

Electrolytes, Interfaces and Interphases

Fundamentals and Applications in Batteries

Electrolytes, Interfaces and Interphases

Fundamentals and Applications in Batteries

By

Kang Xu

Email: kang_xu@hotmail.com



Print ISBN: 978-1-83916-310-4
EPUB ISBN: 978-1-83916-617-4

A catalogue record for this book is available from the British Library

© Kang Xu 2023

All rights reserved

Apart from fair dealing for the purposes of research for non-commercial purposes or for private study, criticism or review, as permitted under the Copyright, Designs and Patents Act 1988 and the Copyright and Related Rights Regulations 2003, this publication may not be reproduced, stored or transmitted, in any form or by any means, without the prior permission in writing of The Royal Society of Chemistry or the copyright owner, or in the case of reproduction in accordance with the terms of licences issued by the Copyright Licensing Agency in the UK, or in accordance with the terms of the licences issued by the appropriate Reproduction Rights Organization outside the UK. Enquiries concerning reproduction outside the terms stated here should be sent to The Royal Society of Chemistry at the address printed on this page.

Whilst this material has been produced with all due care, The Royal Society of Chemistry cannot be held responsible or liable for its accuracy and completeness, nor for any consequences arising from any errors or the use of the information contained in this publication. The publication of advertisements does not constitute any endorsement by The Royal Society of Chemistry or Authors of any products advertised. The views and opinions advanced by contributors do not necessarily reflect those of The Royal Society of Chemistry which shall not be liable for any resulting loss or damage arising as a result of reliance upon this material.

The Royal Society of Chemistry is a charity, registered in England and Wales, Number 207890, and a company incorporated in England by Royal Charter (Registered No. RC000524), registered office: Burlington House, Piccadilly, London W1J 0BA, UK, Telephone: +44 (0) 20 7437 8656.

Visit our website at www.rsc.org/books

Printed in the United Kingdom by CPI Group (UK) Ltd, Croydon, CR0 4YY, UK

Dedication

To my grandmother (1918–2003), who was not a scientist but opened my eyes to science.

To my mentor Austen Angell (1933–2021), who taught me how to do science.

Foreword by Khalil Amine

The invention and successful commercialization of lithium-ion batteries revolutionized our lives in the 21st century. Now more than ever, we rely on electrical energy efficiently packed in these tiny electrochemical devices to drive our cars, to stay connected with our co-workers, friends and families, and to calculate, process and store astronomical amounts of information. In these tiny devices, the electrons and ions flow in various directions *via* different predesigned pathways to capture or release the energy, and to do so reversibly thousands of times. Such processes rely on various components that are well synchronized to work with each other.

However, the invention of lithium-ion batteries was blessed by certain fortuitous factors. When the engineers at Asahi Kasei and Sony put the individual components (anode, cathode and electrolyte) together and assembled the first prototype lithium-ion battery, the scientific principles governing these processes were not completely understood. Thanks to the intensive research efforts during the past three decades, gradually we started to understand how the energy is stored and released in the lattices of the anode and cathode, how the ions and electrons transport in the bulk electrolytes and across interfaces and how the irreversible chemistries initiate, grow, terminate and eventually ensure the reversibility of reactions occurring far away from thermodynamical equilibria. However, many questions still remain unanswered.

Electrolytes, their interfaces with both electrodes and their interactions with these electrodes play the key roles in determining the

reversibility of these reactions. Understanding the composite and convoluted phenomena and behaviors of ion solvation, ion transport, charge transfer and sacrificial electrolyte–electrode reactions at the molecular level will allow us to design the next generation of electrochemical energy storage devices with higher power and energy than lithium-ion batteries. Despite such importance, however, there has not been a book that systematically summarizes the knowledge of electrolytes and interfaces. While the books by Bockris, Bard and Faulkner and also Newman all provided solid foundations of basic electrochemistry, ionics and electrodics, there was a gap between these and the practical electrolytes, interfaces and interphases that we are seeing in advanced battery systems.

This book by Kang Xu serves as a link between these fundamental books and the practical electrolyte systems that we deal with in today's battery research. It systematically summarizes all related knowledge of electrolyte materials, ion solvation and transport, charge transfer, interfacial science and interphasial chemistry, from classical understanding to state-of-the-art studies. It is an excellent textbook for those just entering the field of battery chemistry and materials research, and an excellent desktop reference for researchers in the field.

Khalil Amine

Argonne National Laboratory, USA

Foreword by Jeff Dahn

I have been working on lithium and lithium-ion batteries for 44 years, beginning in 1978. I was trained as a materials physicist and up until about 2008 I concentrated most of my work on new positive and negative electrode materials. Only in 2008 did graduate student Aaron Smith (now at Apple) and I realize that the most important remaining frontier in lithium-ion battery research was improving lifetimes to the multi-decade scale to enable electrical energy storage (EES) and second use of EV batteries. At this point, much of the work in our laboratory started to focus on the electrolyte of lithium-ion batteries. This is because the degradation in lithium-ion cells comes about due to unwanted parasitic reactions between the charged electrode materials and the electrolyte. These are the same reactions that also provide the beneficial solid/electrolyte interphase (SEI) layers on the electrode surfaces.

In 2008, I knew virtually nothing about electrolytes and began reading papers from the US Army Research Laboratory (ARL). Kang Xu, Richard Jow, Michael Ding, Oleg Borodin, S. S. Zhang and others at ARL had done an incredible amount of world-class research on all aspects of electrolytes, including electrolyte additives, for lithium-ion cells and had elevated their laboratory to probably the world-leading center for electrolyte research. I began reading their papers. Kang Xu's review article published in 2004 became a "Bible" for our group. In 2014, Kang Xu wrote his second review article on electrolytes for lithium-ion cells which, again, became required reading for students working on long-lifetime lithium-ion cells in our group.

This book which Kang Xu has produced is a complete treatise on electrolytes with a focus on lithium-ion batteries. I read many sections of the book in its prepublication stage and the content is exceptional. Readers of all backgrounds working on lithium-ion batteries will especially appreciate Parts B and C of this book, which focus on practical aspects of electrolytes. For a practical guy like me, Chapters 11, 12, 15 and 16 especially are standouts. Graduate students and researchers working in this space will appreciate the entire book!

Even though this book explains many aspects of electrolytes and electrolyte/electrode interfaces for lithium-ion cells, many mysteries remain. For me, most important is a truly detailed understanding of what makes the best SEI on the negative electrode and the best cathode/electrolyte interphase on the positive electrode. Detailed studies, using surface-sensitive techniques, have identified elements, functional groups, molecules and compounds that are incorporated into good SEI layers and how these can be affected by the presence of one or sometimes two electrolyte additives. However, a true understanding of *why* these particular species yield good interphases is lacking.

As the world moves towards the “electrification of everything”, multi-decade long lifetime and sustainability (not energy density) of lithium-ion, sodium-ion and other batteries will become of paramount importance to reduce the need for recycling and replacement. Understanding all the minute details of the electrolyte/electrode interphase will be essential to create batteries that can last a century.

This book is the best place for researchers embarking on that journey to start.

Jeff Dahn

Dalhousie University, Halifax, Nova Scotia, Canada

Foreword by M. Stanley Whittingham

It is now about 50 years since the concept of intercalation reactions for storing energy in electrochemical cells was discovered in the Corporate Research Laboratory of Esso (now ExxonMobil). Now they dominate portable energy storage and, having enabled the communications revolution, are ready to enable the electrification of transportation and intermittent renewable electric generation, such as solar and wind. The original lithium batteries used lithium-metal anodes and ether-based electrolytes, because lithium plating is much more efficient with the latter. With the advent of the higher voltage layered oxides and graphitic anodes, the electrolytes switched to organic carbonates, which are more stable at the higher potentials of the oxides. These are still the predominant electrolytes used today. However, they are not thermodynamically stable relative to the anode and often also to the cathode, so protective films must be generated. These so-called solid/electrolyte interphase (SEI) films present challenges to the operation of the cells with additional costs during the formation process at the manufacturing plant. Today's commercial cells achieve less than 25% of their theoretical energy density, but to achieve higher levels will demand pushing all the materials to their limits. This in turn demands that we understand and then eliminate all side reactions. Many of these undesired side reactions are related to the reactivity of the electrolyte, so we must better understand the electrolyte.

This book by Kang Xu addresses this critical need, which has been neglected in most research over the last several decades addressing

Electrolytes, Interfaces and Interphases: Fundamentals and Applications in Batteries

By Kang Xu

© Kang Xu 2023

Published by the Royal Society of Chemistry, www.rsc.org

mostly the cathode. The author has previously published two critically acclaimed reviews in *Chemical Reviews*, and this book now presents the more fundamental underpinning needed for significant advances to be made. It does not restrict itself to the electrolyte alone but also covers the critical interactions with the electrodes, namely the interfaces and interphases. It concludes with a discussion of the other cell components.

It is my expectation that this book will enable researchers to discover new more stable and less costly electrolytes that will allow batteries with energy densities exceeding 500 W h kg^{-1} and 1000 W h L^{-1} . I wish you good reading and great research. Let us move to the next level and create a greener environment for our children and their children.

M. Stanley Whittingham

2019 Nobel Laureate in Chemistry Binghamton, NY, USA

Foreword by Martin Winter

Today we are witnessing gigantic expectations on the impact of electrochemical energy conversion and storage on the future benefit of society, which is well reflected by the prominent role that mainly batteries, but also fuel cells and supercapacitors, play in megatrends such as clean mobility (including robotics) and storage of renewable energies. Negative and positive electrodes together with the electrolyte are the major ingredients of any electrochemical system. From the very early findings of Galvani, Volta and Ritter until today, the electrolyte has always been *the* enabler of novel electrochemical technologies.

There are not many good things to say about Covid, but the unavoidable lockdown period during the pandemic gave Kang Xu the time to realize one of his many dreams. With this book, Kang has most successfully shaped a comprehensive up-to-date treatise targeting at marrying the enormous knowledge of the electrochemical basics of electrolytes with modern electrochemical technology and applications.

In this easy-to-read textbook, batteries, the major playground of the author for many decades, play a major role among the various electrochemical technologies that rely on the capabilities of the electrolyte used. The key role of the electrolyte in batteries is very often reflected in the name of the particular technology. A lead–acid battery contains a sulfuric acid electrolyte and alkaline aqueous and non-aqueous battery chemistries use electrolytes of the same type.

We can even go so far as to say that without looking for and eventually finding proper electrolytes, commercial applications as well as R&D of contemporary and future battery technologies such as lithium-ion

batteries, lithium-metal batteries and solid-state batteries would not be possible. Because this is very often not well recognized either in academia or in industry, electrolytes may be considered as *the “hidden champion” material class of advanced and future batteries*.

The electrolyte is without doubt a true system component of any battery type. Hence understanding electrolytes is key for developing better batteries. This understanding includes bulk electrolyte properties, such as viscosity, ion solvation, ion–ion interactions and, of course, ion transport, which among other good reads are discussed in the first chapters of the book.

As the electrolyte is an inevitable and essential part of both electrode/electrolyte interfaces, it is concomitantly married to the 3D interphases [the solid/electrolyte interphase (SEI) and cathode/electrolyte interphase (CEI) are interphases, not interfaces] that originate from the high reactivity of the electrodes and the intrinsic instability of electrolyte components. In almost all cases, electrolyte formulations and their *ad hoc* interfacial/interphasial chemistries dictate and govern the fate of each battery chemistry and its performance, which is discussed in later chapters of the book.

Electrolytes are a complex and also complicated topic. Not everybody in the battery community is able to make distinguished contributions to the progress of this subject and even fewer of us are as competent to write a book on this topic as Kang Xu.

I have had the honor to know Kang Xu for many years and have spent a considerable amount of time with him on scientific and less scientific occasions. While Kang may not be able to distinguish any difference between Cabernet Sauvignon, Merlot and Shiraz, he is *the one* who knows everything about the enormously broad and multifaceted field of liquid electrolytes – he is a walking encyclopedia! We are privileged that he now shares his incomparable knowledge with us through this wonderful book.

Martin Winter

Münster Electrochemical Energy Technology, University
of Münster, Münster, Germany

Preface

The thought of writing a book on electrolytes has been lingering in my mind since 2015. While the idea of such a book project has always appeared tantalizing, the reality of my day job prevented me from starting. The folder I created for this project remained on my desktop untouched for 5 years. This was also the 5 year period when research on electrochemical energy storage (*aka* batteries) witnessed exponential growth around the world. Although I never started writing, I also never stopped planning its chapters and contents.

Then, in the spring of 2020, the whole world ground to a sudden halt due to the Covid 19 pandemic. Like most people, I was forced to telework, to attend and speak at tiresome online meetings and seminars, while having only occasional privileges to visit the laboratory and office physically. After a few weeks, I decided that it was the time to start this book.

The time could not have been more perfect. As scientists from around the world were forced away from their benches, experimental advances in electrochemical energy storage materials and chemistry research were bound to slow down compared with the previous hectic decade. This relative tranquility gifted us a precious opportunity to look back and think.

Meanwhile, there has not been a book of this kind available that links fundamental knowledge in ionics and electrodics to the basic applications of electrolytes in energy storage devices.

On the one hand, research papers, reviews, perspectives and monographs are being published in such record numbers that the individual researcher often finds it impossible to follow them all, but all of these

publications are almost exclusively intended for veteran researchers in the field, providing little or no introductory ramp for readers new to the field, such as students and postdocs.

On the other hand, in basic electrochemistry, there are many excellent books that teach fundamental knowledge, among which are the three “Bibles”: (1) *Modern Electrochemistry* by Bockris and Reddy, (2) *Electrochemical Methods: Fundamentals and Applications* by Bard and Faulkner, and (3) *Electrochemical Systems* by Newman and co-authors, which have been published in several editions. These three exceptional treatises laid out the rigorous mathematical and thermodynamic foundations of the basic principles in electrochemistry, ionics and modern electrodics. However, in the fast-evolving fields of energy storage science and technology, especially lithium-ion batteries and the emerging battery chemistries and materials, one often has difficulty in establishing direct lineage and relevance from the fundamental knowledge taught in these books.

One example is *Modern Electrochemistry*. In its most recent edition, published in 2000, the authors predicted the hydrogen fuel cell to be the prevalent power source for future vehicles, with only fleeting mention of batteries, and the lithium-ion battery, although already commercialized and in extensive use for nearly a decade by then, was not even mentioned in the book. Needless to say, the interphases and the associated chemistries and kinetics in those advanced batteries went beyond what the classical ionics and electrodics can describe.

The world has changed significantly in this new millennium, and the lithium-ion battery has played an indisputable role in this. The recognition of Professors Stanley M. Whittingham, John B. Goodenough and Dr Akira Yoshino by the award of the Nobel Prize in Chemistry in 2019 marked the apex of this great invention, and research on new energy storage chemistries and mechanisms is becoming ever more important in the new era after the pandemic of 2020–2022.

This book aims to fill the gap mentioned above. It intends to be a friendly yet authoritative “textbook” that will help beginners to overcome the learning curve, and bring them to an eventually sophisticated stage by the end of it. These “beginners” could be students or postdocs who want to enter the fields of electrochemical energy storage, electrochemistry, and materials science and engineering, or any researchers new to these subjects.

The book assumes that readers have a chemistry or materials background, already armed with a knowledge of basic thermodynamics and chemistry. It starts with fundamental knowledge before moving on to applications. Emphasis is placed on established knowledge, but

new findings important to the field are also discussed. Special efforts are made to link the fundamentals to the actual problems encountered with real-life devices. Given the success of lithium-ion batteries in shaping our mobile life, and the research on diverse battery materials and chemistries being pursued as an essential part of our energy future, an unsymmetrical emphasis will inevitably be placed on the electrolytes and interphases in batteries.

Some mathematics is presented order to show the beauty of the fundamental knowledge of electrolytes in bulk and at interfaces, but one could completely skip the derivations and jump directly to the conclusions without losing comprehension of the overall storyline.

This book is not intended to be a comprehensive review of past work or a monograph covering recent advances, hence for well-established facts I do not see the necessity of providing all the available literature references. Instead, only selected classic and seminal works that constitute the foundational knowledge are cited.

All illustrations in the book, with the exception of Figures 12.6, 12.7 and 14.11, were created by me. In 1977, when China was still struggling to exit the suffocating shadow of the Cultural Revolution, my grandmother bought me a special book that suddenly opened my horizons: the Chinese translation of *One Two Three ... Infinity: Facts and Speculations of Science* by Professor George Gamow. In that masterpiece, all the cartoons were drawn by the author. Looking back, the impact of these artistic, humorous, yet inspiring drawings on a boy who was first touched by modern science can never be overestimated. I possess talents neither in science nor arts that can be comparable to those of Professor Gamow, but I hope that, with my humble efforts with the illustrations in this book, I pay homage to him for his influence on me.

Kang Xu

Acknowledgements

I want to thank Prof. Huang Zhigui (Southwest University) for his mentoring and support, especially during my most difficult days in college some 40 years ago. Happy 90th birthday, Prof. Huang!

It is my greatest honor to have had the support of the 2019 Nobel Laureate, Prof. M. Stanley Whittingham. I have received tremendous inspiration and great help from him during my entire scientific career; he not only invited me to compile two wide-ranging review articles on electrolytes for special issues of *Chemical Reviews* in 2004 and 2014, but also graciously agreed to write a Foreword for this book.

Also joining him to write Forewords for this book are three of my longstanding friends, Prof. Khalil Amine (Argonne National Laboratory, USA), Prof. Jeff Dahn (Dalhousie University, Canada) and Prof. Martin Winter (Münster Universität/MEET, Germany), who are established authorities in battery and materials research.

I owe much to the late Prof. John O'M. Bockris, whose colloquial style in teaching a sophisticated mathematical topic had a significant influence on me. Between 1995 and 1997, when he was working on the second edition of the monumental textbook *Modern Electrochemistry*, I was lucky enough to assist him as a contributor of exercise problems for that book. This unique experience benefited me considerably as a student, a researcher and a scientific writer.

Significant influences also came from my PhD advisor, the late Prof. Austen Angell, who not only shaped my career but also continued to help me long after I graduated from his group. He showed me what a scientist should be like.

Despite the invitation from the editors in mid-2015, I had been procrastinating until my friend Prof. Lidan Xing (South China Normal University) encouraged me to start this ambitious project in the spring of 2020. My colleague and friend Dr Janet Ho (US Army Research Laboratory) provided much inspiration and material support during the writing. She is also credited for taking the photograph of me while finishing this book.

Professors Ping Liu (University of California San Diego), Shirley Meng (University of California San Diego), Chunsheng Wang (University of Maryland College Park) and Lidan Xing (South China Normal University) provided valuable suggestions from a teaching perspective.

Dr Lin Ma (ARL/University of Maryland) helped me to access many literature sources, Dr Jenel Vatamanu (US Army Research Laboratory) provided assistance in simulating how charges distribute on an inert electrode surface and Dr Oleg Borodin (US Army Research Laboratory) engaged in fruitful discussions about many fundamental topics related to ion solvation, ion transport and ion assembly on interfaces, and helped me to understand how computer simulation works. My son Michael helped with some of the mathematics and illustrations.

Professors Nitash Balsara (Lawrence Berkeley National Laboratory) and Paul Albertus (University of Maryland) provided invaluable help with the understanding of the Newman formalism of ion transport and discussions on Newman's concentrated solution theory. The comments and views on the limitations of Newman's theory, however, only reflect my personal perspective.

Many respected colleagues assisted me with either scientific literature, images or discussions on specific topics during my writing. They are Prof. Martin Bazant (Massachusetts Institute of Technology), Dr Ratnakumar Bugga (Jet Propulsion Laboratory, NASA), Prof. Jeff Dahn (Dalhousie University), Dr Lei Cheng (Argonne National Laboratory), Dr Michael S. Ding (US Army Research Laboratory), Dr Tao Gao (University of Utah), Dr Rongzhong Jiang (US Army Research Laboratory), Prof. Bernhard Roling (Philipps-Universität Marburg), Prof. Monika Schönhoff (Universität Münster), Dr Marshall Smart (Jet Propulsion Laboratory), Prof. Yicheng Song (Shanghai University), Dr Karen Thomas-Alyea (Verdox Inc.), Prof. Chunsheng Wang (University of Maryland College Park), Prof. Masayoshi Watanabe (Yokohama National University), Prof. Martin Winter (Westfälische Wilhelms-Universität Münster/MEET), Dr Wu Xu (Pacific Northwest National Laboratory), Dr Zhou Yu (Argonne National Laboratory), Dr Jason Zhang (Pacific Northwest National Laboratory) and Prof. Shengshui Zhang (US Army Research Laboratory).

I am grateful to the Joint Center of Energy Storage Research (JCESR), an energy hub funded by the Department of Energy Office of Science and led by Dr George Crabtree and Dr Venkat Srinivasan of Argonne National Laboratory. The JCESR not only supported the research activities in my group on multivalent cation electrolytes, but more importantly granted me the opportunity to work alongside so many brilliant scientists from whom I have learned so much.

Although this book was written outside my official working hours, I want to thank the US Army and DEVCOM Army Research Laboratory for continually supporting my scientific exploration. My first-line supervisors Dr Cynthia Lundgren and then Dr Kyle Grew did their best to create the optimal environment to cultivate the culture of encouraging scientific exploration.

I want to thank the RSC editorial staff Ms Katie Morrey for her assistance in planning and contracting, and her patience with me during 2 years, and Ms Amina Headley for her proofreading. Their enormous efforts made this book possible. Thanks also to the RSC Production team, Dr Helen Potter, Mr Connor Sheppard and Dr Caroline Knapp for their efforts during the production process.

Finally, I want to thank my wife, whose understanding and tolerance for my long hours in the office and in my study allowed me to take on and finish this ambitious project.

Kang Xu
Potomac, Maryland, USA

Author Biography

Kang Xu graduated with a BSc in Chemistry (Southwest University, China), MSc in Polymer Chemistry (Lanzhou Institute of Chemical Physics, Academy of Sciences, China) and PhD in Chemistry (Arizona State University, USA). He is currently a Fellow of the Electrochemical Society, a Laboratory Fellow of the US Army Research Laboratory, Team Leader of Aqueous Electrochemistry at the US Army Research Laboratory and an Adjunct Professor at University of Maryland College Park.

He has been carrying out research on electrolyte materials and interphasial chemistry for over 30 years. His representative research studies include the design and synthesis of new electrolyte materials (solvents, lithium salts, additives, non-flammable electrolytes) and understanding fundamental interfacial and interphasial processes and chemistries. His reports on super-concentrated aqueous electrolytes, battery chemistries and related studies on interphases (*Science*, 2015, 2021 and 2022, and *Nature*, 2019) were considered trailblazing.



Taken on 6th August 2022, during the writing of this book.

Photo credit: Janet S. Ho.

Among his 300+ publications, 25 patents and five books and book chapters, he is best known by young scientists new to the fields of batteries and materials for his two comprehensive review articles published in *Chemical Reviews* in 2004 and 2014, respectively, which have been regarded as desktop references by researchers around the world. His historical accounts on the development of lithium-ion batteries and materials (*Chemical Reviews* in 2018 and *Nature Energy* in 2021) were believed to be the most impartial and accurate recordings of the events. Since 2020 he has been considered one of the 0.1% “highly cited authors” around the world by Clarivate®, and one of the top 0.05% most influential scientists as evaluated by *The Standardized Citation Metrics Author Database Annotated for Scientific Field* published by Stanford University.

Among his multiple recognitions and awards, he was the recipient of the 2015 Invention of the Year Award of the University of Maryland, the 2017 International Battery Association Technology Award, the 2017 Scientist-of-the-Quarter by the US Department of Defense and the 2018 Electrochemical Society Battery Division Research Award.

List of Acronyms

Ac	Acetate
AC	Alternating current
AGG	Aggregates
AN	Acceptance number
AN	Acetonitrile
CE	Counter electrode(s)
CE%	Coulombic efficiency
CEI	Cathode/electrolyte interphase
CIP	Contact ion pair
DC	Direct current
DEE	1,2-Diethoxyethane
DEC	Diethyl carbonate
DEDOHC	Diethyl-2,5-dioxahexane carboxylate
DMC	Dimethyl carbonate
DMDOHC	Dimethyl-2,5-dioxahexane carboxylate
DME	1,2-Dimethoxyethane
DN	Donor number
DOL	1,3-Dioxolane
EA	Ethyl acetate
EC	Ethylene carbonate
ecm	Electrocapillary maximum
EIS	Electrochemical impedance spectroscopy
EMC	Ethyl methyl carbonate
emf	Electromotive force (<i>E</i>)
eNMR	Electrophoretic nuclear magnetic resonance
EP	Ethyl propionate
ES	Ethylene sulfite
ESI-MS	Electrospray ionization mass spectrometry

GC	Glassy carbon electrode
GIC	Graphite intercalation compound
GR	Graphite electrode
HER	Hydrogen evolution reaction (from reductive decomposition of water)
HOMO	Highest occupied molecular orbital
IHP	Inner-Helmholtz plane (layer): assembly of naked ions on an electrode surface
LEDC	Lithium ethylene dicarbonate
LEMC	Lithium ethylene monocarbonate
LGPS	$\text{Li}_{10}\text{GeP}_2\text{S}_{12}$, a solid electrolyte
LiAsF₆	Lithium hexafluoroarsenate
LiBF₄	Lithium tetrafluoroborate
LiBOB	Lithium bis(oxalato)borate
LiClO₄	Lithium perchlorate
LiCoO₂	Lithium cobalt oxide (<i>aka</i> LCO)
LiDFOB	Lithium difluoro(oxalato)borate
LiFePO₄	Lithium iron phosphate (<i>aka</i> LFP)
LiFSI	Lithium bis(fluorosulfonyl)imide
LiMn₂O₄	Lithium maganese oxide (<i>aka</i> LMO)
LiNi_xCo_yAl_zO₂	lithium nickel cobalt aluminum oxide (<i>aka</i> NCA)
LiNi_xMn_yCo_zO₂	Lithium nickel manganese cobalt oxide (<i>aka</i> NMC)
LiPF₆	Lithium hexafluorophosphate
LiPON	Lithium phosphorus oxynitride, a glassy solid electrolyte
LiTFSI	Lithium bis(trifluoromethanesulfonyl)imide
LPS	Lithium thiophosphate ($\text{Li}_7\text{P}_3\text{S}_{11}$), a solid electrolyte
LTO	Lithium titanate
LUMO	Lowest unoccupied molecular orbital
m	Molal (moles of solute in 1 kg of solvent)
M	Molar (moles of solute in 1 L of solution)
MB	Methyl butyrate
MC	Monte Carlo (a classical computer simulation)
MD	Molecular dynamics
MP	Methyl propionate
N_A	Avogadro's number
NMR	Nuclear magnetic resonance
OER	Oxygen evolution reaction (from oxidative decomposition of water)
OHP	Outer-Helmholtz plane (layer): assembly of solvated ions on an electrode surface
ORR	Oxygen reduction reaction (the reversal of OER)
PC	Propylene carbonate
pfg-NMR	Pulsed field gradient nuclear magnetic resonance
PMS	Propargyl methyl sulfonate
pzc	Point of zero charge

rds	Rate-determining step
QM	Quantum mechanics
RE	Reference electrode(s)
RHE	Reversible hydrogen electrode(s)
SC	Succinimide
SEI	Solid/electrolyte interphase (usually dedicated to the one on the anode surface)
SHE	Standard hydrogen electrode (an RHE at standard conditions)
SSIP	Solvent-separated ion pairs
SSE	Solid-state electrolyte(s)
Sulfolane	Tetramethylene sulfone
THF	Tetrahydrofuran
VC	Vinyl carbonate
WE	Working electrode(s)
WiSE	Water-in-salt electrolyte(s)
γBL	Gamma-butyrolactone

Timeline of Important Events in Electrochemistry

- 1600: Gilbert coined “electric” from Greek word “*ἤλεκτρο*” (amber).
- 1791: Galvani discovered the convulsion of a frog’s leg stimulated by an electric current.
- 1799: Volta invented the first battery (Voltaic Pile) by piling alternate Ag/Zn plates separated with pasteboard pre-soaked with saline water.
- 1807: Davy isolated Na and K by electrolyzing their hydroxides using a voltaic pile.
- 1821: Brande isolated Li by electrolyzing lithia (Li_2O) using a voltaic pile.
- 1833: Faraday named “electrolytes”, “cathode”, “anode”, “ions”, etc., and established “Faraday’s law” quantifying electricity and mass.
- 1939: Grove reversed the water splitting reaction, invented the H_2 fuel cell.
- 1874: Kohlrausch established “Kohlrausch’s law of independent ionic migration”.
- 1887: Arrhenius proposed the ionization and partial ionization concept.
- 1893: Nernst established “Nernst’s law”.
- 1900: Kohlrausch established the empirical law for the non-linear relation between molar conductivity and salt concentration.

- 1905: Tafel discovered the empirical law for the exponential relation between applied overpotential and responsive current for hydrogen generation.
- 1905: Einstein established a series of relations for ionic transport.
- 1921: Lewis and Randall discovered ionic strength and empirical law.
- 1923: Debye and Hückel established the Debye–Hückel Model by applying the concept of “ionic atmosphere”, discovered the Debye–Hückel limiting law that explains the Lewis–Randall empirical law.
- 1924: Butler and Volmer independently established the rate equation for charge-transfer at electrolyte/electrode interfaces, the variation of which explains the Tafel empirical law and Nernst equation.
- 1927: Onsager, refinement of the Debye–Hückel model, explains the Kohlrausch non-linear law.
- 1933: Bernal and Fowler proposed the solvation sheath model consisting of primary and secondary sheaths.
- 1938: Pourbaix developed a series of phase diagrams for aqueous solutions.
- 1940s: Frumkin published his seminal work on electrodics.
- 1948: Hasted *et al.* correlated dielectric constant and solvation number.
- 1950s: Bockris and Conway built foundations for physical electrochemistry.
- 1957: Frank and Wen proposed the solvation two-layer model.
- 1961: Davis refined the Debye–Hückel model.
- 1970: Bockris and Reddy refined the interfacial model by treating the electrode surface as a giant 2D ion.
- 1976: Whittingham invented TiS₂ intercalation chemistry.
- 1979: Peled proposed the concept of the solid/electrolyte interphase (SEI) to describe the kinetic stability of lithium and other alkali metals in non-aqueous electrolytes.
- 1980: Goodenough invented LiCoO₂ intercalation chemistry.
- 1980: Armand proposed the concept of the “dual-intercalation battery”.
- 1983: Asahi Kasei scientists Yoshino, Kubribayashi and Nakajima started the assembly of a “lithium metal-free” battery in laboratory cells.
- 1986: The first prototype lithium-ion battery was assembled by Asahi Kasei scientists at Battery Engineering, Boston, MA.

- 1990: Sony commercialized the first-generation “lithium-ion battery”.
- 1990: Dahn and colleagues transplanted the concept of SEI from lithium metal to graphite surface.
- 1990: Fujimoto and colleagues achieved the first electrochemical synthesis of lithiated graphite (LiC_6) in EC-based electrolytes.
- 2019: Nobel Prize for Chemistry awarded to Whittingham, Goodenough and Yoshino for their invention of the lithium-ion battery.

Contents

PART A. FUNDAMENTALS: ELECTROLYTES IN GENERAL	1
1 What Is an Electrolyte?	3
References	5
2 Modern Electrolytes	6
2.1 Types of Electrolytes	6
References	10
3 In Bulk Electrolytes: Ionics	11
3.1 Solvent Molecules: Dipole and Dielectric Medium	12
3.2 Dielectric Constant: Capability of a Solvent to Resist an External Electric Field	13
3.3 Dissolution of Solutes in Solvents: Solvation Sheath	17
3.4 Revisiting the Dielectric Constant: How Ions Affect It, and Its Unexpected Application	20
3.5 Activity Coefficients, Ionic Strength and a Few Empirical Laws	23

3.5.1 Activity Coefficients	23
3.5.2 Kohlrausch's Law on Non-linearity and Independent Movements of Ions	25
3.5.3 Ionic Strength and Lewis–Randall Empirical Law	26
References	28
<hr/>	
4 Quantification of Ion–Ion Interaction: Debye–Hückel Theory	29
4.1 The Ionic Cloud	29
4.2 The Poisson Equation for the Spatial Distribution of an Ionic Cloud	31
4.3 The Boltzmann Equation for the Spatial Distribution of an Ionic Cloud	33
4.4 Linearization of the Boltzmann Equation	35
4.5 Combining the Poisson and Boltzmann Equations	36
4.6 Verifications of the Debye–Hückel Model	40
4.6.1 The Total Excess Charge in an Ionic Cloud	40
4.6.2 The Lewis–Randall Empirical Law	41
4.6.3 The Kohlrausch Empirical Law	45
4.7 Revisiting Constant K : Debye–Hückel Thickness	46
4.8 Refinement of the Debye–Hückel Model: Finite-sized Central Ion	50
4.9 Refinement of the Debye–Hückel Model: Ion-pair Formation and Bjerrum Length	53
4.10 A Quick Comparison Between Debye–Hückel Thickness and Bjerrum Length	56
4.11 Refinement of the Debye–Hückel Model: Ion–Solvent Interaction	57
4.12 The Successes and Limitations of the Debye–Hückel Model	61
4.13 Liquid Structures: From Dilute to Concentrated and to Super-concentrated Regimes	62
References	64
<hr/>	
5 Ion Transport in Electrolytes	65
5.1 Ion Transport in the Absence of an External Field: Diffusion	65
5.1.1 Fick's First Law: Steady-state Diffusion and Random Walk of Ions	66

5.1.2 Einstein–Smoluchowski Equation	70
5.1.3 Fick's Second Law: Non-steady-state Diffusion	72
5.1.4 Solving Fick's Second Law for a Few Practical Scenarios	78
5.2 Ion Transport Driven by an External Field: Migration (Conduction)	82
5.2.1 A Few Transport Quantities and Their Relations	83
5.2.2 Nernst–Einstein Relation	98
5.2.3 Stokes–Einstein Relation	99
5.2.4 Walden's Rule	101
5.2.5 Nernst–Planck Flux Equation	102
5.2.6 Ion Transport with Ion–Ion Interaction: Onsager's Laws	105
5.2.7 Ionics in Non-aqueous Electrolytes	116
5.2.8 Abnormal Proton Transport: Grotthuss Mechanism	121
5.2.9 Electrolytes Without Solvents: Ionic Liquids	124
References	129

6 When Electrolyte Meets Electrodes: Interface

131

6.1 Why Does Interface Matter?	131
6.2 Interfaces Are Electrified: The Electric Double Layer	135
6.2.1 The Potential Across an Individual Interface Is Immeasurable	137
6.2.2 Two Extremities of Interfaces: Polarizable and Non-polarizable	139
6.3 Classical Understanding of the Electric Double Layer	141
6.3.1 Gibbs Surface Excess	141
6.3.2 Quantification of Surface Excess: Electrocapillarity	143
6.4 Structure of an Electrified Interface	150
6.4.1 Helmholtz–Perrin Model: A Simple Capacitor	150
6.4.2 Gouy–Chapman Model: Diffuse Ionic Assembly	153
6.4.3 Stern Model: Combination of Simple Capacitor and Diffuse Charge	155
6.4.4 Grahame and Bockris–Devanathan–Müllen (BDM) Models	156
6.4.5 Contemporary Illustrations of Interfacial Structure	162
6.5 When Charge Transfers Across an Interface: Electrodics	163
6.5.1 What Is Charge Transfer?	164

6.5.2 Kinetics of Charge Transfer Across Interfaces	168
6.5.3 Dynamic Equilibrium at an Interface	171
6.5.4 Butler–Volmer Equation	173
6.5.5 Three Scenarios Predicted by the Butler–Volmer Equation	177
6.5.6 Quantifying Polarizable and Non-polarizable Interfaces	180
6.5.7 How Much Does the Butler–Volmer Equation Depend on Interface Structure?	181
6.5.8 What is β ?	182
6.5.9 Butler–Volmer Equation in Electrochemical Devices	186
References	191

7 Linking Ionics With Electrodics 192

7.1 Steady State	194
7.2 Galvanostatic and Potentiostatic	196
7.3 Nernst Diffusion Layer	200
7.4 Limiting Current	202
7.5 Ambipolar Ionic Transport at an Interface	203
7.6 Further Caution When Applying Diffusion-Originated Equations	206
References	208

8 When an Electrode Operates Beyond Electrolyte Stability Limits: Interphase 209

8.1 Interface <i>vs.</i> Interphase	210
8.2 Electrochemical Stability Window	212
8.2.1 Electrochemical Stability Windows of Aqueous and Non-aqueous Electrolytes	214
8.2.2 Expanded Electrochemical Stability Window by an Interphase	216
8.2.3 The Function of Interphases	218
8.3 Correlation Between Electrochemical Stability Window and Interphases	220
References	221

**PART B. APPLICATIONS: ELECTROLYTES
IN DEVICES** **223**

9 Electrochemical Devices **225**

9.1 How Does an Electrochemical Energy Device Work?	228
9.1.1 Fuel Cells	230
9.1.2 Electrochemical Double-layer Capacitors	235
9.1.3 Batteries	245
9.1.4 Pseudo-capacitors	277
9.1.5 Comparison and Transition Between Capacitors and Batteries	279
References	291

**10 Lithium-metal, Lithium-ion and
Other Batteries** **292**

10.1 Why Lithium?	293
10.2 The Quest for the Holy Grail: Lithium-metal Batteries	294
10.2.1 Irreversibility	298
10.2.2 Dangerous Morphology	299
10.3 Circumventing Irreversibility and Safety Hazards	304
10.3.1 The Bypass <i>via</i> Dual Intercalation	305
10.3.2 The Birth of Lithium-ion Chemistries	306
10.4 Emerging Chemistries and Electrolytes	331
10.4.1 Anode	333
10.4.2 Cathode	352
References	370

**PART C. PROPERTIES OF ELECTROLYTES,
INTERFACES AND INTERPHASES** **373**

11 Phase Diagrams of Liquid Electrolytes **379**

11.1 Phase Diagram of a Pseudo-binary Non-aqueous Electrolyte	382
11.2 Experimental Mapping of Pseudo-binary Phase Diagrams	384

11.3 Thermodynamic Calculation of Higher Order Phase Diagrams	388
References	399
12 Ion Solvation	400
12.1 Bernal–Fowler Three-layer Model	400
12.2 The Four Basic Questions	401
12.2.1 Solvating Site	402
12.2.2 Solvation Number	405
12.2.3 Preferential Solvation	408
12.2.4 Ion Solvation in the Concentrated Regime	418
12.3 Solvation Sheaths, Solvation Cages and Solvation Sites	426
12.4 Anion Solvation	429
References	433
13 Static Stability of Electrolytes	435
References	438
14 Ion Transport	439
14.1 Phenomenological Understanding: Ion Conductivity	440
14.1.1 Why AC (Alternating Current) Techniques?	444
14.1.2 Ion Conductivity for Practical Battery Electrolytes	466
14.1.3 Electrolyte Engineering for Battery Applications	472
14.1.4 Ionicity	477
14.2 Mechanistic Understanding: Speciation	489
14.2.1 Ideality of Electrolytes: Revisiting the Einstein Equations	490
14.2.2 The Real Meaning of Ion Transport Number	493
14.2.3 In Practical Electrolytes: Transport Number (T_+ or T_-) versus Transference Number (T_+ or T_-)	501
14.2.4 A Few Classical Approaches to Transference Numbers	504
14.2.5 Reference Frame for Ionic Transference	543
14.3 Ionics for Non-ideal Electrolytes	548
14.3.1 At the Initial Instant	554
14.3.2 At the Steady State	555
14.3.3 What are these Onsager Transport Coefficients?	559

14.3.4 Revisiting Ambipolar Diffusion: Salt Diffusion	563
14.3.5 Multicomponent Electrolytes	565
14.4 Newman's Ion Transport Theory: A Brief Introduction	568
14.4.1 Concentrated Solution Theory	575
14.4.2 Limitations of Newman's Concentrated Solution Theory	588
References	589
15 Interfaces	592
15.1 Defining an Interface	592
15.1.1 Ionic Fluxes in Bulk and Across an Interface	595
15.1.2 Concentration Profiles in the Bulk Region	596
15.1.3 Concentration Profiles in the Interfacial Region	599
References	601
16 Interphases	602
16.1 Defining an Interphase	603
16.2 An Interphase is Created by Electrode–Electrolyte Mismatch in Electron Energy Levels	605
16.3 What Is a Good Interphase?	609
16.4 Charge Transfer in the Presence of 2D Interfaces and 3D Interphases	612
16.5 Two Distinct Manners of Forming Interphases	613
16.5.1 Proto-interphase and Interphase in an “Anode-free” Lithium-metal Cell	617
16.5.2 Rationale Behind Electrolyte Additives	618
16.6 Chemistry of Interphases	620
16.6.1 In Lithium-ion Batteries	621
16.6.2 In Lithium-metal Batteries	644
16.6.3 Interphasial Chemistries Brought by Additives	651
16.6.4 In “Beyond Lithium-ion” Chemistries	657
16.6.5 Stability of Interphasial Ingredients	665
16.6.6 Interphasial Components Under Debate	675
16.6.7 How Working Ions Travel Across Interphases	680
16.6.8 How Interphases Evolve	685
16.7 Mechanism of Formation of Interphases: Solvation–Interphase Correlation	686
16.7.1 Interfacial Structure	687
16.7.2 Interphasial Chemistry	690
References	708

17 New Concepts and Tools **714**

17.1 Super-concentrating: Unusual Properties	715
17.1.1 Ethers Could Be Anodically Stable	717
17.1.2 Esters Could Be Cathodically Stable	720
17.1.3 Exotic Solvents Could Be Electrochemically Stable	721
17.1.4 Water Could Have a Wide Electrochemical Stability Window	722
17.1.5 Locally Concentrated Electrolytes, Aqueous–Non-aqueous Hybrid Electrolytes	727
17.2 Beyond Liquid Phases: Liquefied Gas and Frozen Ice	729
17.3 Solidifying Electrolytes	731
17.3.1 Polymer Electrolytes	732
17.3.2 Liquid–Inorganic Interfacing	735
17.3.3 True Solid Electrolytes and Their Interfaces/Interphases	737
17.4 Nano-confining Electrolytes	744
17.5 Artificial Interphases	746
17.6 Dynamic Interphases	748
17.7 New Characterization Techniques	750
17.8 Computer Simulations	751
17.8.1 Molecular Simulations	752
17.8.2 Prediction of Properties and Performances	757
17.8.3 Computational Design of Materials	758
References	759

18 Outlook **765****Further Reading** **769****Subject Index** **778**

PART A

Fundamentals: Electrolytes in General

In this Part, we systematically summarize the fundamental knowledge about ideal electrolytes that consists of two major components: Ionics and Electrodics. The former studies how ions and solvent molecules interact and move in the bulk electrolyte, and the latter deals with how the electrolyte interacts with an electrode. The electrolytes investigated here are assumed to be ideal, whereas non-ideal behaviors are discussed in Part C.

1 What Is an Electrolyte?

The word *electrolyte* was created by Faraday in his famous treatise of 1834,¹ when he was trying to explain why certain aqueous solutions can conduct electricity when placed between a pair of “electric poles” polarized by a *voltaic pile* (which was the very first battery, invented by Alessandro Volta in 1799). Since such conduction is accompanied in some cases by the generation of new species at the poles, such as oxygen, hydrogen, chlorine or metal deposition, many researchers before him, including Volta and Berzelius, had already inferred that some sort of decomposition occurred, in which the originally neutral solution is split by electric force into oppositely charged species. Faraday therefore coined a new word from ancient Greek etymology ήλεκτρολυτός, where the prefix ήλεκτρο (ēlectro-) indicates “electricity”, while λυτός (*lytos*) implies that it is “able to be taken apart”. In the same seminal article, he also introduced the terms *electrode* (the way for electricity), *cathode* (westward way) and *anode* (eastward way), based on an analog to the magnetism of the Earth that was induced by an imaginary current. Accordingly, the species that move towards the cathode and anode are a *cation* (westward going) and an *anion* (eastward going), respectively. The cation and anion share a generic name of *ion* (Greek “*iōv*”, or “going”). Considering that at the time there was no molecular-level understanding about electrolytes, the electron was not discovered until some 60 years later (in 1897 by Thomson), and the structure of an atom was not proposed until nearly 80 years later (in 1911 by Rutherford), one is amazed at how prophetic the insight of Faraday was, because all of these terms are still in use

today in electrochemistry and materials science after appropriate modifications!

Perhaps the most interesting and prescient statement that Faraday made was about the surface of the electrodes, which he considered as the “*most important place of action*”.¹ This incredible foresight precisely describes the importance of the electrode/electrolyte *interface* in enabling electrochemical reactions. In fact, it is such interfaces that differentiate electrochemistry from conventional chemistry. Such a two-dimensional interface becomes a three-dimensional *interphase* when the potential of the electrode goes beyond the stability limit of an electrolyte, which is usually the case in most of the advanced batteries such as lithium-ion batteries. Electrolytes and interphases are therefore two sides of the same coin.

However, Faraday was at least partially wrong in one aspect: he thought that ions generated from a neutral species were the result of an electrochemical decomposition. This belief is incorrect for most electrolyte solutes (salts, acids and bases).

A more accurate understanding of the chemical nature of liquid electrolytes came from breakthroughs made in studies on thermodynamics. When Pfeffer was investigating the osmotic pressure of aqueous solutions against neat water, he found that aqueous electrolytes (such as a solution of sodium chloride) induce a much higher pressure difference than non-electrolytes (such as an aqueous solution of sucrose).² Inspired by the rationale established by van't Hoff regarding how vapor pressure was generated, he correctly inferred that the pressure, like that in the gas phase, was also caused by the collision of tiny particles.³ In other words, a solution of sodium chloride has many more particles than a solution of sucrose at the same stoichiometric concentration. Given the fact the former conducts electricity and the latter does not, it became obvious that an electrolyte must have dissociated from the electrically neutral crystalline salt into a larger number of particles bearing opposite charges. These are the cations and anions that Faraday had predicted.

Arrhenius inherited such thinking, and conducted the first systematic study on electrolytes and proposed that ions are thus produced,⁴ but his bold hypothesis sounded too heretic at the time and was not warmly received by his doctoral advisers, which almost ruined his career. Fortunately, Ostwald and van't Hoff recognized the genius of Arrhenius's contribution. With their enthusiastic support, this generalized concept of an electrolyte *via* dissociation of neutral species was gradually accepted by the scientific community. In retrospect,

thanks to these pioneers (Ostwald, Pfeffer and Arrhenius), the quantities studied (osmotic pressure and conductivity) happened to be extremely sensitive to the addition of trace amounts of solutes (salt, acid or base), which allowed them to quantify these changes accurately in correlation with the solute concentration in the very dilute regime using 19th century techniques. Thus, the clever interpretations of the relation between a thermodynamic quantity (osmotic pressure) and an electrochemical quantity (conductivity) set the foundation of a new branch of science, the modern *Physical Chemistry*, and further on *Electrochemistry*.

From here on, we depart from the antiquity era of electrolytes, and enter the classical understanding of them.

References

1. M. Faraday, *On Electrochemical Decomposition*, 1834, pp. 11–44.
2. W. Pfeffer, *Osmotische Untersuchungen: Studien zur Zellmechanik*, Verlag Von Wilhelm Engelmann, Leipzig, Germany, 1877.
3. J. van't Hoff, Osmotic pressure and chemical equilibrium, Nobel Lecture, 13 December 1901, <https://www.nobelprize.org/uploads/2018/06/hoff-lecture.pdf>.
4. S. Arrhenius, Development of the theory of electrolytic dissociation, Nobel Lecture, 11 December 1903, <https://www.nobelprize.org/uploads/2018/06/arrhenius-lecture.pdf>.

2 Modern Electrolytes

The modern definition of an electrolyte consists of two parts:¹ it is an ion conductor; and² it is an electronic insulator. Whenever something is referred to as an electrolyte, or is said to possess an “electrolyte nature”, it carries the implications of being an “*ionic conductor but electronic insulator*”.

The fundamental knowledge concerning electrolytes is mainly involved with 1) how these positive and negative ions distribute in the electrolyte; 2) how these ions move; and 3) how these ions and the electrolyte solvent molecules, if there are any, interact with the electrode surfaces. In classical electrochemistry, the first two categories constitute the contents of *Ionics*, whereas the third is the subject of studies of interfaces, or *Electrodics*.

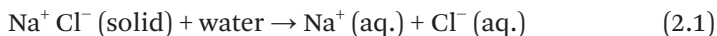
2.1 Types of Electrolytes

The Ancient Greeks believed that gods need only four elements to construct the universe: earth, water, air and fire. While that belief was an excessive oversimplification for the complicated universe that we live in, there are indeed only four ways that one needs to construct a multitude of electrolytes, which often involve water (as the most popular polar solvent molecule), fire (as energy to turn a static ionic lattice into a molten salt or ionic liquid) or earth (as an ion host lattice for ceramic-type electrolytes).

These are the four ways by which an electrically neutral substance can become electrically conducting with the ions as charge carriers.¹ Accordingly, electrolytes can be classified into four types. The first three types are considered closely related because ion transport mechanisms in them are all “liquid like”, although not all of them are liquids macroscopically. The last type stands out alone as the real solid ion conductor, in which the ions become mobile due to a special combination of chemistry and structure.

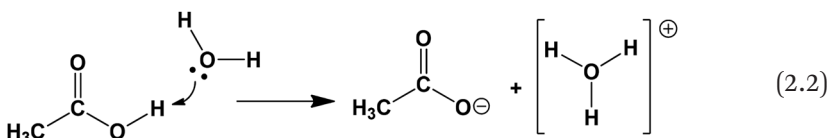
Among the four types of electrolytes, those based on the dissociation of electrolyte solutes by liquid (aqueous or non-aqueous) solvents (Types I and II) constitute the majority of the electrolytes both in our daily life (saline water as an “elixir” in our body) and in industry (the lithium-ion battery being the most prominent representative):

(I) *Ionophores*, or “the bearer of ions”, which already exist in the form of discrete cations and anions in the neutral state. They just need help from solvents to dissociate into free-moving cations and anions. Most salts are ionophores, and sodium chloride (NaCl) represents a typical example. As shown by X-ray diffraction (XRD), the crystalline lattice of NaCl consists of separate sodium cations (Na^+) and chloride anions (Cl^-). A solvent such as water rips the lattice apart and sets Na^+ and Cl^- free:



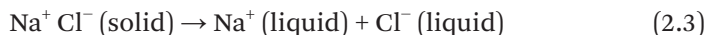
where “aq.” indicates that those ions are helped (solvated) by water molecules (I, Route A in Figure 2.1).

(II) *Ionogens*, or “the producer of ions”, which exist as neutral molecules without any ions, but, in the presence of a solvent, could produce ions by associating with the solvent molecules. Most organic acids belong to this class, and acetic acid (HOAc) represents a typical example. XRD reveals that HOAc, no matter whether in the vapor or crystalline state, remains neutral. However, once dissolved in water, its O–H bond breaks under the action of a water molecule, and loses the proton to the oxygen in water. This process produces a hydronium cation (H_3O^+) and an acetate anion (OAc^-):



Sometimes there is no clear demarcation between ionophores and ionogens, as the bond in certain species could contain both ionic and covalent natures, examples of which include salts based on multivalent cations such as CaBr_2 and AlCl_3 . Therefore, one can view those first two types as a single class of liquid electrolytes that need solvent molecules to assist dissociation. Additionally, when the solvent molecules are macromolecules, the resultant electrolytes (*solid polymer electrolytes*) could be in “solid” form, but the local environments that the ions experience are still “liquid-like” (II, Route A in Figure 2.1).

(III) *Molten salts*, also called *ionic liquids*, which, unlike the first two types, do not need assistance from a solvent. They require heat instead, so that the ordered crystalline lattice of the originally neutral substance collapses and produces separate cations and anions that are free moving. Most ionophores can become molten salt electrolytes if the temperature is high enough. For example, at 801 °C NaCl melts and produces Na^+ and Cl^- (III, Route B in Figure 2.1):



Certain salts containing organic cations (such as imidazolium) melt at rather low temperatures, therefore these salts are in a molten state even under ambient temperature, and are hence named “*room-temperature ionic liquids*” or simply “*ionic liquids*”. Note that since molten salts or ionic liquids consist of neat cations and anions only, without any solvent, they constitute a unique class of electrolytes that distinctly differ from either ionophore or ionogen electrolytes. Hence classical electrolyte theory and models established for aqueous or non-aqueous electrolytes no longer apply to them, and for this reason they have attracted intense interest in recent decades.

It should be noted that, in recent years, the discovery of new salts has enabled researchers to expand the library of electrolytes by making wider combinations of solutes and solvents in concentration ranges that would have been impossible previously. Such findings have significantly obscured the boundaries between Types I, II and III. In these so-called “*super-concentrated electrolytes*”, the high salt concentration in fact has created a middle ground between the classical ionophoric or ionogenic solutions and the ionic liquids. The presence of solvent in those electrolytes is neither as abundant as the former, so that it can be treated as a dielectric continuum to an approximation, nor as negligible as the latter, so it can be

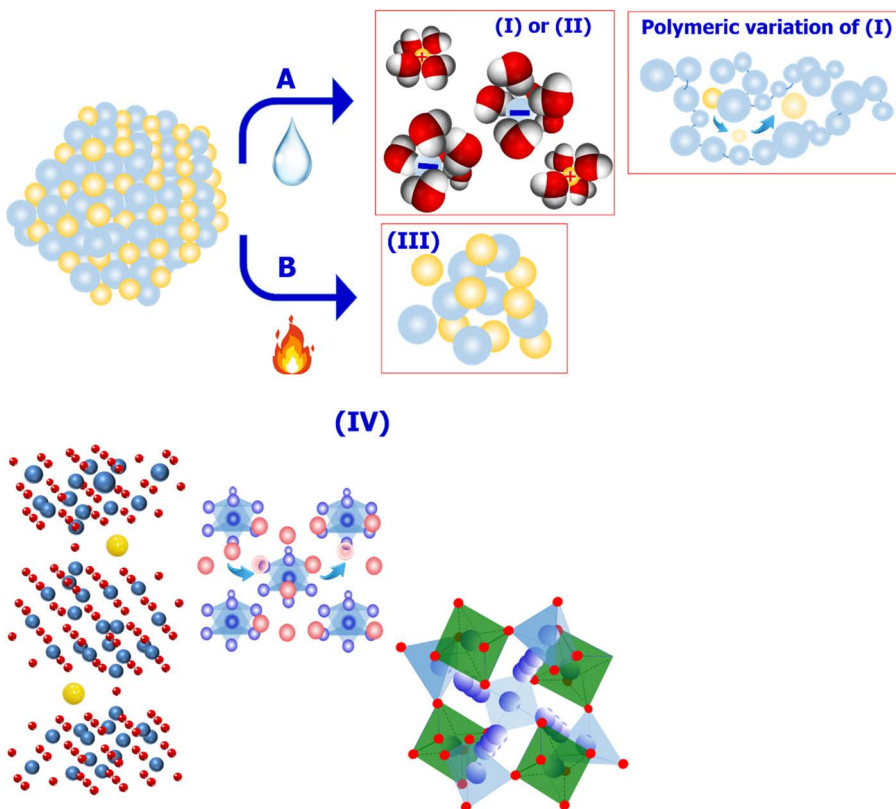


Figure 2.1 Four types of electrolytes created by liberating ions for free movement. (I and II) Dissociation of ions from the lattices of ionophores or ionogens assisted by solvent molecules, leading to *liquid electrolytes*, which are the most common type; a *solid polymer electrolyte* is actually a special variation of this class with the solvent molecules being macromolecular. (III) Destruction of ionophore lattice structure by heat, leading to *molten salt electrolytes (ionic liquid)*. (IV) *Inorganic solid electrolytes* where the ions are mobile because of the decoupled cation-anion interaction in the open structures created by the polyhedral skeletons and the defects/vacancies on the lattices. β -Alumina, LISICON and garnet structures were selected as examples here.

completely ignored. A number of unexpected properties, both bulk and interfacial, arise from such unusually high salt concentrations.

(IV) *Inorganic solid electrolytes*, either crystalline or amorphous, where structurally open channels exist for ions to move, and chemically at least one ionic species (cations most of the time, but occasionally anions also) is decoupled from the polyionic lattice and

encouraged to hop between sites by thermal fluctuation (IV, Figure 2.1). The ion solvation and transport in this class of electrolytes follow significantly different disciplines.

Most electrolytes that we encounter, no matter whether in scientific study or in everyday life, belong to the first two types. Following the conventional nomenclature adopted in electrochemistry, we call these ionophoric or ionogenic species “*solutes*”. Both ionophores and ionogens dissolve in solvents to produce *solutions*, which conduct electricity *via* the movement of the dissociated or generated ions, and are called the “*electrolyte solution*” or simply “*electrolyte*”.

The study of electrolytes hence is the understanding of the interactions among ions and solvent molecules. The way in which they influence each other's movement defines most of their behavior in the electrochemical devices that we study. While classical electrochemistry consists of *Ionics* (the behavior of ions and solvent molecules in the bulk of electrolytes) and *Electrodics* (the behavior of ions and solvent molecules at the electrolyte/electrode interfaces), the emergence of advanced batteries such as the lithium-ion battery, in which the electrodes are operating at potentials far away from the thermodynamic stability limits of electrolytes, has brought a new component, *i.e.* interphases, at the junctions where electrode and electrolyte meet. The understanding of interphases represents the newest addition to electrolyte knowledge.^{2,3}

References

1. J. O' M. Bockris and A. K. N. Reddy, *Modern Electrochemistry*, Plenum Press, New York, 2nd edn, 1998.
2. K. Xu, Non-aqueous liquid electrolytes for lithium-based rechargeable batteries, *Chem. Rev.*, 2004, **104**, 4303–4417.
3. K. Xu, Electrolytes and interphases in Li-ion batteries and beyond, *Chem. Rev.*, 2014, **114**, 11503–11618.

3 In Bulk Electrolytes: Ionics

Ionics studies the behaviors of ions and solvent molecules in bulk electrolytes, *i.e.* how the ions interact with the solvent molecules (ion–solvent interaction) or among themselves (ion–ion interaction), and how they move under the action of a concentration gradient or an external electric field.

The mathematical model proposed by Debye and Hückel in 1923 for ion–ion interactions constitutes the core knowledge of ionics.¹ It started from a basic atomic model, which after a series of simplifications led to a few experimentally verifiable quantities (*e.g.* average activity coefficients), and successfully explained a few empirical laws established earlier (Kohlrausch's non-linear conductivity law and Lewis's ionic strength law). Its simplicity and success influenced numerous investigators thereafter, who made refinements to the original Debye–Hückel model and developed a more thorough understanding of ion–ion interactions (ion pairs, ionic clusters), ion–solvent interactions (solvation) and ionic movement (ionic diffusivity, mobility, conductivity). We will therefore build our ionic learning around this model.

However, before diving into the mathematical details of the Debye–Hückel model, let us first familiarize ourselves with a few basic and critically important concepts along with a couple of empirical laws established before this model. That will enable us to appreciate fully the beauty of the model of Debye and Hückel.

3.1 Solvent Molecules: Dipole and Dielectric Medium

Water is the most prevalent solvent on Earth, hence the earliest investigations on electrolytes were primarily performed on “*aqueous electrolytes*”.

A single water molecule (H_2O) consists of two hydrogen (H) atoms forming covalent bonds with one oxygen (O) atom. What usually is not shown is the positioning of the lone pair of electrons sitting on O, which point away from the O nucleus in such a way that they constitute a distorted tetrahedron with the two H nuclei. It is because of the repulsion by this lone electron pair that the angle between the two O–H bonds deviates slightly from what a normal tetrahedron should adopt (109.28°), but instead is *ca.* 108° (Figure 3.1a). Owing to the large difference between the capabilities of O and H atoms to withdraw electrons (*i.e.* electronegativity, 2.20 for H and 3.40 for O), an O–H bond is highly polarized, with most of the electrons being situated near O. With two such O–H bonds, taking into account the angle between them, the overall polarity of the water molecule should be structured in such a manner that the partial negative charge and the partial positive charge are situated on a line bisecting the angle between these two O–H bonds. In other words, one can simplify the water as a dipole, the polarity of which can be quantified as 1.87 debye (D). Such a simplification proved to be very useful in mathematical treatments when one tries to describe how water molecules coordinate with ions.

The water molecule is *bipolar*, with both its positive and negative termini well exposed and easily accessible (Figure 3.1a). Such easy accessibility to both positive and negative termini enables it to interact effectively with both cations and anions. This is an important reason why water is such an excellent solvent that can dissolve most ionophores and ionogens.

Non-aqueous solvent molecules often lack such bipolarity. A typical example is ethylene carbonate (EC), which is the prevalent solvent used in lithium-ion batteries. Although it has a higher dipole moment than water owing to the strong polarization between carbon and oxygen in the carbonyl configuration, its positive terminus is buried in the middle of the ring structure. Such spatial hindrance actually makes it a “*monopole*”, the interaction of which with cations is much more intensive than with anions (Figure 3.1b). Other non-aqueous solvent molecules, such as ethers, nitriles and esters of various organic

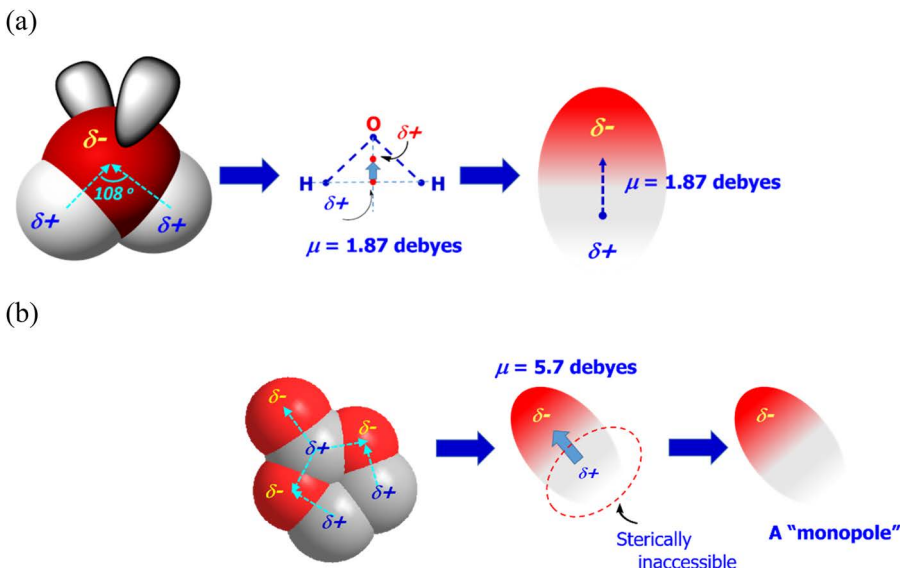


Figure 3.1 (a) The most universal solvent on Earth, water: its molecular structure (left), the “centers of gravity” for both positive and negative charges (middle) and its equivalent dipole (right). (b) A non-aqueous solvent, ethylene carbonate, whose positive terminus of the dipole is spatially hindered by its ring structure, hence in electrolytes it acts as if it is a “monopole” that interacts only with cations.

and inorganic acids, are not as monopolar as EC, but invariably they are more capable of solvating cations rather than anions. Thus, the prevalent solvation behavior in non-aqueous electrolytes is directed at cations, whereas the anions remain relatively free for most of the time. The only exceptions are a few classes of organic compounds, known as “*anion receptors*”, which preferentially solvate anions owing to their specially designed electron-deficient structures.

3.2 Dielectric Constant: Capability of a Solvent to Resist an External Electric Field

It was noted very early on that the electric field established by a pair of plate electrodes becomes weaker if one fills the vacuum space between these electrodes with a solvent. Apparently, compared with a vacuum, these solvent molecules produce a certain resistance against the applied external field. This resistance originates from the reorientation of the dipoles in those solvent molecules upon application

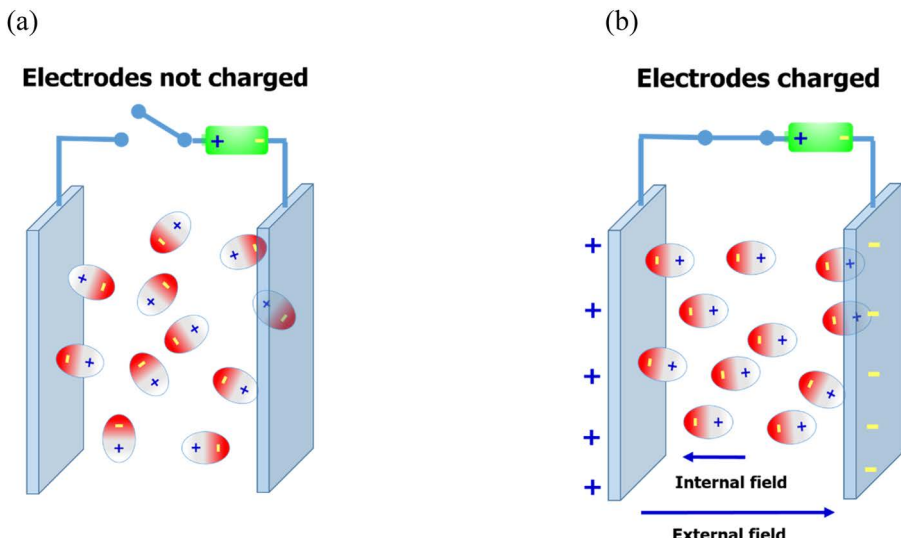


Figure 3.2 Solvent molecules as dipoles resist an external field. (a) When the electrodes are not charged, the dipoles of solvent molecules are randomly oriented; (b) at the instant an electric field is established, the dipoles align themselves in response to this applied field in such a manner that their positive and negative termini point towards the electrode of opposite charge. Such alignment induces an internal field that is in the reverse direction of the external field, thus creating the artifact that the overall field, which is actually measurable, is “weakened” by the presence of these solvent molecules.

of the external field, which is always in the opposite direction to the applied electric field (Figure 3.2).²

Experimentally, we define this behavior as “*dielectric*”, and quantify this property with a quantity called the *dielectric constant* (ϵ), which is the ratio between the field strengths of a vacuum (X_V) and a space filled with the investigated solvent molecules (X_S):

$$\epsilon = \frac{X_V}{X_S} \quad (3.1)$$

Sometimes the dielectric constant is also known as “*permittivity*”. For convenience, we also define the dielectric constant of a vacuum (ϵ_0) as 1.0, hence the relative dielectric constant (ϵ_r) can be expressed as

$$\epsilon_r = \frac{\epsilon}{\epsilon_0} \quad (3.2)$$

Table 3.1 gives the relative dielectric constants for some common solvents. The dielectric constant defines how much the solvent molecule can polarize under an external electric field.

Table 3.1 Dielectric constants for selected common solvents.

Solvent	Structure	Dielectric constants (at 25 °C unless otherwise denoted)
Vacuum		1.0 (by definition)
Water		78.4
Ethylene carbonate		89.8 (40 °C)
Propylene carbonate		64.9
Dimethyl carbonate		3.11
Ethylmethyl carbonate		2.96
Diethyl carbonate		2.81
Acetonitrile	$\text{H}_3\text{C}-\text{C}\equiv\text{N}$	37.5
Methanol		32.7
Ethanol		24.3
Ethylene glycol		37
Dimethyl ether		5.02
Diethyl ether		4.33
Dimethoxyethane		7.20
Tetrahydrofuran		7.58
Tetraglyme		7.79

As an excellent solvent, water possesses one of the highest dielectric constants among the known solvents. Thus, there is certain relation between the dielectric constant of a solvent and its capability to dissolve solutes. However, such a relation is by no means singular, as there are other factors that also contribute to a solvent's capability to dissolve solutes. Examples are the ethers listed in Table 3.1, the dielectric constants of which are not the highest in comparison with most of the esters, but they all demonstrated a remarkable capability to dissolve alkaline salts, which makes them frequent candidates as solvents for non-aqueous electrolytes.

Like conductivity, the dielectric constant is usually measured under alternating current (AC) instead of direct current (DC) conditions (we will explain the reason behind such a choice in Chapter 14), which means that the direction of the applied externally field is switching back and forth. It was noticed that, while the dielectric "constant" for a certain solvent remains a true constant at most low to medium frequencies, it suffers a sudden loss in a threshold region above which only a fraction of the original dielectric constant value can be retained. For water (Figure 3.3), this threshold region is centered around 10 GHz (1.0×10^{10} Hz).

What does this transition mean?

When an external electric field is on, the dipoles of solvent molecules flip in response to the field direction and make their contribution to diminish the electric field strength as shown in Figure 3.2. If this external field switches back and forth in direction, these solvent molecules will flip back and forth as the direction changes. However, if the field switches at a rate that is too fast for the solvent molecules to catch up, their dipoles can no longer align themselves in time against the field, and the contribution of their dipole is gradually lost, until a

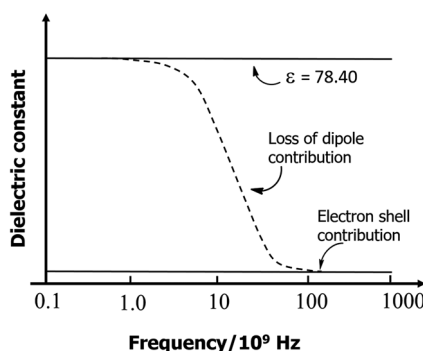


Figure 3.3 Frequency dependence of the dielectric constant of water.

frequency value where their dipoles are completely blind to the alternating field as if it does not exist. At that frequency, only the electrons in the outer shell can still respond to the applied field, but their contribution to the dielectric constant is only a tiny fraction of the overall dielectric constant when measured at low/medium frequencies. For water, this high-frequency region is *ca.* 98 GHz, which means that the maximum flipping speed of water molecules is *ca.* 1.02×10^{-11} s.

Note that so far we have not introduced any ions into the dielectric medium. Therefore, a dielectric constant itself represents the property of a neat solvent, not necessarily an electrolyte. However, the dielectric constant of a solvent describes its capability to react towards an electric field, including the local electric field introduced by an individual ion. In other words, at the microscopic level, the dielectric constant of a solvent quantifies its capability to interact with an ion by reorienting and aligning with its Coulombic field, whereas at the macroscopic level, the dielectric constant of a solvent reflects how effectively the solvent could dissociate a salt and solvate the resultant ions.

Later we will see that this concept lends significant support to Debye and Hückel, who simplified the role of the solvent to a single dielectric constant in their mathematical treatment.

3.3 Dissolution of Solutes in Solvents: Solvation Sheath

Consider a typical ionophore such as NaCl that dissolves in a solvent such as water and turns into an electrolyte (Figure 3.4). Apparently, this dissolution process is spontaneous. Energetically speaking, the change in Gibbs free energy (ΔG) must be negative:

$$\Delta G = \Delta H - T\Delta S < 0 \quad (3.3)$$

Since the stable crystalline lattice of NaCl is completely disintegrated by the dissolution, the so-called lattice stabilization energy has to be compensated in some manner in order to make ΔG negative. A significant contribution comes from the entropy (ΔS), because when Na^+ and Cl^- leave the ordered lattice structure and enter the solution, the entire system becomes very much more chaotic. In addition to entropy, a contribution should also come from the enthalpy (ΔH), which is caused by the stabilization of individual ions by solvents when these solvent molecules use their dipole nature to interact with the ions, in such a manner that the positive terminus

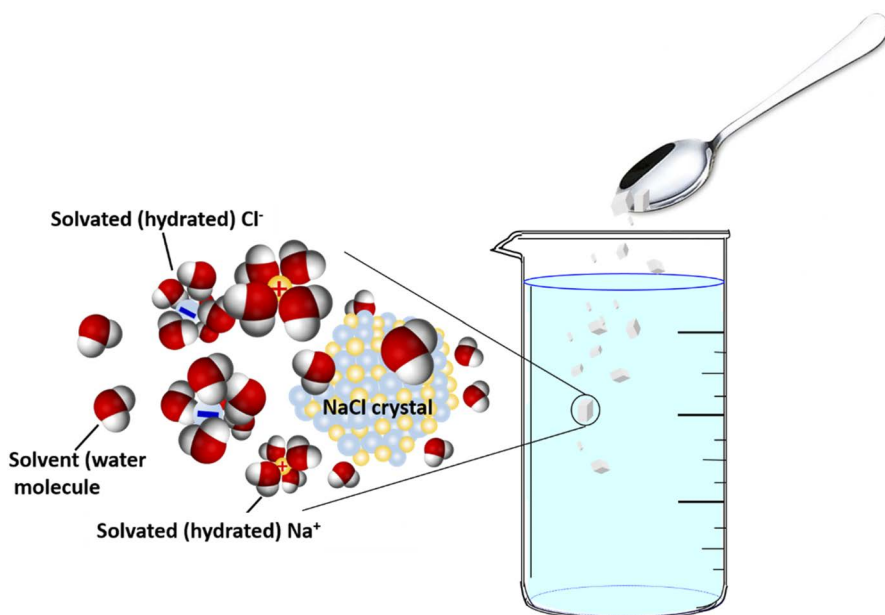


Figure 3.4 Dissolution of table salt (NaCl) in water: the stable NaCl lattice is disintegrated under the interaction between its ions (Na^+ and Cl^-) and solvent molecules (water). Owing to the bipolarity of water molecules, both the cation and anion are solvated. The process is spontaneous because the lattice energy is compensated by the contributions from both enthalpy and entropy.

of the dipole coordinates with the anion, and the negative terminus with the cation. Such stabilization is called “*solvation*” (or *hydration* if the solvent is water). The solvated (or hydrated) ions can be viewed as a discrete species, as the solvent molecules are associated with the ions *via* Coulombic force. Such association or binding ensures that the solvent molecules move with the ion during its translational motion.

One direct consequence of such ion–solvent interactions is the structure within electrolytes called the “*solvation sheath*”. Bernal and Fowler were the first to suggest a three-layer model consisting of *primary solvation sheath*, *secondary solvation sheath* and *bulk solvent molecules* (Figure 3.5).³ They proposed that the solvent molecules immediately associated with the central ion constitute the primary solvation sheath, in which the solvent molecules are bound by the strong Coulombic interaction between their dipole and the ion, so that they are forced to move with the ion during the translational movement. Owing to such strong association and the relative stability, the central

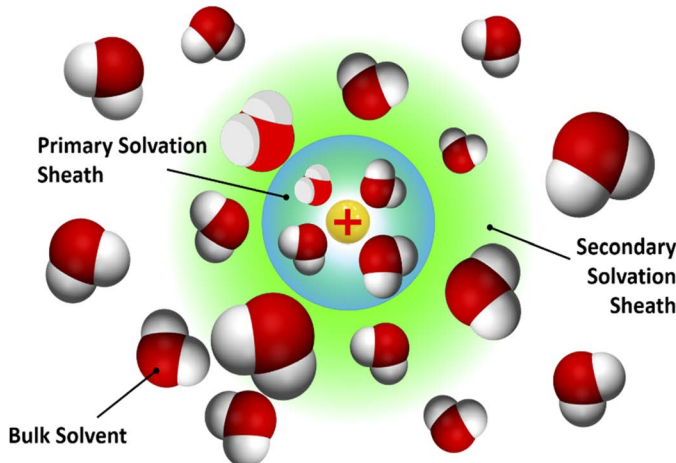


Figure 3.5 The classical solvation sheath model of three layers according to Bernal and Fowler: the innermost layer of solvent molecules and the central ion constitute the primary solvation sheath, the solvent molecules immediately outside constitute the secondary solvation sheath and the solvent molecules further out constitute the bulk.

ion plus the solvent molecules in the primary solvation sheath can be viewed as a discrete species, *i.e.* *solvated ion* (or *hydrated ion*). The average number of solvent molecules in a single primary solvation sheath is called the “*solvation number*”.

The solvent molecules immediately outside the primary solvation sheath are close enough to feel the electric field exerted by the central ion, hence their dipoles are more or less oriented towards the central ion; but they are not close enough to be strongly associated so that they move with the central ion during its translational movement. This immediate layer of solvent molecules constitutes the secondary solvation sheath. Owing to their dipole orientation towards the central ion, these solvent molecules differ from those in the bulk, which are oriented randomly, hence this secondary layer is also named a “*structure broken*” layer, meaning that they disrupt the pristine structure of bulk solvents.

It must be emphasized that the stability of the primary solvation sheath as implied by Figure 3.5 could be misleading. In fact, such *stability* is dynamic rather than static. That is, while an individual solvent molecule could stay for a very short duration with a certain central ion, its departure should be immediately replaced with another solvent molecule, so that the central ion maintains “fully populated” primary and secondary solvation sheaths.⁴

In such a sense, the stability of the primary solvation sheath is time averaged. Even the most strongly associated molecules still experience a very rapid exchange of positions with the solvent molecules in secondary or bulk layers, and the time scale involved is at the level of picoseconds (ps, 10^{-12} s). Hence only fast spectroscopic tools such as infrared or Raman spectroscopy with fast Fourier transformation can distinguish the solvent molecules in the different solvation states, whereas spectroscopic methods with lower temporal resolution such as X-ray scattering and absorption or nuclear magnetic resonance (NMR) can see only one kind of solvent molecules in the electrolytes.

3.4 Revisiting the Dielectric Constant: How Ions Affect It, and Its Unexpected Application

With the knowledge of the solvation sheath, we now revisit the concept of the dielectric constant and consider how the solvent molecules will react to the external electric field when solutes (ions) are introduced.

As mentioned in the preceding sections, a polar solvent molecule such as water could be simplified to be a dipole that orients either towards an external electric field (Figure 3.2) or towards an ion with which it interacts (Figure 3.6). When the external electric field and ions exist simultaneously, the solvent molecules obviously have to make a choice about which field to obey.

The solvent molecules in the primary solvation sheath are in the immediate vicinity of the ions, hence they are unlikely to change the

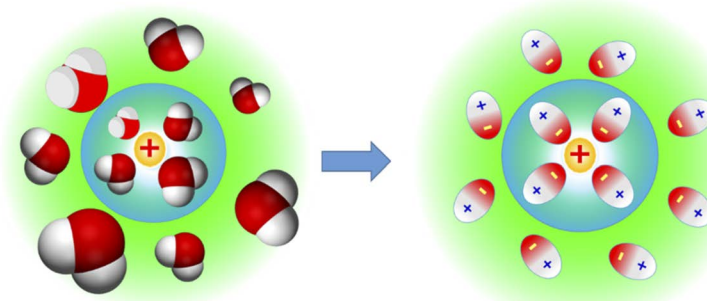


Figure 3.6 The polar water molecules can be viewed as simple molecular dipoles in the simplified solvation sheath structure, as if they were in an electric field created by a pair of external electrodes.

orientation of their dipole when an external electric field is applied. These molecules are considered “*dielectrically saturated*”. At the other extreme, the solvent molecules in the bulk should be free of the influence of the central ions’ electric field, and they should act as they do in the absence of any ions, *i.e.* in neat solvent. The solvent molecules in the secondary solvation sheath layer, however, reside in an intermediate state and could answer to both electric fields, depending on their location between the electrodes. Overall, the presence of these ions introduces a higher degree of chaos to the whole dipole orientation of the solvent molecules. Thus, the net result caused by the introduction of ions in the solution is that there are now not as many solvent molecules that will reorient in response to the external electric field. In other words, the applied electric field meets with less resistance (Figure 3.7a and b).

Note that by logical thinking, we have now established a relation between the dielectric constant of an electrolyte (which is relatively easy to measure by experiment) and the number of solvent molecules that *still* respond to the external electric field, or the number of solvent molecules that *no longer* respond to the external electric field because they are within the primary solvation sheaths. The latter is the “solvation number”, an important quantity defined in the preceding section, which would otherwise be difficult to measure directly.

Thus an unexpected approach to solvation number is now available from the dielectric constant of the electrolytes.

Hasted *et al.* analyzed the above relation between dielectric constant and solvation in aqueous electrolytes.⁵ They found that at 1 M salt concentration, the overall dielectric constant of these electrolytes was reduced by 10–20%. Assuming that the water molecules inside the primary solvation sheath still contribute a dielectric constant of 6 despite solvation, which was estimated from an extreme concentration where no bulk water was available, they derived a simple equation for the dielectric constant of electrolytes:

$$\varepsilon_{\text{soln}} = 80 \left(\frac{55 - c_i n_i}{55} \right) + 6 \frac{c_i n_i}{55} \quad (3.4)$$

where the first term represents the contribution from water molecules in the bulk (outside the primary solvation sheaths) and the second term represents the contribution from those water molecules in the primary solvation sheath, n_i is the total number of water molecules held by the ion at concentration c_i , and “80” and “55” represent the dielectric constant of bulk water and the total number of water

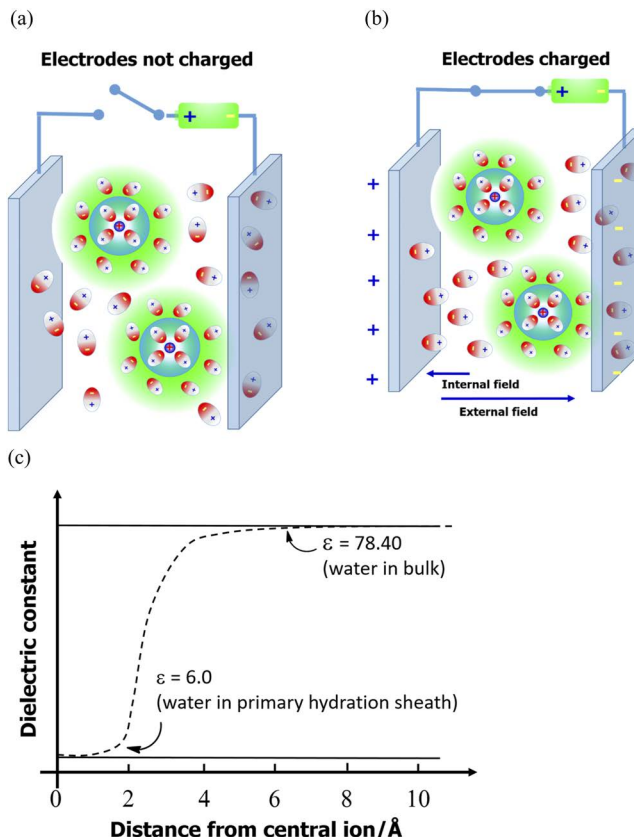


Figure 3.7 The presence of ions in the electrolytes reduces the number of solvent molecular dipoles that respond to the applied external electric field. Those solvent molecules bound in the primary solvation sheaths are considered “dielectrically saturated” owing to their intimate interactions with the ions. For clarity, only cations are shown. (a) The population of molecular dipoles in the bulk section of the electrolyte is reduced because of the recruitment by ions into the solvation sheaths. (b) Upon application of an external electric field, only those molecular dipoles in the bulk can effectively respond and align against the applied field, creating a much weaker internal field. (c) Dependence of dielectric constant on the distance from a central ion at $r = 0$.

molecules (in moles), respectively. Of course, eqn (3.4) holds true only when there are sufficient water molecules to form complete solvation around the ions. In other words, in concentrated or super-concentrated electrolytes, where the population of water *versus* population of ions crosses a certain threshold, the difference between “bulk water” with an ϵ of 80 and the “solvation sheath water” with an ϵ of

6 vanishes. The water molecules in those electrolytes would all be a part of the “solvation environment” and behave neither as bulk nor as solvation sheath.

Table 3.2 gives the hydration numbers for a series of alkali metal (M^+) and alkaline earth metal cations (M^{2+}) obtained in such a manner. It should be noted that in general M^{2+} ions have much higher hydration numbers than M^+ ions, because their electric charge being twice as high requires stabilization from more solvent molecules.

Eqn (3.6) implies that in an electrolyte the solvent molecules will have only two extreme dielectric constants (80 for bulk and 6 for the primary solvation sheath). This is clearly an oversimplification. As mentioned above, the solvent molecules in the secondary solvation sheath take an intermediate state, and their contribution to the dielectric constant should also be somewhere between those two extremes. A more rigorous mathematical treatment was later provided by Conway *et al.*,¹⁰ who described how rapidly the dielectric constant increases as the distance from the central ion goes beyond the primary solvation sheaths (Figure 3.7c).

3.5 Activity Coefficients, Ionic Strength and a Few Empirical Laws

As mentioned in Chapter 1, the birth of an electrolyte in the modern concept owes much to the advances in thermodynamics, especially to the discovery of the so-called “*colligative properties*” of solutions. Ironically, the further understanding of electrolytes revealed that the properties of electrolytes such as ion conductivity do not obey the colligative law; instead, most properties deviate from the colligative law, especially at high solute concentrations.

3.5.1 Activity Coefficients

In the late 1800s, it was noticed that certain properties of solutions are dependent on the number of solute particles but independent of the nature of the species. Such properties include melting point

Table 3.2 Hydration numbers obtained from dielectric constant measurements.

Ion	H^+	Li^+	Na^+	K^+	Rb^+	Mg^{2+}	Ba^{2+}	La^{2+}
Solvation number	10	6	4	4	4	14	14	22

depression, boiling point elevation, vapor pressure reduction and osmotic pressure generation. In 1891, Ostwald coined the term “*colligative*” to differentiate this phenomenon from the “*constitutional properties*” that *do* depend on the chemical nature of the particles, such as melting point, boiling point and vapor pressure themselves, or the “*additive properties*”, which are the sum of the properties of the constituent particles, such as mass, weight or number of moles.⁶ The word came from the Latin root “*colligatus* (bound together)”, meaning that the properties share a common feature of relating to particle numbers while being blind to their individual physical or chemical nature.

Soon it was observed that not all solutes behaved in the same way. For example, dissolving sucrose and NaCl in water at the same concentration generates a significant difference in the changes of those “*colligative properties*”, so significant that it seems that NaCl generates many more particles than sucrose. Combined with the fact that an NaCl solution conducts electricity whereas a sucrose solution does not, it became apparent that something had happened when NaCl dissolved, generating the ions defined by Faraday. This observation led to the realization of how ionophores dissociate into ions that were discussed in the preceding sections. The systematic work carried out by Arrhenius on salt dissociation corrected what was proposed by Faraday earlier that an electric current was required to produce those ions, and earned him the Nobel Prize in Chemistry in 1903.⁷

However, a new problem soon arose. Even at low solute concentrations, the properties of these electrically conducting solutions do not adhere quantitatively to the colligative law. In their studies on electric conductivity, Ostwald and Arrhenius attempted to explain this departure from the colligative law by arguing that some solutes do not dissociate completely into ions, which applies to ionogens such as acetic acid, but this modification still failed to account for those departures occurring with solutes that completely dissociate in water.

Following an empirical practice adopted in thermodynamics for colligative properties, the above departure can be accommodated with an apparent solute concentration called *activity* (a), so that the colligative law can still appear to be obeyed. The ratio between the solute concentration c and activity a is called the *activity coefficient* (γ):

$$a = \gamma c \quad (3.5)$$

In ideal electrolyte solutions, the activity coefficients of all the ions are equal to 1.0, hence there is no difference between the stoichiometric

concentration and the activity. Since the activity coefficients of a single ion cannot be measured experimentally (because it is impossible to form an electrolyte solution containing a single ion), a *mean activity coefficient* (γ_{\pm}) was defined:

$$\gamma_{\pm} = \sqrt{\gamma_+ \gamma_-} \quad (3.6)$$

For an electrolyte of formula A_nB_m , the mean activity coefficient would be

$$\gamma_{\pm} = \sqrt[n+m]{\gamma_A^n \gamma_B^m} \quad (3.7)$$

Note that the application of an activity coefficient only corrects the departure of the electrolyte properties from the colligative law by merely introducing an artificial quantity. It does not explain why such a departure occurs from a molecular perspective. However, it does set the stage for the Debye and Hückel model, because this quantity will pop up to verify the success of their mathematical approach.

3.5.2 Kohlrausch's Law on Non-linearity and Independent Movements of Ions

By the early 1900s, researchers believed that there are two types of electrolytes: “strong” and “weak”. At the time, they did not recognize high-temperature molten salts as a distinct type of electrolyte, and room-temperature molten salts (or ionic liquids) were not known until the late 1950s. Here “strong” and “weak” refer to how complete the solute undergoes dissociation according to Arrhenius’s theory, and strong electrolytes provide higher conductivity than weak electrolytes because of the much higher ion population.

When normalizing the conductivity (σ) of strong electrolytes against the solute concentration:

$$\Lambda_m = \frac{\sigma}{c} \quad (3.8)$$

Kohlrausch found that the resultant molar conductivity Λ_m is in a non-linear relation with the concentration (c) of the solute:⁸

$$\Lambda_m = \Lambda_m^0 - K\sqrt{c} \quad (3.9)$$

where Λ_m^0 is the molar conductivity at infinite dilution ($c \approx 0$), or a limiting molar conductivity that can be extrapolated from the above equation, and K is the Kohlrausch constant, which depends mainly on the chemical nature of the specific salt in solution.

Kohlrausch's law is extracted from experimental results and is therefore completely empirical. However, its underlying mechanism is that ion–ion interactions actually hinder ion transport, hence the molar conductivity achieves its maximum value when the solute concentration approaches zero.

A derivative law, also called the *Kohlrausch independent ion migration law*, was more well known.⁸ It states that in diluted states, the cations and anions are moving freely from each other's influence. Hence molar conductivity can be considered as independent contributions from individual ions.

Both laws are valid only at low electrolyte concentrations, and both can be derived from the Debye–Hückel model with suitable simplification.

3.5.3 Ionic Strength and Lewis–Randall Empirical Law

When Lewis and Randall examined the activity coefficients of “strong electrolytes” such as NaCl, it was realized that the departure from ideal behavior was so enormous that it cannot be explained by Arrhenius's partial dissociation hypothesis.⁹ Given that NaCl solutions are much more conductive than “weak electrolytes” such as acetic acid solutions, Lewis and Randall believed that such departures must be incurred by the much stronger “electromotive force” in those strong electrolytes. Hence the interactions between the oppositely charged ions, the populations of which are much higher in NaCl than in acetic acid, must have a heavy influence on the “colligative properties”. The more ionic an electrolyte is, the more those properties will depart from colligative behavior.

To quantify how “ionic” an electrolyte solution is, Lewis and Randall created a new quantity, “*ionic strength (I)*”:

$$I = \frac{1}{2} \sum_{i=1}^n c_i z_i^2 \quad (3.10)$$

where c_i and z_i represent the concentration and valence, respectively, of each individual ion.⁹ Apparently the multivalent ions have a higher influence on the ionicity of the electrolyte.

For example, the ionic strength of a 1 M NaCl solution in water is

$$I_{\text{NaCl}} = \frac{1}{2} \sum_{i=1}^n c_i z_i^2 = \frac{1}{2} [c_{\text{Na}} z_{\text{Na}}^2 + c_{\text{Cl}} z_{\text{Cl}}^2] = \frac{1}{2} [(1 \times 1^2) + (1 \times 1^2)] = 1.0 \quad (3.11)$$

whereas 1 M solutions of MgCl₂ and CaSO₄, assuming they are fully dissociated, would increase the ionic strength to

$$I_{\text{MgCl}_2} = \frac{1}{2} \sum_{i=1}^n c_i z_i^2 = \frac{1}{2} [c_{\text{Mg}} z_{\text{Mg}}^2 + c_{\text{Cl}} z_{\text{Cl}}^2] = \frac{1}{2} [(1 \times 2^2) + (2 \times 1^2)] = 3.0 \quad (3.12)$$

$$I_{\text{CaSO}_4} = \frac{1}{2} \sum_{i=1}^n c_i z_i^2 = \frac{1}{2} [c_{\text{Ca}} z_{\text{Ca}}^2 + c_{\text{SO}_4} z_{\text{SO}_4}^2] = \frac{1}{2} [(1 \times 2^2) + (1 \times 2^2)] = 4.0 \quad (3.13)$$

respectively. By comparison, super-concentrated aqueous electrolytes such as a water-in-salt electrolyte (WiSE) consisting of 21 m lithium bis(trifluoromethanesulfonyl)imide in water (or 4.9 M) would have an ionic strength of

$$I_{\text{WiSE}} = \frac{1}{2} \sum_{i=1}^n c_i z_i^2 = \frac{1}{2} [c_{\text{Li}} z_{\text{Li}}^2 + c_{\text{TFSI}} z_{\text{TFSI}}^2] = \frac{1}{2} [(4.9 \times 1^2) + (4.9 \times 1^2)] = 5.5 \quad (3.14)$$

The most concentrated aqueous electrolyte is perhaps the “63 molal electrolyte”, which is a hybrid of 42 m (or 3.33 M) of lithium bis(trifluoromethanesulfonyl)imide plus 21 m (1.67 M) of tetraethylammonium bis(trifluoromethanesulfonyl)imide. Its ionic strength should be

$$\begin{aligned} I_{63\text{m}} &= \frac{1}{2} \sum_{i=1}^n c_i z_i^2 = \frac{1}{2} [c_{\text{Li}} z_{\text{Li}}^2 + c_{\text{N}} z_{\text{N}}^2 + c_{\text{TFSI}} z_{\text{TFSI}}^2] \\ &= \frac{1}{2} [(3.33 \times 1^2) + (1.67 \times 1^2) + (5.0 \times 1^2)] = 5.0 \end{aligned} \quad (3.15)$$

The ionic strength tells us that the degree of ionicity of a given electrolyte is determined not only by the concentration of the solute, but to a much greater extent by the charge that these ions carry. It is actually related to the strength of ion–ion interactions in an electrolyte. Like activity coefficients, ionic strength will also naturally appear in the mathematical treatment of Debye and Hückel.

In addition to activity coefficient and ionic strength, a few empirical laws established by experimentalists also provide strong evidence for the Debye–Hückel model. Therefore, it is necessary for us to visit them briefly here, although a detailed discussion of ion conductivity will be provided in later sections dedicated to ion transport behaviors in electrolytes.

Ionic strength is in fact a measure of the electric field introduced by the ions. Its influence on the departure of an electrolyte from ideal colligative properties is expressed by the *Lewis empirical law*.

Based on their extensive measurement and analysis of experimental data, Lewis and Randall established an empirical relation, in which the mean activity coefficient is linearly related to the square root of ionic strength:

$$\log(\gamma_{\pm}) = -C\sqrt{I} \quad (3.16)$$

where C is a constant for a given solute–solvent system. Like Kohlrausch's non-linearity and independent movement law, this relation also remains true only for strong electrolytes in a very dilute range (<0.01 M).

So far we have discussed a series of basic concepts and empirical laws, and have mentioned that most of them will appear naturally in the mathematical treatment of Debye and Hückel or become verified by it. Now we will take a detailed look at the efforts of Debye and Hückel in their attempts to describe electrolytes mathematically *via* a bottom-up approach.

References

1. P. Debye and E. Hückel, Zur Theorie der Elektrolyte. I. Gefrierpunktserniedrigung und verwandte Erscheinungen, *Phys. Z.*, 1923, **24**, 185–206.
2. J. O'M. Bockris and A. K. N. Reddy, *Modern Electrochemistry*, Plenum Press, New York, 2nd edn, 1998.
3. J. D. Bernal and R. H. Fowler, A Theory of Water and Ionic Solution, with Particular Reference to Hydrogen and Hydroxyl Ions, *J. Chem. Phys.*, 1933, **1**, 515–548.
4. O. Borodin, J. Self, K. Persson, C. Wang and K. Xu, Uncharted waters: super-concentrated electrolytes, *Joule*, 2020, **4**, 69–100.
5. J. B. Hasted, D. M. Ritson and C. H. Collie, Dielectric properties of aqueous ionic solutions, *J. Chem. Phys.*, 1948, **16**, 1–21.
6. W. Ostwald, *On catalysis*, Nobel Lecture, 12 December 1909, <https://www.nobel-prize.org/prizes/chemistry/1909/ostwald/lecture/>.
7. S. Arrhenius, *Development of the theory of electrolytic dissociation*, Nobel Lecture, 11 December 1903, <https://www.nobelprize.org/uploads/2018/06/arrhenius-lecture.pdf>.
8. F. Kohlrausch, *Leitvermögen der Elektrolyte*, Benedictus Gotthelf Teubner, Leipzig, 1898.
9. G. N. Lewis and M. Randall, *Thermodynamics and the Free Energy of Chemical Substances*, McGraw-Hill Book Co., New York, 1st edn, 1923.
10. B. E. Conway, The temperature and potential dependence of electrochemical reaction rates, and the real form of Tafel Equations, in *Modern Aspects of Electrochemistry*, Plenum Press, New York and London, 1985, vol. 16.

4 Quantification of Ion-Ion Interaction: Debye-Hückel Theory

Differing from their precedents, Debye and Hückel were the first to attempt to treat strong electrolytes with mathematical rigor at the atomic level, rather than just summarizing experimental data in an empirical manner. Their landmark contribution made in the 1920s successfully correlated molecular properties with macroscopically observable quantities. Despite its many flaws and oversimplifications, this model provided a starting point for modern treatments of non-ideality of electrolyte solutions.

4.1 The Ionic Cloud

Based on prior observations made by Arrhenius, Ostwald, Lewis and Kohlrausch that strong electrolytes also display significant departures from ideal behaviors as anticipated from colligative laws, Debye and Hückel correctly inferred that ion-ion interactions must be responsible for such departures. Thus, the central mission of their efforts was to establish a mathematical model of how these ions of opposite charges distribute around each other.¹

They first assumed that all ions can be viewed as point charges ($z_1 e_0$, $z_2 e_0$, ... $z_i e_0$), and that interactions between any two ions are governed by Coulomb's law:

$$F = \frac{z_1 z_2 e_0^2}{4\pi\epsilon_0\epsilon_r r^2} \quad (4.1)$$

where F is the Coulombic force (in most parts of this book F is used to represent the Faraday constant except where stated otherwise). It should be noted that in this assumption, the role of solvent molecules is simplified as a dielectric continuum without structure, as represented by the dielectric constant ϵ_r .

Hence a cation will most likely find anions around its immediate neighborhood, whereas an anion will most likely find cations around its immediate neighborhood (Figure 4.1a). The sum of such Coulombic forces will determine how cations and anions distribute spatially throughout the whole electrolyte solution.

It sounds simple enough, but considering an extremely dilute strong electrolyte, such as a solution of NaCl in water, even at a concentration of 0.001 M the total number of Na^+ and Cl^- ions in the solution is still $2 \times 0.001 \times 0.001 \times 6.02 \times 10^{23} = 1.20 \times 10^{18}$ per cubic centimeter! Such a magnitude makes it essentially impossible to treat each ion individually, although the law governing their interactions [eqn (4.1)] is already known. In mathematics, this is a typical “*multi-body problem*”, which

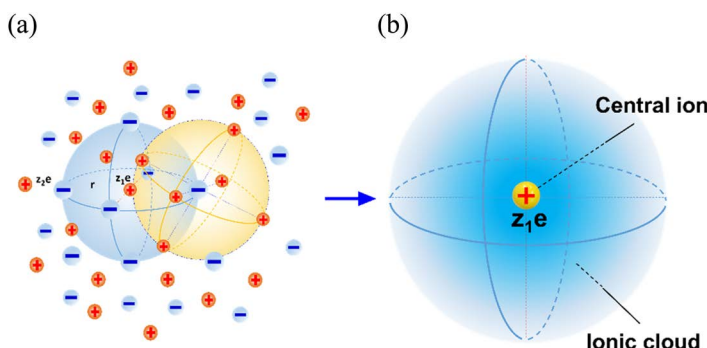


Figure 4.1 A core simplification adopted by Debye and Hückel turns a multi-body problem into a simple two-body problem: (a) Coulombic force governs the distribution of ions throughout the electrolyte solution, with each cation or anion surrounded by ions of opposite charges that consist of a 3D multi-body system; (b) the whole electrolyte solution can be simplified to consist of a single central ion surrounded by an ionic cloud.

does not have analytical solutions once the number of bodies needed to be treated is above three. Approximations have to be applied.

To address this challenge, Debye and Hückel made a very bold but rather clever approximation. They viewed the whole electrolyte solution as if it consists of a single central ion and its surroundings. In this simplification, all of the ions in the solution, with the exception of the central ion, lose their individuality and merge into an integrated collection (Figure 4.1b).

If the charge carried by this central ion is $z_i e_0$, then the corresponding “surroundings” must carry a net charge of $-z_i e_0$, so that the whole solution can maintain its electroneutrality. Thus, the impossible mathematical nightmare of calculating the spatial distribution of the entire ionic population collapses into a relatively simple procedure in which only the spatial distribution of a charge of $-z_i e_0$ needs to be considered.

Is the charge of $-z_i e_0$ distributed evenly throughout this surrounding?

Of course not. As one can imagine, in the immediate vicinity of the central ion the probability of its opposite charge is higher, and as the distance from it increases, the probability gradually fades. Hence the charge of $-z_i e_0$ smears out throughout the surroundings, which is thus named an “*ionic cloud*” (Figure 4.1b).

Thus, the core problem that Debye and Hückel faced now becomes how to derive a rigorous mathematical model to express the continued charge distribution around a central ion. To do this, they took a parallel approach, applying both Poisson and Boltzmann functions to the charge distribution, and then combining the two for a rational solution.

4.2 The Poisson Equation for the Spatial Distribution of an Ionic Cloud

As Figure 4.1b demonstrates, the question now simplifies into how a charge of $-z_i e$ spatially distributes in the surroundings of a central ion carrying a charge of $z_i e$. To simplify the question further, we can place the central ion in a spherical surrounding so that the charge density at a certain distance from the central ion (ρ_r) is spherically symmetric. Now the question becomes how ρ_r changes with r . As the spatial distribution of ρ_r is governed by the Coulombic force, let us set the electrostatic potential at r as ψ_r , and the electric field at r is X_r .

Because the sphere is a closed space, Gauss’s law applies here, which states that the net electric flux through the surface of such

space (Φ_E) must be equal to the total charge within that closed surface (Q) divided by the dielectric constant of the space:

$$\Phi_E = \frac{4\pi}{\epsilon_0 \epsilon_r} Q \quad (4.2)$$

The flux Φ_E is actually the surface integral of the field at r , i.e. field (X_r) times the surface area of the sphere at r :

$$\Phi_E = X_r 4\pi r^2 \quad (4.3)$$

While the total charge within the sphere is the space integral of ρ_r from 0 to r , we assume that the central ion is a point charge without dimension:

$$Q = \int_0^r 4\pi r^2 \rho_r dr \quad (4.4)$$

Combining eqn (4.2)–(4.4), we obtain

$$X_r 4\pi r^2 = \frac{4\pi}{\epsilon_0 \epsilon_r} \int_0^r 4\pi r^2 \rho_r dr \quad (4.5)$$

It is easy to rearrange eqn (4.5) into

$$r^2 X_r = \frac{4\pi}{\epsilon_0 \epsilon_r} \int_0^r r^2 \rho_r dr \quad (4.6)$$

Meanwhile, the definition of electrostatic potential ψ_r gives

$$\psi_r = - \int_0^r X_r dr \quad (4.7)$$

Differentiating both sides of eqn (4.7) with respect to r , we obtain the expression for the field as

$$X_r = - \frac{d\psi_r}{dr} \quad (4.8)$$

Inserting eqn (4.8) back into eqn (4.6), we obtain a differential equation describing the relation between ρ_r and ψ_r :

$$r^2 \frac{d\psi_r}{dr} = -\frac{4\pi}{\epsilon} \int_0^r r^2 \rho_r dr \quad (4.9)$$

which can be turned into eqn (4.10) if we differentiate both sides with respect to r :

$$\frac{d}{dr} \left(r^2 \frac{d\psi_r}{dr} \right) = -\frac{4\pi}{\epsilon} r^2 \rho_r \quad (4.10)$$

Rearranging eqn (4.10), we obtain the famous Poisson equation, which describes the distribution of a charge of $-z_i e$ in space of spherical symmetry as shown in Figure 4.1:

$$\frac{1}{r^2} \frac{d}{dr} \left(r^2 \frac{d\psi_r}{dr} \right) = -\frac{4\pi}{\epsilon} \rho_r \quad (4.11)$$

4.3 The Boltzmann Equation for the Spatial Distribution of an Ionic Cloud

The Poisson equation describes the relation between ρ_r and ψ_r for an ionic cloud. However, despite its elegant look, it does not give us any useful quantity that can be verified by experimental measurement.

Now, Debye and Hückel had to try to link these quantities to parameters that we either know or that we can measure, for example, the solute concentration, which defines the total number of ions. They turned to Boltzmann's statistical law of distribution for help.

Let us consider an infinitesimally small volume element dV at a distance r from the central ion (Figure 4.2). According to assumptions adopted in the preceding section, the charge density distributed in this small volume follows the Poisson equation. In this volume, the excess charge density ρ_r should be the sum of all ions of both positive and negative charges:

$$\rho_r = \sum n_i z_i e_0 \quad (4.12)$$

where n_i and z_i are the number and valence of each ion in the volume element and e_0 is the electronic charge.

In other words, n_i is the concentration of that ion if we set the volume element as unity (*i.e.* concentration is defined as the number of ions in a unit volume). Note that we know the bulk ion concentration

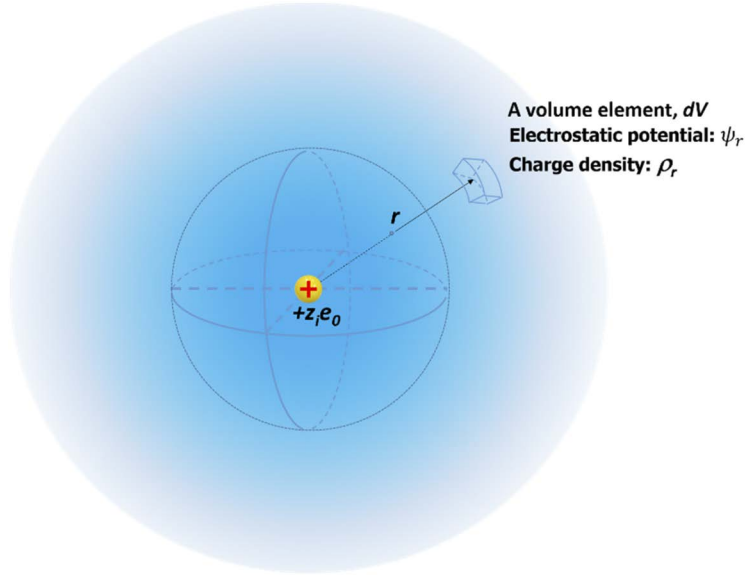


Figure 4.2 A volume element in the ionic cloud at a distance r from the central ion that carries a charge of $+z_i e_0$, where the electrostatic potential is ψ_r and the excess charge density is ρ_r .

n_i^0 because it is equal to the solute concentration (strong electrolytes). However, owing to the ion–ion interaction:

$$n_i^0 \neq n_i \quad (4.13)$$

In other words, the ion–ion interaction, which includes both attraction between ions of opposite charges and repulsion between ions of the same charge, prevents the ions from having an even distribution. The Coulombic force responsible for such an uneven distribution creates a potential difference (U) between n_i^0 and n_i .

Here enters the *Boltzmann distribution law* of classical statistical mechanics, which should govern the relation between n_i^0 and n_i :

$$n_i = n_i^0 e^{-\frac{U}{k_B T}} \quad (4.14)$$

where k_B is Boltzmann's constant. When $U = 0$, $n_i^0 = n_i$, i.e. in the absence of ion–ion interactions the concentration of all ions in the volume element should be the same as the bulk solute concentration. Since the potential energy between n_i^0 and n_i is Coulombic in nature, by definition U should be

$$U = z_i e_0 \psi_r \quad (4.15)$$

Then the Boltzmann distribution law becomes

$$n_i = n_i^0 e^{-\frac{z_i e_0 \psi_r}{k_B T}} \quad (4.16)$$

Using this expression for n_i , we can express the excess charge density ρ_r as

$$\rho_r = \sum n_i z_i e_0 = \sum n_i^0 z_i e^{-\frac{z_i e_0 \psi_r}{k_B T}} \quad (4.17)$$

Here we must remember that n_i^0 , which is the solute concentration in the bulk, is known, and n_i , which is the excess population of ions in that volume element, is unknown. We have finally tied the excess charge density (ρ_r) in the volume element at a distance r from the central ion to something we can measure experimentally.

4.4 Linearization of the Boltzmann Equation

Debye and Hückel then made an important assumption that further simplified the mathematics. They argued that the average electrostatic potential ψ_r is far smaller than the thermal energy kT , hence

$$z_i e_0 \psi_r \ll k_B T, \text{ or } \frac{z_i e_0 \psi_r}{k_B T} \ll 1 \quad (4.18)$$

What does this assumption mean?

In statistical thermodynamics, $k_B T$ represents the amount of energy that the particles (ions, solvent molecules) are required to overcome in order to achieve maximum entropy (or randomness). In other words, if a counter force exists for those particles, $k_B T$ sets a threshold for the counter force to disrupt the distribution governed by the thermal motion of these particles.

In our electrolyte solutions consisting of ions of opposite charges, the motion and distribution of these ions are thus subject to two different forces: (1) Coulombic force that acts *via* an electrostatic field and places ions in an uneven distribution throughout the ionic cloud and (2) the random thermal movement of both ions and solvent molecules that will try to disrupt the Coulombic order and rearrange them

into random disorder. If the energy barrier created by the Coulombic field is too large compared with the thermal energy $k_B T$, the distribution of the ions would be completely governed by their thermal motion, *i.e.* the ionic cloud would become an evenly distributed body of cations and anions. This is obviously not what happens in the electrolytes. On the contrary, since the beginning of this chapter, we have been discussing how Coulombic force determines the distribution within the ionic cloud.

Hence the assumption of $z_i e_0 \psi_r / k_B T \ll 1$ was already hidden in the picture of the ionic cloud. With this assumption, the exponential section of the Boltzmann distribution equation, eqn (4.17), can be expanded into a *Taylor series*:

$$e^{-\frac{z_i e_0 \psi_r}{k_B T}} = 1 - \frac{z_i e_0 \psi_r}{k_B T} + \frac{1}{2} \left(\frac{z_i e_0 \psi_r}{k_B T} \right)^2 + \dots \quad (4.19)$$

To a decent approximation one can ignore the terms after the first two, hence the Boltzmann distribution transforms into

$$\rho_r = \sum_i n_i^0 z_i e_0 \left(1 - \frac{z_i e_0 \psi_r}{k_B T} \right) = \sum_i n_i^0 z_i e_0 + \sum_i \frac{n_i^0 z_i^2 e_0^2 \psi_r}{k_B T} \quad (4.20)$$

The first term $\sum_i n_i^0 z_i e_0$ actually represents the charge in the whole electrolyte, which is zero due to the electroneutrality of the electrolyte. Now we are left with

$$\rho_r = \sum_i \frac{n_i^0 z_i^2 e_0^2 \psi_r}{k_B T} \quad (4.21)$$

Here we have managed to move ψ_r outside the exponential, which is easier to solve because it is now in a linearized form.

4.5 Combining the Poisson and Boltzmann Equations

So far we have obtained two sets of expressions for the excess charge density (ρ_r) in a volume element as shown in Figure 4.2, from Poisson and Boltzmann, respectively. These two equations describe the same thing, hence Debye and Hückel combined them.

We bring back the Poisson equation for ρ_r :

$$\frac{1}{r^2} \frac{d}{dr} \left(r^2 \frac{d\psi_r}{dr} \right) = -\frac{4\pi}{\epsilon} \rho_r \quad (4.22)$$

We rearrange this to

$$\rho_r = -\frac{\epsilon}{4\pi} \left[\frac{1}{r^2} \frac{d}{dr} \left(r^2 \frac{d\psi_r}{dr} \right) \right] \quad (4.23)$$

Combining the above expressions for ρ_r by Poisson and Boltzmann, we have

$$\frac{1}{r^2} \frac{d}{dr} \left(r^2 \frac{d\psi_r}{dr} \right) = \left[\frac{4\pi}{\epsilon k_B T} \sum_i n_i^0 z_i^2 e_0^2 \right] \psi_r \quad (4.24)$$

which is known as the linearized Poisson–Boltzmann equation. Lumping together the constants into a new constant K^2 so that we do not have to write all these constants related to the bulk solute concentration, valence and electronic charge and dielectric constant:

$$K^2 = \frac{4\pi}{\epsilon k_B T} \sum_i n_i^0 z_i^2 e_0^2 \quad (4.25)$$

We can further simplify the linearized Poisson–Boltzmann equation to

$$\frac{1}{r^2} \frac{d}{dr} \left(r^2 \frac{d\psi_r}{dr} \right) = K^2 \psi_r \quad (4.26)$$

This is a second-order differential equation, the solution of which is straightforward and in the general form

$$\psi_r = A \frac{e^{-Kr}}{r} + B \frac{e^{Kr}}{r} \quad (4.27)$$

where A and B are constants that come up when integrating the partial differential equation. The values of A and B cannot be obtained from a pure mathematical perspective. One has to “cheat” by placing the electrolyte being studied under certain actual border conditions, so that the mathematical equation “makes sense”, and we can “guess” these quantities that cannot be obtained merely *via* mathematics.

First, B can be eliminated when we apply the boundary condition of the electrolyte at a distance far enough from the central

ion where the potential caused by the excess charge must approach zero, *i.e.*

$$\psi_r \rightarrow 0 \text{ as } r \rightarrow \infty \quad (4.28)$$

Hence

$$0 = A \frac{e^{-\infty}}{\infty} + B \frac{e^{\infty}}{\infty} \quad (4.29)$$

In order to satisfy the above condition, B must be zero. Therefore, the final relation between ψ_r and r is rather simple:

$$\psi_r = A \frac{e^{-Kr}}{r} \quad (4.30)$$

Second, to evaluate A , one can “cheat” again by considering a strong electrolyte in an extremely dilute state, so that the average distances between the ions are much longer compared with the radius of the central ion. In other words, the electrostatic field around the central ion is purely generated by its own charge of $z_i e_0$, as defined by Coulomb’s law, without interference from the other ions:

$$\psi_r = \frac{q}{4\pi\epsilon_0} \frac{e}{r^2} \quad (4.31)$$

Meanwhile, the solute concentration approaches zero, hence $n_0 \approx 0$. This will lead to $K \approx 0$, or $e^{-kr} \approx 1$. One would have

$$\psi_r = \frac{A}{r} \quad (4.32)$$

Combining eqn (4.31) and (4.32), we obtain

$$A = \frac{z_i e_0}{\epsilon} \quad (4.33)$$

Inserting this value of A obtained through the above approximation, we finally obtain the solution to the linearized Poisson–Boltzmann equation:

$$\psi_r = \frac{z_i e_0}{\epsilon} \frac{e^{-Kr}}{r} \quad (4.34)$$

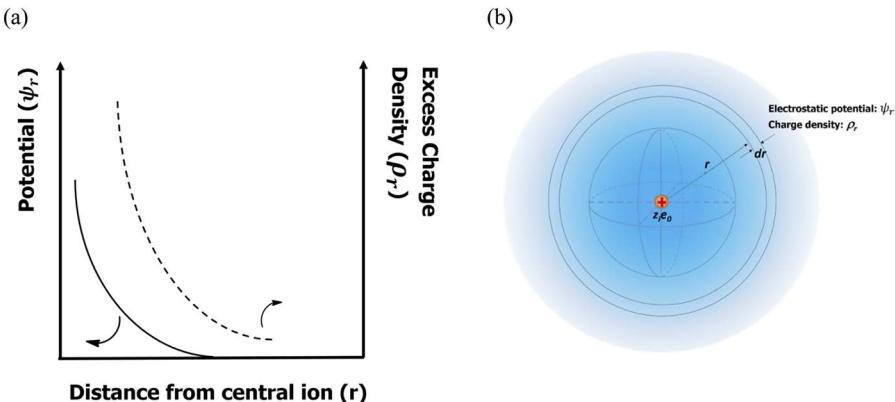


Figure 4.3 (a) Variation of potential (ψ_r) and excess charge density (ρ_r) in a volume element at a distance r from the central ion. (b) The total charge contained in a shell of thickness dr around the central ion can be calculated from the Debye-Hückel model, and the integration of this charge with respect to r gives the total charge contained in the entire ionic cloud, which is $z_i e_0$.

Eqn (4.34) shows, in a very simple and elegant way, how the electrostatic potential ψ_r varies with the distance r from a central ion carrying charge $z_i e_0$. It will be our powerful tool in deriving many experimentally verifiable quantities for strong electrolytes. Figure 4.3 provides a graphical representation.

Now that we have obtained the electrostatic potential (ψ_r) as a function of r in the ionic cloud, what about excess charge density (ρ_r)?

Before combining it with the Boltzmann equation, the Poisson equation describes such a relation, although its solution seemed impossible:

$$\frac{1}{r^2} \frac{d}{dr} \left(r^2 \frac{d\psi_r}{dr} \right) = -\frac{4\pi}{\epsilon} \rho_r \quad (4.35)$$

After combining the Poisson equation with the Boltzmann law of distribution, we have

$$\frac{1}{r^2} \frac{d}{dr} \left(r^2 \frac{d\psi_r}{dr} \right) = K^2 \psi_r \quad (4.36)$$

Then a much simpler relation can be obtained:

$$K^2 \psi_r = -\frac{4\pi}{\epsilon} \rho_r \text{ or } \rho_r = -\frac{\epsilon}{4\pi} K^2 \psi_r \quad (4.37)$$

Inserting the solution obtained from linearized Poisson–Boltzmann equation, eqn (4.34), we now should have

$$\rho_r = -\frac{z_i e_0}{4\pi} K^2 \frac{e^{-Kr}}{r} \quad (4.38)$$

This is the spatial distribution of excess charge with distance from the central ion, the graphic representation of which is also displayed in Figure 4.3a along with the potential.

Eqn (4.34) and (4.38) are the core achievements of the Debye–Hückel model. As we will see in later chapters, the exact expressions of potential and charge distributions in space are of paramount importance. In elegant mathematical language, they describe how the Coulombic field dictates the distribution of ions in an electrolyte solution. Such equations come from an atomistic model, so their accuracy in describing the real world needs to be verified.

4.6 Verifications of the Debye–Hückel Model

Any theory, no matter how elegant it is, needs experimental verification. Now let us apply these equations to derive a few experimentally measurable quantities to verify the correctness of the Debye–Hückel model.

4.6.1 The Total Excess Charge in an Ionic Cloud

First, let us consider a thin shell of infinitesimal thickness dr in the ionic cloud as shown in Figure 4.3b. Since everywhere in this shell is at a distance r from the central ion, both eqn (4.34) and (4.38) hold true:

$$\psi_r = \frac{z_i e_0}{\epsilon} \frac{e^{-Kr}}{r} \quad (4.34)$$

$$\rho_r = -\frac{z_i e_0}{4\pi} K^2 \frac{e^{-Kr}}{r} \quad (4.38)$$

The total charge contained in such a thin shell should be

$$dQ = \rho_r 4\pi r^2 dr \quad (4.39)$$

If we integrate the charge contained in such a thin shell of infinitesimal thickness dr with respect to the radius r of the ionic cloud, then we can obtain the charge contained in the entire ionic cloud, *i.e.*

$$Q_{\text{cloud}} = \int_0^{\infty} \rho_r 4\pi r^2 dr \quad (4.40)$$

The lower limit of the integration is set at 0 because we have considered the central ion as a point charge with a radius of zero, while the upper limit is set as ∞ because we want to make sure that all charges in the ionic cloud are encompassed. Inserting the expression for ρ_r obtained from the linearized solution of the Poisson-Boltzmann equation, we will have

$$Q_{\text{cloud}} = \int_0^{\infty} \frac{z_i e_0}{4\pi} K^2 \frac{e^{-Kr}}{r} 4\pi r^2 dr = -z_i e_0 \int_0^{\infty} e^{-Kr} (Kr) d(Kr) \quad (4.41)$$

The integration is easy, and the result is apparent as

$$Q_{\text{cloud}} = -z_i e_0 \quad (4.42)$$

In other words, in an ionic cloud around a central ion that carries a charge $+z_i e_0$, the entire ionic cloud itself must contain a net excess charge of $-z_i e_0$.

Well, this result is nice but not surprising, because that was what we assumed in the first place. Nevertheless, being able to derive this result from the Debye-Hückel model with mathematical rigor does give us confidence in the model and its accuracy after all of these simplifications and assumptions.

4.6.2 The Lewis-Randall Empirical Law

The most famous verification of the Debye-Hückel model perhaps comes from the derivation of the Lewis-Randall empirical law.² Remember that the law was established based on extensive experimental data and related mean activity coefficient (γ_{\pm}) to ionic strength (I) as follows:

$$\log(\gamma_{\pm}) = -C\sqrt{I} \quad (4.43)$$

At first glance, one would find it unthinkable to derive such a relation from the Debye-Hückel model, as neither γ_{\pm} nor I exists in the core expressions of the Debye-Hückel model for ψ_r or ρ_r . However, let us first expand ψ_r into a non-exponential form by using

$$e^{-x} \approx 1-x \text{ if } x \ll 1 \quad (4.44)$$

Hence e^{-Kr} will turn into

$$e^{-Kr} \approx 1 - Kr \quad (4.45)$$

and the Debye–Hückel solution for ψ_r becomes

$$\psi_r = \frac{z_i e_0}{\epsilon} \frac{e^{-Kr}}{r} = \frac{z_i e_0}{\epsilon r} - \frac{z_i e_0}{\epsilon} K \quad (4.46)$$

Let us examine this new linearized equation for the electrostatic field (ψ_r) in the ionic cloud at a distance r from the central ion. It should immediately become apparent that the first term is the electrostatic field established by the central ion carrying a charge of $+z_i e_0$.

What does the second term represent, then?

According to the additive nature of field, the overall electrostatic field (ψ_r) in the ionic cloud at r must be the net result after the fields from the central ion and the ionic cloud cancel each other out. Therefore, the second term is the electrostatic field provided by the ionic cloud itself:

$$\psi_{\text{cloud}} = -\frac{z_i e_0}{\epsilon} K = -\frac{z_i e_0}{\epsilon K^{-1}} \quad (4.47)$$

Remember that earlier in eqn (4.25) we introduced the new constant K as a convenience to circumvent the trouble of writing long equations. However, now this parameter K seems to carry a certain physical meaning. By comparing the second term with the first term, K^{-1} seems to stand for a quantity that represents some sort of dimensional length. We will come back to revisit this point later, as now we must continue the effort to correlate mean activity coefficient (γ_{\pm}) with ionic strength (I).

Having obtained the electrostatic field exerted by the ionic cloud itself, we can now evaluate the electric work (W_e) required for the ionic cloud to establish such a field, that is, charging up an imaginary ion from zero charge to the full charge $z_i e_0$, which should be

$$W_e = \int_0^{z_i e_0} \psi_r d(z_i e_0) = \int_0^{z_i e_0} \left(-\frac{z_i e_0}{\epsilon K^{-1}} \right) d(z_i e_0) \quad (4.48)$$

This simple integration yields W_e as

$$W_e = -\frac{1}{2} \frac{1}{\epsilon K^{-1}} (z_i e_0)^2 \quad (4.49)$$

Now it is time to recall that, according to our very initial assumption, it was this electric work that forces the electrolyte solutions to depart from the ideal behaviors observed with dilute non-electrolyte solutions and, in order to account for such a departure, mean activity coefficients (γ_{\pm}) were introduced. In other words, the chemical potential μ_i of the i th ion is distorted by this electric work from that of the ideal solution *via*

$$\mu_i = \mu_i^0 + kT \ln(a_i) + W_e \quad (4.50)$$

where μ_i^0 and a_i are the standard chemical potential and activity, respectively, of the i th ion, and k is the Boltzmann constant. Here, the activity coefficient finally shows up *via* the activity (a_i):

$$W_e = \mu_i - \mu_i^0 - kT \ln(a_i) = kT \ln(\gamma_i) = \frac{1}{2} \frac{1}{\varepsilon K^{-1}} (z_i e_0)^2 \quad (4.51)$$

or, after rearrangement:

$$\ln(\gamma_i) = -\frac{(z_i e_0)^2 K}{2 \varepsilon k_B T} \quad (4.52)$$

We have mentioned previously that the activity coefficient for an individual ion is not experimentally measurable, hence we bring back the mean activity coefficient for an electrolyte of formula $A_n B_m$:

$$\bar{\gamma}_{\pm} = \sqrt[n+m]{\gamma_A^n * \gamma_B^m} \quad (4.53)$$

or

$$\ln(\bar{\gamma}_{\pm}) = \frac{n}{n+m} \ln(\gamma_A) + \frac{m}{n+m} \ln(\gamma_B) \quad (4.54)$$

In an electrolyte, electroneutrality requires that $nZ_A = mZ_B$, where Z_A and Z_B are the valences of these ions. After some algebraic manipulations and simplifications, we obtain

$$\ln(\bar{\gamma}_{\pm}) = -|Z_A Z_B| \frac{e_0^2 K}{2 \varepsilon k_B T} \quad (4.55)$$

It is time to bring back the definition of K :

$$K^2 = \frac{4\pi}{\varepsilon k_B T} \sum_i n_i^0 z_i^2 e_0^2 \quad (4.25)$$

and to rewrite n_i^0 therein in terms of concentration (c_i):

$$n_i^0 = \frac{c_i N_A}{1000} \quad (4.56)$$

$$K^2 = \frac{4\pi}{\varepsilon k_B T} \frac{N_A e_0^2}{1000} \sum c_i z_i^2 \quad (4.57)$$

Remember the definition of ionic strength, I :

$$I = \frac{1}{2} \sum_{i=1}^n c_i z_i^2 \quad (4.58)$$

We then have the expression of K as

$$K^2 = \frac{8\pi N_A e_0^2}{1000 \varepsilon k_B T} I \quad (4.59)$$

The ionic strength (I) finally shows up!

We insert the above expression into eqn (4.55) for the mean activity coefficient:

$$\ln(\gamma_{\pm}) = -|Z_A Z_B| \frac{e_0^2}{2 \varepsilon k_B T} \sqrt{\frac{8\pi N_A e_0^2}{1000 \varepsilon k_B T}} \sqrt{I} \quad (4.60)$$

This is exactly the empirical relation established by Lewis and Randall:

$$\log(\gamma_{\pm}) = -C \sqrt{I} \quad (4.61)$$

We can now appreciate the beauty of the Debye–Hückel model, where the bold simplification was made by viewing all other ions around the central ion as an ionic cloud, and an elegant mathematical relationship was derived that finally connected to an experimentally observed quantity in a quantitative manner. Of course, based on the assumptions adopted during its derivation, the relation holds true only for strong electrolytes at extremely dilute concentrations, just as Lewis and Randall found. Thus, eqn (4.60) was also known as the *Debye–Hückel limiting law*, where “limiting” stands for infinite dilution.

Excellent experimental agreement has been found for this law in various 1:1 strong electrolyte solutions (such as NaCl) at extremely dilute concentrations (10^{-4} – 10^{-2} M). However, significant deviations

still occur for 2:2 electrolytes (such as magnesium sulfate, MgSO_4) or 2:3 electrolytes [such as aluminum sulfate, $\text{Al}_2(\text{SO}_4)_3$] or for all electrolytes at high solute concentrations. Nevertheless, an extremely simplified model as represented in Figure 4.1 provides accurate predictions of an experimentally observable quantity, hence the significance of the Debye-Hückel model in the theoretical understanding of electrolytes can never be overestimated.

4.6.3 The Kohlrausch Empirical Law

In addition to the Lewis-Randall empirical law, the Debye-Hückel model can also be transformed into the Kohlrausch empirical law,³ which we will discuss here only briefly, leaving the details to a later section on ion transport.

At the instant a central ion is placed under an external electrostatic field, it moves with the driving force applied by the field, and hence departs from the spherical center of the ionic cloud. As the central ion continues to move under a constant field, it continues to recruit new ions into the ionic cloud at its front (because these new ions are entering its Coulombic field), while losing ions at its tail (because those old ions are leaving the grip of its Coulombic field). Now the ionic cloud loses its spherical symmetry and becomes elongated along the path of the ionic movement (Figure 4.4). Such distortion of the ionic cloud will create two separate forces on the movement of the central ion:

1. The distorted ionic cloud now has an electric center that is no longer overlaid with the central ion, but instead is situated at a

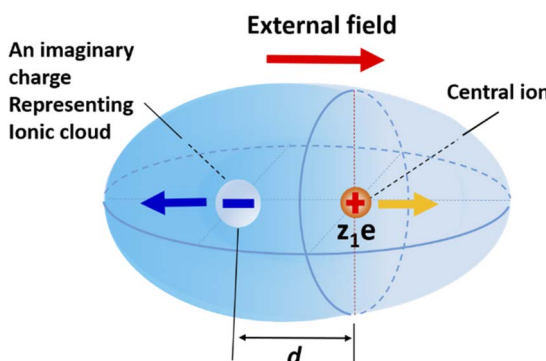


Figure 4.4 When the central ion moves under an external electrostatic field, its ionic cloud loses its spherical symmetry, and exerts counterforces on the moving central ion.

certain distance (d) away from the central ion. This equates to an additional field that opposes the external field applied. This effect is called the “*relaxation field*” from the ionic cloud because it relies on the continuous build-up and decay of the ionic cloud at the front and the tail, respectively.

2. While the central ion moves with the external field, its ionic cloud, which is of opposite charge, will move the other way. This introduces an additional force that drags the central ion. This effect is called the “*electrophoresis effect*” from the ionic cloud.

Both relaxation and electrophoresis are against the moving of the central ion. Onsager took into account those counterforces in the migration of ions, and was able to derive a theoretical expression for the molar conductivity (Λ_m) when measured under an AC field:

$$\Lambda_m = \Lambda_m^0 - (A + B\Lambda_m^0)\sqrt{c} \quad (4.62)$$

where A and B are constants that depend only on known quantities such as temperature, the charges on the ions and the dielectric constant and viscosity of the solvent. Eqn (4.62), known as the Debye–Hückel–Onsager equation, completely reproduces the empirical law of Kohlrausch at a more fundamental level.⁴

4.7 Revisiting Constant K : Debye–Hückel Thickness

We have mentioned earlier that K , although introduced initially as a convenience, turns out to carry a special physical meaning. This meaning becomes very clear when one compares the expression for the electrostatic field for the central ion (Coulomb's law):

$$\psi_{\text{central ion}} = \frac{z_i e_0}{\epsilon r} \quad (4.63)$$

with that for the ionic cloud:

$$\psi_{\text{cloud}} = -\frac{z_i e_0}{\epsilon} K = -\frac{z_i e_0}{\epsilon K^{-1}} \quad (4.64)$$

It is immediately apparent that K^{-1} is a length quantity and acts like an imaginary radius of the ionic cloud if one views the ionic cloud not as a diffused continuum but as a point charge (Figure 4.5).

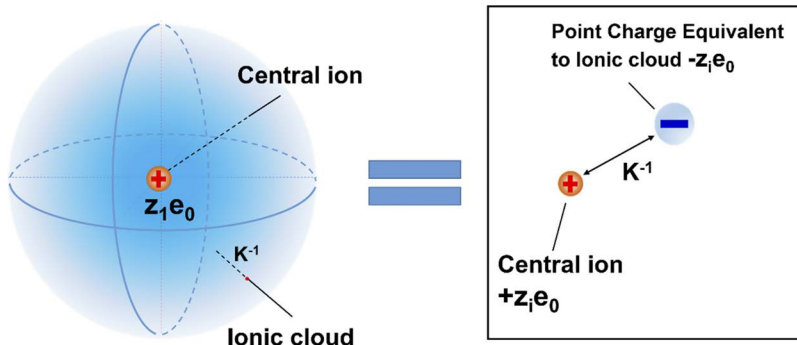


Figure 4.5 The physical meaning of K^{-1} : an ionic cloud can be viewed as a point charge sitting at a distance K^{-1} from the central ion.

More details about the physical meaning of K can be derived from further analysis performed on the amount of charges that an ionic cloud contains. As we have indicated, the total excess charge in a shell of thickness dr is given by

$$dQ = \rho_r 4\pi r^2 dr = -z_i e_0 K^2 r e^{-Kr} dr \quad (4.65)$$

Thus this charge amount varies with the distance from the central ion (r) and should reach a maximum in the middle. This maximum value would be given by

$$0 = \frac{dQ}{dr} = \frac{d}{dr} \left[-z_i e_0 K^2 (e^{-Kr} r) \right] = -z_i e_0 K^2 \frac{d}{dr} (e^{-Kr} r) \quad (4.66)$$

$$0 = \frac{dQ}{dr} = -z_i e_0 K^2 (e^{-Kr} - rKe^{-Kr}) \quad (4.67)$$

Because $z_i e_0 K^2$ is a non-zero quantity, the above relation remains true only if

$$0 = e^{-Kr} - rKe^{-Kr} \quad (4.68)$$

or, after rearrangement:

$$e^{-Kr} = rKe^{-Kr} \quad (4.69)$$

In other words:

$$r = K^{-1} \quad (4.70)$$

This is a very interesting result, meaning that at $r = K^{-1}$, the value of the excess charge contained in a spherical shell of infinitesimal thickness dr reaches the maximum (Figure 4.6a). For this reason, K^{-1} can

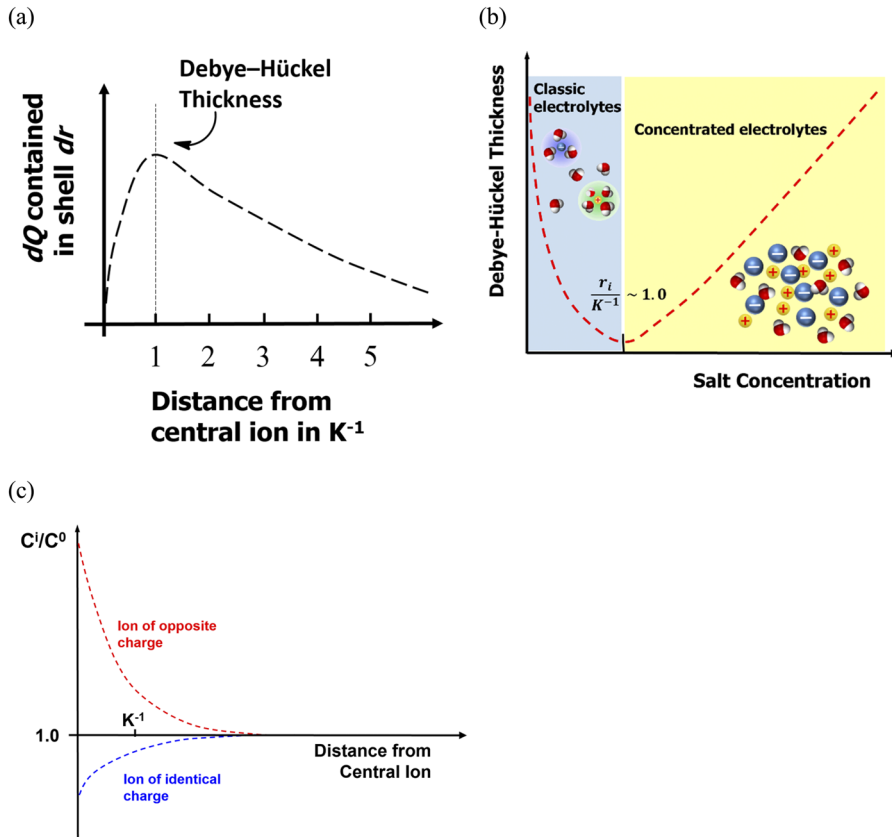


Figure 4.6 (a) Dependence of charge contained in a shell of infinitesimal thickness dr on the distance of the shell from the central ion. The distance is now measured in units of K^{-1} . (b) Concentration dependence of the Debye-Hückel thickness: in dilute electrolytes, the Debye-Hückel thickness decreases with increase in salt concentration, as predicted by eqn (4.25); in concentrated electrolytes, the Debye-Hückel thickness shows an abnormal deviation that is governed by ion size effects (steric and volume exclusion) and also the intensified interionic correlations. (c) Distribution of ions that bear charges identical with or opposite to that of the central ion with distance from the central ion.

be viewed as the effective radius of the ionic cloud. Researchers often referred to K^{-1} as the *Debye-Hückel thickness* (sometimes also known as the *Debye length* and denoted λ_D):

$$K^{-1} \text{ (or } \lambda_D) = \sqrt{\frac{\varepsilon k_B T}{4\pi} \frac{1}{\sum_i n_i^0 z_i^2 e_0^2}} \quad (4.71)$$

Apparently, the Debye-Hückel thickness varies with both ionic strength (or valence) and concentration. Table 4.1 lists K^{-1} for various electrolyte types at different concentrations, which are on the nm (10^{-9} m) scale. Higher ionic strengths and higher concentrations compress the Debye-Hückel thickness of ions, whereas at higher temperatures thermal agitation promotes the random movement of the ions, thus rendering the ionic cloud more diffuse with greater Debye-Hückel thickness. At a salt concentration of 0.1 M and a temperature of 25 °C, the Debye-Hückel thickness is estimated to be *ca.* 0.96 nm if the salt is monovalent (such as NaCl), which is approximately equivalent to the diameter of four water molecules, whereas at a lower salt concentration of 0.001 M, the Debye-Hückel thickness increases to 9.6 nm, which is a thick layer consisting of ~40 water molecules. However, eqn (4.71) applies only in dilute electrolytes, where the ionic sizes are far smaller than both the Debye-Hückel thickness and the average interionic distances, where the interionic correlations can be ignored. As the salt concentration increases to a certain threshold, an abnormal concentration dependence of the Debye-Hückel thickness occurs (Figure 4.6b). The minimum Debye-Hückel thickness seems to occur when its predicted value approached the size of the ion (r_i).

Finally, it should be noted that the concept of Debye-Hückel thickness is not confined to electrolytes. It actually describes in general how charged particles become distributed under the influence of a Coulombic field, no matter where the Coulombic field is generated. For example, the concept of Debye-Hückel thickness can be extended to define the effective thickness of electrode/electrolyte interfaces,

Table 4.1 Debye-Hückel thickness/nm calculated for various electrolyte types at different concentrations.

Type	Concentration/M			
	0.0001	0.001	0.01	0.1
1:1 (e.g. NaCl)	30.4	9.6	3.04	0.96
1:2 (e.g. MgCl ₂)	17.6	5.55	1.76	0.55
2:2 (e.g. MgSO ₄)	15.2	4.81	1.52	0.48

provided that one views the electrode as a giant, two-dimensional ion, which is discussed in more detail in Chapter 15. The Debye–Hückel thickness also transforms into an important parameter, the Garrett–Brattain thickness, when describing the distribution of space charge in semiconductors. An extreme scenario of the Debye–Hückel thickness exists in space plasmas such as solar wind and interstellar media, where the charged particle density is so low (10^{-17} – 10^{-23} M) that the Debye–Hückel thickness of these particles may reach macroscopic values ranging from 1 m to 100 km!

4.8 Refinement of the Debye–Hückel Model: Finite-sized Central Ion

So far we have been treating the central ion as a point charge, *i.e.* without size. This assumption is reflected in eqn (4.72) when the excess charge (dQ) contained in a shell of infinitesimal thickness dr was integrated from “zero” to infinity in order to obtain the overall charge quantity contained in the ionic cloud:

$$Q_{\text{cloud}} = \int_0^{\infty} \rho_r 4\pi r^2 dr \quad (4.72)$$

However, ions in reality, including the smallest of all (protons), are particles of finite size. How would the approximation of point charge impact the accuracy of the solutions that we have obtained so far?

Examination of Table 4.1 reveals that, as the solute concentration increases from 0.0001 to 0.1 M, the ionic cloud radius (Debye–Hückel thickness) decreases from \sim 30 to <1 nm. Obviously the central ion would look less and less like a point charge when the solute concentration increases, making the approximation of the Debye–Hückel model less valid. This is one of the reasons (but not the only reason!) behind the fact that the Debye–Hückel model demonstrates large departures in predicting properties such as molar conductivity and mean activity coefficients in concentrated electrolytes.

A simple thought would be that the above integration should start not at zero but instead at some distance (a) from the central ion. Reviewing the process that we have gone through so far, we found that the solution of the linearized Poisson–Boltzmann equation did not involve the point charge assumption:

$$\psi_r = A \frac{e^{-kr}}{r} \quad (4.73)$$

However, the evaluation of parameter A did so. Therefore, we can start over from the effort of calculating excess charge contained in a volume element of infinitesimal thickness dr :

$$dQ = \rho_r 4\pi r^2 dr \quad (4.74)$$

The charge density ρ_r is thus

$$\rho_r = -\frac{\varepsilon}{4\pi} \left[\frac{1}{r^2} \frac{d}{dr} \left(r^2 \frac{d\psi_r}{dr} \right) \right] = -\frac{\varepsilon}{4\pi} K^2 \psi_r = -\frac{\varepsilon}{4\pi} K^2 A \frac{e^{-Kr}}{r} \quad (4.75)$$

Then the integration for the total excess charge in an ionic cloud becomes

$$Q_{\text{cloud}} = \int_a^\infty dQ dr = -AK^2 \varepsilon \int_a^\infty e^{-Kr} r dr = -A\varepsilon \int_a^\infty Kr e^{-Kr} d(Kr) \quad (4.76)$$

Here a is set as a lower limit, which represents the starting point of an ionic cloud, or the smallest distance to the central ion that an ionic cloud could approach. On the other hand, we know that the result of the above integration must be $-z_i e_0$ as required by the electroneutrality of the whole electrolyte solution. Inserting this condition into eqn (4.76), we can solve for a new value for A , where no point charge assumption is involved:

$$A = \frac{z_i e_0}{\varepsilon} \frac{e^{Ka}}{1 + Ka} \quad (4.77)$$

With this new expression for A , we can obtain a less approximated expression for the potential ψ_r at a distance r from a central ion of finite size:

$$\psi_r = \frac{z_i e_0}{\varepsilon} \frac{e^{Ka}}{1 + Ka} \frac{e^{-Kr}}{r} \quad (4.78)$$

Since eqn (4.78) is a generalized expression for the potential as a function of distance from the central ion, one could combine it with eqn (4.16) (the ion concentration as a function of distance from the central ion governed by a Boltzmann distribution) and recalculate how ions of different charges distribute around a central ion. Figure 4.6c demonstrates the results of such a calculation assuming that both cation and anion are monovalent.

It is apparent that, while the ratio of the two ions approaches 1.0 at distances sufficiently far away from the central ion, the concentration of the ions that bear the *opposite* charge to the central ion increases exponentially in the vicinity of the central ion, because of the Coulombic attraction. Conversely, the concentration of the ions that bear a charge *identical* with that of the central ion decreases dramatically, because of the Coulombic repulsion. At the Debye–Hückel thickness K^{-1} there is a significant difference between the concentrations of the two ions, hence we can state that the ionic cloud acts as if it is an ionic shield carrying opposite charge around the central ion at a distance of K^{-1} .

Also derived from eqn (4.78), the expression for the mean activity coefficient is modified to

$$\log(\gamma_{\pm}) = -A(Z_A Z_B) \frac{\sqrt{I}}{1 + a / K^{-1}} \quad (4.79)$$

In practice, the parameter a in eqn (4.78) and (4.79) is called the *ion size parameter*, the value of which is considered to be situated somewhere between the sum of the cationic and anionic radii in the crystal and the sum of their corresponding solvated sheath sizes (Figure 4.7). This intermediate value (a_2) is known as the *effective ionic radius* in electrolyte solutions.

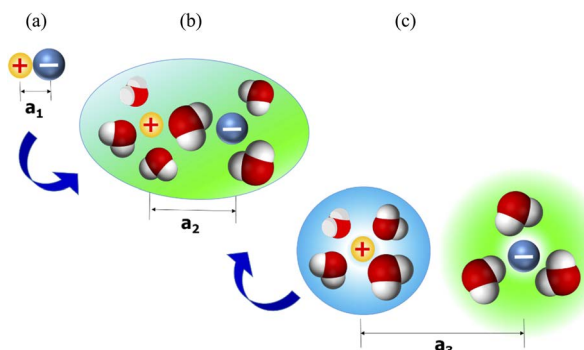


Figure 4.7 The three possible scenarios for the ionic parameter a : (a) the sum of the ionic radii of cation and anion from their distance in the crystal; (b) the interionic distance between cation and anion in a condensed solvation sheath; (c) the sum of the radii of the respective solvation sheaths.

4.9 Refinement of the Debye-Hückel Model: Ion-pair Formation and Bjerrum Length

The Debye-Hückel model paints a static picture of how charged particles (ions) are distributed when governed by a Coulombic field. In fact, by assuming $z_i e_0 \psi_r \ll k_B T$ in order to linearize the Poisson-Boltzmann equation, Debye and Hückel implied that the distribution of ions is dictated by the Coulombic force while subject to little influence from the random thermal motions of the ions. However, this assumption could be problematic, as in reality thermal motions of both solvated ions and solvents are pervasive, while slight deviations from randomness caused by Coulombic interactions lead to excess charges in the ionic cloud. Hence the possibility always exists that an anion in the ionic cloud occasionally approaches closer to a cation than it should in an ionic cloud at equilibrium. Such an intimate encounter between ions of opposite charge would lead to a strong attraction between the two, so strong that the thermal translational energy would not be sufficient for the cation and anion to escape from the Coulombic trap on a certain time scale. Bjerrum suggested that an *ion pair* forms as the result.⁵

Such an ion pair can be viewed as an ionic dipole: it is neutral as a whole entity, hence it makes no net contribution to the ionic cloud, nor does it feel the Coulombic field from the central ion. Its existence is dynamic, as eventually the thermal collisions from solvent molecules or other ions could break the cation and anion apart, but on average a certain fraction of ion pairs is always present throughout the ionic cloud.

To estimate this fraction, let us consider again a spherical shell of infinitesimal thickness dr . The probability of the presence of an anion in this shell (P_r^-) is proportional to the following factors: (1) the volumetric fraction of the shell to the whole sphere ($4\pi r^2/V$, where V is the sphere volume); (2) the total anion populations (N_-) in the sphere; and (3) the Boltzmann factor $\exp(-U/k_B T)$, where U is the potential energy of the anion at a distance r from a cation. P_r^- can therefore be expressed as

$$P_r^- = 4\pi r^2 dr \frac{N_-}{V} e^{-\frac{U}{k_B T}} \quad (4.80)$$

Since N_-/V is the bulk concentration of the anion n_-^0 , and the potential energy U is defined as

$$U = -\frac{z_+ z_- e_0^2}{\epsilon r} \quad (4.81)$$

we can write P_r^- as

$$P_r^- = (4\pi n_-^0) r^2 e^{\frac{z_+ z_- e_0^2}{\varepsilon r k_B T}} dr \quad (4.82)$$

If we introduce a new quantity λ_B :

$$\lambda_B = \frac{z_+ z_- e_0^2}{\varepsilon k_B T} \quad (4.83)$$

Then

$$P_r^- = (4\pi n_-^0) r^2 e^{\frac{\lambda_B}{r}} dr \quad (4.84)$$

This is the probability of finding an anion in the ionic cloud shell at a distance r from the central cation. A similar equation should exist for the probability of finding a cation P_r^+ in the ionic cloud shell at a distance r from the central anion, or in general, the probability of finding an ion in the ionic cloud shell at a distance r from the central ion of opposite charge:

$$P_r^i = (4\pi n_i^0) r^2 e^{\frac{\lambda_B}{r}} dr \quad (4.85)$$

When r is sufficiently small, P_r^i is dominated by the exponential term $e^{\frac{\lambda_B}{r}}$ while r^2 is insignificant, so P_r^i increases at an exponential rate in the tiny region of the ionic cloud close to the central ion. On the other hand, when r is sufficiently large, P_r^i would be dominated by r^2 and increase with interionic distances. In other words, P_r^i reaches a minimum at intermediate r (Figure 4.8). This dependence of P_r^i on the interionic distance r can be understood in a simpler manner: when r is small, *i.e.* in a shell close to the central ion, ions of the opposite charge are more likely to appear; When r is large, the sheer ion population contained in the shell volume of $4\pi r^2 dr$ ensures that ions of opposite charge will exist.

One must remember here that P_r only represents the probability of ions of opposite charge coexisting. However, such coexistence does *not* necessarily guarantee the formation of ion pairs. To form an ion pair, the ions of opposite charge must be close enough so that their Coulombic interaction could overcome the random thermal motions

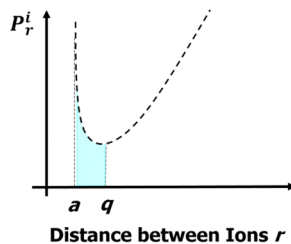


Figure 4.8 The probability of oppositely charged ions coexisting at a distance r , and the probability of ion-pair formation as represented by the shaded area under the curve between distances a and q .

that would otherwise knock them apart. In other words, the high probability P_r found at large r does not really help ion-pair formation.

We therefore define an upper limit of distance q , above which, although ions of opposite charge find each other, they are too far away from each other to form ion pairs. Hence the probability of ion-pair formation is the integral of P_r with respect to r between a lower limit a (the closest interionic distance possible) and an upper limit q :

$$\theta = \int_a^q P_r dr = \int_a^q 4\pi n_i^0 e^{-\frac{\lambda_B}{r}} r^2 dr \quad (4.86)$$

We have previously discussed the possible values of a , also known as the effective ionic radius for ions of finite sizes. The integration is shown as the shaded area under the curve in Figure 4.8 between ion-ion distances a and q , and Bjerrum argued that ion-pair formation is only possible in such a shadowed area. The value of q , which corresponds to the distance r_{\min} at the minimum of P_r , can be obtained by

$$0 = \frac{dP_r}{dr} = \frac{d}{dr} \left[\left(4\pi n_i^0 \right) r^2 e^{-\frac{\lambda_B}{r}} \right] = 4\pi n_i^0 e^{-\frac{\lambda_B}{r}} 2r - 4\pi n_i^0 r^2 e^{-\frac{\lambda_B}{r}} \frac{\lambda_B}{r^2} \quad (4.87)$$

Solving for r that corresponds to the minimum P_r :

$$2r_{\min} = 2q = \lambda_B \quad (4.88)$$

or

$$q = \frac{\lambda_B}{2} = \frac{z_+ z_- e_0^2}{2\epsilon k_B T} \quad (4.89)$$

Like the Debye–Hückel thickness, λ_B also has the unit of length. It is known as the *Bjerrum length*, which defines the upper limit of ion-pair formation: if the distance between two ions of opposite charge is larger than $\lambda_B/2$, these ions can be considered free; otherwise, they are likely captured by each other's Coulombic trap and become a pair.

Apparently, the dielectric constant of the medium, *i.e.* the solvent molecules, plays a major role in determining the Bjerrum length, and hence the degree of ion pairing. For example, in a dilute (0.1 m) electrolyte consisting of a lithium salt in water, the Bjerrum length is estimated to be 0.7 nm, because the water molecule is such a strongly dielectric medium ($\epsilon = 78$) that can effectively shield the Coulombic field of an ion. However, in a polymer electrolyte consisting of a polyether medium ($\epsilon = 7.5$), the Bjerrum length is 7.0 nm. An increase in the Bjerrum length significantly lowers the threshold for the formation of ion pairs.

The ion-pair fraction in a given electrolyte can be estimated based on the above definition:

$$\theta = 4\pi n_i^0 \int_a^{\frac{\lambda_B}{2}} e^{-\frac{\lambda_B}{r}} r^2 dr \quad (4.90)$$

Hence the ion-pair fraction in a given electrolyte can be calculated if the ion effective radius, dielectric constant and solute concentrations are known.

4.10 A Quick Comparison Between Debye–Hückel Thickness and Bjerrum Length

While both parameters stand for distances, what difference and commonality exist between Debye–Hückel thickness (λ_D) and Bjerrum length (λ_B)?

$$\lambda_D = \sqrt{\frac{\epsilon k_B T}{4\pi} \frac{1}{\sum_i n_i^0 z_i^2 e_0^2}} \quad (4.91)$$

$$\lambda_B = \frac{z_+ z_- e_0^2}{\epsilon k_B T} \quad (4.92)$$

Both were derived when we were looking at a shell of infinitesimal thickness dr in an ionic cloud that is located at a distance r from a central ion. The former describes the location where the quantity

of excess charge in the shell reaches a maximum, while the latter describes the upper distance below which the ions of opposite charge can be viewed as ion pairs. Both depend on the dielectric constant of the solvent but in a reversed manner: when the solvent is more polar (*e.g.* water), the Debye-Hückel thickness becomes greater because the electrostatic field from the central ion can affect other ions at further distances, hence the corresponding ionic cloud is larger; however, the Bjerrum length becomes smaller, and the ions are less likely to form ion pairs unless they are found at an extremely small distance.

On the other hand, the Debye-Hückel thickness varies with solute concentration: when the electrolyte becomes more concentrated, the ionic cloud radius is compressed, as Table 4.1 shows, but the Bjerrum length itself is independent of solute concentration, and remains a constant for a given solute-solvent system.

Finally, for most aqueous and non-aqueous electrolytes, the values of the Debye-Hückel thickness and Bjerrum length both lie in the range 10^{-1} - 10^1 nm. This heavy overlapping indicates that, even at low solute concentrations in solvents of high dielectric constant, the formation of ion pairs is inevitable.

4.11 Refinement of the Debye-Hückel Model: Ion-Solvent Interaction

So far, solvents have been treated as a homogeneous continuum of dielectric media without structure, represented by a simple constant (ϵ_r) in the Debye-Hückel model. Such a simplification obviously ignored the complicated features of solvents, which are much more than just a dielectric medium. In fact, soon after Debye and Hückel published their work, the question was raised whether ion-ion interactions were in fact overestimated compared with the contribution from the solvent molecules. After all, the primary driving force for the formation of an electrolyte is the solvation of ions by solvents, which overcomes the ion-ion interaction in ionophoric crystals. Ignoring ion-solvent interactions is destined to lead to trouble.

Such a suspicion was confirmed by the “weird” departure of the experimental mean activity coefficient from what was predicted by the Debye-Hückel model at high solute concentrations (Figure 4.9), where the activity coefficients become larger than unity!

Why is this weird?

Let us recall how the activity coefficient was created. Because of the ion-ion interactions in electrolytes, the ions are not behaving as if

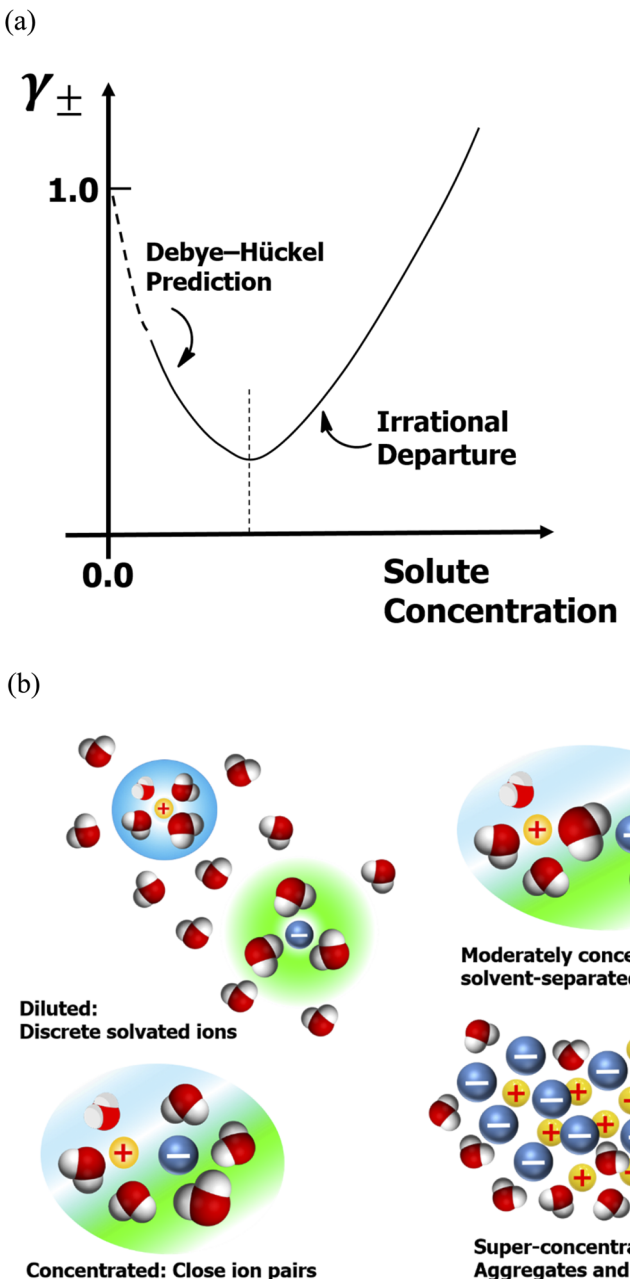


Figure 4.9 (a) The “irrational” departure of the mean activity coefficient from what is predicted by the Debye–Hückel model at high solute concentrations. (b) Transition from “dilute” to “super-concentrated” is accompanied by a change of liquid structures from “discrete solvated ions” to “solvent-separated ion pairs” and

there are fewer of them in the solution. In other words, the colligative properties show a negative departure from ideal behavior. To maintain apparent compliance with the ideal behavior, activity a was created as an apparent correction for the stoichiometric concentration c :

$$a = \gamma c \quad (4.93)$$

Therefore, $\gamma < 1.0$ provided that $c \geq 0$. However, a γ larger than 1.0 would mean a collapse of the above definition, because now a solute at a stoichiometric concentration of 1.0 M would behave as if there is 1.5 M solute in the electrolyte!

How was this possible? It turned out to be the consequence of ignoring ion–solvent interactions.

As we discussed earlier, the dielectric nature of polar solvent molecules makes them dipoles, which not only reorient themselves towards the electrostatic field of the ions, but also contribute to stabilization of the dissociated ions by forming solvation sheaths. The solvent molecules recruited by ions into their solvation sheath also cease to behave like the solvent molecules in the bulk.

When the solute concentrations are extremely low (*e.g.* 10⁻³ M), the number of solvent molecules in these solvation sheaths would be negligible. However, at 1 M solute concentration, the fraction of solvent molecules in the solvation sheaths would be high enough to affect the predictions made from the Debye–Hückel model. Taking an aqueous electrolyte as an example, assuming that the solvation (or hydration) numbers for the cation and anion are 4, then at 1 M solute concentration there would be 8 M water molecules in the cation and anion solvation sheaths in total, which accounts for *ca.* 14% (= 8/55.55) of the entire water molecules available in the electrolyte!

It was therefore suspected that the sharp “irrational” departure of the Debye–Hückel model from experimental data for the mean activity

“close ion pairs”, until “aggregates and networks”. In discrete solvated ions, each solvation sheath consists of three layers, the primary and the secondary solvation sheaths and the bulk free solvent, whereas in a super-concentrated electrolyte the solvation sheath is no longer discernible owing to the insufficiency of solvent molecules and the presence of anions in the close vicinity of the central cation. The intermediate states between these two extremes represent the most frequently encountered liquid structures of the electrolytes in actual electrochemical devices.

coefficient is induced by such a reduction of bulk solvent molecules at high solute concentration (Figure 4.9).

To account for such a departure, one can qualitatively imagine that, at very high solute concentrations, the number of effectively free solvent molecules is significantly reduced because of the population of those solvent molecules recruited into the solvation sheaths. Remember that the purpose of the activity coefficient is to multiply the stoichiometric solute concentration so that it will match the properties measured experimentally. Hence, at high concentrations, the many fewer effectively free solvent molecules push the real solute concentration even higher than the stoichiometric number implies. The net consequence is therefore an apparent increase in the activity coefficient being artificially applied, so that its multiplication effect can catch up with this high solute concentration. Sometimes these increases in activity coefficients are more than what is required to compensate the loss caused by ion–ion interactions, and the irrational departure ($\gamma > 1.0$) occurs as shown in Figure 4.9a.

A more rigorous and quantitative approach was adopted by Stokes and Robinson,⁵ who compared how the solute concentration (C) would be impacted as water molecules are removed as effective solvents at high concentration:

Before water removal: $C_1 = n/(n_w + n)$, where n and n_w represent the moles of solute and water, respectively. After water removal: $C_2 = n/(n_w + n - n_h)$, where n_h represents the moles of water in the hydration sheath. Such removal of water molecules as the result of solvation sheath recruitment would thus incur a change in free energy when the ions are solvated by the solvent molecules. The details of the mathematical treatment will not be covered here. The final revised form of the mean activity coefficient becomes

$$RT \log(\gamma_{\pm}) = -\frac{A\sqrt{I}}{1 + Ba\sqrt{I}} - 2.303 RT \frac{n_h}{n} \log(a_w) + 2.303 RT \log\left(\frac{n_w + n}{n_w + n - n_h}\right) \quad (4.94)$$

where a_w is the activity of water, which should be 1.0 in neat water and <1 when there is solute.

A quick glance at the equation would identify the first term as the Coulombic factor, which we are already familiar with, while the second and third terms obviously are related to the ion–solvent interactions that the original Debye–Hückel model ignored. Since $a_w < 1.0$, both solvent terms should be positive, and their competition with

the Coulombic term determines how the mean activity coefficient changes with solute concentration.

At very low solute concentrations, both solvent terms approach zero because

$$n_h \rightarrow 0, a_w \rightarrow 1.0 \text{ and } \frac{n_w + n}{n_w + n - n_h} \approx 1.0 \quad (4.95)$$

Hence we would be left with the Coulombic term, indicating that the water removal effect is negligible, and the ion-ion interaction prevails, hence $\gamma < 1.0$.

At very high solute concentration, however, the sum of these two solvent terms could overwhelm the Coulombic term and drive the mean activity coefficient to higher values. At a certain intermediate concentration, when the Coulombic and solvent terms cancel each other out, the mean activity coefficient experiences a minimum, which is exactly what experimentalists observed.

Stokes and Robinson applied this refined Debye-Hückel model to aqueous NaCl solutions, and found that it can now accurately predict the mean activity coefficients up to 5 M!

4.12 The Successes and Limitations of the Debye-Hückel Model

We have spent most of this chapter discussing the Debye-Hückel model, its mathematical solutions and its refinements. The importance of this model can never be overestimated, as it set the foundation for the modern understanding of electrolyte solutions. Before Debye and Hückel, all studies on electrolytes were experimental and empirical; it was Debye and Hückel who showed us that it is possible to establish an atomistic model and then link it to properties that are macroscopically verifiable. The significance of the Debye-Hückel model actually goes beyond electrolytes, as it provides a general description of how charged particles or objects interact with each other, examples of which include an electrified surface with dielectric media, electrons/holes in semiconductors, suspensions of colloids and even solar winds and plasma in interstellar space.

On the other hand, the many simplifications adopted by Debye and Hückel imposed constraints on the model, and departures from experiments occur whenever these simplifications are challenged, such as high solute concentrations (*e.g.* super-concentrated electrolytes for

batteries), incomplete dissociation of solutes (“weak” electrolytes), ion-pair formation in less polar solvents, ions with shapes that are far from spherical or with polyatomic structures (*e.g.* polyfluorinated anions used in lithium-ion batteries) or solvent molecules whose bipolar structure is spatially hindered (*e.g.* the carbonate solvents used in lithium-ion batteries), *etc.* For those electrolytes of practical importance in real devices, recent developments in computation chemistry using techniques such as *ab initio* quantum chemistry calculations or molecular dynamics provide increasingly accurate predictions, while empirical approaches are still necessary.

4.13 Liquid Structures: From Dilute to Concentrated and to Super-concentrated Regimes

What the Debye–Hückel model describes is actually a liquid structure for an ideal electrolyte, which consists of discrete solvated ions that are surrounded by solvent molecules to form their solvation sheaths. Each of these solvated ions affects each other’s behavior *via* the Coulombic force, which is strong at short distances, but rapidly disappears with the square of distance.

Such a picture exists only for dilute electrolytes at extremely low concentrations (<0.01 M). However, in practical electrochemical devices, such dilute electrolytes cannot provide sufficient ion transport to support the cell reactions, hence they find only limited applications in real life. The electrolytes used in practical electrochemical devices such as batteries, capacitors and electrolytic cells, on the other hand, are much more concentrated,⁶ where the solvated ions are forced into such close separations that the discrete solvation sheaths can no longer be discerned clearly. Hence transitioning from dilute electrolytes to more concentrated regimes experiences a gradual change of the liquid structures (Figure 4.9b).

There are no well-accepted and quantitative definitions to differentiate what concentration regime an electrolyte is in, but researchers often follow the customary standard as follows:

1. Dilute electrolytes (<0.01 M), where sufficient solvent molecules are available for the ions to recruit, and the solvation sheath takes the classical three-layer structure as proposed by Bernal and Fowler, in which the most immediate solvent molecules forms while the solvent molecules far away from the ion maintain

the undisturbed bulk structure. Somewhere between these two regions is an intermediate layer, the bulk structure of which is broken by the Coulombic field of the ion but their distance is not close enough to associate themselves with the moving ions (secondary solvation sheaths).

2. Moderately concentrated electrolytes ($\sim 1.0\text{ M}$), where the ions of opposite charges have sufficient opportunities to feel the Coulombic effect from each other. But overall, the cations and anions are still separated by solvent molecules. Electrolytes of this class are most widely used in diverse electrochemical devices, including lithium-ion batteries, mainly because the maximum ion conductivity occurs around this concentration.
3. Concentrated electrolytes ($>2.0\text{ M}$), where the insufficiency of solvent molecules leads to more intense cation–ion collisions, while solvent molecules have to be shared by different ions. In such cases, the average interionic distance frequently becomes smaller than half the Bjerrum length ($\lambda_B/2$) (Figure 4.8). Hence an appreciable fraction of ions spend most of the time in pairs.
4. Super-concentrated electrolytes ($>5\text{ M}$), where the extreme insufficiency of solvent molecules forces the cations and anions into more frequent and closer encounters, leading to the complete disappearance of solvation sheaths. In such an extreme scenario, the anion–cation distances are so compressed that they enter the primary solvation sheaths of each other. On a larger length scale, these ions exist in the form of aggregates, in which cations, anions and solvent molecules form interpenetrating but percolating networks, and the distribution of the ions and networks could be inhomogeneous owing to the uneven preferences of each ion for interacting with its neighboring species statistically.

Since the 2010s, the study of diversified super-concentrated electrolytes has led to the discovery of a host of unexpected properties, ranging from transport, thermal and mechanical to electrochemical, interfacial and interphasial, that are otherwise unavailable with moderately concentrated electrolytes.^{7,8} The primary limiting condition on whether a super-concentrated electrolyte can be formulated or not is apparently the solubility of a salt in a given solvent, which is related to the melting point of solvates, disorder and crystallization kinetics that can give rise to crystallinity and gaps at high salt concentrations. Only a few salts permit the formation of super-concentrated electrolytes, the most extreme and best known of which is perhaps the so-called “water-in-salt” electrolytes (WiSE),⁸ consisting of 21 m

of lithium bis(trifluoromethanesulfonyl)imide (LiTFSI) dissolved in water. Its solvent:salt ratio ($\text{H}_2\text{O}:\text{Li}^+$) is 2.64.

In WiSE, the above-mentioned inhomogeneity leads to a significant “disproportionation” in the Li^+ solvation sheath, resulting in a unique liquid structure where a high proportion (~40%) of Li^+ ions are exclusively surrounded by water molecules only, whereas the remainder (~60% of Li^+ ions) are mainly surrounded by TFSI.

In later derivatives of WiSE, the salt concentration has even been increased to 63 m, with the solvent:salt ratio ($\text{H}_2\text{O}:\text{salt}$) being 0.88. Such extreme insufficiency of water molecules per Li^+ ensures the disappearance of the hydrogen bond network that usually exists in water, and most chemical or electrochemical confinements imposed on conventional aqueous electrolytes are hence breached.

References

1. P. Debye and E. Hückel, Zur Theorie der Elektrolyte. I. Gefrierpunktserniedrigung und verwandte Erscheinungen, *Phys. Z.*, 1923, **24**, 185–206.
2. G. N. Lewis and M. Randall, *Thermodynamics and the Free Energy of Chemical Substances*, McGraw-Hill Book Co., New York, 1st edn, 1923.
3. F. Kohlrausch, *Leitvermögen der Elektrolyte*, Benedictus Gotthelf Teubner, Leipzig, 1898.
4. L. Onsager, Theories and problems of liquid diffusion, *Ann. N. Y. Acad. Sci.*, 1945, **46**, 241–265.
5. R. A. Robinson and R. H. Stokes, *Electrolyte Solutions*, Butterworths, London, 2nd edn, 1965.
6. K. Xu, Electrolytes and interphases in Li-ion batteries and beyond, *Chem. Rev.*, 2014, **114**, 11503–11618.
7. O. Borodin, J. Self, K. Persson, C. Wang and K. Xu, Uncharted waters: super-concentrated electrolytes, *Joule*, 2020, **4**, 69–100.
8. L. Suo, O. Borodin, T. Gao, M. Olguin, J. Ho, X. Fan, C. Luo, C. Wang and K. Xu, ‘Water-in-Salt’ Electrolyte Enables High Voltage Aqueous Li-ion Battery Chemistries, *Science*, 2015, **350**, 938–943.

5 Ion Transport in Electrolytes

So far, the ions that we have looked into were stationary. Now let us study how they move, either on their own (*diffusion*), or driven by an external field (*migration*). The former, induced by either Brownian motion of the ions and solvent molecules in the electrolytes, is random and does not create any global charge flow, whereas the latter creates a global directional movement of charges, or current, which is essential for an electrochemical device to sustain its operation. Migration is sometimes also called *conduction*. These two modes of motion (diffusion and migration) are not completely separated; on the contrary, they are closely interconnected, as both depend on how mobile the ions are in the electrolytes.

5.1 Ion Transport in the Absence of an External Field: Diffusion

Even when no external force (such as an external electric field) is applied, the ions are not stationary but instead are constantly moving in random directions, driven by the thermal collisions among the solvent molecules and fellow ions and any local uneven distribution of the ions. Such motion of particles, random in both direction and speed, has been well described in classical statistical mechanics that deals with gas behaviors. Most of the basic concepts and laws established therein apply to the strong electrolytes at dilute solute concentrations.

5.1.1 Fick's First Law: Steady-state Diffusion and Random Walk of Ions

Although the random motion of ions driven by thermal collisions does not create any net charge displacement (*i.e.* global current), it does cause local and instantaneous inequilibria in ion concentrations, which will produce group movement of ions in a preferred direction to eliminate such inequilibria. The instantaneous ionic movement will disappear momentarily when the concentration inequilibrium is eliminated, hence no sustained current is possible. Such inequilibria occur at every moment throughout the entire electrolyte solution, and the associated group movement of ions is possible in every direction. The “stationary” electrolyte solution is the statistical net result of such a dynamic “inequilibria-equilibria” process.

Imagine that in a local region and during an extremely short time interval Δt , a group of certain ion species i is moving in a given direction (say along an imaginary x -axis) because of the concentration difference (Figure 5.1). In this short interval Δt , we have a momentary ion transport, the rate of which is described by *flux*, defined as the number of moles of i passing a reference plane of unit area in unit time. Since the driving force for this ionic movement is the concentration gradient along the x -axis, *Fick's first law* applies:¹

$$J = -D \frac{dc_i}{dx} \quad (5.1)$$

where D is diffusivity (also called diffusion coefficient). It reflects how mobile the ions are given a certain concentration difference.

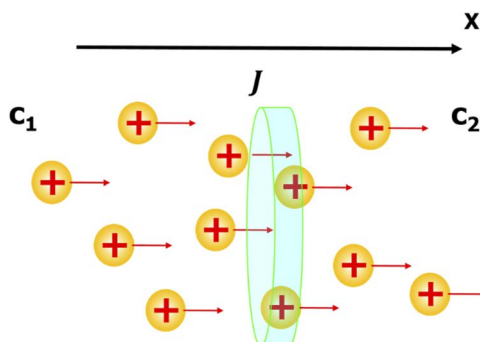


Figure 5.1 Diffusivity describes how mobile the ions are if given a concentration gradient.

Fick's first law is an empirical equation initially established for the diffusion of gaseous species, and its validity has been confirmed under steady-state conditions, where both the concentration gradient and the flux are constant and do not change with time. In a real electrolyte solution, the local concentration gradient is *constantly changing*, so the steady-state condition does not apply. However, as shown later, we can derive non-steady-state relations (*Fick's second law*) on its basis.

It must also be pointed out that the original Fick's law deals with gaseous species that are neutral molecules without charge, whereas in electrolytes ion–ion interactions strongly affect each other not only in the stationary distribution in space (Debye–Hückel model) but also in movement. The illustration in Figure 5.1 does not consider the presence of the counterions (*i.e.* the anions) and their Coulombic attraction on the moving cations, hence the ionic movement can only be ideally diffusional in nature when the electrolyte is extremely dilute, where ion–ion interactions are negligible compared with thermal collisions.

Ion–ion interactions also affect diffusivity, which depends on the activities of the ions. However, when only strong electrolytes at extreme dilutions are considered, ionic diffusivity can be treated as a constant independent of ion concentration.

Under ideal conditions mentioned above (strong electrolytes, extreme dilution), the ions in electrolytes can be considered as particles moving in random directions at random speeds. How far on average can an ion travel given a fixed time interval? This question is actually the famous "*drunken sailor's random walk*" problem in mathematics.

Imagine a drunken sailor emerges from a bar. In deep intoxication, he is able to move around but has completely lost orientation, hence each step he takes could be in any direction possible. Then, after certain time Δt , how far would he be from the origin?

To simplify the problem, we assume that the sailor lives in a one-dimensional world, where from the origin, each step he takes is either $+s$ or $-s$, where s is the length of a single step.

Let us suppose that at Δt he is ready to take the N th step, and his distance from the origin (the bar) is already x_{N-1} , thus the distance after he takes the N th step would be either $(x_{N-1} + s)$ or $(x_{N-1} - s)$, depending on in which direction his feet carry him:

$$x_N = x_{N-1} + s \quad (5.2)$$

$$x_N = x_{N-1} - s \quad (5.3)$$

We would have, respectively:

$$x_N^2 = x_{N-1}^2 + 2x_{N-1}s + s^2 \quad (5.4)$$

$$x_N^2 = x_{N-1}^2 - 2x_{N-1}s + s^2 \quad (5.5)$$

Adding these two equations together, we obtain

$$2x_N^2 = 2x_{N-1}^2 + 2s^2 \quad \text{or} \quad x_N^2 = x_{N-1}^2 + s^2 \quad (5.6)$$

Remember that x_{N-1} is the exact distance of the sailor before the N th step. In reality, we cannot know it for sure, but rather an average value $\langle x_{N-1}^2 \rangle$. In such a case, we rewrite the equation as

$$\langle x_N^2 \rangle = \langle x_{N-1}^2 \rangle + s^2 \quad (5.7)$$

What we do know for sure is that before the first step the sailor is at the origin:

$$\langle x_0^2 \rangle = 0 \quad (5.8)$$

at the first step:

$$\langle x_1^2 \rangle = \langle x_0^2 \rangle + s^2 = s^2 \quad (5.9)$$

at the second step:

$$\begin{aligned} \langle x_2^2 \rangle &= \langle x_1^2 \rangle + s^2 = 2s^2 \\ &\vdots \end{aligned} \quad (5.10)$$

and consequently at the N th step:

$$\langle x_N^2 \rangle = Ns^2 \quad (5.11)$$

where $\langle x_N^2 \rangle$ is the *mean square distance* that the sailor has traveled from the origin after a certain time t .

We started by trying to figure out how far the sailor is from the origin after a finite number of steps of random walk, but at the end of the

mathematics we did not obtain a distance, but instead a quantity that is the square of distance. How does this help us?

The calculation of uncertain quantities such as the probabilities of an occurrence within a given segment of time and/or space is impossible to conduct by a *deterministic* approach. Instead, we must take *stochastic* approaches, and learn to make use of non-deterministic results.

Since each step taken by the sailor is in a completely unexpected direction, it is impossible to tell accurately where he is after a finite time interval Δt . However, the theory of probability tells us that, since each step could be in either direction, the chance of $+s$ or $-s$ is equal (50%); therefore, as long as he walks for long enough (*i.e.* the number of steps he takes approaches infinity), he would most likely be back to where he started: the bar. In other words, the mean distance $\langle x_N \rangle$ must approach zero.

This result does not help us. In order to avoid such an unhelpful quantity, the mean square distance $\langle x_N^2 \rangle$ as a positive, non-zero quantity, while also related to the average distance traveled by the sailor, would offer much more help.

Let us return to the equation that links the mean square distance to the number of steps taken (N). Since N is proportional to the time (assuming that the sailor walks at a constant pace, which would be unusual for someone who is drunk but it simplifies the math here):

$$N = kt \quad (5.12)$$

We have

$$\langle x_N^2 \rangle = kts^2 = At \quad (5.13)$$

This is the general solution to the random walk problem. Although it was derived in a one-dimensional world, the result is universal for a two- or three-dimensional world. It tells us that, after a certain time interval, although we do not know where the drunken sailor is exactly, or where a randomly traveling ion is from the origin, the mean square distance in each case is proportional to the time, with A being the proportionality constant. Apparently, A reflects how agile the sailor is, or how mobile the ion is, because A is determined by two factors: the frequency of the steps and the length of each step.

Now we must evaluate what A is.

5.1.2 Einstein-Smoluchowski Equation

Consider an electrolyte solution in which the concentration of ion i varies along the x -axis, with concentration on the right-hand side of the reference plane (c_2) slightly higher than that on the left-hand side (c_1). For convenience, we set the area of the reference plane as unity and then place two additional planes of the same area at a distance $\sqrt{\langle x^2 \rangle}$ from the reference plane on both sides (Figure 5.2), so that the region of interest is partitioned by these three planes into two separate chambers of equal volume V :

$$V = \sqrt{\langle x^2 \rangle} \quad (5.14)$$

Hence the number of moles of ions in the left-hand chamber is $\sqrt{\langle x^2 \rangle}c_1$ and the number in the right-hand chamber is $\sqrt{\langle x^2 \rangle}c_2$. At time t , all these ions are doing a random walk. Since there is an equal chance that ions will move in either direction (*i.e.* $+x$ or $-x$), the number of moles of ions in the left-hand chamber that move in the $+x$ direction should be $\frac{1}{2}\sqrt{\langle x^2 \rangle}c_1$ and the number in the right-hand chamber that move in the $+x$ direction should be $\frac{1}{2}\sqrt{\langle x^2 \rangle}c_2$. Since $c_2 > c_1$, a net flow of ions occurs from right to left. In other words, the net flux of ions that cross the reference plane in unit time is

$$j = \frac{1}{2} \frac{\sqrt{\langle x^2 \rangle}}{t} (c_2 - c_1) \quad (5.15)$$

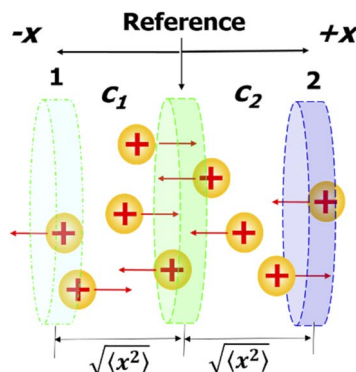


Figure 5.2 The one-dimensional random walk of ions in two chambers of equal volume ($V = \sqrt{\langle x^2 \rangle}$) adjacent to a reference plane of unit area.

Apparently, such a net flow of ions was driven by the concentration gradient along the x -axis and in the direction of $c_2 \rightarrow c_1$, which can be expressed as

$$\frac{dc}{dx} = -\frac{c_2 - c_1}{\sqrt{\langle x^2 \rangle}} \quad (5.16)$$

This can be rearranged into

$$c_2 - c_1 = -\sqrt{\langle x^2 \rangle} \frac{dc}{dx} \quad (5.17)$$

Inserting this expression of $(c_2 - c_1)$ into eqn (5.15):

$$j = \frac{1}{2} \frac{\sqrt{\langle x^2 \rangle}}{t} (c_2 - c_1) = -\frac{1}{2} \frac{\sqrt{\langle x^2 \rangle}}{t} \sqrt{\langle x^2 \rangle} \frac{dc}{dx} = -\frac{1}{2} \frac{\langle x^2 \rangle}{t} \frac{dc}{dx} \quad (5.18)$$

Comparing this equation with Fick's first law:

$$J = -D \frac{dc_i}{dx} \quad (5.1)$$

we obtain

$$D = \frac{1}{2} \frac{\langle x^2 \rangle}{t} \quad (5.19)$$

On rearranging this equation, we now have a new equation for the mean square distance $\langle x^2 \rangle$:

$$\langle x^2 \rangle = 2Dt \quad (5.20)$$

This is the *Einstein–Smoluchowski equation*.^{2,3} Through Fick's first law, this equation links the mean square distance for the random walk of ions to the diffusivity. On comparison with eqn (5.13), we also see what the proportionality constant A is

$$A = 2D \quad (5.21)$$

We have mentioned earlier that the constant A derived from the random walk should reflect how mobile the ions are. It is actually the diffusivity of the ions.

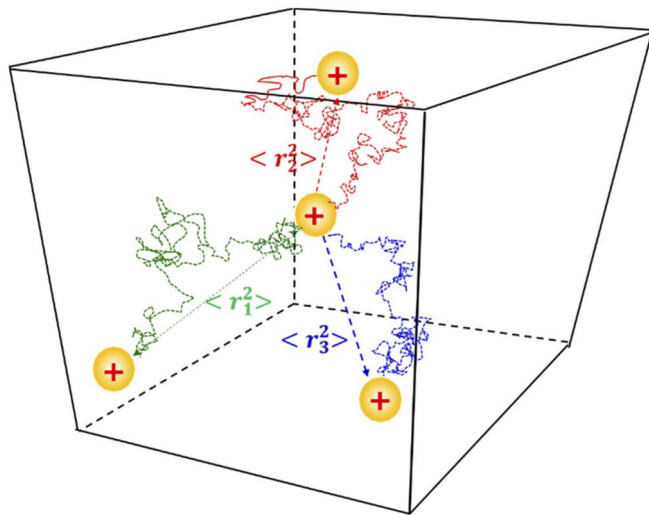


Figure 5.3 The random flight of an ion in a three-dimensional space still obeys the Einstein-Smoluchowski equation after slight modification.

Again, although the diffusion considered in Figure 5.2 is one-dimensional, the result can be extended to two- and three-dimensional situations. In a real electrolyte solution, ions fly randomly in three-dimensional space (Figure 5.3), and in a radial coordinate the Einstein-Smoluchowski equation can be modified to

$$\langle r^2 \rangle = 6Dt \quad (5.22)$$

As with Fick's first law, this result was only valid without taking into account the ion-ion interactions, so it should be regarded as an approximation of the ideal electrolyte (complete dissociation, extremely diluted).

5.1.3 Fick's Second Law: Non-steady-state Diffusion

Remember that Fick's first law was derived under steady-state conditions, *i.e.* both flux and concentration gradient are independent of time. In real electrochemical systems, such a steady state almost never exists or, if it does, only for transient moments. In most electrochemical devices and for most of the time, the diffusion of ions is created by inequilibria at concentrations that vary with time.

A typical example of such inequilibria is the lithium-ion battery, which is constructed on a pair of intercalation hosts as electrodes that sandwich a thin layer of electrolyte containing Li^+ ions (Figure 5.4a). In a simplified scenario (*i.e.* if we do not consider any external field or the existence of an interphase, which will be covered in later chapters), an equilibrium exists between the Li^+ ions in the electrode and

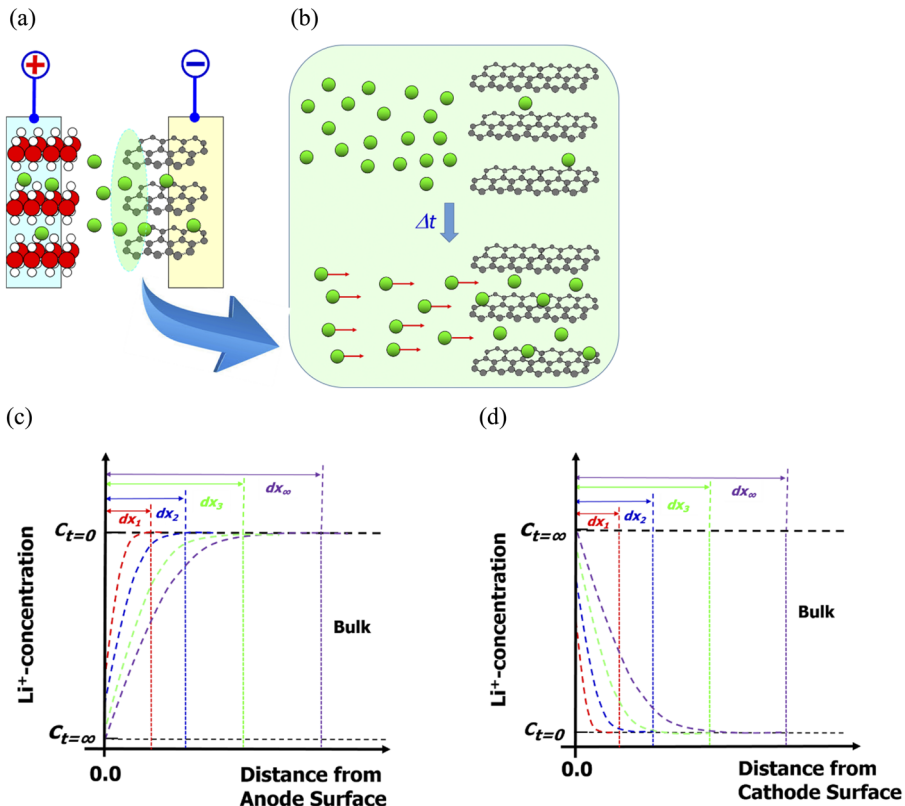


Figure 5.4 Real-life examples of non-steady-state ion diffusion. A lithium-ion battery (a) is plugged into a charger that applies a constant-current charging protocol (b), where Li^+ ions within the electrolyte/electrode interfacial regions suddenly are under an inequilibrium that drives them from the bulk electrolyte into the anode (graphite). (c) At the instant when the equilibrium is breached, a time-dependent concentration gradient is established, where not only does the concentration of Li^+ ions at the graphite/electrolyte interface (or interphase) change with both time (Δt) and distance (x) from the surface, but also the “front” facing the bulk concentration progresses into the bulk (dx). (d) A similar but reverse process occurring at the cathode/electrolyte interface region.

in the electrolyte (Note: here the equilibrium does not mean equal Li^+ concentrations, but rather equal chemical potentials determined by their respective solvation/bonding in the electrolyte and in the electrode interior). However, once the battery is plugged into a charger, the above equilibrium is breached, and Li^+ ions in the interface region face a concentration gradient that changes rapidly with time (Figure 5.4b), until a new equilibrium is established.

Suppose we are looking at the anode side, *e.g.* a graphite electrode, where Li^+ is intercalated in the charging process. Most chargers would apply a constant-current protocol at the beginning, hence a net and constant flux of Li^+ into the graphite is required. On the one hand, the Li^+ ions are being consumed by the electrode (the rate of which is controlled by the *charge-transfer limit* across the interface/interphase and within the electrode); on the other hand, the bulk electrolyte struggles to supply more Li^+ to the interfacial region (the rate of which is controlled by the *mass-transport limit* of the electrolyte), leading to part of the original interfacial regions also being depleted of Li^+ (Figure 5.4c). An equal but reverse process occurs at the cathode side during charging (Figure 5.4d): under the constant-flux mandate from the charger, Li^+ are released from the cathode layer structure and instantaneously accumulate at the cathode/electrolyte interface at $t = 0$. These released Li^+ ions diffuse into the bulk electrolyte (again, without considering the electric field and the existence of an interphase on the cathode surface), creating a time-dependent concentration gradient, and the rate of diffusion of Li^+ depends on how fast the electrolyte can transport these excess Li^+ ions into the bulk.

A new equilibrium will eventually be established at $t = \infty$, which will depend on the relative kinetics within the electrolyte and also within both electrodes (and their respective interphase if there is any). Identification of the controlling factor constitutes the key knowledge for designing a lithium-ion battery with a fast charging capability.

Of course, the above scenario is not confined just to lithium-ion batteries. In general, any electrochemical device that either consumes or generates a species at constant flux (or constant current) would fit into this description, examples of which include electrolyzers that perform electrochemical syntheses.

Another practical example of non-steady-state diffusion is called the “*instantaneous plane source*”, which is often encountered in the electroplating and corrosion industry.

Imagine that a metallic electrode is anodically (*i.e.* oxidatively) dissolved to provide a certain amount of metallic ions as source, which will be deposited at the other electrode. At $t = 0$, a pulsed current (i_p)

is applied to the electrode for a very short duration, then the current is switched off. The ions generated are accumulated at the electrode surface at $t = 0$, but soon this sheet of ions starts to diffuse into the bulk electrolyte driven by the concentration gradient created by the presence of this ionic sheet (Figure 5.5a). This concentration gradient fades with time, so the flux of ions gradually dies down. Eventually, a new equilibrium is established when the ion concentration at the electrolyte/electrode interface region and in the bulk electrolyte equalizes (Figure 5.5b). Again, this scenario is not confined just to electrolyzers or electroplating. For example, a lithium-ion battery that experiences a sudden pulse discharge in a cell phone would release a burst of Li^+ ions, which accumulate at the anode surface and then gradually diffuse into the bulk electrolyte. These Li^+ ions would serve as the instantaneous plane source, and how fast their built-up concentration at the anode can dissipate dictates how fast the lithium-ion battery can release energy (pulse discharging capability).

In both examples of “constant flux” and “instantaneous plane source”, one needs to know not only the concentration gradient (dc/dx) at an instant t , but also the change of the concentration gradient with time (dc/dt) at any x . This is exactly what Fick’s second law tried to solve, to establish a function for c and solve it under various initial and boundary conditions:

$$c = f(x, t) \quad (5.23)$$

To do that, let us now consider a region in the electrolyte enclosed by two planes of unit area at a distance dx , where the concentration gradient for a certain ion (dc/dx) is instantaneous and dynamic (Figure 5.6).

Assume that the concentration at the left-hand plane is c_1 , then the concentration at the right-hand plane (c_2) should be

$$c_2 = c_1 + \left(\frac{dc}{dx} \right) dx \quad (5.24)$$

Because of such a concentration gradient, there should be a net flux of ions passing through the region, the direction of which depends on the relative values of c_1 and c_2 . If $c_1 > c_2$, then according to Fick’s first law, the flux into the region from the left-hand plane is given by

$$J_{\text{in}} = -D \frac{dc}{dx} \quad (5.25)$$

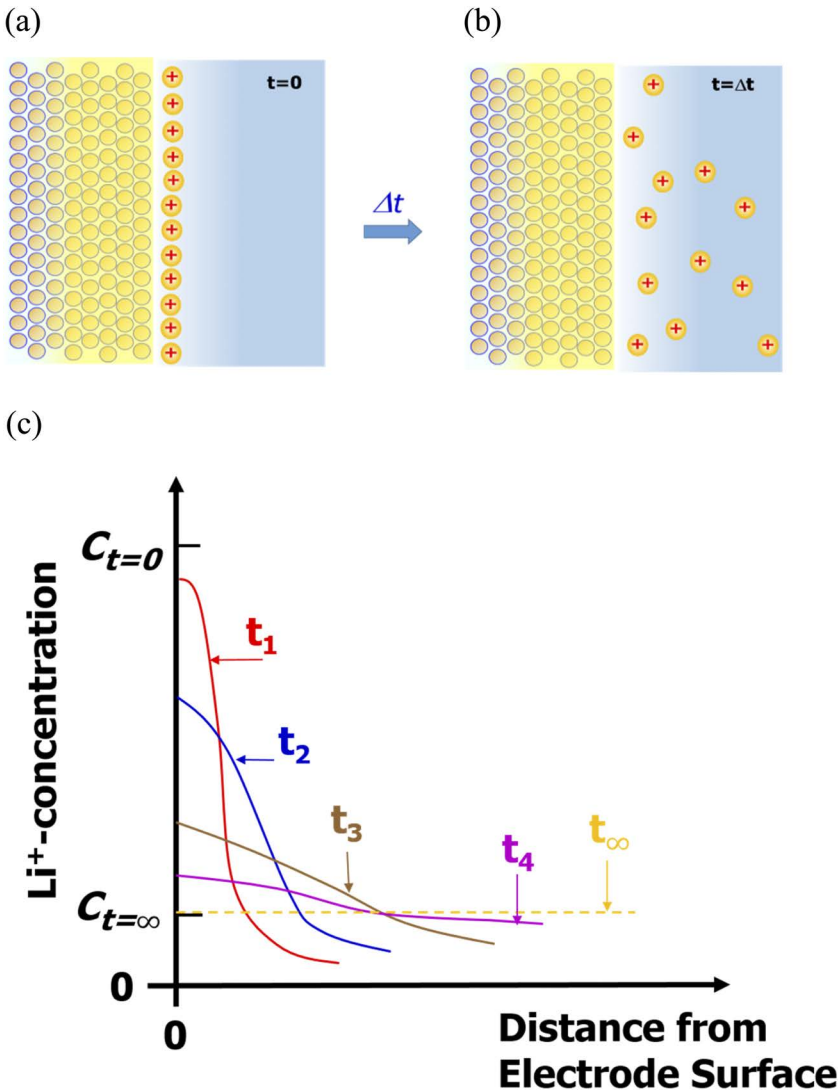


Figure 5.5 The “instantaneous plane source” problem. (a) A metallic electrode experiences a pulsed current that lasts a short duration Δt , releasing a given amount of ions, which diffuse into the bulk electrolyte with the lapse of the time. (b) The time-dependent distribution of these ions in the electrode/electrolyte interfacial region. (c) A lithium-ion battery experiences a sudden pulse discharge in a cell phone, releasing a burst of Li⁺ ions to the cathode/electrolyte interface.

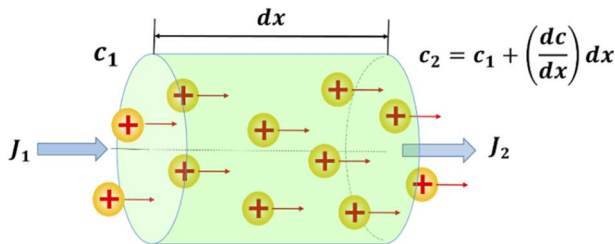


Figure 5.6 The flux of ions under non-steady-state conditions in and out of a volume enclosed between two planes of unit area with a distance dx .

while the flux out of the region from the right-hand plane is

$$J_{\text{out}} = -D \frac{d}{dx} \left(c + \frac{dc}{dx} dx \right) = -D \frac{dc}{dx} - D \frac{d^2 c}{dx^2} dx \quad (5.26)$$

Hence the net flux out of the region is

$$J_{\text{net}} = J_{\text{out}} - J_{\text{in}} = -D \frac{d^2 c}{dx^2} dx \quad (5.27)$$

Thus, in unit time, the net flux of ions leaving a region of unit volume dx is $D(d^2c/dx^2)dx$. By definition, this net flux is exactly the variation of concentration with time (dc/dt) that we have been looking for. Since in this situation the concentration varies with both time (t) and space (along the x -axis), we need to replace the total differential sign (d) with a partial differential sign (∂) and rearrange the above equation into

$$\frac{\partial c}{\partial t} = D \frac{\partial^2 c}{\partial x^2} \quad (5.28)$$

This partial differential equation is known as the *Fick's second law*.¹ It constitutes the foundation for treating the non-steady-state diffusion that occurs throughout the entire electrolyte.

The solution to partial differential equations is much more complicated than total differential equations such as the linearized Poisson-Boltzmann equation. Among the numerous ways to solve Fick's second law, the most popular approach requires a versatile math tool called *Laplace transformation*, which, by multiplying a function $y = f(x)$ with an integral function $\int_0^\infty e^{-px} dx$, converts the partial differential

equation into a total differential equation. We do not intend to explain the mathematical details of the Laplace transformation here because it is a universal tool, which should have been covered in most advanced thermodynamics and materials or chemical engineering classes. Here we just jump directly to the form of Fick's second law after Laplace transformation:

$$\int_0^\infty e^{-pt} \frac{\partial c}{\partial t} dt = \int_0^\infty e^{-pt} D \frac{\partial^2 c}{\partial x^2} dt \quad (5.29)$$

where p is a positive quantity unrelated to t . Solving both sides, Fick's second law under Laplace transformation becomes

$$-c_{t=0} + \int_0^\infty e^{-pt} c dt = D \frac{\partial^2}{\partial x^2} \int_0^\infty e^{-pt} c dt \quad (5.30)$$

where $c_{t=0}$ is the initial value of concentration. This is now a total differential equation with t as the only variable. Since by definition $\int_0^\infty e^{-pt} c dt$ is the Laplace transformation of c , we write it as \bar{c} , and the above equation becomes

$$p\bar{c} - c_{t=0} = D \frac{d^2 \bar{c}}{dx^2} \quad (5.31)$$

Now we have successfully converted a partial differential equation for c , eqn (5.28), which is a function of both x and t , into a total differential equation for \bar{c} , eqn (5.31), which depends on only one variable, x .

5.1.4 Solving Fick's Second Law for a Few Practical Scenarios

As we said previously when dealing with the linearized Poisson–Boltzmann equation, a pure mathematical treatment cannot give us all the answers for a practical system. The same remains true for the differentiation equation derived from Fick's second law, the solution of which requires the application of a physical understanding of the system.

We can now revisit the above-mentioned constant flux example of the lithium-ion battery with Laplace-transformed Fick's second law. Consider the anode (graphite) side first: at the instant it is plugged into the charger, the Li^+ concentration at the anode/electrolyte interface should be the same as the bulk concentration c_0 :

$$c_{t=0} = c_0 \quad (5.32)$$

This is called the *initial condition*.

After a sufficiently long time, the constant flux of Li^+ ions into anode eventually reaches a new equilibrium, in which the Li^+ concentration at the anode/electrolyte interface has dropped to a new value c_∞ , whereas at a sufficient enough distance from the electrode surface ($x = \infty$), the Li^+ concentration remains at the bulk value:

$$c_{x=\infty} = c_0 \quad (5.33)$$

Meanwhile, as soon as the battery is plugged into the charger, a constant current is established, which forces the Li^+ ions to flow into the anode at a constant flux. Therefore, at any instant, the flux at the interface ($x = 0$) is a constant and obeys Fick's first law:

$$J_{x=0} = -D \left(\frac{\partial c}{\partial x} \right)_{x=0} \quad (5.34)$$

These two equations together are called the *boundary conditions*.

The above initial and boundary conditions set the constraints on Fick's second law when describing the scenario of constant flux as illustrated in Figure 5.4. We will again skip some mathematical details in solving the total differential eqn (5.31) and jump directly to its solution:

$$c = c_0 - \frac{J}{\sqrt{D}} \left[2 \sqrt{\frac{t}{\pi}} e^{-\frac{x^2}{4Dt}} - \frac{x}{\sqrt{D}} \operatorname{erfc} \sqrt{\left(\frac{x^2}{4Dt} \right)} \right] \quad (5.35)$$

where erfc is the *Gauss error function complement*, defined as

$$\operatorname{erfc}(x) = 1 - \frac{2}{\sqrt{\pi}} \int_0^x e^{-u^2} du \quad (5.36)$$

Likewise, for the simultaneous Li^+ concentration on the cathode/electrolyte surface, a solution can be obtained:

$$c = c_0 + \frac{J}{\sqrt{D}} \left[2 \sqrt{\frac{t}{\pi}} e^{-\frac{x^2}{4Dt}} - \frac{x}{\sqrt{D}} \operatorname{erfc} \sqrt{\left(\frac{x^2}{4Dt} \right)} \right] \quad (5.37)$$

The positive sign after c_0 indicates that the Li^+ concentration increases at the cathode/electrolyte interface, because the cathode is releasing Li^+ ions into the electrolyte, which must transport these excess Li^+ ions into the bulk region.

Eqn (5.35) and (5.37) provide a general description of how the concentration of a species (c) that is being either consumed or generated by an electrode varies with both time (t) and distance from the electrode surface (x). Obviously, the shapes of both solutions are deeply affected by erfc. What does this component look like then?

Let us first take a look at the error function itself, which is defined as

$$\text{erf}(x) = \frac{2}{\sqrt{\pi}} \int_0^x e^{-u^2} du \quad (5.38)$$

Examination of this expression reveals that the “new” variable u is just an assisting parameter that will disappear once the integral limits (0 and x) are introduced. Its most important characteristics include the following:

1. at $x = 0$, $\text{erf} = 0$, $\text{erfc} = 1.0$;
2. at $x \geq 2$, $\text{erf} = 1$, $\text{erfc} \approx 0$;
3. and at $x = 0$, the slopes of erf and erfc are, respectively,

$$\frac{d[\text{erf}(x)]}{dx} = \frac{2}{\sqrt{\pi}} \quad (5.39)$$

$$\frac{d[\text{erfc}(x)]}{dx} = \frac{d[1 - \text{erf}(x)]}{dx} = -\frac{2}{\sqrt{\pi}} \quad (5.40)$$

In other words, erf takes the shape of a “saturation type” of curve when plotted at fixed t against x , whereas its complement erfc looks like its mirror image along an imaginary axis of $y = 0.5$ (Figure 5.7). The boundary condition of $x \geq 2$ actually sets the upper limit, beyond which the ion concentration no longer departs from the bulk value. This also defines the thickness of the so-called “diffuse layer” that changes with time. In Figure 5.4c and d this changing diffuse layer was represented by various “dx”.

In an actual electrochemical device such as a lithium-ion battery, given the diffusion coefficient of ions and the time scale involved in the cell operation, the diffusion thickness could span the entire distance from anode to cathode. In reality, the growth of diffusion thickness is restricted by the limited supply of ions in the electrolyte created by their population and mobility. In other words, the electrolyte in the entire cell is under “*diffusion control*”.

One can modify Fick’s second law for other ionic transport scenarios by simply changing the initial and boundary conditions. For example,

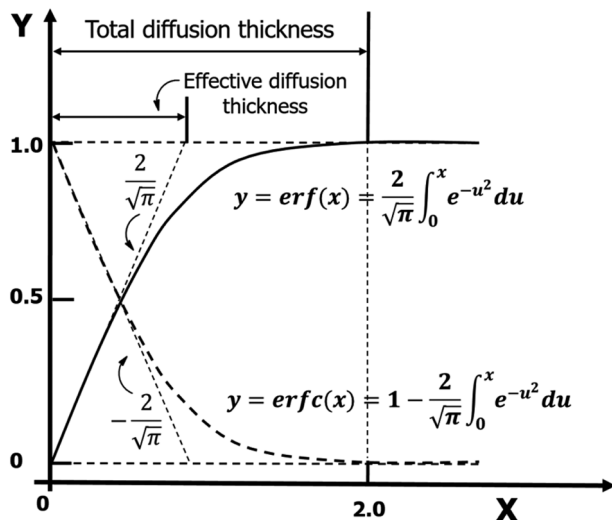


Figure 5.7 The shape and characteristics of the error function (erf) and its complement function (erfc). Their influence on the concentration profiles near the electrode/electrolyte interfaces goes far beyond the two examples given here. Many solutions to Fick's second law under different boundary conditions include erf or erfc components.

in the “instantaneous plane source” problem, we can view the pulse of an instantaneous flux (J_{pulse}) as the time derivative of a constant flux (J):

$$J_{\text{pulse}} = \frac{d}{dt} J \quad (5.41)$$

The solution to eqn (5.31) will become

$$c = c_0 - J_{\text{pulse}} \frac{1}{\sqrt{\pi D t}} e^{-\frac{x^2}{4 D t}} \quad (5.42)$$

If the initial ion concentration at the surface is set as zero:

$$c_{t=0} = c_0 = 0 \quad (5.43)$$

then the ion concentration varies with distance (x) and time (t) in the expression

$$c = -\frac{J_{\text{pulse}}}{\sqrt{\pi D t}} e^{-\frac{x^2}{4 D t}} \quad (5.44)$$

which represents a half bell-shaped distribution as graphically illustrated in Figure 5.5c.

5.2 Ion Transport Driven by an External Field: Migration (Conduction)

In the absence of an external electric field, although all the ions are moving they do not create any current, because their movement is completely random in both speed and direction. On a macroscopic scale and by time average, there is zero net flux of ions in any direction.

When an external electric field is applied to an electrolyte, a preferred direction for ionic movement appears, with cations traveling towards the electrode with excessive negative charge (anode) and anions towards the other. Although on an atomistic level the random movement of an individual still exists, on a macroscopic scale and by time average there is now clearly a net flux (J) of ions (Figure 5.8). Because this flux carries charges, it is an electric current (i). What sets this current apart from the current that one can generate in metallic

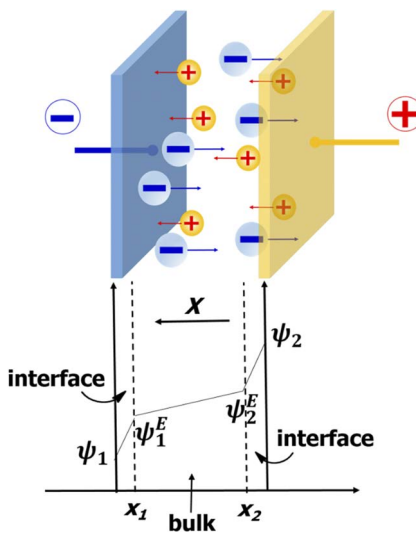


Figure 5.8 Top: The directional movement of ions in an electrolyte under an external electric field. Bottom: The electric field applied to the electrolyte is only part of the overall external field, as there are potential drops in the interfacial regions. The potential change across the interfacial regions were assumed to be linear. As will be seen in Chapters 6, 14 and 15, it is not always the case but still a good approximation in cases of high electrolyte solute concentration region ($>0.1\text{ M}$).

conductors is the charge carriers: this is an ionic current rather than electronic current.

Both cations and anions contribute to this current, hence the sum of their respective fluxes (J_i) constitutes the overall flux, and the current by definition should be

$$i = \sum_i z_i e_0 N_A J_i = F \sum_i z_i J_i \quad (5.45)$$

where $F = N_A e_0$ is Faraday's constant and N_A is Avogadro's number (6.02×10^{23}). In SI units $F = 96\,485 \text{ C mol}^{-1}$ or $96\,485 \text{ A s mol}^{-1}$. Remember that flux (J) describes the number of moles of certain species passing through unit area per second; current (i) should have units of either amperes or coulombs per second.

5.2.1 A Few Transport Quantities and Their Relations

There are numerous quantities that are often used to describe the movement of ions throughout electrolytes, all of which are based on the intrinsic agility of the ions in responding to an external force, be it chemical (created by "chemical potential", or simply concentration difference), mechanical (such as collisions among ions and solvent molecules created by convection) or electrostatic (such as an applied external field).

5.2.1.1 Conductivities (σ , A_m and A)

When an external field is applied to the electrolyte as shown in Figure 5.8, it creates a potential difference ($\psi_2 - \psi_1$) across the entire cell. However, not all of the applied potential works on the electrolyte. At each electrode/electrolyte interface, there is an electrified double layer that constitutes the interfacial region, and there is accordingly a certain potential drop in each of these interfacial regions (a topic that will be discussed in Chapters 6, 8, 15 and 16), hence the actual potential exercised on the electrolyte itself is a reduced value ($\psi_2^E - \psi_1^E$). By definition, the *field strength* X should be

$$X = -\frac{\psi_2^E - \psi_1^E}{\Delta x} = -\frac{\psi_2^E - \psi_1^E}{x_2 - x_1} \quad (5.46)$$

Strictly, Δx should be the length of the electrolyte excluding both interfacial regions. However, in reality, the interfacial thicknesses are usually very difficult to measure accurately, while their relative scale (in nanometers) is negligible compared with the electrolyte thickness,

hence we normally consider Δx as the distance between two electrodes. Note the negative ($-$) sign in the equation, which indicates that a positive ion moves against the positive field gradient.

We have assumed a linear drop of the field across the electrolyte, which is usually true for a liquid electrolyte, which is homogeneous in structure and composition. However, for solid electrolytes (either polymeric or ceramic), the composition and morphology across the system might be inhomogeneous, and the field strength is more precisely defined as

$$X = -\frac{d\psi}{dx} \quad (5.47)$$

Under steady-state conditions, the flux of a given ionic species can be considered to be linearly proportional to the field strength if the field is small enough:

$$J = BX \quad (5.48)$$

This relation will be proven later when we solve the Butler–Volmer equation to the low-field approximation, but here we will just accept it as a fact.

Since J describes the number of moles of a given ionic species passing through a unit area per second, the current density j can be written as

$$j = JzF = zFBX \quad (5.49)$$

which describes how many coulombs (or ampere seconds) of charge are passing through the unit area. We now can define a new constant σ by merging these constants:

$$\sigma = zFB \quad (5.50)$$

Therefore,

$$\sigma = \frac{1}{X} j \quad (5.51)$$

We have already defined that the field strength X , in the case of a homogeneous electrolyte, is linear across the entire electrolyte length Δx :

$$X = -\frac{\psi_2^E - \psi_1^E}{\Delta x} = -\frac{\Delta\psi}{\Delta x} \quad (5.52)$$

In addition, the total current (I) should be

$$I = jA \quad (5.53)$$

where A is the area of the electrodes. Combining eqn (5.51), (5.52) and (5.53), we have a new expression for the introduced quantity σ :

$$\sigma = \frac{\Delta x}{\Delta\psi} \frac{I}{A} \quad (5.54)$$

What does this new quantity σ mean? We can rearrange eqn (5.54) into

$$\Delta\psi = \frac{\Delta x}{\sigma A} I \quad (5.55)$$

Now, recalling that in Figure 5.8 $\Delta\psi$ is the voltage applied across the electrolyte, while A and Δx represent the geometric parameters of the cell, then the above equation is in a very similar format to Ohm's law:

$$V = IR \quad (5.56)$$

with the equivalent resistance R being

$$R = \frac{\Delta x}{\sigma A} = \rho \frac{\Delta x}{A} \quad (5.57)$$

where ρ is the conventional resistivity as defined by Ohm's law. Hence, based on the nature of σ being the reciprocal of resistivity, we name it *conductivity*. It describes how mobile the ions are in response to an external electric field. In an ideal situation as shown in Figure 5.8, it can be evaluated based on the resistance (R) measured under a direct current (DC) field and the cell parameter ($\Delta x/A$):

$$\sigma = \frac{1}{R} \frac{\Delta x}{A} \quad (5.58)$$

In reality, conductivity is often measured under alternating current (AC) rather than DC conditions, because other phenomena (concentration polarization, double-layer capacitance, charge transfers at the

surface of either electrode, *etc.*) often arise under DC conditions in an electrochemical cell, thus complicating the accurate measurement of resistances. We will revisit this topic with more details in Chapter 14.

Differing from resistivity in a metallic conductor, the ion conductivity in an electrolyte can be adjusted *via* both amount and species of solute dissolved therein. In other words, the conductivity depends not only on the solute concentration but also on the type of solute. The latter can be quantified by the ionic strength, as discussed in Section 3.5.3. In order to normalize conductivity against the concentration and valence of the ion, two related concepts were defined: molar conductivity (Λ_m) and equivalent conductivity (Λ):

$$\Lambda_m = \frac{\sigma}{c} \quad (5.59)$$

$$\Lambda = \frac{\sigma}{cz} \quad (5.60)$$

where z is the valence of the ionic species under study.

As discussed earlier, Kohlrausch performed meticulous measurements of ion conductivities for a large number of aqueous electrolytes and, by deriving both molar and equivalent conductivities and plotting them against concentration and comparing across solute types, he established two empirical laws:

1. non-linearity *versus* solute concentration:

$$\Lambda = \Lambda^0 - K\sqrt{c} \quad (5.61)$$

2. independent migrations for cations and anions:

$$\Lambda^0 = \lambda_+^0 + \lambda_-^0 \quad (5.62)$$

where Λ^0 , λ_+^0 and λ_-^0 represent the equivalent conductivity as the solute concentration approaches zero, and the equivalent conductivity contributed by the cation and anion, respectively.

These laws hold true only when the solute concentration approaches zero, and the fundamental reason underlying such a condition is that the ion–ion interaction can be neglected only when the electrolyte is sufficiently dilute, as shown in the Debye–Hückel model.

In actual applications, the conductivity (σ), not molar conductivity (Λ_m) or equivalent conductivity (Λ), is the most useful quantity,

because it directly reflects how much ionic current a given electrolyte can provide to support cell reactions.

5.2.1.2 Mobility (μ)

As briefly mentioned at the beginning of this section, the so-called directional movement of ions as implied by Figure 5.6 or 5.8 is only on a macroscopic scale and by time average. At an atomistic level, the random walk by an individual ion is still maintained even after the external electric field is switched on, while migration in the preferred direction occurs simultaneously (Figure 5.9a). The actual trajectories of the ions should be more like that shown in Figure 5.9b. In other words, the applied electric field only affects the movement of these

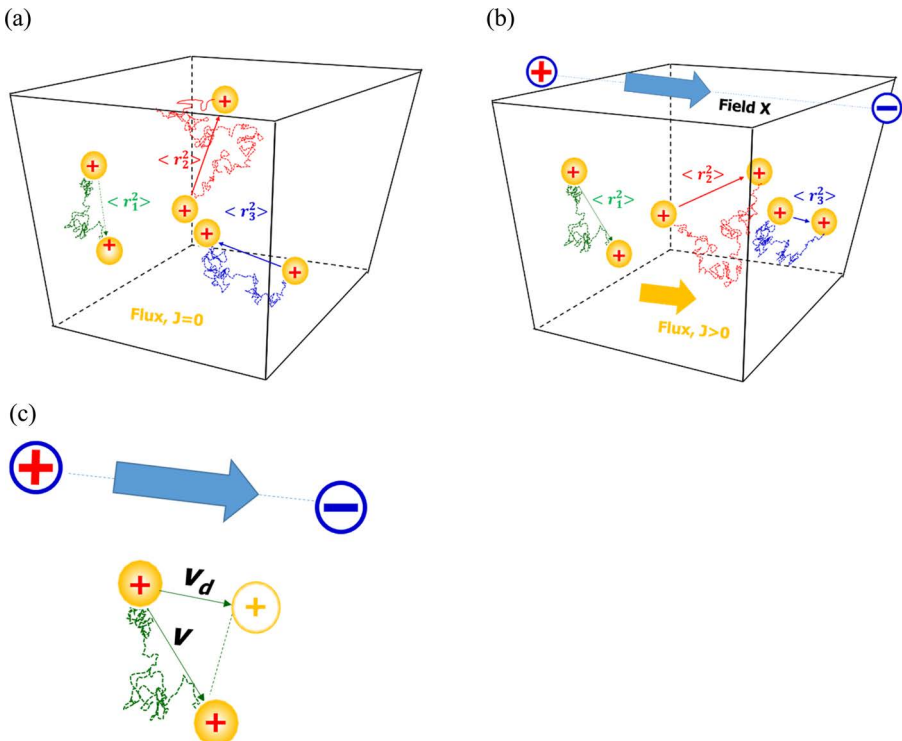


Figure 5.9 (a) The random ionic movement does not create any net flux. (b) An applied external electric field does not stop the random movement; instead, it causes the cations to drift towards (and anions against) the direction of the field by applying a velocity component on their already existing random movement, thus creating a net flux in the direction of the field. (c) The drift velocity is the component that aligns towards the applied field.

individual ions by applying a velocity component that aligns with the direction of the field. We call this velocity component the drift velocity (v_d), which is the projection of its overall velocity on the direction of the field (Figure 5.9c).

Now let us take a detailed look at these ions at an atomistic level.

The applied electrostatic field exerts a force on each individual ion, which is defined by Newton's second law as

$$\vec{F} = ma = m \frac{dv}{dt} \quad (5.63)$$

where \vec{F} is the driving force applied by the field on the ion, m is the mass of the ion and a is the acceleration. If there is no hindrance, the ion would accelerate and speed through the electrolyte with time. However, its collision with other ions (of both same and opposite charges) and solvent molecules keeps occurring. These collisions change the direction and velocity of an ion at each collision, and try to make its trajectory as random as possible. On the other hand, the applied field always tries to correct such deviations of this ion by driving it towards (if it is a cation) or against (if it is an anion) the field. The superimposition of the above two movements accounts for the actual motion of an ion depicted in Figure 5.9b.

Between two collisions, the ion of course follows Newton's second law to adopt the directional motion and contribute to the net flux, until the next collision changes its course. The overall net flux is thus the sum of the contributions from all of the ions during their directional movement, *i.e.* between their collisions. Since such collisions occur completely randomly, we cannot predict precisely the velocity and direction of an individual ion; however, if we assume statistically that the mean time between collisions is τ , and that N collisions occur in a time t , then

$$\tau = \frac{t}{N} \quad (5.64)$$

Since during this mean time τ the investigated ion must follow Newton's second law, its drift velocity (v_d) is given by

$$v_d = \frac{dv}{dt} \tau = \frac{\vec{F}}{m} \tau \quad (5.65)$$

Therefore, the contribution from a given ion to the directional movement of ions (*i.e.* the current) is described by its drift velocity, which is

proportional to the force working on it and the average time between collisions, but inversely proportional to its mass. Since both m and τ can be viewed as intrinsic properties of an electrolyte, whereas F is an external factor, a new quantity, *ionic mobility* (μ), can be defined:

$$\mu = \frac{\tau}{m} = \frac{v_d}{F} \quad (5.66)$$

Hence mobility is the drift velocity of an ion under the action of a unit force, and its dimension in the SI system is $\text{m s}^{-1} \text{N}^{-1}$. It describes how agile the ion is in response to the force. In real life, however, the force acting on an electrolyte is often not as convenient as the applied electric field to measure, hence a modified form of ionic mobility is usually used in the literature, which looks at the drift velocity induced by a *unit field* instead of unit force. This new form of mobility, sometimes referred to as “*conventional mobility*”, will hence have the unit $\text{m s}^{-1} \text{V}^{-1}$ or $\text{cm s}^{-1} \text{V}^{-1}$, while the mobility by the original definition is called “*absolute mobility*”. Since the relation between electrostatic force F on an ion bearing a charge of $z_i e_0$ and the applied electric field X is

$$F = z_i e_0 X \quad (5.67)$$

the conversion between these two mobility forms should be

$$\mu_{\text{Conv}} = z_i e_0 \mu_{\text{Abs}} \quad (5.68)$$

Most of the time, researchers do not indicate exactly what mobility they are using in the literature, which could cause confusion. Therefore, one must pay attention in order to differentiate, and the key clue might be found in the units used for the mobility ($\text{m s}^{-1} \text{N}^{-1}$ or $\text{m s}^{-1} \text{V}^{-1}$).

Table 5.1 lists the conventional mobilities for some selected ions in aqueous electrolytes at ambient temperature along with their diffusion coefficients.

Now let us revisit Figure 5.9 before concluding this section.

To have a more quantitative picture of the relative diffusional and migrational distances that an ion covers simultaneously, we can extract diffusion coefficient and mobility data from Table 5.1 and do a simple calculation.

Let us consider an aqueous electrolyte consisting of KCl. The diffusional distance travelled by a K^+ ion in 1 s could be calculated using its diffusion coefficient ($1.57 \times 10^{-5} \text{ cm}^2 \text{ s}^{-1}$) and the

Table 5.1 Diffusion coefficients (D) and mobilities (μ) of selected ions in aqueous and non-aqueous electrolytes at ambient temperature (25–30 °C).

Ion	$D/\text{cm}^2 \text{ s}^{-1}$	$\mu/\text{cm}^2 \text{ V}^{-1} \text{ s}^{-1}$
H ⁺	7.60×10^{-5}	3.62×10^{-3}
Li ⁺	1.03×10^{-5}	
Na ⁺	1.33×10^{-5}	
K ⁺	1.57×10^{-5}	7.62×10^{-4}
NH ₄ ⁺	1.86×10^{-5}	7.63×10^{-4}

Einstein–Smoluchowski equation [eqn (5.22)] to be 97 µm. Meanwhile, an electric field of 1.0 V cm⁻¹ is applied to this electrolyte, and in response this K⁺ ion would migrate along the applied field, whose distance covered in 1 s would be only 7.62 µm, or less than one-tenth of its diffusional distance!

5.2.1.3 Relationships among D , σ , v_d and μ

So far we have defined a few quantities that describe how mobile the ions are, either on their own (diffusion coefficient D) or under an external electric field (conductivity σ , drift velocity v_d and mobility μ). How are these quantities related?

Let us consider a cation species moving in an electrolyte at a drift velocity v_+ , creating a net flux of positive ions J_+ (Figure 5.10a). Remember that flux is the number of moles of such a cation passing through a unit area per second. Assume that the cation concentration is c_+ in this electrolyte, then in 1 s the number of moles of this cation passing through the area enclosed by dashed lines would be the whole population of the cation (N_+) contained in a volume V :

$$J_+ = N_+ = AVc_+ = Vc_+ \quad (\text{because } A \text{ as unit area} = 1.0) \quad (5.69)$$

Apparently, the volume V is given by how fast the cations are moving:

$$V = A v_+ \quad (5.70)$$

Hence

$$J_+ = v_+ c_+ \quad (5.71)$$

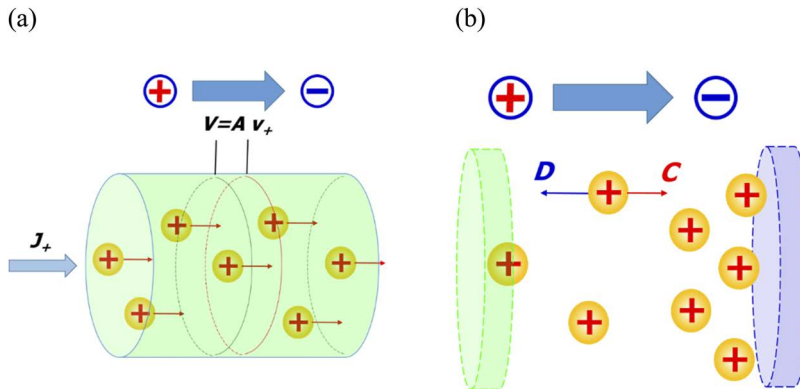


Figure 5.10 (a) Relationship between flux, current density and drift velocity. (b) Einstein's thought experiment of balanced diffusion and conduction for an ion species.

The current density (j_+) corresponding to the flux is

$$j_+ = z_+ F v_+ c_+ \quad (5.72)$$

where F and z are the Faraday constant and this cation's valence. Remember that all ions, no matter whether cations or anions, contribute to the net flux of ions under the external electric field, hence the overall current i should be given:

$$j = \sum_i j_i = \sum_i z_i F v_i c_i \quad (5.73)$$

Now we have linked the drift velocity of each ion with its contribution to the current. Since drift velocity is related to mobility by eqn (5.66), whereas conductivity is related to field strength X by eqn (5.51), after substitution and rearrangement we obtain the following relationship between conductivity and mobility:

$$\sigma = \frac{j}{X} = \sum_i z_i F c_i \mu_i \quad (5.74)$$

If we substitute the Faraday constant F with

$$F = N_A e_0 \quad (5.75)$$

and define charge carrier number n_i as

$$n_i = N_A c_i \quad (5.76)$$

then we will obtain another more popular form of the above relation that is often found in the electrolyte literature:

$$\sigma = \sum n_i z_i \mu_i e_0 \quad (5.77)$$

In the special case of a $z:z$ -type electrolyte (such as NaCl or MgSO₄), it reduces to

$$\sigma = z F c [\mu_+ + \mu_-] \quad (5.78)$$

Likewise, molar and equivalent conductivity can be related to mobility in a similar manner:

$$\Lambda_m = \frac{\sigma}{c} = z F [\mu_+ + \mu_-] \quad (5.79)$$

$$\Lambda = \frac{\sigma}{cz} = F [\mu_+ + \mu_-] \quad (5.80)$$

One should keep in mind here that, although eqn (5.77)–(5.80) all appear to be expressed in *scalar quantities*, *i.e.* quantities without directions, they actually contain *vector elements*, *i.e.* with directions, because the migration of an ion could make either a positive or a negative contribution to the conductivity, depending on whether it moves *along with* or *against* the applied electric field. The latter (“against”) means that a cation moves towards the positively charged electrode and an anion moves towards a negatively charged electrode. In extremely dilute or ideal electrolytes, such ionic movement in the “wrong” direction can be ignored, and it is this implication that renders these equations with a scalar appearance. However, in super-concentrated electrolytes or ionic liquids, movement in the “wrong” direction could occur, and one has to remember that quantities such as charge and mobility intrinsically introduce a vector nature.

5.2.1.4 Einstein Relation

We have successfully related conductivities (σ , Λ_m and Λ) and mobility (μ), but what about diffusion coefficient?

Einstein performed a clever thought experiment and established a link between these two quantities that describe random walk and directional motion of ions, respectively (Figure 5.10b). He imagined an electrolyte system in which the concentration gradient for a certain ionic species creates a diffusional flux J_D :

$$J_D = -D \frac{dc}{dx} \quad (5.81)$$

He then applied an external electric field to induce a conduction flux J_C , which precisely balanced the diffusional flux, so that the net flux is zero:

$$J_D + J_C = 0 \quad (5.82)$$

From the previous section, we know that

$$J_C = cv_d = c\vec{F}\mu \quad (5.83)$$

so we have

$$c\vec{F}\mu - D \frac{dc}{dx} = 0 \quad (5.84)$$

or

$$\frac{dc}{dx} = \frac{c\vec{F}\mu}{D} \quad (5.85)$$

Since this system is at equilibrium, Einstein applied a Boltzmann distribution to obtain the distribution of ionic concentration:

$$c = c^0 e^{-\frac{U}{k_B T}} \quad (5.86)$$

where c^0 is the ion concentration when the electric field is zero and U is the potential energy of an ion in the applied field. Therefore,

$$\frac{dc}{dx} = -c^0 e^{-\frac{U}{k_B T}} \frac{1}{k_B T} \frac{dU}{dx} = -\frac{c}{k_B T} \frac{dU}{dx} \quad (5.87)$$

By definition, the force induced by the field on the ions is

$$\vec{F} = -\frac{dU}{dx} \quad (5.88)$$

Therefore,

$$\frac{dc}{dx} = \frac{c}{k_B T} \vec{F} \quad (5.89)$$

Combining these two expressions for dc/dx , we obtain

$$\frac{c}{k_B T} \vec{F} = \frac{c \vec{F} \mu}{D} \quad (5.90)$$

Now we can finally correlate diffusion coefficient with mobility:

$$D = \mu k_B T \quad (5.91)$$

This equation is the *Einstein relation*.² Note that the mobility used here is the “*absolute mobility*”, i.e. the drift velocity created by unit force. To apply the conventional mobility frequently used in the literature, one needs to convert it by multiplying by $z_i e_0$, as discussed previously.

This sets the foundation for the many important relationships regarding ion transport. In a general sense, and beyond ionic movement in electrolytes, it describes the relationship between random movement of small particles and the orientational movement of the same particles induced by an external force such as electric, magnetic, gravitational or even mechanical.

On the basis of the Einstein relation, we can further establish the relation between diffusion coefficients and conductivity through mobility:

$$\sigma = \sum \frac{n_i z_i D_i e_0}{k_B T} \quad (5.92)$$

In summary, all these quantities (σ , D , μ) describe how agile the ions are in their electrolytes when responding to a “driving force”. Such a driving force can be either the concentration gradient (for diffusion coefficient) or the electric field (for mobility and conductivity). They are interdependent and are proportional to each other in a linear manner.

5.2.1.5 Transport Number (t_+ and t_-)

Since both cations and anions contribute to the overall ion conductivity (σ), sometimes it is important to know which ionic species is the major contributor. For example, in a lithium-ion battery, the cell reactions rely on the transport of Li^+ whereas the movement of other ionic species (especially the anion) is often considered parasitic and harmful to the cell reactions. Knowing the exact contribution of Li^+ to the current could help determine how fast the battery can be charged and discharged at a constant flux of ions. In a broader context, the performance of batteries often relies on the movement of only one specific working ion, hence it is important to know the contribution from such an ion of significance to the cell reaction.

In order to quantify such contributions, the *transport number* (t_i) is defined to reflect the contribution to the current by an individual ion i :

$$t_i = \frac{j_i}{\sum_i j_i} = \frac{z_i F c_i \mu_i}{\sum_i z_i F c_i \mu_i} \quad (5.93)$$

where c_i is the concentration of ionic species i .

In most cases (such as in lithium-ion battery electrolytes), one is only interested in differentiating cationic and anionic contributions to the current, hence the cationic transport number (t_+) and anionic transport number (t_-) were defined as

$$t_+ = \frac{\sum J_+}{(\sum J_+ + \sum J_-)} = \frac{\sum z_i^+ F c_i^+ \mu_i^+}{\sum (z_i^+ F c_i^+ \mu_i^+ + z_i^- F c_i^- \mu_i^-)} \quad (5.94)$$

and

$$t_- = 1.0 - t_+ \quad (5.95)$$

For a $z:z$ -type electrolyte such as NaCl or MgSO_4 in water, the expressions for the transport numbers could be further simplified:

$$t_+ = \frac{\mu^+}{\mu^+ + \mu^-} = \frac{D_+}{D_+ + D_-} \quad (5.96)$$

In lithium-ion battery electrolytes, because the non-aqueous solvents used are often “monopolar” owing to the spatial hindrance to the positive terminus (Figure 5.11), the cation (Li^+) is often much

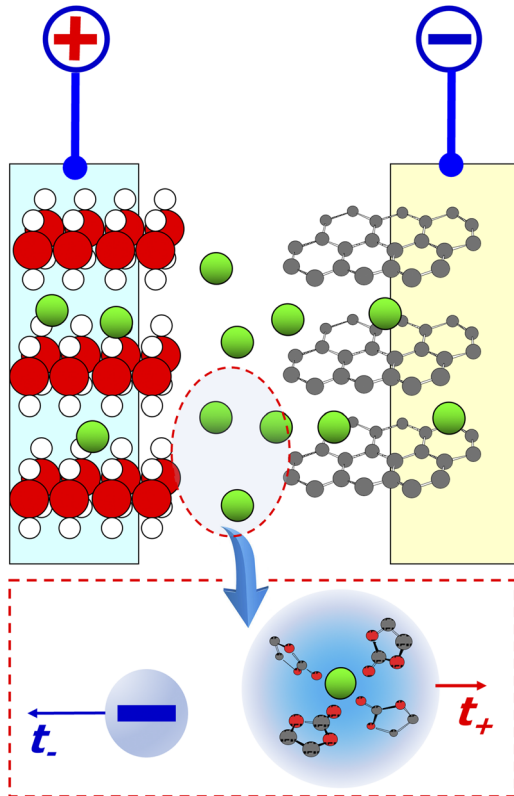


Figure 5.11 In a non-aqueous electrolyte that contains lithium salts, the positive transport number is often far smaller than the negative transport number, owing to the unsymmetrical solvation of cations and anions by the “monopolar” non-aqueous carbonate solvents.

more solvated than the anion. This creates a severely unsymmetrical transport number bias, *i.e.*

$$t_+ < t_- \quad (5.97)$$

In other words, in the measured ion conductivity of a given non-aqueous electrolyte, most of the current is conducted by the anion movement, because the bulky solvation sheath of Li^+ severely slows its mobility (Figure 5.11). This is disadvantageous to the cell reaction, as we have mentioned that the current carried by anions is considered parasitic and not supportive for the cell reactions.

In aqueous electrolytes, the difference between the cationic and anionic transport numbers is smaller, and in some cases the above

Table 5.2 Cationic transport numbers in typical aqueous and non-aqueous electrolytes.

Electrolyte	0.1 M NaCl–H ₂ O	0.1 M KCl–H ₂ O	0.1 M HCl–H ₂ O	21 m LiTFSI–H ₂ O	1.0 M LiPF ₆ –EC-DMC ^a	1.0 M Et ₄ NPF ₆ –AN ^b
<i>t</i> ₊	0.39	0.49	0.83	0.73	0.15–0.4	0.4–0.5

^aLithium hexafluorophosphate dissolved in a mixture of ethylene carbonate (EC) and dimethyl carbonate (DMC). This is the skeleton composition for most electrolytes used in commercial lithium-ion batteries, although the exact composition may vary.

^bTetraethylammonium hexafluorophosphate dissolved in acetonitrile. This is the most common electrolyte used for electrochemical double-layer capacitors. A range is given because very scattered results were obtained using different methods.

trend can be reversed, because the water molecule is bipolar and could solvate both cations and anions. Table 5.2 gives transport numbers for a few important electrolytes that we frequently encounter in life.

The significance of transport number not only lies in predicting the power density of lithium-ion batteries, but also helps in the design of electrolyte systems, in which the transport of one given ion could be manipulated for desired purposes. Such an example can be found in analytical electrochemistry, where Fick's second law is often utilized to solve for ionic transport behaviors under different initial and boundary conditions. To do so, the movement of ions must be exclusively diffusional in an electrochemical cell, *i.e. without any migration*. This could be difficult for an ion that is rather mobile, as it was mentioned in previous sections that the overall motion of ions is actually the superimposition of random walk (diffusion) and directional drift (migration). The presence of migration severely affects the solution of Fick's laws.

For example, consider 0.1 M HCl solution in water, where *t*₊ and *t*₋ are 0.83 and 0.17, respectively. Placing this electrolyte in any electric field, the current is heavily distributed on H⁺ rather than Cl⁻, thus making it almost impossible to observe the diffusion behavior of H⁺.

To address this challenge, one can now add a supporting salt, *e.g.* KCl, to the solution, until KCl becomes the major salt, with K⁺/H⁺ = 1000. Then

$$\frac{t_K}{t_H} = \frac{c_K \mu_K}{c_H \mu_H} = \frac{1}{1000} \times \frac{6 \times 10^{-4}}{30 \times 10^{-4}} = 200 \quad (5.98)$$

Despite the much higher mobility of H⁺, the sheer number advantage of K⁺ ensures that, once an external electric field is applied, the contribution of H⁺ to the cationic current is suppressed to 5%! If one

counts the contribution of anions to the current, then the transport number in this new electrolyte containing an overwhelming proportion of KCl would be

$$t_{\text{H}} = \frac{c_{\text{H}}\mu_{\text{H}}}{c_{\text{H}}\mu_{\text{H}} + c_{\text{K}}\mu_{\text{K}} + c_{\text{Cl}}\mu_{\text{Cl}}} \approx 0.001 \quad (5.99)$$

The near-zero transport number of H⁺ indicates that, in an electrochemical cell under a certain electric field, the current is mainly provided by the movements of K⁺ and Cl⁻, whereas any flux of H⁺ detected at the electrode must be provided *via* its diffusion, which would allow for a much more precise solution of Fick's second law.

Hence in most electrochemical analyses, a *supporting electrolyte* is required, the role of which is to support the migration so that the targeted ion can transport mostly *via* diffusion.

The definition of ion transport number in eqn (5.94) is based on two assumptions: (1) the electrolyte solute (*i.e.* the salt) is completely dissociated into free ions; and (2) these free ions are moving independently of the influence of each other. In other words, the definition is valid for an “ideal electrolyte” only. In most practical electrolytes, these two assumptions do not hold because of the intensified interionic correlations at high salt concentrations (*i.e.* repulsion between ions of the same charge and attraction between the ions of opposite charge), incomplete dissociation, as well as ion–solvent associations. Such ion–ion and ion–solvent interactions become especially important in super-concentrated electrolytes and ionic liquids. In that situation, the ion movements become heavily entangled and correlated, and the ion transport number can no longer follow the simplistic summation as defined in eqn (5.94). We revisit this more complicated topic in Chapter 14.

5.2.2 Nernst–Einstein Relation

The Einstein relation established an important link between diffusion and migration

$$D = \mu k_{\text{B}} T \quad (5.91)$$

On the basis of this relation, a few more important relations can be derived.

Earlier we established that equivalent conductivity is related to ionic mobility in the following manner:

$$\Lambda = z_i e_0 F (\mu^+ + \mu^-) \quad (5.100)$$

Substituting the Einstein relation for the mobilities, we now have

$$\Lambda = \frac{z_i e_0 F}{k_B T} (D_+ + D_-) = \frac{z_i F^2}{RT} (D_+ + D_-) \quad (5.101)$$

This is the *Nernst–Einstein relation*,² which relates equivalent conductivity to the independent contributions from the cationic and anionic diffusion coefficients. Of course, this can only be true in extremely dilute electrolytes, where ion–ion interactions are negligible; but more importantly, this equation implicitly assumes that all ions that diffuse also contribute to the migration, which is not true for ion pairs. An ion pair diffuses, but is electroneutral, therefore it cannot feel the electric field and makes no contribution to carrying the current. Only with extremely dilute electrolytes can the ion pairing be completely eliminated.

5.2.3 Stokes–Einstein Relation

In hydrodynamics, the transport of particles in a condensed phase would encounter a viscous drag. Stokes proved that, when the Reynolds number (Re) of the medium is much less than unity, *i.e.* there is no turbulence and convection, and the particles move through the medium smoothly in the laminar flow, the viscous drag (F_V) felt by a spheritic particle would be

$$F_V = 6\pi r\eta v \quad (5.102)$$

where r is the radius of the particle, η the viscosity of the medium and v the velocity of the particle. In appearance, such a relation describes a macroscopic particle of known geometric shape moving in a structureless continuous medium. It should not be directly applicable to the ions moving in an electrolyte solution for a number of reasons: (1) the size of the ions is comparable to the size of the solvent molecules, hence the medium is no longer structureless and continuous; (2) the geometric shape of most ions is not perfectly spherical; (3) the radius of the ion here is no longer a finite number owing to its solvation by the solvent molecules; and (4) the viscosity, which is a bulk and macroscopic property, should be very different from what an ion can feel in its local environment.

Nevertheless, against all these odds, Einstein made an audacious “guesstimate”, and directly adopted Stokes’s law. He visualized that an

ion in electrolyte is experiencing both a random walk driven by local concentration inequilibrium (diffusion) and a drift velocity imposed by an external electric field. Under steady-state conditions, these two forces should be equal to each other:

$$\frac{dc_i}{dx} = -6\pi\eta rv_d \quad (5.103)$$

where dc_i/dx is the concentration gradient according to Fick's first law and v_d is the drift velocity. Since the concentration gradient takes the form of a force F responsible for the drift velocity, we will have

$$\mu = \frac{v_d}{F} = \frac{v_d}{-\frac{dc_i}{dx}} = \frac{v_d}{6\pi\eta rv_d} = \frac{1}{6\pi\eta r} \quad (5.104)$$

We now introduce the Einstein relation:

$$D = \mu k_B T \quad (5.91)$$

Then we have a new relation between a microscopic property (D) and a macroscopic property (η):

$$D = \frac{k_B T}{6\pi\eta r} \quad (5.105)$$

This is the *Stokes–Einstein relation*.²

One might feel that the above derivation of the Stokes–Einstein relation is non-rigorous. Einstein made this very bold extension of Stokes's law into the microscopic world almost by instinct rather than rigorous mathematical derivation. However, he was correct, and the accuracy of eqn (5.105) is astonishing and has been confirmed in many different scenarios.

5.2.3.1 An Unexpected Use of the Stokes–Einstein Relation

In a rather unexpected development, this relation was used by some to achieve the earliest precise measurement of Avogadro's number (N_A).

We have learned from the Einstein–Smoluchowski equation that for a small particle that moves randomly, the mean square distance travelled in a given duration t would be given by

$$\langle x^2 \rangle = 2Dt \quad (5.20)$$

In other words, the diffusion coefficient is given by

$$D = \frac{\langle x^2 \rangle}{2t} \quad (5.106)$$

Inserting eqn (5.106) into the Stokes–Einstein relation [eqn (5.105)], we obtain

$$\frac{\langle x^2 \rangle}{2t} = \frac{k_B T}{6\pi\eta r} = \frac{RT}{6\pi\eta r N_A} \quad (5.107)$$

and rearrangement of eqn (5.107) gives

$$N_A = \frac{RT}{6\pi\eta r D} = \frac{RTt}{3\pi\eta r \langle x^2 \rangle} \quad (5.108)$$

In other words, at a given temperature T , if one knows the viscosity η of the medium and the radius r of the particle, it only takes the measurement of the mean square distance traveled by this particle in a given duration t to calculate Avogadro's number (N_A).

The French physicist Perrin was the first one who actually conducted such an experiment.⁴ In 1909 he was studying the Brownian motion of microscopic particles in water, and read about Einstein's work. Thus, he suspended gamboge seeds, which have an almost uniform radius of 0.53 μm, in a drop of water and, using a high-power microscope, he meticulously measured the distance that such a microscopic particle travels in a given time interval. Since the viscosity of water and room temperature were known, based on multiple experiments he was able to calculate Avogadro's number to be in the range $6.5\text{--}6.9 \times 10^{23}$, which was an overestimate compared with the accurate value that we know today (6.02×10^{23}) but was of the correct order of magnitude.

For this initial effort that provided the most accurate value for Avogadro's number at the time and his work on Brownian motion, Perrin was awarded the Nobel Prize in Physics in 1926.

5.2.4 Walden's Rule

Diffusion coefficient was connected with equivalent conductivity by the Nernst–Einstein relation and with viscosity by the Stokes–Einstein relation. Is there a relation between equivalent conductivity and viscosity, then?

A simple algebraic rearrangement leads to

$$D = \frac{k_B T}{6\pi\eta r D} = \frac{RT}{zF^2} A \quad (5.109)$$

Therefore, the molar conductivity for a given ion is expressed as

$$\Lambda = \frac{zF^2 k_B}{6\pi\eta r R} \quad (5.110)$$

Inserting $F = N_A e_0$ and $R = k_B N_A$, we will have

$$\Lambda = \frac{zFe_0}{6\pi\eta r} \quad (5.111)$$

or in its more popular form

$$\Lambda\eta = \frac{zFe_0}{6\pi r} = \frac{\text{constant}}{r} \quad (5.112)$$

This is *Walden's rule*, an empirical rule actually established long before Einstein's work.⁵ Its verification once again confirms the validity of the Stokes–Einstein relation. Likewise it only works in extremely dilute electrolytes. In recent studies, Walden's rule has been adopted as a useful empirical descriptor for the “*ionicity*” of an electrolyte, as discussed in more detail in Chapter 14.

5.2.5 Nernst–Planck Flux Equation

The last equation of major importance also benefitted from the Einstein relation but does not bear Einstein's name.

We mentioned above that an ion's motion in an electrolyte can be viewed as the superimposed movements of two different natures: (1) random walk due to a concentration gradient and (2) migration due to an electric field.

For migration, the nature of the force acting on the ion is beyond any doubt: it is the Coulombic force (F_C) from the electric field, and can be expressed as

$$F_C = z_i e_0 X = -z_i e_0 \frac{d\psi}{dx} \quad (5.113)$$

where X is the field and $d\psi/dx$ is the electrostatic potential gradient.

What force drives the diffusion?

As Fick's law has already told us, the motion is driven by the concentration gradient:

$$J_i = -D \frac{dc_i}{dx} \quad (5.114)$$

Analogously, the concentration gradient dc_i/dx can be viewed as a field that generates a force of chemical nature. From thermodynamics, we know that such a chemical force originated from the chemical potential μ_i :

$$\mu_i = \mu_i^0 + RT \ln c_i \quad (5.115)$$

the gradient of which should determine the “chemical field” that an ion feels. Note that here μ_i represents chemical potential rather than ionic mobility.

If one considers the superimposed motion of ions as the result of both of those two forces, then under steady-state conditions the overall ionic flux created by the combined forces should obey Fick's first law in a new form that reflects both fields:

$$J_i = -\frac{D_i c_i}{RT} \left(z_i F \frac{d\psi}{dx} + \frac{d\mu_i}{dx} \right) = -\frac{D_i c_i}{RT} \frac{d}{dx} (z_i F \psi + \mu_i) \quad (5.116)$$

Eqn (5.116) is actually just a more quantitative expression for the statement already qualitatively made in Section 5.2.1. The first part of the term represents the electrostatic potential applied by the external field, which is responsible for the migration, and the second part of the term is related to the concentration gradient. We call this term $(z_i F \psi + \mu_i)$ the *electrochemical potential* ($\overline{\mu}_i$):

$$\overline{\mu}_i = \mu_i + z_i F \psi \quad (5.117)$$

It dictates the movement of an ion in an electrolyte. The above equation can be simplified to

$$J_i = -\frac{D_i c_i}{RT} \frac{d\overline{\mu}_i}{dx} \quad (5.118)$$

Of course, the above analogous process is not rigorous. For a more rigorous mathematical derivation, one could refer to *Modern*

Electrochemistry by Bockris and Reddy or *Electrochemical Systems* by Newman and Balsara (see Further Reading).

Now we insert the Einstein relation into eqn (5.118):

$$D_i = \mu_i k_B T \quad (5.91)$$

and, replacing the absolute mobility with conventional mobility:

$$\mu_{\text{Conv}} = z_i e_0 \mu_{\text{Abs}} \quad (5.119)$$

we obtain

$$J_i = -\frac{D_i c_i}{RT} \frac{d\bar{\mu}_i}{dx} = -\frac{\mu_{\text{Abs}} k_B T c_i}{RT} \frac{d\bar{\mu}_i}{dx} = -\frac{\mu_{\text{Conv}} k_B T c_i}{z_i e_0 RT} \frac{d\bar{\mu}_i}{dx} \quad (5.120)$$

$$J_i = -\frac{\mu_{\text{Conv}} c_i}{z_i F} \frac{d\bar{\mu}_i}{dx} \quad (5.121)$$

This is the *Nernst–Planck flux equation*, which correlates the flux of a charged species with the total driving force from the electrochemical potential, which can be split into an electrostatic part and a chemical part:

$$J_i = -\frac{D_i c_i z_i F}{RT} \frac{d\psi}{dx} - D_i \frac{dc_i}{dx} = \frac{D_i c_i z_i F}{RT} X - D_i \frac{dc_i}{dx} \quad (5.122)$$

This relation explains certain electrochemical phenomena where the ion transport occurs against what the electrostatic force orders them to. Examples include the plating of aluminum from either ionic liquid or non-aqueous electrolytes containing AlCl_4^- :



or the plating of silver from electrolytes containing AgCN_2^- :



In both cases, the negatively charged ions AlCl_4^- and AgCN_2^- must travel to the negative electrode and receive electrons there in order to be reduced. This phenomenon cannot be explained if ionic migration

is the only form of ion transport. Hence the chemical field corresponding to the concentration gradient must serve as the driving force to make aluminum and silver depositions possible in the above examples. Provided that the diffusion term $D_i(dc_i/dx)$ overwhelms the migration term $(D_i c_i z_i F/RT)X$, the ions can travel to the electrode bearing the same charge.

5.2.6 Ion Transport with Ion-Ion Interaction: Onsager's Laws

Based on what we did throughout Chapter 4, the reader may be bothered by the following question: *Where is the ionic cloud in these equations for ion diffusion or migration?* Indeed, for all the ion transport equations discussed so far, the ion-ion interaction has been conveniently ignored, which is why we repeatedly emphasized that these equations hold true only at extremely dilution, where ion-ion interactions are not pronounced. The reason behind this disconnection is the parallel development of the theories on ion distribution and ion transport in the early 1900s.

Such a disconnection was resolved by Onsager, who re-examined the ion transport behaviors with the concept of an ionic cloud.^{6–8} In Section 4.6, when showing how the Debye–Hückel model verified the empirical Kohlrausch's law, we mentioned briefly that the distortion of an ionic cloud creates two separate counterforces on the movement of the central ion: relaxation force (F_R) and electrophoresis force (F_E), so that the net force (F_{Net}) felt by the moving central ion would be

$$F_{\text{Net}} = F_C - (F_R + F_E) \quad (5.125)$$

where F_C is the force applied by the external Coulombic field. Correspondingly, the drift velocity should be modified by correcting the two velocity components generated by these two counterforces:

$$v_d = v_0 - (v_R + v_E) \quad (5.126)$$

We will not go into details about how Onsager treated the complicated interactions among ions during their movement, in the absence or presence of an applied electric field, until Chapter 14 (Section 14.3). At the moment, we will just examine how these two counterforces are treated with mathematical rigor, and how this treatment leads to the verification of Kohlrausch's empirical law by the Debye–Hückel model.

5.2.6.1 Relaxation Force

Apparently, the relaxation force generated by the trailing ionic cloud as shown in Figure 4.4 depends on the departure of the central ion from the charge center of the ionic cloud. This departure is represented by the distance d , which quantifies the asymmetric degree of the ionic cloud, and is sometimes called “*distortion parameter*”. So, what determines the distortion parameter d ?

Since such a distortion is created by the movement by the central ion, it depends on the relative rates of how fast the frontal section of ionic cloud is built and how fast the tail section of the ionic cloud is dissipated. Under this dynamic equilibrium, the relaxation time (τ_R) describes the average time that an ionic cloud would require to adjust itself with the moving central ion.

Debye performed a thought experiment to determine this relaxation time. He imagined that at time $t = 0$, the central ion is suddenly taken away, then the ionic cloud left behind by this central ion is no longer under the influence of its Coulombic field, and the thermal force would take over in redistributing these ions. The ions are thus taking a random walk to eradicate the previous distribution dictated by the Coulombic field of the central ion, as described by the Einstein–Smoluchowski relation:

$$t = \frac{\langle x^2 \rangle}{2D} \quad (5.127)$$

Then, how long will it take for the left-over ionic cloud to reach a new equilibrium as if the former central ion never existed? In other words, what mean square distance should we use in the above equation?

One may recall that in the ionic cloud, we defined a Debye–Hückel thickness (K^{-1} or λ_D):

$$K^{-1} (\text{or } \lambda_D) = \sqrt{\frac{\varepsilon k_B T}{4\pi} \frac{1}{\sum_i n_i^0 z_i^2 e_0^2}} \quad (5.128)$$

which is actually the imaginary radius of the ionic cloud. Then it is reasonable to assume that, if the random walk of the ions in the left-over ionic cloud takes them to a distance equal to the Debye–Hückel thickness, one can consider that such an ionic cloud has been completely dissipated by the thermal force. Hence the relaxation time (τ_R) can be derived from the Einstein–Smoluchowski relation by replacing the distance x with K^{-1} :

$$\tau_R = \frac{(K^{-1})^2}{2D} = \frac{(K^{-1})^2}{2\mu k_B T} \quad (5.129)$$

We now put the central ion back and apply an external field, then we can calculate the average distance that an ionic cloud travels during time τ_R , or the distortion parameter d , as

$$d = \tau_R v_0 = \frac{v_0 (K^{-1})^2}{2\mu k_B T} \quad (5.130)$$

Remember that in Section 4.7 we simplified the picture of a static central ion surrounded by its ionic cloud as two point charges separated by a distance K^{-1} (Figure 4.5). The force between these two point charges is of course Coulombic in nature, and given by

$$F_R = \frac{z^2 e_0^2}{\epsilon (K^{-1})^2} \quad (5.131)$$

Now the ionic cloud is distorted by a degree d , with its charge center no longer coinciding with the central ion but instead moving further away from it. Hence the additional counterforce exerted by this distortion, which is also the relaxation force we are trying to derive, should be proportional to the ratio of this distortion over the Debye–Hückel thickness (d/K^{-1}):

$$F_R = \frac{z^2 e_0^2}{\epsilon (K^{-1})^2} \frac{d}{K^{-1}} \quad (5.132)$$

Substituting d from eqn (5.130), we obtain

$$F_R = \frac{z^2 e_0}{\epsilon (K^{-1})^2 K^{-1}} \frac{v_0 (K^{-1})^2}{2\mu k_B T} = \frac{z^2 e_0^2 K v_0}{2\epsilon k_B T \mu} \quad (5.133)$$

Since the drift velocity (v_0) arises from the applied external field X , the ratio of v_0 to the mobility (μ) is actually the electrostatic force generated by the external field:

$$F = \frac{v_0}{\mu} = z e_0 X \quad (5.134)$$

The relaxation force is then expressed as

$$F_R = \frac{z^3 e_0^3 K X}{2 \varepsilon k_B T} \quad (5.135)$$

In the above treatment, we have assumed that the central ion and its ionic cloud move *only* along or against the direction of the applied field, which is actually inaccurate. We discussed in Section 5.2.1 that the directional migration of ions is only a component superimposed on their already existing random walk, and that the actual trajectories of the ions are still erratic in direction, although with a preferential direction on average along or against the direction of the applied field. After considering the effect of a random walk on the ionic cloud relaxation, Onsager modified the expression for F_R with a correction factor $\omega/2z^2$:

$$F_R = \frac{z e_0^3 K \omega}{6 \varepsilon k_B T} X \quad (5.136)$$

where ω is related to the ionic strength and is defined as

$$\omega = z^2 \frac{1}{1 + \frac{I}{\sqrt{2}}} \quad (5.137)$$

From the relaxation force F_R we now have the drift velocity component generated by it as

$$v_R = \mu F_R = \frac{z e_0^3 K \omega}{6 \varepsilon k_B T} \mu X \quad (5.138)$$

or, if we substitute the absolute mobility with conventional mobility as defined in eqn (5.119):

$$v_R = \frac{e_0^2 K \omega}{6 \varepsilon k_B T} \mu_{\text{Conv}} X \quad (5.139)$$

5.2.6.2 Electrophoresis Force

Under an externally applied field X , the central ion would experience an electrophoretic force of

$$F = z e_0 X \quad (5.140)$$

This force is equally felt by its ionic cloud. At the steady state, both the central ion and ionic cloud move at a constant speed, and this force should be counterbalanced by the Stokes viscous force (F_S):

$$F_S = 6\pi r\eta v \quad (5.141)$$

For the ionic cloud, its radius is defined as the Debye–Hückel thickness (K^{-1}), and the velocity is v_E :

$$ze_0 X = 6\pi K^{-1} \eta v_E \quad (5.142)$$

Then the electrophoresis component of the drift velocity should be

$$v_E = \frac{ze_0 X}{6\pi K^{-1} \eta} \quad (5.143)$$

5.2.6.3 Debye–Hückel–Onsager Equation

Now we have contributions from both relaxation (v_R) and electrophoresis (v_E) to the drift velocity. Substituting v_R and v_E , we have

$$\begin{aligned} v_d &= v_0 - (v_R + v_E) \\ &= v_0 - \left(\frac{e_0^2 K \omega}{6\epsilon k_B T} \mu_{\text{Conv}} X + \frac{ze_0 X}{6\pi K^{-1} \eta} \right) \\ &= v_0 - \frac{X}{K^{-1}} \left(\frac{e_0^2 \omega}{6\epsilon k_B T} \mu_{\text{Conv}} + \frac{ze_0}{6\pi \eta} \right) \end{aligned} \quad (5.144)$$

Rearrangement gives

$$\frac{v_d}{X} = \frac{v_0}{X} - \frac{1}{K^{-1}} \left(\frac{e_0^2 \omega}{6\epsilon k_B T} \mu_{\text{Conv}} + \frac{ze_0}{6\pi \eta} \right) \quad (5.145)$$

By definition, velocities divided by field X (v_d/X and v_0/X) are actually the corresponding mobilities generated by that force, therefore

$$\mu = \mu_{\text{Conv}} - \frac{1}{K^{-1}} \left(\frac{e_0^2 \omega}{6\epsilon k_B T} \mu_{\text{Conv}} + \frac{ze_0}{6\pi \eta} \right) \quad (5.146)$$

Here we have obtained an expression for mobility showing that it is a function of Debye–Hückel thickness, which in turn changes with

solute concentration, and is basically what Kohlrausch's empirical law suggested.

The equivalent conductivity was earlier defined as the sum of cation and anion contributions in the form

$$\Lambda = z_i e_0 F (\mu^+ + \mu^-) \quad (5.147)$$

Substituting mobility expressions for both cation and anion:

$$\begin{aligned} \Lambda &= z_i e_0 F \left[\mu_{\text{Conv}}^+ - \frac{1}{K^{-1}} \left(\frac{e_0^2 \omega}{6 \varepsilon k_B T} \mu_{\text{Conv}}^+ + \frac{z_+ e_0}{6 \pi \eta} \right) \right] \\ &\quad + z_i e_0 F \left[\mu_{\text{Conv}}^- - \frac{1}{K^{-1}} \left(\frac{e_0^2 \omega}{6 \varepsilon k_B T} \mu_{\text{Conv}}^- + \frac{z_- e_0}{6 \pi \eta} \right) \right] \end{aligned} \quad (5.148)$$

If the electrolyte is of the symmetrical type ($z_+ = z_- = z$), such as NaCl or MgSO₄, this expression can be simplified to

$$\Lambda = z_i e_0 F (\mu_0^+ + \mu_0^-) - \frac{1}{K^{-1}} \left[\frac{e_0^2 \omega}{6 \varepsilon k_B T} F (\mu_0^+ + \mu_0^-) + \frac{ze_0 F}{3 \pi \eta} \right] \quad (5.149)$$

The term $z_i e_0 F (\mu_0^+ + \mu_0^-)$ represents the equivalent conductivity when the solute concentration approaches zero, or the limiting equivalent conductivity (Λ^0) defined by Kohlrausch, therefore we can rearrange the above equation to

$$\Lambda = \Lambda^0 - \frac{1}{K^{-1}} \left[\frac{e_0^2 \omega}{6 \varepsilon k_B T} \Lambda^0 + \frac{ze_0 F}{3 \pi \eta} \right] \quad (5.150)$$

Inserting the expression for the Debye–Hückel thickness for a symmetric electrolyte:

$$K = \sqrt{\frac{4\pi}{\varepsilon k_B T} \sum_i n_i^0 z_i^2 e_0^2} = \sqrt{\frac{8\pi N_A e_0^2 z^2 c}{1000 \varepsilon k_B T}} \quad (5.151)$$

we obtain

$$\Lambda = \Lambda^0 - \sqrt{\frac{8\pi N_A e_0^2 z^2 c}{1000 \varepsilon k_B T}} \left[\frac{e_0^2 \omega}{6 \varepsilon k_B T} \Lambda^0 + \frac{ze_0 F}{3 \pi \eta} \right] \quad (5.152)$$

This is the *Debye–Hückel–Onsager equation*, which describes ion conduction while considering the ion–ion interaction. After condensing the constant, it takes the general format of Kohlrausch's law:

$$\Lambda = \Lambda^0 - \sqrt{c} (A + B \Lambda^0) = \Lambda^0 - \text{constant} \times \sqrt{c} \quad (5.153)$$

Thus, we have completed the verification of Kohlrausch's law by the Debye–Hückel model, which was left incomplete in Section 4.6.3, with assistance from Onsager's treatment. The Debye–Hückel–Onsager equation can accurately predict the ion transport properties in aqueous electrolytes such as NaCl, KCl, HCl and AgNO₃ provided that their concentration remains lower than 0.003 M. Because it started from an atomistic model of how ions interact with each other, even after nearly a century it is still regarded as the zenith of physical chemistry. There have been numerous attempts to extend its applicability into higher concentration regimes, but most of those approaches were empirical and cannot quite match the fundamental significance of the original Debye–Hückel model and its application to ion transport by Onsager's treatment.

It is worth mentioning that the measurement of ion conductivities is usually carried out using alternating current (AC) instead of direct current (DC) conditions, whose rationale and underlying mathematics will be discussed in Chapter 14 of this book. One might wonder how an ionic cloud would behave when the externally applied electric field keeps changing direction. This question actually relates to how fast an ionic cloud could relax in response to the moving central ion.

As we briefly discussed in Section 3.2, the dipole of solvent molecules will eventually be unable to catch up with the change of the external field (Figure 3.7). The same applies to the ionic cloud. It was observed that, while the ion conductivities measured under AC conditions remain independent of frequency in the low- and medium-frequency range, an increase in conductivity occurs at a critical frequency of $\sim 10^6$ Hz. That is where the ionic cloud stops responding to the external field, the direct result of which is the disappearance of both relaxation and electrophoresis effects. A central ion losing these opposing forces would appear to move at a faster speed, until at higher frequencies the central ion will also stop feeling the influence from the external field and seemingly cease to move. In other words, the ion transport in the above transition frequency region becomes decoupled from the ion–ion interaction. This phenomenon is known as the *Debye–Falkenhagen effect*.

5.2.6.4 Ambipolar Ionic Movement

Whereas the Debye–Hückel–Onsager approach considered the movement of an individual ion by treating the influence of other ions as the response from an ionic cloud towards the externally applied field, there is an alternative way in which we can look at the simultaneous movement of ions and counterions in a collective manner.

Let us consider the simple case of a binary electrolyte consisting of one kind of cation and one kind of anion, such as an aqueous solution of NaCl. At the instant when an external electric field is applied, Na^+ and Cl^- ions would move in opposite directions, but at different speeds. According to Table 5.2, at a concentration of 0.1 M, Na^+ ions move more slowly as their transport number is only 0.39, whereas Cl^- ions move faster with a transport number of $1 - 0.39 = 0.61$.

This inequality in migration would soon create an imbalance of charge distributions in local regions of the electrolyte, that is, more cations are statistically distributed in the regions closer to the anode, whereas more anions are statistically distributed in the regions closer to the cathode. Such a distribution in fact induces an internal field that is opposite in direction to the externally applied field, and forces the anions to slow down their migration and makes the cations speed up. When a *quasi-equilibrium* is reached, the cations and anions are eventually moving at the same speed.

In other words, even in the ideal electrolyte, the movements of cations and anions are coupled. Such coupling is referred to as *ambipolar ion transport*.

For a simple binary electrolyte such as NaCl solution, we can assume that the total mass-transport flux J_{MT} consists of two parts, one induced by a concentration gradient (diffusion, J_{Diff}), and the other induced by the applied electric field (migration, J_{Mig}):

$$J_{\text{MT}} = J_{\text{Diff}} + J_{\text{Mig}} \quad (5.154)$$

where both J_{Diff} and J_{Mig} have contributions from both anions and cations:

$$J_{\text{MT}}^- = J_{\text{Diff}}^- + J_{\text{Mig}}^- \quad (5.155)$$

$$J_{\text{MT}}^+ = J_{\text{Diff}}^+ + J_{\text{Mig}}^+ \quad (5.156)$$

where the superscripts “−” and “+” stand for anions and cations, respectively. The diffusion part can be defined from Fick’s first law as

$$J_{\text{Diff}}^- = -D_- \frac{\partial}{\partial x} c_- \quad (5.157)$$

$$J_{\text{Diff}}^+ = -D_+ \frac{\partial}{\partial x} c_+ \quad (5.158)$$

where c_- and c_+ represent the bulk concentrations of the anion and cation, respectively.

The migration part, assuming that the externally applied electric potential gradient is dV/dx , would be expressed as

$$J_{\text{Mig}}^- = -\mu_- c_- \frac{\partial V}{\partial x} \quad (5.159)$$

$$J_{\text{Mig}}^+ = \mu_+ c_+ \frac{\partial V}{\partial x} \quad (5.160)$$

where μ_- and μ_+ represent the ionic mobility of the anion and cation, respectively.

Note that for cation the sign in front of mobility is positive, because it moves in the direction of the applied field, whereas the anion moves against the applied field.

Now, the total mass-transport flux can be expressed as the summation of these four components:

$$\begin{aligned} J_{\text{MT}} &= J_{\text{Diff}} + J_{\text{Mig}} = J_{\text{Diff}}^- + J_{\text{Diff}}^+ + J_{\text{Mig}}^- + J_{\text{Mig}}^+ \\ &= -\mu_- c_- \frac{\partial V}{\partial x} - D_- \frac{\partial}{\partial x} c_- + \mu_+ c_+ \frac{\partial V}{\partial x} - D_+ \frac{\partial}{\partial x} c_+ \end{aligned} \quad (5.161)$$

When quasi-equilibrium is established, the total anion flux should be equal to the total cation flux:

$$J_{\text{MT}}^- = J_{\text{MT}}^+ \quad (5.162)$$

or in the form

$$J_{\text{Diff}}^- + J_{\text{Mig}}^- = J_{\text{Diff}}^+ + J_{\text{Mig}}^+ \quad (5.163)$$

which leads to

$$-\mu_- c_- \frac{\partial V}{\partial x} - D_- \frac{\partial}{\partial x} c_- = \mu_+ c_+ \frac{\partial V}{\partial x} - D_+ \frac{\partial}{\partial x} c_+ \quad (5.164)$$

Solving for $\partial V/\partial x$, one would obtain the expression

$$\frac{\partial V}{\partial x} = \frac{1}{(\mu_+ c_+ + \mu_- c_-)} \left[D_+ \frac{\partial}{\partial x} c_+ - D_- \frac{\partial}{\partial x} c_- \right] \quad (5.165)$$

Here we further assume, to a good approximation again, that the local concentrations of anions c_- and cations c_+ are equal to the initial bulk salt concentration c_0 , then eqn (5.164) turns into a simpler expression:

$$\frac{\partial V}{\partial x} = \frac{(D_+ - D_-)}{(\mu_+ + \mu_-) c_0} \frac{\partial c_0}{\partial x} \quad (5.166)$$

Inserting eqn (5.166) back into eqn (5.155) and (5.156) to eliminate the terms depending on potential ingredient, applying the new assumption that $c_- = c_+ = c_0$, and performing rearrangement, we obtain

$$\begin{aligned} J^- &= J_{\text{Diff}}^- + J_{\text{Mig}}^- = -D_- \frac{\partial c_0}{\partial x} - \mu_- c_0 \frac{(D_+ - D_-)}{(\mu_+ + \mu_-) c_0} \frac{\partial c_0}{\partial x} = -D_- \frac{\partial c_0}{\partial x} - \frac{\mu_- D_+ - \mu_- D_-}{\mu_+ + \mu_-} \frac{\partial c_0}{\partial x} \\ &= - \left[D_- - \frac{\mu_- D_- - \mu_- D_+}{\mu_+ + \mu_-} \right] \frac{\partial c_0}{\partial x} = - \left[\frac{\mu_+ D_- + \mu_- D_+}{\mu_+ + \mu_-} \right] \frac{\partial c_0}{\partial x} \end{aligned} \quad (5.167)$$

Likewise:

$$J_{\text{MT}}^+ = J_{\text{MT}}^- = - \left[\frac{\mu_+ D_- + \mu_- D_+}{\mu_+ + \mu_-} \right] \frac{\partial c_0}{\partial x} \quad (5.168)$$

Eqn (5.167) and (5.168) both have an interesting form that is rather similar to the expression of Fick's first law [eqn (5.1)], which suggests that, upon the establishment of quasi-equilibrium between the externally applied electric field and the internally induced electric field, due to the inequality in cationic and anionic transport numbers, the coupled cation and anion movement in fact creates an impression that both ions are diffusing under a composite diffusion coefficient that is determined by the intrinsic diffusion coefficient and mobility of each individual.

We define this imaginary diffusion coefficient as the *ambipolar diffusion coefficient* (D_{ambp}):

$$D_{\text{ambp}} = \frac{\mu_+ D_- + \mu_- D_+}{\mu_+ + \mu_-} \quad (5.169)$$

The cross-product of μ_+D_- and μ_-D_+ unequivocally demonstrates the coupling of cations and anions when they move in a binary electrolyte.

Eqn (5.169) can be turned into a more elegant form by replacing the ionic mobility with the diffusion coefficient of individual ions *via* the Einstein relation [eqn (5.91)]:

$$\mu_+ = \frac{D_+}{k_B T} \quad (5.170)$$

$$\mu_- = \frac{D_-}{k_B T} \quad (5.171)$$

Therefore,

$$D_{\text{ambp}} = \frac{\mu_+ D_- + \mu_- D_+}{\mu_+ + \mu_-} = \frac{\left[\frac{D_- D_+}{k_B T} + \frac{D_- D_+}{k_B T} \right]}{\frac{D_+ + D_-}{k_B T}} = \frac{2 D_- D_+}{D_+ + D_-} \quad (5.172)$$

This new quantity is also known by a series of different names, such as *convective diffusion coefficient*, *salt diffusion coefficient*, *electrolyte diffusion coefficient* and *electrolyte average diffusivity*. On the other hand, the diffusion coefficient of individual ions that we have been dealing with previously is sometimes called the *self-diffusion coefficient*. The various terms mentioned above indeed could cause confusion to beginners. In a brief effort to differentiate the self-diffusion coefficient and ambipolar diffusion coefficient, one could view the former as the free behavior of each individual ion (hence “*self*”), whereas the latter represents the weighted average of the diffusivity of cations and anions. It should be noted again here that eqn (5.169) and (5.172) are specific to binary electrolytes consisting of monovalent cations and monovalent anions, such as NaCl solutions. A more generalized expression will be derived later in Chapter 14.

In considering the influence of oppositely charged ions on each other, the above approach represents a major advance from the classical electrolyte studies established on the Debye–Hückel model, where the salt concentrations must be kept infinitesimally small, so that the distribution and transport of the ions could be treated as if each ion behaves independently of other ions. In those classical studies, the macroscopically measurable quantities such as diffusion coefficients, mobilities and ion conductivities are simply the summation of all

the individual behaviors of ions. Representative equations are those derived directly from the Debye–Hückel model as well as various Einstein equations regarding ion transport.

However, the consideration of ambipolar transport of ions only stays at a collective level to examine ion–ion interactions, *i.e.* the quasi-equilibrium established upon an additional field that is induced by the relative accumulation and depletion of ions in a given region. It still does not take account of direct interactions between ions bearing both the same and opposite charges.

In more concentrated electrolytes, such as the “super-concentrated electrolytes” that have been extensively explored in recent decades, the close encounter between cations and anions and the direct interactions among these individual ions become inevitable, where ions of opposite charges could even form close pairs or large clusters. Under such circumstances, additional parameters such as friction coefficients have to be introduced to reflect the intensified interactions (both attraction and repulsion) between the individual ions and their effect on the distribution and relative movement of ions. Often the differential equations thus derived become extremely complicated, and could not be solved given the many boundary conditions required. We will return to this topic in Chapter 14 when discussing non-ideal electrolytes.

5.2.7 Ionics in Non-aqueous Electrolytes

Water is the most prevalent solvent on Earth, hence most classical understanding about electrolytes was achieved on aqueous solutions. As an excellent electrolyte solvent, bipolar water displays unparalleled capabilities in solvating ions, which benefits from the combination of its high dielectric constant and its tendency to form a network of hydrogen bonds. The direct consequence of sufficient solvation is high ion conductivity, which in classical *ionics* has been the primary, if not exclusive, requirement for an electrolyte.

However, in terms of *electrodics*, which is covered in the next chapter, water is not so useful. Specifically, water is very unstable against both reduction and oxidation if placed under an electric field.

Imagine that a researcher places a pair of electrodes in an aqueous solution of NaCl, and then applies a DC voltage, say 5 V, across the electrodes. From the chemical formula of NaCl, the worker might naively expect that at the anode reduction would produce sodium metal:



while at cathode oxidation would produce chlorine gas:



Well, they will be very disappointed, because only part of the anticipated reactions actually happened. Although oxidation at the cathode does produce a lot of gas, analysis reveals that only part of the gas is chlorine, with the rest being oxygen, and the ratio of these two gases depends on the pH of the solution. At the anode, however, not a trace of sodium metal is produced; Instead, a large amount of gas generated at the anode surface is observed, and analysis reveals that this gas is hydrogen.

In other words, the expected electrochemical reactions of the electrolyte solute are kidnapped by the electrolyte solvent, *i.e.* water. This is a typical example that water cannot serve as a good solvent under many circumstances where one would hope that it would remain inert and not interfere with the desired cell reaction. The underlying reason for water's unsuitability as a solvent is its poor electrochemical stability against reduction and oxidation. Water often interferes with the dominant reactions in the electrochemical process, as it did in the above example of attempted NaCl electrolysis, because it is much more easily reduced than Na^+ , and is as easily oxidized as Cl^- . In other words, it is electrochemically more reactive than its solute NaCl.

In electrochemistry and materials science, such stability of electrolytes can be quantified by a parameter called the "*electrochemical stability window*", or simply "*voltage window*", which is the region between the reductive and oxidative decomposition of the electrolyte components (solutes or solvents, whichever decomposes first). Apparently, in order for an electrolyte to remain inert towards a cell reaction, it must have a stability window that is wide enough to encompass the desired cell reactions.

We will discuss this property of electrolytes in more detail in the next chapter and the related topic of how to expand such a stability window for practical applications such as advanced batteries, but at the moment we would just note that the electrochemical stability window of water is only 1.23 V, which is defined by its reduction to hydrogen and oxidation to oxygen. The specific potential for reduction and oxidation of water depends on the pH value, as does the specific reaction mechanism, but the window remains constant at 1.23 V if every process occurs at thermodynamic equilibrium. Such a thermodynamic relation among these electrode potentials, reaction mechanism

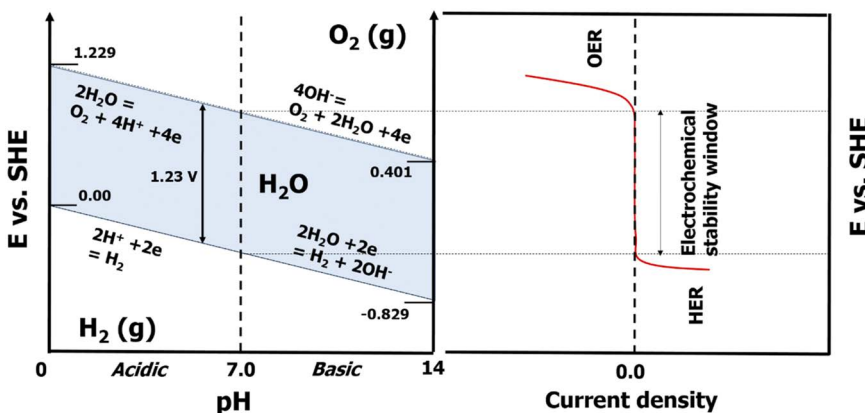


Figure 5.12 The Pourbaix diagram of aqueous electrolytes (left) defines the region where water is electrochemically stable, and the electrochemical stability window of most aqueous electrolytes (right), which is 1.23 V if everything is at thermodynamic equilibrium, as marked by the potential where oxidation (OER) and reduction (HER) of water start. In reality, the actual stability window of aqueous electrolytes is usually ~1.50 V because of kinetic factors of OER. The narrow window of aqueous electrolytes in general imposes a restriction on their application in electrochemical devices where higher voltages are required, such as lithium-ion batteries normally operating at >4.0 V. Such a gap mandates the use of non-aqueous electrolytes.

and pH is best expressed in the so-called “*Pourbaix diagram*” (Figure 5.12),⁹ where the electrochemical stability window of water is represented by the shaded region confined between the two parallel lines that changes with pH value. Above the upper limit, water is unstable as the electrochemical oxidation turns it into oxygen, whereas below the lower limit, it is also unstable as the electrochemical reduction turns it into hydrogen.

In reality, the reactions that generate hydrogen [*hydrogen evolution reactions (HER)*] most likely occur at thermodynamic equilibrium, but the *oxygen evolution reactions (OER)* often encounter a higher kinetic barrier. Such kinetic sluggishness results in a slightly wider electrochemical stability window (~1.5 V) for most aqueous electrolytes, and benefits the aqueous battery chemistry with an operating potential of 1.5 V, as represented by the diverse dry batteries sold in drug stores, which provide a standard voltage of 1.5 V.

However, for those cell reactions that sit way beyond the upper and lower stability limits as defined by the Pourbaix diagram, such as the reduction of sodium ion to sodium metal, water has to give up its role of electrolyte solvent in favor of non-aqueous solvents.

Non-aqueous electrolyte solvents are often organic molecules that are both polar and *aprotic*, *i.e.* not containing a hydrogen atom that can be dissociated into a proton. In today's world, perhaps the most popular non-aqueous solvents are the alkyl esters of carbonic acids, more simply known as carbonates, which are literally in everybody's hands because of their use as electrolyte solvents in all lithium-ion batteries manufactured throughout the world.

Neither the Debye–Hückel model nor the Einstein equations specify that the solvent must be water, hence the general mathematical treatment remains true, but significant differences are expected in both ion solvation and ion transport because of the unique properties of the non-aqueous solvents that differ from those of water.

First, most non-aqueous solvents possess much lower dielectric constants than water. Two immediate consequences thus arise:

1. The Debye–Hückel thickness of the central ion would be much smaller compared with aqueous electrolytes:

$$K^{-1} = \sqrt{\frac{\varepsilon k_B T}{4\pi} \frac{1}{\sum_i n_i^0 z_i^2 e_0^2}} \quad (4.71)$$

We have learned previously that the Debye–Hückel thickness is actually the effective distance between the central ion and its ionic cloud (Figure 4.5). In non-aqueous electrolytes, this average distance would be much shorter, hence the ion–ion interaction intensifies.

2. We have also learned in Section 3.2 that the dielectric constant quantifies the solvent molecule's capability of shielding the Coulombic charge of the ions. A low dielectric constant means that a given central ion could have a far more penetrating Coulombic force, so that the ions far away can now feel its presence.

The combined effects of these two consequences imply that the ions in non-aqueous electrolytes are in a much more intimate relationship than they are in aqueous counterparts, and such a closer interaction between ions of opposite charge would turn into higher population of ion pairs, as predicted by the Bjerrum length, within which all the ions of opposite charges should be considered as an ion pair:

$$\lambda_B = \frac{z_+ z_- e_0^2}{\varepsilon k_B T} \quad (4.83)$$

In fact, in addition to ion pairs, higher orders of ion–ion association also occur, such as triple ions or larger ion clusters. From dilute electrolytes to super-concentrated electrolytes, the ion associations intensify at the expense of the ion conductivities.

The ion–solvent interaction also directly affects ion transport. As discussed earlier, in order to pull ions from their lattice and form an electrolyte solution the solvent molecules must provide sufficient energy compensation, and this often requires the solvent molecules to be polar. Water is an effective dipole that interacts strongly with both cations and anions (Figure 3.1a). Organic molecules, however, are often “monopoles” that preferentially solvate cations while leaving anions relatively free (Figure 3.1b). This unsymmetrical ion–solvent interaction inevitably makes cations much clumsier than their anionic counterparts. Mathematically, this will be reflected in the Stokes–Einstein equation:

$$\mu_+ = \frac{z_+ e_0}{6\pi\eta} \frac{1}{r_+} \quad (5.175)$$

$$\mu_- = \frac{z_- e_0}{6\pi\eta} \frac{1}{r_-} \quad (5.176)$$

where r_+ and r_- are the solvated ionic radii of the cation and anion, respectively. Apparently, with its larger solvation sheath, the cation would have a much lower mobility (μ_+) and much lower cationic transport number than in aqueous electrolytes:

$$t_+ = \frac{\mu_+}{\mu_+ + \mu_-} \quad (5.177)$$

One peculiarity of ion transport in non-aqueous electrolytes is the existence of an apparent maximum conductivity, which is seldom, if ever, observed in aqueous electrolytes (Figure 5.13). The appearance of such conductivity maxima is the result of two competing factors that contribute to the ion transport: (1) the number of free ions available and (2) the mobility of these ions. The latter is dependent not only on the ionic radius but also on the viscosity of the medium as stated in the Stokes–Einstein equation. In non-aqueous electrolytes, the mobility/viscosity issue becomes pronounced even at rather low solute concentrations, creating a maximum conductivity often in the neighborhood of ~1.0 M or m (there is little difference between these two units in dilute electrolytes). However, in aqueous

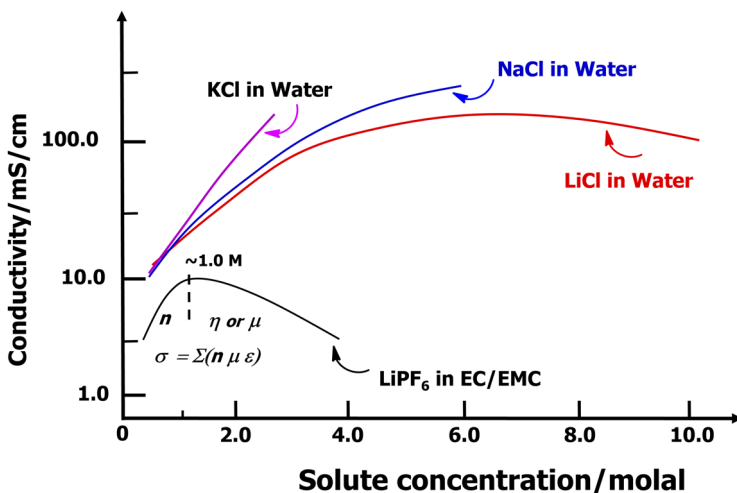


Figure 5.13 Concentration dependence of isothermal conductivity for typical aqueous and non-aqueous electrolytes.

electrolytes, thanks to the superior solvation power of water molecules, the suppressing effect of mobility/viscosity does not appear until a very high solute concentration (such as with LiCl), or simply does not appear at all until the solubility limits of the solutes are reached (such as NaCl and KCl).

5.2.8 Abnormal Proton Transport: Grotthuss Mechanism

The proton (H^+) represents an exception to all the diffusion and migration behaviors described so far.

The proton is the smallest ion in the entire Universe, hence it enjoys a certain uniqueness in comparison with all other ions. One might already have noticed in Table 5.1 that its diffusion coefficients are far higher than other ions, which strongly hints at a transport mechanism that is different from what we have discussed so far.

The ion transport discussed in the previous sections, no matter whether *via* diffusion or migration, involves the individual ions physically traveling from point A to point B, and during the process the ion interacts with its surroundings (solvent medium). It is this interaction that actually constitutes the foundation of Stokes's law. However, extensive experiments showed that the H^+ transport does not obey Stokes's law. In a particular manner, H^+ seems to be decoupled from

the surroundings, and instead of physically traveling the distance, it “teleports” from point A to point B.

In 1806, de Grotthuss proposed such a teleporting mechanism.¹⁰ He stated that “*electrolytic reaction occurs such that each oxygen atom simultaneously passes and receives a single hydrogen atom*”. This transport mechanism does not require the proton to physically travel. This mechanism is similar in a way to “*Newton’s cradle*” (Figure 5.14a), where ball number 1 passes its momentum from position A to position B without actually going there. If one visualizes the momentum as another physical property, *i.e.* the positive charge carried by the proton, then the swinging balls in Figure 5.14a illustrate the proton transport between positions A and B.

Unfortunately, at the time, not only was the concept of ions unknown (remember that Faraday introduced the concept in 1834; see Chapter 1), but also the molecular structure of water was also mistakenly thought to be OH instead of H₂O. de Grotthuss’s prescient idea soon

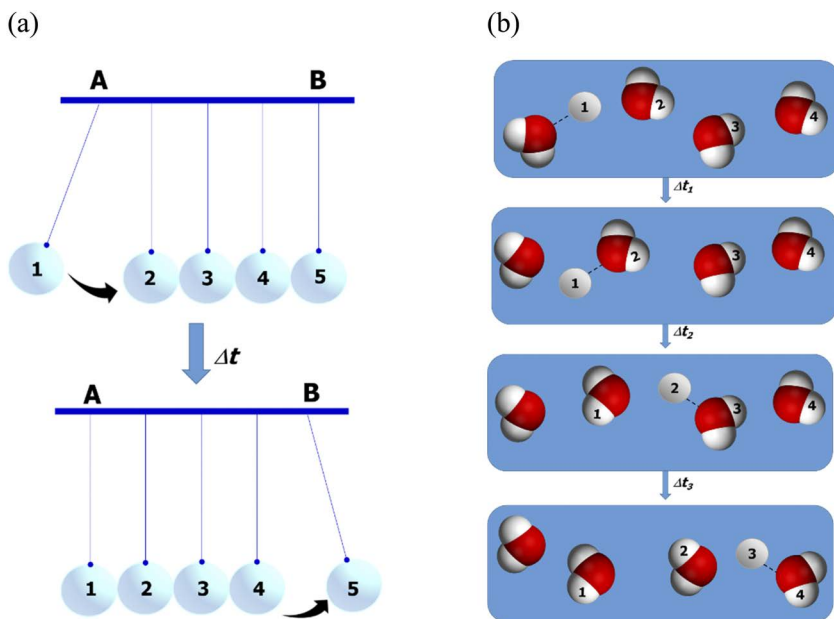


Figure 5.14 Grotthuss mechanism for proton transport. (a) Newton’s cradle, where balls pass momentum from position A to position B without physically traveling. If one visualizes the property of charge (+) as equivalence of the property momentum, then the model represents proton transport. (b) Illustration of how a proton “travels” by a sequence of associating with and dissociating from the water molecules nearby.

fell into oblivion, and the Stokes-like picture of ions trudging across a viscous medium prevailed.

In 1933, while attempting to rationalize the unusual transport of proton in water, Bernal and Fowler revisited the concept of de Grotthuss and borrowed the gist from it.¹¹ They proposed that while a proton in the aqueous solutions exists in the form of a hydronium ion (H_3O^+), neither the heavy hydronium ion nor the proton itself has to physically move from point A to point B. Rather, *via* a sequence of dissociation and association with the neighboring water molecules, the positive charge is transmitted from point A to point B without the long-distance movement of any ions (Figure 5.14b). In this way, the proton transport (or we should say “charge transport” now because the original proton never leaves the original water molecule with which it associates) does not experience the viscous drag from the medium, and is completely decoupled from Stokes’s law.

Further refinement of this mechanism was made both by Bernal and Fowler and by Bockris and Conway (see Further Reading list at the end of the book), who revealed that such a unique transport mechanism may exist only for the proton because it must satisfy two critical requirements for “teleporting”:

1. A decent probability of quantum tunneling through the dissociation/association energy barrier. The so-called Gamow probability according to quantum mechanics is determined by

$$P_t \propto e^{-\frac{4\pi L}{\hbar} \sqrt{m(E-U)}} \quad (5.178)$$

where m is the mass of the tunneling particle, L is the jumping distance and E and U are the total and potential energies of the tunneling particle, respectively. An electron is known to quantum tunnel rather easily, whereas an ion would have to overcome its tremendous mass compared with an electron (a proton is 1370 times heavier than an electron). However, since the proton is the smallest ion in the Periodic Table (it is essentially a nucleus!), its small radius requires a small jumping distance, and eventually makes the probability of proton tunneling as illustrated in Figure 5.14b be at least 0.01.

2. The hydrogen bonding in the water network dictates the orientation of neighboring water molecules, thus preparing them to accept the incoming protons and significantly increasing the probability.

Such uniqueness would cease to exist for any other ions, because a network similar to hydrogen bonding hardly exists in electrolytes based on any other ions, not to mention that as the ionic mass increases the probability of quantum tunneling rapidly vanishes at an exponential rate. For example, the Gamow probability for the next stable ion in the Periodic Table that is lighter than all other ions except the proton, *i.e.* lithium ion (Li^+), would be only $2.19 \times 10^{-33}!$

5.2.9 Electrolytes Without Solvents: Ionic Liquids

So far, we have employed solvents, either water, non-aqueous or polymeric, as assistants to pull ions apart from their fixed positions located in the crystalline lattice, consequently making them mobile (Route A in Figure 2.1). Examples include NaCl solutions in water, lithium hexafluorophosphate in alkyl carbonate esters and lithium perchlorate in poly(ethylene oxide). In these electrolytes, the solvation heat corresponding to the formation of solvation sheaths compensates the loss of lattice stabilization energy, and the mobile species in these electrolytes are actually the solvated ions.

However, we mentioned in Chapter 2 that there are alternative ways to make the ions mobile without involving any solvent molecules.

One such way is to compensate the loss of lattice stabilization energy *via* external heating until the lattice collapses due to melting (Route B in Figure 2.1). The electrolytes thus formed are called *molten salts*. An example is the liquid resulting from NaCl after being heated to 801 °C. In principle, any salt that can remain chemically stable above its melting point (*i.e.* without decomposition) can be turned into a molten salt electrolyte. For some salts consisting of quaternary nitrogen, phosphorus or tertiary sulfur cations (“onium cations”) and large organic anions, the melting occurs at or below ambient temperature. These molten salts are called “*room-temperature ionic liquids*” or simply “*ionic liquids*”.

The other way of making ions mobile without solvation involves the decoupling of ions from the solid matrices, so that at least one ion is mobile within the polyionic framework formed by the other ions (see Figure 2.1). This class of electrolytes includes solid ion conductors usually based on inorganic ceramic compounds in either crystalline or amorphous (glassy) forms. Note that we exclude the so-called “*polymer electrolytes*” from this class, because even in solvent-free *solid polymer electrolytes* (SPEs) the ions remain solvated, with the polymers actually serving as a macromolecular ether solvent, whereas in *gel polymer electrolytes* (GPEs) the ions are solvated by the same organic

polar solvents as they are in conventional non-aqueous electrolytes. The ionics in SPEs and GPEs still falls under the principles described for liquid electrolytes (Route A in Figure 2.1).

We will discuss these “solvent-free” electrolytes in a little more detail in Part B, placing emphasis on their respective applications in electrochemical devices such as batteries. But now we need to discuss briefly the unique aspects of ionics in molten salts and inorganic solid electrolytes before completing this chapter.

5.2.9.1 Molten Salts or Ionic Liquids

Upon melting, crystalline solids turn into liquids, which are similar to most molecular liquids above their corresponding melting points in terms of numerous properties such as fluidity and diffusion coefficient. However, to the surprise of most people, the local structure of these liquids still maintains its ordered arrangement of ions as if they are still in the lattice, although such ordering rapidly vanishes at the scale of nanometers. In other words, the molten salts are ordered in the short range but disordered in the long range. Early structural studies using X-ray or neutron diffraction/scattering techniques found that the interionic distances in molten salts are comparable to or even smaller than those measured in crystalline lattices. Considering that most salts experience a volume expansion of 10–20% upon melting, it is logical to infer that a large number of “voids” are created in the molten state. It is such voids, also known as “free volume”, that allow ions to transport. Theoretical calculations based on the work of forming such holes in liquids revealed that the average size of these holes is approximately the size of the ions comprising the molten salt. For example, in molten NaCl the mean hole radius is 0.17 nm, whereas the radii for Na and Cl are 0.116 and 0.172 nm respectively.

Among the ion transport equations established for liquid electrolytes, the Stokes–Einstein equation was found to roughly hold true for most molten salt electrolytes, which is rather surprising because, as we have mentioned before, the derivation of the Stokes–Einstein equation is not exactly rigorous. The original Stokes relation was supposed to be applicable to the movement of macroscopic spheres in structureless fluids, but in either electrolyte solutions or molten salts the ions are moving against a medium consisting of particles that are roughly their own size. Nevertheless, the Stokes–Einstein equation demonstrated surprising universality.

Unfortunately, this is not the case for the Nernst–Einstein equation, which was found always to overestimate the conductivity of

molten salt electrolytes if one calculates it from the measured diffusion coefficients:

$$\Lambda = \frac{zF^2}{RT} (D_+ + D_-) \quad (5.101)$$

This departure from experiment is attributed to the much higher ion-pair populations in molten salts than in liquid electrolytes.

Remember that in liquid electrolytes (Section 4.9), the presence of solvent molecules, no matter whether aqueous or non-aqueous, effectively separates ions from each other, and the probability of ion-pair formation is constrained by the Bjerrum length (λ_B):

$$\lambda_B = \frac{z_+ z_- e_0^2}{\epsilon k_B T} \quad (4.83)$$

which defines the upper limit of interionic distance for ion-pair formation. Since λ_B is inversely proportional to the dielectric constant of solvents, a highly polar solvent can effectively prevent ion-pair formation by shielding the Coulombic field of the ions.

Ionic liquids, however, are not subject to such shielding. The absence of any solvent implies that all ions are intrinsically within distance of forming ion pairs with their neighbors. Since all ion pairs are electroneutral in charge, their movement makes a contribution to diffusion but not to conduction. Therefore, a correction term must be introduced to modify the Nernst–Einstein equation as

$$\Lambda = \frac{zF^2}{RT} (D_+ + D_-) - \frac{zF^2}{RT} D_{\text{ion pair}} \quad (5.179)$$

Apparently, a high population of ion pairs would have led to a much higher molar conductivity as predicted by the Nernst–Einstein equation than the actual value if its contribution to diffusion is not subtracted.

We have shown how the ion–solvent interaction significantly alters ion transport behavior in electrolyte solutions, which is strongly reflected in the cation transport number, especially when the solvent is “monopolar” organic molecules. Such a solvation effect also ceases to exist in molten salts, and consequently cations should move with much higher agility owing to their smaller ionic radii. The cationic transport numbers t_+ calculated from diffusion coefficients often range from 0.6 to 0.8 in most inorganic molten salts.

It should be mentioned that recent studies challenged the authenticity of these transport numbers as they were derived based on the assumption that the electrolytes remain ideal (*i.e.* dilute). In fact, as the solute concentration increases, intensified ion–ion interactions lead to ion aggregates and clusters, which complicates the simple picture of cations and anions conducting their own migrations independently. It was suggested by Balsara and co-workers that, in such a highly concentrated environment, the transport number for a given ion (Li^+ or Na^+) could depart from the “normal” range of 0–1.0 and wander into negative territory (Section 14.2; Table 14.3).¹²

So, what does a negative transport number for a cation suggest? Imagine that one applies an electric field across an electrochemical cell: what happens now is that the cation migrates towards not the negative but instead the positive electrode. In other words, its contribution to the overall current is now negative. This is possible only if the cation is “kidnapped” by an aggregate that bears an overall charge of negative sign, such as a triplet consisting of one cation and two anions. It is expected that such negative transport numbers would prevail if ion aggregates and clusters exist in high populations, as in super-concentrated electrolytes or molten salts.

5.2.9.2 Inorganic Solid Electrolytes

Inorganic solid electrolytes are based on a wide variety of materials with different chemistries and structures, where the ionics differs significantly from the classical discipline for liquid electrolytes. In these solid matrices, the ions are situated at lattice sites coordinated by neighboring counterions, with a certain similarity to solvation sheaths in liquid electrolytes. However, such solvation sheaths cannot move with the ions when the ions hop between neighboring sites. Sometimes these immobile local solvation structures are referred to as “*solvation sites*”.

In such a mode of transport, the mobile ions would show a transport number of 1.0. However, in doing so, not only must they overcome the energy barriers created by their electrostatic interaction with the framework, but also they require an open channel structure to travel through and available vacancies in the neighborhood to wait for them. Consequently, the two most important factors dictating how mobile ions could originate from compositional and structural requirements for the materials, respectively: the former determines how deep the Coulombic traps for the ions are in the 3D framework, and the latter provides the mandatory spatial freedom for ion hopping.

One can imagine that, most of the time, an ion vibrates around its equilibrium lattice site owing to the confinement by the solvation cage until, occasionally, the thermal fluctuations become sufficiently high that the ion is sufficiently excited to climb out of the Coulombic trap, hop to the neighboring site and fall into a new solvation cage. Since these solvation cages are immobile, the moving ion would experience a series of periodic bottleneck points, which constitute energetic barriers that separate the neighboring equilibrium lattice sites in Coulombic traps (Figure 5.15, left). This is in strong contrast to the transport of solvated ions in liquid electrolytes, where a solvation sheath traveling with the ions together with rapid exchange of solvent molecules inside and outside the primary solvation sheath creates a relatively uniform surrounding around the ions, leading to a rather flattened potential profile (Figure 5.15, right).

Chemically, a solid electrolyte can be metal or non-metal oxides, sulfides or phosphates, while structurally any crystalline lattice type that could form polyhedral skeletons with a large lattice volume and open channels is favored, examples of which include lithium superionic conductor (LISICON), sodium superionic conductor (NASICON), argyrodite, perovskites and antiperovskites. The mobile ions in those solid ion conductors are mostly monovalent cations such as H^+ , Li^+ , Na^+ , K^+ , Cu^+ and Ag^+ , but multivalent cations such as Mg^{2+} and Ca^{2+} and anions such as F^- , Cl^- and O^{2-} can also be mobile. Naturally, the monovalent ions are much more mobile than multivalent ions owing to the weaker Coulombic forces they experience in the local structure. A similar trend also exists in liquid electrolytes, but such a valence

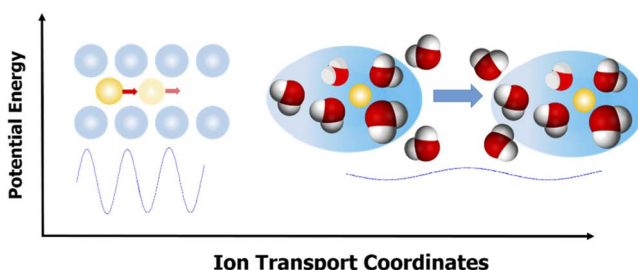


Figure 5.15 The potential energy changes that an ion must experience in an inorganic solid electrolyte (left), where the immobilized solvation cages formed by the polyhedral structure constitute a series of Coulombic traps for the mobile ion in its transport pathway, in sharp contrast to the ion transport in liquid electrolytes, where the portable solvation sheaths along with rapid exchange of solvent molecules ensures an almost constant potential environment for the mobile ion (right).

dependence is much more severe in solid ion conductors owing to the absence of assistance provided by solvation.

Amorphous ceramics that lack long-range order structures could also allow ions to be mobile, examples of which include the commercially available thin-film electrolytes based on lithium phosphorus oxynitride (LiPON) and its many variants. In theory, ion transport in amorphous solids may suffer from the absence of well-ordered channels in the long range, but in reality it may also benefit from the absence of structural heterogeneities and anisotropy. Therefore, there is no absolute favor for or disfavor against either a crystalline or an amorphous nature of the materials.

Whereas amorphous solid ion conductors are morphologically homogeneous, most crystalline solid electrolytes are not (unless they are made single crystalline in extremely rare cases). Instead, they consist of myriads of polycrystalline regions. Hence the ion transport in most crystalline ion conductors must overcome not only the energy barrier of breaking loose from their local Coulombic trap, but also the inter-grain resistances. This introduces extra complexity to the ionics.

It was generally accepted that within the crystalline bulk the ion conductivity is given by

$$\sigma = \frac{\sigma_0}{T} e^{-\frac{E_A}{k_B T}} \quad (5.180)$$

where E_A is the activation energy for ion hopping. At grain boundaries where a crystal interfaces with another crystal or even a different material, however, the spatial redistribution of charges and vacancies, the chemical reactions and the formation of new interphases often lead to unexpected changes in ion diffusion properties that are highly specific to the materials. This remains an area that is little understood so far but has started to attract high activity. No further effort will be made here to cover this rapidly evolving frontier, as most of the fundamental understanding and models proposed are still highly empirical and rudimentary.

References

1. A. Fick, Über Diffusion, *Ann. Phys. Chem.*, 1855, **95**, 59–86.
2. A. Einstein, Über die von der molekularkinetischen Theorie der Wärme geforderte Bewegung von in ruhenden Flüssigkeiten suspendierten Teilchen, *Ann. Phys.*, 1905, **322**, 549–560.
3. M. Smoluchowski, Zur kinetischen Theorie der Brownschen Molekularbewegung und der Suspensionen, *Ann. Phys.*, 1906, **326**, 756–780.

4. J. B. Perrin, *Discontinuous Structure of Matter*, Nobel Lecture, 11 December 1926, <https://www.nobelprize.org/prizes/physics/1926/perrin/lecture/>.
5. P. Walden, Molecular weights and electrical conductivity of several fused salts, *Bull. Russ. Acad. Sci.*, 1914, 405–422.
6. L. Onsager, Reciprocal Relations in Irreversible Processes I, *Phys. Rev.*, 1931, **37**, 405–426.
7. L. Onsager, Reciprocal Relations in Irreversible Processes II, *Phys. Rev.*, 1931, **38**, 2265–2279.
8. L. Onsager, Theories and problems of liquid diffusion, *Ann. N. Y. Acad. Sci.*, 1945, **46**, 241–265.
9. M. Pourbaix, *Atlas of Electrochemical Equilibria in Aqueous Solutions*, National Association of Corrosion Engineers, 2nd edn, 1974.
10. C. J. T. de Grotthuss, Sur la décomposition de l'eau et des corps qu'elle tient en dissolution à l'aide de l'électricité galvanique, *Ann. Chim.*, 1806, **58**, 54–73.
11. J. D. Bernal and R. H. Fowler, A Theory of Water and Ionic Solution, with Particular Reference to Hydrogen and Hydroxyl Ions, *J. Chem. Phys.*, 1933, **1**, 515–548.
12. D. P. Shah, H. Q. Nguyen, L. S. Grundy, K. R. Olsen, S. J. Mecham, J. M. DeSimone and N. P. Balsara, Difference between approximate and rigorously measured transference numbers in fluorinated electrolytes, *Phys. Chem. Chem. Phys.*, 2019, **21**, 7857–7866.

6 When Electrolyte Meets Electrodes: Interface

When an ion in the bulk electrolyte looks around, it sees the same spatial distribution of other ions and solvent molecules in every possible direction, hence its ionic cloud can be considered spherically symmetric, and it is situated in a homogeneous environment. However, when the electrolyte eventually meets an electrode, such symmetry is broken. At the junction between electrolyte and electrode, both phases see a sudden discontinuity in chemistry, in morphology, in spatial distribution of charges and in the field strength they feel.

This inhomogeneous and transitional region between electrolyte and electrodes is the *interface*, which Faraday credited as the “*most important place of action*” in his 1834 article.¹ Its thickness usually lies below tens of nanometers (10^{-8} – 10^{-9} m), but it plays the key role in determining the direction and nature of the electrochemical reactions, their kinetics and sometimes their reversibility. It is in this extremely small length that charge transfer occurs between the electronic conductor (electrode) and the ionic conductor (electrolyte).

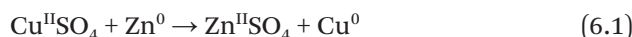
6.1 Why Does Interface Matter?

Apparently, an interface is situated at the critical location in an electrochemical device.

When Faraday made that prescient statement on the importance of an interface, he was merely referring to the phenomena visible at the

electrode surfaces, *i.e.* the signs of reactions such as metal dissolution or deposition, or gas generation, *etc.* What he may not have realized at the time is that this junction between electrode (an electronic conductor) and electrolyte (an ionic conductor) is actually the key component that distinguishes *electrochemistry* from the conventional *chemistry*.² In an electrochemical device, the *interface is the only legitimate location where charge transfer can occur*.

To demonstrate this, let us now consider a redox reaction between zinc metal powder (Zn^0) and a cupric (Cu^{2+}) salt, say copper sulfate ($\text{Cu}^{\text{II}}\text{SO}_4$):



When we mix Zn^0 with an aqueous solution of $\text{Cu}^{\text{II}}\text{SO}_4$ in a beaker (Figure 6.1a), we observe that the beautiful deep blue color of the aqueous solution (characteristic of hydrated Cu^{2+}) gradually fades away, while the gray metal powder suspended in the solution turns reddish brown, and the whole reaction vessel warms up.

Chemically, we explain the above reaction by the more active metal Zn^0 (dark gray) displacing Cu^{II} from its oxidative form (deep blue in aqueous solution) and turning it into metallic form Cu^0 (reddish brown). In doing so, two electrons flow from Zn^0 to Cu^{2+} , and this electron exchange occurs wherever the two are in contact, *i.e.* on the surface of every zinc particle. Thermodynamically, this reaction is spontaneous, meaning that at normal temperature and pressure, the corresponding change in Gibbs free energy (ΔG) is negative. Energy is thus produced from this process, and in the case shown in Figure 6.1a the energy is released in the form of heat:

$$\Delta G = \Delta H - T\Delta S \quad (6.2)$$

This is how conventional chemistry proceeds.

Now, imagine that we physically separate the two reactants (Zn^0 and Cu^{2+}) by placing them in different chambers as shown in Figure 6.1b, so that direct electron exchange between them becomes impossible. Instead, the two electrons lost by Zn^0 (the anode) must now travel *via* an external pathway and arrive at the other side (the cathode) in order to be received by Cu^{2+} . Chemically, the reaction is now split into two separate half-reactions:



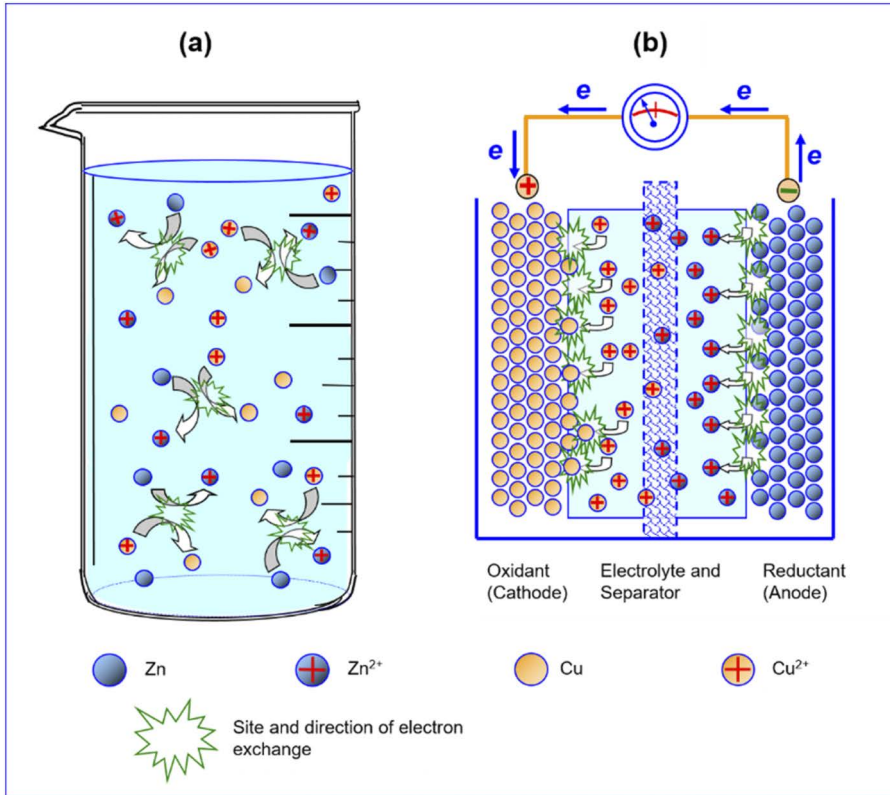
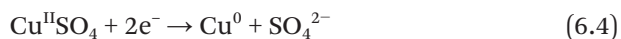


Figure 6.1 Interface separates electrochemistry from chemistry: (a) Zn powder reacts with CuSO_4 solution in a beaker where chaotic collision between reactants is accompanied by disordered electron exchanges; (b) physical separation of reactants confines the electron exchange sites to the two electrolyte/electrode interfaces, forcing the orientational movement of electrons through an external circuit.



while thermodynamically the change in Gibbs free energy, which remains constant in value, is released in the form of electricity, because the electron flow from Zn^0 to Cu^{2+} , thanks to the location confinement, becomes directional:

$$\Delta G = -nF\Delta V \quad (6.5)$$

where ΔV is the potential difference between the two electrodes in the setup in Figure 6.1b. When there is no net current passing, the

difference is actually the open-circuit cell voltage, which is often called “*electromotive force (emf)*”.

This electron flow does useful work, in the form of electricity.

Note that the major difference between chemistry and electrochemistry is that in the latter, the electron exchange, or “charge transfer”, cannot happen just anywhere but instead must occur at a legitimate location, which is the two electrolyte/electrode interfaces. This is how electrochemistry proceeds.

Figure 6.1b actually represents a “*Daniell cell*”, one of the earliest batteries, invented by John Frederic Daniell in 1836. It harnesses the energy associated with the spontaneous reaction between Zn^0 and Cu^{2+} into electric form. Here, for clarity and simplicity, we have deliberately ignored the configuration details of the Daniell cell, such as how to choose either electrode material to enable a desired reaction but circumventing undesired parasitic reactions, or how these two reactants are separated while still allowing ionic transport between the two chambers, *etc.*

In fact, a critical component ensuring that the electron exchanges (or charge transfers) occur only at these interfaces is the physical barrier that separates the two reactants. This barrier must be conductive to ions and solvent molecules, if there are any, between the two chambers, otherwise the reaction cannot proceed owing to rapidly built-up resistances from both mass and charge imbalances. This barrier must also be insulating to any electron transport, otherwise the electrons may not choose to travel *via* the external pathway but instead directly across the electrolyte itself (internal short-circuit).

In other words, *this barrier is an electrolyte*.

We have learned from early definitions that an electrolyte must be an ionic conductor. Here we introduce another requirement for a typical electrolyte: *it must be an electron insulator*.

These basic requirements for electrolytes hold true for all electrochemical devices. In certain practical electrochemical devices, these principles seem to be obscured owing to diversified cell design or unique chemistries, such as primary lithium-metal batteries or redox flow batteries, in which the so-called “electrolytes” are either liquefied electrode materials or electrode materials dissolved or suspended in true electrolytes. These materials are able to participate directly in charge-transfer reactions and hence are electron conducting themselves. Nevertheless, the true electrolytes therein still perform the basic duties of maintaining ionic and mass transportation, while these electrode materials as “foreign” ingredients *must not* establish any direct electronic pathway between the two electrodes within the cell.

6.2 Interfaces Are Electrified: The Electric Double Layer

To study ion transport across an interface, we must first understand what it is (chemistry of the accumulation or depletion of charged species) and how it is structured (spatial distribution of charges and potential). Now consider the most common scenario of a liquid electrolyte interfacing a metallic electrode.

The liquid electrolyte is an ionic conductor that consists of ions solvated by solvent molecules, as well as free solvent molecules outside the solvation sheaths.

The metal electrode is an electronic conductor that consists of metal ions sitting on fixed lattices and free electrons in the conduction band that are delocalized from the cation framework.

In the bulk of either material, the spatial distribution of charges is symmetrical at any given reference point. That is, if one looks around in the bulk of an electrode or an electrolyte, one will see in any direction completely the same spatial distribution of charges, and in any given elemental volume the electroneutrality is maintained. In the electrolyte, such a spatial distribution of charge and the subsequent electroneutrality are described by the Debye–Hückel model (see Chapter 4). In metallic conductors, the delocalization of electrons is described by the Fermi level in the metal, while the quantum nature of the electrons obscures the boundary of the metal surface by introducing additional freedom; these aspects are well beyond the scope of this book.

At the junction where the electrolyte and electrode meet, however, a sudden discontinuity occurs in both phases. Therefore, an ion at the interface would feel a completely different field in the direction towards the electrode surface from what it feels in the direction of the electrolyte bulk, and the same anisotropy applies for the electrons at the electrode side.

A direct consequence of such anisotropy is the accumulation of one charge and depletion of the other. In other words, at the surfaces of both phases, the equilibrium established between the ions to maintain regional electroneutrality is now lost, and a new equilibrium must arise, which would be governed by a completely different field. Such accumulation and depletion of charges at the surfaces of the electrode and electrolyte would lead to an electrified surface (Figure 6.2a). Assuming that the electrode surface will see excess negative charges (*which, in real life, constitutes most of the scenarios*), then the electrolyte would respond correspondingly with excessive positive charges in

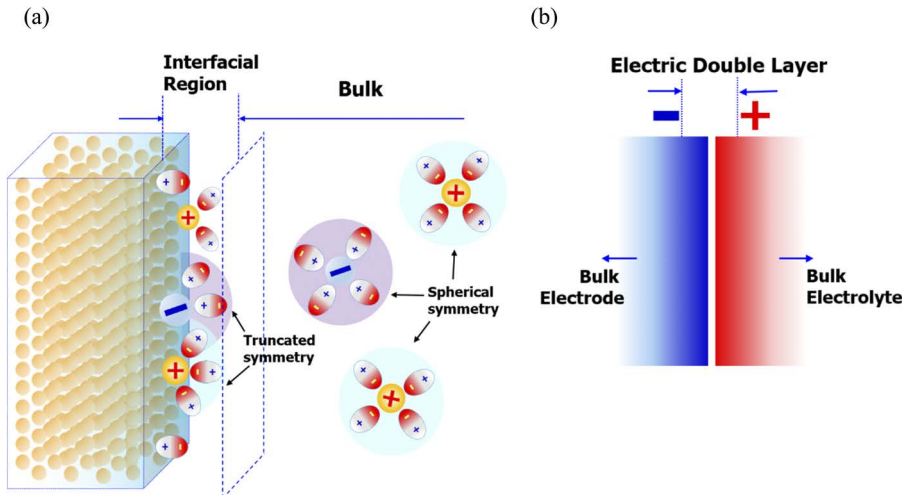


Figure 6.2 When an electrolyte meets a metallic electrode, the spherical symmetry enjoyed by an ion and its ionic cloud is lost. The truncated symmetries induce charge redistribution on both sides of the interface. (a) The interface witnesses discontinuity in both phases. Assume that at the electrode surface an excess amount of electrons enriches; an equal amount of excess positive charge would arise at the electrolyte side, contributed by both cation adsorption and solvent dipole orientation. (b) This corresponding anisotropy in both phases leads to a structure of charge distribution that is equivalent to an electric double layer.

equal amount at its surface facing the electrode, so that the interfacial region as a whole still maintains electroneutrality. In such an arrangement, the excessive negative charge on the electrode side would be the enrichment of electrons (as represented by the strength of shading in Figure 6.2a), while the excess positive charges on the electrolyte side would be contributed by the preferential adsorption of cations as well as oriented dipoles.

The accumulation of excess charges on both sides of the phases is in fact equivalent to an *electric double layer* (Figure 6.2b). Its thickness depends on both the nature of the electrode and the electrolyte materials, and is usually in the range between ångstroms and tens of nanometers (10^{-10} – 10^{-8} m), but this thickness does not have a clear demarcation; instead, it is quite diffuse.

In a broader context, the formation of such an electric double layer is by no means a unique phenomenon between the electrode and electrolyte in electrochemical devices only. It exists universally wherever two phases meet and anisotropy arises, no matter whether the phases

involved are solid, liquid or gaseous. Prominent examples include any solid particles in contact with a solution or gas, two different solid materials interfacing each other and two different immiscible liquid phases interfacing each other. What makes the interfaces in electrochemical devices unique is that one can control the chemistry and structure of interfaces therein *via* an external field, while most interfaces spontaneously formed in Nature are determined by the chemical nature of both phases, which cannot be easily and quantitatively controlled. This is exactly the reason why electrochemical interfaces are the most investigated and well understood thus far.

An applied external field could strengthen, weaken or even completely reverse the charge distribution in an electric double layer, by adjusting both the field strength and polarity. At one specific point, the applied potential can completely erase all the charges on the double layer. This unique scenario represents the *point of zero charge*, a concept that played an important role in the quantitative understanding of interfaces.

6.2.1 The Potential Across an Individual Interface Is Immeasurable

Let us now consider the scenario where an external electric field is applied on the interface. To do so, one has to construct a complete circuit (Figure 6.3), in which the specific interface that we want to investigate is only one of the two interfaces established in such a circuit, and we refer to this electrode as the “*working electrode*” and the other electrode(s) as either *reference* or *counter* electrodes. To make the discussion simple, the reference and counter electrodes can be merged into one, as shown in Figure 6.3, but in more delicate experiments researchers often prefer an independent reference electrode for more accurate potential reading.

Suppose the output voltage of the external power source (such as a battery) is V_{cell} . Is it possible to measure the potential difference across the interface that we want to investigate?

According to Kirchhoff’s law, the applied voltage difference should be distributed among at least three cell components:

$$V_{\text{cell}} = \Delta V_1 + \Delta V_2 + \Delta V_3 \quad (6.6)$$

where ΔV_1 and ΔV_3 are the potential drops across two interfaces including the one we want to investigate, and ΔV_2 is the potential drop across the bulk electrolyte. While ΔV_2 can be estimated based on the

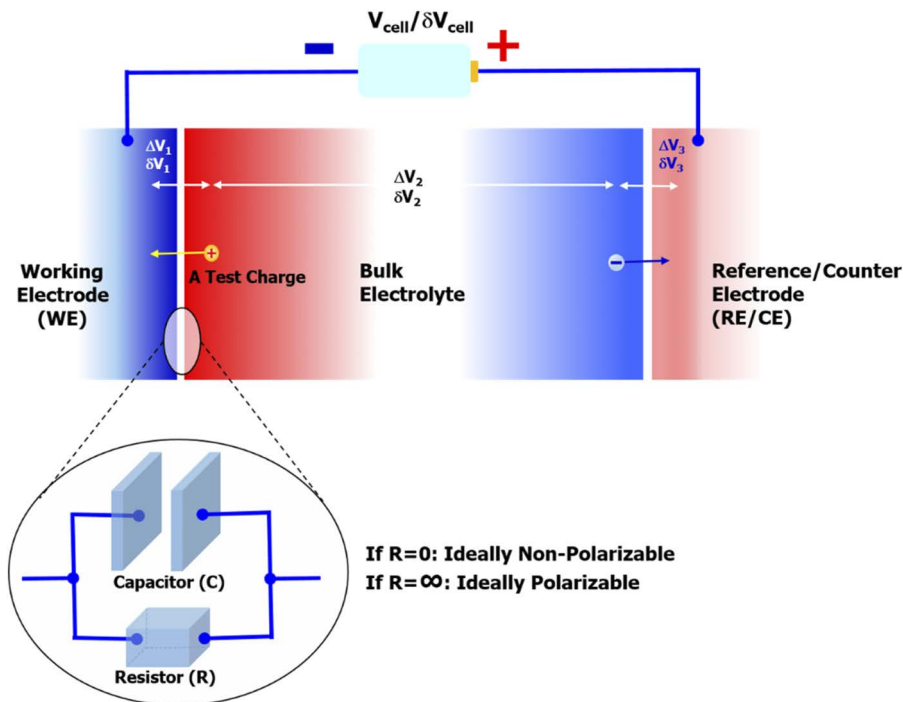


Figure 6.3 An external electric field is applied on an electrochemical cell by a power source, the voltage of which, V_{cell} , is distributed across the cell on three components (top). The interface under investigation (between the working electrode and electrolyte) can be represented by an “equivalent circuit” consisting of a resistor and a capacitor in a parallel arrangement (bottom). The polarizability of the interface depends on how “leaky” the circuit is.

electrolyte’s resistance (or conductivity), the two interfacial components are closely coupled and it is impossible to know how the voltage drop is distributed between these two individual interfaces.

One might suggest that it is still possible to do so by inserting a third electrode close to the interface that we are investigating. If such an electrode is placed close enough to the interface under investigation, then the unknown potential drop across the interface that we are not interested in (ΔV_3) could be circumvented, and we can directly measure the potential difference that we want to know (ΔV_1).

However, it must be remembered that, at the instant such an electrode is inserted into the electrolyte, a new interface is created between this new electrode and the electrolyte, accompanied by a new unknown potential difference ($\Delta V'_3$). What is measured remains the

sum of potential drops across the two interfaces and the electrolyte sandwiched between the two electrodes:

$$V_{\text{cell}} = \Delta V_1 + \Delta V'_2 + \Delta V'_3 \quad (6.7)$$

Hence we are back where we started. It is apparent now that *the potential difference across an individual interface is immeasurable*. One must circumvent this fundamental barrier.

It turns out that, although the absolute potential difference ΔV_1 across a given interface cannot be measured, if one varies the voltage applied by an amount δV_{cell} , it is possible to measure accurately *the change of potential drop across an interface* δV_1 , provided that the two interfaces involved meet certain requirements. This leads to the concept of *interface polarizability*.

6.2.2 Two Extremities of Interfaces: Polarizable and Non-polarizable

Consider that, under the force of an applied field, a test charge moves towards an interface (Figure 6.3). As we have mentioned before, the interface is not an open boundary to physical species, but the charge carried by this ion can be transferred across the interface. How easy this charge-transfer process is defines the polarizability of this interface.

For some interfaces, the charge transfer occurs with almost zero resistance. The fast kinetics ensures that, within certain voltage limits, increasing the external voltage applied on the circuit as shown in Figure 6.3 will not significantly build up more charges at the interface, and consequently the potential of the electrode remains relatively stable. Such interfaces are called *non-polarizable interfaces*. The most typical non-polarizable interface is one that involves the redox reaction between hydrogen gas and proton (H_2/H^+) on a platinum surface. Such non-polarizability makes hydrogen an excellent reference when one tries to measure accurately the potential of another electrode. It is often referred as the *reversible hydrogen electrode* (RHE). If standard conditions are applied (activity of proton 1.0, pressure of hydrogen 1 atm and temperature 298 K), the RHE becomes a *standard hydrogen electrode* (SHE). Similar non-polarizable electrodes also include those based on the calomel redox couple ($\text{Hg}_2\text{Cl}_2/\text{Cl}^-$), and a lithium-metal electrode (Li/Li^+) in non-aqueous electrolytes can also provide a non-polarizable interface under certain conditions.

A non-polarizable electrode is friendly towards charge transfer, hence in practical applications such an electrode is very useful whenever one wants the reaction to proceed at the maximum rate. For example, in fuel cells, in order for hydrogen reduction to occur with minimal resistance, the presence of platinum on the electrode surface is always preferred, despite the high cost associated.

For other electrodes, the charge transfer encounters high resistance at the interfaces, while any attempt to accelerate charge transfer by increasing the external voltage applied would induce the accumulation of more ions at the interface. Consequently, the charge density in the electric double layer intensifies, leading to a significant shift of the electrode potential. Thus we say that this electrode has been polarized. Such interfaces are called *polarizable interfaces*. A typical polarizable electrode is the mercury (Hg) electrode.

As one could imagine, a polarizable electrode makes it harder for a certain charge transfer to occur. Such an electrode is also useful in electrochemical devices whenever one does not want a certain reaction to happen. An example is the traditional alkaline batteries. In order to prevent hydrogen evolution at anode surfaces from intervening in the designed electrochemical reactions, mercury was often used as the negative electrode (anode). The use of mercury has been gradually phased out in recent decades owing to concerns over its toxicity.

Researchers often use so-called “equivalent circuits” to simplify the electrochemical characteristics of interfaces (and other more complicated systems, as we will consider later), as shown in Figure 6.3 (inset), which consists of a capacitor and a resistor in parallel. An ideally non-polarizable electrode would have *zero resistance* ($R = 0$) in the resistor, while an ideally polarizable electrode would have *infinite resistance* ($R = \infty$) in the resistor. In real life, there is no electrode with ideal polarizabilities or non-polarizabilities, and most polarizable and non-polarizable electrodes only demonstrate desired polarizability behaviors under confined conditions such as voltage limits, electrolyte concentration, etc.

We have mentioned in the preceding section that, although the absolute potential difference across an interface is immeasurable, it is possible to measure the change of interfacial potential when the applied external voltage changes. Such a possibility exists only when one uses a polarizable electrode as the working electrode and couple it with a non-polarizable electrode.

Thus, in Figure 6.3, suppose that the working electrode is ideally polarizable, and the reference/counter electrode is ideally non-

polarizable. When one introduces a fraction of voltage change (δV_{cell}), we have

$$\delta V_{\text{cell}} = \delta V_1 + \delta V_2 + \delta V_3 \quad (6.8)$$

For a non-polarizable electrode, its potential is independent of the applied voltage, hence

$$\delta V_3 = 0 \quad (6.9)$$

The potential difference across the electrolyte bulk can be estimated based on its resistance, and in certain cases can be made negligible ($\delta V_2 \approx 0$). Therefore, the change in potential difference across the interface under investigation (δV_1) has thus become measurable:

$$\delta V_{\text{cell}} = \delta V_1 \quad (6.10)$$

This unique scenario, made possible by the combination of a polarizable electrode serving as the working electrode and a non-polarizable electrode as the reference electrode, set the foundation for the classical quantitative understanding of interfaces.

6.3 Classical Understanding of the Electric Double Layer

Before techniques of modern characterization and computational simulation became available, the classical understanding of the elusive interfaces mainly originated from thermodynamic approaches, which link the microscopic (or atomistic) properties of interfaces to certain macroscopic properties that can be measured experimentally. The apex in this discipline is *electrocapillarity*, which mathematically describes the quantitative correlation between interfacial tension and charge densities accumulated or depleted on the interfaces.

6.3.1 Gibbs Surface Excess

When an electrode meets the electrolyte, the anisotropy induces either accumulation or depletion of charges at the interface, where the charges are either electrons on the electrode side or ions on the

electrolyte side. Gibbs defined the “excess” of a given charge in the interfacial region as its departure from the bulk value Γ , which could be either positive (standing for accumulation) or negative (standing for depletion), as shown in Figure 6.4.

Suppose the bulk density for a given charge is c^0 , then at $t = 0$ when the interface has not been electrified the interfacial concentration of this charge is the same as that in the bulk. At $t = \infty$, the interface has been electrified and an electric double layer has been established, then the interfacial concentration (c' or $-c'$) for this charge departs from the bulk value and, depending on whether this charge is accumulated or depleted, becomes higher or lower. The interface excess Γ , as represented by the shaded areas in Figure 6.4, should be

$$\Gamma = \int_0^\infty [c'(x) - c^0] dx = \int_0^\infty c(x) dx \quad (6.11)$$

where $c(x)$, also called the “perturbation”, is the departure from the bulk value and is defined as

$$c(x) = [c'(x) - c^0] \quad (6.12)$$

The upper limit for the integral is infinity, but in actuality the interfacial region usually ends within tens of nanometers (10^{-8} m), beyond which the excess becomes negligible.

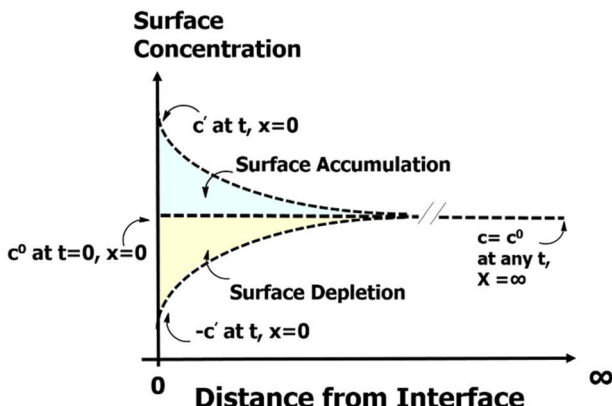


Figure 6.4 Quantification of charges accumulated or depleted at an interface: the Gibbs excess Γ is represented by the shaded areas.

6.3.2 Quantification of Surface Excess: Electrocapillarity

Having defined interface excess, the next step is to figure out how this quantity can be measured. As discussed in Section 6.2.1, the potential difference across a given interface is immeasurable, but its change could be measurable if the interface we choose to study is an *ideally polarizable* electrode and its reference/counter electrode is *ideally non-polarizable*. Although there are no ideally polarizable or non-polarizable electrodes in reality, they can be approximated if we apply certain confinements and restrictions.

The *reversible hydrogen electrode* (*RHE*) serves as such an approximation to a non-polarizable electrode, and *mercury* (*Hg*) as a polarizable electrode. Thus, their coupling should make a meaningful contribution to the study of interfaces. In particular, the unique nature of mercury, being liquid and metallic at the same time, makes it an ideal electrode material that allows us to observe, even with primitive experimental setups, the interfacial changes that would otherwise be extremely difficult to observe on a solid electrode.

6.3.2.1 Surface Tension on a Mercury Electrode

As early as 1800 it had already been noticed that, if a drop of mercury in sulfuric acid is touched by a wire connected to a battery, it contracts, and upon removal of the wire, it resumes its original shape. When Lippman saw this demonstration around 1872, he immediately realized that this behavior must result from the change in the surface tension γ of the mercury drop under electric polarization, and there must exist a relation between the surface tension, which is reflected by the physical shape of the mercury drop, and the charges accumulated at the double layer.

Following this line of thought, he started his seminal work on the capillary behavior of mercury under electrification (*i.e. electrocapillarity*), which led to a series of significant inventions (*e.g.* Lippmann electrometer, polarographic analysis), but for the readers of this book the most important significance of this phenomenon comes from its contribution to the understanding of interfaces at a fundamental (thermodynamic) level,³ because mercury provides an almost ideally polarizable interface, the surface tension of which can be precisely measured using a device as shown in Figure 6.5, and related to the charge density placed by the polarization potential at the double layer.

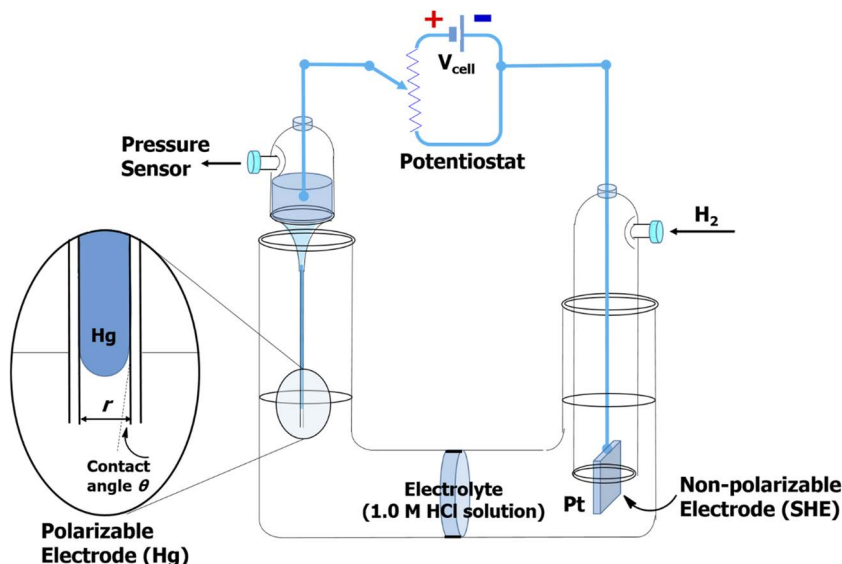


Figure 6.5 Electrocapillarity led to the earliest understanding about interfaces: the coupling of a polarizable working electrode (mercury) and a non-polarizable reference/counter electrode (SHE) makes it possible to measure accurately the potential change occurring at the Hg/electrolyte interface, while the surface tension of Hg is directly correlated with the charge accumulation/depletion at the Hg surface, which can be described mathematically.

Started by Lippmann in the 1870s and followed by Gouy in the 1900s and Frumkin in the 1920s, all of whom used a device as shown in Figure 6.5 or its variations, the potential dependences of the surface tension γ and differential capacitance C were measured for mercury in diverse electrolytes. Whereas the capacitance often displays a complicated behavior, heavily dependent on the salt concentration in electrolyte and characterized with a minimum and a hump in the middle, the surface tension always shows a nearly perfect parabolic shape with almost no exceptions (Figure 6.6). The potential at which the maximum tension occurs is called the *electrocapillary maximum* (*ecm*), which is a characteristic quantity that we will discuss in more detail later.

Here, we need to note that this parabolic shape is *nearly* symmetrical, but *never* perfectly symmetrical. Instead, obvious differences always arise in the positive potential region. In other words, the anion species, which accumulate on the mercury surface in the positive potential region, display somewhat different behaviors among themselves when assembling on the electric double layer, whereas most

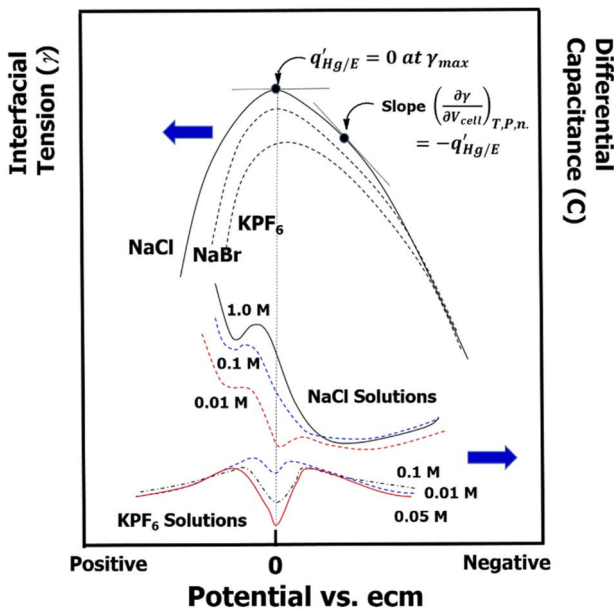


Figure 6.6 Top: the universal dependence of the mercury/electrolyte interfacial tension γ on the mercury potential in a few typical aqueous electrolytes as labeled. According to thermodynamic treatment, the slopes of the parabolas at any potential represent the charge density accumulated at the interface, while the maximum interfacial tension occurs at an interface with zero charge accumulation. Bottom: the differential capacitance at interfaces between mercury and NaCl or KPF₆ solutions when the salt concentrations change.

cations, with only a small number of exceptions, behave almost identically when they accumulate at the interfaces.

Why are such relations always parabolic? And what useful information about interfaces can we derive from such relations?

6.3.2.2 Thermodynamics of the Mercury/Electrolyte Interface

Consider a mercury electrode as shown in the inset in Figure 6.5. The weight of the mercury column in the capillary tube should be

$$W_{Hg} = \pi r^2 h \rho g \quad (6.13)$$

where r is the radius of the capillary, h the height of mercury column, ρ the mercury density and g the gravitational constant. By applying a

voltage V_{cell} , a certain interfacial tension γ is developed in the capillary where mercury meets the electrolyte, which ensures that the mercury column is stationary. At such an equilibrium, the weight of the mercury column must be balanced by the tension force (F_γ) exercised at the interface, which should be proportional to the contact perimeter of mercury ($2\pi r$) and the projection of interfacial tension γ on the vertical direction ($\gamma \cos \theta$):

$$F_\gamma = 2\pi r \gamma \cos \theta \quad (6.14)$$

where θ is the contact angle. Here we have ignored the height of the electrolyte as its density ($\sim 1.0 \text{ g cm}^{-3}$) is negligible in comparison with mercury (13.6 g cm^{-3}). Thus

$$2\pi r \gamma \cos \theta = \pi r^2 h \rho g \quad (6.15)$$

The interfacial tension is then obtained:

$$\gamma = \frac{\pi r^2 h \rho g}{2\pi r \gamma \cos \theta} = \frac{rh \rho g}{2 \cos \theta} \quad (6.16)$$

Given the small contact angle θ , we can reasonably assume that $\cos \theta = 1.0$, hence

$$\gamma = \frac{rh \rho g}{2} \quad (6.17)$$

This relation makes the mercury/electrolyte (Hg/E) interfacial tension γ a quantity that can be measured precisely or even controlled using a device similar to the setup in Figure 6.5. Any change of potential will induce a change of charge density at the double layer, and consequently the surface tension of the mercury/electrolyte interface, which would automatically seek a new equilibrium by adjusting the mercury column height. In the early days an optical magnifying glass was used to read the height of the mercury column, but in the modern era this task has become easier with computer-controlled high-precision pressure sensors by the mercury electrode side.

Under such an equilibrium between mercury column weight and Hg/E interfacial tension, let us consider that an increase in potential δV_{cell} is applied on the mercury electrode in Figure 6.5, which already carries an excess charge of q_{Hg} on the Hg/E interface corresponding

to n mol of surface excess. Application of the first and second laws of thermodynamics to this open system that involves all these energy and mass terms related to the surface change gives

$$SdT - VdP - Ad\gamma - q_{Hg/E}\delta V_{Hg/E} - \sum n d\mu = 0 \quad (6.18)$$

where $\delta V_{Hg/E}$ is the potential change across the Hg/E interface and μ the change in chemical potential caused by the potential change. Assuming that all these occur at constant temperature ($dT = 0$) and pressure ($dP = 0$), we can reduce and rearrange the above equation to

$$q_{Hg/E}\delta V_{Hg/E} = -Ad\gamma - \sum n d\mu \quad (6.19)$$

Since mercury is almost ideally non-polarizable whereas its reference/counter electrode (SHE) is, ideally, almost completely non-polarizable, when we increase the voltage applied on the circuit, the change δV_{cell} will be completely reflected on the mercury electrode, hence

$$\delta V_{Hg/E} = \delta V_{cell} \quad (6.20)$$

Thus, we have

$$d\gamma = -\frac{q_{Hg}}{A} \delta V_{cell} - \sum \frac{n}{A} d\mu \quad (6.21)$$

Meanwhile, when the excess species is adsorbed on the 2D interface, its concentration is represented by n/A . Hence, according to the definition of surface excess in Section 6.3.1,

$$\Gamma = \int_0^\infty [c'(x) - c^0] dx = \frac{n}{A} - \frac{n_0}{A} \quad (6.22)$$

Therefore,

$$\sum \frac{n}{A} d\mu = \sum \Gamma d\mu + \sum \frac{n_0}{A} d\mu \quad (6.23)$$

Under constant temperature and pressure, we know from the Gibbs–Duhem relation that

$$\sum \frac{n_0}{A} d\mu = 0 \quad (6.24)$$

Therefore,

$$\sum \frac{n}{A} d\mu = \sum \Gamma d\mu \quad (6.25)$$

Inserting into the expression for interfacial tension, we now have

$$d\gamma = -\frac{q'_{\text{Hg/E}}}{A} \delta V_{\text{cell}} - \sum \Gamma d\mu = -q'_{\text{Hg/E}} \delta V_{\text{cell}} - \sum \Gamma d\mu \quad (6.26)$$

where $q'_{\text{Hg/E}}$ represents the *charge density* on the interface, that is, the total charge $q_{\text{Hg/E}}$ thereon normalized by the interfacial area A .

To simplify the situation further, all experiments are conducted at a fixed electrolyte composition, therefore $d\mu = 0$ and $\sum \Gamma d\mu = 0$, and the above relation is reduced to

$$d\gamma = -q'_{\text{Hg/E}} \delta V_{\text{cell}} \quad (6.27)$$

or, in its more famous form:

$$\left(\frac{\partial \gamma}{\partial V_{\text{cell}}} \right)_{T, P, \text{Const. comp.}} = -q'_{\text{Hg/E}} \quad (6.28)$$

This the *Lippmann equation*. It basically states that the slope at any point on the parabolas as shown in Figure 6.6 reflects the charge density on the interface at the potential corresponding to that point. With the changes in the applied potential, the charge accumulated from the electrolyte on the interface switches sign according to the electric double-layer definition, *i.e.* at the negative potentials cations are accumulated at the interface, whereas at positive potentials anions are accumulated. The different mobility and adsorption behaviors of anions and cations contribute to the asymmetry of these parabolas. Most importantly, the charges on the interface switch sign somewhere in the middle, and exactly at the maximum interfacial tension (γ_{\max}), which corresponds to the ecm, the slope is zero:

$$\left(\frac{\partial \gamma}{\partial V_{\text{cell}}} \right)_{T, P, \text{Const. comp.}} = -q'_{\text{Hg/E}} = 0 \quad (6.29)$$

meaning that *the interface is free of any charge*. This point is what we referred to as the point of zero charge (pzc) or ecm previously, which always corresponds to the so-called *electrocappingillary maximum*.

Why must the interfacial tension become maximum if there is no charge on the interface?

To explain the reason underlying the electrochemical capillary minimum, one must understand what surface tension is. Briefly, when a species tries to enter a new phase, it will cause a series of changes in the properties of that phase, one of which is surface tension. The addition of this new species will induce a surface area increase of the new phase, and surface tension is the resistance it must overcome. Now imagine an electrified interface, where charges of the same sign (either cation or anion) accumulate. These charges repel each other and, if a new species tries to enter the interfacial region under this situation, it will face a reduced surface resistance (tension) because the repulsion among these charges provides help in repelling the new species.

At the point where the interface is not electrified at all ($q^{\text{int}} = 0$), such a benefit from Coulombic repulsion disappears, and the new species must encounter the highest resistance (γ_{\max}) in order to enter the interface.

Going further, if we view the Hg/E interface as a location to store charges, it behaves as a capacitor, the differential capacitance of which is defined as

$$C_{\text{Hg/E}} = \frac{dq}{dV} = \left(\frac{\partial q'_{\text{Hg/E}}}{\partial V_{\text{cell}}} \right) = - \left(\frac{\partial^2 \gamma}{\partial V_{\text{cell}}^2} \right) \quad (6.30)$$

The electrocapillarity took advantage of the unique nature of mercury being liquid and metal at the same time, which allowed precise measurements of a sensitive interfacial property that would be otherwise difficult for a solid electrode. Eventually, elegant thermodynamic treatment of the results led to a valuable understanding of the electric double layer structures in this unique interface.

Following the classical work of Lippmann and others on mercury, the electrocapillarity was also confirmed on other liquid metal electrodes such as gallium (Ga) and various alloys of mercury with other metals (amalgams).

However, do these principles apply to interfaces between solid electrodes and electrolytes?

The answer is yes, because during the mathematical treatment of the whole topic, the phase state of any material involved, be it electrode or electrolyte, was not under consideration. For this reason, the results obtained should be universally applicable to solid electrodes and solid electrolytes as well. In fact, enabled by modern technologies

using high-precision sensors and laser beams, such as those adopted in atomic force microscopes and interferometers, it has become possible to measure accurately the tension on a solid electrode, which unequivocally proved that the Lippmann equation applies universally to all interfaces, provided that the potential of the electrode rests within the electrochemical stability window of the electrolyte components.

The classical study of electrocapillarity formed the foundation of the modern understanding of electrode/electrolyte interfaces.

6.4 Structure of an Electrified Interface

Electrocapillarity confirmed the existence of an electric double layer at interfaces, and taught us in a quantitative manner how interfacial charges vary with the applied cell voltage. However, as the knowledge was derived from thermodynamic considerations, it cannot tell us how such an electric double layer is structured at the atomistic level.

An electric double layer is instantaneously established when a metallic electrode (in fact, any electronic conductor) is brought into contact with a liquid electrolyte. Since such an interfacial phenomenon occurs at the nanometric scale in a transient nature, even with today's characterization technology their structure remains elusive to direct observation. Instead, most classical understanding of interfaces was derived from model building, against which measurable electrochemical quantities are derived and these models gradually evolved while being confirmed or rejected.

6.4.1 Helmholtz–Perrin Model: A Simple Capacitor

The simplest model for an electric double layer was proposed in the late 1800s by Helmholtz and Perrin, who visualized the respective surfaces of electrodes and electrolytes as a pair of 2D sheets populated by discrete charges: electrons on the electrode side and ions on the electrolyte side (Figure 6.7a, top).⁴ This model actually represents a simple capacitor, the capacitance of which is

$$C = \frac{dq}{dV} = \frac{\epsilon\epsilon_0}{d}A \quad (6.31)$$

where d is the distance between the two sheets of charge, A the surface area of the interface, ϵ the dielectric constant of the material in the interfacial region and ϵ_0 the permittivity of vacuum, which is a

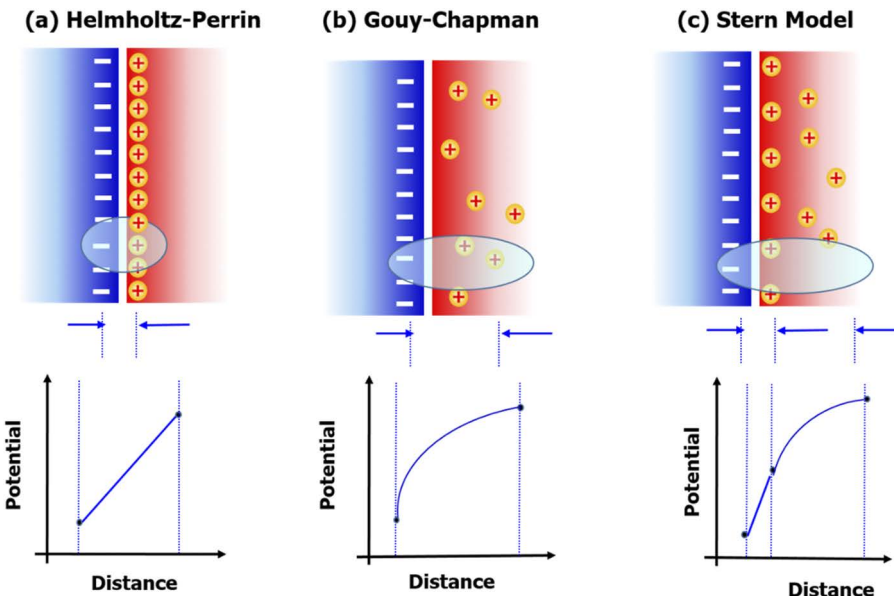


Figure 6.7 Evolution of early interface models. (a) Helmholtz-Perrin model that visualizes EDL as a simple capacitor with a linear potential across it. (b) The Gouy-Chapman model sees a rather diffuse distribution of ions because of the disordering thermal movements. The potential distribution takes a mathematical form similar to the ionic cloud described in the Debye-Hückel model for ions. (c) The Stern model combines the two, while acknowledging that certain ions may adsorb preferentially on the electrode surface, also considering the effect of thermal force. The potential distribution therefore displays a hybrid behavior, the linear section corresponding to the adsorbed ions as in the Helmholtz-Perrin model and the non-linear section corresponding to the diffuse layer as in the Gouy-Chapman model.

constant ($8.85 \times 10^{-12} \text{ C}^2 \text{ J}^{-1} \text{ m}^{-1}$). Accordingly, the potential across this interface of an ideal capacitor nature is linear (Figure 6.7a, bottom):

$$dV = \frac{d}{A\epsilon\epsilon_0} dq \quad (6.32)$$

Now let us apply the Lippmann equation:

$$\left(\frac{\partial \gamma}{\partial V_{\text{cell}}} \right)_{T,P,\text{Const. comp.}} = -q \quad (6.33)$$

After rearranging and replacing dV , we have

$$d\gamma = -q dV = -q \frac{d}{A\epsilon\epsilon_0} dq \quad (6.34)$$

Integrating both sides, we obtain

$$\int d\gamma = -\frac{d}{A\epsilon\epsilon_0} \int q dq \quad (6.35)$$

or, after integration, we have the expression for interfacial tension:

$$\gamma + \text{constant} = -\frac{dq^2}{2A\epsilon\epsilon_0} \quad (6.36)$$

In order to evaluate the integration constant, we can apply the electrochemical capillary minimum condition, which is

$$(q)_{\gamma_{\max}} = 0 \quad (6.37)$$

Therefore,

$$\text{constant} = -\gamma_{\max} \quad (6.38)$$

Finally, the relation between interfacial tension γ and interfacial charge density q becomes

$$\gamma = \gamma_{\max} - \frac{dq^2}{2A\epsilon\epsilon_0} \quad (6.39)$$

while the relation between interfacial tension γ and interfacial potential difference becomes

$$\gamma = \gamma_{\max} - \frac{A\epsilon\epsilon_0 V^2}{2d} \quad (6.40)$$

This equation is encouraging because it shows a parabola-shaped relation with the maximum point at γ_{\max} ; however, it would be a perfectly symmetric parabola, which does not agree with the experimental findings.

A further discrepancy arises from the differential capacitance, which should be a constant with applied potential according to the

simple capacitor model. Impedance analyses revealed that the differential capacitance has an unequivocal dependence on the cell potential or the potential difference across the interfaces, which often takes the characteristic shapes of inverted parabolae or humps.

Clearly, the Helmholtz–Perrin model needs to be modified.

6.4.2 Gouy–Chapman Model: Diffuse Ionic Assembly

Like Figure 5.8 misleading us with an oversimplified picture of ionic migration along the applied field while ignoring the effect of thermal and random movements of these same ions, the Helmholtz–Perrin model made the same mistake. In 1910, Gouy proposed that, on the electrolyte side of the interface, the ions cannot possibly form an ionic sheet in an orderly manner to counter the charges accumulated on the electrode side; instead, the thermal motions of the ions and solvent molecules, which are responsible for the random walk of the ions even under an externally applied electric field, would disrupt an ordered assembly of these ions and turn them into a diffuse ionic assembly.

With more detailed mathematical treatments, this modified interfacial vision later became the *Gouy–Chapman model* (Figure 6.7b, top),⁵ in which the distribution of ions near the electrified interface must experience both the electrostatic field that originated from the charges accumulated on the electrode side and the random thermal force from the electrolyte side.

Does this sound familiar?

Yes, that was exactly the same consideration that Debye and Hückel introduced when studying the distribution of ions around a given central ion. The difference here is that the central ion is a point charge, and the electrostatic field that originated from it has spherical symmetry, while the electrode is a 2D plane of infinite area, and the electrostatic field that originated from it has planar symmetry.

In other words, we can just view the electrode as a giant 2D ion and apply principles established in the Debye–Hückel model.

Thus, the field gradient at a distance x from the interface is given by

$$\frac{d\psi}{dx} = -\sqrt{\frac{8k_B T c_0}{\epsilon \epsilon_0}} \sinh\left(\frac{ze_0 \psi_x}{2k_B T}\right) \quad (6.41)$$

where c_0 is the concentration of species in the bulk of the electrolyte solution and ψ_x the potential difference between point x and the bulk solution.

With this field expression, one could apply Gauss's law that we once used in deriving the Debye–Hückel equation and obtain the distribution of charges at any point x away from the interface:

$$q = \epsilon\epsilon_0 \frac{d\psi}{dx} = -\sqrt{8\epsilon\epsilon_0 c_0 k_B T} \sinh\left(\frac{ze_0\psi_0}{2k_B T}\right) \quad (6.42)$$

Correspondingly, the potential distribution ψ_x can be obtained from the integration of the field gradient. By assuming the approximation that

$$\sinh\left(\frac{ze_0\psi_x}{2k_B T}\right) \approx \frac{ze_0\psi_x}{2k_B T} \quad (6.43)$$

ψ_x can be solved as

$$\psi_x = e^{\left[-\sqrt{\frac{2c_0z^2e_0^2}{\epsilon\epsilon_0k_B T}}x + \text{constant}\right]} \quad (6.44)$$

or, in a simpler form:

$$\ln\psi_x = -\sqrt{\frac{2c_0z^2e_0^2}{\epsilon\epsilon_0k_B T}}x + \text{constant} \quad (6.45)$$

One may immediately notice the familiar term

$$\frac{2c_0z^2e_0^2}{\epsilon\epsilon_0k_B T}$$

which is the reciprocal of the Debye thickness K^{-1} . To evaluate the integration constant, we apply the boundary conditions:

As $x = 0$ (at the interface), $\psi_x = \psi_0$; therefore,

$$\psi_x = \psi_0 e^{-Kx} \quad (6.46)$$

This equation tells us that the potential at the interface decays exponentially as the distance into the electrolyte increases (Figure 6.7b, bottom), while the diffuse charges on the electrolyte side are very similar to an ionic cloud around a central ion. Analogously to what we did in Section 4.7 (Figures 4.5 and 4.6), we can visualize the electrified interface as the equivalent of placing the diffuse charge q_d at a distance K^{-1} away from the accumulated charges q_M on the electrode side.

In fact, the above diffuse charge concept and equation were reported by Gouy and Chapman in 1910, a decade earlier than the work of Debye and Hückel, but it attracted much less attention than the latter. According to Bockris and Reddy,² this clearly reflected the focused interest in the early days of electrochemistry on bulk rather interfacial properties.

In addition to potential difference, we can derive the differential capacitance at such an interface by considering that $q_M = -q_d$:

$$C = \left(\frac{\partial q_M}{\partial V} \right) = - \left(\frac{\partial q_d}{\partial \psi_M} \right) = \sqrt{\frac{2c_0 z^2 e_0^2}{\epsilon \epsilon_0 k_B T}} \cosh \frac{ze_0 \psi_M}{2k_B T} \quad (6.47)$$

which not only is a function of the interface potential (or applied external voltage), but also predicts that the relation should be an inverted parabola because of the shape of cosh, which agrees with experiments.

This was a triumphal moment for the Gouy–Chapman model over the Helmholtz–Perrin model. However, this triumph did not last long: soon experiments revealed that the predicted inverted parabolas occur only near the point of zero charge and only in extremely dilute electrolytes.

6.4.3 Stern Model: Combination of Simple Capacitor and Diffuse Charge

In 1924, Stern combined the Helmholtz–Perrin and Gouy–Chapman models by suggesting that some of the ions are indeed in direct contact with the electrode surface, while the others are distributed in a diffuse manner.⁶ Thus the electrolyte side of the interface consists of two sections, the “inner” Helmholtz–Perrin (H–P) layer and the “outer” Gouy–Chapman (G–C) layer (Figure 6.7c, top). The total charge on the electrolyte side of the interface (q_E) can therefore be divided into two parts:

$$q_E = q_{H-P} + q_{G-C} \quad (6.48)$$

where q_{H-P} and q_{G-C} represent the charges in these two layers, respectively.

An interface with such a discrete structure should see two distinct regions where the potential difference follows the linear trend of Helmholtz–Perrin and the exponential trend of Gouy–Chapman (Figure 6.7c, bottom), respectively. Accordingly, the differential capacitance

across such a hybrid interface consists of two capacitances connected in series:

$$\frac{1}{C} = \frac{1}{C_{\text{H-P}}} + \frac{1}{C_{\text{G-C}}} \quad (6.49)$$

Such a model could, in theory, predict the variation of differential capacitance in a wide range of electrolyte concentrations. In a dilute electrolyte, the Helmholtz–Perrin layer almost disappears, and the whole charge can be considered as diffuse, whereas the differential capacitance follows what the Gouy–Chapman model predicts. However, when the electrolyte is highly concentrated, the diffuse layer is very compressed against the electrode, as predicted by the much smaller Debye thickness, and the interface will adopt more characteristics of the Helmholtz–Perrin model.

Although the Stern model achieved more success than the Helmholtz–Perrin and Gouy–Chapman models, it still encounters challenges with certain electrolytes, where the experimental results for differential capacitance sharply disagree with the prediction.

Further modification is needed.

6.4.4 Grahame and Bockris–Devanathan–Müllen (BDM) Models

It seems that the validity of the Stern model has a strong dependence on electrolyte composition, in particular its anion species. For example, it works reasonably well with aqueous solutions of NaCl, NaBr and NaI, but deviates significantly for NaF. Considering that the first three salts are well dissociated in water, whereas NaF is hardly dissociated, it is apparent that the solvation sheaths of these anions play an important role in dictating the electrocapillary and differential capacitance of the interfaces.

On the basis of the Stern model, in 1947 Grahame proposed that some ions tend to form a monolayer with *specific adsorption* on the electrode.⁷ Here specific adsorption implies that the interaction between these ions and the electrode surface could defy the electrostatic force, *i.e.* charges could adsorb on an electrode even when they share the same charge sign, and adsorb directly on the electrode surface *via* chemical affinity. A few anions, *e.g.* Cl[−] and Br[−], that normally have weak solvation sheaths in aqueous solutions were identified as candidates for such specific adsorption. As a result, the interface can be divided into three substructural regions (Figure 6.8a, top): (1) the

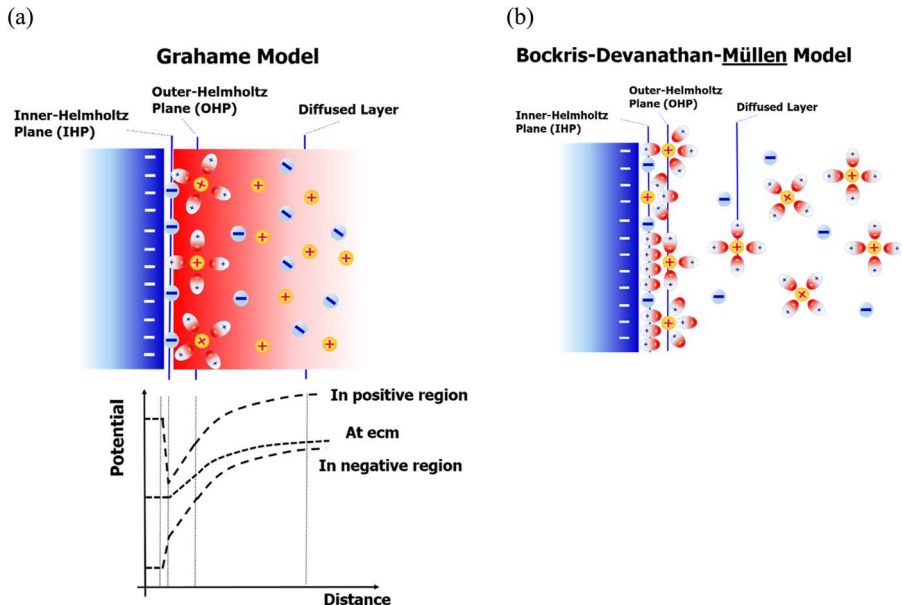


Figure 6.8 (a) Grahame model with the specifically adsorbed ions at the inner-Helmholtz plane and the corresponding potential differences as measured on a mercury electrode in 0.5 M NaCl solution, where Cl⁻ serves as the specifically adsorbed ion; (b) Bockris-Devanathan-Müllen model that considers the aligned adsorption of water molecules at the inner-Helmholtz plane together with specifically adsorbed ions. The closest solvated ions constitute the OHP.

inner-Helmholtz plane (IHP) passes through the centers of those specifically adsorbed ions, (2) an outer-Helmholtz plane (OHP) passes through the centers of solvated ions at the distance of their closest approach to the electrode and (3) the diffuse layer as suggested by Gouy and Chapman is situated beyond the OHP. By now, the double layer has turned into a triple layer.

These specifically adsorbed ions, despite their small fraction, could significantly alter the interfacial structure and incur a serious experimental departure from what is predicted by those models that ignored their presence. The potential difference and differential capacitance now see a strong dependence on which voltage region the electrode is polarized. Figure 6.8a (bottom) schematically illustrates such a situation at the interface of mercury and 0.5 M NaCl solution under three typical polarization scenarios. Obviously, under positive polarization, the high abundance of Cl⁻ at the IHP constitutes a distinct potential change profile, which disappears at the

point of electrochemical capillary minimum (or point of zero charge) or negative polarization.

Experimentally, it has been found that specific adsorption would more likely to occur for anions rather than cations. In fact, the slight asymmetry of the electrocapillary curve that was mentioned in Section 6.3.2.1 actually arises from this: anions adsorb at negative polarization, and their presence at the IHP results in a strong influence on the shape of the electrocapillary curve, whereas cations mostly prefer to remain at the OHP, hence the effect of cation species on the electrocapillary curve is negligible (Figure 6.6).

On the basis of the Grahame model, Bockris, Devanathan and Mullen (BDM) further proposed a modified structure of electrode/electrolyte interface in 1963.⁸ They argued that, since an electrode can be visualized as a giant 2D ion, then the primary solvation sheath of this ion should consist of solvent molecules instead of counterions, provided that there are sufficient solvent molecules available (Figure 6.8b). *For an electrode, its primary solvation sheath is the IHP.*

Thus, the IHP of an electrode in an electrolyte should be occupied not only by those specifically adsorbed ions, but also, more likely, by the solvent molecules (or water molecules if the electrolyte is aqueous), given their high population in the electrolyte. In particular, the dipole nature of water molecules allows them to orient towards or away from the electrode no matter whether the electrode is positively or negatively polarized. Only at the electrochemical capillary minimum could the water molecules be randomly oriented.

The presence of solvent molecules in the IHP could be affected when the salt concentration reaches an extremely high level such that there is no longer a sufficient number of solvent molecules available. In other words, the “central ion” (*aka* the electrode) can now have the opportunity of seeing its counterions, and form an “ion pair”. Here the same quantitative standard as established in the Debye–Hückel–Bjerrum model (Section 4.9) for ion pairing should apply to the possible appearance of ions in the IHP that are not specifically adsorbed.

In this particular scenario, the IHP structure of an electrode is altered, and more ions could enter this important region, causing a cascade of electrochemical changes. The so-called “super-concentrated electrolyte” concept formulated in the 2010s represented this new frontier. In those systems, the electrode/electrolyte interfaces are more populated with ions that are usually not there, and unique new properties emerge to benefit practical applications. One such prominent example is the “water-in-salt” electrolyte that can operate in an extremely wide electrochemical stability window, making high-voltage aqueous batteries a possibility.

Since these solvent molecules at the IHP are strongly oriented towards the electrode, their dielectric constants differ from those in the bulk but are similar to those in the primary solvation sheath of the ions (see Section 3.4).

The Grahame and BDM models added a monolayer of specifically adsorbed ions or adsorbed solvent molecules to the interface structure as visualized by the Helmholtz–Perrin and Gouy–Chapman models. How does this layer affect the potential difference across the interface and the differential capacitance?

According to analysis by Bockris *et al.*,⁸ the contribution from the adsorbed and completely oriented dipoles (*i.e.* water molecules) to the interfacial capacitance is negligible compared with that from the adsorbed ions q_{IHP} . Hence only the specifically adsorbed ions need to be considered. The potential difference across the interface, *i.e.* from the electrode (ϕ_M) into the electrolyte bulk (ϕ_S), now consists of three distinct regions:

$$\phi_M - \phi_S = (\phi_M - \phi_{\text{IHP}}) + (\phi_{\text{IHP}} - \phi_{\text{OHP}}) + (\phi_{\text{OHP}} - \phi_S) \quad (6.50)$$

each of which corresponds to an individual contribution to the overall differential capacitance:

$$C_{M-\text{IHP}} = \frac{q_{\text{IHP}}}{\phi_M - \phi_{\text{IHP}}} \quad (6.51)$$

$$C_{\text{IHP}-\text{OHP}} = \frac{q_{\text{OHP}}}{\phi_{\text{IHP}} - \phi_{\text{OHP}}} \quad (6.52)$$

$$C_{\text{OHP}-S} = \frac{q_d}{\phi_{\text{OHP}} - \phi_s} \quad (6.53)$$

where q_{OHP} and q_d represent the charges distributed on the OHP and in the diffuse layer into the electrolyte, respectively. Electroneutrality requires that

$$q_M = q_{\text{IHP}} + q_{\text{OHP}} + q_d \quad (6.54)$$

Meanwhile the overall capacitance is defined as

$$C = \frac{dq_M}{\phi_M - \phi_S} \quad (6.55)$$

while it can be viewed as three distinct capacitors in series:

$$\frac{1}{C} = \frac{1}{C_{M-IHP}} + \frac{1}{C_{IHP-OHP}} + \frac{1}{C_{OHP-S}} \quad (6.56)$$

After approximation that assumes that the potential difference between the OHP and bulk electrolyte can be ignored compared with the charges at the IHP and OHP, the final expression for the overall interfacial capacitance hence becomes

$$\frac{1}{C} = \frac{1}{C_{M-OHP}} - \left(\frac{1}{C_{M-OHP}} - \frac{1}{C_{M-IHP}} \right) \frac{dq_A}{dq_M} \quad (6.57)$$

Apparently, the differential capacitance depends on the ratio of the ions that are contact-adsorbed over the whole interfacial charge.

Eqn (6.57) could represent the best approach so far to the experimentally observed potential dependence of differential capacitance on mercury electrodes, which often has a complicated shape, being almost constant under negative polarization, followed by a hump and then a minimum near the electrochemical capillary minimum before increasing exponentially under positive polarization (Figures 6.6 and 6.9).

Thus, the understanding of the interface structure evolves based on the discrepancies between the experimental observations and the previous models. Both the IHP and OHP prove to be critical components of the interface. Many reversible charge-storage processes, such as double-layer capacitance and pseudocapacitance, occur there, while their structure dictates the formation and chemistry of *interphases*, the critical component that enables anode chemistries in lithium-ion batteries.

Finally, according to both calculation and experimental observations that were enabled by modern characterization means, the thickness of the IHP is estimated to be a few ångstroms ($\sim 10^{-10}$ m), whereas the diffuse layer could extend to hundreds of ångstroms ($\sim 10^{-8}$ m), depending on the electrolyte concentration and the salt solvation. The thickness of the diffuse layer would vanish rapidly as the salt concentration increases. Hence, to a good approximation, one could ignore the charge distribution within the diffuse layer for simplicity. This is particularly true in electrolytes for practical applications, where the salt concentrations are usually high.

The Stern model, which integrates the compact ionic layer suggested by the Helmholtz–Perrin model and diffuse charge layer

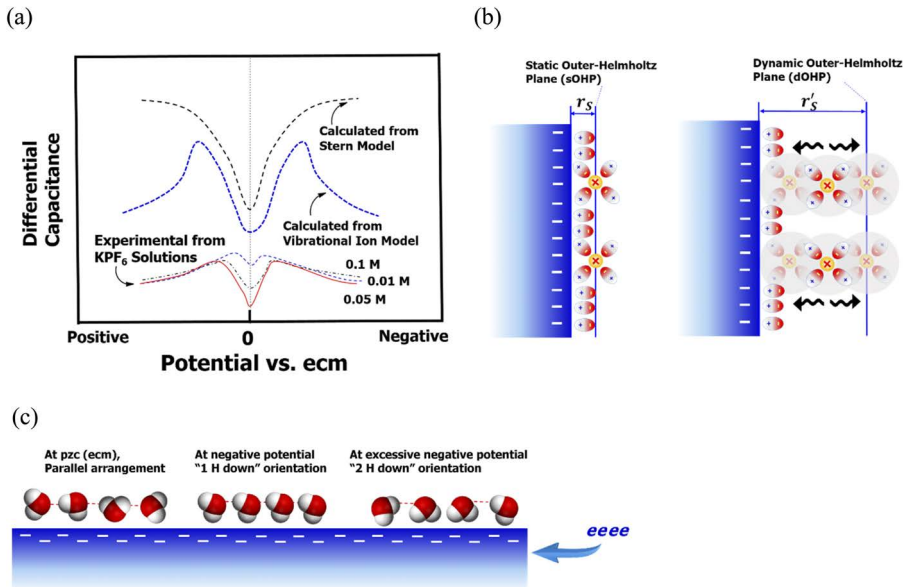


Figure 6.9 Modern illustrations of interfaces at the atomistic scale. (a) Potential dependence of differential capacitance at a mercury/1.0 M KPF₆ aqueous solution interface as measured experimentally and those calculated from the classical Stern model with a static OHP and a modified “vibrational ion model” with dynamic OHP. (b) In the vibrational ion model the distance from the electrode surface to the OHP is much more diffuse. (c) The orientation of water molecules in the IHP of an electrode varies with the electrode potential, from the predominant “parallel” arrangement at point of zero charge (or electrochemical capillary minimum) dictated by the intermolecular hydrogen bonding, to a “1 H down” arrangement at negative polarization, and eventually to a “2 H down” arrangement at highly negative polarization. Source: reconstructed from C.-Y. Li *et al.*, *Nat. Mater.*, 2019, **18**, 697–701.⁹

proposed by the Gouy–Chapman model, can explain the minimum of the differential capacitance at the point of zero charge, as this is where the electrode/electrolyte is least charged. With a fixed distance from the electrode surface to the OHP (also called the *Stern thickness*, r_s), it also predicts that, at large polarizations, the OHP will become saturated with charges on the electrolyte side, hence the differential capacitance should experience a plateau at both extreme polarizations (Figure 6.9, top). This is, however, not what is observed in experiments. In most cases, a gradual decrease in differential capacitance occurs, at either positive or negative polarizations, once the polarization potential becomes excessive (Figure 6.9, bottom). To further approach the

experimental results, we need to have an atomistic-level knowledge of the interfacial structures assisted by better imaging techniques as well as modeling.

6.4.5 Contemporary Illustrations of Interfacial Structure

Modern characterization means and computation techniques make it possible to probe the structural details of interfaces at molecular and atomistic levels that have never been available before.

A recent study attempted to explain the potential dependence of differential capacitance as observed experimentally in Figure 6.9a.⁹ It suggests that the OHP is not entirely static as the classical models imply. Instead, the solvated ions vibrate at the OHP, thus making the OHP quite diffuse (Figure 6.9b). The corresponding Stern thickness between the electrode surface and the OHP (r'_S) is therefore much larger than that of the static OHP. Such vibrations should be minimal at the point of zero charge, but will intensify as the overpotential applied on the electrode increases, in a similar manner to how the vibrational energy is transmitted from electrode to electrolyte in Marcus charge-transfer theory. In fact, this vibrating ion model should describe what the interface looks like before the overpotential reaches the threshold value of driving a charge transfer across the interface.

Thus, the effective distance between the electrode and the OHP, r'_S , increases with increase in polarization potential, accompanied by a decrease in differential capacitance. The calculation based on this assumption of a dynamic OHP indeed reproduces the basic shape of the potential dependences as observed experimentally, a minimum at point of zero charge followed by a maximum (hump), and then a steady decrease (Figure 6.9a).

On the other hand, when Bockris *et al.*⁸ proposed treating an electrode surface as a giant 2D ion, an atomic layer of water molecules is supposed to reside at the IHP serving as the primary solvation sheath of such a giant ion (Section 6.4.4). They proved that it is experimentally impossible to measure the actual potential drop across this dipole layer, while its contribution can be neglected, because once ions appear in the OHP, their contribution to the potential is overwhelming.

However, accurately knowing the dipole contribution still carries significance, especially when there is no charge accumulated at the interface (*i.e.* at point of zero charge). Fortunately, computation chemistry has made it possible to calculate such a potential drop. Based on first principles, *ab initio* molecular dynamic (AIMD) simulations have

been used to analyze charge polarizations at the interface between a Pt(111) crystal and water, which showed that the atomic structure of water layers leads to an oscillatory behavior of the averaged electrostatic potential. The calculation revealed that the potential disturbance induced by the dipole layer, as quantified by the departures from that of a platinum surface in vacuum, mainly occur at the first layer of water on the electrode surface, which fluctuates throughout the interfacial region and rapidly dissipates in a length scale of 5–20 ångstrom. Given the small interfacial thickness, the field strength in the interface could as high as $10^{7\text{--}10}$ V m⁻¹!

More details on this atomic layer of water molecules can be obtained when combining *in situ* spectroscopic and computation techniques. For example, surface-enhanced Raman spectroscopy assisted by AIMD simulations revealed how the water molecules at the IHP of an Au(111) crystal surface change their orientation with the applied overpotential (Figure 6.9c).⁹ At point of zero charge, the arrangement of these water molecules adopts a parallel configuration dictated by the hydrogen bonding. Such a configuration was disrupted when a negative overpotential (-1.29 to -1.85 V vs. point of zero charge) was applied, when the water molecules reoriented themselves by pointing one H-terminus at the electrode surface (called a “1 H down arrangement”). When the applied overpotential became excessive (<-1.85 V vs. point of zero charge), a “2 H down arrangement” appeared, with most of the water molecules turned around with both of their H termini pointed towards the electrode surface. As the structure in the atomic water layer experiences the above evolution, the hydrogen bonding also undergoes two corresponding transitions.

These atomic-level structural details, enabled by modern *in situ* characterization probes and computation techniques, are far beyond what classical models and thermodynamic treatment could teach us. It is expected that many more such details will become available in the years to come, perfecting our fundamental understanding of this vitally important phenomenon in electrochemistry and indispensable subcomponent in electrochemical devices.

6.5 When Charge Transfers Across an Interface: Electrodics

So far we have covered how electrolytes behave when they encounter an electrode: anisotropy electrifies both sides and forms an electric double layer. Now we shift our attention to how charges could travel

across such an electrified double layer. The study of the kinetics of charge transfer at interfaces is called *electrodics*.

6.5.1 What Is Charge Transfer?

Before we dive into electrodics, it is necessary to clearly define charge transfer.

The interfaces are often not open boundaries for the physical transport of species. For example, an electron can travel alone freely in the bulk of an electrode but cannot do so in the bulk of an electrolyte, while, *vice versa*, an ion or any charge-carrying molecular species can travel freely in an electrolyte bulk but will lose its mobility at the interface. Hence “charge transfer” is not necessarily associated with the physical transport of either ions or electrons across an interface. Instead, it only focuses on the process in which a *formal charge* is transmitted from one side of the interface to the other.

Let us consider two typical charge-transfer scenarios at an electrode/electrolyte interface.

The first scenario involves an ion M^{n+} that travels from the electrolyte, accepts n electrons from the electrode and deposits on the electrode surface as M^0 (Figure 6.10a):

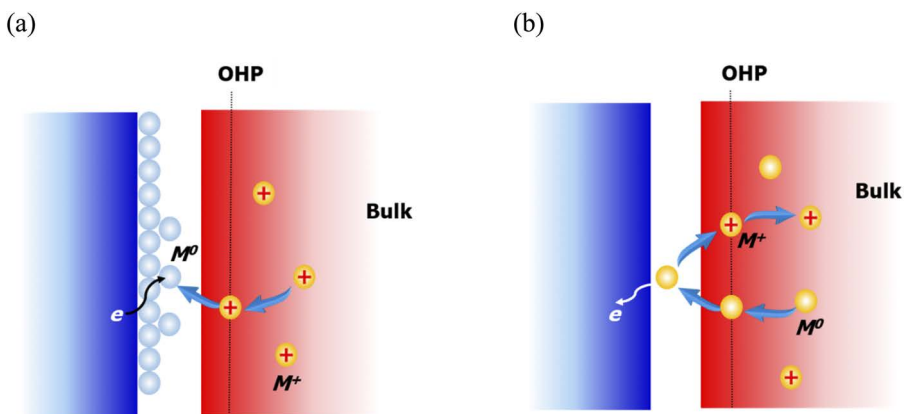
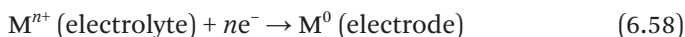


Figure 6.10 Two typical scenarios of charge transfer across an interface. (a) Reduction (electronation) of an ion followed by its deposition on an electrode surface. (b) Oxidation (de-electronation) of a neutral species at an electrode surface, producing an ion that is soluble in electrolytes. For clarity, the ion is shown as a monovalent cation, and its solvation sheath is omitted.

where n is a positive integer, but we will assume $n = 1$ in the following discussion for simplicity.

Such a process represents a variety of electrochemical reactions of practical significance, such as electroplating, electrochemical synthesis of alkali metals and battery chemistries involving metal electrodes, with Li deposition from an electrolyte as a prominent example.

As a monovalent M^+ ion approaches the IHP of the interface, it receives an electron from the conduction band of the electrode and becomes one M^0 atom. Since this M^0 atom is not soluble in the electrode, it remains on the electrode surface and forms the initial lattice for an M crystal. Here, the “charge transfer” refers to the net result of the *transport of a negative charge from the electrode to the electrolyte* across the electrode/electrolyte interface. Later, this specific M^0 atom may diffuse further into the bulk of the electrode (depending on whether the specific electrode material used allows it to do so), but that process is chemical diffusion (mass transfer) inside the electrode and is not part of the charge transfer.

So how do we view the charge transfer during its reverse process, *i.e.* the dissolution of M^0 from the electrode?

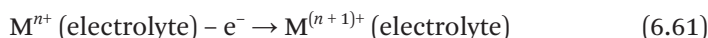
When an M^0 atom loses its valence electron to the electrode and becomes an M^+ ion, the resultant M^+ is soluble in the electrolyte. It becomes solvated at the electrode surface (assuming that the solvent molecules are available near the IHP), and it consequently leaves the interfacial region and diffuses into the bulk electrolyte, the net result of which is the transport of a negative charge *from the electrolyte to the electrode* across the electrode/electrolyte interface. Now one might be puzzled here, as it is hard to imagine how an electron can be transmitted from the electrolyte side while no physical species in the electrolyte side is oxidized. In fact, we can view the process as the bulk electrode losing a *positron p⁺* (or an “antielectron”, *aka* a hole, which is of equal mass but opposite charge to an ordinary electron), which is accepted by one M^0 atom sitting at the electrode surface, and consequently carried by it in the form of an M^{n+} to the electrolyte side:



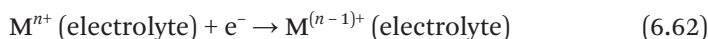
However, researchers are more used to the following form, which is equivalent to the above:



The second scenario involves a neutral species M^0 or charged species M^+ , which is soluble in the electrolyte and does not have to carry a formal charge. When it travels to the IHP of the electrode, it loses an electron and becomes a cation (or, if preferred, one can consider it accepting an electron and becoming an anion, which will not affect the outcome of the discussion below). The product, a cation M^+ , then experiences the same process of becoming solvated and leaving the interfacial region (Figure 6.10b). Such a process represents an even wider variety of electrochemical reactions, such as the reversible electrochemical redox reactions between ferric ion (Fe^{3+}) and ferrous ion (Fe^{2+}) at an inert electrode:



or



where n could be zero or an integer (both positive and negative).

In such reactions, both reactants and products are soluble in the electrolytes, and neither stays at the electrode except for the brief instant of accepting or losing an electron. The charge transfer again refers to the process of electron relocation.

Hence charge transfer is a process of transmitting a property, not physical species. The latter is called “*mass transfer*”.

The charge can be carried by different species, and its transfer across interfaces often does not involve the physical relocation of these species across the interfaces. In other words, the charge transfer corresponds to an electron lost or gained by a species at the interface. Its net result is the *electronation* or *de-electronation* of certain species from the electrolyte at the interface.

In electrochemical devices, the charge transfer across an interface is called “*Faradaic charge transfer*” or the “*Faradaic process*”. In contrast, under some circumstances where the charges are forbidden to travel across the interface owing to extremely high interfacial resistances as in the case of an ideally polarizable electrode, the ions and solvent molecules could adsorb, physically or chemically, on the electrode surface, in response to the change of electrode potential. Such an assembly of ions and solvent molecules is called a “*non-Faradaic process*”. The Faradaic process constitutes the foundation to conduct a redox reaction in the electrochemical pathway (Figure 6.1).

As briefly mentioned in Section 6.2.2, whether the electrodic process happening at an interface is Faradaic or non-Faradaic depends on the polarizability of the interface. An *ideally* polarizable interface forbids any charge transfer across it due to the interfacial resistance being infinite ($R_i = \infty$), hence all processes happening there are non-Faradaic, *i.e.* the assembly of ions and solvent molecules at the electrode surface. This is also known as ideal capacitance behavior. On the other hand, an ideally non-polarizable interface readily allows charge transfer across it, with the interfacial resistance being zero ($R_i = 0$).

It should be mentioned again that, in reality, there is *no* ideal polarizable or non-polarizable interface, hence the interfacial resistance is always a finite number. Therefore, what we encounter in actual electrochemical devices are interfaces with a mixture of polarizability and non-polarizability. That is, under certain rigorous conditions (such as a narrow potential range), an interface could closely approach the ideal behavior of either polarizable or non-polarizable interfaces, but the interface could soon depart from these “close to ideal” behaviors once the condition is breached. A good example is the mercury electrode, the interface of which with most aqueous electrolytes displays close to ideal polarizability, but this perfect polarizability occurs *only* within a narrow potential range of around 0–1.0 V *vs.* SHE, outside which the interface would see either the oxidation of mercury (if the electrode is positively polarized) or the reduction of protons (if the electrode is negatively polarized). Hence the applied potential eventually breaches the ideal polarizability, and the interfacial resistance is no longer infinite but a finite number.

This applies equally to non-polarizable interfaces. First, the interfacial resistance could never be really zero. Therefore, as charge transfer occurs, there is always a fraction of polarizability that induces the assembly and aggregation of ions and solvent molecules at the electrode surfaces. In other words, *a Faradaic process is always accompanied by non-Faradaic processes*, although the latter could be both transient and insignificant in magnitude. Second, this finite interfacial resistance is not a constant but would depend on both the applied potential and the electrolyte, because different processes occur at different potentials.

Therefore, the real interfaces that we encounter in actual electrochemical devices are always a hybridized composite of both polarizable and non-polarizable characteristics. The “equivalent circuit” shown in the inset in Figure 6.3 reflects such mixture of capacitance (non-Faradaic) and resistance (Faradaic) behaviors.

Similar to the study of ionics, the most investigated charge-transfer phenomena in electrodics are those between metallic electrodes and liquid electrolytes (Type I or II in Figure 2.1), *i.e.* aqueous or non-aqueous solutions of ionophores or ionogens. The majority of classical electrodics understanding has been achieved in this way. However, most principles thus established are still applicable, after modifications, to other interfaces, such as that between a liquid electrode and solid electrolyte, or that between an electrolyte and an electrode that are both solids.

6.5.2 Kinetics of Charge Transfer Across Interfaces

Now let us consider the first scenario discussed above, *i.e.* the deposition of a metal M^0 after the corresponding ion M^+ is reduced in the charge transfer (Figure 6.10a).

First, we assume that there is no external electric field applied on the electrode, which is immersed in an electrolyte containing monovalent cations M^+ . At equilibrium, myriads of M^+ ions assemble at the electrode/electrolyte interface and populate the OHP in the double layer. To simplify the discussions here, we assume that there are no specifically adsorbed ions at the IHP, and the potential differences caused by the solvent molecules oriented at the IHP and by the charges distributed throughout the diffuse layer are negligible. In other words, this is a Helmholtz–Perrin model, where the potential drop is simply linear (Figure 6.11, top and middle).

What is the probability of an M^+ ion crossing the interface and approaching the electrode IHP so that it could be reduced to M^0 ?

Electrochemically this is a half reaction:



According to rate process theory, the rate of such a reaction (v_M), in the absence of any electrochemical assistance, depends on the activation energy in an exponential manner expressed as

$$v_{M^+} = \frac{k_B T}{h} c_{M^+} e^{-\frac{\Delta G_1^\ddagger}{RT}} \quad (6.64)$$

where c_M is the concentration of M^+ in the bulk electrolyte and ΔG_1^\ddagger is the standard free energy change required to climb the barrier as shown in Figure 6.11 (bottom). For convenience later, we define a rate constant that is independent of the concentration:

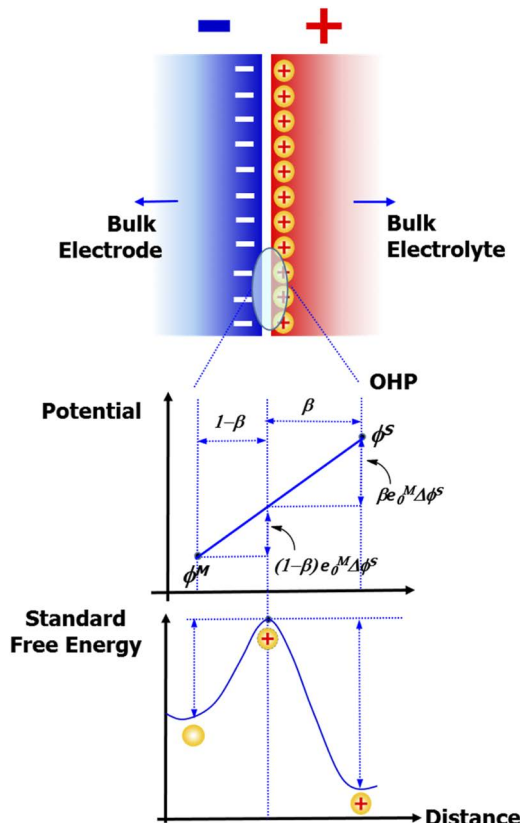


Figure 6.11 Kinetics of charge transfer across an interface. At a Helmholtz-Perrin interface, the potential difference across the electric double layer either helps or impedes the charge transfer associated with the reduction of M^+ or oxidation of M^0 , both of which have to experience a transition-state point that marks the activation energy barrier.

$$k_{\text{chem}} = \frac{k_B T}{h} e^{-\frac{\Delta G^\ddagger}{RT}} = \frac{v_{M^+}}{c_{M^+}} \quad (6.65)$$

where the subscript “chem” indicates that this rate constant is under no influence of an electric field.

Now let us consider the influence of the electric field created by the electric double layer on this moving ion M^+ .

Since M^+ carries a monovalent charge, when it passes through a region where an electric field exists, there must be electric work done, the amount of which is determined by the product of the potential

difference ($\Delta\phi$) and the charge of M^+ (e_0). This electric work will contribute to modifying the activation energy barrier.

Suppose that the potential of the metal electrode φ^M is lower than that of the bulk electrolyte φ^S , then potential difference across the interface, *i.e.* from the OHP to the surface of the electrode ($\Delta^M\varphi^S$), actually helps M^+ to overcome *part* of the activation energy barrier. We emphasize “*part*” here because the highest point in the free energy map of the journey of M^+ occurs somewhere between the OHP and the electrode surface (Figure 6.11, middle), and that point reflects a highly unstable transition state. In other words, the height of this transition state in the free energy map corresponds to the activation energy ΔG^\ddagger required for the reaction.

So, how much help can M^+ get from the potential difference?

We use the transition state to divide the potential drop across the interface into two regions, and assume that the region on the right takes a portion of β in this division (Figure 6.11, bottom). Apparently, this parameter β should be governed by

$$0 \leq \beta \leq 1 \quad (6.66)$$

Then, the part of the potential that helps an M^+ ion reach the transition state is $\beta\Delta^M\varphi^S$, and its contribution to decreasing the activation energy barrier is the electric work $\beta e_0\Delta^M\varphi^S$. For convenience later, we will use $\beta F\Delta^M\varphi^S$ instead for 1 mol of M^+ traveling across the interface.

Thus, with this assistance from potential change in the electric double layer, the activation barrier for the electrochemical reaction of M^+ to M^0 becomes

$$\Delta G_1^{\text{EC}} = \Delta G_1^\ddagger + \beta F\Delta^M\varphi^S \quad (6.67)$$

where the superscript “EC” stands for the new, composited activation energy barrier under the influence of an electric field. Note that in this case

$$\Delta^M\varphi^S = \varphi^M - \varphi^S < 0 \quad (6.68)$$

hence the resultant activation barrier (ΔG_1^{EC}) is lower than the chemical free energy change (ΔG_1^\ddagger).

Correspondingly, the reaction rate for M^+ to travel from right to left becomes

$$\bar{v}_{M^+} = \frac{k_B T}{h} c_{M^+} e^{-\frac{\Delta G_1^\ddagger + \beta F \Delta^M \phi^S}{RT}} \quad (6.69)$$

Here we have introduced an arrow above the rate v_M to indicate the direction of the ion movement from right to left as required for M^+ to be reduced to M^0 .

Since this rate stands for the number of M^+ ions crossing the interface in unit time and unit area, and since M^+ carries a monovalent charge, we can easily convert it to the number of charges passing this interface in unit time and unit area, *i.e.* the current density \bar{i}_{M^+} :

$$\begin{aligned} \bar{i}_{M^+} &= F \bar{v}_{M^+} = F \frac{k_B T}{h} c_{M^+} e^{-\frac{\Delta G_1^\ddagger + \beta F \Delta^M \phi^S}{RT}} \\ &= F k_{\text{chem}}^{-1} c_{M^+} e^{-\frac{\beta F \Delta^M \phi^S}{RT}} \end{aligned} \quad (6.70)$$

6.5.3 Dynamic Equilibrium at an Interface

In the preceding section, we only considered the interfacial kinetics for the reduction of M^+ to M^0 . In fact, since all reactions are microscopically reversible, the oxidation of M^0 atoms could also occur at the same time by losing one electron to the electrode:



The M^+ ions produced are then solvated by solvent molecules in the electrolyte, and eventually diffuse away from interface into the bulk electrolyte.

To complete this sequence, the nascent M^+ ions generated at the electrode surface must travel in the opposite direction to the process discussed in the preceding section, *i.e.* from the surface of the electrode (ϕ^M), passing through a transition state, to the bulk of the electrolyte (ϕ^S), and it must now work *against* the part of potential difference corresponding to $(1 - \beta)\Delta^M \phi^S$, which in fact raises the electrochemical activation energy barrier from the original ΔG_2^\ddagger (Figure 6.11, bottom).

Thus, the activation barrier for the electrochemical reaction of M^0 to M^+ should be

$$\Delta G_{2,EC}^\ddagger = \Delta G_2^\ddagger - (1 - \beta)F\Delta^M \phi^S \quad (6.72)$$

Again, remember that

$$\Delta^M \phi^S < 0 \quad (6.73)$$

so the activation energy barrier is *increased* because of the electric field across the interface.

Following the same analysis, the current density corresponding to the oxidation of M^0 to M^+ is

$$\vec{i}_{M^0} = F k_{\text{chem}}^2 c_{M^0} e^{\frac{(1-\beta)F\Delta^M \phi^S}{RT}} \quad (6.74)$$

where the arrow above the current density i indicates the movement of M^+ from left to right, c_{M^0} represents the concentration of M^0 atoms on the electrode surface and k_{chem}^2 is the rate constant corresponding to the activation barrier ΔG_2^\ddagger that defines the oxidation reaction of M^0 :

$$k_{\text{chem}}^2 = \frac{k_B T}{h} e^{-\frac{\Delta G_2^\ddagger}{RT}} \quad (6.75)$$

Thus, at an interface, there are two reactions occurring simultaneously and in opposite directions. At equilibrium, these two reactions must occur at the same rate and negate each other:

$$\vec{i}_{M^+} = \vec{i}_{M^0} \quad (6.76)$$

while the net current across the interface i_{net} is

$$i_{\text{net}} = \vec{i}_{M^+} - \vec{i}_{M^0} = 0 \quad (6.77)$$

In other words, an interface is the site of two-way traffic for charge transfers, and equilibrium there only means the opposite traffics being equal in numbers. *Such an equilibrium is dynamic in nature*, although the net result being zero might mislead one to think that “*nothing is happening*”.

To quantify how open an interface at equilibrium is towards such two-way traffic, a new term, *exchange current density* (i_0), is created:

$$i_0 = \vec{i}_{M^+} = \vec{i}_{M^0} \quad (6.78)$$

The higher the exchange current density, the faster are the kinetics of charges to cross the interface, and the lower the interfacial resistance R_i .

6.5.4 Butler-Volmer Equation

Imagine that, when one immerses an electrode in an electrolyte, there is no equilibrium, hence the two opposite reactions occurring there are not equal in rate, and an instantaneous net current would arise.

However, this inequilibrium will not last long. Soon the products of the faster reaction will result in net excess accumulation or depletion of a charge on the double layer, and the electric field across the interface changes accordingly to slow down this reaction and accelerate its opposing reaction, until an equilibrium is eventually established. This process will not take longer than 10^{-10} s. By then the two opposite reactions governed by the standard free energy change and the potential change across the interface will reach an identical rate, and the potential of the immersed electrode and the potential difference across the interface will stabilize at a given value to enable this equilibrium. This equilibrium potential (measured as $\Delta\varphi_e$ against a non-polarizable reference electrode) of the electrode is a characteristic property of the material of the electrode, while also being a function of the temperature, electrolyte composition and concentration or partial pressure of the species involved in the reactions, etc.

Can we breach this equilibrium to favor one of the reactions over the other?

Yes, we can do so by applying an external electric field on the interface.

A schematic diagram is presented in Figure 6.12a, which shows the change of $\Delta G_{EC_2}^{EC}$ (different from the change in standard free energy ΔG_2^\ddagger as shown in Figure 6.11 but a composite value that includes the influence of the electric field) as a result of the applied potential. Here we assume that the applied potential only alters the electron Fermi level within the electrode, and that the potentials of M^+ in bulk electrolyte and the transition state remain unaffected. This assumption is not accurate in reality as the transition-state energy can also be affected by the electrode side, but this simplification does not affect the discussions below.

Suppose an external voltage is applied, so that the absolute potential of the electrode is lowered. In other words, the electrode is negatively polarized. The consequent change in $\Delta G_{EC_2}^{EC}$ is represented by curve 2, which has a much higher activation energy barrier than the equilibrium represented by curve 1. Accordingly, the reduction reaction of M^+ will be favored against the oxidation reaction of M^0 . The net current density is now

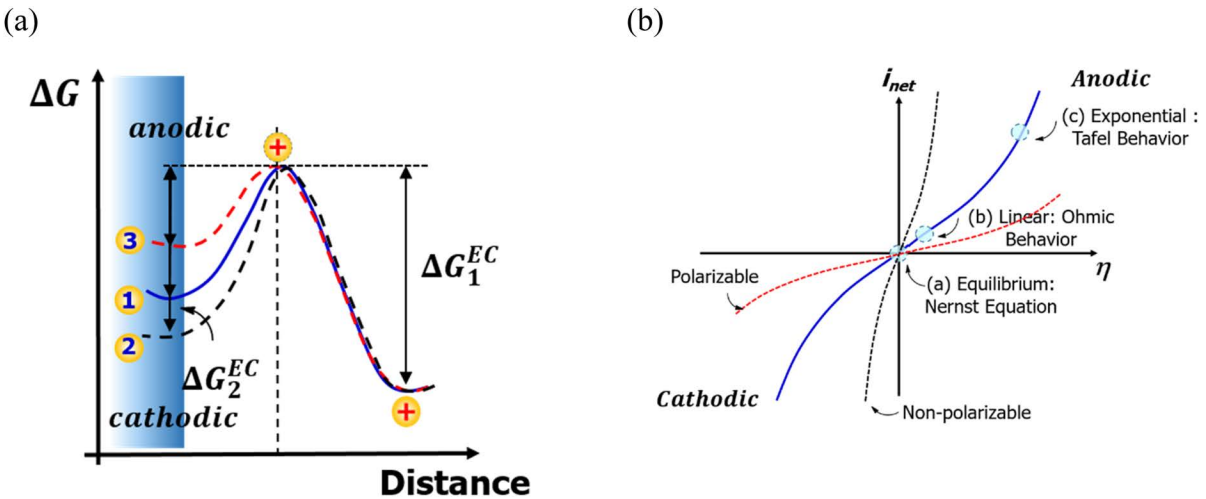


Figure 6.12 (a) Application of an external electric field on the interface allows one to manipulate the direction and rate of the reduction or oxidation reactions by changing the activation energy barriers. (b) Butler-Volmer equation: the dependence of net current density across an interface on the applied overpotential, in which three unique scenarios of distinctly different charge-transfer behavior can be predicted.

$$\vec{i}_{\text{net}} = \vec{i}_{M^+} - \vec{i}_{M^0} > 0 \quad (6.79)$$

Now the net result of the charge transfer is that electrons flow from electrode into electrolyte, which is defined as *cathodic current*.

On the other hand, if we raise the electrode potential, *i.e.* positively polarizing the electrode, the consequent change in ΔG_2^{EC} is reflected by *curve 3*, which presents a much lower activation energy barrier than the equilibrium. Accordingly, the reduction reaction of M^+ will be disfavored against the oxidation reaction of M^0 . The net current density is now

$$\vec{i}_{\text{net}} = \vec{i}_{M^+} - \vec{i}_{M^0} < 0 \quad (6.80)$$

Now the net result of the charge transfer is that electrons flow from electrolyte into electrode, which is defined as *anodic current*.

Thus, by adjusting the voltage applied on the interface, we can easily dictate in which way the equilibrium is biased so that a desirable reaction is favored over its competition reaction.

The applied field, often from an external power source such as a battery or a potentiostat, will deviate the potential difference across interface ($\Delta^M \varphi^S$) from its equilibrium value ($\Delta \varphi_e$). The departure from the equilibrium potential is defined as *overpotential* (η):

$$\eta = \Delta^M \varphi^S - \Delta \varphi_e \quad (6.81)$$

or

$$\Delta^M \varphi^S = \eta + \Delta \varphi_e \quad (6.82)$$

Inserting this new expression for potential difference across the interface $\Delta^M \varphi^S$, we obtain

$$\vec{i}_{M^+} = F k_{\text{chem}}^{-1} c_{M^+} e^{-\frac{\beta F(\eta + \Delta \varphi_e)}{RT}} \quad (6.83)$$

and

$$\vec{i}_{M^0} = F k_{\text{chem}}^2 c_{M^0} e^{\frac{(1-\beta)F(\eta + \Delta \varphi_e)}{RT}} \quad (6.84)$$

Therefore, the net current density, which should not be zero under the applied overpotential, becomes

$$\begin{aligned} i_{\text{net}} &= \bar{i}_{\text{M}^+} - \bar{i}_{\text{M}^0} = Fk_{\text{chem}}^1 c_{\text{M}^+} e^{-\frac{\beta F(\eta + \Delta\phi_c)}{RT}} - Fk_{\text{chem}}^2 c_{\text{M}^0} e^{\frac{(1-\beta)F(\eta + \Delta\phi_c)}{RT}} \\ &= Fk_{\text{chem}}^1 c_{\text{M}^+} e^{-\frac{\beta F\Delta\phi_c}{RT}} e^{-\frac{\beta\eta F}{RT}} - Fk_{\text{chem}}^2 c_{\text{M}^0} e^{\frac{(1-\beta)F\Delta\phi_c}{RT}} e^{\frac{(1-\beta)\eta F}{RT}} \end{aligned} \quad (6.85)$$

Now, remember that

$$i_0 = Fk_{\text{chem}}^1 c_{\text{M}^+} e^{-\frac{\beta F\Delta\phi_c}{RT}} = Fk_{\text{chem}}^2 c_{\text{M}^0} e^{\frac{(1-\beta)F\Delta\phi_c}{RT}} \quad (6.86)$$

Therefore, i_{net} can be written in a very elegant form:

$$i_{\text{net}} = i_0 \left[e^{-\frac{\beta\eta F}{RT}} - e^{\frac{(1-\beta)\eta F}{RT}} \right] \quad (6.87)$$

This is the famous *Butler–Volmer equation*.¹⁰ In a very elegant form, it sets the foundation for modern electrodics. It is valid under the assumption that the reaction species involved are abundant near the interface, therefore their movement is completely dictated by the charge-transfer kinetics across the interfaces.

This relation, initially derived by Butler and later refined by Volmer, reveals the exponential dependence of reaction rate (as represented by current density \bar{i}_{M^+}) on the electrode overpotentials, which could be precisely controlled *via* an external power source provided that the reference or counter electrode is non-polarizable.

Earlier, we mentioned that the interface separates electrochemistry from chemistry. Now the Butler–Volmer equation serves as a link between the two.

If we plot the Butler–Volmer equation against different overpotentials and β values, we obtain a curve with the shape shown in Figure 6.12b. Previously β was just an arbitrary parameter that we selected to divide the potential change in the interface into two distinct sections. Now we see that β actually determines the symmetry of the Butler–Volmer equation. While for most aqueous electrolytes and reversible electrochemical couples β is roughly 0.5, leading to symmetrical anodic and cathodic current curves, the unsymmetrical curves often result from those interfaces where passivation occurs so that a specific reaction is hindered, especially in the scenarios where non-aqueous electrolytes are involved.

6.5.5 Three Scenarios Predicted by the Butler–Volmer Equation

The Butler–Volmer equation describes the relation between current density across an interface and the overpotential applied on the interface. Its universality was unexpected even to Butler and Volmer themselves. Here let us examine three unique scenarios where, with specific constraints applied, the equation condenses into three classical scenarios.

6.5.5.1 At Equilibrium: Nernst Equation

At equilibrium, the two opposing reactions occur at the same rate:

$$i_{\text{net}} = \vec{i}_{\text{M}^+} - \vec{i}_{\text{M}^0} = 0 \quad (6.88)$$

In other words:

$$Fk_{\text{chem}}^1 c_{\text{M}^+} e^{-\frac{\beta F \Delta \phi_e}{RT}} = Fk_{\text{chem}}^2 c_{\text{M}^0} e^{\frac{(1-\beta) F \Delta \phi_e}{RT}} \quad (6.89)$$

which can be transformed into

$$\ln[Fk_{\text{chem}}^1] + \ln c_{\text{M}^+} - \frac{\beta F \Delta \phi_e}{RT} = \ln[Fk_{\text{chem}}^2] + \ln c_{\text{M}^0} + \frac{(1-\beta) F \Delta \phi_e}{RT} \quad (6.90)$$

Rearranging and treating c_{M^+} and c_{M^0} as reactant and product in a reaction at equilibrium (and in fact they are), we obtain

$$\Delta \phi_e = \frac{RT}{F} \ln \frac{Fk_{\text{chem}}^1}{Fk_{\text{chem}}^2} + \frac{RT}{F} \ln K \frac{c_{\text{M}^+}}{c_{\text{M}^0}} \quad (6.91)$$

Since the first term is not concentration dependent, we can condense it into a new constant K :

$$\Delta \phi_e = K + \frac{RT}{F} \ln \frac{c_{\text{M}^+}}{c_{\text{M}^0}} \quad (6.92)$$

This is in fact a variation of the famous *Nernst equation*. It can be proved that K is actually the equilibrium potential difference across the interface under standard condition $\Delta \phi_e^0$ (standard temperature, pressure and activities for all species involved).

It should be noted that the Nernst equation was derived about 25 years before Butler and Volmer's work *via* thermodynamic treatment of electrochemical systems at equilibrium. The condensation of the Butler–Volmer equation into the Nernst equation further confirms the theoretical correctness of the former.

6.5.5.2 At a Small Overpotential: Ohmic Behavior

From Figure 6.12b, it can be seen that, as the electrode potential departs from equilibrium, the current density experiences an initial slow start, which is then followed by a rapid rise.

If we assume that the overpotential is smaller than $RT/\beta F$, which is around 50 mV at ambient temperature in most cases, then the Butler–Volmer equation could be simplified *via* Taylor expansion to

$$i = i_0 \frac{\eta F}{RT} \quad (6.93)$$

In other words, under a small polarization, the current density is linearly proportional to the overpotential applied. It actually represents an Ohmic resistor, where

$$i = \frac{1}{r_i} \eta \quad (6.94)$$

r_i being the resistance of the interface. We deliberately avoid using the popular R to represent resistance here because there is already an R (gas constant) in the preceding equations.

6.5.5.3 At a High Overpotential: Tafel Behavior

On the other hand, when the applied overpotential is much larger than $RT/\beta F$, we have

$$e^{-\frac{\beta\eta F}{RT}} \gg e^{\frac{(1-\beta)\eta F}{RT}} \quad \text{if } \eta < 0 \text{ (negative polarization)} \quad (6.95)$$

$$e^{-\frac{\beta\eta F}{RT}} \ll e^{\frac{(1-\beta)\eta F}{RT}} \quad \text{if } \eta > 0 \text{ (positive polarization)} \quad (6.96)$$

The Butler–Volmer equation will be simplified under these two scenarios to, respectively,

$$i_c = i_0 e^{-\frac{\beta\eta F}{RT}} \quad (6.97)$$

$$i_a = i_0 e^{\frac{(1-\beta)\eta F}{RT}} \quad (6.98)$$

where subscripts “c” and “a” stand for “cathodic” and “anodic”, respectively.

In either case, the current density increases in an exponential manner with the applied overpotential. If we rearrange these relations:

$$\ln i_c = \ln i_0 - \frac{\beta\eta F}{RT} \quad (6.99)$$

$$\ln i_a = \ln i_0 + \frac{(1-\beta)\eta F}{RT} \quad (6.100)$$

Thus

$$\eta_c = \frac{RT}{\beta F} \ln i_0 - \frac{RT}{\beta F} \ln i_c \quad (6.101)$$

$$\eta_a = -\frac{RT}{(1-\beta)F} \ln i_0 + \frac{RT}{(1-\beta)F} \ln i_a \quad (6.102)$$

Now these equations actually are equivalent to the so-called *Tafel empirical law*, which, based on what Tafel observed experimentally, states that the applied overpotential induces an exponential increase in current density:

$$\eta = a - b \log i_c \quad \text{when the negative polarization is sufficiently high} \quad (6.103)$$

$$\eta = a + b \log i_a \quad \text{when the positive polarization is sufficiently high} \quad (6.104)$$

Note that Tafel's law was derived *ca.* 30 years before the Butler–Volmer equation.

This exponential relation between current density (or reaction rate) and applied potential is characteristic of electrochemistry and can be used for practical purposes. In conventional chemistry, researchers often manipulate the direction and extent of reactions by using species concentration, temperature or pressure. The Butler–Volmer equation actually teaches us that we can do so with exponential effectiveness by controlling the electrode potential. This is one advantage provided by electrochemical reactions that is hardly rivaled by conventional chemistry.

6.5.6 Quantifying Polarizable and Non-polarizable Interfaces

In Section 6.2.2, we qualitatively defined a polarizable interface as one that resists charge transfer across the double layer, hence the charge accumulated or depleted at the interface causes a shift of its potential, and a non-polarizable interface as one that readily allows charge transfer across the double layer, hence its potential remains static. We also mentioned that these two ideal scenarios do not exist in real life. In fact, most of the electrodes sit in between, with both polarizable and non-polarizable characteristics. We choose those with a more polarizable nature as the working electrodes to study the interfacial structure, such as the mercury electrode, and those with a more non-polarizable nature as the reference or counter electrodes to provide not only an accurate reference but also, more importantly, a reliable “fulcrum” so that most of the applied potential change is placed on the working electrode instead of the counter electrode.

But how do we quantitatively define polarizability?

Earlier we defined a new quantity representing the resistance of the interface when the charge-transfer behavior is still linear:

$$r_i = \frac{1}{i} \eta \quad (6.94)$$

Here, in analogy with Ohm’s law, we generalize this resistance as the charge-transfer resistance of an interface, r_{ct} :

$$r_{ct} = \frac{\partial \eta}{\partial i} = \frac{RT}{i_0 F} \quad (6.105)$$

Obviously the exchange current density i_0 directly determines how polarizable an interface is. On the plots of net current densities (i_{net}) against overpotential (Figure 6.12b), the exchange current density is not explicitly shown, but a non-polarizable interface should be represented by a “steep” curve, whereas a polarizable interface should be represented by a “flattened” curve.

At room temperature (298 K), the exchange current density on a mercury/sulfuric acid interface is $10^{-9.3}$ mA cm⁻², which corresponds to a charge-transfer resistance of 50 000 000 Ω cm⁻². This is a very polarizable interface.

Meanwhile, the exchange current density on an SHE is $\sim 1.0 \text{ mA cm}^{-2}$, which corresponds to a charge-transfer resistance of $25 \Omega \text{ cm}^{-2}$. This is a rather non-polarizable interface and therefore an excellent reference point.

The above numbers inject a quantitative nature into the equivalent circuit as shown in Figure 6.3 for polarizable and non-polarizable interfaces.

6.5.7 How Much Does the Butler–Volmer Equation Depend on Interface Structure?

At this point, one might have a question lingering in the mind: in Section 6.4, we went to great lengths to show that the structure of an interface is not as simple as the Helmholtz–Perrin model indicated, but instead is rather complicated by the diffuse charge layer, specifically adsorbed ions and solvent molecules as represented by the modifications of Gouy–Chapman, Stern, Grahame and Bockris–Devanathan–Müllen. However, when we derived the Butler–Volmer equation in Sections 6.5.2–6.5.4 we only used a simple Helmholtz–Perrin model. How would this simplification affect the accuracy of the Butler–Volmer equation?

If the charges on the electrolyte side are not confined to the OHP only but instead are distributed in a diffuse layer as the Stern model stated, then the potential change across the interface cannot be linear from the electrode surface to the OHP. Hence the potential difference experienced by an ion moving from the bulk electrolyte to the electrode surface should consist of two parts, as shown in Figure 6.7c, *i.e.*

$$\varphi_M - \varphi_S = (\varphi_M - \varphi_{OHP}) + (\varphi_{OHP} - \varphi_S) \quad (6.106)$$

The first part is still linear, while the second part follows a non-linear behavior similar to the ion distribution of an ionic cloud in the Debye–Hückel model as predicted by the Gouy–Chapman model.

Since charge transfer can occur only at the closest proximity to the electrode, it is reasonable to assume that the part of the potential change mainly responsible for assisting or impeding ion movement should be just the one across the electrode surface to the OHP, *i.e.*

$$(\varphi_M - \varphi_{OHP}) = (\varphi_M - \varphi_S) - (\varphi_{OHP} - \varphi_S) \quad (6.107)$$

The section across the region from the OHP to the bulk electrolyte should still be linear, but its value should be only a fraction of the

overall potential change. Meanwhile, owing to the potential difference now existing between the bulk electrolyte and the OHP, the concentration of the ionic species ($c_{M^+}^{OHP}$) also differs from that of the bulk (c_{M^+}). Instead, according to the Boltzmann distribution, the former should be given as

$$c_{M^+}^{OHP} = c_{M^+} e^{-\frac{F(\phi_{OHP} - \phi_b)}{RT}} \quad (6.108)$$

Accordingly, the equation for the exchange current should be modified to a more accurate form:

$$\bar{i}_{M^+} = Fk_{chem}^{-1} c_{M^+}^{OHP} e^{-\frac{\beta F[(\phi_M - \phi_b) - (\phi_{OHP} - \phi_b)]}{RT}} = Fk_{chem}^{-1} c_{M^+} e^{-\frac{F(\phi_{OHP} - \phi_b)}{RT}} e^{-\frac{\beta(F\phi_M - \phi_{OHP})}{RT}} \quad (6.109)$$

How much correction does this more accurate form of exchange current, and consequently the modified Butler–Volmer equation, introduce?

Experiment shows that, provided the solute concentration in the electrolyte is sufficiently high (>0.1 M), the diffuse charge layer becomes negligible, and the above modification does not cause a significant correction to what is predicted by the Butler–Volmer equation. Hence this approximation is satisfactory for most practical electrochemical devices, where the electrolytes are normally more concentrated than 1.0 M.

A much more serious interference to the Butler–Volmer equation comes from the specifically adsorbed ions, which was shown in the Grahame model as an additional ionic layer at the iHP. Most ions that can specifically adsorb on electrode surfaces are anions with weak solvation sheaths, such as Cl^- and Br^- in aqueous solutions. Not only does the presence of these ions at the IHP significantly alter the potential change across the interface, but also they physically occupy the electrode surface and render it “deactivated” for interactions with the incoming M^+ ions.

The specific adsorption could become especially pronounced in non-aqueous electrolytes, because the anions are usually weakly solvated or barely solvated thanks to the “monopolar” characteristic mentioned in Section 3.1 (Figure 3.1b). A more significant departure from the Butler–Volmer equation could be expected.

6.5.8 What is β ?

During the derivation of the Butler–Volmer equation, β was introduced as a dimensionless parameter that divides the potential change across the interface into two sections, which are individually responsible for reducing or increasing the activation barriers of either forward

or reverse reactions (Figure 6.11, middle). Since we assumed that β corresponds to the activation energy maximum, its range should be between 0 and 1. In most theoretical extensions of the Butler–Volmer equation, β has often been assumed to be 0.5 for convenience. The implication underlying this assumption is that the activation energy barrier as shown in Figure 6.11 would be completely symmetrical. We made this assumption for all three exchange current densities when we first plotted net current density against overpotential in Figure 6.12 according to the Butler–Volmer equation, and the resultant curves are all symmetrical with respect to the origin point. For this reason, β is often referred to as a “*symmetric parameter*”, and in some literature it also as “*charge-transfer coefficient*”.

But how authentic is the assumption of β being 0.5? And what will Butler–Volmer equation behave if β is not 0.5?

If we assume that $\beta = 0$ or $\beta = 1.0$, the Butler–Volmer equation would generate two completely biased curves for current density and overpotential. In fact, these interfaces now behave as a diode that allows only one direction of the reaction to proceed (Figure 6.13).

On the other hand, various experiments have proven that, in most interfaces between a metal electrode and a liquid electrolyte, β sits in very close proximity to 0.5. For example, in the high overpotential approximation we discussed in Section 6.5.5.3, if we compare the following equations:

$$\eta_c = \frac{RT}{\beta F} \ln i_0 - \frac{RT}{\beta F} \ln i_c \quad (6.101)$$

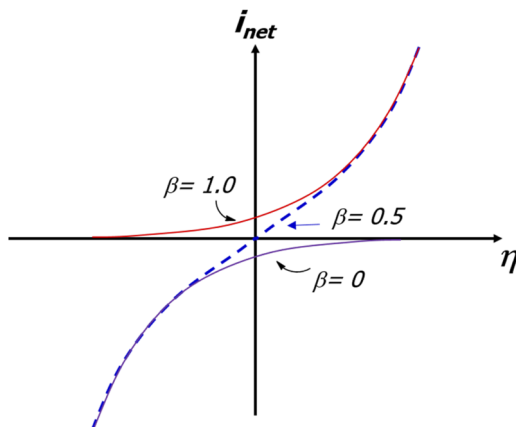


Figure 6.13 Effect of charge-transfer coefficient β on the shape of the Butler–Volmer equation. $\beta = 0$ and 1.0 are plotted in comparison with $\beta = 0.5$.

$$\eta_a = -\frac{RT}{(1-\beta)F} \ln i_0 + \frac{RT}{(1-\beta)F} \ln i_a \quad (6.102)$$

with the corresponding Tafel empirical relations:

$$\eta = a - b \log i_c \quad (6.103)$$

$$\eta = a + b \log i_a \quad (6.104)$$

we can obtain the slope b as

$$b_c = \frac{RT}{\beta F \log e} \quad (6.110)$$

$$b_a = \frac{RT}{(1-\beta)F \log e} \quad (6.111)$$

Hence, at 298 K, if $\beta = 0.5$, then the slope b for both cathodic and anodic polarizations should be 0.116.

Numerous Tafel polarization experiments applying voltages higher than 0.1 V on metal/aqueous electrolyte interfaces often obtain a slope between 0.11 and 0.12, confirming that, in most of these classical interfaces, the activation energy required for forward and reverse reactions is indeed close to being symmetrically distributed.

Since β is related to the free energy changes of these reactions, its being close to 0.5 is by no means a coincidence but instead has a more fundamental origin at the atomistic level.

Marcus, Levich and many others treated the charge-transfer process at interfaces from the quantum mechanics perspective.¹¹ They viewed the activation energy barrier and its maximum as the product of intersections by two separate free energy parabolas (Figure 6.14a), the one on the right representing the travel of an ion from the bulk electrolyte to the interface, and the one on the left representing the electron jump from the metal electrode. Those two synchronized steps construct the entire charge-transfer process for the reduction reaction of the ion. As an approximation, the intersecting region can be viewed in a linear manner as shown in the inset in Figure 6.14a.

In such a graphic representation, reducing the electrode potential by a value of η is equivalent to vertically shifting the free energy curve for the electrons downwards by a value of $F\eta$, or raising the free energy

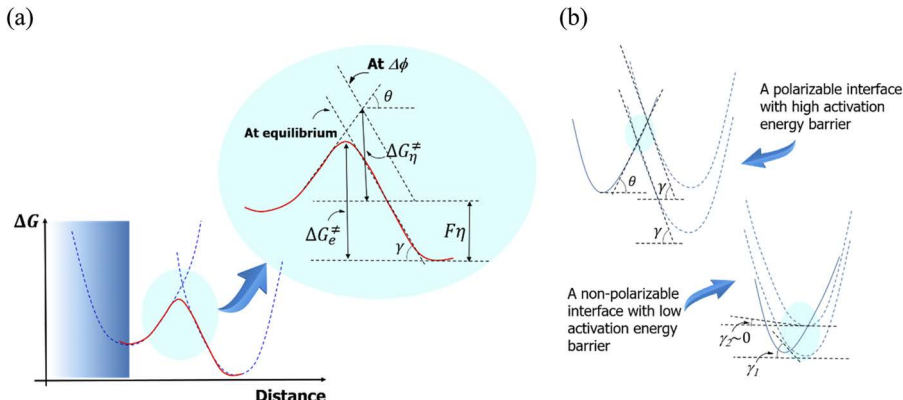


Figure 6.14 (a) The atomistic origin of the symmetry factor β , which depends on the relative slopes of free energy curves for the reaction species involved (ion and electron in this case). (b) Where these free energy curves determine whether the symmetry factor β is independent of the applied overpotential: top, a polarizable interface with high activation barrier – the two free energy curves intersect at linear sections of each other, so the vertical shift of one free energy curve does not induce changes in the relative slopes as determined by γ and θ ; bottom, a non-polarizable interface with low activation barrier – the two free energy curves intersect at non-linear sections of each other, so the vertical shift induces changes in the relative slopes.

curve for the ions upwards by a value of $F\eta$. It is possible to solve the simple geometry shown in Figure 6.14a and obtain the resultant change in the activation energy barrier ($\Delta G_e^\ddagger - \Delta G_\eta^\ddagger$). Their ratio leads to a quantitative expression for β :

$$\beta = \frac{\tan \gamma}{\tan \theta + \tan \gamma} \quad (6.112)$$

Apparently, at the molecular level, β represents the relative slopes (θ and γ) of the free energy curves for the reaction species involved, which are determined by the quantum natures of the particles involved at the atomistic scale.

Is β a constant, then?

Closer examination of Figure 6.14a reveals that, provided the free energy curves for electrode and incoming charge-carrying species intersect in a linear region, the vertical shift of one of the curves does not induce relative changes in the slopes as determined by γ and θ (Figure 6.14b, top). On the other hand, if the intersection occurs in a region where one of the curves departs from linearity, then these two

angles γ and θ are rather sensitive to the extent of vertical shift (Figure 6.14b, bottom).

In other words, for interfaces of high activation energy barrier, low exchange current density or high polarizability, the symmetry parameter β is independent of the applied overpotential. Accordingly, for interfaces of low activation energy barrier, high exchange current density or high non-polarizability, the symmetry parameter β depends on the applied overpotential.

In one particular case, where the two free energy curves intersect near their minima at rather high overpotential, β approaches zero because γ is now close to zero (Figure 6.14b, bottom).

6.5.9 Butler–Volmer Equation in Electrochemical Devices

The Butler–Volmer equation was derived on a rather fundamental basis for a single-step reversible reaction that involves the transfer of a single charge (one electron) across an interface:



Earlier, we showed that for such reversible reactions the net rate is

$$i_{\text{net}} = i_0 \left[e^{-\frac{\beta\eta F}{RT}} - e^{\frac{(1-\beta)\eta F}{RT}} \right] \quad (6.87)$$

where the exchange current is

$$i_0 = Fk_{\text{chem}}^1 c_{\text{M}^{[\text{O}]}} e^{-\frac{\beta\eta F}{RT}} = Fk_{\text{chem}}^2 c_{\text{M}^{[\text{R}]}} e^{\frac{(1-\beta)\eta F}{RT}} \quad (6.86)$$

where we have replaced the original M^+ and M^0 with more general form of the reactants $\text{M}^{[\text{O}]}$ and $\text{M}^{[\text{R}]}$.

At equilibrium, the Nernst equation governs that

$$E_{\text{red}} = E_{\text{red}}^0 - \frac{RT}{F} \ln \frac{c_{\text{M}^{[\text{R}]}}}{c_{\text{M}^{[\text{O}]}}} \quad (6.114)$$

Therefore,

$$\Delta\phi_e = E_{\text{red}} - E_{\text{red}}^0 = -\frac{RT}{F} \ln \frac{c_{\text{M}^{[\text{R}]}}}{c_{\text{M}^{[\text{O}]}}} \quad (6.115)$$

We multiply both sides of the equation with the charge-transfer coefficient β :

$$\beta\Delta\phi_e = -\beta \frac{RT}{F} \ln \frac{c_{M^{(R)}}}{c_{M^{(O)}}} \quad (6.116)$$

and transform it into

$$\left[\frac{c_{M^{(R)}}}{c_{M^{(O)}}} \right]^\beta = e^{-\frac{\beta F \Delta \phi_e}{RT}} \quad (6.117)$$

Now we can insert the above expression back into the exchange current expression, obtaining

$$\begin{aligned} i_0 &= F k_{\text{chem}}^{-1} c_{M^{(O)}} e^{-\frac{\beta F \Delta \phi_e}{RT}} \\ &= F k_{\text{chem}}^{-1} c_{M^{(O)}} \left[\frac{c_{M^{(R)}}}{c_{M^{(O)}}} \right]^\beta = F k_{\text{chem}}^{-1} \left[c_{M^{(O)}} \right]^{(1-\beta)} \left[c_{M^{(R)}} \right]^\beta \end{aligned} \quad (6.118)$$

Eqn (6.118) adopts the form that has often been used in the literature to model the charge-transfer problems in various electrochemical devices. However, it must be remembered that the Butler–Volmer equation should not be directly applied to multi-step, multi-electron transfer processes, which are more often than not the reactions that occur in actual electrochemical devices. Nevertheless, numerous efforts have been made attempting to modify the Butler–Volmer equation for those complicated scenarios. For example, in proton fuel cells, the reduction/oxidation of proton/hydrogen gas at the anode is a single-electron charge-transfer process:



and the equation becomes

$$i_{\text{net}} = i_0 \left(\frac{c_{\text{H}_2}}{c_{\text{H}^+}} \right)^{\gamma_{\text{H}_2}} \left[e^{\frac{\beta F \Delta \phi_e}{RT}} - e^{-\frac{(1-\beta)F \Delta \phi_e}{RT}} \right] \quad (6.120)$$

For advanced batteries that will be discussed in Part B, the reactions are not confined to the interface only, because the associated high capacities rely on electrochemical insertions of the reactants

into the bulk lattice or matrices of the electrodes. For example, at the anode of advanced lithium ion batteries, Li^+ reversibly intercalates/de-intercalates in the graphite lattice (Figure 5.4) or alloys/de-alloys in the amorphous matrix of silicon:



where $x \geq 6$ and $y \leq 3.75$.

If we assume that the charge transfer of these reactions occurs at the interface, then the rate of the reactions now must be related not only to the reactant concentration on the electrolyte side ($c_{\text{Li}^+}^e$), but also the available vacancies in the bulk of the electrode. For a host such as graphite or silicon, there is an upper limit in terms of how many Li^+ ions they can accommodate. For graphite this limit is LiC_6 [$x = 6$ in eqn (6.121)], corresponding to a specific capacity of 372 mAh g⁻¹, and for silicon the limit is $\text{Li}_{3.75}\text{Si}$ or $\text{Li}_{4.4}\text{Si}$ [$y = 3.75$ or 4.40 in eqn (6.122)], corresponding to specific capacities of 3600 and 4212 mAh g⁻¹, respectively. Beyond these limits, the batteries will go beyond the scope of “lithium ion” in nature, because the anode now will become dangerous because of the presence of lithium metal.

Let us now set the concentration of Li^+ in these anode materials at these upper limits to be c_{max} . At such concentrations, the cathodic reaction (Li^+ insertion) will cease to proceed, because there is no vacant site available. However, if only a fraction of those sites are occupied, *i.e.* the actual concentration of Li^+ therein is c_x , then the number of corresponding empty sites ($c_{\text{max}} - c_x$) would drive the cathodic reaction, together with the concentration in the electrolyte ($c_{\text{Li}^+}^e$) (Figure 6.15). According to the rate equation in chemical kinetics, the reaction rate is proportional to the product of these two concentrations ($c_{\text{Li}^+}^e$ and $c_{\text{max}} - c_x$):

$$v_c = k_c \prod c_i^n = k_c [c_{\text{Li}^+}^e (c_{\text{max}} - c_x)]^\beta \quad (6.123)$$

and accordingly the current density for the reaction under an electrochemical overpotential becomes

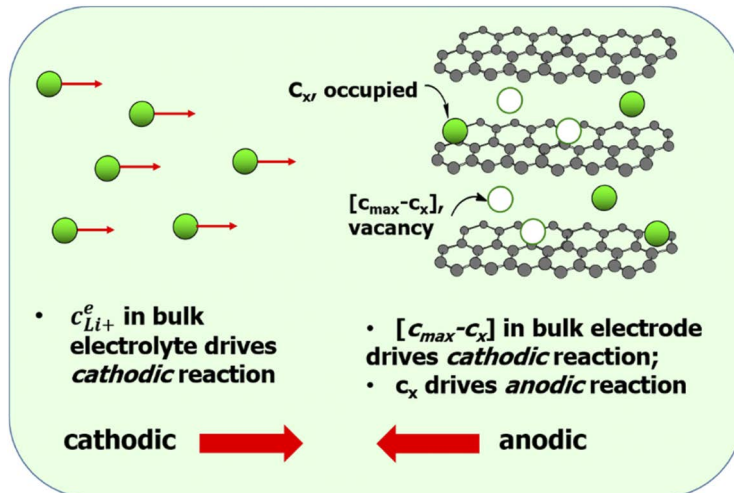


Figure 6.15 An example of the Butler–Volmer equation being applied on an actual electrochemical device, the graphite intercalation host for Li^+ intercalation. Here we completely ignore the existence of an interphase that separates the graphite anode and the bulk electrolyte, and assume that the charge transfer occurs at the interface.

$$i_c = Fk_c \left[c_{\text{Li}^+}^{\text{e}} (c_{\text{max}} - c_x) \right]^{\beta} e^{-\frac{\beta F \Delta \phi_c}{RT}} \quad (6.124)$$

In the other direction, the number of sites occupied (c_x) serves as the concentration to drive the anodic reaction (Li^+ de-insertion):

$$i_a = Fk_a c_x^{(1-\beta)} e^{\frac{(1-\beta)F \Delta \phi_c}{RT}} \quad (6.125)$$

Hence we can rewrite the Butler–Volmer equation as

$$i_{\text{net}} = i_c - i_a = Fk_c \left[c_{\text{Li}^+}^{\text{e}} (c_{\text{max}} - c_x) \right]^{\beta} e^{-\frac{\beta F \Delta \phi_c}{RT}} - Fk_a c_x^{(1-\beta)} e^{\frac{(1-\beta)F \Delta \phi_c}{RT}} \quad (6.126)$$

At equilibrium, the following Nernstian expression can be obtained after we perform similar operations to those described earlier in this section:

$$i_0 = Fk_{\text{chem}} \left(c_{\text{Li}^+}^{\text{e}} \right)^{\beta} \left(c_{\text{LiC}_6}^{\text{max}} - c_{\text{Li}^+}^{\text{s}} \right)^{\beta} \left(c_{\text{Li}^+}^{\text{s}} \right)^{1-\beta} \quad (6.127)$$

while the Butler–Volmer equation takes a new form after inserting these concentrations:

$$i_{\text{net}} = Fk_{\text{chem}}^1 \left(c_{\text{Li}^+}^{\text{e}} \right)^{\beta} \left(c_{\text{LiC}_6}^{\max} - c_{\text{Li}^+}^{\text{s}} \right)^{\beta} \left(c_{\text{Li}^+}^{\text{s}} \right)^{1-\beta} \left[e^{\frac{\beta F \Delta \phi_e}{RT}} - e^{-\frac{(1-\beta)F \Delta \phi_e}{RT}} \right] \quad 6.128$$

The above equations have been extensively adopted in the simulation of lithium-ion batteries, and applied not only to the charge-transfer processes at the anode but also those at the cathode or even the entire cell. However, it must be cautioned that there are many tacit approximations adopted when doing so.

First, we have completely ignored the existence of *interphases* on the electrode surface. Interphases, as a key ingredient in advanced battery chemistries and inevitable for most anode materials especially, will be discussed in Chapter 8. In short, it is an independent phase that has its own chemical composition, morphology and structure, hence the potential drop across it differs completely from what the Helmholtz–Perrin model would predict.

Second, in the presence of the interphase, the assumption that “*the charge transfer of these reactions occurs at the interface*” no longer holds true either. In fact, the existence of the interphase creates two new “interfaces” between itself and the bulk electrode and bulk electrolyte, respectively. Since the most important function of the interphase is to insulate the electron transfer, the charge-transfer process cannot possibly occur either on the electrolyte side of the interphase or within it.

So, does charge transfer occur at the interface between the electrode and interphase?

Not quite either.

For those electrochemical reactions of an insertion nature, the ions participating in the reactions never stop at the interface, nor are they really reduced to the atomic state at the anode (an important reason why the most popular battery used today is called the “lithium-ion battery” instead of the “lithium battery”). The charge transfer in those cases can be viewed as the process of alkali metal ions associating themselves, in the form of Coulombic bonding, with the conducting band of the host materials (graphite or silicon). The latter are the actual recipients of electrons.

Despite these approximations, the Butler–Volmer equation is still applied to numerous actual electrochemical devices after performing necessary modifications and assumptions. More or less, these variants maintained the basic form of the Butler–Volmer equation.

References

1. M. Faraday, *On Electrochemical Decomposition*, 1834, pp. 11–44.
2. J. O. M. Bockris, and A. K. N. Reddy, *Modern Electrochemistry*, 2nd edn, Plenum Press, New York, 1998.
3. G. Lippmann, Relation entre les phénomènes électriques et capillaires, *C. R. Séances Acad. Sci., Ser. C*, 1873, **76**, 1407–1408.
4. H. Helmholtz, Ueber einige Gesetze der Vertheilung elektrischer Ströme in körperlichen Leitern mit Anwendung auf die thierisch-elektrischen Versuche, *Annu. Rev. Phys. Chem.*, 1853, **165**, 211–233.
5. M. Gouy, Sur la constitution de la charge électrique à la surface d'un électrolyte, *J. Phys.*, 1910, **9**, 457–468.
6. O. Stern, Zur Theorie der Elektrolytischen Doppelschicht, *Z. Elektrochem.*, 1924, **30**, 508.
7. D. C. Grahame, The Electrical Double Layer and the Theory of Electrocapillarity, *Chem. Rev.*, 1947, **41**, 441–501.
8. J. O. M. Bockris, M. A. V. Devanathan and K. Müllen, On the structure of charged interfaces, *Proc. R. Soc. London, Ser. A*, 1963, **274**, 55–79.
9. C.-Y. Li, J.-B. Le, Y.-H. Wang, S. Chen, Z. L. Yang, J. F. Li, J. Chen and Z.-Q. Tian, *In situ* probing electrified interfacial water structures at atomically flat surfaces, *Nat. Mater.*, 2019, **18**, 697–701.
10. J. A. V. Butler, Hydrogen overvoltage and the reversible hydrogen electrode, *Trans. Faraday Soc.*, 1932, **28**, 379.
11. R. A. Marcus, On the Theory of Electron-Transfer Reactions. VI. Unified Treatment for Homogeneous and Electrode Reactions, *J. Chem. Phys.*, 1965, **43**, 679–701.

7 Linking Ionics With Electrodics

So far, we have covered two major aspects describing electrolytes: *ionics*, which governs the interactions among ions and solvent molecules and their transport in the bulk, and *electrodics*, which governs the interaction of an electrolyte with an electrode, and the interfacial structure, the subsequent potential profile, as well as the charge transfer across the interfaces.

While doing so, we have acted as if each aspect exists independently. For example, when discussing the second scenario as shown in Figure 6.10b, we were concerned only with how the incoming species climbs the activation energy barrier and subsequently interacts with the electrode, which serves as either a source or sink of electrons. We did not worry about whether there is a sufficient supply of the incoming species from the electrolyte bulk, or whether the species produced can travel away from the interfacial regions fast enough so that this reaction site would not be clogged.

Hence we assumed, without explicitly stating it, that the only sluggish step (often called the “*rate-determining step*” or “*rds*” in kinetics) is the charge transfer at the interface, which consists of the incoming species diffusing from the OHP to the electrode surface and subsequently completing the transaction of electronation or de-electronation. There is neither depletion of the reacting species in the bulk electrolyte nor accumulation of the produced species in the interfacial region. The rate of the reaction relies solely on how fast the reactants can climb the activation barriers defined by the respective free energy curves.

In real life, however, this is not true.

In addition to charge transfer, there is *mass transfer*, which is related to the diffusion and migration of the species into and away from the interfacial region, and is governed by ionics in the bulk electrolyte. These steps are responsible for transporting species needed by the reaction to the interfacial region, and then transporting the species produced by the reaction away from the interfacial region.

If we re-examine the entire process for a typical electrochemical reaction as shown in Figure 6.10b, we can see that it consists of consecutive steps, and any particular step could become the rds provided that it is slower than the remainder of the processes (Figure 7.1a).

But what determines which step could be the rds?

In earlier sections, we have shown that the tremendous activation energy barrier across the interface often makes the charge transfer thereat the most sluggish step, and even earlier we also discussed the activation energy barriers encountered by an ion when traveling in a liquid electrolyte, which is relatively small and flattened in amplitude (Figure 5.15).

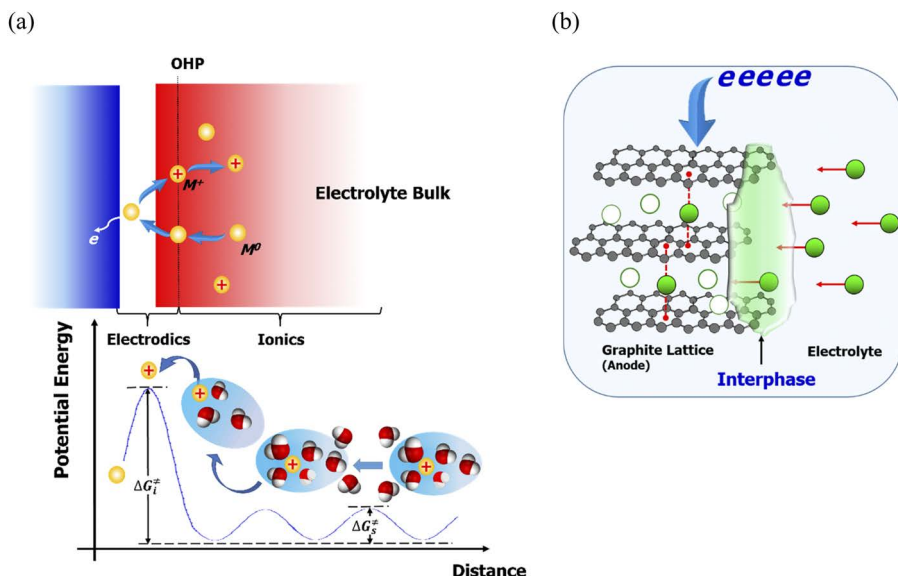


Figure 7.1 (a) The long journey of an ion from the bulk electrolyte to the interfacial region before charge transfer. The activation barrier height, although important given its exponential location in the rate equation, is not the only determining factor. (b) The actual “charge-transfer” process occurring at the graphitic anode of a lithium-ion battery is far more complicated than what the simple Helmholtz-Perrin model presents.

Does this mean that the ionics part of the journey should not have the opportunity of constituting an rds?

Not quite.

Remember that the dominant role of the free energy change ΔG_i^\ddagger in determining the rate (or current density) for a given reaction step is given by its exponential location:

$$v_{M^+} = \frac{k_B T}{h} c_i e^{-\frac{\Delta G_i^\ddagger}{RT}} \quad (6.64)$$

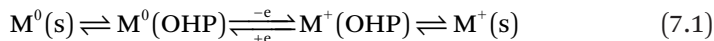
However, in addition to the exponential term, there are still pre-exponential factors that can affect the overall rate, among which is c_i , the number of available reactant species (ions or molecules). Hence, if any mass-transfer step lags behind and fails to supply reactant species to the interfacial region, it could still become the rds. Therefore, although the activation barriers encountered by diffusing or migrating species are much smaller in amplitude compared with that at the interface or interphase (Figure 7.1b), they must be given proper consideration.

Furthermore, the graphic illustration in Figure 7.1 only concerns the incoming species. However, if the leaving species encounters diffusion or migration resistances, their exodus from the interfacial region could also become the rds. Such resistances could arise from either concentration or potential barriers at the OHP, which are induced by the accumulation of product in the bulk electrolyte or by electrostatic pull from the electrode, respectively.

Therefore, ionics and electrodics should be considered together when studying an actual electrochemical reaction, which consists of mass transfer from the bulk electrolyte to the interface, then the charge transfer thereat, followed by mass transfer (if there is any) away from the interface.

7.1 Steady State

Let us look again at the consecutive steps described in Figure 7.1a, which can be written as



Among these consecutive steps, if any single one with a higher ΔG_i^\ddagger becomes the rds, no matter what that step is (charge-transfer step at the interface, or mass-transfer steps in the electrolyte that either

precede or follow the charge-transfer step), its sluggishness will cause either depletion of reactants or accumulation of products at its junction with other steps. Given enough time, this step will effectively decelerate the other steps with lower ΔG_i^\ddagger by reducing their pre-exponential term, and eventually force all those faster steps to proceed at the same speed. Then this reaction has reached the so-called “*steady state*”, in which the reactants needed by this rds step will be produced by the preceding step at a suppressed speed, while the species produced by this step will be immediately consumed by the step following it.

Based on this characteristic of the steady state, the charge-transfer current density (i_{CT}) should correspond to the flux of mass transfer (J_{MT}) according to the following relation:

$$i_{\text{CT}} = nFJ_{\text{MT}} \quad (7.2)$$

Now it must be remembered that, in a real electrochemical device, the mass-transfer flux across the bulk electrolyte could be contributed by two distinct modes of movement, *i.e.* diffusion and migration of the species. For example, if the reactant or product is a neutral species that does not carry any formal charge, its movement across the bulk electrolyte may have been dictated by its concentration gradient from the bulk to the interfacial region, and we can rewrite the above equation by resorting to Fick's first law:

$$i_{\text{CT}} = nFJ_{\text{MT}} = -nF \frac{dc_{\text{M}^0}}{dx} \quad (7.3)$$

However, if the reactant or product is an ion, then the corresponding mass-transfer flux should come from those ions driven by both concentration gradient and the electrostatic force:

$$J_{\text{MT}} = J_{\text{Diff}} + J_{\text{Mig}} \quad (7.4)$$

To simplify this convoluted contribution, researchers in classical electroanalytical chemistry often try to “eliminate” the migration contribution from the above equation, so that the mass-transfer flux is dictated solely by the diffusion. To do so, an inert electrolyte solute that does not participate in the electrochemical reactions is used at high concentration, so that the fraction of migration flux carried by the investigated ion is negligible, as exemplified by the example of transport numbers for proton and potassium in Section 5.2.1.5.

Hence, by keeping the flux purely diffusional, one could apply the solutions to Fick's first and second laws as taught in Section 5.1 under the constraints of different initial and boundary conditions, and derive how charge-transfer current density is related to the diffusion coefficient and bulk concentration of the investigated species, and how such current density varies with the applied external field and time. This is the reason why "supporting electrolytes" are necessities in analytic electrochemistry.

7.2 Galvanostatic and Potentiostatic

In Section 5.1.4, we analyzed how the concentration of a species being either consumed or produced at a constant rate (J_D) varies with distance and time from a reference plane at $x = 0$:

$$c = c_0 - \frac{J}{\sqrt{D}} \left[2\sqrt{\frac{t}{\pi}} e^{-\frac{x^2}{4Dt}} - \frac{x}{\sqrt{D}} \operatorname{erfc} \sqrt{\left(\frac{x^2}{4Dt} \right)} \right] \quad (5.35)$$

$$c = c_0 + \frac{J}{\sqrt{D}} \left[2\sqrt{\frac{t}{\pi}} e^{-\frac{x^2}{4Dt}} - \frac{x}{\sqrt{D}} \operatorname{erfc} \sqrt{\left(\frac{x^2}{4Dt} \right)} \right] \quad (5.37)$$

Now we use the OHP of the interface as the reference plane, at a distance x away from the OHP and at a time t after the constant flux is switched on, the concentration of this species is given by the solution of Fick's second law as

$$c_{x,t} = c_0 - \frac{2J_D \sqrt{t}}{\sqrt{D\pi}} e^{-\frac{x^2}{4Dt}} + \frac{J_D x}{D} \operatorname{erfc} \frac{x}{\sqrt{4Dt}} \quad (7.5)$$

$$c_{x,t} = c_0 + \frac{2J_D \sqrt{t}}{\sqrt{D\pi}} e^{-\frac{x^2}{4Dt}} + \frac{J_D x}{D} \operatorname{erfc} \frac{x}{\sqrt{4Dt}} \quad (7.6)$$

where c_0 represents the concentration of this species in the bulk electrolyte, D is the diffusion coefficient and "+" or "-" after c_0 indicates whether the species is consumed or produced at the interface.

Now, remember that flux is related to the current density via

$$J_D = \frac{i_{CT}}{nF} \quad (7.7)$$

We will have

$$c_{x,t} = c_0 - \frac{2i_{CT}}{nF} \sqrt{\frac{t}{D\pi}} e^{-\frac{x^2}{4Dt}} + \frac{i_{CT}x}{nFD} \operatorname{erfc} \frac{x}{\sqrt{4Dt}} \quad (7.8)$$

$$c_{x,t} = c_0 + \frac{2i_{CT}}{nF} \sqrt{\frac{t}{D\pi}} e^{-\frac{x^2}{4Dt}} + \frac{i_{CT}x}{nFD} \operatorname{erfc} \frac{x}{\sqrt{4Dt}} \quad (7.9)$$

Earlier we applied Fick's second law to describe how the Li^+ concentration gradient varies with time (Figure 5.4c and d) and obtained the same solution. Here we have generalized the problem to any species that participates in an electrochemical reaction at the OHP of an electrode/electrolyte interface. If we plot the concentration of this species in 3D space with both time and distance axes, we will have the concentration profile as shown in Figure 7.2, where a few important relations could be derived under various constraints, as shown in the framed boxes.

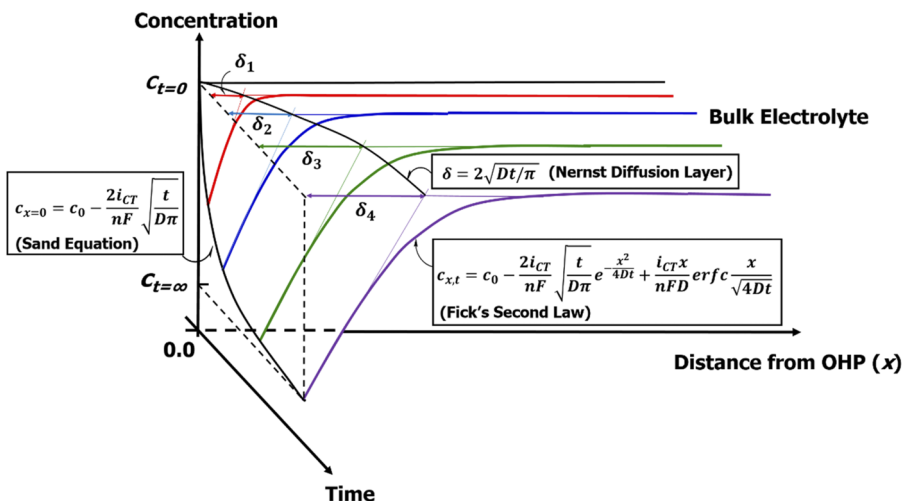


Figure 7.2 Concentration profiles of an electrochemically active species in 3D space as a function of distance and time under galvanostatic conditions. Here only the consumption scenario of the species is shown. The time variation of the interfacial concentration (Sand equation) is represented by the solid curve on the *concentration-time plane* at $x = 0$, and dependence of the Nernst diffusion layer thickness on time is represented by the solid curve on the *distance-time plane* at $c_{t=0}$. Note that both the Sand equation and Nernst diffusion layer thickness are proportional to the square root of time.

Most of the time, one is more interested in knowing how the concentration of this species at the OHP (*i.e.* $c_{x=0}$) changes with time; then, after making x zero, the above expressions become

$$c_{x=0} = c_0 - \frac{2i_{\text{CT}}}{nF} \sqrt{\frac{t}{D\pi}} \quad (7.10)$$

$$c_{x=0} = c_0 + \frac{2i_{\text{CT}}}{nF} \sqrt{\frac{t}{D\pi}} \quad (7.11)$$

If we define a constant P as

$$P = \frac{2i_{\text{CT}}}{nF} \sqrt{\frac{1}{D\pi}} \quad (7.12)$$

Then we obtain

$$c_{x,t} = c_0 - P\sqrt{t} \quad (7.13)$$

$$c_{x,t} = c_0 + P\sqrt{t} \quad (7.14)$$

This is the *Sand equation*, which tells us that, under a constant-current (or *galvanostatic*) mode the interfacial concentration of a given reacting species decays with the square root of time. This relation is represented in Figure 7.2 by the curve on the concentration–time plane at $x = 0$.

Thus, at a constant rate of consuming or producing an interfacial species, the interfacial concentration of the species would eventually reach either infinity ($+\infty$) or negative infinity ($-\infty$) when t is sufficiently large ($t \approx \infty$). In reality, however, practical limits always step in and apply additional restrictions to keep these values realistic.

For example, in the consumption scenario, the interfacial concentration of the species will become infinitesimally small, which means that as soon as a reactant ion or molecule appears at the OHP, it will participate in the reaction, be consumed and be converted into other species. This is similar to the metastable reaction intermediates in a series of reactions. At this time, we often treat the interfacial concentration of the species as zero.

Such a specific time τ , where the concentration of this species drops to zero, is known as *Sand's time* (τ_{Sand}),¹ which could be obtained from the follow relation:

$$c_{x=0} = c_0 - \frac{2i_{CT}}{nF} \sqrt{\frac{\tau_{Sand}}{D\pi}} = 0 \quad (7.15)$$

$$\tau_{Sand} = \pi D \left(\frac{nFc_0}{2i_{CT}} \right)^2 \quad (7.16)$$

In the electrodeposition phenomenon, Sand's time is an important parameter that will affect the morphology of the nascent metal species deposited on the electrode surface, such as the dendritic deposition of metals. However, in that scenario, since a metallic cation is the only conducting species that contributes to the charge transfer, while anions would accumulate at the other electrode surface, creating an additional concentration gradient as well as an internal electric field that is opposite to the externally applied electric field, some adjustment will have to be made to reflect the interactions between the cation and anion. In particular, when a supporting electrolyte is absent, which is most likely the case in most real electrochemical devices, the ambipolar diffusion of the cations and anions should be taken into account, resulting in a different Sand's time. We will discuss this adjustment in Section 7.5.

On the other hand, for the production scenario, the interfacial concentration of the species produced will increase with time, while its diffusion away from the OHP into the electrolyte bulk will try to decrease it. The net result of these two competing processes will determine whether the interfacial concentration can reach an equilibrium. In the case that an excessive overpotential is applied on the electrode so that the diffusion cannot transport the produced species away fast enough, the accumulation of the species at the OHP will encounter its solubility limitation, and the product leaves the OHP in the form of precipitation.

Now let us consider if, instead of a constant flux, a constant potential (*i.e.* *potentiostatic*) is applied at the interface to drive the consumption or production of a given species, how would the interfacial concentration and current density change? Cottrell² applied such potentiostatic constraints on Fick's second law and obtained the corresponding concentration profile as a function of time and distance from the interface:

$$c_{x,t} = c_0 \operatorname{erf} \left[\frac{x}{\sqrt{4Dt}} \right] \quad (7.17)$$

where c_0 is the concentration of the species in the bulk electrolyte.

The corresponding flux depends on the concentration of the species at the OHP of the interface, *i.e.* $x = 0$, and should follow Fick's first law as

$$J_D = -D \frac{\partial c_{x,t}}{\partial x} = -D \left[\frac{c_0}{\sqrt{\pi D t}} e^{-\frac{x^2}{4 D t}} \right]_{x=0} = -c_0 \sqrt{\frac{D}{\pi t}} \quad (7.18)$$

while the current density i_{CT} is related to the diffusional flux by

$$i_{CT} = -nFAJ_D = nFAc_0 \sqrt{\frac{D}{\pi t}} = Kt^{-\frac{1}{2}} \quad (7.19)$$

This is the *Cottrell equation*,² which states that, under a potentiostatic condition, the diffusion-control current density would decay with the reciprocal square root of time.

Note that neither the concentration profile nor the current density relies on the overpotential applied, but rather on the capability of the bulk electrolyte to provide the reactant (*via* the terms c_0 and D).

The Sand and Cottrell equations describe in a quantitative manner how concentration, interfacial potential and charge-transfer current density change under galvanostatic and potentiostatic conditions, respectively. One can observe a similarity between the two: the square root of time (\sqrt{t}). These two ideal scenarios represent the most important electrochemical elements that one could apply to control the reactions, and they are present, in varying manners, in most advanced electrochemical techniques such as *potentiometry*, *coulometry*, *voltammetry* and their variations, including cyclic voltammetry, chronoamperometry, polarography, *etc.* As a consequence, the factor \sqrt{t} often appears in the quantitative treatments of transient responses of either concentration, current or voltage.

7.3 Nernst Diffusion Layer

From Figure 7.2, one can easily see that, under galvanostatic conditions, at a given time, the concentration of the species under investigation experiences a continuous increase from $c_{x=0,t}$ at the OHP all the way into the bulk electrolyte, where it reaches a bulk concentration

value of $c_{t=0}$. Note that the former ($c_{x=0,t}$) is a function of time, whereas the latter ($c_{t=0}$) is a constant. Between these two boundary values there is a transition region defined by eqn (7.13). Nernst proposed a simplified quantification of this transition region. He extrapolated the linear section of the concentration profile at the interface as well as the line representing bulk concentration value. The two lines intersect, and Nernst defined the distance from the OHP to this intersection as the “diffusion layer”.³ It is hence called the “*Nernst diffusion layer*”, the thickness of which is denoted δ and illustrated in Figure 5.7. Apparently δ also changes with time.

What is the physical significance of that straight line at the OHP? Its slope, *i.e.* $(dc/dx)_{x=0}$, is in fact the concentration gradient at the interface:

$$\left(\frac{dc}{dx}\right)_{x=0} = \frac{c_{t=0} - c_{x=0,t}}{\delta} \quad (7.20)$$

According to Fick’s first law, this concentration gradient determines the flux and the charge-transfer current density across the interface:

$$J_D = -D\left(\frac{dc}{dx}\right)_{x=0} = \frac{i_{CT}}{nF} \quad (7.21)$$

Hence

$$J_D = -D \frac{c_{t=0} - c_{x=0,t}}{\delta} = \frac{i_{CT}}{nF} \quad (7.22)$$

which can be rearranged to

$$c_{t=0} - c_{x=0,t} = -\frac{\delta i_{CT}}{nDF} \quad (7.23)$$

On the other hand, we have shown earlier that, under galvanostatic conditions, the concentration at the OHP should be

$$c_{x=0,t} = c_{t=0} + \frac{2i_{CT}}{nF} \sqrt{\frac{t}{D\pi}} \quad (7.11)$$

Combining these two expressions, we obtain

$$\frac{\delta i_{CT}}{nDF} = \frac{2i_{CT}}{nF} \sqrt{\frac{t}{D\pi}} \quad (7.24)$$

One can then easily obtain the expression for δ :

$$\delta = 2\sqrt{\frac{Dt}{\pi}} \quad (7.25)$$

In other words, the Nernst diffusion layer also increases with the square root of time, which is represented by the solid curve on the distance-time plane at $c_{t=0}$ (Figure 7.2).

Similarly, one can obtain the expression for the Nernst diffusion layer under potentiostatic conditions:

$$\delta = \sqrt{\pi Dt} \quad (7.26)$$

In both cases the diffusion layer thickness increases with the square root of time. For most practical electrochemical devices, after a short transient time, the diffusion layer would prevail over the entire cell, until diffusion control steps in and interferes. Thus, how fast the ions can transport across the electrolyte often determines whether mass transport would become the rate-determining step of the cell reaction.

7.4 Limiting Current

Consider an electrode under either galvanostatic or potentiostatic polarization for a while: when equilibrium is reached all the mass-transport and charge-transfer steps proceed at the same rate, as we discussed at the beginning of this chapter, and the concentration of the species that is consumed at the interface becomes essentially infinitesimally small. In this case, at a given time, the concentration gradient at the OHP, *i.e.* $(dc/dx)_{x=0}$, reaches its maximum at that given time:

$$\left(\frac{dc}{dx}\right)_{x=0} = \frac{c_{t=0} - c_{x=0, t}}{\delta} = \frac{c_{t=0}}{\delta} \quad (7.27)$$

The maximum concentration gradient corresponds to a maximum flux and maximum charge-transfer current density, as defined by

$$i_{CT} = -nFJ_D = -nFD\left(\frac{dc}{dx}\right)_{x=0} = -nFD \frac{c_{t=0}}{\delta} \quad (7.28)$$

We call this maximum current density at a given time the limiting current (i_L):

$$i_L = -nFD \frac{c_{t=0}}{\delta} \quad (7.29)$$

In any electrochemical system, the current density cannot be higher than this value, because it is the maximum flux that mass transport can provide.

7.5 Ambipolar Ionic Transport at an Interface

Now we should recall that the interfacial quantities such as surface concentration, diffusion layer thickness and limiting current derived in earlier sections of this chapter were all based on Fick's laws under the assumption that *all* ionic transport is carried by ionic diffusion, and that migration under the applied electric field does not exist.

Experimentally, the latter condition can often be met with the use of a stable supporting electrolyte (Section 5.2.1.5). However, in real-life electrolytes, such as those used in advanced batteries, it is neither practical nor possible to use supporting electrolytes. Hence most of the equations presented in the earlier sections no longer hold true because of the presence of ionic migration. The new complications that arise from ionic migration are not only an additional driving force for ionic transport, but also bring the difference between cationic and anionic responses to the externally applied electric field (as reflected by their respective ionic mobility or transport numbers) and their coupling due to Coulombic interactions.

One practical approach to resolve the complications induced by ionic migration in a binary electrolyte was briefly discussed in Section 5.2.6.4, where it was shown that it is possible, under a series of simplifications and assumptions, to describe the ionic transport driven by both diffusion and migration in a form as if it is a neat diffusional process:

$$J_{MT}^c = J_{MT}^a = - \left[\frac{\mu_c D_a - \mu_a D_a}{\mu_c + \mu_a} \right] \frac{\partial}{\partial x} c_0 \quad (5.168)$$

where the term in front of the concentration gradient can be viewed as an imaginary diffusion coefficient called the ambipolar diffusion coefficient (D_{ambp}):

$$D_{ambp} = \frac{\mu_c D_a + \mu_a D_c}{\mu_c + \mu_a} \quad (5.169)$$

Such a quantity represents the combined effects of diffusion and migration as well as the coupled movement of cations and anions, hence providing a convenient tool to investigate the interfacial charge-transfer process. Benefiting from this simplification, we could rewrite both Fick's laws in the forms

$$J = -D_{\text{ambp}} \frac{\partial c}{\partial x} \quad (7.30)$$

and

$$\frac{\partial c}{\partial t} = D_{\text{ambp}} \frac{\partial^2 c}{\partial x^2} \quad (7.31)$$

Application of eqn (7.30) and (7.31) allows us to study the interfacial scenarios that are closer to real-life electrochemical devices, instead of the idealized charge-transfer scenarios that are induced by pure ionic diffusions as described in Figure 7.2.

For example, we can now look at the electrodeposition problem of a metallic ion from a binary electrolyte, such as Cu^0 deposition from an aqueous electrolyte consisting of CuSO_4 in the Daniell cell described in Figure 6.1, or Li^0 deposition from an ether-based polymeric electrolyte. In these scenarios, the electrodeposition of M^{n+} is driven by both diffusional and migrational movement of cations and anions, in the absence of any supporting electrolyte. For Cu^0 deposition, the charge transfer occurs at an interface that can be considered as a classical electrified double layer, because the potential of Cu^0 sits well within the electrochemical stability window of aqueous electrolytes. However, Li^0 deposition presents a new complication because of its reactivity with electrolyte components and the formation of an interphase (see Chapter 8), which constitutes an independent existence between the Li^0 electrode and electrolyte, and insulates electron exchange. Hence the real charge-transfer sites in this case should be underneath the interphase and near the Li^0 metal surface.

Nevertheless, we can temporarily ignore the existence of an interphase and assume that the interface between Li^0 metal and an ether-based polymer electrolyte remains classical. This assumption has its basis in the fact that, among all the non-aqueous electrolytes investigated so far, ether-based polymers demonstrated the least reactivity with Li^0 , hence the presence of an interphase thereon should be minimal.

At the surface of the metallic electrode ($x = 0$), the current (or flux) should arise only from the cationic movement, and the anion would not participate in the charge transfer. Hence

$$i_{\text{CT}} = i^{\text{c}} = nFJ_{\text{MT}}^{\text{c}} \quad (7.32)$$

$$i^{\text{a}} = nFJ_{\text{MT}}^{\text{a}} = 0 \quad (7.33)$$

Therefore, for the two fluxes at a metallic electrode surface described by eqn (5.168), we could have

$$J_{\text{MT}}^{\text{c}} = \mu_{\text{c}} c_{\text{c}} \frac{\partial V}{\partial x} - D_{\text{c}} \frac{\partial}{\partial x} c_{\text{c}} \quad (7.34)$$

$$J_{\text{MT}}^{\text{a}} = -\mu_{\text{a}} c_{\text{a}} \frac{\partial V}{\partial x} - D_{\text{a}} \frac{\partial}{\partial x} c_{\text{a}} = 0 \quad (7.35)$$

Again, we solve for the potential-dependent term $\partial V / \partial x$ from eqn (7.35):

$$\frac{\partial V}{\partial x} = -\frac{D_{\text{a}}}{\mu_{\text{a}} c_{\text{a}}} \frac{\partial}{\partial x} c_{\text{a}} \quad (7.36)$$

Inserting eqn (7.36) into eqn (7.34), and assuming that, under quasi-equilibrium conditions, the electroneutrality ensures that $c_{\text{c}} = c_{\text{a}}$, we will have

$$J_{\text{MT}}^{\text{c}} = -D_{\text{a}} \frac{\mu_{\text{c}} c_{\text{c}}}{\mu_{\text{a}} c_{\text{a}}} \frac{\partial}{\partial x} c_{\text{a}} - D_{\text{c}} \frac{\partial}{\partial x} c_{\text{c}} = -\frac{\mu_{\text{a}} D_{\text{c}} - \mu_{\text{c}} D_{\text{a}}}{\mu_{\text{a}}} \frac{\partial}{\partial x} c_{\text{c}} \quad (7.37)$$

or we can rewrite it as an expression for the cationic concentration gradient at the interface ($x = 0$), so that it could be conveniently used in Fick's first law:

$$\left[\frac{\partial}{\partial x} c_{\text{c}} \right]_{x=0} = -J_{\text{MT}}^{\text{c}} \frac{\mu_{\text{a}}}{\mu_{\text{a}} D_{\text{c}} - \mu_{\text{c}} D_{\text{a}}} \quad (7.38)$$

Remember the definition of ambipolar diffusion coefficient D_{ambp} in eqn (5.172), which can be introduced into eqn (7.38) by dividing both the numerator and denominator by $(\mu_{\text{a}} + \mu_{\text{c}})$ followed by rearrangement:

$$\left[\frac{\partial}{\partial x} c_{\text{c}} \right]_{x=0} = -\frac{J_{\text{MT}}^{\text{c}}}{D_{\text{ambp}} \left(1 + \frac{\mu_{\text{c}}}{\mu_{\text{a}}} \right)} = -\frac{i^{\text{c}}}{nFD_{\text{ambp}} \left(1 + \frac{\mu_{\text{c}}}{\mu_{\text{a}}} \right)} \quad (7.39)$$

Using this new boundary condition for electrodeposition, we could revisit the solution of Fick's second law under galvanostatic conditions as we did in Section 7.2. Without going into details, the new expression for the cationic concentration profile at the interface ($x = 0$), or Sand's equation, becomes

$$c_{x=0} = c_0 - \frac{2i^c}{nF} \frac{\mu_a}{\mu_a + \mu_c} \sqrt{\frac{t}{D_{amb}\pi}} \quad (7.40)$$

or in a simpler form

$$c_{x=0} = c_0 - \frac{2i^c t_a}{nF} \sqrt{\frac{t}{D_{amb}\pi}} \quad (7.41)$$

where t_a is the anion transport number as defined in eqn (5.96) in Section 5.2.1.5.

Interestingly, we see again in the product term $i^c t_a$ that the deposition of a metallic cation is coupled with the movement of an anion.

7.6 Further Caution When Applying Diffusion-Originated Equations

Before we conclude this chapter, a few words must be said about applying these charge-transfer and mass-transport equations to practical electrochemical devices, especially those devices whose electrodes operate beyond the electrochemical stability limits of the electrolytes, such as lithium-ion batteries, lithium-metal batteries and any advanced batteries working at high voltages.

One must remember that an important assumption adopted while deriving these equations is that all mass transports between interface and bulk electrolyte are diffusion driven, without a contribution from migration. While electroanalytical chemists can approximate their investigated systems to such an assumption with the help of supporting electrolytes (see Section 5.2.1.5 and discussions earlier in this chapter), such a "luxury" is often not available for many practical electrochemical reactions, because in those cases a qualifying supporting electrolyte simply does not exist. Lithium-metal and lithium-ion battery electrolytes represent typical examples.

To serve as a qualified supporting electrolyte, all components of such an electrolyte (solvent molecule, salt cation and anion) must

remain inert to any electrochemical reactions while providing high ion conduction, so that the migrational contribution from the species under investigation could be suppressed to a negligible level.

However, the extreme potentials of most reactions related to either Li^+ reduction (-3.04 V vs. SHE), Li^+ intercalation in graphite (-2.94 V vs. SHE) or silicon hosts (-2.60 V vs. SHE) exclude almost any known electrolyte component, because at those potentials no known electrolyte component can withstand the reduction and remain inert.

Hence, when investigating the mass-transport and charge-transfer processes in lithium or lithium-ion batteries, one must keep in mind that the basic assumption that mass transport is dictated by diffusional movements of species does not hold, as the movement of charge carriers such as Li^+ is not only driven by a concentration gradient, but is also affected (assisted or resisted) by the electrostatic forces exerted by the electrode potentials. The combined effect of such interactions is ambipolar diffusion, which provides a remedy to resolve such convoluted cation and anion movements in a binary electrolyte system, as we have briefly shown in Section 7.5. However, such a remedy still over-simplifies the complicated interactions among electrolyte components, especially in the concentrated or super-concentrated electrolytes that are gaining more and more importance in new applications.

What complicates the situation even more is the presence of interphases, which we will briefly discuss in Chapter 8, and then discuss in a more thorough manner in Part B.

Because of the presence of interphases, charge transfer no longer occurs at the location where the electrode and electrolyte meet, and the ion transport across the interphases introduces an additional step in the consecutive mass-transport and charge-transfer steps as shown in Figure 7.1. More importantly, the step at an interphase is often the rate-determining-step.

Nevertheless, the equations that we derived in the previous two chapters are still extensively used to model, calculate, predict and explain behaviors in lithium and lithium-ion batteries, in both the bulk electrode and bulk electrolyte or across the interfaces, with varying degrees of modification to correct the departures induced by the disturbances from both the migration-driven transport and the presence of interphases. Examples include the direct application of Sand's time to the growth of dendritic Li^0 (Chapter 10, Section 10.2.2) and that of the modification of the Butler–Volmer equation to Li^+ intercalation/de-intercalation at a graphitic anode [Section 6.5.9, eqn (6.128)].

However, one must keep in mind that most of these corrections are semiempirical, and are no longer built on the solid mathematical and thermodynamic foundations that the classical ionics and electrodics were.

For these semiempirical efforts applying modifications of classical theories to approach reality, perhaps an interesting analogy can be found in astronomy. Before Copernicus revealed that the Earth orbits around the Sun, the Ptolemaic model based on geocentrism could explain essentially everything we observe in the sky, and predict within a certain accuracy most of the astronomic events such as solar and lunar eclipses. Those explanations and predictions were made computationally equivalent with what the Copernican model of heliocentrism can generate, by sheer mathematical tricks, but they are grounded on completely wrong scientific foundations.

Such approaches work to a certain extent, but eventually we need to develop new and more scientifically correct models, now that we know about the existence of interphases.

References

1. H. J. S. Sand, On the concentration at the electrodes in a solution, with special reference to the liberation of hydrogen by electrolysis of a mixture of copper sulphate and sulphuric acid, *Proc. Phys. Soc., London*, 1899, **17**, 496–534.
2. F. G. Cottrell, Der Reststrom bei galvanischer Polarisation, betrachtet als ein Diffusionsproblem, *Z. Phys. Chem.*, 1903, **42U**(1), 385.
3. W. Nernst, *Studies in chemical thermodynamics*, Nobel Lecture, 12 December 1921, <https://www.nobelprize.org/uploads/2018/06/nernst-lecture.pdf>.

8 When an Electrode Operates Beyond Electrolyte Stability Limits: Interphase

When the potential of an electrode ventures beyond what the electrolyte components can withstand, reactions occur. In some *but not all* cases the reactions are irreversible decompositions of various electrolyte components (solvent molecules, cations, anions, *etc.*), and they may generate solid products, which consequently deposit on the surface of the electrode, forming a physical layer with inhomogeneity in chemical composition, morphology and thickness.

Furthermore, some *but not all* of these solid depositions may constitute such a unique physical barrier on the electrode surface that it insulates electrons from traveling across, hence stopping the undesired irreversible reactions of the electrolytes from going further, while at the same time still allowing certain ions that are essential to the cell reactions to travel across. Such a *selective insulation/conduction property*, *i.e.* *insulating* to electrons so that undesired charge transfer is blocked but still *conductive* to ions so that the mass transfer needed for the desired charge transfer can still proceed, makes this solid deposition layer an *interphase*.^{1,2}

An interphase does not always form – it forms only when a set of conditions are simultaneously met, and we cannot yet predict precisely when and how it can be formed.

As a relatively new electrochemical concept, the interphase was not discovered until 1979, when Peled attempted to explain why alkali and alkaline earth metals can remain stable in certain non-aqueous

and aprotic solvents despite the thermodynamics.³ More thorough studies on interphases, however, would not start until the commercialization of lithium-ion batteries in the 1990s. Most of the fundamental knowledge about interphases was obtained thereafter.^{4,5} However, so far, we still do not fully understand what it is, how it is structured, how ions transport across it and under what conditions it can be constructed.

What we do know is that there is a closely intertwined relation between electrolytes and interphases.

Given its importance in modern electrochemical devices, we will discuss the concept of the interphase from a few different perspectives here, but leave the detailed knowledge about its formation mechanism and chemistries to Chapter 16.

8.1 Interface vs. Interphase

The interface that we have discussed so far in preceding chapters is merely a location where two different phases (*i.e.* electrode and electrolyte) meet. It is electrified and structured as a double layer because both phases experience a sudden discontinuity in their chemical composition, morphology and charge distribution at the junction.

However, such an interface does not have a fixed chemical composition and structure. Its structure is dynamic, and is responsive to changes of the externally applied overpotential for rather short time lengths (usually $<10^{-3}$ s). The double-layer structure may even disappear, if the applied potential falls on the point of zero charge (“pzc”) potential (Section 6.3).

In other words, the interface is transient and reversible in terms of both structure and chemical composition (Figure 8.1a).

Differing from the interface, the interphase is an independent phase between electrode and electrolyte. It has a relatively permanent chemistry, morphology and structure. In some cases, its chemistry and structure could still evolve, but do so in a much longer time period (hours to days or even months). Most importantly, an interphase must conduct ions while insulating electrons. In other words, the charge transfer across an interface as shown in Figure 6.10 cannot occur across an interphase by principle.

Interphases form as the consequence of irreversible reactions, which are induced by overpolarizing an electrode beyond the electrochemical stability window of the electrolyte (Figure 8.1b). Therefore, the electrochemical stability window of an electrolyte is an important

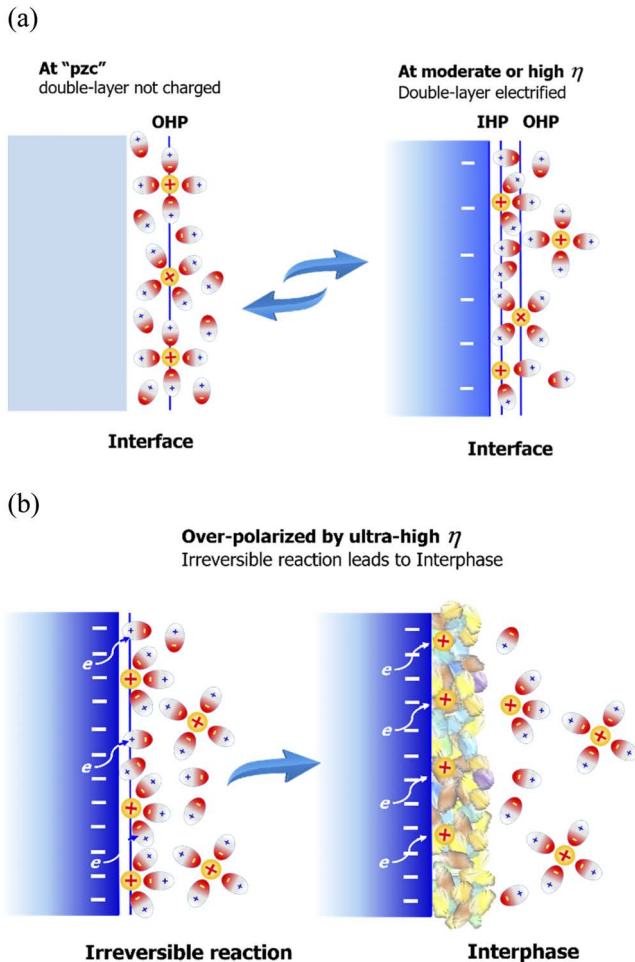


Figure 8.1 Comparison between interface and interphase. (a) At the "pzc" the interface is not electrified, hence the double-layer structure does not exist. As the electrode departs from the "pzc" owing to the applied overpotential, the interface is electrified, and a double-layer structure arises. At this stage, the electrode remains in the electrochemical stability window of the electrolyte, hence the interface is dynamic and reversible. Both the structure and chemical composition of the double layer change with the applied potential. (b) As the electrode potential ventures beyond the electrochemical stability window of the electrolyte, irreversible reactions occur, which may form a solid product deposited on the electrode surface. If such solid deposition has selective conduction, i.e. conductive to ions but insulating to electrons, it constitutes an interphase. Thus, the interphase has a relatively permanent structure and chemical composition.

descriptor that helps us to determine whether an interface or an interphase exists.

However, one must remember that, for an interphase to actually form, going beyond the electrochemical stability window is a necessary but not sufficient condition, because *not all* irreversible reactions lead to solid decomposition products, while even fewer lead to solid products with selective conductivity to ions.

8.2 Electrochemical Stability Window

The electrochemical stability window is an extensively used descriptor that reflects how much electrochemical stress (*i.e.* overpotential) an electrolyte can withstand before irreversible decomposition occurs. In a simple definition, it is the voltage range between its reduction limit and oxidation limit. Cyclic voltammetry, a potentiodynamic technique, is often used to determine these stability limits because it can express such limits in the most visual manner (Figure 8.2), although other electroanalytical techniques (coulometry, titration, potentiostatic or galvanostatic/dynamic, *etc.*) could also be used.

It must be pointed out that the electrochemical stability window is not a mathematically rigorous quantity, because its determination, no matter what technique is used, often depends on some arbitrary standards set by the user. In cyclic voltammetry, such an arbitrary standard is the “threshold current density level”, above which a decomposition reaction should be considered as “significant”, hence the limit should be considered “reached”.

Despite its non-rigorous nature, the electrochemical stability window is a very useful quantity. For example, if an electrolyte is intended for battery applications, its electrochemical stability window would set an upper limit on the battery voltage that it can support, because the *cathode* (positive electrode) material should not operate beyond its *anodic* (oxidation) limit, and the *anode* (negative electrode) material should not operate beyond its *cathodic* (reduction) limit. Such requirements become more stringent if the electrochemical device needs to operate on reversible cell reactions, such as in rechargeable batteries.

As mentioned above, all the interfacial charge-transfer processes discussed in the preceding chapters apply only to interfaces, which should be “clean”, in the absence of any additional phase or barrier caused by solid depositions. In other words, the charge-transfer kinetics described by the Butler–Volmer equation or its derivatives should not be valid in presence of any interphase. For those equations to

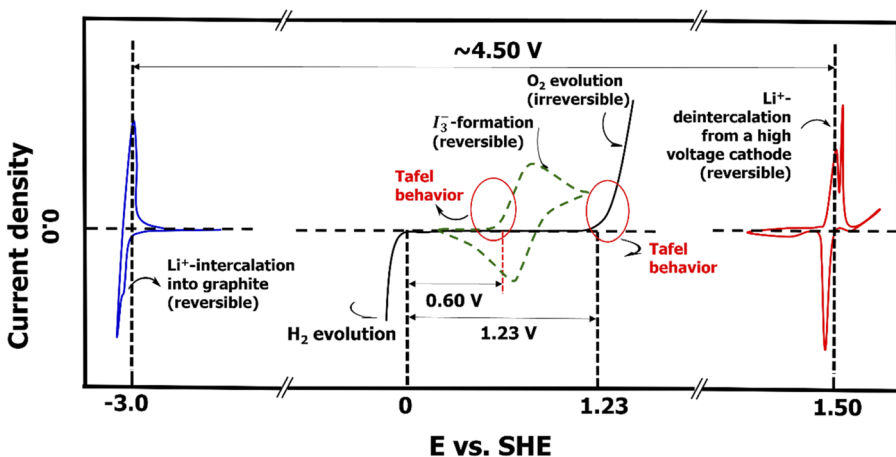


Figure 8.2 The electrochemical stability window is defined by the oxidation and reduction limits of the most reactive components in the electrolyte. An aqueous solution of lithium bis(trifluoromethanesulfonyl)imide (LiTFSI) has an electrochemical stability window of ~ 1.23 V, because TFSI is a stable anion that can be oxidized only at potentials higher than the oxygen evolution reaction (OER), whereas Li^+ is a stable cation that can be reduced to Li^0 only at potentials lower than the hydrogen evolution reaction (HER). Hence the upper and lower limits of the window in this case are defined by the decomposition reactions of the electrolyte solvent, water. However, the electrochemical stability window of aqueous sodium iodide solution is only ~ 0.60 V because iodide is much easier to oxidize than water, thus imposing a lower oxidation limit. Also shown as comparison are the reversible intercalation/de-intercalation processes of lithium ion with a graphite host at the cathodic side, and with a high-voltage cathode material, lithium nickel manganese oxide ($\text{LiNi}_{0.5}\text{Mn}_{1.5}\text{O}_4$), at the anodic side.

remain true, the only reaction occurring there should be the investigated charge-transfer process and its corresponding electrochemical reaction. In most cases, such reactions are reversible upon reversal of the applied overpotential.

To satisfy these requirements for a clean and reversible interface, which has a dynamic double-layer structure and a surface chemistry in the absence of irreversible reactions, a particular condition has to be met: the electrode must stay within the stability limits of the electrolyte components. Otherwise, the interface could be (although not always) replaced by an interphase.

We have learned that an electrolyte consists of solvents and salts. The latter, upon dissolution, dissociate into discrete cations and anions. Each of these components may undergo their own electrochemical

reactions, provided that they see a sufficiently high overpotential applied on the electrode in either a positive (anodic) or negative (cathodic) direction.

In other words, any specific electrolyte component can be electrochemically decomposed, provided that the overpotential applied on the electrode is high enough, in either a negative or positive direction. Hence, in order to maintain a strictly clean interface so that the charge-transfer equations in Chapters 6 and 7 could remain true, the overpotentials on the interface must be applied with caution such that not only do no other undesired electrochemical reactions occur apart from the investigated reaction, but also the investigated reaction itself occurs within the electrochemical stability window of the electrolyte.

The electrochemical stability window for an electrolyte is often defined by the onset of oxidative and reductive decompositions of its most vulnerable components, although such a definition is in fact not rigorous owing to the arbitrary choice of where the onset is. We call these onsets “*oxidation limit*” and “*reduction limit*”, respectively. The oxidative and reductive limits do not necessarily come from the same species.

To illustrate how the electrochemical stability window is correlated with the interface and interphase, we will use two typical electrolytes as examples.

8.2.1 Electrochemical Stability Windows of Aqueous and Non-aqueous Electrolytes

As briefly discussed in Section 5.2.7, aqueous electrolytes based on inorganic or organic salts dissolved in water have an electrochemical stability window of ~ 1.23 V (Figure 5.12), which is essentially set by the oxidation and reduction of the solvent therein, *i.e.* the water molecule.

On the cathodic side, the limit is set by the hydrogen evolution reaction (HER) produced by the reductive decomposition of water, and the corresponding chemical equation depends on the pH value of the aqueous electrolyte:

In *acidic* ($\text{pH} < 7.0$) aqueous electrolytes:



In *alkaline* ($\text{pH} > 7.0$) aqueous electrolytes:



The HER usually needs very little overpotential to occur. In other words, the interface that corresponds to the equilibrium between proton and hydrogen gas is highly non-polarizable. This is the main reason why the standard hydrogen electrode (SHE) serves as a reliable reference electrode.

On the anodic side, the limit is set by the oxygen evolution reaction (OER) produced by oxidative decomposition of water. Again, the exact chemical equation depends on the pH value of the aqueous electrolyte: In *acidic* ($\text{pH} < 7.0$) aqueous electrolytes:



In *alkaline* ($\text{pH} > 7.0$) aqueous electrolytes:



Unlike the HER, the kinetics of the OER are much more sluggish owing to its higher activation energy barrier, and it therefore often requires a high overpotential to proceed. The main reason is that such a process involves the transfer of multiple electrons. Consequently, the interface corresponding to the equilibrium between oxygen gas and water or hydroxide is highly polarizable.

In fact, how to minimize the overpotential for both the OER and its reversible reaction, the oxygen reduction reaction (ORR), has been a central question in fuel cell as well as electrocatalysis research. It often requires expensive noble metals such as platinum as catalysts to reduce the energetic barriers between oxygen gas and water molecules.

Confined by the electrochemical stability of water, if researchers want to study the reduction of a very electropositive metal ion, such as lithium ion (Li^+) or sodium ion (Na^+), or the oxidative decomposition behavior of a very stable anion, such as bis(trifluoromethanesulfonyl)imide (TFSI), they should not choose an aqueous solution of this salt (LiTFSI or NaTFSI), because they will never see the deposition of lithium or sodium metal (Li^0 or Na^0), or the oxidative decomposition of TFSI. Instead, on the cathodic side of the cyclic voltammogram, they will see only the HER, and on the anodic side only the OER, both being the result of the water decomposition (Figure 8.2).

In order to observe either the reduction of these alkali metal ions or the oxidation of a very stable chemical species like TFSI, one must avoid aqueous electrolytes and consider using electrolytes based on non-aqueous and aprotic solvents, so that the limits imposed by

the HER and OER would no longer intervene. For example, certain non-aqueous electrolytes based on sulfolane or alkane nitriles are sufficiently oxidation resistant to allow one to observe the oxidation process of salt anions. On the other hand, the reduction of alkali metal ions occurs at such low potentials that there is essentially no known electrolyte, even those based on non-aqueous and aprotic solvents, that can remain thermodynamically stable to support their reversible deposition. Hence an expanded electrochemical stability window is needed, with the help of interphases. This is especially true for lithium or lithium-based battery chemistries, in which non-aqueous and aprotic solvents have to be used despite the intrinsic issues associated with these solvents, such as high flammability, toxicity to the environment and cost.

However, if the researcher only wants to investigate the oxidative decomposition of iodide (I^-), then an aqueous electrolyte is a convenient choice, because the oxidation of iodide to triiodide (I_3^-) or iodine (I_2) occurs at *ca.* 0.55–0.60 V, well below that of the OER and within the electrochemical stability window of water. Note that such an oxidation reaction of iodide, differing from the oxidative decomposition of water, is reversible, because the product I_3^- or I_2 remains in the electrolyte. They can be readily reduced if the potential on the electrode is reversed, unlike oxygen, which escapes from the system. Such a reversible process in cyclic voltammetry is characterized by a closed shape (Figure 8.2), whose current peaks for anodic (shown as positive by convention) and cathodic (shown as negative by convention) processes are separated by only a narrow gap.

Accordingly, because the anodic limit of the electrolyte is now defined by the oxidation of iodide, not by the oxidation of water, the electrochemical stability window of an aqueous solution of sodium iodide narrows to only 0.60 V (Figure 8.2). Its applicability as an electrolyte becomes further limited.

8.2.2 Expanded Electrochemical Stability Window by an Interphase

As mentioned in the previous section, there is no known electrolyte that can provide a thermodynamically stable voltage range to accommodate the electrochemical reactions occurring at extreme potentials, such as the reduction of alkali metal ions. However, the fact is that reduction or intercalation reactions of these alkali metal ions do occur reversibly in selected non-aqueous electrolytes, upon which a few rechargeable battery chemistries, including the commercially mature lithium-ion battery, are based.

Why is there such a discrepancy? The answer is the interphase.

An interphase has a selective conductivity nature, *i.e.* conductive to ions but insulating to electrons. In other words, it essentially acts as an additional electrolyte. The conduction of ions across it would ensure a continuous electrochemical reaction that involves these essential ions, while the insulation of electron transfer across it prevents electronation or de-electronation, *i.e.* reduction or oxidation, of the electrolyte components.

Hence, once an interphase is formed on an electrode, it in fact expands the effective electrochemical stability window of an electrolyte to frontiers where the thermodynamic stability of these electrolyte components would otherwise not be capable of withstanding. The cyclic voltammograms for the reversible intercalation/de-intercalation processes of lithium ion in a graphite host at the cathodic side (*ca.* -3.0 V vs. SHE), and in a high-voltage cathode material, lithium nickel manganese oxide ($\text{LiNi}_{0.5}\text{Mn}_{1.5}\text{O}_4$), at the anodic side (*ca.* 1.5 V vs. SHE), are shown in Figure 8.2. The expanded 4.5 V electrochemical stability window benefits from the kinetic stability provided by the interphases, which is the fruition of the electrode and electrolyte “working together”.

Thanks to the existence of interphases, diverse lithium-ion intercalation reactions with various hosts could be realized in non-aqueous electrolytes, making it possible for one to construct lithium-ion batteries with a variety of chemistries (Figure 8.3).

An interphase used to be thought to be possible only in non-aqueous electrolytes based on either ether or carbonate esters as solvents,

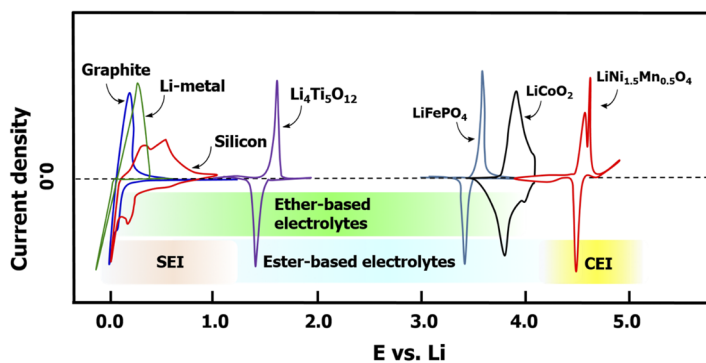


Figure 8.3 Comparison between the operating potentials of a few typical anode and cathode chemistries used in state-of-the-art lithium-ion batteries, and lithium metal itself, and the electrochemical stability windows of the two classes of commonly used electrolytes: ethers and carbonate esters as marked by the shaded bands.

which serve as the chemical source for the formation of the solid products. However, more recent studies by Xu, Wang, Yamada and co-workers since 2015 demonstrated that, by guiding the chemical source of the interphase away from solvent molecules, it is possible to form interphases even in aqueous electrolytes.^{6–8}

In advanced electrochemical systems with interphases, a new electrolyte is always accompanied by a new interphase. In fact, most of the electrolyte design and engineering research is actually the quest for new interphase chemistry.

The expanded electrochemical stability window makes it appear that reversible charge transfer can occur at extreme electrode potentials that would otherwise destroy electrolytes. However, one needs to keep in mind that, in such situations, these charge-transfer equations derived for interfaces no longer remain true, because the interphase as an independent phase of electrolyte nature has altered the foundation for the Butler–Volmer equation.

8.2.3 The Function of Interphases

The interphase has a major uniqueness for high-voltage devices such as lithium-ion batteries. By strict definition, interfaces as discussed in Chapters 6 and 7 do not exist in lithium-based batteries, or in any advanced electrochemical devices whose electrodes operate at potentials beyond the thermodynamic stability limits of the electrolyte components. Therefore, the mathematical treatments of the charge-transfer process as we have discussed in these chapters cannot be applied directly to those advanced devices. A rule of thumb is that, if an electrochemical device operates at an output voltage above 3 V, it is almost certain that some form of interphase will exist therein, on either the positive or negative electrode, or both.

The unique characteristics of the interphase enable certain electrochemical reactions to occur reversibly at potentials far beyond the equilibria required by the thermodynamic properties of the electrode materials or electrolyte materials. In other words, an interphase makes electrochemical reactions *kinetically* reversible at extreme potentials, where these same reactions would otherwise be irreversible if only thermodynamics is considered.

Electrochemical devices benefit from such kinetic stability. They can operate at these extreme potentials and deliver extraordinary performances not expected based on thermodynamic considerations.

The most prominent and successful example is lithium-ion batteries. Their impressively high energy densities and reversibility are realized at extreme potentials of the anode (*ca.* −3.00 V *vs.* SHE) and cathode (up to 1.5 V *vs.* SHE), with the kinetic stability provided by interphases (Figure 8.3).

In most cases, the interphase is produced by the irreversible reactions between the electrode and the electrolyte. Sometimes, with a sufficient understanding of the chemistry and morphology of the interphase, one can even design and apply artificial interphases on electrode surfaces.

Because of the commercial success of lithium-ion batteries, the most commonly investigated interphases are naturally those in such batteries. Those on the anode surface are often called “*solid-electrolyte interphases*” (SEI), while those on cathode surface are called “*cathode-electrolyte interphases*” (CEI). Both were named after the electrolyte nature of the interphases, *i.e.* conductive to ions essential to the electrochemical reactions, but insulating to electrons to prevent irreversible reductive or oxidative decompositions of the electrolytes, as defined in Section 8.1 (Figure 8.1b). SEI should come from reductive decomposition reactions of the electrolyte components, and CEI from oxidative decomposition reactions of electrolytes, although in some cases the “shuttling” of reduced or oxidized species across the cell complicates this clear classification.

In a more general context, a wide electrochemical stability window is by no means just a requirement for lithium-ion batteries. While any battery chemistry would favor a wider electrochemical stability window to maximize the energy that it can store, this requirement actually also comes from many other electrochemical processes, in which certain desired reactions occur only at extreme potentials forbidden by thermodynamics. In those cases, ensuring that the desired reaction will proceed while suppressing parasitic reactions becomes a major function of interphases, examples of which include electroplating, anti-corrosion and electrosynthesis.

Despite the facts that the awareness of interphases started with lithium metal, and a better understanding of them was achieved with lithium-ion batteries, interphases were a common component that existed in many electrochemical devices long before Peled discussed them,³ when they were collectively called “passivation layers”. Therefore, understanding what an interphase is, how it is structured and how it is formed constitutes key knowhow in modern electrochemistry and materials science.

8.3 Correlation Between Electrochemical Stability Window and Interphases

Finally, let us examine the intertwined relation between the electrochemical stability window and interphases.

In Section 6.5.5.3, when discussing the high overpotential scenario for the Butler–Volmer equation, we mentioned that the Tafel behavior actually provides us with an extremely powerful tool to accelerate electrochemical reactions, where an increase in electrode potential could induce an exponential response in the latter:

$$i_c = i_0 e^{-\frac{\beta \eta F}{RT}} \quad (6.97)$$

$$i_a = i_0 e^{\frac{(1-\beta)\eta F}{RT}} \quad (6.98)$$

Compared with conventional chemistry, where species concentration, temperature or pressure are used, applying an overpotential *via* an electric circuit is undoubtedly much more convenient.

However, this powerful tool is not always available – it only works under certain conditions. One such critical condition is a “*clean*” interface that was described in the previous chapter, because the presence of an additional phase, such as solid deposition on the electrode surface, will inevitably alter the foundation upon which the Butler–Volmer equation was derived. In other words, in order for the above Tafel relations to remain true, there should be no interphase present.

To be more precise, the *condition of sufficiency* for the above Tafel relations to remain true, or for any relations derived from the Butler–Volmer equation to remain true, is that the applied overpotential remains within the electrochemical stability window of the electrolytes.

However, it is not a *condition of necessity*, because when the potential of an electrode ventures beyond its electrochemical stability window, the irreversible reactions thus induced do not necessarily produce solid products that will deposit on the electrode surface. In such scenarios of no effective interphase formation, the Tafel relations may still remain true for the current–overpotential relation, although various side reactions could proceed simultaneously.

Based on the above discussions, a plausible correlation between the electrochemical stability window and interphase can be summarized as follows:

1. When an electrode operates within the electrochemical stability window of the electrolyte, interfaces prevail, and relations quantifying the charge-transfer kinetics, such as the Butler–Volmer equation and Tafel relations, remain true.
2. When an electrode operates beyond the electrochemical stability window of the electrolyte, irreversible reactions occur, which may or may not turn an interface into an interphase.

So, how can one determine which scenario is valid?

In the majority of cases, a reaction is made irreversible because of the nature of its products. If at least one of its products leaves the equilibrium or becomes inaccessible to electrons, the reaction cannot be reversed kinetically. This happens when the product is either a gas that escapes, a liquid that phase separates from the bulk electrolyte or a solid that deposits on the electrode surface but is an insulator to electrons. However, an irreversible reaction does not ensure the formation of an interphase.

Among these three scenarios, the first two, *i.e.* the generation of gas or phase-separated liquid products, may still keep an interface “clean”, hence the rate of their production may still follow Tafel behavior. In the last scenario, a new solid phase emerges at the electrode/electrolyte interface which is an independent phase. However, it still is not necessarily an interphase, because it may conduct electrons. Examples include a metal deposition layer, as depicted in Figure 6.10a. Only if this solid deposition insulates electrons would it become an interphase.

Figure 8.1 shows schematically how an interface evolves into an interphase, which requires not only over-polarization of the electrode surface beyond the electrochemical stability window of the electrolyte, but also that the irreversible reaction must produce appropriate solid products of selective conductivity.

More details of electrolytes and the interphases accompanying them will be discussed as the central topic in Chapter 16.

References

1. K. Xu, Non-aqueous liquid electrolytes for lithium-based rechargeable batteries, *Chem. Rev.*, 2004, **104**, 4303–4417.
2. K. Xu, Electrolytes and interphases in Li-ion batteries and beyond, *Chem. Rev.*, 2014, **114**, 11503–11618.
3. E. Peled, The Electrochemical Behavior of Alkali and Alkaline Earth Metals in Non-aqueous Battery Systems—The Solid Electrolyte Interphase Model, *J. Electrochem. Soc.*, 1979, **126**, 2047–2051.

4. R. Fong, U. von Sacken and J. Dahn, Studies of lithium intercalation into carbons using nonaqueous electrochemical cells, *J. Electrochem. Soc.*, 1990, **137**, 2009–2013.
5. D. Aurbach, M. D. Levi, E. Levi and A. Schechter, Failure and stabilization mechanisms of graphite electrodes, *J. Phys. Chem. B*, 1997, 2195–2206.
6. L. Suo, O. Borodin, T. Gao, M. Olguin, J. Ho, X. Fan, C. Luo, C. Wang and K. Xu, Water-in-Salt' Electrolyte Enables High Voltage Aqueous Li-ion Battery Chemistries, *Science*, 2015, **350**, 938–943.
7. Y. Yamada, K. Usui, K. Sodeyama, S. Ko, Y. Tateyama and A. Yamada, Hydrate-melt electrolytes for high-energy-density aqueous batteries, *Nat. Energy*, 2016, **1**, 16129.
8. K. Xu and C. Wang, Batteries: widening voltage windows, *Nat. Energy*, 2016, **1**, 1–2.

PART B

Applications: Electrolytes in Devices

In this Part, we introduce practical electrochemical devices and their characteristics, along with the uniqueness and commonality of the electrolytes used therein. In the days of Volta and Faraday, electrochemical devices were merely arcane contraptions for a handful of enthusiasts, often locked up in cryptic laboratories and only occasionally demonstrated as novelties to the curious public.

Nowadays, electrochemical devices are in everyone's hands, the most ubiquitous example of which is the lithium-ion battery. This invention of the 1990s now essentially rules how we lead our daily lives by powering our smartphones and electric vehicles, in addition to other lesser applications such as diverse electronic gadgets and grids. According to statistics from the Avicenne Consulting Group (http://www.avicenne.com/reports_energy.php), in 2019 the world produced *ca.* 200 GWh lithium-ion batteries of various formats and chemistries, in which *ca.* 230 000 tonnes of liquid non-aqueous electrolytes serve as the "blood" in those devices. These numbers are still growing at an approximate rate of 20% per year, despite the Covid pandemic in 2020–2022. On the other hand, fuel cells and electrochemical double-layer capacitors, although dwarfed by the gigantic market of batteries, still occupy niche applications in various power systems, from tiny electronic gadgets to automobiles and to power grids. It is not an exaggeration to state that the future of our civilization depends on how efficiently we can produce and store energy electrochemically,

which dictates the decarbonization of human economy activity on this fragile planet.

Beyond applications related to energy, electrochemical sensors are also becoming pervasive in our lives, used as high-precision detectors to monitor the blood glucose level of diabetic patients, to guard us against a multitude of toxic gases in natural environments and buildings and to identify drunken drivers through the electrochemical oxidation of ethanol. Electrocardiography and electroencephalography represent the zenith of electrochemical devices in medical applications.

Electrochemical processes also offer elegant surface treatments for various materials *via* electroplating (deposition of metals) or electropolishing (removal of metals), which constitute a toolkit of vital importance for microfabrications in the semiconductor and electronics industry. Most importantly, almost all metal structures in architecture require electrochemical principles to suppress corrosion, especially those on oil-drilling platforms standing in the ocean, where high salt and high humidity (hence aqueous electrolytes) make the electrochemical oxidation of metal materials especially facile.

Finally, we rely on the electrochemical synthesis of many basic chemical materials in astronomical quantities that feed the global industry, which include alkali metal hydroxides, halogens, oxygen, hydrogen peroxide, aluminum, titanium, *etc.*, and most of which would eventually make it into the products that we use every day. In fact, certain chemicals, such as alkali metals (lithium, sodium, potassium, *etc.*) have to be produced *via* electrolysis, because chemically there are no alternative approaches to make them: these metals are such electropositive elements that there are hardly any other chemicals that can reduce them from ionic to elemental form, as reflected by their extremely negative potentials.

Looking into the future, numerous technologies still under development evolve around electrochemistry as the nexus: new battery chemistries and fuel cells, solar-to-electricity conversion in diverse photo-electrochemical junctions, thermal, bio- and acoustic energy-harvesting devices, water desalination and purification, *etc.*

Electrochemistry is and will continue to be an indispensable part of our lives, and so are the electrolytes and interphases as indispensable components in these electrochemical devices.

9 Electrochemical Devices

An electrochemical device performs chemical reactions and manipulates how the reactions proceed by controlling the direction and quantity of electron flows. For this purpose, all reactions employed by an electrochemical device involve the electronation (reduction) or de-electronation (oxidation) of species, *aka* redox reactions. Other chemical reactions that do not involve electron exchange between reactants, such as acid–base neutralization, precipitation caused by simple ion exchange and complexation between ion and ligands, are usually very difficult, if not completely impossible, to conduct in an electrochemical manner.

In order to conduct a redox reaction, the electrochemical device must separate such a reaction into two half-reactions, so that the reactants do not interact directly with each other. Instead, all electron exchanges between the reactants must occur at the electrode/electrolyte interface (Figure 6.1), followed by directional flows of electrons through an external circuit. The role of the electrolyte and interfaces/interphases there is (1) to ensure the physical separation of the reactants so that electrons do not “leak” directly between the reactants and (2) to maintain the mass transport so that the species needed can be sufficiently supplied or the species produced can be immediately removed (Figure 6.10).

Depending on the spontaneity of the reaction, the device either generates electric energy, which drives an external load, or requires a feed of electric energy, which is supplied by an external source.

The contemporary nomenclature for the electrodes in an electrochemical device adopted the names suggested by Faraday in his famous treatise of 1834 (Chapter 1), with the more accurate definition that the *cathode* is where reduction reactions occur and the *anode* is where oxidation reactions occur.

In a not very rigorous classification, there are generally four types of electrochemical devices according to their designed purposes:

1. *An electrochemical device that produces materials by consuming electric energy.*

Examples of this type include *electrolysis* or *electrosynthetic* devices that produce chemicals that are otherwise impossible or too expensive to produce, such as lithium, sodium and aluminum, or *electroplating* devices that form metallic depositions in unique morphologies so that exquisite decorative or functional properties can be displayed. In the electronics industry, copper, gold and other rare metals electroplated into sophisticated 2D and 3D geometric shapes to construct circuits of micrometer-level resolution on printed circuit boards represent the apex of such technology.

2. *An electrochemical device that produces electric energy by consuming materials.*

Examples of this type include fuel cells and primary (non-rechargeable) batteries. The traditional distinction between a fuel cell and a primary battery used to be whether the electrochemical device adopts an open configuration. A fuel cell is open, so that the reactants can be continuously fed into the system, and the electric energy can be produced as long as the “fuel tank” maintains the supply; a battery is closed, so that the materials cannot be replenished, making the energy contained in a battery limited. However, this demarcation becomes obscure in some “batteries” that deviate from the traditional closed configuration, examples of which include some *metal-air batteries*, in which the cathode material, oxygen, comes from the air, while the metal anode such as zinc can be replaced, and “flow batteries” that are equipped with external and removable tanks that contain the reactants.

The colloquial name for this class of electrochemical devices is “*power generation devices*”.

3. *An electrochemical device that is reversible (rechargeable), so that in one direction of the reaction it produces electric energy by consuming materials, while in the other direction it produces materials by consuming electric energy.*

Rechargeable batteries and *capacitors* belong to this group, although by strict definition the *electrochemical double-layer*

capacitor does not consume any materials, as no chemical reaction is involved.

Since the reaction/process therein can be reversed, such devices actually cause a “nomenclature crisis” in the above-mentioned convention that the cathode is where reduction reactions occur and the anode is where oxidation reactions occur. A given electrode in such rechargeable devices could be the cathode during discharge, but it will inevitably become the anode during charge, and *vice versa* for its counter-electrode.

To avoid such possible nightmarish confusion, the rechargeable battery community adopted a nomenclature that is decoupled from the nature of the reactions on the electrode: the electrode that always operates at *higher* potential (*i.e. positive* electrode) is called the cathode, and the electrode that always operates at *lower* potential (*i.e. negative* electrode) is called the anode. The consequence of this alternative nomenclature is that the Faraday convention only applies during the discharge of a rechargeable battery, *i.e.* when it is doing work. When the battery is being charged, the Faraday convention does not apply because the device is considered to be “on vacation”. Although the terms “*positive electrode*” and “*negative electrode*” would cause less confusion, they are rarely used in the scientific literature.

The colloquial name for this class of electrochemical devices is “*energy storage devices*”. They differ from power generation devices in that they can store energy and release it on demand, similarly to a container of electricity, whereas the latter behave more similarly to a thermal engine that continuously converts materials into energy.

4. An electrochemical device that detects the electric current generated from specific reactions with the purpose of monitoring certain substances, phenomena or processes.

Electrochemical sensors belong to this group. Differing from all the devices mentioned above, electrochemical sensors require high sensitivity, real-time response and a precise relation between species concentration and current/voltage, rather than high conversion efficiency, high capacity for energy or high reaction rates that are essential to the electrochemical energy and power devices.

In this book, we will only discuss the electrolytes, interfaces and interphases in electrochemical energy and power devices, with the focus placed on rechargeable batteries.

9.1 How Does an Electrochemical Energy Device Work?

Electrochemical energy and power devices harness the energy changes *via* charge separation and charge recombination.¹ Such separation and recombination processes could be realized through a pure physical process, such as in electrochemical double-layer capacitors, where no chemical reaction is invoked and no new chemical species is produced, or through a chemical process, such as in batteries, where the redox reactions are forced to proceed in an electrochemical manner, and whose free energy change is forced to be expressed in the form of electron flow when charges are separated or recombined.

A good example of the latter was shown in Figure 6.1, which depicts how a conventional redox chemistry between zinc metal and cupric ion (Cu^{2+}) is turned into an electrochemistry that forms a battery, while correspondingly the energy released from this spontaneous reaction is turned into electric work. In the process of turning chemistry into electrochemistry, the role of the electrolyte is critical, because it is the presence of an electrolyte that creates the presence of interfaces with the electrodes, which split the redox reaction into two separate half-reactions, and serve as the only “legitimate” locations for electron exchange.

Hence electrolytes and interfaces enforce a detour of electrons into orientational flow through an external circuit.

We discussed in Chapter 8 how the interface becomes an interphase when the electrodes in an advanced electrochemical device must operate at extreme potentials. The interphase is usually an electronic insulator. In this unique case, the electron exchange (or charge transfer) can no longer occur at the interphase separating the electrode from the electrolyte. Instead, the actual electron exchange should occur at the junction region where the ions meet with the electrode bulk, *i.e.* the first encounter of the ions with the electrode material after the ions migrate across the interphase. This difference was outlined in Figure 8.1. However, despite this difference, the important fact remains that, no matter whether there exists an interface or interphase in an electrochemical device, the electron exchange must not occur within the electrolyte, as it does in the chemical redox reaction depicted in Figure 6.1a, so that an orderly flow of electrons could be ensured.

On a very fundamental level, the energy change involved in the charge-separation and charge-recombination processes is basically related to the electric work that a charged particle does when traveling across a certain potential difference.

Let us suppose that a single particle (ion or electron) carrying an elemental charge travels across a potential difference ΔV , then the corresponding electric work (W_e) is

$$W_e = e\Delta V \quad (9.1)$$

Accordingly, if 1 mol of charged particles, each of which carries a valence n , make the same travel across ΔV , then the work involved becomes

$$W_e = q\Delta V = nF\Delta V \quad (9.2)$$

where F is the Faraday constant ($96\,485\text{ C mol}^{-1}$).

In eqn (9.1) there is actually a hidden assumption that the potential difference (ΔV) remains constant despite the movement of the charge. In reality, ΔV will inevitably change if the charge separation is physical as in an electrochemical double-layer capacitor, unless the charge involved is infinitesimally small. However, in a battery or fuel cell, where the charge separation is mainly determined by the difference between the *eigenpotentials* of the anode ($\overline{\mu_A}$) and cathode ($\overline{\mu_C}$), *i.e.* the difference between the energy levels of the electrons in the anode and cathode materials, respectively, there is a unique case that ΔV could remain nearly constant despite the large amount of charge traveling, which we will discuss in Section 9.1.3.3.

If such electric work is done at constant temperature and pressure, then according to thermodynamic laws, this electric work reflects the change in Gibbs free energy (ΔG) in the electrochemical system:

$$\Delta G = -W_e = -nF\Delta V \quad (6.5)$$

In fact, we encountered this equation back in Section 6.1.

As we briefly discussed in Section 6.1, in electrochemistry the potential difference between two electrodes in a device is named the *electromotive force (emf)* when these electrodes are at equilibrium with the electrolytes when the net current is zero. The emf is often denoted by \mathcal{E} .

Hence eqn (9.2) would take a more famous form:

$$\Delta G = -nF\mathcal{E} \quad (9.3)$$

This relation in fact translates the energy change in chemistry into electrochemistry. It is the mathematical expression of Figure 6.1b.

Differing from the units recommended in the *Système International* (SI), the energy in electrochemistry is often expressed in units of *watt-hours* (W h) instead of *joules* (J): 1 W h is defined as the electric work done by 3.73296×10^{-2} mol of charges (ions or electrons) traveling across a potential difference of 1.0 V, which is equivalent to 3600 J. When evaluating the capability of an electrochemical device to produce or store energy, *energy densities* by weight or volume are often used, denoted *gravimetric* (W h kg⁻¹) or *volumetric* energy densities (W h L⁻¹), respectively.

9.1.1 Fuel Cells

It was mentioned earlier that a fuel cell is often called a “power conversion device” because it acts more like a combination of thermal engine and generator, with its open configuration designed to consume materials to produce electric energy. However, there is one fundamental difference between a fuel cell and any thermal engine, be it internal combustion, steam or Sterling, *etc.*, namely that a fuel cell is not subject to the *Carnot limit* as those thermal engines are, because the fuel fed into a fuel cell experiences no direct combustion but instead direct electrochemical reactions. For this reason, the power conversion efficiency of a fuel cell could theoretically be 100%. In reality, however, numerous factors such as kinetics, parasitic reactions, *etc.*, prevent an actual fuel cell from reaching this ideal efficiency. The highest conversion efficiencies of fuel cells that operate on hydrogen gas normally range between 60 and 70%, which is already an amazing value compared with the 20–30% efficiencies known for most thermal engines.

All fuel cells use a “free” cathode material from atmospheric air. *i.e.* oxygen gas, whereas the fuel, which is actually the active anode material, varies from hydrogen gas to various alcohols, aldehydes and even hydrocarbon compounds.² Each of these cathode and anode materials is a well-defined chemical with its own characteristic *eigenpotential*, and the difference between the eigenpotentials of the cathode and anode materials sets the upper limit of the cell emf. The actual voltage of the cell is determined by more complicated factors, as the energy levels of the electrons in each electrode material are unique, which accordingly confers upon the electrode a unique eigenpotential when the electrode establishes chemical equilibrium with the electrolytes, as described by the Nernst equation. Additionally, the activation

energy barrier to the charge transfer across the interfaces further affects the above equilibrium.

The simplest fuel cell chemistry is based on hydrogen gas, and the cell reaction therein is just the reverse of the electrochemical decomposition reaction of water as shown in eqn (8.1) and (8.3) in Section 8.2.1, *i.e.* the electrochemical recombination of hydrogen and oxygen into water in their respective half-reactions.

In order for these gaseous reactants to be fully utilized, both electrodes not only require pre-engineered channels to guide the gas flow, but also must be constructed from porous materials, so that oxygen and hydrogen gases can remain fully in contact with the electrolyte (liquid or polymer saturated with water) and the electrode (solid) in a triphasic manner. Catalysts also have to be used at the electrodes with the purpose of accelerating the reactions, which are especially necessary for the sluggish four-electron reduction process of oxygen gas. The most effective catalysts are platinum and other rare metals neighboring platinum in the Periodic Table. The expense of these catalysts constitutes a major barrier in the extensive commercialization of room-temperature fuel cells.

Most hydrogen fuel cells operate under acidic conditions, therefore the corresponding half-reactions on each electrode should proceed as follows:

At the anode side:



At the cathode side:



Note that since the reactants in both the cathode and anode half-reactions are in a gaseous state, the physical “anode” and “cathode” in a fuel cell only serve as charge-transfer media. They must provide channels to allow access by these gaseous reactants, and must also conduct electrons to or from the reactants. However, they do not participate in the electrochemical reactions.

The electrolyte in a fuel cell must satisfy the needs of charge transfer and mass transfer from these reactions. The most popular electrolyte used in hydrogen fuel cells is based on the polymeric material Nafion, which was invented by du Pont in the 1960s. Nafion is a highly fluorinated polyolefin material with sulfonic anion groups covalently

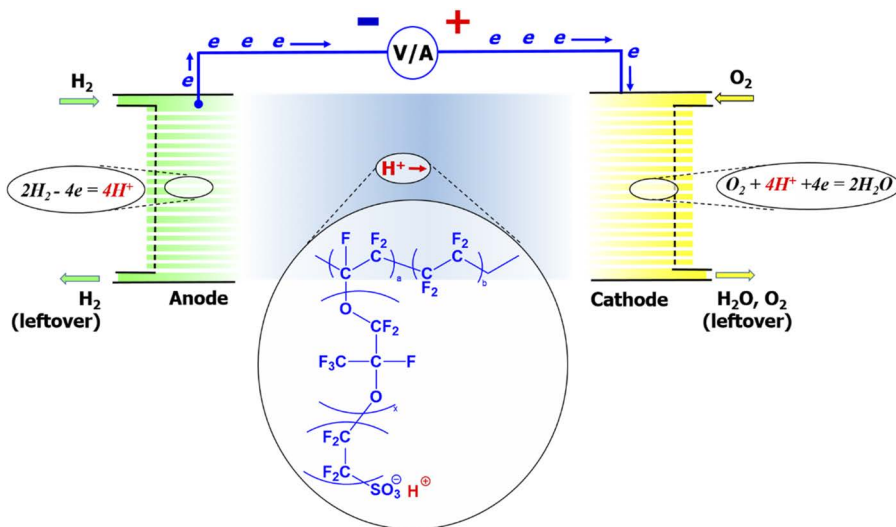


Figure 9.1 Schematic illustration of a hydrogen fuel cell and its polymeric electrolyte membrane based on Nafion. The single-ion electrolyte is actually aqueous in nature, which conducts hydrated protons (H_3O^+) via hopping between neighboring sulfonate sites. Since both electrodes are made porous to allow gaseous access, the real electrode/electrolyte interfaces are within the interior of both electrodes, instead of on the planar geometric surfaces of these electrodes.

attached to the macromolecular skeleton (Figure 9.1), so that protons (or any cation) could transport through the polymeric electrolyte membrane, whereas anions are immobile due to their covalent bond with the polymeric chain.

The nature of the Nafion-based electrolyte membrane used in a fuel cell remains aqueous, because the actual conducting species therein are hydrated protons (H_3O^+), hence the Nafion polymer electrolyte membrane could only work under certain humidity conditions to ensure sufficient proton conductivity. In fact, one could view it as an aqueous solution of one special sulfonic acid whose anion (the sulfonate group) is too large to move, therefore the only ion conductivity available from such an electrolyte is from the cation, *i.e.* proton. Such an electrolyte is known as a “*single-ion electrolyte*” or “*polyelectrolyte*”.

Single-ion electrolytes can be made from polymer materials, in which one of the ions is covalently immobilized to the polymer skeleton as Nafion. They can also be obtained from inorganic materials, in which the immobile lattice consists of one ion, either cation or anion, while the other ions are free to hop between neighboring sites, such as the inorganic solid electrolytes (Figure 2.1).

In Section 8.2.1 we mentioned that the electrochemical stability window of most aqueous electrolytes is only *ca.* 1.23 V, whose anodic and cathodic limits are imposed by the oxidative and reductive decomposition onsets of water (Figure 8.2). Correspondingly, an electrochemical device that is intended to produce energy based on the recombination reaction of hydrogen and oxygen cannot operate at a cell voltage higher than 1.23 V. In fact, owing to kinetic and other losses, most fuel cells offer an open-circuit voltage in the vicinity of 1.0 V. Since such a voltage resides comfortably within the electrochemical stability window of aqueous electrolytes, including Nafion, no interphase is formed in fuel cells. In other words, most of the kinetics-based equations such as the Butler–Volmer equation still hold true at the electrolyte/electrode interfaces in fuel cells.

Just as the water decomposition could occur under either acidic or alkaline conditions [eqn (8.2) and (8.4) in Section 8.2.1], the electrochemical recombination reaction of hydrogen and oxygen could also proceed in alkaline electrolytes:

At the anode side:



At the cathode side:



Obviously, the cell reaction now requires the mass transport of hydroxide anions (OH^-) across the cell, hence Nafion can no longer serve as the electrolyte. Alkaline electrolytes have to be used in this case, the most popular form of which consists of ammonium or other cations covalently attached to various polymeric skeletons, so that its corresponding anion (OH^-) could be mobile.

Such alkaline electrolytes are still aqueous in nature, and for the same reason mentioned above no interphase is formed where either electrode meets the electrolytes.

The eigenpotentials of both cathode (oxygen) and anode (hydrogen) materials depend on the pH of the electrolyte. However, their dependences on pH are identical, as represented by the two parallel lines in the Pourbaix diagram (Figure 5.12), which could be easily derived from eqn 8.1, 8.2, 8.3 and 8.4 as follows:

For hydrogen:

$$E_{\text{H}}^\circ = 0.00 - 0.0591 \times \text{pH} \quad (9.8)$$

For oxygen:

$$E_O^\circ = 1.228 - 0.0591 \times \text{pH} \quad (9.9)$$

Therefore, the cell voltage for both acidic and alkaline fuel cells is a constant of 1.228 V at equilibrium and under standard conditions (*i.e.* 25 °C, 1.0 atm partial pressure for all gaseous species and an activity of 1.0 for all reactants in solution). In reality, however, various kinetic factors will reduce this cell voltage to ~1.0 V.

Compared with acidic fuel cells, alkaline electrolytes encounter one challenge that its acidic cousin (Nafion) does not, namely carbon dioxide (CO₂) poisoning. The fuel cell is often an open system that uses oxygen from the ambient air as the cathode material, but ambient air contains not just oxygen. In addition to dust and other impurities that could clog the air channels in the cathode or deactivate the catalysts, CO₂ presents the most severe challenge to alkaline electrolytes because it reacts readily with hydroxide and forms often insoluble carbonate salts.

Finally, one might wonder why polymeric single-ion electrolytes are used so extensively in fuel cells, as represented by Nafion for proton-exchange membrane fuel cells operating under acidic conditions, but are rather rare elsewhere in other electrochemical devices such as capacitors and batteries.

In fact, all electrochemical devices would desire a single-ion electrolyte if it were available. Such an electrolyte would be ideal because it allows only the ion essential to the cell reaction to move, while blocking the other ions not directly involved in the cell reaction, such as the counterions of the essential ions. The resultant advantage is a transport number of unity (*e.g.* $t_{\text{H}^+} = 1.0$), in the absence of any concentration polarization caused by the migrational movement of the counterions.

However, the problem is that single-ion electrolytes are not available for all cell reactions. Taking Nafion as an example, if one replaces the protons in the polymer matrix with Li⁺ ions, the ion conductivity would experience a precipitous drop of *10 000-fold*, *i.e.* from the typical range of 0.1–0.2 S cm⁻¹ for protons at room temperature to 10⁻⁵ S cm⁻¹ at room temperature or 10⁻⁴ S cm⁻¹ at 70 °C for Li⁺ ions! Although the transport number of the Li⁺ ion now becomes 1.0, such a low ion conductivity cannot support cell reactions at meaningful rates.

What is the reason behind such a drastic drop? The answer was in fact already given in Section 5.2.8 (Figure 5.14).

Proton transport *via* the Grotthus mechanism (Section 5.2.8, Figure 5.14) was made possible by the preferred orientation of water molecules *via* the hydrogen network and the plausible probability of achieving quantum tunneling benefiting from the fact that proton is a simple nucleus. Therefore, its ultra-fast transport in aqueous electrolytes can afford a certain loss caused by the immobilization of its counterion to a polymeric skeleton. In other words, the application of polymeric single-ion electrolytes in fuel cells is a direct fruition from the unique proton transport mechanism.

However, for Li^+ , or any ion other than the proton, none of the above luxuries exists. Hence we have to employ electrolytes, in which both the cation (Li^+) and anion are mobile, for practical ion conductivity. Such a compromise exists in most electrochemical devices, where the need for a practical mass-transport rate often outweighs the consideration of transport number.

In addition to the consideration of ion conductivity and transport number, a more important factor for the use of polyelectrolytes in fuel cells is that any electrochemical device needs a physical barrier between its cathode and anode, so that the reactants do not have direct contact with each other and do not engage in a direct chemical reaction. In batteries and capacitors, such physical barriers are often provided by thin-film porous polymeric materials such as non-woven polyolefins or polyimides. However, the gaseous reactants in fuel cells, *i.e.* oxygen and hydrogen, could easily transport across such inert polymer materials. A single-ion conductor such as Nafion successfully resolves this challenge arising from the unique state of gases, as the barrier now only allows cations such as the proton to pass *via* an ion-exchange mechanism. This would minimize the reactant crossover.

9.1.2 Electrochemical Double-layer Capacitors

In Chapter 6, we showed that an interface between an electrode and an electrolyte is usually electrified into a double-layer structure, because of the charge accumulation or depletion caused by the sudden discontinuity of both phases (Figure 6.2).³

Assuming that the two sides of the interface carry a charge of $+q$ and $-q$, the electrostatic field (X) across this interface would be given by Coulomb's law:

$$X = \frac{q}{A\epsilon} \quad (9.10)$$

where A and ϵ are the area of the interface and the dielectric constant of the medium that sits between the two layers of opposite charges, respectively.

According to the Bockris–Devanathan–Müllen model (Figure 6.8), this dielectric medium should be the water or solvent molecules specifically adsorbed at the IHP. However, since these solvent molecules are “dielectrically saturated”, their dielectric constants are substantially lower than those of their counterparts in the bulk. For example, the dielectric constant of water should be ~6, instead of 78 (Section 3.4).

The potential drop (dV) across this interface would be

$$dV = Xd = \frac{qd}{A\epsilon} \quad (9.11)$$

where d is the thickness of the interface, which should be defined as the distance from the electrode surface to the OHP. In most situations, this thickness is estimated to be 0.2–0.5 nm.

The capacitance across such an interface is defined as

$$C^i = \frac{q}{\Delta V} = \frac{A\epsilon}{d} \quad (9.12)$$

Note that eqn (9.12) is merely an isomorphic form of eqn (6.31) in Section 6.4.1 if one lumps together the dielectric terms.

Now one must remember that eqn (9.12) only describes the capacitance for an individual electrode/electrolyte interface. A real electrochemical device consists of two electrodes, and each has an interface like this. The capacitance of the device (C_{Total}) should therefore be

$$\frac{1}{C_{\text{Total}}} = \frac{1}{C_1^i} + \frac{1}{C_2^i} \quad (9.13)$$

Since such an electrified double layer is at an equilibrium, if one constructs an electrochemical cell using two identical electrodes the resultant symmetric capacitor does not produce any net voltage (Figure 9.2a), because the potential drops across the interfaces would cancel each other out:

$$\frac{1}{C_{\text{Total}}} = \frac{1}{C_1^i} + \frac{1}{C_2^i} = \frac{q}{\Delta V_1^i} + \frac{q}{\Delta V_2^i} = 0 \quad (9.14)$$

where $\Delta V_1^i = -\Delta V_2^i$.

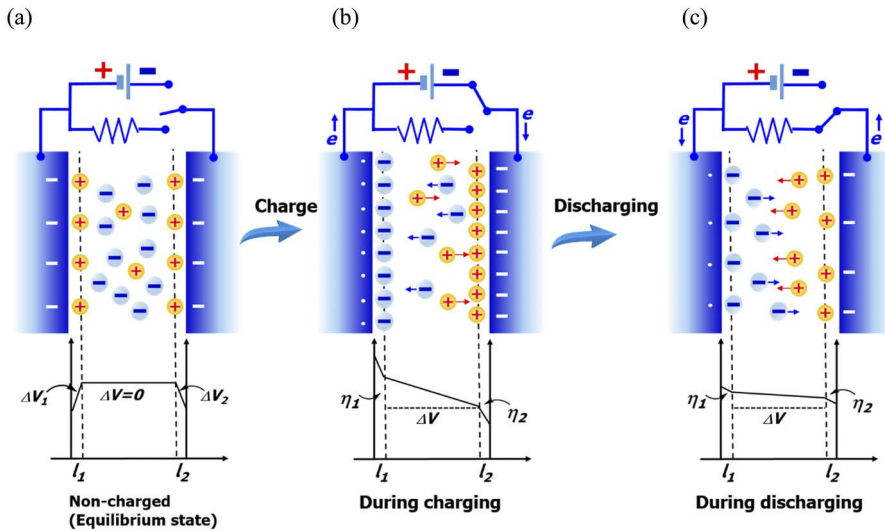


Figure 9.2 An electrochemical double-layer capacitor consisting of two identical electrodes (a) at a *non-charged state*, where the two double layers are electrified but produce no voltage difference between the electrodes; (b) during *charge*, an external power source injects an electron into one electrode (negative electrode) and removes an electron from the other (positive electrode, where the electron deficiency is represented by dots) with a corresponding response from the electrolyte side that generates ionic assemblies; and (c) during *discharge*, the electronic and ionic assemblies dissipate, with the charges separated in the electrolyte resuming a Debye-Hückel distribution, and the electrons flowing from the negative electrode towards the positive electrode, driving the load.

9.1.2.1 How They Work

To make a useful device, one has to apply an external electric field, so that these interfaces are further charged, *i.e.* injecting electrons into one electrode while removing electrons from another electrode using an external power source (Figure 9.2b). Induced by such an overpotential η , excessive charges, Q , are hence accumulated at such interfaces:

$$C_1^i = \frac{Q}{\eta_1} = \frac{A\varepsilon_1}{d_1} \quad (9.15)$$

$$C_2^i = \frac{Q}{\eta_2} = \frac{A\varepsilon_2}{d_2} \quad (9.16)$$

Note that, in addition to the surface area, the charges involved at both interfaces are also identical but of opposite sign.

In this way, we have separated excess charges by applying a voltage.

We can make further simplifications by assuming that the dielectric constant, potential drop and OHP thickness are also identical for these interfaces if the same electrode material is used to construct a symmetrical cell:

$$\varepsilon_1 = \varepsilon_2 = \varepsilon_i \quad (9.17)$$

$$\eta_1 = \eta_2 = \eta_i \quad (9.18)$$

$$d_1 = d_2 = d_i \quad (9.19)$$

In reality, such approximations can only be approached but can never be strictly true, because the assembly behaviors of cations and anions at electrode surfaces cannot be exactly the same. This fundamental difference between cation and anion is responsible for the asymmetry of the electrocapillary curves (Figure 6.6).

Can we now apply eqn (9.14) to derive the capacitance for the entire device?

Not quite.

One must remember that, upon application of an external electric field, charges (cations and anions) in the electrolyte also experience excessive polarization, hence a potential drop (ΔV) also now exists across the bulk electrolyte. This charge separation inside the bulk electrolyte actually creates an additional capacitance C_{Bulk} that is of the same area and charge, but over a different potential difference and across a different length:

$$C_{\text{Bulk}} = \frac{Q}{\Delta V} = \frac{A\varepsilon_{\text{Bulk}}}{L} \quad (9.20)$$

where $\varepsilon_{\text{Bulk}}$ and L are the dielectric constant of the bulk electrolyte and the cell thickness, respectively.

The total capacitance of the cell now can be expressed as

$$\begin{aligned} \frac{1}{C_{\text{Total}}} &= \frac{1}{C_1^i} + \frac{1}{C_2^i} + \frac{1}{C_{\text{Bulk}}} = \frac{\eta_1}{Q} + \frac{\eta_2}{Q} + \frac{\Delta V}{Q} \\ &= \frac{d_1}{A\varepsilon_1} + \frac{d_2}{A\varepsilon_2} + \frac{L}{A\varepsilon_{\text{Bulk}}} \end{aligned} \quad (9.21)$$

Applying eqn (9.17)–(9.19), and after algebraic operation and rearrangement, we obtain

$$C_{\text{Total}} = \frac{A\epsilon_i\epsilon_{\text{Bulk}}}{2d_i\epsilon_{\text{Bulk}} + L\epsilon_i} \quad (9.22)$$

Since the interface thickness ($l_i < 1.0$ nm) is negligible compared with the cell thickness ($L \gg 1000$ nm), and ϵ_i and ϵ_{Bulk} are fairly close on the order of magnitude scale (6 vs. 78 for water, for example), the above expression for the capacitance of a symmetrical electrochemical device further simplifies to

$$C_{\text{Total}} \approx \frac{A\epsilon_i\epsilon_{\text{Bulk}}}{L\epsilon_i} = \frac{A\epsilon_{\text{Bulk}}}{L} = \frac{Q}{\Delta V} \quad (9.23)$$

This approximation is very beneficial, as the interfacial quantities that are usually difficult to determine are eliminated. Thus, the capacitance of a device is equivalent to a simple capacitor with charge Q separated over a voltage difference ΔV on the scale of the cell thickness. Nevertheless, we should always keep in mind that the actual charge separation occurs on a pair of electrified interfaces, each consisting of a layer of excessive charge with an *electronic nature on the electrode side* and a corresponding layer of excessive charge with an *ionic nature on the electrolyte side* (Figure 9.2b).

We can be more specific regarding the charge separation at each interface. At the negative electrode, the interface consists of a layer of excess electrons at the electrode side because of the injected electrons, and a layer of cations at the electrolyte side; while at the positive electrode the interface consists of a layer of electron deficiency (or holes) at the electrode side because of the removed electrons, and a layer of anions at the electrolyte side.

As discussed in Section 6.4.4, the ions that assemble on the interface should be solvated. In other words, the ions should be located at the OHP (Figure 6.8), and a layer of “dielectrically saturated” solvent molecules should construct an IHP, unless the ions can be specifically adsorbed on the electrode surface.

At extremely high salt concentrations, both the IHP and OHP could disappear, while discrete and fully solvated ions are replaced by a continuous liquid structure, as represented by super-concentrated electrolytes as well as ionic liquids.

Upon removal of the externally applied electric field, if one connects these charged electrodes with a load, both interfaces tend to resume

the original equilibrium state, which is accompanied by the dissipation of the ionic layers on both interfaces into the bulk electrolyte, as well as the electron flow *via* the external circuit from the negative electrode to the positive electrode. In other words, the discharge of the interfaces is realized with the electrons doing the electric work (Figure 9.2c).

Alternatively, if one places the charged electrodes at open circuit, *i.e.* making the load on the external circuit infinity ($R_L = \infty$), this electrochemical device would retain the excess charges at the two interfaces, which could be released later on demand, with a flip of the switch.

This is exactly what an energy storage device is designed to do.

The above mechanism of employing an electrified double layer to store electrochemical energy is known as an *electrochemical double-layer capacitor* or simply a *double-layer capacitor*. In some cases, the process that does not involve charge-transfer reactions is referred to as a “*non-Faradaic process*”, and the electrochemical double-layer capacitor is a device that employs non-Faradaic processes to store energy.

Based on eqn (9.23), such a mechanism can be viewed as a process of separating the charges carried by the cations and anions in the electrolyte, during which these ions are pulled away from their distribution equilibrium as described by the Debye–Hückel model.

What one should note in particular is that, during the entire charging and discharging, *there is only charge separation and no charge transfer*. Hence, in a counterintuitive manner, *no electrochemical reactions occur in an electrochemical double-layer capacitor*.

According to what we have learned about the interfaces (Chapter 6), the length between the ionic and electronic charge layers should be on the same scale as the thickness of the outer-Helmholtz layer (~0.5 nm). Because neither charge transfer across the interface nor mass transfer within the solid electrode is involved, the reversible assembly and disassembly of these ionic and electronic charge layers often occurs extremely rapidly. For this reason, an electrochemical double-layer capacitor is considered as a device of high power density, not high energy density.

The amount of energy associated with such a storage mechanism depends on both the amount of charge separated (Q) and the voltage difference (ΔV) by which they are separated, and is given by

$$E = \frac{1}{2} C_{\text{Total}} \Delta V^2 \quad (9.24)$$

As a convention we use “positive electrode” and “negative electrode” instead of “cathode” or “anode” for capacitors, partly because

there is no charge transfer across the interfaces in such devices, hence the original definition of “cathode” and “anode”, at the beginning of Chapter 8, based on reduction and oxidation no longer holds true.

It should be cautioned here that, although eqn (9.3) holds true for the energy change involved in all charge-separation processes, no matter whether redox reactions occur or not, the voltage in an electrochemical double-layer capacitor varies with the amount of charges separated. In other words, once there is current during the charge or discharge, the potential difference between the two electrodes, which is no longer emf, changes in a linear manner that is proportional to the charges separated.

This basic characteristic distinguishes an electrochemical double-layer capacitor from other electrochemical devices such as batteries, the voltage of which is determined by the chemical natures (eigen-potentials) of the two electrodes, and remains almost constant even when the net current is not zero. We have witnessed such a constant cell voltage in fuel cells (Section 9.1.1), and will discuss this difference in more detail at the end of this chapter when comparing the electrochemical characteristics of capacitors and batteries.

To ensure that there are no charge-transfer reactions or formation of an interphase, the voltage applied on a capacitor must always remain within the electrochemical stability window of the electrolytes used therein. However, in reality it is often impossible to keep these interfaces perfectly clean. Certain irreversible reactions always occur in the very first few cycles, passivating the electrode surfaces with some deposits, and one could regard these as “interphases”. Despite the presence of these plausible interphases, one major difference between an electrochemical double-layer capacitor and other electrochemical energy devices such as fuel cells or batteries remains that, in the former, there is only charge accumulation or depletion at these interfaces or interphases, without any charge-transfer reactions occurring or any new species produced.

9.1.2.2 Limiting Factors

According to the charge accumulation and depletion mechanism described in Figure 9.2, the assembly of electronic and ionic layers at the electrode/electrolyte interfaces depends not only on the *polarization voltage*, which directs charges to migrate in response to the electric field applied, but also on the *quantity of ions* that participate in the formation of the double layer.

The former factor (applied voltage) is restricted by the electrochemical stability window of the electrolyte, while the latter (ion quantity)

is restricted by the surface area of the electrodes, because the ionic assemblies could very likely prefer only a single layer of ions separated by proper distances, owing to the strong Coulombic repulsion among ions of the same charge.

Which of these two factors constitutes the limiting component on the energy of the whole device? The answer depends on the following.

If only the apparent geometric area of the electrodes is to be utilized, then the surface area would likely be the limiting factor, because that limited area will be rapidly populated by ions of the same charge. Even at a rather small voltage polarization, such a population could reach such an extent that Coulombic repulsion among these ions prevents any more ions from assembling, unless more voltage polarization is applied to overcome such resistance. This is the fundamental reason why there is a maximum capacitance on a unit area.

According to extensive experiments, the double-layer capacitance of most carbonaceous materials is almost constant within a narrow range of $10\text{--}40 \mu\text{F cm}^{-2}$, which means that, if one applies a voltage of 1 V across the interface, each 1 cm^2 area of the electrode surface can only accommodate between 1.0×10^{-10} and 4.0×10^{-10} mol of ions, or $6.02 \times 10^{13}\text{--}2.4 \times 10^{14}$ ions.

Assuming that a solvated ion has a diameter of 0.5 nm (or 5×10^{-8} cm), then each ion will have a sectional area of

$$S_i = \pi r_i^2 = 3.14 \times (2.5 \times 10^{-8} \text{ cm})^2 = 1.96 \times 10^{-15} \text{ cm}^2 \quad (9.25)$$

The total sectional area of all the ions on the surface will then be

$$S_T = N_i \times S_i = 1.96 \times 10^{-15} \times 2.4 \times 10^{14} \text{ cm}^2 = 0.47 \text{ cm}^2 \quad (9.26)$$

In other words, about half of the area is actually populated by the ions, which are kept at the maximum “social distance” from each other by their Coulombic repulsion. According to MD simulations, the average distance between two neighboring ions is therefore *ca.* 1.0 nm, or about twice the radius of a solvated ion (Figure 9.3a). That will place all ions within the Coulombic field of their neighbors.

In order to increase the population of ions on a given surface area, one could increase the polarization voltage. However, as discussed in the preceding sections, there is a restriction on the maximum voltage that one can apply, which is set by the electrochemical stability window of the electrolytes.

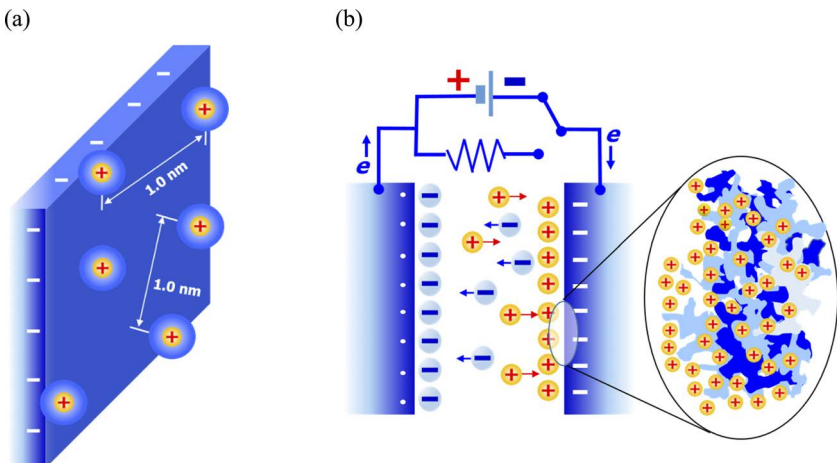


Figure 9.3 Overcoming the factors that limit the ionic density at the electrolyte side of the interface. (a) The highest density of ions that can assemble at the interface is dictated by the Coulombic repulsion among the ions. At 1 V polarization, the average interionic distance between two neighboring ions is ca. 1.0 nm, which corresponds to a specific capacitance of $\sim 20 \mu\text{F cm}^{-2}$. (b) To increase the overall capacitance of an electrochemical double-layer capacitor, one effective strategy is to increase the actual area of an electrode, so that the ionic density on a given geometric electrode area can be maximized without invoking interionic Coulombic repulsion. In this case, the reversible assembly and disassembly of electronic and ionic double layers actually occur at the electrode/electrolyte interfaces within the porous structure of the electrodes.

An alternative, and easier, approach without expanding the electrochemical stability window of the electrolytes is to maximize the *actual electrode surface area* that is accessible by the ions, so that a much larger ionic population could be accommodated by the limited geometric area of an electrode. In fact, this factor was already implied by eqn (6.31), which shows that the total capacitance is proportional to the accessible electrode surface.

For this fundamental reason, porous electrode materials based on carbon became the perfect candidates, thanks to their huge surface area along with exceptional electronic conductivity and low cost. Now the ions can assemble and disassemble on the vast electrode/electrolyte interface without saturating the electrode surface (Figure 9.3b).

Because of its extremely high surface area of up to $1000 \text{ m}^2 \text{ g}^{-1}$, activated charcoal has dominated the commercial market of

electrochemical double-layer capacitors, which can provide a specific capacitance of 150–200 F g⁻¹.

Emerging materials such as graphene and metal–organic framework (MOF) compounds have been pushing the limit further, and surface areas as high as 3000–10 000 m² g⁻¹ have been reported. In other words, the surface area provided by 1 g of such materials would be larger than the area of a football field (5350 m²). Consequently, the highest energy density of the corresponding electrochemical double-layer capacitors has been claimed to be approaching those of typical batteries ($\sim 10^2$ W h kg⁻¹).

With these huge surface areas, the electrodes are capable of accommodating a high ionic population without reaching interionic repulsion, while the voltage polarization limit, imposed by the electrochemical stability window of the electrolyte, becomes the new limiting factor. This shift has induced a transition from aqueous to non-aqueous electrolytes in recent decades.

On the other hand, the advances in nanostructure science and engineering achieved in recent decades have also made diverse candidate materials available, with porous structures under 1 nm, a length close to or even smaller than the radii of most solvated ions. Hence, in order to access these subnanometer pores, the solvation sheaths of ions in electrolytes would have to be stripped or deformed, which leads to abnormal capacitance behaviors differing from the classical capacitance behaviors described by the Helmholtz, Gouy–Chapman, Stern and Bockris models. This emerging front has remained little explored thus far, and could provide opportunities for new science applicable to electrodes, electrolytes and interfaces.

9.1.2.3 Electrolytes

The electrolytes used in electrochemical capacitors could be either aqueous or non-aqueous.

The former, represented by aqueous solutions of sulfuric acid or potassium hydroxide at high concentrations, offer higher ion conductivities, hence enabling these interfaces to store and release charges extremely rapidly. Such capacitors are being used for high power density applications such as pulse discharges (up to 10⁴ W kg⁻¹).

The latter, represented by ammonium salts dissolved in ester, ether or nitrile solvents, offer a much wider electrochemical stability window (~ 3.0 V vs. <1.5 V for aqueous capacitors), hence they can be charged to much higher voltage limits than their aqueous counterparts. Remember that, for capacitors, the energy stored is proportional

to the square of the device voltage [eqn (9.24)], hence an expansion of the electrochemical stability window would bring exponential benefits to energy density. However, the typical energy density that can be achieved by electrochemical double-layer capacitors (10 W h kg^{-1}) is still very small in comparison with batteries. For example, a state-of-the-art lithium-ion battery could deliver an energy density approaching 400 W h kg^{-1} at the cell level.

Therefore, up to 2020, electrochemical double-layer capacitors have still been viewed as high-power instead of high-energy devices, despite the overly optimistic reports in the literature where emerging materials based on graphene or MOFs are used as electrodes.

Nevertheless, electrochemical double-layer capacitors enjoy two advantages that batteries do not: extremely high power density ($10^3\text{--}10^4\text{ W kg}^{-1}$) and an essentially indefinite cycle life ($10^5\text{--}10^6$ cycles). Both of these advantages accrue from the nature of the non-Faradaic charge-separation mechanism, which occurs only at the interfaces and does not involve the often sluggish processes of either charge transfer across the interfaces or mass transport within the solid electrode materials.

9.1.3 Batteries

Unlike electrochemical double-layer capacitors, the energy storage of which is realized *via* the physical assembly and disassembly of charges on the electrode surfaces on two-dimensional interfaces without redox reactions, batteries operate with redox reactions, in which the original chemical species are consumed and new chemical species are produced.⁴ These Faradaic processes go beyond the two-dimensional interfaces and penetrate further into the interior and bulk of the electrode materials.

Like fuel cells, batteries consume materials and produce electric energy during their application (discharge). However, for rechargeable batteries, this process could be reversed during the charging process, where energy provided by an external power source is consumed to produce materials that are the original electrochemical active species in those batteries before discharging. In other words, the electrochemical process at the charging stage of a rechargeable battery is similar to what occurs in an electrolysis or electrochemical synthesis.

Historically, this reversible mechanism in rechargeable batteries led to complications regarding the nomenclature of electrodes, as the cathode and anode had been defined according to the nature of the

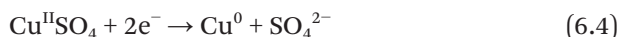
reactions happening thereon, *i.e.* reduction on the cathode and oxidation on the anode.

Now let us look at Figure 6.1b again and use the Daniell cell as an example. Upon discharge, the zinc plate loses electrons, passes them through the external circuit, where they become zinc ions (Zn^{2+}), and eventually these Zn^{2+} ions travel across the zinc/electrolyte interface to become solvated in the bulk electrolyte. This half-reaction is an oxidation reaction:



Meanwhile, the copper plate receives electrons from the external circuit and passes them, across the interface between the copper plate and the electrolyte, to the cupric ions (Cu^{2+}) at the interface. The cupric ions are thus reduced to the elemental form (Cu^0), which is deposited on the copper plate.

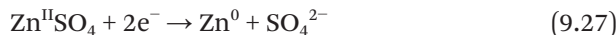
This half-reaction is a reduction:



Hence one is justified in calling the copper plate the “cathode” and the zinc plate the “anode”.

However, the Daniell cell is actually a rechargeable cell. If one applies an external power source, such as another battery or a galvanostat/potentiostat to the copper and zinc electrodes in such a way that the potential of the copper electrode is raised to a more positive value, and the potential of zinc is driven to a more negative value, then the above reactions would be reversed.

Thus, on the copper plate Cu^0 will be oxidized to cupric ions (Cu^{2+}), whereas on the zinc plate the zinc ions (Zn^{2+}) are reduced to the elemental form (Zn^0), which is deposited on the zinc plate:



Now copper should be called the “anode”, and zinc the “cathode”.

Therefore, in all rechargeable batteries, the same electrode would experience both reduction and oxidation reactions, during charge and discharge, respectively, and serve as both cathode and anode accordingly.

In real-life situations, however, it would be very confusing if an electrode is called a “cathode” during its charge and “anode” during its discharge, and *vice versa* for the other electrode. Eventually, as a commonly accepted convention, the electrodes in rechargeable batteries came to be named the “cathode” if its operating potential is higher than that of the other electrode and the electrode of lower potential is the “anode”.

Hence the copper electrode in a Daniell cell would always be the “cathode”, no matter what reaction is happening there, because the potential of the half-reaction expressed in eqn (6.4) is at +0.337 V *vs.* SHE, which is always higher than the potential of the half-reaction expressed in eqn (6.3) for zinc (−0.763 V *vs.* SHE). For the same reason, the zinc electrode would always be the “anode” in a Daniell cell.

This nomenclature actually corresponds to the nature of the reactions during discharge. A simpler alternative is to call these electrodes “positive electrode” and “negative electrode”, because their relative potentials are never reversed even when the reactions on the electrodes are reversed.

Finally, unlike fuel cells, most batteries are closed systems, with the active materials (anode and cathode) pre-sealed in the system. These materials cannot be replenished upon consumption. Therefore, the energy contained in a battery is a fixed number.

There are exceptions, though, as represented by certain open-configuration batteries such as redox flow batteries and metal–air batteries. The latter in particular blur the borderline between fuel cells and batteries, because the cathode material is also the oxygen gas from the ambient air, while one can consider the metal anode (such as aluminum, magnesium or zinc) as a “*solid fuel*” that can be replenished when consumed.

9.1.3.1 How They Work

Since the reductant (anode) and oxidant (cathode) that participate in redox reactions are chemically well-defined species, they already have their own eigenpotentials. Hence a battery upon assembly would have a characteristic voltage that is determined by the difference between the eigenpotentials of these materials.

Using the Daniell cell as an example again, the cathode would be situated at an eigenpotential of +0.337 V *vs.* SHE and the anode at an eigenpotential of −0.763 V *vs.* SHE, when there is no net current between the two electrodes. Hence the Daniell cell has a standard emf of 1.10 V.

When the cell experiences discharge, *i.e.* when the current between the two electrodes is no longer zero, these potentials would change, which would drag the cathode potential lower and the anode potential higher. Therefore the actual cell voltage would be lower than the emf. Such a change is referred to as “*polarization*”, the extent of which depends on how polarizable the electrode/electrolyte interface is, as discussed in Section 6.2.2, and on various kinetic barriers encountered by the reactions, such as the rate of charge transfer at the interfaces and the rate of mass transport within the bulk of both electrodes and electrolyte.

Nevertheless, the cell voltage is determined by the nature of both electrodes, or on the reaction equilibria established at the electrode/electrolyte interfaces, and would remain almost constant during the charge or discharge of the battery, until one of the active electrode materials is completely consumed.

In addition to our favorite example of the Daniell cell, batteries containing a lithium-metal anode would strongly exemplify how the cell voltage depends on the eigenpotential of the electrodes, because lithium not only represents an extremely non-polarizable electrode, it is also the most electropositive metal in the whole Periodic Table, with a redox potential of -3.04 V vs. SHE at room temperature.

Thus, a thin lithium foil is already at such an eigenpotential once it has been assembled into a cell. Upon oxidation during the cell discharge, lithium turns into Li^+ , but its potential remains *relatively* constant despite the current. Here we emphasize “*relatively*” because, depending on the discharge rate, the lithium metal will be more or less polarized towards positive potentials, but such a shift is negligible (usually within 10 mV).

However, the potential would experience a sudden change, such as a jump towards positive values, once the lithium has been completely consumed. If the lithium electrode is sitting on a metallic substrate such as copper, then the electrode would immediately display the eigenpotential of that substrate material at the instant the lithium is completely dissolved.

When both electrodes in a battery act in such a manner, *i.e.* being relatively non-polarizable while displaying their own eigenpotentials, the voltage of the battery would be relatively constant.

We mentioned at the beginning of this chapter that the energy change relating to an electrochemical device is realized *via* charge separation as described by eqn (6.5) or (9.3). If the voltage of a cell is maintained at a nearly constant value, then the energy released from a battery would be delivered at an almost constant voltage until

the active material at one of the electrodes is completely consumed, which is a three-dimensional process that goes well into the interiors of these electrodes, such as the bulk of zinc, copper or lithium metal.

This is a major difference from capacitors, which deliver energy not at a constant but at a constantly changing voltage.

9.1.3.2 Thermodynamics Behind Batteries: Nernst Equation

Now let us consider a generalized battery consisting of a cathode, an anode and an electrolyte that contains ions that are at equilibria with both the cathode and anode (Figure 9.4). This battery is now in an open-circuit state, where the difference between the eigenpotentials of the cathode (ϕ_C) and anode (ϕ_A) is the emf (\mathcal{E}) as expressed in eqn (9.3).

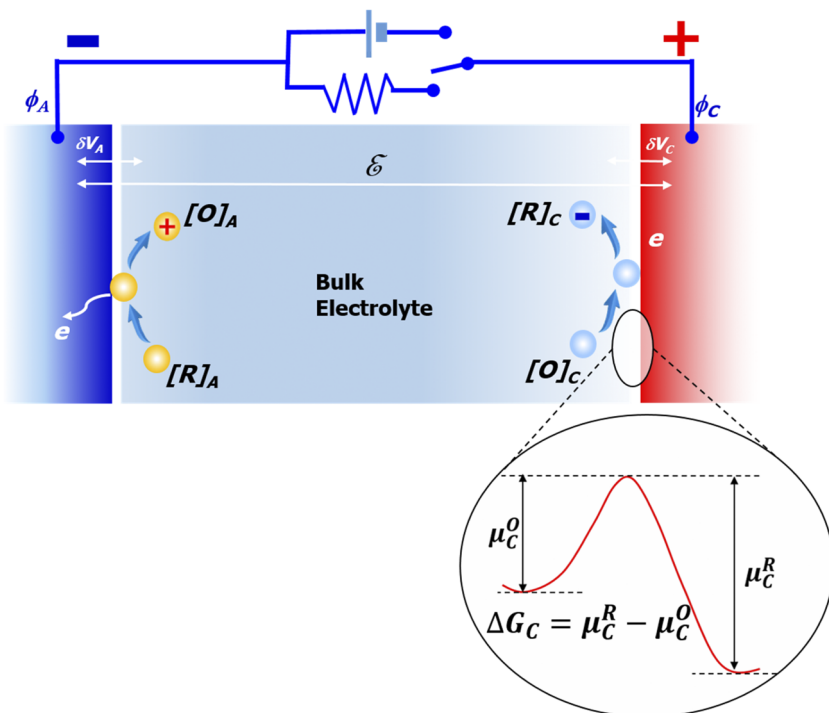


Figure 9.4 A generalized battery without interphases consisting of a cathode, an anode and an electrolyte in the open-circuit state. The reactions at both the cathode/electrolyte interface and anode/electrolyte interface are assumed to be single-electron processes, both of which are at equilibrium. Inset: The energy barriers to the electronation reaction and its counter reaction de-electronation at the cathode/electrolyte interface. There is a similar equilibrium at the anode/interface, not shown here.

Thus, we have the following reactions at the cathode/electrolyte interface and anode/electrolyte interface, respectively:



where $[\text{O}]$ and $[\text{R}]$ represent the activities of the oxidized and reduced species for the reactions at each electrode, and the subscripts A and C denote cathode and anode, respectively.

For the established equilibria at each electrode, an exchange current as described by the Butler–Volmer equation [eqn (6.87)] always exists in both directions (if we do not consider factors such as inter-phases), which forms the foundation for the charge transfers across the interfaces. Therefore, both of these cathodic and anodic reactions are reversible, and the equilibria require that the rates of reactions in reverse directions must be equal.

We will now look at the cathode/electrolyte interface only. Suppose that the free energy barrier to the electronation of $[\text{O}]_{\text{C}}$ is $\mu_{\text{C}}^{\text{O}}$, and that to the de-electronation of $[\text{R}]_{\text{C}}$ is $\mu_{\text{C}}^{\text{R}}$, then the rates of the electronation (v_e) and de-electronation (v_d) reactions should be, respectively

$$v_e = k_e [\text{O}]_{\text{C}} e^{-\frac{\mu_{\text{C}}^{\text{O}}}{k_{\text{B}}T}} \quad (9.31)$$

$$v_d = k_d [\text{R}]_{\text{C}} e^{-\frac{\mu_{\text{C}}^{\text{R}}}{k_{\text{B}}T}} \quad (9.32)$$

where k_e and k_d are the rate constants for the electronation and de-electronation reactions, respectively, and k_{B} is Boltzmann's constant.

At equilibrium, v_e and v_d should be equal, therefore

$$k_e [\text{O}]_{\text{C}} e^{-\frac{\mu_{\text{C}}^{\text{O}}}{k_{\text{B}}T}} = k_d [\text{R}]_{\text{C}} e^{-\frac{\mu_{\text{C}}^{\text{R}}}{k_{\text{B}}T}} \quad (9.33)$$

Rearranging this equation, we obtain

$$\frac{[\text{R}]_{\text{C}}}{[\text{O}]_{\text{C}}} = \frac{k_e}{k_d} e^{-\frac{(\mu_{\text{C}}^{\text{O}} - \mu_{\text{C}}^{\text{R}})}{k_{\text{B}}T}} \quad (9.34)$$

Applying natural logarithms on both sides, the above equation becomes

$$\ln \frac{[R]_c}{[O]_c} = \ln \frac{k_e}{k_d} - \frac{(\mu_c^o - \mu_c^r)}{k_B T} = K + \frac{\Delta G_c}{k_B T} \quad (9.35)$$

where the constant K is introduced to merge the two rate constants, and ΔG_c is the free energy change corresponding to the electronation reaction (or the negative value for the free energy change for the de-electronation reaction):

$$\Delta G_c = \mu_c^r - \mu_c^o \quad (9.36)$$

In the ideal state where $[R]_c = [O]_c = 1.0$, the change in free energy becomes the change in standard free energy ΔG_c^o , hence the constant K can be solved:

$$K = -\frac{\Delta G_c^o}{k_B T} \quad (9.37)$$

Inserting eqn (9.37) into eqn (9.35), we now have

$$\ln \frac{[R]_c}{[O]_c} = -\frac{\Delta G_c^o}{k_B T} + \frac{\Delta G_c}{k_B T} \quad (9.38)$$

which can be rearranged to give

$$\Delta G_c = \Delta G_c^o + k_B T \ln \frac{[R]_c}{[O]_c} \quad (9.39)$$

Remember that Boltzmann's constant k_B and the gas constant R are related by

$$k_B = \frac{R}{N_A} \quad (9.40)$$

where N_A is Avogadro's number, which is further related to the Faraday constant F and elemental charge e_0 by

$$F = N_A e_0 \quad (9.41)$$

We can turn eqn (9.39) into a very well-known form:

$$\Delta G_c = \Delta G_c^\circ + \frac{RT}{F} e_0 \ln \frac{[R]_c}{[O]_c} \quad (9.42)$$

Dividing both sides of this equation by the elemental charge e_0 :

$$\frac{\Delta G_c}{e_0} = \frac{\Delta G_c^\circ}{e_0} + \frac{RT}{F} \ln \frac{[R]_c}{[O]_c} \quad (9.43)$$

Here we need to recall that ΔG_c° and ΔG_c represent the change in free energy across the cathode/electrolyte interface under ideal and non-ideal conditions, respectively. Assuming that the corresponding potential change across this interface is δV_c , then the work done by a single charge across such an interface (W_e) should be

$$W_e = qdV = e_0 \delta V_c = -\Delta G \quad (9.44)$$

Therefore, eqn (9.43) becomes

$$\delta V_c = \delta V_c^\circ - \frac{RT}{F} \ln \frac{[R]_c}{[O]_c} \quad (9.45)$$

We mentioned in Section 6.2.1 that the potential change across an individual interface is actually immeasurable. However, its relative value against a non-polarizable interface can be measured experimentally, similarly to the imaginary reference points/planes in physics. Therefore, it can be replaced with the single-electrode potential ϕ_c , which is measurable against a certain common reference point, such as the bulk electrolyte. Thus eqn (9.45) turns into

$$\phi_c = \phi_c^\circ - \frac{RT}{F} \ln \frac{[R]_c}{[O]_c} \quad (9.46)$$

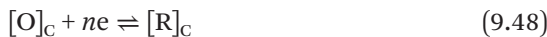
where ϕ_c° is the standard electrode potential, *i.e.* the activities of all species involved are 1.0, the temperature is 298 K, the pressure is 1 standard atmosphere, *etc.* This equation is the *Nernst equation* for an individual electrode, the isomeric form of which was derived in Section 6.5.5.1 when applying the special scenario of zero overpotential, *i.e.* at equilibrium, to the Butler–Volmer equation.

Eqn (9.46) describes the equilibrium between electronation and de-electronation reactions at the cathode/electrolyte interface. A similar equilibrium also exists at the anode/electrolyte interface, for which we will skip the step-by-step derivation and jump directly to the corresponding Nernst equation:

$$\phi_A = \phi_A^0 - \frac{RT}{F} \ln \frac{[R]_A}{[O]_A} \quad (9.47)$$

Note the subscripts A now indicate the location of the equilibrium at the anode/electrolyte interface.

In the generalized half-reactions shown in eqn (9.29) and (9.30), we assumed both reactions to be single electron for simplicity. For reactions involving multiple electrons (such as Zn^{2+}/Zn^0 and Cu^{2+}/Cu^0 in the Daniell cell), we would have



Then, the electric work done by a charge ne_0 across a potential change δV_C should be

$$W_e = qdV = ne_0\delta V_C = -\Delta G \quad (9.50)$$

Accordingly, we divide both sides of eqn (9.42) by ne_0 , and eventually obtain the corresponding potential change across the electrode/electrolyte interfaces as

$$\phi_C = \phi_C^0 - \frac{RT}{nF} \ln \frac{[R]_C}{[O]_C} \quad (9.51)$$

$$\phi_A = \phi_A^0 - \frac{RT}{nF} \ln \frac{[R]_A}{[O]_A} \quad (9.52)$$

where n represents the valence of the ions involved.

The emf of the battery shown in Figure 9.4 should be given by the difference of the electrode potentials at the equilibria, where the net current across the battery is zero:

$$\mathcal{E} = \phi_C - \phi_A = (\phi_C^0 - \phi_A^0) - \frac{RT}{nF} \ln \frac{[R_C][O_A]}{[O_C][R_A]} \quad (9.53)$$

We now define the term $(\phi_C^0 - \phi_A^0)$ as the standard emf \mathcal{E}^0 , which is the cell open-circuit voltage under standard conditions, and eqn (9.53) would take the famous form of the Nernst equation for a full battery:

$$\mathcal{E} = \mathcal{E}^0 - \frac{RT}{nF} \ln \frac{[R_C][O_A]}{[O_C][R_A]} = \mathcal{E}^0 - \frac{RT}{nF} \ln Q \quad (9.54)$$

where Q is called the *reaction quotient*, which represents the activities of all species involved that participate in the cell reactions in a battery.

We will now use eqn (9.54) as the basis to analyze how energy is stored in or released from a battery.

9.1.3.3 What Does the Nernst Equation Teach Us?

What does the Nernst equation teach us about a battery?

First, although at the beginning of this chapter we started to examine the reaction equilibria in a generalized battery configuration, it is apparent that *the applicability of the Nernst equation goes beyond just batteries*: it describes the thermodynamic properties of any electrochemical system that involves a redox reaction. However, the applicability of the Nernst equation excludes electrochemical double-layer capacitors, which only involve the physical separation of charges, without chemical reactions and charge transfers at the interfaces.

Second, *the equilibria required by the Nernst equation correspond to zero current*. In real life, a working electrochemical device cannot be at perfect equilibrium because it must deliver a current flow. However, the Nernst equation still approximates and approaches real electrochemical devices near equilibria provided that the current is infinitesimally small.

Third, *the Nernst equation predicts the upper limit of the voltage that a battery could generate if its electrodes are known*. We have done so for the electrode pair of Zn^0 vs. Cu^{2+} in a Daniell cell (Section 9.1.3.1) or H_2 vs. O_2 in a fuel cell (Section 9.1.1). Furthermore, *via* eqn (9.3), the upper limit of the energy that could be delivered by a battery is also predicted by the Nernst equation. Such limits can be approached but never exceeded. Most importantly, *via* eqn (9.3), we can calculate the theoretical energy available from almost any battery consisting of an electrode pair, provided that the standard *Gibbs free energy* of

formation (ΔG_f) is known for each species involved. This is made possible by a rich database of ΔG_f values available for millions of chemical species, thanks to the development of thermodynamics over the past two centuries.

Last, the Nernst equation tells us that the upper limits for both battery voltage and energy are determined by the natures of the electrodes only. This is the reason why in the battery community and industry the electrode materials are often referred to as “battery chemistries”.

But what do the electrolyte and interface affect? They determine both battery voltage and energy at non-equilibria, i.e. when the battery is working in real-life situations. This is because, provided that there is a non-zero current flowing across the cell, both the battery voltage and energy as predicted by the Nernst equation would suffer losses. Such kinetic losses, usually called “cell polarization”, are mostly contributed to by transport factors occurring within the bulk electrolyte and in particular at the interfaces, such as the mass transport across the bulk electrolyte, the charge transfer across the interfaces and ion migrations across interphases.

And what about interphases? The presence of an interphase, as briefly discussed in Sections 8.2.2 and 8.2.3 (Figure 8.3), allows the use of electrode materials the operating potentials of which reside outside the electrochemical stability window of the electrolytes. Therefore, an interphase would enable a higher voltage and energy that would otherwise be impossible because of the electrolyte instability. Since an interphase is located between the electrode and electrolyte, its presence also inevitably contributes to the cell polarization.

In summary, although electrolytes, interfaces and interphases do not directly determine the voltage and energy of a battery, they do so indirectly via cell polarization and stabilization of the electrode/electrolyte at extreme potentials.

9.1.3.4 Revisiting “Charge Separation”

Before we proceed further to explore more specific characterizations of batteries, it is time to examine the “charge separation” concept once again and try to understand how it applies to batteries.

We have mentioned that the energy storage and release in an electrochemical device are realized through charge separation and charge recombination. Although this concept can be easily (and visually) understood for electrochemical double-layer capacitors (Figure 9.2), in which the charges are physically pulled away from, and subsequently returned to, the equilibrium state of the bulk electrolyte as

described by the Debye–Hückel model, during charging and discharging, respectively, it is much less apparent for batteries and fuel cells, in which each electrode already possesses its own eigenpotential upon assembly into a battery, and the charge separation seems to be predetermined by the chemistries of the electrodes even before they are placed in an electrochemical cell.

In a battery or a fuel cell, charge separation occurs only when the electrodes are paired in an electrochemical cell.

For example, a standalone zinc plate does not feel any “charge separation”, nor would it feel such if it is paired with another zinc plate in an electrochemical cell. However, the instant when it is paired with another electrode of different eigenpotential (copper, lithium, *etc.*), in an electrochemical cell that contains electrolytes with proper ions (Cu^{2+} , Zn^{2+} or Li^+) for corresponding electrolyte/electrode equilibria, it would immediately “feel” the charge separation, even when the electrochemical cell is at open circuit.

Therefore, if the other electrode is copper, the $\text{Zn}^0/\text{Zn}^{2+}$ equilibrium at the zinc/electrolyte interface would be at a more negative potential (-0.763 V vs. SHE) compared with the $\text{Cu}^0/\text{Cu}^{2+}$ equilibrium at the copper/electrolyte interface (0.337 V vs. SHE). Such a potential difference attracts the electrons carried by a zinc atom and makes it break free, leaving Zn^{2+} behind:



while these two electrons, driven by the potential difference, combine with Cu^{2+} at the other interface:



Hence, at this near-equilibrium state (it is no longer a perfect equilibrium as these electrons travel from zinc to copper, making the current non-zero), these two electrons travel across a potential difference of 1.10 V , releasing electric work that corresponds to the energy stored during the original “charge separation”. In this case, zinc is the anode (negative electrode), and copper is the cathode (positive electrode).

If the other electrode is lithium, then the $\text{Zn}^0/\text{Zn}^{2+}$ equilibrium at the zinc/electrolyte interface would be at a more positive potential (-0.763 V vs. SHE) compared with the Li^0/Li^+ equilibrium (-3.04 V vs. SHE) at the lithium/electrolyte interface. Such a potential difference

attracts the electrons carried by a lithium atom and makes it break free, leaving Li^+ behind:



while this electron, driven by the potential difference, combines with Zn^{2+} at the other interface:



Accordingly, at this near-equilibrium state, this electron travels across a potential difference of 2.277 V, releasing electric work that corresponds to the energy stored during the original “charge separation”. In this case, zinc is the cathode (positive electrode), and lithium is the anode (negative electrode).

Because of its extremely low potential, lithium is almost always the anode in electrochemical cells.

Now we can see that the “charge separation” in a battery is caused by a “*virtual chemical reaction*” that would occur if the two electrodes are paired in an electrochemical device, and how the charges are separated is a relative term depending on how the electrodes are paired.

9.1.3.5 Capacity and Energy

Hence the energy involved in a battery is determined by the charge separation created by the difference in eigenpotentials between the two electrodes. In the near-equilibrium state, where the current flow is non-zero but infinitesimally small, the energy stored or released, corresponding to n mol of ions with a valence of z being separated or recombined across a potential difference ΔV , would be given by the electric work done by these charges:

$$W_e = q\Delta V = nzF\Delta V \quad (9.2)$$

Note that the potential difference (ΔV , or cell voltage at open circuit, or emf) is an *intensive quantity*, which is independent of the amount of the electrode materials unless they completely disappear due to consumption, whereas the amount of charge carried by the ions (nzF) is an *extensive quantity*, which reflects the amount of the active species available from the electrode materials, and is normally known as *capacity*.

It is important to differentiate capacity as defined here from *capacitance* as defined earlier in Section 9.1.2 [eqn (9.12)]. Confusion sometimes arises because in the older literature these two terms were sometimes used interchangeably. Capacitance is the relative ratio between the amount of charges accumulated on the electrode surface (an extensive quantity) and the overpotential applied across the electrodes (an intensive quantity), therefore it is apparently an intensive quantity itself that is independent of the amount of electrode materials.

If the potential difference ΔV remains constant during the entire movement of the n mol of charge, then the energy expected from such an ideal battery would be the simple product of cell voltage (or emf) and capacity:

$$E_{\text{cell}} = q \times \Delta V = q \times \mathcal{E} \quad (9.59)$$

In this case, if one plots the cell voltage of a battery against the cell capacity, one would obtain the dashed line in Figure 9.5a, which is a constant until the capacity reaches nzF , *i.e.* all of the active species in one of the electrodes has been completely consumed. The corresponding energy would be represented by the area of the shaded rectangle.

However, as already mentioned, the cell voltage would suffer from kinetic losses provided that the current is non-zero, and such kinetic losses would deteriorate when the current flow becomes more substantial. As the result, the cell voltage would depart from the emf represented by the dashed line and become a curve, which is lower than what the emf would produce, while the capacities that can be accessible under such kinetic polarization also depart from the theoretical value of nzF (Figure 9.5a). The combination of the two factors is reflected in the amount of energy available from the battery, which, as represented by the various shaded areas under the corresponding cell voltage curves, decreases with increase in current, and can be expressed as

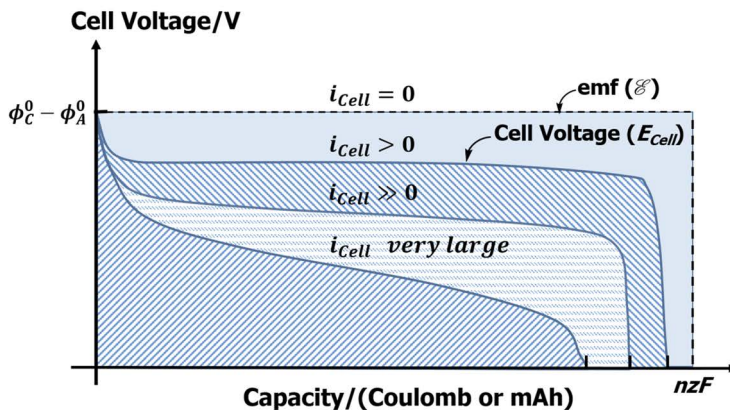
$$E_{\text{cell}} = \int_0^{nzF} V(q) dq \quad (9.60)$$

where $V(q)$ indicates that the cell voltage is a function of capacity.

The capacity by its nature is the quantity of charge, therefore it can be expressed in moles of ions whose valence is known, or in coulombs (nzF). Thus, a redox reaction involving 1 mol of Li^+ corresponds to 1 mol of elementary charge, which is

$$C_{\text{Li}} = N_A e_0 = 6.0221 \times 10^{23} \times 1.6022 \times 10^{-19} = 96\,485.333 \text{ coulombs} \quad (9.61)$$

(a)



(b)

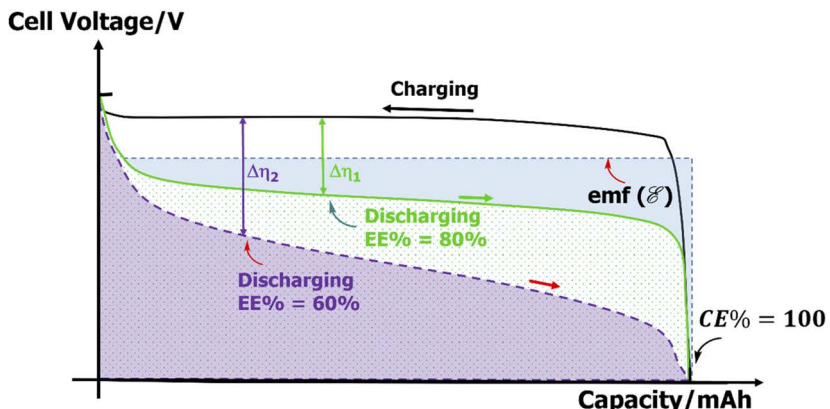


Figure 9.5 (a) Schematic plots of the cell voltage of a battery against its capacity at both equilibrium/near-equilibrium and working states of varying currents. The energy released from the battery is represented by the shaded areas under the corresponding cell voltage curves. (b) Comparison between Coulombic efficiency and energy efficiency, and the accompanying potential hysteresis, for an imagined rechargeable battery. The voltage profile of the charging process is plotted inversely against the capacity axis for convenience of comparison.

which is Faraday's constant by definition.

However, another more popular (and more convenient) unit is often used in electrochemistry and battery communities, namely ampere-hours (A h) or milliampere-hours (mA h). Remember that 1 coulomb in SI units is 1 ampere-second, hence the capacity corresponding to the redox reaction of 1 mol of Li^+ is

$$C_{\text{Li}} = 96485.333(\text{As}) \times \frac{1000 \left(\frac{\text{mA}}{\text{A}} \right)}{3600 \left(\frac{\text{s}}{\text{h}} \right)} = 26801.481 \text{ mAh} \quad (9.62)$$

Naturally, a redox reaction involving 1 mol of Zn^{2+} or 1 mol of Al^{3+} would correspond to twice (192 970 coulombs or 53 602.962 mA h) or three times (289 456 coulombs or 80 404.444 mA h) as much capacity, respectively, which has been the primary driving force recently behind efforts to explore battery chemistries employing multivalent cations such as Zn^{2+} , Ca^{2+} , Mg^{2+} and Al^{3+} .

When considering the valence of the active species, a generalized form of eqn (9.61) is

$$C_M = z_M N_A e_0 = z_M F \text{ (coulombs)} = 0.2778 z_M F \text{ (mA h)} \quad (9.63)$$

where z_M is the valence of M and F is the Faraday constant.

Although the multivalence of these ions allows a higher capacity (and possibly energy), they are much heavier than Li^+ , which raises the question of which ion provides the more efficient way to store energy. In other words, from a practical perspective, what matters to a battery is not only how much total capacity and energy it delivers, but also how much capacity and energy *per unit weight* or *per unit volume* of the materials could be provided by the materials. Therefore, we will define the *specific capacity* corresponding to the redox of a *unit mass* (1 g) of Li^+ (or Li^0) as

$$C_{\text{Li}}^s = \frac{0.2778 z_{\text{Li}} F}{M_{\text{Li}}} = \frac{26801.481 \text{ mAh mol}^{-1}}{6.95 \text{ mol}^{-1}} = 3856 \text{ g}^{-1} \quad (9.64)$$

Likewise, we can obtain the specific capacities for Zn^{2+} and Al^{3+} as

$$C_{\text{Zn}}^s = \frac{0.2778 z_{\text{Zn}} F}{M_{\text{Zn}}} = \frac{53602.962 \text{ mAh mol}^{-1}}{65.38 \text{ g mol}^{-1}} = 820 \text{ mAh g}^{-1} \quad (9.65)$$

$$C_{\text{Al}}^s = \frac{0.2778 z_{\text{Al}} F}{M_{\text{Al}}} = \frac{80404.444 \text{ mAh mol}^{-1}}{26.98 \text{ g mol}^{-1}} = 2980 \text{ mAh g}^{-1} \quad (9.66)$$

Apparently, Li^+ is the more efficient ion that one could employ to do electric work! However, Li^+ is not the most efficient ion, because beryllium (Be), which provides divalent chemistry, reaches the perfect balance between low atomic weight and high valence and produces the highest specific capacity known for all electrode materials:

$$C_{\text{Be}}^{\text{s}} = \frac{0.2778 z_{\text{Be}} F}{M_{\text{Be}}} = \frac{53602.962 \text{ mAh mol}^{-1}}{9.0122 \text{ g mol}^{-1}} = 5948 \text{ mAh g}^{-1} \quad (9.67)$$

Despite this impressive capacity, the extremely high toxicity and low abundance of Be actually make it an impractical choice as an electrode material. Hence Li became the “winner”, often referred to as the “Holy Grail”, for battery anodes, and has been driving most of the efforts seeking new battery chemistries.

Now, we must remember that the specific capacities expressed in eqn (9.64)–(9.67) were only normalized against the weight of a single electrode material. These “single-electrode” specific capacities are often used to quantify the potential significance of a given material. However, a single electrode cannot make a battery, which should consist of at least two electrodes.

So, how does one calculate the capacity of an electrochemical cell that consists of two electrodes?

One must always remember that, in an electrochemical cell, the reaction occurring at one electrode is only a half-reaction, hence it must have a corresponding half-reaction at another electrode, so that both the charge transfer and mass transport that a sustained whole reaction needs could be provided. For example, let us consider a conceptual rechargeable battery consisting of an Li^0 anode and an oxygen cathode. Let us further assume that oxygen has to be provided in a closed-cell environment, *i.e.* oxygen is not from the ambient air, so that carbon dioxide and other impurities could be kept away to ensure the cell reversibility. In this case, the masses of both anode and cathode active materials contribute to the overall mass of the cell.

How should we construct the cell to achieve the optimum capacity and energy?

In such an enclosed lithium/oxygen battery, the anode half-reaction was already given by



and the cathode half-reaction would be



Note that the reduction of oxygen here is a two-electron process leading to the formation of peroxide (O_2^{2-}), which differs from the

four-electron process as represented in eqn (9.5) and (9.7), where oxygen experienced a complete reduction to the oxide state (O^{2-}). This partial reduction of oxygen is necessary for better reversibility of the Li/oxygen battery.

In this battery, every mole of Li^0 reduction at the anode would require only 0.5 mol of oxygen oxidation at the cathode. If one constructs such a battery using equimolar amounts of Li^0 and oxygen, then half of the cathode would be in excess, which does not participate in the cell reaction and remains as an inert mass. Since the battery is a closed system, the presence of inert materials always comes at the expense of the specific capacity and energy density of the whole cell.

Following this logic, the capacity of a whole battery is actually determined by the electrode that has a smaller capacity. In order to optimize the capacity (and energy) that a cell could deliver, one should try to minimize the inert mass caused by the excessive electrode material. In the ideal situation, such a mass should be zero, and the capacities of the anode and cathode should be exactly matched.

At this optimum state, what is the relation between the specific capacity for the whole cell (*i.e.* normalized against the whole cell mass) and the specific capacities of the two electrodes?

Let us consider a generalized battery consisting of an anode and cathode, whose specific capacities, C_A^s and C_C^s , respectively, are given by definition as

$$C_A^s = n_A z_A F = \frac{0.2778}{M_A} z_A F \quad (9.69)$$

$$C_C^s = n_C z_C F = \frac{0.2778}{M_C} z_C F \quad (9.70)$$

At the ideally optimized state mentioned above, the masses of the anode (w_A) and cathode (w_C) are so arranged that the capacities from each are identical, hence there is no excess mass at either electrode. Such capacities from each electrode would be given by

$$C_A = \frac{0.2778 w_A}{M_A} z_A F \quad (9.71)$$

$$C_C = \frac{0.2778 w_C}{M_C} z_C F \quad (9.72)$$

while the capacity for the whole cell (C_{cell}) should be the same as C_A and C_C :

$$C_{\text{cell}} = C_A = C_C \quad (9.73)$$

Now, remember that the total mass of the cell should be

$$w_{\text{cell}} = w_A + w_C \quad (9.74)$$

Hence the specific capacity of the whole cell should be given by

$$C_{\text{cell}}^s = \frac{C_{\text{cell}}}{w_{\text{cell}}} = \frac{C_{\text{cell}}}{w_A + w_C} \quad (9.75)$$

Note that the total mass of the whole cell does not include the masses of the electrolytes and other inactive materials, such as separator, current collector, cell packaging, etc. To make it more rigorous, eqn (9.75) should be modified to

$$C_{\text{cell}}^s = \frac{C_{\text{cell}}}{w_{\text{cell}}} = \frac{C_{\text{cell}}}{w_A + w_C + w_I} \quad (9.76)$$

where w_I represents the sum of all other inactive masses. However, eqn (9.75) and its derivative forms are still used by most workers for simplicity.

We rewrite eqn (9.75) in its reciprocal form so that it will be easier to simplify:

$$\frac{1}{C_{\text{cell}}^s} = \frac{w_A + w_C}{C_{\text{cell}}} = \frac{w_A}{C_{\text{cell}}} + \frac{w_C}{C_{\text{cell}}} \quad (9.77)$$

Substituting eqn (9.73) into eqn (9.77), we obtain

$$\frac{1}{C_{\text{cell}}^s} = \frac{w_A}{C_A} + \frac{w_C}{C_C} = \frac{w_A M_A}{0.2778 w_A F} + \frac{w_C M_C}{0.2778 w_C z_C F} = \frac{M_A}{0.2778 z_A F} + \frac{M_C}{0.2778 z_C F} \quad (9.78)$$

Inserting eqn (9.69) and (9.70), we obtain the relation between the specific capacity of the whole cell and the specific capacities of the two individual electrodes:

$$\frac{1}{C_{\text{cell}}^s} = \frac{1}{C_A^s} + \frac{1}{C_C^s} \quad (9.79)$$

or, in a form that can be directly used for practical examples:

$$C_{\text{cell}}^{\text{s}} = \frac{C_{\text{A}}^{\text{s}} C_{\text{C}}^{\text{s}}}{C_{\text{A}}^{\text{s}} + C_{\text{C}}^{\text{s}}} \quad (9.80)$$

For example, applying this equation to the Li/oxygen battery, we can obtain the cell-level theoretical specific capacity as

$$C_{\text{cell}}^{\text{s}} = \frac{C_{\text{Li}}^{\text{s}} C_{\text{O}}^{\text{s}}}{C_{\text{Li}}^{\text{s}} + C_{\text{O}}^{\text{s}}} = \frac{3856 \times 1675}{3856 + 1675} = 1167.74 \text{ mA h g}^{-1} \quad (9.81)$$

What else does eqn (9.80) tell us? It also indicates that, in a battery (or any electrochemical device), the whole cell capacity is determined by the specific capacities of the two individual electrodes in a coupled manner. This coupling implies that the best way to improve the specific capacity of a battery is through simultaneous improvements of both electrodes.

For example, if one individual electrode has a far higher specific capacity than the other, the specific capacity and energy density of the corresponding battery are mostly dictated by the specific capacity of the other electrode, which serves as a “bottleneck”. It is immediately apparent if one assumes an extreme case where the specific capacity of an ideal anode is infinity ($C_{\text{A}}^{\text{s}} = \infty$), then

$$C_{\text{cell}}^{\text{s}} = \frac{C_{\text{A}}^{\text{s}} C_{\text{C}}^{\text{s}}}{C_{\text{A}}^{\text{s}} + C_{\text{C}}^{\text{s}}} = \frac{C_{\text{A}}^{\text{s}} C_{\text{C}}^{\text{s}}}{C_{\text{A}}^{\text{s}}} = C_{\text{C}}^{\text{s}} \quad (9.82)$$

This is the major reason why in lithium-ion battery research the development of cathode materials has dominated most resources and attention, because the anode (graphitic carbon) already has a much higher specific capacity (372 mA h g^{-1} , or 339 mA h g^{-1} if one counts the overall mass of LiC_6 ; see Section 9.1.3.6) than most of the cathode materials based on transition metal oxides ($<250 \text{ mA h g}^{-1}$).

A more quantitative understanding of this issue can be achieved by considering an imaginary cell that consists of two electrodes with different capacities. Here let us use three model anode materials with different specific capacities as templates, *i.e.* graphite (339 mA h g^{-1}), silicon (2010 mA h g^{-1} ; see Section 9.1.3.6) and lithium metal (3856 mA h g^{-1}), and allow the cathode capacity to vary. The resultant full cell capacities governed by eqn (9.80) would be represented by three distinct curves as shown in Figure 9.6.

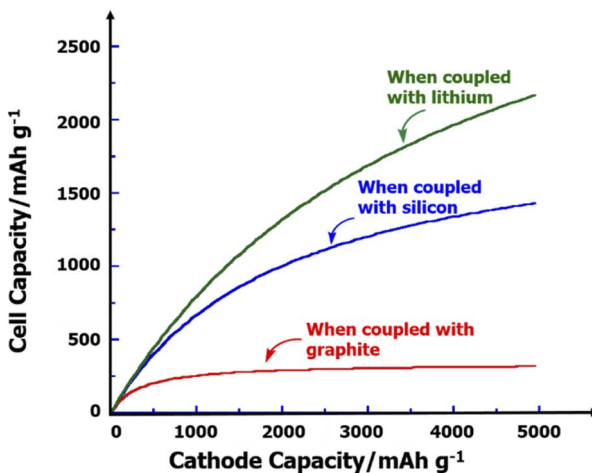


Figure 9.6 The specific capacity of a full cell consisting of imaginary cathode materials with varying capacity that are coupled with three different anode materials, graphite, silicon and lithium metal.

Apparently, thanks to the coupling between the cathode and anode, once the specific capacity of a cathode exceeds that of the anode, any gain in the full cell capacity induced by an increase in the capacity of the cathode would slow and eventually become suppressed. Conversely, for a cathode with a high specific capacity, coupling it with an anode of moderate capacity would also reduce its contribution to increase the full cell capacity.

Hence the optimum improvement of the full cell capacity would be achieved in the scenario when the cathode and anode have identical specific capacities. For example, the ideal match for a cathode of 1000 mA h g^{-1} would be an anode of the same specific capacity, the consequence of which is a maximized gain in the full cell capacity. Of course, in reality there is always a mismatch between the two.

Finally, from a different perspective, eqn (9.80) also implies that the specific capacity or energy output of a whole battery consisting of two *given* electrodes would be optimized if the capacities of each electrode are *completely matched*. Any excess capacity above the matched value, no matter which electrode, would be useless in the whole cell operation, and the excess amount of the electrode would just become “dead weight”, dragging down the energy density of the whole cell.

Knowing the theoretical capacity at cell level allows us to estimate the *maximum theoretical specific energy* (MTSE) for batteries, provided that the theoretical cell voltage is known, which can be calculated as

emf based on thermodynamic data such as the Gibbs free energy of formation under standard conditions:

$$E_{\text{cell}}^{\text{s}} = C_{\text{C}}^{\text{s}} \times \mathcal{E} \quad (9.83)$$

However, materials researchers more frequently use a similar equation to estimate the MTSE of individual electrode materials:

$$E_{\text{M}}^{\text{s}} = C_{\text{M}}^{\text{s}} \times \mathcal{E}_{\text{M}} \quad (9.84)$$

where \mathcal{E}_{M} represents the estimated cell potential if one couples this electrode with an imaginary counter-electrode. This will be especially convenient if one needs to evaluate the potential significance of a new material. Examples include the typical cathode materials used in lithium-ion batteries, such as lithium cobalt oxide (LiCoO_2 , 3.8 V, $\sim 1000 \text{ W h kg}^{-1}$), lithium nickel manganese cobalt oxide ($\text{LiNi}_x\text{Mn}_y\text{Co}_z\text{O}_2$, 4.0~4.3 V, $\sim 700 \text{ W h kg}^{-1}$) or lithium iron phosphate (LiFePO_4 , 3.5 V, $\sim 500 \text{ W h kg}^{-1}$), where the voltages were all *versus* the Li^0 potential.

Caution must be exercised here, because these MTSE numbers were calculated using the mass of a single electrode, without even considering the mass of the other electrode, hence they do not reflect the energy available from a full battery. In fact, the highest cell-level energy density of lithium-ion batteries achieved as of 2022 is still below 400 W h kg^{-1} based on a cathode with a high nickel content and an anode with a high silicon content. Normally, the inert mass of the electrolyte, separator and cell packaging materials would reduce the MTSE of the single electrode by at least half!

9.1.3.5.1 Rechargeable Batteries: Coulombic and Energy Efficiencies

If a battery is rechargeable, its chemistry must be reversible. That is, when the cell reaction proceeds spontaneously, the battery releases energy to the user, and when the user applies a voltage that is higher in value but opposite in direction to the battery, the cell reaction is forced to go backwards, and in principle all starting materials (active species in both the anode and cathode) will be regenerated.

Not all cell chemistries are reversible. In fact, since Volta invented the first battery more than 200 years ago, fewer than two dozen rechargeable battery chemistries have been discovered. Among them, the lithium-ion battery is the newest, the most energetic and the most efficient.

There are two separate quantities that describe the reversibility of cell chemistries in rechargeable batteries, corresponding to capacity and energy, respectively.

The most popular quantity is *Coulombic efficiency* (CE%). Basically, it counts how many electrons one puts into a battery during charging, and then how many electrons one can obtain from the spontaneous cell reaction during discharging. The ratio of these two quantities, often expressed as a percentage, is CE%, which is by nature the capacity ratio of the discharging and charging processes:

$$\text{CE\%} = \frac{\text{capacity released during discharging}}{\text{capacity injected during charging}} \quad (9.85)$$

A less frequently used quantity is *energy efficiency* (EE%), sometimes known as *round trip energy efficiency*. Basically, it is the ratio between the energy one injects into a battery during charging and the energy the battery releases during discharging:

$$\text{EE\%} = \frac{\text{energy released during discharging}}{\text{energy injected during charging}} \quad (9.86)$$

We have mentioned before that, once the cell current is non-zero, the cell voltage departs from the ideal cell voltage that the emf would produce (Figure 9.5a). This actually applies to both charging and discharging processes. The only difference is that during the charging process, such a deviation is positive, which results in a higher potential curve than the dashed line representing emf, whereas during the discharging process the deviation is negative (Figure 9.5b). In other words, when using a rechargeable battery, one would always obtain less energy during discharging than what is entered into the battery during charging.

In most cases, EE% is lower than CE%, because the former is subjected to not only the lower capacity accessible when the cell current is non-zero, but also the voltage loss caused by the same kinetic barriers.

Most of the time, we do not really care what the ideal cell voltage predicted from the emf is, but instead care more about the difference between the charging and discharging voltages. Such a difference, which varies at different capacities, is called *voltage hysteresis* ($\Delta\eta$). Voltage hysteresis directly affects EE%.

Finally, as an example to differentiate what CE% and EE% represent, let us examine the charging/discharging behavior of an imaginary

rechargeable battery as shown in Figure 9.5b. At different discharging currents, the reversible capacity accessed in this battery is almost constant and approaches the theoretical value, which would predict a CE% of ~100%. However, owing to the reduction in discharging voltage when the discharging current is high, the EE% could be much smaller, because the actual energy delivered, as represented by the shaded areas under the voltage curves, becomes increasingly smaller.

Such interesting behavior is by no means fictitious. It is frequently encountered in certain scenarios such as chemistries involving oxygen redox reactions, the four-electron process of which becomes sluggish at high current densities, or multivalent chemistries, where the movement of cations bearing formal charges higher than +1 faces extra resistances from their environment (solvation sheath, lattice coordination, *etc.*).

When this scenario arises, CE% alone would provide deceptive information regarding the reversibility of the battery chemistry. Instead, one should look at EE% as a basis to judge how rechargeable the battery is.

One might wonder, at 100 CE%, which obviously hints that the original chemical state of the battery (*i.e.* the starting materials at both the cathode and anode) has been completely restored after complete utilization of all active materials, what a much lower EE% represents?

It tells us that extra energy has to be consumed, during both charging and discharging, in order to utilize the active materials completely and restore the original chemical state of the battery completely. The extra energy, which is defined as the difference between the charging and discharging energies, is mostly lost in the form of heat, which is created by the movement of ions in a highly resistive environment.

9.1.3.6 A Mistake Often Made

A persistent yet usually overlooked error regarding specific capacities deserves a separate section for clarification.

The specific capacity that has been expressed in eqn (9.64)–(9.67) and eqn (9.69) and (9.70) can be generalized for any species *i* in the following form:

$$C_i^s = \frac{0.2778}{M_i} z_i F \quad (9.87)$$

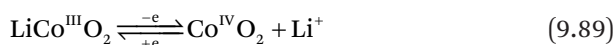
where M_i and z_i represent the molecular weight and valence of the redox species, respectively.

For simple elemental materials such as metallic lithium, zinc, aluminum and beryllium, the meaning of M_i is unambiguous: the atomic weight of the corresponding metals [eqn (9.64)–(9.67)]. However, when the species is a compound consisting of multiple elements, the situation becomes more ambiguous and, to make things more confusing, two separate standards have been adopted by the materials community. Both are correct and have their own justifications, but their mixed use could create confusion.

For example, the accepted theoretical specific capacity of the typical cathode material in a lithium-ion battery, LiCoO_2 (LCO), is 273.87 mA h g⁻¹, calculated as

$$C_{\text{LCO}}^s = \frac{0.2778}{M_{\text{LCO}}} z_{\text{LCO}} F = \frac{0.2778}{97.883} \times 96485.33 = 273.87 \text{ mA h g}^{-1} \quad (9.88)$$

which is based on an assumed electrochemical lithiation/de-lithiation (*i.e.* oxidation/reduction) of LiCoO_2 :



and the molecular weight of the whole compound LiCoO_2 (97.883).

On the other hand, the accepted theoretical specific capacity of the typical anode material in a lithium-ion battery, graphite (GR), is 372 mA h g⁻¹, calculated as

$$C_{\text{GR}}^s = \frac{0.2778}{M_{\text{GR}}} z_{\text{GR}} F = \frac{0.2778}{72} \times 96485.33 = 372 \text{ mA h g}^{-1} \quad (9.90)$$

and based on an assumed electrochemical lithiation/de-lithiation (*i.e.* oxidation/reduction) of graphite:



where every six carbons can stoichiometrically accommodate up to one Li^+ , hence the molecular weight of C_6 (72) was used.

What is the difference between eqn (9.88) and eqn (9.90)? In the former, the molecular weight of the whole compound LiCoO_2 was used, whereas in the latter, if graphite is viewed as a “container” for Li^+ in such intercalation chemistry (to be discussed in Chapter 10), then *only the weight of the container* (72) was counted, with the contents in the container (Li^+) completely ignored. The justification behind this peculiar “container-only” approach seemed to have stemmed from

the fact that graphite (and some other anode hosts) can be used in its non-lithiated state as an electrode, whereas most cathode materials such as LiCoO₂ are used in the lithiated state, because their crystalline lattice needs stabilization provided by the Li⁺ intercalated therein.

Extending this “container-only” approach to silicon, another anode host for lithium-ion batteries, since each silicon atom is believed to be able to accommodate up to 4.4 Li⁺:



we would obtain the corresponding specific capacity for silicon:

$$C_{\text{Si}}^s = \frac{0.2778}{M_{\text{Si}}} z_{\text{Si}} F = \frac{0.2778}{28.08} \times 4.4 \times 96485.33 = 4199 \text{ mA h g}^{-1} \quad (9.93)$$

which, like that for graphite, is a widely used number in the literature.

Recalling that we have calculated the specific capacity of Li⁰ to be 3856 mA h g⁻¹ [eqn (9.64)], one could very likely be tempted to draw the conclusion that “silicon provides a higher specific capacity than lithium metal”. In fact, the author has seen similar statements multiple times in peer-reviewed publications, proposals and presentations, some of which were even from rather senior researchers.

But is it correct? *Clearly it does not make any sense.*

Silicon is a “container” for Li⁺. No matter how many Li⁺ it can accommodate, it cannot possibly provide a higher specific capacity than a neat Li⁰ metal electrode, which can be considered as “container-less” ($M_i = 0$). In other words, if one applies the same “container-only” approach to a neat Li⁰ metal electrode, its specific capacity should be infinity!

Therefore, in this context, the 372 mA h g⁻¹ for graphite or 4199 mA h g⁻¹ for silicon cannot be directly compared with 3856 mA h g⁻¹ for Li⁰ metal, although for graphite this mistake does not seem so apparent owing to its much smaller specific capacity. In order to be evaluated against Li⁰ metal, these capacities have to be recalculated by considering the molecular weight of the whole species involved, such as

$$C_{\text{GR}}^s = \frac{0.2778}{M_{\text{C}_6\text{Li}}} z_{\text{GR}} F = \frac{0.2778}{78.95} \times 96485.33 = 339.50 \text{ mA h g}^{-1} \quad (9.94)$$

$$C_{\text{Si}}^s = \frac{0.2778}{M_{\text{SiLi}_{4.4}}} z_{\text{Si}} F = \frac{0.2778}{58.66} \times 4.4 \times 96485.33 = 2010.50 \text{ mA h g}^{-1} \quad (9.95)$$

Now these numbers make much better sense, and can be compared with the 3856 mA h g^{-1} for Li^0 metal. Note that since each silicon atom must accommodate so many lithium atoms, the overall mass of the eventual lithiated state more than doubles, and the specific capacity correspondingly is halved from 4199 to 2010 mA h g^{-1} .

The “take-home message” of this section is that when one wants to compare the specific capacities of different single-electrode materials, attention must be paid to ensure that these specific capacities were calculated from the same standard, no matter whether it is “entire molecular weight” or “container-only”.

In a broader sense, the same discretion should be exercised when evaluating the capacities reported in the literature, which have been calculated on diverse standards for different purposes. Some count only the mass of a single electrode and hence are only valid to evaluate a new material when its full cell configuration remains unknown, some count the masses of both the cathode and anode while ignoring the “inert” masses of the electrolyte, separator and cell packaging materials, and some count the entire cell masses that include everything.

9.1.3.7 Energy Quality

In Section 9.1.3.5, we mentioned that the energy involved in an electrochemical device is determined by both capacity and cell voltage [eqn (9.59)], which is realized by the electric work done by a charge travelling across the potential difference. In a visual manner, such energy could be represented by the area enclosed by the curves in Figure 9.5.

This leads to the question of whether, given the fixed amount of energy, it matters at what voltage the energy is delivered. The answer is yes, and this leads to the concept of “*energy quality*”, which describes, in general, the efficiency for one form of energy to be converted to useful work or another form of energy.

With a given amount of energy, the voltage at which the energy is delivered is an important parameter that determines what applications a battery can be used for. This could be easily understood by analogy with either hydraulic energy delivered at various water-level differences or thermal energy delivered at various temperature differences: the smaller these differences are, the less useful the energy is. Thus, at higher water-level differences, water flows faster, and has a much greater impact on the blades of the turbine, while water-level differences below a certain value would fail to push the turbine (Figure 9.7). Likewise, the efficiency in various heat engines also

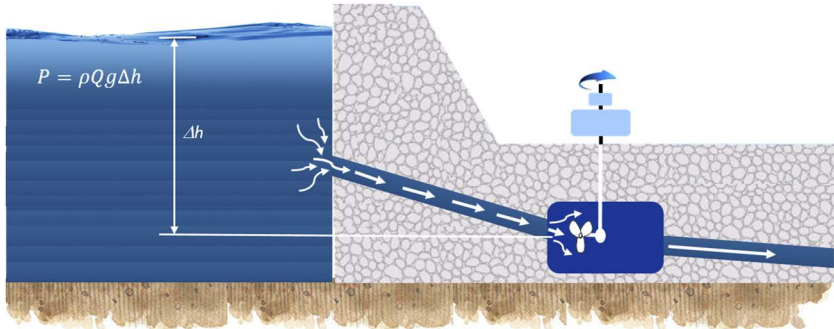


Figure 9.7 The energy quality describes the efficiency of converting one form of energy into another form or doing useful work. In hydroelectric power generation, the quality of the energy released by a water reservoir is proportional to the difference in water levels (“hydraulic head”, Δh), which is a critical factor to drive the load, and is closely analogous to temperature differences (ΔT) in thermal energy or potential (voltage) differences (ΔV) in electric energy. Energy quality is also directly associated with how fast the energy can be available (i.e. power) from the system.

directly relies on the temperature difference, as described quantitatively by the Carnot limit in thermodynamics.

For electric energy, if one uses it to drive a load of fixed resistance R , the effect of voltage is best reflected in the *power* (P), defined as the energy released in unit time:

$$P = \frac{dE}{dt} \quad (9.96)$$

From eqn (9.60), we have

$$dE = Vdq \quad (9.97)$$

Hence

$$P = \frac{dE}{dt} = V \frac{dq}{dt} = Vi \quad (9.98)$$

where i is current, defined in Section 5.2 as the quantity of charge passing through unit area in unit time [eqn (5.45)]. According to Ohm’s law:

$$i = \frac{V}{R} \quad (9.99)$$

which turns eqn (9.98) into

$$P = \frac{V^2}{R} \quad (9.100)$$

Thus, the usefulness of a battery in powering a load such as an electric motor is particularly sensitive to its voltage. Examples include electric lawn mowers and blowers, where the rpm of the motor cannot be sustained when the battery voltage is below a certain level, or electric vehicles, where banks of batteries have to be connected in series to generate an output voltage of at least 300 V.

Huggins proposed a rough energy quality quantification for batteries, in which he ranked those delivered below 1.5 V as low quality, those between 1.5 and 3.0 V as medium quality and those at 3.0 V and above as high quality.⁴ While most commercial lithium-ion batteries can deliver energy at a nominal 4.0 V, active research has been conducted seeking 5 V class chemistries.

In high-voltage batteries, the electrolytes play a critically important role, because they must not only support the mass transport of needed chemical species in the bulk, but must also withstand such high electrochemical stress without decomposing.

The severity of such electrochemical stress caused by high voltages can be exemplified by the Tafel behavior discussed in Section 6.5.5.3, where we demonstrated that any increase in overpotential could trigger an exponential increase in current. It is under such electrochemical stress that high-voltage electrolytes must remain inert, which has to be realized through the formation of interphases on both electrodes.

9.1.3.8 Battery Chemistries: Conversion Reaction vs. Intercalation

Since Alessandro Volta invented the very first battery in 1799, numerous chemistries have been employed to harness the energy held therein; however, despite the diverse chemistries, whether primary or rechargeable, and no matter whether they are aqueous or non-aqueous in nature, we can divide all of them into just two categories: *conversion reaction* and *intercalation*.

Before the invention of lithium-ion batteries, *most battery chemistries were based on the conversion reaction type* (Figure 9.8a), in which the structure of the electrode is replaced with a new structure during the cell reaction. The advantage of such chemistries is obviously the high capacity and energy associated with the reactions, because every

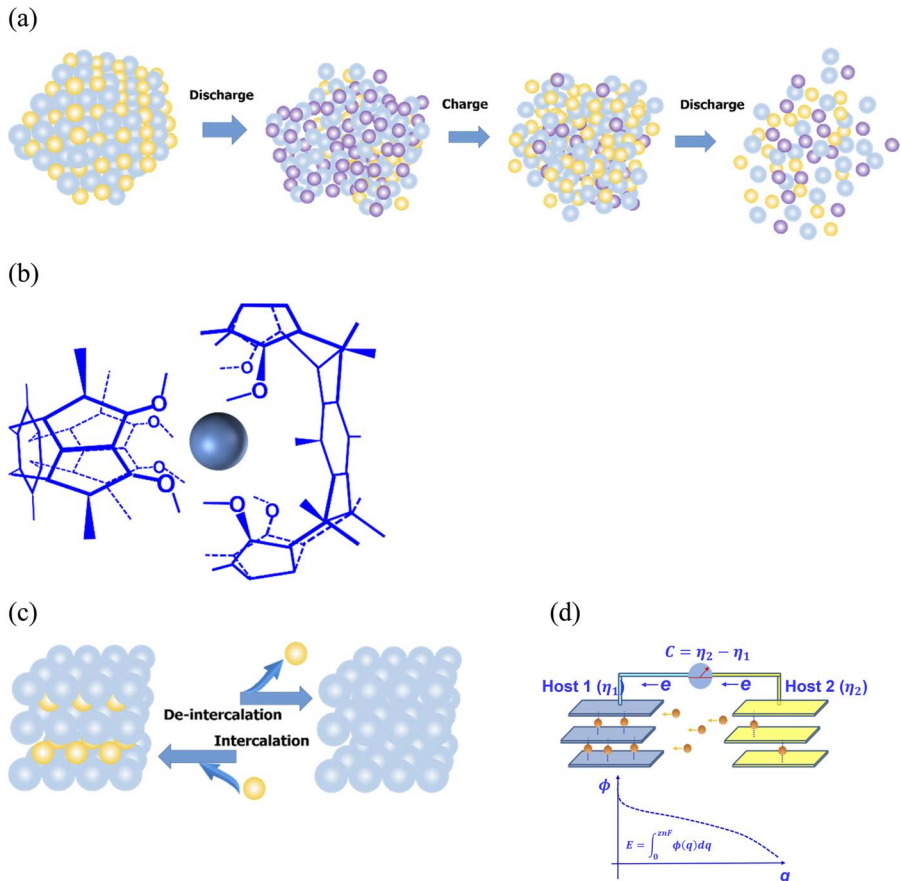


Figure 9.8 The two basic types of battery chemistries. (a) Conversion reaction type, where the electrode structures experience complete destruction and re-formation, hence the reversibility is poor. (b) A typical host-guest complex consisting of a guest cation trapped in a chelation cage formed by an ether-based supermolecular structure. (c) Intercalation reaction, where the scaffold structures of the host electrodes experience little change as the guest ion intercalates into or de-intercalates from the host. In intercalation chemistry, the redox reactions occur on the host, while the entry and exit of the guest ions cooperate to ensure the balance of charge. (d) The dual-intercalation cell design proposed by Armand in 1980, which was later adopted in lithium-ion batteries. In the 1980s, no anode intercalation host was available, owing to the absence of key knowledge on electrolytes and interphases.

component participates in the cell reaction. The disadvantage is their reversibility, which becomes a “fatal” weakness if one wants to recharge such batteries. Since the original structure of the electrode has been entirely destroyed, it is almost impossible to restore the original structure precisely by putting every component back to their original location. Such irreversibility occurs during every charge-discharge cycle, whose accumulation over the time leads to complete failure of the chemistry (Figure 9.8a).

Examples of conversion reaction chemistries include that of the Daniell cell and all metallic anode materials such as Li^0 .

The other type of battery chemistry is *intercalation*, in which the basic electrode structures remain relatively static (“*topotactic*”) during the redox reactions, while the charge separation is created by the intercalation of guest ions in the scaffold of the electrode hosts (Figure 9.8c).

Intercalation electrode chemistry can be considered a natural electrochemical extension of the so-called “*host-guest chemistry*” concept that emerged in the 1960s. The core concept of host-guest chemistry is that new properties and functions emerge following the association between host molecule and guest molecule, while such properties and functions could be reversible provided that the bonding between the host and guest is non-covalent in nature (Figure 9.8b). In other words, the bonding involved in the host-guest chemistry is mainly *via* Coulombic force, hydrogen bonding or van der Waals force. The supermolecular structure thus formed dictates both the properties and the reversibility of the host-guest complexes, as exemplified by molecules as simple as crown ethers or as complex as enzymes. For their trailblazing work in host-guest chemistry, Cram, Lehn and Pedersen were awarded the Nobel Prize in Chemistry in 1987.⁵

As the electrochemical version of host-guest chemistry, an intercalation electrode is actually a host attached to an electrode, so that the entry and exit of the guest species, often an ion, can be quantitatively and reversibly controlled *via* the electrons injected or withdrawn *via* the electrodes. Apparently, the reversibility of such electrode chemistries should be much superior to that of the conversion reaction type, because the changes in electrode structures are confined to a minimum, in strong contrast to the conversion reactions where severe phase and lattice changes in each cycle of charging and discharging occur accompanied by destruction and re-formation of chemical bonding.

However, the excellent reversibility of intercalation chemistries come at the expense of the specific capacity and energy density, as

these inert scaffold lattices do not participate in the cell reaction, and introduce certain “penalties”.

While the earliest application of the intercalation concept on electrodes was achieved by Whittingham in 1976 with the demonstration of a layer-structured chalcogenide, lithium titanium disulfide (LiTiS_2),⁶ and improved by Goodenough and co-workers in 1980 by switching from sulfides to oxides,⁷ the test batteries they built were actually hybrid in nature, as the anode used therein was still lithium metal, Li^0 , which is a conversion reaction by nature. In other words, the excellent reversibility anticipated from intercalation chemistries could not be unlocked owing to the presence of conversion reaction materials in the cell.

The initial *dual-intercalation battery* concept was proposed by Armand in 1980 (Figure 9.8d),⁸ and represented the exact configuration of lithium-ion batteries used nowadays, in addition to many other metal-ion batteries under development since the 2000s, including sodium-ion and magnesium-ion batteries. The foundation for such dual-intercalation chemistry is that one must find two intercalation hosts, which, upon intercalating a guest ion, must display electrode potentials sufficiently different from each other that a meaningful battery could be created. However, in the 1980s, most intercalation materials known were transition metal chalcogenides or oxides, the potential differences of which are not large enough to make such dual-intercalation batteries meaningful, while the graphite host intercalated with Li^+ (LiC_6), although known since the 1950s, could not be synthesized *via* electrochemical means at the time. Hence such innovative design could only remain on the drawing board. It took decades of efforts by numerous scientists and engineers to finally produce a carbonaceous anode host for Li^+ , which led to the commercialization of lithium-ion batteries in the early 1990s by Sony. In such processes, the knowledge of the correct electrolytes and the interphase chemistries on the anode surface constitutes the key knowhow.

The typical intercalation chemistries currently used in lithium-ion batteries include cathodes based on transition metal oxides such as LiCoO_2 or its homologs with similar layered structures, and carbonaceous anode materials with varying graphitic contents. Li^+ accommodated in those crystalline structures could generate a potential difference in the range 3.5–5.0 V, which is characterized with excellent reversibility, as represented by a cycle life of up to thousands of times.

As the first battery employing dual-intercalation chemistry, the lithium-ion battery has changed our lives significantly since the 1990s. Its invention was recognized in 2019 by the award of the Nobel Prize in

Chemistry to Whittingham, Goodenough and Yoshino. Yoshino was responsible for integrating the cathode, anode and electrolyte into a working cell in the mid-1980s at Asahi Kasei, although at the time the anode was still amorphous carbon with a negligible degree of graphitization, owing to the lack of knowledge on the interphasial chemistry between the electrolyte and graphite.⁹

Three decades after the emergence of the first-generation lithium-ion batteries, the capacities and energy densities of intercalation chemistries seem to be approaching their ceilings. Hence conversion reaction-type materials are being more and more frequently revisited by researchers pursuing next-generation battery chemistries with higher performances, in the hope that their intrinsic reversibility issue could be resolved with the new knowledge, tools and techniques achieved in the areas of nanostructure, *in situ/operando* characterization and electrolytes and interphases.

9.1.4 Pseudo-capacitors

In Sections 9.1.1–9.1.3 we covered two major classes of energy storage devices, electrochemical double-layer capacitors that operate exclusively with non-Faradaic processes at two-dimensional interfaces, and batteries and fuel cells that operate exclusively with Faradaic processes in the three-dimensional structure of the electrode materials.

Whereas the three-dimensional nature of Faradaic reactions would be most apparent in batteries, for fuel cells this characteristic may seem less obvious, as the electronation and de-electronation reactions of oxygen and fuels occur in the triphasic region involving liquid (electrolyte), solid (inert electrode substrate) and gas (electrode active materials), which appear to be two-dimensional in nature also. However, one must remember that the actual electrode materials here are oxygen and hydrogen gases (or other fuels). Complete consumption of these electrode materials, of course, mandates that the redox reactions proceed deep into the interior of both materials.

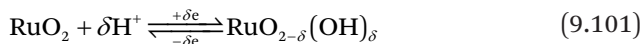
Between these two extremes of *two-dimensional non-Faradaic capacitance behavior* and *three-dimensional Faradaic behavior*, there is an intermediate class of electrochemical devices, which operate on Faradaic reactions to generate or store energy, but all of these Faradaic charge-transfer processes are confined to the two-dimensional interfaces between electrode and electrolyte (or at least “near” such interfaces), without penetrating the bulk of the electrodes. Such behavior is called *pseudo-capacitance*.¹⁰ Since the electronation and

de-electronation of species therein are confined to the electrode surface, such reactions are also referred to as “*quasi-two-dimensional reactions*”.

As an intermediate between typical capacitance and Faradaic behaviors, pseudo-capacitance displays an array of properties with mixed characteristics derived from the two. On the one hand, the power density (up to 10^3 W kg^{-1}) and reversibility (up to 10^5 cycles) of pseudo-capacitors are similar to those of electrochemical double-layer capacitors (10^4 W kg^{-1} and 10^6 cycles) thanks to the two-dimensional nature of the reactions; on the other, their energy densities ($>10 \text{ W h kg}^{-1}$) enabled by the Faradaic process are somewhat higher than those of electrochemical double-layer capacitors, but still far below what batteries can achieve.

However, based on the electrochemical signatures to be discussed in the next section, the pseudo-capacitance bears a much higher resemblance to capacitance than a typical battery, such as a rectangular cyclic voltammogram and sloping linear galvanostatic responses.

The nature of the redox reactions involved in pseudo-capacitance depend on the electrode materials and the electrolyte. Most pseudo-capacitors function in acidic aqueous electrolytes, and usually operate with the protonation/de-protonation of certain noble metals, such as platinum (Pt) or gold (Au), or oxides based on transition or noble metals, such as manganese (MnO_2), titanium (TiO_2) or ruthenium (RuO_2). Such reactions normally involve only a monolayer or quasi-monolayer of these oxides. A typical example of this class is RuO_2 , the reversible protonation of which generates a specific capacitance of $200\text{--}400 \text{ F g}^{-1}$ (compared with $150\text{--}200 \text{ F g}^{-1}$ for pure double-layer capacitance):



The majority of pseudo-capacitance relies on the charge-transfer process in a conversion reaction manner. However, the emergence of nanostructured materials in recent decades has gradually obscured the demarcation between bulk and surface, and hence transformed certain typical intercalation reactions into pseudo-capacitance. The most notable example is the flagship intercalation compound for lithium-ion batteries, LiCoO_2 , whose intercalation sites for Li^+ that were originally located within the layered structure become surface adsorption sites for Li^+ if the surface area of the LiCoO_2 is sufficiently large, while its electrochemical behavior experiences a corresponding shift towards pseudo-capacitance.

In order to differentiate such pseudo-capacitance from the “*intrinsic pseudo-capacitance*” demonstrated by the reversible protonation of RuO₂ as shown in eqn (9.101), which is independent of the particle size of the materials, some researchers called it “*extrinsic pseudo-capacitance*”, which becomes available only when the surface area of the materials is sufficiently large that these bulk intercalation sites become surficial.

Finally, an effort should be made to clear up the confusion caused by the use of semantics.

A rather vague but very popular term, “*supercapacitor*” or “*ultracapacitor*”, often appears in the scientific literature and also popular media to describe either electrochemical double-layer capacitors or pseudo-capacitors, or both. The initial purpose of coining such a term was to differentiate these capacitors from the more traditional *dielectric capacitors* (also known as *electrostatic capacitors*), which rely on dipole orientations in dielectrics to achieve energy storage, very similar to what was described in Figure 3.2. The energy densities available from such partial charge separations are significantly lower than those from either electrochemical double-layer capacitors or pseudo-capacitors ($\sim 1.389 \times 10^{-3}$ W h kg⁻¹), but they can deliver such energy on a much shorter time scale ($\sim 10^{-6}$ s) at much higher voltages (10^2 – 10^3 V), in comparison with $\sim 10^{-3}$ s and 1–3 V for electrochemical double-layer capacitors and pseudo-capacitors.

Since dielectric capacitors involve no electrochemical reactions or processes, they are beyond the scope of this book.

9.1.5 Comparison and Transition Between Capacitors and Batteries

Previously, we compared the energy contained in a battery with the energy held by a *huge* body of water, the *nearly infinite volume* of which ensures that the difference between water levels (Δh) remains almost constant during the flow of the water (Figure 9.7). As mentioned in Section 9.1.3, the almost constant cell voltage of a battery is enabled by the constant eigenpotential of each electrode material, which is determined solely by the chemical nature of the material and is independent of the amount of the electrode materials. Therefore, *the cell voltage (ΔV) and charge quantity (Q) are decoupled from each other*:

$$\Delta V = \text{constant} \quad (9.102)$$

while the energy contained in such a battery (E_B) is expressed as

$$E_B = Q \times \Delta V \quad (9.103)$$

In fact, both eqn (9.102) and (9.103) have been expressed in different forms in the preceding sections. Here we will retain these simpler forms for the convenience of discussion in this section.

From a similar perspective, the appropriate analog for electrochemical double-layer capacitor should be a water reservoir of *finite volume*, where the water level *constantly changes* with the amount of water in the tank (Figure 9.9a). As mentioned in Section 9.1.2, in this case the cell voltage is proportional to the quantity of charges separated. In other words, *the cell voltage and charge quantity are coupled together*:

$$\Delta V = k \times Q \quad (9.104)$$

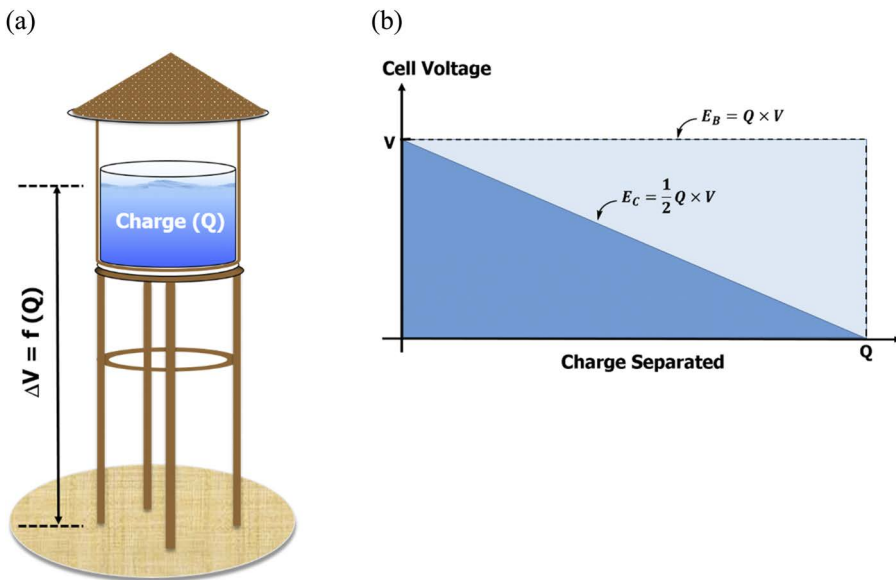


Figure 9.9 (a) The energy stored in electrochemical double layers is similar to the potential energy contained in a body of water that is of finite volume, because the potential difference between the two electrodes (ΔV) incurred by the charge separation is a function of the quantity of charge separated (Q), just like the height of the water level Δh varying with the volume of water. (b) With an identical quantity of charge Q separated at an identical voltage V , the energy held in an electrochemical double-layer capacitor is half of that held in a battery.

which is actually a variation of eqn (6.32), and k is the reciprocal capacitance ($1/C$). Therefore, the energy contained in such an electrochemical double-layer capacitor (E_C) is given by

$$E_C = \int_0^Q V(Q) dQ = \int_0^Q \frac{Q}{C} dQ = \frac{1}{2C} Q^2 \quad (9.105)$$

Inserting the expression of Q from eqn (9.104):

$$Q = C \times \Delta V \quad (9.106)$$

we will have the energy of the electrochemical double-layer capacitor when a quantity of charge Q is separated at a cell voltage ΔV :

$$E_C = \frac{1}{2C} (C \times \Delta V)^2 = \frac{1}{2} C \times \Delta V^2 \quad (9.107)$$

which, in fact, has already been encountered as (eqn (9.24)) in Section 9.1.2.2. We can further transform eqn (9.107) by expressing the energy E_C as a function of only amount of charge Q and cell voltage ΔV by replacing the capacitance C with

$$C = \frac{Q}{\Delta V} \quad (9.23)$$

Then the energy E_C becomes

$$E_C = \frac{1}{2} \frac{Q}{V} \times \Delta V^2 = \frac{1}{2} Q \times \Delta V \quad (9.108)$$

What can we extract from eqn (9.103) and (9.108)? They indicate that, under ideal conditions, with an *identical quantity of charge* Q separated at an *identical potential difference* ΔV , the energy held by an electrochemical double-layer capacitor is only *half* of that held by a battery. In other words, if the battery energy can be represented by the area of a square in the plot of cell potential *versus* capacity (V - Q plot) as shown in Figure 9.9b, then the capacitor energy should be the area of a triangle that halves the square.

Furthermore, the actual quantity of charge separation in an electrochemical double-layer capacitor is, more often than not, far smaller than that separated in a battery at the same potential difference.

For example, let us consider a typical aqueous electrochemical double-layer capacitor consisting of two identical activated carbon

electrodes, each with a specific surface area of $1000 \text{ m}^2 \text{ g}^{-1}$ and a specific capacitance of $20 \mu\text{F cm}^{-2}$. If one polarizes such a capacitor at 1.5 V, then the charge separated at a single electrode should be (remembering that by definition of capacitance *1 farad* is *1 coulomb per volt*, 1 C V^{-1}):

$$\begin{aligned} Q &= C \times V = 20 \times 10^{-6} \text{ CV}^{-1} \text{ cm}^{-2} \times 1000 \times 10^4 \text{ cm}^2 \text{ g}^{-1} \times 1.5 \text{ V} \\ &= 300 \text{ Cg}^{-1} \end{aligned} \quad (9.109)$$

Recalling eqn (9.63) to convert coulombs into mA h:

$$Q = 300 \times 0.2778 \text{ mA h g}^{-1} = 83 \text{ mA h g}^{-1} \quad (9.110)$$

This is for a single electrode, while the overall charge separation for the capacitor should be $\sim 40 \text{ mA h g}^{-1}$ of cell. If such an electrochemical double-layer capacitor can be polarized to 3.0 V, which is the maximum potential that an electrochemical double-layer capacitor could approach in non-aqueous electrolytes, then the charge separation is 166 mA h g^{-1} , which is comparable to but still lower than those of most battery electrodes.

Meanwhile, the charge separated in battery electrodes, if measured on single electrodes, is usually on the order of $100\text{--}200 \text{ mA h g}^{-1}$ for cathodes and $372\text{--}1000 \text{ mA h g}^{-1}$ for anodes. According to the coupled relation between cathode and anode capacities [eqn (9.80)], the overall charge separation (or, as often called in the battery community, capacity) for a battery should be in the range $80\text{--}160 \text{ mA h g}^{-1}$ of cell. Thus, even in the most favored situation for capacitors, the constant voltage of the battery ensures twice as much energy.

Because of the combination of the above factors, a battery usually contains much more energy than an electrochemical double-layer capacitor.

9.1.5.1 Electrochemical Signatures of Capacitance and Faradaic Reactions: Cyclic and Linear Voltammetry

The fundamental difference between the behaviors of batteries and capacitors, as exemplified by their distinct $V\text{-}Q$ plots (Figure 9.9b), serves as the root of their characteristic responses to certain electrochemical stimulations. Such responses are often used as unique signatures to identify whether a particular electrochemical process behaves more like a battery or an electrochemical double-layer capacitor.

The most frequently used electrochemical characterization techniques consist of two main categories: (1) one that controls the

current, by either keeping it constant (called *galvanostatic*) or varying it at a constant rate (called *galvanodynamic*), while monitoring the potential response; and (2) one that controls the electrode potential, by either keeping it constant (called *potentiostatic*) or varying it at a constant rate (called *potentiodynamic*), while monitoring the current response.¹¹

In the former category, galvanostatic characterization is often used to measure quantities such as charge separation (capacity) and energy under a *constant charge or discharge current*. This is a favored method because it simulates real application scenarios where these electrochemical energy devices are used to drive a load of fixed resistance.

In galvanostatic charge and discharge tests, one often plots the change of cell voltage (V) against the capacity (Q) involved, as already demonstrated by the V - Q plots for both a battery and an electrochemical double-layer capacitor in Figure 9.9b. Of course, when the current is non-zero, the cell polarization induced by kinetic barriers in charge-transfer and mass-transport processes would deform the standard rectangular or triangular shapes in Figure 9.9b. The effect of such polarization was shown schematically in Figure 9.5 for a battery, and a similar effect is expected for a capacitor, with the actual cell voltage departing negatively from the ideal straight line during discharge and an accessible capacity lower than that predicted theoretically.

In the latter category, potentiodynamic characterization is more useful than potentiostatic characterization, because it can determine the precise potential for a certain electrochemical process to occur, be it a redox reaction in an electrode or an irreversible decomposition reaction of the electrolyte. In this method, the potential of a working electrode (V_{WE}) is gradually changed against that of a reliable reference electrode:

$$V_{\text{WE}} = V_{\text{WE}}^i \pm rt \quad (9.111)$$

where V_{WE}^i is the initial potential of the working electrode, r the scanning rate (in V s^{-1}) and t the time and the \pm sign indicates whether the direction of scan is anodic (+) or cathodic (-). Under this quasi-equilibrium condition, the occurrence of the investigated reaction would be indicated by the level of current.

Sometimes, the potential change of the working electrode is one way only, from the initial potential V_{WE}^i to terminal potential V_{WE}^t , and the method is called *linear sweep voltammetry* (LSV). In other cases, the potential of the working electrode would be brought back to its

original value V_{WE}^0 after reaching a vertex value, and the method is called *cyclic voltammetry* (CV). CV is very useful for determining how reversible a reaction is.

In both potentiodynamic and potentiostatic characterizations, current or current density (i) is plotted against the electrode potential (V_{WE}). In such i - V plots, as with V - Q plots, the non-Faradaic nature of a capacitor and the Faradaic nature of a battery would generate completely different responses.

For an electrochemical double-layer capacitor, the current response by definition is

$$i = \frac{dQ}{dt} \quad (9.112)$$

Since the charge separation quantity Q is determined by the capacitance of the electrode C_e via

$$C_e = \frac{Q}{V_{\text{WE}}} \quad (9.113)$$

We have

$$i = \frac{d(C_e V_{\text{WE}})}{dt} = C_e \frac{dV_{\text{WE}}}{dt} \quad (9.114)$$

Suppose the potential scan direction is anodic, therefore

$$\frac{dV_{\text{WE}}}{dt} = r \quad (9.115)$$

Hence

$$i = C_e \frac{dV_{\text{WE}}}{dt} = C_e r \quad (9.116)$$

At a constant scanning rate r , the current response should be a constant that is proportional to the electrode capacitance and scan rate but independent of the electrode potential V .

Of course, here a hidden assumption is that the scanning is conducted within the electrochemical stability window of the electrolyte.

Thus, in an i - V plot, the current response from a standard electrochemical double-layer capacitor is just a straight line parallel to the V -axis and located at $C_e r$ (Figure 9.10). By measuring the current i , one

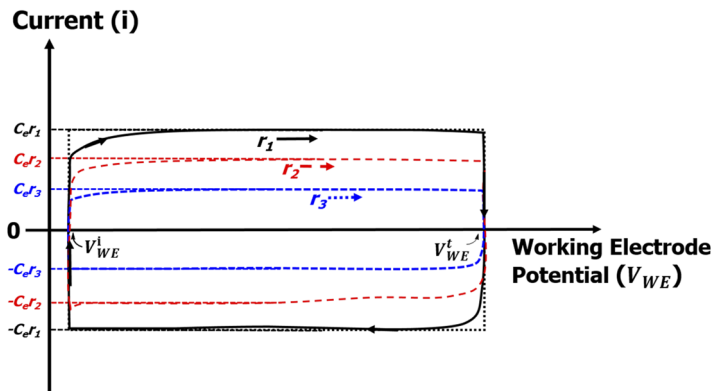


Figure 9.10 The electrochemical signatures of non-Faradaic capacitance under potentiodynamic conditions (cyclic voltammetry with an initial potential of V_{WE}^l and a terminal potential of V_{WE}^t). The arrows on the plots indicate the directions that the electrode potential is scanned.

can easily calculate the electrode capacitance because the scanning rate r is a known experimental parameter.

If cyclic voltammetry is applied, the complete potentiodynamic scanning consists of both anodic and cathodic progressions. Thus, in cathodic scanning, the corresponding current response would be

$$i = C_e \frac{dV_{WE}}{dt} = -C_e r \quad (9.117)$$

which is, of course, another straight line parallel to the V -axis but now located at $-C_e r$ (Figure 9.10).

Combining eqn (9.116) and (9.117), the standard i - V plot of an electrochemical double-layer capacitor in cyclic voltammetry should be shaped like a closed rectangle (Figure 9.10), with the length of the vertical side being $2C_e r$.

Note that the most interesting feature of such an i - V plot is that, at the terminal potential V_{WE}^t , the current would immediately vanish to zero, and upon reversing the direction of the voltage scanning, the current would immediately become $-C_e r$. This reflects the nature of the charge separation realized on a 2D surface: as soon as the electrode potential ceases to increase, the assembly of ionic species at the surface stops, causing the anodic current $C_e r$ immediately to drop to zero, whereas as soon as the electrode potential starts to decrease, the separated ionic charges at the electrode surfaces are released, producing the cathodic current $-C_e r$.

In reality, such a perfect rectangle would be deformed owing to various kinetic factors. However, since all of the current response in an electrochemical double-layer capacitor arises from non-Faradaic processes, *i.e.* pure electrostatic charge separation *via* ionic assemblies at the electrode surfaces, the processes are independent of charge transfers across the interfaces. Therefore, even under the non-equilibrium condition of non-zero current, the i - V plots of most electrochemical double-layer capacitors are still capable of maintaining a rectangular-like shape, with minimal departures from the ideal rectangle as predicted by eqn (9.116) and (9.117).

For a battery electrode, or any electrode that experiences a Faradaic process, the current response is much more complicated, because it is subject to both charge transfer across the electrode/electrolyte interfaces and mass transport within the bulk of the electrolytes, as depicted schematically in Figure 7.1a.

Let us consider an oxidation reaction that occurs on a working electrode at an equilibrium potential φ_e^0 , which could be considered the eigenpotential of the electrode material, or some other species in the electrolyte that is oxidized at the electrode surface:



If the voltammetric scan starts at an initial potential (V_{WE}^i) that is more negative than φ_e^0 , then there was only a negligible anodic current (called *background current*) corresponding to the above reaction, as seen in zone I in Figure 9.11. With the positively progressing potential approaching φ_e^0 , obvious oxidation of $[R]$ at the electrode surface starts, indicated by the rising anodic current in zone II. Such an anodic current is expected to increase further as the electrode potential goes beyond φ_e^0 , as predicted by the Tafel behavior [eqn (6.98)]. On the other hand, however, the increasingly rapid consumption of reactant $[R]$ or accumulation of product $[O]$ at the interface eventually brings in the restriction by mass transport, which sets a limit on the exponential increase in reaction rate (current) and slows the reaction.

The compromise of these two competing factors leads to the appearance of a peak in the current in zone III. In other words, the maximum current (often denoted i_p in the literature, where p stands for “peak”) is the result of charge-transfer rate determined by the Butler–Volmer equation at the interfaces and the mass transport from the bulk electrolyte to the interfacial region determined by Fick’s laws.

In most potentiodynamic experiments, the scan rate r in eqn (9.111) is slow enough (usually on the scale of 10^{-3} V s $^{-1}$) for us to assume

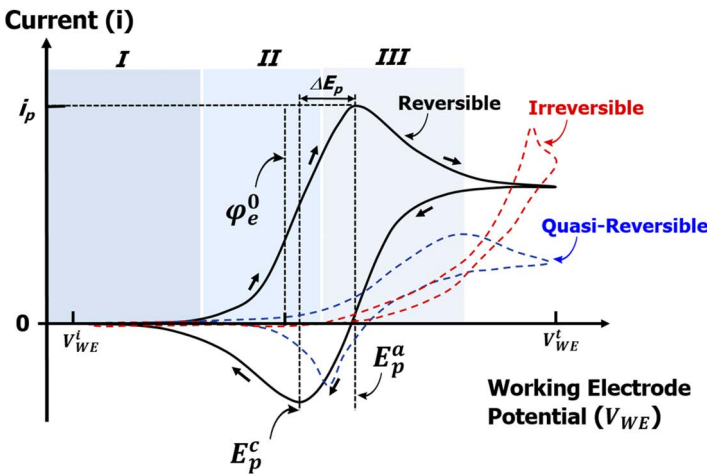


Figure 9.11 The electrochemical signatures of non-Faradaic capacitance versus Faradaic battery behaviors under potentiodynamic conditions (cyclic voltammetry with an initial potential V_{WE}^t and terminal potential V_{WE}^t). The arrows on the plots indicate the direction of the electrode potential.

that all Faradaic processes occur at near equilibrium; therefore, for simplicity, we can directly apply the Nernst equation to the activities in zone II:

$$V_{WE}^t - \varphi_e^0 = \frac{RT}{nF} \ln \frac{c_{[O]}}{c_{[R]}} \quad (9.119)$$

where $c_{[O]}$ and $c_{[R]}$ are the concentration of reactant and product at the interface, respectively. Recalling eqn (9.111) for the anodic scenario, and rearranging the above equation to express the concentration ratios of [O] and [R], we obtain

$$\frac{c_{[O]}}{c_{[R]}} = e^{\frac{nF}{RT}(V_{WE}^t - \varphi_e^0)} = e^{\frac{nF}{RT}(V_{WE}^t + rt - \varphi_e^0)} \quad (9.120)$$

At each electrode potential, in the infinitesimally small time interval, the concentrations of these species are related to their corresponding concentrations in the electrolyte bulk by the following initial conditions:

$$c_{[O]}(x, 0) = 0 \quad (9.121)$$

$$c_{[R]}(x,0) = c_{[R]}^0 \quad (9.122)$$

and boundary conditions:

$$c_{[O]}(\infty, t) = 0 \quad (9.123)$$

$$c_{[R]}(\infty, t) = c_{[R]}^0 \quad (9.124)$$

where $c_{[R]}^0$ is the concentration of [R] in the bulk electrolyte. These initial and boundary conditions actually correspond to the potentiostatic scenario that was briefly discussed in Section 7.2, except that here the potential is not exactly constant, but constantly changing. Nevertheless, we can still approximately assume that at each infinitesimally small time interval the electrode sits at a constant potential, and all species obey the above initial and boundary conditions.

The differential equations derived from Fick's second law under these initial and boundary conditions can only be solved numerically; the details of which will not be covered here but can be found, for example, in the book by Bard and Faulkner.¹¹ The general form of the peak current i_p is thus given as

$$i_p = 0.447 nF A c_{[R]}^0 \sqrt{\frac{nFD_{[R]}r}{RT}} \quad (9.125)$$

where A is the electrode area and $D_{[R]}$ the diffusion constant of [R] in the bulk electrolyte. The maximum current i_p is proportional to the reactant concentration in the bulk electrolyte $c_{[R]}^0$ and square root of scanning rate r . Eqn (9.125) is also known as the *Randles–Sevcik equation*.

If the above reaction is reversible, upon reversal of the potential scan the reduction of the formed [O] species would start. At this moment, the net current as measured in the i -V plots is actually a mixture of both anodic and cathodic currents due to these two competing reactions. Hence the net current continues to decrease as a result of the combined effects of both mass-transport limitation and the coexistence of anodic and cathodic reactions, which eventually produces a cathodic peak when the potential is sufficiently negative that the mass-transport limitation from [O] species emerges.

These responses render the characteristic shapes of the i -V plots in cyclic voltammetry, as represented by the solid curve in Figure 9.11.

The typical i - V plots in cyclic voltammetry obtained from various lithium-ion battery electrode materials in proper electrolytes, which we briefly discussed in Section 8.2.3 (Figure 8.3), demonstrated such basic symmetric behaviors with varying extents of variations.

The gap between the potentials for anodic and cathodic peaks, ΔE_p , is often used to quantify how reversible the Faradaic process is:

$$\Delta E_p = \frac{E_p^a - E_p^c}{2} = \frac{2.3RT}{nF} \quad (9.126)$$

which is independent of scanning rate r . At room temperature (298 K) and for single-electron reactions, this gap is 56.5 mV.

This gap could be smaller if the Faradaic process involves no mass-transport steps. Such scenarios include the reactant being insoluble and deposited on the electrode, therefore they are directly available without requiring diffusion from the bulk electrolyte to the interfacial region. Examples of these highly reversible reactions include electrode surfaces that are decorated with active species, or lithium deposition and stripping on an inert substrate.

It must be cautioned here again that, since eqn (9.125) and (9.126) were both derived from Fick's laws, *they hold true only under ideal electroanalytical conditions*, i.e. all ionic movements are purely by diffusion instead of migration. In practical battery electrolytes, especially lithium-based electrolytes, such requirements are difficult to meet, hence cyclic voltammetry is mostly used for *qualitative* rather than *quantitative* purposes, as exemplified by the numerous cyclic voltammetric curves in Figure 8.3, which are more useful in revealing at what potential certain Faradaic reactions start and whether they are reversible, rather than determining the concentration of reactant concentration or its diffusion coefficient.

One can see that the voltammetric responses for some electrodes or electrolyte materials in Figure 8.3 do not even have the maximum i_p , such as the cathodic section of graphite, silicon and lithium-metal electrodes. Instead, the current continues to increase until the terminal preset potential limit. This happens very often, because the high population of Li^+ in the electrolyte and the fast Li^+ conduction ensure that, under the experimental conditions employed (e.g. the cathodic limits where the electrode is polarized, the active material loading per unit area and the scan rate), the depletion of Li^+ because of a mass-transport shortage never occurs. Such a departure from the "ideal" behavior predicted by eqn (9.125) and (9.126) actually benefits practical applications.

Some Faradaic reactions are so sluggish that their reverse reactions need a much higher electrochemical driving force to start. Such a requirement for an excessive overpotential will be reflected in a much wider gap between the potentials for anodic and cathodic peaks (ΔE_p), and these processes are often referred to as “*quasi-reversible*” (Figure 9.11).

For completely irreversible reactions, such as the decomposition of electrolyte components on an electrode surface when the potential of the electrode goes beyond its electrochemical stability window, the current corresponding to the reverse reaction becomes negligible (Figure 9.11), and the peak current of such a decomposition process can be given as

$$i_p = 0.22nFAC_{[R]}^0 k_{app} e^{-\alpha \frac{nF}{RT}(E_p - E_0)} \quad (9.127)$$

Before we conclude this chapter, we should be aware that Faradaic (battery) and non-Faradaic (capacitance) behaviors, although distinct in their own electrochemical signatures in typical situations, are sometimes indistinguishable. On the one hand, as mentioned in Section 9.1.4, the high percentage of surface *versus* bulk in nanostructured materials obscures the Faradaic and non-Faradaic processes; on the other, the currents induced by capacitance exist in all batteries, as the electrodes in an electrochemical device inevitably have surfaces. In most situations, the current arising from the capacitance effect is negligible compared with that arising from Faradaic sources. However, this could change if the electrodes have especially high surface areas (unlikely in most batteries owing to interphasial considerations to be discussed in Chapter 12) or when the batteries are subject to especially high charging or discharging currents, because the capacitance current is proportional to the rate at which the potential of an electrode changes (Figure 9.10).

The techniques discussed above, galvanostatic (Figures 9.5 and 9.9) and potentiodynamic (Figures 9.10 and 9.11), are the two most popular characterizations used by researchers whenever a new material, be it electrode, electrolyte, interface or interphase, is examined for its potential application in energy storage. Therefore, although their quantitative foundations as expressed by the equations in this chapter may no longer exist for practical electrode or electrolyte systems, the electrochemical signatures described here are helpful in understanding new materials from a fundamental perspective.

References

1. J. O'M. Bockris and A. K. N. Reddy, *Modern Electrochemistry*, Plenum Press, New York, 2nd edn, 1998.
2. M. Winter and R. Brodd, What Are Batteries, Fuel Cells, and Supercapacitors?, *Chem. Rev.*, 2004, **104**, 4245–4270.
3. B. E. Conway, *Electrochemical Supercapacitors: Scientific Fundamentals and Technological Applications*, Springer, New York, NY, 1999.
4. R. A. Huggins, *Advanced Batteries: Materials Science Aspects*, Springer, New York, NY, 2009.
5. D. J. Cram, The Design of Molecular Hosts, Guests, and Their Complexes, *Science*, 1988, **240**, 760–767.
6. M. S. Whittingham, Electrical Energy Storage and Intercalation Chemistry, *Science*, 1976, **192**, 1126–1127.
7. K. Mizushima, P. C. Jones, P. J. Wiseman and J. B. Goodenough, Li_xCoO_2 ($0 < x < 1$): A New Cathode Material for Batteries of High Energy Density, *Mater. Res. Bull.*, 1980, **15**, 783–789.
8. M. B. Armand, Intercalation Electrodes, in *Materials for Advanced Batteries*, ed. D. Murphy, Plenum Press, New York, 1980, p. 145.
9. M. Winter, B. Barnett and K. Xu, Before Li Ion Batteries, *Chem. Rev.*, 2018, **118**, 11433–11456.
10. B. E. Conway, V. Birss and J. Wojtowicz, The role and utilization of pseudo-capacitance for energy storage by supercapacitors, *J. Power Sources*, 1997, **66**, 1–14.
11. A. J. Bard and L. R. Faulkner, *Electrochemical Methods. Fundamentals and Applications* Wiley, New York, 2nd edn, 2001.

10 Lithium-metal, Lithium-ion and Other Batteries

If a layperson casually skims scientific journals for battery-related literature, they will be surprised to see that over 99% of the work reported is more or less related to materials based on or containing lithium.

Despite being one of the three primordial elements formed within the first few minutes of the “*Big Bang*”, the abundance of lithium in our universe is rather low, in fact even far lower than the abundance of those heavier elements (carbon, oxygen, nitrogen, *etc.*) that require harsher conditions (nuclear fusion at the center of stars, supernova explosions, *etc.*) to be nucleosynthesized. The reserve of lithium in the Earth’s crust is not only very small, but also distributed in a very uneven manner. The richest lithium reserve is concentrated in a rather small triangular region intersected by the borders of Bolivia, Chile and Argentina, the so-called “*Lithium Triangle*”, which is blessed with myriads of salt lakes rich in lithium (Figure 10.1), among which *Salar de Uyuni* (salt flat of Uyuni) located in Bolivia is the largest. It is a giant salt lake with an area of 10 000 km² that is clearly visible on satellite photographs, with an estimated reserve of lithium ranging from 9 million to 100 million tons, accounting for 50–80% of the global reserve.¹ Although confined by industrial infrastructure as well as politics in the region, *Salar de Uyuni* remains underdeveloped, it undoubtedly holds the key to the energy future of the Earth, if no other emerging battery chemistries that contain no lithium can replace lithium-ion batteries in a timely manner. In addition, the *Atacama* salt flat in Peru and other smaller reserves in the USA, Russia, China and Australia

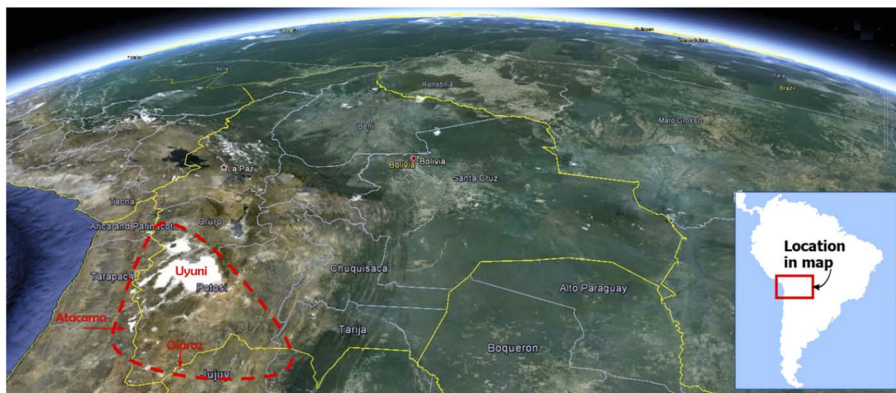


Figure 10.1 The “*Lithium Triangle*” region takes a prominent share in the global reserve of lithium, benefiting from myriads of salt lakes scattered in the region intersected by the borders of Bolivia, Chile and Argentina. Among them, Salar de Uyuni (salt flat of Uyuni) in Bolivia is the largest and remains little developed as of 2022.

feed the global lithium-ion battery and electric vehicle industries with most of the mined and processed lithium-containing raw materials (in the form of lithium carbonate, chloride and hydroxide).

So, what unique properties of lithium make it so attractive when researchers and others are contemplating potential battery chemistries?

10.1 Why Lithium?

There are two independent factors that contribute to making lithium the ultimate battery material, which are closely related to the two factors that dictate the energy of a battery.²

As we covered in Section 9.1.3.7, the energy that can be stored and delivered by a battery is determined by the cell voltage and capacity (Figure 9.5). Therefore, the first factor is the *electrode potential* of lithium metal.

In 1913, the electrode potential of lithium was first accurately measured using Li–Hg alloy (amalgam) by Lewis and Keyes, who found that, when coupled with a calomel reference electrode (+0.268 V vs. SHE), the cell produced 3.3044 V, “*the highest hitherto measured*”, which translates to a lithium potential of *ca.* −3.0364 V vs. SHE.³

The conclusion drawn by Lewis and Keyes remains true today, and it is not likely to change in the future, because among *all the known*

solid elements in the Periodic Table, there is no other element that has a lower electrode potential than lithium. A few exceptions exist, such as monovalent Ca^+ and Mg^+ cations, but these are not only in a form that is difficult to access as electrode materials (*i.e.*, not in solid form), but also, more importantly, they are extremely unstable intermediates that do not exist under normal conditions.

With the lowest electrode potential (or the highest *electropositivity* in thermodynamic terms), lithium serves as a very powerful anode, because when it is coupled with any given cathode, the cell would produce the highest cell voltage.

The second factor is the specific *capacity* of lithium metal. As we covered in Section 9.1.3.5, the overall cell specific capacity is related to the specific capacity of individual electrodes *via* eqn (9.79) or (9.80), where a high-capacity electrode on either side is desired.

For lithium metal, this specific capacity was already given by eqn (9.64) as 3856 mAh g^{-1} . Although it is not the highest capacity, because the highest is provided by Be [5948 mAh g^{-1} , eqn (9.67)], the even lower abundance and much higher toxicity of Be automatically disqualify it as a practical electrode material.

Hence lithium is the eventual “winner”.

The combination of these two factors, electrode potential and specific capacity, makes lithium the ultimate anode material that is impossible to replace. For this reason, lithium is often referred to as the “*Holy Grail*” by battery and materials scientists. However, as the term Holy Grail also implies, it is extremely difficult to harness the tremendous power held by lithium.

10.2 The Quest for the Holy Grail: Lithium-metal Batteries

Soon after lithium was recognized as the “most powerful” anode material, efforts were made to unlock its potential. However, people soon found that its most valuable advantage, the lowest electrode potential, is also its greatest problem, because such an extremely low electrode potential means extremely high activity in reacting with other materials.

Hence the high promise of energy density and the major challenge of stability are two sides of the same coin, that is, the extreme electrode potential of lithium metal. Thermodynamically speaking, lithium should be the most reactive metal to exist. And, in reality, nothing has been discovered that does not react with lithium metal. Even the

most inert organic compounds such as *n*-hexane react with Li⁰ and form a thin passivated layer on the surface.⁴

In the early days, it was the activity of lithium metal that made it difficult for researchers to find a suitable electrolyte, especially the electrolyte solvents, for any possible battery that contains a lithium-metal electrode.

Aqueous electrolytes are of course out of the question, because of the narrow electrochemical stability window defined by the oxidative and reductive decompositions of water (Figures 5.12 and 8.2). The same applies to all the non-aqueous but protic solvents, such as alcohols and amines. Furthermore, even solvents being both non-aqueous and non-protic cannot guarantee that lithium metal will remain stable. Examples include nitromethane and acetonitrile, the α -hydrogen of which, activated by strongly electron-withdrawing functionalities, becomes acidic enough for the strong Lewis base lithium metal.

Only with a limited number of *both non-aqueous and non-protic* solvents could lithium metal maintain its chemical stability. Examples include most ethereal solvents and a number of esters, especially the dialkyl esters of carbonic acid (Table 10.1). Studies much later found that even in those “stable” non-aqueous and non-protic solvents, lithium metal still reacts, but a process similar to surface passivation occurs there, preventing sustained reaction between lithium metal and the electrolyte solvents. Such stability is “*kinetic*” in nature, and is provided by the interphase that we will focus on later.⁵

The discovery of the non-aqueous and non-protic solvents led to the formulation of electrolytes that are chemically stable with lithium metal, and eventually enabled the commercialization of a few primary (non-rechargeable) lithium-metal batteries. These batteries, such as lithium thionyl chloride batteries, can still be found today in limited applications, such as wireless transponders for highway toll collection, and in military missions where the energy density (Wh kg⁻¹) far outweighs other concerns such as cost and the environment.

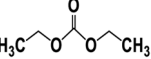
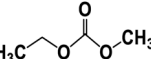
However, *the greatest challenge remaining is to make lithium-metal electrodes rechargeable.*

The *kinetic stability* between lithium metal and these non-aqueous and non-protic solvents is still static in nature, which is not difficult to achieve provided that the instantaneous reaction between Li⁰ and solvents produces an electronically insulating interphase, so that sustained reactions could be stopped.

However, a rechargeable electrode always produces new surfaces, which would then induce new reactions and new interphases. The continuous irreversible reactions on these newly exposed surfaces not

Table 10.1 Selected non-aqueous and aprotic solvents kinetically stable with lithium metal.

Solvent molecule	Structure	Molecular weight	Melting T _m (°C)	Boiling T _b (°C)	Viscosity η/ cP (25 °C)	Permittivity ε (25 °C)	Dipole moment (debye)	Density d/g cm ⁻³ (25 °C)
Dimethoxy ethane (DME)		90	-58	84	0.46	7.2	1.15	0.86
1,3-Dioxolane		74	-95	78	0.59	7.1	1.25	1.06
Tetraglyme		222.28	-30	275	3.29	7.78	2.60	1.009
Ethylene carbonate (EC)		88	36.4	248	1.90 (at 40 °C)	89.78	4.61	1.321
Propylene carbonate (PC)		102	-48.8	242	2.53	64.92	4.81	1.200
Vinyleno carbonate (VC)		86	20	170		126	4.51	1.35
Fluoroethylene carbonate (FEC)		106.05	18	212	4.1	78.4	4.97	1.454
Gamma-butyrolactone (γ BL)		86	-43.5	204	1.73	39	4.29	1.057

Dimethyl carbonate (DMC)		90	4.6	91	0.59 (at 20 °C)	3.107	0.76	1.063
Diethyl carbonate (DEC)		118	-74.3	126	0.75	2.805	0.96	0.969
Ethylmethyl carbon- ate (EMC)		104	-53	110	0.65	2.958	0.89	1.006

only induce the loss of active material (which is Li⁰ in this case), but more seriously constitute the underlying root of safety hazards.

This barrier originating from the extreme reactivity of lithium metal still stands between us and the “Holy Grail” as of 2022, despite the astronomical efforts and resources invested in addressing it.

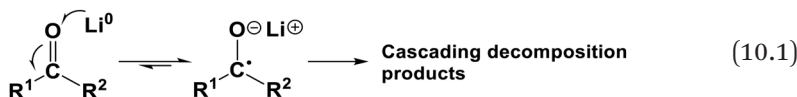
10.2.1 Irreversibility

As defined in Section 9.1.3.5.1, the most popular and simplistic descriptor used in electrochemistry for reversibility (or irreversibility) is *Coulombic efficiency* (CE%). It quantifies the fraction of charge that one can recover after injecting a certain amount of electric charge:

$$\text{CE\%} = \frac{\text{capacity released during discharging}}{\text{capacity injected during charging}} \quad (9.85)$$

For a reaction occurring at an electrode, there are various ways to determine CE%, including both voltammetry (by controlling the voltage) and galvanometry (by controlling the current), or their numerous variations such as coulometry and amperometry, the details of which will not be discussed here. One can again resort to *Electrochemical Methods. Fundamentals and Applications* by Bard and Faulkner (see ref. 43) to learn the specifics of these techniques. However, despite the diversity, the essence of each of these techniques focuses on how to count the charges in and out accurately.

For an electrodic reaction to be perfectly reversible, an ideal CE% should be 100%. However, owing to parasitic reactions, CE% is always less than that. In particular, the extreme reactivity of a lithium-metal electrode represents tremendous potential opportunities for such parasitic reactions, thus presenting the most severe challenge to CE%. In ester-based electrolytes, a lithium-metal electrode can only achieve a CE% in the region of 70–90%, because the carbonyl functionality (C=O) in esters is chemically reactive towards reducing agents such as Li⁰:



which has been the foundation for a series of well-known organometallic reactions.

Ethers are chemically less reactive with Li⁰, therefore ethereal-based electrolytes in general yield better CE% than their ester-based counterparts, somewhere above 90%.

However, as of 2022 when this chapter was written, with the most recent advances and innovations in electrolyte materials, interfacial chemistries, electrode architectures at atomistic scale, *etc.*, the highest CE% achieved for a lithium-metal electrode was still only 99.5%.⁶ Although this may appear to be a very high value, one must remember that a battery is a closed system (Section 9.1.3), and a lithium-metal battery is particularly so, owing to the high sensitivity of Li⁰ to ambient moisture and other impurities, hence the possibility of replenishing electrode active materials is essentially zero. In other words, any loss is permanent.

Hence for a rechargeable battery using a lithium-metal electrode in the best electrolyte available, each cycle of discharge (Li⁰ oxidation, or often called *stripping*) and charge (Li⁺ reduction, or often called *plating* or *deposition*) would suffer a 0.5% loss of Li. With the accumulation of losses over repeated cycles, the capacity of the cell would gradually fade. At the 100th cycle, such a battery would retain only *ca.* 60% of its original capacity:

$$(0.995)^{100} = 0.606 \quad (10.2)$$

Obviously, 99.5% is not good enough.

The state-of-the-art lithium-ion batteries, using graphite as anode intercalation host for Li⁺, can retain at least 80% of the initial capacity over thousands of cycles. This clearly benefits from the extremely high CE% of 99.99%:⁷

$$(0.9999)^{2000} = 0.818 \quad (10.3)$$

In fact, such a high CE% of lithium-ion batteries comes not only from the anode but also from the cathode, as the overall CE% of a battery would be determined by the lower CE% of the electrode therein.

10.2.2 Dangerous Morphology

Aside from Coulombic loss, a more menacing problem for lithium-metal electrodes is the dangerous morphology of Li⁰ when crystallizing under electrochemical conditions. That is, when one tries to reduce Li⁺ from the electrolyte at the interface and then plate the Li⁰

atoms obtained onto the electrode surface, the location for such a Faradaic process to occur is not evenly distributed across the electrode surface. Instead, the incoming Li^+ will display heavy biases and preferences when choosing which locations to land on. Such a phenomenon is known as “*dendrite formation*”, because needle-like crystals with a very large aspect ratio are often the consequence over repeated depositions.⁸

The underlying mechanism of uneven crystal growth under an electric field is in fact universal for *all metal depositions*. When a given electric field is applied on an electrode, the distribution of the surface field strength cannot be homogeneous across the rough terrain. Instead, a more intensified field strength would be generated around the locations with “*protrusions*” (Figure 10.2). Such a higher than average field strength would induce metal cations to approach and deposit thereon preferentially, and the deposition would further increase the height and roughness of the protrusions. This self-propagating mechanism eventually magnifies the protrusions into dendrites with the accumulation of preferential metal cation migration over repeated depositions.

The early theoretical understanding of dendritic growth during metal deposition was based on the simpler case of copper deposition from aqueous electrolytes, where a clear correlation was seen between

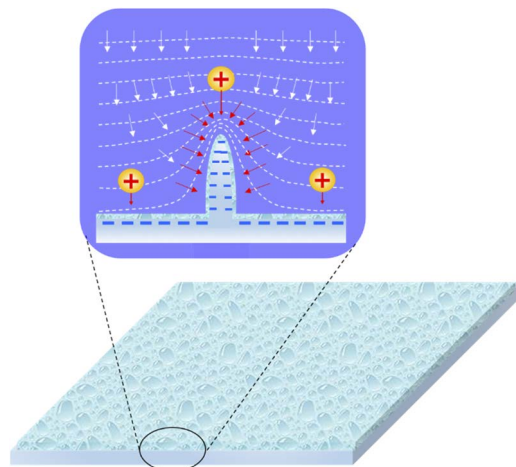


Figure 10.2 The uneven electrodeposition of metal cations on a rough surface of an electrode is induced by the inhomogeneity in the distribution of electric field. Around the “protrusions”, the cations feel a much stronger Coulombic force, and hence tend to deposit preferentially.

the fractal pattern crystal and current density applied on the electrode. It was proposed that, above a certain threshold current density, the concentration of the metal cations near the Helmholtz planes of the electrode surface can no longer maintain a sufficient supply to cover the electrode fully. Consequently, the insufficient cations, once arriving at the interface, would be preferentially attracted by those sites where the electric field strength is stronger than in the surrounding neighborhood, and eventually deposit and accumulate there.

Sand's time (τ_{Sand}), which was described in Section 7.2 and defined by eqn (7.16), has often been chosen to represent the threshold to mark the end of uniform electrodeposition and the start of preferential cation deposition around the protrusions.⁹ Under ambipolar cation and anion movements, Sand's time can be solved from

$$c_{x=0} = c_0 - \frac{2i^c t_a}{nF} \sqrt{\frac{\tau_{\text{Sand}}}{D_{\text{ambp}} \pi}} = 0 \quad (7.41)$$

which leads to

$$\tau_{\text{Sand}} = D_{\text{ambp}} \pi \left(\frac{c_0 nF}{2i^c t_a} \right)^2 \quad (10.4)$$

Apparently, a high current shortens the Sand's time and accelerates the non-uniform deposition, whereas slower cation transport (*i.e.* high t_a) deteriorates the non-uniformity.

However, the direct transplanting of the dendritic growth model from copper to lithium is problematic, because Cu^0 is not reactive with the aqueous electrolyte, and no interphases have been formed thereon, whereas the reactivity of Li^0 with electrolytes, especially with non-aqueous electrolytes based on esters, ensures that an interphase always stands between the Li^0 surface and the electrolyte, hence the two-dimensional interface no longer exists.

The presence of such an interphase on the Li^0 surface as an additional factor further deteriorates the unevenness of electrodeposition.

The chemical source of the interphase is the insoluble reaction products between Li^0 and the electrolyte components (solvents, salt anion, *etc.*). In most cases, these products thus generated consist of a complicated mixture of inorganic and organic compounds with varying chemical structures and physical properties, and they are distributed across the lithium metal surface in a rather random manner. It makes perfect sense that some of these products are more conductive

to Li^+ than others, hence the location of those more conductive products would also naturally attract more Li^+ during the deposition process.

Hence the combination of surface roughness (physical protrusions) and interphase inhomogeneity (more conductive interphasial spots) creates preferential locations for the deposition of Li^0 . When such a preference accumulated over repeated cycles, the deposited Li^0 naturally develops into long, needle-shaped crystals with branches (Figure 10.3).

The dendritic form of Li^0 is extremely dangerous in a battery. It has a high surface area and high aspect ratio, with a length reaching as far as $10^2 \mu\text{m}$, which is much longer than the gap between the anode and cathode in most electrochemical cells. For example, the commonly adopted anode–cathode gap in a lithium-ion battery, often defined by the polymeric separators used therein, is just $20\text{--}50 \mu\text{m}$. A dendrite electrically connecting the opposite electrodes in a cell would create an “internal short”, which not only ruins the cell chemistry because of the undesired electronic pathway (see Section 6.1 and Figure 6.1) but also, while doing so, triggers the violent discharge that frequently leads to a catastrophic end, such as fire and explosion.

An even more dangerous by-product from dendrites is the so-called “dead Li^0 ”.¹⁰ Owing to the extreme reactivity of Li^0 , one can imagine

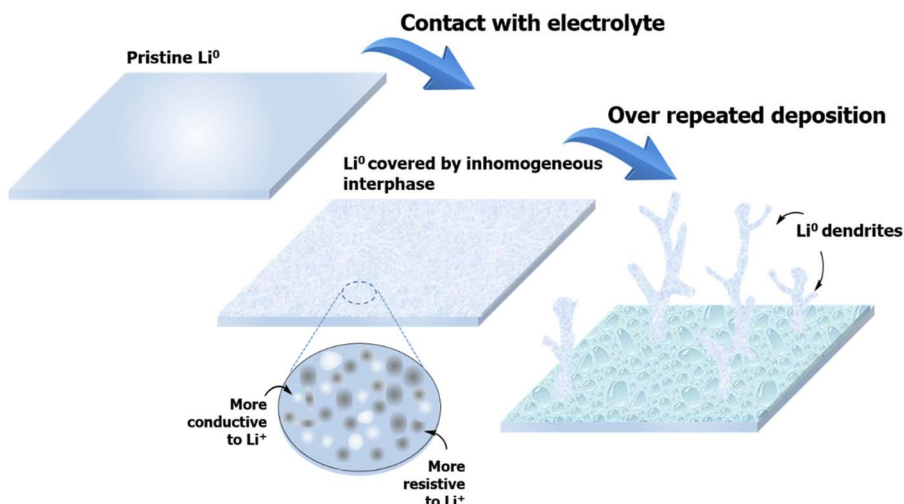


Figure 10.3 Schematic diagram of the formation process of dendritic Li^0 . It arises from the uneven deposition of Li^0 caused by the surface inhomogeneity of interphases, driven by the extreme reactivity of Li^0 with electrolytes.

that the interphase, which is the inevitable product from the reaction between Li^0 and the electrolyte, also covers the surfaces of the myriads of Li^0 whiskers. For the same reason as explained above, on those dendrites there are also spots that are more conductive to Li^+ than others. Hence, when those dendrites are subject to electrochemical dissolution (stripping), these spots would become the preferential location where Li^0 becomes oxidized and then exits to the electrolyte. When such electrochemical dissolution occurs near the bottom of a dendrite, the upper section of the dendrite would be physically severed and become electrically isolated from the bulk electrode (Figure 10.4). Those isolated particles of the dendrite, often of micro-to nanometric sizes, are *electrochemically dead*, because they can no longer participate in the cell reactions. However, *chemically* they are extremely reactive because they are still Li^0 and have a high surface area that is in contact with the electrolytes. Most fire and explosions of lithium-metal and even lithium-ion batteries were caused by these dead Li^0 .

The presence of Li^0 dendrites and dead Li^0 is the main reason why rechargeable lithium-metal batteries are not safe. Together with *Coulombic inefficiency* that reflects the irreversible loss of lithium during each cycling, they constitute the three major obstacles to the practical

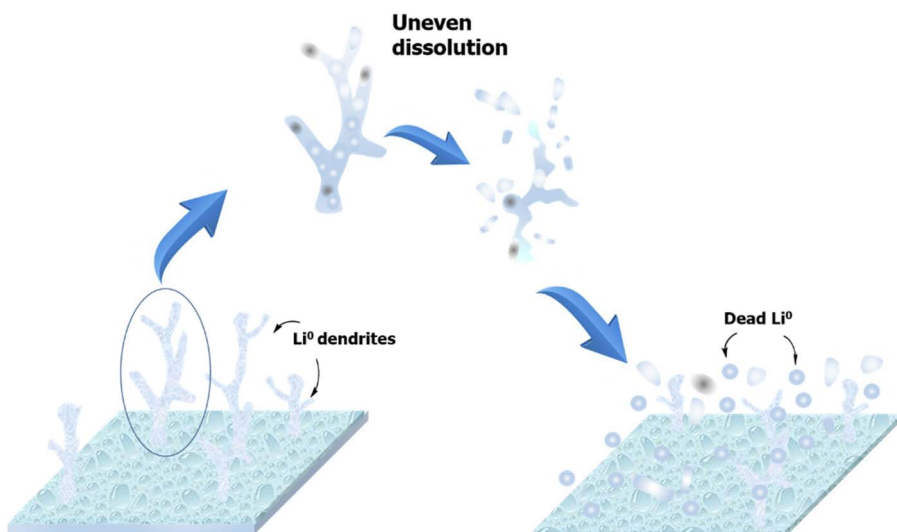


Figure 10.4 Schematic diagram of the formation process of dead Li^0 . It arises from the uneven stripping of Li^0 caused by the surface inhomogeneity of interphases, driven by the extreme reactivity of Li^0 with electrolytes.

commercialization of lithium-metal batteries, despite the tantalizing energy densities that a lithium-metal anode promises.

Looking from a higher level, Li^0 dendrites and dead Li^0 stem inevitably from the general irreversibility of conversion reaction-type cell chemistries (Figure 9.8). In such chemistries, for every complete charge–discharge cycle, one must destroy the original electrode structure and create a new one, while hoping that, when the cell reaction is reversed, every active species would go back to its original arrangement. The realization of reversibility for such reactions with drastic phase changes requires precise control of the reaction kinetics, morphology and interfacial structure at a level well below the nanometric scale, which has not been achieved as of 2022.

10.3 Circumventing Irreversibility and Safety Hazards

It was the poor reversibility and the accompanying safety hazards of lithium-metal electrodes that had kept the Holy Grail of lithium-ion batteries beyond our reach. So far, the closest attempt at reaching the Holy Grail was made by Moli Energy, which in 1988 commercialized a rechargeable lithium-metal battery using molybdenum disulfide (MoS_2) as the cathode.

MoS_2 is an intercalation host that accommodates Li^+ at *ca.* 2.0 V, therefore the Li/MoS_2 battery operates on an intercalation cathode and a conversion reaction-type anode. Such a “half-intercalation” cell configuration was very common in the 1970s–1980s, when researchers were still hopeful of harnessing the gigantic power of lithium metal. Needless to say, the reversibility of such cells is entirely determined by the lithium-metal electrode.

Only 4 months after the initial shipment of these Li/MoS_2 “half-intercalation” batteries to electronics manufacturers, widespread fire and explosion accidents were reported, which forced Moli Energy to recall all these products and declare bankruptcy. The post-mortem diagnosis of the recalled batteries identified the culprits of these fire and explosion incidents: the Li^0 dendrites and dead Li^0 , which seemed to be more easily formed during the irregular charging–discharging cycles in users’ hands rather than the periodic galvanostatic charging–discharging cycles on laboratory battery testers.

The impact of this incident was significant and way beyond Moli Energy itself, because at that time numerous companies in the USA and Japan were in the process of developing their own “half-intercalation”

batteries, using a lithium-metal anode and various cathodes. Moli Energy's fallout eventually terminated the efforts of the mainstream battery industry to commercialize a rechargeable lithium-metal battery, and forced them all to look away from lithium metal, at least for the time being, and to seek a bypass around the dangerous morphology of lithium electrodes.

10.3.1 The Bypass via Dual Intercalation

A feasible pathway to circumvent the irreversibility and dangerous morphology of conversion reaction chemistries had in fact already been proposed, at least in concept, by Armand a decade before the Moli Energy incident (Section 9.1.3.8). He suggested in 1980 that a cell employing intercalation hosts at both the anode and cathode sides should be immune from the drastic changes in phase, volume and chemical states of the electrodes, and therefore enjoy the benefits of excellent reversibility brought by the minimal structural changes in the topotactic reactions.¹¹

However, there was one problem to realizing such a dual-intercalation cell: at the time, it was not known what intercalation host can serve at the anode side.

Following the pioneering work of Whittingham and Goodenough, by the 1980s researchers had already discovered a series of intercalation compounds based on transition metal sulfides and oxides, but most of these compounds intercalate Li^+ at potentials close to each other but far above that of lithium metal. On the other hand, the key to realizing Armand's dual-intercalation cell relies on a couple of intercalation hosts that accommodate Li^+ at potentials that differ sufficiently that a meaningful cell voltage could be generated. This absence of intercalation compounds with proper intercalation potentials hindered the development of dual-intercalation batteries.

However, a more important reason was that, before the Moli Energy incident occurred, the development of lithium-metal electrodes was still believed by most researchers to be hopeful. Under this circumstance, it was natural that little enthusiasm was inspired in seeking an anode intercalation host that would certainly be inferior to lithium metal itself in terms of both potential and specific capacity.

Following Armand's proposal, there were only two different efforts that directly or indirectly adopted the concept of dual intercalation.

One was made in 1977 by Whittingham's colleagues at Exxon Corporate Research, who used Whittingham's LiTiS_2 as the cathode host and aluminum as the anode host for Li^+ .¹² Considering that aluminum

in fact forms an alloy instead of an intercalation compound with Li^+ , what was achieved there was actually another conversion reaction-type chemistry, the reversibility of which is even worse than that with Li metal itself owing to the huge volume change of the Li-Al alloy during insertion and de-insertion of Li^+ . However, since there was no Li metal in this cell, it can also be called a “lithium-ion battery”.

Another effort, made in 1980 by Lazari and Scrosati, employed different transition metal oxides (M_xO_y , where M is iron, tungsten, titanium or vanadium) as both anode and cathode hosts for Li^{+} .¹³ Although the difference in the operating potentials of these transition metal oxides was certainly not high enough (~2.0 V), and the energy penalty was high owing to the high masses of these transition metal oxides, the cell configuration itself bears a much closer resemblance to modern lithium-ion batteries, with intercalation lattices at both electrodes remaining topotactically unchanged during lithiation and de-lithiation (Figure 9.8c). Hence Scrosati’s cell should be considered as an ancestral prototype of modern lithium-ion batteries.

10.3.2 The Birth of Lithium-ion Chemistries

A serious effort to develop a dual-intercalation battery was made by a team of engineers led by Yoshino and Kuribayashi at the Japanese company Asahi Kasei in the mid-1980s, who did so by integrating Goodenough’s intercalation cathode LiCoO_2 with a carbonaceous anode host.¹⁴ The motivation for selecting carbonaceous materials was partially due to the fact that Asahi Kasei was a petrochemical company, hence it owned a huge tonnage of carbonaceous materials of diverse chemical compositions, structures and morphologies as side products from oil refinery processes, but more importantly, it was known as early as the 1950s that graphite, a unique crystalline form of carbonaceous materials, can intercalate Li^+ and form a stage I intercalation compound with the stoichiometry LiC_6 . This compound displayed a series of physical and chemical properties distinctly different from the parental host, graphite, such as golden color, high reactivity with water and other protic solvents and high ionic and electronic conductivities.

Researchers have long wondered whether LiC_6 can be used as a surrogate anode material for lithium metal, but up to the mid-1980s LiC_6 could still only be synthesized *chemically*, *i.e.* *via* direct reaction between graphite and molten lithium metal or its vapor. However, for LiC_6 to serve as a rechargeable anode, it has to be synthesized *electrochemically*, and the process has to be reversible for thousands of times

as an electrode would experience in a rechargeable battery. Such new LiC₆ electrochemistry requires knowledge of electrolyte formulations and interphase chemistry that was unavailable until the early 1990s, hence a decade-long disbelief lingered in the minds of materials scientists and electrochemists that graphite cannot be electrochemically lithiated.

Influenced by this disbelief, the engineers at Asahi Kasei circumvented graphite and placed their focus on carbonaceous materials with less ordered structures, such as polyacetylene, carbon fiber and various soft and hard carbons. Eventually, they identified one of the soft carbon materials, petroleum coke, as the anode host in their “lithium metal-free battery”. In the summer of 1986, the Asahi Kasei team assembled a prototype of such batteries consisting of an LiCoO₂ cathode, a petroleum coke anode and non-aqueous electrolytes based on lithium perchlorate dissolved in propylene carbonate (PC). This prototype “lithium metal-free battery” marked the birth of modern lithium-ion batteries, although its specific energy density (90 W h kg⁻¹) was far lower than that of the commercial lithium-ion batteries we use so extensively nowadays (> 300 W h kg⁻¹).

The improvements in the energy density of lithium-ion batteries are certainly the result of continuing optimization of materials and cell engineering over the years, but a major factor responsible for such improvements is the graphitic anode, which was not adopted in lithium-ion batteries until after 1994.

Nevertheless, in 1990, Sony announced the commercialization of the first-generation lithium-ion battery, in an almost identical configuration with the Asahi Kasei prototype.¹⁵ This marked the beginning of a new era that would be characterized by mobile electronics, electrification of transportation and clean and renewable energy.

As the very first intercalation battery chemistry, the lithium-ion battery has reshaped our lives in the twenty-first century. Its invention was eventually recognized by the award of the Nobel Prize in Chemistry to Whittingham, Goodenough and Yoshino in 2019.¹⁶

10.3.2.1 Graphite as Li⁺ Host

The adoption of graphite, which is a much more ideal anode host for Li⁺, occurred after the commercialization of the first-generation lithium-ion battery by Sony.

Graphite is a highly ordered carbonaceous material. Its basic structure consists of sp²-hybridized carbon atoms connected with three nearest neighbors at a bond angle of 120°, forming an endless sheet

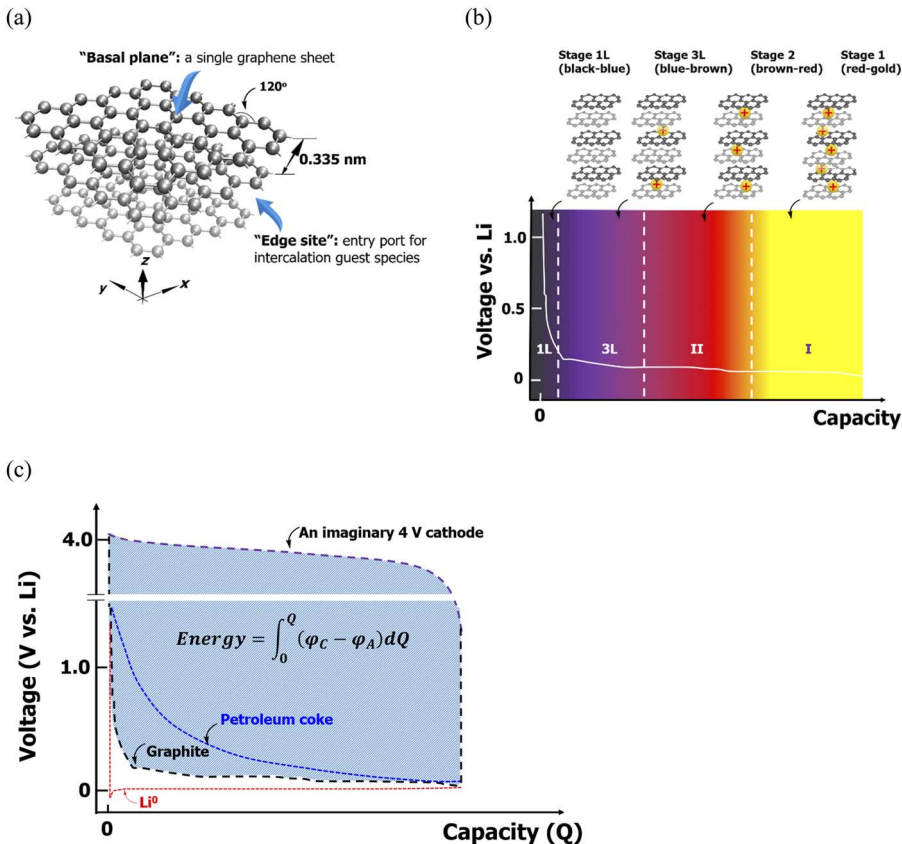


Figure 10.5 The graphite structure provides an excellent host to accommodate Li⁺ at low potential, but its electrochemical synthesis challenges the knowledge of electrolytes and interphases. (a) The structure of graphite; (b) the stoichiometry of staged Li⁺ intercalation compounds in graphite with accompanying color descriptors; (c) comparison of the lithiation potential between lithium metal (Li⁺), graphite and petroleum coke. The shaded area represents the energy held by the lithium-ion battery that consists of a graphitic anode and an imaginary 4 V cathode.

of fused hexagonal rings (Figure 10.5a). These 2D sheets (known as *graphenes*) are then stacked upon each other vertically (*i.e.* in the *z*-direction) at an interlayer distance of 0.335 nm. Carbon atoms within the same graphene sheet are connected covalently, hence those hexagonal rings are strongly bonded and nearly indestructible. However, the various graphene layers are held together only by rather weak van der Waals force and π–π interactions, thanks to the free electron provided by every sp²-hybridized carbon atom. These free electrons are

highly mobile, delocalized from the carbon atoms, and form a continuous conduction band in the x - and y -directions (along the planes).

Such a unique hierarchical architecture renders graphite a series of *anisotropic* properties. For example, whereas the C–C bonds of the hexagonal rings are almost indestructible except under extremely harsh conditions, the graphene layers being weakly held together can easily be taken away from each other in a process commonly known as “*exfoliation*”. This characteristic not only makes graphitic material an excellent solid lubricant, it also allowed Geim and Novoselov to mechanically exfoliate graphite layers by layer simply using household Scotch tape, until they obtained single graphene layers. For this work they were awarded the Nobel Prize in Physics in 2010. On the other hand, whereas electrons are highly mobile within the layers, the electronic conductivity perpendicular to the layers is 100–10 000 times lower, depending on how “perfect” the crystal lattice of the graphite is. The wide range reflects the diversity of graphitic materials. Indeed, as a naturally occurring element, carbon adopts more than 500 allotropes, most of which are more or less graphitic with extensively varying amorphous fractions, morphologies and superstructures.

Most important to us, the weakly held together graphene layers are “hospitable hosts”, in which the interlayer space provides accommodation for diverse guest species, which could be neutral molecules such as ammonia or ionic species such as alkali metal cations (Li^+ , K^+) and anions [hydrosulfate, HSO_4^- ; hexafluorophosphate, PF_6^- ; bis(trifluoromethanesulfonyl)imide, TFSI^-].⁴

The intercalation of Li^+ into graphite was known as early as the 1950s when Hérold reacted graphite directly with molten lithium and obtained a golden compound. Soon after, it was discovered that the intercalation reactions occurs *via* certain stages, forming various intercalation compounds with discrete stoichiometries and characteristic colors (Figure 10.5b).¹⁷ Although it is beyond the scope of this book to discuss the details of these intercalation compounds and their stages and crystalline structures, it must be pointed out that the maximum lithiation of graphite is a stage I compound with the stoichiometry LiC_6 , which corresponds to a golden color and a specific capacity of 372 mAh g⁻¹ if only counting the graphite mass, or 339 mAh g⁻¹ if counting the entire mass of LiC_6 (as we calculated in Section 9.1.3.6).

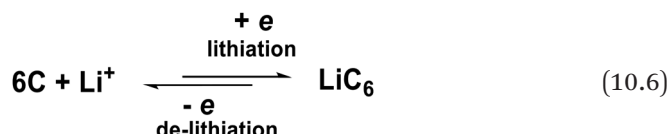
However, before the 1990s, researchers only knew how to make such Li^+ intercalation compounds LiC_x *via chemical approaches*, *i.e.* by immersing a piece of graphite into a pool of molten Li^0 at temperatures

higher than 180 °C, or reacting a piece of graphite with Li⁰ vapor in a sealed ampoule at lower temperature but under vacuum:



Such a chemical process involves a “one-way” diffusion of Li⁰ into the graphite lattice, and is hardly reversible.

Now, here is the problem. To make LiC₆ an anode Li⁺ host in a rechargeable battery, one has to ensure that the process could be carried out in an electrochemical manner, and it must be reversible thousands of times, *i.e.*



where the Li⁺ comes from the electrolyte. This process involves a single-electron reduction (during the lithiation) or oxidation (during the de-lithiation).

Even if researchers can pre-synthesize LiC₆ chemically and then assemble it into an electrochemical cell as the anode (as many did, according to the claims made in patent applications during the early to mid-1980s), this anode, after the first discharge, will need to be charged, *i.e.* LiC₆ needs to be restored electrochemically.

Hence the electrochemical synthesis of LiC₆ constitutes the key for enabling graphite to be used as the reversible host for Li⁺ at the anode. It was this key that frustrated battery scientists and electrochemists for decades, convincing people that graphite is an unlikely anode host for Li⁺ in a rechargeable battery, until a “magic” electrolyte solvent is identified, which will be discussed in the next section.

Once the electrochemical synthesis of LiC₆ was made possible by a “magic” electrolyte solvent (or, more precisely, by the unique interphase chemistry that the solvent brings), the advantage of graphite as an anode host was fully unleashed: it intercalates Li⁺ at a flat potential plateau very close to that of Li⁰ (~0.10 V to Li). Compared with the less ordered carbonaceous materials such as petroleum coke, the perfectly crystalline structure of graphite ensures that Li⁺ intercalation occurs at an almost constant potential (Figure 10.5c).

For an anode, this low and flat potential means a higher energy that can be delivered at a steady voltage because, as mentioned in Section

9.1.5 (Figure 9.9), the energy contained in a battery is determined by the amount of charges (*i.e.* capacity) separated at a potential difference (*i.e.* cell voltage). In other words, the energy contained in a battery can be represented graphically by the area enclosed by the potential curves of the anode and cathode, because the cell voltage (V or ΔV) is simply the difference between the potentials of the cathode and anode ($\varphi_C - \varphi_A$). By coupling with any given cathode, graphite doubtlessly provides a better energy density to the extent of 30–50%, depending on the cathode chemistries and cell engineering.

Therefore, graphite or other carbonaceous materials of high graphitic degree prevailed as the optimum anode host for Li^+ in essentially all lithium-ion batteries manufactured after 1995 until today.

The “magic” electrolyte solvent responsible for enabling the adoption of graphite is ethylene carbonate (EC), which has become an indispensable electrolyte component in all lithium-ion batteries manufactured nowadays despite the varying electrolyte formulations adopted by each individual battery maker, provided that the anode is graphite.

10.3.2.2 The “Magic” EC-Graphite Chemistry

The fundamental reason for the difficulty of graphite being electrochemically lithiated comes from two separate but closely intertwined factors:

1. As an intercalation host, graphite is an excessively “hospitable host” that welcomes almost anything in the interlayer spaces, which often leads to uncontrollable side reactions. Structurally, this is because the graphene layers are only “loosely” held together by the van der Waals force, hence the edge sites of graphite tend to open easily for the incoming guest species provided that they bear the “right charges”, be it the Li^+ , or the solvent molecules “kidnapped” by Li^+ , *i.e.* in the primary solvation sheaths.
2. The Li^+ intercalation occurs at a very low potential where most electrolyte components cannot remain stable. In other words, the graphite lithiation potential is below the reduction stability limits of almost any electrolyte component, hence Li^+ intercalation is always accompanied by irreversible decompositions of some electrolyte components (salt anion, solvent molecules, *etc.*). This is actually the legacy from the highest electropositivity of Li^0 discussed in Section 10.1.

The combination of these two factors makes a graphite electrode extraordinarily sensitive to the electrochemical intercalation of Li^+ . When one attempts to lithiate graphite electrochemically, this involves negatively polarizing the graphite electrode, so that Li^+ can migrate, approach the graphite edge sites and eventually enter. However, since Li^+ is always solvated by the solvent molecules in these electrolytes (Section 3.3, Figure 3.5), what is brought to the edge site of graphite is not a naked Li^+ , but actually a solvated Li^+ , that is, Li^+ along with solvent molecules in its primary solvation sheaths.

Hence Li^+ intercalation is *always* accompanied by the co-intercalation of the solvent molecules in its primary solvation sheaths, and these solvent molecules, after being accommodated between the graphene layers, would decompose there because of the low electrode potential. Such irreversible reductions, often accompanied by the generation of gaseous products, may cause irreparable damage to the fragile graphitic structure.¹⁸

So, under what circumstances would the destruction of the graphitic structure be avoided?

We will leave the discussion of the interphase formation mechanism to the next chapter, and jump directly to the answer here: *the structure of these solvent molecules in the primary solvation sheath of Li^+ dictates whether the graphitic structure can avoid the fate of destruction when lithiated.*¹⁹ The same conclusion has been confirmed to apply also in the case of other cations, such as sodium, zinc and magnesium. Hence it might very likely be a universal law for the intercalation of cationic species into graphite. It also makes perfect sense because, as one can imagine, any cation intercalation process must be preceded by its solvation sheath approaching the graphite edge sites.

The uniqueness, or the “magic” chemistry, of EC is that, when an Li^+ solvation sheath populated by EC molecules approaches the graphite, the EC molecules reductively decompose and form an interphase that seals off the graphite surface wherever the graphite and electrolyte are in direct contact (Figure 10.6).²⁰ Such an interphase is electronically insulating so that the continuous reduction of EC is terminated, and ionically conductive so that Li^+ can migrate across it in both directions to support the mass transport required by the cell reaction. Mechanically, it also serves as a “glue” that holds together the graphene layers and prevents their exfoliation, a “filter” that forces a solvated Li^+ to desolvate and only allows naked Li^+ to pass through, and a surface film with flexibility that tolerates the *ca.* 10% volume change between pristine graphite and its fully lithiated state LiC_6 .

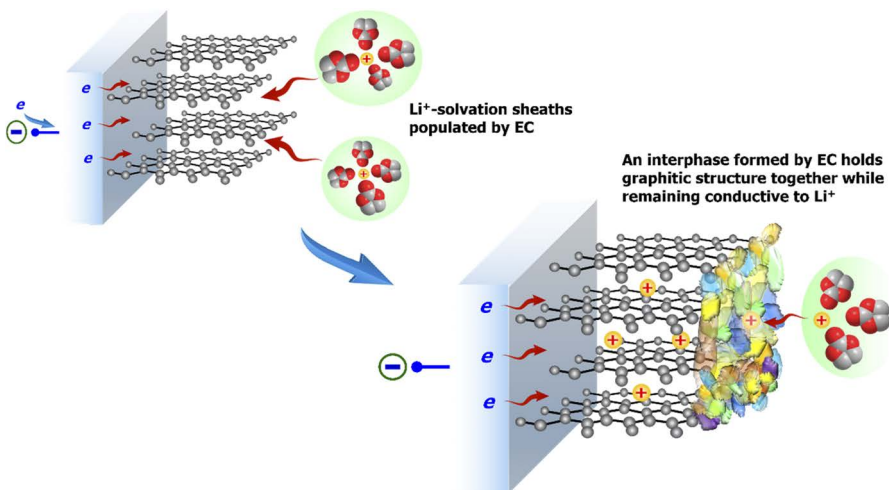


Figure 10.6 The unique chemistry between EC and graphite: EC forms an interphase, allowing intercalation of naked Li^+ while holding the graphitic structure together.

All of these characteristics of the EC-derived interphase contribute to making the electrochemical synthesis of LiC_6 possible.

However, after nearly three decades of using EC as a “magic” electrolyte solvent to permit the electrochemical synthesis of LiC_6 , the mechanism of how EC achieves this remains not fully understood, despite numerous theories and models.^{21,22} What we do know for sure is that, among the hundreds of non-aqueous and aprotic solvent molecules investigated, EC seems to be one of the very few (fewer than six), all of which are carbonate esters, that could do this *at moderate to dilute (<1.0 M) lithium salt concentration*, and there seems to be no clear correlation between the solvent structure and the interphase effectiveness. This phenomenon merits further efforts to deconvolute on a molecular level.

It should be noted that “*moderate to dilute lithium salt concentration*” was emphasized above because as the lithium salt concentration crosses a certain limit, the above solvent confinement could be breached, as the reliance on an effective interphase would then shift from solvent to salt anion. This is the mechanistic foundation behind the “super-concentration” concept that has prevailed after 2010, which will be discussed in more detail in Part C.²³

Although not fully elucidated, the unique EC-graphite chemistry makes EC the indispensable electrolyte solvent used in billions of lithium-ion batteries manufactured nowadays.

10.3.2.3 The Three Electrochemical Scenarios of Graphite

As mentioned in the preceding section, the combination of two factors discussed therein imposes an extremely rigorous requirement on the electrolyte composition in order for the graphite to be reversibly lithiated, and EC turns out to be the answer for lithium-ion batteries. However, if the solvent is not EC, what would happen to the graphite? In addition to the scenario of successful lithiation of graphite to the stage I compound LiC_6 (Figure 10.6), there are generally two other scenarios depending on the solvent molecules.

The first scenario occurs when the solvent co-intercalated with Li^+ is unstable, and the reductive decomposition fails to form an effective solid interphase to stabilize the graphitic structure. Eventually no lithiation of graphite could be achieved, and the graphite is exfoliated (Scenario I, Figure 10.7). The mechanism underlying the exfoliation could be the decomposition products of these electrolyte solvent molecules in the primary solvation sheath of Li^+ , which are generated between the graphene layers and are often gaseous. The reactions that occur between the graphene layers very likely would overcome the weak interlayer attraction and repel these graphene layers apart.

The majority of the non-aqueous and aprotic solvent molecules lead to Scenario I, including those carbonate molecules that are close structural analogs of EC. The most interesting example is PC, which differs from EC by only one methyl group, but instead expresses a strong tendency to exfoliate the graphitic structure at ~ 0.70 V without lithiating (Figure 10.8). Historically, the close structural similarity but distinctly different interphasial chemistry between EC and PC created the disbelief that graphite could not be electrochemically lithiated. This disbelief could have postponed the emergence of lithium-ion batteries for decades. Its details will be covered in the next section as an exemplary case for the importance of interphase chemistry in lithium-ion batteries and all the advanced batteries developed thereafter and to be developed in the future.

Scenario II occurs when the solvent molecules exhibit strong resistance towards reduction even at potentials close to that of Li^0 . Therefore, when these solvent molecules are brought by Li^+ into the graphite interlayers, the entire solvated Li^+ could remain stable, at least within a certain time frame. The co-intercalation of Li^+ and these solvent molecules into the graphitic structure forms a so-called “*ternary graphite intercalation compound*” (Scenario II, Figure 10.7). Here the term “ternary” describes the presence of three different components that make up the new host–guest complex, *i.e.* graphite, Li^+ and

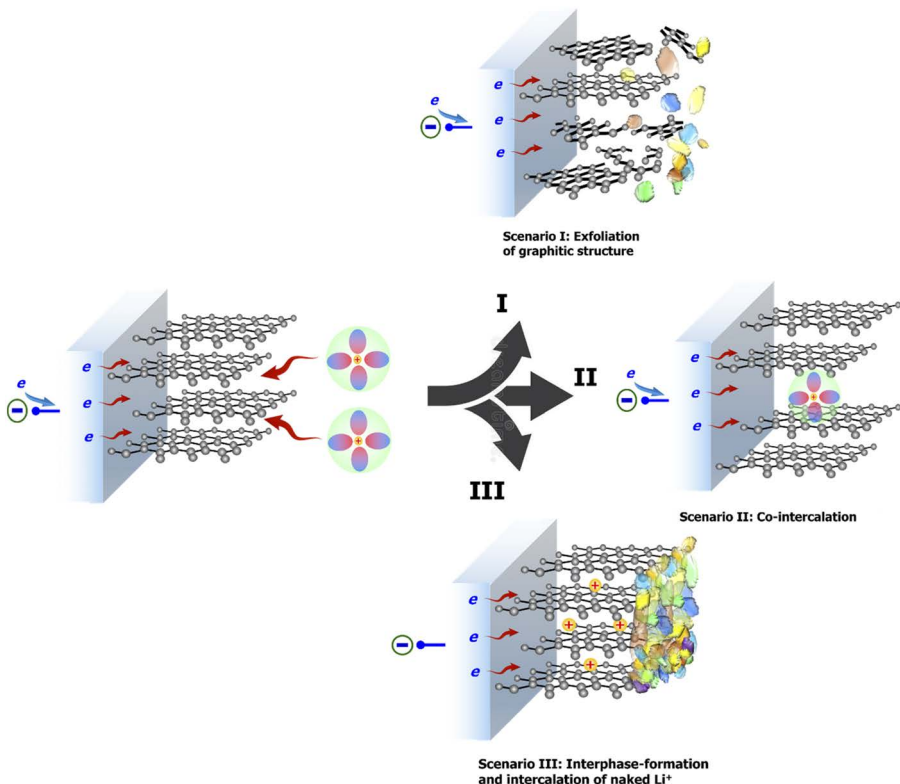


Figure 10.7 The three electrochemical scenarios of graphite when polarized negatively in an electrolyte, only one of which (Scenario III) achieves electrochemical lithiation, and the interphase is the key. This scenario occurs only in certain electrolyte compositions with either special selection of solvent molecules (such as EC) or salt (such as LiBOB), or simply high salt concentrations (such as in super-concentrated electrolytes).

the accompanying solvent molecules. The potential for the co-intercalation to occur is much higher than that of naked Li^+ by *ca.* 0.3–0.5 V depending on which solvent molecules are used, while the solvated ions, because of their much larger sizes than the naked Li^+ , cannot be accommodated in graphite at densities as high as LiC_6 .

Although these ternary intercalation compounds present interesting structures and chemistries to study, they are generally not good candidates for electrodes. Not only would lower capacity and energy density arise from the lower intercalation stoichiometry and higher intercalation potential, the reversibility of such ternary graphite intercalation compounds is also poor, because the intercalation of these

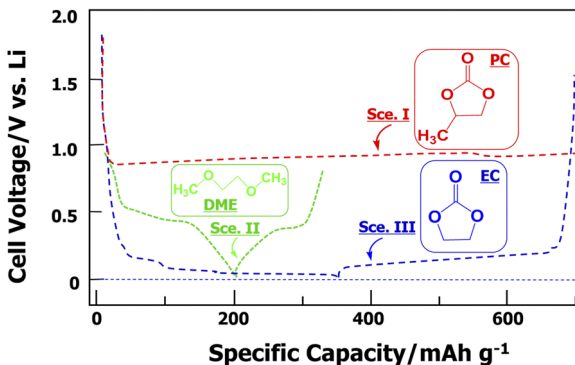


Figure 10.8 Potential profiles for the three electrochemical scenarios of graphite being polarized negatively in an electrolyte containing lithium salt. Scenarios I and III highlight the *EC-PC disparity*, *i.e.* close structural similarity but distinctly different interphasial chemistries. In PC-based electrolytes graphite exfoliates at a potential around 0.7–0.8 V vs. Li, generating gaseous products from the decomposed electrolyte solvents and fragments of graphite electrode; in EC-based electrolytes, a protective interphase derived from the decomposition products of EC holds the graphitic structure together, and ensures the intercalation of naked Li⁺ at low potentials as small as 0.01–0.1 V vs. Li. Scenario II is exemplified by graphite being polarized negatively in an electrolyte based on dimethoxyethane (DME), where the “lithiation” process at ~0.45 V vs. Li is actually dominated by the co-intercalation of Li⁺ and DME molecules solvating it.

“giant” solvated ions would introduce very high stress into the graphitic structure, which gradually degrades during the repeated co-intercalation and de-co-intercalations.

Recently, it was found that the co-intercalation of solvated Na⁺ presents much better reversibility than solvated Li⁺, perhaps owing to the less aggressive intercalation potential (~0.5 V vs. Li). Nevertheless, the lower intercalation stoichiometry and lower energy of the ternary intercalation compounds still make them fall short of being ideal intercalation materials for electrochemical energy storage.

The majority of the non-aqueous and aprotic solvent molecules leading to Scenario II belong to ethereal families, because an ethereal linkage is intrinsically stable against electrochemical reduction compared with other solvent molecules that possess unsaturated functionalities, such as the carbonyls in esters [Section 10.2.1, eqn (10.1)]. However, sulfoxide also incurs Scenario II despite the unsaturation of its S=O functionality.

The third scenario, which was discussed in Section 10.3.2.2 (Figure 10.7), is of course a reversible intercalation chemistry that

a lithium-ion battery needs: the solvent molecules in the solvation sheath of Li^+ are unstable against reduction once having been brought into the edge sites of graphite, but their decomposition product provides a self-terminating mechanism that prevents further reductions of the solvent molecules in the bulk electrolyte. These products, in a self-limiting manner, deposit on the graphite surface as a robust but flexible interphase, conductive to ions but insulating to electrons. Once this interphase is formed, it would only allow naked Li^+ to be intercalated, the high stoichiometry of which (LiC_6) promises a rather high specific capacity (372 mAh g⁻¹ graphite).

The realization of Scenario III relies on the “magic” chemistry between EC and graphite, the discovery of which experienced a rather tortuous pathway.

10.3.2.4 EC Versus PC

As discussed in Section 10.3.2.1, in the 1950s researchers already knew that graphite can accommodate alkali metal cations such as Li^+ , K^+ and Cs^+ (Na^+ is an odd exception: it cannot be intercalated as a naked ion, but its solvated form with ether molecules can be reversibly co-intercalated; the science behind this phenomenon is beyond the scope of this book). However, at the time all these compounds were made *via* chemical means, *i.e.* by direct reactions between graphite and molten alkali metals or their vapor. The electrochemical synthesis of these intercalation compounds obviously turned out to be much more complicated, as evidenced by the three scenarios we have just covered (Figure 10.7). Specifically for Li^+ , its electrochemical intercalation into graphite requires the “magic” chemistry from EC, the atomic origin of which is still not fully understood, despite numerous models and theories.

Most of the non-aqueous electrolytes introduced since the 1950s were formulated by using non-aqueous and aprotic solvent molecules selected from two major organic compound families, ethers and esters. Therefore, whenever one tries to lithiate a graphite electrode in an electrolyte, the graphite most likely would encounter either Scenario I (exfoliation, immediate destruction of the graphitic structure) or Scenario II (co-intercalation with low capacity and poor reversibility). A large number of electrolytes were also formulated with mixtures of both esters and ethers, *e.g.* PC and DME, hence the mixed scenarios of exfoliation/decomposition and co-intercalation occurred simultaneously.

So, why was EC not used any earlier?

In fact, also in the 1950s, when researchers were still seeking the Holy Grail, EC was already recognized as a non-aqueous and aprotic solvent molecule that can effectively dissolve lithium salts. However, compared with its structural cousin PC, one conspicuous disadvantage of EC stood out: its melting point is 36.4 °C, which makes it almost a solid at room temperature, in contrast to PC, which does not freeze until –48.8 °C (Table 10.1). This high melting point can be attributed to the highly symmetrical molecular structure of EC, which can be easily packed into an orderly crystal lattice and would require high energetic compensation (e.g. heat) when one tries to disrupt such a lattice. PC, on the other hand, is an asymmetric molecule, the methyl group of which introduces significant disruption of its packing efficiency into an ordered manner. In fact, the broken molecular symmetry of PC is far more severe than the structure drawn in Figure 10.8 would imply, because one must realize that the carbon where the methyl group is located is a stereocenter, the chirality of which is determined by how the methyl group is situated relative to the plane of the ring structure (Figure 10.9). In other words, given its non-chiral synthesis process, the commercial PC solvent is actually a racemic mixture of its *R* and *S* stereoisomers, each of which accounts for 50% in the mixture. With such complications in symmetry, it is understandable how much more difficult it is to pack these highly asymmetric molecules into crystalline lattices, and how much easier it is to turn such mixtures into liquids.

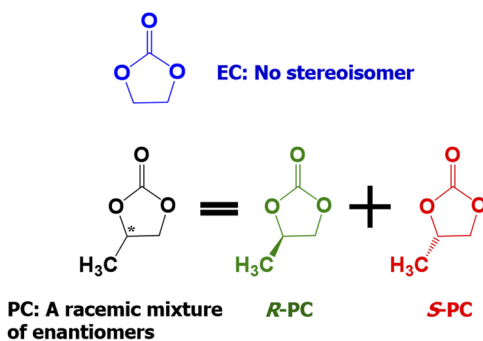


Figure 10.9 EC versus PC: EC is a symmetric molecule with no stereoisomers, whereas the methyl group in PC breaks its molecular symmetry not only with the bulky volume of the methyl group, but also the chirality introduced by the methyl group that makes the carbon where the methyl sits a stereocenter (as marked with an asterisk). Hence the PC solvent from commercial sources, unless specifically labeled, is a racemic mixture of equimolar *R* and *S* enantiomers.

It was such a divergence in molecular symmetry and the resultant difference in melting behavior that placed PC in a much more favored position over EC when being considered as candidates as solvents for electrolytes.²⁴ Natural instinct drives us to choose a liquid over a solid to formulate a liquid electrolyte, especially when their structural similarity would imply that their chemical and electrochemical properties are similar. Unfortunately, EC and PC represent two extremely different interphasial chemistries, as shown in Figure 10.8, and the “magic” chemistry between EC and graphite would take more than three decades (1958 to 1990) to be found. However, even after we identified EC as the “magic chemical” to permit a graphitic structure for reversible Li⁺ intercalation, we are still not sure why there is such a distinct difference in their interphasial behaviors that could only arise from a minor structural variation.

There have been numerous models and theories attempting to explain the EC–PC disparity, such as the difference in solubility of their reduction products (*i.e.* those derived from EC tend to “glue” to the graphitic surface, whereas those derived from PC prefer to dissolve in the bulk electrolyte),²¹ or the difference between the Li⁺ solvation sheath structures in two solvents (*i.e.* the Li⁺ solvation sheath in EC is more receptive towards the partial association with PF₆⁻ anion, thus allowing its involvement in the interphase formation process as a fluoride donor, whereas PC tends to bind more tightly with Li⁺ and exclude anion participation),²² or the difference in how these solvated Li⁺ ions partially desolvate immediately before they co-intercalate into graphite at the edge sites, *etc.*

Nevertheless, these models and theory still cannot convincingly explain why, as of 2022, despite the large number of organic solvents examined, very few have demonstrated a similar “magic” chemistry that EC shows towards graphite. The complete elucidation of this mystery requires further efforts.

10.3.2.5 Evolution of Non-aqueous Electrolytes

The exact formulations of electrolytes used in modern lithium-ion batteries vary significantly with each individual manufacturer and often remain trade secrets that cannot be easily accessed in the open literature. However, they are all based on a skeleton formula: lithium hexafluorophosphate (LiPF₆) dissolved in mixed solvents, which consist of EC and at least one linear carbonate ester, including dimethyl carbonate (DMC), diethylene carbonate (DEC) and ethylmethyl carbonate (EMC).^{25,26} Such a skeleton formulation was the fruition of a lengthy

evolution that synchronized with the evolution of electrode materials, during which our understanding of electrolyte science evolved accordingly.

10.3.2.5.1 Solvents

The *solvent* part of this skeleton formulation experienced a more tortuous pathway.

As mentioned earlier, the very first non-aqueous and aprotic electrolytes were formulated using solvents selected from two structural families: alkyl esters and alkyl ethers.

When Whittingham invented the first Li intercalation cathode (titanium disulfide, TiS_2) in 1972, he used an electrolyte based on carbonate, ether or even chloroformate as solvents, because the operating potential of TiS_2 is so moderate (<3.0 V vs. Li) that all these solvents, no matter how exotic, could comfortably encompass the operating potentials of both the anode (lithium metal in this case) and cathode without interfering with their own decompositions. However, after Goodenough identified transition metal oxides (*e.g.* lithium cobalt oxide, LiCoO_2) as better cathode materials with higher operating potentials and higher specific capacities, an inevitable shift from ether to ester occurred, because the ethers generally experience oxidative decomposition around 4.0 V, which disqualifies them as electrolytes for high-voltage chemistries.

Thus, *the first constraint* on the solvent formulation was imposed by the cathode.

The ester family includes alkyl esters of carboxylic acids, such as γ -butyrolactone, ethyl acetate or carbonate esters, such as EC and PC. Because of its high melting point (~36.4 °C), EC was often heavily disfavored, while PC was preferred as the most popular ester solvent. During the 1950s–1990s, typical non-aqueous electrolytes often consisted of various lithium salts dissolved in a mixture of several solvents that contained more or less PC. Such a preference for PC was of course unfortunate, as we have shown in Figure 10.8 that PC happens to be the solvent that induces Scenario I. The misbelief that it is impossible to intercalate Li^+ into graphite electrochemically was thus created due to repeated failures to do so in PC-based electrolytes.

By the time Yoshino and colleagues at Asahi Kasei began to invent a “lithium metal-free” battery, this misbelief drove them to turn to carbonaceous materials with less crystallinity as the anode host for Li^+ , and eventually identified petroleum coke (an amorphous carbon) as an acceptable anode host for Li^+ . In the claims of their original patent, graphite was even specifically excluded using crystallinity

quantified by X-ray diffraction. This self-imposed restriction apparently came from PC-centric electrolytes. Their efforts eventually led to the first-generation lithium-ion battery, which was commercialized by Sony in 1990. The electrolytes therein were based on PC. However, other researchers did not give up on graphite, or EC, or both.

A year after the Sony's announcement, Fujimoto and colleagues at Sanyo were trying to find a carbonaceous anode that did not conflict with the Asahi patent. By July 1991, they realized that graphite might present the only opportunity, as was claimed in an early Sanyo patent by Ikeda and co-workers, who used an ether-based electrolyte therein and apparently achieved co-intercalation of an Li^+ -ether complex with limited reversibility and specific capacity (Scenario II).

In order to realize the full specific capacity promised by LiC_6 , they needed to find an electrolyte that does not exfoliate the graphitic structure. After screening a vast number of possible combinations, EC was identified as the "magic" solvent. Considering the high melting point and the high viscosity of EC, Fujimoto and colleagues added linear carbonate esters such as DMC and DEC as diluent, because they can be intermixed with EC at almost any ratio. Their patent was filed in November 1991, which defined the skeleton electrolyte solvent formula for modern lithium-ion batteries: a mixture that must contain EC and at least one linear carbonate ester selected from DMC, DEC and ethylmethyl carbonate (EMC).⁴⁴

The *second constraint*, therefore, was imposed by the graphitic anode materials, or more precisely by the interphasial chemistry required by the extreme potential and fragile structure of graphite.

In fact, identical electrolyte compositions (EC-DEC) had appeared in a patent filed slightly earlier by Okuno and colleagues at Matsushita, but that patent did not specifically claim graphite as anode host, nor did it present any evidence for LiC_6 formed in such EC-centric electrolytes.

On the other hand, much earlier, in the 1980s, Dahn and colleagues at Moli Energy had already used an electrolyte based on an EC-PC mixture for Li-metal batteries with molybdenum sulfide (MoS_2) as cathode, although that cell chemistry, similar to that of the TiS_2 used by Whittingham, works well in ether-based electrolytes. By late 1988, Dahn and co-workers also discovered the "magic" chemistry between EC and graphite. However, this electrolyte formula still carries the irreversible signature of Scenario I from the PC, hence such a solvent formulation was not widely adopted as a modern LIB electrolyte. In a seminal article published in 1990, Dahn and co-workers reported that a solid-electrolyte interphase (SEI) formed by EC must serve as the key

to enable the electrochemical synthesis of LiC_6 .²⁰ This insight guided the research on electrolytes in a new direction that examines the interphasial chemistries, in addition to bulk properties.

10.3.2.5.2 Salts

The solute (*i.e.* salt) part of the skeleton electrolyte formulation evolved *via* a relatively more straightforward pathway, with part of the reason being that, compared with the wide range of organic molecules available as solvent candidates, there is a very limited number of salt anions from which to choose. A more important reason, however, is that the anions do not play an important role in interphasial chemistries. This anion insensitivity of interphasial chemistries originates from two aspects.

On the *anode side*, the anion participation in anode interphasial chemistry is suppressed by the Coulombic repulsion between a negatively charged electrode (anode) and a negatively charged ion (anion), which significantly reduces the population of anions in the Helmholtz layers, thus decimating their opportunity of being reduced and becoming part of interphases thereat (Figure 10.10).

Although a few anions were indeed identified as key participants in the formation of interphases on a graphitic anode surface, the most pronounced example being bis(oxalato)borate (BOB), they would have to overcome such Coulombic repulsion to become part of the interphase on graphite. BOB does so with an extraordinarily high reduction potential, ~1.8 V *vs.* Li, therefore when its reductive decomposition occurs, the potential of the graphitic anode has not become excessively negative to drive it completely out of the Helmholtz layers.^{27,28} Eventually the decomposition products from BOB, *i.e.* lithium salts of oxalates and borates, deposit on the graphite surface and become the main chemical source of the interphase thereat.

In fact, benefiting from the extraordinarily high reduction potential of BOB, the interphase chemistry derived from a LiBOB-containing electrolyte is so dominated by the anion-derived chemical species that even EC becomes no longer indispensable but optional. Convincing evidence comes from an electrolyte consisting of LiBOB dissolved in PC, which stabilizes the graphitic structure as does EC, and yields a voltage profile almost identical with that shown for Scenario III from EC electrolyte in Figure 10.8.

PF_6^- represents an alternative example of anions participating in the anode interphase chemistry. Its sensitivity to trace moisture in the electrolyte always generates a small fraction of pentafluorophosphorus (PF_5) and phosphoryl trifluoride (POF_3) molecules and other

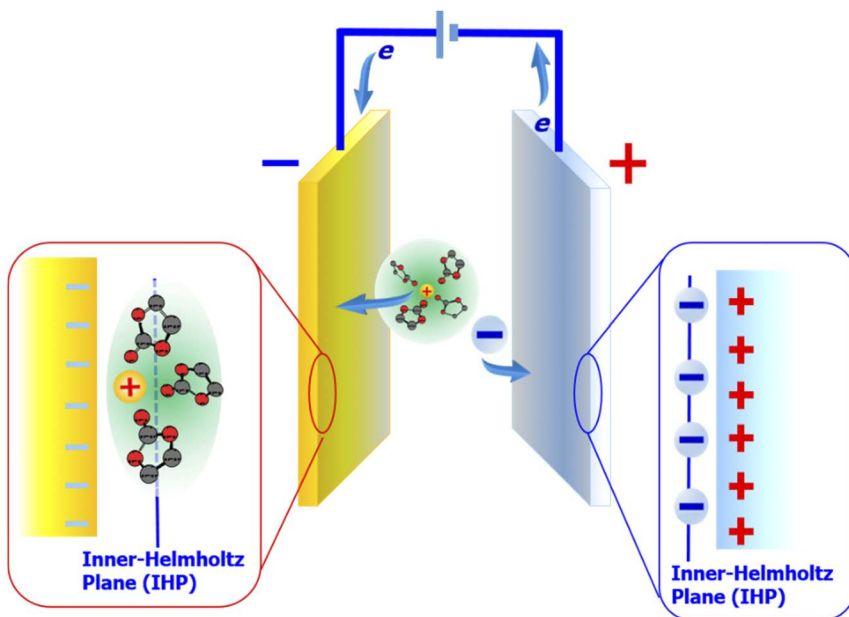


Figure 10.10 The fundamental origin of the biased sensitivity of interphasial chemistry towards solvent molecules and anions at the anode and cathode. (a) At the anode, the negatively polarized electrode repels the negatively charged ions (anions) away from the Helmholtz layers, thus suppressing their opportunity to participate in the interphase formation process at the anode surface. Meanwhile, the negatively polarized electrode attracts the cations and solvent molecules in their solvation sheaths, thus granting these solvent molecules more opportunity to determine the interphasial chemistry. The EC-graphite “magic” occurs in such a context. (b) At the cathode, the positively polarized electrode attracts the anions, thus promoting the influence of anions on the cathode-electrolyte interphase (CEI) chemistry. It should be mentioned that the anions are mainly free in non-aqueous electrolytes, without the well-defined solvation sheaths that cations normally carry.

fluorine-containing species. These neutral species are insensitive to the Coulombic repulsion from the anode surface, and therefore can migrate to the Helmholtz layers and further decompose there, donating various organic and inorganic fluorides to the eventual solid-electrolyte interphase on a graphitic anode. The same mechanism is believed to be responsible for the improved interphases enabled by a few other lithium salts based on anions that are better fluorine contributors, such as bis(fluorosulfonyl)imide (FSI⁻) and its structural homologs.

Nevertheless, for salt anions, there is no parallel to the uniqueness of the “magic” EC-graphite chemistry.

On the *cathode side*, although Coulombic attraction between a positively charged electrode (cathode) and a negatively charged ion (anion) favors anions to populate in its Helmholtz layers (Figure 10.10), the cathode structure in general is much more inert towards co-intercalation and exfoliation of solvent molecules, and consequently less sensitive to their structures or the physical and chemical properties of their decomposition products. This is because the cathode structures are much more robust, with the slabs of cations and polyanions held together by rather strong Coulombic forces, in sharp contrast to the fragile graphitic structures held together by weak van der Waals force and π - π interactions between the graphene layers.

What further reduces the sensitivity of cathode interfaces towards electrolyte decomposition reactions is the anion solvation sheath, or the non-existence of it.

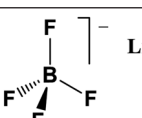
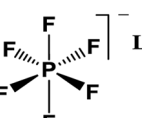
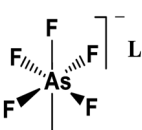
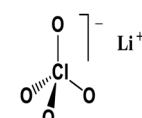
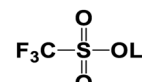
Anions in non-aqueous electrolytes are rather weakly solvated, in sharp contrast to cations. This is the consequence of two coincidental factors.

First, all the salt anions favored as conducting solutes in non-aqueous electrolytes are not simple “*point charges*” but complex structures of large size, and most of them are fluorinated (Table 10.2). Such choices were mainly the result of natural selection enforced by the attempts to maximize the solubility of lithium salts in generally low-polarity non-aqueous solvents. In fact, it was for solubility considerations that most commonly accessible simple anions are excluded.

Therefore, in those complex anions, the formal negative charge is not localized on the central atom, but instead is well delocalized from the central atom throughout the entire complex anion structure thanks to the high electronegativity of the fluorine substitutions. Such delocalization of the formal charge throughout the entire structure inevitably dilutes the Coulombic field exerted by the anion on its neighboring solvent molecules, as opposed to what these solvent molecules would feel from a “*point charge*” cation. If one applies the “*line of electric field*” concept proposed by Faraday to describe the strength of the Coulombic fields felt by solvent molecules, one can easily see that the cationic Coulombic field generated by a point charge cation is much more intense than the anionic Coulombic field generated by a complex-structured and well-delocalized anion, as reflected by the “density” of field lines (Figure 10.11).

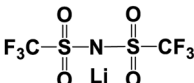
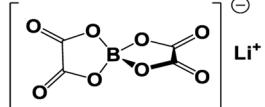
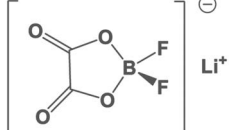
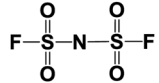
Second, as discussed in Section 3.1, most non-aqueous and aprotic solvent molecules are “*monopolar*”, *i.e.* their *negative termini* (such as

Table 10.2 A few lithium salts commonly used as electrolyte solutes.

Lithium salts	Structure	M. Wt	T_m (°C)	σ (mS cm ⁻¹) ^b	Chemical stability	Electrochemical stability ^c	
						Cathodic	Anodic
Lithium tetrafluoroborate (LiBF ₄)		93.9	293 ^a	4.9	Moisture-sensitive, corrosive		
Lithium hexafluorophosphate (LiPF ₆)		151.9	200 ^a	10.7	Extremely mois- ture-sensitive, corrosive		
Lithium hexafluoroarsenate (LiAsF ₆)		195.9	340	11.1	Moisture-sensitive, corrosive		
Lithium perchlorate (LiClO ₄)		106.4	236	8.4	Hygroscopic		
Lithium trifluoromethane sul- fonate (LiOTf, triflate)		155.9	>300 ^a		Hygroscopic		

(continued)

Table 10.2 (continued)

Lithium salts	Structure	M. Wt	T_m (°C)	σ (mS cm ⁻¹) ^b	Chemical stability	Electrochemical stability ^c	
						Cathodic	Anodic
Lithium bis(trifluoromethane sulfonyl)imide (LiTFSI)		286.9	234	9.0	Hygroscopic		
Lithium bis(oxalate)borate (LiBOB)		193.9	>300 ^a	7.5	Moisture-sensitive	1.7 V	4.2 V
Lithium difluorooxaborate (LiDFOB)		143.9	~270		Moisture-sensitive	1.8 V	>4.5 V
Lithium bis(fluoro-sulfonyl) imide (LiFSI)		187	145		Moisture-sensitive		

^aDecomposition without melting.^bAt room temperature (25 °C), in EC/DMC (50:50).^cDetermined by voltammetry scans without taking interphase-formation into account.

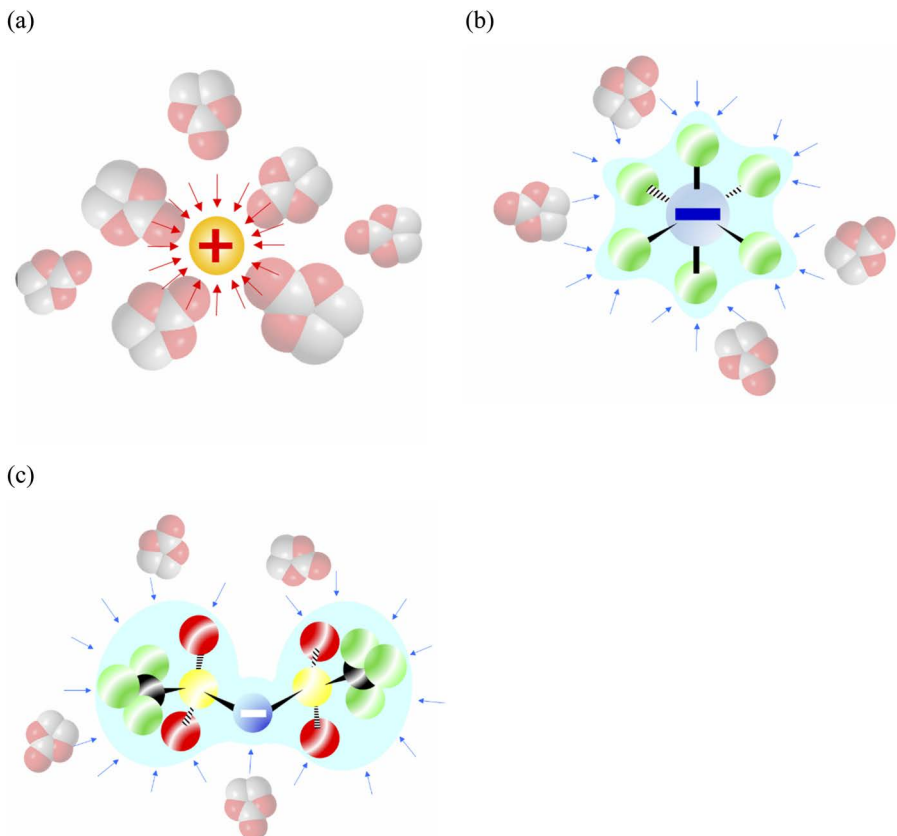


Figure 10.11 The difference between the solvation behaviors of a cation and an anion. (a) The cations are essentially a point charge, the intense and focused Coulombic field of which exerts a strong attraction to those solvent molecules around it, so that the solvated cations (Li^+ , Na^+ , Mg^{2+} , etc.) often display collective transport and electrochemical behaviors. (b), (c) The formal charge in those complex and fluorinated anions (PF_6^- and TFSI are used as examples here) is well delocalized, so that the Coulombic field felt by the surrounding solvent molecules is rather ‘‘diluted’’, and the anion-solvent interaction is much weaker. Here we applied the field line concept proposed by Faraday to express the difference in Coulombic fields from the cation and anion, respectively, with an arbitrary use of 18 field lines for one formal charge. Meanwhile, in ester solvent molecules such as EC depicted in the graph, the termini bearing partial negative charges (carbonyl oxygen) are the preferred sites that interact with cations, while their interaction sites with anions are not well defined.

the carbonyl oxygen of the ester functionalities) are well exposed to solvate cations, but their positive termini are relatively hidden sterically by the structure, making it harder for them to solvate an anion (Figure 3.1). This selective solvation behavior of non-aqueous solvents in favoring cations but disfavoring anions is in strong contrast to water, the “*bipolar*” nature of which enables it to solvate both cations and anions.

For these two reasons, the anion solvation sheath, if it exists, is a very loose association between the anion and solvent molecules,²⁹ and when an anion enters the Helmholtz layers of the cathode surface, such a weak anion–solvent association exerts very little influence on the reactions or processes thereat.³⁰

In summary, the combination of the above factors renders salt anions not as decisive as solvents to interphase chemistries in a battery, and the constraints placed on the selection of lithium salts came mainly from the requirements for more desirable physical and chemical characteristics of a conducting electrolyte solute, such as solubility and conductivity, rather than from interphasial chemistry considerations. After all, before any interfacial property can be considered, the salt has to be dissolved by the non-aqueous solvents first and then conduct.

It was realized very early on that the average dielectric constants (permittivities) of non-aqueous and aprotic solvents are generally lower than that of water (78 at room temperature), as revealed by the comparison between Tables 3.1 and 10.1. Although there are a few exceptions, such as EC (89.78) and PC (64.92), whose dielectric constants are comparable to or even higher than that of water, the overall dielectric constants of the actual electrolyte solutions lie in the range 10–30, because linear carbonates such as DMC, EMC and DEC as co-solvents inevitably reduce such values with their own low dielectric constants.

As discussed in Sections 3.1 and 3.4, the dielectric constant of a solvent directly reflects how efficiently the salt can be dissociated into discrete ions and how the resultant ions can be solvated by such solvent molecules. Obviously, unlike aqueous electrolytes, the salts in those non-aqueous and aprotic solvents are expected to encounter issues of effective dissolution as well as dissociation. This can be evidenced by (1) the much lower salt solubility and (2) the much lower ion conductivity of the non-aqueous electrolytes in comparison with their aqueous counterparts.

Thus, for a lithium salt to be sufficiently dissociated in those media with moderate dielectric constants, one would want the corresponding

anion to come from a strong acid. Therefore, the low *Lewis basicity* of the corresponding anion would encourage the salt to dissociate rather than associate and aggregate. Meanwhile, since the anions also conduct in the electrolytes and interact with the anode and cathode surfaces, their electrochemical stability, especially the stability against oxidative decomposition at the cathode surface, must be taken into account (Figure 10.10).

The application of these constraints excluded a lot of anions that are commonly accessible, such as simple halides (fluorides are barely soluble in any non-aqueous solvent, while chlorides, bromides and iodides are easily oxidized at low anodic potentials), carboxylates (acetates, whose oxidation also occurs at low anodic potential) or inorganic anions with oxygens as the charge barriers (nitrates, sulfates and sulfonates, which offer low solubility in most non-aqueous solvents). Eventually, the anion structures were narrowed down to a few that are invariably fluorinated, such as PF_6^- , hexafluoroarsenate (AsF_6^-), tetrafluoroborate (BF_4^-) and bis(trifluoromethanesulfonyl) imide (TFSI). These fluorinated complex anions display high solubility, high dissociation constants and high ionic conduction in these non-aqueous and aprotic solvents despite the generally low dielectric constants.

Among these, LiPF_6 does not always offer the best single performance, but instead provides a series of physical, chemical and electrochemical properties that are well balanced (Table 10.2), from *bulk* (high solubility in carbonate solvent mixtures even when the overall dielectric constant is only ~ 30), to *ion transport* (ion conductivities around 10 mS cm^{-1} at room temperature), and to *interface* (remain stable against oxidation at the cathode up to 4.5 V, and participate in forming fluoride-containing interphases at the anode).

Equally if not more important from the cell engineering perspective is that PF_6^- also effectively stabilizes aluminum foil at these high potentials by coating it with a passivation film with fluoride and phosphate ingredients, an apparent benefit from its instability against trace moisture. This enabled aluminum to be adopted as a practical substrate for high-voltage cathode materials and circumvented the more noble (and more expensive) metals.

After the 1990s, LiPF_6 became the standard lithium salt adopted by the entire lithium-ion battery industry. In research communities, however, other lithium salts (LiBF_4 , LiTFSI , LiBOB and LiAsF_6) are still frequently being used, despite the overwhelming use of LiPF_6 .

After 2010, a modified version of LiTFSI , lithium bis(fluorosulfonyl)imide (LiFSI), emerged as a potential replacement for LiPF_6 , as it

provides a series of favorable properties over LiPF₆, such as higher solubility and better ionic conduction. It is especially favored for various new battery chemistries, such as high nickel oxide cathodes such as lithiated nickel manganese cobalt oxide [LiNi_{0.8}Mn_{0.1}Co_{0.1}O₂ (NMC 811)]. It has also attracted extensive interest in the research realm, especially for conversion reaction electrode materials including a lithium metal anode, sulfur/sulfide or metal fluoride cathodes and a few new electrolyte concepts, such as super-concentration. As of 2020, the production of LiFSI at an industrial scale has forced its cost to fall substantially to a level comparable to or even lower than that of LiPF₆, raising the possibility that LiPF₆ could be eventually be replaced with LiFSI.

10.3.2.6 The Modern Lithium-ion Battery

By early 1991, the skeleton electrolyte formulation for the modern lithium-ion battery had been defined as LiPF₆ dissolved in a mixed carbonate solvent consisting of EC and at least one of the linear carbonates selected from DMC, EMC and DEC. Such EC-centric electrolytes can form stable and protective interphases on graphitic carbon and stabilize the aluminum substrate at the cathode side, while providing fast Li⁺ conduction. It soon prevailed in all lithium-ion batteries and enabled graphite to be adopted as a universal anode host.

The use of EC-based electrolytes and a graphitic anode increased the energy density of the third-generation lithium-ion battery by 30–50% compared with the amorphous carbonaceous anodes used in the first- and second-generation lithium-ion batteries. The EC-graphite combination became a standard combination in all the lithium-ion batteries manufactured after 1994. The basic configuration of modern lithium-ion batteries has remained unchanged until today: a graphitic structure as an anode intercalation host for Li⁺, a transition metal oxide or metal phosphate of layered or other structures as the cathode intercalation host for Li⁺ and an electrolyte consisting of LiPF₆ dissolved in a mixture containing EC and other carbonate esters (Figure 10.12).

Nowadays, the exact electrolyte compositions in commercial lithium-ion batteries remain the trade secrets of individual manufacturers, especially when the application of electrolyte additives becomes the most economical approach to tailor the desired properties for new battery chemistries. However, the skeleton electrolyte formulation initially proposed by Fujimoto and co-workers has not experienced any drastic change.

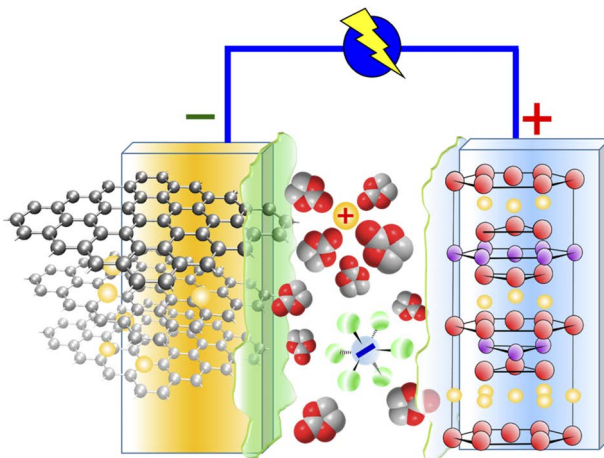


Figure 10.12 The dual-intercalation configuration eventually adopted in modern lithium-ion batteries: an anode intercalation host based on the layered structures of graphitic materials, a cathode intercalation host based on layered, spinel or tunnel structures of transition metal oxide or transition metal phosphate materials (LiCoO_2 is shown here as an example) and a non-aqueous electrolyte consisting of LiPF_6 dissolved in an EC-centric mixed carbonate solvent. Linear carbonates (DMC, EMC or DEC) have been omitted for clarity.

Undoubtedly, electrolyte formulations will continue to evolve with new battery chemistries emerging. As history has taught us, the electrolyte is closely associated with the electrode materials that it interfaces.

By the time Whittingham, Goodenough and Yoshino received the Nobel Prize in Chemistry in 2019, the lithium-ion battery had already become *the most popular electrochemical device* ever invented in the history of humankind. It has changed the lives of almost every individual on Earth, powering their digital gadgets, driving their vehicles or delivering energy to their households *via* grids, and its application frontier is still being expanded almost every day. Until it is completely replaced with a new battery chemistry, it will continue to play an essential part in our daily life.

10.4 Emerging Chemistries and Electrolytes

History advances in a non-linear manner. Occasionally it seems to have returned to the same spot, but in fact at a different height. Therefore, some of the so-called “emerging” chemistries may have in fact

emerged before in a different form. They were never realized simply because they presented difficulties in reversibility by pushing the materials, especially electrolytes and interphases, to extremities that were beyond our capability to accommodate and to compromise at the time.

Intercalation chemistry successfully circumvented the reversibility challenge of conversion reaction chemistries, but at the expense of specific capacities and energy densities, because the intercalation lattice of the electrode does not participate in the reaction, therefore bringing inert masses to the cell (Figure 9.8). Such expense was well worthwhile when the lithium-metal anode was found to present insurmountable safety concerns, and the safe rechargeable batteries available at the time were based on aqueous chemistries with both low capacity/energy and poor reversibility.

After the overwhelming success of lithium-ion batteries, however, such expense appears to be more and more excessive, and especially after thoroughly studying lithium-ion batteries since the 1990s, we believe that we have understood so much about electrodes, electrolytes and interfaces, and have mastered the necessary techniques in controlling and tailoring both materials and chemistries at nanometric and even atomic scales.

The energy density of lithium-ion batteries has been steadily improved since the 1990s thanks to incremental progress achieved in materials innovation and manufacturing engineering, from the initial 90 W h kg^{-1} of the first-generation lithium-ion battery (Sony, 1991) to the level approaching 300 W h kg^{-1} of the state-of-the-art lithium-ion batteries in 2022. However, sooner or later the intercalation chemistry will face a ceiling to its maximum energy density, which is imposed by these intrinsic inert masses brought by the intercalation framework. Various studies have estimated that such a ceiling is somewhere between 350 and 400 W h kg^{-1} .

At the materials level, in order to break the intercalation ceiling, the conversion reaction type of battery chemistry has to be revisited as an alternative way out, on both the anode and cathode sides. It is hopeful that what was impossible a few decades ago could now be achieved, or at least be manageable. An optimism is prevailing in the battery and materials community: having been armed with knowledge and techniques that were unavailable in the 1970s, we might eventually approach the Holy Grail.

Of course, given the highly irreversible nature of conversion reaction chemistries, where bonds are constantly broken and rebuilt,

the electrolytes and interphases have to face unprecedented challenges.

10.4.1 Anode

We have shown that there is no other material that has a lower eigenpotential than Li^0 . This unique character, arising from the electropositivity of Li, is inherited by many materials that contain Li, in which Li could exist in a state between an ion and an atom. The most pronounced example is what the lithium-ion battery adopts as its anode host: a graphite intercalation compound containing Li^+ .³¹ According to both experimental and computation studies, the ionicity of Li^+ intercalated in LiC_x varies with the composition: at diluted stages (Stages 1L to 3L, Figure 10.5b), lithium retains its ionic state, but as the stages becomes more concentrated, the intercalated Li^+ gradually gains more atomic (Li^0) nature. At the fully lithiated stage (Stage 1, LiC_6), the lithium therein could be considered as existing in a hybridized state ($\text{Li}^{\delta+}$), which is the result of charge transfer from the elections in the p-bands of the sp^2 -hybridized carbon atom to the intercalated Li^+ . This partially atomic nature of $\text{Li}^{\delta+}$ is reflected by the low eigenpotential of LiC_6 , which is only 0.01–0.2 V vs. Li.

The same rule applies to a series of elements or compounds with which lithium can form alloys, and these alloys often become the preferred candidates as anode hosts to accommodate Li^+ . Differing from graphite, where the basic graphitic structure does not experience drastic change without the breaking of old bonds and re-formation of new bonds, the alloying is always accompanied by the breaking and re-formation of intermetallic bonds, as shown schematically in Figure 9.8a. Such an Li^+ storage mechanism can certainly achieve much higher stoichiometry than that of LiC_6 .

10.4.1.1 Aluminum, Tin, Silicon

There are many elements, or alloys of them, that could form intermetallic alloys with Li^0 , such as aluminum, bismuth, silver, gold, tin, antimony, indium, *etc.*

Like LiC_6 , there is also a chemical and an electrochemical approach to synthesize these alloys. In the former, one simply mixes the host metal (M^0) and Li^0 at high temperature, which form a homogeneous mixture:



In the latter, Li^+ from the electrolyte is reduced at the interface between the host and the electrolyte in a single-electron process, and the Li^0 formed subsequently diffuses into the matrix of the host M^0 :



These alloys could be either stoichiometric compounds or solid solutions without a certain stoichiometry.

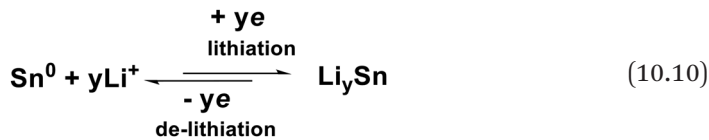
We have mentioned that in the 1970s, colleagues of Whittingham at Exxon Corporate Research adopted aluminum (Al^0) as an alloy host for Li^+ . Al^0 mixes with Li at almost any ratio, but as an anode host the maximum usable capacity is 2980 mAh g⁻¹ down to a voltage of around 0.3 V, corresponding to AlLi_3 . Although the volume change during lithiation and de-lithiation of Al (~94%) is not too severe compared with 300–400% of both tin (Sn) and silicon (Si), the cycling stability of Al is in fact especially poor and proves extremely difficult to improve. Unlike Sn or Si, efforts to make Al nanostructured are impractical, because Al itself at small particle scales is a very energetic material that often finds military or civilian applications as a propellant or explosive. Its potential as an electrode material, therefore, is outshone by Sn and Si.

Among all these elements, Sn and Si are doubtless the favorites and eventually reached practical batteries with varying degree of success.

Just 5 years after Sony's commercialization of the first lithium-ion battery, attention was already turned on to alloy hosts. Researchers at Fuji Photo Film Co. proposed in 1995 an amorphous tin-based composite oxide (TCO) as the anode host. In fact, TCO itself is not the direct host for Li^+ , and must experience an initial irreversible "activation" process to become Sn^0 particles before Li^+ could have an accommodation host:



Here, what is significant is that both Sn^0 and Li_2O are generated on the nanoscale. Nano-Sn⁰ now serves as a reversible host for Li^+ at extremely large capacity (y could be as high as 4.4):



It should be noted that the activation process as expressed by eqn (10.9) is one-time and irreversible, hence the $x\text{Li}^+$ involved therein is considered permanently consumed. That is the price to pay for this conversion reaction chemistry. Theoretically, a specific capacity of 993 mAh g⁻¹ could be obtained, corresponding to the formation of Li_{4.4}Sn down to a potential of ~0.6 V vs. Li.

One might ask why researchers had to go through such trouble of losing capacity in a seemingly useless step such as eqn (10.9). Why could they not skip that irreversible activation and directly design a nano-Sn⁰?

The answer is that making non-noble metallic elements into a nanostructure often destabilizes the material. The nanostructure increases their contact area with air, and makes them easier to oxidize. For those elements that are “active” in the *electrochemical series* (*i.e.* those with a standard potential more negative than that of H₂ in Table 10.3), a

Table 10.3 Standard potentials (*electrochemical series*) for selected metallic elements.

Metallic element	Electrode reaction	Standard potential/V vs. SHE (25 °C, 1 atm)
Li	$\text{Li}^+ + \text{e}^- \rightarrow \text{Li}^0$	-3.045
Cs	$\text{Cs}^+ + \text{e}^- \rightarrow \text{Cs}^0$	-3.026
Rb	$\text{Rb}^+ + \text{e}^- \rightarrow \text{Rb}^0$	-2.981
K	$\text{K}^+ + \text{e}^- \rightarrow \text{K}^0$	-2.925
Ca	$\text{Ca}^{2+} + 2\text{e}^- \rightarrow \text{Ca}^0$	-2.866
Na	$\text{Na}^+ + \text{e}^- \rightarrow \text{Na}^0$	-2.714
Mg	$\text{Mg}^{2+} + 2\text{e}^- \rightarrow \text{Mg}^0$	-2.371
Al	$\text{Al}^{3+} + 3\text{e}^- \rightarrow \text{Al}^0$	-1.66
Zn	$\text{Zn}^{2+} + 2\text{e}^- \rightarrow \text{Zn}^0$	-0.763
Fe	$\text{Fe}^{2+} + 2\text{e}^- \rightarrow \text{Fe}^0$	-0.440
Sn	$\text{Sn}^{2+} + 2\text{e}^- \rightarrow \text{Sn}^0$	-0.136
Fe	$\text{Fe}^{3+} + 3\text{e}^- \rightarrow \text{Fe}^0$	-0.04
H ₂	$2\text{H}^+ + 2\text{e}^- \rightarrow \text{H}_2$	0.00 (reference)
Cu	$\text{Cu}^{2+} + 2\text{e}^- \rightarrow \text{Cu}^0$	+0.337
Ag	$\text{Ag}^+ + \text{e}^- \rightarrow \text{Ag}^0$	+0.799
Hg	$\text{Hg}^{2+} + 2\text{e}^- \rightarrow \text{Hg}^0$	+0.854
Pt	$\text{Pt}^{2+} + 2\text{e}^- \rightarrow \text{Pt}^0$	+1.188
Au	$\text{Au}^{3+} + 3\text{e}^- \rightarrow \text{Au}^0$	+1.52

nanostructure even makes them energetic materials such as explosives or propellants, e.g. Al^0 or magnesium.

An extreme example, of course, is *nanostructured Li⁰*, which is simply dendritic Li⁰ or dead Li⁰, the number one culprit for the fire hazards of lithium-ion and lithium-metal batteries.

By using TCO as the starting material, the process represented by eqn (10.8) and (10.9) cleverly circumvented the difficult task of making reactive nano-Sn⁰ either mechanically or chemically, instead doing so by employing the electrochemical approach in an enclosed reaction vessel (the electrochemical cell).

The additional benefit of this approach is the formation of nano-Li₂O, which acts as structural scaffold and buffer, and turns out to be critical in keeping the electrode integrity when Li_ySn experiences a volume change of ~300% during lithiation and de-lithiation. Of course, one has to pay the price of irreversible loss of $x\text{Li}^+$ in the activation step [eqn (10.9)].

In recent decades, there have been many similar approaches to forming unstable nanostructured materials *via* electrochemical means, which went beyond the areas of battery or energy storage materials.

The effort of making a TCO-based anode host for Li⁺ eventually went into commercial lithium-ion batteries 10 years later, in 2005, when Sony announced a new lithium-ion battery chemistry, named “*Nextlion*”, in which a composite anode consisting of graphite and tin oxide was adopted. However, TCO was used in only limited amounts in order to minimize the irreversibility induced by its volume change. The adoption of this alloy anode host did not become the industry mainstream owing to limited gains in capacity and energy at the expense of the extra cost caused by processing. It was unclear what electrolyte was used in this lithium-ion cell, but because of the small presence of nano-Sn⁰ after the activation, its impact on the interphase is limited, and carbonate-based electrolytes can still do the job.

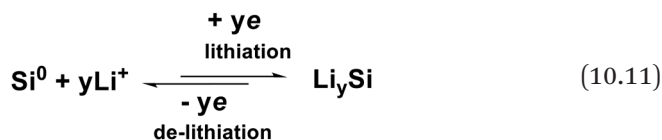
The efforts to make Si an anode host were much more serious, mainly driven by its astonishing theoretical specific capacity of 4199 mAh g⁻¹, corresponding to Li_{4.4}Si down to a potential of ~0.4 V vs. Li. Note that, given the same ratio of lithiation in the final alloy (Li_{4.4}M, M = Sn or Si), the much higher specific capacity of Si is the benefit from its much lower atomic weight (28.081) compared with Sn (118.71). The advantage of Si over Sn is further consolidated by advantages such as its much higher natural abundance (in fact, Si is the second most abundant element in the Earth’s crust, after oxygen, which makes its potential cost literally as low as “dirt”), its more stable chemical nature (which makes it possible to synthesize nanostructured Si⁰ directly) and its low lithiation/de-lithiation potential (0.2–0.40 V vs. Li).

However, there is a catch.

The extra high capacity of 3579 mAh g⁻¹ (or 4199 mAh g⁻¹, depending how much Li⁺ can be inserted into Si⁰) comes at a price, *i.e.* the volume change of the Si⁰ host. With so many guests accommodated, the host becomes especially bloated with a 300–400% volume expansion; when the guests leave the host, the volume would have to shrink back to its pristine level. Such a drastic volume change presents an unprecedented challenge to both the integrity of the Si⁰ electrode in addition to the stability of the electrolyte and interphase.

A sharp comparison is the graphitic structure, which experiences a volume change of only ~10% during lithiation and de-lithiation.

Hence, although the great potential promised by Si⁰ as a rechargeable anode host has been known for some time, its adoption in lithium-ion batteries has been deterred by its rather poor reversibility, which results from the nightmarish combination of its *tremendous volume change* (300–400%) during lithiation and de-lithiation and its *low operating potential* (0.2–0.4 V vs. Li):



where y is between 3.75 and 4.4, corresponding to a specific capacity between 3579 and 4199 mAh g⁻¹.

While the low potential of an Si⁰ anode requires an electronically insulating interphase to be formed, so that the sustained irreversible reactions between Si⁰ surface and bulk electrolyte could be prevented, as discussed in Section 8.1, the dramatically expanding and shrinking Si⁰ electrode, caused by the repeated entry and exit of up to 4.4 Li⁺ per Si⁰, keeps creating new Si⁰ surfaces. This means that the interphases formed are persistently broken, and new interphases immediately form again on these newly created Si⁰ surfaces.

This destruction-reformation cycle of the interphase synchronizes with the expansion-shrinking of Si⁰ compounded and produces two serious consequences: (1) the irreversible consumption of solvent molecules and Li⁺ from the electrolyte, which provide chemical sources for interphase formation and re-formation, and (2) the disintegration and irreversible loss of active material Si⁰, which occurs in a similar manner to the formation of dead Li⁰ (Figure 10.4). These two irreversible processes combine to drive the rapid fading of lithium-ion batteries with Si⁰ as the anode.

The revival of the Si⁰ anode occurred about a decade ago, when Cui and colleagues demonstrated that the structural integrity of Si⁰ could be maintained provided that it is architected into nanostructures under a length scale of <200 nm.⁴⁵ Hence the persistent loss of Si⁰ due to electrode “*pulverization*” is circumvented, with electrolyte consumption simultaneously minimized. Since then, a large number of various nano-Si⁰, including zero-dimensional nanoparticles, one-dimensional nanowires, two-dimensional thin films, three-dimensional networks and elegant porous, hollow, core–shell and yolk–shell architectures, have been designed and demonstrated, which are beyond the scope of this book.

Of course, nanostructure alone is not enough to enable Si⁰ to be adopted as a practical anode material. It requires a synchronized approach from other components.

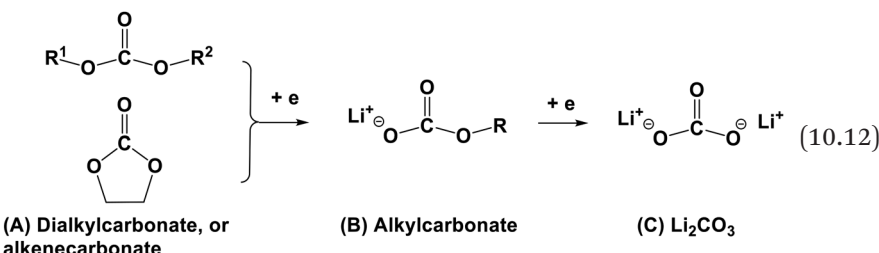
New polymer binders of both high elastic strength and electronic conductivity were developed, so that Si⁰ can remain in electrical contact even when volume expansion disconnects these nanowires and nanoparticles from the bulk electrode. Equally important are various new electrolytes that ensure the formation of new interphasial chemistries to accommodate the volume change of the Si⁰ electrode with minimum breakage and maximum flexibility.

Remember that the skeleton electrolyte compositions for the state-of-the-art lithium-ion batteries were the result of simultaneous constraints imposed by high-voltage transition metal oxide cathodes and graphitic carbon anodes. Now with the graphite removed from the equation while the transition metal oxide cathodes remain, esters are still preferred as the solvents owing to the high voltage consideration, but EC is no longer indispensable.

More importantly, given the volume change characteristic of the electrode, the emphasis becomes how to form an interphase that is either tough enough to contain the mechanical pressure, or flexible enough to accommodate it. Despite the advances made in recent decades in understanding the fundamental science beneath the formation and chemistry of interphases (to be discussed in Chapter 11), the majority of the efforts in tailoring interphasial chemistry and structure are still Edisonian trial-and-error, *via* adjusting the structure of both salts and additives to alter the inorganic and organic ingredients in the interphases.

With the purpose of tailoring such interphases, most of the new electrolytes for Si⁰ electrodes employ exotic lithium salts and electrolyte co-solvents or additives. The main co-solvent extensively used is a fluorinated version of EC, *fluoroethylene carbonate* (FEC), while the most

frequently used additive is the unsaturated version of EC, *vinylene carbonate* (VC) (Table 10.1). The interphase components originating from the combination of FEC and VC consist of polymerized carbonate, as well as LiF, Li₂CO₃ or *lithium alkylcarbonate*. The latter, alkylcarbonate, could be viewed as a partially reduced form of the carbonate solvents because it still retains half of the organic functionality, *i.e.* an alkyl group [eqn (10.12)], hence it is also known as a “*semicarbonate*”.



In fact, Li₂CO₃ can be viewed as the fully reduced form of carbonate solvents, while carbonate solvents could be viewed as the stabilized forms of carbonate anion (CO₃²⁻) or carbon dioxide gas (CO₂). This is the reason on the molecular level why CO₂ is always produced during the operation of modern lithium-ion batteries, not only during the initial stage of interphase formation where a small portion of carbonate solvent molecules participate in the reduction to provide chemical sources, but also when the battery is placed under conditions that deviate from the designed electrochemistry, such as high temperatures, or high voltage induced by overcharging, or even under normal operating conditions for a long time.

Alkylcarbonate is not unique in interphases formed on Si⁰ surfaces. In fact, it is a universal interphasial component provided that the electrolyte solvents are based on carbonate esters. We will come back to revisit this topic in more detail when discussing interphase chemistry and formation in Chapter 12.

Imide-based lithium salts, LiTFSI and especially LiFSI, are often favored salts for Si⁰-compliant electrolytes, along with lithium bis(oxalato)borate (LiBOB) and its half-fluorinated version lithium difluoro(oxalato)borate (LiDFOB) (Table 10.2).

More exotic co-solvents have also found application in Si⁰-compliant electrolytes, which include phosphorus-based (*e.g.* triphenyl phosphate, TPP), silane- or siloxane-based and sulfone-based compounds (*e.g.* dimethyl methylphosphonate, DMMP), along with other fluorinated or unsaturated versions of carbonate molecules, as

well as room-temperature ionic liquids based on large organic cations such as pyrrolidinium, imidazolium, ammonium and phosphonium and organic anions such as FSI and TFSI. This large library of electrolyte compositions is expected to continue to grow, as the removal of the restrictions imposed by a graphite anode indeed provides a high degree of freedom in forming Si⁰-compliant electrolytes.

10.4.1.2 Lithium Metal

It was mentioned earlier that the two major classes of non-aqueous solvents are esters of organic acids (such as carbonate or carboxylate esters) and ethers. Whereas esters are intrinsically reactive with Li⁰ [eqn (10.1)], ethers are relatively stable with Li⁰. For this reason, the early electrolytes capable of producing a Coulombic efficiency higher than 90% were almost exclusively based on ethereal solvents, such as dimethoxyethane (DME), 1,3-dioxolane and glymes of varying chain lengths (Table 10.1). This trend of favoring ethers continued when lithium metal was revisited as a rechargeable anode material in the early 2010s, although in recent years, thanks to the advances in fundamental understanding, esters can also be applied as electrolyte solvents provided that the interphasial chemistry is tailor designed.

However, even in ether-based electrolytes, there is interphase formation on the surface of Li⁰, and such a passivation process occurs instantaneously when Li⁰ is in contact with an electrolyte, because of the low eigenpotential of Li⁰. For those ether solvents that are almost inert towards Li⁰, the interphasial chemistry is entirely dictated by the reduction of the lithium salt anion. For this reason, the interphasial chemistry component most commonly encountered on a lithium-metal surface is LiF, due to the universal presence of fluorine in the anions of the lithium salts used (Table 10.2).

Although the concept of interphase was transplanted from lithium metal to other anode hosts (such as carbonaceous, silicon or other alloys), there is a conspicuous and unique, but often ignored, character of interphases on lithium-metal surfaces that differs significantly from all other anode hosts.

The eigenpotential of lithium metal is extremely low and beyond the electrochemical stability limits of almost all electrolytes. Therefore, before lithium metal is brought into contact with any electrolyte, it is already covered with a native passivation film, the majority chemical ingredients of which are lithium oxide (Li₂O), lithium hydroxide (LiOH) and lithium carbonate (Li₂CO₃). We cannot call this native passivation film an interphase just yet, because it is not thick enough

(<2 nm) to insulate electron tunneling. Upon exposure of lithium to an electrolyte, the electrolyte components, whether solvents or salt anion, would instantaneously and indiscriminately react with both the native passivation film and the underlying Li^0 , producing an interphase that insulates electron tunneling but conducts Li^+ . During this process, the original chemical components of the native passivation film that are alkaline in nature would be mostly consumed by the reactions between them and the salt anions of an acidic nature.

In other words, the interphases on lithium metal are formed in a surface *chemical* process that involves the electrolyte solvents, salt anion, the native passivation components and Li^0 itself.

In sharp contrast, the interphases on graphite, silicon or other anode host materials are formed in an *electrochemical* process, because the eigenpotentials of these host materials are mostly within the electrochemical stability window of most electrolytes and the reduction of electrolyte components does not start until the potential of the anode host is brought down to a point beyond the electrochemical stability limits of the electrolyte. In this case, the reduction occurs in a step-wise rather than indiscriminate manner, making it easier to tailor an interphase chemistry. This is actually the foundation of using electrolyte additives to manipulate interphase chemistry.

Finally, one might wonder whether there is any solvent, organic or inorganic, that is thermodynamically stable with Li^0 .

In fact, there are indeed some. For example, the non-polar hydrocarbon compounds, either aliphatic or aromatic, are almost non-reactive towards Li^0 , examples being *n*-hexane, benzene and toluene. However, the non-polar nature of these molecules gives them an extremely weak capability to dissolve any ionophoric or ionogenic compounds, hence they are nearly useless as electrolyte solvents. This fact highlights the dilemma that we face when formulating new electrolyte systems, because one has to consider the numerous requirements that an electrolyte must simultaneously satisfy in an electrochemical device.

In the “*lithium renaissance*” that started in the 2010s, various approaches have been taken to circumvent the dangerous morphologies of dendritic Li^0 and dead Li^0 , such as a pre-constructed anode host *via* nanostructure design, separator materials designed to regulate Li^+ flux, application of artificial interphases and novel electrolyte concepts.³²

It had been hoped that the adoption of solid electrolytes based on inorganic materials such as ceramics and glasses could completely resolve the Li^0 morphology challenge, but recent findings cast doubt on this simple belief. According to Monroe and Newman, in order for

the growth of lithium dendritic crystals to be physically suppressed, a surface layer with a shear modulus of 6 GPa or higher must be present.³³ Such high mechanical strength is available from glasses or oxide-based solid electrolytes, but difficult to acquire when sulfide-based electrolytes are used. Even with the harder oxide-based materials such as garnet, the grain boundaries in the polycrystalline matrices always provide an opportunity for both dendritic Li⁰ and dead Li⁰ to grow. In fact, numerous studies found that both Li⁰ morphologies are present in solid electrolytes. In addition to the argument that the dendritic Li⁰ growth is mainly enabled by the grain boundaries within the polycrystalline solid electrolytes, others attribute the dendritic Li⁰ growth to the intrinsic electronic conductivity of these ceramic materials at the level of 10^{-7} – 10^{-8} S cm⁻¹, which is higher than those of liquid electrolytes by at least three orders of magnitude. Such moderate electronic conductivity allows Li⁺ to be reduced in the bulk of the solid electrolytes, producing both dendritic Li⁰ and dead Li⁰. While solid electrolytes remain a highly promising option for lithium-metal anodes, their practical application in devices cannot entirely depend on its “solid” nature alone; additional surface treatments might be required, so that the above-mentioned electronic conductivity could be minimized, while creating an intimate interfacing between the solid electrolytes with lithium metal.

The most extensive efforts in developing a rechargeable lithium-metal anode were still focused on tailoring new liquid electrolytes, employing new solvents, new salts, new additives and new liquid structures.

One particular approach deserves to be mentioned here because it attempted to suppress the growth of dendritic Li⁰ directly *via* basic electrochemistry.

We mentioned earlier that a major factor responsible for the growth of dendritic Li⁰ is the uneven distribution of electric field on a rough surface, where any protrusion could serve as the precursor for the budding site of dendrites due to the intensified electric field strength around it (Figure 10.2). Thus, if one can find an inert cation that could resist electrochemical reduction at the potential of Li⁰ deposition, then such an inert cation could enrich and assemble around these protrusions, forming an electrostatic shield against the approach of Li⁺, forcing the Li⁺ to deposit somewhere else, and consequently preventing these protrusions from developing into dendrites (Figure 10.13).

But what cation could remain inert at the same potential when Li⁺ started deposition? At first glance at this question, the intuitive

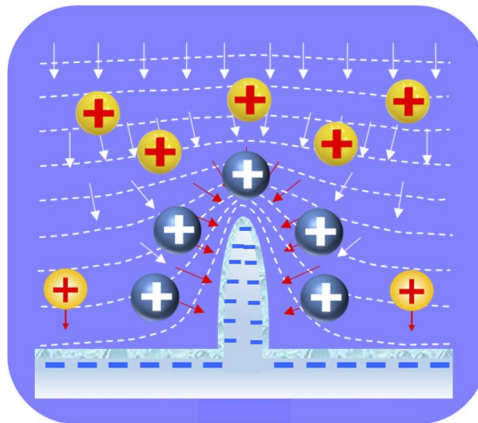


Figure 10.13 The electrostatic shield formed by an inert cation effectively drives away the approaching Li^+ ions and forces them to deposit somewhere else, thus preventing the budding protrusions on an electrode from developing into dendrites.

answer would be “none”, as we have discussed in previous sections that Li^0 is the most electropositive element in the Periodic Table, and its standard reduction potential is the lowest (-3.04 V vs. SHE , Table 10.3). There should be no cation that could remain inert at the potential of Li^+ reduction.

However, one must remember that all of the reduction potentials listed in Table 10.3 are the so-called “*standard potentials*”, *i.e.* these are the values measured under strictly standard conditions, such as 298 K (25°C), the activity of all involved species in liquid being 1.0 and the partial pressure of all species involved in the gaseous phase being 1.0 atm.

The actual reduction potential of a species in the electrolyte is governed by the Nernst equation, which was described in Chapters 6 and 9 in various forms [eqn (6.76), (6.98) and (9.22)], but with the same message that such potentials vary with the ratios of the activities or partial pressures of the species involved. From these equations, we can derive one variation for a cationic species M^+ (oxidized form) that experiences reduction to become elemental M^0 (reduced form) by assuming that the activity of M^0 (α_{red}) is simply 1.0:

$$E_{\text{red}} = E_{\text{red}}^\varphi - \frac{RT}{zF} \ln \frac{\alpha_{\text{red}}}{\alpha_{\text{ox}}} = E_{\text{red}}^\varphi - \frac{0.05916\text{V}}{z} \log_{10} \frac{1}{\alpha_{\text{ox}}} \quad (10.13)$$

where R , T , α , F and z are the universal gas constant, absolute temperature, chemical activity for related species, Faraday constant and the valence number of the species involved, respectively.

Therefore, it is possible to find a few elements with reduction potentials that are in close proximity to that of Li^0 , and to manipulate their actual reduction potentials by adjusting their activities α_{ox} so that they could be inert against reduction at Li^0 . There are only a few elements that meet this requirement, and cesium (Cs) and rubidium (Rb) are among them (Table 10.3). Indeed, when their concentration (and activity) in an electrolyte is lower than 0.1 M, their reduction potentials would cross that of Li^+ and they become inert against reduction at the potential where Li^+ deposition starts (Table 10.4).

Thus, using Cs^+ and Rb^+ at additive levels could create the so-called “electrostatic shield” and prevent continuous Li^+ deposition at those budding sites into dendrites, and Li^+ would be forced to adjacent regions and be deposited thereon. The net consequence is the overall “leveling” of the metallic lithium surface.

Such a strategy was confirmed experimentally.³⁴ Not only was the dendrite formation suppressed in the presence of a Cs^+ salt at different concentrations, but also the already formed dendrites gradually disappeared in the presence of the additive. However, it should be cautioned that the safety margins created in reduction potentials by concentration (or activity) difference are rather fragile, and accidental deviation from these quasi-equilibrium values, induced by a high charging current or local polarization, would result in consumption of these additive cations and loss of the protective mechanism.

Of course, such a strategy also only works when the Li^+ concentration is far from that of the inert cation. Fortunately, this requirement is often readily met because, as the major working ion in the cell chemistry, Li^+ has a concentration that is almost always in the neighborhood of 1.0 M, and in super-concentrated electrolytes its concentration could be much higher.

Table 10.4 The actual reduction potentials (E°/V vs. SHE) of Rb^+ and Cs^+ compared with that of Li^+ at low concentrations.

Cation	Concentration/M				
	1.0	0.001	0.01	0.05	0.1
Li^+	-3.040				
Rb^+	-2.981	-3.157	-3.098	-3.057	-3.039
Cs^+	-3.026	-3.203	-3.144	-3.103	-3.085

Most of the efforts attempting to make lithium-metal electrodes safely reversible resorted to innovations in the electrolytes and interphases.

Thanks to the in-depth understanding of interphasial chemistries that have been driven by and benefited from the commercial success of lithium-ion batteries since the 1990s, and assisted by advanced characterization and powerful computation techniques, the interphasial chemistries can be manipulated in a qualitative manner. It should be emphasized that we still do not have precise knowledge about how each electrolyte component participates in the interphase formation, or how each identified interphasial component functions; however, that does not prevent us from addressing this challenge *via* a trial-and-error and semi-empirical approach.

Among the numerous interphasial components identified so far, fluorine-rich species, such as LiF and fluorocarbons, have generally been considered as more effective ingredients in suppressing dendritic Li^0 and dead Li^0 , while maintaining the Coulombic efficiency at a level above 99%. This does not mean, however, that simply increasing the fluorine content would accomplish these aims. It seems that how these fluorine species exist and are distributed across the interphases are as important as their content. The semiempirical rule obtained from recent efforts shows that the fluorine has to be pre-stored in either the solvent molecular structure or salt anion structure in some way, which, upon electrochemical decomposition, will be released to become part of the interphases. For this purpose, numerous fluorinated solvent molecules have been designed and tested, including not only fluorinated esters but also ethers, which were known to be more stable with Li^0 but less stable against an oxidative environment on the cathode.

On the other hand, the salt anions are already highly fluorinated, as exemplified by PF_6^- , TFSI and FSI. A simple approach is to increase the salt concentration, so that the opportunity for the fluorine from those anions to become part of the interphase would correspondingly increase. This is part of the basis of the so-called “super-concentrated electrolytes” that prevailed after the 2010s.

One particular non-fluorinated salt anion, nitrate (LiNO_3), deserves to be mentioned here, owing to its successful and extensive use as an interphase additive in lithium–sulfur chemistries. It was believed that dense and compact layers of interphases consisting of LiN_xO_y and lithium nitride (Li_3N) are formed due to the reduction of NO_3^- by Li^0 . To exploit further the advantage of a nitride-rich interphase, researchers even proposed the use of lithium azide (LiN_3) as an electrolyte

additive, which indeed results in better interphases containing higher amounts of Li₃N. However, one must caution against the excessive use of these nitrogen-based salts and additives in electrolytes when considering safety aspects. After all, the combination of sulfur, nitrate and carbon (the omnipresent electrode ingredient) is reminiscent of the familiar formula of black gunpowder, let alone the fact that azide itself has a strong chemical tendency to release nitrogen gas.

10.4.1.3 Sodium and Potassium Metals

Inspired by the success of lithium-ion batteries and driven by the limited lithium reserves in the Earth's crust, sodium (Na) and potassium (K), as the closest analogs of lithium in the Periodic Table, have been attracting interest as potential replacements in battery chemistries.³⁵ Like lithium metal, both sodium and potassium are extremely reactive (Table 10.3), which renders them naturally advantageous in terms of cell voltage and energy density when coupled with given cathode materials, but at the same time also raises concerns over safety, reversibility and dangerous morphologies of dendritic and dead Na⁰/K⁰. Of these two metals, sodium has been more favored because of its higher abundance in both the Earth's crust and oceans, and also the associated higher specific capacity.

Research on sodium- and potassium-based batteries has followed similar lines to that on lithium-metal and lithium-ion batteries. This is reflected not only in the similar non-aqueous solvents adopted to dissolve sodium and potassium salts, but also in the practice of seeking a carbonaceous host to accommodate Na⁺ or K⁺ so that the corresponding metal anodes are circumvented.

The initial hope of intercalating Na⁺ into graphite was not realized because the binary graphite intercalation compound NaC_x is thermodynamically unstable unless the Na⁺ is in an extremely diluted state, such as $x = 48\text{--}80$, corresponding to insignificant capacities in the range 27–46 mAh g⁻¹. Such values are impractical compared with the binary graphite intercalation compound of graphite and Li⁺, whose fully lithiated state LiC₆ corresponds to 372 mAh g⁻¹. As a consequence, researchers were forced to look at non-graphitic carbonaceous materials such as hard carbon, which can accommodate Na⁺ to a capacity of ~330 mAh g⁻¹. This value may appear to be close to that delivered by Li⁺ intercalation in graphite, but in reality the energy delivered by an actual sodium-ion battery is much lower, for two reasons. (1) The calculation of such a capacity is based on the neat weight of the host (*i.e.* carbon host), and the mass of the guest ion (Li⁺ or K⁺)

is not counted (see related discussions in Section 9.1.3.6). However, in real-life batteries all materials have to be counted, and the much heavier Na^+ (atomic weight 22.98 g mol⁻¹ for Na^+ vs. 6.95 g mol⁻¹ for Li^+) would undoubtedly further reduce the actual capacity and energy of the device. (2) The sodiation voltage profile of hard carbon is not only high but also steep, similar to the lithiation profile of petroleum coke but distinctly different from the flat plateau of graphite lithiation, as shown in Figure 10.5. There is a corresponding loss of energy in such steep voltage profiles as the energy is represented by the area enclosed by the voltage profiles of the anode and cathode. The combination of these factors renders a sodium-ion battery a much less energy-dense device than a lithium-ion battery, and their future markets seems to be mostly confined to applications where energy density is not as important as cost, such as in stationary grid energy storage rather than in portable electronics or vehicle electrification.

The typical electrolytes used in sodium-metal and sodium-ion batteries are very similar to those used in corresponding lithium-metal and lithium-ion cells, *i.e.* NaPF_6 , NaTFSI or NaFSI dissolved in carbonate solvents. Since hard carbon has a disordered structure, the restriction on PC-rich electrolyte formulations is lifted, and PC could be used as a major solvent for sodium electrolytes. SEI would still be expected to form considering the low sodiation potential (-2.7 V vs. SHE) at the hard carbon anode, which will be discussed in Chapter 12.

Most cathode intercalation hosts for Na^+ chemistry, based on variants of either transition metal oxides or phosphates, operate below 4.5 V, hence the requirement for anodic stability was not particularly challenging in comparison with lithium-ion battery cathode materials.

Ether-based electrolytes such as DME were also explored for sodium-metal and sodium-ion batteries, where higher ion conductivities were achieved at the expense of electrochemical stability. On the other hand, the optimized systems often consisted of mixtures of carbonates similar to the electrolytes used for lithium-ion batteries, but with much lower linear carbonate ratios, mainly because sodium salts are much less soluble than their lithium counterparts, and usually require the use of polar solvents with dielectric constants above 10.

Of particular interest is the finding that, as in similar studies conducted on Li^+ electrolytes, Na^+ also favors EC in its solvation sheath over acyclic carbonate (DMC or EMC), as evidenced by Raman spectra and also electro-spray ionization mass spectra (ESI-MS) results, and this preferential solvation of Na^+ by EC would be directly linked to the interphasial chemistry on hard carbon, as discussed in Chapter 12.

In addition to non-aqueous electrolytes based on carbonates, polymer gel and ionic liquid electrolytes were also evaluated for sodium-ion batteries. However, as for lithium-ion batteries, most of these systems remain experimental curiosities rather than practical electrolyte systems, because more issues were introduced that need to be resolved, such as insufficiently high ion conductivity, interfacial contacts with electrode surfaces and electrochemical stabilities.

The safety aspects of sodium-ion chemistry were investigated using accelerating rate calorimetry (ARC), in which the reactivity of fully sodiated hard carbon Na_xC_6 was compared with that of its lithiated counterpart Li_xC_6 . A rather surprising result was obtained: an NaPF_6 -based electrolyte showed higher reactivity towards Na_xC_6 than an LiPF_6 -based electrolyte towards Li_xC_6 , hence making sodium-ion batteries less safe than lithium-ion batteries despite the higher energy of the latter. This paradox arises from the more effective passivation imposed by the unstable LiPF_6 on the charged anode. Here, the kinetics once again outperforms the thermodynamics.

Between cyclic and linear carbonates, Na_xC_6 was found to react more readily with the former, and XRD analyses identified the formation of semicarbonates, probably *via* similar reaction mechanisms known for Li^+ electrolytes. The preferential solvation of Na^+ by EC also seemed to affect the reactivity between Na_xC_6 and the electrolyte, as the activation of the polar solvent molecules by the Coulombic force of the cation has been accepted as a key factor dictating the reactivity of the solvent molecule. Since EC would be preferentially “recruited” by Na^+ when a sodium salt was present, leaving mostly acyclic carbonate molecules such as DMC or DEC in the bulk, the reaction between Na_xC_6 and cyclic carbonate would also be encouraged owing to the higher effective concentration of the latter at the interfaces with the carbonaceous anode.

Potassium can intercalate into the graphitic structure and form binary graphite intercalation compounds at relatively high concentration. The fully potassium state KC_8 corresponds to a theoretical capacity of 279 mAh g⁻¹, again a value that does not count the mass of the even heavier potassium (39.09 g mol⁻¹). The actual capacity achieved approaches this value (~273 mAh g⁻¹) when mixed carbonate electrolytes are used, but reversibility is generally inferior compared with not only lithium-ion but also sodium-ion batteries. Both carbonate ester and ether electrolytes have been used for potassium-metal and potassium-ion batteries. The potassium salts are more soluble than sodium salts, hence the choice of solvents shows better

flexibility. The enthusiasm for potassium-based batteries is moderate, apparently because of their moderate energy output, greater challenges and higher cost compared with sodium-based batteries.

10.4.1.4 Multivalent Cation Chemistries

While lithium has *one* of the highest specific capacities (3856 mAh g⁻¹) among all the elements in the Periodic Table, *the* highest specific capacity is shown by beryllium, because the beryllium cation (Be²⁺) is a divalent cation, the divalent nature of which compensates its higher atomic mass (Section 9.1.3.5):

$$\begin{aligned} C_{\text{Be}}^{\text{s}} &= \frac{0.2778z_{\text{Be}}F}{M_{\text{Be}}} = \frac{0.2778 \times 96 | 485 \times 2 \text{ mAh mol}^{-1}}{9.0122 \text{ g mol}^{-1}} = \frac{53|602.962 \text{ mAh mol}^{-1}}{9.0122 \text{ g mol}^{-1}} \\ &= 5948 \text{ mAh g}^{-1} \end{aligned} \quad (9.67)$$

Of course, we cannot use Be as a battery electrode material, because of its low abundance (even lower than lithium) and its high toxicity; however, this fact reveals that there is a certain advantage in multiple cation chemistries, especially when their abundance in the Earth's crust is high. Therefore, calcium, magnesium, zinc and even aluminum have been actively considered as viable working ions beyond lithium-ion battery concepts, because their high valence at least partially offsets their heavier mass.³⁶

$$C_{\text{Mg}}^{\text{s}} = \frac{0.2778z_{\text{Mg}}F}{M_{\text{Mg}}} = \frac{53\ 602.962 \text{ mAh mol}^{-1}}{24.30 \text{ g mol}^{-1}} = 2205.88 \text{ mAh g}^{-1} \quad (10.14)$$

$$C_{\text{Ca}}^{\text{s}} = \frac{0.2778z_{\text{Ca}}F}{M_{\text{Ca}}} = \frac{53\ 602.962 \text{ mAh mol}^{-1}}{40.08 \text{ g mol}^{-1}} = 1337.39 \text{ mAh g}^{-1} \quad (10.15)$$

$$C_{\text{Zn}}^{\text{s}} = \frac{0.2778z_{\text{Zn}}F}{M_{\text{Zn}}} = \frac{53\ 602.962 \text{ mAh mol}^{-1}}{65.38 \text{ g mol}^{-1}} = 820 \text{ mAh g}^{-1} \quad (9.65)$$

$$C_{\text{Al}}^{\text{s}} = \frac{0.2778z_{\text{Al}}F}{M_{\text{Al}}} = \frac{80\ 404.444 \text{ mAh mol}^{-1}}{26.98 \text{ g mol}^{-1}} = 2980 \text{ mAh g}^{-1} \quad (9.66)$$

With these promises comes the challenge of moving these multivalent cations.

In the preceding chapters, Li^+ has been described as a point charge with a strong Coulombic force field, which recruits solvent molecules around itself, strongly binds them and forms a solvation sheath that results in relatively slow Li^+ movement compared with anions.

In comparison, these multivalent cations, after losing electrons in their valence shells, would have ionic radii that are comparable to or even smaller than that of Li^+ (Table 10.5). With the multiple formal charge ($2\times$ or $3\times$) that they carry, the Coulombic field emitted from them is naturally much stronger, and the solvent molecules in their solvation sheaths are much more tightly trapped.

Such strong interactions between multivalent cations and their environments makes it extremely difficult for them to move, not only through the bulk electrolytes but even more so across the interphases and through the solid electrode lattices. In fact, it was believed for a very long time that there should be *no interphase* present on the surface of electrodes for these multivalent cations, otherwise the interphase will immediately prohibit the migration of the corresponding multivalent cations and terminate the operation of cell chemistry.

The “interphase-free” belief has been the central concept dictating the design and development of most Mg and Ca electrolytes, because the reduction potentials of these two cations are rather low (Table 10.5), where most electrolytes, especially those based on esters, tend to experience reduction and subsequently form interphases on these metals. Requiring the electrolytes to remain inert at these potentials places an extremely harsh restriction on the choice of electrolyte solvents and also salt anions. Eventually, the only electrolytes that can pass this rigorous selection criterion are those that can intrinsically resist reduction, such as salts with anions based on Grignard reagents or borohydrides and solvents that are essentially ethers.

The bonds between Mg^{2+} or Ca^{2+} and these organometallic anions are actually more covalent rather than ionic by nature, and the

Table 10.5 Ionic radii and reduction potentials of Li^+ and selected multivalent cations.

Parameter	Cation					
	Li^+	Be^{2+}	Mg^{2+}	Ca^{2+}	Zn^{2+}	Al^{3+}
Ionic radius/pm (10^{-12} m)	90	59	86	114	88	67.5
Reduction potential/V vs. SHE	-3.04	-1.85	-2.371	-2.866	-0.763	-1.166

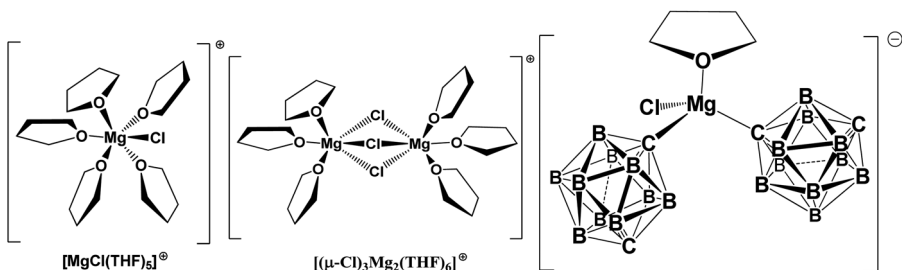


Figure 10.14 Selected conductive species identified in various Mg electrolytes.

conducting species in these electrolytes are often complex clusters consisting of dimeric or polymeric cations with halide bridges (Figure 10.14), hence the freedom of Mg^{2+} and Ca^{2+} was significantly restricted, as reflected in the sluggish kinetics of Mg^{2+} and Ca^{2+} deposition and usually low ion conductivities of these Grignard-like electrolytes.

More importantly, although these electrolytes indeed remain stable at low potentials with Mg^0 and Ca^0 , and successfully allow reversible deposition/stripping of Mg and Ca at high Coulombic efficiencies, they face a dilemma, because their reductive nature also implies a readiness to experience oxidation, *i.e.* their resistance against oxidative decomposition is weak. In fact, neither these organometallic anions nor ethers could withstand the oxidation at potentials above 3 V. This anodic instability imposes a limit on the upper voltage for the possible cathode materials under development for the multivalent cation chemistries, and hence restricts the realization of their potentially high energy density promised by the multivalency.

As a possible solution to such a dilemma, a few recent findings reversed the previous belief that multivalent ions cannot transport across interphases. Instead, both Mg^{2+} and Zn^{2+} were found to conduct through certain interphases formed on Mg^0 and Zn^0 surfaces. In some cases, the interphases must be preformed with these multivalent cations embedded inside, so that a conducting channel could be maintained; in others, the interphases can be directly formed from the decomposition of electrolytes. These interphases will be discussed in more detail in Chapter 16.

Nevertheless, the possibility of an interphase conducting multivalent ions implies that it is possible to lift the strict “interphase-free” requirement, which would allow ester-based electrolytes to be used in these multivalent cation chemistries. Such decoupling of the need

for interfacial stability from the bulk composition is exactly what lithium-ion batteries are constructed upon. It opens up the scope for developing high-voltage (4 V class) cathode materials with diverse structures, and might become a main direction in the future to seek new multivalent ion electrolytes.

10.4.2 Cathode

As discussed in Section 9.1.3.5, the specific capacity of a battery is determined by the specific capacities of individual electrodes *via* eqn (9.80):

$$C_{\text{cell}}^s = \frac{C_A^s C_C^s}{C_A^s + C_C^s} \quad (9.80)$$

which dictates that the electrode of lower specific capacity constitutes a bottleneck to the whole cell specific capacity. For a lithium-ion battery, this bottleneck is apparently on the cathode side, as shown graphically in Figure 9.6, because the maximum specific capacity provided by various transition metal oxides is still around 200 mAh g^{-1} , while the specific capacity actually realized on a graphitic anode is already above 300 mAh g^{-1} . The adoption of lithium metal would further push the anode specific capacity up to 3856 mAh g^{-1} , leaving the improvements in the whole cell capacity more constrained by the cathode side.

It was because of this asymmetry of capacity that most resources in battery research nowadays are allocated to the cathode side, because the incentives to find a better cathode are of greater urgency.

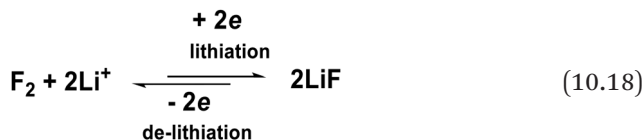
From the perspective of electrochemical redox potential, one ideal conversion reaction cathode material is fluorine (F_2), which promises a high specific capacity that outperforms the majority of elements in the Periodic Table:



$$C_{\text{F}}^s = \frac{0.2778 z_{\text{F}_2} F}{M_{\text{F}_2}} = \frac{53 | 602.962 \text{ mAh mol}^{-1}}{37.98 \text{ g mol}^{-1}} = 1411.32 \text{ mAh g}^{-1} \quad (10.17)$$

Such a high specific capacity, in combination with its high redox potential ($\sim 5.91 \text{ V vs. Li}$ or 2.87 V vs. SHE), makes it *the ultimate cathode*. When combined with *the ultimate anode*, lithium metal, one could

build a 6 V super-battery, with the cell chemistry, whole cell specific capacity and energy density given by



$$C_{\text{cell}}^s = \frac{C_A^s C_C^s}{C_A^s + C_C^s} = \frac{3856 \times 1411}{3856 + 1411} = 1033 \text{ mAh g}^{-1} \quad (10.19)$$

$$E_{\text{cell}}^s = C_{\text{cell}}^s \times \Delta V = 1033 \times 5.91 \text{ mW h g}^{-1} = 6105 \text{ W h kg}^{-1} \quad (10.20)$$

However, such a powerful battery chemistry can only exist on paper.

The extreme reactivity and danger of F_2 (much greater than those associated with lithium metal), together with its gaseous nature, make it an especially unlikely cathode material. More realistic cathode materials from the Periodic Table, therefore, are those based on the redox reactions of either oxygen or sulfur.

10.4.2.1 Oxygen

Oxygen (O_2) is also gaseous, but chemically it is much less aggressive than F_2 . More importantly, it is available from the ambient air. The latter advantage makes it possible to extract cathode active material directly from the ambient air with an open-cell design, although under most circumstances O_2 is still supplied in neat form in an enclosed cell structure, because impurities from the ambient air, CO_2 in particular, often render the cell chemistries irreversible. Distinctions can often, but not always, be made whether to call the battery a “lithium/oxygen battery” or a “lithium/air battery”.

Chemically, an oxygen cathode would be identical with the cathode in a fuel cell as described in Section 9.1.1 (Figure 9.1), with the exception that the oxygen in a fuel cell does not require recharging, because the fuel cell is a conversion device, not a storage device. To keep the oxygen cathode reversible upon recharging is the main challenge faced by a lithium/oxygen or lithium/air battery.³⁷ More often than not a compromise has to be made in terms of energy and capacity for reversibility.

O_2 as a cathode material could experience either a two-electron ($2e^-$) reduction as described by eqn (9.68), forming peroxide (O_2^{2-}):



with $z_{O_2} = 2$, and a corresponding specific capacity of

$$C_O^s = \frac{0.2778 z_{O_2} F}{M_{O_2}} = \frac{53\,602.962 \text{ mAh mol}^{-1}}{31.998 \text{ g mol}^{-1}} = 1675.19 \text{ mAh g}^{-1} \quad (10.22)$$

or a four-electron reduction, forming the more completely reduced form, oxide (O^{2-}):



with $z_{O_2} = 4$ and a corresponding specific capacity of

$$C_O^s = \frac{0.2778 z_{O_2} F}{M_{O_2}} = \frac{107\,205.93 \text{ mAh mol}^{-1}}{31.998 \text{ g mol}^{-1}} = 3350.334 \text{ mAh g}^{-1} \quad (10.24)$$

The redox potential of these reactions varies with both pH value and solvation environment of the related species in either aqueous or non-aqueous electrolytes. For example, as Figure 5.12 indicates, the four-electron chemistry of oxygen usually occurs between 1.229 and 0.401 V vs. SHE (or between 4.269 and 3.441 V vs. Li).

Nevertheless, by adopting a median voltage value of 3.0 V, we can roughly estimate that, when coupled with a lithium-metal anode, the above chemistries would proceed respectively according to



promising specific capacities of

$$C_{cell}^s = \frac{C_A^s C_C^s}{C_A^s + C_C^s} = \frac{3856 \times 1675}{3856 + 1675} = 1167 \text{ mAh g}^{-1} \quad (10.26)$$

$$C_{\text{cell}}^{\text{s}} = \frac{C_{\text{A}}^{\text{s}} C_{\text{C}}^{\text{s}}}{C_{\text{A}}^{\text{s}} + C_{\text{C}}^{\text{s}}} = \frac{3856 \times 3350}{3856 + 3350} = 1792 \text{ mAh g}^{-1} \quad (10.27)$$

and energy densities of

$$E_{\text{cell}}^{\text{s}} = C_{\text{cell}}^{\text{s}} \times \Delta V = 1167 \times 3.0 \text{ mW h g}^{-1} = 3501 \text{ W h kg}^{-1} \quad (10.28)$$

$$E_{\text{cell}}^{\text{s}} = C_{\text{cell}}^{\text{s}} \times \Delta V = 1792 \times 3.5 \text{ mW h g}^{-1} = 5376 \text{ W h kg}^{-1} \quad (10.29)$$

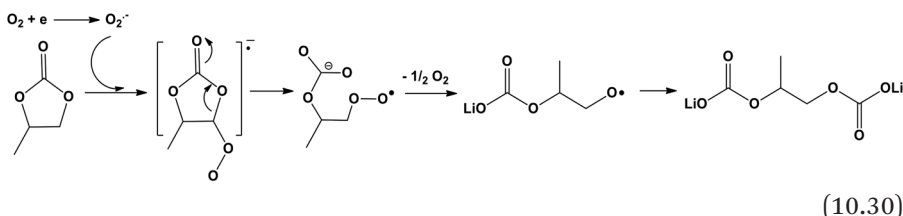
In the popular science news media, a lithium/oxygen or lithium/air battery is often cited as a battery that could compete with gasoline in an internal combustion engine, boasting an energy density of $>10\,000 \text{ W h kg}^{-1}$. Apparently such high numbers are based on a single electrode only, mainly in the hope that the cathode material O_2 can be directly extracted from the ambient air and hence not contributing mass to the cell. So far, this has been just an optimistic wish, as in most cases the hope of using free oxygen cathode material from the ambient air has not been realized.

Nevertheless, the numbers given by eqn (10.28) and (10.29) are still astonishing, comparable to or even higher than the 6 V Li/ F_2 superbattery. In real cells, even after discounting by considering the mass of oxygen active material and the cell packaging, the eventual energy density could still remain at a high level, if the promised potential of oxygen redox reactions could be fully accessed.

Here again, the multivalency of oxygen chemistry provides a sharp competitive edge in terms of promised capacity and energy. However, in reality, the multivalency often results in reversibility issues that most multivalency chemistries are known to suffer, which involve more electrons and higher kinetic barriers. To mitigate the reversibility of oxygen chemistries, researchers have often tried to confine the chemistry to the two-electron stage, as peroxides encounter a much lower kinetic barrier to oxidation.

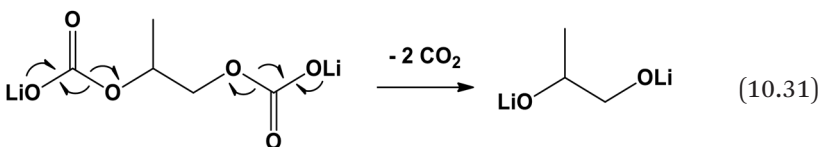
The challenges faced by electrolytes in a lithium/oxygen battery include not only the long-known problem of protecting and stabilizing the lithium-metal anode, but also the new requirements such as the ability to dissolve and transport O_2 molecules and stability against the reactive O_2 reduction products such as peroxides (Li_2O_2) or even superoxide intermediates (LiO_2).

Despite their success in lithium-ion batteries, carbonate esters are unstable against either the lithium-metal anode or the highly reactive peroxides or superoxides, which would initiate nucleophilic attack on the electron-deficient center in the carbonate molecules, *i.e.* the carbonyls:



in which the reaction proceeds *via* a carbonate-peroxide intermediate, eventually breaking down into semicarbonates. It is believed that only a superoxide can initiate such nucleophilic attacks, as peroxides are rather unreactive towards carbonate molecules. Unfortunately, the former is an inevitable intermediate during the reduction chemistry of oxygen.

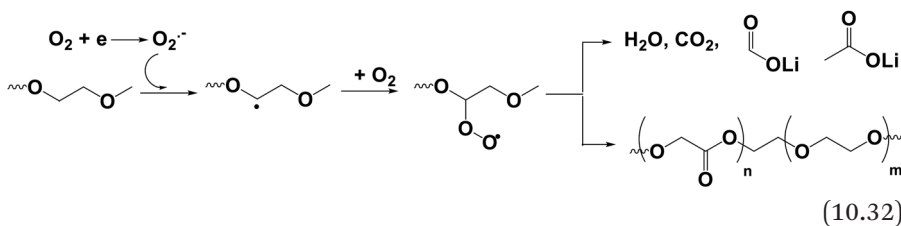
What brings more complications to the situation is that, since the semicarbonates formed are situated on the cathode, they could oxidatively decompose upon recharging to >4.0 V:



These parasitic reactions compete with the oxygen reductions, and lead to a mixture of inorganic species such as Li_2CO_3 , carboxylate, Li_2O , *etc.*, along with H_2O and CO_2 , the presence of which significantly affects the reversibility of Li/O_2 battery chemistries and contributes to the hysteresis between charging and discharging potentials, an indicator for poor round-trip energy efficiencies. In fact, the “rechargeable Li/O_2 batteries” reported in the early 2010s were actually an artifact created by the reactivity of these carbonate molecules towards superoxides, and the subsequent oxidation of these products.

Eventually, the incompatibility between carbonate esters and oxygen chemistry forced researchers to seek new non-aqueous electrolytes based on ethers and other exotic solvent molecules.

Ethers are not ideal owing to their low anodic stability, although they favor the two-electron reduction of oxygen to peroxide, the preferable end product for oxygen chemistry in terms of reversibility. However, ethers could still undergo reactions with superoxide, which extracts the α -hydrogen from the ether linkage and eventually oxidizes ethers to compounds with carbonyl functionalities:



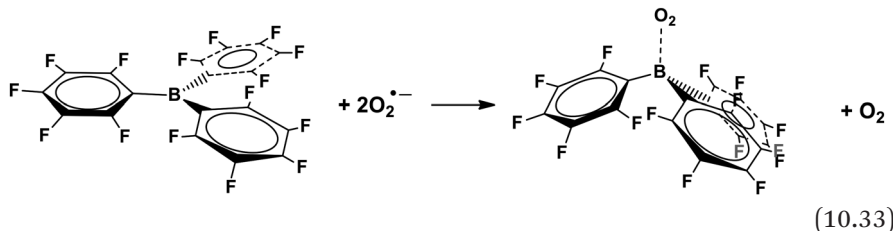
Once these new species with carbonyls have been formed, a new vicious cycle described by eqn (10.30) and (10.31) starts.

Exotic solvent molecules such as nitriles, alkylamides, sulfoxides, lactams and ionic liquids seem to behave better, but still none of these allow an Li/O₂ battery to be truly “rechargeable”. It seems that the two constraints that an ideal Li/air electrolyte solvent must satisfy simultaneously are often inversely correlated, *i.e.* (1) low electrophilicity in order to remain stable against the attack from strong nucleophiles such as superoxide, O₂^{·-}, and (2) high ionization in order to remain stable against oxidation. Ether and ester compounds happen to serve as examples at two extremes of these paradoxical criteria, as the former were generally less susceptible to nucleophilic attack from O₂^{·-} but vulnerable to oxidation, whereas the latter were known for better anodic stability against oxidation but reacted readily with O₂^{·-}. Other requirements such as solubility and transport properties of both Li⁺ and oxygen just add to the already stringent requirements.

Fluorinated compounds are well known for their capability in dissolving O₂. Partially fluorinated or perfluorinated compounds such as fluorinated phosphites and phosphates and tris(perfluorobutyl) amine all led to certain improved kinetics and efficiency.

Various electrolyte additives are used to stabilize peroxides and superoxides, so that they do not react with non-aqueous electrolyte solvents such as carbonate esters. For example, crown ethers with suitable cavities can be used as additives to capture Li⁺, so that the corresponding peroxide could be solvated; ammonium cations, NR₄⁺, can be used to coordinate with superoxide radicals based on the hard–soft acid–base (HSAB) model, because the ammonium–superoxide

complex should be considered a “soft–soft” interaction; an anion receptor such as tris(pentafluorophenyl)borane could serve as a scavenger for peroxide anions, which forms a strong complex to promote the reoxidation of peroxide with better kinetics:



Despite these innovative efforts, the Li/O₂ battery remains a remote future prospect, and its electrolyte is by no means the only challenge that it needs to overcome. In fact, every component of Li/O₂ battery chemistry faces unique challenges, including the lithium-metal anode, the electrolyte, which must meet all of the above-mentioned criteria, and the triphasic reaction sites at the air cathode, which must simultaneously access gas, liquid and solid reactants. The sum of all these challenges only magnifies the multitude of efforts needed.

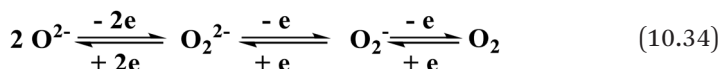
In addition to the tantalizing energy densities promised by the Li/O₂ battery, one also needs to consider the potential risks once such promises have been realized. Peroxides and superoxides have always been a topic of safety training for chemistry undergraduates, and their coexistence with organic molecules such as ethers and acetones increases such concerns. However, in Li/O₂ chemistry they are either the intended or the inevitable products if the electrochemistry proceeds as desired. Furthermore, during the complicated interactions between the reduced oxygen species and the electrolyte or electrode components, the possibility of forming compounds of similar or even higher instability cannot be excluded. The combination of these species with the most energetic anode material (metallic lithium) and flammable non-aqueous electrolytes makes the general safety of Li/O₂ chemistry a legitimate concern, as with any high energy density battery chemistry.

The research on small laboratory devices has thus far found low risks associated with the chemistry, but when the performance of Li/O₂ or Li/air batteries reaches a certain maturity for practical deployment, their safety has to be more rigorously examined before substantial scale-up efforts are made.

An alternative pathway to leverage oxygen redox chemistry takes a compromise approach between intercalation and conversion reaction chemistries.

Oxygen species exist as oxide anions (O^{2-}) in the layered, spinel or olivine structures of transition metal oxides. By design, they would not participate in electrochemical redox reactions. Thus, in potential regions <4.5 V, the redox reactions always occur at the transition metal sites, accompanied by intercalation/de-intercalation of Li^+ . This is the intercalation chemistry already employed with lithium-ion batteries.

However, it was observed that, when a typical lithium-ion battery cathode, such as $LiCoO_2$ or $LiMn_2O_4$, is charged to extremely high potentials (usually >4.5 V), oxygen is always released. This is because at these high potentials, the energy band of the electrons in the 3d orbitals of a transition metal overlaps with the 2p electrons of these oxides, hence oxygen participates in the oxidation sequentially:



Normally, such processes are irreversible and considered harmful to the cell, because they are often accompanied by the collapse of lattice structures and the generation of highly active singlet oxygen atoms. The vigorous reactions between this singlet oxygen and the electrolyte components result in catastrophic failure of the battery.

However, in certain circumstances, when an electrode material is properly structured, it is possible to confine these reactions to some extent, so that the process is reversible. This creates the possibility of harnessing these oxygen redox reactions for additional energy storage capacity. Since the oxygen atoms are already immobilized in the form of oxides on lattice structures, they do not experience the transport and diffusion difficulties that neat oxygen gas must encounter in the conventional Li/O_2 or Li /air batteries.

Since such a class of new “oxygen cathode” materials is still under exploration, the requirements that an electrolyte must meet remain to be elucidated. However, solvent molecules that can resist chemical reactions with oxidative species such as peroxides or superoxides, and also resistance against electrochemical oxidation on the surface of cathode materials, should be a direction for future electrolyte research.

10.4.2.2 Sulfur

In the Periodic Table, sulfur essentially behaves similarly to oxygen in its two-electron redox chemistry:



$$C_s^s = \frac{0.2778z_s F}{M_s} = \frac{53\,602.962 \text{ mAh mol}^{-1}}{32.065 \text{ g mol}^{-1}} = 1671.69 \text{ mAh g}^{-1} \quad (10.36)$$

The redox potential of sulfur (2.1–2.5 V) is lower than that of oxygen (>3.0 V), hence the corresponding specific capacity and energy density, assuming an average operating potential of 2.15 V, available from its coupling with lithium metal should be

$$C_{\text{cell}}^s = \frac{C_A^s C_C^s}{C_A^s + C_C^s} = \frac{3856 \times 1671}{3856 + 1671} = 1165 \text{ mAh g}^{-1} \quad (10.37)$$

$$E_{\text{cell}}^s = C_{\text{cell}}^s \times \Delta V = 1165 \times 2.15 \text{ mW h g}^{-1} = 2504 \text{ W h kg}^{-1} \quad (10.38)$$

The major difference between oxygen and sulfur, both advantageous and disadvantageous, is that sulfur is a solid.³⁸ Being a solid means that it is easier to handle as an electrode material than gaseous oxygen, and the cell configuration could adopt a more traditional design with a hermetic seal, which excludes interference from the ambient environment. However, not directly available from the ambient air means a lower energy density and higher cost, if the potential promises of the oxygen cathode could be fully realized. The abundance of highly pure sulfur in the Earth's crust ensures that sulfur chemistry is not expensive, even if the sulfur is not completely free. Rather, the immediate challenge in sulfur chemistry is its complications in non-aqueous electrolytes, despite the simplicity that eqn (10.35) might suggest.

Sulfur atoms show a strong tendency for catenation, forming long homoatomic chains or homocyclic rings of various sizes. The most abundant and stable form of sulfur in Nature is the cyclic octamer S₈, which is crystalline at room temperature. During its reduction, it experiences a serial stepwise reaction that starts with ring opening, *via* the formation of various intermediates called *polysulfides*, until it reaches the final reduced form S²⁻.

Whereas both the starting material S₈ and the final reduction product (Li₂S if the anode is lithium metal) are solids with minimal

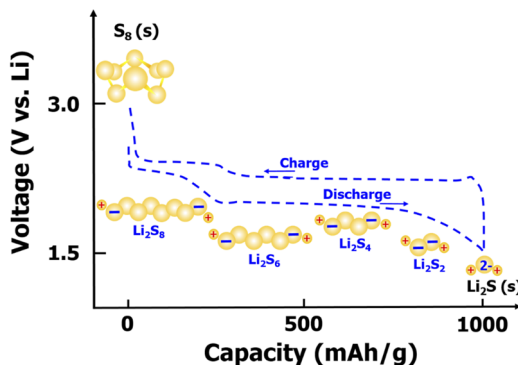


Figure 10.15 Voltage profile of a lithium/sulfur cell in an ether-based non-aqueous electrolyte. The partial reduction of sulfur leads to the formation of polysulfides of various lengths, which in turn correspond to the different sections of voltage plateaus.

solubility in non-aqueous electrolytes, these polysulfide intermediates, especially the higher ordered ones, are very soluble in most non-aqueous solvents. In non-aqueous electrolytes, the formation of these polysulfides corresponds to a two-stage voltage plateau at 2.3 and 2.1 V *vs.* Li, which represent the sequential conversions of S_8 to Li_2S_6 , Li_2S_4 and Li_2S (Figure 10.15). Upon charging, Li_2S would be sequentially oxidized to Li_2S_6 , Li_2S_4 and eventually S_8 , thus completing a reversible cycle, or at least one would hope so.

Thus, during this conversion reaction cycle, the electrochemically active material is first available as a solid only from the bulk electrode. Then the electrochemically active material turns into the liquid state and is only available from the electrolyte, which must simultaneously remain in electronic contact with the bulk electrode for electron access. Finally, the electrochemically active material must return to the surface of the bulk electrode in order to deposit as solid Li_2S , so that the electrochemically active material would not be lost. The complexity and irreversibility for conversion reaction type materials is best represented here.

What makes the situation more complicated is that both the fully charged state (S_8) and the fully discharged state (Li_2S) are insulators to both ionic and electronic conduction, making it very difficult to access the active species at the start and end stages of the cell chemistry.

On the other hand, these soluble polysulfides can diffuse or migrate freely within the bulk electrolyte, and have a high chance of interacting with the lithium anode. Such direct encounters between the cathode (polysulfides) and anode (lithium metal) are not desirable

because, as mentioned in Section 6.1 (Figure 6.1), they lead to direct chemical reaction between the oxidant (cathode) and the reductant (anode), thus defeating the purpose of trying to harness the energy contained in this chemistry electrochemically.

In battery design, such a direct exchange caused by the shuttling of soluble electrochemically active materials in electrolytes such as polysulfides is referred to as “*internal short-circuit*” or “*self-discharge*”. It consumes the active materials on both electrodes, as evidenced by the gradual loss of cell voltage and capacity.

Summing up all these complications, one can easily imagine what challenge this solid–liquid–solid conversion reaction process presents. Perhaps the complication is second only to the solid–liquid–gas triphasic reactions in lithium/air batteries.

In fact, in the conversion reaction chemistry of lithium/sulfur cells, the electrode and the electrolyte are intertwined in such a way that a clear demarcation between electrode and electrolyte is no longer possible: for most of the cell operation, the electrochemically active material, or the electrode, is soluble and being constantly transported together with the conducting salts within the bulk electrolyte. There is now no clear interface between the sulfur cathode and the electrolyte.

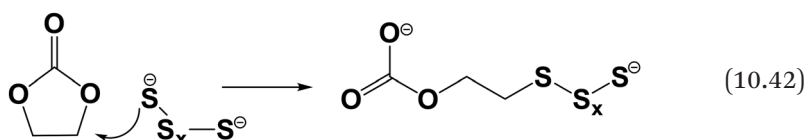
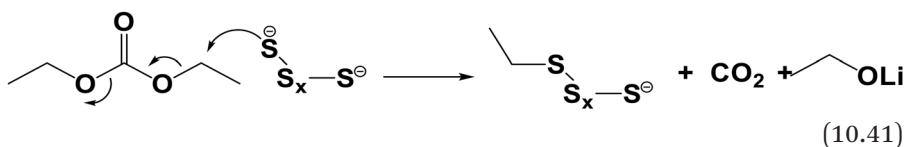
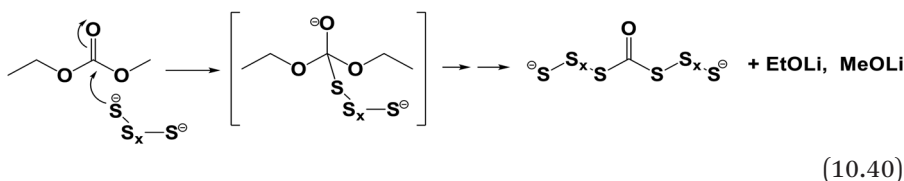
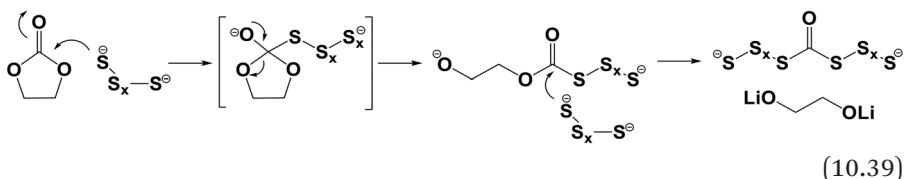
Most of the efforts to address these challenges were made on the design and architecture of the electrode structure, so that sulfur and all the polysulfides or Li_2S could be confined in the carbonaceous host, which not only provides electronic contact but also serves as a physical barrier to the free wandering of polysulfides.

However, completely segregating sulfur and polysulfides from the electrode structure also brings its own problems, because the electronic contact among species within the electrode structure, which is now solid–solid by nature, is not sufficient to ensure that all sulfur species could be accessed for their capacity. The dissolution of polysulfides, in contrast, is key to the full utilization of the promised capacity of sulfur.

Hence a dilemma appears: dissolution of polysulfides in electrolytes ensures a high degree of utilization of the sulfur capacity, but the free shuttling of polysulfides across the bulk electrolyte causes parasitic reactions that gradually consume the active species (lithium, sulfur) of the cell. This is the central challenge faced by lithium/sulfur chemistry that has not been fully resolved as of today.

Since the operational potential of the sulfur chemistry is reasonably moderate (<3.0 V vs. Li), the corresponding electrolytes are not required to be stable at high potentials. For this reason, the

anodic stability of ether-based electrolytes is sufficient. However, what makes ether-based electrolytes the favored electrolyte systems for sulfur chemistry is the fact that the carbonate ester molecules react irreversibly with these polysulfides, which are strong nucleophiles for the carbonyl groups or other positively charged sites in esters, leading to the formation of thioethers or thiocarbonates [eqn (10.39)–(10.42)]:



Carbonate-based electrolytes may still be used, however, only when the sulfur or the polysulfides are physically sequestered or covalently immobilized in certain host structures. In those cases the resultant lithium/sulfur cells normally yield much better cycling stability, because the self-discharge effect caused by the dissolution and shuttling of polysulfide species would be eliminated.

In ether-based electrolytes, lithium nitrate (LiNO_3) is a frequently used additive to protect the lithium anode, which we briefly covered

in Section 10.4.1.2. Together with the main conducting salt such as LiTFSI or LiFSI dissolved in the ethereal mixtures, the actual composition of the electrolyte during cell operation is quite complicated, as it would contain all these polysulfides dissolved in the electrolytes in addition to their reaction products with the electrolyte components or the interphases formed by the TFSI⁻, FSI⁻ and NO₃⁻ anions.

The chemical composition of the interphase on a lithium anode is also under the influence of all these factors. At dilute salt concentrations, most of the interphasial components are contributed by the decomposition products of the solvent molecules, especially those cyclic ethers that are less stable against reduction reactions. For example, the electrolyte composition frequently used for lithium/sulfur batteries often consists of a mixture of a linear ether, dimethoxyethane (DME), and a cyclic ether, 1,3-dioxolane (DOL). At 1.0 M LiTFSI concentration, the major contributor to the interphase on lithium metal is often the ring-opening reduction product from DOL, such as alkoxide (ROLi), oligomers with -OLi edge groups, as well as Li₂O. An increase in salt concentration or inclusion of other solvent molecules would alter the interphasial chemistry, as evidenced by the much higher abundance of LiF in the interphase if LiTFSI or LiFSI is dissolved at high concentration (>1.05 M), or upon addition of fluoroethylene carbonate (FEC), or Li₃N and Li_xNO_y species upon the addition of LiNO₃.

These inorganic interphasial components seem to be effective in mitigating the shuttling of polysulfides; meanwhile, the reactivity of polysulfides with Li⁰, although unwanted in terms of retaining lithium active material, contributes to suppressing the growth of dendritic Li⁰. The presence of polysulfides could have been essential in ensuring a layered structure of interphase on lithium metal, the top layer consisting of oxidized products of polysulfides, which thermodynamically can be oxidized by LiNO₃, and the bottom layer consisting of the reduced products of polysulfides and LiNO₃.

Given the reactivity between LiNO₃ and Li⁰ or polysulfides, it should be cautioned that LiNO₃ is progressively consumed during the cell cycling, hence its effect is not in permanent existence.

Also benefiting from the low operating potential of sulfur chemistry, non-aqueous electrolytes based on exotic solvents other than ethers and esters were possible, such as phosphate or phosphite esters, nitriles, sulfoxides, sulfates or sulfonic esters, as well as various ionic liquids.

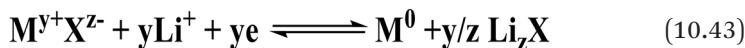
Despite the tremendous efforts and resources invested, as of the end of 2020 the commercialization of a practically rechargeable battery

constructed on the basis of lithium/sulfur chemistry remains remote, because its realization relies not only on the successful harnessing of sulfur chemistry with novel electrode design and the matching electrolytes, but also, or even more so, on the successful stabilization of the lithium-metal anode.

10.4.2.3 Metal Oxides, Sulfides and Halides

The neat forms of oxygen, sulfur and halogens, especially fluorine, are difficult to harness as electrode materials. In an alternative approach, the metal compounds of these electronegative elements are much easier to use as electrode materials, and they could experience conversion reactions that correspond to higher capacities than the intercalation chemistries of transition metal oxides could provide.³⁹ This is because, when breaking down the lattice structure of these metal oxides, sulfides or halides, the number of Li⁺ ions that can be accommodated in the process is determined by the valence of the metal, as a complete conversion reaction would produce the elemental form of the metal (M⁰). This is in strong contrast with the majority of intercalation chemistry, where each transition metal would usually allow the accommodation of only one Li⁺ ion.

Thus, the conversion reactions of these metal compounds follow the general scheme



where M represents a metallic element such as iron, copper, cobalt, etc., X represents oxygen, sulfur and various halogens and y and z are their valences. In particular, the high electronegativity of fluorine pushes the redox potential of the metal compounds into a region higher than 3 V, making the conversion reaction chemistries of various metal fluorides especially attractive.

As mentioned in Section 9.1.3.8, the capacity and energy promised by conversion reaction chemistries are often beyond reach, both because of the general difficulty in conversion reaction reversibility that arises from the impossibility of precisely guiding the breaking and re-forming of chemical bonds (Figure 9.8), and because of the specific difficulty with these metal compounds, which form elemental metal particles of nanometric size that show high reactivity towards the electrolytes.

The irreversibility of conversion reaction chemistries thus comes from the combined contributions of several factors: (1) the repeated

breaking/re-forming of M-X bonds in each conversion is made difficult by the poor ion and mass transport of the products in the multicomponent matrix, where certain components are insulating both ionically and electronically, such as LiF, and where phase transformation and phase separation frequently occur; (2) volume changes accompanied by mechanical failure of the nanostructured electrode particles induced by these repeated breaking and re-formation of bonds; (3) the low energy efficiency arising from the large voltage hysteresis, which is the potential difference between the charging and discharging plateaus of the electrode, a consequence of the high energy barriers between repeated bond breaking and re-formation; and (4) the direct electrolyte consumption by the reaction with nano-sized metal particles.

As one can see, these challenges cannot be resolved by electrolytes alone, therefore the majority of the efforts at conversion reaction chemistries are focused on the design of better electrode chemistries and structures so that their reversibility could be improved. Needless to say, nano-structure design and synthesis take the central stage.

Nevertheless, advanced electrolytes are still needed, together with the nano-structuring efforts, to minimize the parasitic consumption of electrolytes. Various highly fluorinated solvent molecules were found to be effective in doing so by forming fluorine-rich interphases, which consist of both inorganic (LiF , MF_y) and organic (C-F) species at the nano-scale.

It should be mentioned that such a preference for fluoride in interphasial chemistry has been universal, as numerous studies on diverse battery chemistries have revealed that fluorides, either inorganic or organic, usually serve as better chemical building blocks for interphases than other ingredients provided that they are formed in nano-sizes and arranged in proper morphology. Precise chemical and morphological understanding has not been achieved, and an empirical approach has often been adopted in the battery materials and chemistry community, where fluorinated organic molecules are used as the source of fluorine. Such pre-stored fluorine must be chemically stable in the electrolyte, but will release fluorine in the form of inorganic or organic fluorides upon electrochemical reduction or oxidation. Only in such a manner can the presence of fluorine in the interphases bring positive effects.

In other words, the presence of fluorine in an interphase alone cannot guarantee a better interphase, and a lot depends on how the fluorine exists chemically and distributes morphologically.

10.4.2.4 Anion Intercalation Chemistries

The intercalation of Li^+ (or any cation) into a crystal lattice is a *reduction* process, during which the electrons are injected into the lattice (Figure 10.16a). Depending on the chemical nature of the host lattice, the intercalation process could occur at different potentials. Those occurring at low potentials, examples of which include graphite (C_6 , ~ 0.01 V vs. Li) and lithiated titanate ($\text{Li}_4\text{Ti}_5\text{O}_{12}$, ~ 1.5 V vs. Li), could serve as ideal anode hosts for Li^+ , whereas those occurring at high potentials, examples of which include lithium cobalt oxide (LiCoO_2 , ~ 4.2 V vs. Li) and lithium iron phosphate (LiFePO_4 , ~ 3.5 V vs. Li), could serve as ideal cathode hosts for Li^+ .

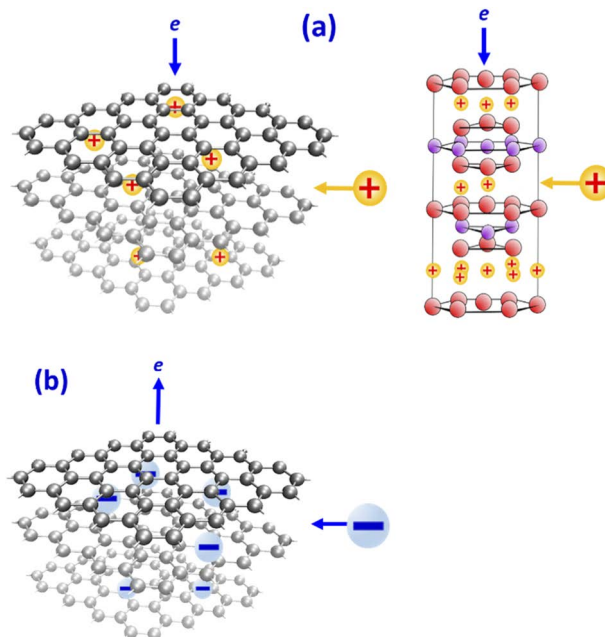


Figure 10.16 Redox reactions accompanying the intercalation process. (a) The intercalation of a cation such as Li^+ is a reduction process, during which the electrons are injected into the lattice. The diverse intercalation host materials with various intercalation potentials make it possible for lithium-ion batteries to be constructed. (b) The intercalation of an anion is an oxidation process, during which the electrons are removed from the lattice. A graphite lattice is used here. Like cation intercalation, an anion intercalation host could also serve as either the anode or cathode host depending on the potentials where the intercalation occurs.

Lithium-ion battery chemistry benefited from the discovery of those host materials that can intercalate Li^+ at very different potentials, so that a meaningful cell voltage above 3.0 V is possible.

On the other hand, an anion could also intercalate into a crystal lattice, and its intercalation is, of course, an oxidation process (Figure 10.16b), during which the electrons are removed from the lattice.⁴⁰ Depending on the potentials where anion intercalation occurs, such materials could also be used as either the anode or cathode host. However, unlike cation intercalation chemistries, not so many anions or corresponding lattice hosts have been identified. The most commonly used host lattice is graphite, which is very amenable to accommodating intercalants, and the potentials involved are usually especially high. For example, the intercalation of PF_6^- , BF_4^- , TFSI and FSI anions all occur around 5 V vs. Li, thus presenting especially stringent challenges towards the electrolytes, because almost none of the known non-aqueous electrolytes could support such high-voltage reversible chemistries in the long term. Even additives or solvents with high fluorination could only provide short-term stability with a high fading rate. Other anions such as BOB cannot even form a stable graphite intercalation compound, because their intercalation potentials are so high that neither electrolyte solvents nor the anion itself could withstand them. On the other hand, the intercalation of simple halide anions such as chloride (Cl^-) and bromide (Br^-) into graphite, however, presents an exception, because the potential for such intercalations to occur is moderate (~4.0 V).⁴¹

In addition to the high-voltage constraint, the specific capacity of anion intercalation in graphite is also usually much lower than that of cations such as Li^+ and Na^+ , because the much larger size of the anions induces higher stress on the lattice, hence accommodating a high density of anions in full intercalation stages becomes especially challenging for lattices such as those of graphite, which are only kept together by rather weak van der Waals forces between the graphene layers. For example, the intercalation of PF_6^- into graphite can only lead to rather diluted intercalation compounds with stoichiometry $[\text{PF}_6^-]\text{C}_{20}$ even when the electrode is brought to ~5.2 V, corresponding to a specific capacity of only 112 mAh g⁻¹. This comes in sharp contrast to the fully lithiated graphite with stoichiometry $[\text{Li}^+]\text{C}_6$, corresponding to a specific capacity of 372 mAh g⁻¹.

The most pronounced disadvantage of anion intercalation chemistry is exposed in the construction of actual electrochemical cells, which requires it to be coupled with another chemistry to form a pair of matching electrodes. Unlike Li^+ or other alkali metal cations (Na^+ ,

K^+ , etc.) that have been found to be able to intercalate into diverse host materials (hence it is possible to find a pair of lattice hosts with meaningful potential differences for the same ion), the intercalation host materials for anions are much rarer and limited. Therefore, most of the time, an anion intercalation chemistry has to be coupled with the intercalation of its counterion, as exemplified by Figure 10.17, which depicts an electrochemical cell consisting of a *graphitic anode* and a *graphitic cathode*, which intercalate cations (Li^+) at the anode and anions (such as PF_6^-) at the cathode at the same time. Such a cell is called a “*dual-ion intercalation cell*”, because both ions participate in their own intercalation chemistry at different electrodes.

Dual-ion intercalation chemistry requires a sufficient supply of both cations and anions for each electrode. Since these ions are stored in the electrolyte, such requirements brought an unwanted factor for cell design, namely that the amount of electrolyte can no longer be minimized as it is in lithium-ion batteries. This not only increases the weight of the electrolyte used in the cell, thus reducing energy densities, but also introduces complications in electrolyte design, because most salts have limited solubility in non-aqueous solvents, and electrolytes become rather viscous and resistive at high salt concentrations. In addition more concentrated electrolytes imply higher cost.

The combination of modest gain (low specific capacity and energy density) and great difficulty (electrolytes of extremely high voltage stability, limited host material candidates, salt solubility limit and potential high cost) led to dual-ion intercalation cells being little explored. However, a recent study published in 2019 found that the co-intercalation of equimolar Cl^- and Br^- into graphite, forming an intercalation/conversion reaction compound $\text{C}_{3.5}(\text{Br}_{0.5}\text{Cl}_{0.5})$, could be

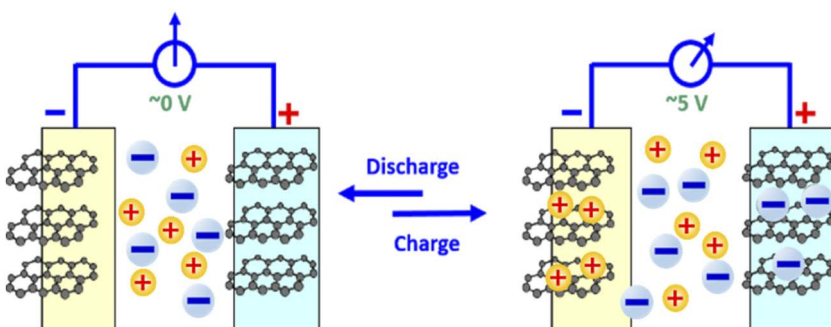


Figure 10.17 A 5 V dual-ion intercalation cell that employs symmetrical graphite electrodes, which accommodate Li^+ at the anode and its counterion PF_6^- at the cathode.

realized by pre-storing these ions in the solid electrode instead of in a liquid electrolyte, thus circumventing most of these challenges.⁴² The partial oxidation of these halide anions reduces the Coulombic repulsion among them in the graphite lattice, thus allowing the formation of a stage I graphite intercalation compound. Since such cathode materials do not contain any transition metal elements but promise specific capacity or energy densities near to or even higher than those of the state-of-the-art cathode materials in lithium-ion batteries, they could attract further interest as a sustainable alternative.

Finally, it should be emphasized that it is important to differentiate this “dual-ion intercalation cell” from the “*dual-intercalation cell*” that was discussed in Section 9.1.3.8 (Figure 9.8d). The latter simply means that *both electrodes* are intercalation hosts, but they are for *the same ion*. For example, the modern lithium-ion battery shown in Figure 10.12 is a dual-intercalation cell but *not* a dual-ion intercalation cell, because Li⁺ is the only intercalant ion therein, and the anion does not participate in any cell reaction by design, although it should not be excluded that an insignificant degree of anion intercalation might also occur at the cathode, especially considering that cathode materials normally contain carbon as conductive additives, the graphitic structure of which therein could allow anion intercalation when the battery is charged to very high voltages.

References

1. S. Fletcher, *Bottled Lightning: Superbatteries, Electric Cars, and the New Lithium Economy*, Hill and Wang, 1st edn, 2011.
2. R. A. Huggins, *Advanced Batteries: Materials Science Aspects*, Springer, New York, 2009.
3. G. N. Lewis and F. G. Keyes, The Potential of the Lithium Electrode, *J. Am. Chem. Soc.*, 1913, **35**, 340–344.
4. M. Winter, B. Barnett and K. Xu, Before Li Ion Batteries, *Chem. Rev.*, 2018, **118**, 11433–11456.
5. E. Peled, The Electrochemical Behavior of Alkali and Alkaline Earth Metals in Nonaqueous Battery Systems—The Solid Electrolyte Interphase Model, *J. Electrochem. Soc.*, 1979, **126**, 2047–2051.
6. X. Cao, X. Ren, L. Zou, M. H. Engelhard, W. Huang, H. Wang, B. E. Matthews, H. Lee, C. Niu, B. W. Arey, Y. Cui, C. Wang, J. Xiao, J. Liu, W. Xu and J.-G. Zhang, Monolithic solid-electrolyte interphases formed in fluorinated orthoformate-based electrolytes minimize Li depletion and pulverization, *Nat. Energy*, 2019, **4**, 796–805.
7. C. P. Aiken, E. R. Logan, A. Eldesoky, H. Hebecker, J. M. Oxner, J. E. Harlow, M. Metzger and J. R. Dahn, Li[Ni_{0.5}Mn_{0.3}Co_{0.2}]O₂ as a Superior Alternative to LiFePO₄ for Long-Lived Low Voltage Li-Ion Cells, *J. Electrochem. Soc.*, 2022, **169**, 050512.
8. Y. Li, Y. Li, A. Pei, K. Yan, Y. Sun, C.-L. Wu, L.-M. Joubert, R. Chin, A. L. Koh, Y. Yu, J. Perrino, B. Butz, S. Chu and Y. Cui, Atomic structure of sensitive battery materials and interfaces revealed by cryo-electron microscopy, *Science*, 2017, **358**, 506–510.

9. H. J. S. Sand, On the concentration at the electrodes in a solution, with special reference to the liberation of hydrogen by electrolysis of a mixture of copper sulphate and sulphuric acid, *Proc. Phys. Soc., London*, 1899, **17**, 496–534.
10. C. Fang, J. Li, M. Zhang, Y. Zhang, F. Yang, J. Z. Lee, M.-H. Lee, J. Alvarado, M. A. Schroeder, Y. Yang, B. Lu, N. Williams, M. Ceja, L. Yang, M. Cai, J. Gu, K. Xu, X. Wang and Y. S. Meng, Quantifying inactive lithium in lithium-metal batteries, *Nature*, 2019, **572**, 511–515.
11. M. B. Armand, Intercalation Electrodes, in *Materials for Advanced Batteries*, ed. D. Murphy, Plenum Press, New York, 1980, p. 145.
12. B. M. L. Rao, R. W. Francis and H. A. Christopher, Lithium–Aluminum Electrode, *J. Electrochem. Soc.*, 1977, **124**, 1490–1492.
13. M. Lazzari and B. Scrosati, Cyclable Lithium Organic Electrolyte Cell Based on Two Intercalation Electrodes, *J. Electrochem. Soc.*, 1980, **127**, 773–774.
14. I. A. Kuribayashi, *Nameless Battery with Untold Stories*, ed. Private Press, KEE Corporation, Union Press, Kanagawa, Japan, 2015.
15. T. Nagaura and K. Tozawa, Lithium Ion Rechargeable Battery, *Prog. Batteries Sol. Cells*, 1990, **9**, 209–217.
16. M. S. Whittingham, The origins of the lithium battery, Nobel Lecture, 8 December 2019, <https://www.nobelprize.org/uploads/2019/10/whittingham-lecture.pdf>.
17. A. Hérold, Synthesis of graphite intercalation compounds, in *Chemical Physics of Intercalation*, ed. A. P. Legrand and S. Flandrois, Springer, Boston, MA, 1987.
18. M. Winter and J. O. Besenhard, Lithiated Carbons, in *Handbook of Battery Materials*, ed. J. O. Besenhard, VCH, Weinheim, Germany, 1999, vol. 3, pp. 383–418.
19. K. Xu, Y. Lam, S. S. Zhang, T. R. Jow and T. B. Curtis, Solvation sheath of Li^+ in non-aqueous electrolytes and its implication of graphite/electrolyte interface chemistry, *J. Phys. Chem. C*, 2007, **111**, 7411–7421.
20. R. Fong, U. von Sacken and J. R. Dahn, Studies of Lithium Intercalation into Carbons Using Nonaqueous Electrochemical Cells, *J. Electrochem. Soc.*, 1990, **137**, 2009–2013.
21. K. Xu, Whether EC and PC Differ in Interphasial Chemistry on Graphitic Anode and How, *J. Electrochem. Soc.*, 2009, **156**, A751–A755.
22. L. Xing, X. Zheng, M. Schroeder, J. Alvarado, A. von W. Cresce, K. Xu, Q. Li and W. Li, Deciphering EC–PC Mystery in Li-ion Battery, *Acc. Chem. Res.*, 2018, **51**, 282–289.
23. M. Li, C. Wang, Z. Chen, K. Xu and J. Lu, New concepts in electrolytes, *Chem. Rev.*, 2020, **120**, 6783–6819.
24. G. Pistoia, M. D. Rossi and B. Scrosati, Study of the Behavior of Ethylene Carbonate as a Non-aqueous Battery Solvent, *J. Electrochem. Soc.*, 1970, **117**, 500–502.
25. K. Xu, Nonaqueous Liquid Electrolytes for Lithium-Based Rechargeable Batteries, *Chem. Rev.*, 2004, **104**, 4303–4418.
26. K. Xu, Electrolytes and Interphases in Li-ion Batteries and Beyond, *Chem. Rev.*, 2014, **114**, 11503–11618.
27. K. Xu, S. Zhang, T. R. Jow, W. Xu and C. A. Angell, LiBOB as salt for lithium-ion batteries: a possible solution for high temperature operation, *Electrochem. Solid-State Lett.*, 2001, **5**, A26–A29.
28. K. Xu, S. Zhang, B. A. Poese and T. R. Jow, Lithium bis(oxalato)borate stabilizes graphite anode in propylene carbonate, *Electrochem. Solid-State Lett.*, 2001, **5**, A259–A262.
29. A. von W. Cresce, M. Gobet, O. Borodin, J. Peng, S. M. Russell, E. Wikner, A. Fu, L. Hu, H.-S. Lee, Z. Zhang, X.-Q. Yang, S. Greenbaum, K. Amine and K. Xu, Anion solvation in carbonate-based electrolytes, *J. Phys. Chem. C*, 2015, **119**, 27255–27264.
30. O. Borodin, X. Ren, J. Vatamanu, A. von W. Cresce, J. Knap and K. Xu, Modeling insight into battery electrolyte electrochemical stability and interfacial structure, *Acc. Chem. Res.*, 2017, **50**, 2886–2894.
31. J. R. Dahn, Phase diagram of Li_xC_6 , *Phys. Rev. B*, 1991, **44**, 9170–9177.
32. W. Xu, J. Wang, F. Ding, X. Chen, E. Nasybulin, Y. Zhang and J.-G. Zhang, Lithium metal anodes for rechargeable batteries, *Energy Environ. Sci.*, 2014, **7**, 513–537.

33. C. Monroe and J. Newman, Dendrite growth in lithium/polymer systems – a propagation model for liquid electrolytes under galvanostatic conditions, *J. Electrochem. Soc.*, 2003, **150**, A1377–A1384.
34. F. Ding, W. Xu, G. L. Graff, J. Zhang, M. L. Sushko, X. Chen, Y. Shao, M. H. Engelhard, Z. Nie, J. Xiao, X. Liu, P. V. Sushko, J. Liu and J.-G. Zhang, Dendrite-free lithium deposition via self-healing electrostatic shield mechanism, *J. Am. Chem. Soc.*, 2013, **135**, 4450–4456.
35. T. Hosaka, K. Kubota, A. S. Hameed and S. Komaba, Research Development on K-Ion Batteries, *Chem. Rev.*, 2020, **120**, 6358–6466.
36. M. E. A. Domínguez, A. Ponrouch, P. Johansson and M. R. Palacín, Achievements, Challenges, and Prospects of Calcium Batteries, *Chem. Rev.*, 2020, **120**, 6331–6357.
37. T. Liu, J. P. Vivek, E. W. Zhao, J. Lei, N. Garcia-Araez and C. P. Grey, Current Challenges and Routes Forward for Nonaqueous Lithium–Air Batteries, *Chem. Rev.*, 2020, **120**, 6558–6625.
38. A. Manthiram, Y. Fu, S.-H. Chung, C. Zu and Y.-S. Su, Rechargeable Lithium–Sulfur Batteries, *Chem. Rev.*, 2014, **114**, 11751–11787.
39. M. N. Obrovac and V. L. Chevrier, Alloy Negative Electrodes for Li-Ion Batteries, *Chem. Rev.*, 2014, **114**, 11444–11502.
40. J. A. Read, *In situ* studies on the electrochemical intercalation of hexafluorophosphate anion in graphite with selective cointercalation of solvent, *J. Phys. Chem. C*, 2015, **119**, 8438–8446.
41. J. A. Read, A. v. Cresce, M. H. Ervin and K. Xu, Dual-Graphite Chemistry Enabled by a High Voltage Electrolyte, *Energy Environ. Sci.*, 2014, **7**, 617–620.
42. C. Yang, J. Chen, X. Ji, T. P. Pollard, X. Lü, C.-J. Sun, S. Hou, Q. Liu, C. Liu, T. Qing, Y. Wang, O. Borodin, Y. Ren, K. Xu and C. Wang, Aqueous Li-ion battery enabled by halogen conversion–intercalation chemistry in graphite, *Nature*, 2019, **569**, 245–250.
43. A. J. Bard and L. R. Faulkner, *Electrochemical Methods: Fundamentals and Applications*, Wiley, New York, 2nd edn, 2001.
44. M. Fujimoto, N. Yoshinaga and K. Ueno, Li-ion Secondary Batteries, *Japanese Patent*, 3229635, 1991.
45. C. K. Chan, H. Peng, G. Liu, K. McIlwrath, X. F. Zhang, R. A. Huggins and Y. Cui, High-performance lithium battery anodes using silicon nanowires, *Nat. Nanotechnol.*, 2008, **3**, 31–35.

PART C

Properties of Electrolytes, Interfaces and Interphases

In this Part, we dive even deeper to describe the major properties of modern non-aqueous electrolytes, covering their phase behaviors and the approaches of constructing phase diagrams, the ion solvation and the preferences in both solvating sites and solvent molecular structures, the ion conductivity, ionicity, transference number and the related classical and modern techniques and tools to determine these properties. Emphases are placed on the mathematical derivations of AC impedance and also the ion concentration profiles and potential distribution in electrolytes that are placed in operational electrochemical devices. The treatment of ion transport in practical electrolytes, under the influence of strong interionic correlations, is conducted in Onsager formalism, while a brief introduction to Newman theory, which was mainly constructed in the inverted Stefan–Maxwell formalism, is also included.

In Part A, we focused on the fundamental knowledge of electrolytes in general, including the ion–ion interactions and ion and mass transport in bulk (Ionics) and at interfaces (Electrodics). Most of the knowledge does not carry particular prerequisites that the electrolytes are working in a battery environment and that they must be subjected to corresponding chemical and electrochemical constraints.

The general knowledge covered the fundamental aspects of electrolytes, from how the ions interact among themselves and with the

solvents (*Ionics*), how the solvated ions interact the electrode surfaces (*Electrodics*), to how the solvated ions move, either by themselves (*Diffusion*) or under external fields (*Migration*).

However, the majority of such knowledge was acquired from the end of the nineteenth century (1890s) to the middle of the last century (1960s) on aqueous electrolyte systems. On the other hand, the most popular electrochemical devices nowadays, the lithium-ion battery being the prominent example, are running on non-aqueous electrolytes and the concomitant interphases, about which the understanding on a fundamental level is still developing. Most classical models and laws taught in textbooks were established for strong electrolytes in water and at extremely dilute concentrations, and therefore are no longer applicable directly, because the structures of both solvent molecules and ions (anions in particular) can no longer be ignored.

After Part B introduced typical electrochemical devices and a description of each type of batteries, starting from the first chapter in this Part, Chapter 11, we will switch our focus to the fundamental knowledge of the “practical” electrolytes designed to work in battery environments, particularly lithium-ion batteries. The physical properties, which, by definition, do not involve either chemical or electrochemical reactions, will be discussed in Chapters 11, 12 and 14. Falling into this category are the properties related to phase diagrams, ion solvation, ion transport and extended solution structure, *etc*. The interface and interphasial processes, which involve Faradaic reactions and charge transfers across the interfaces or interphases, will be discussed in Chapters 15 and 16. Carbonate-based electrolytes will be given the utmost attention as they constitute the skeletal electrolyte formulations in lithium-ion batteries. Other electrolyte systems still under research and development, especially those based on ether-based solvents, will also be covered as long as knowledge is available.

Needless to say, the lithium-ion battery is the most popular electrochemical device ever invented in the history of humankind. If anyone conducts a random survey on any street around the globe, the lithium-ion battery will be found in the palms of almost every individual encountered or on their bodies, and most of these individuals carry more than one to power their various portable electronic gadgets.

It is such popularity and commercial success of lithium-ion batteries that propelled the basic science of intercalation battery materials, chemistries and mechanisms. It is therefore not surprising that most of the modern knowledge about non-aqueous electrolytes, interfaces and interphasial chemistries were derived from the studies on lithium-ion battery systems. Nevertheless, the fruition of these studies,

especially the understanding of interphase chemistry and formation mechanisms, has provided inspiration in the development of electrolytes and interphases for other advanced battery chemistries.

C.1 A Quick Retrospect: What Qualifies an Electrolyte?

In a battery, the electrolyte is the only component that is in intimate contact with every other component, be it an active component such as the anode and cathode, or an inactive component such as a polyolefin separator, metallic current collectors for both the anode and cathode and conducting additives and polymeric binder therein, in addition to tabs and packaging materials. Such a special position places many constraints on the electrolyte as it must work with every component in a synchronized manner. For this reason, the electrolyte has often been the “last piece of the puzzle in place”, as we have seen in the development history of the lithium-ion battery, and it will most likely be so during the development of the next generation of advanced battery chemistries.^{1–3}

These constraints from other components can be summarized into a long list, but the core requirements remain the following four:

1. *Ion transport*, which is the primary function of an electrolyte to supply the cell reactions at both electrodes with necessary materials, otherwise the cell reactions would be unsustainable.
2. *Electronic insulation*, which is essential to ensure that electron exchange must proceed where the electrolyte and electrode meet, instead of within the bulk electrolyte, so that orientational movement of electrons could be produced *via* an external circuit, otherwise parasitic reactions within the electrolyte would lead to high self-discharge and a short shelf life of the battery.
3. *Chemical and electrochemical stability*, which is essential to ensure that the electrolyte would remain inert to the cell reaction. For most aqueous electrolytes, such stability is achieved by making sure that the cell reactions occur at potentials within the window encompassed by the decomposition of water (~1.23 V). For non-aqueous electrolytes, however, such stability could be achieved *via* the formation of interphases through the sacrificial decomposition of electrolytes on electrode surfaces. Electrochemical stability is especially important for the reversible cell reactions, *i.e.* rechargeable batteries.

It should be noted that the chemical and electrochemical stability of the electrolyte is required not only with the anode and cathode, although these two components are often the most important, but also with all other components in the battery, such as the separator, the current collectors, the polymeric binder and the electrode tabs, because an electrolyte must interface with each and every one of these components. Any instability in the above combinations could become the “*Achilles’ heel*” that causes the battery to fail. Considering that the battery must be rechargeable, the “inertness” of electrolytes towards all these components must be maintained throughout the entire lifespan of the battery.

4. *Phase stability*, no matter whether the electrolyte is a liquid, a polymer, a ceramic or a glass solid. This is because phase transformation is often accompanied by drastic changes in structures and properties, and many such changes are not welcome as the cell reactions are designed based on the expected properties of the electrolytes. The phase transformations could be induced by changes of temperature, pressure, chemical composition or electrode potential.

In addition to these four core requirements, there is a long list of additional requirements that are contingent upon the designed cell chemistry, the nature of the electrolytes and the intended applications.

For example, in diverse lithium-ion batteries, where graphitic carbons serve as anode hosts and transition metal oxides as cathode hosts, the most commonly used electrolytes are liquid electrolytes based on mixtures of alkyl esters of carbonic acid (*i.e.* carbonates). They must meet the following requirements, which are in some cases the derivatives from the above four core requirements:

1. *Forming protective interphases*, especially on graphitic carbons, *via* sacrificial decomposition, which must produce solid depositions on electrode surfaces that display an “electrolyte nature”, *i.e.* ionically conductive and electronically insulating. Remember that it was such an electrolyte nature that interphases were named after: SEI (solid/electrolyte interphase).
2. *Low surface tension, or “high wettability”*, on all solid surfaces involved, including polyolefin separators and both electrodes that consist of active materials (graphitic carbon and transition metal oxides) as well as inert components such as conductive

additives and polymer binders. This capability of the electrolyte ensures that the pore structures of these components could be sufficiently populated and accessible to the ions.

3. *Wide liquid range*, which would be quantitatively defined by the *liquidus, solidus* and *solvus* lines and *bubble point/boiling point* lines in the phase diagram of the corresponding carbonate mixtures. Phase transformation occurs beyond the liquid range defined by these lines and induces undesirable property changes, such as salt precipitation, partial or complete freezing of the electrolyte system and electrolyte composition changes due to loss of solvents *via* evaporation, *etc.*

These requirements only take into account the needs from the technical perspective to permit reversible cell reactions. A more comprehensive list should also include other peripheral but nonetheless just as important needs, such as safety, toxicology, environmental friendliness, cost and sustainability.

Even after doing so, the list is still not complete, and it will never be complete because it is dynamic and constantly evolving with the emergence of new cell chemistries and the development of new electrolyte materials.

C.2 Another Quick Retrospect: What Does an Electrolyte Do?

An electrolyte is responsible for transporting masses between the two electrodes, so that the cell reaction could proceed sustainably. These masses are almost always in ionic form, therefore their movement represents charge transport.

Both capacity and energy, as discussed in Section 9.1.3, are determined by the two electrodes coupled together, and in theory the electrolyte plays no role in determining either property.

Instead, the electrolyte directly dictates the rate at which the above capacity and energy could be accessed. In particular, the interfaces and interphases often play a critical role in determining the power density of the battery, because the ionic transport across the interfaces or the interphases would usually constitute the bottleneck of mass transport, as compared with the electron diffusing/hopping/tunneling within the electrodes or the ion transport within the bulk electrolytes.

This is by no means to say that capacity and energy are completely independent of the electrolyte and the interfaces or interphases associated with it.

In reality, the electrolyte, interfaces or interphases *indirectly* affect the capacity and energy of a battery by defining what electrode could be used. They do so by defining the electrochemical stability window for stable electrode operation, beyond which the electrode materials should be excluded. This is especially important for rechargeable batteries, in which the reversibility of the cell chemistry must meet a more stringent requirement. The most pronounced example of such an indirect influence on the capacity and energy is the EC-containing electrolytes developed for lithium-ion batteries, without which the high-capacity graphitic carbon and transition metal oxide could not be coupled together to form modern lithium-ion batteries. In the science of advanced battery chemistries, designing a better electrolyte often implies designing better interphases.⁴

In a few particular cell chemistry designs, such as redox flow batteries, the once clear demarcation between electrode and electrolyte is vanishing, because the electrolyte therein contains active materials that would directly determine the capacity and energy of a battery.

References

1. K. Xu, Non-aqueous liquid electrolytes for lithium-based rechargeable batteries, *Chem. Rev.*, 2004, **104**, 4303–4417.
2. K. Xu, Electrolytes and interphases in Li-ion batteries and beyond, *Chem. Rev.*, 2014, **114**, 11503–11618.
3. M. Li, C. Wang, Z. Chen, K. Xu and J. Lu, New concepts in electrolytes, *Chem. Rev.*, 2020, **120**, 6783–6819.
4. Y. S. Meng, V. Srinivasan and K. Xu, Designing better electrolytes, *Science*, 2022, **378**, eabq3750.

11 Phase Diagrams of Liquid Electrolytes

The most basic *physical* properties of liquid electrolytes include their liquid range (phase diagram), solvation of the ions therein and their movements, as well as the interfacial behaviors of the solvated ions at the electrode surface at various polarization potentials. The word “*physical*” here emphasizes the absence of chemical changes of the pristine electrolyte composition, such as the electrochemical or chemical decompositions of the electrolyte components.

The majority of the electrolytes used today are still in the liquid state, including the electrolytes used in lithium-ion batteries. Historically, the overwhelming preference for liquids over solids is based on the fact that most electrode materials are in the solid state, and the intimate interfacing between a solid and another solid is always challenging. Poor interfacing between electrodes and electrolytes not only makes the ion transport across the two phases extremely difficult, it also prevents sufficient access of the capacities in the electrodes by ions in the electrolyte. In fact, the most challenging hurdle that an all-solid battery faces today is still the difficulty of interfacing a solid electrode with a solid electrolyte.

However, when one of them is a liquid, the interfacing becomes much easier, and a liquid electrolyte becomes the natural choice.

Solid electrodes separated by liquid electrolytes have been the most popular battery configuration ever since Alessandro Volta’s first battery, in which brine water (an aqueous solution of NaCl) served as the electrolyte and copper and zinc as electrodes. There have been limited exceptions to this general configuration, as exemplified by the

high-temperature Na/S battery, where both electrodes (sodium and sulfur) are in the liquid (or molten) state and separated by a ceramic membrane of β -alumina serving as solid electrolyte, or the lithium/thionyl chloride battery, where one of the electrodes (thionyl chloride cathode) is in the liquid state while the actual electrolyte is a thin layer of “passivation” formed *in situ* on the lithium metal surface by thionyl chloride.

A liquid electrolyte can only function as designed in its liquid range, which is thermodynamically stable within certain boundary conditions, such as temperature, pressure and composition. In physical chemistry, these phase-stable regions are often defined graphically by the *phase diagram*, which delineates the occurrence of phase transformations at a certain temperature, pressure and composition. Figure 11.1 displays the phase diagram of the most popular electrolyte solvent, water. Since water is a neat solvent without an electrolyte solute (salt), it is a unary system with the composition as a constant (molar fraction $x_{\text{Water}} = 1.0$), and its phase diagram can be expressed with two variables: temperature and pressure.¹

Upon addition of an electrolyte solute (salt), the electrolyte solution becomes a binary system, and its phase diagram immediately becomes

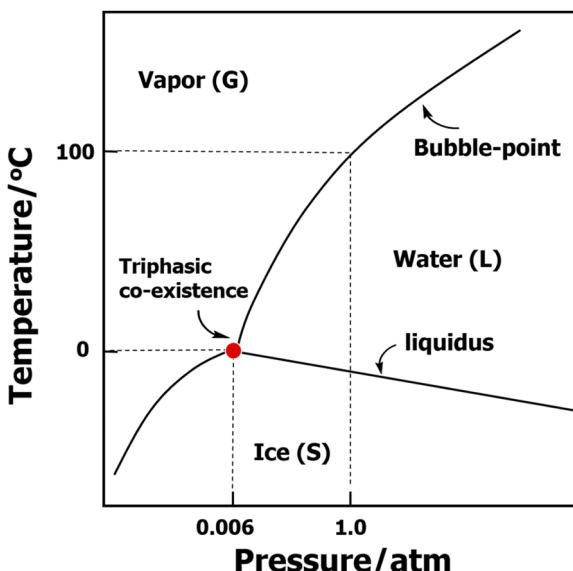


Figure 11.1 The phase diagram of water. The lines represent the temperature and pressure where the two phases coexist at equilibrium. The triphasic (ice-liquid water-vapor) coexistence is located at a fixed temperature and pressure.

much more complicated, as there are three free variables that affect the phase equilibrium, *i.e.* temperature, pressure and composition, while various “compounds” could form between the solvent and salt, which is determined by their molecular interactions in both the liquid and solid states. The phase diagram therefore cannot be easily drawn on a 2D space without simplifications. The most common convention adopted is to remove one variable by assuming that it is a constant. For liquid systems, such a variable is usually the pressure, because as in the case of electrolytes, we are most interested in how the system behaves at standard 1 atmosphere (atm) or its neighborhood, while high-vacuum or high-pressure conditions are seldom the typical environments for the application of liquid electrolytes.

Figure 11.2 displays the phase diagram of the most popular electrolyte in our lives, an aqueous solution of NaCl, at 1 atm pressure.² It still looks complicated, and the complications arise from the many “compounds” that NaCl and water can form at different temperatures and compositions, which will not be discussed here because it is beyond the scope of this book. What we need to focus on is the liquid range as represented by the shaded area, which is enclosed by a *bubble-point* line at the top, and three *liquidus* lines at low-temperature and high-salt regions. These individual lines indicate the temperatures where two phases coexist at equilibrium: bubble-point line for

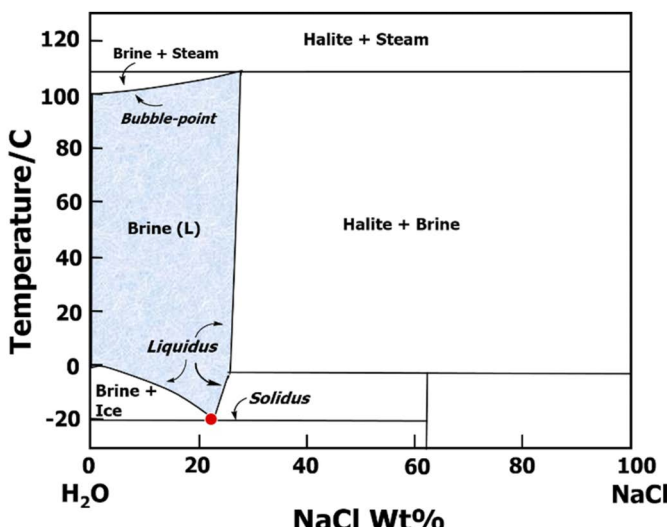


Figure 11.2 The phase diagram of an aqueous solution of NaCl. Its liquid range is represented by the shaded area enclosed by the liquidus and bubble-point lines.

liquid–vapor equilibrium and liquidus for brine–ice equilibrium. When the temperature drops to a threshold value as marked by the *solidus* line, everything is frozen, and the equilibrium is established between two solids: ice and NaCl crystals.

If one intends to use aqueous NaCl electrolyte in a battery, such as the voltaic pile, the shaded area sets the phase-stable region of this electrolyte, otherwise the battery performance would face sudden changes in properties, such as ion conductivity.

11.1 Phase Diagram of a Pseudo-binary Non-aqueous Electrolyte

Of course, aqueous NaCl solution cannot result in a high-energy battery, because its electrochemical stability window, confined by the water decompositions, is only 1.23 V (Figures 5.2 and 8.2), which is insufficient to support meaningful battery chemistries that operate at extreme potentials. However, the principle still applies to non-aqueous electrolytes, the phase-stable region of which is likewise defined by the temperature where the lowest boiling component starts to evaporate and the temperature where the highest melting component starts to freeze.

In most cases, the upper temperature limit (the so-called *bubble point*) is more related to the solvent, whereas the lower temperature limit (the so-called *liquidus*) is more related to the salt. This phase-stable region again sets the maximum service temperature range of the electrolyte, because above the upper limit the electrolyte tends to vaporize, which would build up pressure inside a sealed battery and eventually vent catastrophically, while below the lower limit the electrolyte gradually loses ion transport capability (ion conductivity) until it completely freezes at the solidus temperature and becomes an ionic insulator.

The service temperature range for a battery thus projected only reflects consideration from the electrolyte perspective, while the actual service temperature range of the battery could be much narrower, because other factors might start to weigh in before the environment temperature hits either the upper or lower temperature limit. For example, the interphasial resistance could rapidly deteriorate at low temperature before the electrolyte completely freezes, or one of the electrolyte components such as fluorinated salt anions or the interphase starts to decompose or react with other components at elevated temperature before the lowest boiling solvent starts to evaporate. However, the service temperature range predicted by the phase-stable region still serves as an extremely useful reference.

The practical electrolyte systems used in lithium-ion batteries are seldom based on a single solvent. The simplest and most typical electrolyte is 1.0 M LiPF₆ dissolved in a mixture of EC and DMC at various solvent ratios. This makes the electrolyte a ternary system, and its phase diagram hence becomes even more complicated because of the five free variables (the temperature, the pressure and the electrolyte compositions that can be expressed in molar fractions of three components that can be represented by the molar fractions of the two solvent molecules and salt, x_A , x_B and x_{Salt} , with the cation and anion molar fractions constrained by the salt formula). In addition, one also needs to consider the much higher number of possible “compounds” formed among the two solvents and the salt.

All these factors together determine the phase equilibrium. It is therefore no longer possible to construct phase diagrams in 2D graphs such as Figures 11.1 and 11.2 even with simplifications.

In an attempt to simplify the situation further, researchers often disregard the presence of salt, and just measure or calculate the phase diagram of the solvent mixtures. In the case of a solvent mixture consisting of two solvent molecules, the composition can be represented simply by the molar fractions (x_A and x_B). This is a *pseudo-binary electrolyte system*, the phase diagram of which can now be described on a 2D plane.

The bubble point, liquidus and solidus of the actual electrolyte could then be estimated by following the laws of colligative properties such as *Raoult's law*, *van't Hoff's law* and *Henry's law*, under the assumption that the salt is completely dissociated. Of course, at high salt concentrations (as used with most practical electrolytes), such an estimation is not precise and needs further corrections. Nevertheless, the phase diagrams of the solvent mixtures provide a valuable reference foundation to predict the phase behaviors of an electrolyte.

Finally, considering that liquid–vapor transformation has limited significance for the service temperature range of a battery, because other factors such as thermal instability and chemical reactivity of either electrolyte or interphasial components often weigh in at high temperatures, further simplification could be made by neglecting the liquid–vapor transformation (bubble point) in the phase diagrams of electrolytes.

With all these simplifications and approximations applied simultaneously, the typical electrolyte used in lithium-ion batteries thus turns into a *pseudo-binary* system, in which we need to consider only two variables, *i.e.* temperature and composition, to locate a phase

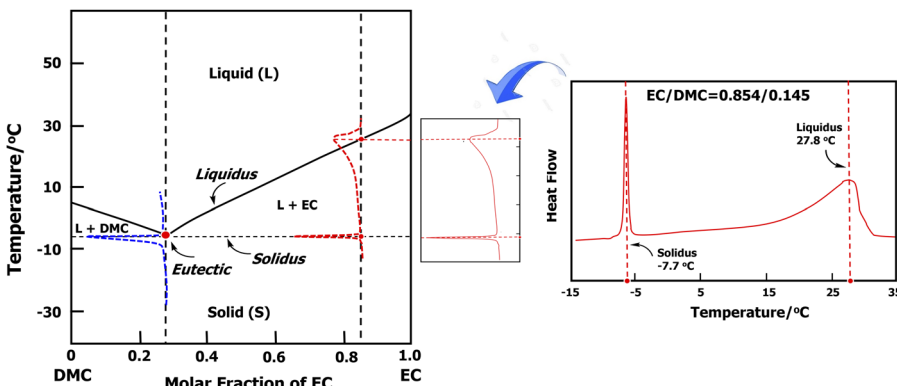


Figure 11.3 Left: The phase diagram of EC-DMC demonstrates a typical simple eutectic system, because these carbonate molecules mix with each other in an almost ideal manner; Right: The construction of the EC-DMC phase diagram using a calorimetric technique. The liquidus and solidus display characteristic thermal responses, while the composition at the eutectic point would display only a single solidus peak. Reconstructed based on data from Ding's seminal work.^{3,5,6}

equilibrium. The phase diagram of EC-DMC thus plotted is shown in Figure 11.3 (left), which is a typical binary system with simple eutectic behavior.³ Of the two solvents, EC has a higher melting temperature than DMC (EC 36.4 °C, DMC 4.6 °C), so it raises the liquidus line on the EC-rich side of the electrolyte, and imposes a more restrictive requirement for the liquid range. The eutectic point, or the solidus transition, occurs at *ca.* -7.7 °C, setting the threshold temperature where the entire solvent system would be frozen. An electrolyte based on this binary solvent mixture, even considering the depression of the melting point caused by the addition of salt, would not be much lower than -10 °C. The earlier versions of lithium-ion batteries manufactured in the 1990s cannot be used in a sub-zero climate, mainly because of the binary and EC-rich electrolytes used therein. An electrolyte without any EC was eventually formulated in 2016, which is freed from the temperature constraint imposed by EC.⁴

11.2 Experimental Mapping of Pseudo-binary Phase Diagrams

There are numerous ways to map the phase diagrams. Since a phase transition is always accompanied by a sudden change of properties such as enthalpy, entropy and heat capacity, the most convenient and

straightforward approach is a calorimetric technique, and the most mature and popular calorimetric technique is differential scanning calorimetry (DSC). In such an experiment, one slowly heats a sample from a temperature far below the solidus line, so that every component therein is frozen, and monitors the thermal responses from the sample, which, when experiencing a phase transition, may absorb heat (*endothermic*) or release heat (*exothermic*). Here the scan rate must be “slow” enough to ensure that sufficient time is allowed for the equilibria to be established once phase transition starts to occur.

As shown in Figure 11.3 (right), upon gradual heating, the frozen sample of an EC–DMC mixture at molar fractions $x_{\text{EC}} = 0.854$ and $x_{\text{DMC}} = 0.145$ displays two endothermic events, a very sharp peak at -7.7°C , and a broad peak at 27.8°C . The former indicates the melting of the mixture of solid EC and solid DMC, leading to the solid–liquid equilibrium in a binary phase region, while the latter indicates the complete melting of the sample into a homogeneous liquid phase consisting of EC and DMC at the nominal composition. Enclosed between the solidus and liquidus lines is the binary phase region, where the liquid phase consisting of EC and DMC mixture establishes equilibrium with the solid EC, because the sample is EC-rich. On the other side of the eutectic point, a binary phase also exists, enclosed by the same solidus line and another liquidus line corresponding to the equilibrium between a liquid phase consisting of EC–DMC mixture and the solid DMC.³

Even though the addition of salt would push down the temperature of both liquidus and solidus lines, an EC-rich electrolyte such as the sample studied in Figure 11.3 ($x_{\text{EC}} = 0.854$ and $x_{\text{DMC}} = 0.145$) apparently still cannot allow the battery to operate at low temperatures below 0°C .

To maximize the liquid range of EC–DMC binary electrolytes, DMC-rich compositions are therefore preferred, with EC–DMC (30:70 v/v) being the most popular both in research and in some commercial lithium-ion batteries. This volumetric composition corresponds to molar fractions $x_{\text{EC}} = 0.353$ and $x_{\text{DMC}} = 0.647$, which is located very close to the eutectic composition of $x_{\text{EC}} = 0.292$ and $x_{\text{DMC}} = 0.708$. The reason behind the slightly higher EC content is the consideration from an interphasic chemistry perspective that graphitic carbon in lithium-ion batteries needs more EC molecules to form a sufficiently protective SEI.

All simple eutectic binary systems display thermal events in their DSC traces similar to that shown in Figure 11.3 (right), *i.e.* two separate melting processes corresponding to solidus and liquidus, before the system turns into a complete single liquid phase.^{5,6} By conducting

the scan depicted in Figure 11.3 (right), one can determine the liquidus and solidus points for a given composition and, conducting a series of such scans for each composition, from $x_{EC} = 0$ to $x_{EC} = 1.0$, one can construct the phase diagram for this simple eutectic system as shown in Figure 11.3 (left) by connecting all the liquidus and solidus points across the composition range.

As the system composition approaches that of the eutectic, the solidus and liquidus points approach each other and eventually merge at the eutectic composition. Here, the entire system experiences only one melting process, which turns it into a homogeneous solution. For the EC-DMC binary system, the eutectic composition is located at $x_{EC} = 0.292$ and $x_{DMC} = 0.708$, and melting occurs at a temperature identical with the solidus point, $-7.7\text{ }^{\circ}\text{C}$. This is also the lowest temperature at which an EC-DMC mixture could remain liquid.

One advantage demonstrated by such simple eutectic behavior is that the mixture always yields a wider liquid range than the single solvent, as its liquidus is always lower than the melting temperature of neat EC or DMC.

In order to expand the liquid range of carbonate-based electrolytes, researchers started to experiment with carbonate mixtures based on lower melting carbonate molecules, or to adopt higher order carbonate mixtures, such as ternary, quaternary or even systems with up to six co-solvents. The molecular homologs of DMC, such as EMC (melting temperature $-53\text{ }^{\circ}\text{C}$) and DEC (melting temperature $-74.3\text{ }^{\circ}\text{C}$), are the most frequently employed candidates (Table 10.1). However, since EC is an indispensable component required by interphasial chemistry to stabilize the graphitic carbon anode material, the progress in this approach has been limited.

We mentioned earlier that the high melting point of EC ($36.4\text{ }^{\circ}\text{C}$) sets a limit on how much improvement the other carbonate cosolvents could achieve to push the solidus line downwards. In fact, simply coupling EC with a carbonate of low melting temperature could work in exactly the opposite direction: the mismatch between the high-melting EC and the low-melting linear carbonate would produce a very steep liquidus – so steep that the phase diagram almost loses the resemblance to a simple eutectic system – that would eventually narrow the liquid range of the usable electrolyte composition.

This counterintuitive effect can be seen in Figure 11.4a, where EC is coupled with DMC, EMC and DEC, respectively.^{5,6} Although the solidus lines are indeed pushed down by the introduction of DEC or EMC, the steep liquidus line on the EC-rich side confines these low-melting liquid phases into a rather narrow strip that is very rich in either EMC or

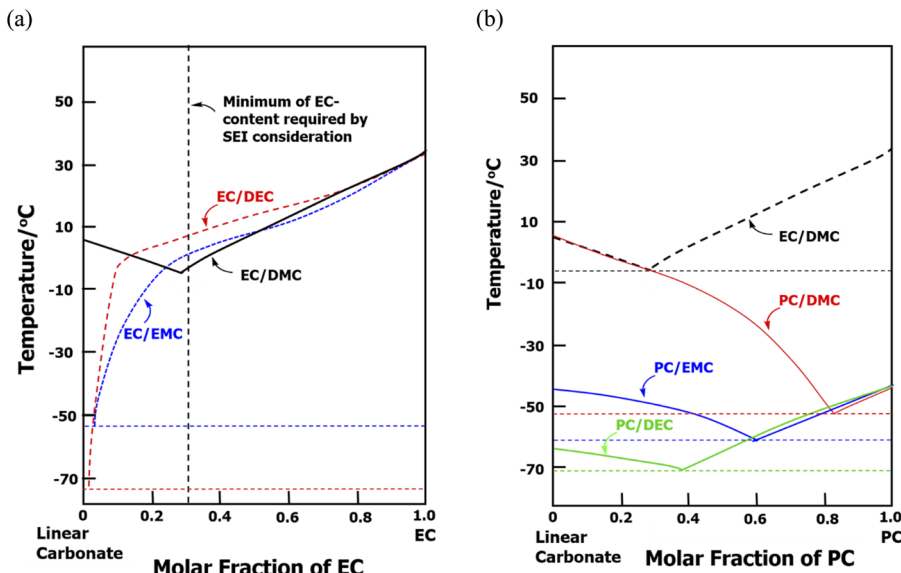


Figure 11.4 (a) The liquid range for the binary electrolyte compositions ($x_{\text{EC}} \geq 0.30$) that can support the intercalation chemistry of a graphitic anode actually becomes narrower when carbonates with very low melting temperatures are coupled with EC. (b) Coupling PC with various linear carbonates creates fairly wide liquid ranges, but the constraint imposed by interphasial chemistry requirements often excludes the use of such electrolytes. Reconstructed based on data from Ding's seminal work.^{3,5,6}

DEC. To meet the needs from interphasial chemistry considerations mentioned above, the minimum molar fraction of EC in the electrolyte is usually ~ 0.30 . This constraint essentially excludes those low-melting liquids on the EMC- or DEC-rich side of the eutectic point. Thus, an EC-DEC or an EC-EMC mixture provides a comparable or even narrower liquid range for lithium-ion batteries if these binary systems are adopted.

It should be mentioned that PC, as the cyclic homolog of EC, has a rather low melting temperature (-48.8°C), and its coupling with most linear carbonate solvents would not produce the melting temperature mismatch described in Figure 11.4a. Therefore, the liquid ranges provided by PC-containing electrolytes are in general much wider (Figure 11.4b). However, the PC-containing electrolytes face the dilemma that the graphitic carbon anode experiences exfoliation because of the unstable interphases (Section 10.3.2.3, Figure 10.8). In emerging battery chemistries that no longer rely on a graphitic carbon anode, such as lithium-metal batteries, sodium-ion batteries or other metal anode

batteries of multivalent cations (Mg, Zn or Ca), the protection of graphitic carbon is no longer required, hence the constraint from EC-derived interphase chemistry can be removed. The use of PC-based electrolytes could see much more opportunities in the future.

Nevertheless, to overcome this melting temperature mismatch of EC-centric electrolytes, either higher order than binary mixtures or solvent molecules other than carbonates must be used. Carboxylate esters such as methyl butyrate and ethyl acetate can effectively push down the solidus temperature of the electrolyte systems, and are hence often adopted as cosolvents in many low-temperature electrolytes, but these improvements in low-temperature performances (down to $-60\text{ }^{\circ}\text{C}$) are often achieved at the expense of cycling stability.

In recent decades, the emerging battery chemistries removed the constraint imposed by the graphitic carbon anode and its interphasial chemistry, and many exotic solvents became available, significantly expanding the liquid range of the electrolytes. For example, fluorinated ethers and localized super-concentration electrolytes could work with a lithium-metal anode battery at temperatures as low as $-70\text{ }^{\circ}\text{C}$, while even lower temperature limits ($\sim -100\text{ }^{\circ}\text{C}$) have been achieved with aqueous electrolytes with a super-concentrated multivalent cation salt. Some research even crossed the borderline between liquid and gas phases, and employed halocarbon compounds that would be gaseous under normal pressure. These liquefied electrolytes have to be used in hermetically sealed cells under pressure.⁷

11.3 Thermodynamic Calculation of Higher Order Phase Diagrams

Binary phase diagrams have been exhaustively mapped in a systematic manner for all possible combinations among the commonly used cyclic and linear carbonate solvents, including EC, PC, DMC, EMC and DEC, and these phase diagram all demonstrate simple eutectic behavior.

However, the actual electrolytes used in state-of-the-art lithium-ion batteries often consist of more than two solvents, even if one ignores the presence of salts and additives. In theory, a phase diagram could still be constructed in a similar approach for these high-order systems, provided that one collects enough data points *via* DSC scans for various compositions. However, with more than three free variables (temperature plus molar fractions for $N - 1$ of the N solvents),

experimentally mapping such systems becomes so complicated that it is virtually impossible.

Instead of exhaustive and laborious experiments, a more feasible approach is calculation.

Unlike kinetic behaviors such as transport and interfacial structure or electrochemical/chemical reactions such as interphasial chemistries, a phase transition occurs at equilibrium, and the phase diagram is merely the graphical representation of thermodynamics through minimizations of free energy. Therefore, a phase diagram can be precisely predicted based on the known thermodynamic properties of the carbonate molecules, such as enthalpy, entropy, heat capacity and Gibbs free energy, which have been thoroughly investigated and can be found in numerous databases. As most of the liquid systems in which we are interested are typically studied and used at constant temperature and pressure, Gibbs free energy should be the quantity to be minimized in calculating phase equilibria. In fact, there is a very mature sub-field of computational thermodynamics that specializes in the calculation of phase diagrams *via* Gibbs free energy minimization, often referred to as *CALPHAD*.⁸ Although we cannot cover all the details of this technique here, the basic principles of this methodology are introduced below.

Now, let us first consider the mixing process of two solvent molecules A and B, which produces a binary system. Assume that these two components are miscible with each other at any ratio, and the intermolecular forces between A and B molecules are identical with the intermolecular forces between A and A molecules or B and B molecules. In other words, when A and B molecules see each other, there is neither attraction nor repulsion, and both molecules treat each other exactly as their own kind. This mixing is hence called “*ideal mixing*”, which is roughly the case among all the alkyl carbonate molecules.

The major driving force for this ideal mixing would be the mixing entropy S_{mix}° , which is described by *Boltzmann's entropy relation* as

$$S_{\text{mix}}^{\circ} = k_{\text{B}} \ln W \quad (11.1)$$

where k_{B} is Boltzmann's constant and W is the total number of microstates when A and B molecules mix into a homogeneous solution. W can be expressed as

$$W = \frac{N!}{n!(N-n)!} \quad (11.2)$$

where N is the total number of sites available for occupation by solvent molecules and n and $(N - n)$ represent the sites occupied by A and B molecules, respectively. In other words, the molar fractions of A and B can be expressed as

$$x_A = \frac{n}{N} \quad (11.3)$$

$$x_B = \frac{N-n}{N} \quad (11.4)$$

Now the mixing entropy expressed in eqn (11.1) becomes

$$S_{\text{mix}}^\circ = k_B \ln \frac{N!}{n!(N-n)!} \quad (11.5)$$

and we apply Sterling's approximation to expand the permutations into

$$S_{\text{mix}} = k_B [N \ln N - n \ln n - (N-n) \ln (N-n)] \quad (11.6)$$

Inserting the expressions for the molar fractions of A and B molecules, we can obtain the entropy change during the mixing of A and B molecules:

$$S_{\text{mix}}^\circ = -Nk_B(x_A \ln x_A + x_B \ln x_B) \quad (11.7)$$

When we are considering that in total there is 1 mol of molecules, N is actually *Avogadro's number*, N_A , therefore

$$R = N_A k_B \quad (11.8)$$

where R is the gas constant. Hence the ideal mixing of A and B molecules is driven by an entropy change of

$$S_{\text{mix}}^\circ = -R(x_A \ln x_A + x_B \ln x_B) \quad (11.9)$$

while the change in Gibbs free energy during this mixing process is

$$G_{\text{mix}}^\circ = -TS_{\text{mix}}^\circ = RT(x_A \ln x_A + x_B \ln x_B) \quad (11.10)$$

On the other hand, if A and B molecules do not recognize each other as one of their own, there will be either attraction or repulsion when

they see each other; such a mixing process is known as “*non-ideal mixing*”, and a correction term should be added to eqn (11.10):

$$G_{\text{mix}}^{\text{XS}} = x_A x_B \Omega \quad (11.11)$$

where Ω is a descriptor of the intermolecular force between A and B molecules. The correction term is also known as “*excess Gibbs mixing energy*”. In eqn (11.11), if $\Omega > 0$, A and B molecules repel each other and tend to mix with their own, thus creating a driving force that counters the effect of entropy and favors phase separation; if $\Omega < 0$, A and B molecules attract each other, thus creating a driving force to form discrete compounds.

Hence the total Gibbs energy of mixing (G_{mix}^\ddagger) for non-ideal mixing is

$$G_{\text{mix}}^\ddagger = G_{\text{mix}}^\circ + G_{\text{mix}}^{\text{XS}} = RT(x_A \ln x_A + x_B \ln x_B) + x_A x_B \Omega \quad (11.12)$$

while the total Gibbs energy of the system is given by

$$G_{\text{Total}} = G^\circ + G_{\text{mix}}^\ddagger \quad (11.13)$$

where G° represents the standard Gibbs free energy for A and B molecules at reference states and can be assumed to be zero for convenience.

Eqn (11.13) set the foundation for the “*regular solution model*” that has been extensively used to predict the phase diagrams of binary systems.

Expanding the above line of thought to a liquid system consisting of multiple solvent components, we would have the ideal Gibbs energy of mixing as

$$G_{\text{mix}}^\circ = RT \sum_i x_i \ln x_i \quad (11.14)$$

and the excess Gibbs mixing energy as

$$G_{\text{mix}}^{\text{XS}} = \sum_{i=1}^n \sum_{j=i+1}^{n+1} x_i x_j [\Omega_{ij}^0 + \Omega_{ij}^1 (x_i - x_j) + \Omega_{ij}^2 (x_i - x_j)^2 \dots] \quad (11.15)$$

However, here we should stay with the simple binary system and examine further how a binary phase diagram is calculated.

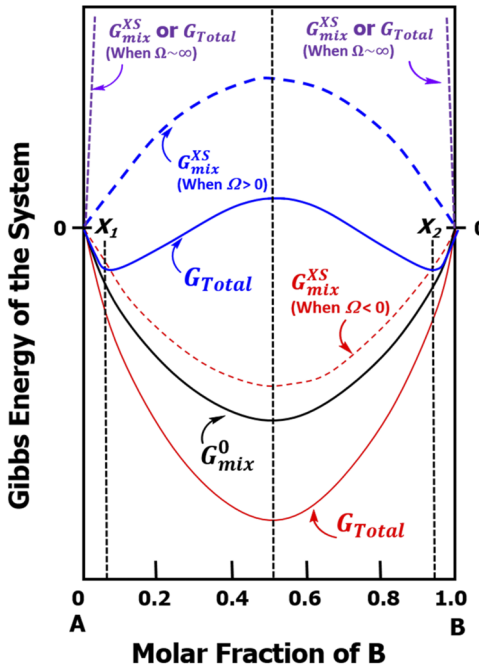


Figure 11.5 Schematic illustration of the composition dependence of total Gibbs free energy (G_{Total}) for a binary system consisting of A and B molecules. For ideal mixing, there is a single minimum in G_{Total} located at the composition where equimolar A and B molecules mix homogeneously. For non-ideal mixing, the nature of the intermolecular force between A and B molecules determines whether a homogeneous mixture could be formed. Carbonate solvents adopt two extremities while in liquid and solid states with $\Omega^L \approx 0$ and $\Omega^S \approx \infty$.

Now let us consider the general case of A and B molecules mixing, which could be either liquid or solid state. Figure 11.5 shows graphically how the different excess Gibbs mixing energy ($G_{\text{mix}}^{\text{xs}}$) affects the total Gibbs energy of the system (G_{Total}) in this case, given the same ideal Gibbs mixing energy G_{mix}^0 .

The ideal mixing, with neither attraction nor repulsion between A and B molecules, results in a lower total Gibbs free energy for the system, because mixing entropy (S_{mix}^0) is the only driving force behind the mixing. The total Gibbs free energy for the system reaches a single minimum that is located at an equimolar composition of A and B molecules ($x_A = x_B = 0.5$), corresponding to the state of complete and thorough mixing of the two molecules.

The non-ideal mixing, however, depends on the nature of the intermolecular force between A and B molecules.

When the force is attractive, *i.e.* A and B like each other more than they like one of themselves, the excess Gibbs mixing energy $G_{\text{mix}}^{\text{xs}}$ is negative because of a negative intermolecular force factor ($\Omega < 0$), thus rendering the total Gibbs free energy even more negative than the scenario of ideal mixing. This additional force drives the complete and thorough mixing of the two molecules, but the resultant total Gibbs free energy would not necessarily be symmetrical, so the minimum of the total Gibbs free energy for the system could depart from the equimolar composition.

On the other hand, when A and B molecules repel rather than attract each other, the excess Gibbs mixing energy $G_{\text{mix}}^{\text{xs}}$ becomes positive with a positive intermolecular force factor ($\Omega > 0$). Depending on the relative magnitude of Ω , a positive $G_{\text{mix}}^{\text{xs}}$ could completely reshape the total Gibbs free energy by creating additional local minima, as exemplified by the minima at two compositions x_1 and x_2 in Figure 11.5. The consequence of such local minima in Gibbs free energy induced by repulsive interaction between A and B molecules is the formation of a two-phase region whenever the nominal composition of the mixture falls between x_1 and x_2 , because the system thereat would automatically seek a lower Gibbs free energy at given temperature and pressure. Again, the locations of these minima, depending on the nature and magnitude of intermolecular forces between A and B molecules, do not have to be symmetrical as represented in Figure 11.5.

Finally, when A and B molecules shows zero solubility towards each other, the intermolecular force factor Ω becomes very large, or approaches infinity, which makes both $G_{\text{mix}}^{\text{xs}}$ and G_{Total} very high when one tries to mix A and B molecules. This corresponds to a sharp rise in Gibbs free energy in the composition range $0 < x_A$ or $x_B < 1.0$, which ensures that only neat substance A or B exists independently, without the formation of any so-called “solid solutions” such as either A in B or B in A.

Specifically for the carbonate molecules, which are frequently used as electrolyte solvents in commercial lithium-ion batteries and also in most battery research work, the intermolecular force factor therein, Ω , adopts two extremities depending on whether the carbonates are in liquid or solid states.

For carbonate molecules in liquid states, their intermolecular force is negligible ($\Omega^L \approx 0$), and their mixing is more similar to ideal mixing as represented by G_{mix}° in Figure 11.3.

However, for the same carbonate molecules in solid states, their intermolecular force is extremely large ($\Omega^S \approx \infty$), hence there is virtually no solubility of carbonate molecules in each other at the solid state. Consequently, the mixing of solid A and B molecules at the solid state would face a sharply rising Gibbs free energy. In other words, once the

temperature drops to a certain value such that solid A or B molecules precipitate, these solid forms are either pure A or B crystals, without any solid solutions of A in B or B in A.

The above two basic characteristics work together to determine how a simple eutectic phase diagram would take shape.

As mentioned earlier, the phase diagram is simply a graphical representation of phase equilibria. In our case, what interests us most is the liquid range of the solvent mixtures, *i.e.* the phase equilibria along the liquidus lines. In order to understand how a given component, in a simple binary system consisting of A and B molecules, could coexist in both liquid and solid states, we must analyze how their Gibbs free energy changes during the mixing first, then apply the thermodynamics rule of equilibria.

Consider the Gibbs free energy change of the above binary system of A and B molecules at a given temperature T and constant pressure, where both A and B molecules have reached equilibria in both liquid and solid phases, while A and B molecules are miscible like ideal species in the liquid state, and do not dissolve each other at all in the solid state. Thus we have four independent species coexisting, that is, solid A, solid B, liquid A and liquid B that are ideally mixed into a homogeneous solution. The corresponding total Gibbs free energy of these species could therefore be plotted in a similar manner to Figure 11.5, but now include both liquid and solid forms of A and B molecules (Figure 11.6). Note that we take the solids A and B in pure form as the reference points by placing their Gibbs free energy at zero in the upper panel of Figure 11.6, while the liquids A and B in pure form would be at higher points G_A° and G_B° than the reference point. Under constant temperature and pressure, these higher Gibbs free energies simply become the fusion enthalpies (ΔH_A° and ΔH_B°) for A and B molecules that are readily measurable, thus eqn (11.13) can be refined for a solid and a liquid as

$$G_{\text{Total}}^S = G_{\text{mix}}^\circ + G_{\text{mix}}^{\text{XS}} \quad (11.16)$$

$$G_{\text{Total}}^L = \Delta H_A^\circ + G_{\text{mix}}^\circ + G_{\text{mix}}^{\text{XS}} \quad (11.17)$$

For those species to be at equilibrium with others, thermodynamics teaches us that their *chemical potentials* must be equal, which is in fact the partial derivative of the Gibbs free energy with respect to composition at constant temperature and pressure:

$$\mu_i = \left(\frac{\partial G}{\partial x_i} \right)_{T,P} \quad (11.18)$$

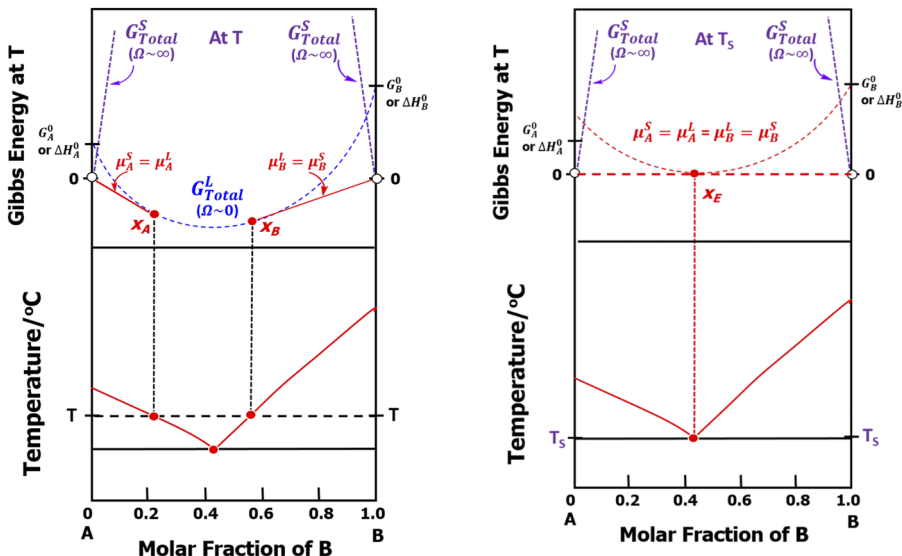


Figure 11.6 The thermodynamics behind the construction of a binary phase diagram at given temperatures T (left) and T_s (right), and how the phase equilibria translate into the liquidus lines as well as the eutectic point in the phase diagram. The two slanted lines representing the total free energy of two solid phases (G_S^{Total}) are drawn with a very high slope on the assumption that these two solid phases have extremely low solubility towards each other. If the inter-solubility is zero, those two lines should be perfectly vertical and hence overlap with the y -axis. Reconstructed based on data from Ding's seminal work.^{3,5,6}

Hence we can write a host of chemical potential equations to describe the equilibria that are established among these four species, solid A, solid B, liquid A and liquid B, but the most important are the following two. Considering that solid A and solid B show zero solubility or miscibility towards each other, the Gibbs free energy for them becomes just a point on the y -axis, and that liquid A and liquid B mix as ideal solution components, hence we can treat them as a single component:

$$\mu_A^S = \mu_A^L = \left(\frac{\partial G_{\text{Total}}^L}{\partial x} \right) \quad (11.19)$$

$$\mu_B^S = \mu_B^L = \left(\frac{\partial G_{\text{Total}}^L}{\partial x} \right) \quad (11.20)$$

Mathematically speaking, since chemical potentials are the first derivative of the Gibbs free energy, they can be represented graphically by the slope of a family of tangents on the plots of G_{Total}^S and G_{Total}^L versus composition. For the equilibrium between solid A and liquid A, or the equilibrium between solid B and liquid B, there is only one tangent from that family that matters, as it must represent the equal chemical potentials between solid and liquid species; in other words, the tangents involved must have the same slope.

Hence, as shown in the top left panel of Figure 11.6, at a given temperature T the equilibrium between solid A and liquid A is represented by the tangent line on the left, which intersects with G_{Total}^L at a composition x_A , because it equates the chemical potentials μ_A^S and μ_A^L . Likewise, the equilibrium between solid B and liquid B is represented by the tangent line on the right, which intersects with G_{Total}^L at a composition x_B , because it equates the chemical potentials μ_B^S and μ_B^L .

Since at this given temperature T these two tangent lines have different slopes, which stand for two different chemical potentials, there should exist two separate phases, one corresponding to solid A in equilibrium with a liquid mixture that consists of x_A of A and $(1 - x_B)$ of B, and another corresponding to solid B in equilibrium with a liquid mixture that consists of $(1 - x_B)$ of A and x_B of B. These two tangent points thus translate into two separate points on the liquidus line at temperature T in the phase diagram, as shown in the bottom left panel of Figure 11.6.

When the temperature approaches solidus T_s , the slopes of those two tangent lines gradually approach each other, and eventually merge into a single tangent line that intersects with a direct line linking the two pure solid phases solid A and solid B (Figure 11.6, right). That single tangent point would correspond to the eutectic point in the binary phase diagram.

When one repeats the above process for every temperature, all points on the liquidus line could be calculated based on the known thermodynamic properties of A and B molecules, and a complete phase diagram such as those in Figure 11.4 can be constructed. The well-established thermodynamic database for almost all known compounds makes the CALPHAD approach rather easy, as there are various commercial software packages available. In fact, applying CALPHAD to most carbonate solvents has already produced phase diagrams very close to those measured experimentally, therefore there is high confidence in this approach.

It was also discovered that, by comparing the calculated and experimentally measured phase diagrams, intermolecular forces between any pair of linear carbonates were nearly constant, while the attraction

between a linear and a cyclic carbonate molecule is considerably weaker than the average of the linear–linear and cyclic–cyclic attractions. These corrections, after being applied to the assumption that carbonate molecules mix as an ideal solution, allow the calculated phase diagrams to approximate the actual electrolyte solvent mixtures with higher accuracy.

Based on the calculated binary systems, one can construct phase diagrams of higher orders, so that the liquid and phase equilibria in these highly complicated mixtures could be projected. Figure 11.7

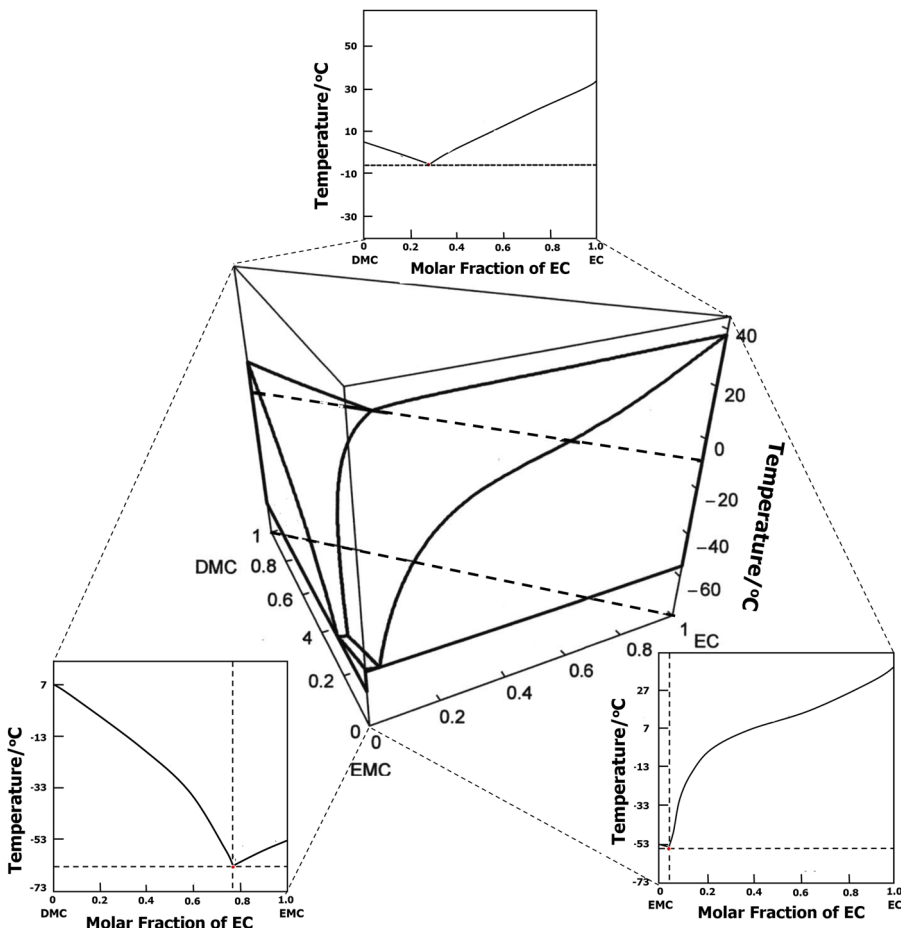


Figure 11.7 The construction of a ternary phase diagram from the related binary phase diagrams. The system of interest here consists of EC, DMC and EMC, the three most commonly used carbonate solvents in lithium-ion batteries. Reconstructed based on data from Ding's seminal work.^{3,5,6}

displays a calculated ternary carbonate system that has frequently been employed for low-temperature and high-power applications, in which the liquidus lines turn into liquidus planes, and determine the liquid range of the resultant solvent mixtures.

A closer examination of this ternary phase diagram reveals that, as mentioned earlier, simply adding a component with a low melting temperature could work to the opposite effect. In fact, the greater the difference between the melting temperatures of the components, the more steeply the liquidus plane on the higher melting component side would convex upwards, thus compressing the liquid range of the solvent combination. This effect can be clearly seen when one compares how the liquidus plane is raised by the presence of EC in Figure 11.7. The most effective way to expand the liquid range of lithium-ion battery electrolytes would be to mix carbonate molecules with closely matching melting temperatures, as exemplified by the ternary system consisting of PC, EMC and DEC, which produces a eutectic temperature below -90°C (Figure 11.8a).

The three-dimensional representation of a ternary phase diagram is usually inconvenient to use, therefore most of the time researchers prefer to render it into a pseudo-two-dimensional diagram as shown in Figure 11.8b. The conventions used to represent the ternary composition are covered in fundamental thermodynamic textbooks and will not be explained in detail here. The temperatures expressed on the z-axis in the three-dimensional diagram are now reduced to a series of contour lines representing identical temperatures.

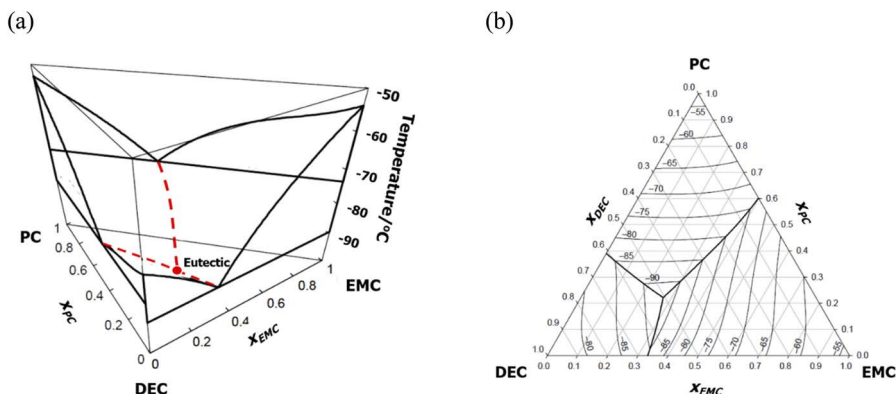


Figure 11.8 (a) The ternary phase diagram for a carbonate mixture consisting of PC, DEC and EMC. (b) A two-dimensional rendering of the same ternary phase diagram. Reconstructed based on data from Ding's seminal work.^{3,5,6}

It should be remembered that all of the phase diagrams shown in the previous and the present sections are those for neat solvent mixtures in the absence of salt. The addition of salt would further suppress the liquidus lines or planes, and in some cases would form distinct compounds owing to various bondings and interactions arising from the solvation of cations and anions.

Since the CALPHAD method was established based on thermodynamic generalities, theoretically it could be expanded to any system by altering the conditions that are specific to carbonates.

References

1. P. Gallo, K. Amann-Winkel, C. A. Angell, M. A. Anisimov, F. Caupin, C. Chakravarty, E. Lascaris, T. Loerting, A. Z. Panagiotopoulos, J. Russo, J. A. Sellberg, H. E. Stanley, H. Tanaka, C. Vega, L. Xu and L. G. M. Pettersson, Water: a tale of two liquids, *Chem. Rev.*, 2016, **116**, 7463–7500.
2. X. Yang, V. Neděla, J. Runštuk, G. Ondrušková, J. Krausko, L. Vetráková and D. Heger, Evaporating brine from frost flowers with electron microscopy and implications for atmospheric chemistry and sea-salt aerosol formation, *Atmos. Chem. Phys.*, 2017, **17**, 6291–6303.
3. M. Ding, K. Xu and T. Jow, Phase diagram of EC-DMC binary system and enthalpic determination of its eutectic composition, *J. Therm. Anal. Calorim.*, 2000, **62**, 177–186.
4. L. Ma, S. L. Glazier, R. Petibon, J. Xia, J. M. Peters, Q. Liu, J. Allen, R. N. C. Doig and J. R. Dahn, A guide to ethylene carbonate-free electrolyte making for Li-ion cells, *J. Electrochem. Soc.*, 2016, **164**, A5008–A5018.
5. M. S. Ding, K. Xu and T. R. Jow, Liquid-solid phase diagrams of binary carbonates for lithium batteries, *J. Electrochem. Soc.*, 2000, **147**, 1688–1694.
6. M. S. Ding, K. Xu, S. Zhang and T. R. Jow, Liquid/solid phase diagrams of binary carbonates for lithium batteries, Part II, *J. Electrochem. Soc.*, 2001, **148**, A299–A304.
7. C. S. Rustomji, Y. Yang, T. K. Kim, J. Mac, Y. J. Kim, E. Caldwell, H. Chung and Y. S. Meng, Liquefied gas electrolytes for electrochemical energy storage devices, *Science*, 2017, **356**, eaal4263.
8. N. Saunders and A. P. Miodownik, *CALPHAD, Calculation of Phase Diagrams: A Comprehensive Guide*, Pergamon Materials Series, 1st edn, 1998.

12 Ion Solvation

The ability of an electrolyte to conduct ions starts with the generation of discrete and free ions, which can be done either *via* dissociating a solute as suggested by Arrhenius, where the solute could be ionic compounds (ionophores) or polar molecular compounds (ionogens), or *via* simple heating (Types I–III, Section 2.1, Figure 2.1). In both instances, the close association between ions of opposite charges is broken apart, by polar solvents in the former case or by simple heating in the latter. Such “charge separation” at local length (ångstroms to nanometers) needs energy, which is provided by the solvation enthalpy and entropy of ions by these polar solvent molecules, or by the external heat that turns the ionophores into a molten state, respectively. Of course, for the special group of molten salts with low melting temperatures, *i.e.* room-temperature ionic liquids, the ambient environment can be considered as the external heating source.

This section covers the ion solvation that occurs when ionophores or ionogens are dissociated by molecular solvents (Types I and II), because they represent the majority of the electrolytes used in advanced battery chemistries.

12.1 Bernal–Fowler Three-layer Model

In the classical Debye–Hückel model of electrolyte solutions, the role of the solvent was deliberately simplified into a dielectric continuum for mathematical convenience. Bernal and Fowler were the first to model quantitatively how the introduction of an ion into bulk water induces structure breaking by reorienting the dipoles of the

neighboring water molecules so that they align with the Coulombic field emitted from the ion.¹ The consequence of such reorientation is that the immediately neighboring water molecules next to the central ion deviate from the original bulk structure dictated by hydrogen bonding, but such a highly directional arrangement is only locally confined to the first layer of water molecules, *i.e.* the so-called primary solvation sheath. At distances further away, the water molecules gradually transition from a secondary solvation sheath, where they are partially affected by the Coulombic field from the ion, to the bulk water, where the influence of the ion completely disappears. This “three-layer” model was discussed in Section 3.3 (Figure 3.5).

This model could be directly transplanted to non-aqueous electrolytes by removing hydrogen bonding and by considering the “monopolar” nature of the non-aqueous solvents (Section 3.1, Figure 3.1). However, it should be noted that Bernal and Fowler’s three-layer model actually assumes that there are sufficient solvent molecules available when an ion recruits its solvation sheath members, hence it applies only to dilute electrolyte systems.

This condition would no longer apply at high salt concentrations, where the insufficiency of solvent molecules would lead to the disappearance of the bulk and secondary solvation sheaths, while the solvent molecules are forced to be shared by different ions.² At extreme scenarios, the anion–cation distances are so compressed that they enter the primary solvation sheaths of each other. Such disruption of the classical solvation sheath not only alters the local solvation environment around the ions, but also introduces liquid structures at long range due to the aggregation of ions.³

12.2 The Four Basic Questions

The typical electrolytes adopted by lithium-ion batteries belong to Type I, where the Li⁺ and its counter-anion are solvated by polar solvents. At the most favored salt concentration, *i.e.* around 1.0 M, there is a sufficient population of solvent molecules, therefore the ions enjoy the luxury of the three-layer model when forming their discrete solvation sheaths.

Because of the “monopolar” nature of most non-aqueous solvent molecules (Section 3.1, Figure 3.1), the cation–solvent interaction should outweigh that between the anions and solvent. In the case of lithium-ion electrolytes, the discrepancy between cation and anion solvation behaviors is further intensified by the facts that Li⁺ is the second

smallest cation, second only to proton, therefore it is almost a point charge with a strong Coulombic field on its surroundings, while anions are exclusively based on fluorinated complex structures, in which the formal charge is well delocalized (Section 10.3.5.2, Figure 10.11).

Hence the strong binding of cations to nucleophilic sites on these non-aqueous solvent molecules leads to a more stable cation solvation structure, while anions remain very loosely bound by solvent molecules, leading to the consequence that cation solvation has far more significance than anion solvation in both bulk ion transport properties, interfacial structures and interphasial chemistries.

Since the revelation of the unexpected relation between solvation and interphasial chemistry, the interaction of Li^+ with non-aqueous electrolyte solvents has been extensively explored using many spectroscopic techniques. The emphasis has been placed on answering the following four basic questions:

1. Which nucleophilic sites of non-aqueous solvent molecules, especially carbonates, interact with Li^+ ?
2. How many solvent molecules can a single Li^+ accommodate in its solvation sheath?
3. Does Li^+ display any preference when being solvated in a mixture of non-aqueous solvent molecules?
4. How does the solvation sheath structure evolve with salt concentration?

Thanks to the extensive investigations performed in the past two decades employing a wide range of techniques, there are now definite answers for most of these questions, while others remain ambiguous and controversial.

Most of these studies were carried out using lithium-ion battery electrolytes as targets, but the understanding of Li^+ solvation not only allows the prediction of ion transport and interphasial chemistry in lithium-ion batteries or other lithium-based batteries, but also goes beyond lithium and helps with the efforts to design new electrolytes and interphases for other emerging chemistries.

12.2.1 Solvating Site

The least controversial question is the solvating site in carbonates and other polar solvents, as both experimental and computation studies unequivocally pointed to the carbonyl oxygen of carbonate molecules as the binding site for Li^+ .

Quantum calculations of free energy and molecular dynamics (MD) simulations of various lithium salts in typical non-aqueous electrolytes found that Li^+ is surrounded by a number of carbonyl groups from carbonate molecules, the lone-pair electrons of which should be most effective in neutralizing the Coulombic attraction of the small cation (Figure 12.1).⁴

The most convincing evidence comes from the more site-specific spectroscopic technique nuclear magnetic resonance (NMR) that probes ^{17}O nuclei, which would be in direct interaction with Li^+ .⁵ Significant changes in the chemical environment of ^{17}O nuclei can be detected in both EC and DMC, which is reflected in the displacement of chemical shifts. For carbonyl ^{17}O nuclei, this chemical shift displacement could be as high as 20 ppm upon addition of a lithium salt. Interestingly, such displacement occurs *upfield*, indicating that ^{17}O nuclei on carbonyl become “shielded” by more electron cloud compared with the neat solvent mixture without lithium salt. Meanwhile, the ethereal ^{17}O nuclei experience a much smaller displacement in chemical shift, but in the opposite direction, *i.e.* *downfield*, indicating that these ^{17}O nuclei become depleted of electron clouds when lithium salt is added.

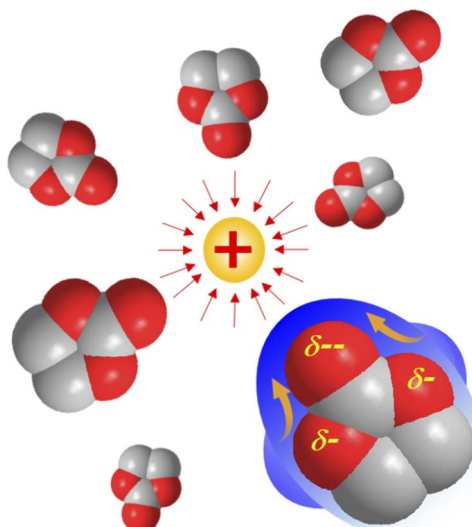


Figure 12.1 The primary solvating site on a carbonate molecule for a cation is its carbonyl oxygen. The Coulombic field of a cation polarizes the EC molecule shown, and induces its overall electron cloud in the molecular orbital to shift towards the carbonyl oxygen, which partially depletes the electron cloud on ethereal oxygens.

The divergent behaviors of carbonyl and ethereal ^{17}O nuclei may at first glance seem to be rather perplexing, but it makes perfect sense: under the influence of the Coulombic field exerted by Li^+ (or any other cation), the entire electron cloud in the molecular orbital of the carbonate molecule shifts along the field lines towards the cation center, hence enriching locally on the carbonyl ^{17}O nuclei while partially depleting the ethereal ^{17}O nuclei (Figure 12.1). In other words, the entire carbonate molecule is polarized under the Coulombic field of the cation such as Li^+ , and its molecular dipole moment should be significantly increased. This change in dipole moment has been confirmed by *ab initio* quantum calculations.

Of course, the depletion of the electron cloud essentially excludes ethereal oxygen as an effective binding site for the cations.

Consistent results are also obtained from ^{13}C NMR spectroscopy, but since ^{13}C nuclei do not directly coordinate with Li^+ , they are not as sensitive to the Li^+ solvation as ^{17}O nuclei, and the induced chemical shift displacements are much less significant (<1.0 ppm).

The temporal resolution of NMR spectroscopy ($\sim 10^{-6}$ s) is usually not high enough to differentiate the different kinds of solvent molecules that are either binding to ions or are free, because the exchange between molecules inside and outside the solvation sheath occurs on the scale of 10^{-12} – 10^{-10} s, depending on how strongly the ions and solvents interact. Therefore, what ^{17}O and ^{13}C NMR spectra represent is the time-averaged result of solvation.

On the other hand, techniques with high temporal resolution such as Fourier transform infrared or Raman spectroscopy can effectively differentiate these two kinds of molecules, as evidenced by the appearance of new peaks upon addition of lithium salts. Studies using these techniques led to the same conclusion mainly based on the asymmetric stretching vibration of carbonyl ($\nu_{\text{C=O}}$) at $\sim 1800 \text{ cm}^{-1}$, which was observed to be strongly shifted with Li^+ solvation.

For ether solvents, the ethereal oxygen atoms in the structure are the only solvating sites for cations. The lone electron pairs on these oxygen atoms provides such strong coordination towards the central cation that they form a so-called “*solvation cage*”, in which the central cation is in fact tightly trapped (Figure 12.2).

The strong ion–solvent interaction ensures sufficient dissolution of salts to form electrolyte. However, it also constitutes a resistance to the charge transfer at electrode/electrolyte interfaces or interphases, because when a solvated ion such as Li^+ reaches the electrode surface to participate in cell reactions, the solvation sheath must be disrupted,

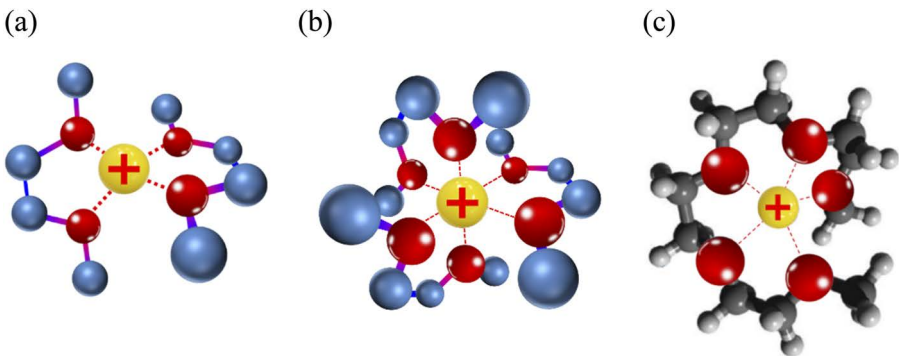


Figure 12.2 The solvation of Li^+ by ethers and polyethers. (a) An Li^+ ion solvated by two dimethoxyethane (DME) molecules forms a stable tetrahedral chelation structure, which is the dominant species detected by electrospray ionization mass spectrometry (ESI-MS); (b) an Li^+ ion solvated by three DME molecules forms an octahedral chelation structure, which is the dominant species generated by molecular dynamics simulations; (c) an Li^+ ion solvated by a polyether, tetraethylene glycol dimethyl ether (tetruglyme), whose multiple solvation sites form a chelation structure of high denticity. In these “super-stable” solvation cages Li^+ is essentially trapped. It requires tremendous desolvation energy to free the Li^+ .

and these inner solvent molecules must be stripped away. In other words, a substantial proportion of the interfacial kinetics comes from the energy needed to desolvate the solvated ion.

According to numerous experimental and computational studies, such desolvation energy is estimated to be in the range $20\text{--}50 \text{ kJ mol}^{-1}$ for carbonate molecules and $50\text{--}100 \text{ kJ mol}^{-1}$ for ethers. In given circumstances, such an energy barrier could become the rate-determining step in the cell reaction. For example, the desolvation process of Li^+ at a graphite surface is such a case, which is part of the reason why lithium-ion batteries usually cannot be charged at a fast rate.

12.2.2 Solvation Number

There is little controversy regarding this question.

Although it remains challenging to measure directly the accurate structures of solvation sheaths in the liquid state, various studies have attempted to determine the number of solvent molecules in the solvation sheath of a cation from the solid (often crystalline) solvates, which precipitate from liquid solution when either the salt

concentration rises above a certain threshold or the temperature drops below a certain threshold. These solvates, often with stoichiometric compositions, are considered the “living fossil” for solvation sheaths in liquid electrolytes, as they should maintain the most favored solvation composition of ions before the solubility limit of the salt forces them to exit the solution. The structures determined in this manner were hoped to offer remote but still reasonable clues to project the actual coordination picture between Li^+ and solvent molecules in typical electrolytes.

For Li^+ , numerous reports using such approaches have estimated the number to be between 4 and 6, depending on the size of the solvent molecules, based on both X-ray single-crystal and powder diffraction measurements. Especially when the solvent is EC, Li^+ seems to prefer a tetrahedrally coordinated configuration in the precipitated crystals, hence $\text{Li}(\text{EC})_4$ was believed to be the most favored solvation species in corresponding dilute solutions. On the other hand, when acetonitrile was used as the solvent, the overwhelming crystalline solvates formed from both LiPF_6 and LiTFSI salts had the stoichiometry $\text{Li}(\text{AN})_6$.⁶

Based on these remote (because these structures reflect what exists in solid instead of liquid states) but still relevant clues, the widely accepted picture of the Li^+ solvation sheath in typical carbonate-based electrolytes is a central Li^+ tetrahedrally coordinated by four solvent molecules. This simplistic picture reflects the generally accepted argument that the solvation number of Li^+ is 4, which is also true for most monovalent cations dissolved in non-aqueous electrolytes at low salt concentrations. However, this number is by no means static, but instead averaged over a long time frame owing to the fast exchange rate for solvent molecules within or outside the solvation sheath.

The number also depends closely on the size and polarity of the solvent molecules. For example, all the oxygen coordination sites of glymes are intramolecular, therefore they are densely packed in a rather small space. Combined with the strong tendency from the lone electron pairs on these oxygen atoms, the solvation sites of Li^+ in glymes could be as high as 6 (Figure 12.2). On the other hand, each carbonate molecule has only one carbonyl oxygen, hence the space around Li^+ could not accommodate more than five carbonate molecules in the primary solvation sheath, therefore high solvation numbers are less likely to occur.

Many calculations reveal that, among the solvent molecules coordinated with the central ion, the individual ion-solvent interaction strength varies with the solvation number. For example, assuming that there are four EC molecules in the primary solvation sheath of

Li^+ , the energy barrier encountered when removing the first EC molecule is so small that Li^+ with a solvation number of 3 and 4 could interconvert to each other at a rather fast rate. However, as the central Li^+ gradually desolvates, it becomes increasingly difficult to remove the remaining EC molecules, while the last EC molecule would be the most tightly held by the Li^+ , as there are now no dipoles from other solvent molecules to partially neutralize the Coulombic field from the Li^+ . The desolvation energies mentioned in the previous section were derived from experiments where Li^+ is completely intercalated or deintercalated from an anode host such as graphite or lithiated titanate, and the values of 20–50 kJ mol^{-1} for carbonate molecules or 50–100 kJ mol^{-1} for ethers should be the accumulated desolvation energy needed to remove all solvent molecules.⁷

The phenomenon of partial desolvation has been confirmed by many experiments, including ESI-MS (Figure 12.3), where solvation

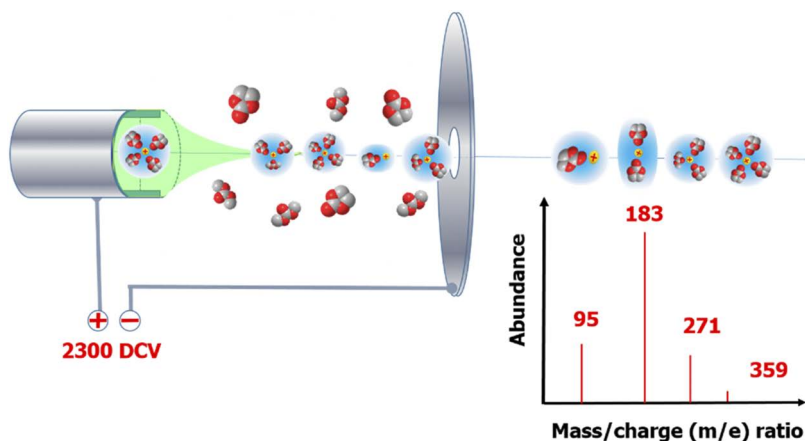


Figure 12.3 Schematic illustration of the use of electrospray ionization mass spectrometry (ESI-MS) to determine the solvation sheath structure of a typical electrolyte based on an EC-DMC binary mixture. An electrolyte droplet feels the DC voltage of 2300 V applied between the nozzle and the target and flies in the electric field, during which time the solvent molecules not coordinated with Li^+ will be stripped away, whereas the solvated ions will eventually pass through the aperture on the target plate and be detected and counted by the mass spectrometer. The exact solvation structure can be derived based on the mass-to-charge ratio of the peaks, and the population of the solvent species inside a solvation sheath can be quantitatively determined. Since the solvated ions would be partially desolvated during the flight, the abundance of the tetrahedrally coordinated Li^+ ions would take only a very small portion.²⁸

numbers smaller than 4 always dominate the species detected, and $[\text{Li}(\text{solv})_2]^+$ ions are usually the most abundant,⁸ or electrochemical co-intercalation experiments, where solvated cations such as Li^+ or Na^+ are allowed into certain hosts under special conditions, and $[\text{M}(\text{solv})_3]^+$ ions are detected as the main intercalants.⁹

For multivalent cations, the charge is doubled or tripled on particles with radii comparable to or even smaller than those of monovalent ions, therefore the Coulombic field emitted by these cations would be much more intensified, not only on surrounding solvent molecules but also on the counterions. In many cases, the latter factor becomes so strong that it directly affects the solubility of the salts. In fact, the effective dissolution of most multivalent salts in solvents, be they non-aqueous or aqueous, relies on the competition between solvent molecules and anions towards the cations. The direct consequence of the strong cation–anion interaction is the presence of ion pairs and aggregates, which also occurs in electrolytes of monovalent cations at high salt concentrations, but occurs almost universally in multivalent electrolytes, especially when the anions are monovalent themselves. In fact, the formation of cation–anion pairs can be viewed as the invasion of anions into the solvation sheath of the cations, an indication that the dipole of solvent molecules can no longer effectively “neutralize” the strong Coulombic field of multivalent cations. In these ion pairs and aggregates, the anions often form bridge-like structures between cations.

According to free energy analysis on solvation structures for divalent cations in low-dielectric solvents based on ethers, multiplicity arises for the thermodynamically stable cation solvation configurations, *i.e.* there could be several minima in the free energy, which reflects more than one possible solvation configurations that coexist in those electrolytes. This is in strong contrast to monovalent cations such as Li^+ , which often provide one most favored solvation configuration. Hence the ion pairs and aggregates should be the natural results from such multiplicity.

12.2.3 Preferential Solvation

This question still faces certain controversy, but more and more convincing evidence, both experimental and computational, now point towards the conclusion that solvation preference by Li^+ occurs in typical lithium-ion battery electrolytes, and the cyclic carbonates are in general favored over linear carbonates.^{10–13}

As mentioned in earlier sections, the electrolytes actually employed in lithium-ion batteries or any other advanced batteries seldom

consist of a single solvent. Instead, salts dissolved in binary and ternary mixed solvents or even higher order solvent mixtures make up the overwhelming majority of electrolyte systems. This tradition apparently came from the practical considerations of maximizing performance, but raises a question of great importance to ion transport, interphase chemistry and interfacial kinetics: in such mixtures, does Li^+ prefer any solvent more than others in its solvation sheath?

The underlying basis for a mixed solvent is optimum ion transport, because an ideal electrolyte needs both effective dissolution of salts into free ions, which requires a strong ion–solvent interaction, and facile movement of the free ions, which requires low viscosity of the medium. More often than not, those two requirements conflict with each other, as a strong ion–solvent interaction often leads to high viscosity. The strategy for mixtures essentially separates these two functions and assigns them to different solvent molecules. Specific to lithium-ion battery electrolytes, if one takes the typical EC–DMC as an example, the high dielectric constant of EC (89 at room temperature) enables it to interact strongly with Li^+ , whereas the highly fluid DMC is responsible for reducing the overall viscosity of the entire system.

This high dielectric constant–low viscosity combination strategy actually applies to all carbonate-based electrolytes used in lithium-ion batteries. If one examines the physical properties listed in Table 10.1 closely, it is apparent that the cyclic carbonate molecules such as EC and PC are those solvents with a high dielectric constant, whereas linear carbonates such as DMC, DEC and EMC are those with low viscosity. From this perspective, the typical mixtures often used in lithium-ion batteries all follow this general formulation, examples of which include EC–DEC, EC–DMC, PC–DEC and PC–DMC and higher ordered mixtures such as EC–PC–DMC and EC–DMC–DEC–EMC.

Based on this rationale, it would therefore be reasonable to assume that, during the dissolution process of a certain salt lattice in these mixed solvents, the solvation of ions by a solvent molecule with a higher dielectric constant would be energetically favored over that of a solvent molecule with lower dielectric constant. It would be equally expected that, once equilibrium has been established in the solution, the ions would have solvation sheaths that are mainly composed of solvents with a high dielectric constant on a statistical average.

Hence a general picture of how such ions move, interact with interfaces or form interphases could be painted: the ions surrounded by solvents of high dielectric constant such as EC or PC swim in the matrix consisting mainly of low-viscosity solvent molecules such as DMC, DEC or EMC.

Meanwhile, some counter arguments to the above belief came from simulations and computational deconvolution of Raman or other vibrational spectra, which propose either that no preferential solvation exists or that a linear carbonate such as DMC is preferred. The basis for the above controversy could be partially due to the complexities in deconvoluting vibrational spectra, and partially due to the very short time scales (10^{-12} – 10^{-9} s) involved in most simulations *versus* the macroscopic and experimentally measurable consequences (ion conduction, interfacial kinetics and interphasial chemistries, *etc.*) resulting from possible preferential solvation.

However, with the advances made in super-computing capability and improvements in force fields, more and more simulations and the related deconvolution of vibrational spectra started to point the other way, and a preference for cyclic carbonate over linear carbonate by Li^+ gradually became a mainstream concept. For example, both molecular mechanics and quantum calculations reveal that, in the radial distribution, the average distance between Li^+ and EC (0.212–0.214 nm) is smaller than that between Li^+ and DMC (0.216–0.218 nm), in solvation energy analysis DMC and DEC could be readily replaced with a cyclic carbonate such as EC or PC and the interpretation of Raman spectra could be completely reversed depending on how the composite peaks are deconvoluted, *etc.*¹⁰

More convincing evidence come from those spectroscopic techniques whose results are so unambiguous that they require little or no computational deconvolution, and those spectroscopic techniques that can reflect the change in chemical environments due to Li^+ solvation on a longer time scale ($>10^{-6}$ s) than what computer simulations could sense (10^{-12} – 10^{-9} s). Mounting evidence has become available on this topic. For example, the decomposition product of an EC–DMC (30:70 molar ratio) electrolyte on different electrodes consists almost exclusively of lithium ethylene dicarbonate (LEDC), which is the reduction product from EC, instead of lithium methyl carbonate (LMC) from the reduction of DMC, despite the fact that DMC is the predominant solvent in the electrolyte.¹¹ When using an EC–PC mixture, the competition between the graphite exfoliation by PC and reversible Li^+ intercalation enabled by EC quantitatively follows the PC–EC competition for the Li^+ solvation sheath composition *via* the change of the Coulombic efficiency of graphite lithiation.¹² When electrolytes consisting of EC–DMC or EC–DEC mixtures were subjected to liquid secondary ion mass spectrometry (LSIMS) or temperature coefficient studies, the results invariably pointed to an EC-favored solvation sheath structure.^{13,14}

The most convincing evidence came from the experiments that directly probed the solvation sheath structure. Among these were NMR techniques that probe either ^{13}C or ^{17}O nuclei, which see much larger displacements in chemical shifts for EC carbonyl than DMC carbonyl, and ESI-MS, which quantitatively measures the composition of the Li^+ solvation sheath.¹⁵ The time-average nature of these two techniques actually represents an advantage, because as of today simulations cannot reach such a time scale, while most of the experimentally observable consequences are the result of the long time scale interactions between ions and solvent molecules.

Here ESI-MS deserves a more detailed description, as not only has it been applied on many typical lithium-ion battery electrolytes in a systematic manner, but also it reveals the Li^+ solvation sheath structure in a quantitative manner that has not been available from other spectral means.¹⁵

In ESI-MS, the bulk electrolyte is sprayed by a nozzle into fine droplets of micrometer size. When these droplets, which already carry formal charges because of the dissolved salt, are suspended in a chamber, the applied DC voltage directs the cation (or anion) to fly from the nozzle towards the target plate with an aperture in the center. By switching the polarity of the applied voltage, one could choose to study either positively charged droplets (*i.e.* solvated cations) or negatively charged droplets (*i.e.* solvated anions).

During the flight to the target aperture, these charged droplets experience partial desolvation, and lose those solvent molecules unbound or loosely bound to the central ion. The droplets that eventually arrive at the aperture normally consist of a single ion surrounded by solvent molecules. When these solvated ions pass through the aperture, they are then picked up by a mass spectrometer, which can precisely identify what solvent molecules are present within the solvation sheath of the ion and how many there are, simply based on the mass-to-charge ratio of the corresponding peaks (Figure 12.3). On the other hand, the abundance of each peak, when expressed with respect to all peaks detected, reflects the statistical population of a given solvent molecule in a solvation sheath.

Thus, the quantitative picture painted by these results unequivocally reveals that a solvated Li^+ ion is primarily surrounded by EC molecules provided that EC is mixed with a linear carbonate molecule. Figure 12.4 displays the relation between the population of EC found within the Li^+ solvation sheath *versus* the bulk electrolyte composition, where a characteristic “positive deviation” is always observed for any binary combination of EC with a linear carbonate such as DMC, EMC or DEC.

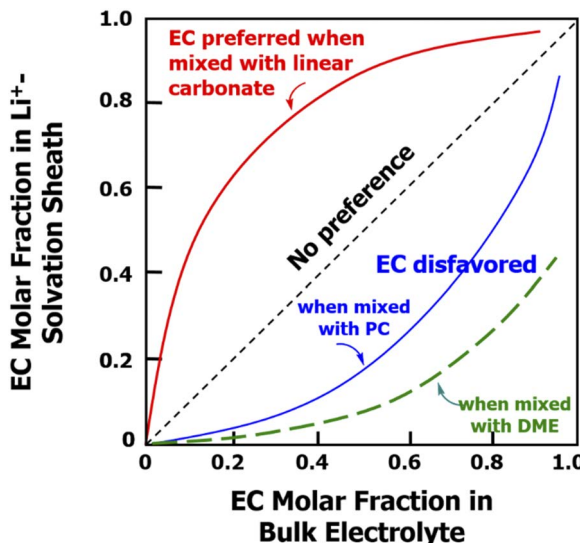


Figure 12.4 The preferential solvation of Li⁺ by solvent molecules. In mixed solvents consisting of EC and a linear carbonate, EC is preferred, as indicated by the positively deviated curve. However, in mixtures consisting of EC and PC or EC and DME, EC is disfavored by Li⁺, and PC or DME becomes the preferred solvent, as indicated by the negatively deviated curves. Since most lithium-ion battery electrolytes are based on EC mixed with linear carbonates with no or little PC and DME, EC should dominate the solvation sheath structure of Li⁺.

To understand what such a deviation means in Figure 12.4, let us imagine that a lithium salt is dissolved in a mixture of solvents and a naked Li⁺ is looking for solvent molecules to recruit into its solvation sheath. If this Li⁺ is an “equal opportunity employer”, it would pull every solvent molecule into its solvation sheath with an identical probability, and statistically its solvation sheath structure would completely reflect the electrolyte bulk composition, *i.e.* without any preference for any solvent. Under such a circumstance, if one plots the EC molar fraction detected in the Li⁺ solvation sheath structure *versus* the EC molar fraction in the bulk electrolyte, a diagonal straight line (the dashed line in Figure 12.4) would be obtained, because there is no preference in the solvation.

In other words, any deviation from that diagonal straight line represents preferential solvation. A positive deviation above the diagonal straight line means that there is a greater fraction of EC in the Li⁺ solvation sheath than in the bulk electrolyte composition, hence EC is

preferred, while a negative deviation below the diagonal straight line means that EC is disfavored in the Li^+ solvation sheath.

All binary electrolytes subjected to ESI-MS exclusively display a positive deviation, provided that EC is coupled with a linear carbonate, be it DMC, DEC or EMC.^{15,16} Such a positive deviation is quite universal, and is essentially independent of salt species and salt concentration, revealing that EC is indeed preferred by Li^+ .

When will EC be disfavored? That will happen when a cosolvent more preferred by Li^+ is mixed with EC to form a binary solvent mixture. Such cosolvents that can outcompete EC for Li^+ could be PC or DME, whose solvation cage is shown in Figure 12.2a.

When PC or DME is mixed with EC, the preference is completely reversed. Hence the curves representing the EC molar fraction in the Li^+ solvation sheath follow a negative deviation from the “equal opportunity employer” straight line (Figure 12.4).¹² Since most lithium-ion battery electrolytes are based on EC mixed with linear carbonates with no or little PC and DME (Figure 10.7, Scenarios I and II, respectively), such PC- or DME-dominated Li^+ solvation sheaths would be rare in real batteries. It is known that PC cannot provide the interphasial chemistry required by graphitic anode materials; this undesired preference by Li^+ solvation prevents the extensive use of PC in lithium-ion battery electrolytes, although it promises a much wider liquid range and lower service temperature limits (Section 11.3, Figure 11.8).

The use of DME in lithium-ion battery electrolytes is also disfavored, but for an entirely different reason. The ethers are extremely stable against reductive decomposition, hence they rarely participate in the formation chemistry of interphases (to be discussed in Chapter 16). This stability, in combination with their tight coordination with Li^+ as depicted in Figure 12.2, renders Scenario II as depicted in Figure 10.7 the dominant intercalation chemistry if an ether-based electrolyte is used. This co-intercalation scenario prevents the formation of the fully lithiated graphite LiC_6 that corresponds to a high capacity of 372 mA h g^{-1} and hence must be avoided. In fact, in the early days of lithium-ion battery development, this unwanted property of $[\text{Li}(\text{ether})_n]^+$ to be able to intercalate into the graphitic structure as an intact complex kept researchers away from graphite when looking for carbon materials as anode hosts, until the introduction of the interphase concept and the discovery that EC-based all-carbonate electrolytes could form such interphases.

As will be discussed later, the above asymmetric distribution of cyclic and acyclic carbonate molecules in the Li^+ primary solvation sheath has a profound influence on the interphasial chemistry and processes

on the graphitic anode within a lithium-ion battery. One immediate consequence of preferential solvation is that Li^+ preference for solvent molecules of higher dielectric constant (ϵ) or higher solvation power would exclude the solvent molecules of lower dielectric constant or lower solvation power from the solvation sheath and leave the latter as free, non-coordinating solvent molecules. As a result, the media in which the solvated ions migrate are mainly composed of these free solvent molecules, which impart their low viscosity (η) to benefit the movement of the solvated ions. In this way, a synergistic participation from both high- ϵ and low- η solvents contributes to the optimization of ion transport that we will discuss later.

12.2.3.1 Quantifying Solvation Power

ESI-MS,¹⁷ ^{17}O NMR and other spectroscopic techniques provide reliable resolution regarding the important question of preferential ion solvation, but one might wonder whether there is any standard quantification that can be used to describe the solvation power of solvent molecules.

In the previous sections, we used the dielectric constant as such a quantity, but the relative preference of Li^+ towards EC and PC proves that the dielectric constant might not be a reliable descriptor that can be applied in all scenarios, because both EC and PC are cyclic carbonates with dielectric constants far higher than those of linear carbonates (Table 10.1); however, EC has a higher dielectric constant (89.78) than PC (64.92), which conflicts with the experimental proof that PC is preferred over EC by Li^+ .

Historically, there are two separate ways to quantify the capability of a molecule to interact with ion: dielectric constant (ϵ) and “*donor number*” (DN). The former describes the polarizability of a molecule under the influence of a Coulombic field, as shown schematically in Figure 12.1, which has been discussed in Chapter 3, Section 3.2 (Figures 3.2 and 3.3, Table 3.1). The latter describes the availability of an electron lone pair on a molecule to a standard Lewis acid, such as a cation.

Gutmann proposed the use of antimony pentachloride (SbCl_5) as such a standard Lewis acid, and quantified the tendency of a molecule to donate electrons by measuring the enthalpy released by coupling that molecule with SbCl_5 in a non-coordinating solvent, 1,2-dichloroethane.¹⁷ Therefore, DN is actually not only a relative number, but also a number measured against an arbitrary standard, which is not necessarily applicable to the situation that we are facing with battery electrolytes. Especially, antimony is significantly larger than Li^+ in size, and it may not be sensitive enough to steric hindrance and

chelating effects, which are important for Li^+ . This can be evidenced by the fact that the DN of DMC (17.2) is even higher than that of EC (16.4), yet EC has been demonstrated to be a much more powerful solvent than DMC towards Li^+ .

In reality, neither ϵ nor DN reflects the whole picture of ion–solvent interactions, which is determined by many factors, *e.g.* the molecular polarizability, the availability of the electron lone pair, the spatial hindrance that might prevent the accessibility of a Lewis acid to the electron lone pair, and the molecular structure and conformation that might assist in the coupling of the Lewis acid and the electron lone pair. Especially important for Li^+ is the concept of “*denticity*”, that is, if a molecule is so structured that multiple intramolecular coordination sites are available to coordinate with Li^+ , then the solvation becomes “*chelation*”, and the solvation sheath of Li^+ actually becomes a cage. In such a cage of chelation, the added-up ion–solvent binding would be extremely strong to outcompete the singular binding sites such as the carbonyl group in EC.

A more recent study attempted to establish a relatively universal quantitative measure that takes into account of all of the above factors.¹⁸ Such a quantity, named “*relative solvation power*” (χ_s), is defined as the ratio between the coordination percentage of a test solvent (S) against that of a reference solvent (R) when a binary mixture of S and R is exposed to salts of either lithium or any other cation:

$$\chi_s = \frac{\alpha_s}{\alpha_r} \quad (12.1)$$

The success of such a quantity relies on the accurate determination of the relative percentage of each solvent being recruited by Li^+ into its solvation sheath. Most vibrational spectroscopic tools such as infrared and Raman spectroscopy encounter difficulty in differentiating unambiguously the solvent molecules inside and outside Li^+ solvation sheaths, and this becomes more challenging when the electrolyte is a binary mixture.

Once again NMR spectroscopy proves to be a powerful tool in making such differentiations and quantifications. A diffusion ordered spectroscopy (DOSY) technique based on NMR spectroscopy was recently developed and applied to various ester and ether solvents. For each category, a reference was selected, such as EMC for esters and 1,3-dioxolane (DOL) for ethers, and the solvation power of a given solvent molecule could be evaluated by mixing it with the reference solvent to form a binary mixture, the relative diffusivities of which are compared before and after the addition of lithium salts. Based on the

changes in their relative diffusivity, it is possible to calculate quantitatively the molar fraction of each solvent in the binary mixture that is affected by the Li^+ , which leads to the relative solvation power (χ). In theory, this method could be expanded to any cation beside Li^+ .

Table 12.1 lists the relative solvation powers of a series of esters and ethers towards Li^+ . Also listed for comparison are dielectric constants and DNs, when available. The highly fluorinated ethers as represented by TTE and BTFE are rendered essentially non-polar by the presence of multiple fluorine substitutions, which significantly reduces the electron availability on the ethereal oxygen therein. Therefore, these molecules display nearly zero solvating power towards Li^+ . Although this characteristic disqualifies them as effective electrolyte solvents, it makes them very useful non-solvating diluents in attempts to formulate a class of pseudo-concentrated electrolytes, *i.e.* “*localized highly concentrated electrolytes*”, which will be discussed in the following chapters.

Apparently, the relative solvation power serves as a much more reliable descriptor for evaluating the opportunity of a solvent molecule to be recruited by Li^+ in its solvation sheath. Nevertheless, one can still tell that there is a general trend that those solvent molecules with higher dielectric constants will display a stronger solvation power, although the correlation is by no means linear.

The above quantifying system based on NMR spectroscopy still does not provide a real universal metric, as different references have to be used for ethereal and ester categories, otherwise the differences in the solvation power among certain solvents become rather indiscernible. This not only introduces inconveniences when evaluating the solvation power for a given solvent molecule, but also makes the comparison between solvent molecules of different categories difficult. More resources should be invested in this meaningful effort, and the rapid developments in super-computing capabilities, assisted by deep machine learning and artificial intelligence, could eventually make it possible to predict precisely the ion–solvent interactions on a long time scale.

Before concluding this section, it must be remembered that, given the widely accepted preferential solvation, the solvation sheath itself is not a static structure, hence neither the solvation number nor the solvation members are constant. As mentioned earlier, the exchange among the solvent molecules within and outside the solvation sheath is extremely fast, and could be on the time scale of 10^{-12} s. The concept of “preferential solvation” is only valid on average. For example, a Li^+ ion is most likely surrounded by EC at a given time in its primary solvation sheath, and when every 10^{-12} s a given EC molecule

Table 12.1 Relative solvation power (χ) of selected solvent molecules towards Li^+ .

Solvent molecule	Structure	Solvation power (χ) ^a	Permittivity (ϵ)	DN
γ -Butyrolactone		1.95	39	
PC		1.46	64.92	15.1
EC		1.41	89.78	16.4
DMC		1.02	3.107	17.2
EMC		1.00	2.958	
FEC		0.63	78.40	
DME		6.44	7.2	20
THF		2.75	7.5	20
Me-THF		2.26		
MtBE ^b		0.93	2.6	
DOL		1.0	7.1	21.2
TTE ^c		0		
BTFE ^d		0		

^aNote that the solvation powers for esters and ethers were referenced against EMC and DOL, respectively, therefore the data for those two classes of solvents are not directly comparable.

^bMtBE: methyl *tert*-butyl ether.

^cTTE: 1,1,2,2-tetrafluoro-3-(1,1,2,2-tetrafluoroethoxy)propane.

^dBTFE: 1,1,1-trifluoro-2-(2,2,2-trifluoroethoxy)ethane.

is displaced by a solvent molecule from outside the solvation sheath, the newcomer is also most likely an EC molecule.

12.2.4 Ion Solvation in the Concentrated Regime

As the salt concentration increases and passes a certain threshold, the classical solvation sheath structure as proposed by Bernal and Fowler¹ that consists of three layers of solvent molecules (Figure 3.5) no longer exists, because the high ion population makes it impossible for each single ion to afford the luxury of a Bernal–Fowler solvation sheath. Instead, the ions are forced to approach each other so closely that their solvation sheaths, or the perimeter of their Coulombic fields, significantly overlap. As a result, these originally discrete solvation sheaths gradually merge into each other, where counterions start to enter the solvation sheath of each other, and the Coulombic fields from ions of opposite charges act on solvent molecules at very close vicinities and redistribute them. Such a close interaction between ions, counterions and solvent molecules leads to a series of new ionic species, from “solvent-separated ion pairs” (SSIPs), to “close ion pairs” or “contact ion pairs” (CIPs), to “aggregates” (AGGs), as discussed in Section 4.11 (Figure 4.9b).²

However, not every salt can support the formation of concentrated or super-concentrated electrolytes. After all, the dissolution of salts into ions is the result of the interplay between ion–ion interactions and ion–solvent interactions (Figure 12.5). For example, if the interionic attraction between a cation and an anion is so strong that it outperforms that of an ion–solvent interaction, then CIPs would prefer to adopt the kind of ionic arrangement as in a salt lattice, hence salt precipitation from the electrolyte could start. This usually occurs with most of the inorganic salts, such as NaCl and LiCl, the maximum concentration of which in water can reach 6 and 10 molal (m), respectively (Section 5.2.7, Figure 5.13). At those concentrations, although the solvent:salt ratio is as high as 9 and 6, respectively, meaning that there are still sufficient numbers of solvent molecules for each ion to form a Bernal–Fowler-type solvation sheath despite the high salt concentration, the strong cation–anion attraction overcomes the solvation power of the water molecules and they recombine into the lattice of solid NaCl and LiCl. Note that water is an extremely powerful solvent, but the cation–anion attractions in these inorganic salts are so strong because both ions are in fact “point charges”.

One of the few exceptions to inorganic salts is lithium nitrate (LiNO_3), which can be dissolved in water at concentrations as high as

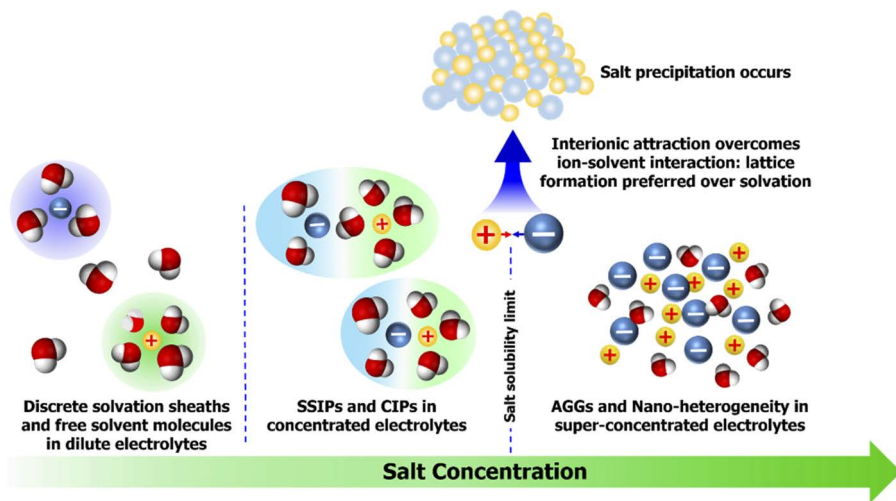


Figure 12.5 The evolution from dilute to concentrated and super-concentrated electrolytes is accompanied by changes in both the local solvation environment and extended liquid structure. The interplay between ion–ion interactions and ion–solvent interactions determines whether the formation of super-concentrated electrolyte is possible, which mainly relies on two competing factors: (1) the Coulombic attraction between an ion and its counterion and (2) the capability of the solvent molecule to coordinate with the ions (especially the cations) and to prevent them from approaching each other too closely.

23.5 m, where the solvent:salt ratio is nearly 2.35, and can be considered as a super-concentrated electrolyte. According to both molecular dynamics simulations and experimental studies such as the atomic pair distribution function based on X-ray diffraction, such high concentrations force the Li^+ to share water molecules in a manner where Li^+ , NO_3^- and water are arranged as if they are in the crystal lattice of hydrated LiNO_3 , except that the local structure of the aggregates consisting of $[\text{Li}(\text{H}_2\text{O})_2]^+$ chains adopts a much more relaxed conformation than in the crystal, so that Li^+ ions still remain mobile in such semi-crystalline structures. This state can be considered as being situated midway between a crystal and a classical solution.

On the other hand, if the ion–solvent interaction could outcompete the ion–ion interaction, then it is more likely that super-concentrated electrolytes will form, where the solvent:salt ratio can be reduced to a level approaching or even below 1.0. In reality, this was achieved not by increasing the ion–solvent interaction, but by reducing the attraction between cations and anions *via* altering the anion structure. Typical examples are highly fluorinated and large anions such as

bis(trifluoromethanesulfonyl)imide (TFSI), bis(fluorosulfonyl)imide (FSI) and their derivatives, in which the formal charges are well delocalized across a large structure. So far, almost all super-concentrated electrolytes, no matter aqueous or non-aqueous, were based on such anions. The highest salt concentration achieved is 63 m, where the solvent:salt ratio is reduced to 0.88.¹⁹

The super-concentration of salts in electrolytes can be considered as an intermediate region between classical diluted electrolytes and ionic liquids. The presence of high salt concentrations induces a series of unusual properties that are otherwise unavailable from electrolytes at normal salt concentrations. We will dedicate a section to their discussion.

Of course, so far there has been no quantitative and unified definition regarding what exact salt concentration is considered “super”, as the emergence of those unusual properties is highly dependent not only on the solvent but also on the nature of the properties.

12.2.4.1 Solvation Disproportionation

At super-concentration, the individual solvation sheaths of the classical Bernal–Fowler structures are forced to approach each other and eventually merge, and the ion–ion and ion–solvent interactions intensify significantly. Induced by such “densified” Coulombic fields emitted from ions of opposite charges at a small length scale, the changes that occur to the solvation sheath are no longer homogeneous. Instead, the distribution of solvent molecules among different central ions becomes uneven.

To explain what this uneven distribution refers to, let us look at a specific example: an aqueous electrolyte based on LiTFSI.

At a dilute concentration of 1 m, there are plenty of water molecules available (55.55 water molecules per Li^+ ion) for the Li^+ to recruit into its solvation sheath, hence one should expect a classical Bernal–Fowler solvation sheath structure for each ion that is well separated by an ample number of free solvent molecules, forming SSIPs.

When the TFSI concentration is increased to 10 m, the water:salt ratio (*ca.* 5:1) still ensures that there are sufficient water molecules to constitute a Bernal–Fowler solvation sheath, if one assumes that the solvation number of Li^+ is 4 and the anion is barely solvated. However, such Bernal–Fowler solvation sheaths are no longer as well separated from each other as in dilute electrolytes, because now there are not so many free solvent molecules. As a result, these solvation sheaths have a much greater opportunity to encounter and collide with each other,

and these occasional encounters between cations and anions could produce a high population of CIPs as defined by the Bjerrum length (Section 4.9, Figure 4.8).

When the TFSI concentration is further increased to 20 m, the electrolyte becomes a water-in-salt electrolyte (WiSE), and the water:salt ratio becomes 2.8, which can no longer support the formation of Bernal–Fowler solvation sheaths. Under such a circumstance, one would imagine that solvation sheaths in a WiSE should be forced to take an average solvation arrangement of 2.8, forming a solvation sheath so depleted of solvent molecules that different ions have to share the solvent molecules, or a continuous AGG.

However, the above picture turns out to be over-simplistic, as both computer simulation and experiments revealed that the distribution of solvent molecules among different ions is by no means homogeneous: some Li^+ ions acquire more solvent molecules than others, so that they can still afford to construct a Bernal–Fowler solvation sheath consisting of four water molecules, whereas other Li^+ ions are so deprived of solvent molecules in their neighborhood that they have to allow the anions to enter their primary solvation sheath perimeter, forming percolating cation–anion aggregates. In other words, there is severe *disproportionation* with respect to the structure of the Li^+ solvation sheath in the super-concentration regime (Figure 12.6).²⁰

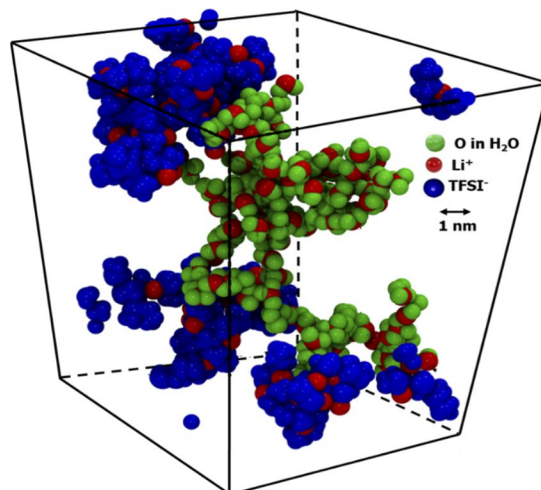


Figure 12.6 Molecular dynamics snapshot of a WiSE consisting of 21 m LiTFSI dissolved in water, where disproportionation in the solvation sheath occurs and leads to heterogeneous aggregations at the nano-scale. Reproduced from ref. 20 with permission from American Chemical Society, Copyright 2020.

According to molecular dynamics simulation, at 20 m LiTFSI in water about 40% of Li^+ ions in a WiSE are only surrounded by water molecules in a tetrahedrally coordinated configuration, taking up about 57% of the entire water population; while the remainder of the Li^+ ions are both coordinated by two TFSI anions and two water molecules. In other words, the severe disproportionation ensures that nearly half of the Li^+ ions are in the classical tetrahedrally coordinated configuration with a solvation number of 4, at the expense of the remainder of the Li^+ ions, which are essentially trapped in an anion-based network. It was speculated that Li^+ ions in the former coordination environment $(\text{Li}[\text{H}_2\text{O}]_4)^+$ would serve as the mobile species and be responsible for the ion conduction, whereas Li^+ ions in the AGGs would have much more difficulty in moving.

However, such disproportionation seems to be a unique phenomenon with aqueous electrolytes only, probably because of the bipolarity of water molecules to coordinate with both cations and anions. Non-aqueous electrolytes at similar solvent:salt ratios have not been found to behave similarly. For example, acetonitrile (AN) is a rare non-aqueous solvent that can dissolve lithium salts to concentrations that are comparable to a WiSE. In super-concentrated (3.5–5 m) solutions of various salts in AN, the solvent:salt ratio has reached 2, and the Li^+ ions therein can only access half of the solvent molecules needed to complete its first solvation sheath. Both computation simulation and spectroscopy revealed that in these electrolytes the Li^+ solvation sheath receives similar contributions from the solvent and anions, that is, on average two solvent molecules and two anions per Li^+ , in the absence of any disproportionation.

Whether the disproportionation phenomenon is exclusive to aqueous electrolytes remains to be verified. As new non-aqueous and aprotic solvent molecules or new salts are developed, more non-aqueous electrolytes in super-concentration regimes need to be investigated to reach a universal conclusion.

12.2.4.2 Nano-heterogeneity in Extended Liquid Structures

When an electrolyte ventures into the super-concentration regime, drastic changes induced by the solvation disproportionation not only occur in the local environment of ions and solvent molecules, but also to a larger length scale (1–100 nm) beyond the local arrangement of ions and solvent molecules.

At a large length scale, the overall liquid structure of the electrolyte, which is homogeneous and “smooth” because of the random thermal

motions of ions and solvent molecules, would become “grainier” owing to the intensified ion–ion and ion–solvent interactions. Such an inhomogeneous structure arises from the uneven distribution of solvent molecules around ions. The clusters of ions with the same solvation sheath structure are more likely to aggregate, forming local regions of heterogeneity at the nanometric scale, as shown in Figure 12.6. The existence of such nano-heterogeneity was predicted by molecular dynamics simulations, and has been verified by various experiments including scattering spectroscopy using both neutron and X-ray techniques, and vibrational spectroscopy using infrared and Raman techniques. Here the strong ability of water to solvate both Li^+ and anions was considered a key factor responsible for such inhomogeneous liquid structures. In those liquid structures of nano-heterogeneity, the “water-rich” domains often consist of cations solvated only by water molecules, such as $[\text{Li}(\text{H}_2\text{O})_x]^+$, while the “anion-rich” domains are mostly $[\text{TFSI}-\text{Li}^+-\text{TFSI}]$ complexes with little presence of water. These nano-domains could be viewed as two different percolating networks that interpenetrate each other.

When the salt concentration enters the extreme super-concentrated regions, the distribution of these nano-domains changes accordingly. For example, in the 63 m electrolyte that consists of 42 m LiTFSI and 21 m trimethylethylammonium bis(trifluoromethanesulfonyl)imide ($\text{Me}_3\text{EtN}\cdot\text{TFSI}$), the water molecules become such a minority in the electrolyte that the water-rich domains are isolated and discontinuous, while most of the liquid structure consists of anion–cation pairs (Figure 12.7).^{19,21} Interestingly, the solubility limit of LiTFSI itself in the water is only *ca.* 22 m, while $\text{Me}_3\text{EtN}\cdot\text{TFSI}$ alone cannot dissolve in water at all. However, when used as a co-salt of each other, a total of 42 m LiTFSI could be dissolved along with 21 m $\text{Me}_3\text{EtN}\cdot\text{TFSI}$, pushing the solvent:salt ratio to an unprecedented level of 0.88. In other words, not only are there insufficient water molecules for Li^+ to form the luxury of a Bernal–Fowler solvation sheath, but also, on average, there are insufficient water molecules to satisfy even the minimum demand of a single water molecule per cation. This strongly implies that the larger tetraalkylammonium cation, which is a so-called chaotropic cation and hence much weaker Lewis acid than Li^+ , actually does not require water solvation but instead serves as an effective weakly polar medium to help stabilize the anions.

Finally, it should be remembered again that, like the solvation sheath structures, the liquid structures as shown in Figures 12.6 and 12.7 are highly dynamic, and they rapidly change on a temporal scale of nano- or even picoseconds. Nevertheless, their presence causes

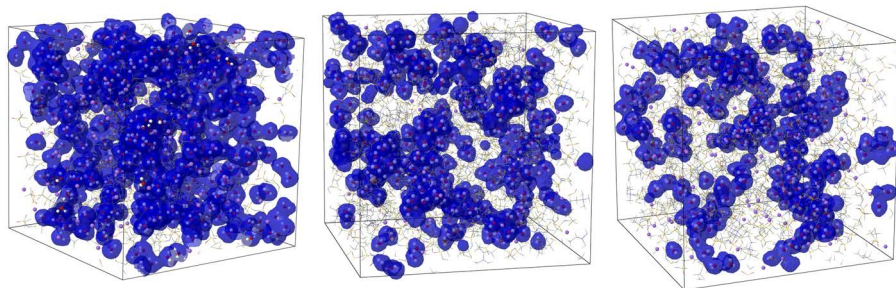


Figure 12.7 Evolution of heterogeneous liquid structure with salt concentration: snapshots of a molecular dynamic simulation box showing the connectivity of $\text{Li}^+(\text{H}_2\text{O})$ chains as represented by solid spheres in electrolytes consisting of (left) WiSE (21 m LiTFSI in water), (center) WiSE with additional 21 m ammonium co-salt trimethylethylammonium bis(trifluoromethanesulfonyl) imide ($\text{Me}_3\text{EtN-TFSI}$) and (right) a 63 m super-concentrated electrolyte consisting of 42 m LiTFSI and 21 m ammonium co-salt $\text{Me}_3\text{EtN-TFSI}$. The disruption of hydrogen bond network is reflected in the disconnection of the $\text{Li}^+(\text{H}_2\text{O})$ domains. Reproduced from ref. 19 with permission from American Chemical Society, Copyright 2020.

significantly different transport and interfacial behaviors that differ from those of the electrolytes with dilute salt concentrations.

12.2.4.3 “Salt Solvate” Electrolytes

A special class of concentrated electrolytes deserves a dedicated section, namely the so-called “salt solvate” electrolytes that have been systematically studied by Watanabe and co-workers, who not only investigated these equimolar or highly concentrated electrolytes for new properties, but also attempted to rationalize them on a fundamental level. This class of concentrated electrolytes were also sometimes referred to as “quasi-ionic liquid” systems.^{22–24}

These electrolytes are most frequently based on multi-glymes of varying length (G_n , where n represents the number of ether units in $\text{CH}_3[\text{CH}_2\text{CH}_2\text{O}]_n\text{OCH}_3$), which provide ethereal oxygen atoms to form chelate structures with cations, and represent an intermediate concentration range between the conventional dilute electrolytes and super-concentrated electrolytes, because the population of solvent molecules therein is just enough to complete the first solvation sheath of Li^+ . In many such electrolytes there is a certain molar stoichiometry

between the solvent and the cation. A typical structure of a salt solvated electrolyte based on an $[\text{Li}-\text{G}_n]^+$ complex is shown in Figure 12.2. Because of the high denticity of these glymes, the solvation cages that they form for the cations are often extremely tight and strong, which leads to a series of unusual properties including thermal, ion transport and electrochemical.

These properties could be desirable or undesirable. For example, the glymes are usually very volatile solvent molecules, but once they form equimolar mixtures with various lithium salts the resultant liquids becomes rather viscous and non-volatile, with thermal stability (as measured by the capability of maintaining the weight) up to 200 °C. Spectroscopic evidence reveals that all glyme molecules are tightly coordinated by Li^+ , which would outcompete EC or even PC as the most favored solvent molecules in an ESI-MS experiment as shown in Figure 12.4. However, the solvation cages also make the cation movement especially clumsy, which reduces not only the cationic transport number even further but also the overall ion conductivity.

Of course, solvent molecules other than ethers could also form salt solvate electrolytes, including carbonates, nitriles and sulfones. By constructing phase diagrams, various crystalline solvates, $[\text{Li}(\text{EC})_1\text{LiTFSI}]$ and $[\text{Li}(\text{EC})_3\text{LiTFSI}]$, together with an amorphous phase around the stoichiometric composition $[\text{Li}(\text{EC})_2\text{LiTFSI}]$, have been identified. Raman spectroscopy revealed that about 95% of EC molecules in this salt solvate composition were coordinated with Li^+ . In sulfones, the formation of an $[\text{LiBF}_4(\text{sulfolane})_2]$ complex seems to establish a relatively immobile and anionic framework.²⁵

Polymeric ethers could form similar solvation structures, as represented by the “polymer-in-salt” concept first demonstrated by Angell and co-workers,²⁹ which in fact served as the ancestor for the later “solvent-in-salt” electrolytes and WiSE systems. However, the polymer salt solvate electrolyte systems often suffer from high crystallinity and high melting temperature in addition to slow ion transport.

In addition to ethers and carbonates, various cyclic and linear amides and nitriles of varying lengths were also found to form salt solvate electrolytes, in which the lone pair of electrons on the nitrogen serves as the major electron donor in coordination with Li^+ . In most cases, the electrolytes do not demonstrate a clear stoichiometry between the cation (mostly Li^+) and the solvent molecules, hence it is difficult to delineate a clear demarcation between salt solvate electrolytes and ordinary concentrated electrolytes.

12.3 Solvation Sheaths, Solvation Cages and Solvation Sites

In Section 2.1, Figure 2.1, we displayed four distinct types of electrolytes. However, despite how drastically distinct these electrolytes may appear, the solvation environments of ions experience a continuous rather than sudden transformation in these electrolytes (Figure 12.8).²⁶

In typical liquid electrolytes with low to moderate salt concentrations, we have established that ions therein possess discrete Bernal-Fowler solvation sheaths that consist of three layers of solvent molecules, *i.e.* primary and secondary solvation sheaths and bulk. If the solvent molecules are non-aqueous and aprotic, then the cations are especially solvated, with the electronegative termini of these solvent molecules selectively coordinated with the cation, often adopting the most popular tetrahedral configurations. Although the Brownian motion of other entities in the electrolytes, such as neighboring ions, or solvent molecules from the secondary solvation sheath or the bulk electrolyte, constantly disrupts such Bernal-Fowler solvation sheaths, knocking off the solvent molecules within the primary solvation sheath and replacing them with new solvent molecules, the ion–solvent interactions are often strong enough to survive the solvent exchange. Hence such solvation structures are considered dynamically static on the time scale of the ion transport; in other words, the ions can be considered to be traveling with their own solvation sheaths.

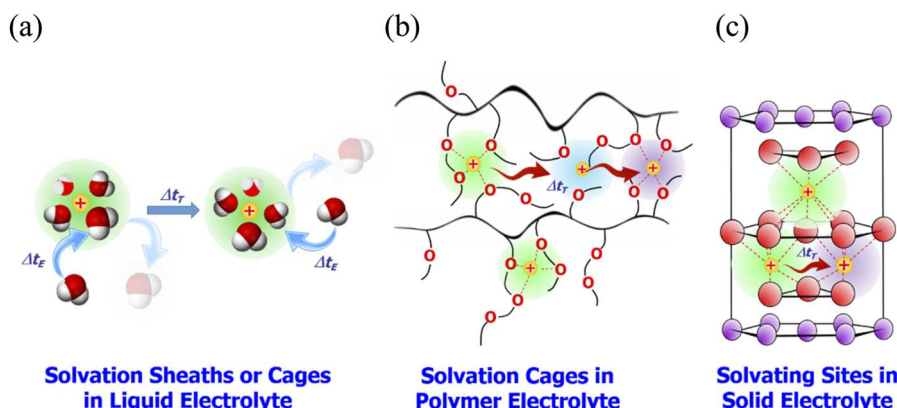


Figure 12.8 The transition of the ion solvation environment from (a) solvation sheaths/solvation cages in typical liquid electrolytes to (b) solvating cages in polymer electrolytes and (c) solvating sites in solid electrolytes.

For those solvent molecules that display especially strong solvation power towards cations thanks to their high donicity and denticity, such as ethers like DME or polyglymes (Table 12.1), the solvent exchange rate could be so slow that the solvation sheath essentially remains intact during the translational movement of ions on large length scales (of the order of nanometers according to both simulations and experiments). Such static solvation sheaths are often called “solvation cages”, because the strong tendency to trap the ions often constitutes high energy barriers for the ions to desolvate at electrode/electrolyte interfaces or interphases.

No matter whether solvation sheath or solvation cage, the solvation environment of mobile ions in these liquid or liquid-like electrolytes is dynamically static, and translates with mobile ions on length scales depending on the ion-solvent interaction.

On the other hand, in inorganic solid electrolytes as exemplified by ceramic or glassy ion conductors, the counterions are often immobilized on the framework, whereas the mobile ions, which are often cations such as Li^+ or Na^+ , have to hop from one coordination site to the next. If one views the environment of the mobile ions at a given coordination site as a solid solvation sheath, and the ligands that coordinate with the mobile ions as solvent molecules, then this solid solvating sheath would remain completely immovable when the ion hops. We should then name such static solvation sheaths “solvating sites”, where the word “site” implies that the solvation environment does not move. In other words, the “solvation sheaths” in true solid electrolytes face zero disruption from Brownian motion, whereas the mobile ions would have to completely shed their “solvation sheaths” when moving.

Hence the solvation environment of mobile ions in these true solid electrolytes is perfectly static, and does not translate with the mobile ion.

A somehow intermediate state exists between the typical liquid electrolytes and typical inorganic solid electrolytes. In polymer electrolytes based on ethereal molecules, such as poly(ethylene oxide) (PEO) or other variations of the macromolecular ethers, the ions would experience a solvation environment that shares similarities with both the “solvation cage” in liquid electrolytes and “solvating sites” in solid electrolytes. On the one hand, although the polymeric electrolyte may appear to be “solid” with macroscopic dimensional stability, what an ion sees inside these electrolytes microscopically is still a liquid-like structure, the ethereal solvation cage of which does not differ much from that in a liquid electrolyte based on ethereal solvents. On the other hand, despite the strong interaction between the mobile ion and the ether cages, those ether units are covalently linked to the

polymeric chains, hence they are much less mobile when trying to cooperate with the movement of the mobile ion. The compromise result of such a conflict is that, at a certain length scale, the solvation cage can no longer travel together with the mobile ion, and the ion has to shed its original solvation cage and “hop” into a new solvation cage or coordination site as a mobile ion in an inorganic solid electrolyte does.

Therefore, the solvation environment of a mobile ion in these polymeric, or semi-solid, electrolytes is relatively static, and translates with the mobile ion to a certain extent.

These differences in the solvation characteristics have been leveraged to differentiate how the ion transport occurs in these electrolytes, which leads to the definition of “vehicular” or “structural” modes of ion transport, with the former referring to the ions that travel with their solvation sheaths or solvation cages, and the latter to the ions that hop between different solvating sites. Of course, there is no absolute demarcation between the two modes. What most likely happens in a liquid or polymer electrolyte is the mixed transport mode from both vehicular and structural manners, and the definition of what is vehicular or structural largely depends on two questions of “how long” and “how far”, *i.e.* how long do the solvent molecules stay with the solvation sheath and how far do the solvent molecules have to travel with the central ion? A widely accepted standard is that, if a given solvation sheath maintains its integrity during the time required for the ion to travel the length of an entire solvation sheath (of the order of nanometers), then it can be considered as vehicular. On the other hand, since there are more than one solvent molecule in the solvation sheath, what could also very likely happen in the liquid and polymer electrolytes is that the solvation sheath is only partially broken, with some of the solvent molecules being replaced with new solvent molecules while the others remain in the solvation sheath until the completion of the trip (Figure 12.8a). In such a case, the demarcation between vehicular and structural manners becomes really ambiguous, and one could only evaluate the ion transport mode from a statistical perspective. One quantity developed from molecular dynamics simulation is the so-called “residence time”, τ_R , which measures the average time a solvent molecule spends with its central ion. For example, τ_R for a carbonate molecule such as EC with an Li^+ ion is estimated to be 0.2 ns at room temperature, whereas for ethers τ_R is about five times longer, which reflects the much stronger solvation power of ethers towards Li^+ because of the chelation structure (Figure 12.2).

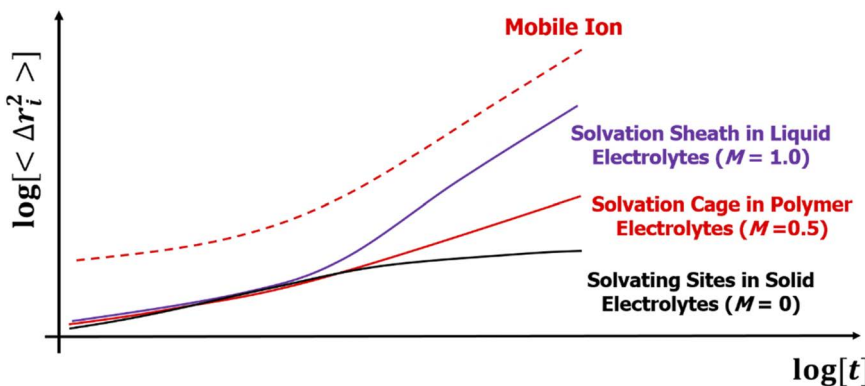


Figure 12.9 The various types of electrolytes could be quantitatively differentiated by how the solvation sheaths of ions move with them. Here an order parameter M was defined as the ratio of mobility between the solvation environment and the mobile ion. When the time scale is long enough, the mean square displacement achieved by the mobile ion and its solvation sheath/solvation cage/solvating site distinctively reveals characteristic behaviors of liquid, polymer and solid electrolytes.²⁶

Other quantities are also derived so that one can differentiate these diversified types of electrolytes. For example, Balsara and colleagues defined an “*order parameter*” M based on the relative mobility of an ion (α_+ , assuming the mobile ion is a cation) and its solvation environment (α_i), such as solvent molecules or the coordination sites:

$$M = \frac{\alpha_i}{\alpha_+} \quad (12.2)$$

In liquid electrolytes, since the mobile ions travel with the solvation sheath, both entities are of similar mobility, and the ratio M is approximately 1.0. In ceramic or glassy electrolytes, the mobile ions are decoupled from the solvation environments and move alone, and the ratio M should be zero. Polymer electrolytes serve as a transition state between the two, with the ratio M being 0.5 (Figure 12.9).²⁶

12.4 Anion Solvation

Most anions used in lithium-ion batteries and other emerging advanced batteries are based on complex structures, where the formal negative charge is well delocalized over a large size. Typical examples

are PF_6^- , BF_4^- , TFSI^- and FSI^- (Table 10.2). The high contents of fluorine in these structures are by no means a coincidence; instead, the extremely high electronegativity of fluorine makes it a strong electron-withdrawing substituent, which ensures sufficient delocalization of the formal charge from the central atom. The consequence of such delocalization is that the anions are turned from the original “point charge” into a large body that carries the same amount of charge, hence the accompanying Coulombic field emitted is much less intense (Figure 10.9).

Meanwhile, on the solvent side, as discussed in Section 3.1, most of these non-aqueous and aprotic molecules are essentially “monopolar” (Figure 3.1), because their positive termini are usually sterically hindered and hence difficult to access for anions.

The combination of these two factors resulted in a much weaker anion–solvent interaction compared with that between cations and solvent.²⁷ In fact, applying the same ESI-MS experiment as shown in Figure 12.3 on electrolytes by reversing the polarity of the DC voltage applied, one would detect the naked anions as the overwhelming major species in the mass spectrometer, while the anion–solvent association is only sporadically detected and in rather small populations. Similar results were also reported by both experimental and computation means, such as liquid secondary ion mass spectrometry (SIMS),¹⁴ multinuclear NMR,⁵ FTIR and Raman spectroscopy, and also calculation of solvation enthalpy. For example, in typical carbonate solvents, the solvation enthalpy for Li^+ is estimated to be between 20 and 50 kcal mol⁻¹, whereas for anions (PF_6^- and TFSI^-) the value is below 10 kcal mol⁻¹.²⁷ The direct consequence of this preferred solvation of cations over anions is the difference in their transport behaviors: the anions are generally much more mobile than the cations, and the difference is much more pronounced in non-aqueous than aqueous electrolytes, because water is a bipolar solvent molecule that can solvate both cations and anions, whereas non-aqueous solvent molecules are mostly monopolar, as pointed out in Chapter 3, Section 3.1 (Figure 3.1).

This seems to be a universal trend, not only for all the complex anions listed above (PF_6^- , BF_4^- , TFSI^- and FSI^-), but also for both ester and ether solvents. Thus, the general belief is that a well-defined solvation sheath for anions does not exist.

However, exception arises when the solvent molecules are equipped with electron-deficient centers, such as boron in the so-called “anion receptors”. One example of an anion receptor was shown in eqn

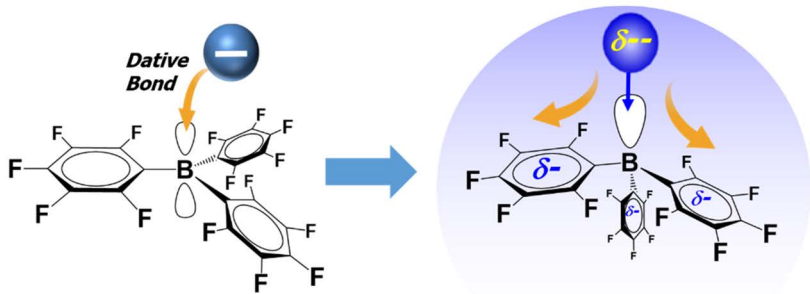
(10.33). In this case, the “solvent” molecules are no longer electron donors but electron acceptors, and can selectively “solvate” anions by forming a giant complex anion that is similar in many ways to the complex anion themselves, *i.e.* delocalizing the charge over an extended space. This can be achieved by using electron-withdrawing substituents such as fluorine, or by forming conjugated bonding systems such as aromatic structures where the formal charge can be redistributed *via* resonances, or both, using fluorinated aromatic substituents on aromatic rings (Figure 12.10). Here the interaction nature between the empty orbital on boron and the electron donor of the complex anion is a so-called “*dative bond*”.

Since most of the complex anions themselves are held together by covalent bonds between a central atom and multiple fluorine substituents, one complication brought by these anion receptors is that the dative bond between the electron-deficient central boron and the electron donor from the complex anion becomes so strong for these covalent bonds that the complex anion could be ripped apart, causing decomposition. Such a process was already observed in those anions, such as PF_6^- and BF_4^- , in which the anion receptor took only a fluoride anion instead of the entire complex anion, producing the gaseous products PF_5 and BF_3 , which could trigger a chain of decompositions to the other solvent molecules (Figure 12.10b).

Note that all P–F and B–F bonds in PF_6^- and BF_4^- should be identical in terms of bond length and angle; however, the P–F or B–F bond that participates in the dative bond with boron is elongated compared with other bonds, as reflected in Figure 12.10b.

For water, the cation-preferred solvation behavior does not exist, as both anions and cations can be solvated by this bipolar solvent molecule. In fact, it is the water-TFSI association that ensures the formation of super-concentrated electrolytes at solvent:salt ratios approaching 1.0, where unusual solvation structures arise, such as the solvation disproportionation and the nano-heterogeneity network that we already discussed (Figures 12.6 and 12.7).^{3,20,21} It remains an open question whether these unusual solvation behaviors occur only in aqueous electrolytes, but apparently the weak solvation behavior of anions in non-aqueous and aprotic solvents makes it much more difficult for non-aqueous electrolytes to demonstrate these unusual behaviors, as exemplified by the acetonitrile-based electrolytes, the concentration of which approaches that of a WiSE but neither solvation sheath disproportionation nor nano-heterogeneity was observed therein.

(a)



(b)

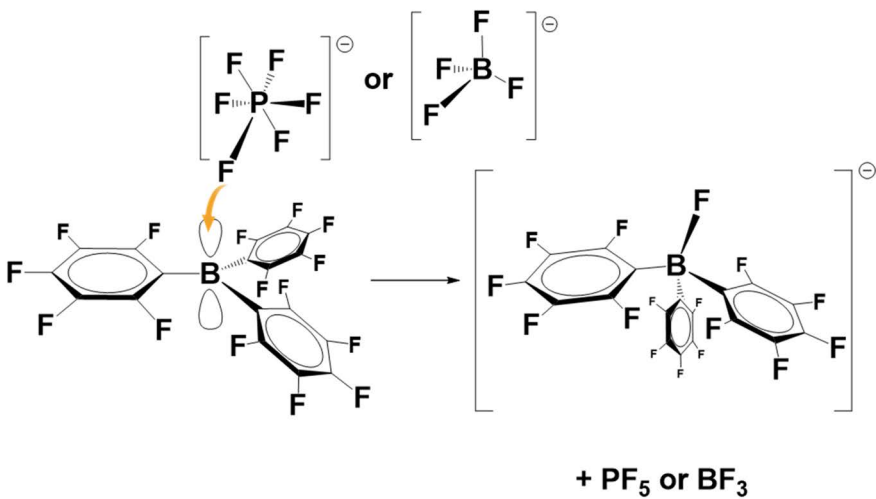


Figure 12.10 (a) The formal charge on an anion is accommodated in the empty orbital on the central atom boron, the electron-deficient nature of which is intensified by the multiple fluorine substitutions on the three aromatic rings that conjugate with boron. The dative bond formed between the anion receptor and the original complex anion turns the latter from a non-point charge into an even larger anion, where the formal charge is further delocalized. (b) If the original anion consists of labile bonds, such as PF_6^- and BF_4^- , the strong interaction between the anion receptor and the electron donor in the labile bonds may tear apart the original anion and form a new complex anion, producing harmful Lewis acids such as PF_5 and BF_3 .

References

1. J. D. Bernal and R. H. Fowler, A Theory of Water and Ionic Solution, with Particular Reference to Hydrogen and Hydroxyl Ions, *J. Chem. Phys.*, 1933, **1**, 515–548.
2. O. Borodin, J. Self, K. Persson, C. Wang and K. Xu, Uncharted Waters: Super-concentrated Electrolytes, *Joule*, 2019, **4**, 69–100.
3. O. Borodin, L. Suo, M. Gobet, X. Ren, F. Wang, A. Faraone, J. Peng, M. Olguin, M. Schroeder, M. S. Ding, E. Gobrogge, A. von W. Cresce, S. Munoz, J. A. Dura, S. Greenbaum, C. Wang and K. Xu, Liquid structure with nano-heterogeneity promotes cationic transport in concentrated electrolytes, *ACS Nano*, 2017, **11**, 10462–10471.
4. O. Borodin, X. Ren, J. Watamanu, A. von Wald Cresce, J. Knap and K. Xu, Modeling Insight into Battery Electrolyte Electrochemical Stability and Interfacial Structure, *Acc. Chem. Res.*, 2017, **50**, 2886–2894.
5. X. Bogle, R. Vazquez, S. Greenbaum, A. von W. Cresce and K. Xu, Understanding Li⁺-Solvent Interaction in Nonaqueous Carbonate Electrolytes with ¹⁷O NMR, *J. Phys. Chem. Lett.*, 2013, **4**, 1664–1668.
6. D. M. Seo, O. Borodin, S.-D. Han, P. D. Boyle and W. A. Henderson, Electrolyte solvation and ionic association II. Acetonitrile-lithium salt mixtures: highly dissociated salts, *J. Electrochem. Soc.*, 2012, **159**, A1489–A1500.
7. K. Xu, A. v. Cresce and U. Lee, Differentiating contributions to “ion transfer” barrier from interphasial resistance and Li⁺ desolvation at electrolyte/graphite interface, *Langmuir*, 2010, **26**, 11538–11543.
8. A. v. Cresce and K. Xu, Preferential solvation of Li⁺ directs formation of interphase on graphitic anode, *Electrochim. Solid-State Lett.*, 2011, **196**, 3906–3910.
9. H. Kim, J. Hong, G. Yoon, H. Kim, K.-Y. Park, M.-S. Park, W.-S. Yoon and K. Kang, Sodium intercalation chemistry in graphite, *Energy Environ. Sci.*, 2015, **8**, 2963–2969.
10. J. Vatamanu, O. Borodin and G. D. Smith, Molecular Dynamics Simulation Studies of the Structure of a Mixed Carbonate/LiPF₆ Electrolyte near Graphite Surface as a Function of Electrode Potential, *J. Phys. Chem. C*, 2012, **116**, 1114–1121.
11. G. V. Zhuang, K. Xu, T. R. Jow and P. N. Ross, Study of SEI layer formed on graphite anodes in PC/LiBOB electrolyte using IR spectroscopy, *Electrochim. Solid-State Lett.*, 2004, **7**, A224–A227.
12. A. Cresce, O. Borodin and K. Xu, Correlating Li⁺ Solvation Sheath Structure with Interphasial Chemistry on Graphite, *J. Phys. Chem. C*, 2012, **116**, 26111–26117.
13. H. Wang, S. C. Kim, T. Rojas, Y. Zhu, Y. Li, L. Ma, K. Xu, A. T. Ngo and Y. Cui, Correlating Li-ion solvation structures and electrode potential temperature coefficients, *J. Am. Chem. Soc.*, 2021, **143**, 2264–2271.
14. Y. Zhou, M. Su, X. Yu, Y. Zhang, J.-G. Wang, X. Ren, R. Cao, W. Xu, D. R Baer, Y. Du, O. Borodin, Y. Wang, X.-L. Wang, K. Xu, Z. Xu, C. Wang and Z. Zhu, Real-time mass spectrometric characterization of the solid-electrolyte interphase of a lithium-ion battery, *Nat. Nanotechnol.*, 2020, **15**, 224–230.
15. K. Xu and A. von Wald Cresce, Li⁺-solvation/desolvation dictates interphasial processes on graphitic anode in Li ion cells, *J. Mater. Res.*, 2012, **27**, 2327–2341.
16. K. Xu and A. von Cresce, Interfacing electrolytes with electrodes in Li ion batteries, *J. Mater. Chem.*, 2011, **21**, 9849–9864.
17. V. Gutmann, Solvent effects on the reactivities of organometallic compounds, *Coord. Chem. Rev.*, 1976, **18**, 225–255.
18. C.-C. Su, M. He, R. Amine, T. Rojas, L. Cheng, A. T. Ngo and K. Amine, Solvating power series of electrolyte solvents for lithium batteries, *Energy Environ. Sci.*, 2019, **12**, 1249–1254.

19. L. Chen, J. Zhang, Q. Li, J. Vatamanu, X. Ji, T. P. Pollard, C. Cui, S. Hou, J. Chen, C. Yang, L. Ma, M. S. Ding, M. Garaga, S. Greenbaum, H.-S. Lee, O. Borodin, K. Xu and C. Wang, A 63 m Superconcentrated Aqueous Electrolyte for High-Energy Li-Ion Batteries, *ACS Energy Lett.*, 2020, **5**, 968–974.
20. Z. Yu, L. A. Curtiss, R. E. Winans, Y. Zhang, T. Li and L. Cheng, Asymmetric composition of ionic aggregates and the origin of high correlated transference number in water-in-salt electrolytes, *J. Phys. Chem. Lett.*, 2020, **11**, 1276–1281.
21. L. Ma, J. Vatamanu, N. T. Hahn, T. P. Pollard, O. Borodin, V. Petkov, M. A. Schroeder, Y. Ren, M. S. Ding, C. Luo, J. L. Allen, C. Wang and K. Xu, Highly reversible Zn metal anode enabled by sustainable hydroxyl chemistry, *Proc. Natl. Acad. Sci. U. S. A.*, 2022, **119**, e2121138119.
22. K. Yoshida, M. Nakamura, Y. Kazue, N. Tachikawa, S. Tsuzuki, S. Seki, K. Dokko and M. Watanabe, Oxidative-stability enhancement and charge transport mechanism in glyme-lithium salt equimolar complexes, *J. Am. Chem. Soc.*, 2011, **133**, 13121–13129.
23. K. Dokko, N. Tachikawa, K. Yamauchi, M. Tsuchiya, A. Yamazaki, E. Takashima, J.-W. Park, K. Ueno, S. Seki, N. Serizawa and M. Watanabe, Solvate ionic liquid electrolyte for Li-S batteries, *J. Electrochem. Soc.*, 2013, **160**, A1304–A1310.
24. K. Ueno, K. Yoshida, M. Tsuchiya, N. Tachikawa, K. Dokko and M. Watanabe, Glyme-lithium salt equimolar molten mixtures: concentrated solutions or solvate ionic liquids?, *J. Phys. Chem. B*, 2012, **116**, 11323–11331.
25. K. Dokko, D. Watanabe, Y. Ugata, M. L. Thomas, S. Tsuzuki, W. Shinoda, K. Hashimoto, K. Ueno, Y. Umebayashi and M. Watanabe, Direct Evidence for Li Ion Hopping Conduction in Highly Concentrated Sulfolane-Based Liquid Electrolytes, *J. Phys. Chem. B*, 2018, **122**, 10736–10745.
26. D. J. Siegel, L. Nazar, Y. M. Chiang, C. Fang and N. P. Balsara, Establishing a unified framework for ion solvation and transport in liquid and solid electrolytes, *Trends Chem.*, 2021, **3**, 807–818.
27. A. von W. Cresce, M. Gobet, O. Borodin, J. Peng, S. M. Russell, E. Wikner, A. Fu, L. Hu, H.-S. Lee, Z. Zhang, X.-Q. Yang, S. Greenbaum, K. Amine and K. Xu, Anion solvation in carbonate-based electrolytes, *J. Phys. Chem. C*, 2015, **119**, 27255–27264.
28. A. von Cresce and K. Xu, *Electrochem. Solid-State Lett.*, 2011, **14**, A154–A156.
29. C. A. Angell, C. Liu and E. Sanchez, Rubbery solid electrolytes with dominant cationic transport and high ambient conductivity, *Nature*, 1993, **362**, 137–139.

13 Static Stability of Electrolytes

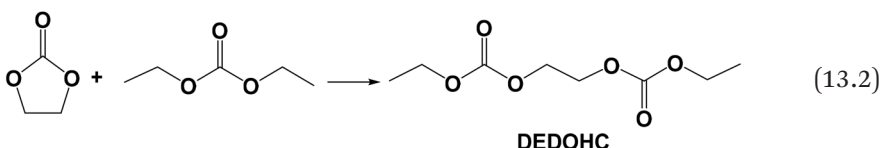
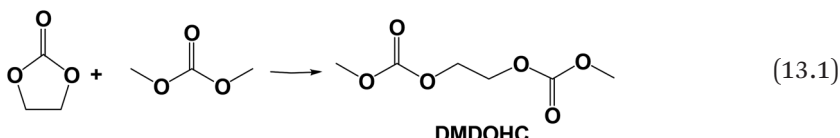
How stable an electrolyte is during its long-term and static storage remains a topic of high practical importance but often neglected. Only limited research has been conducted on the typical carbonate-based electrolytes used in lithium-ion batteries.

Here “*static stability*” refers to the resistance of the electrolyte composition against spontaneous conversions and transformations, *i.e.* in the absence of any external chemical or electrochemical driving forces. However, we will treat “external heat” as an exception, because most of these spontaneous reactions are accelerated at elevated temperatures.

In our conventional belief, once a salt or a mixture of salts has been dissolved in a solvent, the electrolyte composition is fixed and permanent. One then puts a label on the container, implying the permanency of such a composition. This is true for most aqueous electrolytes, such as an aqueous solution of NaCl, the composition of which does not change if we ignore the natural evaporation of the solvent.

However, this belief no longer holds true for most typical non-aqueous electrolytes used in lithium-ion batteries. In such electrolytes based on mixed carbonate molecules, both the cation and the highly fluorinated anions (*e.g.* PF₆⁻ and BF₄⁻) are strong Lewis acids or precursors for strong Lewis acids, which, upon their solvation with polar carbonate solvent molecules, could act as catalysts to trigger a series of spontaneous reactions among the solvents. The best-known example is the so-called “*transesterification reaction*”, which produces new molecules that are originally not present in

the electrolyte. For example, in the most commonly used electrolyte compositions (1.0 M LiPF₆ in EC-DMC or EC-DEC), two new carbonate molecules, dimethyl-2,5-dioxahexane carboxylate (DMDOHC) and diethyl-2,5-dioxahexane carboxylate (DEDOHC), have been identified by liquid and gas chromatography, NMR spectroscopy and absorption, scattering and other spectroscopic techniques:¹

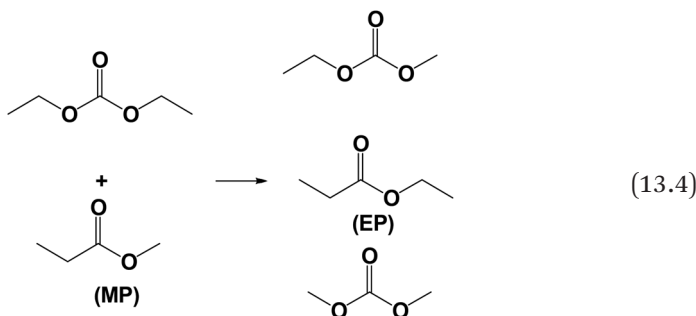


These linear diester products apparently originate from the ring opening of the cyclic carbonate EC *via* an ester exchange process with the linear carbonate molecules. Since the neat EC-DMC and EC-DEC solvent mixtures, *i.e.* without the lithium salt, do not demonstrate visible conversions as shown in eqn (13.1) and (13.2), these reactions must have been initiated or catalyzed by the acidic lithium salts used therein, which generate a series of species that would interact with the carbonate solvents, such as HF, PF₅ and PO_xF_y that are generated by the decomposition or the hydrolysis of LiPF₆ by trace moisture. The presence of these longer chain linear diesters, when at a high percentage, causes an increase in the viscosity of the electrolyte, thus slowing down ion transport while reducing effective solvation to the Li⁺ and they would also have an adverse effect on the capability of the electrolyte to form effective interphases.

A similar ester exchange also occurs between linear carbonates. For example, a significant amount of EMC has been found in a solvent mixture of DMC and DEC:



EMC, ethyl propionate (EP) and DMC were generated from the original solvent mixture of DEC and methyl propionate (MP):



Again, these reactions would not occur in the absence of lithium salts.

Fortunately, such transesterification reactions are found to proceed gradually at room temperature and become pronounced only during storage for long time periods ($t \approx 10^6$ s or up to months). On the other hand, these reactions could be thermally activated, the kinetics of which are accelerated in an Arrhenius-like manner. Therefore, the adverse effect of these reactions could become rather significant during storage. On the other hand, in a recent work by Dahn and coworkers, DMDOHC was deliberately synthesized and used as a solvent for a high temperature electrolyte, based on the argument that the transesterification produces a more thermodynamically stable product.²

According to more rigorous analyses carried out using liquid chromatography and gel permeation chromatography, there might be other parasitic reactions occurring, which produce higher molecular weight species with longer retention times on the chromatogram. Oligoether and poly(ether carbonate) compounds were proposed, which resulted from the polymerization of EC, but their exact structure remains to be determined. The precise identification of high polymeric species is always a challenge, no matter whether in bulk electrolytes or in interphases.

Interestingly, by monitoring the change in the ratio of EC to DMC over time, researchers noticed that the amount of EC decreased at a faster rate than that of DMC. This serves as strong evidence that the Lewis acid catalysts such as PF₅ preferentially attack the cyclic structure of EC rather than linear carbonates. Considering that the cyclic structure of EC actually represents an unsaturation that is equivalent to a C=C double bond, it should not be surprising that a ring-opening reaction is the initial step of the reaction sequence, the ion radicals of which eventually lead to polymeric reactions in addition to transesterification.

The existence of the spontaneous transesterification reactions among carbonate solvents serves as an important indication that the real electrolyte formulation might be different from what the label on an electrolyte container states, unless the electrolyte is freshly prepared or has been stored at low temperatures. One should always be cautious about the “face value” of these labels, and try to use electrolytes that have been carefully preserved or freshly prepared, so that a reliable correlation could be established between the electrolyte composition and electrochemical performance.⁴

Once placed in cells, the electrolytes in a battery environment could be subject to more complicated stimulus. The efforts at mechanistic studies seemed to identify the free radicals of these carbonate molecules as the source of static instability, which could be generated by either acidic or alkaline impurities, active sites on electrode surfaces or simply electrochemical reductions or oxidations.³ All of these factors are universal in almost any electrochemical device, and especially in batteries whose electrodes operate at extreme potentials. However, even when the electrolytes are not placed in the battery environment, other external factors could still generate these radicals, such as heat, light or exposure to acidic species that are always present from the partial hydrolysis of the common salt anions (PF_6^- and BF_4^-), or even oxygen. Hence the static instability of electrolytes in these electrochemical devices is an intrinsic tendency that could hardly be avoided. On the other hand, it was recently discovered that certain electrolyte additives, such as vinylene carbonate (VC) and lithium difluorophosphate (LiPO_2F_2), which were originally designed to manipulate interphasial chemistries, actually suppress the transesterification reactions in the bulk. Hence a hidden but important feature of these additives may concern the stabilization of the “face formula” of the electrolytes, which might be as critical as the participation of additives in interphasial chemistries.⁴

References

1. E. S. Takeuchi, H. Gan, M. Palazzo, R. A. Leising and S. M. Davis, Anode Passivation and Electrolyte Solvent Disproportionation: Mechanism of Ester Exchange Reaction in Lithium-Ion Batteries, *J. Electrochem. Soc.*, 1997, **144**, 1944–1948.
2. T. Taskovic, A. Eldesoky, W. Song, M. Bauer and J. R. Dahn, High Temperature Testing of NMC/Graphite Cells for Rapid Cell Performance Screening and Studies of Electrolyte Degradation, *J. Electrochem. Soc.*, 2022, **169**, 040538.
3. E. Endo, M. Ata, K. Sekai and K. Tanaka, Spin Trapping Study of Gradual Decomposition of Electrolyte Solutions for Lithium Secondary Batteries, *J. Electrochem. Soc.*, 1999, **146**, 49–53.
4. Y. Qian, S. Hu, X. Zou, Z. Deng, Y. Xu, Z. Cao, K. Kang, Y. Deng, Q. Shi, K. Xu and Y. Deng, How electrolyte additives work in Li-ion batteries, *Energy Storage Mater.*, 2019, **20**, 208–215.

14 Ion Transport

As the primary requirement that differentiates electrolytes from non-electrolytes, ion transport has received the most thorough investigation since the earliest days of electrolyte science. In fact, it was the high sensitivity of ion transport to ion numbers (*i.e.* ion conductivity being measurable even in extremely dilute electrolytes) that initiated the classical studies on electrolytes conducted by Arrhenius, Ostwald and Kohlrausch.

In Chapter 5, we discussed the general ion transport phenomena and the foundational scientific interpretations. We learned that, in order to describe accurately how well an electrolyte functions in an electrochemical device, be it fuel cell, battery, electrochemical double-layer capacitor or electrolyzer, one needs to know the “triad” of transport properties: ion diffusion coefficient (D_i), ion conductivity (σ_i) and the associated ion transport numbers (t_+ or t_-). Among the three, the accurate determination of ion conductivity is the most mature and least controversial. Ion conductivity accurately reflects the overall contributions from all mobile ionic species in the electrolyte to its capability of carrying current, and has been widely adopted in all electrolyte investigations. On the other hand, the accurate determination of the ion diffusion coefficient, sometimes referred to as the “self-diffusion coefficient” of ions, has become easy and widely available owing to the advances in nuclear magnetic resonance (NMR) techniques made in recent decades, although its application is inevitably restricted to those ions or molecules that contain at least one kind of NMR-active nuclei.

In contrast, the ion transport number proves to be the most challenging quantity among the three to determine. The complications

arising from ion transport numbers can be witnessed not only from the fact that a generally applicable technique for its accurate determination has not been developed, but also from the lack of consensus even on its definition in the highly concentrated regimes such as ionic liquids or super-concentrated electrolytes.

In this chapter, we will explore these transport properties in more depth from two different perspectives: phenomenological and mechanistic. The former treats an electrolyte like a “black box”, focusing on the overall performance of the electrolytes in practical scenarios while paying little attention to understanding how the ions behave at atomic and molecular levels. The latter attempts to shed light on how the ions and solvent molecules interact with each other when attractions and repulsions among them can no longer be ignored as we did in Chapter 5, since these interactions are inevitable in electrolytes with practical salt concentrations. In fact, even in dilute electrolytes, we have seen that the Coulombic interactions among ions cannot be completely ignored, and the movements of cations and anions are coupled in an ambipolar manner [Section 5.2.6.4, eqn (5.169) or (5.172)].

We will analyze the complicated nature of ion transport in electrolytes at salt concentrations in the range of practical interest, such as lithium-ion batteries, and also the concentrated and super-concentrated regimes of interest to emerging battery chemistries, and reveal that, in those practical electrolytes, the seemingly simple ion transport phenomena actually involve complications that still cannot be accurately described or determined as of today.

14.1 Phenomenological Understanding: Ion Conductivity

In Section 5.2.2.1, we defined ion conductivity as the flux of all charges that pass through a unit area in unit time when responding to an externally applied electric field that is of unit strength:

$$\sigma = \frac{1}{X} j \quad (5.51)$$

When considering an electrochemical cell of area A and inter-electrode distance Δx under a DC (direct current) polarization with a potential difference $\Delta\psi$, the ion conductivity, which is essentially the inverse of resistivity, can be written in the familiar form of Ohm's law:

$$\sigma = \frac{\Delta x}{\Delta\psi} \frac{I}{A} \quad (5.54)$$

$$\sigma = \frac{1}{R} \frac{\Delta x}{A} \quad (5.58)$$

These equations appear to be very straightforward, and may often mislead one to believe that ion conductivity could be measured under DC conditions.

However, unlike metallic conductors, where electrons are often the only charge carriers with unlimited numbers available and negligible associations with their parental cations (*i.e.* the metallic atoms that lose these electrons to the conduction bands), ion conduction is much more complicated. The numbers of ions are limited in the electrolytes, there are strong interactions among the ions themselves or between them and the solvent molecules through the Coulombic fields, and each ion could behave differently at the electrolyte/electrode interfaces.

Now, let us consider a simple electrolyte system consisting of one cation and one anion sandwiched between a pair of electrodes with area A and inter-electrode distance Δx . At time $t = 0$, an external electric field $\Delta\psi$ is applied. Usually this applied potential $\Delta\psi$ is chosen to be large enough to induce ion migration but small enough not to induce undesired charge transfers at the electrolyte/electrode interfaces. In other words, the applied $\Delta\psi$ ensures all actions are within the electrochemical stability window of the electrolyte, and no substantial electrolyte decompositions should occur at these interfaces. Almost instantaneously upon application of an external electric field, these actions and anions start to move in opposite directions, accumulating and depleting both cations and anions in different interfacial regions, in addition to creating charge separation within the bulk electrode (Figure 14.1).

What happens next depends critically on the nature of the electrodes or, more precisely, it depends on how the electrolyte and electrode interact.

In most experiments, the electrodes are “inert” by nature, that is, there is no chemical reaction between the electrolyte components (cation, anion and solvents) and the electrode itself. In this case, these electrodes are called “blocking electrodes”, and the cations and anions in the electrolyte cannot do anything once they arrive at the electrolyte/electrode interfaces apart from accumulating at the anode and cathode surfaces, respectively (left panel of Figure 14.1). This is in fact an electrochemical double-layer capacitor that we discussed in Section 9.1.2.

The corresponding current response during the charging of this electrochemical double-layer capacitor takes the typical form of a

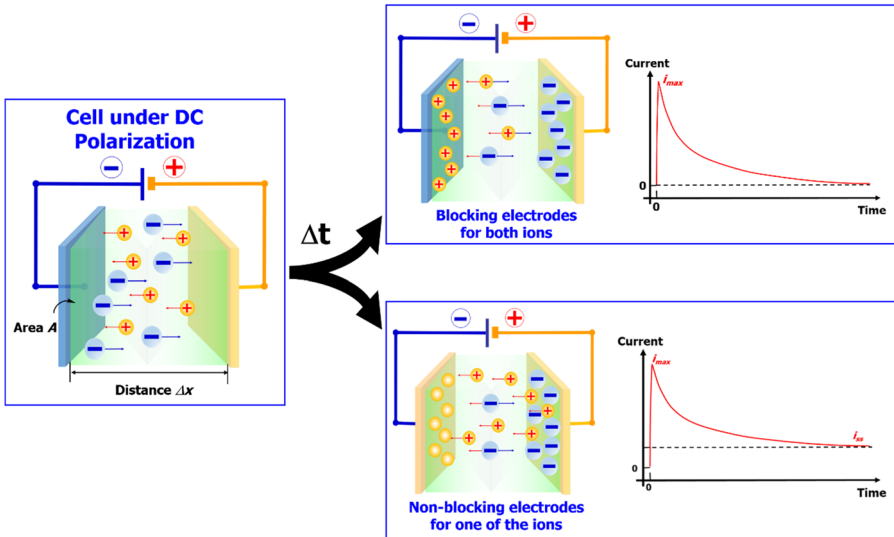


Figure 14.1 When an electrochemical cell is under DC polarization, the ions start to move in response to the applied electric field instantaneously, and the ion transport behavior after the initial transient response depends on the nature of the electrodes. Two different scenarios are displayed here: (top right panel) the electrodes are blocking to both ions, hence the electrochemical cell behaves like an electrochemical double-layer capacitor; (bottom right panel) the electrodes are non-blocking to one of the ions, where a steady-state current would be attained based on the ion that experiences charge transfer.

capacitive behavior (top right panel of Figure 14.1). The time needed for the cell current to approach the peak (i_{max}) is usually on the scale of micro- to milliseconds ($10^{-6}\text{--}10^{-3}$ s) or less, while the entire decay process approaches zero on the scale of seconds or longer, both of which are functions of ion conductivity, the true surface area of the electrodes, the specific capacitance of the electrodes and the Coulombic attractions and repulsions among the ionic species as described by eqn (5.169) if no other interionic interaction is considered.

When the cell current becomes zero, the cations and anions remaining in the bulk electrolyte would not contribute any net movement despite the applied cell potential $\Delta\psi$, because the driving force from the internal electric field established by the charge separation and the concentration gradient of both cations and anions exactly counterbalances any migration induced by the externally applied electric field $\Delta\psi$. We call this equilibrium the “*steady state*”.

Apparently, it is difficult to resolve the intrinsic resistance of the electrolytes sandwiched in such electrochemical cells as the current response changes so rapidly and depends on so many factors.

Another scenario, also frequently encountered in real-life situations, is an electrochemical cell with electrodes that are non-blocking to *one of the ions*. A typical example is a symmetrical cell consisting of a pair of lithium metal electrodes that are immersed in a Li⁺-containing electrolyte. In this cell, both electrodes are non-blocking to Li⁺ but blocking to whatever anion is in the electrolyte. Upon application of an external electric field, both ions move instantaneously, in similar manner to the blocking electrode scenario. However, very soon the anions cease to have any net movement, because of the concentration gradient established by the accumulation and depletion of anions at the other end of the bulk electrolyte. On the other hand, however, the cation (Li⁺) does not cause either accumulation or depletion at either electrode, because the DC polarization $\Delta\psi$ applied to the cell generates Li⁺ at the positive electrode and consumes Li⁺ at the negative electrode by depositing Li⁰ on the lithium electrode surface.

At the positive electrode:



At the negative electrode:



Hence the evolution of the overall cell current would be represented schematically by the bottom right panel of Figure 14.1, in which the initial current peak contains the contributions from the movement of both cations and anions, but with time elapsing, when the cell reaches the steady state the cell current (i^{ss}) would become overwhelmingly carried by the movement of Li⁺.

This second scenario is often known as a “*semi-blocking condition*”, or specifically when we discuss cells such as lithium-metal or lithium-ion batteries, “*anion-blocking condition*”. It is an important scenario that we will return to when conducting a more thorough examination in the following sections.

Again, the intrinsic ion conductivity of the bulk electrolyte cannot be directly resolved from such an experiment, although the steady-state current could be a very useful quantity *if everything is in an ideal state*. In fact, such a quantity was leveraged by Bruce and Vincent when

they attempted to develop a methodology to determine Li⁺ transport number, which is discussed in more detail in Sections 14.2.4 and 14.3. However, the assumption that “*if everything is in the ideal state*” is critically important here, and it does not hold true in most practical electrolyte systems.

Of course, there are many other scenarios that could introduce even more complications, such as only one of the electrodes being made non-blocking to the ions (a typical example of which is a hybrid battery–capacitor), or both electrodes being made non-blocking to one of the ions but at very different potentials (a typical example of which is the lithium-ion battery, both of whose electrodes can accommodate Li⁺ *via* intercalation), or electrodes being made non-blocking to both ions (typical examples of which include a hydrogen fuel cell or a dual-ion intercalation battery consisting of electrodes that intercalate cations and anions at different potentials). We do not intend to cover all of these scenarios here, but it is clear that these complications do not help to resolve the intrinsic ion conductivity of the bulk electrolytes.

Therefore, despite the simple and straightforward looks of eqn (5.54) and (5.58), the measurement of ion conductivity is by no means simple and straightforward. It is very difficult to carry out under DC field polarization.

14.1.1 Why AC (Alternating Current) Techniques?

The ultimate difficulty with DC techniques originates from the ion accumulation and depletion, which induce counter-migrations and interionic couplings *via* the building of an internal resisting field as well as the concentration gradient. Such accumulation and depletion are inevitable under DC conditions because all of the ions *persistent*ly move in one direction driven by the applied DC field.

To circumvent such accumulation and depletion, a simple approach is to change frequently the direction of the field applied, so that the ions do not have a consistent direction to follow. This is the basic logic underlying AC techniques, in which the ions would oscillate in response to the applied AC field, which keeps switching its direction at a certain frequency. Therefore, provided that the frequency adopted is faster than that which the ion translational movement could keep pace with, these ions would never be able to build up accumulations or depletions in any local regions of the bulk electrolyte (Figure 14.2).

Among the various AC techniques, *AC impedance spectroscopy*, or *electrochemical impedance spectroscopy* (EIS) as it is often referred to in the literature, provides a very easy and precise tool for the accurate

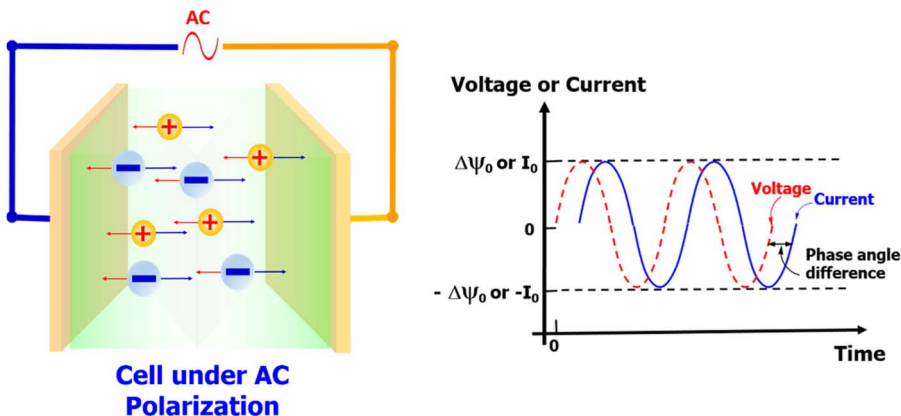


Figure 14.2 The application of an alternating electric field could circumvent the buildup of ion accumulation and depletion, so that the ion concentration throughout the bulk electrolyte maintains the original state, and the intrinsic resistance (or conductance) of the electrolyte could be resolved *via* mathematical analysis. Here a blocking electrode cell is shown, although in experiments the electrodes could be made non-blocking to one of the ions or to both ions.

determination of ion conductivity, and has been adopted as the standard protocol for almost all electrolyte studies.^{1,2} In this technique, an AC field of amplitude $\Delta\psi_0$ is applied as a sinusoidal function of time t , which can be expressed in a complex plane by

$$V(t) = \Delta\psi_0[\cos(\omega t) + i \sin(\omega t)] \quad (14.3)$$

where ω is the angular frequency, related to the frequency of the AC field f by

$$\omega = 2\pi f \quad (14.4)$$

and i is the imaginary unit by its universal definition:

$$i = \sqrt{-1} \quad (14.5)$$

The applied AC potential normally has a rather small amplitude, often in the range from a few millivolts to tens of millivolts (10^{-3} – 10^{-4} V), so that the electrochemical stability window of the electrolyte is observed, and no undesired reactions would be induced. The AC

current in response to the AC potential also takes a sinusoidal form but with some delays due to the time needed for the ions to respond to the applied field (Figure 14.2, right). The ratio of the applied potential to the current should generate a quantity that is similar in nature to the resistance in Ohm's law for a DC field:

$$Z = \frac{V(t)}{I(t)} \quad (14.6)$$

We name this resistance-analogous quantity *impedance*. Since both potential and current are complex quantities with a real and an imaginary part, the impedance Z should also be a complex quantity that can be expressed as a vector in a complex plane:

$$Z = Z_{\text{real}} - iZ_{\text{imag}} \quad (14.7)$$

where the projections of Z on the x - and y -axes are its real and imaginary components, respectively (Figure 14.3). For simplicity, in the literature Z_{real} and Z_{imag} are also often written as Z' and Z'' , respectively.

The real *versus* imaginary component plot as shown in Figure 14.3 is called a *Cole–Cole plot* in AC impedance spectra. Sometimes a misnomer, *Nyquist plot*, is also used. We will soon find how useful such plots are.

In most AC impedance spectra, the frequency (f and ω) of the applied AC field is varied in a certain range, typically between 10^{-3} and 10^6 Hz (but it could be as wide as 10^{-4} – 10^9 Hz for special purposes), so that a series of impedances could be generated as a function of frequency. This series of data constitute the impedance spectra, which contain

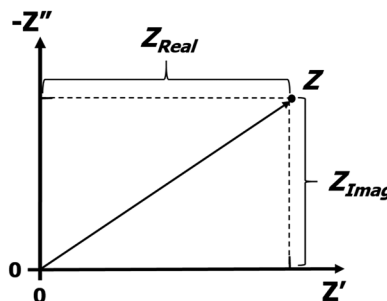


Figure 14.3 An impedance value Z can be expressed as a vector in the complex plane, whose projections on the x - and y -axes are its real and imaginary components, respectively.

the target value that we want to determine, *i.e.* the intrinsic resistance (or conductance) of the electrolyte. To solve for this resistance *via* the complicated spectra, we need to perform rigorous mathematical analysis on how the impedance changes with the frequency of the applied AC field.

14.1.1.1 Equivalent Circuits

Before we venture into the mathematical details of resolving the intrinsic resistance of the electrolyte from AC impedance spectra, we will first try to simplify the electrochemical cell structures into a few elemental components that are easier to be treated mathematically.

We should start with the simplest scenario shown in Figure 14.1, where the electrodes are *blocking to both ions*. We have said earlier that this is in fact an electrochemical double-layer capacitor, but a closer look allows us to dissect it further into a few more elemental components.

First, let us assume that the *intrinsic resistance of the bulk electrolyte* is R_B , which is what we want to measure and can be represented by a *pure resistor* (Figure 14.4, left).

Then, at the two separate electrolyte/electrode interfaces, there are corresponding *double-layer capacitances* that can be represented by two *pure capacitors*. If the two electrodes are identical (as in the case of symmetrical cells), then these two double-layer capacitors on the left and right sides of the cell should also be identical, which can be merged into a single component represented by C_{DL} . The resistor R_B and the capacitors C_{DL} should be connected *in series*, because an ion traveling in the electrolyte cannot pass these two electrolyte/electrode interfaces.

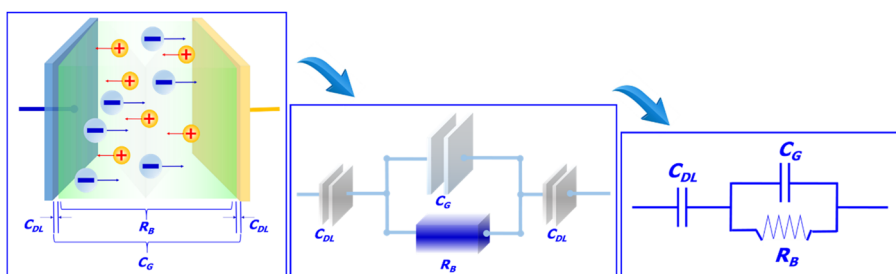


Figure 14.4 Simplifying an electrochemical cell with electrodes blocking to all ions into equivalent circuits.

Finally, one component that could often escape our attention is the *geometric capacitance* between the two electrodes, which can be represented by another pure capacitor C_G . Differing from these two C_{DL} , this capacitor should be connected with the resistor R_B *in parallel*, because an ion traveling in the electrolyte can easily pass this capacitor by overcoming the resistance of the electrolyte.

Summarizing all these considerations, one should easily obtain an *equivalent circuit* for the electrochemical cell consisting of blocking electrodes (Figure 14.4, middle). Again, since the two double-layer capacitors are identical in a symmetrical cell, such an equivalent circuit could be further simplified into what is shown on the right in Figure 14.4, which is often encountered in the literature.

Now let us turn our attention to the electrochemical cell consisting of electrodes that are *non-blocking to at least one of the ions*, which is the second scenario shown in Figure 14.1.

The intrinsic resistance of the bulk electrolyte R_B is still connected *in series* with the two separate double-layer capacitors C_{DL} . However, now the electrodes are no longer blocking to the ions, hence an ion traveling in the electrolyte could pass these double-layer capacitors at the interface. We know that when the ion crosses the interfaces, charge transfer occurs (Chapter 6), for which the ion should experience a certain resistance, which, therefore, can be represented by another *pure resistor*, R_{CT} . In other words, the two separate double-layer capacitors C_{DL} should be connected *in parallel* with the charge-transfer resistor R_{CT} .

Putting these considerations together, one obtains the equivalent circuit for an electrochemical cell consisting of non-blocking electrodes (Figure 14.5, middle). Again, if the two double-layer capacitors and the two separate charge-transfer resistors are identical, they should be merged into a single component, respectively, and such an equivalent circuit takes the form often encountered in the literature (Figure 14.5, right).

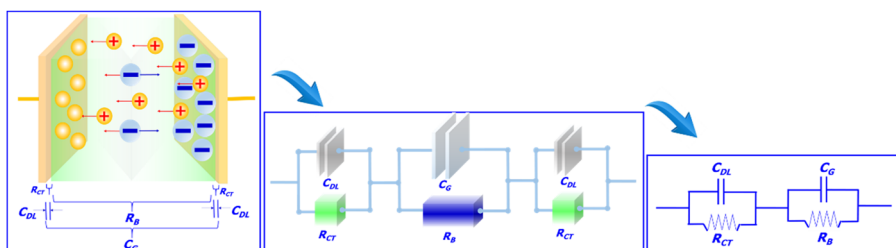


Figure 14.5 Simplifying an electrochemical cell with electrodes non-blocking to at least one of the ions into equivalent circuits.

However, it should always be kept in mind that, if the cell is asymmetric, such as a lithium-ion battery consisting of an anode at low potential and a cathode at high potential, the double-layer capacitors and the charge-transfer resistors at the two electrode/electrolyte interfaces are not identical. Although one could still use an equivalent circuit shown on the right in Figures 14.4 and 14.5, the double-layer capacitance and the charge-transfer resistance should reflect the average values of these capacitors and resistors at each electrode.

Finally, an aspect that is often ignored by researchers using these equivalent circuits is the interphases, the presence of which on electrodes is not recognized in these equivalent circuits. Understandably, ions traveling across the interphases must also experience extra resistances, which should be represented by an independent component R_{SEI} that is again connected in parallel to the double-layer capacitors C_{DL} but in series with the charge-transfer resistor R_{CT} . In some literature, such interphasial resistance is considered as part of the charge-transfer process, hence R_{CT} in this case represents the overall contributions from the ion migration across the interphases and its reaction after crossing interphases. However, one should always remember that ion movement across interphases and its subsequent charge transfer are two processes distinct not only in chemical nature but also in kinetics and the time scale on which they respond to the applied AC field.

In the modern literature on battery research, the definition of R_{CT} has been extended to almost any process at the interface/interphase. For example, in the case of lithium-metal deposition, R_{CT} could be the overall resistances encountered by a Li^+ when crossing the interphase, or receiving the electron from the electrode, or nucleating on the electrode surface into depositions.

The equivalent circuits shown in Figures 14.4 and 14.5 represent the two most typical scenarios that researchers often encounter in laboratory cells. In electrochemical devices such as lithium-ion batteries consisting of various chemistries, the real-life equivalent circuits could be much more complicated, but they can usually be broken down into basic equivalent circuits similar to the two shown in Figures 14.4 and 14.5.

14.1.1.2 Elements in AC Impedance Spectra: Resistor, Capacitor, Inductor, Constant-phase Element and Warburg Element

In these equivalent circuits, there are two basic elements, resistor R and capacitor C , hence such circuits are sometimes called “*RC networks*” in electronics.

Now let us perform analysis on the simplest element, a pure resistor R , and derive what its impedance should be when an AC field described by eqn (14.3) is applied on it. There is no doubt that this resistor follows Ohm's law all the time despite how the applied AC field varies with time, therefore the current response would be described by

$$I(t) = \frac{V(t)}{R} = \frac{\Delta\psi_0}{R} [\cos(\omega t) + i \sin(\omega t)] = I_0 [\cos(\omega t) + i \sin(\omega t)] \quad (14.8)$$

where I_0 is the current response when the AC field reaches its maximum value at $\Delta\psi_0$.

Apparently, the current is also a sinusoidal function with time, and it is completely synchronized with the applied AC potential, *i.e.* the phase angle difference as marked on the right in Figure 14.2 is zero. The corresponding impedance Z_R , as defined in eqn (14.6), should be

$$Z_R = \frac{V(t)}{I(t)} = \frac{\Delta\psi_0}{I_0} = R \quad (14.9)$$

This impedance Z_R has only a real part. In other words (although it might sound slightly redundant), *the impedance of a pure resistor is just its resistance*.

Then, how about a pure capacitor?

We have learned in Section 9.1.2 [eqn (9.12), (9.20) and (9.23)] that, when a potential difference ΔV is applied on the capacitor, the accumulation or dissipation of the charge on the capacitor is described by

$$Q = C \times \Delta V \quad (14.10)$$

where C is the specific capacitance of the capacitor.

The same principle applies when the applied field is AC instead of DC, and the corresponding charge accumulated or dissipated would also become a function of time:

$$Q(t) = C \times V(t) \quad (14.11)$$

Inserting the expression for $V(t)$ from eqn (14.3), we obtain

$$Q(t) = C \Delta\psi_0 [\cos(\omega t) + i \sin(\omega t)] \quad (14.12)$$

The current response of such capacitor is by definition the change of charge amount in unit time:

$$I(t) = \frac{dQ(t)}{dt} = \frac{d(C\Delta\psi_0 [\cos(\omega t) + i \sin(\omega t)])}{dt} = C\Delta\psi_0 \frac{d[\cos(\omega t) + i \sin(\omega t)]}{dt} \quad (14.13)$$

Applying the known trigonometric relations

$$\frac{d \cos(\omega t)}{dt} = -\omega \sin(\omega t) \quad (14.14)$$

$$\frac{d \sin(\omega t)}{dt} = \omega \cos(\omega t) \quad (14.15)$$

We transform eqn (14.13) into

$$I(t) = \omega C \Delta \psi_0 [-\sin(\omega t) + i \cos(\omega t)] \quad (14.16)$$

and the impedance associated with this pure capacitor Z_C is

$$Z_C = \frac{V(t)}{I(t)} = \frac{[\cos(\omega t) + i \sin(\omega t)]}{\omega C \Delta \psi_0 [-\sin(\omega t) + i \cos(\omega t)]} \quad (14.17)$$

To simplify the denominator, we substitute one of its terms with

$$-\sin(\omega t) = i^2 \sin(\omega t) \quad (14.18)$$

Then eqn (14.13) turns into a more elegant and shorter form:

$$Z_C = \frac{[\cos(\omega t) + i \sin(\omega t)]}{i \omega C \Delta \psi_0 [\cos(\omega t) + i \sin(\omega t)]} = \frac{1}{i \omega C} \quad (14.19)$$

Hence the impedance of a pure capacitor is simply $1/i\omega C$ or $-i/\omega C$.

It should be noted that the current response is no longer perfectly synchronized with the applied AC field. In other words, the phase angle difference is no longer zero. We can rewrite eqn (14.12) into the following form by applying basic conversion between trigonometric relations:

$$I(t) = \omega C \Delta \psi_0 \left[\cos\left(\omega t - \frac{\pi}{2}\right) + i \sin\left(\omega t - \frac{\pi}{2}\right) \right] \quad (14.20)$$

which reveals that the current leads the applied AC potential by 90° . However, if it might be thought that, since current is the result of the applied potential, it would be weird to have an effect “leading” its cause, then we can rephrase it by saying that the current lags behind the applied AC potential by 270° . Either way, the phase angle difference between $V(t)$ and $I(t)$ is 90° .

These two elements, pure resistor and pure capacitor, constitute the most frequently used components used by researchers to construct equivalent circuits. In addition to these, there are two other elemental components that need to be used occasionally, because the complicated AC impedance spectra encountered in real-life electrochemical cells often cannot be well accounted for by these pure components.

One such element is *inductance*, represented by L , whose impedance Z_L will be

$$Z_L = \frac{i}{\omega L} \quad (14.21)$$

which reflects the tendency of a component to oppose the change in the electric current flowing through it. Such resistance is a consequence of the electromagnetic disturbance created by the fluctuations in the current flow. The inductance often arises from the wires and cables constituting the circuits, and its presence is often responsible for the negative reading in imaginary impedances and the loops in the complex plane.

The other elementary component is the *constant-phase element* (cpe), which can be considered a hybrid between a resistor and a capacitor, or often referred to as a “leaky capacitor”, the impedance Z_{cpe} of which is expressed as

$$Z_{\text{cpe}} = k(i\omega)^{-p} \quad (14.22)$$

where k is a constant and p is a real number between 0 and 1.0. Inserting eqn (11.5) into eqn (11.22) to substitute the imaginary unit i , we can rewrite it as

$$Z_{\text{cpe}} = \frac{k}{(\omega)^p} (-1)^{\frac{p}{2}} \quad (14.23)$$

To further simplify the expression for Z_{cpe} into a typical complex quantity, we need to perform a trick by invoking *Euler's formula*:

$$e^{ix} = \cos(x) + i \sin(x) \quad (14.24)$$

which indicates that when $x = \pi$,

$$e^{ix} = \cos(\pi) + i \sin(\pi) = -1 \quad (14.25)$$

Substituting the term -1 in eqn (14.23) with eqn (14.25), we obtain

$$Z_{\text{cpe}} = \frac{k}{(\omega)^p} \left[e^{i\pi} \right]^{-\frac{p}{2}} = \frac{k}{(\omega)^p} e^{\left(-\frac{p\pi}{2} \right)} \quad (14.26)$$

Applying Euler's formula eqn (14.24) one more time to rewrite the exponential term, we obtain

$$Z_{\text{cpe}} = \frac{k}{(\omega)^p} \left[\cos\left(-\frac{p\pi}{2}\right) + i \sin\left(-\frac{p\pi}{2}\right) \right] = \frac{k}{(\omega)^p} \left[\cos\left(-\frac{p\pi}{2}\right) - i \sin\left(\frac{p\pi}{2}\right) \right] \quad (14.27)$$

Now eqn (14.27) expresses the impedance of the cpe in a typical complex number form consisting of a real component and an imaginary component, which allows us to evaluate how a cpe behaves with different values of p .

If $p = 0$:

$$Z_{\text{cpe}} = k[\cos(0) - i \sin(0)] = k \quad (14.28)$$

Because k is a constant independent of the frequency, the cpe behaves like a pure resistor, the resistance R_{cpe} of which is simply k .

If $p = 1.0$:

$$Z_{\text{cpe}} = \frac{k}{\omega} \left[\cos\left(\frac{\pi}{2}\right) - i \sin\left(\frac{\pi}{2}\right) \right] = -\frac{ki}{\omega} \quad (14.29)$$

The similarity between eqn (14.29) and eqn (14.19) implies that the cpe now behaves like a capacitor, the capacitance C_{cpe} of which based on comparison between these two equations should be $1/k$.

In cases when p resides between 0 and 1.0, the cpe should behave like a hybrid of a pure resistor and a pure capacitor. For example, if $p = 0.5$:

$$Z_{\text{cpe}} = \frac{k}{\sqrt{\omega}} \left[\cos\left(\frac{\pi}{4}\right) - i \sin\left(\frac{\pi}{4}\right) \right] = \frac{k(1-i)}{\sqrt{2\omega}} \quad (14.30)$$

In fact, $p = 0.5$ represents a special case of the cpe known as a “*Warburg element*” or “*Warburg diffusion element*”, which is a straight line that intersects the real axis at a constant angle of 45° . It is unique among cpes because both real and imaginary components are equal at all frequencies and both depend upon $\omega^{-\frac{1}{2}}$. It is often used to describe the semi-infinite linear diffusion at low frequencies.

With the impedances for these four elemental components expressed mathematically, we can now proceed to construct equivalent circuits.

14.1.1.3 Connecting AC Impedance Elements into Circuits

Equipped with these elements, we can now start thinking of constructing equivalent circuits as shown in Figures 14.4 and 14.5.

When one connects these elements either in series or in parallel to construct a circuit, their impedances follow the same rules that pure resistors follow, *i.e.* although the natures of the elements involved are resistors, capacitors, inductors or constant-phase elements, the total impedance Z_{Total} for elements in series is given by

$$Z_{\text{Total}} = \sum_{i=1}^n Z_i \quad (14.31)$$

whereas for the elements in parallel the total impedance Z_{Total} follows the reciprocal summation rule:

$$\frac{1}{Z_{\text{Total}}} = \sum_{i=1}^n \frac{1}{Z_i} \quad (14.32)$$

14.1.1.3.1 R-C in Series

Now, let us first connect a resistor and a capacitor *in series* (inset in Figure 14.6a). Its total impedance should be given by eqn (14.31), *i.e.* adding together the impedance of a pure resistor Z_R as expressed by eqn (14.9) and the impedance of a pure capacitor Z_C as expressed by eqn (14.19):

$$Z_{\text{Total}} = Z_R + Z_C = R - \frac{i}{\omega C} \quad (14.33)$$

This already takes the typical form of a complex quantity as expressed in eqn (14.7), with the real and imaginary components being expressed as, respectively

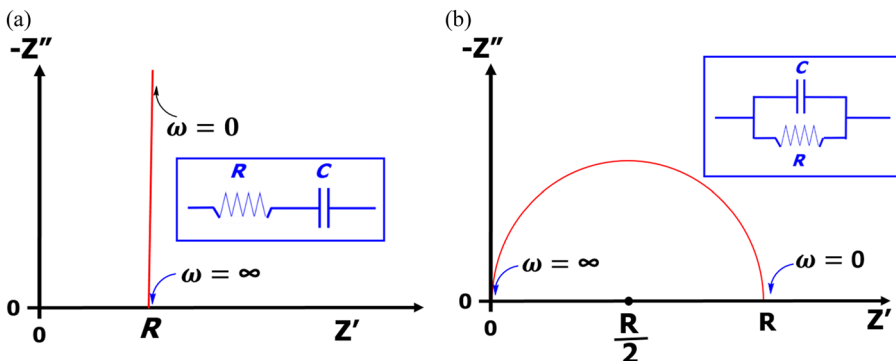


Figure 14.6 The two basic connections of RC elements: (a) a resistor and a capacitor are connected *in series*, where the real part is a constant at R independent of the frequency of the AC field applied, while the imaginary part varies with the frequency; (b) a resistor and a capacitor are connected *in parallel*, where both the real and imaginary parts vary with the frequency but obey an equation of a semi-circle.

$$Z' = Z_R = R \quad (14.34)$$

$$Z'' = Z_C = \frac{i}{\omega C} \quad (14.35)$$

In other words, Z' is the resistance R and Z'' is the impedance contributed by the capacitor. At infinite frequency ($\omega = \infty$) the imaginary component ($Z'' = i/\omega C$) vanishes, while at near-zero frequency ($\omega = 0$) the imaginary component approaches infinity. If one plots all the total impedance values that are measured at all frequencies in the complex plane, the resultant spectra would simply look like a vertical line that intersects the real axis at the location R (Figure 14.6a).

14.1.1.3.2 R - C in Parallel

Next, let us try to connect a resistor and a capacitor *in parallel* (inset in Figure 14.6b). Its total impedance should be given by eqn (14.34), *i.e.* its reciprocal is the summation of the reciprocal of a pure resistor Z_R as expressed by eqn (14.9) and the reciprocal of the impedance of a pure capacitor Z_C as expressed by eqn (14.19):

$$\frac{1}{Z_{\text{Total}}} = \frac{1}{R} - \frac{\omega C}{i} = \frac{1}{R} + i\omega C = \frac{1 + i\omega CR}{R} \quad (14.36)$$

Hence the total impedance of this parallel circuit is given by

$$Z_{\text{Total}} = \frac{R}{1 + i\omega CR} \quad (14.37)$$

Because Z_{Total} as expressed by eqn (14.37) does not take the typical complex quantity form defined by eqn (14.7), we need to simplify it by eliminating the imaginary unit i from the denominator. This can be done by multiplying the denominator with its conjugate quantity, *i.e.* $(1 - i\omega CR)$, and remembering that $i^2 = -1$, which leads to

$$Z_{\text{Total}} = \frac{R(1 - i\omega CR)}{1 + (\omega CR)^2} = \frac{R}{1 + (\omega CR)^2} - i \frac{\omega CR^2}{1 + (\omega CR)^2} \quad (14.38)$$

Now the total impedance of the parallel circuit takes the form we want, which consists of a real and an imaginary component given by, respectively

$$Z' = \frac{R}{1 + (\omega CR)^2} \quad (14.39)$$

$$Z'' = \frac{\omega CR^2}{1 + (\omega CR)^2} \quad (14.40)$$

At infinite frequency ($\omega = \infty$), both the real component Z' and the imaginary component Z'' approach zero. However, at near-zero frequency ($\omega = 0$), the imaginary component is still zero, while the real component becomes R .

What would Z' and Z'' be when the frequency is at intermediate values between zero and infinity? And what would the impedance spectra look like in the complex plane?

To answer these questions, let us first try to establish a relation between Z' and Z'' :

$$(Z')^2 + (Z'')^2 = \frac{R^2 + (\omega CR^2)^2}{[1 + (\omega CR)^2]^2} = R^2 \frac{1 + (\omega CR)^2}{[1 + (\omega CR)^2]^2} = R^2 \frac{1}{1 + (\omega CR)^2} \quad (14.41)$$

Inserting eqn (14.39) to replace the fraction term in eqn (14.41), we obtain

$$(Z')^2 + (Z'')^2 = RZ' \quad (14.42)$$

Rearranging the above equation and adding a term $R^2/4$ to both sides, eqn (14.42) turns into

$$(Z')^2 + (Z'')^2 - RZ' + \frac{R^2}{4} = \frac{R^2}{4} \quad (14.43)$$

or, in a more revealing form:

$$\left(Z' - \frac{R}{2} \right)^2 + (Z'')^2 = \frac{R^2}{4} \quad (14.44)$$

The significance of eqn (14.44) goes far beyond just an algebraic trick. In fact, it tells us that, in a complex plane, the relation between the real and imaginary components of the impedances corresponding to the equivalent circuit shown by the inset in Figure 14.6b obeys the equation of a *semi-circle*. Such a semi-circle would have a radius $R/2$ and be centered at the location $(R/2, 0)$, with the ends at the origin of the complex plane when the frequency approaches infinity and at $(R, 0)$ when the frequency approaches zero.

Now we can finally take on a real-life equivalent circuit.

14.1.1.3.3 Circuits with Blocking Electrodes

The simplest electrochemical cell in real life is the one with blocking electrodes (Figure 14.4), where the bulk resistance of the electrolyte (R_B , our ultimate goal in this whole section) is connected with the geometric capacitor C_G in series, while the double-layer capacitor is connected with this RC unit in parallel. Since both electrodes are blocking to both ions, there is *no* resistor connected in parallel with these double-layer capacitors, or alternatively one can say that the interfacial resistor in parallel with the capacitors has a resistance of infinity.

For the *parallel RC* unit consisting of R_B and C_G , the impedance Z_P should be given by eqn (14.38):

$$Z_P = \frac{R(1 - i\omega C_G R_B)}{1 + (\omega C_G R_B)^2} \quad (14.45)$$

while the impedance from the series contributor, *i.e.* the double-layer capacitor, should be given by eqn (14.19):

$$Z_S = \frac{1}{i\omega C_{DL}} = -\frac{i}{\omega C_{DL}} \quad (14.46)$$

The total impedance Z_{Total} is the summation of the two components Z_p and Z_s :

$$Z_{\text{Total}} = \frac{R(1-i\omega C_G R_B)}{1+(\omega C_G R_B)^2} - \frac{i}{\omega C_{\text{DL}}} \quad (14.47)$$

Rearranging this into the typical complex quantity expression, we obtain

$$Z_{\text{Total}} = \frac{R}{1+(\omega C_G R_B)^2} - i \frac{\left[1 + (\omega C_G R_B)^2 \left(1 + \frac{C_{\text{DL}}}{C_G} \right) \right]}{\omega C_{\text{DL}} \left[1 + (\omega C_G R_B)^2 \right]} \quad (14.48)$$

Despite the fact that this is the simplest circuit in real life, the expression of the impedance is already rather complicated. When plotted in a complex plane, the impedance consists of a semi-circle and a vertical line at its low-frequency end (solid lines in Figure 14.7), which meets one's intuitive expectation that it should look like the hybrid of the vertical line from $R-C$ in series (Figure 14.6a) and the semi-circle from $R-C$ in parallel (Figure 14.6b).

In such a plot, we can finally resolve the bulk resistance R_B of the electrolyte from the location where the semi-circle and the vertical line intersect with the real axis. If the cell geometry (electrode area

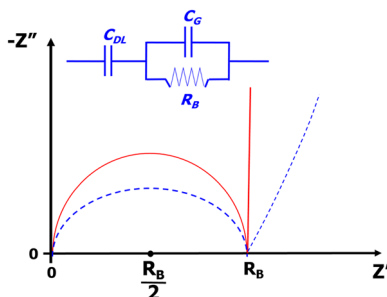


Figure 14.7 The impedance spectra generated by the simplest electrochemical cell, where both electrodes are blocking to all ions in the electrolyte. If the elementary components are pure resistors and capacitors, the impedance plot should consist of a semi-circle and a vertical line (solid lines), both of which intersect the real axis at R_B , giving us the ion conductivity of the electrolyte. However, real-life electrochemical cells always generate a depressed semi-circle and a tilted line (dashed lines).

A and inter-electrode distance Δx) is known, the conductivity of the electrolyte can be determined from eqn (5.58).

In fact, the impedance plot represented by the solid lines in Figure 14.7 is already very close to what we see in the literature. However, upon closer examination, we can still sense some difference. First, the semi-circles from the real-life electrochemical cells are always somehow “depressed” rather than being a perfect semi-circle; Second, the line contributed by the double-layer capacitance is never perfectly vertical, but instead is inclined and often slightly curved, as represented by the dashed lines in Figure 14.7.

We must find out what causes such departures from a vertical line and a perfect semi-circle, and how much it could affect the accuracy in determining R_B .

14.1.1.3.4 Correcting with Constant-phase Element

The above-mentioned departures were observed in the early days of impedance studies, and it was for the purpose of correcting such departures that the cpe concept was introduced. The impedance of a cpe is given by eqn (14.27):

$$Z_{\text{cpe}} = \frac{k}{(\omega)^p} \left[\cos\left(\frac{p\pi}{2}\right) - i \sin\left(\frac{p\pi}{2}\right) \right] \quad (14.27')$$

Now replacing the pure capacitor in the circuit of $R-C$ in series (inset of Figure 14.6a) with such a cpe, its expression then becomes

$$Z_{\text{cpe}} = \frac{R}{(\omega)^p} \left[\cos\left(\frac{p\pi}{2}\right) - i \sin\left(\frac{p\pi}{2}\right) \right] \quad (14.49)$$

while the total impedance becomes

$$Z_{\text{Total}} = Z_R + Z_{\text{cpe}} = R \left[1 + \frac{1}{(\omega)^p} \cos\left(\frac{p\pi}{2}\right) \right] - i \frac{R}{(\omega)^p} \sin\left(\frac{p\pi}{2}\right) \quad (14.50)$$

the real and imaginary components of which are, respectively

$$Z' = R \left[1 + \frac{1}{(\omega)^p} \cos\left(\frac{p\pi}{2}\right) \right] \quad (14.51)$$

$$Z'' = \frac{R}{(\omega)^p} \sin\left(\frac{p\pi}{2}\right) \quad (14.52)$$

Now the impedance should take the form of a straight line, whose projection on the real axis (*i.e.* Z') varies with frequency but would have a minimum of R when the frequency approaches infinity, where the impedance intersects with the real axis at an angle of $p\pi/2$ (Figure 14.8a).

The scenario of $R-C$ in parallel could be treated in a similar manner by replacing the pure capacitor with a cpe, so the total impedance is given as

$$\frac{1}{Z_{\text{Total}}} = \frac{1}{R} + \frac{1}{Z_{\text{cpe}}} = \frac{1}{R} + \frac{1}{\frac{R}{(\omega)^p} \left[\cos\left(\frac{p\pi}{2}\right) - i\sin\left(\frac{p\pi}{2}\right) \right]} \quad (14.53)$$

The simplification of eqn (14.53) into an obvious graphical representation like eqn (14.44) becomes rather complicated and lengthy, and is impossible to cover in this short section, therefore we will jump directly to the result. The cpe in the parallel connection rotates the semi-circle around the origin by an angle $p\pi/2$, hence depressing the semi-circle by a distance D (Figure 14.8b). Fortunately, despite this deformation from the ideal situation of a pure capacitor connected

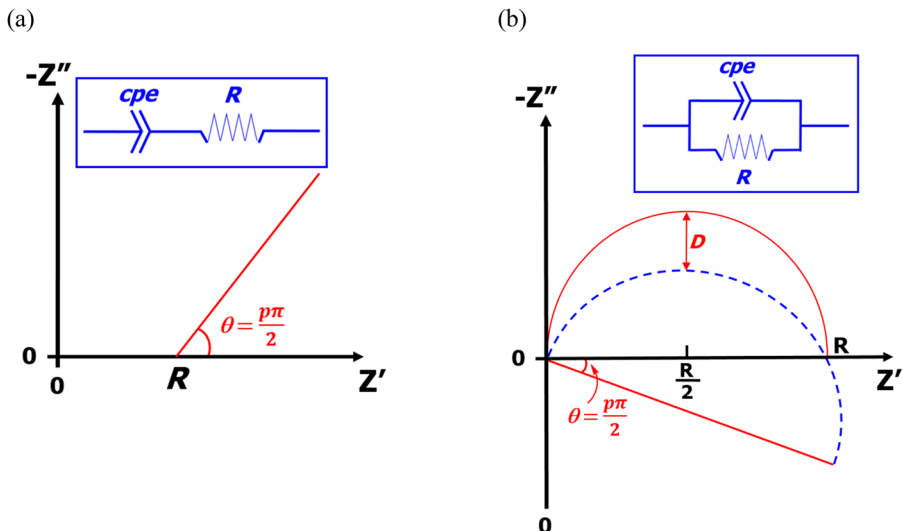


Figure 14.8 The correction brought by the cpe accounted for (a) the tilted line contributed from the “leaky capacitor” connected with a pure resistor in series and (b) the depressed semi-circle when the “leaky capacitor” is connected with a pure resistor in parallel.

with a pure resistor in parallel, the semi-circle would still intersect the real axis at R , hence the bulk resistance, or the ion conductivity, of the electrolyte could still be resolved from the AC impedance spectra using cells with blocking electrodes.

Therefore, the electrochemical cells with blocking electrodes as shown in Figure 14.4 have become the standard cell setup for determining ion conductivity.

14.1.1.3.5 Circuits with Non-blocking Electrodes

For practical electrochemical cells that involve charge transfer, such as a lithium–lithium symmetrical cell (where both electrodes are non-blocking to Li^+ but blocking to the anion), or a lithium-ion battery (where both electrodes are non-blocking to Li^+ but do so at very different potentials), or fuel cells and dual-ion intercalation batteries (where both electrodes are non-blocking to both cations and anions while doing so at very different potentials), the corresponding equivalent circuits must consider the inclusion of many more elements, the mathematical expressions for which become rather lengthy and complicated. Instead of delving into the details of resolving these complicated scenarios, we therefore refer interested readers to the extensive literature available on the topic, some of which is listed in Further Reading. The simplified treatment by Macdonald is especially recommended for those who wish to learn more about the solution of equivalent circuits with non-blocking electrodes.

However, before we conclude this section, we need to demonstrate what the impedance spectra of the simplest non-blocking circuit look like, because it is the most frequently encountered scenario in battery research. Consider a lithium–lithium symmetrical cell that contains an electrolyte that we assume is thermodynamically stable with lithium metal. Such an electrolyte does not exist in reality (at least as of 2022), but ether-based electrolytes could closely simulate such a situation.

As discussed in Section 14.1.1.1 (Figure 14.5), the equivalent circuit for such a cell should consist of two $R\text{-}C$ parallel units connected in series (Figure 14.9a), which correspond to the impedances arising from ion transport in the bulk electrolyte and the charge transfer at the electrolyte/electrode interfaces, respectively. Hence the total impedance of the circuit should be described as the summation of the impedances of these two $R\text{-}C$ parallel units Z_1 and Z_2 :

$$Z_{\text{Total}} = Z_1 + Z_2 \quad (14.54)$$

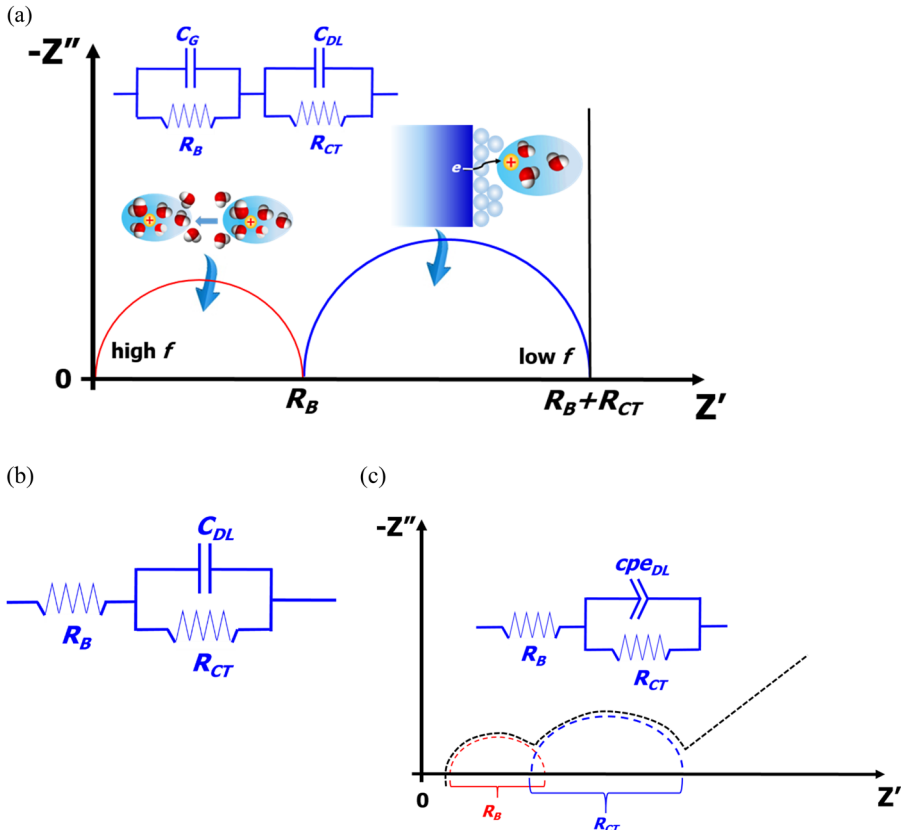


Figure 14.9 AC impedance spectra generated by an electrochemical cell with non-blocking electrodes to one of the ions. (a) The two semi-circles emerged should correspond to the two R - C parallel units that are induced by ion transport within the bulk electrolyte and charge transfer at the two electrolyte/electrode interfaces, respectively. (b) The simplified equivalent circuit often adopted to describe an electrochemical cell with non-blocking electrodes, where the cell geometric capacitance is neglected. (c) The real impedance spectra generated by such an electrochemical cell could be a lot less ideal looking, and deconvolution assisted by commercial software is necessary to solve for the bulk resistance.

For the first unit consisting of geometric capacitance C_G and electrolyte bulk resistance R_B , its impedance obeys the relation

$$\frac{1}{Z_1} = \frac{1}{Z_G} + \frac{1}{Z_B} = \frac{1}{R_B} + i\omega C_G \quad (14.55)$$

while for the second unit consisting of double-layer capacitance C_{DL} and charge-transfer resistance R_{CT} , a similar relation holds:

$$\frac{1}{Z_2} = \frac{1}{Z_{\text{DL}}} + \frac{1}{Z_{\text{CT}}} = \frac{1}{R_{\text{CT}}} + i\omega C_{\text{DL}} \quad (14.56)$$

The total impedance is then expressed as

$$Z_{\text{Total}} = \frac{1}{\frac{1}{R_{\text{B}}} + i\omega C_{\text{G}}} + \frac{1}{\frac{1}{R_{\text{CT}}} + i\omega C_{\text{DL}}} \quad (14.57)$$

In the literature, the geometric capacitance C_{G} can sometimes be neglected, which leads to the simplified version of the equivalent circuit shown in Figure 14.9b, and the expression of total impedance becomes

$$Z_{\text{Total}} = \frac{1}{R_{\text{B}}} + \frac{1}{\frac{1}{R_{\text{CT}}} + i\omega C_{\text{DL}}} = R_{\text{B}} + \frac{R_{\text{CT}}}{1 + i\omega C_{\text{DL}} R_{\text{CT}}} \quad (14.58)$$

Multiplying the conjugate quantity of the denominator $1 + i\omega C_{\text{DL}} R_{\text{CT}}$ transforms eqn (14.53) into

$$Z_{\text{Total}} = R_{\text{B}} + \frac{R_{\text{CT}} - iR_{\text{CT}}^2 \omega C_{\text{DL}}}{1 + [\omega C_{\text{DL}} R_{\text{CT}}]^2} = \left[R_{\text{B}} + \frac{R_{\text{CT}}}{1 + [\omega C_{\text{DL}} R_{\text{CT}}]^2} \right] - i \frac{R_{\text{CT}}^2 \omega C_{\text{DL}}}{1 + [\omega C_{\text{DL}} R_{\text{CT}}]^2} \quad (14.59)$$

the real and imaginary parts of which are, respectively

$$Z' = R_{\text{B}} + \frac{R_{\text{CT}}}{1 + [\omega C_{\text{DL}} R_{\text{CT}}]^2} \quad (14.60)$$

$$Z'' = \frac{R_{\text{CT}}^2 \omega C_{\text{DL}}}{1 + [\omega C_{\text{DL}} R_{\text{CT}}]^2} \quad (14.61)$$

From eqn (14.60), we obtain

$$[\omega C_{\text{DL}} R_{\text{CT}}]^2 = \frac{R_{\text{CT}}}{Z' - R_{\text{B}}} - 1 \quad (14.62)$$

where one could solve for the frequency ω :

$$\omega = \frac{1}{C_{\text{DL}} R_{\text{CT}}} \sqrt{\frac{R_{\text{CT}}}{Z' - R_{\text{B}}} - 1} \quad (14.63)$$

Inserting eqn (14.63) into the expression of the imaginary part, eqn (14.61):

$$\begin{aligned} Z'' &= \frac{R_{CT}^2 C_{DL} \times \frac{1}{C_{DL} R_{CT}} \sqrt{\frac{R_{CT}}{Z' - R_B} - 1}}{1 + [C_{DL} R_{CT}]^2 \left[\frac{1}{C_{DL} R_{CT}} \sqrt{\frac{R_{CT}}{Z' - R_B} - 1} \right]^2} = \frac{R_{CT} \sqrt{\frac{R_{CT}}{Z' - R_B} - 1}}{1 + \frac{R_{CT}}{Z' - R_B} - 1} \\ &= [Z' - R_B] \sqrt{\frac{R_{CT} - Z' + R_B}{Z' - R_B}} \end{aligned} \quad (14.64)$$

or

$$\begin{aligned} (Z'')^2 &= [Z' - R_B]^2 \frac{R_{CT} - Z' + R_B}{Z' - R_B} = [Z' - R_B][R_B + R_{CT} - Z'] \\ &= 2Z'R_B + Z'R_{CT} - (Z')^2 - (R_B)^2 - R_B R_{CT} \end{aligned} \quad (14.65)$$

Now eqn (14.65) takes the familiar form of a quadratic equation of two variables Z' and Z'' . We perform an algebra trick similar to that which we did before by rearranging it into

$$(Z'')^2 + (Z')^2 + (R_B)^2 - Z'R_{CT} - 2Z'R_B + R_B R_{CT} = 0 \quad (14.66)$$

followed by adding an identical term $(R_{CT}/2)^2$ to both sides of the equation, which turns it into

$$(Z'')^2 + (Z')^2 + (R_B)^2 - Z'R_{CT} - 2Z'R_B + R_B R_{CT} + \left(\frac{R_{CT}}{2}\right)^2 = \left(\frac{R_{CT}}{2}\right)^2 \quad (14.67)$$

Once again, eqn (14.67) can be compressed into an equation for a semi-circle:

$$\left[Z' - R_B - \frac{R_{CT}}{2} \right]^2 + (Z'')^2 = \left(\frac{R_{CT}}{2} \right)^2 \quad (14.68)$$

On a complex plane, eqn (14.68) represents a semi-circle with a diameter R_{CT} that intersects with the real axis at (R_B) and $(R_B + R_{CT})$ at the high- and low-frequency ends, respectively (Figure 14.9a).

Remember that before we perform these simple but lengthy algebraic operations, we have assumed that the geometric capacitance C_G can be neglected. The consequence of such simplification shrinks

the first semi-circle corresponding to the R_B-C_G parallel unit into a single point on the real axis at R_B , which would otherwise be represented by an independent semi-circle as described by eqn (14.44). In other words, the full graphical representation of the equivalent circuit as shown in Figure 14.9a should be two consecutive semi-circles that intersect with the real axis at $(0, R_B)$ and $(R_B, R_B + R_{CT})$, respectively. Naturally, the diameters of these two semi-circles are R_B and R_{CT} , respectively.

The semi-circle at higher frequency with a diameter of R_B arises from the R_B-C_G parallel unit and is often considered responsible for ion transport in the bulk electrolyte. This semi-circle intersects the real axis at R_B , and gives us the information for the ion conductivity in the bulk electrolyte.

The semi-circle at lower frequency with a diameter of R_{CT} arises from the $R_{CT}-C_{DL}$ parallel unit and is usually considered responsible for the charge transfer at an interface/interphase. In the ideal situation, the charge-transfer conductance ($G_{CT} = 1/R_{CT}$) quantifies the ion transport carried by the only ion that can cross the interfaces, and therefore the transport number of that ion could be calculated by

$$t_i = \frac{I_i}{\sum_i^n I_i} = \frac{R_B}{R_{CT}} \quad (14.69)$$

Hence the resistance corresponding to R_{CT} is always higher than R_B .

We will return later (Section 14.2.4) to discuss further the applicability and hidden assumptions of eqn (14.69).

In addition to the relative value in impedances, the semi-circle corresponding to the $R_{CT}-C_{DL}$ unit also occurs at much lower frequency than that corresponding to the R_B-C_G unit, because the speed of ion migration across the interfaces is always slower than that of ion movement across the bulk electrolyte, with very few exceptions.

However, the impedance spectra from real life electrochemical cells often depart significantly from the above ideal scenarios, where the two semi-circles are not only depressed but also shifted and merged, while the spike is not only tilted but also curved (Figure 14.9c). In particular, the non-aqueous electrolytes used in commercial lithium-ion batteries, the ion conductivities of which are around 10 mS cm^{-1} at room temperature, often display a severely depressed semi-circle corresponding to the R_B-C_G unit that almost shrinks into a single interception point on the real axis when compared with the semi-circle corresponding to the $R_{CT}-C_{DL}$ unit. This constitutes the basis for the

simplified version of the equivalent circuit shown in Figure 14.9b that we adopted to perform the mathematical analysis above.

These irregularities encountered in real life can be partially resolved by modifying the equivalent circuits with elements such as an inductor, cpe, Warburg diffusion element, *etc.* In commercially available impedance analyzers, various equivalent circuits are provided as part of the software, and one could always find a “perfect fit” of the experimental data provided that a proper equivalent circuit is selected (Figure 14.10). However, one must keep in mind that in such complicated scenarios, the interpretation of the graphical meanings associated with impedance already becomes rather ambiguous. Sometimes we cannot even confidently assign a certain semi-circle to any specific process, as the bulk and interfacial/interphasial processes tend to merge and overlap in similar frequency domains.

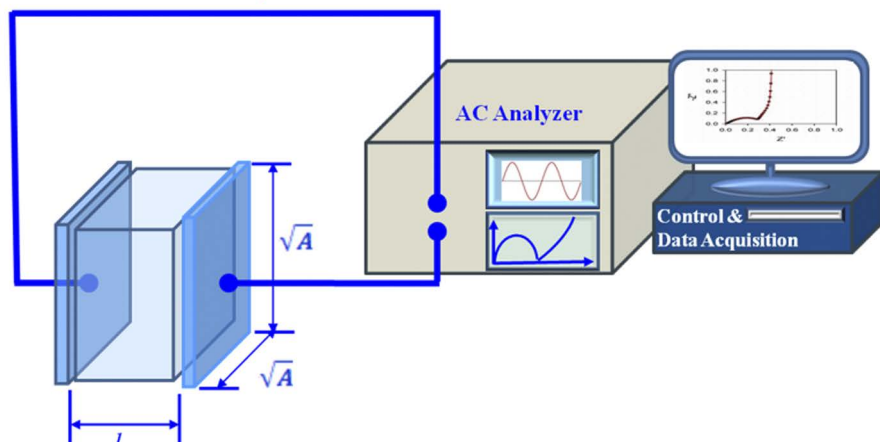
After all, AC impedance spectra are just a phenomenological tool that treats the electrolyte as a “black box” and cannot differentiate precisely what motion from which component causes a change in impedance behavior. To do that, we will need mechanistic analysis, which will be discussed in the latter half of this chapter.

14.1.2 Ion Conductivity for Practical Battery Electrolytes

Provided that caution is exercised against over-interpretation of data to derive contributing components such as bulk and interfacial/interphasial processes, AC impedance spectra still serve as a very mature, accurate and easy-to-access tool in determining ion conductivity. In particular, the blocking electrode cell setup shown in Figure 14.4 has been extensively used by the research community, generating highly accurate and reproducible ion conductivity data.

Leveraging such a tool and cell setup, Ding and co-workers carried out exhaustive efforts to map the ion conductivities of essentially all skeleton electrolyte formulations used in lithium-ion batteries using LiPF₆ salt and mixed carbonate solvents.^{3,4,5} Despite the fact that the work was completed nearly two decades ago, the data generated are still highly relevant, because the developments in electrolyte materials have been relatively static compared with the advances in electrode materials and interphasial chemistries. Such a situation changed only since the 2010s. Even after 2010, most of these skeleton electrolytes based on carbonate esters are still being used extensively today in industry, while persistent formula variations caused by the use of various additives did little to alter the ion transport behavior in bulk electrolytes.

$$I(t) = \frac{V(t)}{Z_{Total}} = \frac{\Delta\psi_0[\cos(\omega t) + i \sin\omega t]}{Z' - iZ''}$$



$$V(t) = \Delta\psi_0[\cos(\omega t) + i \sin\omega t]$$

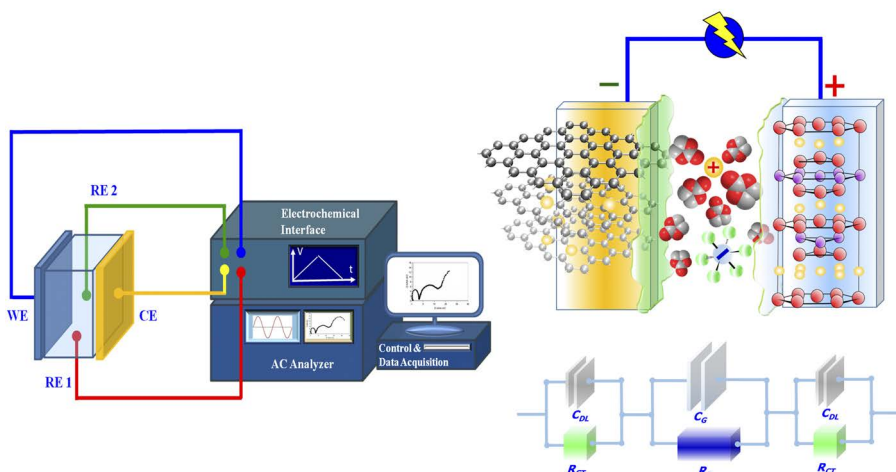


Figure 14.10 The powerful software accompanying the universal commercial impedance analyzers can always find a “perfect fit” to experimental data, no matter whether in blocking (top) or non-blocking (bottom) electrochemical cells, provided that a proper equivalent circuit is selected. However, one must remain cautious that AC impedance spectra as a phenomenological tool do not have the capability of differentiating the complicated components contributing to the spectra. Over-interpretation of data should be avoided, especially when analyzing a complicated systems such as a lithium-ion battery. The contributions from various components to the impedance are no longer discrete but coupled and merged.

In their exhaustive ion conductivity mapping, Ding and co-workers considered ion conductivity as a function of two variables, *i.e.* salt concentration (mol kg^{-1} of LiPF_6 , or its molality m) and solvent composition (x_{EC} as the molar fraction of EC in any binary electrolyte). For example, such an ion conductivity surface could be generated for the binary electrolyte LiPF_6 in EC-EMC at 30 °C as shown in Figure 14.11a.³

This process was then repeated at every temperature of interest to complete the final mapping, which, based on the close fit of the experimental data to a fourth-degree trivariate polynomial function, can be expressed in a polynomial equation with 33 terms:

$$\begin{aligned}\sigma(m, x, T) = & -3.37115 + 12.5608m - 7.89593m^2 + 3.51922m^3 - 1.1547m^4 + 18.1863x \\ & - 6.22756mx - 13.6916m^2x + 8.43904m^3x - 7.83732x^2 + 19.607mx^2 - 18.4529m^2x^2 \\ & - 30.6369x^3 + 29.2mx^3 - 0.04299187T + 0.180877mT - 0.0836202m^2T + 0.0230098m^3T \\ & + 0.195946Tx + 0.0676686mTx - 0.14134m^2Tx + 0.147429Tx^2 + 0.173059mTx^2 \\ & - 0.51634Tx^3 - 0.000223097T^2 + 0.000111233mT^2 + 0.000049528m^2T^2 \\ & + 0.000952777T^2x + 0.00117334mT^2x - 0.000619157T^2x^2 - 3.46897 \times 10^{-7}T^3 \\ & - 2.75041 \times 10^{-6}mT^3 - 5.57653 \times 10^{-6}T^3x\end{aligned}\quad (14.70)$$

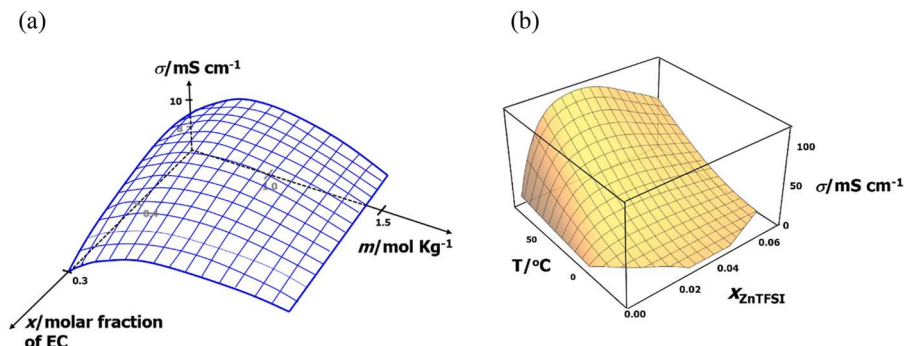


Figure 14.11 Mapping ion conductivity in 3D space as a function of salt concentration, solvent composition and temperature. (a) The conductivity surface of a typical skeleton lithium-ion battery electrolyte of composition LiPF_6 -EC-EMC at 30 °C. The two variables shown are salt concentration (molality, m) and solvent composition (expressed as molar fraction of EC in this binary system). (b) The conductivity surface of an aqueous electrolyte $\text{Zn}(\text{TFSI})_2$ as a function of temperature and salt concentration [expressed as molar fraction of the salt $\text{Zn}(\text{TFSI})_2$ in the electrolyte]. Reproduced from ref. 5 with permission from American Chemical Society, Copyright 2020.

Although such understanding still stays at the phenomenological level, it does help with the design and tailoring of existing electrolyte formulations when considering specific needs from applications. For example, analyzing Figure 14.11a, one can qualitatively summarize how ion conductivity changes with these three parameters:

1. *Salt concentration (m)*: At low salt concentrations (<1.0 m), the number of free ions increases with increase in salt concentration, because the presence of free ion carriers depends on the salt population. However, at excessively high salt concentrations, a maximum ion conductivity always occurs for such non-aqueous electrolytes (Figure 14.12a), after which the ion conductivity falls steadily. This behavior differs from that of many aqueous electrolytes, as discussed in Section 5.2.7 (Figure 5.13), and it occurs as a compromise between the number of free ions (n) and the increasing ion–solvent interaction (high viscosity, η) and ion aggregation (low ion mobility, μ). The location of such a maximum conductivity depends on the dielectric constant of the solvents as well as temperature; however, it is always in the neighborhood of 1 M salt concentration, which was the primary reason why traditional studies of non-aqueous electrolytes were

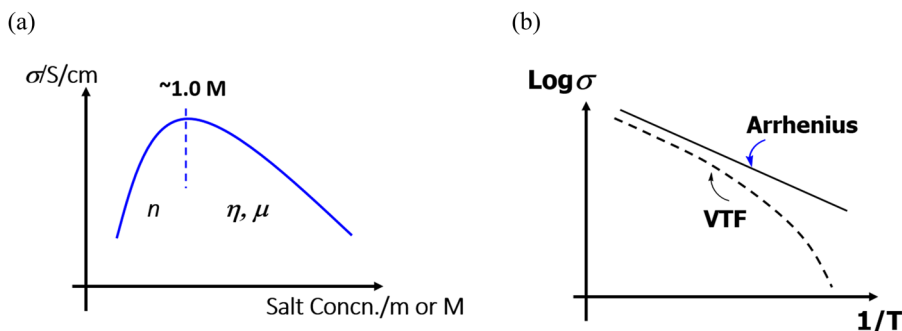


Figure 14.12 Ion transport behavior in liquid or liquid-like electrolytes. (a) The ion conductivity in most non-aqueous electrolytes experiences a maximum, which represents a compromise between two sets of competing factors: the number of free ions available from sufficient salt dissociation, and the increasing ion–ion and ion–solvent interactions in the high salt concentration region. (b) The non-Arrhenius transport behavior in amorphous (liquid, polymeric, glassy) electrolytes characteristically differs from that in crystalline solid electrolytes, and a modified Vogel–Tammann–Fulcher equation was proposed to describe such transport behavior that requires more cooperation from the solvating environment.

almost exclusively confined to the 1 M region while demonstrating a reluctance to go beyond this local region. Not until recently have the efforts with super-concentrated electrolytes breached this confinement imposed by the desire to seek high ion conductivities.

2. *Solvent composition (x_{EC})*: Generally, a higher dielectric constant would shift the occurrence of ion pairing to higher salt concentrations, because the Coulombic field of the central ion would be better shielded by such solvent molecules. This is in fact reflected in the Bjerrum length discussed in Section 4.9, which is minimized by the dielectric constant of the medium, making the definition of ion-pair formation much stricter, or making it more difficult for such ion pairs to form:

$$\lambda_B = \frac{z_+ z_- e_0^2}{\epsilon k_B T} \quad (4.92)$$

Hence solvent molecules represented by cyclic esters such as EC, PC or γ BL (Table 10.1) should be favored, because an ion in these solvents would have a higher probability of staying free at a given salt concentration and ion association would be less likely to occur. Unfortunately, these solvents also have high boiling temperatures and high viscosities (Table 10.1). It was such a conflict between desired properties that set the foundation for why mixtures of solvents are always used in practical batteries. For example, at a given salt concentration of 1.6 m, solvents with a higher x_{EC} are favored at high temperatures ($>50^\circ\text{C}$) because the influence of viscosity is less pronounced and σ increases monotonically with x_{EC} . At low temperatures ($<10^\circ\text{C}$), this relation is reversed because of the predominant effect of viscosity. At intermediate temperatures (between 20 and 40 $^\circ\text{C}$), σ peaks *versus* x_{EC} , indicating that at neither high nor low x_{EC} is able to optimize ion conduction. Similarly, salt concentration also affects the dependence of conductivity on solvent composition, and produces the various shapes in σ - x_{EC} relations, including single maximum curves and monotonic increases or decreases at different salt concentrations and temperatures.

3. *Temperature (T)*: With other variables remaining the same, ion conductivity increases monotonically with increase in temperature, until at very high-temperature regions where the dielectric constant outweighs the viscosity in affecting ion conduction.

Such high-temperature domains (well above 100 °C), however, are usually beyond the range of practical interest, until recently, when Dahn and colleagues demonstrated that lithium-ion batteries, with electrolytes formulated with the transestrification products between EC and DMC, could perform at temperatures approaching 100 °C.⁴³ In this newly expanded temperature regime, the effect of dielectric constant tends to become more pronounced, hence the overall trend of increase in ion conductivity with increase in temperature would gradually slow. Conversely, the ion conductivity at sub-ambient temperatures is predominantly determined by the increase in solution viscosity, although the dielectric constant becomes higher simultaneously.

A higher salt concentration accelerates the decrease in ion conductivity with decrease in temperature, because it contributes to a higher viscosity. This constitutes a barrier to the application of super-concentrated electrolytes for low-temperature scenarios. The combined effect of higher viscosity and low temperature is shown by the steeper σ - T curves at higher concentration. Solvent composition, on the other hand, also has a definite although mild influence on the temperature dependence of ion conductivity. The surface plots in Figure 14.11a reveal that the change in conductivity with temperature accelerates as the solvent becomes richer in EC, although different mechanisms involving either predominant ε or η at low or high salt concentrations, respectively, are believed to be at work.

It was recognized long ago that the temperature dependence of ion conductivity in amorphous electrolytes (which include liquid, polymeric and glassy electrolytes) differs from those in crystalline solids such as ceramic solid electrolytes. In the latter, since the ions hop between the various “solvating sites” immobilized in the lattices (Figure 12.8c), it requires an activation energy (E_A) to climb out of the energy wells associated with each solvating site, hence the relation between the logarithm of ion conductivity and reciprocal temperature takes a linear form governed by the Arrhenius relation:

$$\sigma(T) = Ae^{-\frac{E_A}{RT}} \quad (14.71)$$

where A is a pre-exponential factor. In an amorphous medium, the ions are surrounded by various solvation sheaths or cages, which could move with the ions for a certain time scale. Thus,

the movement of ions requires a lot more cooperation from the solvating environment (Figure 12.8a and b). This different ion transport mechanism is reflected in the temperature dependence that departs from linear Arrhenius behavior. Instead, a modified Arrhenius formalism called the Vogel–Tamman–Fulcher equation was proposed, which can account for the ion transport in an amorphous medium in a phenomenological manner (Figure 14.12b):

$$\sigma(T) = AT^{-\frac{1}{2}}e^{-\frac{B}{R(T-T_0)}} \quad (14.72)$$

where A and B are constants characteristic of the conduction process and T_0 is the vanishing conductivity temperature, which can be determined through fitting. Experimentally, T_0 values were found to be closely related to the glass transition temperatures of the solution systems, which agreed with the general assumption that ion transport in liquids or any non-crystalline polymer media is coupled with the solvation environment, which becomes frozen at the glass transition temperature.

In summary, these conductivity surfaces generated against the variables m , x_{EC} and T can be consistently interpreted to reveal useful knowledge of engineering electrolytes for optimum ion transport. These factors and their effects on ion conductivity are by no means unique to the system illustrated (LiPF_6 –EC–EMC) but are general guidance on how ion conductivities of other electrolyte systems with similar compositions would change with these same variables, and constitute a useful database for the understanding of more complex systems, such as ternary or quaternary mixtures.

In recent years, the same approach has been applied to generate conductivity surfaces for many emerging electrolyte systems, such as the aqueous super-concentrated electrolyte containing both monovalent and multivalent salts, among which $\text{Zn}(\text{TFSI})_2$ is displayed as an example in Figure 14.11b.^{4,5}

14.1.3 Electrolyte Engineering for Battery Applications

Before lithium-ion batteries, the early efforts at electrolyte engineering concentrated on the optimization of ion transport capability while paying little attention to the properties related to the interface and electrochemical stability window.

An equation extensively cited in the literature for ion conductivity is

$$\sigma = \frac{J}{X} = \sum z_i F c_i \mu_i \quad (5.74)$$

the derivation of which was discussed in Section 5.2.1.3. In fact, as we will discuss in subsequent sections, this equation comes with three significant assumptions that can hardly be met with practical electrolytes: (1) the salt completely dissociates into free ions, (2) all ions participate in migration and (3) all ions move independently of each other. Therefore, eqn (5.74) requires significant correction before being applied to practical electrolytes. Nevertheless, this equation still provides qualitative guidance in designing electrolytes, if ion transport is the only consideration.

Most efforts to improve ion conductivity have revolved around eqn (5.74), *i.e.* aiming at increasing either the ion population (c_i) or the ionic mobility (μ_i). Since these two factors are decided simultaneously by the physicochemical natures of the salt and solvents, different approaches involving either of these electrolyte components have been adopted.

For lithium electrolytes, the only variable in salt structure is the anion. In a given non-aqueous solvent system, the dissociation of a lithium salt would be facilitated if the anion is well stabilized by electron-withdrawing functionalities. Successful examples of such anions include PF_6^- and TFSI, where the formal charge is well delocalized (Figure 10.11), and the cation (Li^+) dissociates readily.

On the other hand, the mobility of an ion is known to vary inversely with its solvation radius r_i according to the Nernst–Einstein equation (and Stokes–Einstein relation):

$$\mu = \frac{1}{6\pi\eta r} \quad (5.104)$$

Again, it should be cautioned that this equation and also the Nernst–Einstein equation (also subject to the three assumptions mentioned above) should only be used qualitatively here.

So far, very few attempts at improving ion conductivity *via* the salt engineering approach have been successful, because the choice of anions suitable for lithium electrolyte solutes is rather limited and the synthesis of new structures is very difficult, and as additional constraints, electrochemical stability window requirements may exclude many anion structure designs based on central atoms of high reactivity, such as oxides (as in carboxylates and alkoxides), halides, sulfides, *etc.*

Alternatively, solvent composition tailoring has been the main tool for electrolyte engineering due to the availability of a vast number of candidate solvents. Considerable knowledge has been accumulated on the correlation between solvent properties and ion conductivity, and the most important are the two bulk properties of the solvents, dielectric constant ϵ and viscosity η , which determine the charge carrier number (n_i) and ion mobility (μ_i), respectively.

When solvated ions migrate within the electrolyte, the drag force applied by the surrounding solvent molecules is measured by the solvent viscosity η . Thus, in a solvent of lower viscosity, the solvated ions would move more easily in response to an applied electric field as expressed by eqn (5.104). Solvents of low viscosity have always been considered ideal candidates for electrolyte applications; however, their actual use was restricted because most of these solvents also display low dielectric constants (Table 10.1) and cannot dissociate ions effectively enough to prevent ion pairing.

Since a high dielectric constant and low viscosity usually cannot be integrated into a single solvent, a solvent mixture became the natural answer to formulating electrolytes for lithium batteries, usually with one of the components selected for ϵ and the other for η , in the hope that a balance between these two properties could be arrived at *via* such mixing. The concept has been rapidly accepted by researchers since the 1980s, usually using cyclic carbonates for their high ϵ and linear or cyclic ethers for their low η . In almost all cases, the ion conductivity in mixed solvents is superior to that in single solvents.

The physical foundation for such a mixed solvent approach was laid down by Matsuda and colleagues, who systematically explored mixtures of a cyclic carbonate and an ether, PC-DME.⁴⁴ They meticulously investigated the dependence of vapor pressure, dielectric constant and viscosity on solvent composition, and correlated the variations with ion transport properties. They revealed that the dielectric constant varied with solvent composition following an almost linear relation, with slight positive deviations, whereas viscosity always showed a pronounced negative deviation from what a linear relation would predict. For such binary solvent systems, approximate quantifications of the solvent mixing effect on these two properties were given:¹

$$\epsilon_s = (1 - x_2)\epsilon_1 + x_2\epsilon_2 \quad (14.73)$$

$$\eta_s = \eta_1^{(1-x_2)} \times \eta_2^{x_2} \quad (14.74)$$

where ϵ_s , η_s , ϵ_b , η_i and x_i are the dielectric constant and viscosity of the mixture or the pure solvent components and the volume fraction of the individual solvent component, respectively.

Either ϵ_s or η_s varies with solvent composition in a monotonic way, and the additive effect of each term seems to be able to account for the manner in which ion conductivity varies with solvent composition. At low DME concentration in the PC–DME system, the mixture has a high dielectric constant so that the salt dissociates more completely. However, in this region, the high viscosity, which impedes ionic movement, dominates the ion conduction. With increasing DME content, the dielectric constant remains relatively high, but the system viscosity falls drastically and the solvated ions migrate with higher mobility. As a result, a net increase in ion conductivity is achieved. Further increases in DME content (or low PC content) result in a very low dielectric medium where the effect of ion-pair formation outweighs that of low viscosity, hence the ion conductivity decreases with increase in DME content. Therefore, the maximum in ion conductivity *versus* solvent composition is actually the result of the compromise between the effects of the dielectric constant and viscosity. Such a compromise illustrates the superiority of mixed-solvent *versus* single-solvent electrolytes.

A simple mathematical treatment based on this model successfully reproduced the variation of ion conductivity with solvent composition as observed in experiments on numerous different systems. It also proposed that, in an ideal situation where no ion-pair formation is present, the change in ion conductivity should follow a linear relation as predicted by a semiempirical Walden's rule, the origin of which was discussed in Section 5.2.4:

$$\Delta\eta = \text{constant} \quad (14.75)$$

The Walden product ($\Delta\eta$) can be viewed as an ion conduction metric that is normalized against both the solvent viscosity and the salt concentration (*i.e.* the number of free ions if no ion pairing occurs); therefore, its value serves to a first approximation as a quantification of the degree of ion dissociation in electrolytes with either a given solvent or a given salt. We will explore further what this quantity could teach us in evaluating the interionic correlations in different electrolyte systems.

Although Matsuda and co-workers' systematic study was conducted on mixtures of cyclic carbonate PC with ethers, the most conclusive correlations remain qualitatively true for mixtures of cyclic and linear

carbonates, *i.e.* compositions of the state-of-the-art lithium electrolytes. Most likely, it was the work by Matsuda and co-workers that delineated the basic guidelines for electrolyte formulation, which eventually led to the formulations of the state-of-the-art lithium-ion electrolytes by Fujimoto and colleagues using cyclic (high- ϵ) and linear (low- η) carbonate mixtures.⁴⁵

Further analysis of related studies seems to argue that the success of the high ϵ -low η combination might not be due to the simple additive effect of these two properties but, rather, a synergistic action of these two variables through a mechanism that involves the solvent's preference for cations in its solvation sheath. During the dissolution process of a certain salt lattice in mixed solvents, the solvation of the ions by a solvent molecule with a higher dielectric constant would be energetically favored over the one with a lower dielectric constant. Consequently, it would be reasonable to expect that after equilibrium has been established in the solution, the ions would have solvation sheaths that are mainly populated with the high- ϵ solvents.

Modeling results using molecular quantum mechanics support this hypothesis by showing that the less favored solvent molecules (with low ϵ) actually could be readily replaced with the favored solvent molecules. Thus, in the EC-EMC binary system, the solvation sheath should be predominantly composed of EC, whereas in the EC-PC binary system, the solvation sheath favors PC.

We have presented evidence for such preferential solvation trends in Section 12.2.3 (Figure 12.4), although recent findings revealed that the most preferred solvent may not be judged merely by its dielectric constant, but a more comprehensive metric such as solvation power (Table 12.1).

The preferential solvation by ions not only concerns ion transport but also further relates to the electrochemical stability of the electrolytes in lithium-ion cells, because these solvent molecules in the solvation sheath, such as EC or PC, migrate with the ions to electrode surfaces, are enriched there, and are probably more involved in the oxidative or reductive processes than the less coordinating, low ϵ -low η solvent molecules, such as the linear carbonates. This difference has a profound impact on the chemical nature of the electrolyte-electrode interphases to be discussed in the next chapter.

The apex of such mixed solvents was achieved by Fujimoto and colleagues in 1990 when they found that a mixture of cyclic carbonate with linear carbonate not only optimizes ion transport but also could enable the electrochemical synthesis of LiC₆ by forming an interphase mainly derived from the EC reduction process. Such electrolyte

engineering serves as the skeleton formulation that is currently working in the most popular electrochemical device ever invented by humankind.

14.1.4 Ionicity

One important index arising from the phenomenological studies on ion transport is the so-called “*ionicity*”,⁵ which has been used as a quantitative indicator to measure how “ionic” an electrolyte is, or how close an electrolyte is from its ideal state, which, in real life, only extremely dilute electrolytes could approach.

In the ideal state of an electrolyte, the salt is completely dissolved and dissociated into ions, all ions participate in the ion transport and no ion feels the presence of the other ions, hence ion-pair formation is zero. In other words, the average interionic distance is so much larger than the Bjerrum length that statistically interionic collisions are impossible.

However, in reality, practical electrolytes must contain a salt concentration higher than 0.01 M (or 0.01 m) in order to provide ion conductivity at a practical level. In those concentration regions, and especially in the so-called “super-concentrated” domains and ionic liquids, none of the above ideal prerequisites could be met. Instead, the ions feel a strong presence of other ions, of both the same and opposite charge, hence the formation of ion pairs as well as large aggregates exists universally. Equally important is that the solvent molecules, which in extremely dilute electrolytes would remain uncoordinated with ions and serve as a static reference medium, now become closely associated with the ions in those ion pairs, aggregates or large networks (Figures 12.6 and 12.7).

Ions in these non-ideal electrolytes therefore cannot move as freely, as they are in the ideal state. Their contribution to the overall ion transport, as evaluated by the normalized quantity molar conductivity Λ , is hence significantly lower than it should be if the ions are in the ideal state. In other words, we think that these electrolytes are not as “ionic” as they should be.

Ionicity represents the effort to quantify such deviations from the ideal state, and is derived from the semiempirical *Angell–Walden plot*.^{6,7}

14.1.4.1 Walden Analysis and Haven Ratio

In Section 5.2.4 we derived Walden’s rule from the Nernst–Einstein equation and Stokes–Einstein relation, which relates the molar ion

conductivity Λ_i of a specific ion to its radius r_i and the viscosity of the medium η :

$$\Lambda_i \eta = \frac{zFe_0}{6\pi r_i} = \text{constant} \quad (14.72)$$

where the constant is temperature dependent.

As the molar ion conductivity of a specific ion is difficult to measure independently by experiment, Angell and colleagues extended the above relation to the overall molar ion conductivity of the electrolyte Λ_E , and simplified the relation to

$$\Lambda_E \eta = \text{constant} \quad (14.76)$$

or in logarithmic form

$$\log \Lambda_E = K \log(\eta^{-1}) \quad (14.77)$$

which in fact is based on the assumptions that the overall ion conductivity is the simple sum of those of each individual ion, and that all ions are fully independent of the influence of each other's Coulombic field. Hence the electrolyte described by eqn (14.77) represents an ideally ionic state for electrolytes. Only a few selected electrolytes, when in extremely dilute states, meet such requirements, and an aqueous solution of potassium chloride (KCl) is one of them. In aqueous solutions, not only is KCl completely dissociated into free K^+ and Cl^- ions, but also these two ions have approximately identical diffusion coefficients. In fact, it is this unique characteristic that made aqueous KCl solutions the "standard electrolyte" that researchers often use as a reference to calibrate instrumentation, or as a "salt bridge" in electrochemical analytic devices.

Thus, eqn (14.77) indicates that, when the logarithm molar conductivity ($\log \Lambda_E$) of an ideal electrolyte such as aqueous KCl solution is plotted against the logarithm of its reciprocal viscosity [$\log(\eta^{-1})$, or logarithm of the fluidity], one should obtain a straight line. By selecting a standard aqueous KCl solution at 0.01 M and using proper units for the molar conductivity (in $S \text{ cm}^2 \text{ mol}^{-1}$) and viscosity (100 mPa s), such a straight line would be perfectly diagonal and pass directly through the origin (Figure 14.13). This plot of $\log \Lambda_E$ versus $\log(\eta^{-1})$ is known as the *Walden plot* or *Angell–Walden plot*.⁷

Since the accurate determination of overall ion conductivity is easy thanks to the AC impedance spectra, and the accurate determination of viscosity is also readily available, an extensive database of both

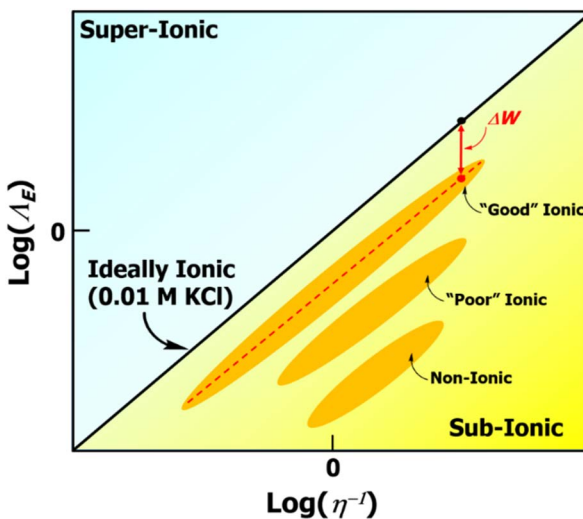


Figure 14.13 The Angell–Walden plot that defines ionicity. An aqueous solution of 0.01 M KCl is used as the standard ideally ionic electrolyte, the ion transport of which follows almost perfectly what the Nernst–Einstein equation predicts.

parameters has been accumulated in the literature for diverse electrolyte systems. These databases enabled researchers to compare a wide range of electrolyte systems by placing them in the Angell–Walden plot, no matter whether they are aqueous or non-aqueous, polymeric or ionic liquids.

The results are rather interesting. Most of the electrolytes thus evaluated indeed exhibit linear behavior, but deviate from the reference line generated by the ideally ionic electrolyte, aqueous KCl solutions. Such deviations could be quantified by the difference between the expected molar conductivity from the ideal electrolyte and the actually measured electrolytes (ΔW in Figure 14.13):

$$\Delta W = \Lambda_{\text{NE}} - \Lambda_E \quad (14.78)$$

where Λ_{NE} is the so-called Nernst–Einstein molar conductivity expected from an ideal electrolyte.

Angell and colleagues attributed the deviation to the incomplete dissociation of salts, formation of ion pairs and ion aggregations, and therefore a new quantity called “*ionicity*” (I) can be defined as

$$I = \frac{\Lambda_E}{\Lambda_{\text{NE}}} = \left(1 - \frac{\Delta W}{\Lambda_{\text{NE}}} \right) \quad (14.79)$$

For an ideal electrolyte, $I = 1.0$.

It should be mentioned that in studies on inorganic solid electrolytes, a related quantity, the *Haven ratio* (H_R), was defined as the ratio of theoretical ion conductivity as predicted from the Nernst–Einstein equation (σ_{NE}) to that actually measured (σ_{exp}):

$$H_R = \frac{\sigma_{NE}}{\sigma_{exp}} \quad (14.80)$$

In this sense, ionicity is in fact the inverse of the Haven ratio:

$$I = \frac{1}{H_R} \quad (14.81)$$

Since the majority of these inorganic solid electrolytes are essentially single-ion conductors, *i.e.* with only one mobile ion, while the counterion of which is immobilized on a lattice or framework, the Haven ratio reflects how the mobile ion is correlated with the lattice or framework. The Haven ratio is usually less than 0.50, indicating the “super-ionic” nature of these solid electrolytes, as will be discussed below.

14.1.4.2 Classification of Electrolytes: Ionic, Super-ionic and Sub-ionic

Most practical electrolytes fall below the reference straight line representing an ideally ionic electrolyte, therefore their ionicity ranges between 0 and 1.0. These electrolytes are consequently named “*sub-ionic*”. Depending on how far they deviate from the ideal ion conductivity value, they are further broken down into the groups “*good ionic*”, “*poor ionic*” and “*non-ionic*” (Figure 14.13).⁷

These electrolytes all demonstrate negative deviations, which are attributed to the presence of incomplete ion dissociation, because the presence of ion pairs and ion aggregates reduces the effective populations of free ions expected from the salt concentration, which is indirectly reflected in the viscosity of the electrolytes.

However, when Walden analysis was applied to certain molten salts or ionic liquids, such as metal halides (ZnF_2 or $ZnCl_2$) or silicates (SiO_2), an “abnormality” emerged, as these electrolyte systems reside above the ideally ionic line. This positive deviation produces an ionicity higher than 1.0. In other words, these electrolyte systems exhibit higher molar ion conductivities than expected from the salt concentration or viscosity. Such electrolytes are named “*super-ionic*”.

It is very important to emphasize that being super-ionic does not necessarily mean that the electrolyte system is super-conductive. It simply means that, *considering the given viscosity of that system*, the ion conductivity exhibited exceeds what one would predict from the Nernst–Einstein equation. These inorganic halides in their molten state are extremely viscous, therefore even mediocre ion conductivity, after being normalized against viscosity, places these systems far above the ideally ionic line.

In fact, an ionicity above 1.0 should not be as beyond comprehension as it may appear. For example, all solid-state electrolytes, no matter whether polymeric, glassy or ceramic, should be super-ionic by definition, because their viscosity approaches infinity and the mobile ions are essentially decoupled from the immobile and solid environment, which is why these solid electrolyte systems are sometimes called “super-ionic conductors”. However, the classification generated from Walden analysis is mostly applicable to liquid electrolytes as a semiquantitative measure of the ion association, ion-pair formation and ion aggregation.

The typical non-aqueous electrolytes used in lithium-ion batteries have been thoroughly analyzed by many researchers using Walden analysis, which revealed that, even at extremely low salt concentrations (0.1 M LiPF₆) and high EC content, the ion association effect is still very severe, as reflected by the average ionicity of 0.3–0.5.

Usually, the salts and solvents used have the most direct effect on ionicity. Compared with other most commonly used lithium salts, LiPF₆ has been shown to be the most dissociated in the non-aqueous solvents, and when evaluated in identical carbonate solvent mixtures it presents the highest ionicity, whereas LiBF₄ and LiBOB appear to be the least dissociated salts, with LiTFSI and LiFSI being intermediate. The presence of solvent molecules of high dielectric constant, such as EC, PC or γ BL (Table 10.1), certainly leads to higher ionicity as they promote more ion dissociation.

On the other hand, electrolytes based on ethereal solvents, such as those “salt solvate electrolytes” that were discussed in Section 12.2.4.3, generally have much higher ionicity in the range 0.5–0.6, thanks to the excellent solvating and chelating power provided by the polyether structures.

Surprisingly, even higher ionicity is found for ionic liquids and molten salts, where the absence of solvent molecules and the closer interionic distances would have led us to believe that interionic association should be much stronger therein. This trend is demonstrated not only in those “abnormal” super-ionic systems mentioned above, but also more universally with the majority of the non-lithium ionic liquid

systems based on onium cations, where the ionicities are higher than 0.5 in almost all cases but could be as high as 0.8. Only when Li^+ is added to those systems does their ionicity decrease dramatically. In other words, the ionic liquids based on those large onium cations, be it ammonium, imidazolium, pyrrolidinium, *etc.*, are much more dissociated in comparison with the rather small cations such as Li^+ and Na^+ , which severely constrains ionic motion.

These examples (solvated salt electrolytes and ionic liquid electrolytes) serve as vivid examples to remind us that high ionicity does not automatically mean good electrolytes, as the most desired property from the perspective of practical application is the actual ion conductivity.

Walden analysis was applied to super-concentrated aqueous electrolytes by Yamada *et al.*, which revealed a pronounced cation–anion decoupling behavior despite the high salt concentration, which apparently benefited from the well-dissociated lithium salts in H_2O , and strongly suggested an ionic hopping process that is relatively independent of the anion movement.⁸ This should arise directly from the liquid structure with nano-heterogeneity that we discussed in Sections 12.2.4.1 (Figure 12.6) and 12.2.4.2 (Figure 12.7), which allows a high fraction of free Li^+ *via* a vehicular motion through the water-rich domains. However, as will be discussed in Section 14.1.5, the movement of the free Li^+ actually occurs in the form of $\text{Li}^+(\text{H}_2\text{O})_4$ through the 3D percolating network in the WiSE, hence Li^+ moves with its solvation sheath instead of doing so independently.

14.1.4.3 Modifications to Walden Analysis

The concept of electrolyte ionicity *via* Walden analysis has been extensively applied in electrolyte studies, especially on ionic liquids and molten salt electrolytes. In recent decades, various modifications were also introduced, aimed at making its theoretical foundation more rigorous, or making the quantification more accessible as a universal descriptor, or circumventing the irrationality that it induces such as the case of super-ionicity.

14.1.4.3.1 Correction of Ionic Radii

When Angell and colleagues directly jumped from eqn (5.112) to eqn (14.76), they actually made an assumption that average ionic radii for both cations and anions could be adopted without inducing serious departures from the underlying Stokes–Einstein relation. However, by doing so, irregularities inevitably arose, because the diverse electrolyte systems compared on the Angell–Walden plot involve very

different salt species containing cations and anions of varying sizes and shapes. The varying ion sizes thus directly affect how agile these ions are when moving in the viscous media, and result in ion transport behaviors that deviate from what would have been expected from their viscosity or concentration.

MacFarlane *et al.* attempted to account for such deviations by going back to the original point where Angell and colleagues made the assumption.⁹ At an ideally ionic state, the Nernst–Einstein molar ion conductivity should have been given by the simple summation of the contributions from each individual ion:

$$\Lambda_{\text{NE}} = \lambda_+^0 + \lambda_-^0 = \frac{F^2}{RT} (z_+ D_+ + z_- D_-) \quad (5.101)$$

Assuming that each individual ion follows the Stokes–Einstein relation [eqn (5.105)] for an electrolyte with monovalent cations and anions, we should have the Nernst–Einstein molar ion conductivity expressed as

$$\Lambda_{\text{NE}} = \frac{F^2}{RT} \left[\frac{k_B T}{6\pi\eta r_+} + \frac{k_B T}{6\pi\eta r_-} \right] = \frac{\text{constant}}{\eta} \left[\frac{1}{r_+} + \frac{1}{r_-} \right] \quad (14.82)$$

where r_+ and r_- are effective ionic radii for cations and anions, respectively.

Eqn (14.82) allows us to take the difference in the cation and anion radii into account by plotting $\log \Lambda_E$ versus $\log \left(\eta^{-1} \left[\frac{1}{r_+} + \frac{1}{r_-} \right] \right)$. The adjusted Angell–Walden plot therefore should provide a more rigorous quantification for the electrolyte diversity.

However, its disadvantage is also obvious, because compared with the original Angell–Walden plot, which employs only two easily measurable quantities (molar ion conductivity and viscosity), the required effective ionic radii for different ions are not always available. It should be noted that the ionic radii readily available in databases or in the Periodic Table should not be used here, because those numbers were usually obtained from the corresponding crystal lattices, whereas in liquid electrolytes those ions, especially the cations, are solvated. Hence r_+ and r_- in eqn (14.82) should be represented by the so-called “*Stokes radii*” of ions that accounted for the solvation sheaths, which are not widely available thus far. Table 14.1 gives Stokes radii for Li^+ and TFSI anion in selected solvents that were estimated from the measurement of self-diffusion coefficients obtained

Table 14.1 Stokes radii for Li⁺ and TFSI anion in selected solvents.^a

Stokes radius	Solvent					
	EC	PC	DMC	THF	DME	Tetraglyme
R_{Li^+} / Å	2.20	2.15	2.75	2.18	2.8	1.8
R_{TFSI} / Å	1.35	1.30	2.65	1.75	2.45	1.6

^aSource: ref. 31.

via NMR spectroscopy. Apparently, the Stokes radii vary with the solvent, as the size of the latter dictates the size of the solvation sheaths. More interestingly, despite the variations and errors in experimental fitting, the Stokes radius of Li⁺ is persistently larger than that of the TFSI anion, although the latter is doubtless much larger if one considers only the size of the atoms. Therefore, the Stokes radii displayed in Table 14.1 serve as convincing evidence for the conclusion we drew in Sections 10.3.2.5.2 and 12.4 that, in non-aqueous electrolytes, Li⁺ is well coordinated by solvent molecules, whereas anions remain relatively free (Figure 10.11).

More importantly, the original Stokes law [eqn (5.102)] was based on a more basic assumption that the ions are perfectly spherical, which no longer holds true for most of the ions we are now working with, typical examples of which include odd-shaped anions such as TFSI and FSI and asymmetrically substituted organic onium cations such as various tetraalkylammonium, imidazolium and pyrrolidinium ions (Table 14.2). In addition to their non-spherical shapes, their Stokes radii also remain unknown for most electrolyte systems, as the radii depend on how these ions are solvated by specific solvent molecules and require independent determination. The combination of these irregularities of ion properties certainly presents challenges in classifying the complicated electrolyte systems via the over-simplified phenomenological comparison established on Walden analysis.

14.1.4.3.2 Correction via NMR Spectroscopy

Around the mid-1990s, the decade-long studies on gradients of magnetic field and radiofrequency field in nuclear magnetic resonance (NMR) spectroscopy, accompanied by continuing improvements in both hardware and software, finally led to a practical technique that allows us to probe directly the translational movement of NMR-active nuclei, hence providing an accurate, non-invasive and reliable way of measuring the self-diffusion coefficient of ions and molecules that contain these nuclei. This “clean” technique, pulsed field gradient

Table 14.2 Structures and shapes of selected commonly used ions.

Ion		Structure	Approximate shape
Li^+	Li^+		
Trimethylpropylammonium			Spherical Asymmetrically pyramidal
1-Methyl-3-propylimidazolium			Elongated planar
1-Methyl-1-butylpyrrolidinium			Distorted planar
Hexafluorophosphate (PF_6^-)			Octahedral
Tetrafluoroborate (BF_4^-)			Tetrahedral
Bis(trifluoromethanesulfonyl)imide (TFSI^-)			Elongated dumbbell
Bis(fluorosulfonyl)imide (FSI^-)			Elongated dumbbell

spin-echo (PGSE-NMR or pfg-NMR), immediately displays overwhelming advantages over other existing methods of measuring diffusion coefficients, which were either unreliable regarding accuracy, such as scattering techniques, or laborious, costly and “messy”, as best exemplified by the labeling of samples with radioactive isotopes so that their motion could be monitored.

The pfg-NMR technique was rapidly made available on most commercially available NMR spectrometers around the beginning of the

millennium, and has since been extensively recognized as a standard approach by electrolyte researchers.

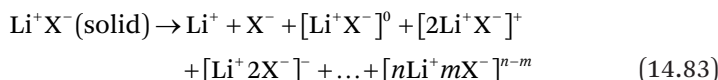
The primary restriction of this NMR technique, of course, is the availability of or access to suitable hardware, which used to be very costly and available only in major universities and research centers funded by governments. However, this restriction has been receding as NMR facilities have become increasingly accessible to most laboratories at reasonable cost.

The second restriction arises from the limited sensitivity of NMR techniques, *i.e.* only those nuclei with odd numbers of protons and neutrons can be detected, while those with even numbers of protons and neutrons are NMR-inactive. Examples of the latter include some of the most common isotopes that we encounter, such as ^{12}C , ^{16}O and ^{14}N . Although the nuclei of these elements' rare isotopes, such as ^{13}C , ^{17}O and ^{15}N , have odd numbers of protons and neutrons and are therefore NMR-active, the low natural abundances of these isotopes often make the application of pfg-NMR techniques extremely challenging, unless isotope-enriched samples are made available.

Fortunately for electrolyte researchers, the second restriction does not impose too many problems, as the most important components in electrolytes often contain NMR-active nuclei, such as ^7Li and ^{23}Na in cations, ^{19}F in various fluorinated anions such as PF_6^- , BF_4^- , TFSI^- and FSI^- , and ^1H in organic solvent molecules. Hence the pfg-NMR technique rapidly gained high popularity, and became the favorite tool of electrolyte researchers in measuring the self-diffusion of not only ions but also the solvent or polymeric matrix.

We do not intend here to cover the principles of how the pfg-NMR technique works, because it is a rather specialized area. Those interested can find relevant material in the Further Reading list at the end of this book. Briefly, this technique permits the rapid determination of self-diffusion coefficients for all these NMR-active nuclei, no matter whether they are in an ion, a molecule, ion pairs or ion aggregates. The self-diffusion coefficients obtained are averages in nature, because the temporal resolution of NMR spectroscopy is on the scale of 10^{-9} – 10^{-10} s, which is much slower than the ion responding to random walk in the electrolytes and interacting with other ions or solvent molecules.

As a specific example, let us consider a monovalent lithium salt Li^+X^- , which at practical salt concentrations (1 M or higher) dissociates into various species with solvation by electrolyte solvent molecules:



The self-diffusion coefficients of Li^+ or X^- measured by pfg-NMR spectroscopy (assuming both are NMR-active) are hence averaged across all these species for either Li^+ or X^- , no matter whether they are free, associated in the neutral ion pair or confined in complex aggregated species.

Leveraging this technical advance, Watanabe and colleagues redefined the determination of ionicity by combining pfg-NMR spectroscopy with AC impedance spectroscopy.¹⁰ They adopted the definition of ionicity as the ratio of the actual molar ion conductivity of the electrolyte Λ_E to the ideal molar ion conductivity as predicted by the Nernst–Einstein equation (Λ_{NE}):

$$I = \frac{\Lambda_E}{\Lambda_{\text{NE}}} \quad (14.79')$$

They argued that Λ_E can be determined by the overall ion conductivity (σ) measured via AC impedance spectroscopy by normalizing against the salt concentration c :

$$\Lambda_E = \frac{\sigma}{c} \quad (5.59)$$

which collectively reflects the migration of ions under the applied external electric field.

On the other hand, Λ_{NE} can be calculated following the Nernst–Einstein equation using the self-diffusion coefficients for the individual ions (D_+ and D_-) as measured by pfg-NMR spectroscopy:

$$\Lambda_{\text{NE}} = \frac{z_i F^2}{RT} (D_+ + D_-) \quad (5.101)$$

which assumes that *ALL diffusing species detected by pfg-NMR spectroscopy should contribute to the molar conductivity*, which is possible only in the ideally ionic electrolytes. In other words, Λ_{NE} reflects the upper limit of molar ion conductivity because it takes into account the contributions not only from those nuclei in free ions, but also from those nuclei in species that are either non-conducting under an electric field because they are neutral (such as $[\text{Li}^+\text{X}^-]^0$), or that are much more slowly moving because of the heavier mass (such as $[\text{2Li}^+\text{X}^-]^+$), or those moving in the “wrong” direction and contributing negatively to the overall conductivity (such as $[\text{Li}^+\text{2X}^-]^-$).

Therefore, in an electrolyte with a practical salt concentration, where ion-pair formation and ion aggregation inevitably exist, Λ_{NE}

would overestimate the molar ion conductivity, hence the ionicity should always be confined as

$$0 \leq I = \frac{A_E}{A_{NE}} \leq 1.0 \quad (14.84)$$

With such a definition, the category of “super-ionic” would cease to exist because the macroscopic viscosity is no longer a factor to be considered.

In reality, eqn (14.84) has been verified extensively by experimental data for the vast majority of electrolyte systems. The values of ionicity thus obtained are similar to the results obtained from Walden analysis, but with much higher sensitivity towards changes in the structure (size, shape) or valence of ions.

The real advantage of Watanabe’s modification is its universality. Even when this approach is applied to systems with extremely high or infinite viscosities, such as semi-solid polymeric electrolytes or inorganic glassy and ceramic electrolytes, eqn (14.84) still holds true, in sharp contrast to Walden analysis.

The only exceptions are those systems that contain protons (H^+) as conducting ions, such as aqueous solutions of super-acids (HTFSI, H_2SO_4 , etc.) or protic ionic liquids (e.g. ethylmethylimidazolium with HTFSI or ethylammonium nitrate $[EtNH_3]^+NO_3^-$), the ionicities of which determined *via* pfg-NMR spectroscopy are above 1.0, indicating that the actually molar ion conductivity measured by AC impedance spectroscopy is higher than that expected from the ideally ionic state as described by the Nernst–Einstein equation. This “abnormal” ion transport behavior obviously arises from the Grotthuss mechanism that governs the motion of protons, benefiting from the fact that H^+ is the smallest ion with certain quantum characteristics (Section 5.2.8).

The modification of ionicity determination proposed by Watanabe and colleagues possesses overwhelming advantages over the original Walden analysis, because it not only eliminates the requirement for electrolyte viscosity measurement, but also circumvents the inconveniences that are intrinsically associated with Walden analysis in the case of nearly infinite viscosities for solid electrolyte systems. This correction extended the applicability of the ionicity concept to a much broader scope.

In retrospect, since ionicity describes how well the ions are dissociated from each other in an electrolyte system, it should not involve the system viscosity, as this quantity is related not only to interionic correlations but also very much to the ion–solvent interactions. Adopting

aqueous KCl solution as the standard reference line in Walden analysis and defining ionicity based on the deviation from such a standard inevitably involves the viscosity of aqueous KCl solution as an indirect measure of ion association. Hence the failure of the Angell–Walden plot approach would be natural when facing systems where the solvent molecules (as in polymeric electrolytes) or one of the anions (as in glassy or ceramic solid electrolytes) are immobile.

Again, high ionicity does not necessarily guarantee an excellent electrolyte. The typical carbonate-based electrolytes work very well in lithium-ion batteries with their superior ion conductivity (*ca.* 10^{-2} S cm $^{-1}$ at room temperature), but their ionicity is only *ca.* 0.3. The “salt solvate”, polymeric or ionic liquid electrolytes provide much higher ionicity, but their actual overall conductivity (*ca.* 10^{-5} – 10^{-3} S cm $^{-1}$) cannot provide sufficient ion transport to support the cell reactions required. In this sense, whether the ions in an electrolyte are completely dissociated does not matter.

14.2 Mechanistic Understanding: Speciation

So far, we have learned how to determine the overall ion conductivity of an electrolyte system, and derived a few quantities such as ionicity that allow us to conceptualize indirectly how ions are transported in the electrolytes. However, knowing only ion conductivity does not indicate how well the electrolyte would function in a practical electrochemical device, because what we really care about is the current carried by the working ions, not the overall contribution from both cations and anions. For example, in a lithium-ion battery, the qualification of an electrolyte rests with its capability to conduct Li $^{+}$ to support the half-reactions on each electrode, not by its capability to conduct anions, as the anions would be blocked by both electrodes, and anionic migration would eventually be counterbalanced at the steady state by its own diffusion (Figure 14.1).

Therefore, the maximum working current that a battery can deliver relies on the Li $^{+}$ transport number t_{+} . This limitation would be especially felt in the scenarios of fast charging or discharging of the lithium-ion battery.

What complicates the situation even more is the intensified interionic correlations at practical salt concentrations, where diverse ionic species form as suggested by eqn (14.83). In this case, the movements of both cations and anions and all these ionic species are inter-correlated, while the ion transport number as defined in Section

5.2.1.5 [eqn (5.93)] becomes no longer valid, because the movement of a specific ion is no longer directly related to the fraction of effective current carried by this ion. In other words, one must differentiate the *ion transport number* (t_+ and t_-) and *ion transference number* (T_+ and T_-) that we discuss in the sections that follow.

Hence, to describe better how useful an electrolyte is, one must know not only how fast the ions move *collectively* in the electrolyte, but also how the ions interact with each other and with solvent molecules, and what the contributions are from these mobile ionic species to the overall ion conductivity. Seeking knowledge of *electrolyte speciation* during the ion migration constitutes the central mission of the modern understanding of ionics in practical electrolytes, which differs from the classical understanding achieved in electrolyte systems of ideality that were discussed in Chapters 3–5, and requires mechanistic analysis of ion transport (and also mass transport) on the molecular level.

14.2.1 Ideality of Electrolytes: Revisiting the Einstein Equations

Before we dive deeper, it is beneficial to revisit briefly the classical ionics knowledge about ion transport covered in Chapter 5, especially the Einstein equations, the validity of which has been repeatedly emphasized to be applicable only in extremely dilute electrolytes, ideally below 0.001 M.

When we examined the ion migration driven by an external electric field, we started from the definition of electric current [eqn (5.45)] and ion conductivity [eqn (5.50) and (5.74)], and derived the Nernst-Einstein relation [eqn (5.101)], Walden's rule [eqn (5.112)] and the expressions for transport number [eqn (5.93)] and molar or equivalence conductivity [eqn (5.62)]:

$$i = \sum_i z_i e_0 N_i J_i = \sum_i z_i F J_i \quad (5.50)$$

$$\Lambda^0 = \lambda_+^0 + \lambda_-^0 \quad (5.62)$$

$$\sigma = \frac{j}{X} = \sum_i z_i F c_i \mu \quad (5.74)$$

$$t_i = \frac{J_i}{\sum_i J_i} = \frac{z_i F c_i \mu_i}{\sum_i z_i F c_i \mu_i} \quad (5.93)$$

$$\Lambda = \frac{z_i e_0 F}{k_B T} (D_+ + D_-) = \frac{z_i F^2}{RT} (D_+ + D_-) \quad (5.101)$$

$$\Lambda \eta = \frac{zFe_0}{6\pi r} = \frac{\text{constant}}{r} \quad (5.112)$$

Behind all these equations, there are three hidden assumptions: (1) the salt is completely dissociated into free ions, (2) all free ions participate in the diffusion and migration and (3) each free ion, wrapped in a classical Bernal–Fowler solvation sheath, does not feel the existence of any other ions, and hence moves independently. Such electrolytes are characterized with “ideality”.

On the other hand, the other Einstein equations, such as the Einstein–Smoluchowski equation [(eqn (5.20)], Einstein relation [eqn (5.91)] and Stokes–Einstein equation [eqn (5.105)], all appear to be of more general applicability and hence do not require ideality as described by the above three assumptions:

$$\langle x^2 \rangle = 2Dt \quad (5.20)$$

$$D = \mu k_B T \quad (5.91)$$

$$D = \frac{k_B T}{6\pi \eta r} \quad (5.105)$$

However, one should not forget that these relations were initially derived for Brownian motions of neutral particles traveling in liquid or gaseous states. For example, the concept of mobility was originally defined as the ratio of the particle’s terminal drift velocity to an applied force, which was only extended to the force imposed by an electric field on charged particles at a much later stage. Apparently, no consideration was given to the interionic Coulombic attraction and repulsion forces in the derivation of these relations, and consequently their validity still faces departures from ideality in practical electrolytes with high salt concentrations.

While electrolyte ideality might be approached only in extremely dilute electrolytes, the practical electrolytes used in most electrochemical devices, such as lithium-ion batteries, have to stay away from ideality, because in order for the electrolytes to support a meaningful function of these electrochemical devices, they have to employ salt concentrations at levels far above 0.01 M, usually in the neighborhood of 1 M, otherwise they cannot provide sufficiently high fluxes of ions.

In those concentrated electrolytes, none of the above three assumptions would hold true.

At these high salt concentrations, each individual ion feels the Coulombic attraction or repulsion from the other ions, and its movement is inevitably affected by the presence of the other ions, no matter whether they have the same or opposite charge. *Vice versa*, its own charge and Coulombic field also have an equal influence on those other ions. The overall result from this interionic cross-influence is the observed deviation of ion transport behaviors from ideality represented by all the “reality-dependent” equations mentioned above.

It should be noted that such deviations already become rather pronounced in moderately concentrated electrolytes with salt concentrations above 0.01 M but well below 1 M. In highly concentrated electrolytes (above 2 M but below 10 M) and super-concentrated electrolytes (above 10 M), the substantial formation of diverse ionic species, such as ion pairs, aggregates and the extended liquid structures of nano-heterogeneity as shown in Figures 12.5–12.7, would further drive the deviation from the ideality.

In Section 5.2.6, we briefly discussed the interionic coupling issue when demonstrating how Onsager treated ion movement in an applied electric field, in which the influence of the other ions on the central ion was simplified into a continuous “ionic cloud” exerting both relaxation and electrophoresis drags on the central ion when it tries to move. We also defined a new quantity, the ambipolar diffusion coefficient D_{ambp} , to describe how the coupled cations and anions move in an entangled and convoluted manner that is determined by the intrinsic diffusion coefficient and mobility of both ions:

$$D_{\text{ambp}} = \frac{\mu_+ D_- + \mu_- D_+}{\mu_+ + \mu_-} \quad (5.169)$$

which describes the ion coupling that is already present even in ideal electrolytes.

In the sections that follow, we will examine in a more rigorous and systematic manner the ion transport in those electrolytes that are moderately, highly or super-concentrated. For convenience of discussion, we would name an electrolyte as an “*ideal electrolyte*” if it follows the Nernst–Einstein equation (and all the derivative equations mentioned above). Otherwise, we would call it a “*practical electrolyte*”, which would encompass the regimes of moderately, highly or super-concentrated electrolyte solutions.

14.2.2 The Real Meaning of Ion Transport Number

Let us first consider the ideal electrolyte as a relatively easy start.

In this ideal electrolyte, the ion transport number t_i is defined by eqn (5.93), which simplifies to eqn (5.96) and (5.95) if this ideal electrolyte is a binary electrolyte consisting of two monovalent ions M^+ and X^- :

$$t_+ = \frac{\mu^+}{\mu^+ + \mu^-} = \frac{D_+}{D_+ + D_-} \quad (5.96)$$

$$t_- = 1.0 - t_+ \quad (5.95)$$

Needless to say, there is a hidden assumption that the only ionic species present in the electrolyte are the free cation M^+ and anion X^- together with their individual solvation sheaths, which is a natural extension of the three ideality conditions discussed in the previous section.

According to such a definition, the lowest transport number for either cation or anion is zero and the highest is 1.0:

$$0 \leq t_+ \leq 1.0 \quad (14.85)$$

$$0 \leq t_- \leq 1.0 \quad (14.86)$$

These equations appear very straightforward. However, they carry more information than they appear to, even in the simplest case of ideal electrolytes.

In order to extend the above definition of transport number beyond its “face value”, let us apply it to a simple electrochemical cell, such as that shown in Figure 14.1, which contains this ideal electrolyte of monovalent ions M^+ and X^- . We briefly discussed in Section 14.1 that this cell is semi-blocking to one of the ions, and the cell current would experience a gradual decay before eventually reaching a steady state. Now let us analyze such a current decay in a more rigorous manner (Figure 14.14). For convenience, we assume that the anion is the blocked ion here and the cation is the one participating in cell reactions, hence the *working ion*.

When one applies an external electric field at instant $t = 0$, both ions in the electrolyte respond instantaneously by migrating in opposite directions according to the sign of their charge. Since these ions

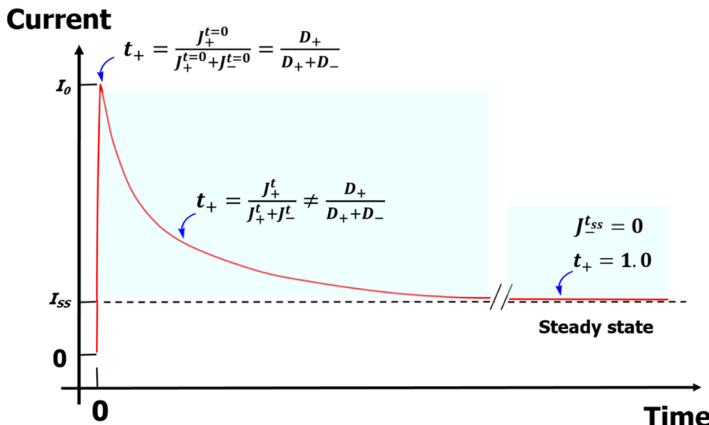


Figure 14.14 The current decay of an electrochemical cell under “DC polarization”, where one ion (cation) is not blocked by electrodes and the other (anion) is blocked. Note that t without a subscript represents time, while t_+ and t_- represent cationic and anionic transport numbers, respectively.

migrate independently without interacting with each other, their movements can be described by the simplified picture in Figure 5.8, or if one wants to consider a more realistic picture, Figure 5.9, which indicates that migration is actually a fraction of the composite movement of ions projected in or against the direction of the applied electric field.

At this instant ($t = 0$), if an electric charge of Q coulombs is passed across the cell, then one fraction of it, *i.e.* Qt_+ , is carried by the cations and the remainder, Qt_- , is carried by the anions. Also at this instant, the migration of these ions is the only factor responsible for the ionic fluxes across the cell, because any diffusive flux generated by their local concentration variations would be random in direction and hence make a zero contribution to the ionic current or to the half-reactions occurring at the electrolyte/electrode interfaces. Based on what we discussed in Section 5.2.5 [eqn (5.116) and its derivatives], the independent fluxes of cation ($J_+^{t=0}$) and anion ($J_-^{t=0}$) at this instant can be expressed, respectively, as

$$J_+^{t=0} = -\frac{D_+ c_+}{RT} \frac{d}{dx}(F\psi + \mu_+) = -\frac{FD_+ c_+}{RT} \frac{d\psi}{dx} \quad (14.87)$$

$$J_-^{t=0} = -\frac{D_- c_-}{RT} \frac{d}{dx}(F\psi + \mu_-) = -\frac{FD_- c_-}{RT} \frac{d\psi}{dx} \quad (14.88)$$

because the concentration gradient (or chemical potential gradient) for either ion is zero at $t = 0$:

$$\left[\frac{d\mu_+}{dx} \right]_{t=0} = \left[\frac{d\mu_-}{dx} \right]_{t=0} = \left[\frac{dc_+}{dx} \right]_{t=0} = \left[\frac{dc_-}{dx} \right]_{t=0} = 0 \quad (14.89)$$

At this instant, *and only at this instant*, the electric current in the cell would be divided into cationic and anionic contributions strictly according to their corresponding transport numbers:

$$t_+ = \frac{J_+^{t=0}}{J_+^{t=0} + J_-^{t=0}} = \frac{D_+}{D_+ + D_-} \quad (14.90)$$

Of course, to reach eqn (14.90) one needs to recall that in an ideal electrolyte consisting of monovalent cations and anions, the concentration of each ion is equal:

$$c_+ = c_- = c_{\text{salt}} \quad (14.91)$$

For most of the electrochemical devices that we are interested in, the lithium-ion battery being the most preeminent example, only one of these two ions participates in the half-reactions occurring at the electrolyte/electrode interfaces, hence only the fraction of current carried by that ion matters. The remainder of the current carried by the counterion is hence parasitic, which not only makes a zero contribution to propelling the cell reaction, but also creates a counter-effect to the migration induced by the applied electric field. Because these inert but mobile ions are neither consumed nor produced at electrolyte/electrode interfaces, their directional migration leads to their depletion and accumulation at two interfaces of the cell. The direct consequence of such a depletion and accumulation of the blocked ions is the establishment of a concentration gradient within the electrolyte, which generates an ionic diffusion that is no longer random and directionless, but in a direction opposite to the migration of this ion. Since we have assumed that the anion is the blocked ion, then

$$\left[\frac{d\mu_-}{dx} \right]_t = \left[\frac{dc_-}{dx} \right]_t \neq 0 \quad (14.92)$$

At this time, the ion transport number as defined in eqn (5.95) and (5.96) no longer determines the actual cationic and anionic contributions in the cell current. Instead, since anion migration is

counter-balanced by its diffusion, the cationic fraction of the cell current is rising, although the overall cell current is dropping (Figure 14.14).

In any practical electrochemical cell where one ion is blocked and the other is not (hence “semi-blocking”), the existence of the above concentration gradient and its resistance to the applied electric field is called “*concentration polarization*”. It reduces the cell efficiency and other performances from what could be expected from an ideal electrochemical cell where *all ions* are allowed across the interfaces, and is an inevitable parasitic process for all semi-blocking electrochemical cells. As time elapses, this concentration gradient increases.

Given sufficient time ($t = t_{ss}$), the concentration polarization by the blocked ion would be built up to a level such that the corresponding diffusional ionic flux that it produces reaches an equilibrium with the migrational ionic flux:

$$\frac{dF\psi}{dx} = -\frac{d\mu_-}{dx} \quad (14.93)$$

so that the net ionic flux of the blocked ion becomes zero:

$$J_-^{t_{ss}} = -\frac{D_- c_-}{RT} \frac{d}{dx}(F\psi + \mu_-) = 0 \quad (14.94)$$

This would be the “steady state” represented by the plateau in cell current in Figure 14.1, bottom right panel. Apparently at this equilibrium, the cell current is contributed only by the flux of the ion that is not blocked by the electrodes, which is the cation in our assumption. Therefore, at the steady state, the magnitude of this cell current is dictated solely by the self-diffusion coefficient of this working ion and the electric field applied on the electrolyte:

$$J_+^{t_{ss}} = -\frac{FD_+ c_+}{RT} \frac{d\psi}{dx} \quad (14.87)$$

In reality, the non-blocked ion could also build up a concentration gradient, which could be either against or along its migrational movement, depending on the kinetics of the ion at each electrode, then the cationic flux would also have contributions from both migrational and diffusional components. We will return to this topic for a more rigorous analysis in Section 14.2.4.

Since the working ion is the only ion that actually performs the current-carrying task for the cell chemistry at the steady state, its transport number (t_+^{ss}) now becomes unity:

$$t_+^{ss} = 1.0 \quad (14.95)$$

while that of the blocked ion becomes zero:

$$t_-^{ss} = 0.0 \quad (14.96)$$

The time it takes for an electrolyte to reach its steady state depends on how fast the blocked ion could travel from electrolyte bulk and assemble on the electrolyte/electrode interfaces to counter completely any further accumulation. It ranges from seconds to hours to days.

Now, one might be perplexed: if the transport number of the working ion in a semi-blocking electrochemical cell would eventually become unity, then why is its transport number t_+ as defined in eqn (5.96) still meaningful?

Rearranging eqn (5.96), we could obtain

$$D_+ = \frac{t_+ D_-}{1 - t_+} = \frac{t_+ D_-}{t_-} \quad (14.97)$$

which after being inserted into eqn (14.87) leads to

$$J_+^{t_{ss}} = -\frac{t_+ D_-}{t_-} \frac{Fc_+}{RT} \frac{d\psi}{dx} \quad (14.98)$$

Therefore, the transport numbers (together with the associated self-diffusion coefficients) are still meaningful, because they dictate the eventual magnitude of the maximum cell current. This is an important parameter for the electrolyte, as it tells us how much current an electrolyte can provide to support the cell reaction.

Meanwhile, the establishment of the steady-state equilibrium depends on how fast a concentration gradient for the blocked ion could be built up to counter the migrational flux. In other words, the time it takes for the cell to reach equilibrium depends on the rate of the blocked ion to move from the electrolyte bulk into these two interfacial regions. The rate of such depletion and accumulation is described by the ambipolar diffusion of the ions:

$$D_{\text{ambp}} = \frac{\mu_+ D_- + \mu_- D_+}{\mu_+ + \mu_-} = \frac{2D_- D_+}{D_+ + D_-} \quad (5.172)$$

which can be transformed into

$$D_{\text{ambp}} = \frac{2D_+}{\frac{D_+}{D_-} + 1} = \frac{2D_+}{\frac{t_+}{t_-} + 1} = 2D_+ t_- \quad (14.99)$$

Hence the transport number of the blocked ion is also meaningful in determining how fast the equilibrium at the steady state could be established.

In summary, under semi-blocking conditions, even in the ideal electrolyte, the transport numbers as defined by eqn (5.95) and (5.96) *do not reflect the actual current fraction during the cell operation*. Instead, they are transient properties for both ions at the very first instant when the external electric field is just applied, and their influences are only reflected in both the rate of establishing the steady state and the magnitude of the maximum current when the equilibrium at the steady state is reached.

Therefore, if someone reads in the literature that the Li^+ transport number is 0.3 in a typical lithium-ion battery electrolyte (*e.g.* LiPF_6 dissolved in a mixture of EC and DMC, which is in fact not an ideal but a practical electrolyte, but let us ignore that fact temporarily), they should not translate this number into a superficial understanding that, in this lithium-ion battery, only 30% of the electric current is carried by Li^+ , while PF_6^- carries the remaining 70%. No – it simply means that, if the overall ion conductivity of this electrolyte as measured by AC impedance spectroscopy is 10 mS cm^{-1} , the Li^+ conductivity (σ_{Li}) available is only 3 mS cm^{-1} , which can provide a maximum current density of

$$i_{\text{max}} = E \times \sigma_{\text{Li}} = 4.0 \frac{V}{0.01 \text{ cm}} \times 0.3 \times 10^{-3} \text{ mS cm}^{-1} = 0.12 \text{ A cm}^{-2} \quad (14.100)$$

where E is the electric field applied on the electrolyte by the cathode and anode of the lithium-ion battery, and we assume that the cell voltage of such a lithium-ion battery is 4.0 V (which is the typical working voltage of most lithium-ion batteries nowadays).

Finally, we need to recall that, before starting the above discussion, we assumed above that the movement of the non-blocked ion (cation in our discussion) does not incur any concentration gradient of it across the electrolyte. In reality, of course, this is impossible, because the depletion or accumulation of the working ion at the two

electrolyte/electrode interfaces varies with the rate of charge-transfer at these interfaces/interphases, and such a rate very likely differs from the flux of this ion within the electrolyte. For lithium-ion batteries, the rate of the charge transfer at a graphitic anode (~ 0.01 V vs. Li) is normally the slowest owing to the presence of thick interphases, hence the generation of Li^+ (during discharge) or consumption of Li^+ (during charge) often cannot keep pace with the Li^+ flux in the bulk electrolyte. However, for anode hosts with no or little presence of interphases, such as lithium titanate ($\text{Li}_4\text{Ti}_5\text{O}_{12}$, ~ 1.5 V vs. Li), the generation or consumption of Li^+ is fast enough to ensure an almost constant Li^+ concentration profile in the interfacial region near the anode, unless an extremely high current (charge or discharge) is applied on the cell. Likewise, the rate of the charge transfer at the cathode also varies with the chemistry, where those with no or little presence of interphase, such as lithium iron phosphate (LiFePO_4 , ~ 3.5 V vs. Li), would approach a constant Li^+ concentration profile in the interfacial region near the cathode, while those with obviously thicker interphases, such as high-voltage lithium cobalt phosphate (LiCoPO_4 , ~ 5.1 V vs. Li), lithium nickel manganese oxide ($\text{LiNi}_{0.5}\text{Mn}_{1.5}\text{O}_4$, ~ 4.5 V vs. Li) or high-nickel NMC ($\text{LiNi}_x\text{Mn}_y\text{Co}_z\text{O}_2$, >4.2 V vs. Li), would incur an Li^+ concentration gradient in the interfacial regions near the cathode. Lithium cobalt oxide (LiCoO_2 , ~ 3.8 V vs. Li) presents an intermediate scenario with its moderate operating voltage. Overall, the generation of these Li^+ concentration gradients in these two interfacial regions near the anode and cathode could have very different effects on the Li^+ -migrational flux, depending on the specific anode and cathode chemistries and the kinetics in the electrolytes.

In order to demonstrate how the diffusional and migrational fluxes arising from cationic and anionic movement could contribute to the eventual current-carrying task in a practical electrochemical cell, we now consider a lithium-ion battery that consists of a graphitic anode and a layered-structure transition metal oxide cathode as an example, and schematically depict the relative movements of these fluxes (Figure 14.15). Here we assume that the Li^+ diffusion is also against the migration in considering the interphases, especially that on the graphitic anode surface. In a symmetrical lithium–lithium cell the situation would be reversed, where the combination of faster kinetics at lithium-metal electrodes and minimum interphase presence in polyether-based electrolytes may create concentration gradients that favor the Li^+ movement in the same direction as its migration.

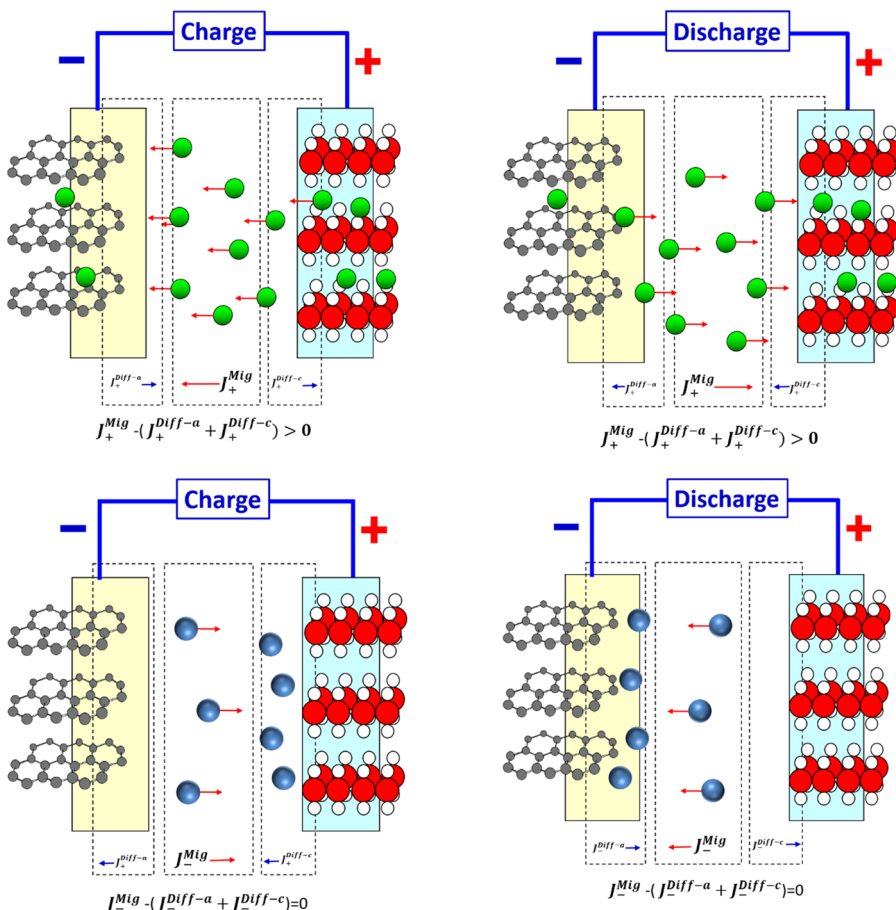


Figure 14.15 Schematic diagram of cationic and anionic flux contributions to the actual cell current inside a lithium-ion battery during charging and discharging scenarios. The cations (top panels) and anions (bottom panels) are shown in separate illustrations, and interphases are omitted for clarity. The subscripts on the fluxes indicate the sign of the charge on the ion, and the superscripts indicate whether the flux is generated by migration or diffusion at the cathode or anode side.

One can see how these various fluxes are convoluted in either an additive or reductive manner to dictate the cell operation. Remember that so far, we are still only dealing with ideal electrolytes, *i.e.* the cations and anions are individual free ions that move independently of the influence of each other. The inter-ionic forces have not been factored in.

14.2.3 In Practical Electrolytes: Transport Number (t_+ or t_-) versus Transference Number (T_+ or T_-)

In electrolytes of practical concentrations, diverse ionic species form, as described by eqn (14.83). Under the applied electric field, each of these charged species would participate in migration according to their own charges, while the neutral species would make a zero contribution to the migration.

Hence an interesting scenario arises: since some of the working ions (Li^+) are now part of the ionic species that bear a negative charge, such as $[\text{Li}^+2\text{X}]^-$, they would move like an “anion”, in the direction opposite to that in which an Li^+ would move. The same applies to those anions in complex species that bear a positive charge, such as $[2\text{Li}^+\text{X}]^+$. In other words, the cations and anions are now convoluted on an entirely new level in dictating the cell current. The neutral species, meanwhile, do not respond to the applied electric field and make no contribution to the migrational flux.

As a result of such convolution, the same electrochemical cell as shown in Figure 14.1 containing such a practical electrolyte would experience a very different chronological decay in cell current, as the non-blocked species and blocked species can no longer be expressed in simple stoichiometry based on the chemical formula of the conducting salt.

As discussed above, in an electrochemical cell that relies on a single working ion to operate, such as a lithium-ion battery, what one really needs to know is, for each coulomb of charge passed, how many Li^+ ions are *actually* transported from one side of the cell to the other? In the previous section, this question met a relatively simple answer if the electrolyte is ideal: at the initial instant ($t = 0$), only t_+ coulombs are carried by the cation, while after sufficiently long time, the entire coulombs are carried by the cation ($t_+ = 1.0$).

However, for a practical electrolyte that experiences a speciation process as in eqn (14.78), the answer becomes rather complicated. Even at the initial instant ($t = 0$), where pure ionic migration dictates the electric current without the interference from any diffusional fluxes of ions, we know that 1 coulomb of charge consists of the transport of Li^+ and $[2\text{Li}^+\text{X}]^+$ along the applied electric field, which moves three Li^+ in that direction, and the transport of X^- and $[\text{Li}^+2\text{X}]^-$ against the applied electric field, which moves one Li^+ in that direction. Suppose that each of these ionic species has its own transport number, then the actual number of Li^+ that have been moved by this 1 coulomb of charge is given by

$$T_{\text{Li}} = t_{\text{Li}^+} + 2t_{[2\text{Li}^+\text{X}^-]^+} - t_{[\text{Li}^+2\text{X}^-]^-} \quad (14.101)$$

This new quantity T_{Li} is called the *transference number* of Li^+ . It quantifies the fraction of an ion of interest moved due to the migration when 1 coulomb of charge is passed across the cell. Of course, more ionic species would be formed in electrolytes at higher salt concentrations, which would further complicate the speciation of eqn (14.83) and subsequently eqn (14.101). Like the transport number, a relation also exists between the transference numbers for the cation and anion in a binary electrolyte:

$$T_+ + T_- = 1.0 \quad (14.102)$$

In the literature, transport number and transference number are often used interchangeably by most authors, but one needs to know how to differentiate them: whereas transport number describes the relative mobility of individual ionic species, which could be a single ion or ionic complexes, transference number describes the overall contribution of a given ion to the migrational flux. The most important difference between the two numbers can be reflected in the fact that, whereas transport numbers are clearly confined by eqn (14.85) and (14.86) to reside between 0 and 1, there is no such confinement of transference numbers, considering that Li^+ ions in some of these ionic species are actually being transported in the “wrong” direction. Theoretically, T_{Li} in eqn (14.101) could be negative (<0) provided that the triplet $[\text{Li}^+2\text{X}]^-$ moves faster than Li^+ and $[2\text{Li}^+\text{X}]^+$, which is possible under certain conditions given that the positively charged ions often attract much more stable and clumsy solvation sheaths than do the negatively charged ions. In this case, the passage of current across the cell leads to the migration of Li^+ in the opposite direction within the cell.

Then one would wonder how such a cell could work if the transference number of its working ion is negative.

In fact, a negative transference number is not as “exotic” or “catastrophic” as one would imagine. An electrochemical cell could still function despite its working ions having a negative transference number provided that such a negative migration flux could be counterbalanced by a positive diffusion flux of this ion or a complex ionic species that contains such ion.

In Section 5.2.5 we encountered such examples, where the working ions (Ag^+ or Al^{3+}) exist as complex ionic species such as $[\text{AlCl}_4]^-$ or $[\text{Ag}(\text{CN})_2]^-$ that carry negative charges. The electrochemical reduction of such complex anions depends solely on the diffusion flux of them

that travels in the opposite direction to the migration flux. Here the constant consumption of these complex anions at the electrolyte/electrode interface ensures that a concentration gradient is maintained and provides a steady supply of these complex anions against the applied electric field.

In fact, the contribution of diffusional fluxes is not confined to these ionic species that carry the opposite charge of the working ions. To a very significant extent, the neutral species, *i.e.* the ion pair $[Li^+X^-]^0$ or larger aggregates such as $[nLi^+nX^-]^0$, while not responding to the applied electric field *via* migration, are also driven by the concentration gradients and participate in the diffusion. Hence they are also transferring Li^+ across the cell and contribute to counterbalancing the negative migrational flux.

Considering ion transport number and ion transference number, the latter is of more relevance to cell chemistry. After all, the operation of lithium-ion chemistry depends on how many moles of Li^+ are being moved, no matter in what form they arrive at the electrolyte/electrode interfaces/interphases. Only in an ideal electrolyte are the transport number and transference number equal, because the speciation would simply collapse into two individual ions Li^+ and X^- .

The above discussion still only considers the initial instant ($t = 0$) when the electric field is applied to the electrolyte. With time elapsing and concentration gradients for each species gradually built up, the net flux of the working ion being transported across the cell would have more intensely convoluted contributions from these various species. Meanwhile, the dynamic interconversion and equilibria among these ionic species as well as component ligands coexist simultaneously, thus rendering the ion transport phenomena in such an electrolyte of seemingly simple binary composition far more complicated and unpredictable than anything that we have dealt with so far.

In fact, the existing theories and models in modern ionics still encounter difficulty in completely resolving such complexities, and an accurate prediction of how the ions are moving in such situations is still unavailable. This difficulty is reflected in the fact that, differing from ion conductivity and diffusivity, there is still no standardized method available to determine ion transport numbers or ion transference numbers with reliability and reproducibility. The determination of these numbers has become such a controversial subject in recent decades that widely scattered results are often reported for the same electrolyte system, depending on which model or technique is being used. Although this book does not intend to delve into these different theories and models still under development, we do need to spend a

little more time on this very important property, which together with ion conductivity and diffusivity constitutes the triad of parameters in defining an electrolyte. In studying and comparing these imperfect theories and models, we could understand better what the challenges are, and the extent to which we can trust an ion transport or ion transference number reported in the literature.

14.2.4 A Few Classical Approaches to Transference Numbers

As differentiated in the previous section, ion transport number (t_+ or t_-) describes the mobility of an individual ionic species, *i.e.* its agility in responding to an applied electric field, be it either a single ion or a complex ionic species. On the other hand, ion transference number (T_+ or T_-) refers to the total moles of an ion of interest (usually the working ion) being transported across the cell with the passage of 1 faraday of charge, no matter the ion of interest travels alone (as the free ion) or in a complex species that could migrate either along with or against the applied electric field. Only in ideal electrolytes, where the speciation no longer exists, are these two quantities identical.

Of the two numbers, the ion transference number is of more relevance in evaluating how well an electrolyte functions in a practical electrochemical cell. There have been numerous efforts at determining this important quantity. The classical methods established usually examine this quantity on a time scale that would allow the establishment of a steady state. Ironically, despite its limited applicability, the oldest method for determining ion transference number, the *Hittorf approach*, remains one of the most accurate, and does not involve any assumption of electrolyte ideality.

14.2.4.1 Hittorf-Tubandt Approach: Direct Chemical Analysis

Historically, Hittorf was perhaps the first to recognize that cations and anions might be moving at different velocities under the influence of the same electric field. In fact, the English word “transference number” was a simple translation from the German word “*Überführungszahl*”, which was coined by Hittorf to quantify the difference in cationic and anion traveling velocities.

From 1853 to 1859, writing in three consecutive seminal publications, Hittorf corrected the long-standing misbelief regarding the ion transport mechanism that *all ions move at the same velocity under*

the same electric field.^{11–13} To prove this argument experimentally, he designed a multi-compartment electrochemical cell, and employed chemical analysis as a direct tool to determine the difference in electrolyte compositions at various locations across the cell after an electric charge is passed.

Figure 14.16a displays schematically the initial design of such a cell by Hittorf, in which a series of compartments are separated by membranes for convenient sampling of the electrolytes. The cell consists of aqueous CuSO_4 electrolyte between a copper positive electrode and a platinum or silver negative electrode, which adopts a vertical orientation. With an applied electric field, copper is oxidized and becomes Cu^{2+} that migrates towards the negative electrode, while the SO_4^{2-} anion migrates in the opposite direction until it is counterbalanced by the diffusional movement driven by its concentration gradient. The copper electrode was intentionally placed at the bottom, so that the more concentrated (and therefore heavier) section of the electrolyte, due to the generation of Cu^{2+} by the copper electrode, would naturally sit at the bottom and would not be disturbed by the gravitational convection. Hittorf further divided the cell into four sections with membranes, and carefully controlled both the applied voltage and the amount of charge passed, so that the Cu^{2+} concentration in the middle two compartments (compartments II and III)

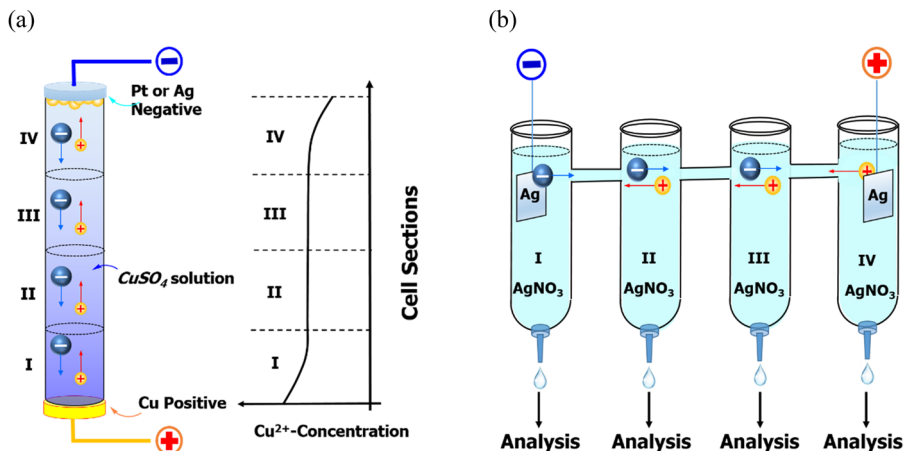


Figure 14.16 The classical approaches to determine ionic transference number. (a) The original Hittorf cell, the compartments of which were separated by membranes; (b) the modified multi-compartment Hittorf cell that adopted a horizontal orientation with manifold outlets that allow for convenient sampling and quantitative chemical analysis.

are identical. This is necessary to ensure that there is zero concentration gradient for Cu^{2+} , therefore the difference between the Cu^{2+} concentrations in compartments I and IV would be entirely caused by migration.

With such meticulous considerations, Hittorf passed a known amount of charge Q across the cell that could be accurately measured by a coulometer, and then took apart the four cell compartments for chemical analysis. Thus, the transference number of Cu^{2+} can be calculated by

$$T_+ = \frac{Q - [c_1 - c_3] z_{\text{Cu}} V F}{Q} = 1 - \frac{2(c_1 - c_3) V F}{i \Delta t} \quad (14.103)$$

where c_1 and c_3 are the Cu^{2+} concentrations in compartments I and III, respectively, V is the volume of the cell compartments (assuming that all four compartments are the same) and Q is the total passage of charge at a current i during a time interval Δt . The concentration difference between compartments I and II can be used as the second set of data for an accuracy check.

The results verified his hypothesis that cations and anions have different migrational velocities. In most electrolytes consisting of various inorganic salts dissolved in water or alcohols, he found that cations always move more slowly than anions, with transference numbers ranging between 0.3 and 0.4, and for certain inorganic salts he even obtained negative cationic transference numbers, such as zinc chloride and silver cyanide and chloroplatinate. Interestingly, he noted that these transference numbers showed a strong dependence on salt concentration. For example, both zinc chloride (ZnCl_2) and cadmium iodide (CdI_2) displayed positive cation transference numbers in dilute aqueous solutions; however, as the salt concentration increased, these numbers gradually shifted into the negative range. A similar shift also occurred when the solvent was changed from water to a less polar solvent such as ethanol or amyl alcohol.

Hittorf correctly attributed such an “abnormal” phenomenon to the formation of complex ionic species, although according to a modern perspective the exact formula that he proposed for those complex ions were incorrect. After all, one must remember that in the mid-1800s the correct electronic structures of atoms were still not known, and would only be elucidated about half a century later by Bohr and Rutherford. On this basis, the understanding achieved by Hittorf was incredibly prescient.

As we know today, these negative ion transference numbers are clear indicators for the formation of complex ionic species in those

electrolytes, such as $[ZnCl_3]^-$, $[AgCN_2]^-$, $[PtCl_6]^{2-}$, etc. The formation of such complex ionic species would be encouraged by a high salt concentration, which compresses cations and anions together in the absence of solvent molecules to separate them, or encouraged by the poorly polar solvent molecules, which, owing to low dielectric constants, fail to act as an electrostatic shield to keep the neighboring cations and anions from feeling the attraction of each other.

Unfortunately, Hittorf's work met with strong opposition at the time, because researchers simply could not understand why cations and anions would move at different velocities. Apparently, at the time, they were more accustomed to thinking of ions as simple charged particles without structure and solvation sheath.

Later, it was suggested that the membranes used in the Hittorf cell to separate the cell compartments might be selective in allowing certain ions to pass at faster speeds while slowing down others, thus distorting the results, hence modifications were made to the Hittorf cell by removing these membranes. Figure 14.16b shows one such version with manifolds to access electrolyte compositions, while other improvements resorted to alternative means of determining electrolyte composition *via* conductivity (if a standard conductivity–concentration curve is established first), so that laborious chemical analysis could be avoided.

In general, Hittorf's method requires laborious steps to determine the exact chemical composition of those compartments. However, once performed in a meticulous manner, it yields a precision as high as ± 0.0001 .

Meanwhile, the disadvantages of this method are also obvious: it is time consuming, requires a large volume of electrolyte and relies on great caution in performing the experiment, especially considering the significant amount of work needed in analyzing the cell compartments. More importantly, it can only be applied to limited electrolytes, where accurate chemical analysis is possible, such as simple inorganic cations like Cu^{2+} , Ag^+ and Zn^{2+} , the quantitative determination of which is made possible by well-established analytical protocols such as titration. Lithium-based electrolytes, unfortunately, do not fall into this category.

A similar method was proposed by Tubandt in 1932 to measure ion transference numbers in a solid electrolyte (be it ceramic or polymer),¹² which could be viewed as a variation of the Hittorf approach. The solid nature of the electrolytes makes the sampling and analysis much easier, as one could directly dismantle the cell after passing charge, and slice the electrolyte into distinct sections for weighing.

From the weight change one could calculate the quantity of immigration or emigration of the working ions.

14.2.4.2 Lodge-Mason Approaches: Moving Boundaries

To circumvent the problems associated with chemical analysis, in 1886 Lodge proposed a new approach that leveraged visible electrolyte/electrolyte interfaces, using which one can directly evaluate how fast cations and anions move under an applied electric field (Figure 14.17).¹⁴ The initial reaction that he adopted is the precipitation of barium sulfate (BaSO_4) from the reaction of barium chloride (BaCl_2) with an indicator electrolyte containing sulfate anions such as Na_2SO_4 . By monitoring the moving boundary of BaSO_4 in the electrochemical cell, one can calculate the transference number of cations as

$$T_+ = \frac{z_+ c_+ \Delta L A F}{Q} = \frac{z_+ c_+ \Delta L A F}{I \Delta t} = \frac{z_+ c_+ A F}{I} v_+ \quad (14.104)$$

where ΔL is the distance that the BaSO_4 boundary moves in a time interval Δt , A is the sectional area of the cell and v_+ is the velocity of the boundary. An approximation was made here by assuming that

$$Q = I \Delta t 14.105$$

which ignores any possible non-linear behaviors of the current and the variation of the ion conductivity in the electrolyte during the passage of current.

Soon it was realized that the actual situation is complicated by the formation of solid particles in the electrolyte, which changes both the

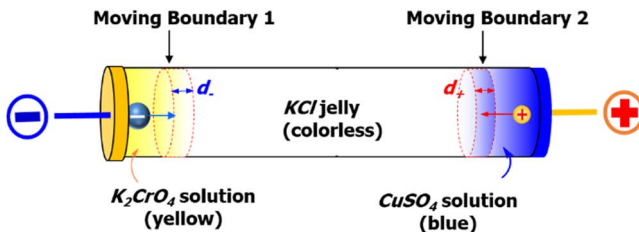


Figure 14.17 The Lodge-Mason moving boundary approach, where electrolytes of different natural colors or refractive indices were employed, so that visible boundaries could be established at electrolyte/electrolyte interfaces. With careful selection of the electrolytes and meticulous control of the experimental conditions, the relative velocity at which each boundary moves reflects the ratio between the migrational velocities of ions.

conductivity and the viscosity of the frontier regions of the moving boundaries, and sometimes even clogs the electrochemical cell. As a result, precipitation reactions were abandoned, and modifications were made to this approach with preferences for those indicators that do not interfere with the electrolyte properties too much, examples of which include acid-base indicators such as bromophenol blue, or electrolytes containing ions of natural colors or of strong optical contrast against the supporting electrolytes.

Figure 14.17 shows schematically an improved “double moving boundary” version of Lodge’s approach by Mason, in which K_2CrO_4 (yellow) and CuSO_4 (blue) solutions were placed at each end of the electrochemical cell, while the main electrolyte consisting of KCl (colorless) immobilized in gel.¹⁵ Upon passage of electric current, the yellow and blue fronts advance towards each other, and their relative velocity reflects the relative transference of CrO_4^{2-} anion and Cu^{2+} cation. Supposing that the distance traversed by the $\text{CrO}_4^{2-}/\text{KCl}$ boundary is d_- , and that by the CuSO_4/KCl boundary is d_+ , then

$$\frac{d_+}{d_-} = \frac{\Lambda_+^0}{\Lambda_-^0} \quad (14.106)$$

where Λ_+^0 and Λ_-^0 are the *limiting molar ion conductivities* of Cu^{2+} and CrO_4^{2-} . Since the total molar ion conductivity Λ_T^0 of CuCrO_4 under limiting conditions, *i.e.* when the salt concentration approaches zero, is easy enough to determine experimentally by extrapolation, which according to the *Kohlrausch law of independent ionic migration* should be related to these two individual limiting molar ion conductivities by

$$\Lambda_T^0 = \Lambda_+^0 + \Lambda_-^0 \quad (14.107)$$

hence the transference numbers for each individual ion can be calculated as

$$T_+ = \frac{\Lambda_+^0 + \Lambda_-^0}{\Lambda_T^0} = \frac{d_+}{d_+ + d_-} \quad (14.108)$$

Obviously the electrolyte solutions used in this experiment need to be dilute enough to approximate ideality.

Nowadays one classical experiment on transference number measurement is still being taught in electrochemistry laboratory classes at some universities, which leverages the difference in refractive indices of different electrolyte solutions instead of natural colors. In such

an experiment, a modified Hittorf-like cell in a vertical orientation is adopted, and three electrolyte solutions of different densities are used, the heaviest of which (such as lithium chloride, LiCl) is placed at the bottom, and the lightest (such as sodium acetate, NaOAc) at the top. The middle electrolyte (such as sodium chloride, NaCl) is the electrolyte to be investigated. Not only must it share a common anion with the bottom electrolyte and a common cation with the top electrolyte, but also its density must be situated between these two “indicator” electrolytes, so that gravitational convection can be minimized. In order to keep the boundaries sharp and well defined, additional sets of conditions must also be met, the most important of which is that, at the lower boundary, the cation of the indicator electrolyte (*i.e.* Li⁺ in LiCl) must not move faster than the cation whose transport number is to be determined (*i.e.* Na⁺ in NaCl), while at the upper boundary, the anion of the indicator electrolyte (*i.e.* OAc⁻ in NaOAc) must not move faster than the anion whose transport number is to be determined (*i.e.* Cl⁻ in NaCl). Otherwise, under the applied electric field, these cations and anions from the indicator electrolyte would overtake their counterparts in the investigated electrolyte, leading to rather diffuse boundaries and poor accuracies. Only by satisfying all these stringent requirements can one ensure that clear boundaries are formed at LiCl/NaCl and NaCl/NaOAc interfaces.

A similar experiment can also be conducted using hydrogen chloride (HCl) and cadmium chloride (CdCl₂) to form a single boundary as in the original Lodge approach.

The applicability of the moving boundary method obviously suffers from these severe restrictions. So far only a limited number of electrolytes could be studied by the Lodge–Mason approaches. A more universal method for determining ion transference numbers that does not require so many laborious precautions is needed.

14.2.4.3 Armand Approach: Electrochemical Concentration Cell

In 1986, Armand and colleagues proposed an interesting way to measure Li⁺ transference numbers for polymer electrolytes.¹⁶ They constructed a lithium–lithium symmetrical cell that consists of two polymeric electrolytes containing the same lithium salt but at different concentrations. In electrochemistry, this is known as a *concentration cell*. In order to understand how this method works, we need first to examine how the cell emf is related to the transference numbers of the ions involved.

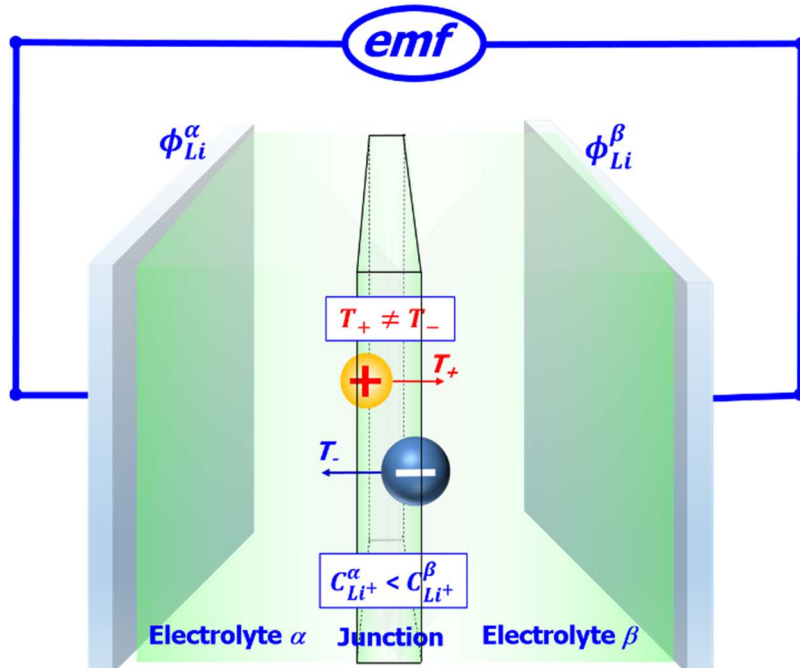


Figure 14.18 A concentration cell consisting of two identical electrodes that sandwich two electrolytes of the same composition but different salt concentrations. The cell is at open circuit, and there is zero current passing through the cell, hence the cell voltage is the emf. This is a “concentration cell with ion transference” because the transference numbers of the two ions are unequal at the junction, thus generating a junction potential E_J .

In such a cell (Figure 14.18), the identical electrode material (Li^0) is at equilibrium with the same electrolytes at different salt concentrations (electrolyte α and electrolyte β), and intuition tells us that there must be a potential difference generated between the two electrodes that can be quantified by the Nernst equation:

$$\phi_{Li}^{\alpha} = \phi_{Li}^0 + \frac{RT}{F} \ln C^{\alpha} \quad (14.109)$$

$$\phi_{Li}^{\beta} = \phi_{Li}^0 + \frac{RT}{F} \ln C^{\beta} \quad (14.110)$$

in which the activity of the lithium metal (Li^0) has been assumed to be 1.0. Apparently, the right lithium-metal electrode (Li_{β}^0) would be situated at a higher potential than the left lithium-metal electrode (Li_{α}^0).

Upon closer examination, the potential difference generated by the Nernstian response is in fact just one part of the overall potential difference, because at the interface between the two electrolytes an additional potential also arises, which is induced by the sharp concentration difference between the two electrolytes. Hence there is a strong tendency for the ions to diffuse from the more concentrated phase (β) towards the more dilute phase (α). Such a potential difference is in fact present anywhere and whenever a concentration gradient exists, hence it is also sometimes called the “*diffusional potential*”, but in classical electrochemical texts it is more often referred to as the “*junctional potential*”.

Thus, the emf of a concentration cell should consist of two parts, Nernstian (E_N) and junction (E_J):

$$\text{emf} = E_N + E_J \quad (14.111)$$

The Nernstian part is simply given by

$$E_N = \phi_{\text{Li}}^\beta - \phi_{\text{Li}}^\alpha = \frac{RT}{F} \ln \frac{C_{\text{Li}^+}^\beta}{C_{\text{Li}^+}^\alpha} \quad (14.112)$$

or if we assume that the electrolytes are not ideal:

$$E_N = \phi_{\text{Li}}^\beta - \phi_{\text{Li}}^\alpha = \frac{RT}{F} \ln \frac{a_{\text{Li}^+}^\beta}{a_{\text{Li}^+}^\alpha} \quad (14.113)$$

where a^α and a^β are the corresponding activities of the lithium salts in the two electrolytes.

The junction part, on the other hand, is decided by the relative tendency of each ion to diffuse from the more concentrated phase towards the more dilute phase in an attempt to eliminate such a concentration gradient. In other words, the junction potential is related to the relative mobility of the ions involved, or their transference numbers.

When one considers the entire equilibria in this concentration cell, it becomes clear that we can divide the processes involved into the electrochemical part, which consists of two half-reactions at each electrode, and the corresponding diffusional charge-transport part at the junction. Now we must keep in mind that the cell is at open circuit, and all the “current” or “charge passing” that we discuss below merely reflect the *tendency* of the ions and the electrodes to do so without actually passing the charge. Once current starts to flow, the equilibrium is breached.

At the left electrode (Li_α^0), because of its lower potential, it tends to experience an oxidation process and release more Li^+ into the electrolyte:



while the higher potential of the lithium-metal electrode at the right side (Li_β^0) drives the reduction of more Li^+ from the electrolyte:

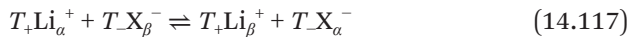


The overall electrodic reaction would be the summation of eqn (14.109) and (14.110):



the corresponding potential difference of which is described by the Nernst equation discussed above [eqn (14.112) or (14.113)].

Accompanying the above electrode half-reactions, there must be corresponding charge transport within the electrolyte in order to maintain electroneutrality, *i.e.* Li^+ produced by the left electrode (Li_α^+) migrates towards the right, whereas the anion (X^-) migrates in the reverse direction. The relative velocities of Li_α^+ and X^- are dictated by their respective ion transference numbers. Hence, at the junction, for an *imaginary* 1 F of charge passing through the cell, there are T_+ mol of Li_α^+ crossing into electrolyte β , accompanied by T_- mol of X_β^- crossing into electrolyte α . In other words, we can write the following equilibrium:



The free energy change corresponding to eqn (14.117) should be

$$\Delta G = -nFE_J = RT\ln Q \quad (14.118)$$

where $n = 1$ in our case (assuming monovalent lithium salt), and Q is the reaction quotient that can be expressed as

$$Q = \frac{\left[a_{\text{Li}^+}^\beta \right]^{T_+} \left[a_{\text{X}^-}^\alpha \right]^{T_-}}{\left[a_{\text{Li}^+}^\alpha \right]^{T_+} \left[a_{\text{X}^-}^\beta \right]^{T_-}} \quad (14.119)$$

Inserting eqn (14.119) into eqn (14.118):

$$-FE_J = RT \ln \frac{\left[a_{\text{Li}^+}^\beta \right]^{T_+} \left[a_{\text{X}^-}^\alpha \right]^{T_-}}{\left[a_{\text{Li}^+}^\alpha \right]^{T_+} \left[a_{\text{X}^-}^\beta \right]^{T_-}} \quad (14.120)$$

Rearranging, we obtain the expression for the junction potential that depends on the ion transference numbers of the two ions at the junction:

$$E_J = -\frac{RT}{F} \ln \frac{\left[a_{\text{Li}^+}^\beta \right]^{T_+} \left[a_{\text{X}^-}^\alpha \right]^{T_-}}{\left[a_{\text{Li}^+}^\alpha \right]^{T_+} \left[a_{\text{X}^-}^\beta \right]^{T_-}} = -T_+ \frac{RT}{F} \ln \frac{\left[a_{\text{Li}^+}^\beta \right]^{T_+}}{\left[a_{\text{Li}^+}^\alpha \right]^{T_+}} - T_- \frac{RT}{F} \ln \frac{\left[a_{\text{X}^-}^\alpha \right]^{T_-}}{\left[a_{\text{X}^-}^\beta \right]^{T_-}} \quad (14.121)$$

If both electrolytes are ideal, we can replace the activities with the salt concentration, and remember that, since the salt is completely dissolved into free ions, the cation concentration would be equal to the anion concentration in the same electrolyte. Hence

$$a_{\text{Li}^+}^\alpha = a_{\text{X}^-}^\alpha = C_{\text{Li}^+}^\alpha = C_{\text{X}^-}^\alpha \equiv C^\alpha \quad (14.122)$$

$$a_{\text{Li}^+}^\beta = a_{\text{X}^-}^\beta = C_{\text{Li}^+}^\beta = C_{\text{X}^-}^\beta \equiv C^\beta \quad (14.123)$$

Eqn (14.121) can be simplified to

$$E_J = (2T_- - 1) \frac{RT}{F} \ln \frac{C^\beta}{C^\alpha} = (T_+ - T_-) \frac{RT}{F} \ln \frac{C^\alpha}{C^\beta} \quad (14.124)$$

Eqn (14.124) represents the two most popular expressions for junction potential used in the majority of electrochemical textbooks. Obviously, if the electrolyte systems possess identical cationic and anionic transference numbers (*i.e.* $T_+ = T_-$), the junction potential becomes zero.

As a digression from what we are discussing here, in classical electrochemical analysis experiments the junction potential often exists as a nuisance because it causes perturbations in the measurement of thermodynamic properties that are determined by the Nernst equation, therefore researchers were always attempting to eliminate its influence. It was for this reason that a salt bridge based on concentrated potassium chloride (KCl) has often been used, because the mobilities of these two ions are very close ($\mu_{\text{K}^+} = 7.619 \times 10^{-4} \text{ cm}^2 \text{ s}^{-1} \text{ V}^{-1}$ and $\mu_{\text{Cl}^-} = 7.912 \times 10^{-4} \text{ cm}^2 \text{ s}^{-1} \text{ V}^{-1}$, leading to $T_{\text{K}^+} \approx 0.49$ and $T_{\text{Cl}^-} \approx 0.51$), hence the junction potential difference is negligible therein.

A concentration cell equipped with such a salt bridge is called a “*concentration cell without ion transference*”. In comparison, the concentration cell shown in Figure 14.18 is a “*concentration cell with ion transference*”. Both are useful for the determination of ion transference number.

The emf of the entire concentration cell can thus be obtained by inserting eqn (14.113) and (14.124) into eqn (14.111):

$$\text{emf} = 2T_- \frac{RT}{F} \ln \frac{C^\beta}{C^\alpha} \quad (14.125)$$

If these electrolytes are not ideal, one needs to maintain the activities for both ions, and the expression of the emf takes a more complicated form:

$$\text{emf} = E_N + E_J = \frac{RT}{F} \ln \frac{a_{\text{Li}^+}^\beta}{a_{\text{Li}^+}^\alpha} - T_+ \frac{RT}{F} \ln \left[\frac{a_{\text{Li}^+}^\beta}{a_{\text{Li}^+}^\alpha} \right]^{T_+} - T_- \frac{RT}{F} \ln \left[\frac{a_{\text{X}^-}^\alpha}{a_{\text{X}^-}^\beta} \right]^{T_-} \quad (14.126)$$

Because it is experimentally impossible to measure the activity coefficients of individual ions, often the mean activity coefficient γ_\pm is adopted:

$$\gamma_\pm = \sqrt{\gamma_+ \gamma_-} \quad (14.127)$$

so that the activity of these two ions can be expressed as

$$a_\pm = \sqrt{a_+ a_-} = \sqrt{C_+ \gamma_+ C_- \gamma_-} = \gamma_\pm \sqrt{C_+ C_-} \quad (14.128)$$

and the expression for the concentration cell emf can be simplified to

$$\text{emf} = 2 \frac{RT}{F} T_- \ln \frac{a_\pm^\beta}{a_\pm^\alpha} = 2(1 - T_+) \frac{RT}{F} \ln \frac{a_\pm^\beta}{a_\pm^\alpha} \quad (14.129)$$

Alternatively, if we do not know the mean activity coefficients of the ions in the investigated electrolytes, we can construct a concentration cell *without ion transference* (WIT) as discussed above, using these same electrolytes but equipped with a salt bridge. Then the corresponding cell emf, designated here as emf_{WIT} , would be merely decided by the Nernstian section:

$$\text{emf}_{\text{WIT}} = \frac{RT}{F} \ln \frac{a_\pm^\beta}{a_\pm^\alpha} \quad (14.130)$$

The transference number T_- would be given as the ratio of these two emfs:

$$T_- = \frac{\text{emf}}{\text{emf}_{\text{WIT}}} \quad (14.131)$$

In practice, T_- is more often derived from the slope of the emf *versus* emf_{WIT} plot using a series of values to ensure better accuracy:

$$T_- = \frac{d(\text{emf})}{d(\text{emf}_{\text{WIT}})} \quad (14.132)$$

This approach does not require any prior knowledge about mean activity coefficients, hence it is often more favored; however, a suitable salt bridge is not always available, especially for non-aqueous electrolytes or solid electrolytes. In the work of Armand and colleagues, for example, they were attempting to determine the Li⁺ transference number in polymeric electrolytes, therefore extra experiments had to be carried out to estimate the mean activity coefficients.¹⁶

So far, we still assumed that the transference numbers T_+ and T_- are constant in the salt concentration range of interest. In reality, they are most likely not. Hence we need to take one more step forward to approach the concentration cells built with practical electrolytes. Since the salt concentration experiences a sharp change at the junction, a more rigorous derivation should consider transference numbers as a function of concentration that experiences a continuous change from C^α in electrolyte α to C^β in electrolyte β . Thus, the junction could be divided into a series of thin sections of infinitesimal thickness, and transporting T_+ mol of monovalent cations and T_- mol of monovalent anions across such thin layers involves a change in electrochemical free energy $d\bar{G}$, expressed as

$$d\bar{G} = \sum_i T_i d\bar{\mu}_i \quad (14.133)$$

where $\bar{\mu}_i$ is the electrochemical potential that we discussed in Section 5.2.5:

$$\bar{\mu}_i = \mu_i + z_i F \psi \quad (5.117)$$

The electrochemical potential consists of a chemical potential part ($\mu_i = \mu_i^0 + RT \ln Q$) and an electrostatic part ($z_i F \psi$). Integrating the

electrochemical free energy from electrolyte α to C^β in electrolyte β , one has

$$\int_{\alpha}^{\beta} d\bar{G} = 0 = \sum_i \int_{\alpha}^{\beta} T_i d\bar{\mu}_i \quad (14.134)$$

The junction potential E_J becomes

$$E_J = -\frac{RT}{F} \sum_i \int_{\alpha}^{\beta} T_i d \ln a_i \quad (14.135)$$

Eqn (14.135) represents the most rigorous description of a concentration cell consisting of practical electrolytes. For a binary electrolyte of monovalent ions, it simplifies to

$$E_J = -\frac{RT}{F} \int_{\alpha}^{\beta} T_- d \ln(a_+ a_-) \quad (14.136)$$

and the transference number can be expressed as

$$T_- = \frac{F}{RT} \frac{dE_J}{d \ln(a_+ a_-)} \quad (14.137)$$

In summary, the junction potential (or the emf of the concentration cell) is indeed related to the ion transference numbers, which provides multiple avenues to determine the latter, provided that a suitable cell configuration could be designed for an accurate solution. However, the challenge in using such an equation also comes from its rigor, as one is often required to know the activity of each individual ion involved at the junction, which is impossible to measure experimentally, while any approximation that one is forced to adopt would inevitably induce a compromise to the mathematical rigor.

Armand and colleagues attempted to determine Li^+ transference in various polymer electrolytes. The concentration cells that they constructed contained polymer electrolytes based on poly(ethylene oxides) of various molecular weights that dissolved different lithium salts [lithium perchlorate (LiClO_4), lithium triflate (LiCF_3SO_3) and lithium iodide (LiI)]. Since the salt concentrations used deviate far from the requirements of ideality, they had to adopt these approximations, including estimating mean activity coefficients and also calibrating salt activities *via* construction of additional anion-reversible cells. The Li^+ transference numbers in these polymer electrolytes were eventually reported to be in a wide range, 0.3–0.8. It should be mentioned

that 0.8 is an incredibly high value that is hardly possible in either liquid non-aqueous or polymeric electrolytes. Apparently, this resulted from the accumulated errors from the approximation and these additional experiments, as the available experimental techniques failed to provide the precision of physical quantities required by the rigorous mathematical considerations.

The application of concentration cells and the concomitant junction potential equations derived above are not just confined to the determination of ionic transference numbers. In fact, they provide a rather powerful approach to measure other quantities that are important for practical electrolytes, such as salt diffusion coefficients, thermodynamic factors, *etc.*, which will be discussed later.

The concentration cells can be applied to liquid electrolytes, but extreme caution has to be taken to ensure physical separation of the two electrolytes, so that no inter-mixing and convection occur while keeping them “ionically connected”, so that ion transference can still occur at the interfacial region. In practice, a porous separator is often used to achieve such dual effects of separation and connection.

14.2.4.4 Modified Hittorf Approach: Perturbed Electrochemical Concentration Cell

As discussed in Section 14.2.4.1, the Hittorf–Tubandt approach allows the direct measurement of transference for specific ionic species as a function of the charge passed across the cell, without consideration of the ideality of the electrolyte and the complicated ionic speciation occurring. However, the approach is “messy” and laborious, usually requires large volumes of samples and is not always feasible if the electrolyte or electrode system is sensitive to the ambient environment, with lithium-based electrolytes being a prominent example.

One modified approach that combines the Hittorf–Tubandt approach and an electrochemical concentration cell provides a compromise way to determine ionic transference number, which is also independent of the assumption of electrolyte ideality and ionic speciation but does not involve the laborious separation and analysis steps of the Hittorf–Tubandt approach.

In this approach, one constructs an electrochemical cell similar to that shown in Figure 14.18, where the two electrolytes are still separated but at the same salt concentration. Such a cell should not have any cell potential because there is chemical equilibrium between the two electrolytes.¹⁷ Then one perturbs this equilibrium by passing a known amount of charge through the cell, hence creating a

concentration difference between the two electrolytes. This needs to be done with great caution, so that the concentration gradients would not be established across the entire cell (a situation that will be discussed later in the Bruce–Vincent approach in Section 14.2.4.6), but just near the two electrode/electrolyte interfaces. In other words, the concentration profile should be like that illustrated in the Hittorf cell in Figure 14.16a, and this requires small perturbations.

Now the cell should exhibit a cell potential emf as we learned in the last section, which is expressed by eqn (14.130), because there is no concentration gradient at the interface separating the two electrolytes. Theoretically, one can derive the transference numbers from the emf without chemically analyzing the concentrations in the anode and cathode compartments, if one knows the exact relationship between emf and the concentration gradient.

Therefore, if the cell polarization is conducted galvanostatically at a constant current i , after a duration Δt the changes in salt concentration in the anode and cathode compartments should be

$$\Delta C_a = (1 - T_+) \frac{i\Delta t}{V_a F} \quad (14.138)$$

$$\Delta C_c = (T_+ - 1) \frac{i\Delta t}{V_c F} \quad (14.139)$$

where V_a and V_c represent the volumes of the anode and cathode compartments, respectively.

The concentration difference between the two electrode compartments is then given by

$$\Delta C = \Delta C_a - \Delta C_c = \frac{i\Delta t}{F} (1 - T_+) \frac{V_a + V_c}{V_a V_c} \quad (14.140)$$

which can be used to solve for cationic transference number:

$$T_+ = 1 - \frac{V_a V_c F}{i\Delta t (V_a + V_c)} \Delta C \quad (14.141)$$

To calculate T_+ , one needs the precise relationship between ΔC and emf. It is here that we encounter some problems, as what dictates emf in eqn (14.130) is salt activity, not concentration. Hence further complications arise with the measurement of mean activity coefficients or thermodynamic factors if one tries to derive an analytical relation

between these two quantities. A more practical approach, however, is to establish experimentally a numerical relationship between ΔC and emf, which allows the direct calculation of T_+ from the measured emf.

14.2.4.5 Sørensen-Jacobsen Approach: AC Impedance Spectra

In 1982, Sørensen and Jacobsen proposed a “universal” approach based on AC impedance techniques.¹⁸ As discussed in Section 14.1.1.3.5, when an electrode is non-blocking to at least one ion, the impedance spectra would display two semi-circles on the complex plane, with intercepts on the real axis at R_B and $(R_B + R_{CT})$, respectively, which are followed by a spike with a certain slope (Figure 14.9). If the frequency of the spectra is further extended to the milli-hertz (10^{-3} Hz) or even sub-milli-hertz (10^{-4} Hz) regimes, the spike would experience a maximum and revert to intercept the real axis, shaping the third and distorted semi-circle (Figure 14.19).

According to Macdonald *et al.*, the emergence of this distorted semi-circle should be attributed to a new *diffusional component* W_s , also known as the *Warburg short element*, which arises because a diffusional layer across the entire electrolyte is established in the sub-milli-Hertz regime ($<10^{-3}$ Hz). The corresponding equivalent circuit is represented by the inset in Figure 14.19. The effect of this diffusional component only matters when the frequency used to generate the impedance spectra is low enough that the ions under the effect of the semi-DC electric field could have sufficient time to establish

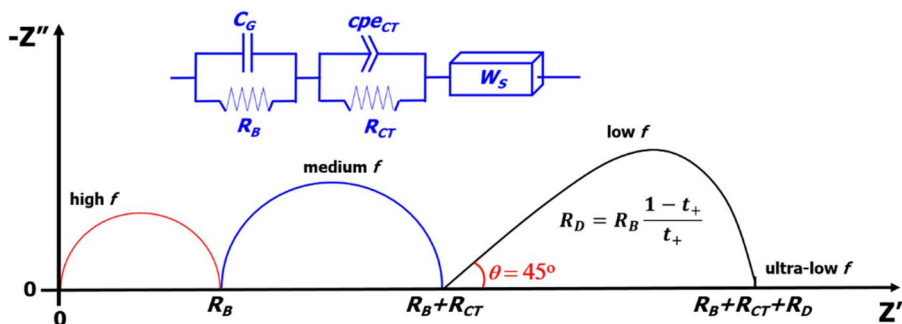


Figure 14.19 AC impedance spectra of an electrochemical cell with non-blocking electrodes to one ion when measured in a wide range of frequency, from mega-hertz (10^6 Hz) to sub-milli-hertz (10^{-4} Hz), where the impedance of the diffusional component W_s could be leveraged to measure the transference number of the non-blocked ion.

a concentration gradient across the entire bulk electrolyte. In such a situation, the concentration gradient builds up for the blocked ion, which is assumed to be the anion here for convenience, would start to counterbalance its own migration. If the capacitance or cpe elements for the bulk and charge-transfer circuits are neglected [remember that we made a similar simplification when solving eqn (14.68) for the non-blocking circuit], the impedance responses of such equivalent circuit can be solved, which was shown by Macdonald *et al.* to be

$$Z_D = R_B \frac{\mu_-}{\mu_+} \frac{\tanh(\alpha)}{\alpha} \quad (14.142)$$

with α defined as

$$\alpha = \sqrt{\frac{i2\pi f}{D_{amb}}} l \quad (14.143)$$

where f is frequency, D_{amb} the ambipolar diffusion coefficient of the salt and l the cell thickness.

Thus, when the frequency is extremely low and the cell extremely thin, α becomes zero, therefore

$$\frac{\tanh(\alpha)}{\alpha} = 1 \quad (14.144)$$

and the diffusional component intersects with real axis at

$$R_D = R_B \frac{\mu_-}{\mu_+} \quad (14.145)$$

If the definition of ion transference number for simple binary electrolyte still holds true:

$$t_+ = \frac{\mu^+}{\mu^+ + \mu^-} = \frac{D_+}{D_+ + D_-} \quad (5.96)$$

$$t_- = 1.0 - t_+ \quad (5.95)$$

then R_D becomes

$$R_D = R_B \frac{1-t_+}{t_+} \quad (14.146)$$

and the cation transference number could be calculated according to

$$t_+ = \frac{R_B}{R_B + R_D} \quad (14.147)$$

Since R_B is easily available with high accuracy from AC impedance spectra, as discussed in Section 14.1, one only needs to extend the frequency range so that both parameters (overall ion conductivity and ion transference number) could be determined in a single experiment.

One might recall that in Section 14.1.1.3.5 we derived a similar but different equation for transference number calculation based on AC impedance spectra:

$$t_i = \frac{I_i}{\sum_i I_i} = \frac{R_B}{R_{CT}} \quad (14.69)$$

How do eqn (14.69) and (14.147) differ?

In fact, these two equations reflect two alternative interpretations of AC impedance spectra. The former treated the charge-transfer component in the equivalent circuit as the sole source of resistance against the migration of the non-blocked ions across the interface, but in fact this component also includes the resistance from the interphases that often form at the electrolyte/electrode interfaces. In other words, the AC impedance cannot effectively differentiate R_{SEI} and R_{CT} , but rather gives us a convoluted component that reflects both processes. The latter is derived from a circuit at ultra-low frequencies, where the diffusion of the blocked ions occurs in the electrolyte to resist the migration. It does not involve the interfacial or interphasial interferences, hence enjoying a more solid foundation than the former. However, the basic assumption on which eqn (14.142) relies is the establishment of a diffusion layer across the entire electrolyte, which may not happen if there is convection in the electrolyte, either natural (as induced by electrolyte density variation, concentration gradient, *etc.*) or artificial (as induced by shaking or vibration of the cell).

Compared with the Hittorf or Lodge approaches, the Sørensen-Jacobsen approach is rather straightforward and “clean”, provided that one has access to ultra-low frequency AC impedance instrumentation, because no laborious and messy electrolyte separation and chemical analysis are required. However, it does come at a price: the final calculation of transference number still invokes the assumption of electrolyte ideality. Therefore, its applicability to practical electrolyte systems remains questionable.

14.2.4.6 Bruce–Vincent Approach: Combining AC and DC Techniques

A “cleaner” approach that combines the DC and AC techniques was proposed by Bruce and Vincent in 1987.¹⁹ Although initially it was proposed only for polymeric electrolytes or any “immobilized” electrolytes, so that the absence of either artificial or natural convection could ensure the establishment of a well-defined concentration profile for rigorous mathematical treatment, this constraint, along with the assumption of electrolyte ideality, was often ignored by most researchers. The Bruce–Vincent approach rapidly gained popularity after its publication, and its extensive adoption was driven both by the surging enthusiasm for lithium-based battery chemistries since the mid-1980s and by its intrinsic elegance and simplicity in execution, which are extremely attractive to most researchers in materials science and engineering who do not have a profound knowledge of ionics or electrodics. This approach deserves full attention here, not only because of its influence in the field, but more because, in the process of dissecting how the ions distribute across the electrolyte and consequently what potential profiles are established, we can get a glimpse of how complicated ion transport is, even when the electrolyte presents the simplest scenario, *i.e.* a binary monovalent electrolyte of ideality. At the central stage of the Bruce–Vincent approach is the steady state achieved during the DC polarization that we briefly discussed in Sections 14.1 (Figure 14.1, left panel) and 14.2.2 (Figure 14.14), in which a constant voltage ΔV is applied across a cell while the decay of current is monitored as a function of time. In fact, we will keep returning to the analysis of such a steady state later, as it sets up a stage to verify the various theoretical models constructed by modern ionics of non-ideal electrolytes.

In this approach, Bruce and Vincent rigorously examined whether the following relation holds true:

$$T_+ = \frac{i^{\text{ss}}}{i_0} \quad (14.148)$$

where i_0 and i^{ss} are the “*initial current*” detected at the instant of voltage application and “*steady-state current*” detected near the end of the polarization, respectively (Figure 14.14). Eqn (14.148) is built on the justification that, since the initial current i_0 has contributions from both cations and anions, whereas the current at the steady state i^{ss} only has a contribution from cations, their ratio should reflect the

fraction of cationic flux in the overall current. However, after all, this justification is only an intuition that needs rigorous mathematical analysis.

14.2.4.6.1 Salt (and Ion) Concentration Profiles at the Steady State

In order to make the analysis as rigorous as possible, Bruce and Vincent strictly defined the cell configuration as a symmetrical lithium–lithium cell, which contains *an ideal polymer electrolyte with a monovalent salt Li⁺X⁻*, so that the concentration profile for each ion and the respective ionic fluxes could be quantitatively derived. To ensure that the electrochemical environment involved is well defined, they further proposed that the applied voltage is high enough to generate sufficient current for accurate measurement, but low enough to prevent extensive electrolyte decomposition at the electrode/electrolyte interfaces. The optimum voltage suggested by them was 10 mV.

At $t = 0$, the cation and anion concentration profiles should be homogeneous across the electrolyte. At this instant, the initial current would be given by

$$i_0 = \frac{\Delta V}{R_B} = \sigma \frac{\Delta V}{d} \quad (14.149)$$

where ΔV is the voltage applied, R_B the bulk resistance of the electrolyte that can be accurately determined by AC impedance spectra, σ the corresponding overall ion conductivity and d the distance between the electrodes. For simplicity, the electrode area has been assumed to be 1.0 here. Applying the Nernst–Einstein equation [(eqn (5.101)] and invoking the definition of molar ion conductivity [eqn (5.60)], we have

$$i_0 = \sigma \frac{\Delta V}{d} = \frac{F^2 C_0}{RT} [D_+ + D_-] \frac{\Delta V}{d} = \frac{F^2 C_0}{RT} [D_+ + D_-] E_{\text{Bulk}}^0 \quad (14.150)$$

where C_0 is the salt concentration, D_+ and D_- are the self-diffusion coefficients of the cations and anions, respectively, and E_{Bulk}^0 is the electric field across the bulk electrolyte at the initial state:

$$E_{\text{Bulk}}^0 = \frac{\Delta V}{d} \quad (14.151)$$

At $t > 0$ (such as t_1, t_2 , etc.), both cations and anions migrate according to the applied voltage, while their respective fates at the electrodes create unique concentration profiles across the cell.

For the cation, more Li^+ would be generated *via* the oxidation at the electrode that is positively polarized (right electrode), and assuming that such kinetics are fast enough, the Li^+ concentration at the right interface would always be *higher* than its concentration in the bulk. At the same time, Li^+ is consumed *via* its reduction to Li^0 at the electrode that is negatively polarized (left electrode), and again assuming that such kinetics are fast enough, the Li^+ concentration at the left interface would always be *lower* than its concentration in the bulk (Figure 14.20a).

For the anion, X^- is driven by the applied voltage to migrate from the negatively polarized electrode (left) towards the positively polarized electrode (right), but since both electrodes are blocking to X^- , it is depleted at the left interface but accumulated at the right interface. The consequence of such depletion and accumulation is that the concentration of X^- at the left interface is always *lower* than its concentration in the bulk, whereas the concentration of X^- at the right interface is always *higher* than its concentration in the bulk (Figure 14.20b).

In summary, the concentration profiles of cations and anions are actually identical at the steady state. Such identical concentration profiles for cations and anions are the natural consequence of the electroneutrality requirement that an electrolyte must satisfy in the bulk. Although the above description is qualitative in nature, a more rigorous derivation of these concentration profiles will be conducted in Chapter 15.

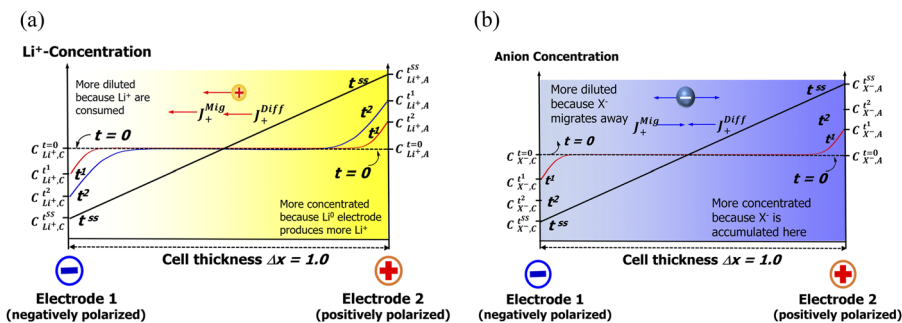


Figure 14.20 Schematic diagram of the concentration gradients of (a) cations and (b) anions in a symmetrical cell, such as that shown in Figure 14.1, right panels, which is under DC polarization at a constant voltage ΔV . Its current response should be similar to that shown in Figure 14.14. At the steady state, the net anionic flux would be zero, because its migration driven by the applied voltage is counterbalanced by its diffusion driven by the anion concentration gradient. However, the cationic flux benefits from both migration and diffusion.

The collective consequence of the above cation and anion concentration gradients is the enrichment of both cations and anions at the right side of the cell and the corresponding depletion of these ions at the left side of cell. This is in fact equivalent to the redistribution of the salt from the left side to the right side of the cell. If one does not differentiate cations and anions in this movement but instead view the dissolved salt as a whole, the net consequence of the corresponding movement of cations and anions is equivalent to the salt diffusing from one side of the cell to the other. This consequence in fact naturally arises from the local electroneutrality requirement for electrolytes in the bulk, and one can separately define a diffusion coefficient for this “salt” species, *i.e.* D_{Salt} , which we have already briefly touched upon as the ambipolar diffusion coefficient in Section 5.2.6.4, and will discuss in more detail in Section 14.3.4.

Such identical concentration gradients for two ions, however, has completely the opposite effect on their respective migration: for anions, the diffusional flux driven by such a concentration gradient *opposes* the migration driven by the applied voltage; for cations, however, its migration is *complemented* by its diffusion as both are in the *same* direction.

According to classical electrodics, if the electrolyte is in the liquid state, the buildup of the above concentration profiles would eventually be terminated by either artificial or natural convection of the electrolytes, which is induced by the drastic density differences in the different sections of the cell. The convection would maintain the original salt concentration C_0 undisturbed in the middle section of the electrolyte, while the concentration gradient is only confined to the local interfacial regions near the electrode surfaces. However, if the electrolyte is solid or semi-solid, be it either polymeric, glassy or crystalline, the absence of convection would ensure the continuous buildup of the above concentration profiles, until the cell reaches the steady state, where the concentration gradient would be represented by a diagonal straight line as depicted in Figure 14.20.

At such a steady state (t^{ss}), within any cross-sectional element of the electrolyte an electroneutrality must exist, which requires

$$C_+^x = C_-^x = C_{\text{Salt}}^x \neq C_0 \quad (14.152)$$

where the superscript x denotes the location of the cross-sectional element, and subscripts denote the species. In other words, the concentration gradients for cations and anions should be identical:

$$\frac{dC_+}{dx} = \frac{dC_-}{dx} = \frac{dC_{\text{salt}}}{dx} \quad (14.153)$$

14.2.4.6.2 Cationic and Anionic Fluxes at the Steady State

Now, let us see what I_0 and I_{ss} are under such concentration gradients.

As discussed briefly in Section 14.2.2, at this steady state the anion migration driven by the applied voltage would be exactly counterbalanced by the anion diffusion driven by the concentration gradient:

$$J_-^{ss} = -\frac{D_- c_-}{RT} \frac{d}{dx}(F\psi + \mu_-) = 0 \quad (14.94)$$

In other words, the electrostatic gradient is equal to but opposite in direction to the chemical gradient (*i.e.* concentration gradient):

$$-F \frac{d\psi}{dx} = \frac{d(\mu_-)}{dx} = \frac{d(\mu_-^0 + RT \ln C_-)}{dx} = RT \left(\frac{1}{C_-} \right) \frac{dC_-}{dx} \quad (14.154)$$

The potential gradient created by the applied voltage across the cell would hence be

$$\frac{d\psi}{dx} = -\frac{RT}{F} \left(\frac{1}{C_-} \right) \frac{dC_-}{dx} \quad (14.155)$$

Meanwhile, the cation moves from the right electrode to the left electrode, initially only *via* migration driven by the applied voltage. With the buildup of the cationic concentration profile, however, part of the cation is also driven by diffusion in the same direction, hence

$$J_+^{ss} = J_+^{\text{Mig}} + J_+^{\text{Diff}} \quad (14.156)$$

where the two parts (migrational and diffusional) can be described by Coulomb's law and Fick's first law, respectively:

$$J_+^{\text{Mig}} = \frac{D_+ C_+ F}{RT} \frac{d\psi}{dx} \quad (14.157)$$

$$J_+^{\text{Diff}} = -D_+ \frac{dC_+}{dx} \quad (14.158)$$

While the concentration gradients for cations and anions are identical, so is the potential gradient felt by both ions. Hence we can insert eqn (14.155), (14.157) and (14.158) into eqn (14.156), which with the elimination of the potential term ($d\psi/dx$) becomes

$$\begin{aligned} J_+^{t_{ss}} &= \frac{D_+ C_+ F}{RT} \frac{d\psi}{dx} - D_+ \frac{dC_+}{dx} = -\frac{D_+ C_+ F}{RT} \frac{RT}{F} \left(\frac{1}{C_-} \right) \frac{dC_-}{dx} - D_+ \frac{dC_+}{dx} \\ &= -D_+ C_+ \left(\frac{1}{C_-} \right) \frac{dC_-}{dx} - D_+ \frac{dC_+}{dx} \end{aligned} \quad (14.159)$$

Since the electrolyte is ideal, therefore

$$C_+ = C_- = C_{\text{Salt}} \quad (14.152)$$

$$\frac{dC_+}{dx} = \frac{dC_-}{dx} = \frac{dC_{\text{Salt}}}{dx} \quad (14.153)$$

Eqn (14.159) hence further simplifies to

$$J_+^{t_{ss}} = -2D_+ \frac{dC_+}{dx} \quad (14.160)$$

Hence

$$J_+^{t_{ss}} = 2J_+^{\text{Diff}} \quad (14.161)$$

or

$$J_+^{\text{Mig}} = J_+^{t_{ss}} - J_+^{\text{Diff}} = J_+^{\text{Diff}} \quad (14.162)$$

Eqn (14.160) and (14.162) present a somewhat unexpected relation: at the steady state and under the concentration gradients depicted in Figure 14.20, *the cationic flux comes from two equal components, i.e. migrational and diffusional*. In other words, the total cationic flux, or current, is carried equally by the cation migration and diffusional fluxes. By definition, the current at the steady state, i^{ss} , should be given as

$$i^{ss} = F J_+^{t_{ss}} = -2FD_+ \frac{dC_+}{dx} = -2FD_+ \frac{dC_{\text{Salt}}}{dx} \quad (14.163)$$

This expression contains a differential term (concentration gradient). To establish further what the concentration gradient at the steady state is, we need to recognize that the concentration gradient across

the electrolyte must be a constant, as suggested by the diagonal straight line in Figure 14.20, because at this state the current i^{ss} has been stabilized at a constant value (Figure 14.14). Therefore, the concentration gradient should be given as

$$\frac{dC_+}{dx} = \frac{dC_{\text{salt}}}{dx} = \frac{\Delta C}{\Delta x} = (C_A^{\text{ss}} - C_C^{\text{ss}}) \quad (14.164)$$

while the steady-state current becomes

$$i^{\text{ss}} = -2FD_+ \frac{dC_{\text{salt}}}{dx} = -2FD_+ (C_A^{\text{ss}} - C_C^{\text{ss}}) \quad (14.165)$$

where the quantities C_A^{ss} and C_C^{ss} represent the salt concentrations at the anode and cathode side of the cell when the steady state is established, respectively, because as Figure 14.20 shows, we can now treat the cation and anion as a neutral association (*i.e.* the “salt”) diffusing and migrating in the electrolyte. One should note that “anode side” and “cathode side” are still within the bulk electrolyte, where the local electroneutrality still holds true, not the interfaces with both electrodes, where the local electroneutrality breaks down. We will discuss how these two quantities change in the interfacial regions in Chapter 15.

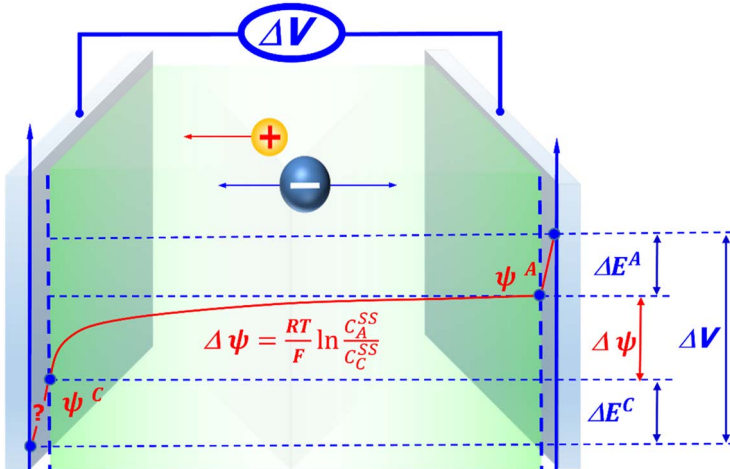
14.2.4.6.3 Potential Profile Across Cell and Electrolyte

Eqn (11.191) is an elegant expression, but it still contains a term ($C_A^{\text{ss}} - C_C^{\text{ss}}$) that is difficult to measure experimentally. Ideally, the steady-state current should be expressed in a form that can be directly comparable to the expression of I_0 [eqn (14.146)]. In other words, we need to find out how the concentration gradient is related to the applied voltage ΔV or the corresponding electric field or E_{Bulk}^0 at the steady state.

To do that, we need to analyze how the potential drop is distributed across the cell at the steady state (Figure 14.21). Suppose that the potential drop across the two electrolyte/electrode interfaces is represented by a single term ΔE , then the potential drop across the bulk electrolyte $\Delta\psi$ should be given by

$$\Delta\psi = \Delta V - \Delta E \quad (14.166)$$

Since the anode and the cathode are in equilibrium with the electrolyte at two distinct concentrations C_A^{ss} and C_C^{ss} , respectively, their



Cell thickness $\Delta x = 1.0$

Figure 14.21 Schematic illustration of potential distribution across the cell when the steady state is reached under potentiostatic conditions. The sum of the potential drops across the two electrolyte/electrode interfaces ($\Delta E^A + \Delta E^C$) is governed by the Nernst equation, while the potential drop across the bulk electrolyte ($\Delta\psi$) can be solved based on the linear concentration gradient as described in Figure 14.20. The potential drop at the interfacial region near the cathode will be discussed in Chapter 15.

respective potentials E_A^{ss} and E_C^{ss} should be given by the Nernst equation:

$$E_A^{ss} = \frac{RT}{F} \ln C_A^{ss} \quad (14.167)$$

$$E_C^{ss} = \frac{RT}{F} \ln C_C^{ss} \quad (14.168)$$

while their difference represents the sum of the potential drops across the two interfaces:

$$\Delta E = E_A^{ss} - E_C^{ss} = \frac{RT}{F} \ln \frac{C_A^{ss}}{C_C^{ss}} \quad (14.169)$$

Then, what about the potential drop across the bulk electrolyte? Since the concentration gradient is linear at the steady state, the salt concentration at a given location in the cell (a distance x from the cathode) should be given by a linear relation:

$$C_x = \frac{dC_{\text{salt}}}{dx} x + C_C^{\text{ss}} = (C_A^{\text{ss}} - C_C^{\text{ss}})x + C_C^{\text{ss}} \quad (14.170)$$

Inserting eqn (14.164) and (14.170) into eqn (14.155), we have the potential gradient expressed in a form free from another differential term (*i.e.* concentration gradient):

$$\frac{d\psi}{dx} = -\frac{RT}{F} \left(\frac{1}{C_-} \right) \frac{dC_-}{dx} = -\frac{RT}{F} \frac{(C_A^{\text{ss}} - C_C^{\text{ss}})}{(C_A^{\text{ss}} - C_C^{\text{ss}})x + C_C^{\text{ss}}} \quad (14.171)$$

or

$$d\psi = -\frac{RT}{F} \frac{(C_A^{\text{ss}} - C_C^{\text{ss}})}{(C_A^{\text{ss}} - C_C^{\text{ss}})x + C_C^{\text{ss}}} dx \quad (14.172)$$

Hence the potential drop across the electrolyte can be obtained by integrating eqn (14.172) across the cell, *i.e.* from $x = 0$ to $x = 1$:

$$\Delta\psi = \frac{RT}{F} (C_A^{\text{ss}} - C_C^{\text{ss}}) \int_0^1 \frac{1}{(C_A^{\text{ss}} - C_C^{\text{ss}})x + C_C^{\text{ss}}} dx = \frac{RT}{F} \ln \frac{C_A^{\text{ss}}}{C_C^{\text{ss}}} \quad (14.173)$$

What is slightly surprising is that eqn (14.173) is *identical* with eqn (14.169)! In other words, the potential drops at the interfaces are identical with the potential drop across the electrolyte:

$$\Delta\psi = \Delta E = \frac{RT}{F} \ln \frac{C_A^{\text{ss}}}{C_C^{\text{ss}}} \quad (14.174)$$

while the applied voltage ΔV can be expressed in terms of the concentrations:

$$\Delta V = \Delta\psi + \Delta E = \frac{2RT}{F} \ln \frac{C_A^{\text{ss}}}{C_C^{\text{ss}}} \quad (14.175)$$

Like eqn (14.161), this relation is also rather unexpected, as it tells us that the applied voltage is *equally divided into two parts*: the potential drop across the interfaces and the potential drop across the bulk electrolyte. However, considering that both potential drops $\Delta\psi$ and ΔE are dictated by the two concentrations C_A^{ss} and C_C^{ss} at the steady state, we should not be too surprised.

One might find it puzzling that the potential drop across the cell, as shown in Figure 14.21, is rather asymmetric, and most of its drop is

concentrated at the cathode side. We will return to discuss this asymmetry in more detail later. As implied by the question mark “?” at the bottom left in Figure 14.21, one should note that so far we have left the potential drop in the interfacial region unexplored until we engage in more detailed discussion about the definition of interfaces in Chapter 15.

14.2.4.6.4 Cationic Transference Number in the Absence of Interphases

With eqn (14.175), we are now only one step away from relating eqn (14.165) to ΔV or E_{Bulk}^0 , and this last step needs an algebraic approximation that stands true when the difference between C_A^{ss} and C_C^{ss} is sufficiently small:

$$C_A^{\text{ss}} - C_C^{\text{ss}} = \frac{C_A^{\text{ss}} + C_C^{\text{ss}}}{2} \ln \frac{C_A^{\text{ss}}}{C_C^{\text{ss}}} \quad (14.176)$$

Inserting eqn (14.176) into eqn (14.165), we will have

$$i^{\text{ss}} = -2FD_+ (C_A^{\text{ss}} - C_C^{\text{ss}}) = -FD_+ (C_A^{\text{ss}} + C_C^{\text{ss}}) \ln \frac{C_A^{\text{ss}}}{C_C^{\text{ss}}} \quad (14.177)$$

Invoking eqn (14.177), while also noting that the following relation exists between C_A^{ss} and C_C^{ss} as the consequence of both concentrations departing from the initial concentration C_0 driven by the applied potential:

$$C_A^{\text{ss}} + C_C^{\text{ss}} = 2C_0 \quad (14.178)$$

Thus, we have a new expression for i^{ss} :

$$i^{\text{ss}} = \frac{F^2 D_+ C_0}{RT} \frac{\Delta V}{d} = \frac{F^2 C_0}{RT} D_+ E_{\text{Bulk}}^0 \quad (14.179)$$

Now i^{ss} can be directly compared with the expression for i_0 [eqn (14.150)]:

$$\frac{i^{\text{ss}}}{i} = \frac{D_+}{D_+ + D_-} \quad (14.180)$$

By definition, this ratio is the cationic transference number in an ideal electrolyte, *i.e.* Eqn (14.148) is confirmed to have a theoretical foundation:

$$T_+ = \frac{D_+}{D_+ + D_-} = \frac{i^{\text{ss}}}{i_0} \quad (14.148)$$

This conclusion basically confirms our earlier intuitive interpretation of the potentiostatic polarization curve as depicted in Figure 14.14, that the current at the steady state is carried only by the cationic movement, and its ratio to the initial current i_0 should give us the measurement of cationic transference number. However, eqn (14.180) was derived in a much more mathematically rigorous manner, and it comes with three stringent confinements: (1) the electrolyte must be ideal so that the Nernst–Einstein relation is observed [eqn (14.148)]; (2) the electrolyte must be “immobilized” so that the steady-state concentration gradient could be established in the absence of any convection (Figure 14.20); and (3) the polarization must be small enough that the concentration difference at two electrodes satisfies the approximation relation as described in eqn (14.176). The small cell voltage of 10 mV as recommended by Bruce and Vincent ensures that the relation is accurate within an error of 1%. However, at 30 mV, the departure from the relation becomes intolerable.

An additional hidden assumption in the above derivation is the absence of interphases. One may argue that the potential drop across the interfaces (ΔE) already accounted for this factor. In reality, however, the interphases are dynamic in both thickness and chemistry, especially when new surfaces of lithium keep being exposed during the lithium deposition and stripping on both electrodes. These factors require corrections to the potentiostatic polarization method as described by eqn (14.148).

14.2.4.6.5 Cationic Transference Number in the Presence of Interphases

As we learned in Section 10.1, lithium metal is unique in that its electrode potential is the lowest among all known metallic elements (-3.0364 V vs. SHE), which gives it extremely high reactivity. Therefore, no matter how small the applied voltage is, the two lithium electrodes react with the electrolyte components (solvent, salt anions) instantaneously upon contact. It is well known nowadays that, in any cell built with lithium-metal electrodes, there is always an interphase existing on the Li^0 surface (Sections 8.1 and 8.2), the presence of which introduces an additional resistance to the passing of the current, and consequently induces a corresponding voltage drop. Hence a correction must be made to address the presence of interphases.

Furthermore, in the potentiostatic polarization process as described in this section, there is constant Li^0 deposition at the cathode (or the

negatively polarized electrode) and constant Li⁺ dissolution from the anode (or the positively polarized electrode). In this context, a new Li⁰ surface is being created at every instant during the entire polarization process, hence the formation of new interphases never stops, as evidenced by the ever-increasing interphasial resistances in such cells. Hence this evolution of interphasial resistance must also be considered when making modifications to the Bruce–Vincent approach.

At $t = 0$, if we assume that the resistance brought by the interphase R_{CT}^0 can be represented by the semi-circle that emerges at lower frequency range in the AC impedance (Figure 14.19), then the expression of the initial current should become

$$i_0 = \frac{\Delta V}{R_B + R_{\text{CT}}} = \frac{\Delta V}{\frac{1}{\sigma} + R_{\text{CT}}^0} \quad (14.181)$$

Therefore, the applied voltage actually consists of two parts:

$$\Delta V = \Delta\psi + \Delta E_T = i_0 \frac{1}{\sigma} + i_0 R_{\text{CT}}^0 \quad (14.182)$$

where $\Delta\psi$ and ΔE_T represent the potential drops across the bulk electrolyte and the interphasial regions. Note that ΔE_T replaces the previously discussed potential drop across the interfaces ΔE .

At the steady state, only cations are contributing to the effective ionic fluxes, while the anion flux becomes zero. Hence the ion conductivity in eqn (14.182) that corresponds to the overall resistance to the movement of both ions should be replaced with the cationic portion of it, *i.e.* the “*cationic conductivity*” σT_+ , which apparently comes from the assumption that cations and anions are independently making their individual contributions to the overall ion conduction *via*

$$\frac{1}{R_B} = \frac{1}{R_+} + \frac{1}{R_-} \quad (14.183)$$

while the interphasial resistance should be replaced with a new value corresponding to a larger semi-circle obtained at the steady state, $R_{\text{CT}}^{\text{ss}}$. This changing interphasial resistance reflects the ongoing reactions between the electrolyte and the newly exposed Li⁰ surfaces. Therefore, the applied voltage at this steady state would become

$$\Delta V = i^{\text{ss}} \frac{1}{\sigma T_+} + i^{\text{ss}} R_{\text{CT}}^{\text{ss}} \quad (14.184)$$

We solve for the bulk conductivity σ from eqn (14.181):

$$\sigma = \frac{i_0}{\Delta V - i_0 R_{CT}^0} \quad (14.185)$$

and solve for the cationic transference number T_+ from eqn (14.184):

$$T_+ = \frac{i^{ss}}{\Delta V - i^{ss} R_{CT}^{ss}} \frac{1}{\sigma} \quad (14.186)$$

Inserting eqn (14.185) into eqn (14.186), we obtain the *Bruce–Vincent equation*:

$$T_+ = \frac{i^{ss}}{i} \frac{\Delta V - i_0 R_{CT}^0}{\Delta V - i_{ss} R_{CT}^{ss}} \quad (14.187)$$

which corrects eqn (14.148) with a term that reflects the potential drop across a dynamic interphase.

Eqn (14.187) constitutes the foundation of a very popular method, *i.e.* the *Bruce–Vincent approach*, which allows the quantitative determination of a very useful parameter, the ion transference number, using highly accessible techniques and simple experiments. It requires the combination of the DC potentiostatic polarization technique, which measures the steady-state current i , and the AC impedance technique, which measures the bulk electrolyte resistance R_B (or ion conductivity σ) and interphase resistances at both initial (R_{CT}^0) and steady state (R_{CT}^{ss}). It should be noted that although i_0 appears to be a quantity associated with the DC polarization (Figure 14.14), it is often extracted from the ion conductivity σ via eqn (14.149) with higher accuracy, because the attempt to directly measure i_0 in the DC method would inevitably encounter the issue of temporal resolution of the instrumentation, *i.e.* how fast the circuit could capture the very first current response, with milliseconds or microseconds making significant differences, while the AC impedance technique provides an effective pathway circumventing such challenges.

One might notice that the derivation of eqn (14.187) does not have a basis of mathematical rigor as did the steady-state equations for the concentration gradient and potential profile in Sections 14.2.4.6.2 and 14.2.4.6.3. In particular, the adoption of a new quantity, cationic conductivity, σT_+ , is intuitive rather than rigorous. However, the elegant form of eqn (14.187) was warmly received by researchers, despite

the stringent restrictions that Bruce and Vincent imposed on its application in their original 1987 paper.¹⁹

When the Bruce–Vincent approach was applied to polymer electrolytes based on poly(ethylene oxide) or other polyethers, the Li⁺ transference numbers were usually found to range between 0.2 and 0.4. Although these polymeric electrolytes clearly do not completely meet the requirement of ideality (*i.e.* salt completely dissociated into free ions and zero ion–ion interactions), the excessive application of the Bruce–Vincent approach was soon extended to essentially *all* electrolytes, including the typical lithium-ion battery electrolytes (LiBF₄ or LiPF₆ in mixed carbonates), with similar Li⁺ transference numbers.

14.2.4.7 Pulsed Field Gradient NMR Spectroscopy

In Section 14.1.4.3.2, we discussed the application of diffusional NMR techniques such as pfg-NMR spectroscopy in measuring the translational movement of certain NMR-active nuclei, thus allowing the determination of the self-diffusion coefficients of ions that contain these nuclei. For studies on battery electrolytes, ⁷Li and ¹⁹F are two “Godsent” nuclei for this technique as they represent the most frequently used cations and anions, respectively. Knowing the self-diffusion coefficients for both ions therefore makes it possible for one to calculate the corresponding cationic or anionic transference numbers from their corresponding self-diffusion coefficients:

$$t_+ = \frac{D_+}{D_+ + D_-} \quad (5.96)$$

With the increasing availability of NMR facilities in universities and major research centers, the transference numbers determined in this manner have been extensively adopted in the battery and materials research communities, and NMR methods have become even more popular than the Bruce–Vincent approach in recent decades owing to their “cleanliness” and non-invasive nature. Hayamizu and colleagues systematically applied this approach to a number of non-aqueous electrolyte systems most commonly used in batteries, and reported Li⁺ transference numbers in the range 0.2–0.4.^{21,31}

One must note that a hidden assumption exists in eqn (5.96), *i.e.* *all* self-diffusing ions contribute to the ionic flux induced by an electric field independently. Again, this is true only in ideal electrolytes. For practical electrolytes, however, ionic speciation occurs as eqn (14.83)

describes, and a certain NMR-active nucleus, in a binary monovalent electrolyte, could exist in a free ion C^+ or A^- , which makes a contribution to ionic migration, or in an ion pair $[C^+A^-]^0$, which is electrically neutral and makes a zero contribution to ionic migration, or in large ionic clusters $[nC^+mA^-]^{(n-m)}$, which make a partial contribution to ionic migration because their effective charges are reduced from the formal charge carried by an independent ion. Nevertheless, NMR methods indiscriminately probe every active nucleus in the electrolyte, neglecting their speciation and assuming that they would all contribute to an electric field by migrating. Hence the use of self-diffusion coefficients as determined by NMR techniques, which are averaged over all these species, would inevitably lead to deviations in ionic transference numbers by eqn (5.96).

In the majority of the scenarios where ion transference numbers determined using different approaches are compared, researchers found that such deviations led almost exclusively to *overestimation* for *cationic* transference numbers (Table 14.3). In fact, most ionic transference numbers as measured by pfg-NMR spectroscopy are scattered around 0.5, a strong indication that cations and anions are closely associated, as they would be in an ion pair.

If we consider that, in an equal manner, either cations or anions would make only zero or partial contributions to ionic fluxes provided that they exist in ion pairs or clusters, a preferential suppression of cationic mobility due to the ion speciation in practical electrolytes should be immediately suspected. For this reason, the ionic transference numbers from pfg-NMR spectroscopy are often treated as the upper limit of ion transference that could be available in a given electrolyte system.

14.2.4.8 Electrophoretic NMR Spectroscopy

One particularly important variation of NMR spectroscopy is the so-called *electrophoretic NMR* (eNMR) technique, which, invented in 1982 by Holz and colleagues, maintains the *in situ* and non-invasive nature of NMR methods but seeks to differentiate the mobile ionic species from those not participating in migrational movement.²⁰ The “electrophoretic” element of the technique refers to the fact that an electric field is placed inside an NMR sample tube so that the ions (or all charged species) are induced to flow. Most frequently, such an electric field is applied when the spin-echo relaxation of cations and anions under pulsed gradient conditions are simultaneously monitored, so that the translational movement observed should be entirely

Table 14.3 Selected Li⁺ transference numbers in electrolytes obtained using different approaches.

Hittorf	Armand	Sørensen-Jacobsen	Bruce-Vincent	pfg-NMR	eNMR	Newman ^a
0.06 ± 0.05 (LiClO ₄ -PEO) ^b	0.70 (LiOTf-PEO) ^c	0.54 (LiSCN-PEO) ^e	0.44–0.48 (LiOTf-PEO) ^k	0.43–0.46 (LiFSI-G4) ^f	0.36–0.43 (LiFSI-G4) ^f	-0.25 to -1.0 (LiFSI-C ₈ -DMC) ^l
0.30 (LiClO ₄ -PEO) ^c	0.015–0.09 (LiFSI-G4) ^{f,g}	0.95–0.68 (LiFSI-C ₈ -DMC) ^l		0.51 ± 0.02 (LiTFSI-G4) ^f	0.58 ± 0.11 (LiTFSI-G4) ^f	-4.38 (NaOTf-PEO) ^m
0.36–0.41 (LiPF ₆ - PC-EC-DMC) ^d	0.025 ± 0.005 (LiTFSI-G4) ^{f,g}	0.37 (NaOTf-PEO) ^m	0.45–0.60 (LiFSI-C ₈ -DMC) ^l			-0.75 to +0.70 (LiTFSI-PEO) ⁿ
	0.16–0.17 (LiTFSI-sulfolane) ^h	0.03–0.25 (LiTFSI-PEO) ⁿ	0.38 (LiTFSI-EC) ^q			
	0.05–0.07 (LiPF ₆ -EC-DMC) ⁱ	0.79–0.82 (LiBETI-glymes) ^o		0.48 (LiTFSI-DMC) ^q		
	0.048–0.062 (LiTFSI-BMP-TFSI) ^j	0.54–0.67 (LiFSI-glymes) ^o		0.39–0.47 (LiPF ₆ -EC-DMC) ⁱ		
		0.51–0.65 (LiTFSI-glymes) ^o				
		0.34 ± 0.0053 (LiPF ₆ -EC-DEC) ^p		0.13 (LiTFSI-BMP-TFSI) ^j		
		0.48 (LiFSI-FDMB) ^q				
			0.45–0.46 (LiTFSI-ethers) ^r			
			0.73 (LiTFSI-H ₂ O) ^s			

^aRigorously defined transference number against solvent reference frame as determined by Newman concentrated solution theory (to be discussed in Section 14.4). Sources: (1) ref. 33; (2) ref. 34.

^bSalt:EO ratio 1:8. Measured at 120 °C. Source: ref. 13.

^cSalt:EO ratio 8–120. Source: ref. 16.

^dConcentration 0.5–2.5 M. Source: ref. 17.

^eSalt:EO ratio 1:4.5. Measured at 80 °C. Source: ref. 18.

^fSalt:solvent ratio ranging between 1:1 to 1:2. Source: ref. 23.

^gSalt:solvent ratio 1:1. Source: ref. 23.

^hConcentration range 0.5–2.7 m. Source: ref. 35.

ⁱConcentration 1.2 M. Source: ref. 30.

^jBMP: 1-butyl-1-methylpyrrolidinium, a cation for room-temperature ionic liquids. Source: ref. 30.

^kSalt : EO ratio 1 : 9. Measured at 90 °C. Source: ref. 36.

^lC₈-DMC: a perfluorinated tetraethylene ether terminated by methyl carbon. Source: ref. 34.

^mSalt concentration: 2.58 M. Source: ref. 37.

ⁿLi : EO ratio 0.01–0.3. Source: ref. 38.

^oLIBETI: lithium bis(pentafluoroethylsulfonyl)imide. Source: ref. 39.

^pSource: ref. 40.

^qFDMB: fluorinated 1,4-dimethoxylbutane. Source: ref. 41.

^rSource: ref. 31.

^sConcentration: 21 m. Source: ref. 42.

attributed to the migrational fluxes. In other words, this technique is a combination of ordinary diffusional NMR techniques such as pfg-NMR spectroscopy discussed above and a DC technique, which is realized by equipping the NMR sample tube with an additional pair of electrodes. Figure 14.22a depicts one of the typical eNMR sample tube designs often used.

When a DC voltage is applied, the drift velocities of cations and anions with NMR-active nuclei are measured and normalized against the force (or field) created by the applied voltage. The ionic transference numbers obtained in this manner should be independent of any assumptions of ideality, nor do they require any knowledge of

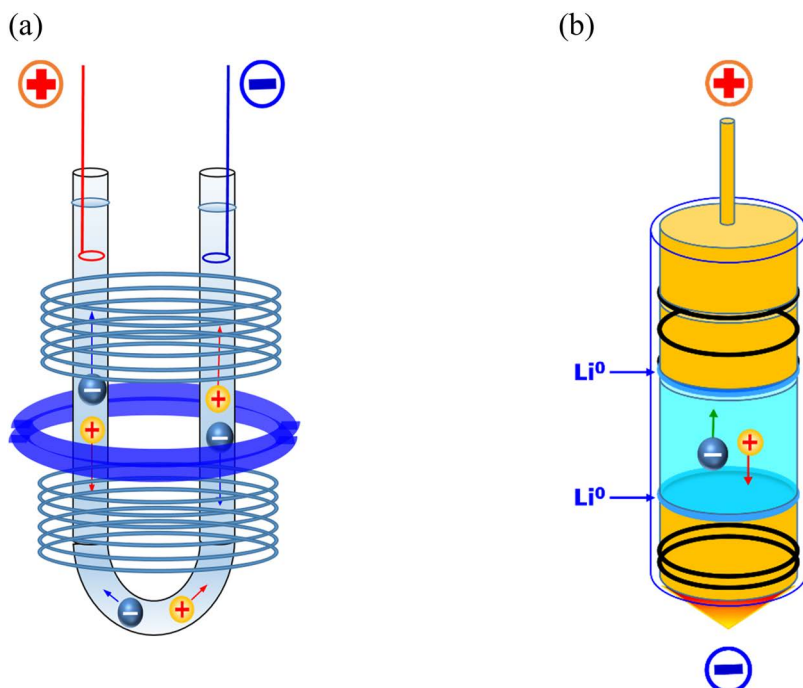


Figure 14.22 (a) A sample tube design that is often adopted in eNMR experiments, in which a pair of electrodes are inserted to apply additional DC voltage while the translational movement of the ions containing the nuclei of interest are measured under pulsed gradient conditions. In order to induce sufficient spatial displacements for ions in the time frame of milliseconds, a high voltage (~100 V) has to be applied. (b) A modified eNMR tube design that adopted lithium-metal electrodes as source and sink for Li^+ , so that the ion transport in the electrolyte could be investigated under conditions that more closely simulate real electrochemical devices: lower DC voltage (<3.0 V) and longer polarization duration (seconds).

ion–solvent or ion–ion interactions, as the method directly measures the actual mobilities of ions under an externally applied electrostatic field, according to the definition of ionic mobility in Section 5.2.1.2:

$$\mu = \frac{\tau}{m} = \frac{v_d}{F} \quad (5.66)$$

and the individual ion transference number can be calculated from

$$T_+ = \frac{\mu_+}{\mu_+ + \mu_-} = \frac{v_d^+}{v_d^+ + v_d^-} \quad (14.188)$$

The voltage used usually lies in the region of ~ 100 V, so that an electric field can be strong enough (~ 100 V cm $^{-1}$) to create a drift velocity of 10^{-4} – 10^{-2} cm s $^{-1}$ in the tiny space of NMR tubes. Hence, on the time scale of milliseconds (10^{-3} s), an ionic translational displacement in the order of microns (μm or $>10^{-6}$ m) would be generated to ensure experimental precision.

eNMR spectroscopy has been applied to numerous electrolytes in recent years, and the ionic transference numbers generated have been used for comparison with the data generated from other approaches. A general gap exists among these diverse ionic transference numbers, as summarized in Table 14.3, which will be further discussed in the next section. Given the nature of the eNMR technique of directly probing the ionic movement under an electric field, the data from eNMR spectroscopy should have higher confidence, and it has been used as a benchmark to make corrections to other approaches or to verify the theoretical models of modern ionics.

Among the limited eNMR data that have been published, of particular interest are those reported by Schönhoff and colleagues,²³ who showed that in an ionic liquid electrolyte system that consists of a lithium salt dissolved in an organic cation-based ionic liquid, Li $^+$ migrates in the “wrong” direction, and its velocity is nearly identical with that of the anions, whereas in non-aqueous electrolytes used in lithium-ion batteries, Li $^+$ and the corresponding anions migrate in their respective “right” directions. The measured Li $^+$ transference numbers range between –0.02 and –0.04 for those ionic liquid electrolytes. These negative cationic transference numbers are believed to arise from the ionic speciation similar to what was described by eqn (14.83), *i.e.* Li $^+$ moves in a vehicular manner in negatively charged complexes or clusters. The effective charges of such complexes or clusters are determined as –1 for LiTFSI dissolved in an imidazolium

ionic liquid, *i.e.* $[\text{Li}(\text{TFSI})_2]^-$, or -2 for LiBF_4 dissolved in the same ionic liquid, *i.e.* $[\text{Li}(\text{BF}_4)_3]^{2-}$. Because these ionic electrolytes work in lithium-ion batteries, there must be a second ion transport mechanism to compensate for the migration of Li^+ in the wrong direction, which should be the diffusional flux of neutral species such as $[\text{LiTFSI}]^0$ or $[\text{LiBF}_4]^0$ driven by the concentration gradient of Li^+ . This conclusion led to some sharp controversy, but it seems that the significant ionic speciation occurring in ionic liquids and super-concentrated electrolytes must have been behind these migrations in the wrong direction. In this sense, the effective transport of Li^+ in the “right” direction within these exotic electrolytes beyond the normal salt concentration range must either be compensated for by diffusional flux or supported by an alternative transport mechanism, such as the structural hopping of ions instead of vehicular transport.

In all the approaches for determining ionic transference numbers, eNMR spectroscopy is a unique method that is not only independent of any assumption of ideality, but also benefits from the combined advantages of NMR techniques, *i.e.* chemical specificity and non-invasive and *in situ* nature. The application of a DC voltage allows direct and quantitative probing of ionic movement under conditions that closely simulate the environment where the electrolyte is used. Moreover, eNMR spectroscopy can detect the movement of not only charged (ions) but also neutral (solvent molecules) species provided that they bear NMR-active nuclei that are sufficiently abundant for detection (such as ^1H , ^{13}C or ^{17}O in non-aqueous solvents). This enables us to see whether ions and solvent molecules are associated or not, and whether such associations are preferential. For example, recent studies revealed that the mobilities of Li^+ and oligoether-based solvent molecules are essentially identical, thus confirming that Li^+ ions in these electrolytes travel in the tight solvation cages as described in Figure 12.2. In other words, these solvated species $[\text{Li}(\text{Solv})_n]^+$ travels in a vehicular instead of structural manner, as discussed in Section 12.3.

However, as we emphasized at the beginning of Section 14.2, there is no perfect technique for determining ionic transference numbers. In addition to the common restrictions that any NMR technique faces, *i.e.* the limited nuclei and ready access to the instrumentation, eNMR spectroscopy requires the application of a DC voltage that is far beyond the electrochemical stability window of any known electrolyte. One can imagine that extensive electrolyte decomposition occurs under such polarization, which would generate both gaseous and solid by-products along with possible interphase formation. Despite the short time

frame where the DC voltage is applied, such decomposition will induce enough interferences to the actual potential drop applied on the bulk electrolyte in the NMR tube, thus preventing accurate calculation of field strength and consequently the ionic transference numbers. It has been estimated that there is a *ca.* 5% voltage loss due to the electrolyte decomposition on the electrode surfaces, depending on the time interval of DC polarization. From this perspective, one would want to minimize the duration of DC polarization; however, an additional source of inaccuracy of the eNMR technique actually comes from the short time frame of the DC polarization. Since the movement of ions is measured only instantaneously during milliseconds, their behavior might differ from what they would experience in a longer time frame. After all, the electrochemical performance of an electrolyte is dictated by the ion movement and speciation on a time scale of minutes to hours.

The adoption of an extremely high voltage and a very short DC polarization duration in fact originated from the same restriction, *i.e.* the electrodes used to generate DC polarization are blocking electrodes to both ions, hence lengthy polarization would induce Li^+ accumulation or depletion at these electrodes, consequently generating unwanted concentration gradients and diffusional flux. In 2006, Hayamizu proposed a modified eNMR tube design (Figure 14.22b) that might circumvent the above disadvantages.²¹ In this design, a pair of lithium-metal electrodes were used instead of inert electrodes made of materials blocking to both cations and anions. These lithium-metal electrodes serve as an electrochemical source (at the anode) or sink (at the cathode) for Li^+ , thus making it possible to polarize the electrolyte in a time frame that is comparable to the actual environments where electrolytes are used.

All things considered, eNMR spectroscopy is still the most promising technique that should experience rapid development and extensive applications in the years to come. The restrictions, especially the requirement associated with excessively high DC voltages and the time scale, could be lifted as result of the advances in technology and improvements in experimental sensitivities and measurement precision.

14.2.5 Reference Frame for Ionic Transference

One issue that is often overlooked in ion transference discussions is what reference frame the ion is moving in.²²

As in classical mechanics, any movement must be studied against a fixed reference frame. In those approaches that involve either direct chemical analysis or visual display of ion movements (Hittorf–Tubandt

approach, Section 14.2.4.1, or Lodge–Mason approaches, Section 14.2.4.2), the ionic transference is calculated based on the changes in the chemical composition of the electrolyte located in the cathode and anode compartments, respectively, and such changes are contrasted against the baseline composition, *i.e.* the “bulk” electrolyte in the middle sections of the cell. In other words, the ionic movement is referenced against an imaginary “stationary” electrolyte phase. In fact, in order to maintain such a stationary phase as a stable reference, care must be taken in Hittorf experiments not to “over-polarize” the cell so that the concentration profile shown in Figure 14.16a would not be disturbed. A major difference can be immediately seen between such a concentration profile and the concentration profile of the steady state in the symmetrical cell in the Bruce–Vincent approach (Figure 14.20).

Hence an extremely important but often tacit precondition for the Hittorf–Tubandt approach and Lodge–Mason approaches is that the solvent molecules, which carry no charge, do not move and serve as the stationary reference frame. Here, “do not move” refers to the zero contribution of solvent molecules to the migrational flux in response to the applied electric field. Again, as discussed in Section 5.2.1.1, the directionless movement, *i.e.* random walk by the solvent molecules, is not considered as violating the definition of “stationary”.

Therefore, all ionic transference numbers determined using the Hittorf–Tubandt approach or Lodge–Mason approaches have in fact been measured against the solvent as the reference frame (Figure 14.23a). This reference frame makes sense in dilute and even in most practical electrolytes, provided that there are free solvent molecules in the bulk electrolytes, because it is those solvent molecules beyond the influence of the Coulombic fields from the ions that can be viewed as the stationary reference. Otherwise, the solvent molecules, either in the primary and secondary solvation sheaths of the ions (Figure 3.5) or in the clusters and nano-heterogeneity structures (Figures 12.6 and 12.7), would be “kidnapped” by ions to participate in the migration in respond to the applied electric field. The solvents would cease to be a stationary reference.

Hence the “internal” reference frame based on solvent would vanish in super-concentrated electrolytes, and especially in the “extremity” of super-concentration: the ionic liquid. The complete absence of free and hence stationary solvent molecules therein makes the definition of ion transference less well defined. For example, in the simplest ionic liquid consisting of only two ions, the passage of electric charge across the cell would not create any concentration gradient for the

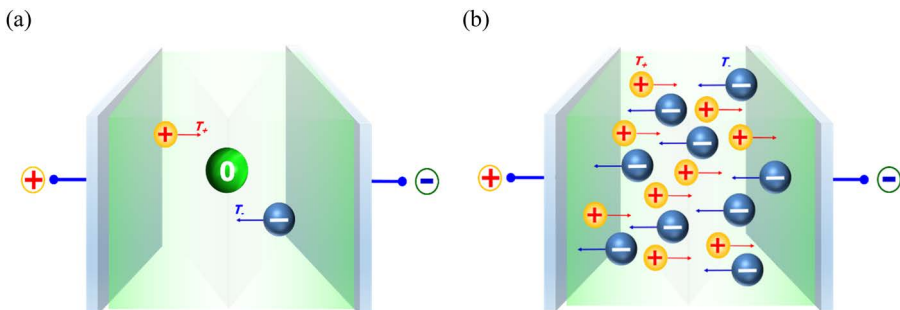


Figure 14.23 (a) The free solvent molecules serve as the internal reference frame for ion transference in the Hittorf-Tubandt approach or Lodge-Mason approaches. (b) The free solvent molecules vanish at super-concentration or in ionic liquids, hence the role of the internal reference frame falls on either of the ions. For an ionic liquid consisting of only two ions, the determination of ionic transference number becomes unnecessary if an internal reference frame is chosen.

ions while the net result of the current would be the transport of the ionic salt from one side of the cell to the other, depending on which ion is not blocked by the electrodes. In this particular electrolyte, the movement of any ion relative to the internal reference frame therein would be meaningless, because the reference frame is the other ion (Figure 14.23b), and the transference numbers should be given as

$$T_+^- = 1.0; T_-^- = 0.0 \quad (14.189)$$

$$T_+^+ = 0.0; T_-^+ = 1.0 \quad (14.190)$$

where the superscript refers to the “internal reference frame” and the subscript to the ion whose transference we are attempting to describe. In other words, if the anion is chosen as the reference frame, the cationic transference number would be 1.0, and *vice versa*. It is unnecessary to determine either in this case.

In a more complicated ionic liquid system consisting of more than two ions, such as the frequently encountered ionic liquid electrolytes used to support lithium or lithium-ion battery chemistries, the transference behavior of the individual ions can be referenced against one of the ions, then the description of the relative contributions of other ions to the migration becomes meaningful. For example, in the popular ionic liquid electrolyte consisting of LiTFSI dissolved in an

onium salt (*e.g.* 1-ethyl-3-methylimidazolium, EMIM^+) with the same anion, the common anion TFSI can be chosen as the internal reference frame, and transference numbers for Li^+ ($T^{\text{TFSI}}_{\text{Li}}$) and EMIM^+ ($T^{\text{TFSI}}_{\text{EMIM}}$) would add up to unity:

$$T^{\text{TFSI}}_{\text{Li}} + T^{\text{TFSI}}_{\text{EMIM}} = 1.0 \quad (14.191)$$

Now it is necessary to determine the value of either Li^+ against the anion reference frame ($T^{\text{TFSI}}_{\text{Li}}$) or EMIM^+ against the anion reference frame ($T^{\text{TFSI}}_{\text{EMIM}}$). Again, the superscript TFSI stands for to the internal reference frame we choose, and the subscript Li or EMIM refers to the ion whose transference we are attempting to describe.

On the other hand, for those who are more interested in the function of electrolytes in transporting charge, an external reference frame would be more useful. Such a reference frame could be either the electrolyte/electrode interfaces or the porous separators in the electrochemical cell. Such an “external” reference frame is also known as the “*laboratory reference frame*”. All of those approaches that employ a reversible electrochemical reaction at the electrolyte/electrode interfaces, such as Armand approach (Section 14.2.4.3), Sørensen–Jacobsen approach (Section 14.2.4.5) or Bruce–Vincent approach (Section 14.2.4.6), determine the ionic transference against the external or laboratory reference frames.

A third reference frame, also considered “internal”, is the “*center-of-mass frame*” (CoM frame), which is often favored in computation simulations. It is based on the statement that, in a closed system, under ideal conditions, the momentum of all moving species must be conserved. Thus, on application of an electric field, with the cations and anions moving in different directions, the total momentum P_{total} should be zero:

$$P_{\text{total}} = \sum_i p_i = \sum_i m_i n_i \vec{v}_i = 0 \quad (14.192)$$

where m_i , n_i and \vec{v}_i are the molecular mass, number and velocity of species i , respectively. Note that \vec{v}_i is a vector with direction. In other words, the CoM for an ideally closed system should be stationary and qualified to serve as a reliable reference frame. It could be a more reliable reference frame than solvent molecules as suggested by the Hittorf–Tubandt approach or Lodge–Mason approaches, especially when the solvent molecules participate in the migration, or when there is no presence of solvent molecules at all, such as super-concentrated electrolytes and ionic liquids.

Thus, when it is possible to determine independently the drift velocity (or mobility) of every component (cation, anion and solvent), the velocity (or mobility) of the CoM against the laboratory reference frame ($\mu_{\text{CoM}}^{\text{LF}}$) could be calculated from the velocities of each individual species against the laboratory reference frame (μ_i^{LF}) along with their molar concentrations (c_i) and molecular masses (M_i):

$$\mu_{\text{CoM}}^{\text{LF}} = \frac{\sum_i \mu_i^{\text{LF}} M_i c_i}{\sum_i M_i c_i} \quad (14.193)$$

Since every component in the electrolyte including solvent must be included in eqn (14.187) and (14.188), the denominator in the latter is actually the density of the electrolyte ρ , thus turning eqn (14.193) into

$$\mu_{\text{CoM}}^{\text{LF}} = \frac{\sum_i \mu_i^{\text{LF}} M_i c_i}{\rho} \quad (14.194)$$

Knowing how fast the CoM drifts against the laboratory frame, one can easily convert the mobilities of individual species into the CoM reference frame by

$$\mu_i^{\text{CoM}} = \mu_i^{\text{LF}} - \mu_{\text{CoM}}^{\text{LF}} \quad (14.195)$$

Schönhoff and co-workers used eNMR spectroscopy to determine the drift velocity (or mobility) of cations, anions and solvent molecules in an electrolyte consisting of LiFSI dissolved in a glyme solvent G4.²³ In such an electrolyte system, Li^+ forms a tight solvation cage similar to that shown in Figure 12.2 (Section 12.2.1) and travels in a vehicular manner, hence every component is migrating under the applied electric field: Li^+ and the solvating solvent G4 move along the electric field, and the FSI anion in the opposite direction. They performed the conversion using eqn (14.194) and (14.195), and found only slight differences between the ion mobilities and the transference numbers when referenced against the laboratory and CoM frames. This was because the CoM drift velocity is nearly negligible in comparison with the drift velocities of cations and anions. However, in real life, it was found that CoM is not always stationary, but instead may drift on its own. This deviation from the conservation of momentum could be caused by imperfections of the experimental cells, which arise from Joule heating by the passage of current, or gravitational or mechanical convections, or asymmetry of the electrochemical reactions, etc.

14.3 Ionics for Non-ideal Electrolytes

From Table 14.3, it is easy to see the chaotic picture of the efforts in understanding ion transport behaviors in the presence of ionic speciation in concentrated electrolytes, which is still a dynamic area and where active debate is ongoing. To shed light from a fundamental perspective on how the ion speciation in concentrated electrolytes affects the ion transport, so that the wide gaps that exist in these ion transference numbers obtained from different approaches could be resolved, various efforts have been made in the last two decades to develop rigorous formulations that govern the transport properties of charged species in electrolytes. The most influential analytical models are constructed upon the frameworks of either *Onsager formalism* or *Stefan–Maxwell formalism*.^{24–26}

Onsager formalism was originally developed to describe the relation between fluxes and the thermodynamic forces driving such fluxes. The thermodynamic driving force X could be any gradient created by chemical, thermal, electrical or magnetic inequilibrium, while the flux for each individual species J is assumed to be in a *linear* relationship with such a driving force, *i.e.*

$$J_1 = L_{11}X_1 + L_{12}X_2 + L_{13}X_3 + \dots \quad (14.196)$$

$$J_2 = L_{21}X_1 + L_{22}X_2 + L_{23}X_3 + \dots \quad (14.197)$$

$$J_3 = L_{31}X_1 + L_{32}X_2 + L_{33}X_3 + \dots \quad (14.198)$$

⋮

where X_j is the thermodynamic driving force and L_{ij} are the *Onsager thermodynamic transport coefficients* or simply *Onsager transport coefficients*, which describe the interactions between species i and j .

Basically, in the Onsager formalism the motions of each species involved are coupled *via* the Onsager coefficients with other species, *i.e.* the motion of species i is no longer independent but instead is correlated with that of every other species j , which can be generalized into

$$J_i = \sum_j L_{ij} X_j \quad (14.199)$$

The linearity in the relation between flux and driving force is in fact not a stranger to us, as we have encountered it previously, for example in Fick's first law (Section 5.1.1), where the driving force X is the concentration gradient dc_i/dx :

$$J_i = -D \frac{dc_i}{dx} \quad (5.1)$$

or in the Nernst–Planck equation, where the driving force X is the electrochemical potential gradient $d\overline{\mu}_i/dx$:

$$J_i = -\frac{\mu_{\text{Conv}} c_i}{z_i F} \frac{d\overline{\mu}_i}{dx} \quad (5.121)$$

where the electrochemical potential can be expanded into electrostatic and chemical portions:

$$\overline{\mu}_i = \mu_i + z_i F \psi \quad (5.117)$$

The key point made by eqn (14.199) is that, in non-ideal electrolytes, the flux of any individual species is no longer dictated just by the driving force acting upon it, but also is being affected by *the driving forces acting on the other species via* the Onsager coefficients. In other words, to understand the transport behavior of a given species, we will not only need to know its own properties such as concentration, charge and self-diffusion coefficient, but also those of other species as well as their correlation coefficients.

Unlike the equations describing flux, conductivity or current discussed in Section 14.2.1, where the summation signs (“ Σ ” or “ $+$ ”) usually imply ideality because of their origin from the Nernst–Einstein equation, no assumption of ideality is made in eqn (14.192)–(14.194), because the Onsager coefficients already accounted for the interionic correlations.

An important principle of Onsager formalism is the *reciprocity* among the Onsager coefficients, which acts in a similar manner to Newton's third law:

$$L_{12} = L_{21} \quad (14.200)$$

$$L_{13} = L_{31} \quad (14.201)$$

$$L_{23} = L_{32} \quad (14.202)$$

⋮

$$L_{ij} = L_{ji} \quad (14.203)$$

In alternative but similar logic the Stefan–Maxwell equations were originally developed to describe the diffusion of particles in the gaseous state, and view the motions of the particles from the perspective of force balance, *i.e.* the thermodynamic force acting on the species i is balanced by the friction between this species with other species j , while such friction is proportional to the velocity differences ($\bar{v}_j - \bar{v}_i$) between this species and the others. For the motion of a charged particle i , whose driving force is again in a linear relationship with the gradient of its electrochemical potential $\bar{\mu}_i$, one can therefore write

$$c_i \frac{d}{dx} \bar{\mu}_i = \sum_{j \neq i} K_{ij} (\bar{v}_j - \bar{v}_i) \quad (14.204)$$

where K_{ij} is the binary drag coefficient describing the friction between species i and species j . K_{ij} is also called the *Stefan–Maxwell transport coefficient* and, as we will see later in Section 14.4.1, it serves a similar purpose as the Onsager coefficients in eqn (14.199).

Constructed upon both Onsager and Stefan–Maxwell frameworks, numerous approaches and models have been developed for non-ideal electrolytes, the most prominent of which is the concentrated solution theory established by Newman and colleagues. We cannot exhaustively review these models in this book, but for those with further interest in their derivation, the foundational book *Electrochemical Systems* by Newman and Balsara²⁴ and follow-up work,^{27,28} and also the seminal experimental work of Roling and colleagues^{29,30} and the modified theoretical approach of Fong and co-workers^{25,26} are recommended. Here, we will only briefly touch upon the topic by demonstrating, within the Onsager formalism, how the ion–ion interactions change the concentration and potential distributions as well as the corresponding ion diffusional and migrational fluxes when DC polarization is applied. It is especially interesting to find, when the DC polarization curve as shown in Figure 14.14 is analyzed in the new perspective of the Onsager formalism, what difference the interionic interaction would cause to the currents observed at the initial state ($t = 0$) and steady state ($t = t_{ss}$).

Let us again consider the simplest electrolyte, *i.e.* an electrolyte consisting of a monovalent salt M^+X^- . Eqn (5.118) told us that the cationic and anionic fluxes are independently driven by the gradient of their own electrochemical potentials:

$$J_i = -\frac{D_i c_i}{RT} \frac{d\bar{\mu}_i}{dx} \quad (5.118)$$

which is no longer true here owing to the interionic correlations. In the Onsager formalism, a linear relation still exists for an ion between its flux and its electrochemical potential gradient, but there is now an interaction term that links the cationic flux with the gradient of anionic electrochemical potential, and *vice versa*, because of the interionic correlations. Hence we can rewrite the cationic and anionic fluxes as follows:

$$J_+ = - \left[L_{++} \frac{d\bar{\mu}_+}{dx} + L_{+-} \frac{d\bar{\mu}_-}{dx} \right] \quad (14.205)$$

$$J_- = - \left[L_{--} \frac{d\bar{\mu}_-}{dx} + L_{-+} \frac{d\bar{\mu}_+}{dx} \right] \quad (14.206)$$

where L_{++} describes the correlations between the movements of different cations and L_- the correlations between the movements of different anions, while L_{+-} and L_{-+} serve as the interaction terms defining the correlations between cations and anions. Remember that owing to reciprocity, these two terms are identical:

$$L_{+-} = L_{-+} \quad (14.207)$$

In an ideal electrolyte, all correlations are absent, while L_+ becomes zero, causing eqn (14.205) and (14.206) to collapse into simple forms described by eqn (5.118). A comparison would immediately find that L_{++} and L_- in ideal electrolytes are just dictated by the self diffusion coefficients of each ion

$$L_{++} = \frac{D_+ c_+}{RT} \quad (14.208)$$

$$L_{--} = \frac{D_- c_-}{RT} \quad (14.209)$$

We can again expand the expressions for electrochemical potentials based on eqn (5.117) into an electrostatic term and a chemical term:

$$\overline{\mu_i} = \mu_i + z_i F\psi \quad (5.117)$$

with $z_+ = +1$ for a cation and $z_- = -1$ for an anion. Moreover, the chemical potential term can be further expanded into

$$\mu_i = \mu_i^0 + RT \ln a_i \quad (5.115)$$

Note that, differing from the original eqn (5.115), activity a_i instead of concentration c_i is used here because we are now dealing with practical and non-ideal electrolytes. Hence the electrochemical potential gradients for cation and anion now become

$$\frac{d\overline{\mu_+}}{dx} = F \frac{d\psi}{dx} + RT \frac{d\ln a_+}{dx} \quad (14.210)$$

$$\frac{d\overline{\mu_-}}{dx} = F \frac{d\psi}{dx} + RT \frac{d\ln a_-}{dx} \quad (14.211)$$

which are then inserted into eqn (14.205) and (14.206), leading to the cationic and anionic fluxes that reflect the consideration of interionic correlations:

$$J_+ = - \left[L_{++} \left(F \frac{d\psi}{dx} + RT \frac{d\ln a_+}{dx} \right) + L_{+-} \left(-F \frac{d\psi}{dx} + RT \frac{d\ln a_-}{dx} \right) \right] \quad (14.212)$$

$$J_- = - \left[L_{--} \left(-F \frac{d\psi}{dx} + RT \frac{d\ln a_-}{dx} \right) + L_{+-} \left(F \frac{d\psi}{dx} + RT \frac{d\ln a_+}{dx} \right) \right] \quad (14.213)$$

We are still dealing with a simple monovalent electrolyte, but the picture already becomes complicated once interionic correlations are considered.

It should be mentioned that, as the activity coefficients for individual ions are difficult to measure, in real life the mean activity coefficients are often used instead:

$$\gamma_\pm = \sqrt{\gamma_+ \gamma_-} \quad (3.6)$$

Hence the individual activity becomes

$$a_+ = a_- = a_\pm = \gamma_\pm c_{\text{Salt}} \quad (14.214)$$

Correspondingly, eqn (14.212) and (14.213) could be rewritten in the following forms, after replacing the mean ion activities with eqn (14.214) and looping together the electrostatic and chemical components, respectively:

$$J_+ = - \left[(L_{++} - L_{+-})F \frac{d\psi}{dx} + (L_{++} + L_{+-})RT \frac{d\ln a_+}{dx} \right] \quad (14.215)$$

$$J_- = - \left[(L_{+-} - L_{--})F \frac{d\psi}{dx} + (L_{--} + L_{+-})RT \frac{d\ln a_\pm}{dx} \right] \quad (14.216)$$

Here we define a new quantity, the “thermodynamic factor” Φ :

$$\Phi = \frac{d\ln a_\pm}{d\ln(C_{\text{Salt}})} = \frac{d\ln(\gamma_\pm C_{\text{Salt}})}{d\ln(C_{\text{Salt}})} = 1 + \frac{d\ln \gamma_\pm}{d\ln(C_{\text{Salt}})} \quad (14.217)$$

and further transform eqn (14.215) and (14.216) into

$$J_+ = - \left[(L_{++} - L_{+-})F \frac{d\psi}{dx} + (L_{++} + L_{+-})RT\Phi \frac{d\ln C_{\text{Salt}}}{dx} \right] \quad (14.218)$$

$$J_- = - \left[(L_{+-} - L_{--})F \frac{d\psi}{dx} + (L_{--} + L_{+-})RT\Phi \frac{d\ln C_{\text{Salt}}}{dx} \right] \quad (14.219)$$

The thermodynamic factor describes the non-ideality of the electrolytes. For an ideal electrolyte it of course collapses into 1.0, but for practical electrolytes it can be determined by using a concentration cell that was described in Section 14.2.4.3 when discussing the Armand approach. In fact, the differential form of eqn (14.129) is better known:

$$d(\text{emf}) = \frac{2RT}{F}(1 - T_+) d\ln a_\pm = \frac{2RT}{F}(1 - T_+) \Phi d\ln(C_{\text{Salt}}) \quad (14.220)$$

which can be rearranged into

$$\frac{d(\text{emf})}{d\ln(C_{\text{Salt}})} = \frac{2RT}{F}(1 - T_+) \Phi \quad (14.221)$$

Thus, one could derive the thermodynamic factor by monitoring the change in cell potential as a function of salt concentration in a concentration cell, provided that one knows the ionic transference number of the electrolyte system. In other words, the ionic transference number and

thermodynamic factor are coupled in eqn (14.220) and (14.221), so one has to know one of them in order to determine the other. To make things more complicated, in the statement above, we have a tacit assumption that the ionic transference number is a constant that does not change with salt concentration, which, in practical electrolytes, does not hold true. Therefore, caution must be exercised when using a concentration cell to determine thermodynamic factors or ionic transference numbers.

The thermodynamic factor is an important quantity for practical electrolytes, in addition to ion conductivity, ionic transference numbers and diffusion coefficients.

14.3.1 At the Initial Instant

Now let us place the above electrolyte in a symmetrical cell as we did before in the Bruce–Vincent approach and then apply a DC polarization. At the initial instant, no concentration gradient (or activity gradient) is established for either ion, and the ionic motion is entirely migrational driven by the electric field. Hence the chemical potential terms in eqn (14.212) and (14.213) could be eliminated, giving

$$J_+ = - \left[L_{++} F \frac{d\psi}{dx} - L_{+-} F \frac{d\psi}{dx} \right] = (L_{++} - L_{+-}) \left(- \frac{d\psi}{dx} \right) \quad (14.222)$$

$$J_- = - \left[L_{--} F \frac{d\psi}{dx} + L_{+-} F \frac{d\psi}{dx} \right] = (-L_{--} + L_{+-}) \left(- \frac{d\psi}{dx} \right) \quad (14.223)$$

In fact, the absence of diffusional terms is also true in AC impedance experiments in the high-frequency domain, where the ion accumulation or depletion does not have sufficient time to be built.

Also at this instant, the electrostatic gradient is actually the initial electric field applied on the bulk electrolyte:

$$\frac{d\psi}{dx} = \frac{\Delta V}{d} = -E_{\text{Bulk}}^0 \quad (14.224)$$

where ΔV is the voltage applied during the DC polarization and d the distance between the two electrodes. Hence we can simplify eqn (14.222) and (14.223) to

$$J_+ = -F(L_{++} - L_{+-})E_{\text{Bulk}}^0 \quad (14.225)$$

$$J_- = -F(L_{--} - L_{+-})E_{\text{Bulk}}^0 \quad (14.226)$$

The total ion flux is then given by

$$J_{\text{Total}} = J_+ + J_- = -F(L_{++} + L_{--} - 2L_{+-})E_{\text{Bulk}}^0 \quad (14.227)$$

while the initial current I_0 should be correspondingly given by

$$i_0 = FJ_{\text{Total}} = -F^2(L_{++} + L_{--} - 2L_{+-})E_{\text{Bulk}}^0 \quad (14.228)$$

Unlike what was said in the previous section that the summation signs therein imply electrolyte ideality, here the summation relation already accounted for the ion–ion correlations.

14.3.2 At the Steady State

When the electrolyte in a symmetrical cell eventually reaches the steady state, a concentration gradient has been established, which generates a diffusional flux that exactly counterbalances the migrational flux of the blocked ion, hence the net anionic flux J_- becomes zero. From eqn (14.213) we will have

$$\left[L_{--} \left(-F \frac{d\psi}{dx} + RT \frac{d \ln a_-}{dx} \right) = -L_{+-} \left(F \frac{d\psi}{dx} + RT \frac{d \ln a_+}{dx} \right) \right] \quad (14.229)$$

which can be rearranged to

$$(L_{--} - L_{+-})F \frac{d\psi}{dx} = L_{+-}RT \frac{d \ln a_+}{dx} + L_{--}RT \frac{d \ln a_-}{dx} \quad (14.230)$$

To simplify the activity gradients at the steady state, we assume that, within every cross-sectional layer of the electrolyte, the electroneutrality is still maintained, as we did in Section 14.2.4.6.1, so that

$$a_+ = a_- = a \quad (14.231)$$

Then eqn (14.230) can be transformed into

$$RT \frac{d \ln a}{dx} = \frac{L_{--} - L_{+-}}{L_{--} + L_{+-}} F \frac{d\psi}{dx} \quad (14.232)$$

Thus, for an electrolyte cross-section layer of thickness dx , the potential drop $d\psi$ is given by

$$d\psi = \frac{L_{--} + L_{+-}}{L_{--} - L_{+-}} \frac{RT}{F} d\ln a \quad (14.233)$$

and we can extrapolate eqn (14.233) into the entire bulk electrolyte sandwiched in the symmetrical cell of thickness d , across which the potential drop $\Delta\psi_{\text{Bulk}}^{\text{ss}}$ should be

$$\Delta\psi_{\text{Bulk}}^{\text{ss}} = \frac{L_{--} + L_{+-}}{L_{--} - L_{+-}} \frac{RT}{F} \Delta\ln a \quad (14.234)$$

where $\Delta\ln a$ is the change in salt activity across the bulk electrolyte. The electric field across the bulk electrolyte at the steady state, $E_{\text{Bulk}}^{\text{ss}}$, is accordingly given by

$$E_{\text{Bulk}}^{\text{ss}} = \frac{\Delta\psi_{\text{Bulk}}^{\text{ss}}}{d} = \frac{L_{--} + L_{+-}}{L_{--} - L_{+-}} \frac{RT}{Fd} \Delta\ln a \quad (14.235)$$

Meanwhile, the electrolyte is also at equilibrium with both electrodes, hence the potential drop across the electrolyte/electrolyte interfaces $\Delta\psi_i^{\text{ss}}$ should be obtained from the Nernst equation [in a similar way to eqn (14.169)] as

$$\Delta\psi_i^{\text{ss}} = \frac{RT}{F} \Delta\ln a \quad (14.236)$$

Comparing the equation couples (14.234) and (14.236) *versus* (14.169) and (14.173), one can immediately see that, when interionic correlations are considered, the potential drop across the bulk electrolyte $\Delta\psi_{\text{Bulk}}^{\text{ss}}$ is no longer the same as the potential drop across electrolyte/electrode interfaces $\Delta\psi_i^{\text{ss}}$, hence a major basis for the Bruce–Vincent approach discussed in Section 14.2.4.6.3 vanishes. Consequently, the cationic transference number can no longer be obtained by using eqn (14.144) or (14.187).

However, the summation of $\Delta\psi_{\text{Bulk}}^{\text{ss}}$ and $\Delta\psi_i^{\text{ss}}$ still adds up to the applied voltage ΔV :

$$\Delta V = \Delta\psi_{\text{Bulk}}^{\text{ss}} + \Delta\psi_i^{\text{ss}} = \left[\frac{2L_{--}}{L_{--} - L_{+-}} \right] \frac{RT}{F} \Delta\ln a \quad (14.237)$$

Meanwhile, the steady-state current i^{ss} is only contributed to by the cationic flux as described by eqn (14.222):

$$\begin{aligned} J_+ &= - \left[L_{++} \left(F \frac{d\psi}{dx} + RT \frac{d \ln a_+}{dx} \right) + L_{\pm} \left(-F \frac{d\psi}{dx} + RT \frac{d \ln a_-}{dx} \right) \right] \\ &= F \frac{d\psi}{dx} (L_{+-} - L_{++}) - RT \frac{d \ln a}{dx} (L_{++} + L_{+-}) \end{aligned} \quad (14.238)$$

In order to eliminate the term with activity, we resort to eqn (14.238) and obtain

$$\frac{d \ln a}{dx} = \frac{L_{--} - L_{+-}}{L_{--} + L_{+-}} \frac{F}{RT} \frac{d\psi}{dx} \quad (14.239)$$

and insert it into eqn (14.234), so that the cationic flux is related only to a potential term:

$$\begin{aligned} J_+ &= F \frac{d\psi}{dx} (L_{+-} - L_{++}) - RT (L_{++} + L_{+-}) \frac{L_{--} - L_{+-}}{L_{--} + L_{+-}} \frac{F}{RT} \frac{d\psi}{dx} \\ &= F \frac{d\psi}{dx} \left[(L_{+-} - L_{++}) - \frac{L_{--} - L_{+-}}{L_{--} + L_{+-}} (L_{++} + L_{+-}) \right] \end{aligned} \quad (14.240)$$

Note that $-d\psi/dx$ actually represents the electric field across the bulk electrolyte at the steady state $E_{\text{Bulk}}^{\text{ss}}$, so we can rewrite eqn (14.240) as

$$J_+ = -F \left[(L_{+-} - L_{++}) - \frac{L_{--} - L_{+-}}{L_{--} + L_{+-}} (L_{++} + L_{+-}) \right] E_{\text{Bulk}}^{\text{ss}} \quad (14.241)$$

Since $E_{\text{Bulk}}^{\text{ss}}$ is still a value that is difficult to measure experimentally, we need to relate it to the applied voltage across the cell, as we did in deriving the Bruce–Vincent approach in Section 14.2.4.6.

The applied voltage ΔV is a constant, no matter whether the cell is at the initial state or steady state, hence the electric field at the initial state E_{Bulk}^0 is given by eqn (14.224). Inserting it into eqn (14.237) and solving for $\Delta \ln a$, we obtain

$$\Delta \ln a = E_{\text{Bulk}}^0 \frac{L_{--} - L_{+-}}{2L_{--}} \frac{Fd}{RT} \quad (14.242)$$

Inserting eqn (14.242) into eqn (14.235), we obtain a new expression for the electric field across the bulk electrolyte at the steady state:

$$E_{\text{Bulk}}^{\text{ss}} = \frac{L_{--} + L_{+-}}{2L_{-}} E_{\text{Bulk}}^0 \quad (14.243)$$

Now, inserting eqn (14.243) into eqn (14.241), we obtain the expression for the cationic flux at the steady state when interionic correlations are considered in the Onsager formalism:

$$J_{+} = F \left[\left(L_{+-} - L_{++} \right) - \frac{L_{--} - L_{+-}}{L_{--} + L_{+-}} \left(L_{++} + L_{+-} \right) \right] \frac{L_{--} + L_{+-}}{2L_{-}} E_{\text{Bulk}}^0 \quad (14.244)$$

and the corresponding current is given by

$$i^{\text{ss}} = F J_{+} = F^2 \left[\left(L_{+-} - L_{++} \right) - \frac{L_{--} - L_{+-}}{L_{--} + L_{+-}} \left(L_{++} + L_{+-} \right) \right] \frac{L_{--} + L_{+-}}{2L_{-}} E_{\text{Bulk}}^0 \quad (14.245)$$

Comparing the two sets of equations eqn (14.150) and (14.179) *versus* eqn (14.227) and (14.245), although these Onsager transport coefficients are unknown, one can already realize how much interionic correlations have complicated the currents measured at both the initial and steady state. Apparently the cationic transference number can no longer be obtained from the simple ratio between i^{ss} and i_0 . Only when L_{+-} becomes zero do i^{ss} and i_0 as expressed in eqn (14.227) and (14.245) collapse to

$$i_0 = F^2 (L_{++} + L_{--}) E_{\text{Bulk}}^0 \quad (14.246)$$

$$i^{\text{ss}} = F J_{+} = F^2 \left[L_{++} - \frac{L_{--}}{L_{--}} L_{++} \right] \frac{L_{--}}{2L_{--}} E_{\text{Bulk}}^0 = F^2 L_{++} E_{\text{Bulk}}^0 \quad (14.247)$$

And it is only under such conditions that the cationic transference number can be obtained from the ratio between i^{ss} and i_0 :

$$\left[\frac{i^{\text{ss}}}{i_0} \right]_{\text{ideal}} = T_{+} = \frac{L_{++}}{L_{++} + L_{--}} \quad (14.248)$$

In non-ideal, practical electrolytes, when all interionic correlations are considered, the ratio between the current at the steady state and the initial state does not yield the true cationic transference number,

but rather takes a complicated form that does not carry any apparent physical significance:

$$\left[\frac{i^{\text{ss}}}{i_0} \right]_{\text{Non-ideal}} = \frac{L_{++} L_{--} - (L_{+-})^2}{L_{++} L_{--} + (L_{--})^2 - 2L_{+-} L_{--}} \neq T_+ \quad (14.249)$$

14.3.3 What are these Onsager Transport Coefficients?

Comparing the equation couples eqn (14.227) and (14.245) again with eqn (14.150) and (14.179), we obtain the two Onsager transport coefficients L_{++} and L_{--} in ideal electrolytes, *i.e.* when there are no cation-anion correlations:

$$L_{++} = \frac{D_+ c_0}{RT} = \frac{\sigma_+}{F^2} \quad (14.250)$$

$$L_{--} = \frac{D_- c_0}{RT} = \frac{\sigma_-}{F^2} \quad (14.251)$$

where σ_+ and σ_- are cationic and anionic conductivities, respectively, which are directly independently determined by their own self-diffusion coefficients D_+ and D_- .

Hence in ideal electrolytes, the overall ion conductivity can be viewed as the summation of the individual conductivity of cations and anions, which are defined as

$$\sigma_+ = T_+ \sigma \quad (14.252)$$

$$\sigma_- = \sigma - \sigma_+ = (1 - T_+) \sigma \quad (14.253)$$

In practical electrolytes, however, not only is L_{+-} no longer zero, but the other two Onsager transport coefficients L_{++} and L_{--} must also take much more complicated forms owing to interionic correlations among the ions of the same charge themselves, *i.e.* the repulsion of cations against cations, and repulsion of anions against anions. In other words, not only is the overall ion conductivity no longer the simple summation of cationic and anionic conductivities; more importantly, the two Onsager transport coefficients L_{++} and L_{--} are affected by the correlations among the ions of the same charge, *i.e.* L_{++} must also account for the interionic correlations among the cations themselves, in addition to the cationic conductivity σ_+ , and L_{--} must

account for the interionic correlations among the anions themselves, in addition to the anionic conductivity σ_- . We name such correlations among the ions of the same charge “*distinct correlations*” to differentiate them from the “*self*” cationic and anionic conductivities (σ_+^s and σ_-^s) induced by their own self diffusion coefficients [*i.e.* σ_+ and σ_- in eqn (14.250) and (14.251)].

In such a context, the expression of the overall ion conductivity should be modified to

$$\begin{aligned}\sigma_{\text{Total}} &= (\sigma_+^s + \sigma_{++}^d - \sigma_{+-}) + (\sigma_-^s + \sigma_{--}^d - \sigma_{+-}) \\ &= \sigma_+^s + \sigma_{++}^d + \sigma_-^s + \sigma_{--}^d - 2\sigma_{+-}\end{aligned}\quad (14.254)$$

The newly added quantities σ_{++}^d , σ_{--}^d and σ_{+-} actually just express the Onsager transport coefficients L_{++} , L_{--} and L_{+-} in an alternative form with conductivity units, and therefore they are also known as “*Onsager conductivity coefficients*”. We just need to remember that they are related to the Onsager transport coefficients *via* a simple relation:

$$\sigma_i = F^2 L_i \quad (14.255)$$

Only when all these “distinct” correlations (σ_{++}^d , σ_{--}^d and σ_{+-}) become zero can the expression of overall ion conductivity collapse into the simple form for ideal electrolytes:

$$\sigma_{\text{Total}} = \sigma_+^s + \sigma_-^s \quad (14.256)$$

Now let us examine what these interionic correlations could be for a simple electrolyte that consists of a monovalent salt $[\text{C}^+\text{A}^-]$ at practical salt concentrations. In such a non-ideal electrolyte, each ion feels the existence of the other ions, no matter whether these ions bear the same or the opposite charge with it.

Considering the ionic species, there should be *three* possible combinations, *i.e.* (1) cation–cation corresponding to σ_{++}^d , (2) anion–anion corresponding to σ_{--}^d and (3) cation–anion corresponding to σ_{+-} .

On the other hand, considering the nature of their interactions, there are *three* possible outcomes, *i.e.* (1) *uncorrelated*, *i.e.* the considered ions do not have any correlation with each other, and their movement in the electrolyte is completely independent; (2) *correlated*, *i.e.* the considered ions are coupled in their transport and move in a preferential direction; and (3) *anticorrelated*, *i.e.* the considered ions repulse each other in their transport and move preferentially in opposite directions.

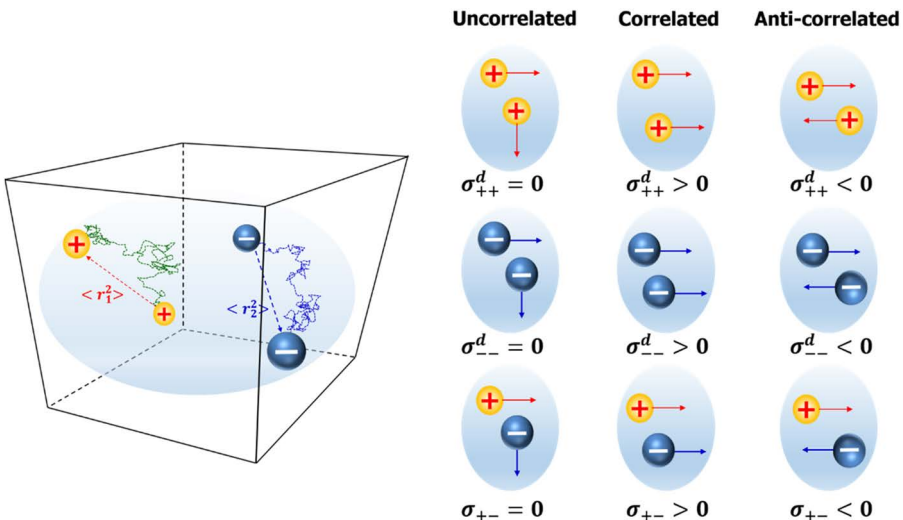


Figure 14.24 Schematic illustration of the nine possible scenarios of interionic correlation in a simple electrolyte consisting of a monovalent salt, which arise from three Onsager conductivity coefficients (σ_{++}^d , σ_{--}^d and σ_{+-}) describing the ionic combinations, and three possible outcomes (uncorrelated, correlated and anticorrelated). The uncorrelated scenario, if holding true for all three situations, i.e. $\sigma_{++}^d = 0$, $\sigma_{--}^d = 0$ and $\sigma_{+-} = 0$, represents the ideal electrolyte.

These three combinations of intercorrelated ionic species and three interaction natures would produce nine possible scenarios in total, which are illustrated schematically in Figure 14.24. Note that only when *all three* ionic species combinations are *simultaneously* uncorrelated ($\sigma_{++}^d = \sigma_{--}^d = \sigma_{+-} = 0$) can the electrolyte be considered ideal.

In addition to eqn (14.208) and (14.209), eqn (14.250) and (14.251) further revealed that, despite the mysterious appearance of these Onsager transport coefficients, they are simply quantities related to the ion transport behaviors. In ideal electrolytes, they would collapse into familiar quantities related to self-diffusion coefficients or ion conductivities. In practical electrolytes where complicated ionic speciation occurs, they reflect the contributions from all kinds of interionic correlations to the transport behaviors of the ions.

The advantage of the result given by eqn (14.250) and (14.251) turns the Onsager formalism into a form that is easier to calculate and therefore often favored in MD simulation studies. In the simulation box, one just needs to place a force on a particle and calculate the

resultant velocities and mobilities thus generated. That allows us to quickly evaluate the Onsager transport coefficients:

$$\mu_+ = \frac{\sigma_+^s + \sigma_{++}^d + \sigma_{+-}}{Fc_0} \quad (14.257)$$

$$\mu_- = \frac{\sigma_-^s + \sigma_{--}^d + \sigma_{+-}}{Fc_0} \quad (14.258)$$

The experimental determination of Onsager coefficients requires the combination of different techniques, because even for a simple electrolyte system consisting of a monovalent salt, there are at least *three* Onsager transport coefficients (L_{++} , L_{--} and L_{+-}), which mathematically need *four* measured properties to solve. If one further breaks it down to *five* Onsager conductivity coefficients (σ_+^s , σ_-^s , σ_{++}^d , σ_{--}^d and σ_{+-}), then more experimentally measurable quantities are needed. These quantities often have to be measured by very different experimental techniques, for example, ion conductivity by AC impedance spectroscopy, ionic transference number by eNMR spectroscopy or low-frequency AC impedance spectroscopy (Sørensen–Jacobsen approach) or potentiostatic polarization (Bruce–Vincent approach), salt diffusion coefficient, thermodynamic factor or mean activity coefficients by concentration cell, and self-diffusion coefficients from pfg-NMR spectroscopy, *etc.* The separate errors arising from each experiment would soon add up and propagate, introducing large uncertainties in the final values of Onsager coefficients.

It was for this reason that there have been very few reports on these Onsager coefficients. Table 14.4 lists those reported in the literature in recent years.

Although one may note that these data are widely scattered even for the same electrolyte (for example, LiTFSI–G4), a general trend can still be found, namely that both distinct coefficients (σ_{++}^d and σ_{--}^d) and the cross-species term (σ_{+-}) are negative.

How do we understand this?

Intuitively, one would expect that the distinct term for cations (σ_{++}^d) should be negative, because the Coulombic repulsion among cations would not encourage all cations to travel in the same direction. Thus, the presence of a cation–cation correlation reduces the overall contribution from cations to the overall ion conductivity. The same logic also governs σ_{--}^d to be negative, as its presence reduces the overall contribution from anions to the overall ion conductivity. Thus, cation–cation and anion–anion inter-correlations are both “anticorrelated” according to Table 14.4.

Table 14.4 Onsager conductivity coefficients in binary monovalent electrolytes determined using different approaches.

Electrolyte	σ_{+}^s	σ_{-}^s	σ_{++}^d	σ_{--}^d	σ_{+-}
LiTFSI-G3 (1:1) ^a	0.78	0.55	-0.62	-0.10	-0.22
LiTFSI-G4 (1:1) ^a	0.78	0.76	-0.65	-0.40	-0.27
LiTFSI-DME (1:2) ^a	0.92	0.82	-0.32	-0.76	-0.18
LiTFSI-DME-G2 (1:1:1) ^a	0.81	0.83	-0.38	-1.02	-0.20
LiTFSI-sulfolane (1:2) ^a	0.90	0.58	-0.18	-0.50	-0.10
LiTFSI-sulfolane (1:3) ^a	0.80	0.60	-0.02	-0.55	-0.10
LiTFSI-G4 (1:1) ^b	1.28 ± 0.06	1.23 ± 0.06	-0.84 ± 0.18	-0.99 ± 0.09	-0.31 ± 0.02
LiFSI-G4 (1:1) ^b	1.37 ± 0.07	1.65 ± 0.08	-1.07 ± 0.10	-1.13 ± 0.18	-0.38 ± 0.01
LiFSI-G4 (1:1.5) ^b	1.52 ± 0.08	1.95 ± 0.10	-1.19 ± 0.10	-1.11 ± 0.42	-0.39 ± 0.04
LiFSI-G4 (1:2) ^b	1.74 ± 0.09	2.29 ± 0.11	-1.33 ± 0.10	-1.15 ± 0.34	-0.45 ± 0.03

^aSalt:solvent molar ratios. Data normalized against the overall ion conductivity. Source: ref. 32.

^bSalt:solvent molar ratios. Source: ref. 23.

The cross-species term, σ_{+-} , however, should depend on many other factors. On the one hand, a strong cation–anion interaction should produce a large population of close ion pairs, the presence of which reduces the overall ion conductivity; on the other hand, in the large clusters that still bear a charge, the concerted movement of a large host of ions contributes positively to the overall ion conductivity. Table 14.4 reveals that all ether-based electrolytes display larger negative values of the cross-species term, implying the severe ion-pairing in those systems as compared with the sulfolane system.

14.3.4 Revisiting Ambipolar Diffusion: Salt Diffusion

In Sections 14.3.1 and 14.3.2, we separately analyzed the cationic and anionic fluxes at the initial and steady states of a practical electrolyte subject to DC polarization under a constant voltage, which correspond to the condition of migrational movements of both ions in the absence of a diffusional contribution, and the condition of anion blocking, respectively.

Now let us examine a unique case, where all the ion transport is driven by diffusional flux *in the absence of a migrational contribution*, and cations and anions move in the same direction. Such a transport mode actually does not produce any electric current, while all the ions therein are intercorrelated during the movement.

Under such a condition, the cationic and anionic fluxes are equal:

$$J_+ = J_- = J_{\text{Salt}} \quad (14.259)$$

Inserting eqn (14.211) and (14.212) into eqn (14.250), we obtain

$$\begin{aligned} \left[(L_{++} - L_{+-})F \frac{d\psi}{dx} + (L_{++} + L_{+-})RT\phi \frac{d\ln C_{\text{salt}}}{dx} \right] = \\ \left[(L_{+-} - L_{--})F \frac{d\psi}{dx} + (L_{--} + L_{+-})RT\phi \frac{d\ln C_{\text{salt}}}{dx} \right] \end{aligned} \quad (14.260)$$

which can be simplified and rearranged into

$$(L_{++} + L_{--} - 2L_{+-})F \frac{d\psi}{dx} = (L_{--} - L_{++})RT\phi \frac{d\ln C_{\text{salt}}}{dx} \quad (14.261)$$

The potential gradient $d\psi/dx$ is thus solved as

$$\frac{d\psi}{dx} = \frac{(L_{--} - L_{++})}{(L_{++} + L_{--} - 2L_{+-})} \frac{RT}{F} \phi \frac{d\ln C_{\text{salt}}}{dx} \quad (14.262)$$

which is then inserted back into eqn (14.213), leading to the expression for the cationic flux as

$$J_+ = J_{\text{salt}} = - \left[(L_{++} - L_{+-})F \frac{(L_{--} - L_{++})}{(L_{++} + L_{--} - 2L_{+-})} \frac{RT}{F} \phi \frac{d\ln C_{\text{salt}}}{dx} + (L_{++} + L_{+-})RT \frac{d\ln a_\pm}{dx} \right] \quad (14.263)$$

Simplification of eqn (14.263) leads to a more condensed form:

$$J_+ = - \left[\frac{L_{++}L_{--} - L_{+-}^2}{(L_{++} + L_{--} - 2L_{+-})} \right] 2RT\phi \frac{d\ln C_{\text{salt}}}{dx} \quad (14.264)$$

Leveraging the characteristic differentiation of a natural logarithm, we have

$$\frac{d\ln C_{\text{salt}}}{dx} = \frac{1}{C_{\text{salt}}} \frac{dC_{\text{salt}}}{dx} \quad (14.265)$$

Inserting eqn (14.265) in eqn (14.264), we obtain an equation that is in similar shape to Fick's first law [eqn (5.1)]:

$$J_+ = -2RT\phi \left[\frac{L_{++}L_{--} - L_{+-}^2}{(L_{++} + L_{--} - 2L_{+-})} \right] \frac{1}{C_{\text{salt}}} \frac{dC_{\text{salt}}}{dx} = -D_{\text{salt}} \frac{dC_{\text{salt}}}{dx} \quad (14.266)$$

where D_{Salt} is a composite quantity defined as

$$D_{\text{Salt}} = 2RT\Phi \left[\frac{L_{++}L_{--} - L_{+-}^2}{(L_{++} + L_{--} - 2L_{+-})} \right] \frac{1}{C_{\text{Salt}}} \quad (14.267)$$

Despite its complicated expression, on analyzing the units of D_{Salt} one would soon find that they are simply $\text{cm}^2 \text{s}^{-1}$, the same as for a diffusion coefficient. Therefore, eqn (14.266) in fact tells us that the transport of cations and anions in the same direction is equivalent to transporting the neutral salt in the electrolyte, the transport behavior of which can be described by a simple Fick's first law if one uses a composite quantity that is determined by the transport of the individual ions as well as their correlation coefficients.

In the ideal electrolyte, where L_{+-} becomes zero, Φ becomes 1.0 and L_{++} and L_{--} each collapse into what eqn (14.250) and (14.251) express, and D_{Salt} would consequently collapse into a quantity with which we are already familiar:

$$D_{\text{Salt}} = \frac{D_+ D_- (C_{\text{Salt}})^2}{(RT)^2} \frac{RT}{C_{\text{Salt}} (D_+ + D_-)} 2RT \frac{1}{C_{\text{Salt}}} = \frac{2D_+ D_-}{D_+ + D_-} \quad (14.268)$$

which is the ambipolar diffusion coefficient D_{ambp} that was defined in Section 5.2.6.4 [eqn (5.172)]. In other words, the ambipolar diffusion described in Section 5.2.6.4 just represents a special case of salt diffusion, which occurs in the ideal electrolyte in the absence of the interionic correlations described by the Onsager transport coefficients, but the movements of cations and anions are still coupled *via* the Coulombic interactions as described by Debye and Hückel in their ionic cloud.

14.3.5 Multicomponent Electrolytes

So far, we have only dealt with the simplest electrolytes consisting of a single monovalent salt, where only two ions, cation and anion, coexist. However, the ionic speciation and the interionic correlations already made the description of ion transport rather complicated. In real life, multiple salts often have to be used, and the number of Onsager transport coefficients (N_{Onsager}) needed increases accordingly, which can be calculated by

$$N_{\text{Onsager}} = \frac{n(n+1)}{2} \quad (14.269)$$

where n is the number of ionic species produced by the salt (ionic speciation is ignored here).

Therefore, for the simplest electrolyte consisting of a monovalent salt such as LiTFSI dissolved in water, we need *three* Onsager transport coefficients (L_{++} , L_- and L_+), but for multiple salt systems, such as a popular ionic liquid electrolyte that consists of a simple lithium salt, LiTFSI, dissolved in an ionic liquid based on an organic cation pyrrolidinium (Py^+) with the same anion (TFSI), *six* Onsager transport coefficients, *i.e.* $L_{\text{Li-Li}}$, $L_{\text{Py-Py}}$, $L_{\text{TFSI-TFSI}}$, $L_{\text{Li-Py}}$, $L_{\text{Li-TFSI}}$ and $L_{\text{Py-TFSI}}$, would be needed to describe completely the interionic correlations among the three ion species (Li^+ , Py^+ and TFSI) in this system. If the lithium salt added is not LiTFSI but LiPF_6^- , which no longer shares a common anion with the ionic liquid, the number of Onsager transport coefficients further increases to 10 in order to describe exhaustively the interionic correlations among the four ion species, *i.e.* Li^+ , Py^+ , PF_6^- and TFSI. Of course, for each of these Onsager transport coefficients there are three possible scenarios: uncorrelated, correlated and anticorrelated.

One could also further split these Onsager transport coefficients describing the correlations among the same kind of ions, *i.e.* $L_{\text{Li-Li}}$ (or $\sigma_{\text{Li-Li}}$), into corresponding “self” and “distinct” components such as $L_{\text{Li-Li}}^s$ and $L_{\text{Li-Li}}^d$ (or $\sigma_{\text{Li-Li}}^s$ and $\sigma_{\text{Li-Li}}^d$), *etc.*, according to the discussion in Section 14.3.3. In this case, the number of coefficients increases by a factor of n :

$$N_{\text{Onsager}} = \frac{n(n+1)}{2} + n = \frac{n(n+3)}{2} \quad (14.270)$$

For such complicated electrolyte systems, it is rather challenging to determine completely all these Onsager transport coefficients by experiment, because the quantities needed to be measured have to come from even more experiments of different natures, each introducing different degrees of uncertainty that rapidly accumulate and propagate.

On the other hand, the computation approaches would not be subject to these physical difficulties. In particular, as mentioned earlier, the Onsager formalism discussed in the above sections provides a very user-friendly framework for the molecular dynamics simulations, in which the trajectories of a large number of ions could be easily calculated. For example, the molar ion conductivity as expressed by the Nernst–Einstein equation (for ideal electrolytes):

$$\Lambda = \frac{zF^2}{RT} (D_+ + D_-) \quad (5.101)$$

could be transformed into a form for molecular dynamics simulations by relating the respective self-diffusion coefficients to the sum of the displacement vectors Δr_i and Δr_j taken by individual ions in a time interval Δt , which is based on the Einstein–Smoluchowski equation:

$$\langle x^2 \rangle = 2D_t \quad (5.20)$$

Thus, a generalized expression for the molar ion conductivity becomes

$$\sigma = \lim_{\Delta t \rightarrow \infty} \frac{F^2}{6RTV\Delta t} \sum_{i=1}^n \sum_{j=1}^n \langle \Delta r_i(\Delta t) \cdot \Delta r_j(\Delta t) \rangle \quad (14.271)$$

where V is the volume of the simulation box and n the number of ions involved (Figure 14.25). Note that here the constraint of electrolyte ideality is no longer necessary as the trajectories of each individual ion are summed over all the species i and j , hence individual jump vectors of both “self”, “distinct” and “cross” are already all taken into account.

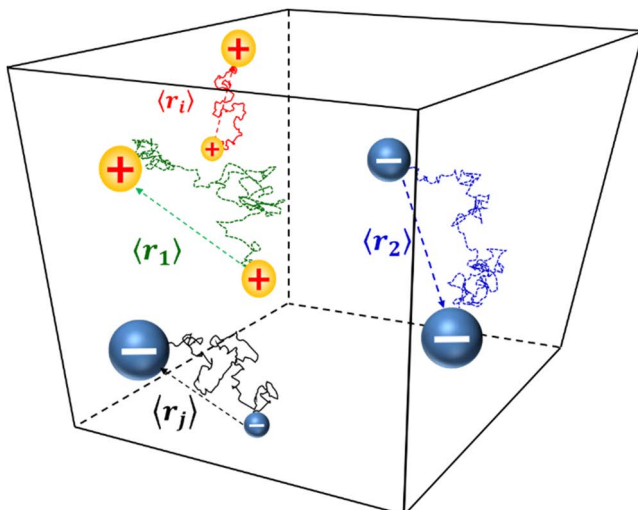


Figure 14.25 Molecular dynamics simulation monitors the displacement vectors taken by each individual ion in a certain time interval, and directly calculates the transport behaviors under the interionic correlation behavior.

14.4 Newman's Ion Transport Theory: A Brief Introduction

Among the numerous theoretical models, the framework established by Newman provides an independent and systematic approach for the rigorous treatment of the ion transport phenomena in electrolytes. Here we will introduce only the basic principles of the framework and its application on concentrated electrolytes, while referring readers with more detailed interest to the monumental book “*Electrochemical Systems*” by Newman and Balsara, which has been published in four editions as of 2021.²⁴

As the foundation of the theory, Newman laid out four elementary statements that express the basic physical laws governing ion transport in an electrolyte solution:

1. *Flux Statement:* The flux of a species i is induced by three possible driving forces, *i.e.* the migration induced by an applied electric potential ψ , the diffusion induced by concentration inhomogeneity and the flow of the bulk electrolyte caused by mechanical convection:

$$J_i = -z_i \mu_i F c_i \nabla \psi - D_i \nabla c_i + c_i \mathbf{v} \quad (14.272)$$

where z_i is the valence of the species, μ_i its mobility, c_i its concentration, D_i its self-diffusion coefficient, and \mathbf{v} the velocity of the bulk electrolyte caused by convection. Note that ∇ is the vector differential operator, the application of which gives the gradient of a quantity. For example, ∇c_i represents the concentration gradient with which we are familiar, but instead of the one-dimensional gradient (dc_i/dx) that we have used for simplification, it represents in a more general sense the concentration inhomogeneity in a three-dimensional space:

$$\nabla c_i = \frac{\partial c_i}{\partial x} + \frac{\partial c_i}{\partial y} + \frac{\partial c_i}{\partial z} \quad (14.273)$$

Thus, the first term on the right-hand side of eqn (14.272) represents the migrational flux induced by the gradient of an electric potential (*i.e.* the electric field) $\nabla \Phi$, the second term the diffusional flux induced by concentration gradient ∇c_i and the last term the convective flux.

So far in our earlier considerations we have assumed the convective flux to be negligible. On applying this constraint

and removing the last term, eqn (14.272) would collapse into a familiar form that relates the flux with the electrochemical potential of a species, such as

$$J_i = -\frac{D_i c_i}{RT} \frac{d}{dx}(z_i F \psi + \mu_i) \quad (5.116)$$

2. *Current Statement:* The electric current is the sum of those fluxes contributed from charged species:

$$i = F \sum_i z_i J_i \quad (14.274)$$

which, after being combined with eqn (14.272), becomes

$$i = -F^2 \nabla \psi \sum_i z_i^2 \mu_i c_i - F \sum_i z_i D_i \nabla c_i + Fv \sum_i z_i c_i \quad (14.275)$$

We have seen an alternative form of this statement before [eqn (5.45)], which stems from the simple relation between the quantity of materials (mol cm^{-2}) and the charge they carry (F cm^{-2}), because flux is the flow of the former, and current is the flow of the latter:

$$i = \sum_i z_i e_0 N_i J_i \quad (5.45)$$

3. *Materials Balance Statement:* The net change in the concentration of a species with time ($\partial c_i / \partial t$) is equal to the difference between the input and exit of the species:

$$\frac{\partial c_i}{\partial t} = -\nabla J_i + R_i \quad (14.276)$$

where the first term represents the exit of the species and the second term represents this species produced by a reaction. R_i is set as zero considering only the ion transport in the bulk electrolyte, but in interfacial regions it represents the rate of the species being produced or consumed.

4. *Electroneutrality Statement:* In any local region within the bulk electrolyte, the cations and anions must exactly balance out each other's charge:

$$\sum_i z_i c_i = 0 \quad (14.277)$$

This statement would eliminate the last term of eqn (14.275) and turn it into

$$i = -F^2 \nabla \psi \sum_i z_i^2 \mu_i c_i - F \sum_i z_i D_i \nabla c_i \quad (14.278)$$

Note that the electroneutrality statement only holds true in the bulk electrolyte. In interfacial regions it would cease to stand, as excess charge and an uneven charge distribution are induced by the discontinuity of the electrolyte and electrode phases. In Chapter 15 we will discuss more details of the breakdown of electroneutrality and how this defines an interface.

Furthermore, in the absence of a concentration gradient, eqn (14.278) further simplifies to

$$i = -F^2 \nabla \psi \sum_i z_i^2 \mu_i c_i = -\sigma \nabla \psi \quad (14.279)$$

where σ is represented by

$$\sigma = F^2 \sum_i z_i^2 \mu_i c_i \quad (14.280)$$

Eqn (14.279) tells us that, under such conditions, the current is in a linear relationship with the potential applied on the electrolyte, an analog of Ohm's law, while the proportionality is just a more generalized expression for ion conductivity that we have encountered in Chapter 5, Section 5.2.1.1.

For an electrolyte, the Materials Balance and Electroneutrality Statements in fact define many useful but often implicit constraints. For example, in the preceding sections we always simplified our discussion by assuming that the electrolyte consists of a binary monovalent salt M^+X^- , in which not only is the valence of both the cation and anion is 1 but also the stoichiometric ratio between the cation and anion is 1:1. However, in real life, we must deal with salts in which the cation and anion have different valences, and accordingly the stoichiometric ratio between them is no longer 1:1. Considering a generalized formula of a salt $M_{v_+}^{z_+} X_{v_-}^{z_-}$, upon dissolution in electrolyte, 1 mol of it would generate v_+ mol of cation with a valence of z_+ (M^{z_+}) and v_- mol of anion with a valence of z_- (X^{z_-}):



In such an electrolyte, the total number of ions (ν) should be given as

$$\nu = \nu_+ + \nu_- \quad (14.282)$$

while the Electroneutrality Statement governs the relation among valence and stoichiometric coefficients:

$$\nu_+ z_+ + \nu_- z_- = 0 \quad (14.283)$$

Furthermore, if the salt concentration (either in molarity or molality) in the electrolyte is c_{Salt} , the concentrations of the cation (c_+) and anion (c_-) should be

$$c_+ = c_{\text{Salt}} \nu_+ \quad (14.284)$$

$$c_- = c_{\text{Salt}} \nu_- \quad (14.285)$$

Rather particularly, in Newman's theory, the electrolyte solvent is treated as an independent component, therefore its own concentration (c_0) must also be considered in most cases, which would become especially important in the super-concentration regime because the population of solvent therein would become comparable to that of other components or even become the minority. Hence the total concentration of the electrolyte (c_T) needs to be defined as

$$c_T = \sum_i c_i = c_+ + c_- + c_0 \quad (14.286)$$

These four basic Statements serve as the foundation of Newman's theory, and may be expanded under different boundary conditions and constraints into various relations with which we are already familiar. For example, if we set ν in eqn (14.272) as zero, *i.e.* in the absence of any bulk electrolyte movement or mechanical convection, and invoke the definition of electrochemical potential [eqn (5.117)] as well as the Einstein relation [eqn (5.91)], the flux expression becomes

$$J_i = -\frac{D_i c_i}{RT} \nabla \bar{\mu}_i \quad (14.287)$$

which is just another form of eqn (5.118) that directly relates flux to the gradient of electrochemical potential when one only needs to consider the systems in one dimension:

$$J_i = -\frac{D_i c_i}{RT} \frac{d\bar{\mu}_i}{dx} \quad (5.118)$$

Alternatively, we can also set both \mathbf{v} and $\nabla\psi$ as zero, *i.e.* in the absence of any mechanical convection and electric field, then the flux would be purely contributed to by diffusional movements:

$$J_i = -D_i \nabla c_i \quad (14.288)$$

which is just another form of Fick's first law [eqn (5.1)] that we derived in one dimension:

$$J = -D \frac{dc_i}{dx} \quad (5.1)$$

Inserting eqn (14.288) into eqn (14.276), and setting the reaction rate R_i as zero, we obtain the change of species concentration with time as

$$\frac{\partial c_i}{\partial t} = \nabla [D_i \nabla c_i] = D_i \nabla^2 c_i \quad (14.289)$$

which is just the Fick's second law [eqn (5.28)]:

$$\frac{\partial c}{\partial t} = D \frac{\partial^2 c}{\partial x^2} \quad (5.28)$$

expressed in a more generalized form.

For a general binary electrolyte consisting of an asymmetric salt that can dissociate into cations of valence z_+ and anions of valence z_- , we can apply the Flux Statement [eqn (14.272)] and Materials Balance Statement [eqn (14.276)] to cations and anions, respectively:

$$\frac{\partial c}{\partial t} + \mathbf{v} \nabla c = z_+ \mu_+ F \nabla (c \nabla \psi) + D_+ \nabla^2 c \quad (14.290)$$

$$\frac{\partial c}{\partial t} + \mathbf{v} \nabla c = z_- \mu_- F \nabla (c \nabla \psi) + D_- \nabla^2 c \quad (14.291)$$

where the ion-specific concentrations (c_+ and c_-) have been replaced with the salt concentration c with application of the Electroneutrality Statement. Combining eqn (14.290) and (14.317), we obtain

$$(z_+ \mu_+ - z_- \mu_-) F \nabla(c \nabla \psi) + (D_+ - D_-) \nabla^2 c = 0 \quad (14.292)$$

Solving the potential term $\nabla(c \nabla \psi)$ and then inserting it back into eqn (14.290) or (14.291), we obtain an expression for the change of species concentration with time ($\partial c / \partial t$):

$$\frac{\partial c}{\partial t} + v \nabla c = \left[\frac{z_+ \mu_+ D_- + z_- \mu_- D_+}{z_+ \mu_+ - z_- \mu_-} \right] \nabla^2 c \quad (14.293)$$

which adopts a similar format to Fick's second law [eqn (5.28)]. As before, we define the composite term in front of the second-derivative operator ∇^2 as a new quantity, the *salt diffusion coefficient* (D_{Salt}), because it has the same units as diffusion coefficient:

$$D_{\text{Salt}} = \frac{z_+ \mu_+ D_- - z_- \mu_- D_+}{z_+ \mu_+ - z_- \mu_-} \quad (14.294)$$

Eqn (14.294) is a more generalized expression for the ambipolar diffusion coefficient [eqn (5.169)] defined in Chapter 5, Section 5.2.6.4 (one needs to remember here that z_+ bears a positive sign whereas z_- bears a negative sign):

$$D_{\text{ambp}} = \frac{\mu_+ D_- + \mu_- D_+}{\mu_+ + \mu_-} \quad (5.169)$$

As we discussed there, in the absence of an applied electric potential, the cationic and anionic species in an electrolyte would behave as a single species governed by the Electroneutrality Statement. The diffusion of this imaginary single species can be described by a quantity that is a compromise between the self-diffusion coefficients of both ions.

On the other hand, if the anion is blocked while the cation serves as the working ion that can cross the electrolyte/electrode interfaces, then at the steady state where the Bruce–Vincent approach was derived, we have

$$J_+ = \frac{i^{\text{ss}}}{z_+ F} = -z_+ \mu_+ F c \nabla \psi - D_+ \nabla c \quad (14.295)$$

$$J_- = 0 = -z_- \mu_- F c \nabla \psi - D_- \nabla c \quad (14.296)$$

Combining eqn (14.295) and (14.296) and eliminating the potential term $\nabla \psi$, we obtain

$$\frac{i^{ss}}{z_+ F} = -\frac{z_- \mu_- D_+ - z_+ \mu_+ D_-}{z_- \mu_-} \nabla c \quad (14.297)$$

Recalling that the transference numbers are now given by

$$T_+ = 1 - T_- = \frac{z_+ \mu_+}{z_+ \mu_+ - z_- \mu_-} \quad (14.298)$$

and the salt diffusion coefficient D_{Salt} is defined in eqn (14.294), one can easily rearrange eqn (14.297) into

$$\frac{i^{ss}}{z_+ F} = -\frac{D_{\text{Salt}}}{1 - T_+} \nabla c \quad (14.299)$$

Therefore, at the steady state, the flux of the working ion depends on the ion transference number, the salt diffusion coefficient and the concentration gradient across the cell. In other words, the cations and anions in this case act as if they are in a neutral species, the salt. This has been implied by the concentration profiles shown in Figure 14.20a and b. As equations that describe the relation between the current at steady state (i^{ss}) and the electrolyte concentration gradient (∇c or dC_{Salt}/dx) under anion-blocking conditions, eqn (14.299) is in fact identical with eqn (14.163) derived in Section 14.2.4.6.2:

$$i^{ss} = F J_+^{ts} = -2 F D_+ \frac{dC_+}{dx} = -2 F D_+ \frac{dC_{\text{Salt}}}{dx} \quad (14.163)$$

which can be easily proven if one sets $z_+ = 1$ and $z_- = -1$ (monovalent electrolyte) and then invoke the Einstein relation [eqn (5.91)] and the definition of transference number in an ideal electrolyte [eqn (5.96)]:

$$D_+ = \mu_+ k_B T \quad (5.91)$$

$$D_- = \mu_- k_B T \quad (5.91)$$

$$T_+ = \frac{D_+}{D_+ + D_-} \quad (5.96)$$

From the above examples, we can see that Newman's framework apparently emphasizes a more generalized and integrated approach to describe ion transport phenomena, and it uses a rather rigorous and elegant mathematical language. The mathematics used therein is often straightforward but rather lengthy and complicated. The real challenge is to rearrange and transform these lengthy terms into some quantities with physical meanings, and Newman is a master of such algebraic tricks. On the other hand, it is this rigorous and generalized mathematical language that makes Newman's framework often less accessible to those unfamiliar with its style.

14.4.1 Concentrated Solution Theory

In concentrated solutions, the statements regarding current, materials balance and electroneutrality still hold true, but the Flux Statement needs modification to reflect the interionic correlations.

Newman treated the interionic correlations within the Stefan–Maxwell formalism as defined by eqn (14.204), which views the motions of a species as the consequence of a balance between the driving force on it and the sum of frictional forces exerted by all other species on it. The latter are linearly proportional to the velocity differences ($\bar{v}_j - \bar{v}_i$) between the species we study (i) and every other species ($j, j \neq i$), and the drag coefficients K_{ij} (sometimes also called *Stefan–Maxwell transport coefficients*) describe the intercorrelations between each pair of the species combinations.

According to the Stefan–Maxwell equations, the Stefan–Maxwell transport coefficients K_{ij} can be expressed in terms of a *binary interaction diffusion coefficient* D_{ij} :

$$K_{ij} = \frac{RTc_i c_j}{c_T \mathfrak{D}_{ij}} \quad (14.300)$$

where c_T is the total concentration of the species and c_i and c_j are the concentrations of the species involved in the interaction, including the solvent. Apparently, Stefan–Maxwell transport coefficients K_{ij} , like Onsager transport coefficients [eqn (14.203)], are governed by the reciprocity principle:

$$\mathfrak{D}_{ij} = \mathfrak{D}_{ji} \quad (14.301)$$

while the relationship among the concentration quantities c_i , c_j and c_T obeys eqn (14.286).

In Newman's theory, eqn (14.204) is written in a more generalized form as

$$c_i \nabla \overline{\mu_i} = \sum_j \frac{RT c_i c_j}{c_T \mathfrak{D}_{ij}} (\overrightarrow{v_j} - \overrightarrow{v_i}) \quad (14.302)$$

Thus, for a simple electrolyte consisting of a binary salt of 1:1 type, there are three such equations governing the driving forces:

$$c_+ \nabla \overline{\mu_+} = \frac{RT c_+ c_0}{c_T \mathfrak{D}_{+0}} (\overrightarrow{v_0} - \overrightarrow{v_+}) + \frac{RT c_+ c_-}{c_T \mathfrak{D}_{+-}} (\overrightarrow{v_-} - \overrightarrow{v_+}) \quad (14.303)$$

$$c_- \nabla \overline{\mu_-} = \frac{RT c_- c_0}{c_T \mathfrak{D}_{-0}} (\overrightarrow{v_0} - \overrightarrow{v_-}) + \frac{RT c_- c_+}{c_T \mathfrak{D}_{-+}} (\overrightarrow{v_+} - \overrightarrow{v_-}) \quad (14.304)$$

$$c_0 \nabla \overline{\mu_0} = \frac{RT c_0 c_+}{c_T \mathfrak{D}_{0+}} (\overrightarrow{v_+} - \overrightarrow{v_0}) + \frac{RT c_0 c_-}{c_T \mathfrak{D}_{0-}} (\overrightarrow{v_-} - \overrightarrow{v_0}) \quad (14.305)$$

where the subscripts +, - and 0 stand for cationic, anionic and molecular species, respectively.

If one adds up these three equations, the left-hand side, if at constant temperature and pressure, should be zero as governed by the Gibbs–Duhem equation:

$$c_+ \nabla \overline{\mu_+} + c_- \nabla \overline{\mu_-} + c_0 \nabla \overline{\mu_0} = 0 \quad (14.306)$$

while the right-hand side also yields zero because of the reciprocity [eqn (14.301)] and these relative velocities cancel each other out:

$$\begin{aligned} \sum_i \sum_j \frac{RT c_i c_j}{c_T \mathfrak{D}_{ij}} (\overrightarrow{v_j} - \overrightarrow{v_i}) &= \frac{RT c_+ c_0}{c_T \mathfrak{D}_{+0}} (\overrightarrow{v_0} - \overrightarrow{v_+}) + \frac{RT c_+ c_-}{c_T \mathfrak{D}_{+-}} (\overrightarrow{v_-} - \overrightarrow{v_+}) \\ &\quad + \frac{RT c_- c_0}{c_T \mathfrak{D}_{-0}} (\overrightarrow{v_0} - \overrightarrow{v_-}) + \frac{RT c_- c_+}{c_T \mathfrak{D}_{-+}} (\overrightarrow{v_+} - \overrightarrow{v_-}) + \frac{RT c_0 c_+}{c_T \mathfrak{D}_{0+}} (\overrightarrow{v_+} - \overrightarrow{v_0}) \\ &\quad + \frac{RT c_0 c_-}{c_T \mathfrak{D}_{0-}} (\overrightarrow{v_-} - \overrightarrow{v_0}) = 0 \end{aligned} \quad (14.307)$$

Because of this constraint, which holds true at constant temperature and pressure, it is often unnecessary to list all three equations for such a simple electrolyte system. In fact, for an electrolyte consisting of N components, $N - 1$ independent equations are sufficient.

Comparing eqn (14.302) with eqn (14.272) (the Flux Statement), one can immediately see that the two seem to be in an inverse relation: The former relates *driving force* linearly to the velocities of the species and the latter relates the *flux* linearly to the *driving force*. Here one needs to remember that flux (number of moles passing through a unit area in unit time, *i.e.* mol m⁻² s⁻¹) is simply the species velocity (m s⁻¹) multiplied by the species concentration (mol m⁻³). We have made similar observations previously that the Stefan–Maxwell formalism is in fact an inverted form of the Onsager formalism. Because driving forces are often experimentally more challenging to measure, it is more useful to have eqn (14.303)–(14.305) inverted into the corresponding flux expressions.

Now let us start from the fact that “the flux is simply the species velocity multiplied by the species concentration”. Since each species has its own velocity \vec{v}_i , the flux induced by the transport of individual species is given by

$$J_i = c_i \vec{v}_i \quad (14.308)$$

Here one needs to differentiate the velocity \vec{v}_i from the bulk electrolyte velocity \vec{v} in eqn (14.267), as \vec{v} only describes a portion of the movement induced by the mechanical convection, while \vec{v}_i is the average velocity of species i induced by the driving force corresponding to the gradient of electrochemical potential $\nabla \bar{\mu}_i$ that already includes the contribution from the electrostatic potential gradient and concentration gradient.

Therefore, by combining eqn (14.308) with the Current Statement [eqn (14.274)], we can obtain an expression for the current in terms of the related velocities of cation and anions:

$$\begin{aligned} i &= F \sum_i z_i J_i = F(z_+ J_+ + Fz_- J_-) = F(z_+ c_+ \vec{v}_+ + z_- c_- \vec{v}_-) \\ &= Fz_+ c_+ (\vec{v}_+ - \vec{v}_-) \end{aligned} \quad (14.309)$$

where we have leveraged the relation $z_+ = -z_-$ as we have assumed earlier that the electrolyte is a simple binary salt of 1:1 type, such as $[\text{Na}^+\text{Cl}^-]$ or $[\text{Ca}^{2+}\text{O}^{2-}]$.

Hence the electric current can be expressed in terms of the relative velocity differences between cations and anions. Introducing the velocity of the solvent molecules \vec{v}_0 into eqn (14.309) by adding and subtracting it, we obtain

$$i = Fz_+ c_+ (\vec{v}_+ - \vec{v}_-) = Fz_+ c_+ [\vec{v}_+ - (\vec{v}_+ - \vec{v}_0)] - Fz_- c_- [\vec{v}_- - (\vec{v}_- - \vec{v}_0)] \quad (14.310)$$

Thus, the electric current remains the same as the movements of cations and anions are measured against solvent molecules as the reference. As we shall soon see, such directly relating of current to species velocity without involving consideration of electrostatic potential will provide significant convenience to the treatment of flux problems in the presence of complicated interionic correlations.

Differing from eqn (14.272) and many other equations that we have dealt with previously, in Section 14.2.4 in particular, where the potential gradient must be considered along with concentration gradients, here the flux of charged species or the corresponding current is just expressed in terms of the velocities of each individual species. This is perhaps the real significance of eqn (14.310) and a unique cleverness, because the potential terms often introduce difficulties in mathematical treatment.

For a general electrolyte salt as described by eqn (14.281):



a relationship exists among the electrochemical (or chemical) potentials for each species:

$$\overline{\mu_{\text{salt}}} = \nu_+ \overline{\mu_+} + \nu_- \overline{\mu_-} \quad (14.311)$$

Note that since the salt is a neutral species, there is no electrostatic portion in its electrochemical potential, which collapses to become simply chemical potential.

Correspondingly, the driving forces for the cationic and anionic species are thus expressed as

$$\begin{aligned} c_+ \nabla \overline{\mu_+} &= K_{0+} (\overrightarrow{\nu_0} - \overrightarrow{\nu_+}) + K_{+-} (\overrightarrow{\nu_-} - \overrightarrow{\nu_+}) \\ &= -\frac{RTc_+ c_0}{c_T \mathfrak{D}_{0+}} (\overrightarrow{\nu_+} - \overrightarrow{\nu_0}) + \frac{RTc_+ c_-}{c_T \mathfrak{D}_{+-}} (\overrightarrow{\nu_-} - \overrightarrow{\nu_+}) \end{aligned} \quad (14.312)$$

$$\begin{aligned} c_- \nabla \overline{\mu_-} &= K_{0-} (\overrightarrow{\nu_0} - \overrightarrow{\nu_-}) + K_{+-} (\overrightarrow{\nu_+} - \overrightarrow{\nu_-}) \\ &= -\frac{RTc_- c_0}{c_T \mathfrak{D}_{0-}} (\overrightarrow{\nu_-} - \overrightarrow{\nu_0}) + \frac{RTc_+ c_-}{c_T \mathfrak{D}_{+-}} (\overrightarrow{\nu_+} - \overrightarrow{\nu_-}) \end{aligned} \quad (14.313)$$

Thus, in Newman's theory, the reference frame comes in naturally because the velocity of any given species must be against other species. The solvent molecule often serves as a convenient stationary reference frame, because owing to its zero charge it feels no driving force generated by the potential gradient.

Adding eqn (14.312) and (14.313), we eliminate the cross terms between cations and anions, $(\bar{\mathbf{v}}_- - \bar{\mathbf{v}}_+)$ and $(\bar{\mathbf{v}}_+ - \bar{\mathbf{v}}_-)$, and obtain

$$c_+ \nabla \bar{\mu}_+ + c_- \nabla \bar{\mu}_- = \frac{RTc_0}{c_T} \left[\frac{c_+}{\mathfrak{D}_{0+}} (\bar{\mathbf{v}}_0 - \bar{\mathbf{v}}_+) + \frac{c_-}{\mathfrak{D}_{0-}} (\bar{\mathbf{v}}_0 - \bar{\mathbf{v}}_-) \right] \quad (14.314)$$

From eqn (14.311), (14.284) and (14.285), we know that the left-hand side of eqn (14.314) is actually the derivative of the chemical potential of the salt, μ_{salt} :

$$c_+ \nabla \bar{\mu}_+ + c_- \nabla \bar{\mu}_- = c_{\text{salt}} \nabla \bar{\mu}_{\text{salt}} \quad (14.315)$$

On the other hand, by invoking eqn (14.284) and (14.285), the right-hand side of eqn (14.315) can be rearranged into

$$\frac{RTc_0 c_{\text{salt}}}{c_T} \left[\frac{\nu_+}{\mathfrak{D}_{0+}} (\bar{\mathbf{v}}_0 - \bar{\mathbf{v}}_+) + \frac{\nu_-}{\mathfrak{D}_{0-}} (\bar{\mathbf{v}}_0 - \bar{\mathbf{v}}_-) \right] \quad (14.316)$$

Combining eqn (14.313) with eqn (14.314) and eliminating c_{salt} , we obtain

$$\frac{c_T \nabla \bar{\mu}_{\text{salt}}}{RTc_0} = \frac{\nu_+}{\mathfrak{D}_{0+}} (\bar{\mathbf{v}}_0 - \bar{\mathbf{v}}_+) + \frac{\nu_-}{\mathfrak{D}_{0-}} (\bar{\mathbf{v}}_0 - \bar{\mathbf{v}}_-) \quad (14.317)$$

which can be rearranged into

$$-\frac{\mathfrak{D}_{0-} c_T \nabla \bar{\mu}_{\text{salt}}}{\nu_- R T c_0} = \frac{\nu_+ \mathfrak{D}_{0-}}{\nu_- \mathfrak{D}_{0+}} (\bar{\mathbf{v}}_+ - \bar{\mathbf{v}}_0) + (\bar{\mathbf{v}}_- - \bar{\mathbf{v}}_0) \quad (14.318)$$

Then applying eqn (14.310) to replace $(\bar{\mathbf{v}}_- - \bar{\mathbf{v}}_0)$, we can introduce the electric current i :

$$-\frac{\mathfrak{D}_{0-} c_T \nabla \bar{\mu}_{\text{salt}}}{\nu_- R T c_0} = \frac{\nu_+ \mathfrak{D}_{0-}}{\nu_- \mathfrak{D}_{0+}} (\bar{\mathbf{v}}_+ - \bar{\mathbf{v}}_0) + (\bar{\mathbf{v}}_+ - \bar{\mathbf{v}}_0) - \frac{i}{F c_+ z_+} \quad (14.319)$$

which after further rearrangement becomes

$$\frac{i}{F c_+ z_+} - \frac{\mathfrak{D}_{0-} c_T \nabla \bar{\mu}_{\text{salt}}}{\nu_- R T c_0} = \left(\frac{\nu_+ \mathfrak{D}_{0-}}{\nu_- \mathfrak{D}_{0+}} + 1 \right) (\bar{\mathbf{v}}_+ - \bar{\mathbf{v}}_0) \quad (14.320)$$

On the other hand, when the interionic correlation is taken into account and the solvent is used as reference frame, the definition of cationic transference number now should become

$$T_+^0 = \frac{z_+ \mathfrak{D}_{0+}}{z_+ \mathfrak{D}_{0+} - z_- \mathfrak{D}_{0-}} = \frac{\nu_- \mathfrak{D}_{0+}}{\nu_+ \mathfrak{D}_{0-} + \nu_- \mathfrak{D}_{0+}} \quad (14.321)$$

where the superscript 0 in T_+^0 marks the reference frame. It should be noted that the choice of reference frame is arbitrary.

Examining eqn (14.320), one can easily identify the term containing the Stefan–Maxwell transport coefficients on the right side of as

$$\frac{\nu_+ \mathfrak{D}_{0-}}{\nu_- \mathfrak{D}_{0+}} + 1 = \frac{1}{T_+^0} \quad (14.322)$$

which turns eqn (14.320) into

$$\overrightarrow{\mathbf{v}_+} - \overrightarrow{\mathbf{v}_0} = \frac{i T_+^0}{F c_+ z_+} - \frac{T_+^0 \mathfrak{D}_{0-} c_T}{\nu_- R T c_0} \nabla \overline{\mu_{\text{Salt}}} \quad (14.323)$$

or

$$c_+ (\overrightarrow{\mathbf{v}_+} - \overrightarrow{\mathbf{v}_0}) = \frac{i T_+^0}{F z_+} - \frac{T_+^0 \mathfrak{D}_{0-} c_T c_+}{\nu_- R T c_0} \nabla \overline{\mu_{\text{Salt}}} \quad (14.324)$$

Further algebraic maneuvers allow us to replace the ion-specific quantities such as c_+ and \mathfrak{D}_{0-} with corresponding salt or electrolyte quantities by invoking eqn (14.282)–(14.285) and (14.294), and eqn (14.324) is eventually turned into

$$c_+ (\overrightarrow{\mathbf{v}_+} - \overrightarrow{\mathbf{v}_0}) = \frac{i T_+^0}{F z_+} - \frac{\nu_+ c_T c_{\text{Salt}} \mathfrak{D}_e}{\nu_- R T c_0} \nabla \overline{\mu_{\text{Salt}}} \quad (14.325)$$

in which \mathfrak{D}_e is defined as the *electrolyte diffusion coefficient* that incorporates the correlations among all electrolyte components *via*

$$\mathfrak{D}_e = \frac{\mathfrak{D}_{0+} \mathfrak{D}_{0-} (z_+ - z_-)}{z_+ \mathfrak{D}_{0+} - z_- \mathfrak{D}_{0-}} \quad (14.326)$$

One needs to note the difference between this electrolyte diffusion coefficient that counts all species including solvent molecules and the salt diffusion coefficient defined in eqn (14.294) that only counts ions. We will discuss their relation further in the next section.

In a similar manner, we can derive an expression for the anionic movement:

$$c_- (\overrightarrow{v}_- - \overrightarrow{v}_0) = \frac{iT_-^0}{Fz_-} - \frac{\nu_\pm c_T c_{\text{salt}} \mathfrak{D}_e \nabla \overline{\mu_{\text{salt}}}}{\nu R T c_0} \quad (14.327)$$

Thus, based on eqn (11.334), the fluxes for cationic, anionic and molecular (solvent) species can be expressed as, respectively

$$J_+ = c_+ \overrightarrow{v}_+ = \frac{iT_+^0}{Fz_+} - \frac{\nu_+ c_T c_{\text{salt}} \mathfrak{D}_e \nabla \overline{\mu_{\text{salt}}}}{\nu R T c_0} + c_+ \overrightarrow{v}_0 \quad (14.328)$$

$$J_- = c_- \overrightarrow{v}_- = \frac{iT_-^0}{Fz_-} - \frac{\nu_- c_T c_{\text{salt}} \mathfrak{D}_e \nabla \overline{\mu_{\text{salt}}}}{\nu R T c_0} + c_- \overrightarrow{v}_0 \quad (14.329)$$

$$J_0 = c_0 \overrightarrow{v}_0 \quad (14.330)$$

Eqn (14.330) is actually redundant as only two independent flux equations are needed for an electrolyte consisting of three species. The solvent molecules often serve as the reference frame for the cationic and anionic movements.

As pointed out at the beginning of this section, eqn (14.307) is in fact an inverted form of the Flux Statement. The above derivation process of eqn (14.328)–(14.330) represents such an inversion. Comparing these equations with the Flux Statement [eqn (14.272)], one can immediately see the striking similarity.

In the Flux Statement, the first term on the right-hand side ($-z_i \mu_i F c_i \nabla \psi$) represents the migrational flux induced by the gradient in an electrostatic field, the second term ($-D_i \nabla c_i$) the diffusional flux induced by the gradient in concentration and the third term ($c_i v$) the velocity of the bulk electrolyte.

On the other hand, in eqn (14.328) and (14.329), the first terms, iT_+^0/Fz_+ and iT_-^0/Fz_- , represent current that is related to electrostatic driving force, the second terms,

$$-\frac{\nu_+ c_T c_{\text{salt}} \mathfrak{D}_e}{\nu R T c_0} \nabla \overline{\mu_{\text{salt}}} \quad \text{and} \quad -\frac{\nu_- c_T c_{\text{salt}} \mathfrak{D}_e}{\nu R T c_0} \nabla \overline{\mu_{\text{salt}}}$$

represent the imbalances among the different species concentrations, and the third terms, $c_+ \overrightarrow{v}_0$ and $c_- \overrightarrow{v}_0$, represent the velocity of the bulk solvent.

14.4.1.1 Self, Ambipolar, Salt and Electrolyte Diffusion Coefficients

So far, we have come across quite a few quantities called “diffusion coefficients”, which include self-diffusion coefficients (D_+ and D_-), ambipolar diffusion coefficients (D_{ambp}), salt diffusion coefficients (D_{salt}) and electrolyte diffusion coefficients (\mathfrak{D}_e). While they all describe how fast species move in an electrolyte, each of them describes the movement under a specific constraint.

The self-diffusion coefficient, as the name implies, reflects the completely free will of the species to move, which occurs without any influence from the presence of other species, no matter whether they are ions of the same or opposite charge or neutral species such as solvent molecules. It is governed by the Einstein–Smoluchowski equation:

$$\langle x_i^2 \rangle = 2D_i t \quad (5.20)$$

To a certain level of approximation, such total freedom of ions is assumed for ideal electrolytes, *i.e.* extremely dilute electrolytes with salt concentrations below 0.001 M (or 0.001 N), but rigorously it is not valid even in those extremely dilute electrolytes, because interionic Coulombic effects are always present, which sets the foundation of the ionic cloud model of Debye and Hückel and is governed by the Electroneutrality Statement.

In such “approximately ideal” electrolytes, the molar or molal conductivity is related to the self-diffusion coefficients according to the Nernst–Einstein equation:

$$\Lambda = \frac{zF^2}{RT} (D_+ + D_-) \quad (5.101)$$

On the other hand, both ambipolar and salt diffusion coefficients take into account the effect of interionic correlations with ion transport, and describe the concerted movement of cations and anions as a single species governed by the Electroneutrality Statement, when there is no externally applied electric field:

$$D_{\text{ambp}} = \frac{\mu_+ D_- + \mu_- D_+}{\mu_+ + \mu_-} \quad (5.169)$$

$$D_{\text{salt}} = \frac{z_+ \mu_+ D_- - z_- \mu_- D_+}{z_+ \mu_+ - z_- \mu_-} \quad (14.294)$$

As discussed previously, D_{Salt} is a more general form of D_{ambp} when the salt under consideration is $\text{M}_{\nu^+}^{z^+}\text{X}_{\nu^-}^{z^-}$ instead of a monovalent salt. So far, the composite correlation between cationic and anionic diffusion coefficients described by both D_{Salt} and D_{ambp} still only reflects the situation of dilute electrolytes, with no consideration given to the universal interionic correlations that occur in practical electrolytes or concentrated solutions.

Like both D_{Salt} and D_{ambp} , the electrolyte diffusion coefficient \mathfrak{D}_e treats the movement of cation and anions as if they behave like a single species when traveling under the Electroneutrality Statement.

Differing from both D_{Salt} and D_{ambp} , \mathfrak{D}_e takes into account not only all possible interionic correlations, no matter whether ions of the same or opposite charge, but also the effect of the solvent molecules on the ion transport, which are all treated in the framework of Stefan-Maxwell formalism in the form of cross-species transport coefficients.

A relation between D_{Salt} and \mathfrak{D}_e could be derived by considering the cationic and anionic fluxes in the absence of an applied electric field.

On the one hand, since both ions are traveling as if they are a single species, *i.e.* the salt, we can write the flux equation for this neutral species as

$$J_{\text{Salt}} = -D_{\text{Salt}} \nabla c_{\text{Salt}} + c_{\text{Salt}} \mathbf{v} \quad (14.331)$$

which simply comes from the Flux Statement [eqn (14.272)] with $\nabla \psi = 0$.

On the other hand, by setting the electric current as zero, the cationic flux [eqn (14.328)] becomes

$$J_{\text{Salt}} = \frac{J_+}{\nu_+} = \frac{J_-}{\nu_-} = -\frac{c_T c_{\text{Salt}} \mathfrak{D}_e}{\nu R T c_0} \nabla \overline{\mu_{\text{Salt}}} + c_{\text{Salt}} \overline{\mathbf{v}_0} \quad (14.332)$$

where, at constant temperature and pressure, the chemical potential of the salt is given by

$$\overline{\mu_{\text{Salt}}} = \left[\overline{\mu_{\text{Salt}}} \right]^0 + \nu R T \ln \alpha_{\text{Salt}} = \left[\overline{\mu_{\text{Salt}}} \right]^0 + \nu R T \ln(\gamma c_{\text{Salt}}) \quad (14.333)$$

and the derivative of $\overline{\mu_{\text{Salt}}}$ would be given as

$$\nabla \overline{\mu_{\text{Salt}}} = \nu R T \nabla \ln(\gamma c_{\text{Salt}}) = \nu R T (\nabla \ln \gamma + \nabla \ln c_{\text{Salt}}) = \frac{\nu R T}{c_{\text{Salt}}} \left(\frac{d \ln \gamma}{d \ln c_{\text{Salt}}} + 1 \right) \nabla c_{\text{Salt}} \quad (14.334)$$

Inserting eqn (14.334) into eqn (14.332), we obtain

$$J_{\text{Salt}} = -\frac{c_T c_{\text{Salt}} \mathfrak{D}_e}{\nu R T c_0} \frac{\nu R T}{c_{\text{Salt}}} \left(\frac{d \ln \gamma}{d \ln c_{\text{Salt}}} + 1 \right) \nabla c_{\text{Salt}} + c_{\text{Salt}} \overrightarrow{\nu}_0 \quad (14.335)$$

Comparing eqn (14.335) with eqn (14.331), we obtain the relation between D_{Salt} and \mathfrak{D}_e as

$$D_{\text{Salt}} = \mathfrak{D}_e \frac{c_T}{c_0} \left[\frac{d \ln \gamma}{d \ln c_{\text{Salt}}} + 1 \right] \quad (14.336)$$

14.4.1.2 Revisiting the Bruce–Vincent Approach in Newman’s Formalism

Leveraging eqn (14.336), we can rewrite the second term in eqn (14.328) and (14.329) as

$$\frac{c_T c_{\text{Salt}} \mathfrak{D}_e}{\nu R T c_0} \nabla \overline{\mu_{\text{Salt}}} = D_{\text{Salt}} \left(1 - \frac{d \ln c_0}{d \ln c_{\text{Salt}}} \right) \quad (14.337)$$

and insert it back into eqn (14.328) and (14.329) to transform them into an expression more similar to the Flux Statement given by eqn (14.272):

$$J_+ = c_+ \overrightarrow{\nu}_+ = \frac{i T_+^0}{F z_+} - \nu_+ D_{\text{Salt}} \left(1 - \frac{d \ln c_0}{d \ln c_{\text{Salt}}} \right) \nabla c_{\text{Salt}} + c_+ \overrightarrow{\nu}_0 \quad (14.338)$$

$$J_- = c_- \overrightarrow{\nu}_- = \frac{i T_-^0}{F z_-} - \nu_- D_{\text{Salt}} \left(1 - \frac{d \ln c_0}{d \ln c_{\text{Salt}}} \right) \nabla c_{\text{Salt}} + c_- \overrightarrow{\nu}_0 \quad (14.339)$$

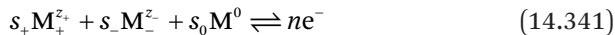
Eqn (14.338) and (14.339) constitute the core of Newman’s theory in treating many transport-related properties. As briefly mentioned earlier in this section, one of the advantages of this approach is that the gradient of electrostatic potential ($\nabla \psi$) is no longer a quantity of necessity, as the migrational contribution has been represented by the relative velocities of various ionic species directly related to electric current, which is much easier to measure experimentally or to simulate computationally.

Inserting eqn (14.338) into the Materials Balance Statement [eqn (14.276)], we obtain

$$\frac{\partial c}{\partial t} + \nabla(c_+ \vec{v}_0) = \nabla \left[D_{\text{Salt}} \left(1 - \frac{d \ln c_0}{d \ln c} \right) \nabla c_{\text{Salt}} \right] - \frac{i \nabla T_+^0}{F z_+ v_+} \quad (14.340)$$

These core equations can be expanded under various boundary conditions and constraints, leading to solutions for numerous real-life problems of interest that we have discussed in the previous sections and chapters.

For example, applying Newman's concentrated solution theory, Balsara and Newman³³ revisited the scenario where the Bruce–Vincent approach was derived (Section 14.2.4.6), *i.e.* a constant potential difference is applied to a symmetrical cell consisting of a simple binary electrolyte $M_{v_+}^{z_+} X_{v_-}^{z_-}$, with M^{z+} as the working cation and X^{z-} as the blocked anion. Since a reference frame is crucial for the Newman formalism, they assumed that the potential $\nabla\psi$ is applied against a reference where the species experience a reversible electrochemical reaction:



Eqn (14.341) is a generalized manner of expressing an electrochemical reaction, where s_i are stoichiometric coefficients for the reversible reaction occurring at the reference electrode. These coefficients differ from the stoichiometric coefficients (v_+ or v_-) in the formula $M_{v_+}^{z_+} X_{v_-}^{z_-}$ and might be zero if the reaction does not involve that species. Taking a lithium reference electrode as an example, the reaction simply collapses to



with $s_+ = -1$, $s_- = 0$ and $s_0 = +1$. At equilibrium, the thermodynamics governs the change of chemical potentials at the reference electrode as

$$s_+ \nabla \mu_+ + s_- \nabla \mu_- + s_0 \nabla \mu_0 = -nF\nabla\psi \quad (14.343)$$

The relationship between the applied potential ψ and the current should be given as

$$i = -\sigma \nabla \psi - \frac{\sigma}{Fz_+ V_+} \left[\frac{z_+ s_+}{n} + \frac{z_+ \mathfrak{D}_{0+}}{z_+ \mathfrak{D}_{0+} - z_- \mathfrak{D}_{0-}} - \frac{s_0 z_+ c_+}{n c_0} \right] \nabla \mu_{\text{Salt}} \quad (14.344)$$

If only the cation and its corresponding metal are involved in the reaction at the reference electrode, eqn (14.344) simplifies to

$$i = -\sigma \nabla \psi - \frac{\sigma}{F} \left[\frac{s_+}{n V_+} + \frac{T_+^0}{z_+ V_+} \right] \nabla \mu_{\text{Salt}} \quad (14.345)$$

At the initial state, the electrolyte is homogeneous across the cell, hence the gradient of the salt concentration or its chemical potential is zero, hence

$$i_0 = -\sigma \nabla \psi \quad (14.346)$$

At the steady state, the anionic flux against the reference frame of solvent (*i.e.* setting $\overrightarrow{v}_0 = 0$) becomes zero, while the cationic flux is solely responsible for the electric current. Invoking eqn (14.329):

$$J_-^{\text{ss}} = \frac{i^{\text{ss}} T_-^0}{Fz_-} - \frac{\nu_- c_T c_{\text{Salt}} \mathfrak{D}_e}{\nu R T c_0} \nabla \mu_{\text{Salt}} = 0 \quad (14.347)$$

$$J_+^{\text{ss}} = \frac{i^{\text{ss}}}{Fz_+} \quad (14.348)$$

From eqn (14.347), one obtains

$$\nabla \mu_{\text{Salt}} = i^{\text{ss}} \frac{T_-^0}{Fz_-} - \frac{\nu R T c_0}{\nu_- c_T c_{\text{Salt}} \mathfrak{D}_e} \quad (14.349)$$

Inserting eqn (14.349) into eqn (14.345), one obtains the relationship between the steady-state current i^{ss} and the applied potential ψ :

$$i^{\text{ss}} = -\frac{\sigma}{1 + N_e} \nabla \psi \quad (14.350)$$

where N_e is a new quantity called the “*Newman number*”, defined as

$$N_e = \frac{\nu}{(\nu_- z_+)^2} \frac{\sigma R T c_0 (T_-^0)^2}{F^2 c_T c_{\text{Salt}} \mathfrak{D}_e} \quad (14.351)$$

Therefore, the ratio between the electric current at the initial and steady states should be

$$\frac{i^{\text{ss}}}{i^0} = \frac{1}{1 + N_e} \quad (14.352)$$

Despite the simple and elegant appearance of eqn (14.352), the ratio between the electric current at the initial and steady states is actually a composite quantity that involves many ion transport properties, including the ion transference number. Therefore, the quantity that was assumed to be the cationic transference number in the Bruce–Vincent approach is actually something else. Only when the salt concentration approaches zero can the Newman number be expressed approximately as

$$\lim_{c \rightarrow 0} N_e = \frac{T_-^0}{T_+^0} \quad (14.353)$$

which validates the Bruce–Vincent approach by

$$\lim_{c \rightarrow 0} \frac{i^{\text{ss}}}{i^0} = T_+^0 \quad (14.354)$$

On the other hand, since N_e contains the transference number, it is theoretically possible to apply the Bruce–Vincent approach for a more rigorous determination of ion transference number. To do so, several quantities need to be measured by various experimental techniques, which include the ion conductivity (σ) obtained from AC impedance spectra, the ratio of the initial and steady-state currents (i^{ss}/i^0) obtained from DC polarization experiments, the salt (D_{salt}) or electrolyte diffusion coefficient (\mathfrak{D}_e), or the thermodynamic factor [$1 + d\ln \gamma_{\pm} / d\ln(C_{\text{salt}})$] obtained from concentration cell measurements. As we have pointed out before, the uncertainties accumulated from these very different experiments may compromise the confidence of such rigorous approaches. In fact, most cationic transference numbers (Li^+ and Na^+) as measured by the Newman approach in a number of polymer electrolytes have been distinctly different from values reported using other approaches, including the relatively more reliable eNMR techniques (Table 14.3). The most controversial are the negative numbers. Although we have pointed out in previous sections that negative ion transference numbers are possible under the circumstances of ion speciation, the negative ion transference numbers generated by the Newman approach are actually composite results from those ionic

clusters that move in the “wrong” direction and the reference frame they are measured against.^{34,35}

14.4.2 Limitations of Newman’s Concentrated Solution Theory

Newman’s concentrated solution theory treated ion transport phenomena with such rigor that all possible variables must be considered, as evidenced by the numerous new quantities often required in order to obtain a full description of ion transport. However, we must remember that we are still just dealing with a simple binary electrolyte system that contains only three components, *i.e.* cation, anion and solvent molecules, whereas most practical electrolyte systems used in real-life electrochemical devices consist of many more components. Taking the practical electrolyte used in lithium-ion batteries as an example, the simplest electrolyte formulation consists of four species, *i.e.* cation, anion and two solvent molecules (*i.e.* mixed carbonates). Hence there would be three independent velocities with one being the reference frame, which requires at least three fluxes or equations to describe the driving forces [such as eqn (14.303) and (14.304)] or fluxes [such as eqn (14.338) and (14.339)] that involve six independent transport coefficients for the inter-species interactions. Such complexity increases with the number of components according to $n(n - 1)/2$, and it is not rare in the lithium-ion battery industry that electrolyte systems of higher order than ternary are adopted. This number would become even higher if one considers the electrolyte additives, which are also often used in multiple numbers.

Therefore, it is extremely challenging to describe accurately these practical electrolytes with multiple components within the Newman formalism.

On the other hand, when the electrolyte in an electrochemical device experiences strong polarization, which is induced either by a high rate of charge or discharge or extreme potentials of the electrodes, strong concentration polarization would arise, with the surface concentration of the working ion becoming zero while its bulk concentration remains high. Under such circumstances, the concentration dependence of all these transport coefficients must be taken into account. Thus far, almost no efforts have been made to measure these transport coefficients rigorously across the full concentration ranges.

Finally, all transport equations in the previous two chapters were derived under the assumption of constant temperature and pressure,

so that the Gibbs–Duhem equation could be applied. In reality, however, the Joule heat generated during ion transport inevitably raises the temperature of the whole electrolyte system. Such an effect would become especially pronounced at high charge and discharge rates. The temperature dependences of concentration gradients and potential profiles across the electrolytes thus become critically important, and this has not been fully addressed in the above framework.

In summary, while the rigor of concentrated solution theory is very compelling, its strict applicability to “real” electrolytes unfortunately is rather limited. In this context, one could even say that it is such rigor that often renders the experimental verification of Newman’s concentrated solution theory very difficult, because most of the quantities required are either experimentally inaccessible or available only with high uncertainties. This reduces the confidence in the results. Extensive application and verification of Newman’s concentrated solution theory depends on the development of new characterization techniques that are both of high temporal, spatial and speciation resolution and *in situ* and *operando* in nature.

References

1. R. G. Linford, in *Electrochemical Science and Technology of Polymers 2*, ed. R. G. Linford, Elsevier Applied Science, London, 1990, p. 281.
2. E. Barsoukov and J. R. Macdonald, *Impedance Spectroscopy Theory, Experiment, and Applications*, John Wiley & Sons, 2nd edn, 2005.
3. M. S. Ding, K. Xu, S. S. Zhang, K. Amine, G. L. Henriksen and T. R. Jow, Change of conductivity with salt content, solvent composition, and temperature for electrolytes of LiPF₆ in ethylene carbonate–ethyl methyl carbonate, *J. Electrochem. Soc.*, 2001, **148**, A1196–A1204.
4. M. S. Ding, K. Xu and T. R. Jow, Conductivity and Viscosity of PC–DEC and PC–EC Solutions of LiBOB, *J. Electrochem. Soc.*, 2005, **152**, A132–A140.
5. M. S. Ding, L. Ma, M. A. Schroeder and K. Xu, Phase Diagram and Conductivity of Zn(TFSI)₂–H₂O Electrolytes, *J. Phys. Chem. C.*, 2020, **124**, 25249–25253.
6. C. A. Angell, Formation of glasses from liquids and biopolymers, *Science*, 1995, **267**, 1924–1935.
7. C. A. Angell, Mobile ions in amorphous solids, *Annu. Rev. Phys. Chem.*, 1992, **43**, 693–717.
8. Y. Yamada, K. Usui, K. Sodeyama, S. Ko, Y. Tateyama and A. Yamada, Hydrate-melt electrolytes for high-energy-density aqueous batteries, *Nat. Energy*, 2016, **1**, 16129.
9. D. R. MacFarlane, M. Forsyth, E. I. Izgorodina, A. P. Abbott, G. Annat and K. Fraser, On the Concept of Ionicity in Ionic Liquids, *Phys. Chem. Chem. Phys.*, 2009, **11**, 4962–4967.
10. A. Noda, K. Hayamizu and M. Watanabe, Pulsed-Gradient Spin–Echo ¹H and ¹⁹F NMR Ionic Diffusion Coefficient, Viscosity, and Ionic Conductivity of Non Chloroaluminate Room-Temperature Ionic Liquids, *J. Phys. Chem. B.*, 2001, **105**, 4603–4610.
11. J. W. Hittorf, *Über die Wanderungen der Ionen*, Wilhelm Engelmann, Leipzig, 1853.

12. C. Tubandt, in *Handbuch der Experimentalphysik*, ed. W. Wien and F. Harms, Akad. Verlag, Leipzig, 1932, vol. XII, Teil 1.
13. P. G. Bruce, M. T. Hardgrave and C. A. Vincent, The determination of transference numbers in solid polymer electrolytes using the Hittorf method, *Solid State Ionics*, 1992, **53/56**, 1087–1094.
14. K. J. Laidler and J. H. Meiser, *Physical Chemistry*, Benjamin Cummings, 1982, pp. 276–280.
15. G. A. Lonergan and D. C. Pepper, Transport numbers and ionic mobilities by the moving boundary method, *J. Chem. Educ.*, 1965, **42**, 82.
16. A. Bouridah, F. Dalard, D. Derog and M. B. Armand, Potentiometric measurement of ionic mobilities in poly(ethylene oxide) electrolytes, *Solid State Ionics*, 1986, **18/19**, 287–290.
17. L. O. Valøen and J. N. Reimers, Transport properties of LiPF₆-based Li-ion battery electrolytes, *J. Electrochem. Soc.*, 2005, **152**, A882–A891.
18. P. R. Sørensen and T. Jacobsen, Conductivity, charge transfer and transport number: an ac-investigation of the polymer electrolyte LiSCN-poly(ethylene oxide), *Electrochim. Acta*, 1982, **27**, 1671–1675.
19. P. G. Bruce and C. A. Vincent, Steady state current flow in solid binary electrolyte cells, *J. Electroanal. Chem. Interfacial Electrochem.*, 1987, **225**, 1–17.
20. M. Holz, Electrophoretic NMR, *Chem. Soc. Rev.*, 1994, **23**, 165–174.
21. K. Hayamizu, S. Seki, H. Miyashiro and Y. Kobayashi, Direct In Situ Observation of Dynamic Transport for Electrolyte Components by NMR Combined with Electrochemical Measurements, *J. Phys. Chem. B*, 2006, **110**, 22302–22305.
22. K. W. Gao, C. Fang, D. M. Halat, A. Mistry, J. Newman and N. P. Balsara, The Transference Number, *Energy Environ. Mater.*, 2022, **5**, 366–369.
23. S. Pfeifer, F. Ackermann, F. Sälzer, M. Schönhoff and B. Roling, Quantification of cation–cation, anion–anion and cation–anion correlations in Li salt/glyme mixtures by combining very-low-frequency impedance spectroscopy with diffusion and electrophoretic NMR, *Phys. Chem. Chem. Phys.*, 2021, **23**, 628–640.
24. J. Newman and N. P. Balsara, *Electrochemical Systems*, Wiley, 4th edn, 2021.
25. K. D. Fong, J. Self, K. M. Diederichsen, B. M. Wood, B. D. McCloskey and K. A. Persson, Ion Transport and the True Transference Number in Nonaqueous Polyelectrolyte Solutions for Lithium Ion Batteries, *ACS Cent. Sci.*, 2019, **5**, 1250–1260.
26. K. D. Fong, H. K. Bergstrom, B. D. McCloskey and K. K. Mandadapu, Transport phenomena in electrolyte solutions: Nonequilibrium thermodynamics and statistical mechanics, *AICHE J.*, 2020, **66**, e17091.
27. D. M. Pesko, K. Timachova, R. Bhattacharya, M. C. Smith, I. Villaluenga, J. Newman and N. P. Balsara, Negative Transference Numbers in Poly(ethylene oxide)-Based Electrolytes, *J. Electrochem. Soc.*, 2017, **164**, E3569–E3575.
28. A. A. Wang, A. B. Gunnarsdottir, J. Fawdon, M. Pasta, C. P. Grey and C. W. Monroe, Potentiometric MRI of a superconcentrated lithium electrolyte: testing the irreversible thermodynamics approach, *ACS Energy Lett.*, 2021, **6**, 3086–3095.
29. N. M. Vargas-Barbosa and B. Roling, Dynamic Ion Correlations in Solid and Liquid Electrolytes: How Do They Affect Charge and Mass Transport?, *ChemElectroChem.*, 2020, **7**, 367–385.
30. F. Wohde, M. Balabajew and B. Roling, Li⁺ transference numbers in liquid electrolytes obtained by very-low-frequency impedance spectroscopy at variable electrode distances, *J. Electrochem. Soc.*, 2016, **163**, A714.
31. A. Noda, K. Hayamizu and M. Watanabe, Pulsed-Gradient Spin-Echo 1H and 19F NMR Ionic Diffusion Coefficient, Viscosity, and Ionic Conductivity of Non-Chloroaluminate Room-Temperature Ionic Liquids, *J. Phys. Chem.*, 1999, **103**, 519–524.
32. K. Shigenobu, et al., *Phys. Chem. Chem. Phys.*, 2020, **22**, 15214–15221.
33. N. P. Balsara and J. Newman, *J. Electrochem. Soc.*, 2015, **162**, A2720–A2722.

34. D. B. Shah, H. O. Nguyen, L. S. Grundy, K. R. Olson, S. J. Mecham, J. M. DeSimone and N. P. Balsara, Difference between approximate and rigorously measured transference numbers in fluorinated electrolytes, *Phys. Chem. Chem. Phys.*, 2019, **21**, 7857–7866.
35. J. S. Ho, O. A. Borodin, M. S. Ding, L. Ma, M. A. Schroeder, G. R. Pastel and K. Xu, Understanding Lithium-ion Transport in Sulfolane-and Tetraglyme-based Electrolytes using Very Low Frequency Impedance Spectroscopy, *Energy Environ. Mater.*, 2021, DOI: 10.1002/eem2.12302.
36. J. Evans, C. A. Vincent and P. G. Bruce, Electrochemical measurement of transference numbers in polymer electrolytes, *Polymer*, 1987, **28**, 2324–2328.
37. M. Doyle and J. Newman, Analysis of transference number measurements based on the potentiostatic polarization of solid polymer electrolytes, *J. Electrochem. Soc.*, 1995, **142**, 3465–3468.
38. D. M. Pesko, S. Sawhney, J. Newman and N. P. Balsara, Comparing Two Electrochemical Approaches for Measuring Transference Numbers in Concentrated Electrolytes, *J. Electrochem. Soc.*, 2018, **165**, A3014–A3021.
39. S. Wei, Z. Li, K. Kimura, S. Inoue, L. Pandini, D. D. Lecce, Y. Tominaga and J. Hassoun, Glyme-based electrolytes for lithium metal batteries using insertion electrodes: An electrochemical study, *Electrochim. Acta*, 2019, **306**, 85–95.
40. S. Zugmann, M. Fleischmann, M. Amereller, R. M. Gschwind, H. D. Wiemhoefer and H. J. Gores, Measurement of transference numbers for lithium ion electrolytes via four different methods, a comparative study, *Electrochim. Acta*, 2010, **56**, 3926–3933.
41. Z. Yu, H. Wang, X. Kong, W. Huang, Y. Tsao, D. G. Mackanic, K. Wang, X. Wang, W. Huang, S. Choudhury, C. V. Amanchuwu, S. T. Hung, Y. Ma, E. G. Lomeli, J. Qin, Y. Cui and Z. Bao, Molecular design for electrolyte solvents enabling energy-dense and long-cycling lithium metal batteries, *Nat. Energy*, 2020, **5**, 526–533.
42. O. Borodin, L. Suo, M. Gobet, X. Ren, F. Wang, A. Faraone, J. Peng, M. Olguin, M. Schroeder, M. S. Ding, E. Gobrogge, A. v. W. Cresce, S. Munoz, J. A. Dura, S. Greenbaum, C. Wang and K. Xu, Liquid Structure with Nano-Heterogeneity Promotes Cationic Transport in Concentrated Electrolytes, *ACS Nano*, 2017, **11**, 10462–10471.
43. T. Taskovic, A. Eldesoky, W. Song, M. Bauer and J. R. Dahn, High Temperature Testing of NMC/Graphite Cells for Rapid Cell Performance Screening and Studies of Electrolyte Degradation, *J. Electrochem. Soc.*, 2022, **169**, 040538.
44. Y. Matsuda and H. Satake, Mixed Electrolyte Solutions of Propylene Carbonate and Dimethoxethane for High Energy Density Batteries, *J. Electrochem. Soc.*, 1980, **127**, 877–879.
45. K. Xu, Li-ion battery electrolytes, *Nat. Energy*, 2021, **6**, 763.

15 Interfaces

In Chapter 8, we set the conceptual foundation of interfaces when discussing the scenarios of an electrolyte meeting an electrode. The phase discontinuity of both materials results in sudden changes of physical and chemical properties. On the electrolyte side, these sudden changes are reflected in the potential distribution and ion concentration profiles. In this chapter, we will attempt to quantify these sudden changes further.

15.1 Defining an Interface

In Section 14.4, Chapter 14, we introduced the Electroneutrality Statement as one of the four cornerstones of Newman's theory on electrolytes, and briefly mentioned that this statement remains true only in the electrolyte bulk.¹ At interfaces, where an electrode meets an electrolyte, there is a sudden discontinuity of the chemistry in both phases, which induces corresponding sudden changes in the distribution of potential and electric charges.² The electroneutrality thus breaks down in local interfacial regions. This departure from electroneutrality can be best represented with the simple picture of an electric double layer as shown in Figure 6.7, where an electrode surface almost always repels one ion while attracting its counterion, thus resulting in excessive charges in these local regions of electrolyte near an electrode. In principle, such a departure from electroneutrality could enable us to define where an interface starts, but the actual situation of the electrode–electrolyte interaction is too complicated for a single and universal definition.

If the electrode and electrolyte are at a static equilibrium, *i.e.* there is neither an electrodic reaction occurring at the interface nor charge transfer across the interface, one could simply view the equilibrium from the electrostatic perspective, and treat the electrode as a giant, two-dimensional ion, hence its interface with the electrolyte as the consequence of an original dielectric continuity being disturbed by the Coulombic charge carried by this giant ion. One might immediately recall that, when deriving the mathematical description of an ionic cloud in Chapter 4, we defined a quantity of length in nature, *i.e.* the Debye–Hückel thickness:

$$K^{-1}(\text{or } \lambda_D) = \sqrt{\frac{\varepsilon k_B T}{4\pi} \frac{1}{\sum_i n_i^0 z_i^2 e_0^2}} \quad (4.71)$$

which represents the imaginary radius of the ionic cloud if one views the ionic cloud not as a diffuse continuity but as a point charge (Figure 4.5, right). Mathematically, at a distance $d = K^{-1}$ from the central ion, the total amount of charge contained in a spherical shell of infinitesimal thickness dr reaches the maximum (Figure 4.6a), hence one could also visualize the ionic cloud as an ionic shielding of thickness K^{-1} around the central ion (Figure 4.5, left).

Extending this concept to the giant, two-dimensional ion (*i.e.* the electrode), the Debye–Hückel thickness could therefore be used to define where the interfacial region starts, because it is in this region that the electroneutrality is no longer obeyed (Figure 15.1). Hence the interface should be on the same length scale as the Debye–Hückel thickness, which in dilute aqueous electrolytes is approximately sub-nanometric ($<10^{-9}$ m). Similarly to the Debye–Hückel thickness of a central ion, the interface thickness thus defined should be proportional to the square roots of both temperature and dielectric constant of the electrolyte, but inversely proportional to the square root of salt concentration. This is because thermal agitation that promotes random ionic motions intensifies at elevated temperatures, extending the interfacial region, while the higher population of ions in the electrolyte tends to compress the deviation from electroneutrality in the vicinity of the electrode.

When there is an electrodic reaction, and charge transfer occurs across the interface by a working ion, the above description of the static ion distribution near the interface no longer applies, and the ionic fluxes across the interface must be accounted for. Here let us examine the simplest case of such a dynamic situation, *i.e.* the ion

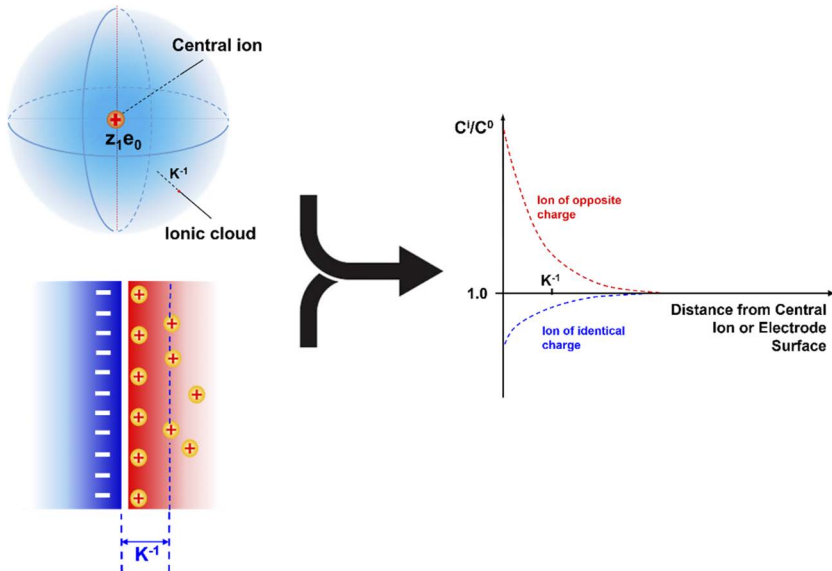


Figure 15.1 The concept of Debye–Hückel thickness applies to both an individual ion and an electrode, provided that one views the latter as a giant 2D ion. Thus, Debye–Hückel thickness can be extended to define the interface based on the deviation from electroneutrality in this region. The thickness of an interface should be on a length scale similar to the Debye–Hückel thickness, which is proportional to the square roots of temperature and dielectric constant of the electrolyte and inversely proportional to the square root of ion concentration.

distribution and the associated deviation from electroneutrality in the interfacial region when there is an ongoing electrodic reaction at the steady state. In other words, we are revisiting the ion transport in a one-dimensional cell at the steady state that has been discussed in the establishment of Bruce–Vincent approach (Section 14.2.4.6),³ but this time we will place more attention on the ion concentrations and the lengths involved instead of the potentials or currents. As before, we assume that the electrolyte sandwiched between a pair of identical electrodes is ideal and without any convection, where the anion of valence z_- is blocked, whereas the cation of valence z_+ serves as the working ion and can experience charge transfer at the electrode/electrolyte interfaces. With a potential difference of $\Delta\psi$ applied across the cell, we have already learned that the salt concentration profile across the electrolyte should be as shown in Figure 14.20. However, we must remember that such a concentration profile only describes the salt and ion distributions *within the bulk electrolyte*, because electroneutrality is still maintained in such distributions.

In the *bulk electrolyte*, the relative concentration of cations and anions must satisfy the Electroneutrality Statement:

$$z_+C_+ + z_-C_- = 0 \quad (15.1)$$

In the interfacial region near the cathode (*i.e.* negatively polarized electrode), however, the Coulombic force exerted by the electrode repels the anion from its vicinity while attracting an excessive population of cations into its vicinity, thus making the interface populated with an overwhelming majority of positive charge. Mathematically, this excess can be expressed as

$$z_+C_+ \gg z_-C_- \quad (15.2)$$

and the interfacial region can be viewed as a closed space with a net electrostatic charge, where Gauss's law and Poisson's equation of electrostatics should apply.

We can leverage the above difference to derive both the concentration and potential distributions in bulk and interfacial regions and discuss how one should quantitatively differentiate them.

15.1.1 Ionic Fluxes in Bulk and Across an Interface

First, while the Electroneutrality Statement is applicable only in the electrolyte bulk, the Flux Statement still holds true anywhere across the cell including the interfacial regions, which for cationic and anionic fluxes should be written as, respectively

$$J_+ = -D_+ \frac{dC_+}{dx} - D_+ C_+ \frac{z_+ F}{RT} \frac{d\psi}{dx} \quad (15.3)$$

$$J_- = -D_- \frac{dC_-}{dx} + D_- C_- \frac{z_- F}{RT} \frac{d\psi}{dx} \quad (15.4)$$

The alternative forms of eqn (15.3) and (15.4) were derived earlier when discussing the Bruce–Vincent approach, and we know that at the steady state the anionic flux J_- is zero because the migration of anions would be exactly cancelled out by their diffusion, hence from eqn (15.4) we have

$$D_- \frac{dC_-}{dx} = D_- C_- \frac{z_- F}{RT} \frac{d\psi}{dx} \quad (15.5)$$

which can be rearranged into

$$\frac{d \ln C_-}{dx} = \frac{z_- F}{RT} \frac{d\psi}{dx} \quad (15.6)$$

and

$$C_- = e^{\frac{z_- F}{RT} \psi(x)} \quad (15.7)$$

Meanwhile, the electric current at the steady state, i^{ss} , is entirely contributed by the cationic flux, hence

$$i^{ss} = z_+ F J_+ = -z_+ F D_+ \left[\frac{dC_+}{dx} - C_+ \frac{z_+ F}{RT} \frac{d\psi}{dx} \right] \quad (15.8)$$

These equations hold true for both bulk and interfacial regions of the electrolyte, and the electric field ($d\psi/dx$, *i.e.* the potential gradient) in these regions dictates how the ion concentration and potential drops are distributed. Considering the significant difference between these two regions, we must examine these equations under corresponding boundary conditions.

In order to do so, let us revisit the ion concentration profiles established at the steady state as shown in Figure 14.20, but this time we need to introduce an imaginary line located at x_i (where the subscript “i” denotes “interfacial”) that marks the border between “bulk” electrolyte and the “*interfacial*” region (Figure 15.2). In the former, the Electroneutrality Statement is satisfied, and eqn (15.1) holds true, whereas in the latter, an excess in cation population is expected, which should be similar to the cation/anion distribution as shown in Figures 4.6c and 15.1, with eqn (15.2) remaining true. In reality, of course, the border of bulk and interfacial regions is not so markedly separated by a single line, but instead it should be represented by a transition region. In that case the ion distributions even in the bulk electrolyte do not strictly obey the Electroneutrality Statement but instead experience a gradual departure from it, a phenomenon that is referred to by some researchers as “*quasi-neutrality*”. However, for mathematical simplicity, here we will treat the border between the two regions as an imaginary line.

15.1.2 Concentration Profiles in the Bulk Region

Now let us consider the bulk region first. From eqn (15.5), we could solve for the electric field:

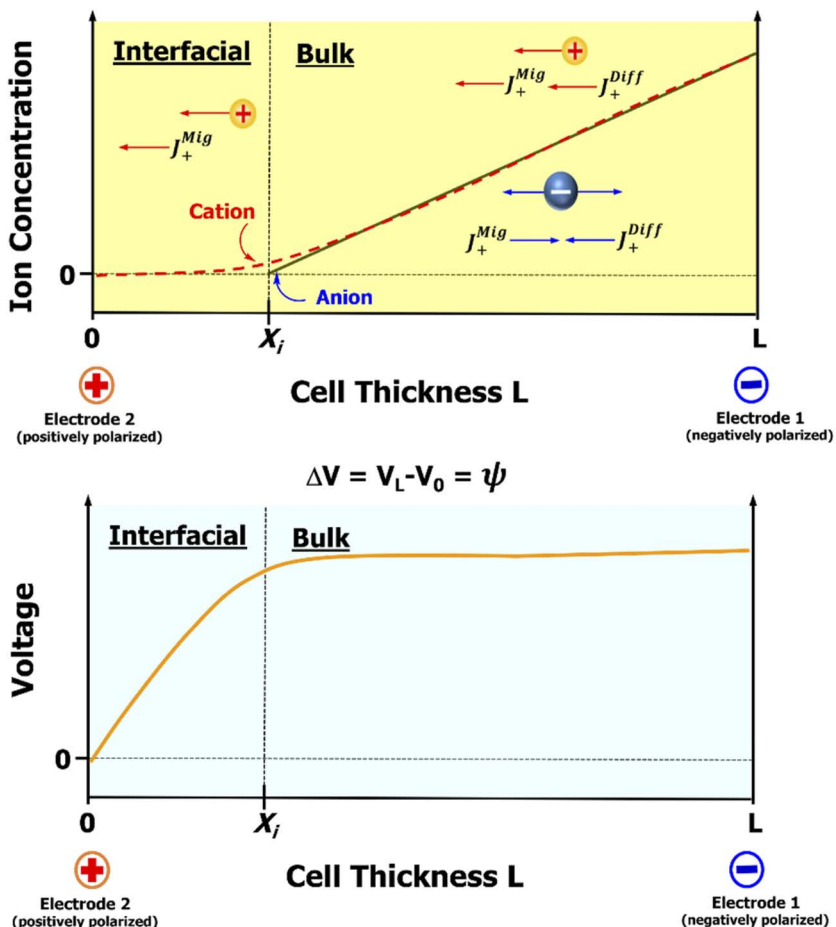


Figure 15.2 Differentiating interfacial from bulk regions. Top: the cationic and anionic concentration profiles in bulk and interfacial regions, respectively, when a steady state is established. Bottom: the corresponding voltage profile in bulk and interfacial regions. Note that in the interfacial regions, the diffusional contribution to the cationic flux can be ignored, where the current is overwhelmingly contributed by the cationic migration.

$$\frac{d\psi}{dx} = \frac{RT}{z_- FC_-} \frac{dC_-}{dx} \quad (15.9)$$

Inserting eqn (15.9) into eqn (15.3), we now have an expression for cationic flux that does not contain the troublesome potential term:

$$J_+ = -D_+ \frac{dC_+}{dx} - D_+ C_+ \frac{z_+}{z_- C_-} \frac{dC_-}{dx} \quad (15.10)$$

The cationic flux is important to us, because at the steady state the electric current would be entirely contributed by it. However, eqn (15.10) is a differential equation with two different concentration gradients (dC_+/dx and dC_-/dx), which makes it inconvenient to solve *via* integration. Fortunately, thanks to the electroneutrality that is assumed to be strictly obeyed here, C_+ and C_- are correlated with each other *via* eqn (15.1), therefore

$$\frac{dC_-}{dx} = \frac{d}{dx} \left[\frac{z_+ C_+}{z_-} \right] = \frac{z_+}{z_-} \frac{dC_+}{dx} \quad (15.11)$$

Inserting eqn (15.11) into eqn (15.10), we obtain

$$J_+ = -D_+ \frac{dC_+}{dx} - D_+ \frac{z_+ C_+}{z_- C_-} \frac{z_+}{z_-} \frac{dC_+}{dx} = -D_+ \left[1 + \frac{z_+}{z_-} \right] \frac{dC_+}{dx} \quad (15.12)$$

which is now a total differential equation. Remember that at the steady state the cationic flux is actually a constant given by

$$J_+ = \frac{i^{ss}}{z_+ F} \quad (15.13)$$

Hence a total differential equation could be transformed by combining eqn (15.12) and (15.13) followed by rearrangement:

$$dC_+ = -\frac{i^{ss}}{z_+ F D_+} \frac{1}{\left(1 + \frac{z_+}{z_-} \right)} dx \quad (15.14)$$

which can be integrated in the range from $x = x_i$ to x (any location in the cell until the anode side) to yield an expression for cation concentration as a function of distance from the interface:

$$C_+ = \int_{x_i}^x \left(-\frac{i^{ss}}{z_+ F D_+} \frac{1}{1 + \frac{z_+}{z_-}} \right) dx = -\frac{i^{ss}}{z_+ F D_+} \frac{1}{1 + \frac{z_+}{z_-}} (x - x_i) \quad (15.15)$$

and correspondingly an expression for anion concentration as a function of distance from the interface:

$$C_- = -\frac{z_+}{z_-} C_+ = \frac{i^{\text{ss}}}{z_- F D_+} \frac{1}{\left(1 + \frac{z_+}{z_-}\right)} (x - x_i) \quad (15.16)$$

Both eqn (15.15) and (15.16) actually represent linear concentration profiles for cations and anions, which become essentially zero at the interface ($x = x_i$). When $z_+ = -z_-$, i.e. an electrolyte consisting of equi-valent ions such as NaCl or MgSO₄, the concentration profiles for cations and anions are identical, which we already witnessed in Figure 14.20a and b. Here in Figure 15.2 (top), these profiles are again shown in the bulk region as marked by the range from $x = x_i$ to L (the anode side of the cell).

With eqn (15.15) and (15.16), the function of potential $\psi(x)$ can also be obtained by inserting either equation back into eqn (15.9) and then integrating it in the range from $x = x_i$ to $x = L$:

$$\psi(x) = \psi(L) + \frac{RT}{z_- F C_-} \ln \frac{x - x_i}{L - x_i} \quad (15.17)$$

The cell voltage gradient in the bulk region is relatively flat (compared with the drastic change in the interfacial region that we are about to discuss), as shown in Figure 15.2 (top) by the range from $x = x_i$ to $x = L$. In fact, we derived such a potential distribution in Section 14.2.4.6.3 from another perspective [eqn (14.173)], and briefly discussed its asymmetric shape that was introduced by the logarithmic term (Figure 14.21). We now understand that such asymmetry is caused by the depletion of ions near the cathode side because of the electroic reaction with fast kinetics, which we assumed when deriving the Bruce–Vincent approach (Section 14.2.4.6).

15.1.3 Concentration Profiles in the Interfacial Region

In the interfacial region defined by $0 < x < x_i$ in Figure 15.2, the cation population far exceeds the anion population, hence we can approximately assume that the net charge density ρ in this enclosed region is given by

$$\rho = z_+ F C_+ \quad (15.18)$$

while the distribution of such a net charge in the interfacial region should be governed by the *Poisson equation*, when the field is created

by the applied potential ψ , which, in combination with Gauss's law, dictates that

$$\frac{d^2\psi}{dx^2} = -\frac{\rho}{\epsilon_0 \epsilon} = -\frac{z_+ F C_+}{\epsilon_0 \epsilon} \quad (15.19)$$

where ϵ_0 and ϵ are the dielectric constants of vacuum and the electrolyte, respectively. In particular, one should note that ϵ here represents the dielectric constant of the electrolyte in the interfacial region, where the solvents and ions are aligned with the strong Coulombic field of the electrode, hence it could differ significantly from the dielectric constants of the electrolyte in bulk that are usually given in the literature.

Also, in this interfacial region, because the electric field is extremely strong, *i.e.* much stronger than that in the bulk, one expects that the cationic flux would overwhelmingly consist of a migration contribution and the diffusional component could be ignored, which turns eqn (15.3) into

$$J_+ = \frac{i^{ss}}{z_+ F} = -D_+ C_+ \frac{z_+ F}{RT} \frac{d\psi}{dx} \quad (15.20)$$

Solving for the potential gradient from eqn (15.20) and then inserting it into eqn (15.19), we obtain

$$-\frac{z_+ F C_+}{\epsilon_0 \epsilon} = \frac{d^2\psi}{dx^2} = \frac{d}{dx} \left[-\frac{i^{ss} RT}{D_+ C_+ (z_+ F)^2} \right] = i^{ss} \frac{RT}{D_+ (C_+ z_+ F)^2} \frac{dC_+}{dx} \quad (15.21)$$

which again becomes a total differential equation with respect to C_+ , and which could be integrated now in the interfacial region defined as $0 < x < x_i$:

$$C_+ = \sqrt{-i^{ss} \frac{RT \epsilon_0 \epsilon}{2(z_+ F)^2 D_+} (x_i - x)} \quad (15.22)$$

A quantitative analysis indicates that, unlike eqn (15.15), the distribution of cations along the distance from the electrode is now no longer linear as eqn (15.15) states; instead, the cation concentration would experience a non-linear trend of increasing within the range of the interfacial region ($0 < x < x_i$), and reaching a maximum at the electrode surface ($x = 0$). In reality, this cannot be true, because of

the actual boundary condition that the cation concentration must be zero at the electrode surface owing to the fast kinetics. Considering this additional constraint, and the fact that both the cation and anion concentrations should already approach zero at the interfacial border ($x = x_i$), the above analytical solution has to be modified in order to match the solutions achieved in both regions.

Likewise, the function of potential $\psi(x)$ can also be obtained:

$$\psi(x) = \psi(0) - \frac{2}{3} \sqrt{-i^{ss} \frac{2RT}{\varepsilon_0 \varepsilon D_+}} (x_i - x)^3 \quad (15.23)$$

By comparing eqn (15.23) with eqn (15.17), one can immediately see that the former describes the potential change from the electrode surface ($x = 0$) to the interfacial border (x_i), while the latter approaches the interfacial border from the other end of the cell. Quantitative analysis indicates that the cell potential will continue the trend of dropping as described by eqn (15.17), while as the distance approaches the electrode surface the drop in potential accelerates.

Combining these constraints, Chazalviel conducted a numerical solution to eqn (15.3) and (15.4).⁴ The profiles for both cation concentration and potential in these two regions are as shown in Figure 15.2, and are considered to represent a close description of the reality in an anion-blocking cell at the steady state. Results from both simulations and various spectroscopic studies have shown that, while the interfacial thickness as defined above varies significantly with both electrode and electrolyte materials as well as the ion–ion and ion–solvent interactions and the dielectric constant of the electrolytes, a general range of 0.5–2 nm usually applies for such two-dimensional interfaces.

References

1. J. Newman and N. P. Balsara, *Electrochemical Systems*, Wiley, 4th edn, 2021.
2. J. O'M. Bockris and A. K. N. Reddy, *Modern Electrochemistry*, Plenum Press, New York, 2nd edn, 1998.
3. C. A. Vincent and P. G. Bruce, Steady state current flow in solid binary electrolyte cells, *J. Electroanal. Chem. Interfacial Electrochem.*, 1987, **225**, 1–17.
4. J.-N. Chazalviel, Electrochemical aspects of the generation of ramified metallic electrodeposits, *Phys. Rev. A: At., Mol., Opt. Phys.*, 1990, **42**, 7355–7367.

16 Interphases

In Chapter 8, we conceptually discussed the scenarios of an interface turning into an interphase when the potential of the electrode ventures into the regions beyond the thermodynamic stability of the electrolyte. In this chapter, we continue this discussion in more detail concerning how interphases are formed from electrolytes (with the possible participation of electrodes also), what factors dictate the formation processes and how the chemical, morphological and architectural characteristics of the resultant interphases affect the advanced battery chemistries, especially the chemistries of lithium-ion, lithium-metal and other lithium-based batteries.

It should be noted that, although an interphase is often associated with rechargeable, and especially lithium-based, battery chemistries, it is by no means confined to rechargeable chemistries only. Instead, it exists universally in almost all electrochemical devices that operate above 3 V. For example, long before the invention of lithium-ion batteries, lithium-metal primary batteries (Li/SOCl_2 , LiMnO_2 or Li/CF_x) commercialized in the 1960s were already based on interphases formed on the lithium-metal surface by either inorganic electrolytes such as thionyl chloride (SOCl_2) or organic electrolytes such as ethers,¹ although at the time the concept of an interphase did not exist, and it was just thought that lithium metal is passivated in non-aqueous, aprotic electrolytes.

Compared with studies on ion solvation and ion transport, the understanding of interphases is still in its infancy. Although the presence of a “passivation layer” on lithium metal was acknowledged as early as the 1950s,² while the formal concept of an interphase was

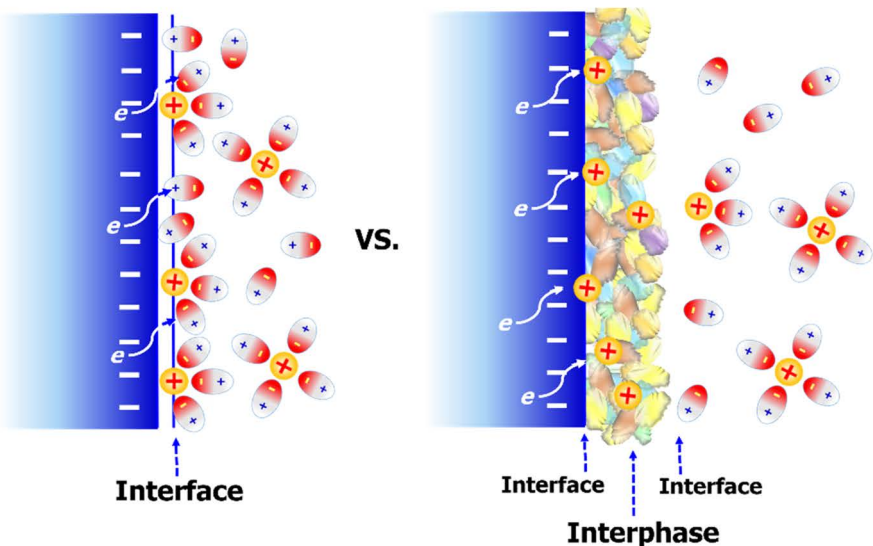
proposed by Peled in 1979 (along with the creation of the popular acronym SEI for “*solid electrolyte interphase*” and the basic definition of SEI being “*Li⁺-conducting and electron-insulating*”),³ the serious investigation of an interphase as an independent component in electrochemical devices did not start until the birth of lithium-ion batteries in the 1990s.⁴ In this sense, most of the knowledge about interphases was accumulated in the short time frame of three decades, and our understanding of this “new” entity remains restricted by the characterization means available.

16.1 Defining an Interphase

Differing from a two-dimensional interface, an interphase is an independent and three-dimensional phase with chemistry and morphology distinct from both the electrodes and electrolyte, therefore an interphase actually has its own interfaces, one between it and the electrode, and another between it and the electrolyte (Figure 16.1a). Since the chemistry and morphology of an interphase are relatively permanent and static after its formation, its definition is usually based on chemical and morphological characterizations. Such a definition is unambiguous on some electrodes, such as graphite and lithium metal, whose interphases have clear boundaries with both the bulk electrode and electrolyte. However, the definition becomes less clear on some other electrodes whose active ingredients also participate in the formation chemistry of interphases. Examples of the latter include certain transition metal oxides such as NMC, the lattice structure of which near the electrolyte often undergoes transformation into structures of less reversibility during the formation of interphases. In this case, the boundaries become rather smeared, and no consensus has been reached regarding whether this transformed surface structure of the cathode should be considered as part of the interphase, or whether only those surface depositions from the decomposition of electrolytes should be considered as the interphase.

Like an interface, the thickness of an interphase also varies significantly with the nature of the electrode, its surface chemistry and its operating potential, and particularly the nature of the electrolytes. According to both computational and experimental studies, the thickness of the interphase falls into a general range of 2–50 nm.^{5,6} If thinner than 2 nm, the interphase is considered susceptible to electron tunneling regardless of what ingredient the interphase is constructed from, hence it could not serve as an effective barrier to undesired

(a)



(b)

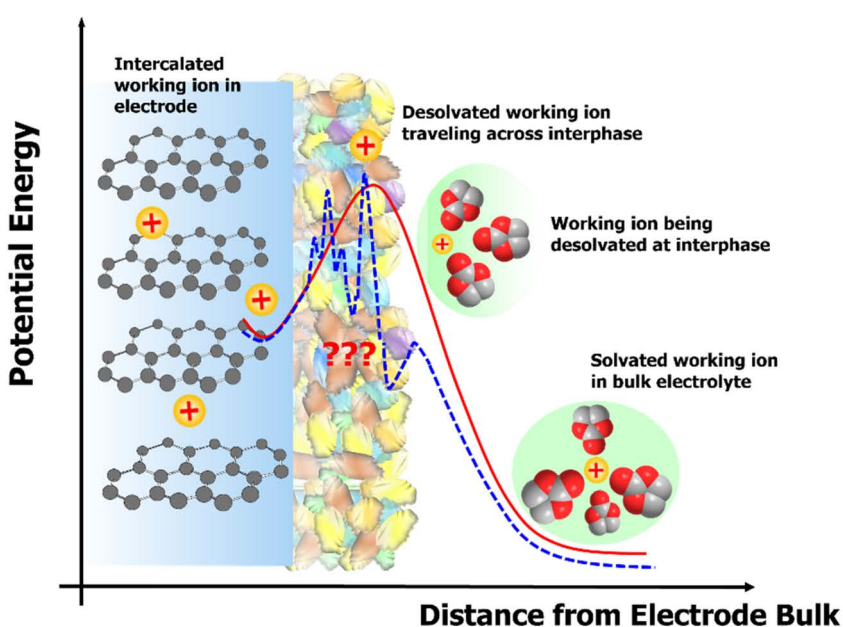


Figure 16.1 (a) A well-defined two-dimensional interface and a poorly defined three-dimensional interphase of heterogeneous chemistries and morphologies. Note that an interphase has its own interfaces with the electrode and electrolyte. (b) The difference in potential energy for an Li⁺ ion traveling from the bulk electrolyte, across an interphase and then into the electrode interior. Here graphite is used as an example of an intercalation host for Li⁺.

reactions; if thicker than 50 nm, an interphase would be too resistive to working ions and cause undesired kinetic losses to the cell chemistry.

As will be discussed below, an interphase is created by the reaction between an electrode and an electrolyte. Most of the interphases studied so far are highly heterogeneous in both chemistry and morphology. Although we have developed an advanced understanding of the chemistry of interphases and their formation processes, their microscopic structure and the way in which they function, *i.e.* transporting working ions, remain little understood. Most importantly, we do not have the knowledge about how ions are distributed across the interphases and how the potential drops across it, as we did for interfaces in the previous chapter. Let us consider the graphitic anode and the associated interphase in a lithium-ion battery as an example (Figure 16.1b). We know the relative potentials of an Li^+ when it is solvated in the bulk electrolyte and when it is intercalated within a graphitic structure, and we know that, between these two terminal states, an Li^+ must have been desolvated somewhere, and that the desolvated Li^+ must migrate across the interphase in order to arrive at the graphite interior. We also know that the potential of Li^+ in those transition states (during desolvation or migrating across the interphase) must be higher than that of its solvated state in the bulk electrolyte or its intercalated state in the graphitic lattice. However, owing to the chemical and morphological heterogeneity of interphases, we do not know how the potential energy of this Li^+ varies while being desolvated at the interphase or moving within the interphase. Most of the knowledge so far is either simulation or pure speculation.

This is still a highly dynamic area of intense studies, where many questions remain unanswered, with many opportunities for exciting science to be done.

16.2 An Interphase is Created by Electrode-Electrolyte Mismatch in Electron Energy Levels

The emergence of an interphase in an electrochemical device is in fact created by our efforts to push such devices to operate at maximum voltages. The motive for doing so could be the benefits of more energy being stored at higher quality (as in the case for electrochemical double-layer capacitors and batteries), or the benefits of enabling reactions that otherwise would not occur under moderate conditions (such as the electrochemical synthesis of lithium or other alkaline

metals). The direct consequence of this voltage maximization places the potential of the electrodes at extreme values, where the electrolyte can no longer remain thermodynamically stable. Electrolyte decompositions occur, and an interphase subsequently forms, if the decomposition products meet certain standards, *i.e.* being solid and retaining an electrolyte nature, as discussed in Section 8.1.

We can better understand how an interphase works in a battery in terms of the electron energy level (Figure 16.2).⁷ Let us take a typical lithium-ion battery as an example, the two electrodes of which are graphitic carbon as anode host and a transition metal oxide as cathode host for Li^+ , while a non-aqueous electrolyte interfaces with both electrodes. Even though each battery component is a mixture of many ingredients, for simplification we can treat each of them as a

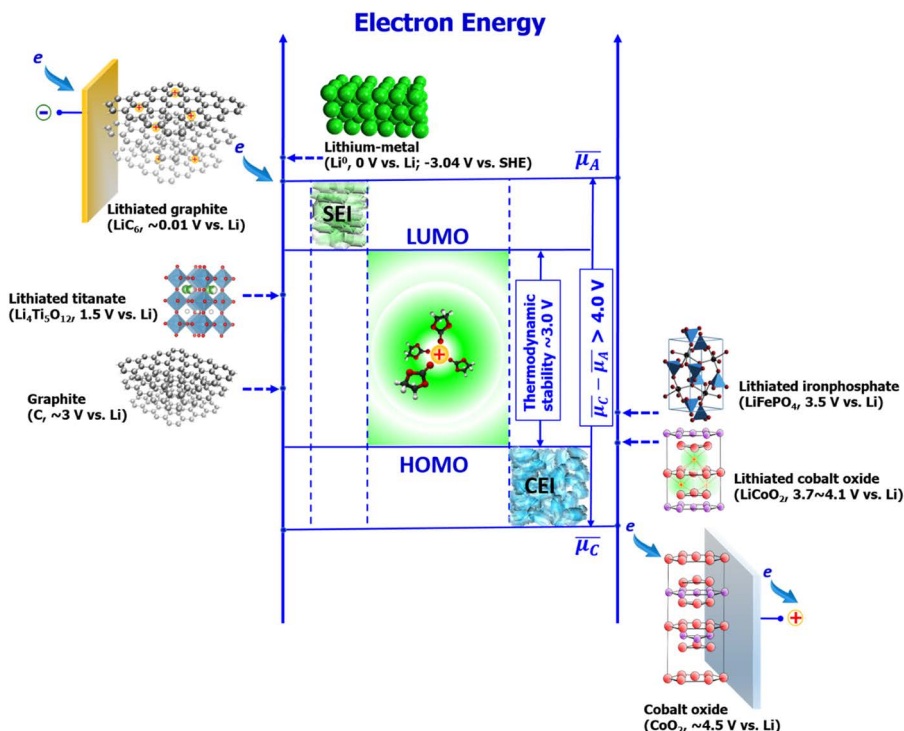


Figure 16.2 Schematic illustration of electron energy levels for each component in a lithium-ion battery and the function of both interphases, *i.e.* solid/electrolyte interphase (SEI) at the anode side and cathode/electrolyte interphase (CEI) at the cathode side, in preventing the irreversible decomposition of the electrolyte by the fully charged anode and cathode surfaces. Also shown are the approximate eigenpotentials of a few representative anode and cathode materials.

component with singular chemical properties. Thus, the energy levels of the electrons in the anode and cathode are represented by their corresponding eigenpotentials $\overline{\mu_A}$ and $\overline{\mu_C}$, respectively, the difference of which is related to the cell voltage ΔV via

$$-e\Delta V = \overline{\mu_C} - \overline{\mu_A} \quad (16.1)$$

For state-of-the-art lithium-ion batteries at the fully charged state, such a difference is usually in the range 4.1–4.5 V. With special cathode materials such as lithium cobalt phosphate (LiCoPO_4), it could be as high as >5 V.

On the other hand, the thermodynamic stability of the electrolyte is defined by the difference between the energy levels of the electrons residing in the *lowest unoccupied molecular orbital* (LUMO) and the *highest occupied molecular orbital* (HOMO) of the electrolyte, which, according to calculations, should not be wider than 3.0 V even for non-aqueous aprotic electrolytes. For aqueous electrolytes, this gap between the LUMO and HOMO is even smaller, namely 1.23 V as shown in Figure 5.12 (Section 5.2.7) and Figure 8.2 (Section 8.2). Note that, since we are treating the electrolyte as a single component, these HOMO and LUMO should be considered as the hybridized molecular orbitals of *all* electrolyte components, which include salt cation, salt anion, solvent molecules and electrolyte additives if there are any.

In conclusion, a mismatch exists between the electrochemical potentials of both electrodes and the thermodynamic stability limits of the electrolyte.

With such a mismatch, if any electrode material with electrons residing at energy levels above the LUMO of the electrolyte is in contact with this electrolyte, there would be a tendency for that material to transfer its electrons to the electrolyte. The result of such a transfer is the *reductive decomposition* of the electrolyte. Likewise, if any material with electrons residing at energy levels below the HOMO of the electrolyte is in contact with this electrolyte, there would be a tendency for that material to extract electrons from the electrolyte. The result of such transfer is *oxidative decomposition* of the electrolyte.

In most cases, these decomposition reactions proceed sustainably until either the electrode material or the electrolyte is completely consumed. The most prominent example is lithium metal in aqueous electrolytes (with only the water-in-salt electrolytes existing as exceptions). We would say that such an electrode is unstable in the given electrolyte, or *vice versa*.

However, in limited cases, the decomposition products formed depositions on the electrode surfaces. If these products remain conductive to the working ion of the cell but are insulating towards electrons, then such deposition serves as a self-limiting interphasial entity, which prevents the sustained reductive or oxidative decompositions. We call these new deposition layers on electrode surfaces *interphases* or, depending on where they are, *solid/electrolyte interphase* (SEI) and *cathode/electrolyte interphase* (CEI).⁸

The emergence of SEIs and CEIs in lithium-ion batteries insulates the electron transfers between electrode and electrolyte in the above-mentioned “mismatch” regions, which in fact extends the electrochemical stability window of the electrolyte from its thermodynamic value of ~3.0 V to the electrochemical potentials of both anode and cathode (Figure 16.2). This is the basic function of an interphase.

Of course, the presence of interphases is by no means unique to lithium-ion batteries, but instead is universal in any electrochemical cell, provided that its electrodes operate beyond the thermodynamic stability limits of its electrolyte. However, it was the commercial success of lithium-ion batteries that brought the significance of interphases into the focus of researchers, hence most knowledge about interphases in the literature is closely relevant to lithium-ion battery chemistries and materials. Historically, recognizing the role of SEI by Dahn and colleagues initiated a revolution in electrolyte science, which guided us into an entirely new direction that designing a new electrolyte must consider not only the bulk properties such as salt dissolution and ion transport, but also the implications of interphase chemistry brought by such electrolytes.⁴

It should be mentioned that there are certain exceptions to interphases in lithium-ion batteries, *e.g.* lithium titanate ($\text{Li}_4\text{Ti}_5\text{O}_{12}$) and lithium iron phosphate (LiFePO_4). The former often serves as the anode and the latter as the cathode in certain lithium-ion battery chemistries, although they are not necessarily used together. They are special because their eigenpotentials (~1.5 V vs. Li for $\text{Li}_4\text{Ti}_5\text{O}_{12}$ and ~3.5 V vs. Li for LiFePO_4) happen to reside within the thermodynamic stability limits of most non-aqueous electrolytes (Figure 12.4). Because of this thermodynamic nature, no interphases should be formed on these electrodes unless they are polarized to potentials beyond the limits as marked by the LUMO and HOMO levels of the electrolytes.

If one assembles a cell consisting of $\text{Li}_4\text{Ti}_5\text{O}_{12}$ as anode and LiFePO_4 as cathode, then it is possible to obtain an “interphase-free” lithium-ion battery. As we said earlier, “*the best interphase is no interphase*” –

such an interphase-free lithium-ion battery should display excellent power density, *i.e.* a capability of providing a high current drain during discharge and a capability of being charged at high rates, because the charge transfer at the electrode/electrolyte interfaces in this battery do not encounter the interphasial resistance that Li^+ has to overcome in most lithium-ion batteries.

Of course, the corresponding expense that one has to pay for the high power density is the mediocre energy density, because a lithium-ion battery constructed with an $\text{Li}_4\text{Ti}_5\text{O}_{12}$ anode and LiFePO_4 cathode can generate a maximum working voltage of only ~ 2.0 V. High-power/low-energy lithium-ion batteries such as these are therefore often restricted to certain niche applications where we need excellent reversibility (long cycle and calendar life) and fast charge/discharge but do not care much about how long the battery could run. Examples of such applications are electric buses operating in urban environments, where the buses could receive pulse charge during their short but frequent stops along their fixed routes.

16.3 What Is a Good Interphase?

We mentioned in Section 6.1 (Figure 6.1) that the two interfaces between electrodes and electrolyte constitute the only legitimate sites for electron exchanges in the electrochemical device, so that the redox reaction could proceed along an electrochemical rather than a chemical pathway.

The presence of interphases at these two interfaces invalidates this statement. As the electrodes are no longer in direct contact with the bulk electrolyte, the electron transfer between electrodes and electrolytes as described by the Butler–Volmer equation (Section 6.5.4) becomes essentially impossible. Instead, the working ions now have to migrate across these interphases, and complete the electron transfer at the junction between the electrode and the inner side of the interphase. In fact, this concept was briefly discussed in Section 6.5.9 (Figure 6.15).

In this sense, an ideal interphase not only should serve as an effective “kinetic barrier” to unwanted electron transfers between electrodes and electrolyte driven by the gaps between the HOMO and $\overline{\mu_c}$ or between the LUMO and $\overline{\mu_A}$, but also should conduct the working ions with minimum resistance. So far, it has been impossible to measure directly the ionic resistivity (or ion conductivity) across interphases, hence the thickness of interphases has been used as an indirect (and inaccurate) quantity to evaluate its quality.

A popular but highly empirical consensus among researchers is that a good interphase should not be thick, because a thin interphase usually implies low resistance towards ionic migration, and indicates that its chemical composition is effective in insulating electron tunneling with a minimized footprint on electrode surfaces. However, there is no quantitative standard regarding “*how thick an SEI is too thick*”.

It has been widely recognized that the lower limit of interphasial thickness should be ~2 nm, because a barrier under such a limit is believed to be susceptible to electron tunneling and hence incapable of preventing unwanted electron transfer. On the other hand, there is no well-accepted value for the upper limit, while the average thicknesses of interphases as measured on lithium metal and lithiated graphitic carbon usually fall in the range 10–20 nm. In early efforts at characterizing SEI on a lithium-metal surface, Peled and Straze found that the interphases formed in most non-aqueous electrolytes based on ethers or carbonate esters range between 2.5 and 10 nm, and proposed an expression for the interphase thickness L using a parallel capacitor model:⁹

$$L = \frac{\varepsilon A}{C_{\text{dl}} \times 3.6 \times 10^{12}} \quad (16.2)$$

where ε is the dielectric constant of the electrolyte near the electrode surface, A the electrode area and C_{dl} the double-layer capacitance created by the interface between the electrode and the electrolyte. This is apparently an oversimplified model and cannot account for the complicated factors that might affect the formation of the interphases. Most important, the chemical building blocks and their physical and chemical properties should be the factors that matter most.

In fact, there should be a general link between the interphase thickness and the electronic conductivity of the chemical ingredients that constitute the interphase. As we briefly discussed in Section 5.2.8, the charge tunneling probability decreases exponentially with the distance:

$$P_r \propto e^{-\frac{4\pi L}{h} \sqrt{m(E-U)}} \quad (5.178)$$

Therefore, it is expected that a highly electronic-insulating chemical ingredient would tend to form a compact and effective interphase, whereas those ingredients with high electronic conductivity cannot achieve the necessary protective function of the interphase without a thick deposit. This is in fact part of the reason why inorganic

ingredients, especially those based on fluorides, are often found in good interphases. However, it must be cautioned that chemistry is only one part of the equation: the morphology and structure of the interphase, *i.e.* how these chemical ingredients are arranged and distributed in the interphase, often play an equally, if not more, important role in determining how good an interphase is.

Shortly after Peled proposed the concept of SEI, a list of requirements for an ideal interphase was compiled:

1. Zero electronic conductivity, otherwise electron tunneling would induce continuous electrolyte decomposition;
2. High conductivity to Li^+ (or the working ion), so that the cell chemistry could be sustainable by needed migration and mass transport;
3. Uniform morphology and chemical composition for homogeneous current distribution, so that Li^0 dendrites would be minimized;
4. Minimum thickness, so that the travel of Li^+ (or the working ion) across the SEI would incur the least amount of overpotential;
5. Good adhesion to the electrode surface, so that the interphase layer would not delaminate during the reversible electrode redox reaction, which is often accompanied by periodic volume expansion and contraction;
6. Good mechanical strength and flexibility, for the same purpose as point 5;
7. Low solubility in electrolytes, so that continuous dissolution of the SEI would not occur, resulting in persistent decomposition of the electrolyte and consumption of the limited source of lithium from the cathode.

As the electrodes and interphases that we deal with evolve from lithium metal to another metal, intercalation or alloy hosts, and the working ion from Li^+ to other emerging chemistry ions such as Na^+ or multivalent ions, the above list remains largely valid, but a perfectly ideal interphase has never been found. The interphase in real life is often a compromise with balanced merits of the above list.

Finally, in a “tongue-in-cheek” expression, we can say that “*no interphase is the best interphase*” because, after all, the presence of interphases is not by choice but a compromise imposed on the electrochemical device as a consequence of electrolyte instability. Any interphase inevitably induces additional resistance to ionic transport. In this sense, a perfectly ideal interphase would be one of zero

thickness. This is the rationale behind the so-called “dynamic interphase” concept, where the interphase does not exist in a permanent form but instead assembles only when the electrode needs protection. We will briefly discuss this new concept in more detail in Chapter 17.

16.4 Charge Transfer in the Presence of 2D Interfaces and 3D Interphases

In a number of electrochemical devices with low working potentials, such as lead–acid and nickel–metal hydride batteries, aqueous electrochemical double-layer capacitors or fuel cells, the working voltages of which are below 1.5 V, the reversible and stable operation of the devices is achieved entirely by the thermodynamic stability of the electrolytes therein, *i.e.* each component of the electrolytes is thermodynamically stable against oxidation or reduction on the surfaces of positive or negative electrodes. There is no interphase in such devices. The interface in these devices conceptually consists of a pair of electrified layers as discussed in Section 6.4, and the thickness of such interfaces, as defined as the distance between electrode surface and the outer-Helmholtz plane, is estimated to be <1 nm. Traditionally, they are regarded as 2D planes.

Because of the sub-nanometer thickness, the electric field strength within the interface is on the order of $10^9 \text{ V}\cdot\text{cm}^{-1}$, which constitutes an energy barrier for any ion transport across the interface. The rate of charge transfer across the interface is governed by the Butler–Volmer equation:

$$i_{\text{net}} = i_0 \left[e^{-\frac{\beta \eta F}{RT}} - e^{\frac{(1-\beta)\eta F}{RT}} \right] \quad (6.87)$$

Compared with the rate of ion diffusion and migration within the bulk electrolyte, this interfacial transport process could most likely, but not always, become the rate-determining step.

This 2D interface, as discussed in Section 8.1 (Figure 8.1a), is the site for charge transfer, and its structure should be dynamic and transient.

However, when the cell voltages increase to >3.0 V, the potential of one of the electrodes (or both electrodes) would generally venture beyond the zone enclosed by the LUMO and HOMO of the electrolyte as depicted in Figure 16.2, inducing the formation of interphases. The chemical composition of the interphases is dictated by both electrodes

and electrolyte and consists of the solid decomposition products from the reactions between the two. Such reactions are irreversible, hence the presence of an interphase on the electrode surface is mostly permanent, and it has relatively static chemical composition, structure and morphology. It is a 3D entity with a certain thickness >2 nm.

Since the interphase is an electrolyte in nature, *i.e.* conducting ions while insulating electron tunneling, it is no longer a site for charge transfer. Instead, the working ions have to travel across the interphase in order to complete the charge transfer for the cell reaction (Figure 16.1). In other words, the charge transfer now occurs only underneath the interphase at the electrode side, or at the “interface” between the electrode and the interphase. Nothing is known about the kinetics of this process, because it is often tightly convoluted with the ion migration process across the interphase. It is reasonable to believe that the kinetics of ion migration across such an independent and 3D phase would encounter a much higher energy barrier than a 2D interface, so the interphase almost always constitutes the rate-determining step in the cell reaction. Owing to the heterogeneous morphology of the interphase, the distribution of electric field across it is also non-linear. Most importantly, in principle, the Butler–Volmer equation no longer directly applies to any charge-transfer processes if an interphase exists. Nevertheless, the Butler–Volmer equation is still frequently adopted in modeling lithium-ion or other advanced batteries, where modifications are made in order for it to appear as if the charge-transfer process in the presence of a 3D interphase is still governed by it. One must be extremely cautious when reading the related literature, and bear in mind that, so far, the efforts to understand interphases have not acquired direct knowledge about ion transport resistance and kinetics across the interphases, let alone differentiating and determining the charge-transfer kinetics at the junction of the interphase electrode. The limited simulation results for the Li^+ diffusion coefficient and conductivity across interphases remain to be verified by experiments.

16.5 Two Distinct Manners of Forming Interphases

Although workers often equate the interphases formed on the lithium-metal surface with the interphases formed on a graphitic carbon surface as found in lithium-ion batteries, on the basis that the eigenpotentials of lithium metal and fully lithiated graphite differ by

only millivolts, there is actually a sharp distinction between these two interphases. They are formed in two completely different manners (Figure 16.3).

The first manner of interphase formation is characterized by the nature of being “*instantaneous and indiscriminating*”. Interphases formed on a lithium-metal surface belong to this category (Figure 16.3a).

As discussed in Section 9.1.3.1, lithium metal has the lowest eigen-potential ($\mu_A = -3.04$ V vs. SHE) known among all the elements. On the energy diagram depicted in Figure 16.2, an electron in lithium metal sits at the very top and doubtless beyond the thermodynamic stability limits of any known electrolyte materials as marked by their LUMOs. A natural consequence of this extreme activity (or reactivity) of lithium metal towards electrolytes is that an interphase would form instantaneously upon contact between the two. In other words, when an electrolyte is injected into a cell that contains lithium metal as one of its electrodes, an interphase is formed in an extremely short time frame, probably on a time scale shorter than nanoseconds. Under such a circumstance, if the electrolyte consists of multiple components, all of which possess LUMOs below that of μ_A , the reduction of these components by lithium metal would be not only instantaneous but also indiscriminating. In other words, the opportunity for each electrolyte component to participate in the interphase formation on lithium metal is relatively equal.

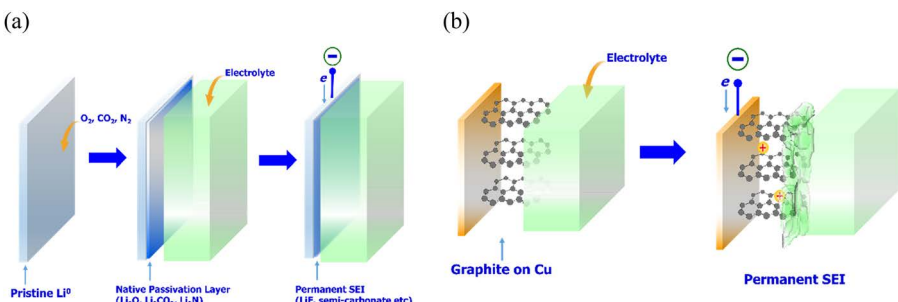


Figure 16.3 Two distinct ways of forming interphases: (a) instantaneous and indiscriminating, as in SEI formation on an Li^0 surface; (b) stepwise and discriminating, as in the SEI formed on the surface of lithiated graphite. Before the Li^0 surface sees the electrolyte, the ambient atmosphere has already reacted with Li^0 and created a native passivation layer, which then reacts with the electrolyte instantaneously. Further electrochemical rearrangement results in a permanent SEI.

Of course, the actual process of interphase formation on lithium metal is even more complicated. Because of its extreme reactivity with almost anything that it comes in contact with, long before the first contact of lithium metal with any electrolyte there is already a thin layer of “passivation film” completely covering its surface. This passivation film results from the reaction of lithium metal with the ambient air in the reaction chamber and dryroom at the manufacturing site, and the major products of such reactions consist of lithium oxide (Li_2O), lithium hydroxide (LiOH), lithium carbonate (Li_2CO_3) and lithium nitride (Li_3N):



Since the thickness of such a passivation film is usually below the threshold level required to prevent electron shuttling (<1 nm), it does not yet qualify to be called an interphase. However, this passivation film has a direct impact on the chemical composition of the eventual interphase, because all these compounds are alkaline in nature, and would react with the electrolytes that are usually acidic in nature due to the lithium salts used. We leave the discussion on the interphasial chemistries to a later section.

This instantaneous and indiscriminating manner applies to any electrode provided that its eigenpotential is situated beyond the thermodynamic stability limits of the electrolyte enclosed by the LUMO and HOMO, regardless of which side the electrode is on. For example, if there is a cathode material whose electron energy level is located below the HOMO of the electrolyte, the interphase formed on this cathode in this electrolyte would also occur in an instantaneous and indiscriminating manner, except that the decomposition reactions would be oxidative instead of reductive in nature. Cathodes with $\overline{\mu_c}$ below the electrolyte HOMO in their pristine states are very rare; examples include certain conversion reaction-type metal fluorides (FeF_3 or CuF_2), or those intercalation-type

transition metal oxides that are de-lithiated before being assembled into cells, such as CoO_2 or NiMnO_2 . Such de-lithiated (and hence fully charged) cathode materials are extremely unstable and difficult to handle, therefore they are seldomly used except for special experimental purposes. The actual cathode materials used in lithium-ion batteries are in their lithiated (and hence fully discharged) state, and the interphases formed on their surfaces follow the second manner.

The second manner is characterized by the nature of being “*step-wise and discriminating*”. Interphases formed on a graphitic anode surface represent a typical example in this category. Also falling into this category are other anode materials such as alloy hosts and conversion reaction-type hosts including silicon, tin and phosphorus, and also most of the cathode materials that are in lithiated states such as LiCoO_2 , $\text{LiNi}_x\text{Mn}_x\text{Ni}_z\text{O}_2$, etc.

Taking graphite as an example, before its graphitic structure is fully loaded with Li^+ and becomes LiC_6 , the eigenpotential of graphite (*i.e.* carbon) sits at ~ 3.0 V *vs.* Li^0 , or nearly 0 V *vs.* SHE, which is located within the thermodynamic stability limits of the electrolyte as marked by its LUMO and HOMO (Figure 16.2). Therefore, when a graphitic anode first comes into contact with an electrolyte, no major reactions should occur. However, during the very first charge of the lithium-ion battery after electrolyte injection, when the cell voltage gradually rises, the potential of the graphite correspondingly decreases and eventually crosses the LUMO of the electrolyte. Only at that time would reductive decomposition of the electrolyte start, generating the first chemical ingredients that subsequently constitute the interphase.

As mentioned above, the electrolyte LUMO shown in Figure 16.2 actually represents a hybridized orbital when we treat the electrolyte as an imaginary single component. The real electrolyte, however, consists of multiple components (salt anion, mixture of solvent molecules, etc.), hence during the gradual decrease in graphite potential, the component that possesses the lowest LUMO would have a greater opportunity to be preferentially reduced, the products of which consequently have a greater opportunity to form an effective interphase, if these decomposition products meet the criteria of forming an interphase as discussed in Section 8.3.

On the other hand, the component that possesses a higher LUMOs might never have the opportunity to be reduced, because the component that possesses a lower LUMO may already form a protective interphase that effectively insulates electron transfer between the electrode and the electrolyte, hence preventing any decomposition of other electrolyte component.

Eventually, the interphases formed in the second manner might consist of products that are contributed to by certain preferred electrolyte components, the chemical signature of which in the interphase far outweighs their footprint in the bulk electrolyte. In this sense, the reduction of electrolyte components by the electrode is *discriminating*.

Furthermore, the potential of the electrodes in lithium-ion batteries shifts progressively during charge, starting from a value within the thermodynamically stable region of the electrolyte, then crosses the electron energy levels marked by the LUMO or HOMO, and eventually reaches the fully charged potentials of various electrode materials. During this process the chemical composition of the interphasial components must also have experienced a progressive transformation, because most likely the initial products are only partially reduced or oxidized, and would be further reduced or oxidized when the electrodes are brought to more extreme potentials. In this sense, the formation of the interphases could be *stepwise*, because the chemical compositions of the eventual interphases are not generated in a single step.

16.5.1 Proto-interphase and Interphase in an “Anode-free” Lithium-metal Cell

An interesting scenario between the above two manners arises from the so-called “*anode-free*” cell configuration that has become increasingly popular in lithium-metal battery research. In this cell design, no active anode material (Li^0) is used on the anode side when the cell is assembled, while the “anode” therein is just a bare electrode substrate (Cu foil). The cell is charged to high voltages corresponding to the potential of the cathode, and during the process the pre-stored Li^+ in the cathode lattice is de-lithiated therefrom, migrates across the electrolyte and eventually is deposited on the Cu foil. In this way, we minimize the amount of lithium metal in the cell to just the exact amount needed for cell operation. The primary benefit of an anode-free cell is of course the energy density, as no excess amount of lithium metal exists as an “inert mass”, and the minimized presence of lithium metal also improves cell safety. Needless to say, such a cell configuration requires excellent reversibility, because any loss of lithium metal due to parasitic and irreversible reactions would be immediately reflected in the fading of the cell capacity. So far, such cells are just used as a sensitive test vehicle to detect Li^0 /electrolyte reactivity.

The interphase formed in anode-free cells would share commonality with both manners of interphase formation discussed above.

Upon cell assembly, the eigenpotential of the anode substrate Cu foil sits in the region between the LUMO and HOMO of the electrolyte. In fact, similarly to that of pristine graphite, it is closer to the HOMO than the LUMO (~3.0 V vs. Li), therefore there is no instantaneous and indiscriminating interphase formation when the electrolyte is injected into the anode-free cell. As the cell is charged for the very first time, the potential of the anode substrate gradually approaches and then crosses the LUMO of the electrolyte, accompanied by gradual and stepwise electrolyte decomposition and subsequent formation of a *proto-interphase*, which could be discriminating towards electrolyte components. Note that, by now Li^+ is still not reduced, because the potential of the anode has not reached the threshold for Li^0 deposition. It is generally believed that such a proto-interphase is not a fully formed interphase, being porous and hence permeable to the bulk electrolyte, and unable to insulate electron tunneling effectively.

However, when the anode potential is further polarized cathodically (*i.e.* approaching and surpassing that of Li^0), the emergence of the nascent Li^0 depositions underneath or beside the proto-interphase would induce a new round of reductive decomposition of the electrolyte, which should occur instantaneously and indiscriminately, similarly to the first manner. This second round of reactions would generate interphasial ingredients more similar to the interphases usually found on a lithium-metal surface formed through the first manner. Meanwhile, the already formed proto-interphases also continue to experience stepwise reduction, eventually turning into a permanent interphase more similar to those formed on a graphitic anode in lithium-ion batteries.

In other words, the interphases formed in lithium-metal batteries in an anode-free configuration should consist of a hybrid chemistry that is contributed to by two different manners of formation.

16.5.2 Rationale Behind Electrolyte Additives

After researchers realized the importance of interphases in the reversibility of rechargeable battery chemistries, it has always been their target to tailor design a more desirable interphase than those formed naturally by the electrode–electrolyte interaction in a cell. The stepwise formation manners of interphases provide such an opportunity, as one can select, or even design and synthesize, certain molecular or ionic structures, the LUMO and HOMO of which ensure their preferential reduction or oxidation before the other components in the electrolytes, hence the eventual interphasial chemistry would be mainly

contributed from such molecular or ionic compounds. Since the only purpose of these compounds is interfacial, *i.e.* to form an interphase, they are not expected to be responsible for other missions such as salt dissolution, ion solvation and ion transport, hence their footprint in the electrolytes could be minimized, sometimes as low as ppm levels. This constitutes the foundation of electrolyte additive practice, which has been extensively adopted by the lithium-ion battery industry.

Initially this concept was proposed by Peled *et al.*, who deliberately selected unstable ingredients in electrolytes such that the SEI formed mainly carries the products from such ingredients.¹⁰ As their initial selection tool, they leveraged the vast databank of rate constants (k_e) for reductions in aqueous electrolytes to screen large numbers of candidates, and focused on those with $k_e > 10^9 \text{ M}^{-1} \text{ s}^{-1}$ as such potential SEI contributors. EC, vinylene carbonate (VC), SO₂ and CO₂ were found to meet such criteria. Later studies confirmed that EC and VC are indeed effective electrolyte additives and they have found extensive applications in the lithium-ion battery industry, and CO₂ is also occasionally used for the formation of special interphases, although its gaseous nature makes it more difficult to be popular.

The approach proposed by Peled *et al.* actually formed the theoretical basis for the later development of electrolyte additives, although nowadays a more powerful screening tool than k_e has been found, namely the energy levels of the LUMO or HOMO, thanks to the increasing popularity of computational chemistry and supercomputing facilities. Almost all developers of electrolytes and additive materials would start their search and design by calculating the LUMO and HOMO energy levels for their target molecules as an important reference.

However, whereas it is relatively easy to manipulate the energy levels of the LUMO or HOMO by designing and synthesizing special structures, it is almost impossible to predict whether the decomposition products generated by such designed additives could meet the criteria for being a good interphase. The study of electrolyte additives is therefore still built on a semiempirical foundation.

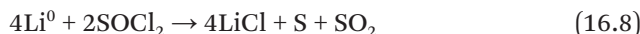
We will discuss the effects of additives on the chemistry and formation mechanism of interphases separately in later sections.

Finally, regardless of whether the formation process is instantaneous or stepwise, the resultant interphase would dictate the performance of the electrochemical devices such as the rechargeability and the kinetics of the cell chemistry during their whole lifetime. Extensive studies have shown that the physicochemical nature of the interphase depends on its chemistry in addition to morphology and structure.

16.6 Chemistry of Interphases

An interphase is created by the extreme potentials of electrodes and the instability of the electrolyte under such extreme potentials. Therefore, the chemical composition and the formation process of interphases involve both electrodes and electrolyte components.

The simplest example is the lithium-metal primary battery based on thionyl chloride (SOCl_2) electrolyte, in which the primary chemical composition of the interphase on lithium metal is lithium chloride (LiCl), which obviously comes from the contribution of both the electrode Li^0 and the electrolyte, although the source of the chloride remains unclear because both salt LiAlCl_4 and solvent SOCl_2 (which also serves as the cathode material in this case) could participate *via* reactions such as



The formation process of this LiCl -based interphase should occur instantaneously at the moment when the electrolyte is injected. On the other hand, in rechargeable lithium-metal or lithium-ion batteries, ester- or ether-based solvents are often preferred because they can withstand higher oxidation potentials, and the chemical ingredients in the corresponding interphases are often found to have origins from the solvents, such as Li_2CO_3 , Li_2O and partial reduction product alkyl carbonate, because these solvents, especially the esters, tend to have higher LUMOs and will be preferentially reduced by the electrodes (Li^0 or LiC_6).

As mentioned earlier, despite the universal existence of interphases in all batteries that operate beyond 3.0 V, serious investigations on interphase chemistry and formation mechanism did not start until the commercial success of lithium-ion batteries in the early 1990s. For this reason, the majority of modern knowledge about this new battery component was accumulated on the specific chemistry of lithium-ion batteries. Only in recent decades (since the 2010s) did interphase studies expand to other emerging battery chemistries. Meanwhile, thanks to the application of the new *in situ/operando* characterization techniques with unprecedented temporal and spatial resolutions, we are

learning a lot more about these interphases than we ever knew before. The constant emergence of new techniques and new materials has made understanding interphases a highly dynamic field. It is very possible that, by the time this book is published, some of the knowledge summarized here might already need modification or correction.

16.6.1 In Lithium-ion Batteries

Although the initial concept of interphases proposed by Peled and co-workers was confined just to the unique surface chemistry of lithium-metal or other alkaline/alkaline earth metal electrodes in non-aqueous electrolytes, in-depth investigations and the extensive popularity of the term “SEI” were driven by the commercial success of lithium-ion batteries, with most knowledge accumulated about the interphasial ingredients formed by the reactions between carbonate-based electrolytes and the graphitic anode. In comparison, the understanding of interphase formation on the cathode surface started much later, accompanied by occasional debate about whether such an interphase exists on the cathode side at all. It is well established nowadays that the presence of either an anode interphase or cathode interphase depends closely on the potentials where the corresponding electrodes operate: whereas the presence of SEIs on lithium metal and lithiated graphite is beyond any doubt, an anode with a moderate potential such as $\text{Li}_4\text{Ti}_5\text{O}_{12}$ could operate without the necessity of forming an SEI. Likewise, while the presence of a CEI on LiFePO_4 is unnecessary (because its potential of 3.5 V resides within the thermodynamic stability limits of the electrolyte), and the presence of a CEI on the LiCoO_2 surface could raise doubts (because its potential of 3.7 V is in the proximity of the electrolyte HOMO), the CEI must be present in high-voltage cathode materials such as high-nickel NMC (~4.2 V), LiCoPO_4 (~5.1 V) and $\text{LiNi}_{0.5}\text{Mn}_{1.5}\text{O}_4$ (~4.6 V).

16.6.1.1 On the Anode: SEI

Interestingly, the awareness of the interphase presence in lithium-ion batteries was not triggered by the emergence of the first-generation product manufactured by Sony in 1990, because a non-graphitic carbonaceous anode (petroleum coke) was used in this earliest version of the chemistry, and the effect of the interphase therein was not pronounced enough to attract attention. Such a pronounced effect was only noticed when Fujimoto and colleagues at Sanyo, in a separate

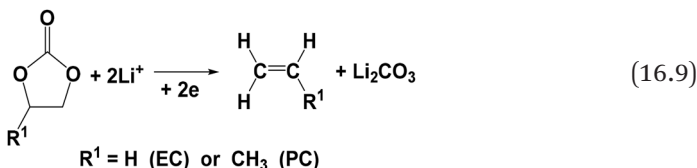
pursuit, discovered the “magic” chemistry between graphitic carbon and electrolytes based on EC solvent,⁸² followed by Dahn and colleagues, who attributed this “magic” combination to the unique interphasial chemistry required by graphite to support the reversible Li⁺ intercalation.⁸³ It was also Dahn who transplanted the term “SEI” from lithium metal to a graphitic surface. In the absence of detailed chemical analysis of this interphase *via* surface analysis at the time, Dahn and co-workers assumed that the basic chemical composition of such an SEI should be Li₂CO₃-based (which was apparently influenced by early work of Dey and co-workers), although they suspected that it may not just be as simple as Li₂CO₃. Their instinct was correct. In fact, the composition of the SEI on a graphitic surface proved to be far more complicated than a single chemical ingredient. Depending on the electrolyte composition and also the formation conditions such as temperature, pressure and electrochemical protocol, the interphase chemistry and morphology could vary widely.

16.6.1.1 Semicarbonates and Their Evolution

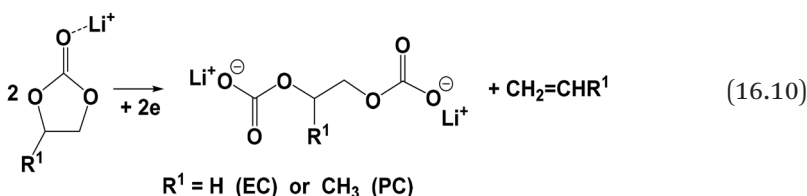
In Section 10.4.1.1 [eqn (10.12)], we briefly discussed that on an Si⁰ surface the carbonate esters could experience a single-electron reduction, which is incomplete and produces alkyl carbonate (or semicarbonate), or a two-electron reduction, which is complete and produces carbonate (Li₂CO₃). In fact, the identification of semicarbonate is by no means specific to the Si⁰ surface alone, but instead it is a universal chemical species that has been found in most electrochemical reductions on anode surfaces. Even when the electrodes are not active battery anodes or cathodes such as graphite, lithium metal or Si⁰, but just inert current substrates (Cu, Ni, or Pt) that are simply polarized to extreme potentials, semicarbonates are always present, provided that the electrolyte solvents are carbonate esters such as EC, DMC or other cyclic or acyclic carbonate esters.^{11–15}

Since carbonate esters serve as universal electrolyte solvents in lithium-ion batteries, their reduction products, semicarbonates, are considered the major chemical ingredients in interphases on the anode surface. There is a well-established consensus in the field that semicarbonates (also known as *alkyl carbonates* in some literature) support the major functions of the SEI by allowing Li⁺ transport while insulating electrons.

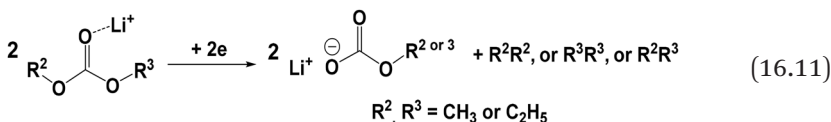
Based on surface spectra analysis, Aurbach and Gofer first proposed¹⁶ that the reduction of carbonate solvents on a graphitic surface does not directly produce Li₂CO₃, which requires a *two-electron pathway* to occur, as suggested by Dey and Sullivan:¹⁷



Instead, an incomplete reduction *via* a *single-electron pathway* occurs as a more likely reaction, producing semicarbonate:



For linear (acyclic) carbonates such as DMC, EMC or DEC, an equivalent single-electron pathway is represented by



Here “*semi*” refers to the fact that the carbonate substructure is half ionic with Li^+ as counterion and half molecular with an alkyl group, making it an ester. Comparing eqn (16.9) against eqn (16.10) and (16.11), one can immediately tell the difference between these two pathways: in the former, an inorganic interphasial ingredient would be produced (Li_2CO_3) because all the organic moieties would be lost in the form of gas (alkenes from the cyclic carbonates EC and PC, or alkanes from the acyclic carbonates DMC, EMC and DEC); in the latter, only half of the organic moieties would be lost as gaseous products, and the other half would be retained as part of the interphase. Numerous experimental evidence generated by X-ray photoelectron, Fourier transform infrared, Raman and NMR spectroscopy and chemical analysis of the released gas, along with a number of newly developed advanced characterization techniques such as electrochemical quartz crystal microbalance (EQCM) measurements and liquid secondary ion mass spectrometry (liq-SIMS), supported the existence of semicarbonates, thus confirming the validity of the single-electron pathways.

Two important details regarding eqn (16.10) and (16.11) should be emphasized here.

First, the definitions of “two-electron” and “single-electron” refer to the number of electrons received by each carbonate ester. The reactions described in each of these equations involve two carbonate esters, hence two electrons in total are consumed to make them “single-electron reductions”.

More importantly, in both eqn (16.10) and (16.11), a Li^+ is always situated close to the carbonyl group of the carbonate esters. This is not written so just to balance the charge of the equations, but more importantly it reflects the fact that the reduced esters are those residing within the solvation sheath of the Li^+ , as shown previously in Figure 10.11a. In fact, calculations have shown that it is rather difficult for a pure solvent molecule to be either reductively or oxidatively decomposed in the absence of any salt. Only after coordinating with Li^+ does its reactivity increase to the level for an electrochemical decomposition to occur. This solvation effect on reactivity is believed to be caused by the polarization of the solvent molecule by the Coulombic field of the Li^+ , which significantly weakens the covalent bonding within the molecule. By this logic, among the solvent molecules in an electrolyte, those residing in the cation solvation sheath would enjoy a preference to be reduced, whereas those beyond the influence of the cationic Coulombic field should remain relatively inert towards electrochemical reduction (Figure 16.4).

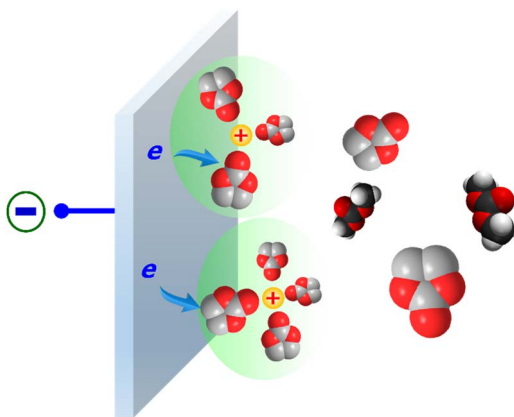
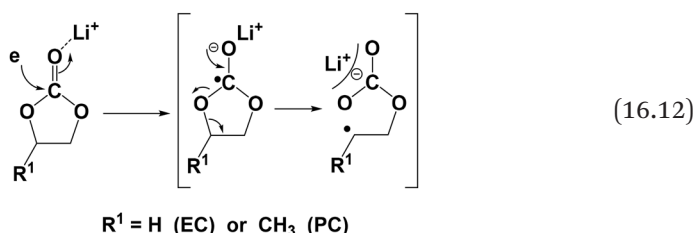


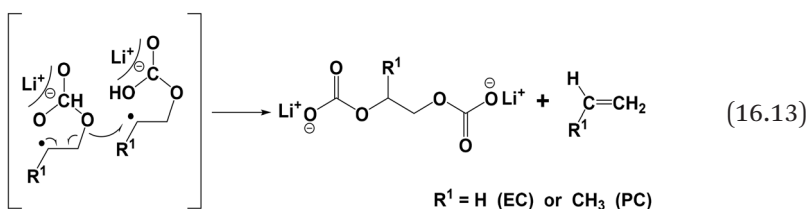
Figure 16.4 At the anode/electrolyte interface of an electrochemical device, the solvent molecules within the primary solvation sheath of Li^+ (or other cations) have a higher preference of being reduced than those not coordinating with Li^+ (or other cations). EC is used as the example solvent here because of its universal use in lithium-ion batteries, and solvated Li^+ and partially desolvated Li^+ are used as examples.

In other words, those solvent molecules within the solvation sheath of Li^+ could have a greater opportunity to participate in interphasial chemistry than those outside due to the activation by the central ion they solvate. This argument actually constitutes the basis for the interphase formation mechanism,^{18,19} and we will return to this topic with a more detailed discussion in the next section.

From the perspective of organic chemistry, the single-electron reduction of a carbonate ester to produce a relatively complicated structure such as semicarbonate could have gone through a series of intermediates or transition states. The most likely route should be direct nucleophilic attack on the most electron-deficient site in the carbonate ester, *i.e.* the carbon in the carbonyl group, by an electron from the electrode, producing an anion radical, which then experiences an intramolecular rearrangement accompanied by a cleavage at one of the *ethereal* C–O sites:



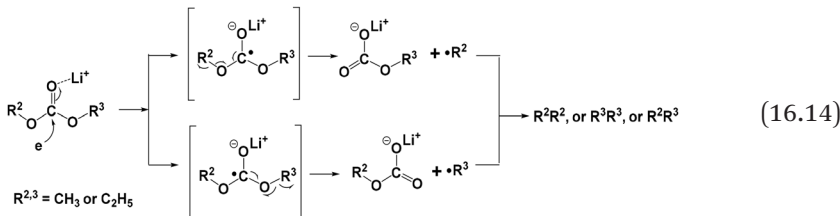
This anion radical should have a sufficiently long lifetime thanks to the stabilization by the positive charge of Li^+ that coordinates with the carbonyl oxygen, and it may have an opportunity to conduct an intermolecular rearrangement with another identical anion radical, producing the semicarbonate while losing 50% of the organic moiety in the form of gaseous alkenes (ethylene if the solvent molecule is EC or propylene if the solvent molecule is PC):



The two semicarbonates produced by the single-electron reductions of EC and PC are *lithium ethylene dicarbonate* (LEDC) and *lithium*

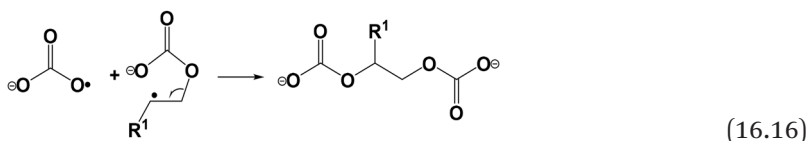
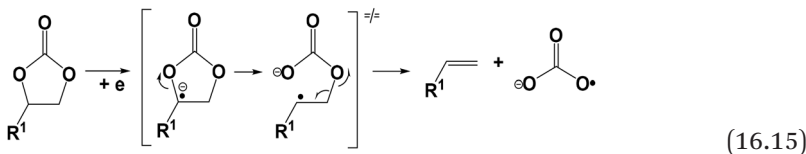
propylene dicarbonate (LPDC), respectively. Because EC is used almost universally in all lithium-ion batteries, and also because EC is especially favored in the solvation sheath of Li^+ (Section 12.2.3) in various electrolyte formulations based on mixed carbonate solvents except PC, LEDC has been identified as a major product in the interphases on a graphitic anode.

For linear carbonates, a similar reaction pathway can be presented:



where the released gaseous products are alkanes (ethane, propane or butanes depending on whether DMC, EMC or DEC is used alone or in a mixture), while the corresponding semicarbonates are *lithium methyl carbonate* (LMC) and *lithium ethyl carbonate* (LEC), respectively. Compared with LEDC, both LMC and LEC constitute only a minor portion, apparently due to the solvation sheath structure of Li^+ , which prefers cyclic carbonates over acyclic carbonates.

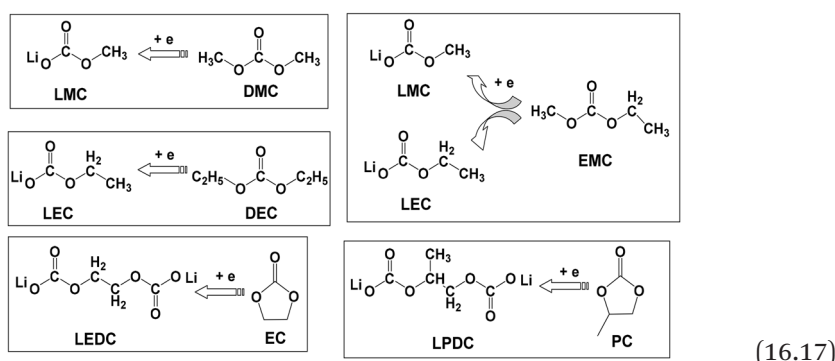
An alternative mechanism leading to semicarbonates, especially for cyclic carbonate molecules, was proposed by Shkrob *et al.* based on their efforts to detect radicals under cryogenic conditions (77 K) using electron paramagnetic resonance spectroscopy:²⁰



Note that this pathway would generate the same gaseous and solid products as the pathway suggested in eqn (16.13), the only difference being a carbonate radical anion $\text{CO}_3^{\cdot-}$.

Given their importance, numerous efforts have been made to confirm the presence of semicarbonates in interphases collected from cycled lithium-ion batteries. For example, radical anions have been detected using electron spin resonance, which determine that such radical anions are very stable and long lived, thus allowing the two molecular reactions as depicted in eqn (16.13) and (16.14); direct analysis on the gaseous products confirmed that alkenes and alkanes are the main products during the initial cycling of cells, where most of the interphase formation occurs. Quantitative analysis performed further on the interphase formation reveals indeed that the charges consumed are much greater than the amount of gaseous products detected, thus supporting the prediction of eqn (16.10) and (16.11) that only half of the organic moieties are retained in the products that constitute the interphase, instead of being completely lost in the form of gas.

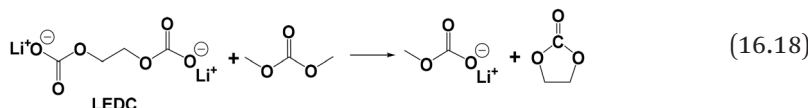
Spectroscopic analysis on electrode surfaces recovered from cycled cells also identifies various signature features of semicarbonates. Two research groups, led by Xu and Dedryvère, respectively, approached the issue in the most fundamental and systematic manner, by laboriously synthesizing the standard semicarbonates that are believed to be single-electron reduction products from all possible carbonate solvent molecules commonly used in lithium-ion battery industry [eqn (16.17)].^{12,21}



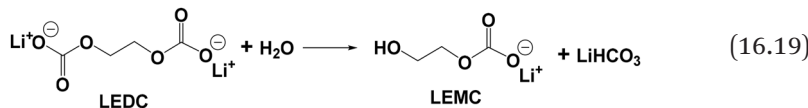
Using these standard compounds in high purity as references, a precise spectroscopic database was thus established for the accurate identification of these species in actual interphases, and enabled the investigation of their bulk properties such as conductivity, electrochemical and thermal stability and chemical reactivity towards the ambient environment and moisture, to be discussed later.

An interesting fact is that unsaturated alkenes are produced from cyclic carbonate esters [eqn (16.13)] whereas saturated alkanes are produced from acyclic carbonate esters [eqn (16.14)], which was verified by various characterizations that analyzed the gaseous products released during the interphase formation stages. This difference actually reflects the basic structural nature of these two classes of carbonates: an implicit degree of unsaturation contained in the ring of EC or PC is eventually expressed in the structures of the decomposition products when they chemically break down.

While semicarbonates, especially LEDC, have been considered as the overwhelming products in interphases on graphitic carbon, a more recent study found that its existence in a battery environment is highly dynamic, and it could further react with fellow solvent molecules and be converted to different structures, for example



In particular, a half-hydrolysis product of LEDC, *lithium ethylene monocarbonate* (LEMC), was identified as the major interphase ingredient after a lithium-ion battery experienced long-term cycling.²² The formation mechanism of this species remains unclear, as there seems to be no direct electrochemical pathway leading to it. Hence it was suggested that the trace moisture in the battery environment, either from residual water in the pristine electrolyte or from the oxidation of electrolyte solvents at the cathode side, is responsible for the formation of LEMC, which induces limited hydrolysis:

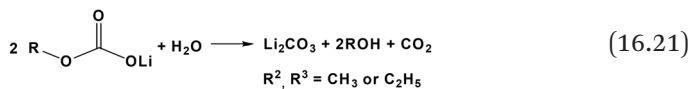
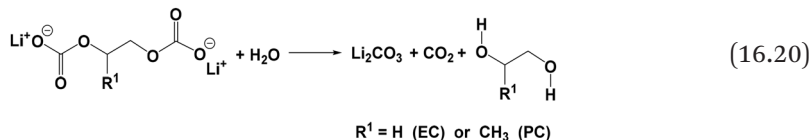


Whether LEMC becomes a universally prevalent interphasial species in all lithium-ion batteries remains to be explored.

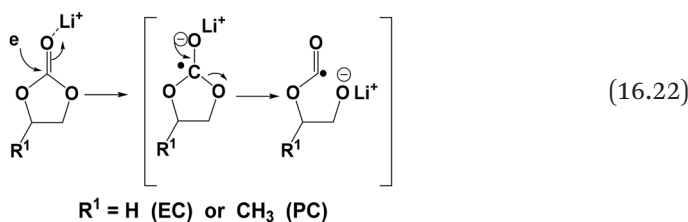
16.6.1.1.2 Other SEI Ingredients

Meanwhile, other chemical ingredients have also been identified, including Li_2CO_3 that could be generated from a direct electrochemical

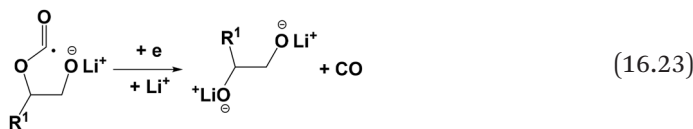
reduction *via* a two-electron pathway [eqn (16.9)] or simply from the complete hydrolysis of the corresponding semicarbonates:



On the other hand, the intermediate shown in eqn (16.12) could also experience cleavage at an alternative site, *i.e.* the *acyl* C–O, instead of cleaving at the ethereal C–O site and leading to semicarbonate as shown in eqn (16.13) and (16.14). This acyl cleavage process was confirmed by Onuki *et al.* using ^{13}C -labeled EC and DEC:²³

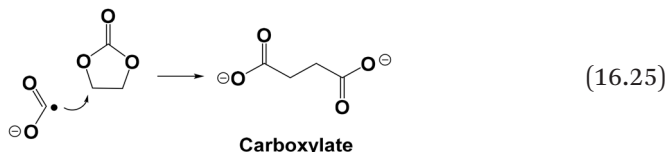
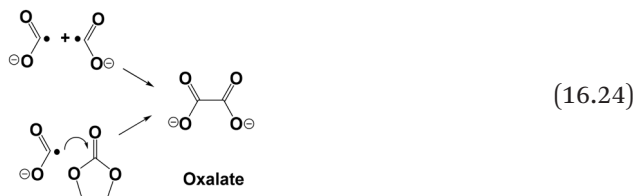


Such an intermediate is further reduced by accepting one electron, and rearranged into *alkoxides* while releasing CO as the gaseous product:

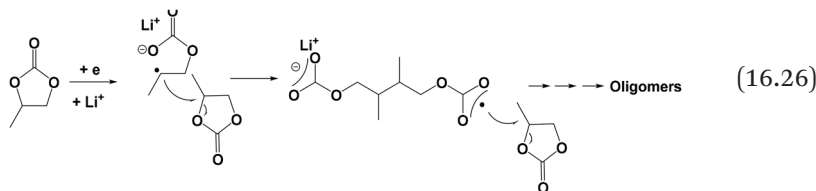


Acyl cleavage can also explain the identification of other minority species often detected in the interphases, such as oxalates and carboxylates, which involve the formation of new C–C bonds, hence the

recombination of carbonyl radicals must have occurred, although the exact pathway needs more investigation:

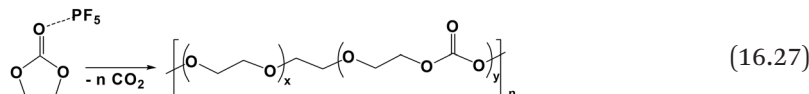


In addition to salts, polymeric or oligomeric species, apparently from reduction of solvent molecules, constitute another class of interphasial ingredients. Because the most frequently used spectroscopic tools (FTIR spectroscopy, XPS, *etc.*) are not especially sensitive enough to characterize these macromolecular structures, our understanding about them was limited to possible oligoether compounds resulting from ring-opening polymerization of cyclic carbonates. Indirect inference based on thermogravimetric analysis combined with mass spectrometry (TG-MS) of graphite anodes also seemed to suggest polymeric moieties. The most explicit identification of polymeric SEI components was provided by a mass spectrometric technique that was tailored to detect macromolecules, namely matrix-assisted laser desorption/ionization mass spectrometry (MALDI-MS).²⁴ It was found that when an inert electrode (Au or Sn) was cycled down to 0.1 V *vs.* Li in a PC- or EC-DMC-based electrolyte, interphasial species are formed, with distinct peaks corresponding to long-chain oligomers with an *m/z* ratio as high as a few thousand, the repeating units of which vary with both solvent composition and electrode materials. Although it is still difficult to identify exactly what these oligomers are, using DFT calculations researchers speculated a mechanism that involved radical initiation/propagation and formation of new C–C bonds, which is the only way to explain how the chain can grow to such a great extent:



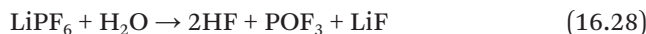
Note that in eqn (16.26) the radical has to attack the alkoxide carbon, which, when compared with the carbonyl carbon, is not necessarily the thermodynamically favored site for such a nucleophilic attack.

Polymeric species could also form with the assistance of the strong Lewis acids such as PF_5 , which could be generated by the salt anion PF_6^- and catalyzes a ring-opening polymerization:



So far, the precise structure of these polymeric species remains unclear, and their presence in interphases could have been significantly underestimated, not only because they are very difficult to identify owing to the lack of appropriate characterization means for macromolecular species, but also because their polar molecular nature often makes them soluble in most solvents, hence they are often lost during the sample washing protocol when preparing for *ex situ* characterizations.

In addition to solvent molecules, the salt anions also participate in the formation chemistry of interphases. The most prevalent inorganic species in interphases is LiF , which apparently comes from the decomposition of the universally used fluorinated anion PF_6^- , but the exact pathway remains unclear, because both chemical and electrochemical reactions could produce LiF , for example²⁵



Studies showed that LiF may have been generated by hybridized and convoluted processes that involve both chemical and electrochemical pathways.

16.6.1.2 On the Cathode: CEI

Most knowledge about the interphases came from studies on SEIs at the anode side, whereas CEI attracted relatively lukewarm interest until recently.²⁵ This bias mainly stems from the following three factors:

1. Most important of all, the potential of the lithiated graphitic anode (and also the lithium-metal electrode) clearly sits far beyond the LUMO of the electrolytes, whereas the potentials of most cathode materials (LiCoO_2 or LiFePO_4) are often located in the vicinity of the electrolyte HOMO (Figure 16.2). As consequence, the presence of an SEI on the anode surface is too pronounced to be ignored, whereas there is less pressing necessity associated with a CEI, and its presence on the cathode surface is often elusive. There have even been certain debates over whether a CEI exists or not. This elusiveness vanishes only when a cathode with an aggressive working potential, such as high-nickel NMC or LiCoPO_4 , is involved.
2. The graphitic anode is especially sensitive to the presence, or absence, of an SEI, because the fragile graphitic structure is held together only by weak van der Waals forces and hence is susceptible to solvent co-intercalation/decomposition, which often leads to structural disintegration (exfoliation); In contrast, the robust cathode structures are held together by Coulombic or covalent bonds and hence are largely insensitive to solvent co-intercalations. The presence of a CEI could only be felt when it becomes too resistive during the long-term cycling.
3. The surface of a graphitic anode, which is mainly sp^2 -hybridized carbon atoms connected into multiple graphene sheets, is comparatively “cleaner”, and the chemical composition relatively “simpler”, if one disregards the minor functionalities and impurities at the edge sites or defects. Therefore, any interphasial deposition during the cell operation could be easily noticed by various microscopic means. On the other hand, the complicated chemical species on cathode surfaces often make it difficult to discern unambiguously whether the interphasial depositions come from electrochemical oxidation of electrolytes, or partially

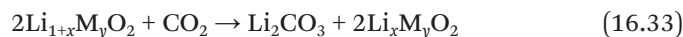
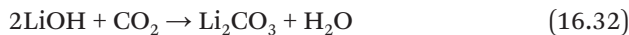
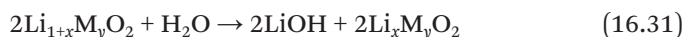
degraded cathode chemistry itself, or simply from the native passivation film that is already on the pristine cathode surface that often consists of Li_2CO_3 , LiOH or Li_2O . Further complications were introduced by the spontaneous reactions of these native film ingredients with acidic electrolyte components (LiF , $\text{LiP}_x\text{O}_y\text{F}_z$, etc.). The convoluted irreversible electrochemical reactions and cathode surface phase transformation occur simultaneously during the initial charging and render the eventual interphase complicated and random in both chemical composition and morphology.

The above characteristics make a CEI often thinner and incomplete in coverage of the cathode surface, in sharp contrast with SEIs, which must completely shield the graphitic anode (and lithium-metal anode). Because of such differences, SEIs on a graphitic anode are usually more resistive than CEIs on a cathode. However, CEIs are often found to increase in magnitude at a faster pace than SEIs during long-term cycling, and eventually become the more resistant component in the cell at a certain point. Cycling with high-voltage cathodes or aging at elevated temperatures accelerates this process.

The formation of a CEI often proceeds *via* at least three stages: (1) the formation of a native passivation film on the cathode during electrode manufacturing/processing; (2) spontaneous chemical reactions of the native passivation film upon its exposure to electrolytes; and (3) electrochemical rearrangement of these chemical species formed in stages 1 and 2 during the initial charging.

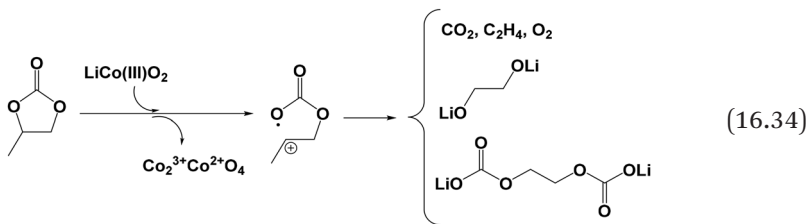
16.6.1.2.1 Native Passivation, Spontaneous Reaction and Preferred Adsorption

Most cathode materials, especially transition metal oxides ($\text{Li}_{1+x}\text{M}_y\text{O}_2$) used in lithium-ion batteries, are strongly alkaline in nature, hence during their manufacturing, processing, storage or transport the surface of these metal oxides react with CO_2 or moisture in the ambient atmosphere and generate various products:



These products cover the surface of the cathode particles as a thin layer of native passivation. Upon contact with electrolytes, which are acidic in nature thanks to the fluorinated anions used in most commercial electrolytes (PF_6^- or BF_4^-) and the prevalent moisture, spontaneous reactions occur, producing LiF and other fluorides such as PO_xF_y species. These reaction products replace the native passivation film with the new passivation film. Here “spontaneous” indicates that the reactions are chemical instead of electrochemical, and no charge transfer is required between the electrode and the electrolyte.

Spontaneous reactions not only occur between the native surface film and electrolytes, they also involve the intrinsic cathode composition. This process is accompanied by the generation of a series of gaseous products that include CO_2 , O_2 and alkanes or alkenes that correspond to the carbonate solvents used. Semicarbonates, Li_2CO_3 , LiF and alkoxides that are similar to the SEI ingredients have all been identified by various spectroscopic analysis methods, in addition to some products that are unique to the cathode chemistry such as Co_3O_4 (from LiCoO_2) or $\lambda\text{-MnO}_2$ (from Mn-based cathode materials such as $\text{Li}_2\text{Mn}_2\text{O}_4$ or $\text{LiNi}_{0.5}\text{Mn}_{1.5}\text{O}_4$). The presence of the latter strongly suggests that redox reactions occur even without the electrochemical charging of the cathode materials, probably *via* radical intermediates that were induced by the electron exchange between transition metal cores and solvent molecules. The speculated reaction mechanism is represented by



where the transition metal center near the cathode surface is reduced to a lower valence while the cyclic carbonate is oxidized to semicarbonate. Note that here the same semicarbonate is produced *via* an oxidative, instead of reductive, pathway. Likewise, alkoxides, alkenes and alkanes are also produced by the spontaneous oxidation. These spontaneous reactions produced the precursors for the permanent CEIs on the cathode surface.

Owing to the importance of spontaneous reactions between cathode materials and electrolyte in determining the final SEI chemistry, it is important to understand how the electrolyte components adsorb on

these diverse cathode material surfaces. Using sum frequency generation (SFG) vibrational spectroscopy, it was found that, in the absence of Li^+ , the polar PC molecules mainly adopted two opposite orientations on the surface of LiCoO_2 , with the carbonyl group pointing at the surface being the favored conformation. However, this preferred orientation would be rapidly disrupted as the result of the introduction of Li^+ in the solution, because Li^+ would assemble carbonate molecules around itself to form a solvation sheath with much stronger Coulombic attractions. On the other hand, when typical carbonate mixtures such as EC–DMC or EC–DEC were used, an obvious preferential adsorption of EC over its acyclic counterparts was detected (Figure 16.5), which was attributed to the higher dielectric constant of

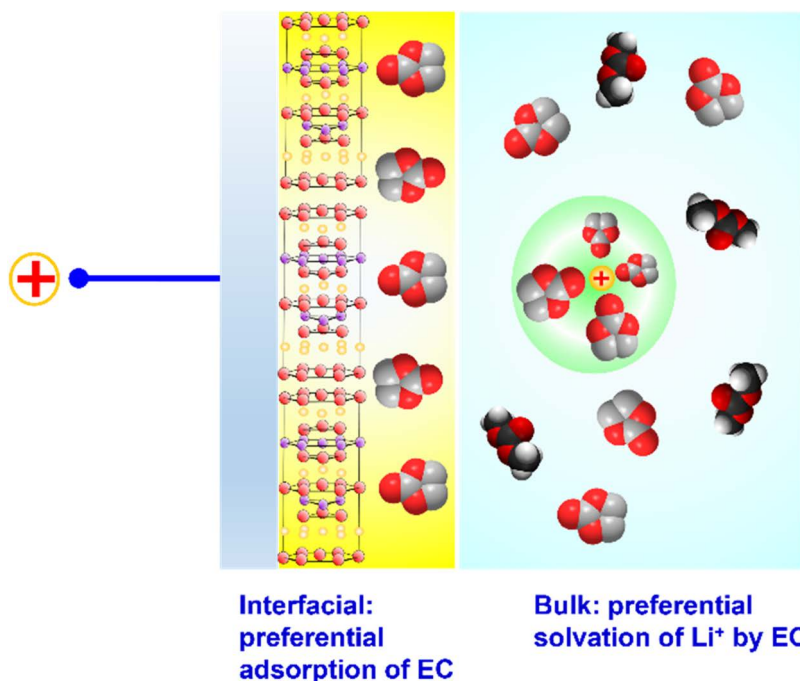


Figure 16.5 Adsorption of carbonate molecules on the surface of lithium cobalt oxide (LiCoO_2), a commonly used cathode material in lithium-ion batteries. The cyclic carbonate molecules such as PC or EC adopt two preferential orientations on the surface, with its carbonyl group pointing either towards or away from LiCoO_2 . If the electrolyte is based on mixed carbonates such as EC and DMC, as often used in lithium-ion batteries, EC molecules preferentially adsorb on the LiCoO_2 surface. The linear carbonate DMC is not preferentially adsorbed either on the electrode surface or in the Li^+ solvation sheath. The anion is omitted from the illustration for clarity.

Table 16.1 Preferential adsorption of EC on the LiCoO₂ surface.^a

Bulk composition	(1) EC in bulk/mol%	(2) EC at LiCoO ₂ surface/mol%
EC-DMC (1:1)	56	95 ± 1
EC-DEC (1:1)	65	92 ± 1
EC-DMC-DEC (1:1:1)	43	93 ± 1

^aSource: (1) ref. 27; (2) ref. 28.

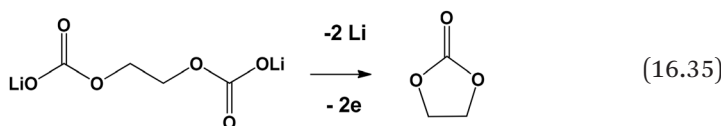
EC compared with the acyclic carbonates. The calculated percentages of EC at the LiCoO₂ surface and in the bulk electrolyte are compared in Table 16.1.^{26–28}

This astonishingly preferential accumulation of EC molecules at the cathode surface could have more profound repercussions on the resultant interphasial chemistry. Upon charging (*i.e.* removal of Li⁺ from LiCoO₂), it was expected that the EC in the vicinity of the cathode surface would capture Li⁺ released by the cathode into the electrolyte; meanwhile, owing to the rising potential of the cathode surface, these same EC molecules could also become the preferred “victims” of oxidation and become part of the cathode interphase.

It should also be noted that, compared with the “EC preference” in the anode interphase that is a direct consequence of preferential solvation (to be discussed in Section 16.7), this potential preference at the cathode surface would be caused by an entirely different reason.

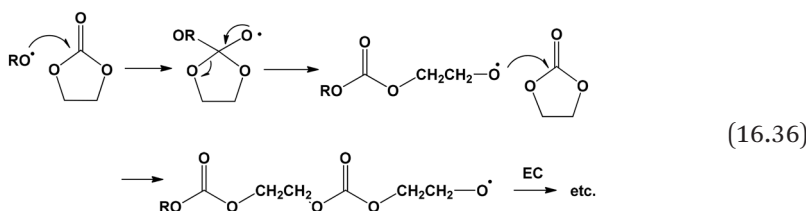
16.6.1.2.2 Electrochemical Rearrangement into Permanent CEI

The remnant native film and the aftermath of its reaction with the electrolyte would experience a new transformation stage during the initial electrochemical charging of the cathode, the exact mechanism of which remained unclear. We only know that the eventual CEI on LiCoO₂ surfaces inherited most chemical signatures from the spontaneous reaction products and electrochemical charging merely made the surface film more “uniform”. On an LiNiO₂ cathode, researchers observed using solid-state ⁷Li and ¹H NMR spectroscopy that changes did occur during the initial charging, and a CEI with a more organic content gradually replaced the original inorganic native film. On an LiMn₂O₄ surface, oxidative dissolution of the “left-over” passivation film occurred as a result of the electrochemical charging, which regenerated electrolyte solvents.²⁹



which implies that under certain conditions the interphasial ingredients are re-oxidizable. This applies not only on the cathode surface but also on the anode surface, provided that the potential reaches a threshold value and the interphasial ingredients are “electrically wired”, *i.e.* accessible to electrons provided by the electrodes. Considering the electron-insulating nature of the interphases, this does not happen easily but is not completely impossible. As we will discuss later, the re-oxidation of the SEI indeed occurs on the anode surface, especially during the initial formation stage, where the proto-SEI or nascent SEI is still electrically in contact with the electrodes.

Polymerization of cyclic carbonates initiated *via* oxidative processes was also possible, as polycarbonate-like species have been found in CEIs. A proposed oxidation mechanism suggested a pathway of oxidative ring-opening polymerization of cyclic carbonates:



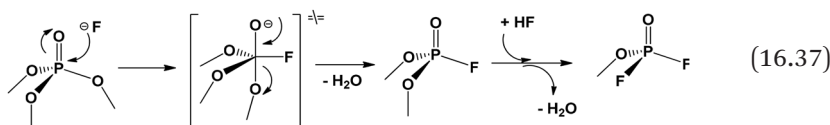
Based on an earlier study of the polymerization of EC, however, there was a suspicion about the chemical stability of polycarbonate due to the high density of carbonyls in the repeating units. Therefore more likely, the polymer would lose part of the carbonyls in the form of CO₂ and result in a copolymer consisting of carbonate and ethylene oxide units.

In addition to Li₂CO₃, semicarbonates and polymeric/oligomeric species, LiF is also an ingredient often found in CEIs. The appearance of LiF is usually attributed to the oxidation of PF₆⁻ by cathode active material, and it is produced only at high potentials (>4.9 V). ⁷Li and ¹⁹F solid-state NMR spectroscopy not only confirmed the formation of LiF on the LiCoO₂ surface during the electrochemical charge, but also revealed, by examining the effect of ⁷Li-⁷Li spin diffusion between LiF and LiCoO₂ on the spin-lattice relaxation time, that these LiF species aggregated as separate macroscopic domains not directly attached to LiCoO₂ particles. This clearly illustrated the inhomogeneous nature of interphase structures. How exactly these inorganics (LiF, Li₂CO₃) and organics (semicarbonates, oligomeric species) are distributed remains a topic of high importance that awaits revelation.

Needless to say, the above process, and also all the reactions described in eqn (16.31)–(16.36), occur at the expense of active cathode materials, leading to dissolution of transition metal and loss of Li⁺ storage sites or transformation of lattice structures that are often inevitably accompanied by degradation of electrochemical performance. However, such processes are usually confined to the surface region of the cathode, therefore its extent may not be as significant as the capacity loss caused by the formation of an SEI on anode side.

For high-voltage cathode materials that operate above 4.5 V, the presence of a CEI becomes more pronounced, the chemical building blocks of which are mainly contributed by sustained electrolyte oxidation, and include polymeric species such as poly(ethylene carbonate) that is generated at potentials above 4.5 V on the surface of LiNi_{0.5}Mn_{1.5}O₄ [eqn (16.36)], or copolymers consisting of ether-carbonate repeating units that correspond to polycarbonates partially losing carbonyls, as well as abundant salt species such as LiF or Li_xP_yO_z. A rather unique work worth mentioning here is a comparative study on both thin-film LiNi_{0.5}Mn_{1.5}O₄, which is in almost pure form, and the corresponding composite consisting of LiNi_{0.5}Mn_{1.5}O₄ in the presence of binders and carbon additives.⁸⁴ Only minimal decomposition of electrolyte components on the former was found, which raises the suspicion that these active cathode materials are intrinsically stable towards carbonate solvents themselves, and the real reason inducing CEI formation is not the potential but the active surface of the electrode that catalyzes the oxidative decomposition of electrolytes.

Compared with spinel LiNi_{0.5}Mn_{1.5}O₄, LiCoPO₄ presented a more severe challenge to electrolyte stability owing to its higher potential (4.8–5.1 V). It was speculated that the instability might involve the chemical composition of the cathode along with electrolyte oxidation, because olivine phosphate moieties in the de-lithiated state could be susceptible to nucleophilic attack from fluorides, which commonly exist in most commercial electrolytes containing LiPF₆ as salt:⁸⁵



The species formed, PO₂F₂⁻, is soluble in the electrolyte, and its leaving the cathode surface leads to a series of progressive damaging steps that include lithium depletion, lattice degradation of LiCoPO₄

and exfoliation of the carbon conductive layer. A number of efforts were made to stabilize electrolytes against these high-voltage cathode materials, among which the use of fluorinated solvents seems to be most effective. The detailed mechanism of how these phosphate or thiophene derivatives work remains to be understood, but from a practical perspective, the fluorination of interphases has now become a common approach to designing both SEIs and CEIs.

16.6.1.3 The Cross-talk Between Anode and Cathode

The interphasial processes that occur at the cathode and anode surfaces were once thought to be isolated from each other, but ever-increasing evidence reveals that certain forms of “conversation” exist between the cathode and anode, as interphasial species generated on one electrode often appear on the other with unexpected impacts. This is a natural consequence of the fact that, in an electrochemical cell, the electrolyte is the only component that interacts with all other cell components, including the active surfaces of the two electrodes.^{5,6}

The earliest cathode–anode dialog recognized was the dissolution of Mn(II) from LiMn_2O_4 and its subsequent deposition as Mn^0 on graphitic anodes or incorporation in the SEI as Mn(II). The appearance of Mn^0 or Mn(II) on the anode side was described as extremely detrimental to the SEI on the anode and subsequently the reversibility of anode intercalation chemistry. According to some researchers, the metallic Mn^0 is embedded in the middle of the interphase, and actually serves as an electrochemical mediator to tunnel electrons through the electronically insulating SEI, the result of which is the sustained reduction of electrolyte components. Other researchers considered, based on X-ray absorption near-edge structure (XANES) spectra, that the Mn species deposited on various anode surfaces remained predominantly in an oxidation state of +2, and the capacity fade caused by Mn(II) dissolution from the cathode lattice was actually the result of an ion-exchange process between Mn^{2+} in the bulk electrolyte solution and Li^+ embedded in the anode interphase. Whatever the form Mn adopts in an SEI, its presence at the wrong side of the cell has been confirmed to be the main reason for most of the capacity loss in lithium-ion batteries.

In a broader context, transition metal cores in almost all layer or spinel structures are susceptible to acid leaching by HF, which is a common impurity in LiPF_6 -containing electrolytes; therefore, the appearance of these metals (Mn, Ni and Co) due to anode–cathode cross-talk should have been held at least partially responsible for

performance degradations. However, only limited efforts have been devoted to its understanding so far.

In addition to transition metal species, other species generated from electrolyte oxidation or reduction could also diffuse or migrate across the cell and reach the other end. For example, when a high-voltage $\text{LiMn}_{1.6}\text{Ni}_{0.4}\text{O}_4$ cathode was coupled with an $\text{Li}_4\text{Ti}_5\text{O}_{12}$ anode, although its moderate redox potential of 1.5 V vs. Li makes it an “SEI-free” electrode, organic species are nevertheless found to accumulate on the $\text{Li}_4\text{Ti}_5\text{O}_{12}$ surface as an obvious result of irreversible oxidation processes occurring on the cathode. Obviously, some species that originated from the oxidative process at the cathode were soluble in the bulk electrolyte and migrated or diffused across the cell before being intercepted and perhaps reduced by the anode. Dahn and co-workers designed an innovative cell configuration of a “pseudo-full cell”, and successfully “interrupted” the cross-cell interaction, thus confirming the existence of the above cross-talk.⁸⁶

Anode–cathode dialog was also found in lithium-metal or anodeless lithium-metal cells, and some researchers believed that the fluorinated species discovered in the SEIs on the anode in fact initially originated at the cathode surface, especially in the case where the salt anion (such as PF_6^- or BF_4^-) is the only fluorine source in the electrolyte. For those negatively charged anions to be reduced at a negatively polarized electrode, these anions have to overcome the Coulombic repulsion from the electrode in order to approach the inner- or outer-Helmholtz layers. Calculations indicated that this process is possible only when the salt concentrations are sufficiently high, and the interfacial regions are effectively compressed. Indeed, for either symmetric cells consisting of Li^0/Li^0 or an anodeless cell consisting of Cu/Li^0 configurations, hardly any fluorinated species are found in the SEIs if the electrolyte is not concentrated (~1.0 M); however, abundant fluorinated species (LiF or partially decomposed anions) appear in SEIs on either Li^0 or Cu surfaces if the same dilute electrolytes are used in full cells consisting of Li^0/NMC or an anodeless cell consisting of Cu/NMC configurations. Apparently, the generation of these fluorinated species requires the presence of a cathode that operates at high potentials. A reasonable inference would be that these fluorinated species, or at least their precursors, have to be generated by a cathode at high potentials, which could be in the form of radicals or cation radicals. These fluorine-containing radical species then subsequently diffuse or migrate to the anode (Li^0 or Cu), where they become a part of the deposited SEI.

In addition to material exchange between the cathode and anode, these two electrodes also influence each other’s operation through a

more “immortal” manner. Dahn and co-workers used high-precision coulometry and revealed how the SEI growth on graphitic anodes induces charge imbalance in a full cell where the Li⁺ source is limited, which eventually led to overcharging of the cathode and subsequent irreversible processes at higher potential than prescribed for the cathode material.⁸⁷ They attributed the high impedance and irreversible consumption of both electrolyte and lithium source to such a gradual cell imbalance.

These discoveries convincingly highlighted the fact that the components within a battery are not isolated from each other; instead, they all are synchronized to work together like a timepiece. To resolve issues associated with one individual component, a holistic system approach is often needed in order to address these strongly interrelated processes.

16.6.1.4 How Do SEIs and CEIs Differ and Resemble Each Other?

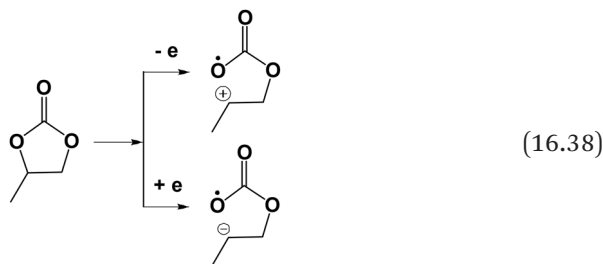
Both SEIs and CEIs are responsible for insulating electrolytes from electrodes electronically, but they are formed at very different potentials. Hence the formation mechanism for an SEI and a CEI must differ: SEI *via* a reductive decomposition process of electrolyte components, whereas CEI *via* an oxidative decomposition process that often involves both electrolyte components and cathode active materials.

However, based on an extensive survey of interphasial chemistries formed in various cell and electrochemical conditions, one would be surprised to find that these two interphases share more similarities than differences, except for a few special cases where unique electrolytes are used. In those exceptions, all ether electrolytes based on highly fluorinated ethers result in an SEI consisting mainly of Li₂O or Li₂O₂ and a CEI consisting mainly of LiF or other fluorinated species.

Such general similarities between SEIs and CEIs are reflected not only in the inorganic components such as carbonates, oxides and fluorides (*i.e.* Li₂CO₃, Li₂O or LiF in lithium-ion or lithium-metal cells), but also in the organic components such as semicarbonates and polymeric or oligomeric species consisting of ethylene oxide repeating units. The frequent identification of these chemical ingredients in both SEIs and CEIs implies at least two characteristics:

1. First, these compounds can be produced through either a reductive or an oxidative pathway. For example, in the formation processes of both semicarbonates and polymeric species, the abstraction of electrons from, and donation of electrons to, the

solvent molecules only serve as an initiating step, which produces either a cation radical or an anion radical, such as



which is then followed by subsequent ring-opening rearrangement or radical propagation and recombination reactions that generate products with very similar or identical structures.

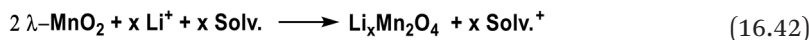
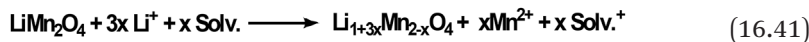
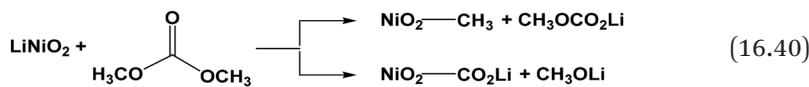
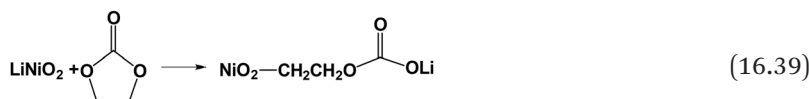
2. These ingredients have been the “common survivors” from the natural selections of both extremely reducing and extremely oxidizing environments. This is the underlying reason why they are found in both SEIs and CEIs, because they are more likely to be able to withstand the harsh environment of both the anode and cathode than most of the ingredients in the bulk electrolyte.

It is easier to understand why these inorganic species are reliable and persistent interphasial components, because they are excellent electronic insulators, and they are strongly resistant against either reduction or oxidation. The latter can be supported by the fact that it is essentially impossible to either reduce and deposit Li^0 or to oxidize and generate gases (O_2 , CO_2 and F_2) from those salts, under normal conditions, *i.e.* in the vicinity of room temperature, pressure and potentials, or in the bulk sizes. In fact, as mentioned in Section 10.4.2, oxidation of oxides or fluorides to gases requires extreme potentials that no known electrolyte solvent could support. The somehow puzzling issue here is that these inorganics are hardly ionic conductors either, and would fail to serve the function for an interphase that the working ion must be allowed to diffuse or migrate across. However, the nanoscale of the interphases, in addition to the nano-size of these inorganic species in either crystalline or amorphous states, alleviates the poor intrinsic ion conductivity of these ingredients and enables the interphases to find a balance between insulating electron tunneling and allowing ionic transport.

For organic species such as polymeric, oligomeric and semicarbonate species, an additional issue beside their ion conductivity would arise regarding their ability to withstand the extreme anodic potential, *i.e.* the oxidative potential of the cathode materials, as most of those organic structures are considered vulnerable against oxidation, which usually starts with electron transfer from the C–H bonds to the cathode, producing either protons (H^+) or cation radicals ($R^{\cdot+}$). Some of these organic species, semicarbonate being an example as we shall see in the next section, could even be re-oxidized at the anode side if the potential is moderately high and if the species remain electrically wired with the electrode, which is the case when the newly formed SEI components are still in their nascent forms and complete electron insulation has not been achieved.

In this sense, CEIs tend to be more inorganic than organic in nature.

One most prominent, but often neglected, characteristic of CEIs that differs distinctly from that of SEIs is the involvement of cathode active ingredients in interphasial chemistry, as implied in eqn (16.31), (16.33), (16.34) and (16.37). Similar processes have also been observed for other cathode chemistries, such as



Hence the interphasial depositions would consist of the mixtures of decomposition products from both electrolyte components and cathode active materials, with the former being oxidized products from solvents or anions, and the latter being reduced products from the transition metal oxides that often exist in the lattice structure or morphology different from the bulk cathode materials. However, traditionally, the parts of interphasial regions containing a transition

metal are often treated as surface degradation of cathode materials, instead of being considered as a sublayer of the CEI. A typical example is the high-nickel NMC cathode ($\text{LiNi}_x\text{Mn}_y\text{Co}_z\text{O}_2$), the surface structure of which is often detected to transform from layered to rock salt when de-lithiated (charged) at high voltage. In fact, this is the result of a process that involves both cathode structure and electrolyte components, and the emergence of the new surface structure should be part of the formed CEI.

In a broader context, this actually is related to how an interphase should be defined. Given that it is the result of the reaction between electrode and electrolyte, should only the ingredients contributed by the electrolyte be considered interphasial? Or should the entire region that differs distinctly from the bulk electrode and bulk electrolyte be considered interphasial?

Such complications do not exist on the anode side, mainly because of the illusion of “clean” surfaces of either lithiated graphite or lithium metal. In both cases the electrodes do contribute to the interphase formation, the former with both Li^+ and oxides or nitrides from the minor functionalities at the edge or defect sites of the graphite, and the latter with Li^+ and oxides, fluorides and other impurity species from the native passivation layers. However, it is often impossible to precisely distinguish the source of these contributions, and a simple definition of interphase was therefore adopted with the hidden assumption that these electrodes (lithiated graphite and lithium metal) are “clean” and do not contribute chemically to the eventual interphases.

16.6.2 In Lithium-metal Batteries

Several decades after circumventing lithium metal as a dangerous anode material of conversion reaction type and successfully developing lithium-ion batteries based on intercalation chemistry, researchers came back to look at lithium metal, and attempted to harness the energy density promised by its high capacity and low electrode potential. The attraction of the ultimate anode material remains tantalizing if its irreversibility and danger could be effectively suppressed, aided by our new knowledge and new techniques.³⁰

In Section 16.5, we discussed the two distinct ways in which interphases are formed. Owing to its extremely low eigenpotential, lithium metal induces instantaneous and indiscriminate interphase formation upon contact with electrolyte. Theoretically, any components in the electrolyte (solvent, salt anion or additive) would have almost

equal opportunity to be reduced by lithium metal and become part of the eventual SEI. In reality, however, even before electrolyte injection, a dense and all-covering passivation film already forms on the lithium-metal surface during its manufacturing, packaging and storage, and mainly consists of lithium oxide, lithium carbonate, lithium hydroxide or lithium nitride [eqn (16.3)–(16.6)]. Given the thickness of such a passivation film (~2 nm), it does not have sufficient capability to insulate electron tunneling, therefore by strict definition it is not yet an interphase, but its existence does make the surface of lithium strongly alkaline in nature. This fact, in combination with the fact that most state-of-the-art electrolytes are acidic in nature, predicts that the instantaneous interphase formed upon electrolyte injection would be the reaction products of those “acids” and “bases”, generating lithium fluoride, lithium phosphate, lithium fluorophosphate and the remnants of these native ingredients (oxides, carbonates, hydroxides and nitrides).

However, this instantaneous interphase would not endure, because during the cycling of lithium-metal cells, new surfaces of the lithium-metal anode would be produced due to the deposition of Li^0 , which further reacts with those oxides, carbonates, hydroxides and nitrides as well as the electrolyte solvents. The eventual chemical composition of the permanent interphase is thus rather complicated and extremely inhomogeneous in both chemistry and morphology. As discussed in Section 10.2.2 (Figures 10.2 and 10.3), such inhomogeneity is a major reason for the uneven Li^0 deposition and the subsequent growth of dendrites.

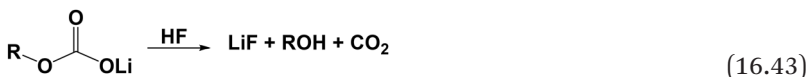
Just as is the case for lithium-ion batteries, there is a direct correlation between the interphasial chemistry and the electrolyte used. The earliest electrolytes used in primary lithium-metal batteries were thionyl chloride and sulfur trioxide, which are actually active cathode materials themselves. They form instantaneous interphases with Li^0 upon contact. Therefore, in these lithium-metal batteries, the real electrolytes are the interphases formed on the lithium-metal surface by these inorganic solvents, such as LiCl , Li_2SO_4 or $\text{Li}_2\text{S}_2\text{O}_4$. Restricted by the chemical nature of these liquid cathode materials, these interphases function only as a passive protective layer to prevent further reactions between Li^0 and these active materials, and are not required to support reversible cell chemistries.

For rechargeable lithium-metal batteries, organic non-aqueous electrolytes are needed to support the reversible Li^0 deposition and stripping. Unlike lithium-ion batteries, the electrolytes of which are confined to carbonate solvents, there are two distinct classes of

organic non-aqueous electrolytes that are often used in lithium-metal batteries: esters and ethers.

16.6.2.1 Esters

The earliest attempt to make lithium-metal anodes rechargeable switched from the inorganic and electrochemically active solvents such as thionyl chloride to more inert organic solvents such as PC, which would generate, in addition to the above-mentioned inorganic salts, semicarbonates (LPDC) according to eqn (16.13). When EC is used as part of the electrolyte, LEDC would be produced as the main interphasial component. Since those semicarbonates are rather sensitive to hydrolysis or acidolysis by trace moisture in both electrolytes and in the experimental analysis, the incompletely and completely hydrolyzed products, *i.e.* Li₂CO₃ and LiHCO₃, of semicarbonates were also found in the interphases. Of course, the semicarbonates are also susceptible to acidic impurities such as HF, and eventually generate LiF.¹²



Alkyl carbonates could also experience continuous electrochemical reduction by Li⁰ and turn into the complete two-electron reduction product, Li₂CO₃, which has been proven experimentally by comparing the nascent interphases formed. Based on this knowledge, Aurbach and co-workers proposed that the SEI might have a multilayer structure within which the simple inorganic species such as Li₂CO₃, Li₂O are more stable and closer to lithium, whereas semicarbonates are more likely to be distributed in the outer layers.⁸⁸ Later this multilayer structure was confirmed for various interphases formed in diverse electrolytes and electrode chemistries.

Like interphases on a graphitic anode surface in lithium-ion batteries, polymeric species are also identified on lithium-metal surfaces. These polymeric films, most likely polyether moieties, are found to be embedded with LiF crystals, leading to the competing SEI model of mosaic architecture. More recent studies revealed that the actual architecture of interphases on lithium metal is especially complicated, owing to the extreme potential of Li⁰ and the constantly emerging new Li⁰ surfaces during its deposition. The chemistry and morphology of interphases therefore depend strongly not only on the chemical

composition of the electrolyte but also on the electrochemical conditions under which they are formed. Diverse architectures, including mosaic, multilayer and monolithic, are possible. A single model is therefore insufficient to account for such complicated phenomena.

The physical and chemical properties of SEIs on lithium metal directly affect the reversibility and morphology of a lithium-metal anode. It is known that the roughness of the SEI depends heavily on the chemical nature of the electrolyte. For example, it was argued that an SEI consisting of LiF/Li₂O would provide a much more uniform current distribution, but in numerous studies it was also observed that trace moisture has a positive effect on the lithium cycling efficiency in non-aqueous electrolytes by assisting in the formation of a compact and uniform SEI, probably owing to the decomposition of semicarbonates into inorganic Li₂CO₃ and LiHCO₃.

In general, probably owing to the intrinsic chemical instability against reduction [Section 10.2.1, eqn (10.1)], esters tend to form rather thick and resistive SEIs on the lithium-metal surface, and the Coulombic efficiencies are usually in the low range 70–90%, unless other cosolvents or additives are used.

16.6.2.2 Ethers

Compared with esters, ether-based electrolytes perform much better in enabling the reversible deposition and stripping of lithium metal, with thinner and less resistive SEIs and also higher Coulombic efficiencies (>90%). These advantages come at least in part from the overall better chemical stability of ethereal molecules against reduction. The eventual interphasial ingredients include inorganic components such as oxides, peroxides, hydroxides, fluorides (if the anion or one of the solvents is fluorinated) and organic components such as oligomeric ethers and alkoxides that are the products from the ether cleavage, radical generation/propagation and subsequent recombination.

One interesting finding relates to the preferential solvation and reduction of the ethereal compounds that seems to be the reverse of what has been discovered about ester-based electrolytes (Table 16.2). Similarly to esters, there are also two classes of ethereal solvents, *i.e.* cyclic ethers such as tetrahydrofuran (THF) and 1,3-dioxolane (DOL), and linear ethers such as dimethoxyethane (DME) or higher order glymes. Compared with esters, these ethers are much more stable chemically against reduction; however, they still do react with Li⁰, producing the inorganic and organic ingredients as mentioned above. When examined by ESI-MS (Section 12.2.2, Figure 12.3), DME or other

Table 16.2 Solvation and reduction preferences for esters and ethers.

Solvent	Structure	
	Cyclic	Linear
Esters	<i>Preferred</i> in solvation Example: $\text{Li}[(\text{EC})_4]^+$ <p><i>Preferred</i> in reduction and interphase contribution</p>	<i>Not preferred</i> in solvation <i>Not preferred</i> in reduction and interphase contribution
Ethers	<i>Not preferred</i> in solvation <i>Preferred</i> in reduction and interphase contribution Example: reductive cleavage of DOL at different sites produces alkoxides	<i>Preferred</i> in solvation Example: $\text{Li}[(\text{DME})_2]^+$ <p><i>Not preferred</i> in reduction and interphase contribution</p>

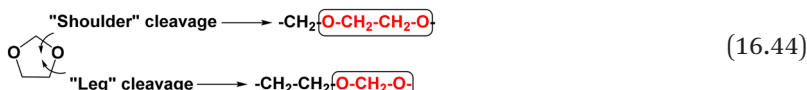
linear ethers apparently are the preferred solvent molecules within the solvation sheath of Li^+ , because they form extremely stable chelating solvation structures. In particular, the solvation structure $[\text{Li}(\text{DME})_2]^+$ shown in Figure 12.2 was identified by ESI-MS as the predominant species in any DME-DOL or DME-THF mixed solvent system, provided that the molar fraction of DME is above 20%. The knowledge about the preferential solvation and preferential reduction of carbonate electrolytes implies that such solvent molecules preferred by Li^+ should become the major interphase contributors.

However, the reality is completely the reverse. When linear and cyclic ethers are used together as mixed solvents, it was found that the cyclic ethers, although not preferred in the Li^+ solvation sheath, would be the solvent that is preferentially reduced, a consensus confirmed by both surface analysis and calculations.

This decoupling between solvation and reduction for ethers appears to originate from a combination of several factors:

- Linear ethers are more flexible in forming a chelating structure, whose multi-oxygen coordination sites enclose Li⁺ and form a five- or six-membered ring solvation structure as shown in Figure 12.2, whereas cyclic ethers cannot do so owing to the constraints imposed by their cyclic skeleton. This makes the Li⁺ solvation sheath overwhelmingly dominated by linear ethers, a typical example being [Li(DME)₂]⁺ detected by ESI-MS as the major species in electrolytes based on mixed ether solvents.
- The ring structure of cyclic esters such as EC or PC aligns the molecular polarity towards the carbonyl functionality (Figure 3.1b), thus rendering the whole molecule highly polar, whereas the more flexible structure of the linear esters such as DMC or EMC partially offsets the polarity. This difference could be clearly seen in the dielectric constants (Table 10.1) or solvation power (Table 12.1) of cyclic carbonates *versus* linear carbonates.
- Unlike esters, the carbonyl functionality of which is highly sensitive to both Li⁺ solvation (Section 12.2.1, Figure 12.1) and reduction [eqn (10.1)], each individual oxygen site in the ethers is nearly equal in terms of both solvating Li⁺ and resisting reduction.
- Under such “leveling” conditions, the only dictating factor that determines the relative reactivity of cyclic *versus* linear ethers becomes the structural unsaturation. As discussed previously, from the perspective of organic chemistry, the ring structure represents a degree of unsaturation, thus making cyclic ethers chemically more susceptible against reduction or oxidation.

The surface analysis and calculation identified two possible sites on the cyclic ether DOL, where the incoming electron cleaves the C–O bonds and creates an anion radical:³¹



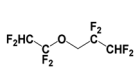
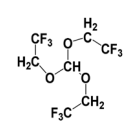
These two cleavage sites are denoted “shoulder” and “leg” according to their relative locations. The unique structure of DOL makes it possible to distinguish the products generated by these two cleavage sites, because the “leg” cleavage would generate species containing O–CH₂–O linkages such as (CH₂CH₂OCH₂OLi)₂ and Li–OCH₂O–(CH₂)₃O(CH₂)₂OLi, whereas the “shoulder”

cleavage would only produce species containing oligoether linkages O–CH₂–CH₂–O such as LiOCH₂CH₂OLi, LiOCH₂CH₂OCH₂CH₂OLi and LiOCH₂CH₂OCH₂CH₂OCH₂CH₂OLi.

Those species with O–CH₂–O linkages have a unique spectroscopic signature similar to a carbonyl structure (such as 289 eV in C1s or 531 eV O1s spectra in X-ray photoelectron spectroscopy, or low-field chemical shifts in NMR spectra for ¹H, ¹³C and ¹⁷O nuclei signals), and are rather stable against further reduction, whereas the species with O–CH₂–CH₂–O linkages can be further reduced to inorganic salts such as Li₂O. This difference in reactivity of various products generated by these two cleavage pathways therefore results in a layered structure of SEI on lithium metal, *i.e.* an inner SEI layer consisting of mainly inorganic species such as Li₂O or Li₂O₂ from those species with O–CH₂–CH₂–O linkages generated by the “shoulder” cleavage, while the outer layer retains a more organic nature.

In recent years, more focus has been shifted towards polyfluorinated ethers as solvents, which tend to form various fluorinated interphasial species (Table 16.3). Although a simple correlation between

Table 16.3 Fluorinated ethers as new electrolyte solvents.

Solvent ^a	Structure	B.p./°C	F:H ^b	HOMO/eV	LUMO/eV	η/cP at 25 °C	$\sigma/\text{mS cm}^{-1}$ at 25 °C
Bis(2,2,2-trifluoroethyl) ether (BTFE)		62–63	1.5	−8.76	−0.5	0.7	4.88
1,1,2,2-Tetrafluoroethyl 2,2,3,3-tetrafluoroethyl propyl ether (TTE)		93.2	2	−9.31	−0.5	1.43	2.44
Tris(2,2,2-trifluoroethyl) orthoformate (TFEO)		143	1.5	−8.84	−0.4	1.97	1.61

^aSource: BTFE, ref. 78; (2) TTE, ref. 79; (3) TFEO, ref. 80.

^bRatio of fluorine to hydrogen in the molecule.

fluorine content and SEI effectiveness or Coulombic efficiency does not exist, it does seem that certain interphases with fluorine present outperform their counterparts with less or no fluorine.³² It has been speculated that, in addition to the fluorine content, how those fluorides exist in interphases also matters, and different experimental and computational techniques indicate that the particle size of the fluorinated ingredients (LiF or organofluorine species) must be on the nanoscale in order to avoid the adverse effect of the ionically insulating nature of fluorinated compounds. On the other hand, in SEIs formed in some of these electrolytes based on fluorinated ethers, LiF or C–F species could become minorities while the presence of Li and O dominates, implying an SEI consisting mainly of inorganic Li₂O or Li₂O₂ species.

The application of new characterization techniques allows us to gain more detailed insights into the fragile and sensitive interphases grown on the surface of lithium metal. For example, cryogenic electron microscopy applied by Cui and colleagues revealed that the chemical composition, structure and morphology of SEIs generated on an Li⁰ surface depend strongly on the electrolyte composition.⁸⁹ In one of the ether electrolytes (1 M LiFSI in DME-TFEO), a monolithic SEI was identified on the Li⁰ surface, in which the distribution of inorganic ingredients, mainly Li and O, seemed to be homogeneous across the entire thickness of 10 nm. Most interestingly, these inorganic ingredients remain in amorphous instead of crystalline states. This is in sharp contrast to the CEI grown in the same electrolyte on a high-nickel NMC cathode surface, the inner layer of which is dominated by LiF and other fluorinated ingredients.⁹⁰

16.6.3 Interphasial Chemistries Brought by Additives

As briefly discussed in Section 16.5.2, the use of electrolyte additives provides an economical way of altering electrode/electrolyte interphases without replacing the major components of the current state-of-the-art electrolyte systems. This allows electrolyte scientists and engineers to decouple the requirements for bulk properties (such as ion solvation and ion transport) from those for interfacial/interphasial properties (such as thermodynamic stability defined by HOMO/LUMO, the interfacial assembly of electrolyte components at the electrode surface, their decomposition chemistries and the kinetic stability provided by interphases formed by the decomposition products). This decoupling is significant, as an electrolyte must face extreme

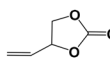
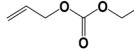
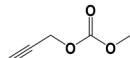
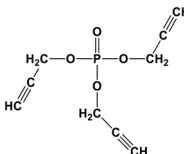
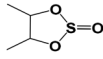
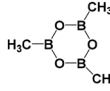
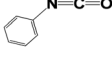
electrochemical conditions at the anode and cathode simultaneously, and these requirements for bulk and interfacial/interphasial properties often conflict with each other, making it essentially impossible to satisfy all of them with a single electrolyte composition. Such conflict would only become severe when more aggressive anode and cathode chemistries are being pursued for higher energy densities, while electrolyte additives could provide an effective solution. In recent years, electrolytes containing additives have also been named “*functional electrolytes*” in the literature.^{33,34}

Just as interphases are more needed on the anode side of lithium-ion or lithium-metal batteries, most additives were developed to target interphasial chemistries on the anode surface, especially on graphitic anodes. The efforts were focused on identifying compounds with a lower LUMO, so that they could be reductively decomposed before most of the main electrolyte components. However, as discussed in Section 12.6.2, such a design strategy remains semi-empirical because although computation can precisely predict the LUMO energy level and the potential of reductive decomposition, it cannot precisely predict whether the subsequent decomposition products possess the physical and chemical properties required by interphases.

Additives have been extensively used in commercial lithium-ion batteries, but owing to commercial confidentiality of each manufacturer, their exact usage has rarely been reported in the open literature, especially those that work most efficiently. Patent disclosures and conference abstracts can reveal certain information about this aspect, although a fundamental insight is usually unavailable in these forms of literature. For example, Dahn and colleagues developed high-precision coulometry and applied it to study how additives impact battery performance. In their study, they often used a combination of multiple additives and selected the most effective electrolyte composition.⁹¹ Although this approach proved to be effective in screening large numbers of possible combinations of salt concentration, solvent composition and additive structure, these additives are actually evaluated in a “black box” manner without revealing the exact underlying mechanism.

Table 16.4 summarizes selected additives that have been reported in the open literature. In most cases, the concentration of these SEI-targeted additives is expected to be kept at a minimum so that the bulk properties of the electrolytes such as ion transport and liquid ranges would not be discernibly affected. In other words, for an ideal anode additive, its trace presence should be sufficient to decouple

Table 16.4 Selected electrolyte additives.

Additive	Structure	HOMO/LUMO/eV or corresponding potential/V vs. Li
Ethylene carbonate (EC) ^a		0.67 eV/-8.28 eV
Vinyl carbonate (VC)		-0.25 eV/-7.21 eV
Monofluoroethylene carbonate (FEC)		0.19 eV/-8.80 eV
Vinylenethylene carbonate (VEC)		
Allyl ethyl carbonate (AEC)		1.50 V
Propargyl methyl carbonate (PMC)		0.83 V
Tris(propargyl) phosphate (TPP)		-1.47 eV/-7.93 eV
Butylene sulfite (BS)		1.8 V
1,3-Propane sultone (PS)		0.70 V
Prop-1-ene-1,3-sultone (PES)		
Trimethylboroxine		
Phenyl isocyanate		1.62 V

(continued)

Table 16.4 (continued)

Additive	Structure	HOMO/LUMO/eV or corresponding potential/V vs. Li
Alkoxyboroxine		
Tris(hexafluoroisopropyl) phosphate (HFIP)		4.2 V

^aEC used as reference for comparison.

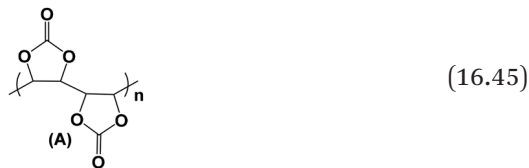
the interphasial chemistry and properties from the bulk properties. There is no official standard defining an upper limit on the additive concentration, but an arbitrary criterion of 10% by weight or volume has been commonly adopted by researchers. Above 10%, the added component will be treated as a cosolvent instead of an additive.

With few exceptions, the additives that are intended to alter SEI chemistries usually have low LUMOs or high reduction potentials, which ensure that these additives are reduced on the anode surface before the bulk electrolyte components are involved. For the same reason, the limited number of additives designed to modify CEI chemistries would have high HOMO or low oxidation potentials. This requirement for higher reactivity than the rest of the electrolyte composition often leads to compounds containing unsaturated, cyclic or heteroatomic structures. Some of these additives listed in Table 16.4 have been extensively used in the lithium-ion battery industry, although electrolyte and cell manufacturers often treated the additives as trade secrets, thus making it difficult to know exactly what or how much additives are used.

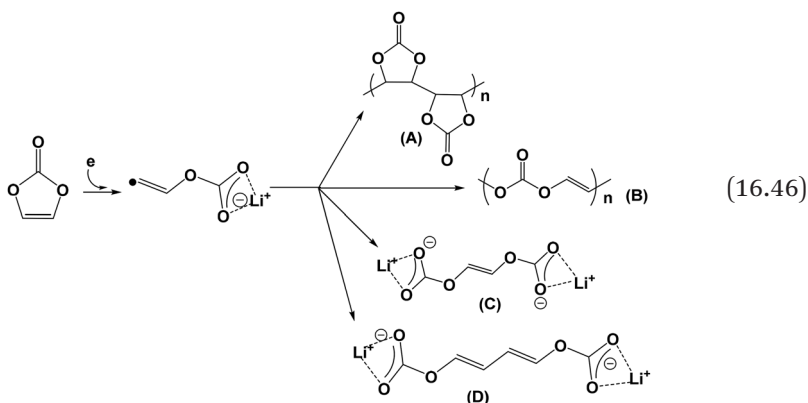
On the fundamental side, there have also been limited efforts made to understand how these additives work, especially *via* what reaction pathway they follow electrochemically or chemically and what eventual products they generate, with the exception of a few well-established additives such as vinyl carbonate (VC) and monofluoroethylene carbonate (FEC).

Unsaturated compounds have always been favored as potential additive candidates, and VC has been the most prominent example. It was proposed *via* both *ab initio* calculation and experimental spectroscopy based on synthesized VC-originated polymers that the

radical polymer product from VC is the main product on both a graphitic anode and an LiCoO₂ cathode:



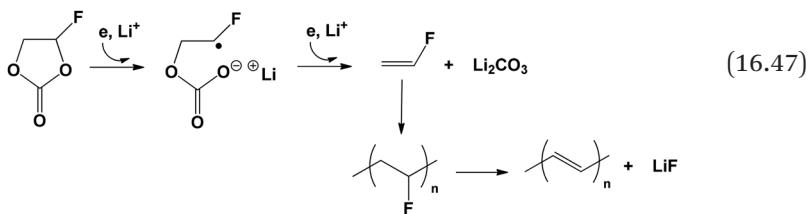
A reaction mechanism was proposed based on the experimental observation that the radical is generated at 2.5 V vs. Li, which initiated the chain reaction and generate a series of polymeric and oligomeric products:



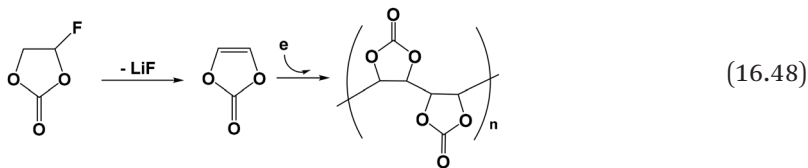
How the same polymeric products end up on the cathode surface is still not clear. A mechanism for the oxidation of VC producing the corresponding radical cation might be possible, and so might a “cathode-anode dialog” mechanism, in which the radical species are sufficiently long-lived to diffuse across the cell and propagate on the opposite electrode surface. According to Dahn and co-workers, the effectiveness of the polymeric interphase generated by VC was actually more pronounced at the cathode rather than at the anode, as quantified by both the Coulombic efficiency and the irreversible capacity consumed in the first cycle.⁹²

In a more general context, unsaturated functionalities (double or triple bonds, cyclic structures, etc.) provide a site for polymerization under both reductive and oxidative initiations.

FEC, on the other hand, could experience different pathways simultaneously. One possible mechanism proposed for FEC involves the nucleophilic attack by an electron at the alkoxide C–O bond that has been activated by the electronegative fluorine, followed by a ring-opening reaction that eventually generates LiF and Li₂CO₃ embedded in polymeric species:



An alternative proposed route also produces LiF, but the FEC molecule experiences dehydrofluorination first to form VC, followed by a cascade of reactions similar to that shown in eqn (16.46) and eventually leads to the formation of poly(vinyl carbonate):



FEC has been found to be especially effective for Si anodes, and has essentially become an indispensable electrolyte solvent for all Si-based lithium-ion batteries as EC once was for graphite-based lithium-ion batteries. Despite the various Si materials used, a general consensus is that FEC-originated interphases tend to be denser and thinner. By examination with diverse surface analytical tools, the chemical composition of FEC-originated interphases was shown to be more enriched in inorganic (LiF) and organic fluorides (C–F), whereas interphases formed in FEC-free electrolytes have more O-containing species, such as Li₂O and lithium salts of alkyl carbonates, apparently from the reduction of carbonate solvents.

The SEI and CEI additives for lithium-ion batteries usually aim at one of two distinct but closely interrelated goals: (1) to minimize the irreversible capacity needed in the first cycle to form the SEI and (2) to minimize the cell impedances during long-term cycling. With new chemistries such as Si or lithium-metal anodes, the SEIs

therein are also expected to help manage the volume contraction and expansion of these anode materials, in addition to suppressing the formation of dangerous morphologies such as dendritic and dead Li⁰.

In the early era of lithium-ion batteries research, Aurbach and colleagues also discovered a variety of gaseous additives, such as CO₂, SO₂ and N₂O, which were introduced into electrolytes under moderate pressure (3–6 atm) and achieved varying degrees of success.⁹³ Although it might seem impractical because the application of pressure would certainly incur additional costs and safety concerns for the commercial cells, the pressurized cell was adopted for certain special application environments such as in space, under water or at extreme temperatures. The recently developed liquefied gas electrolytes represent such examples. On the other hand, researchers also found that, provided the electrolyte system has sufficient solubility for these gaseous additives, pressurized conditions are unnecessary. For example, CO₂ has been used as an effective additive for the WiSE electrolyte, which forms a dense SEI consisting of mainly LiF (from the decomposition of TFSI anion therein) and Li₂CO₃ (from the CO₂ that saturates the WiSE).⁹⁴

16.6.4 In “Beyond Lithium-ion” Chemistries

The intrinsic limit on the energy density of lithium-ion batteries is imposed by the masses of the “inert” intercalation hosts, which comes as the compromise made for higher reversibility. The ratio of this parasitic weight to active ingredient (*i.e.* Li⁺) is especially high on the cathode side, where typically only one Li⁺ could be accommodated per transition metal element in the fully-lithiated state. In order to break through this limit, numerous efforts have been made in recent years to seek cathode chemistries beyond transition metal oxides or phosphates as Li⁺ intercalation hosts, and inert masses are kept to a minimum or completely eliminated.³⁵ This has led to the emerging chemistries based on Li/sulfur, Li/air and various conversion reaction chemistries such as metal sulfides or metal fluorides as discussed in Section 10.4. These “beyond lithium-ion” systems boast energy densities approaching >10 000 W h kg⁻¹. Since they all employ lithium metal as the anode material, the chemistry and morphology of the SEIs involved are in general similar to what was discussed in the previous section, with the exception of Li/sulfur, whose cathode-anode cross-talk *via* polysulfide shuttling introduces sulfur-based interphasic ingredients such as thiocarbonates that were discussed in Section

10.4.2.2 [eqn (10.39)–(10.42)]. Their CEIs, however, differ from those in lithium-ion batteries and vary with the chemistries.

The external limit on lithium-ion batteries, on the other hand, is imposed by the resource restrictions, as the mainstream chemistries employed rely greatly upon a few elements (Li, Ni and Co), the availability of which in the Earth's crust is either rare or with geopolitical or ethical risks. Concerns over cost or such risks drove the efforts to seek alternative and cheaper chemistries based on abundant elements such as Na, K, Mg, Ca or Zn. These “beyond lithium-ion” systems promise less ambitious energy density goals, although the projected volumetric energy densities of these multivalent systems (Mg, Ca or Zn) are actually higher than that of lithium-ion batteries thanks to the storage mechanisms involving multi-electron reactions.

These “beyond lithium-ion” chemistries bring new interphasial challenges.

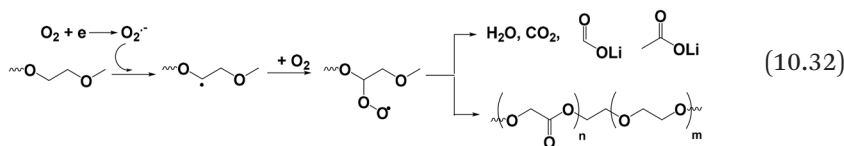
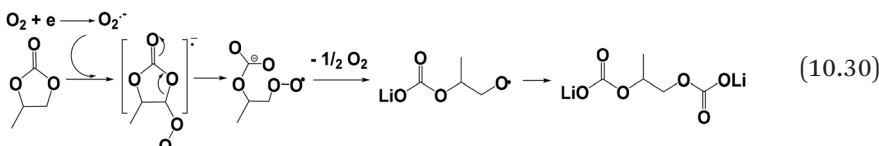
16.6.4.1 CEIs in Li/O₂ and Li/Air Chemistry

Li/O₂ and Li/air chemistry promises extremely high theoretical energy densities that approach gasoline-powered internal combustion engines (13 000 W h kg⁻¹), which has been enabled by the fortuitous combination of the facts that lithium is the metal with the lowest gravimetric density, the lowest atomic number and the lowest electrode potential, and that the active cathode material (O₂) is stored in the ambient environment and often not counted as part of the mass of the device.³⁶ In reality, however, such “super-batteries” face severe challenges with regard to electrolytes and especially interphases.

On the anode side (Li⁰), the challenges of dendritic and dead Li⁰ and the interphases to suppress them have been discussed in Sections 10.2 and 16.6.2. To render the cell rechargeable, one must not only exclude invasive impurities from the environment, such as moisture and CO₂ (which leads to the Li/O₂ rather than Li/air configuration), but also ensure that the electrolyte would favor the formation of peroxide (Li₂O₂) or superoxide (LiO₂) species rather than oxide species (Li₂O) as the discharge products, because Li₂O would render the cell non-rechargeable. Equally important is to ensure that the electrolyte is stable against reactions with those peroxide or superoxide species, otherwise dangerous organic peroxides could be formed. CEIs formed on the air cathode play a central role in the reversibility of the chemistry, in addition to the SEI on the lithium-metal anode. One must realize that, with the challenges at the lithium-metal anode still not resolved, introducing additional challenges at the cathode does

not help. Therefore, among all the “beyond lithium-ion” systems, Li/air or Li/oxygen might be the most remote chemistries for practical applications.

As a direct legacy from the knowledge about lithium-ion and lithium-metal batteries, carbonates and ethers are the two major solvents used in most Li/O₂ research, but their chemical and electrochemical instability against the highly reactive products generated during the discharge of oxygen gas (*i.e.* peroxides or superoxides) is often found to be an issue.³⁷ As described in Section 10.4.2.1, both esters and ethers are susceptible to nucleophilic attack from either peroxide or superoxide species:



Although the above reduction processes may appear to be familiar, and easily remind one of what happens on a graphitic surface in lithium-ion batteries, we must remember that we are looking at a cathode surface now, hence these semicarbonates, alkoxides, carboxylates and polymeric species are generated *via* a process of oxidative rather than reductive nature. This fact reveals again that identical surface compounds could be produced on either side of the battery.

Owing to the sensitivity of most of these species towards impurities such as moisture, acids (HF or partially decomposed fluorinated anions) and CO₂, the eventual CEIs could be more complicated mixtures that also contain more stable species of inorganic nature, such as LiF, Li₂O and Li₂CO₃, *etc.* These secondary reactions are especially likely in Li/air cells, where the oxygen comes from the ambient environment and inevitably brings impurities. Together with semicarbonates, peroxides, superoxides and polymers, these solid products constitute the eventual CEIs on the air cathode. Characterization revealed that the CEIs in Li/O₂ are not static but experience periodic dissolution/reduction and re-formation in each charge and discharge

cycle. Such dynamic CEIs on an air cathode, along with a highly reactive lithium-metal anode and even more dynamic SEIs thereon, constitute extremely severe challenges to Li/O₂ and Li/air chemistries.

16.6.4.2 SEIs on Na⁰/K⁰ Electrodes and Intercalation Hosts for Na⁺/K⁺

The potentials of Na⁰ and K⁰ are close to but slightly higher than that of Li⁰ (Table 10.3), hence the interphases on their surfaces would be similar to the SEIs formed on Li⁰, *i.e.* in an instantaneous and indiscriminate manner. Na⁰ and K⁰ are also covered with a native passivation layer that formed spontaneously during the manufacturing, packaging and storage processes. Likewise, the chemical reactions of these native passivation layers with electrolytes upon cell assembly and the subsequent electrochemical reactions driven by the applied potential and the nascent deposited Na⁰ and K⁰ would jointly determine the chemistries of the eventual SEIs.^{38,39}

Most sodium and potassium electrolyte compositions inherited the legacy from the lithium electrolytes in terms of both materials and knowledge, hence ethers and esters constitute the two major classes of solvents most often used. It is therefore expected, and has been confirmed experimentally, that the SEIs on Na⁰ and K⁰ are very similar to the SEI formed on Li⁰. In carbonate-based electrolytes, the SEIs often adopt a layered structure, with the inner layer having a more inorganic nature and consisting of oxides, fluorides, carbonates (Na₂O, NaF, Na₂CO₃ or K₂O, KF, K₂CO₃) and the outer layer having a more organic nature and consisting of semicarbonates (RO-CO₂Na) and polymeric or oligomeric species. In ether-based electrolytes, the main SEI ingredients are dominated by oxides and fluorides. In electrolytes containing FEC, fluorides (NaF and KF) are prevalent.

One prominent difference does exist, however, in the relative contents of these inorganic and organic species. In SEIs formed in sodium electrolytes, the relative percentage of organic ingredients, especially semicarbonates, is much lower than those found in SEIs formed in either lithium or potassium electrolytes. This inorganic-organic nature of SEIs seems to originate from the solubility differences among these organic salts of Li⁺, Na⁺ and K⁺, because it has been well established that sodium salts are often more soluble in non-aqueous solvents than their lithium or potassium counterparts. This reason behind this solubility order is complicated. On the one hand, the solubility of a salt is in general determined by the Lewis acidity of

the cation, which in this case follows the order $\text{Li}^+ > \text{Na}^+ > \text{K}^+$. Hence sodium salts are more soluble than potassium salts thanks to the stronger Coulombic interaction between Na^+ and solvent molecules than that between K^+ and solvent molecules. On the other hand, Li^+ is a unique cation owing to its extremely small ionic radius, which has led to a series of abnormal properties associated with lithium-related compounds that can be found in most inorganic chemistry textbooks. In this particular case, the extremely strong Coulombic interaction exists not only between Li^+ and solvent molecules, but also between Li^+ and its counter-anions in the corresponding salts, and the eventual solubility is determined by the competition of these two counter-effects. The net result of the competition tilts towards lower solubility of these inorganic or organic lithium salts.

All things considered, the organic salts containing Na^+ are thus the most soluble and least likely to remain in an SEI, even after its formation in the interfacial reactions, hence the SEIs tend to be enriched with inorganic salts of Na^+ ; on the other hand, the relatively lower solubility of Li^+ and K^+ salts ensures that their organic salts (semicarbonates, oxalates and alkoxides) could be retained in the eventual SEIs at a reasonable percentage.

Like lithium-metal electrodes, both sodium- and potassium-metal electrodes tend to form dendritic and dead Na^0 or K^0 , which could be even more dangerous than dendritic and dead Li^0 , which drives the efforts to develop sodium-ion or potassium-ion batteries, which have been following a similar pathway that once led from lithium-metal to lithium-ion batteries. The graphitic structure can only accommodate Na^+ at an extremely dilute level (NaC_{44}) if ester-based solvents are used, with higher Na^+ concentrations disfavored by thermodynamics, whereas solvated Na^+ in ether-based electrolytes can reversibly co-intercalate into graphite and form a ternary graphite intercalation compound, which is similar to Scenario II described in Section 10.3.2.3 (Figure 10.7). In the latter case, the SEI is considered absent despite the irreversible capacities observed in the initial cycles, because once an SEI is formed at the edge sites of the graphite, the solvated Na^+ such as $[\text{Na}(\text{DME})_2]^+$ can no longer enter and exit the graphitic structure.

For this reason, the most popular anode intercalation host used for Na^+ is hard carbon, the non-graphitic nature of which provides numerous adsorption/intercalation sites for Na^+ . Naturally, the SEIs formed on hard carbon in sodium electrolytes differ from those SEIs formed on Na^0 , and should be similar to those formed in lithium-ion batteries, *i.e.* in a stepwise and discriminating manner.

According to various surface spectroscopy studies, the SEIs formed on hard carbon from sodium electrolytes are more similar to those from lithium electrolytes, but in general the content of organic species (semicarbonates, alkoxides) is lower than that of inorganic species, which are mainly fluorides or other fragments generated by the partial decomposition of salt anions such as SO_xF from TFSI or FSI anions. This trend is again probably related to the solubility of these sodium salts. The higher inorganic nature of a sodium SEI also makes the SEI thinner (~ 30 nm) than potassium or lithium SEIs.

Both graphite and hard carbon have been used as anode intercalation hosts in potassium-ion batteries, in which the SEIs are more similar to those formed in lithium electrolytes, with both inorganic and organic ingredients arranged in layer structures.

16.6.4.3 SEIs on Metals With Multivalent Chemistries

As discussed in Section 10.4.1.4, the battery chemistries that attempt to employ multivalent ions such as Mg^{2+} , Ca^{2+} and Al^{3+} as working ions encounter tremendous challenges both in electrolyte composition and in interphases.^{6,40} The extremely strong Coulombic forces exerted by a multivalent ion on its environment, be it solvent molecules, counterions or coordination sites in both the electrode lattice and interphases, induce significant resistance to their movement. In interphases, where the coordination sites are immobilized and cannot move with the ion, the ion has to move in a “structural manner” (Section 12.3, Figure 12.8), hence a multivalent ion must free itself before hopping to the next coordination site to form a new association. The Coulombic traps constituted for structural motion are already much steeper than those for vehicular motion (Figure 5.15), while the multivalence of the ion only makes such energy traps even deeper for it to escape. It was for this reason there has been a long-standing belief that there must not be any interphase formed on the metal anode in multivalent ion battery chemistry. The design of multivalent ion electrolytes has mostly evolved around this central belief, and the solvents and salt anions employed have been almost exclusively confined to those compounds known to resist reduction, such as various hydrides (e.g. borohydrides), organometallic carbanions stabilized by bridging multivalent cations (such as in Grignard reagents) or ethereal solvents. On the other hand, solvent molecules such as esters, nitriles and sulfones are least welcome in this category

of electrolytes, because their intrinsic instability against reduction would inevitably produce solid deposits and interphases on most of these metals, the eigenpotentials of which are low enough to induce reactions (Table 10.3).

The electrolytes based on these reduction-resistant solvents and salts indeed can support excellently the reversible deposition and stripping of multivalent metals, and in some cases a Coulombic efficiency of 100% has been claimed for Mg and Ca. However, a dilemma inevitably arises from such an interphase-free pursuit, namely that most of these exotic electrolytes based on hydrides, ethers or carbanions are unstable against oxidation, hence their use in the electrolytes would exclude the use of high-voltage (>3 V) cathode materials for multivalent batteries, if such cathode materials actually exist. Therefore, from the perspective of developing a practical multivalent metal battery, one has to consider the design, formation and engineering of interphases on either the anode or cathode surfaces of a multivalent battery, so that the conflicting needs of the anode and cathode can be simultaneously accommodated.

Recent advances seem to prove that interphases that allow multivalent ions to conduct are possible. The limited examples include an artificial interphase that was engineered on an Mg surface by the *in situ* polymerization of an acrylonitrile monomer in the presence of an Mg salt, $\text{Mg}(\text{CF}_3\text{SO}_3)_2$.⁴¹ This Mg^{2+} -conducting and electron-insulating polymeric electrolyte layer essentially decouples the anodic and cathodic requirements for Mg electrolytes, and allows the use of carbonate ester electrolytes or aqueous electrolytes in addition to high-voltage Mg^{2+} intercalation cathode materials. Likewise, *via* electrolyte engineering with super-concentration and inert ion crowding at the electrode/electrolyte interfaces, an effective ZnF_2 -based interphase that conducts Zn^{2+} was also identified, which assists in suppressing the dendritic growth of Zn^0 during its repeated deposition and stripping cycles.

These efforts may represent the future directions for developing multivalent electrolytes. As we have learned from the mature example of lithium-ion batteries, the electrolytes therein already face many challenges from almost every component in the cell, hence attempts to comply with thermodynamic stability limits of electrolytes, such as what the interphase-free approach pursues, would inevitably limit the opportunity to be successful. Instead, interphases have been proven to be an effective strategy for decoupling electrolytes from at least some of the key but conflicting requirements, such as stability

against both oxidation and reduction. With the belief that multivalent ions cannot transport across any interphase now overturned, there is plenty of opportunity to explore what interphasial chemistry would support multivalent ions.

16.6.4.4 CEIs on Conversion Reaction Chemistry

As discussed in Sections 9.1.3.8 (Figure 9.8) and 10.4.2.3, conversion reaction chemistries are usually associated with high capacities and high energy densities, but their reversibility suffers from the fact that, in each charge and discharge cycle, the electrode structure must experience complete breaking and re-formation. This presents unique challenges to both electrolytes and the interphases, as long as these electrodes operate beyond the thermodynamic stability limits of the electrolyte.⁴²

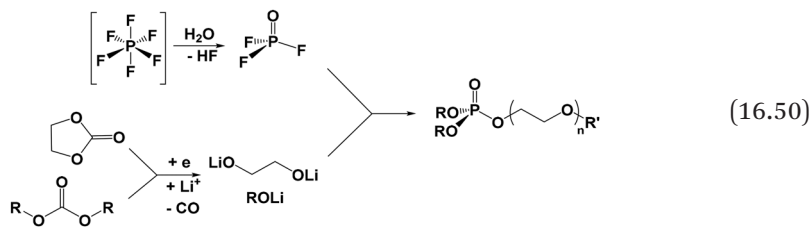
This is the case for the metal sulfides, oxides and halides (especially fluorides) that are being explored as next-generation cathode materials:



where M represents iron, copper, nickel or other transition or non-transition metal and X represents anions such as S²⁻, O²⁻ or F⁻.

One popular approach to improve the reversibility of conversion reaction chemistries is to design various nano-structures, so that both reactants and products are confined in a rather small length scale, which makes the diffusion pathways short enough for the species involved to return to their original locations. A consequence of this nano-structure approach is that the surface area of such conversion reaction cathode materials is very high. In particular, those nascent metal particles M⁰ of nano-size are extremely reactive to electrolytes, and such reactive centers are generated in each cycle, in similar manner to a new Li⁰ surface being generated in each deposition process.

When these conversion reaction cathode materials are discharged in carbonate-based electrolytes, interphasial species consisting of polymeric and phosphate esters of varying lengths are identified, which seem to be the esterification products between phosphoryl fluoride (POF₃) and PEG-like alkoxides, with the former generated from PF₆⁻-anion and the latter from the radical-induced decarbonylation of cyclic or linear carbonate molecules:



Such CEIs are very peculiar as similar esterification processes have never been found in interphases of lithium-ion batteries. Even stranger is that some of these CEI species were found to be formed during the initial discharge, but disappeared upon immediate charging. This reflects the instability of the CEIs in conventional electrolytes based on carbonate esters and the salt LiPF_6^- .

In recent years, highly concentrated electrolytes based on both esters and ethers, especially highly fluorinated ethers, have been used as alternative electrolytes, which helps to mitigate the poor reversibility of these conversion reaction materials. The CEIs formed in those electrolytes originated almost exclusively from the oxidative or reductive decomposition products of the salt anions PF_6^- , TFSI or FSI. One might feel that “reductive” decomposition here does not make much sense as we are discussing cathode materials, but the fact is that most of these conversion reaction materials must be lithiated and delithiated in a wide voltage range, thanks to the poor kinetics associated with the sluggish diffusion processes of both Li^+ and metallic species as well as the structural reorganization. This often drives these cathode materials into low-voltage regions, which induces reductive decomposition of the electrolytes.

Although electrolytes and interphases remain the major challenges for these conversion reaction materials, they are far from being the only challenges. In order to make these cathode materials practical, the structural design of the electrodes should take the center stage, in synchronization with electrolyte and interphase efforts.

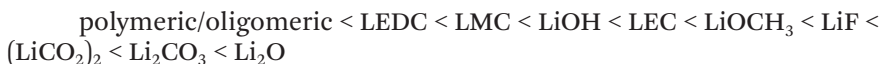
16.6.5 Stability of Interphasial Ingredients

The interphases formed are often regarded as the most fragile components in the battery, not only because they exist on a nanometric scale and are susceptible to mechanical damage, but also because most of the ingredients are often thermally, chemically or electrochemically sensitive. The understanding of the stability of interphases is still

limited owing to the lack of non-invasive and *in situ/operando* tools to probe them.

16.6.5.1 Solubility of Interphasial Components

The majority of battery configurations consist of solid electrodes and liquid electrolytes, hence the interphases must remain in solid form, and the interphasial ingredients must be resistant to dissolution by the electrolyte solvents. The solubilities of most interphasial ingredients, including oxides, alkoxides, carbonates, semicarbonates, fluorides and oxalates, have been evaluated both experimentally and computationally. It was found that the heat of dissolution ranged from an exothermic process for organic salts to an endothermic process for inorganic salts, in the following order:⁴³



Hence the least soluble ingredients should be the inorganic species (Li_2O , LiF) rather than organic species. The solubility of these typical inorganic lithium salts is estimated to be $10^{-5}\text{--}10^{-4}$ mol L⁻¹. If these species can be oxidized/reduced at the opposite electrode after diffusing across the cell, such seemingly “low” concentrations can already incur a self-discharge current at a level of 0.2–2 mA L⁻¹ of electrolyte. Of course, a dynamic equilibrium exists between the dissolution and precipitation of these interphasial species, hence any form of consumption of these dissolved species at electrode surfaces would encourage more dissolution of the interphase, leading to eventual cell impedance buildup.

No matter whether the dissolution process is endothermic or exothermic, the dissolution of these species accelerates with increase in temperature. When the working ion is changed from Li^+ , it is expected that the Na^+ version of these interphasial species will be generally more soluble, the K^+ version is approximately similar to the Li^+ version and the multivalent versions (Mg^{2+} , Ca^{2+} , or Zn^{2+}) are much less soluble.

The above dissolution enthalpy order remains roughly the same in both EC and DMC, the two most commonly used electrolyte solvents not only in commercial lithium-ion batteries but also in most emerging battery chemistry research. The solubilities in EC were generally higher, as expected from the higher solvation power of EC because of its higher molecular polarity. Perhaps the only exception was LEDC, which dissolves less in EC than in DMC. This deviation

can be attributed to the conformational constraint of LEDC, which allows limited accessibility of oxygen atoms in solvent molecules. On the other hand, LEMC, which is the half-hydrolyzed product of LEDC and will be formed after long-term cycling, would be more soluble in non-aqueous solvents than LEDC.

This dissolution of the formed SEI by electrolyte solvents would undoubtedly produce adverse effects on the performance of lithium-ion batteries and would be at least partially responsible for the slow consumption of electrolyte and active lithium inventory in the cell during the entire service life. This is because, during long-term cycling, the damaged SEI has to be constantly repaired by the same electrochemical reactions that occurred in the initial formation process.

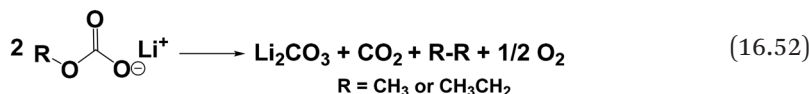
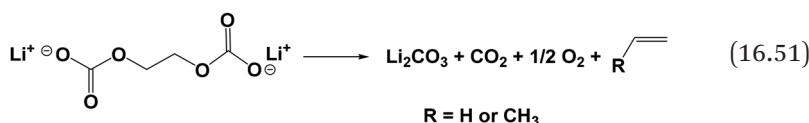
The solubility of interphasial ingredients should not be considered alone in the absence of the electrode on which they are sitting. In particular, the potential of the electrode seems to have a significant influence on the dissolution rate of the interphasial ingredients. It was discovered that the SEI needs much more “repairing” when the lithium-ion battery has to stay in the fully charged state than simply experiencing repeated cycling. Of course, in this scenario the SEI corrosion process is no longer a pure dissolution process, and electrochemical decomposition of the interphases might have been involved. For example, in a fully lithiated graphite, the intercalated Li^+ continuously diffuses from the interior of the graphitic structure through the imperfect SEI coverage and participates in the reaction with electrolyte solvents to replenish the SEI components that have been dissolved by the electrolyte. An equilibrium would exist between the SEI dissolution rate and Li^+ diffusion rate, and this equilibrium naturally shifts with the potential of the electrode. The electrode potential in a battery that experiences cycling swings periodically from extreme potentials to moderate potentials, whereas the electrode potential in a battery that stays stationary in the fully charged state constantly drives the SEI repair at a higher rate.

16.6.5.2 Thermal Stability of Interphases

Aside from accelerated dissolution at elevated temperature, interphasial components, especially those of organic nature (semicarbonates, alkoxides and polymeric/oligomeric species), might also experience thermal decomposition. In certain safety studies of lithium-ion batteries, the thermal instability of the interphasial ingredients was even believed to be the cause of thermal runaway, because the

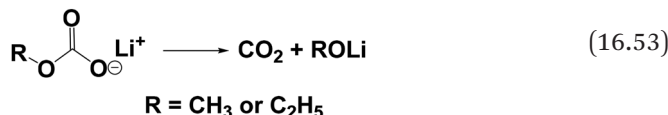
decomposition of these interphasial ingredients at lower temperatures ($\sim 120\text{ }^{\circ}\text{C}$) is usually exothermic, and the heat released in such processes serves as the trigger to activate a series of decomposition reactions that could in turn generate much more heat and then activate more reactions in a chain propagation.

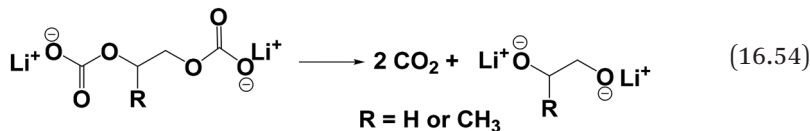
The reactivity of the organic interphasial ingredients seems to be negligible at room temperature, unless one views it in a much longer time frame when prolonged cycling is carried out, and where semicarbonates experience partial hydrolysis and become monocarbonate salts (Section 16.6.1.1.1). On the other hand, such evolution processes could be significantly accelerated by elevated temperature. In the more drastic manner of driving reactions such as heating, the partially decomposed products such as LEMC as shown in eqn (16.19) are rarely detected, and are replaced by the more complete form of the decomposition, such as Li_2CO_3 :



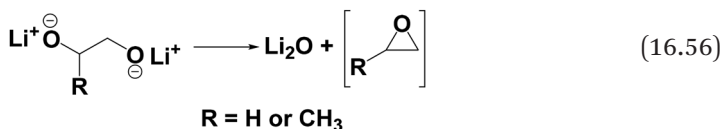
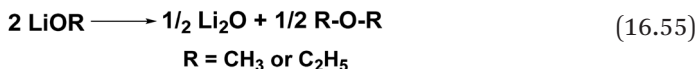
The thermal decomposition pathways depicted in eqn (16.51) and (16.52) should be reliable as they have been confirmed by computational studies and thermal and surface analyses in combination with gas chromatographic analysis. Using the chemically synthesized pure specimens of various semicarbonates [eqn (16.17)], differential scanning calorimetry and thermogravimetric analysis results placed the major thermal decomposition onset in a wide temperature range between 200 and 400 $^{\circ}\text{C}$, which often appears to be preceded by a minor exothermic reaction occurring 120 $^{\circ}\text{C}$.¹²

Alternative pathways also exist, in which the eventual products of the thermal decomposition are alkoxides:





while these alkoxides at higher temperatures (~ 400 °C) would continue the thermal decomposition and generate the completely inorganic and more stable form of oxides:



Eventually, the interphase that experiences thermal decomposition would consist of inorganic species only, which include Li_2CO_3 and Li_2O and also LiF generated during the initial formation of the interphase from the reduction of salt anions PF_6^- and BF_4^- . The formation of these inorganic compounds was confirmed not only by chemical analysis of the products from the thermally decomposed semicarbonate specimen, but also quantitatively from thermogravimetric analysis, where the weight loss recorded seems to favor the pathways leading to Li_2O .

Of course, the above conclusions are of only limited significance for the thermal stability of interphases, as they were drawn from a pure synthesized semicarbonate specimen, whereas the stability of interphases should never be studied alone, as a real interphase has to coexist with the electrodes in the battery environment. The charged state of the electrode expectedly influences the rate and extent of the interphase decomposition, but in this context the decomposition of the interphase is no longer a neat thermal process but is closely convoluted with both chemical and electrochemical decomposition of the interphases.

An interesting observation is that the apparent contents of LiF , Li_2O and Li_2CO_3 in an SEI seem to increase significantly after the thermal decomposition of an *in situ* SEI in a lithium-ion battery. In fact, this is partially due to the direct production of these species by the thermal

and chemical decomposition of semicarbonates and other organic species [eqn (16.43) and (16.51)], but partially due to the stability of LiF, Li₂O and Li₂CO₃ against any thermal decomposition: when the more fragile organic ingredients such as semicarbonates or polymeric/oligomeric species disappear, the relative contents of LiF and Li₂O, and also Li₂CO₃, correspondingly increase.

The thermal stability of CEI ingredients has been less well investigated. Thermogravimetric analysis revealed that the CEIs on transition metal oxide cathode materials such as spinel manganese oxide (LiMn₂O₄) or cobalt oxide (LiCoO₂) experience thermal breakdown in electrolytes at 140 °C, and the reactions apparently propagate to involve the charged cathode materials and bulk electrolyte, eventually producing Mn₂O₃ or Co₃O₄ and releasing CO₂. It is therefore difficult to deconvolute the pure thermal decomposition of the CEI ingredients from the subsequent and more extensive reactions, especially when such reactions also involve the dissolution of the active cathode materials (Mn²⁺, Ni²⁺ or Co³⁺) and corresponding structural transformation of the cathode lattice. Abundant LiF and polycarbonate species left on the cathode surface are often the aftermath of these complicated reactions, revealing the role of the acidic electrolytes that employ anions such as PF₆⁻ or BF₄⁻.

For lithium-ion batteries or other advanced high-energy batteries, the extreme case of thermal instability is the so-called “*thermal runaway*”, which represents the catastrophic chain-like reactions that are triggered by thermally induced decomposition of all cell components that involve not only electrolyte or interphasial ingredients but also the electrode materials. Thermal runaway is believed to start by an exothermic reaction in a local part of the cell, the heat of which cannot be effectively dissipated away within the cell under a nearly adiabatic condition. Such local heat then activates more reactions and eventually involve all potential reactants in a very short length of time (<10 s).

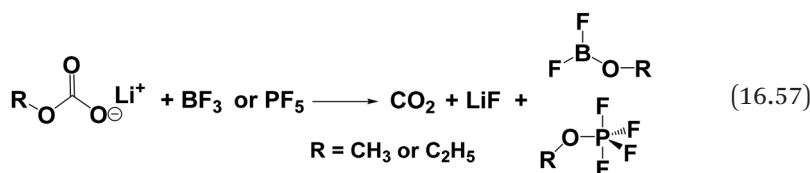
In such chaotic and often violent processes it is usually not possible to identify precisely which component reacts with which, or what the reaction pathway is. Even the analysis of reaction products becomes difficult (and unnecessary) given the complete combustion of the whole cell. The only information that we can rely on in such extreme thermal events is the thermodynamics of all of the cell components, such as the enthalpy or heat expected from the complete reactions among the oxidative cathode materials, reductive anode materials and flammable electrolyte solvents. We know that in these

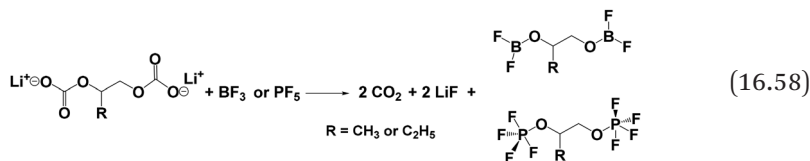
reactions the non-aqueous electrolyte solvents, polymer binder and separators serve as the fuels, and the charged cathode acts as the main contributor of the enthalpy, but various investigations on typical lithium-ion batteries (*i.e.* graphite anode, lithium cobalt oxide cathode and carbonate-based electrolytes) have identified the instability of the SEIs with lithiated graphite as the key that triggers the chain reactions involving all these cell components. This is because, among all these components, the SEIs in these lithium-ion batteries have the highest thermal instability and hence the lowest “onset” temperature threshold (*ca.* 120 °C). However, with the introduction of safer electrolytes with higher degrees of fluorination and more stable SEIs, and also the use of more reactive cathode materials such as high-nickel transition metal oxides, the trigger of thermal runaway could shift to the CEI or electrolyte decomposition on the cathode side, because the de-lithiated cathode materials have a strong tendency to release oxygen gas, which reacts with any organic materials in the cell (separator, binder, *etc.*) even when the electrolyte solvents themselves are non-flammable.

16.6.5.3 Chemical Stability of Interphases

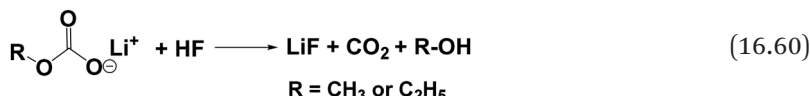
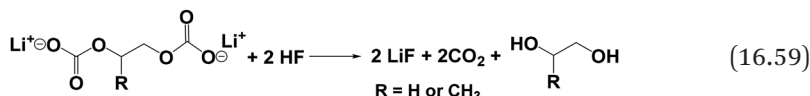
While most organic and inorganic interphasial ingredients are reactive with various impurities in the electrolytes, such as moisture, acid or the decomposed species of the electrolyte salt anion and solvents, LiF is perhaps the only exception because it is stable both chemically and electrochemically.

Surprisingly, despite their alkaline nature, there is negligible reactivity between carbonates and the acidic salts when a synthesized pure specimen of semicarbonates is mixed with typical non-aqueous electrolytes consisting of solutions of LiPF₆ or LiBF₄. However, the corresponding Lewis acids of these salts, *i.e.* BF₃ and PF₅, react violently with the semicarbonates, releasing CO₂. Spectroscopic analysis of the products suggests that the reaction probably proceeds *via* the following pathways:^{6,12}

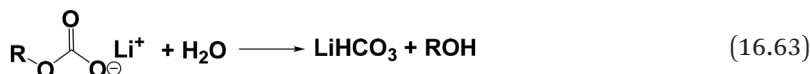
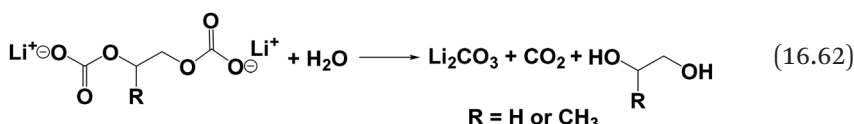
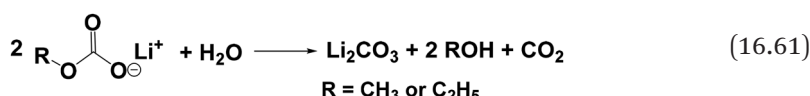


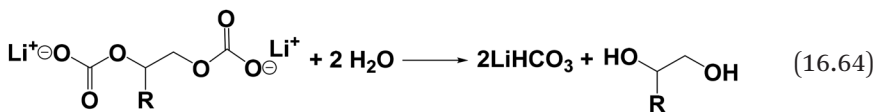


Like Li_2O or Li_2CO_3 , semicarbonates are alkaline in nature and are hence especially sensitive towards acid, which is always present in the form of trace HF in state-of-the-art lithium-ion battery electrolytes. The reaction releases CO_2 and turns the organic interphasial ingredients into LiF :



In addition to acids, semicarbonates are also extremely sensitive to water or moisture from the electrolyte or from the ambient environment, the reactions of which lead to the formation of either Li_2CO_3 or LiHCO_3 , depending on whether there is sufficient water in the system to allow complete hydrolysis:





Since the spectroscopic signatures of these two inorganic species are very close and difficult to distinguish, the unambiguous identification of semicarbonates in interphases has been constantly interfered with by moisture encountered during the surface analysis. This interference is reflected by the many claims made in the literature that Li_2CO_3 is the major ingredient of interphases. As we have seen from the above discussion, the actual situation could be much more complicated. The partial or complete hydrolysis of a semicarbonate could lead to Li_2CO_3 , LiHCO_3 or monocarbonates such as LEMC shown in eqn (16.19) when moisture is extremely rare in the system.

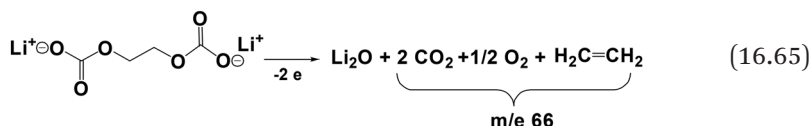
16.6.5.4 Electrochemical Stability of Interphases

Interphase formation is driven by the reactivity between the electrolyte and the electrodes, and the effectiveness of the interphase in insulating electron transport ensures the metastability established between the electrode and electrolyte. Although researchers often view the formation process of an interphase as irreversible, hence the presence of interphase on the electrode surface, once formed, is permanent, reality again turns out to be complicated. In the scenario where the electron insulation is not fully established, the interphasial species formed could still be exposed to electron donation from or extraction by the electrodes, and consequently the interphase could be electrochemically oxidized or reduced after its formation.^{23,44} The identification of LEMC in SEIs [eqn (16.19)] is proof of such evolution as a consequence of chemical or electrochemical instability.²²

Such scenarios of partial electron access occur in the early stages of interphase formation, where the nascent interphases have not been fully isolated from the bulk of the electrodes. Therefore, disappearance of the interphase after its formation has frequently been observed under *in situ/operando* microscopes, such as the optical microscope and atomic force microscope. One example is a graphitic carbon surface polarized to a potential that is low enough for interphase formation but not for Li^+ intercalation, where one can visibly see that the interphase formed in the first cathodic polarization disappears upon reversal of the electrode potential. Such a process has to be related to the electrochemical reaction, *i.e.* the electron exchange between the

electrode and the electrolyte, because the phenomenon is reversible upon cyclic application of the potential. Apparently, the interphasial species that consist of reduction products from the electrolyte components (solvents, salt anions, *etc.*) could be reoxidized under that condition. However, after the graphitic electrode has been polarized to the low potential of Li^+ intercalation, or after the electrode has experienced repeated cycling for long enough, the interphase formed seems to have transitioned into a more permanent presence and becomes less susceptible to reoxidation.

This semi-reversible process reflects the instability of the nascent interphases or proto-interphases on electrode surfaces. Recently, this phenomenon was subjected to careful scrutiny using an advanced quantitative technique employing an *in situ* electrochemical quartz crystal microbalance (EQCM), the quartz crystal of which was attached to a thin graphitic carbon film. From the mass gain detected by the EQCM, the nascent interphases or proto-interphases do not seem to differ in chemical identity from the permanent interphasial ingredient, *i.e.* the interphase is still dominated by the mixture of LiF (from the salt anion PF_6^-) and the single-electron reduction product from EC (LEDC). However, the LEDC in such nascent proto-interphases does not behave similarly to its cousins in a permanent SEI at all, as it is readily oxidizable. The EQCM determined a reproducible mass loss per charge (*m/z*) of 67.1 during this process, and the corresponding mechanism was hypothesized to be two-electron oxidation of LEDC that leads to the formation of Li_2O and release of three gaseous products, CO_2 , O_2 and ethylene:



where the mass loss corresponds to the three gaseous products is

$$\text{mass loss per charge} = \frac{2M_{\text{CO}_2} + 0.5M_{\text{O}_2} + M_{\text{C}_2\text{O}_4}}{2} = \frac{2 \times 44 + 0.5 \times 32 + 28}{2} = 66$$
(16.66)

which is close to what the EQCM measures (*m/z* = 67.1) when considering reasonable experimental errors.

Experiments further confirmed the above reaction pathway with quantitative accuracy: surface analysis (*in situ* Raman and *ex situ*

XPS methods) on the graphitic electrode detects the existence of Li₂O, while chromatographic analysis not only identifies these three gaseous products, but also determines the relative molar ratio of CO₂:O₂:C₂H₄ as 4:1:2. This is a rare example of an interphase study where high accuracy of quantitative results was achieved to directly support a surface reaction mechanism.

16.6.6 Interphasial Components Under Debate

The complications surrounding interphases have been evidenced by the discussions above. As Winter once commented, interphases are “the most important but least understood” component in advanced batteries.⁹⁵ This fact is further highlighted by the controversies that still exist regarding many fundamental issues, despite intensive efforts in recent decades. Paraphrasing an ancient Greek proverb, the more we learn about interphases, the more we know how little we understand it. This paradox will remain as we advance our work to interphases formed on electrodes of the emerging and “beyond lithium-ion” chemistries, where interphasial chemistry becomes more and more intertwined with the redox reactions that occur in both anode and cathode materials.

16.6.6.1 Over Li₂CO₃

Perhaps the most debated item among interphasial ingredients in lithium-ion batteries is Li₂CO₃. Beyond any doubt, Li₂CO₃ was often detected in the SEI on graphitic anodes, and once it was even believed to be the only chemical component of the SEI.

The early belief that Li₂CO₃ originates from a two-electron reduction pathway of carbonate molecules was corrected by Aurbach and co-workers.⁹⁶ Thus, the Li₂CO₃ often identified in surface analysis is actually an artifact, which very likely arises from the aftermath of semi-carbonate hydrolysis due to poor moisture management [eqn (16.61) and (16.62)] with the possible presence of LiHCO₃ also [eqn (16.63) and (16.64)]. However, the correction made by Aurbach and co-workers did not end the controversy, because in the following decade numerous researchers still described Li₂CO₃ as an SEI component, while others strongly disagreed. A few studies compromised the debate and concluded that the presence of Li₂CO₃ might be conditional on both electrolyte composition and cell cycling history. For example, there was a report that Li₂CO₃ was the only major interphasial species identified on graphite after being cycled in an LiTFSI-based electrolyte, while a mixture of both semicarbonate and Li₂CO₃ would be found with an

electrolyte based on a variation of LiTFSI, lithium bis(ethanesulfonyl)imide, or LiBeti. On the other hand, some researchers reported that Li_2CO_3 was observed only on aged graphite electrodes, and no Li_2CO_3 could be detected on freshly cycled graphite. A further discrepancy was reported more recently that LEMC is the major interphasial ingredient, the identification of which needs meticulous control of the moisture level in the characterization environment.

The DFT calculations tend to support the suggestion that the two-electron reductive pathway for carbonates is less likely because of the high energy barrier of 0.5 eV, hence semicarbonate should be favored. However, this barrier might not be high enough to make semicarbonates the exclusive interphasial component, thus a reasonable consequence would be mixtures of semicarbonates and Li_2CO_3 . Other calculations showed that a two-electron reduction mechanism does not necessarily produce Li_2CO_3 ; instead, in the multiple step process following the initial release of CO, the fate of the glyoxide could lead to CO_3^{2-} , CO, alkenes, alkene dicarbonates (such as LEDC) and even polymeric species.

Edström *et al.* attributed this difference to experimental errors.⁴⁵ They noticed that most researchers who employed XPS to study interphasial compositions did not use hermetically sealed sample vessels, hence artifacts arose during the electrode recovery from the cycled battery and the preparation and transport of the electrode samples into the vacuum sample chamber of the XPS instrument, where the ambient moisture instantaneously turns semicarbonates into Li_2CO_3 . In fact, the source of Li_2CO_3 is not confined to semicarbonates. For example, Li_2O , which is also an interphasial ingredient often detected, could also lead to Li_2CO_3 by reacting with CO_2 in the atmosphere if the electrode sample is not handled with rigorous exclusion of moisture and air.

16.6.6.2 Over Fluorides

LiF was another interphase ingredient that raised controversy. As the element most resistive towards both oxidation and reduction, fluorine should be a desired ingredient for both SEIs and CEIs, and this rationale seems to be supported by the discovery of LiF in most interphases. However, the fluorine content in an interphase has been a complicated issue, regarding which there have been numerous conflicting reports.^{32,46-49}

Early efforts at forming effective interphases recognized the solvent decomposition as the main chemical source of SEI on a

graphitic anode, which includes semicarbonates ($\text{RO}-\text{CO}_3^-$), carbonates (CO_3^{2-}), alkoxides, oxalates, oxides and polymeric species. In the associated literature, fluorinated species such as LiF or fluorophosphates (PO_xF_y), although found universally throughout SEIs, were often considered to be harmful ingredients in interphases, as they might have been the inevitable consequences of the hydrolysis of the labile fluorinated salt anions (PF_6^- , BF_4^- or AsF_6^-). This belief was supported by the knowledge that LiF in its bulk state is an excellent insulator to both ionic and electronic transport, hence its presence can only make the interphase less conductive to Li^+ . In those cells that failed because of high impedance, over-fluorinated interphases were often identified, leading to the belief that fluorides are undesirable interphasial ingredients.

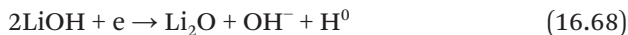
However, other studies, especially those focused on new battery chemistries, started to reverse the above negative impression of fluorides. In most cases, electrolyte systems that could effectively support these aggressive chemistries (cathode materials based on high-voltage or high-nickel layered oxides, or conversion reaction metal fluorides and oxide, or anode materials based on Li^0 or Si^0) often contain rich sources of fluorine, either in the form of salt anions at high concentrations, or in the form of solvent molecules that bear fluorine substituents. These fluorine sources in the electrolyte compositions eventually made their way into the interphases on both sides, and the form of the fluorides included both LiF and organic fluorinated species. The characterization found that most of these fluorinated compounds exist on the nanoscale, in either crystalline or amorphous forms. This observation might imply that the above controversy regarding whether one should introduce fluorinated species in interphases is actually not the essence of the problem. In addition to the identity of chemical composition, equally important are how these fluorinated species exist and are distributed in the interphase, or how they are arranged and interact with other species in the interphase. This is the knowledge that constitutes a key knowhow for designing new electrolyte systems for aggressive battery chemistries of the future, but it is also the knowledge that the battery and materials research community do not possess so far.

16.6.6.3 Over LiH

Lithium hydride (LiH) is a mysterious interphasial component that remains little explored as of 2022.^{50–52} In this species, the hydrogen atom bears a negative charge (*i.e.* H^-), hence it differs from all

hydrogen sources in the electrolyte, no matter whether inorganic (H_2O , LiOH , LiHCO_3) or organic species (C–H in all carbonate solvents and additives), in which the hydrogen atoms more or less are positively charged (*i.e.* H^+ or $\text{H}^{\delta+}$). Hence the formation of LiH must occur on the anode side *via* a reductive process.

Among the diverse reductive decomposition processes on the anode, there is indeed a possibility that a hydrogen in organic species receives an electron from the electrode and becomes a hydride, but this process must compete against other reduction processes, where the electron goes to the more electrophilic sites, such as the carbon next to an oxygen [eqn (16.12) and (16.44), for example], and especially those carbons in a carbonyl functionality. In the energy diagram, the reduction of a C–H is significantly disfavored by the thermodynamics as compared with these ethereal or acyl cleavages, while a positively charged hydrogen such as H^+ or $\text{H}^{\delta+}$ must experience an intermediate state of H^0 , *i.e.* a hydrogen atom or hydrogen gas, before it can be reduced to a negatively charged hydride. The more probable source for hydride formation would be the H^0 already formed in the electrolyte system that has been generated from various active protons in water or LiOH :



The generated H^0 species such as hydrogen gas then reacts directly with Li^0 and is reduced to hydride:



In fact, this was exactly the commercial pathway of synthesizing LiH, except that the reaction has to be conducted at high temperatures ($>300^\circ\text{C}$), where lithium metal is in the molten state.

But does this reaction occur at room temperature and in a battery environment?

Thermodynamically, the above reaction seems impossible at ambient conditions because, if examined under standard conditions, *i.e.* 298 K, 1 atm pressure and activities for all species involved being 1.0, the Gibbs free energy of formation ($\Delta_f G$) associated with this reaction is not negative, owing to the mediocre $\Delta_f G$ for LiH ($-68.3 \text{ kJ mol}^{-1}$)

and the high $\Delta_r G$ for both Li^0 (-127 kJ mol^{-1}) and H_2 (-407 kJ mol^{-1}). However, under electrochemical conditions, and especially in a battery environment and in interfacial confinement, the prediction from thermodynamics based on the standard Gibbs free energy does not necessarily hold true. For example, the hydrogen participating in the reaction in eqn (16.69) should be generated from the reduction of water or LiOH interfacially and *in situ*, thus existing in a rare form of atomic-state hydrogen, the reactivity of which towards lithium metal could deviate from what is predicted from thermodynamics. Besides, the direct electrochemical reduction of such atomic hydrogen without involving Li^0 is also possible:



By exposing the fresh lithium metal to hydrogen gas in a non-aqueous electrolyte and then examining the surface using FTIR spectroscopy, Aurbach and colleagues found that LiH may indeed have been formed, no matter *via* which pathway the reaction took place.⁹⁷ More direct evidence came from some recent studies. For example, on a metal oxide conversion reaction material (ruthenium oxide, RuO_2), LiH was observed when the materials were discharged down to low potentials ($\sim 0.8 \text{ V vs. Li}$), and this was attributed to the electrochemical reduction of LiOH ; or when Li^0 was deposited from ester-based electrolytes and then examined by cryogenic electron microscopy (cryo-EM), where some dendrites were identified as consisting entirely of LiH . However, other studies employing a similar cryo-EM technique or quantitative chemical titration technique did not find any LiH , the dendrites being simply Li^0 nanowires covered with SEIs. Synchrotron-based X-ray diffraction (XRD) and pair distribution function analyses have also been applied to resolve this mystery and it was found that very likely LiH and LiF coexist as a solid solution ($\text{LiF}_{1-x}\text{H}_x$), and the close lattice parameters of the two makes the effort of differentiating difficult. Hence some of the previous studies may have mistaken LiH as LiF . Much more effort is needed for the eventual confirmation or falsification of the presence of LiH in interphases.

Finally, it should be pointed out that LiH , even if it is actually formed by one of the above processes on the electrode surface, is a metastable chemical, which could easily be converted to H_2 or H^0 if there is moisture or oxygen in the electrolyte system. This is likely to have been responsible for the elusiveness and the controversy.

16.6.7 How Working Ions Travel Across Interphases

This is a key feature of interphases that has never been well understood. So far, all knowledge about this critical property of interphases has been based solely on simulations, results from indirect experiments and speculation.^{53–55}

As discussed in previous sections, an interphase must insulate electrons and conduct working ions. Also outlined in previous sections are the major chemical ingredients that constitute interphases in lithium-based batteries, which include inorganic (LiF , Li_2O or Li_2CO_3), organic (oxalates, semicarbonates or alkoxides) and polymeric ($-[\text{CH}_2-\text{CH}_2-\text{O}-]_n$) species. However, these species are all well known to be ion insulators while in the bulk state, the only exception being the polymeric species, the ethylene oxide linkages of which can promote mediocre Li^+ conduction (normally 10^{-5} – 10^{-6} S cm $^{-1}$ at room temperature) *via* their own segmental motion. The minority presence of polymeric ingredients in most SEIs does not seem to be capable of ensuring a percolating network across the entire interphase, hence they cannot be expected to account for the ion transport across interphases. Further on, interphases with simple or even single compositions (such as LiF or Li_2O) have been found or formed, which can conduct Li^+ at a fast rate.

Simulations indicate that the ion conductivities (or ion diffusion coefficients) in all of these compounds are expected to be extremely low (Table 16.5). For example, at room temperature (25 °C), the diffusion coefficient of Li^+ in LiF , Li_2O and Li_2CO_3 is on the scale of 10^{-16} – 10^{-17} m 2 s $^{-1}$, which corresponds to ion conductivities of about 10 $^{-10}$ S cm $^{-1}$ or a similar order of magnitude.

Table 16.5 Calculated self-diffusion coefficients (D_i) and ion conductivities (σ) of selected interphasial ingredients.

Parameter	Interphasial ingredient		
	LiF	Li_2O	Li_2CO_3
D_i at 27 °C/m 2 s $^{-1}$	3.93×10^{-16} ^a	4.01×10^{-16} ^a	4.90×10^{-16} ^a 8.4×10^{-16} ^b (1.1×10^{-11}) ^c
σ /S cm $^{-1}$ ^a	1.46×10^{-9} ^d	1.49×10^{-9} ^d	1.83×10^{-9} ^d (4.11×10^{-5}) ^e

^aSource: ref. 77.

^bSource: ref. 54.

^cThe self-diffusion coefficient if Li^+ adopts the maximized non-stoichiometric coordination state as depicted in Figure 16.6.

^dCalculated from ref. 77.

^eCalculated from ref. 54.

On the other hand, lithium-ion batteries are known to be able to function at extremely high power densities (up to 10^4 W kg^{-1}), which implies that interphases should be quite conductive to the working ion.

We now have an obvious paradox: how could a lithium-ion battery support a high rate of charge and discharge in the presence of SEIs and CEIs that are constructed with these poor ion conductors? On a molecular level, the question becomes: how do the working ions manage to navigate through a phase that should be extremely resistive?

An isotope-labeling experiment designed by Lu and Harris may have been the first attempt to understand this paradox.⁵³ Although it still did not give a molecular-level answer to these questions, it does tell us unambiguously that the interphases are much more conductive to Li^+ than expected from the bulk ion transport properties of these interphasial ingredients.

In this experiment, the researchers formed an SEI on a Cu substrate in an electrolyte that was based on a lithium salt enriched with one isotope, ^6Li , and then recovered and rinsed the Cu from the cell, followed by exposing the ^6Li -SEI to another electrolyte based on the same lithium salt but enriched with another isotope, ^7Li . It was observed that after a short exposure (minutes), extensive ^6Li - ^7Li exchange occurred. In other words, no matter whether these interphasial ingredients are LiF , Li_2O , Li_2CO_3 or organic species such as oxalates, semicarbonates and alkoxides, the majority of Li^+ ions inside these ingredients (up to 99%) are actually highly mobile and replaceable, which far exceeds what is expected from the low conductivities and diffusion coefficients from simulations.

This discovery led to the belief that the conduction of Li^+ across interphases should occur *via* a “knock-off” mechanism that in a certain sense is similar to the Grotthuss mechanism of H^+ conduction as described in Section 5.2.8 (Figure 5.14), except at a much slower pace and in the absence of synchronization with other Li^+ at remote distances.⁵⁴

Qi and colleagues performed computational simulations to gain further insight into such a mechanism. Using crystalline Li_2CO_3 as the template interphasial ingredient, they proposed a molecular mechanism, in which an Li^+ could minimize the energy barrier to its movement by maximizing its “solvation number” with the environment.⁹⁸ As depicted in Section 12.3 (Figure 12.8c), Li^+ can be considered “solvated” in a solid electrolyte, in which oxide (O^{2-}) or sulfide (S^{2-}) anions stabilize a naked Li^+ ion by coordinating with it, and this picture can be extended to interphases (SEIs and CEIs) as they are also by nature “solid electrolytes”. Therefore, in the static state, thanks to

the crystalline structure of the interphasial ingredients, an Li^+ should be stoichiometrically coordinated by the anions on the framework. In Li_2CO_3 , this coordination number is four (left sub-cell, Figure 16.6), as every Li^+ is arranged to be tetrahedrally coordinated by the four oxide anions. It should be noted that, strictly, the three oxygens in a carbonate anion CO_3^{2-} are not identical, with one connected with the sp^2 -hybridized carbon *via* a $\text{C}=\text{O}$ double bond and the other two bearing the formal charges connected with the same carbon *via* a single $\text{C}-\text{O}$ bond, but the conjugation structure of CO_3^{2-} and the subsequent resonance effect equalize these three oxygens, making each of them bear partial charges. Therefore, to a first approximation, we can treat all the oxygens in the Li_2CO_3 lattice as oxide anions.

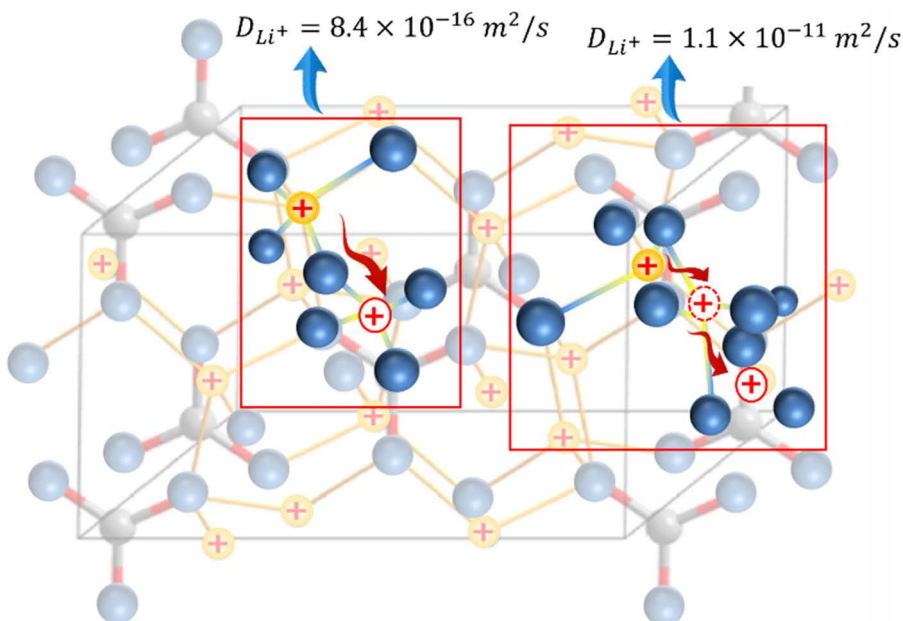


Figure 16.6 A molecular picture of how Li^+ transports across an interphase assuming that crystalline Li_2CO_3 is the sole interphasial ingredient. In the static state, an Li^+ is tetrahedrally coordinated by four oxide anions. Such an Li^+ can hop directly to the neighboring tetrahedral site (marked with a clear circle containing a + sign), which involves a transition state of high energy barrier (left sub-cell), or it can seek stabilization by coordinating non-stoichiometrically (marked with a clear circle with a broken line containing a + sign) with the oxide anions from the neighboring sites. The latter pathway comes with a much-reduced energy barrier and subsequently accelerated Li^+ diffusion coefficient (right sub-cell).

In such an Li_2CO_3 lattice, if an Li^+ ion needs to migrate or diffuse into another neighboring tetrahedral site, it has to break the coordination bonds in the solvation site temporarily, and the corresponding uncoordinated Li^+ represents a metastable and transition state of high energy. The calculated energy barrier ΔE for the above process would be ~ 0.54 eV, while the self-diffusion coefficient of Li^+ can be estimated using the following relation:

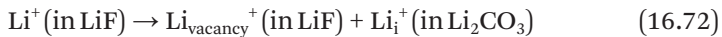
$$D_{\text{Li}^+} = \frac{\nu(\Delta x^2)}{2} e^{-\frac{\Delta E}{k_b T}} \quad (16.71)$$

where ν is the lattice vibrational frequency of Li_2CO_3 , estimated to be roughly 10^{13} Hz, and Δx^2 is the distance required for Li^+ to hop in each step, estimated to be 0.4906 nm based on the lattice parameters of the Li_2CO_3 crystal in channels in the (100) direction. The self-diffusion coefficient of Li^+ thus estimated is *ca.* $8.4 \times 10^{-16} \text{ m}^2 \text{ s}^{-1}$, which is expected from the ion transport properties known for bulk materials as discussed above.

In an alternative pathway, however, the migrating Li^+ does not hop directly between the sites and break off all its coordination relations with the environment. Instead, it remains “solvated” with the neighboring oxide anions even when leaving the tetrahedral site. In such a manner it could be simultaneously coordinated by more than four oxide anions in a distorted solvation environment that deviates from the stoichiometric solvation number of four (right sub-cell, Figure 16.6). This pentacoordinated transition state is significantly stabilized by the coordination of these extra oxide anions, which leads to a reduced energy barrier of 0.31 eV and an Li^+ self-diffusion coefficient ($1.1 \times 10^{-11} \text{ m}^2 \text{ s}^{-1}$) higher by five orders of magnitude.

In their subsequent efforts to simulate a situation closer to reality, Qi and colleagues considered a more heterogeneous rather than singular interphase that consists of two typical ingredients Li_2CO_3 and LiF , and found that additional acceleration of Li^+ transport could occur when these two ingredients interface with each other at nanoscale.⁵⁶ They found *via* calculation that LiF and Li_2CO_3 display entirely different ion transport behaviors when the chemical potential of Li^+ is in equilibrium with typical negative electrode materials such as lithiated Si or graphite: Li_2CO_3 generates excessive interstitial Li^+ (Li_{i}^+), whereas LiF generates a Schottky pair consisting of Li^+ ($\text{Li}_{\text{vacancy}}^+$) and F^- vacancies. Thus, when an LiF particle comes in contact with an Li_2CO_3 particle, a defect reaction driven by the chemical potential difference of the two materials leads to transfer of Li^+ from

the LiF phase to the Li_2CO_3 phase, creating a space-charge region at the junction of the two phases:



In this interfacial region, enrichment of both Li_i^+ and $\text{Li}_{\text{vacancy}}^+$ occurs along the grain boundary between LiF and Li_2CO_3 particles (Figure 16.7). According to calculation, the concentration of major charge carriers (Li_i^+ at the Li_2CO_3 side) would be higher by two orders of magnitude than in the bulk of these materials, hence the high ion transport across interphases could very likely occur along the interfacial regions or grain boundaries of these heterogeneous materials.

Such a space-charge effect fades exponentially with the distance away from the interfacial region between the two materials. Therefore, in order for the ion transport to benefit from such a defect effect, one would naturally come to the conclusion that each interphasial component needs to maximize its contact with other components. The ideal contact situation would be nano-particles of both ingredients.

The above molecular picture of how ions transport across the interphases is partially confirmed by experiments, in which an artificial SEI consisting of nanocrystalline LiF and Li_2CO_3 was fabricated on an Si anode using radiofrequency deposition, and the maximum ${}^6\text{Li}-{}^7\text{Li}$

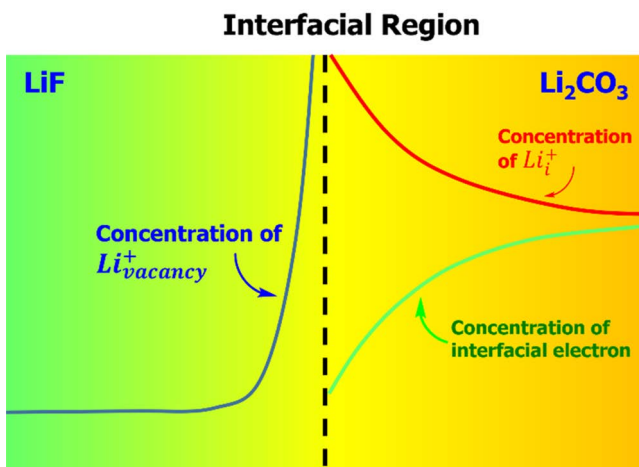


Figure 16.7 The interfacing of two different materials creates excessive charge carriers along the grain boundaries between the particles, which may be responsible for the high ion transport across the interphases. Here LiF and Li_2CO_3 are used as two template interphasial ingredients.⁵⁶

exchange, which can be used as an indirect indicator of Li^+ conductivity within the SEI, was found to occur when the ratio of these two ingredients was nearly 50% each, where maximum interfacing between LiF and Li_2CO_3 occurs.

One additional and more important inference from the above work is that a composite interphase consisting of mixed ingredients should be more ionically conductive than an interphase of singular composition, because the above space-charge effect could only occur between different materials. This inference is consistent with the discovery that most successful interphases (as evidenced by low resistance and effective protection during electrochemical cycling of the cells) were found to consist of chemically diverse ingredients intimately mixed at the nanoscale.

So far, the above molecular picture of working ions navigating across the interphases is the fruit of simulation and speculation, and any direct experimental proof is still difficult to obtain. This is an area of great importance that requires more investment of resources and attention, because a molecular understanding would provide precise and essential guidelines for designing new electrolyte chemistries and interphases.

16.6.8 How Interphases Evolve

Although we stated in Section 16.2 that, unlike two-dimensional and transient interfaces, the chemical composition and morphology of three-dimensional interphases are “permanent”, in fact such permanency is relative. All interphasial ingredients, whether inorganic or organic, demonstrate varying degrees of instability against dissolution and chemical and electrochemical decomposition, which can all be activated and accelerated thermally when the temperature rises. The cell chemistries also often deviate from the designed pathways and generate impurities such as moisture and acids, which further triggers a series of parasitic reactions. Therefore, the actual interphasial chemistry and morphology are constantly evolving on a time scale comparable to the lifespan of the cell. Some of these processes have been discussed in previous sections, but others remain little understood and require further investigation.

On the other hand, instead of the microscopic and mechanistic approaches, one could also view the degradation mechanism of interphases from a macroscopic and statistical perspective. Since the interphase stability (or instability) is inevitably correlated with the reversibility (or irreversibility) of the cell chemistry, theoretically it is

possible to know how an interphase evolves by quantitatively monitoring the rate at which the cell degrades. This perspective was realized by the work of Dahn and co-workers, who developed a high-precision coulometric technique to quantify the exact loss of the active lithium inventory in lithium-ion batteries, and hence discovered a square-root rule that governs the growth of interphases in the cell:⁵⁷

$$\frac{dx}{dt} = \sqrt{\frac{k}{2}} t^{-\frac{1}{2}} \quad (16.73)$$

where x is the hypothetical thickness of an idealized interphase and k is a constant for a given electrolyte-electrode system and temperature. In other words, although the formation of an interphase is supposed to insulate the electron tunneling and prevent the electrolyte from reacting with the electrodes at extreme potentials, this ideal insulation and protection of interphases never exists, hence the growth of the SEI never really stops after its initial formation. It just slows down following the square-root relation shown in eqn (16.73), and such growth continues through the entire lifespan of the cell.

Of course, what eqn (16.73) tells us is just the rate of interphase evolution. It does not tell us anything about the chemistries or electrochemistries behind the relation. It has been speculated that, in typical lithium-ion batteries, most of the interphase evolution occurs at the anode, although when the cathode potential is above 4.5 V, or when the cell is operating at elevated temperatures (>50 °C) or during long-term cycling, parasitic reactions on the cathode surface could dominate, as revealed by impedance, spectroscopic and high-precision coulometric studies.

16.7 Mechanism of Formation of Interphases: Solvation-Interphase Correlation

The interphases are usually formed during the initial activation of the electrochemical cells, when the potentials of the electrodes are pushed to regions beyond the thermodynamic stability limits of the electrolytes for the very first time. Although such a formation process may not be completed during the first activation cycle and could possibly continue during the entire lifespan of the cell, as discussed in the previous section, what happens during this fateful cycle is still doubtless of ultimate importance, as the initial chemistry, morphology and architecture that come into shape in the initial cycle would

directly determine the eventual interphasial chemistry, morphology and architecture after a certain evolution. Understanding the formation mechanism not only helps us to predict better what interphase chemistry to expect from a certain electrolyte composition but also, more importantly, it allows us to design new electrolytes and interphases for future electrochemical devices.

In Section 16.6.1.1.1 (Figure 16.4), we briefly touched on one key aspect of interphase formation mechanisms when discussing why certain carbonate molecules are preferentially reduced over others at the anode surface, that is, the interaction of these preferred molecules with Li^+ plays a critical role in destabilizing them against electrochemical reduction. From another perspective, *i.e.* the perspective of how an interphase is formed when a solvated ion approaches the electrode surface, the same picture in Figure 16.4 actually implies an intrinsic correlation between the electrochemistry's ion solvation sheath structure and the interphase chemistry. Furthermore, in a broader context, such a “*solvation–interphase correlation*” reflects a universal phenomenon in any electrochemical device, *i.e.* when a solvated working ion (assumed to be a cation here as an example) traveling from the electrolyte bulk and approaching an electrode surface (assumed to be an anode here as an example), the solvent molecules in its solvation sheath will also be there because they are “kidnapped” by the Coulombic field of the working ion.^{18,19,58–60} The presence of these solvent molecules within the primary solvation sheath of the working ion naturally affects the electrode/electrolyte interfacial structure (Figure 16.8), which should predict the eventual interphase chemistry, because it is these solvent molecules that ultimately become the precursors of interphasial ingredients that have been discussed in the previous sections. It should be noted that in Figure 16.8 the presence of a counterion (anion) is deliberately neglected for clarity, but one should remember that in the interfacial region electroneutrality is no longer obeyed, hence the anion population in the interfacial region, when the electrode is negatively polarized, should be naturally decimated. The situation would reverse if the potential of the electrode is reversed.

16.7.1 Interfacial Structure

When an electrode is polarized but with potential still residing within the thermodynamic stability limits of the electrolyte as defined by the HOMO or LUMO, there would be no Faradaic reactions in the cell and no charge transfer across the electrode/electrolyte interface.

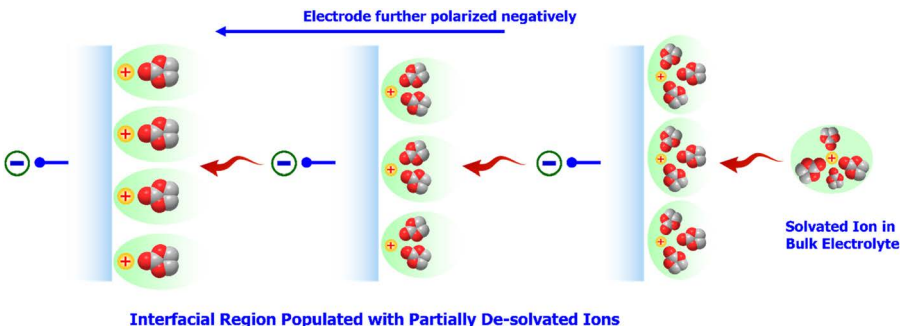


Figure 16.8 An intrinsic correlation exists between the ion solvation structure, a bulk property, and the interfacial structure at the electrode surface. In the illustration, the working ion is assumed to be a cation, which is solvated preferentially by EC molecules (as for Li^+ in typical lithium-ion battery electrolytes), and the electrode is the anode that is negatively polarized. Apparently the interfacial composition and structure closely depend on not only the electrode potential shift but also the ion solvation sheath structure.

However, the applied electric field induces ion transport within the bulk electrolyte, and the solvated ions travel to the electrode surfaces either along or against the field, depending on the sign of their charge. The ions, together with their solvation sheaths if there are any, arrive at the electrode/electrolyte interfaces and subsequently assemble into an interfacial structure (Figure 16.8). This is the two-dimensional interface that we discussed in Chapter 6 as electrified double-layer, and that we attempted to define in a relatively quantitative manner in Chapter 15, but in those discussions we deliberately ignored the presence of an ion solvation sheath, while simply treating ions as point charges. Now we are revisiting the situation by considering the presence of an ion solvation sheath, and the effect of the solvation sheath structure on the interface.

While both the structure and composition of such an interface are transient and dynamic, with a strong dependence on the potential of the electrodes and also the electrolyte composition, it is apparent that an intrinsic correlation exists between the solvation sheath structure of the ions and the interfacial structure and composition.⁶¹ We considered the former in Chapter 12 and learned that, in typical lithium-ion battery electrolytes, the solvation of Li^+ by mixed carbonate solvent molecules is not even. Instead, a strong bias exists for the solvent molecules, as Li^+ prefers cyclic carbonate molecules such as EC or PC over acyclic carbonate molecules such as DMC or EMC (Section 12.2.3,

Figures 12.3 and 12.4). A logical inference is that such a preference should also be inherited by the interfacial structure, as illustrated schematically in Figure 16.8. This selective enrichment of one solvent molecule over others at the electrode/electrolyte interface is a direct result of the correlation between ion solvation and interface.

It has been experimentally difficult to achieve direct observation of interfacial structures, mainly owing to their transient and dynamic nature. However, a recently developed innovative technique based on secondary ion mass spectrometry (SIMS) makes it possible to monitor directly the interfacial structure established at the interfaces between liquid electrolyte and solid electrode as a function of different potentials. The “snapshots” of the interfacial assembly thus obtained by piecing together the fragments as detected by mass spectrometry confirmed the concepts described in Figure 16.8.⁶²

Further confirmation came from molecular dynamics simulations, which is a perfect tool to look at the ion–ion and ion–solvent interactions at electrode/electrolyte interfaces as a function of both applied potential and electrolyte composition (especially salt concentration). It was found that in a typical lithium-ion battery electrolyte consisting of LiPF₆ dissolved in a 30:70 mixture of EC and DMC, the surface concentrations of the cation (Li⁺) and anion (PF₆⁻) distinctly intensify as the potential of the electrode is pushed negatively or positively, respectively (Figure 16.9).^{61,63} Meanwhile, the preferred solvent molecule, which is EC for both cation and anion, simultaneously enriches at the interfaces.

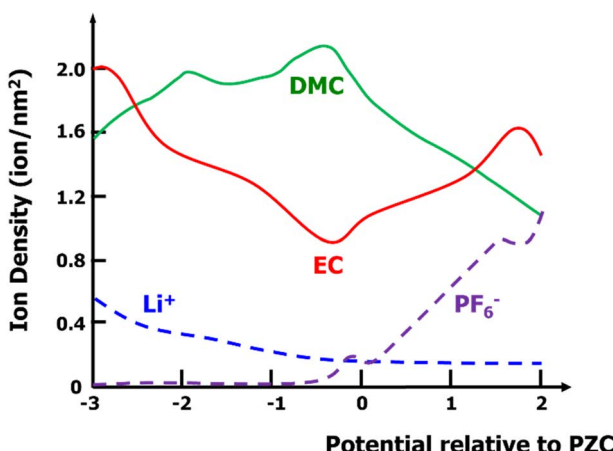


Figure 16.9 Distribution of cation, anion and cyclic (EC) and acyclic (DMC) carbonate molecules at the electrode/electrolyte interface as a function of the potential applied.⁸¹

One interesting finding from the simulation is that, when the salt concentration increases into the so-called “super-concentration” regime, the above distinct distribution of cations and anions according to the Coulombic attractions becomes less pronounced. In other words, even when an electrode is negatively polarized, the opportunity for an anion to be found in the interfacial region is still high, simply because the anion population in the bulk is too high for the electrode to repel. This raises the possibility of altering the interfacial structure and even interphasial chemistries, if the anion is a desired contributor to interphasial chemistry. This concept has been the theoretical foundation for the design of these electrolyte materials with extremely high salt concentrations such as “water-in-salt” electrolytes.

The above description of the correlation between ion solvation and interfacial structure should be universally applicable to all electrochemical systems, no matter whether an interphase is formed eventually or not. However, if an interphase is formed, its chemistry must have a connection with the interfacial structure discussed above.

16.7.2 Interphasial Chemistry

When an electrode is further polarized to the potential where the working ion starts to experience charge transfer, or beyond the thermodynamic stability limits of the electrolyte as defined by its HOMO or LUMO energy levels, whichever comes first, a Faradaic reaction occurs. At this instant, there could be two competing pathways for the Faradaic reaction to proceed. Let us again take the negatively polarized electrode and the interfacial structure as depicted in Figure 16.8 as an example. An electron provided by the electrode could either go to the working ion assembled in the interfacial region, leading to the reduction of the ion to a lower valence state, or the electron could go to the solvent molecules within the solvation sheath of this ion that is also assembled in the interfacial region (Figure 16.10).

In the first pathway, the reaction normally leads to deposition of the metal on the electrode surface, but exceptions exist if the reduced form of the working ion is also soluble in the electrolyte, hence it would diffuse away driven by its concentration gradient. Such examples include Fe^{3+} coordinated in ferrocene. Further complications arise if there is intercalation or an alloy host at the anode side, where a slightly different mechanism is involved that will be discussed in the next section.

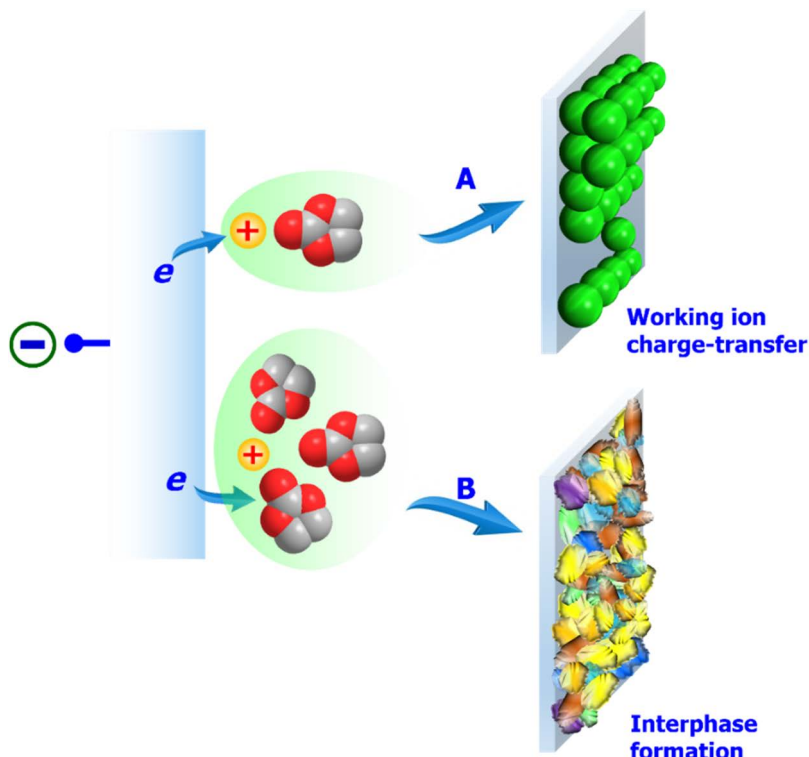


Figure 16.10 Once the potential of the negatively polarized electrode wanders further beyond the electrochemical stability limits of the electrolyte, a Faradaic reaction occurs, which could proceed via two distinct pathways: (A) charge transfer of the working ion already assembled in the interfacial region or (B) decomposition of the solvent molecule within the solvation sheath of the working ion. The former usually corresponds to the reversible cell reaction and the latter to the formation of an interphase. It is apparent that the interfacial structure as depicted in Figure 16.8 has a significant impact on both reaction pathways.

In the second pathway, the solvent molecule is reduced and usually produces an anion, such as a semicarbonate ($R-CO_2-O^-$), carbonate (CO_3^{2-}), oxalate [$O-(CO)_2-O^-$] or fluoride anion (F^-), which could exist in the form of a salt of the working ion [such as $R-CO_2-OLi$, Li_2CO_3 , $LiO-(CO)_2-OLi$ or LiF], and if the reduction product satisfies the requirements as discussed in Chapter 8, *i.e.* it is a solid, and it has an electrolyte nature (conductive to working ions but an insulator to electrons), this pathway leads to the formation of an interphase.

For Li^+ , pathway A in Figure 16.10 almost never precedes pathway B, because of the extreme eigenpotential of Li^0 . In other words, it is almost impossible to find an electrolyte solvent that could remain thermodynamically stable at the potential where Li^+ is reduced to Li^0 . For other ions with less negative reduction potentials, such as Cu^{2+} or Zn^{2+} , it is possible to formulate electrolytes so that the deposition of the corresponding metals could occur without the formation of interphases.

16.7.2.1 Interphase Formation in a Lithium-ion Battery: A Special Case

For lithium-ion batteries, or any batteries that employ either an intercalation or alloy material as structural host to accommodate the working ion, the interphase formation mechanism represents a special case that differs from those depicted in Figure 16.10, because in those chemistries charge transfer no longer occurs between the electrode substrate and the working ion directly, but rather between the electrode substrate and the intercalation or alloy host, which serves as the actual recipient or donor of electrons during the reduction or oxidation process, respectively. In other words, the electron bands within these intercalation or alloy host materials are the reservoirs for electrons that enable the reversible charge transfer to occur. In batteries using these intercalation or alloy hosts, the working ion is supposed to remain ionic, or at least retain most of its ionic state. It was this nature that gave the “lithium-ion battery” its name, and differentiates it from lithium-metal batteries.

Therefore, for any of those “X-ion” batteries, the Faradaic reactions now must involve a third party, *i.e.* those intercalation or alloy hosts whose structural characteristics will add complexities to the two basic Faradaic reaction pathways described in Figure 16.10. Let us again take the anode host material of the lithium-ion battery, *i.e.* graphitic carbon, as an example, because it has been the target of intensive investigations, and most of our knowledge about interphases was accumulated therefrom. In fact, it was the investigation of the SEI formation mechanism on a graphitic structure that led to the discovery of the solvation–interphase correlation.

In Section 10.3.2.1, we learned how the graphitic structure accommodates Li^+ when the potential of the graphitic anode is polarized negatively. An electron injected from the external source eventually goes to the p-orbitals of the sp^2 -hybridized carbon atoms, instead of going to the Li^+ and reducing it to Li^0 . The “reduced” graphitic

framework then accommodates the incoming Li^+ according to the following relation:



in which the maximum Li^+ concentration allowed in the graphite is LiC_6 . Since the electron from the external power source now sits in the p-orbitals of the sp^2 -hybridized carbon atoms, the final product LiC_6 should be written as $[\text{Li}^+\text{C}_6^-]$ to reflect the ionic nature of the Li^+ or, more precisely, as $[\text{Li}^{\delta+}\text{C}_6^{\delta-}]$ because Li^+ is not 100% ionic owing to some partial charge transfer as revealed by solid-state NMR studies.

Nevertheless, pathway A in Figure 16.10 must be modified accordingly to reflect the role of the intercalation host.

As we have also learned, before an Li^+ ion can be intercalated into the graphitic structure, the potential of the graphitic anode will induce the reductive decomposition of the electrolyte, if such an electrolyte is based on carbonate molecules. The solvent decomposition leads to the formation of an SEI that would only allow the intercalation of naked (unsolvated) Li^+ into the graphite, which was depicted as Scenario III in Figure 10.7.⁶⁴ In other words, when an Li^+ ion starts to intercalate into the graphitic structure, there would have been an SEI covering the edge sites of the graphitic material, and the Li^+ therefore has to migrate across the SEI in order to be intercalated. Hence the two electronation pathways shown in Figure 16.10 are no longer *parallel*, but instead *sequential* (Figure 16.11). In either process, the charge transfer occurs between the electrode substrate and the intercalation host. The p-orbitals of the sp^2 -hybridized carbon atoms serve as a reservoir for the electrons, which donates electrons to the solvent molecules during the interphase formation, or retains electrons when interacting with the intercalated Li^+ .

16.7.2.1.1 The Transient State Before Formation of an Interphase: Co-intercalation

For a researcher studying the interphase formation mechanism, the process that is of most importance is the exact sequence of events between states (1) and (2) in Figure 16.11.

To understand this transient state, one needs to perform a thought experiment, and recall the three scenarios of a graphite

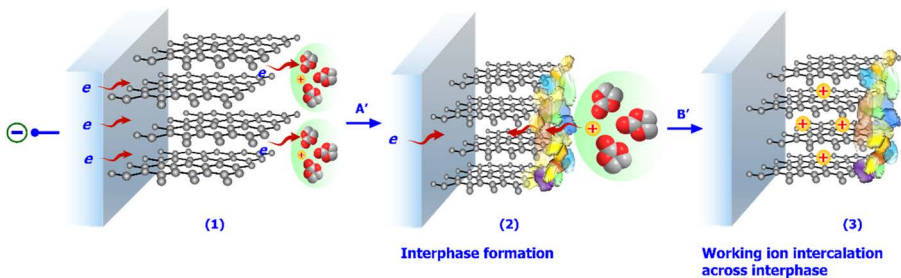
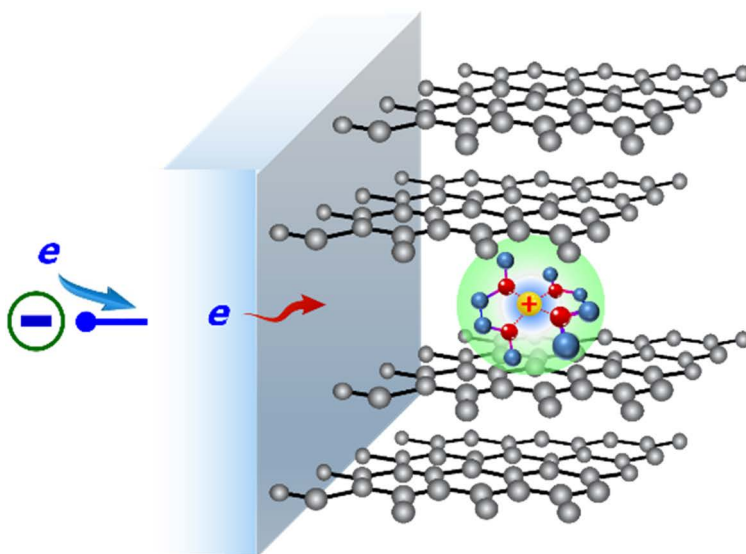


Figure 16.11 SEI formation on a graphitic anode followed by Li^+ intercalation into the graphitic lattice. The p-orbitals of the sp^2 -hybridized carbon atoms serve as a reservoir for the electrons. In step A', the carbonate molecule within the primary solvation sheath of Li^+ (EC) receives the electron from the reservoir, is reductively decomposed and becomes part of the SEI. In step B', the Li^+ migrates into the graphitic structure and interacts with the carbon atoms whose p-orbitals receive the excess electrons.

anode that is negatively polarized in electrolytes (Figure 10.7). In Section 10.3.2.3, the narrative may sound as if these three scenarios are independent situations that are not related to each other, but upon further consideration one cannot help noticing that, at the instant of electrode charging, all solvated cations, no matter what solvent molecules they carry in the primary solvation sheath, will behave similarly by migrating towards the graphite, and then approaching the edge sites. This is because the graphitic structure is highly anisotropic, and the electrons can flow most effectively only along the in-plane direction. This principle in fact applies to any electrode that possesses lattice structures consisting of ion-conducting tunnels or channels.

A logical inference from the thought experiment based on such anisotropy is that all these solvated ions, driven by the applied electric field, would at a certain instant arrive at the edge sites, and attempt to enter the graphitic structure *via* these edge sites. Hence these three scenarios merely reflect the different fates of these solvated ions once they start entering the edge sites, and the difference in their fates should be caused by the different solvent molecules in their solvation sheaths.

Based on this logical connection among all three scenarios with a common transition state, Scenario II in Figure 10.7 in fact represents a special “living fossil” for the interphase formation process, because among the limited number of ternary co-intercalation compounds (Scenario II), the solvent molecules used in the electrolytes are mostly ether based (Figure 16.12), which are known for a



Scenario II: Stable co-intercalation, where solvent molecules are ethers or those strongly reduction-resistant

Figure 16.12 Scenario II depicted in Figure 10.7 in fact provides a “snapshot” of the transient states of the interphase formation scenario, because ether molecules are strongly resistant against reduction, which ensures the stability of this transient state. Shown in the solvation sheath is dimethoxyethane, a well-known ether solvent molecule that forms a solvation cage with Li^+ . The co-intercalated species is drawn as $[\text{Li}(\text{DME})_2]^+$, because it is the most stable solvated species as detected by ESI-MS (as depicted in Figure 12.3), but the actual composition of the co-intercalated species remains unclear.

strong resistance against reduction. Hence there is sufficient reason to hypothesize that the same ternary co-intercalation compounds must also have been formed by carbonate esters and other solvent molecules, but these solvent molecules are too reactive in the reductive environment, and their different decomposition behaviors lead them towards different fates as represented by Scenarios I and III. In a more precise description, Scenarios I (exfoliation) and III (interphase formation) are merely the results of different stabilities of the solvent molecules in the primary solvation sheath of Li^+ .^{18,19}

This hypothesis has been convincingly proven by various electrochemical, spectroscopic and computational simulations, among which is the engineered competition between Scenarios I and III that

was deliberately induced by an electrolyte based on mixtures of EC and PC, which will be discussed in more detail in the next section,⁶⁵ and the capture by *in situ* XRD of the transient ternary graphite intercalation compound formed in PC.⁶⁶

Hence we can now argue that the interphase formation shown in Figure 16.11 (or Scenario III in Figure 10.7) actually experiences a transient co-intercalation state of solvated Li^+ , where the solvation sheath is populated by EC (Figure 16.13). An interphase is formed, because the EC molecules in the solvation sheath are activated by the Coulombic field of Li^+ for reduction as described in Figure 16.4, and the reduction products generated by EC happen to meet the requirements for interphasial ingredients: solid, ionically conductive, electronically insulating, and adhere to the graphite edge sites firmly. The interphase thus formed should penetrate slightly into the edge sites of the graphitic structure rather than being a simple layer of “cover up” on top of the graphite surface.

Likewise, the graphite exfoliation process shown as Scenario I in Figure 10.7 also experiences the same transient co-intercalation state of solvated Li^+ , where the solvation sheath is populated by PC (Figure 16.14). The PC molecules within the solvation sheath of Li^+ are also activated by the Coulombic field of Li^+ for reduction, but the reduction products of PC fail to meet these same stringent criteria for interphasial ingredients. Consequently, the graphitic structure is disintegrated by the fragments generated by PC (Figure 16.14).

Since the co-intercalation compounds involved in both Scenarios I and III are unstable and transient owing to the high reactivity of EC or PC, the direct detection of the presence of these transient states would be challenging, and requires the technique used to possess both structural and temporal resolution, *i.e.* to be capable

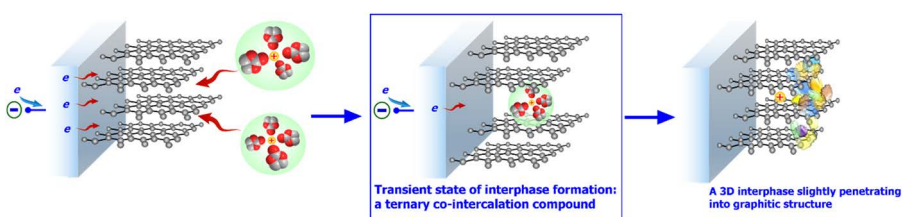
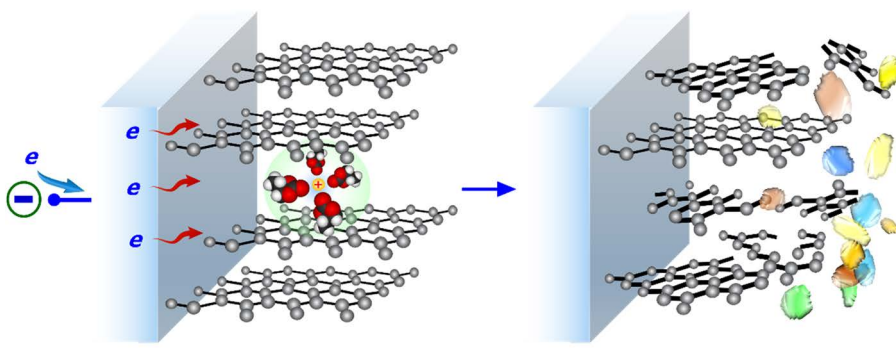


Figure 16.13 Formation of an interphase on graphitic material by EC is preceded by a transient state of ternary co-intercalation compound. The subsequent reduction of EC produces the necessary interphasial ingredients that seal off the edge sites of graphite. Such an interphase should penetrate slightly into the graphitic structure instead of just covering the surface.



Scenarios I: Unstable co-intercalation followed by exfoliation, where solvent molecule is PC

Figure 16.14 The exfoliation of graphite illustrated as Scenario I in Figure 10.7 also starts with a co-intercalation transient state, which can be captured by XRD if the scan is fast enough. In an actual battery, however, where the anode spends much more time at negative potentials, the PC molecules in the primary solvation sheath of Li^+ would be reductively decomposed, and the products failed to serve as effective interphasial ingredients. Eventually, the graphitic structure disintegrates, leading to Scenario I.

of capturing the structural characteristics of these co-intercalation compounds in both a precise and timely manner. Nevertheless, thanks to the intense efforts in the last decade, the above transient-state hypothesis of a co-intercalation intermediate preceding the interphase formation or exfoliation received more and more experimental evidence, such as the transient linear expansion of graphitic materials as measured by *in situ* dilatometry, the *in situ* electrochemical quartz crystal microbalance that can roughly weigh the mass increase before the interphase is formed, and the quantitative breakdown of the irreversible *versus* reversible capacities in the first lithiation cycle of the graphitic anode.

The most direct and convincing evidence came from a prominent discovery by Winter and colleagues, who performed a fast cathodic scan of a graphitic anode in a PC-based electrolyte, and managed to capture the transient formation of a ternary co-intercalation compound corresponding to what is depicted in Figure 16.14 using *in situ/operando* XRD.⁶⁶ When scanned at 10 mV s^{-1} between 3.0 and $\sim 0.50 \text{ V vs. Li}$, a new series of diffraction peaks appearing at $2\theta = 24^\circ$ and 27.5° revealed a much larger interlayer distance ($\sim 1.59 \text{ nm}$), which corresponded to the size of a solvated Li^+ ion with three or four PC molecules in its solvation sheath. Although a similar ternary

graphite intercalation compound has not been reported for EC-based electrolytes, very likely because of the much higher reactivity of EC when co-intercalated with Li^+ within a graphitic structure, one can reasonably infer that a similar mechanism must have been followed. It seems that the higher reactivity of EC requires an *in situ/operando* technique with a higher temporal resolution for real-time detection.

16.7.2.1.2 Preferential Solvation Leads to Preferential Reduction

An important message that we can take from the above hypothesized interphase formation mechanism is the role of ion solvation in interphasial chemistry. As we can see from the inference process illustrated in Figures 16.11–16.14, the Li^+ solvation sheath in fact dictates what solvent molecules are co-intercalated into the graphitic structure, and it is these co-intercalated solvent molecules that are electrochemically reduced between the graphene layers and subsequently become the precursors of the eventual interphase. In other words, the solvent molecules inside the Li^+ solvation sheath should predict the interphasial chemistry.^{18,19,65}

This is an important conclusion that should not be too surprising, because we have already briefly discussed how a bulk property such as solvation sheath structure could affect or even determine the interfacial and interphasial properties. Interphase formation on a graphitic structure specifically, and interphase formation on any anode surface in general, reflect the “solvation–interphase correlation”.

Since we learned in Section 12.2.3 that preferential solvation exists for Li^+ or other cations in electrolytes consisting of mixed solvent molecules, a new question now arises: would such a preference be inherited by interphasial chemistry?

The answer is positive, with mounting experimental evidence from diverse characterizations.

Zhuang and colleagues presented the earliest proof that EC might be selectively reduced. When comparing the FTIR spectra collected from an Ni surface that was negatively polarized to 0.50 V in a DMC-dominant electrolyte (LiPF_6 in 30 : 70 EC–DMC), they were surprised to see that the SEI formed on the Ni surface was almost identical with the standard reference sample of LEDC synthesized *in vitro*, while DMC seems to be completely excluded from the interphasial chemistry, despite its much higher concentration in the bulk electrolyte.^{14,67} As a follow-up, Xu further investigated this issue by applying NMR spectroscopy to a series of SEIs formed in electrolytes containing EC and DMC or EMC in various ratios. A similar conclusion was drawn that the interphases formed on graphite anodes were indeed dominated by

EC reduction products even when the acyclic carbonate populations were overwhelming.¹⁸ Naturally, such a strong preferential reduction of EC molecules over its linear counterparts is a consequence of the Li⁺ solvation preference in electrolytes, which was discussed in Section 12.2.3, and the 3D interphase formation mechanism driven by initial co-intercalation, which was discussed in previous sections.

Xu was the first to formally link ion solvation and interphasial chemistry in 2004 and 2007, respectively.^{5,18} Supporting evidence came later from diverse experiments, including different spectroscopic techniques including FTIR and solution NMR spectroscopy,⁶⁸ and also new approaches using isotope-labelled electrolytes and interphases that were examined by liquid and solid SIMS,^{63,69} and quantitative and *in situ/operando* EQCM accompanied by simulations.²⁵ Based on these systematic studies, it was proved that in non-aqueous electrolytes consisting of mixed carbonate molecules, cyclic carbonates such as EC or PC are always the preferred source of SEIs on graphitic anodes. This preference originates directly from the preferential solvation of Li⁺ discussed previously. Since most lithium-ion battery electrolytes have to rely on EC with little PC present, the SEIs in these batteries bear a heavy chemical signature from EC, and LEDC or its evolutionary form LEMC constitute the main chemical compositions of SEIs. This apparent link between the chemical compositions of the Li⁺ solvation sheath and the interphase serves as strong supporting evidence for the “solvation–interphase correlation” and also the interphase formation mechanism discussed above.

More confirmation of this correlation and mechanism came from studies on PC-based electrolytes, which are known to produce Scenario III after co-intercalating into graphitic structures.⁶⁵ Therefore, its failure to form a protective interphase and the pronounced exfoliation process could be leveraged by various researchers as a convenient “marker” to detect whether a protective interphase is formed, or how effective the interphase is. An interesting example was presented by Xu and colleagues, who polarized graphite negatively in a series of electrolytes consisting of EC–PC mixtures at various molar ratios, and used the relative ratio between irreversible and reversible capacities as a quantitative descriptor for both the “solvation–interphase correlation” and the tendency for preferential reduction.⁹⁹ They found that as the relative population of EC *versus* PC gradually increases, the graphitic anode obviously experiences a competition between Scenario I of exfoliation and Scenario III of interphase formation, with its interphasial chemistry switching from the preferential reduction of PC molecules within the Li⁺ solvation sheath to the eventual reduction of EC to a protective SEI.

A rather puzzling relation observed in that work is that the transition process from Scenario I, as marked by low Coulombic efficiency (~0%) of the first lithiation cycle, to Scenario III, as marked by very high Coulombic efficiency (~90%), is not smooth. Instead, a sudden change occurs at an EC:PC molar ratio of 80% (Figure 16.15), after which the interphase rapidly becomes effective in protecting the graphitic structure from exfoliation by PC.

What lies underneath this mysterious 80% threshold?

In Section 12.2.3, we discussed how to determine the Li^+ solvation sheath structure quantitatively using ESI-MS (Figure 12.3), and showed that EC is often preferred by Li^+ in its solvation sheath when mixed with linear carbonates such as DMC, EMC or DEC, but would become disfavored by Li^+ once there is PC in the system (Figure 12.4). Therefore, in an EC–PC electrolyte, both solvent molecules have to

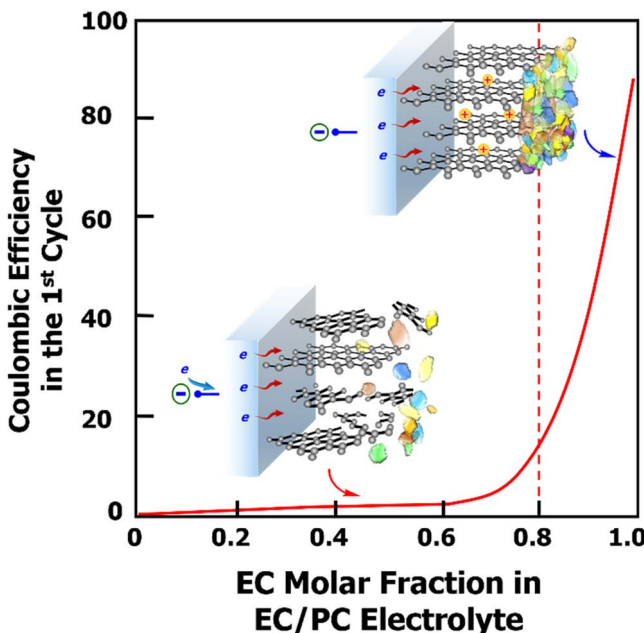


Figure 16.15 Dependence of the Coulombic efficiency in the first lithiation cycle of a graphitic anode in an electrolyte consisting of a mixture of EC and PC at various molar ratios. The poor Coulombic efficiency is caused by the exfoliation of graphite and extensive decomposition of the electrolyte solvent PC, and the high Coulombic efficiency (>70%) indicates effective protection of the graphitic structure by an interphase originating from EC. The transition state between the two extremes reflects the competition between the two solvents in the Li^+ solvation sheath.

compete with each other to enter the solvation sheath, and those in the solvation sheath would then be preferentially reduced on the graphitic surface *via* the transient states as shown in Figures 16.13 and 16.14, leading the graphitic structure to different fates. Hence the Coulombic efficiency curve in Figure 16.15 in fact is a reflection of the “solvation–interphase correlation”.

Applying the same ESI-MS technique, Xu and colleagues systematically mapped the change of solvation sheath structure in the above EC-PC electrolyte, and revealed a non-linear progression from a PC-dominated solvation sheath in the PC-rich composition towards an EC-dominated solvation sheath in the EC-rich composition (Figure 12.4).⁹⁹ This non-linearity, with a strong negative departure from the diagonal line representing non-preferential solvation, is apparently due to the stronger affiliation between Li^+ and PC. The most important discovery in this work was that, when the EC molar ratio in the bulk electrolyte reaches 80%, the Li^+ solvation sheath would consist of 50% EC and 50% PC (Figure 16.16). Therefore, an EC-dominant

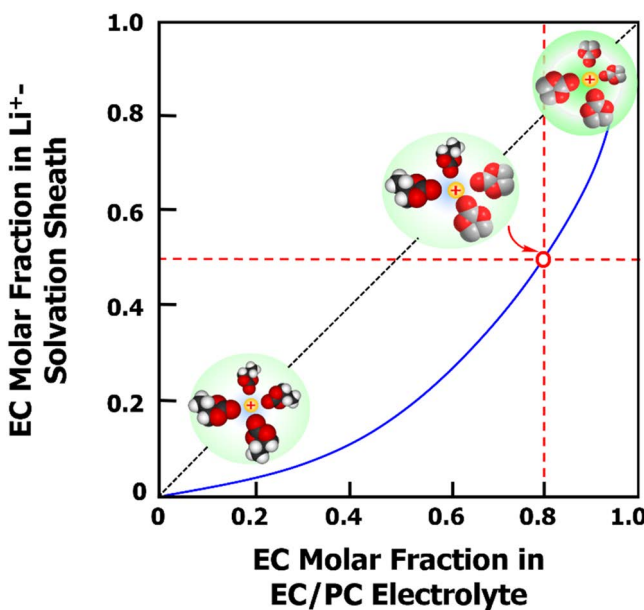


Figure 16.16 The “mysterious” threshold of 80% EC actually represent a turning point in the structure of the Li^+ solvation sheath, above which EC dominates the interphase formation. This serves as the most direct and quantitative support for the “solvation–interphase correlation”. Note that the EC molar fractions in the Li^+ solvation sheath were determined by ESI-MS as discussed in Section 12.2.3, Figure 12.4.

Li^+ solvation sheath is the key for effective interphase formation and rapid improvement of Coulombic efficiency as shown in Figure 16.15.

In most state-of-the-art electrolytes used in lithium-ion batteries, the use of PC is avoided, or at least kept to the minimum, because of its strong tendency to solvate Li^+ and the poor interphasial chemistries that it brings. On the other hand, in a typical electrolyte consisting of mixtures of EC with linear carbonate molecules, such as EC-DMC, EC-EMC, EC-DEC or higher order of mixtures, the Li^+ solvation sheath would be dominated by EC molecules as revealed by Figure 12.4, hence the SEIs formed on the graphitic surface by these electrolytes bear a heavy chemical fingerprint of EC, as represented by the LEDC or its descendant LEMC [Section 16.6.1.1.1, eqn (16.19)].

To change the interphasial chemistry, one needs to change the structure of the Li^+ solvation sheath. This can be done either by using new solvent molecules and additives or by changing the salt concentration so that a new chemical source for the interphase can be used, namely the salt anion.

16.7.2.2 Tailoring Interphase Chemistry by Altering the Ion Solvation Sheath Structure

The discovery of the “solvation–interphase correlation” provided us with a powerful tool to tailor interphasial chemistries.

When discussing SEI chemistry on an anode in Section 16.6.1.1, we learned that interphases are comprised of both organic and inorganic ingredients, with the former most likely from the reduction of solvent molecules, whereas the latter, especially LiF , from the reduction of the salt anion. On the other hand, in Section 10.3.2.5.2, we also showed that, thanks to the Coulombic attraction and repulsion, the solvated cations (which are often the working ions in most battery chemistries) would be more likely to enrich in the vicinity of a negatively charged electrode, whereas their counterions (anions) would be disfavored (Figure 10.10). Such enrichment of solvated cations and depletion of anions near the Helmholtz layers of an anode would naturally lead to an interphasial chemistry with more contributions from the reduction of solvent molecules rather than the reduction of anions.

One way to alter this preference is to increase the salt concentration, which actually sets the foundation for the super-concentration concepts.⁶⁰ The rationale behind this approach is that, within the limits allowed by the maximum solubility of a given salt, one dissolves as

much salt as possible, so that the discrete cation solvation sheath as suggested by Bernal and Fowler (Section 3.3, Figure 3.5) can no longer be formed because of the depletion of solvent molecules relative to the population of ions. Hence the classical three-layer solvation sheath has to be compressed, and anions are forced into the solvation sheath of the cations, forming various types of ion pairs or clusters. Such ionic complexes would carry an average lower formal negative charge or even partial positive charge, hence gaining a greater opportunity to approach the Helmholtz layers of an anode and to be reduced. The final result is an interphasial chemistry with higher contributions from the anion-derived ingredients.

This practice was first confirmed in PC-based electrolytes. Various lithium salts (LiTFSI , LiClO_4 and LiPF_6) at concentrations that are higher than the normal range of ~ 1.0 M were dissolved, and it was found that effective SEIs could be formed to allow stable and reversible lithiation of a graphitic anode in these PC-based or PC-rich electrolytes.^{70,71} Upon thorough characterization using FTIR, diffusion-ordered NMR and energy-dispersive X-ray spectroscopy, it was found that, once the LiPF_6 concentration has reached a certain level (3.0–3.5 M in this case), the Li^+ solvation sheath experienced a transition from solvent-separated ions to contact ion pairs or larger clusters (Figure 16.17). From a solvation perspective, this is equivalent to bringing the anions into the primary solvation sheath of the cation. Now assisted by its close interaction with the cation, the anion would have a greater opportunity to arrive at the Helmholtz layers in the vicinity of the negatively polarized electrode, and eventually be reduced at the electrode surface. For PC-based electrolytes containing high concentrations of LiPF_6 , this means the switching of interphasial chemistry from the PC reduction product LPDC to the anion reduction product LiF . The resultant interphase with a high LiF content is much more effective than LPDC, thus stabilizing the graphitic structure for the formation of LiC_6 (Figure 16.17).

The illustration in Figure 16.17 in fact represents a universal phenomenon in all these electrolytes containing fluorinated anions, which could be LiBF_4 , LiTFSI , LiFSI , etc.

Of course, such a phenomenon is by no means confined to carbonate-based electrolytes. Yamada *et al.* applied it to an acetonitrile-based electrolyte system, which successfully forms a protective SEI on a graphitic anode.⁷⁰ Xu and Wang even carried this practice one step further by dissolving an extraordinarily large amount of LiTFSI in water, which results in a significantly widened electrochemical

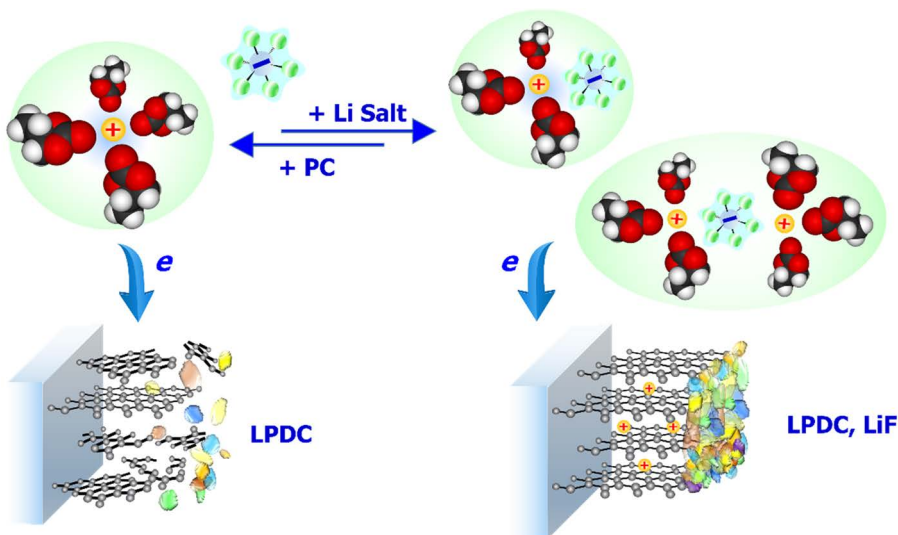


Figure 16.17 The increasing salt concentration forces the anion to enter the solvation sheath of the cation, resulting in various forms of ion pairs or ion clusters. The anions in these complexes face much lower repulsion from the negatively charged electrode, and would become a more pronounced contributor to the interphasial chemistry. Hence the PC-based highly concentrated electrolytes can protect the graphitic structure from exfoliation.⁷¹

stability window that goes far beyond the thermodynamic stability limits imposed by the water molecules.¹⁰⁰ This “water-in-salt” electrolyte approach has been pursued by both Xu’s and Yamada’s groups since 2015, and by other groups around the world in recent years, which eventually expanded the usable electrochemical stability window of aqueous electrolytes to the realm of >4.5 V. The essence of this work is constructed on the concept of the “solvation–interphase correlation”, which allows the solvation sheath structure of the working ion to be altered at high salt concentrations, so that the main contributor to interphasial chemistries is switched from solvent molecules to salt anions.

Before concluding this section, it should be emphasized that the transient state of co-intercalation and the related interphase formation mechanism are not confined to graphite only. Theoretically, they are universal for any electrode host of intercalation chemistries on the anode side. However, the “solvation–interphase correlation” may not be directly applicable on the cathode side, because the interphase formation process on a positively polarized electrode corresponds to de-intercalation of the working ion from the lattice structure,

hence what a working ion experiences is solvation, not de-solvation. Although preferential solvation of the working ions still exists at the electrolyte/cathode interface, the most preferred species on the cathode surface is now the anions, apparently because of the Coulombic attraction. Now facing the advantageous competition from the anions for the positions within Helmholtz layers, the solvent molecules no longer benefit from their interaction with the cations, hence their relative importance in determining interphasial chemistries fades accordingly.

On the other hand, we have been using the graphitic structure as a template to describe the interphase formation mechanism, not only because it is the most investigated electrode surface thanks to the commercial success of lithium-ion batteries, but also because graphite has been intensively studied as an intercalation host for various cations during the past century, and many of its interfacial characteristics are now well understood.

In a broader sense, the “solvation–interphase correlation” is still universally valid in the interphase formation mechanisms on other anode materials with structures different from graphitic, such as the “structureless” metal anode, where the “flat” surfaces of the metal electrode would induce partial desolvation of the working cations in the process of interfacial structure assembly, before those solvent molecules remaining in the solvation sheath of the working ions eventually receive electrons from the electrode, are electrochemically reduced, and become part of the interphase. This correlation has been leveraged in designing new electrolyte materials and interphasial chemistries for aqueous or non-aqueous rechargeable batteries using multivalent ions such as Zn^{2+} as the working ion, where a high salt concentration ensures the formation of an interphase to prevent the reduction of water molecules (Figure 16.18). Such anion-derived interphases, based on either fluorides (MF_2), carbonates (MCO_3) or oxides (MO) of the working cation, allows the migration of these multivalent ions to complete the reversible cell chemistries. However, as will be discussed in the next section, for most of those emerging battery chemistries based on multivalent working ions, super-concentration alone may not provide a sufficient solution, and direct interfacial engineering becomes necessary.^{72,73}

16.7.2.3 Tailoring Interphase Chemistry in Multivalent Ion Electrolytes

Projected as an alternative battery chemistry to lithium-ion batteries, aqueous zinc batteries have received intense attention during the last

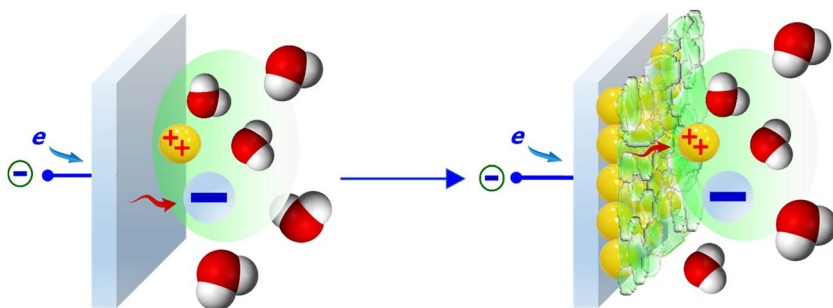


Figure 16.18 The “solvation-interphase correlation” applies universally to anode materials. For example, the aqueous electrolytes for bivalent cations such as Zn^{2+} follow a similar process of polarizing the solvation sheath of Zn^{2+} , reducing the component within this solvation sheath and forming an interphase at the Zn^0 /electrolyte interface if the reduction products meet the strict criteria as mentioned in Section 16.3. For aqueous Zn^{2+} electrolytes, a high salt concentration is necessary because the only reliable source for interphasial chemistry is contributed by the fluorinated anions.

decade. In fact, a zinc-metal anode (Zn^0) is no stranger to the battery world, because it was the first battery anode used by Alessandro Volta to assemble the earliest battery in history, the voltaic pile. Currently, batteries based on Zn^0 , *i.e.* alkaline batteries, are still readily available in shops and supermarkets, providing us with cheap and safe electricity packed up in tiny cans. However, these alkaline batteries are non-rechargeable, owing to the unstable Zn /electrolyte interphase. Among many other issues, the eigenpotential of Zn^0 (-0.76 V *vs.* SHE, *i.e.* more negative than the potential where water starts to be reduced) sits beyond the thermodynamic stability limits of water molecules. This mismatch, similar to what is described in Figure 16.2, destabilizes the reversibility of a Zn^0 anode when one attempts to deposit Zn^0 back on the anode surface. Various problems, such as low Coulombic efficiency, dendritic and dead Zn^0 growth, gas generation and electrolyte depletion, *etc.*, would therefore occur. Researchers in recent decades have been leveraging the knowledge accumulated on lithium-ion and lithium-metal batteries, and redesigned aqueous Zn electrolytes and interphases. One important lesson learned is that the interfacial structure at the Zn^0 –electrolyte junction plays the key role in determining the interphasial chemistry and the reversibility of the Zn^0 anode, which is in turn reliant on the Zn^{2+} solvation sheath.

Unlike monovalent cations such as Li^+ or Na^+ , the solvation sheath of Zn^{2+} is much more difficult to alter by merely increasing the salt concentration, because as a bivalent cation that has an ionic radius

roughly the same as or even smaller than those of Li^+ and Na^+ but bears twice as much charge, Zn^{2+} is stubbornly coordinated with six water molecules in its primary solvation sheath, *i.e.* the so-called “ Zn^{2+} aqua complex” (Figure 16.19). As we learned in the preceding sections, these water molecules are activated by the strong Coulombic field of Zn^{2+} and are extremely vulnerable towards reduction. In order to compete against such strong favoring of H_2O reduction over that of the anion, a super-concentration concept such as “water-in-salt” or a localized high concentration, which have created “miracles” for electrolyte monovalent cations, no longer work as well, and one needs to engineer directly the interfacial structure and the interphasial chemistries.

One effective way to directly alter the interfacial structures is the introduction of certain “onium cations”, *e.g.* ammonium, phosphonium or sulfonium. These so-called “chaotropic” organic cations serve as assisting ions not only to help the dissolution of the working ion salt, but also to actively decorate the electrode surfaces with their hydrophobic nature. Their enrichment in the inner-Helmholtz layers on the both anode and cathode has obviously suppressed the activity of water molecules both within the solvation sheath of the working cations and in the vicinity of the electrode surface, hence during the initial charge transfer electronation would preferentially occur on either the working cation or the anion, whereas the reduction or oxidation of water molecules becomes discouraged. This practice has brought improved reversibility on the side of the Zn^0 anode, as evidenced by the high Coulombic efficiencies and prevention of dendritic or dead Zn^0 , and altered reaction pathways on the side of the air cathode, where the normal four-electron oxygen reduction chemistry is converted into a two-electron process, producing a more reversible

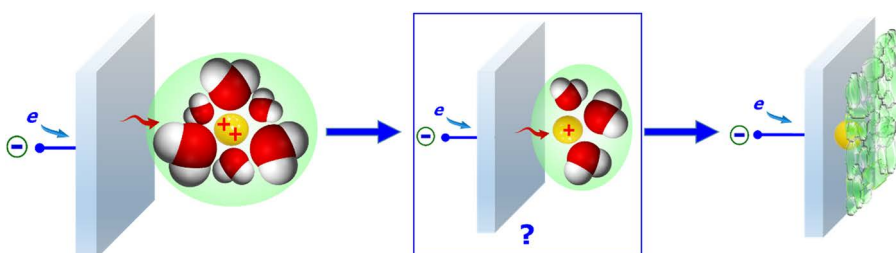


Figure 16.19 The interfacial charge-transfer process and interphasial chemistry involved with multivalent working cations are much more complicated than those with monovalent working cations. The possible existence of the monovalent intermediate introduces new variables in understanding the interphase formation mechanism.

zinc peroxide product. These explorations of tailoring the interfacial structures and interphasial chemistry represent a highly dynamic and active field, which might solve the reversibility issue that has been plaguing Zn⁰ anodes for centuries.

Thanks to intense efforts, more details about the interfacial processes and interphasial chemistries in multivalent electrolytes are being revealed. According to calculations, the reduction of Zn²⁺ to Zn⁰, or in a more universal context the reduction of all multivalent cations such as Mg²⁺ and Ca²⁺ to their elemental states, does not occur directly *via* a process involving transfer of multiple electrons. Instead, it could have gone through an intermediate state of monovalent cation Zn⁺ (or Mg⁺ and Ca⁺), which directly adsorbs on the inner-Helmholtz layer of the anode (Figure 16.19).⁷⁴ Such intermediate monovalent cations are extremely active and therefore short-lived, but increasing evidence has been emerging in support of their existence.^{75,76} How this monovalent, transient and unstable intermediate remains solvated in the interfacial region is undoubtedly a critical factor in determining not only the kinetics, efficiency and reversibility of multivalent ion chemistries, but also the design of new interphases in such batteries. A more thorough understanding is needed in order to shed light on this critical intermediate step.

References

1. *Linden's Handbook of Batteries*, ed. K. W. Beard, McGraw Hill, New York, 5th edn, 2019.
2. C. Zhang, Passivating lithium metal, *Nat. Energy*, 2018, **3**, 251.
3. E. A. Peled, The Electrochemical Behavior of Alkali and Alkaline Earth Metals in Nonaqueous Battery Systems—The Solid Electrolyte Interphase Model, *J. Electrochem. Soc.*, 1979, **126**, 2047–2051.
4. R. Fong, U. von Sacken and J. R. Dahn, Studies of Lithium Intercalation into Carbons Using Nonaqueous Electrochemical Cells, *J. Electrochem. Soc.*, 1990, **137**, 2009–2013.
5. K. Xu, Non-aqueous liquid electrolytes for lithium-based rechargeable batteries, *Chem. Rev.*, 2004, **104**, 4303–4417.
6. K. Xu, Electrolytes and interphases in Li-ion batteries and beyond, *Chem. Rev.*, 2014, **114**, 11503–11618.
7. J. B. Goodenough and Y. Kim, Challenges for rechargeable Li batteries, *Chem. Mater.*, 2010, **22**, 587–603.
8. M. Winter, The Solid Electrolyte Interphase – The Most Important and the Least Understood Solid Electrolyte in Rechargeable Li Batteries, *Z. Phys. Chem.*, 2009, **223**, 1395–1406.
9. E. Peled and H. Straze, The Kinetics of the Magnesium Electrode in Thionyl Chloride Solutions, *J. Electrochem. Soc.*, 1977, **124**, 1030–1035.
10. E. Peled, D. Golodnitsky, C. Menachem and D. Bar-Tov, An advanced tool for the selection of electrolyte components for rechargeable lithium batteries, *J. Electrochem. Soc.*, 1998, **145**, 3482–3486.

11. D. Aurbach, A. Zaban, Y. Ein-Eli, I. Weissman, O. Chusid, B. Markovski, M. D. Levi, E. Levi, A. Schechter and E. Granot, Recent studies on the correlation between surface chemistry, morphology, three-dimensional structures and performance of Li and Li-C intercalation anodes in several important electrolyte systems, *J. Power Sources*, 1997, **68**, 91–98.
12. K. Xu, G. V. Zhuang, J. L. Allen, U. Lee, S. S. Zhang, P. N. Ross Jr and T. R. Jow, Syntheses and characterization of lithium alkyl mono- and dicarbonates as components of surface films in Li-ion batteries, *J. Phys. Chem. B*, 2006, **110**, 7708–7719.
13. E. Goren, O. Chusid and D. Aurbach, The Application of *In Situ* FTIR Spectroscopy to the Study of Surface Films Formed on Lithium and Noble Metals at Low Potentials in Li Battery Electrolytes, *J. Electrochem. Soc.*, 1991, **138**, L6–L9.
14. G. V. Zhuang, K. Xu, H. Yang, T. R. Jow and P. N. Ross, Lithium Ethylene Dicarbonate Identified as the Primary Product of Chemical and Electrochemical Reduction of EC in 1.2 M LiPF₆/EC:EMC Electrolyte, *J. Phys. Chem. B*, 2005, **109**, 17567–17573.
15. K. Xu, Electrolytes and interphasial chemistry in Li ion devices, *Energies*, 2010, **3**, 135–154.
16. D. Aurbach and Y. Gofer, The Behavior of Lithium Electrodes in Mixtures of Alkyl Carbonates and Ethers, *J. Electrochem. Soc.*, 1991, **138**, 3529–3536.
17. A. N. Dey and B. P. Sullivan, The Electrochemical Decomposition of Propylene Carbonate on Graphite, *J. Electrochem. Soc.*, 1970, **117**, 222–224.
18. K. Xu, Charge-transfer process at graphite/electrolyte interface and the solvation sheath structure of Li⁺ in nonaqueous electrolytes, *J. Electrochem. Soc.*, 2007, **154**, A162–A167.
19. K. Xu, Y. Lam, S. S. Zhang, T. R. Jow and T. B. Curtis, Solvation sheath of Li⁺ in nonaqueous electrolytes and its implication of graphite/electrolyte interface chemistry, *J. Phys. Chem. C*, 2007, **111**, 7411–7421.
20. I. A. Shkrob, Y. Zhu, T. W. Marin and D. Abraham, Reduction of Carbonate Electrolytes and the Formation of Solid-Electrolyte Interface (SEI) in Lithium-Ion Batteries. 1. Spectroscopic Observations of Radical Intermediates Generated in One-Electron Reduction of Carbonates, *J. Phys. Chem. C*, 2013, **117**, 19255–19269.
21. R. Dedryvère, S. Leroy, H. Martinez, F. Blanchard, D. Lemordant and D. Gonneau, XPS Valence Characterization of Lithium Salts as a Tool to Study Electrode/Electrolyte Interfaces of Li-Ion Batteries, *J. Phys. Chem. B*, 2006, **110**, 12986–12992.
22. L. Wang, A. Menakath, F. Han, Y. Wang, P. Y. Zavalij, K. J. Gaskell, O. Borodin, D. Iuga, S. P. Brown, C. Wang, K. Xu and B. W. Eichhorn, Identifying the components of the solid-electrolyte interphase in Li-ion batteries, *Nat. Chem.*, 2019, **11**, 789–796.
23. M. Onuki, S. Kinoshita, Y. Sakata, M. Yanagidate, Y. Otake, M. Ue and M. Deguchi, Identification of the Source of Evolved Gas in Li-Ion Batteries Using ¹³C-labeled Solvents, *J. Electrochem. Soc.*, 2008, **155**, A794–A797.
24. H. Tavassol, J. W. Buthker, G. A. Ferguson, L. A. Curtiss and A. A. Gewirth, Solvent Oligomerization during SEI Formation on Model Systems for Li-Ion Battery Anodes, *J. Electrochem. Soc.*, 2012, **159**, A730.
25. T. Liu, L. Lin, X. Bi, L. Tian, K. Yang, J. Liu, M. Li, Z. Chen, J. Lu, K. Amine, K. Xu and F. Pan, *In situ* quantification of interphasial chemistry in Li-ion battery, *Nat. Nanotechnol.*, 2019, **14**, 50–56.
26. S. P. Kühn, K. Edström, M. Winter and I. Cekic-Laskovic, Face to face at the cathode electrolyte interphase: From interface features to interphase formation and dynamics, *Adv. Mater. Interfaces*, 2022, **9**, 2102078.
27. H. Liu, Y. Tong, N. Kuwata, M. Osawa, J. Kawamura and S. Ye, Adsorption of Propylene Carbonate (PC) on the LiCoO₂ Surface Investigated by Nonlinear Vibrational Spectroscopy, *J. Phys. Chem. C*, 2009, **113**, 20531–20534.

28. L. Yu, H. Liu, Y. Wang, N. Kuwata, M. Osawa, J. Kawamura and S. Ye, Preferential Adsorption of Solvents on the Cathode Surface of Lithium Ion Batteries, *Angew. Chem., Int. Ed.*, 2013, **52**, 5753–5756.
29. S. K. Heiskanen, J. Kim and B. Lucht, Generation and Evolution of the Solid Electrolyte Interphase of Lithium-Ion Batteries, *Joule*, 2019, **3**, 2322–2333.
30. W. Xu, J. Wang, F. Ding, X. Chen, E. Nasybulin, Y. Zhang and J. G. Zhang, Lithium metal anodes for rechargeable batteries, *Energy Environ. Sci.*, 2014, **7**, 513–537.
31. Q. Liu, A. Cresce, M. Schroeder, K. Xu, D. Mu, B. Wu, L. Shi and F. Wu, Insight on lithium metal anode interphasial chemistry: Reduction mechanism of cyclic ether solvent and SEI film formation, *Energy Storage Mater.*, 2019, **17**, 366–373.
32. C. Wang, Y. S. Meng and K. Xu, Fluorinating interphases, *J. Electrochem. Soc.*, 2018, **166**, A5184–A5186.
33. S. S. Zhang, A review on electrolyte additives for lithium-ion batteries, *J. Power Sources*, 2006, **162**, 1379–1394.
34. H. Yoshitake, Functional Electrolytes Specially Designed for Lithium-Ion Batteries, in *Lithium-Ion Batteries*, ed. M. Yoshio, R. J. Brodd and A. Kozawa, Springer, New York, NY, 2009.
35. Y. S. Meng, Introduction: Beyond Li-Ion Battery Chemistry, *Chem. Rev.*, 2020, **14**, 6327.
36. W.-J. Kwak, Rosy, D. Sharon, C. Xia, H. Kim, L. R. Johnson, P. G. Bruce, L. F. Nazar, Y.-K. Sun, A. A. Frimer, M. Noked, S. A. Freunberger and D. Aurbach, Lithium–Oxygen Batteries and Related Systems: Potential, Status, and Future, *Chem. Rev.*, 2020, **14**, 6626–6683.
37. W. Xu, K. Xu, V. V. Viswanathan, S. A. Towne, J. S. Hardy, J. Xiao, Z. Nie, D. Hu, D. Wang and J.-G. Zhang, Reaction mechanisms for the limited reversibility of Li–O₂ chemistry in organic carbonate electrolytes, *J. Power Sources*, 2011, **196**, 9631–9639.
38. A. Van der Ven, Z. Deng, S. Banerjee and S. P. Ong, Rechargeable Alkali-Ion Battery Materials: Theory and Computation, *Chem. Rev.*, 2020, **120**, 6977–7019.
39. T. Hosaka, K. Kubota, A. S. Hameed and S. Komaba, Research Development on K-Ion Batteries, *Chem. Rev.*, 2020, **120**, 6358–6466.
40. M. E. Arroyo-de Dompablo, A. Ponrouch, P. Johansson and M. R. Palacín, Achievements, Challenges, and Prospects of Calcium Batteries, *Chem. Rev.*, 2020, **120**, 6331–6357.
41. S. B. Son, T. Gao, S. P. Harvey, K. X. Steirer, A. Stokes, A. Norman, C. Wang, A. Cresce, K. Xu and C. Ban, An artificial interphase enables reversible magnesium chemistry in carbonate electrolytes, *Nat. Chem.*, 2018, **10**, 532–539.
42. F. Wang, R. Robert, N. A. Chernova, N. Pereira, F. Omenya, F. Badway, X. Hua, M. Ruotolo, R. Zhang, L. Wu, V. Volkov, D. Su, B. Key, M. S. Whittingham, C. P. Grey, G. G. Amatucci, Y. Zhu and J. Graetz, Conversion Reaction Mechanisms in Lithium Ion Batteries: Study of the Binary Metal Fluoride Electrodes, *J. Am. Chem. Soc.*, 2011, **133**, 18828–18836.
43. K. Tasaki, A. Goldberg, J. J. Lian, M. Walker, A. Timmons and S. J. Harris, Solubility of lithium salts formed on the lithium-ion battery negative electrode surface in organic solvents, *J. Electrochem. Soc.*, 2009, **156**, A1019–A1027.
44. A. Cresce, S. M. Russell, D. R. Baker, K. J. Gaskell and K. Xu, *In situ* and quantitative characterization of solid electrolyte interphases, *Nano Lett.*, 2014, **14**, 1405–1412.
45. K. Edström, M. Herstedt and D. P. Abraham, A new look at the solid electrolyte interphase on graphite anodes in Li-ion batteries, *J. Power Sources*, 2006, **153**, 380–384.
46. M. Nie, D. Chalasani, D. P. Abraham, Y. Chen, A. Bose and B. L. Lucht, Lithium Ion Battery Graphite Solid Electrolyte Interphase Revealed by Microscopy and Spectroscopy, *J. Phys. Chem. C*, 2013, **117**, 1257–1267.
47. D. E. Arreaga-Salas, A. K. Sra, K. Roodenko, Y. J. Chabal and C. L. Hinkle, *J. Phys. Chem. C*, 2012, **116**, 9072.

48. N. Delpuech, N. Dupré, D. Mazouzi, J. Gaubicher, P. Moreau, J. S. Bridel, D. Guyomard and B. Lestriez, Correlation between irreversible capacity and electrolyte solvents degradation probed by NMR in Si-based negative electrode of Li-ion cell, *Electrochem. Commun.*, 2013, **33**, 72–75.
49. M. S. Kim, Z. Zhang, P. E. Rudnicki, Z. Yu, J. Wang, H. Wang, S. T. Oyakhire, Y. Chen, S. C. Kim, W. Zhang, D. T Boyle, X. Kong, R. Xu, Z. Huang, W. Huang, S. F. Bent, L.-W. Wang, J. Qin, Z. Bao and Y. Cui, Suspension electrolyte with modified Li^+ solvation environment for lithium metal batteries, *Nat. Mater.*, 2022, **21**, 445–454.
50. M. J. Zachman, Z. Tu, S. Choudhury, L. A. Archer and L. F. Kourkoutis, Cryo-STEM mapping of solid–liquid interfaces and dendrites in lithium–metal batteries, *Nature*, 2018, **560**, 345–349.
51. C. Fang, J. Li, M. Zhang, Y. Zhang, F. Yang, J. Z. Lee, M.-H. Lee, J. Alvarado, M. A. Schroeder, Y. Yang, B. Lu, N. Williams, M. Ceja, L. Yang, M. Cai, J. Gu, K. Xu, X. Wang and Y. S. Meng, Quantifying inactive lithium in lithium metal batteries, *Nature*, 2019, **572**, 511–515.
52. Z. Shadike, H. Lee, O. Borodin, X. Cao, X. Fan, X. Wang, R. Lin, S. M. Bak, S. Ghose, K. Xu, C. Wang, J. Liu, J. Xiao, X.-Q. Yang and E. Hu, Identification of LiH and nanocrystalline LiF in the solid–electrolyte interphase of lithium metal anodes, *Nat. Nanotechnol.*, 2021, **16**, 549–554.
53. P. Lu and S. J. Harris, Lithium transport within the solid electrolyte interphase, *Electrochem. Commun.*, 2011, **13**, 1035–1037.
54. S. Shi, P. Lu, Z. Liu, Y. Qi, L. G. Hector Jr, H. Li and S. J. Harris, Direct Calculation of Li-ion Transport in the Solid Electrolyte Interphase, *J. Am. Chem. Soc.*, 2012, **134**, 15476–15487.
55. A. Wang, S. Kadam, H. Li, S. Shi and Y. Qi, Review on modeling of the anode solid electrolyte interphase (SEI) for lithium-ion batteries, *Comput. Mater.*, 2018, **4**, 1–6.
56. Q. Zhang, J. Pan, P. Lu, Z. Liu, M. W. Verbrugge, B. W. Sheldon, Y. T. Cheng, Y. Qi and X. Xiao, Synergetic effects of inorganic components in solid electrolyte interphase on high cycle efficiency of lithium ion batteries, *Nano Lett.*, 2016, **16**, 2011–2016.
57. A. J. Smith, J. C. Burns, S. Trussler and J. R. Dahn, Precision measurements of the coulombic efficiency of lithium-ion batteries and of electrode materials for lithium-ion batteries, *J. Electrochem. Soc.*, 2009, **157**, A196–A202.
58. K. Xu, A. von Cresce and U. Lee, Differentiating contributions to “ion transfer” barrier from interphasial resistance and Li^+ desolvation at electrolyte/graphite interface, *Langmuir*, 2010, **26**, 11538–11543.
59. K. Xu and A. von Cresce, Interfacing electrolytes with electrodes in Li ion batteries, *J. Mater. Chem.*, 2011, **21**, 9849–9864.
60. A. von Cresce and K. Xu, Preferential solvation of Li^+ directs formation of interphase on graphitic anode, *Electrochem. Solid-State Lett.*, 2011, **14**, A154–A156.
61. L. Xing, X. Zheng, M. Schroeder, J. Alvarado, A. von W. Cresce, K. Xu, Q. Li and W. Li, Deciphering the ethylene carbonate–propylene carbonate mystery in Li-ion batteries, *Acc. Chem. Res.*, 2018, **51**, 282–289.
62. Y. Zhou, M. Su, X. Yu, Y. Zhang, J. G. Wang, X. Ren, R. Cao, W. Xu, D. R. Baer, Y. Du, O. Borodin, Y. Wang, X.-L. Wang, K. Xu, Z. Xu, C. Wang and Z. Zhu, Real-time mass spectrometric characterization of the solid–electrolyte interphase of a lithium-ion battery, *Nat. Nanotechnol.*, 2020, **15**, 224–230.
63. O. Borodin and G. D. Smith, Quantum Chemistry and Molecular Dynamics Simulation Study of Dimethyl Carbonate: Ethylene Carbonate Electrolytes Doped with LiPF_6 , *J. Phys. Chem. B.*, 2009, **113**, 1763–1776.
64. M. Winter, B. Barnett and K. Xu, Before Li ion batteries, *Chem. Rev.*, 2018, **118**, 11433–11456.
65. A. Cresce, O. Borodin and K. Xu, Correlating Li^+ Solvation Sheath Structure with Interphasial Chemistry on Graphite, *J. Phys. Chem. C.*, 2012, **116**(50), 26111–26117.

66. M. R. Wagner, J. H. Albering, K. C. Moeller, J. O. Besenhard and M. Winter, XRD evidence for the electrochemical formation of Li(PC)yCn in PC-based electrolytes, *Electrochim. Commun.*, 2005, **7**, 947–952.
67. G. V. Zhuang, H. Yang, P. N. Ross, K. Xu and T. R. Jow, Lithium methyl carbonate as a reaction product of metallic lithium and dimethyl carbonate, *Electrochim. Solid-State Lett.*, 2005, **9**, A64–A68.
68. X. Bogle, R. Vazquez, S. Greenbaum, A. W. Cresce and K. Xu, Understanding Li⁺-Solvent Interaction in Nonaqueous Carbonate Electrolytes with ¹⁷O NMR, *J. Phys. Chem. Lett.*, 2013, **4**, 1664–1668.
69. Y. Zhang, M. Su, X. Yu, Y. Zhou, J. Wang, R. Cao, W. Xu, C. Wang, D. R. Baer, O. Borodin, K. Xu, Y. Wang, X.-L. Wang, Z. Xu, F. Wang and Z. Zhu, Investigation of ion-solvent interactions in nonaqueous electrolytes using *in situ* liquid SIMS, *Anal. Chem.*, 2018, **90**, 3341–3348.
70. Y. Yamada, K. Furukawa, K. Sodeyama, K. Kikuchi, M. Yaegashi, Y. Tateyama and A. Yamada, Unusual stability of acetonitrile-based superconcentrated electrolytes for fast-charging lithium-ion batteries, *J. Am. Chem. Soc.*, 2014, **136**, 5039–5046.
71. M. Nie, D. P. Abraham, D. M. Seo, Y. Chen, A. Bose and B. L. Lucht, Role of Solution Structure in Solid Electrolyte Interphase Formation on Graphite with LiPF₆ in Propylene Carbonate, *J. Phys. Chem. C*, 2013, **117**, 25381–25389.
72. L. Cao, D. Li, T. Pollard, T. Deng, B. Zhang, C. Yang, L. Chen, J. Vatamanu, E. Hu, M. J. Hourwitz, L. Ma, M. Ding, Q. Li, S. Hou, K. Gaskell, J. T. Fourkas, X.-Q. Yang, K. Xu, O. Borodin and C. Wang, Fluorinated interphase enables reversible aqueous zinc battery chemistries, *Nat. Nanotechnol.*, 2021, **16**, 902–910.
73. L. Ma, T. P. Pollard, Y. Zhang, M. A. Schroeder, X. Ren, K. S. Han, M. S. Ding, A. von Cresce, T. B. Atwater, J. Mars, L. Cao, H.-G. Steinrück, K. T. Mueller, M. F. Toney, M. Hourwitz, J. T. Fourkas, E. J. Maginn, C. Wang, O. Borodin and K. Xu, Ammonium enables reversible aqueous Zn battery chemistries by tailoring the interphase, *One Earth*, 2022, **5**, 413–421.
74. P. Quaino, E. Colombo, F. Juarez, E. Santos, G. Belletti, A. Groß and W. Schmickler, On the first step in zinc deposition – A case of nonlinear coupling with the solvent, *Electrochim. Commun.*, 2021, **122**, 106876.
75. Q.-H. Zhang, P. Liu, Z.-J. Zhu, X.-R. Li, J.-Q. Zhang and F.-H. Cao, Electrochemical detection of univalent Mg cation: A possible explanation for the negative difference effect during Mg anodic dissolution, *J. Electroanal. Chem.*, 2021, **880**, 114837.
76. A. Atrens and W. Dietzel, The Negative Difference Effect and Unipositive Mg⁺, *Adv. Eng. Mater.*, 2007, **9**, 292–297.
77. L. Benitez and J. M. Seminario, *J. Electrochem. Soc.*, 2017, **164**, E3159–E3170.
78. X. Cao, P. Gao, X. Ren and Ji-G. Zhang, Effects of fluorinated solvents on electrolyte solvation structures and electrode/electrolyte interphases for lithium metal batteries, *Proc. Natl. Acad. Sci. U. S. A.*, 2021, **118**, e2020357118.
79. X. Cao, X. Ren, L. Zou, M. H. Engelhard, W. Huang, H. Wang, B. E. Matthews, H. Lee, C. Niu, B. W. Arey, Y. Cui, C. Wang, J. Xiao, J. Liu, W. Xu and J.-G. Zhang, Monolithic solid-electrolyte interphases formed in fluorinated orthoformate-based electrolytes minimize Li depletion and pulverization, *Nat. Energy*, 2019, **4**, 796–805.
80. X. Ren, P. Gao, L. Zou and W. Xu, Role of inner solvation sheath within salt-solvent complexes in tailoring electrode/electrolyte interphases for lithium metal batteries, *Proc. Natl. Acad. Sci. U. S. A.*, 2020, **117**, 28603–28613.
81. O. Borodin, X. Ren, J. Vatamanu, A. von Wald Cresce, J. Knap and K. Xu, Modeling insight into battery electrolyte electrochemical stability and interfacial structure, *Acc. Chem. Res.*, 2017, **50**, 2886–2894.
82. M. Fujimoto, N. Yoshinaga and K. Ueno, Li-ion Secondary Batteries, *Japanese Patent*, 3229635, 1991.

83. R. Fong, U. von Sacken and J. R. Dahn, Studies of Lithium Intercalation into Carbons Using Nonaqueous Electrochemical Cells, *J. Electrochem. Soc.*, 1990, **137**, 2009–2013.
84. K. J. Carroll, M.-C. Yang, G. M. Veith, N. J. Dudney and Y. S. Meng, Intrinsic Surface Stability in $\text{LiMn}_{2-x}\text{Ni}_x\text{O}_{4-\delta}$ ($x = 0.45, 0.5$) High Voltage Spinel Materials for Lithium Ion Batteries, *Electrochem. Solid-State Lett.*, 2012, **15**, A72.
85. E. Markevich, R. Sharabi, H. Gottlieb, V. Borgel, K. Fridman, G. Salitra, D. Aurbach, G. Semrau, M. A. Schmidt, N. Schall and C. Bruenig, Reasons for capacity fading of LiCoPO_4 cathodes in LiPF_6 containing electrolyte solutions, *Electrochem. Commun.*, 2012, **15**, 22.
86. S. R. Li, C. H. Chen, X. Xia and J. R. Dahn, The Impact of Electrolyte Oxidation Products in $\text{LiNi}_{0.5}\text{Mn}_{1.5}\text{O}_4/\text{Li}_4\text{Ti}_5\text{O}_{12}$ Cells, *J. Electrochem. Soc.*, 2013, **160**, A1524.
87. R. Petibon, J. Xia, L. Ma, M. K. G. Bauer, K. J. Nelson and J. R. Dahn, Electrolyte System for High Voltage Li-Ion Cells, *J. Electrochem. Soc.*, 2016, **163**, A2571–A2578.
88. D. Aurbach, in *Non-Aqueous Electrochemistry*, Marcel Dekker, NY, Basel, 1999.
89. Y. Li, Y. Li, A. Pei, K. Yan, Y. Sun, C.-L. Wu, L.-M. Joubert, R. Chin, A. L. Koh, Y. Yu, J. Perrino, B. Butz, S. Chu and Y. Cui, Atomic structure of sensitive battery materials and interfaces revealed by cryo-electron microscopy, *Science*, 2017, **358**, 506–510.
90. X. Cao, X. Ren, L. Zou, M. H. Engelhard, W. Huang, H. Wang, B. E. Matthews, H. Lee, C. Niu, B. W. Arey, Y. Cui, C. Wang, J. Xiao, J. Liu, W. Xu and J.-G. Zhang, Monolithic solid-electrolyte interphases formed in fluorinated orthoformalate-based electrolytes minimize Li depletion and pulverization, *Nat. Energy*, 2019, **4**, 796–805.
91. D. Y. Wang and J. R. Dahn, A High Precision Study of Electrolyte Additive Combinations Containing Vinylene Carbonate, Ethylene Sulfate, Tris(trimethylsilyl) Phosphate and Tris(trimethylsilyl) Phosphite in $\text{Li}[\text{Ni}_{1/3}\text{Mn}_{1/3}\text{Co}_{1/3}]\text{O}_2/\text{Graphite}$ Pouch Cells, *J. Electrochem. Soc.*, 2014, **161**, A1890–A1897.
92. R. Petibon, J. Xia, L. Ma, M. K. G. Bauer, K. J. Nelson and J. R. Dahn, Electrolyte System for High Voltage Li-Ion Cells, *J. Electrochem. Soc.*, 2016, **163**, A2571–A2578.
93. D. Aurbach and O. Chusid, In situ FTIR spectroelectrochemical studies of surface films formed on Li and nonactive electrodes at low potentials in Li salt solutions containing CO_2 , *J. Electrochem. Soc.*, 1993, **140**, L155–L157.
94. J. Yue, J. Zhang, Y. Tong, M. Chen, L. Liu, L. Jiang, T. Lv, Y. Hu, H. Li, X. Huang, L. Gu, G. Feng, K. Xu, L. Suo and L. Chen, Aqueous interphase formed by CO_2 brings electrolytes back to salt-in-water regime, *Nat. Chem.*, 2021, **13**, 1061–1069.
95. M. Winter, The Solid Electrolyte Interphase - The Most Important and the Least Understood Solid Electrolyte in Rechargeable Li Batteries, *Z. Phys. Chem.*, 2009, **223**, 1395–1406.
96. O. Chusid, Y. Ein Ely, D. Aurbach, M. Babai and Y. Carmeli, Electrochemical and Spectroscopic Studies of Carbon Electrodes in Lithium Battery Electrolyte Systems, *J. Power Sources*, 1993, **43/44**, 47–64.
97. D. Aurbach and I. Weissman, On the possibility of LiH formation on Li surfaces in wet electrolyte solutions, *Electrochem. Commun.*, 1999, **1**, 324–331.
98. S. Shi, P. Lu, Z. Liu, Y. Qi, L. G. Hector Jr, H. Li and S. J. Harris, Direct calculation of Li-ion transport in the solid electrolyte interphase, *J. Am. Chem. Soc.*, 2012, **134**, 15476–15487.
99. A. Cresce, O. Borodin and K. Xu, Correlating Li^+ Solvation Sheath Structure with Interphasial Chemistry on Graphite, *J. Phys. Chem. C*, 2012, **116**(50), 26111.
100. L. Suo, O. Borodin, T. Gao, M. Olguin, J. Ho, X. Fan, C. Luo, C. Wang and K. Xu, “Water-in-salt” electrolyte enables high-voltage aqueous lithium-ion chemistries, *Science*, 2015, **350**, 938–943.

17 New Concepts and Tools

Designing better electrolytes and the associated interphases holds the key to breakthroughs in materials and chemistries for future batteries.

As of 2022, the energy densities of lithium-ion batteries have reached 300–400 W h kg⁻¹ (or 600–800 W h L⁻¹) in the most popular 18 650 configuration, depending on the chemistry used,¹ which is about three times higher than that of the first-generation lithium-ion battery commercialized in 1991,² with simultaneous improvements in cycle life, power or rate capability and safety, accompanied by a decrease in manufacturing costs. Such improvements were the fruition of both materials innovations with new structures and chemistries as well as cell engineering that pushes these materials to their extremes so that their potentials are fully exploited in commercial cells. Nevertheless, by 2025, the energy densities of lithium-ion batteries would have approached the limits imposed by the intercalation nature of its electrodes, based on all the active electrode materials known at present. Hence tremendous interest and resources are being dedicated to the efforts to seek new battery chemistries, materials and mechanisms. Electrolytes and interphases in these emerging batteries would have to face much more stringent and challenging requirements.³

Thanks to the efforts and resources invested during the past three decades, fundamental knowledge about electrolytes and interphases has been rapidly accumulated.^{4–6} The advances in theoretical models and the ever-increasing computing capability reveal unprecedented pictures at the atomistic length scale and pico-/nanosecond time scale of how ions, solvent molecules and the charged surfaces of electrodes interact, which are properties and behaviors that would otherwise be

inaccessible or unmeasurable in ordinary experiments. Meanwhile, the invention of new characterization techniques of high temporal and spatial resolution, both *in situ/operando* and *ex situ*, shed more and more light on the elusive interfacial and interphasial behaviors, with increasing assistance from computational modeling and simulations, especially with more recent assistance from machine learning (ML) and artificial intelligence (AI).

Based on this progress in both computational and characterization frontiers, we have gradually established a systematic understanding about the once elusive interfaces and interphases. Such knowledge enabled us to design various new concepts to tailor electrolytes and interphases for special application purposes. In particular, the “solvation–interphase correlation” has provided us with a very powerful tool to tailor interphasial chemistries, which were once unpredictable and totally empirical.^{7,8} Many new-concept electrolytes have been developed that benefited directly or indirectly from this understanding.⁴

This chapter only “cherry-picks” a selected number of new concepts recently applied to the design of electrolytes and interphases. Such coverage is inevitably superficial and non-systematic, but it reflects the highly dynamic nature of the field.

The chapter also briefly covers the new tools for understanding and characterizing interfaces and interphases, including a very rudimentary introduction to the applications of computational simulations in this specific area. Of course, the author’s understanding of these fields is also on a rather rudimentary level.

17.1 Super-concentrating: Unusual Properties

One key piece of knowledge achieved in the last decade is that the formation process and chemistry of the solid electrolyte interphase (SEI) in lithium-ion batteries are closely coupled to the ion solvation sheath structure, which, unlike the elusive interfacial and interphasial properties, is relatively easy to predict and tailor.^{7–9} Systematic quantification of solvating power has been established for the most frequently used solvent molecules and ions, while the electrochemical reaction pathways for most of those solvent molecules can be calculated *via* classical or *ab initio* molecular dynamic simulations or quantum mechanics.^{10–12} In such a context, once the electrolyte composition is altered, corresponding changes occur in the solvation sheath structure, which subsequently lead to

changes in the eventual interphasial chemistry. This coupled relation, which we named “solvation–interphase correlation” in previous sections, allows us to predict and even to engineer interphases. It was this line of thought that inspired the “*super-concentration*” concept, although many pioneers studying super-concentrated electrolytes did not necessarily realize this underlying correlation when first reporting their work.

Super-concentration is a relative term and therefore inaccurate by nature. It describes the general approach of deliberately formulating electrolytes at higher salt concentration, with the purpose of achieving certain gains in other targeted properties, while accepting a decrease in ion conductivity as the price to pay. This approach represents an important departure from the classical doctrine in which ion conductivity is the primary, if not the only, consideration, and indicates that there are now other properties of comparable or even greater importance than just ion conduction, hence a certain sacrifice in ion transport is acceptable. These other properties include, but are not limited to, the electrochemical stability window, the underlying interphasial chemistry, selective transference of certain ions, or other physical, chemical, morphological or mechanical considerations, such as flammability, stability against thermal and chemical degradation and corrosion, *etc.*

In super-concentrated electrolytes, the significant deficiency of solvent molecules leads to ion-solvation sheaths that are not structured as in a classical Bernal–Fowler three-layer model (Figure 3.5, or Section 12.1). Instead, the individual ion solvation sheaths are so compressed that they are forced to partially “merge” and share solvent molecules (Figure 12.5), while counterions inevitably appear at distances that are considered to be within the classical primary solvation sheaths (~ 0.2 nm). This “crowding” effect significantly alters the ion solvation structure and in turn induces a series of new properties, some of which have already been discussed in Section 12.2.4.

Of course, not all of these new properties are beneficial to the applications in electrochemical cells.

McKinnon and Dahn were perhaps the first pioneers who ventured into the “super-concentration” regime. They reported in 1985 that a saturated solution of LiAsF₆ in propylene carbonate (PC) could circumvent the co-intercalation of PC into a layered host, although this host, a chalcogenide (Li_xZrSe₂ or Li_xTaS₂), was on the cathode instead of the anode side.¹³ More attention was generated by Angell *et al.* in 1993, who found that unusually high ion conductivity could be achieved by increasing the salt concentration above a certain threshold level,

where the monotonic decrease in ion conductivity with salt concentration was breached because the ionic movement is decoupled from the polymeric segmental motion.¹⁴ The resultant polymeric electrolytes are thus enriched in extra ionic concentration compared with ordinary liquid or polymer electrolytes, a nature that places them somewhere closer to neat ionic liquids. They named this class of electrolyte materials “*polymer-in-salt*” electrolytes, which should be viewed as the ancestors of the later versions of the super-concentrated electrolytes, such as “*solvent-in-salt*”, “*water-in-salt*”, “*water-in-bisalt*”, hydrated electrolytes or locally concentrated electrolytes.

The “unusual” properties vary from electrolyte to electrolyte, and most of the time they are only unusual to that specific electrolyte composition, while other electrolyte systems could offer comparable or even better properties. Therefore, most of the time, these unusual properties have been treated only as laboratory novelties. However, it was through the exploration of these unconventional practices that we gradually learned how to design new electrolyte systems that could truly support the aggressive chemistries employed in the emerging batteries.

The following are just a selection of prominent examples of the unusual properties made possible by super-concentration.

17.1.1 Ethers Could Be Anodically Stable

In strong contrast to carbonates, ethers have found much less commercial success, which can be attributed to their intrinsic chemical, electrochemical and interphasial disadvantages at both cathodes and anodes.

On the cathode side, the intrinsic chemical instability of ethers against oxidation disqualifies them for any application that requires high-voltage (>4 V) cathode materials. On the anode side, although most ethers are chemically stable against reduction (especially compared with esters), their stability prevents them from forming an SEI over graphite but instead enables co-intercalation, *i.e.* Scenario II as depicted in Figure 10.7, which is an undesirable and clumsy intercalation chemistry of mediocre potential, low capacity and poor reversibility. Here the stability of ethers against reduction becomes a disadvantage instead of a merit because of the unique structure of graphite and its requirement for special interphasial chemistry. Only in the limited cases where both lithium metal and a cathode of moderate potential are employed could ethers find a niche, one example of which is the Li⁺/sulfur battery chemistry.

In summary, the intrinsic chemical nature of ethereal molecules renders them fairly stable against reduction but highly susceptible to oxidation, which is the fundamental reason why ether-based electrolytes often outperform other electrolyte systems in interfacing with lithium-metal electrodes but cannot support the reactions at either graphitic or cathode surfaces, especially when the cathode chemistry has to operate at potentials higher than 4.0 V *vs.* Li⁰. Ethers are also typically more volatile and flammable than esters. The volatility is in particular a nuisance to work with. For example, 1,3-dioxolane and dimethoxyethane solvents commonly used in Li⁰/S batteries will evaporate so easily that researchers sometimes have to chill the electrolyte before injection, otherwise the actual electrolyte composition could change during the cell construction.

Increasing the salt concentration in ether-based electrolytes, however, resolves most of these issues. Numerous electrolyte systems have been developed along this line of thought, but the work on “salt solvate” electrolytes by Watanabe and co-workers,^{15–17} which we already briefly introduced in Section 12.2.4.3, represented the most systematic understanding of this class of electrolytes. Using both thermal (DSC, TGA), spectroscopic (NMR, FTIR) and electrochemical methods and computational simulations, they revealed with unequivocal evidence that all ether solvents in these super-concentrated systems are tightly harnessed by Li⁺, while the presence of “free” solvent molecules, *i.e.* uncoordinated with either cations or anions, essentially does not exist.

Such strong interactions led to high thermal stability, low flammability and unusual viscosity. For example, some of these “salt solvate” electrolytes can withstand temperatures up to 200 °C without losing weight. Particularly surprising were the improvements in their electrochemical stabilities towards the cathode and graphitic anode. The basic mechanism behind this seems to come from two separate fronts: (1) the “physical” factor, which is simply related to the decimated ratio of the ether solvent molecules to ions in the electrolyte system and the subsequent total recruitment of all solvents into the solvation sheaths, therefore the activity and reactivity of the ethers towards a cathode surface consequently become weakened, which can be evidenced by the reduced donicity of the lone pair of electrons on the ether oxygen in the super-concentrated realm; and (2) the “chemical” factor, which is related to the increased presence of anions in the electrolyte and the resultant effect of passivating the cathode surface, *via* either cathode electrolyte interphase (CEI) formation or specific adsorption on the cathode surface. The ether-based electrolytes

adopting the super-concentration approach have been reported to be able to support cathode chemistries up to 4.5 V.

The harnessing by Li^+ also eliminates the clumsy and inefficient co-intercalation behavior at a graphitic anode. Apparently the anions, which are now forced into the primary solvation sheath of Li^+ , take the responsibility of forming a protective SEI on graphitic carbon, before the ether solvent molecules, which are also in the Li^+ solvation sheath but now have to coexist with the anions, could co-intercalate. Such unusual properties can all be attributed to the competitive solvation of Li^+ by solvent (glyme) molecules and anions, which does not occur in dilute salt systems. This intimate interaction between cations and anions is of particular significance to the interfacial/interphasial properties that often dictate the electrochemical stabilities of the electrolytes.

As lithium-metal anodes have been revisited since the early-2010s, ether-based super-concentrated electrolytes were explored as a means to provide the desired stabilities on both the Li^0 surface and high-voltage high-Ni cathode surface. Thus far, the best Coulombic efficiencies of a rechargeable Li-metal anode came from ether-based electrolytes (99.5% at 0.5 mA cm^{-2} and 1 mAh cm^{-2}), which is mainly due to the densely packed Li-metal morphology now underlying the new interphasial chemistry that is otherwise unavailable in dilute or in carbonate-based electrolytes.¹⁸ The new SEI on the Li-metal surface now mainly carries the chemical signature from the anions, made possible by the combination of two factors: (1) the high presence of anions in the primary Li^+ solvation sheath, which fluorinated the resulting interphase, and (2) the relative inertness of ether molecules towards the Li surface.

In addition to electrochemical stability, these super-concentrated ether electrolytes also displayed unusual ion transport, thanks to the strong interactions among the Li^+ and anions at high concentration and also the solvent molecules that now can hardly remain “free” of the Coulombic fields of both the Li^+ and anions. Analysis revealed that, when approaching super-concentration, the ionicity as defined in Section 14.1.4 [eqn (14.79), Figure 14.13] counterintuitively increases, despite the expectation that intensified cation-solvent interactions would make the electrolyte depart further away from ideality as predicted by the Nernst–Einstein equation.¹⁹ This fact strongly implies that the ion transport mechanism starts the shift from a vehicular towards a structural manner. Maximum ionicity for “salt solvate” electrolytes was found to occur at a fixed stoichiometric ratio of ether units to Li^+ ($\text{EO} : \text{Li}^+$) of 4, which happens to be a typical Li^+ solvation sheath structure in ether-based solvents. Borodin *et al.*

attributed this behavior to the anti-correlation of the $\text{Li}^+(\text{EO})_4$ solvate and anion motion as required by the conservation of momentum in this highly dissociated electrolyte with little free solvent.¹⁹

17.1.2 Esters Could Be Cathodically Stable

The state-of-the-art electrolytes employed in lithium-ion batteries are based on carbonate esters. This class of electrolytes are blessed by both high dielectric constant and donor number, exhibiting excellent solvating capability towards most lithium salts and, in particular, one of them, ethylene carbonate (EC), possesses a unique ability to form SEIs on the fragile graphitic structure and CEIs on high-voltage cathode materials. However, esters are intrinsically unstable against reduction, especially by Li^0 [eqn (10.1)].

Compared with ether-based electrolytes, the application of the super-concentration concept to ester-based electrolytes has received much less attention. The main underlying reason is the low solubilities offered by ester solvents towards most salts. This is especially true when the most favored carbonate solvent, EC (m.p. 36.4 °C), often solidifies at salt concentrations above 1 M. More freedom was offered by the lower molecular symmetry of PC, which comes with both a low m.p. (-48.8 °C) and strong resistance against crystallization, hence the earliest super-concentrated carbonate electrolytes explored were based on PC.^{20,21} Dilute PC-rich electrolytes are known for graphite exfoliation (Scenario I depicted in Figure 10.7). However, when the concentration of lithium salts is high enough, no matter whether the salt is LiPF_6 , LiClO_4 or LiTSFI , the characteristic graphite exfoliation would be replaced by reversible lithiation/de-lithiation of graphite (Scenario III), apparently because the anions forced into the solvation sheath of Li^+ initiated a new interphasial chemistry that prevents the occurrence of exfoliation.

The emergence of a new salt anion, bisfluorosulfonylimide (FSI), makes it easier to apply the super-concentration concept in carbonate-based electrolytes, as the salts (Li, Na and K) are highly soluble in solvents with low dielectric constants such as linear carbonates and no longer require a solvent with high dielectric constant and high melting point. EC-free electrolytes consisting of a high concentration (~10 m) of LiFSI or NaFSI dissolved in EMC can form protective interphases and support the reversible Li^+ intercalation chemistries in graphitic structures as well as the 5 V class cathode material $\text{LiNi}_{0.5}\text{Mn}_{1.5}\text{O}_4$.²² The SEIs and CEIs generated by FSI apparently play the major role in enabling these chemistries. The implication from this work is that

super-concentration could induce alternative interphasial chemistries in carbonate-based electrolytes, so that the many restrictions that typical lithium-ion battery electrolytes are subject to can now be circumvented. The most prominent example is the presence of EC. In other words, super-concentration could make the presence of EC optional. This opens up opportunities to many “exotic” solvents that have previously been out of the question, especially considering the sensitive and fragile structure of graphitic anodes towards co-intercalation and exfoliation.

17.1.3 Exotic Solvents Could Be Electrochemically Stable

Among the polar, non-aqueous and aprotic organic molecules, only carbonate esters and ethers have received extensive evaluation as electrolyte solvents for most of the battery chemistries under development since the 1980s, while these “exotic” organic molecules were ruled out after stringent criteria were applied to them. Eventually, only carbonate esters made it into the commercial lithium-ion batteries, with EC as the indispensable component until recently.

After the super-concentration concept bestowed various unusual properties upon ether- and PC-based electrolytes, researchers gradually realized the intercorrelations along the chain of “salt concentration, solvation sheath structure or solution structure, interphasial chemistry”, and started applying the super-concentration concept to those solvent molecules which had been regarded as impossible. The exotic electrolyte systems thus generated include nitriles, sulfones and sulfoxides. Among these, prominent examples include acetonitrile, sulfoxide or tetrahydrofuran containing a high concentration ($>3.0\text{ M}$) of LiTFSI that supports reversible Li^+ intercalation chemistry in graphite, as reported by Yamada and colleagues,^{23,24} and sulfolane containing a high concentration of LiTFSI or LiFSI that supports both graphitic and lithium-metal anodes and high-voltage cathodes, as reported by Watanabe and colleagues²⁵ and Xu and colleagues.²⁶ The interphasial chemistries in these super-concentrated electrolytes are based almost exclusively on the formation of rich contents of LiF.

However, so far these exotic electrolyte systems remain laboratory novelties, *i.e.* they are still at the stage of proving that “they can also achieve this” but not yet in the position of “they can replace those state-of-the-art electrolytes because they outperform them”. Nevertheless, the knowledge accumulated helps in setting the foundation for the many more useful super-concentrated electrolyte systems.

As in other electrolyte systems, the effects of super-concentration are not confined to the interphasial aspects only, but also induce a series of unusual behaviors in the ion transport. For example, Watanabe and colleagues demonstrated that in super-concentrated sulfolane electrolytes, Li^+ experiences an apparent transition from vehicular to structural mode, and Li^+ starts to hop from one coordination site (*i.e.* the sulfonyl oxygen on the sulfolane structure) to another without concerted movements of the sulfolane molecules or anion involved.²⁵ This observation raises the possibility that long-range liquid structure could exist universally in all electrolytes, no matter whether aqueous or non-aqueous, provided that a certain threshold salt:solvent ratio is crossed. It should be cautioned here that structural ion transport does not necessarily involve long-range liquid structure, or offer better ion conductivities. Generally, a vehicular mechanism dominates when the solvation sheath consists of solvent molecules that coordinate strongly with cations, such as ethers (Figure 12.2), whereas a weaker cation–solvent interaction, which could arise from the presence of excess anions in the direct neighborhood because of the high salt concentration, leads to a greater structural contribution. In some (but not all) scenarios of super-concentration, where the solvent–anion interaction outmatches that between the cation and solvent, the anions could become less mobile as they are in dilute electrolytes, hence the cation transference number increases. This scenario occurs with sulfolane and FSI or TFSI, where the Li^+ transference is estimated to be ~0.70.

17.1.4 Water Could Have a Wide Electrochemical Stability Window

As briefly discussed in Sections 5.2.7 and 8.2 (Figure 8.2), water-based (aqueous) electrolytes have an electrochemical stability window of only 1.23 V, beyond which the water molecules are reductively or oxidatively decomposed, releasing hydrogen and oxygen gases. The limits of such an electrochemical stability window are reliant on the pH of the electrolyte, and at pH 7 the cathodic and anodic limits are –0.63 and +0.60 V *vs.* SHE, respectively (Figure 5.12). Of course, kinetic factors may well push the window wider than what thermodynamics tells us, especially on the anodic side, because the oxidation of water to oxygen gas involves four electrons, which is a rather sluggish process. However, such a kinetic delay of water decomposition does not involve any protection from interphasial chemistry, simply because none of the decomposition products from water (H^+ , OH^- , H_2 and O_2)

could adopt a solid form in an aqueous electrolyte and subsequently precipitate on the electrode surface as an interphase.²⁷

In this context, “water-in-salt” electrolytes proposed by Xu, Wang, Yamada and colleagues took the concept of super-concentration to the furthest extreme.^{28–31} They showed that, when the salt concentration crosses a certain threshold, the anion becomes the species that reductively decomposes on the surface of the negatively polarized electrodes, and the decomposition products could take the form of a solid precipitate and form an interphase. Of course, the selection of suitable salts here is essential, because (1) the salts have to be soluble enough in order to reach that certain concentration threshold and (2) the anions of the salts have to contain the required ingredients for the interphasial chemistry. Regarding the first requirement, there is no fixed quantitative value for the concentration, but it seems that for lithium salts the threshold needed is higher ($>15\text{ m}$), whereas for sodium it is $\sim 9\text{ m}$, and for multivalent cations the concentration of $3\text{--}5\text{ m}$ should already have crossed the threshold as each cation would bring two or three times the number of anions. Regarding the second requirement, the ingredient needed for interphasial chemistry identified thus far is fluorine, and the favored anions are TFSI, bis(trifluoroethane sulfonyl)imide (Beti) or other versions of fluorinated imide anions. FSI has also been proven effective for those salts (NaFSI and KFSI, for example) that are not as sensitive to hydrolysis as LiFSI.

Both experiments and simulations have revealed that, at those high salt concentrations, the anions are forced into the primary solvation sheaths of the cations, and subsequently activated towards reductive decompositions on the anode surface. In the case of lithium salts, the concentration of LiTFSI is *ca.* 21 m , and the interphase formed significantly suppresses the competitive decomposition reactions, especially those of water, expanding the cathodic stability limits of the aqueous electrolytes from -0.63 to *ca.* -1.6 V vs. SHE (Figure 17.1). Although this stability limit is still not low enough to allow desired anode materials such as graphite, silicon or lithium metal, it has already delayed the thermodynamic reduction of water by nearly 1 V. A similar Li^+ electrolyte system developed by Yamada and colleagues, named “hydrate melt” electrolytes, consists of a mixture of salts at even higher salt concentrations and hence with more reduced water reactivity, resulting in electrochemical stability windows approaching those achieved in non-aqueous electrolytes.³⁰ Various characterizations and simulations were applied to this new class of aqueous electrolytes, and the SEI formed was identified as a dense interphase layer mainly constructed of LiF nanocrystals embedded with “impurities”

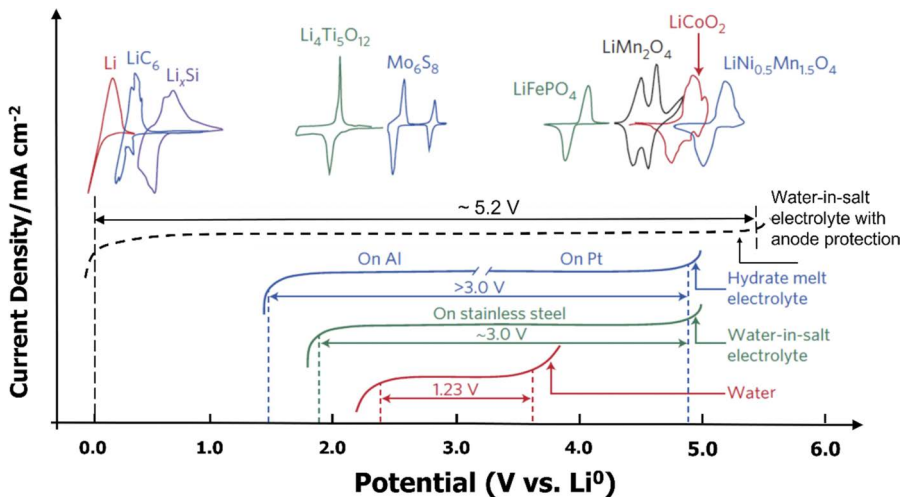


Figure 17.1 Expansion of the electrochemical stability window in aqueous electrolytes *via* the application of the super-concentration concept. Note that the window curve for “hydrate melt” is broken in the middle, because the cathodic and anodic curves were collected on different substrates (cathodic on aluminum and anodic on platinum), while all other curves were collected on a single substrate of stainless steel. The cyclic voltammetry traces for various anode and cathode materials are also shown in the top panel for comparison.

such as Li₂O, Li₂CO₃ and LiOH. As pointed out in Section 16.6.7 (Figure 16.7), the presence of these impurities might be essential for the effective travel of Li⁺ across the LiF-dominant SEI, as the latter is an insulator to both ions and electrons.

As in the case of non-aqueous electrolytes, the presence of an interphase on an anode surface is beyond any doubt, but such a presence on a cathode surface remains rather dubious, because most of the spectroscopic characterizations, either *ex situ* or *in situ*, could not find solid evidence for the presence of an obvious CEI on the cathode surface. Hence it is speculated that a permanent interphase may have never been formed. Instead, it appears that the anodic stability of aqueous electrolytes is mainly contributed to by kinetic factors: the sluggish oxidation process of water is simply made even more sluggish by the highly concentrated aqueous electrolytes. In fact, the kinetic protection of the cathode surface is helped by the fact that upon charging, its positively polarized surface attracts anions preferentially, which could assemble in the Helmholtz planes and form a “hydrophobic” layer. This is actually the concept of a dynamic and transient interphase that will be discussed in more detail in the next section.

However, an anode surface does not have such dynamic and transient protection; on the contrary, the anode surface in aqueous electrolytes faces two natural disadvantages: (1) the energy barrier to water reduction and subsequent hydrogen evolution is rather low, and the reductive decomposition of water is usually very fast, and (2) the negatively polarized surface of the anode preferentially repels anions while attracting Li^+ or other cations, which always bring water molecules within their solvation sheaths. These water molecules, already activated by the Coulombic field of cations, are vulnerable to reductive decompositions, and would compete with the reductive decomposition of the anions. The combination of these two factors creates the so-called “*cathodic challenge*”, which works against the intention of forming SEIs from anion decomposition.

The cathodic challenge could only be suppressed to a certain extent by the application of the super-concentration concept. As illustrated in the bottom panel of Figure 17.1, the anodic stability limits of these super-concentrated aqueous electrolytes are already more or less sufficient to encompass the operating potentials of most *cathode materials* used in lithium-ion batteries; however, the cathodic stability limits are still located far above the operating potentials of these commonly used *anode materials* in lithium-based batteries, such as Li^0 , graphite or silicon. Increasing the salt concentration alone could not overcome this cathodic challenge. To stabilize the aqueous electrolytes with these active anode materials, one needs to explore additional measures. For example, coating of the anode surface with an artificial proto-SEI, normally consisting of fluorine-containing and hydrophobic ingredients, would further expand the electrochemical stability window of aqueous electrolytes to levels comparable to those of non-aqueous electrolytes (Figure 17.1, top panel).³² Here, artificial intervention with a hydrophobic and fluorinated precursor for the eventual SEI helps to counter the natural disadvantages created by the facile water decomposition and the strong Coulombic repulsion of the fluorinated anions by the anode surface. The new interphasial chemistry is still based mainly on LiF and other fluorides, but the fluorine source has been switched from the anions to the hydrophobic layer applied.

Aqueous super-concentrated electrolytes have also been applied to other battery chemistries beyond lithium-metal and lithium-ion chemistries, including a unique chemistry using a sulfur conversion reaction as the anode instead of cathode as well as intercalation chemistries of sodium and potassium ions and multivalent ions such as Mg^{2+} , Ca^{2+} and Zn^{2+} .

In addition to benefits in interphasial chemistry and electrochemical stability, the aqueous nature of such electrolytes also brings stability against the ambient environment. This advantage was most conspicuously demonstrated by an aqueous gel version of Zn electrolytes, which was exposed to ambient laboratory conditions for 40 days and experienced no weight loss, hence allowing an open configuration of a battery with high safety.³³ This comes in strong contrast to devices that rely on non-aqueous electrolytes, the moisture sensitivity of which requires hermetic sealing of the device, which makes it rigid and not easy to use. Thus, the ambient stability introduces unprecedented flexibility, which has been demonstrated on different lithium-ion and lithium-metal chemistries at the pouch cells level.

The attempts to understand the chemistry and formation mechanism of aqueous interphases naturally prompted interest in the *interfacial* structure at electrodes, which should, no matter whether in aqueous or non-aqueous systems, precede any chemical reactions that lead to the actual formation of any interphases, and therefore should in principle predict the interphasial chemistry. When Borodin and co-workers tried to rationalize the “*cathodic challenge*”, they considered the electrode–anion interaction to be mainly responsible as discussed above, and their molecular dynamics simulations revealed that such uneven positioning of cathodic and anodic limits in those super-concentrated aqueous electrolytes stems from the competitive distributions of water molecules and salt anions at the inner-Helmholtz interface of the electrode, which varies as a function of both salt concentration and applied potential.^{33,35} Although super-concentration ensures that the inner-Helmholtz layer of an anode surface is more populated by anions, thus leading to an interfacial structure more inclined towards the formation of an anion-based interphase than would be the case in a dilute aqueous electrolyte, further cathodic polarization would disrupt such a preference by expelling anions and attracting cations solvated by water molecules, as evidenced by the necessity to enforce a fluorinated interphase *via* artificial coating of a proto-SEI layer.³⁴

In addition to interfacial and interphasial considerations, an equally important factor is the presence of a long-range liquid structure resulting from the unique local solvation structures, which were described in Section 12.2.4 (Figures 12.6 and 12.7). Very different conclusions were drawn regarding how Li⁺ or other cations are solvated by water molecules and anions, depending on the force fields applied to the system. Borodin *et al.* argued that in a water-in-salt electrolyte (WiSE), once a threshold salt concentration (~10 m for LiTFSI) is

crossed, the Li^+ solvation sheath structure experiences a significant disproportionation, where the distribution of water molecules and anions around an Li^+ is not averaged according to the bulk composition. Instead, some Li^+ would only see water molecules while the others see anions.³⁵ Such an uneven distribution of solvation sheath structure results in a nanoscale phase separation, *i.e.* the “*nano-heterogeneity*” illustrated in Figures 12.6 and 12.7. Although the exchanges of water molecules and anions around an Li^+ occur on a time scale of picoseconds, the structure could be captured by techniques with high temporal resolution, such as neutron scattering or femtosecond pump–probe infrared spectroscopy.

This nano-heterogeneity of the solution structure is expected to promote preferentially the cation transport, because the anions are now relatively immobilized in a framework of lower mobility. This prediction seems to be supported by the measurement of Li^+ transference numbers using pfg-NMR spectroscopy, which results in $T_+ \approx 0.73$, apparently higher than what it should be in dilute electrolytes (0.2–0.4). Theoretically, the preferential ion transport is believed to benefit the rate performance of a battery chemistry based on the redox reactions of this ion. Hence the capability of WiSE to support high-rate charge/discharge (up to 60C) in diverse chemistries (Li^+ , Zn^{2+}) despite the moderate ionic conductivities seems to stem from such preferential ion transport that was enabled by the unique ion solvation structures and the subsequent long-range liquid structures.

The above nano-heterogeneity argument was supported by some researchers, including Lim and colleagues, who found that dissolved Li^+ ions form a three-dimensional, percolating network that is spontaneously intertwined with nanometric non-solvating water molecules, through which the solvated Li^+ ions move as if they conduct *via* a fast lane that is little affected by the anions.³⁶ However, the results of other studies using different force fields disagree that disproportionation occurs. This is a topic that should be further looked into before a more definite conclusion can be drawn.

17.1.5 Locally Concentrated Electrolytes, Aqueous–Non-aqueous Hybrid Electrolytes

After the super-concentration concept was successfully applied to various aqueous and non-aqueous electrolytes, numerous efforts have been made in attempts to improve further the electrochemical stability, safety, cost and performance of these electrolytes. One direction that has received the most intensive attention is to hybridize the

aqueous systems with non-aqueous components and create an electrolyte that inherits the merits of but circumvents the weaknesses of both systems.

The most pronounced weakness of super-concentrated electrolytes is their high cost. In the lithium-ion battery industry, the electrolyte often constitutes the second most expensive component after the cathode materials, and a lithium salt is often the most expensive among all electrolyte components. While imide anions such as TFSI and FSI are often favored owing to their excellent solubility and electrochemical uniqueness, these uncommon anions must be synthesized and purified *via* rather sophisticated processes, which are costly at present owing to the limited market demand. More recent efforts by the industry have driven down the cost of LiFSI significantly, but even at a cost level comparable to that of LiPF₆ one does not wish to use this component at high concentrations. In addition to cost concerns, super-concentration also suffers from the disadvantages of high bulk viscosity and poor wettability, which make it difficult for the electrolytes to access thoroughly the porous structures of both the electrodes and separators.

A clever approach named "*localized high-concentration electrolytes*" was proposed by Xu, Zhang and colleagues at Pacific Northwest National Laboratory, who attempted to maintain the advantages of super-concentrated electrolytes (interphasial chemistry, preferential cation transport and safety) while eliminating their disadvantages (cost, viscosity, ion conductivity and wettability).^{37–40} The essence of such approaches is a "*non-solvent*", which does not directly dissolve the salt but should form, at least macroscopically, homogeneous mixtures with the bulk electrolyte solvents. This non-solvent, usually a polyfluorinated ether with weak polarity, serves as both a diluent to reduce the overall salt concentration in the bulk electrolyte and a structure interrupter that forces the salt-containing domains to be compressed, so that a similar solvation sheath structure can still be preserved locally. Thus, whereas the local environment of cations (Li⁺ or Na⁺) still maintains the solvation structure of super-concentrated electrolytes, which dictates the interphasial chemistries at electrode surfaces, the bulk properties (ion transport, viscosity or wettability towards the electrodes and separators) were mainly defined by the average composition of the bulk electrolyte that still retains the nature of a more dilute regime. This successful separation of the desired bulk from interfacial properties *via* the engineered solvation structure and long-range liquid structures has enabled a number of exotic solvent systems traditionally thought impossible to be formulated, and raised

the hope that more optimized electrolyte systems should be expected from this effective concept.

In a related approach, Wang *et al.* hybridized aqueous and non-aqueous electrolytes in the hope that the advantages of ion transport and non-flammability from the former could be combined with the interphasial chemistry from the latter.⁴¹ A linear carbonate ester, dimethyl carbonate (DMC), was selected as the non-aqueous component, despite the fact that DMC is immiscible with water in the absence of a lithium salt. Apparently, the water molecules in WiSE differ significantly from the water molecules in the bulk state provided that the salt LiTFSI reaches the super-concentration level, because homogeneous solutions form between DMC and WiSE. The overall concentration of LiTFSI in this hybridized system is still ~14 m, but already significantly lower than the 21 m of WiSE. This aqueous–non-aqueous hybrid electrolyte meets part of the goal: it inherits the non-flammability from the aqueous nature, reduces the concentration and the cost of salt, and further expands the electrochemical stability window to ~4.1 V, which supports the reversible operation of a high-voltage cathode material, $\text{LiNi}_{0.5}\text{Mn}_{1.5}\text{O}_4$. Surface analysis revealed that the carbonate molecule DMC introduced a significant amount of a second component (Li_2CO_3) into the SEI. This approach was soon extended to other battery chemistries, including Na and Zn batteries, while the range of non-aqueous solvents includes PC, nitriles, ethers and sulfolane.⁴²

By obscuring the once clear demarcation between aqueous and non-aqueous regimes, this new class of hybrid electrolytes offers unlimited possibilities to explore.

17.2 Beyond Liquid Phases: Liquefied Gas and Frozen Ice

The traditional boundaries between phases are also breached, allowing us to expand the temperature limits imposed by the liquid state of electrolytes. One new class of electrolytes based on liquefied gas was reported by Meng and colleagues, who used a variety of hydrofluorocarbons (fluoromethane, difluoromethane, fluoroethane, 1,1-difluoroethane, 1,1,2,2-tetrafluoroethane and 2-fluoropropane) as electrolyte solvents.^{43,44} These unconventional “solvents” are all in the gaseous state under ambient conditions. However, under moderate pressure, their mixtures with lithium or ammonium salts (LiTFSI, 1-ethyl-3-methylimidazolium-TFSI and tetrabutylammonium-PF₆) turn into the liquid state, and can serve as electrolytes to support

various battery chemistries including lithium-metal and graphitic anodes and 4 V class cathodes of LiCoO_2 .

Owing to their small molecular size, weak intermolecular attraction, high dielectric constants and low viscosity, these unconventional solvent molecules permit superior solvent dielectric-fluidity factors that are higher than those of typical electrolyte solvents such as esters and ethers, in addition to their extremely low melting points. Additives such as tetrahydrofuran (THF) can be introduced to alter the Li^+ solvation structure, which has been fully populated with fluoromethane molecules. The intrinsic fluorine-rich chemistry and the self-equilibrated pressure permit Li^0 reversibility even at very high current density (10 mA cm^{-2}) and at low temperature. Lithium-metal batteries constructed using this electrolyte display exceptional performance, especially at temperatures as low as -60°C . It was believed that a highly fluorinated interphase was formed on the anode surface upon its contact with these fluorocarbons. Compared with the SEIs generated in carbonate-based electrolytes, the composition of these interphases was found to be highly ceramic-like instead of polymeric/organic in nature, with LiF identified as the major component. Optimized electrolytes in this class demonstrated stable cycling over 500 cycles with a Coulombic efficiency of 99.6%.

Other types of cosolvent could also be employed to widen the operating temperature range, especially at the limit where salt precipitates and ion transport shutdown occurs. More recent use of difluoromethane (CH_2F_2) in combination with dimethoxyethane cosolvent has shown such improvement, and the concept was also extended to multivalent chemistries such as Zn.⁴⁵ This new type of electrolyte, although restricted to limited applications because they require a hermetically sealed stainless-steel case, have significant potential for further development.

On the other side of the phase spectrum, researchers have reported ion conduction behavior in solid ice, which opens up the possibility of a new class of solid-state electrolyte. Conductivities of up to $10^{-3} \text{ S cm}^{-1}$ were reported for various sulfate salts at *ca.* -8°C .⁴⁶ The authors attributed the transport of Li^+ and other alkali metal cations to an ion-hopping mechanism through the ice lattice. Unexpectedly, multivalent ions (Al^{3+} , Mn^{2+} , Zn^{2+} and Cu^{2+}), which are considered rather clumsy because of their strong Coulombic interactions with the environment (solvent molecules, electrode lattices, *etc.*), were found to be fairly conductive, with conductivities between 10^{-4} and $10^{-7} \text{ S cm}^{-1}$ in the low temperature range of -4 to *ca.* -10°C . These working ions were shown to be able to reversibly deposit and strip from such a solid-ice electrolyte onto an electrode.

Although only limited efforts have been made in this direction, new types of electrolytes could be discovered by further breaching the traditional boundaries that confine our thought processes.

17.3 Solidifying Electrolytes

With extremely limited exceptions, almost all electrode materials are in the solid state. Therefore, there is an intrinsic advantage of an electrolyte being in the liquid state, because it can intimately interface with those solid electrodes because of its fluid nature, accessing most of the pore structure of the electrode materials, maximizing the actual contact area, and subsequently ensuring that the charge transfer across the interfaces would not encounter excessive resistance because of limited interfacing. However, a liquid electrolyte also comes with intrinsic disadvantages, which include leakage if the electrochemical cell is broken, making it difficult to contain the spillage of highly toxic ingredients, and also the high flammability of the non-aqueous electrolytes. The latter becomes especially critical when more and more aggressive electrode materials are used to pursue higher capacity, higher power and higher energy of batteries.

It has long been a tantalizing goal to solidify this fluid component in the cell.^{47,48} Serious efforts started with Armand in the 1970s, who proposed to leverage polymeric materials based on ethylene oxide linkages, $[CH_2CH_2O]_n$, to dissolve lithium salts and serve as solid polymeric electrolytes (SPEs).⁴⁹ However, that class of solid electrolytes have encountered the intrinsic dilemma that while a flexible polymeric chain is desired because the ion transport relies on the cooperative motion of the polymer chain these polymeric linkages must also provide strong mechanical support, hence the polymeric chain must be rigid enough. The struggle to balance these two conflicting properties dominated the history of SPEs research during the last four decades, and one indication is that the ion conductivities in SPEs at ambient temperature never achieve a value above $10^{-4} \text{ S cm}^{-1}$.

Consequently, these polymeric electrolytes found only limited applications in batteries, where an elevated temperature ($>60^\circ\text{C}$) is needed to achieve a decent ion conductivity ($>10^{-4} \text{ S cm}^{-1}$) for practically feasible cell reaction rates. Furthermore, despite a 1983 article by Yazami reporting that lithiated graphite can be formed electrochemically in PEO-based SPEs,⁸⁸ these electrolytes are actually incapable of supporting graphitic anodes owing to high interfacial resistances, unless they are plasticized with suitable solvents. This essentially

excludes polyether-based SPEs from commercial lithium-ion batteries and restricts their opportunities to a narrow niche market of lithium-metal anode batteries. Furthermore, the ether linkages in these polymer electrolytes are also susceptible to oxidation at the cathode surface, hence their application in batteries is restricted to those with moderate voltages, such as lithium iron phosphate (LiFePO_4). Efforts were made to circumvent the ion conductivity issue by combining a polymeric electrolyte with a liquid electrode.

Alternatively, another class of ceramic material, β -alumina, was also discovered in the early 1970s as a fast Na^+ conductor, and serious efforts were made to apply it as a solid electrolyte in diverse electrochemical devices including batteries.⁵⁰ Despite its popular name, β -alumina is in fact not an alumina (Al_2O_3) or its polymorph, but instead a non-stoichiometric compound with the general formula $\text{Na}_{1+x}\text{Al}_{11}\text{O}_{17+x/2}$, where the excess amount of Na^+ forms the conducting layer (Chapter 2, Figure 2.1, leftmost structure at the bottom). Although similar structures with different guest conducting ions including proton (H^+), potassium (K^+), silver (Ag^+), lead (Pb^{2+}) and barium (Ba^{2+}) could also be constructed, Na^+ -conducting β -alumina received the most attention, and a battery constructed based on sodium (Na^0)/sulfur chemistry once reached the pre-production stage in early electric vehicle applications. The concept never materialized into a commercial product, because the high temperature ($>700\text{ }^\circ\text{C}$) that is required to maintain fast ion conduction and to keep the two electrode materials in the molten state was inconvenient and highly unsafe. However, these early efforts with β -alumina inspired Whittingham to investigate how ions could transport so fast *via* the interstitials in the solid state, which led to his later discovery of the very first Li^+ intercalation compounds.⁸⁹

In the 2010s, interest in inorganic electrolyte materials was revived. A few classes of such materials in either ceramic or glassy states were discovered, and ion conductivities as high as, or even higher than, those of liquid electrolytes were realized. These materials excited the battery and materials research community to re-examine the possibility of an all-solid-state battery.

17.3.1 Polymer Electrolytes

Strictly, the polymer electrolytes are *semi-solids*, because although *macroscopically* they display certain dimensional stability, *microscopically* the ions in them interact with the solvating environment, the ethylene oxide linkages, and are transported across them as they are

in liquids. This characteristic applies to both SPEs and gel polymer electrolytes (GPEs),⁵ except that in the latter the working ions are solvated by the added small solvent molecules rather than the polymeric linkages.

The search for polymeric linkages other than ethylene oxide that can effectively dissolve lithium salts has not been successful, hence currently, most polymeric electrolytes, especially SPEs, are still mainly constructed with variations of the structures with ethylene oxide units. However, GPEs enjoys much more flexibility, as they rely on small solvent molecules to solvate working ions, and the polymer therein serves only as the framework providing dimensional stability, processability and mechanical support. Hence many polymer and copolymer units based on structural units of acrylonitrile, imides, styrene, *etc.*, have been reported, and the liquid electrolytes employed are usually those mature compositions that have already proven successful in commercial lithium-ion batteries. The “soft” nature of these materials makes their interfacing with electrodes easier than with true solid electrolytes. In particular, the emerging markets for flexible electronics favor batteries based on such semi-solid electrolytes. Modern processing techniques such UV curing and e-beam curing have been widely adopted.

The SPEs, in the absence of any small solvent molecules, still face severe challenges owing to their poor ion transport, but breakthroughs have been reported sporadically when SPEs are interfaced with nano-structured materials, such as silicates (SiO_2), titanate (TiO_2), alumina (Al_2O_3), metal-organic frameworks (MOFs), *etc.*, with ion conductivities well above $10^{-4} \text{ S cm}^{-1}$ at room temperature being achieved. The explanation of how these nano-structures promote ion transport remains unclear: some attributed the improvements to the elimination of crystalline phases of ether linkages, while others resorted to the interactions between the surfaces of these nano-structured materials and the Li^+ and polymeric chain. The argument from Cui and colleagues that the nano-channels provide fast Li^+ -conducting pathways is especially interesting, as it might involve the confinement of solvated Li^+ in an environment that is of comparable size to the solvation sheath.⁵²

In an alternative approach, Aetukuri *et al.* believed that simply blending a ceramic solid electrolyte in a polymer matrix actually did not fully leverage the high conductivity of the former, because these particles are eventually embedded in the less conductive polymer matrix without forming an independent percolating pathway for Li^+ transport.⁵¹ Leveraging a casting-etching technique extensively

used in semiconductor and electronics fabrication to a composite polymer–ceramic electrolyte, they were able to form a single solid electrolyte layer consisting of ceramic particles whose size dispersion was well within the narrow range of ± 15 nm. These particles are firmly embedded in a polymer matrix with their top and bottom surfaces exposed so that a direct ionic pathway is established without going through the polymer matrix. Such a thin membrane (<100 μm) is a flexible polymer–inorganic composite electrolyte that not only offers excellent ion conductivity and mechanical strength, but also proved to be rather effective in suppressing Li^0 dendrites.⁵¹ The latter benefit comes from the fact that the “soft” part (the polymer) is nearly insulating towards Li^+ conduction. Of course, the interfacing issue between such a composite and a solid electrode material remains.

In addition to ion transport, a property more relevant to the high rate capability of cell reactions is the Li^+ transference number. Theoretically, an Li^+ transference number of unity ($T_+ = 1.0$) eliminates concentration polarization and limits the opportunities for Li dendrite formation. However, in reality there is always a significant compromise in both ion conductivity and polymer flexibility once the anions are immobilized on polymeric chains *via* covalent bonds. To resolve this compromise, liquid solvents have been embedded into single-ion conducting polymers, which is a close simulation of fuel-cell Nafion polyelectrolytes plasticized by water. Such a class of single-ion electrolytes, based on aromatic poly(arylene ether)s with pendant lithium perfluoroethylsulfonates and saturated with liquid electrolytes, exhibits a T_+ of nearly unity along with high conductivities ($>10^{-4}$ S cm $^{-1}$) even at low temperatures. According to Archer and co-workers, a high T_+ constitutes a key control over the reversible deposition and stripping of Li-metal anodes.⁵³

Given the instability of ether linkages at high potential, SPEs usually cannot support cathode materials that operate at >4.0 V *vs.* Li, hence the most popular cathode chemistries (LiCoO_2 , $\text{LiNi}_{x}\text{Mn}_{y}\text{Co}_{z}\text{O}_2$ and $\text{Li}_2\text{Ni}_{0.5}\text{Mn}_{1.5}\text{O}_2$) are usually excluded, and LiFePO_4 is often the favored cathode for these polymeric electrolytes. This anodic stability can be circumvented by using a dual-layer SPE, where a polymer material of high anodic stability (polyamide-based) is in contact with the cathode, allowing a 4 V class cathode to be used, while an ether-based SPE is interfaced with the anode. Needless to say, the overall ion conductivity is now defined by the less conducting polymer here, *i.e.* $<10^{-5}$ S cm $^{-1}$ of polyamide at room temperature, if no additional interfacial resistance arises from the junction of the two polymers.

One special class of polymer-based electrolytes leverages the self-healing nature of certain polymers, so that any chemical, electrochemical or mechanical degradation that often occurs with electrodes during long-term cycling could be repaired. This concept mainly employs reversible hydrogen bonding or other non-covalent chemical bonding. Varying degrees of success regarding both interfacial stability with electrodes and capability of self-healing damage at the system level were reported.

Leveraging the mature techniques in the semiconductor and electronics industries such as photo-patterning and lithography, new manufacturing technologies were also used to pattern or etch polymer electrolytes and polymer-based separators for various merits. This allowed the application of the emerging 3D printing technologies. Such approaches are regarded as highly valuable in enabling 3D micro-batteries to be formed directly on chips with fabrication of modulable arrays.

17.3.2 Liquid-Inorganic Interfacing

In 2013, a new class of semi-solid electrolytes was created by Maier and colleagues, who named them “*soggy-sand electrolytes*”, that bridge conventional liquids with solids.⁵⁴ This hybridization strategy aims at combining the liquid-like fast ion transport from a conventional liquid electrolyte with the dimensional stability and high modulus of an inorganic solid framework, which is often based on nano-sized inorganic particles such as silicate, alumina or even various ceramic electrolytes. Thus, the solid could be either an ion conductor itself, or a completely inert structural scaffold. These oxide solids often serve as a preferential adsorption surface for the salt anions, hence the lithium salts dissolved in the liquid phase would be further dissociated, rendering the Li⁺ more mobile than the anions.

The eventual dispersion of the particles in the liquid phase forms a fractal percolating network to accelerate the ion transport. Such dispersion of nanoparticles in the liquid phase is not spatially immobilized, therefore gravitational precipitation could occur once the equilibrium is breached, putting an end to the ion transport network. The introduction of a suitable fraction of inorganic solids into liquid electrolytes usually induces a spike in ion conductivities, which could be improved as much as fivefold, in addition to improved Li⁺ transference number.

The actual ion transport process in these “*soggy-sand*” electrolytes could be much more complicated, involving surface energy,

space charge and surface functionalities of the oxide particles. Similar effects for polymeric electrolytes were discussed in the previous section, and a more recent explanation involves the concept of nano-confinement that will be discussed in more detail in the sections to follow.

Several variations of liquid–inorganic hybrids have been inspired by the “soggy-sand” concept, in which stabilization of the lithium–metal anode surface was specifically targeted. These systems include excess lithium halide salts suspended in non-aqueous electrolytes, ionic liquids tethered to the surface of inorganic particles, anions immobilized on nanoparticles that are dispersed in liquid electrolytes and liquid electrolytes infused into composites of inorganics and polymers.^{55–57} Improvements with varying degrees of success were reported for Li–metal cycling stability, with rationales based on the surface energy of the electrolyte/Li interface. More recently, further concepts also evolved and were extended to many other inorganic particles with meso-, nano- or hierarchical structures, including oxides such as Al₂O₃, SiO₂, ZrO₂ ad CeO₂ or even metal–organic frameworks (MOFs) and covalent organic frameworks (COFs). Generally, the liquid electrolytes were thought to be trapped *via* either physical (non-covalent) forces or chemical interactions in the meso- or nanopores of these inorganic scaffolds, with benefits such as decent ion conductivities ($>1.0\text{ mS cm}^{-1}$), improved Li⁺ transference numbers (~ 0.6) or an additional capability to suppress Li–metal dendrites. In particular, Archer and colleagues described a so-called “*ionic rectifier*”, where a liquid electrolyte physically constrained in the narrow pores of α -Al₂O₃ demonstrate Li⁺ transference numbers of nearly unity, owing to the blocking of anion transport by the pore wall that bears the same charge.⁹⁰ Again, the effect of nano-confinement should apply here, considering that the nano-sized pores, voids and channels in these frameworks serve as an essential factor in enabling all these unusual properties that are otherwise unavailable in conventional liquid or solid electrolytes.

Although the semi-solid electrolyte approaches represent a new class of promising materials for the next-generation battery chemistries, with high Li⁺ transference numbers as the main attraction, most of the materials are still yet to be rigorously characterized under electrochemical conditions close to a real battery environment. In particular, their stability against high-capacity and high-voltage cathode chemistries remains to be manifested. Most important, this is an emerging new area, and there has not been a unified framework in the understanding of the phenomenon.

17.3.3 True Solid Electrolytes and Their Interfaces/Interphases

In the battery and materials communities, the term *solid-state electrolytes* (SSEs) or simply *solid electrolytes* (SEs) is often reserved for the class of ceramic or glassy materials that are capable of conducting ions, *i.e.* the fourth type electrolyte discussed in Section 2.1 (IV in Figure 2.1). The first SSE seriously considered as an electrolyte in an actual battery was β -alumina, which was not successful because of its poor ion conductivity at room temperature.⁵⁰

Since the 2010s, lithium-ion batteries have been gradually adopted in electric vehicles, in attempts to fight climate change and acquire independence from a reliance on fossil fuels. Accompanying the popularization of lithium-ion batteries is the increasing public concern over their safety, as highlighted by more frequent media coverage of the fire hazards caused by thermal runaway of lithium-ion batteries.

Such high-profile incidents are the inevitable result of the extensive application of these high-energy electrochemical devices in our daily life. Strictly speaking, the safety of the battery is determined by a combination of two factors, one being the energy contained in the enclosed device and the other the rate at which such energy could be dissipated when the designed electrochemical pathway encounters a failure. Therefore, at least in part, the highly flammable electrolytes in these electrochemical devices should be held responsible for these catastrophic cell failures, because of their metastability with the reactive electrodes, which is kinetically maintained by the presence of SEIs and CEIs, and this serves as the major weakness to allow the instantaneous dissipation of large amounts of energy.

To minimize the safety concern with high-energy batteries, one needs to remove at least one of these two factors. It is unrealistic to make a battery less energetic, because it would defeat the original purpose of new battery research. The only remaining factor to consider is the electrolyte. Theoretically, solidifying the electrolyte with inorganic materials with ceramic or glassy structures would provide a more robust kinetic barrier that should withstand a higher degree of cell abuse and slow the energy dissipation when the cell fails.

Extra benefits could also be generated from the inorganic SSEs. For example, the mechanical strength of these materials is expected to be sufficiently high to suppress the formation of Li^0 dendrites, so that this ultimate anode becomes feasible; the lattice or matrices of true SSEs would only allow Li^+ or other working ions to pass, providing a transference number of unity ($T_+ = 1.0$); the anode–cathode dialog

caused by the cross-over of parasitic electrode reactions, such as the polysulfide species generated in the sulfur chemistry, could be completely shut off; and the higher gravimetric or volumetric energy densities brought by the more efficient packing because of the high density of SSEs, *etc.*

The above challenges and potential merits drove the discovery of new classes of SSEs since the 2010s, and there have been numerous major materials that were claimed to be close to practical applications, such as the garnet type, the antiperovskite type and diverse sulfide types including argyrodites.

The newly discovered SSEs, especially those based on sulfide-type materials, have provided ion conductivities (10^{-3} – 10^{-2} S cm $^{-1}$) that approach or are even higher than those of the state-of-the-art non-aqueous electrolytes ($\sim 10^{-2}$ S cm $^{-1}$). Therefore, the most severe challenge facing the SSEs remains the interfacial issues between two solid phases, and consists of two separate parts: (1) the poor physical solid–solid contacts and (2) the chemical or electrochemical reactivity between the electrolytes and the electrodes, which is especially pronounced for sulfide-type materials as they have a rather narrow electrochemical stability window and are unstable against either reductive or oxidative decompositions.^{58,59}

The decompositions of SSEs, especially those based on sulfides, have been well documented with both experimental evidence and theoretical predictions. Overall, the nature of how the SSE interfaces with electrode materials directly dictates the performance of the solid-state batteries, with four possible scenarios: (1) SSE materials that are inherently stable against the active material and will not form an appreciable interphase; (2) the decomposition products of SSEs are electrically conductive, resulting in the continuous decomposition of SSEs and cell degradation; (3) SSEs are susceptible to decomposition but will generate products that are of electrolyte nature, *i.e.* allowing the conduction of working ions but insulating electrons; and (4) the products from the decompositions of SSEs either cannot conduct or only poorly conduct both electrons and ions. While the first scenario might only exist if an SSE with a wide electrochemical stability window, such as garnet, is interfaced with electrodes of moderate operating potentials, most SSEs fall into the last three scenarios. In particular, the third scenario actually closely resembles the concept of interphases in the case of liquid electrolytes.

The products from these interfacial reactions form extra interlayers of different chemical natures between bulk electrolyte and bulk electrodes. In most cases they bring an increase in interfacial impedance,

loss of mechanical integrity and strength, and volume changes and worsening of physical contacts between solid and solid phases.

Despite the high expectations that SSEs would have sufficient mechanical strength against Li^0 dendrite growth, such growth has been still identified from time to time. Differing from the relatively free growth in liquid electrolytes, Li dendrites seems to move preferentially through the interconnecting pores and grain boundaries within the SSE.⁶⁰ However, there is already a report revealing that, even with a single-crystalline SSE, where grain boundaries do not exist, dendrite growth still occurs.⁶¹ Wang and colleagues argued that this is an intrinsic issue associated with the much higher electronic conductivity of these inorganic SSEs, which can only be resolved with the formation of an interlayer standing between the bulk SSEs and the Li^0 electrode.⁶² Such an “interlayer” is in fact an artificial interphase.

Because dendrite growth had been thought to start with the depletion of the Li^+ concentration at the interfaces, according to the prediction of Sand's time [Section 7.2, eqn (7.16)], the relatively low Li^+ conductivity of some SSE materials has also been blamed. However, the dendrite growth should more likely follow a diffusion-controlled mode of growth. This is in contrast to the mossy and diffusion-controlled modes of liquid electrolyte systems. Since liquid electrolytes ensure intimate contact with the newly formed dendritic Li^0 , mossy dendrites grow, and lead to constant impedance buildup. For SSEs, however, the contact between newly formed Li^0 and SSEs is rather limited and highly heterogeneous; instead, SSEs are more prone to decomposition, which will increase impedance. When combined with the typically lower conductivity (as a result of both bulk SSE ionic conductivity and interface resistance between active material and the SSE), the formation of dendrites could occur even at seemingly low current densities. Nevertheless, under conditions of internal short-circuit created by these dendrites, batteries using SSEs will still be safer compared with liquid electrolytes.

17.3.3.1 Garnet-type SSEs

Garnet-type materials typically have the general formula $\text{Li}_x\text{La}_3\text{Zr}_2\text{O}_{12}$ (LLZO) and differ between one another mostly in the addition of various metal dopants such as Ti^{4+} and Ga^{3+} .^{58,59} In contrast to sulfide-based SSEs, garnets are significantly more stable, in both chemical and electrochemical senses, because they are oxides by nature. We have witnessed a similar stability transition when

the research on intercalation materials was switched from chalcogenides (TiS_2) to transition metal oxides (Section 9.1.3.8). This advantageous aspect of garnets make them an attractive electrolyte candidate when coupling with aggressive electrode materials such as lithium metal is considered. However, at higher voltages, they will still decompose. The weakness of garnet-type materials, on the other hand, is the generally lower ion conductivity compared with those of sulfide-type materials. The most conductive phase, the cubic phase, is difficult to achieve without additives. Moisture can interact with garnet SSEs, during which Li^+ exchanges with H^+ , leading to the formation of LiOH and Li_2CO_3 species, both of which are highly insulating to Li^+ .

The synthesis of garnets, or any oxide-based SSE, requires a high sintering temperature, especially for the highly conducting cubic phase (1230 °C), which will likely induce increased manufacturing costs compared with the sulfide-based SSEs. Garnet-based materials also show poor processibility, because their oxide nature renders the garnet particles rather hard and consequently the corresponding SSEs very brittle.

The hard and brittle nature of garnets also makes their interfacing with solid electrode materials rather challenging, especially when the electrode material itself is also hard and brittle in nature. Hence most of the interfacing issues arise at the electrolyte/cathode interface instead of the electrolyte/anode interface, because both lithium metal and graphite are soft and compliable whereas transition metal oxides are not. To overcome such interfacing issues, garnet-type SSEs often require a co-sintering process to achieve intimate contact with the active electrode materials.

The chemical stability between garnet-type SSEs and lithium metal is still uncertain owing to their rather close redox potentials, but evidence has been found that an oxygen-deficient interphase could have been formed between deposited Li and mechanically polished LLZO. The mechanism of the formation of such interphases could have proceeded *via* the elimination of oxygen by reaction with Li^0 , which is then charge compensated by the reduction of Zr^{4+} in LLZO. On changing the dopant element to tantalum (Ta), niobium (Nb) or aluminum (Al), the composition and properties of the interphases change accordingly.

One special interfacial challenge that LLZO faces is its lithiophobicity, *i.e.* the molten Li^0 and its surface repel each other due to the high surface energy. To improve the wettability of LLZO towards Li^0 ,

various artificial coating techniques have been applied, including the use of alumina (Al_2O_3) and lithium nitride (Li_3N).

While garnet-type particles may possess sufficient mechanical strength against the stress induced by Li^0 dendrite growth, the grain boundaries between particles have been considered a weakness against Li^0 dendrites, as they offer clear pathways for the propagation of Li^0 dendrites. This could be related to the effect of space charge on ion transport at the interparticle boundaries that was discussed in Section 16.6.7 (Figure 16.6) when considering the ion transport mechanism across the interphases, but a more recent study by Wang and colleagues also attributed the Li^0 dendrite growth along these grain boundaries to the relatively high electronic conductivities of SSEs.⁹¹ In other words, the Li^+ migrating along the grain boundaries could encounter electrons and then charge transfer occurs at these sites, producing isolated and nanometric Li^0 .

What seems to support this argument is the report that Li_2CO_3 and LiOH , often the by-products generated during LLZO synthesis, help to eliminate the Li^0 dendrite growth when located at the grain boundaries. These ingredients are often identified in interphases of lithium-ion batteries and are known for their excellent electron insulation, hence their presence at the grain boundaries must have introduced a new interphasial chemistry to mitigate Li^0 dendrite growth *via* blocking electron conduction. The practical application of SSEs thus relies on the complete understanding of the Li^0 dendrite growth mechanism, especially how interface engineering along these grain boundaries could help counter the relatively high electronic conductivities of SSEs.

17.3.3.2 Antiperovskite-type SSEs

This type of SSE, also known as inverse perovskite, has the general formula Li_3OX (where X = Cl, Br or other halides). They are named after their structural similarity to perovskite materials of ABO_3 cubic, $Pm\bar{3}m$ structure, but with reversed cation and anion placements.^{58,59}

Antiperovskite-type SSEs typically possess comparatively higher ionic conductivity owing to the excess Li^+ content, lower melting point and better processibility than garnet-type materials, and can also be synthesized at much lower temperatures. One representative antiperovskite, Li_3OCl , is predicted to be thermodynamically stable against Li^0 , which is very rare, if not unique, among the

known electrolytes. Furthermore, the soft nature of antiperovskites also makes it easier to reduce grain boundaries during synthesis. These properties are very helpful for incorporating the SSEs in an all-solid-state battery.

Unfortunately, Li_3OCl is unstable under ambient conditions, and will spontaneously decompose into Li_2O and LiCl at room temperature. In general, antiperovskites are also rather hygroscopic or moisture sensitive, and will extract water from the ambient atmosphere, altering their conductivity at different degrees of hydration. Although the moisture absorbed from the environment increases ion conductivity, this effect has created confusion throughout the literature regarding its true chemical composition and reproducibility. Aside from chemical instability, electrochemically Li_3OCl is predicted to decompose at >2.5 V vs. Li^0 into Li_2O_2 and LiClO_4 .

An alternative antiperovskite, lithium halide hydroxide (Li_2OHX), has become very popular in recent years. Its synthesis conditions are even more challenging owing to the material's tendency to strip metal ions from reaction vessels, furthering the complexities and confusion in the literature regarding its constantly changing ionic conductivity and the difficulty with precise control.

The main benefit of Li_2OHX materials is their relatively higher conductivity compared with Li_3OCl . Spectroscopic studies and calculations have revealed that there is likely to be a rotating motion of the OH^- groups, which accelerates the transport of Li^+ in a "paddle wheel"-like mechanism. Replacement of the OH^- with F was found to increase the Li^+ ion conductivity in addition to increasing the voltage stability.

One encouraging aspect of antiperovskites is that Li^0 dendrites do not seem to be formed in them. This could be an indication of the higher thermodynamic stability with Li^0 together with low electronic conductivity, but further studies are needed for a full understanding.

17.3.3.3 Sulfide-type SSEs

The sulfide-type SSEs stemmed from the original LISICON (lithium superionic conductor) structure composed of various cations paired with oxygen.^{58,59} Compared with their oxygen analogs, the thio derivative LISICONs consistently possess significantly higher conductivities owing to the more polarizable electron cloud of sulfur. In fact, the representative SSEs of this class, $\text{Li}_7\text{P}_3\text{S}_{11}$ (LPS) and $\text{Li}_{10}\text{GeP}_2\text{S}_{12}$ (LGPS), possess the highest Li^+ conductivities ever reported, 1.7×10^{-2} and 1.2×10^{-3} S cm⁻¹, respectively, which are well into the realm of liquid

electrolyte systems. Accordingly, sulfide-type SSEs have become the most popular and promising class of materials under investigation, with industry projecting its application in electric vehicles before 2025.

The most severe challenge that sulfide-type SSEs face is their chemical and electrochemical instability, because thermodynamically a sulfide (S^{2-}) can be oxidized before 3.0 V vs. Li^0 , and its complexation with other elements from Groups 13–17 in the Periodic Table fails to change this nature, but instead introduces further instability against reductive decomposition. Cation substitution in the form of Ge into the more traditional baseline composition of Li_3PS_4 has offered significant improvements in conductivity. Similar results were obtained with Si and Sn.

Upon reductive decomposition by Li^0 , both LPS and LGPS will form lithiated phases such as Li–Ge, Li–Si and Li–Sn, which are more conductive. Anion substitution of LPS generates another popular SSE type, argyrodites, which have the general formula Li_6PS_5X , where X = I, Br or Cl. The argyrodites have been shown to have higher stability against complete de-lithiation, but they are unstable against oxidative decomposition by cathode materials based on transition metal oxides. More recently, simulations predicted that a highly defective $Li_{1+2x}Zn_{1-x}PS_4$ at $x \geq 0.5$ should have a conductivity of >50 mS cm $^{-1}$ at room temperature, but experimentally only 0.8 mS cm $^{-1}$ was achieved. On the other hand, another argyrodite, $Li_7P_{2.9}Mn_{0.1}S_{10.7}I_{0.3}$, exhibited an extremely high ionic conductivity of 5.6 mS cm $^{-1}$ at room temperature, and an even higher Li^0 conductivity of up to 25 mS cm $^{-1}$ has been reported at room temperature for $Li_{9.54}Si_{1.74}P_{1.44}S_{11.7}Cl_{0.3}$, against which not every aqueous electrolyte could compete.

Unfortunately, all these highly conductive SSEs have significant compromises in their chemical or electrochemical stability, and usually they are accompanied by high interfacial resistances, as a result of the reactions with both anode and cathode materials. To make it worse, the products from these parasitic reactions could not serve as effective interphases, because they conduct both ions and electrons. In contrast, $Li_{9.6}P_3S_{12}$ exhibited high anodic stability, but with a compromise in Li^0 conductivity (~ 1 mS cm $^{-1}$).

Various coating approaches have also been adopted to modify the solid/solid interface, which includes some of the common electrode materials such as $Li_4Ti_5O_{12}$ (LTO), $LiNbO_3$ (LNO) and simple inorganic salts such as lithium iodide (LiI). The chemical nature of sulfides requires interfacial stabilization in order to support the high energy

density electrode materials such as lithium metal and high nickel layered transition metal oxides.

17.4 Nano-confining Electrolytes

In the preceding chapters, we learned how important the solvation sheath structure of working ions is for the key properties of the resultant electrolytes, ranging from salt dissolution and dissociation, to ion diffusion and migration, and all the way to the interfacial reactions and interphasial chemistries. We have also discussed the diverse efforts to alter the ion solvation sheath structures in an attempt to manipulate these key properties, including super-concentrating the electrolytes to extreme ion densities in the electrolytes or localizing such super-concentrations with the use of non-solvents.

However, all these efforts were still made in the presence of ion solvation, where ion–solvent interactions dictate the reversible redox reaction of the former and the stability/reactivity of the latter.

What will happen if solvation of the working ion is completely absent?

One might argue that it is impossible, because thermodynamics governs that the ions must be solvated so that the solvation enthalpy could energetically compensate the loss of lattice stabilization (Figure 3.4). However, upon further examination, one could soon realize that it is entirely possible to find an alternative source of stabilization for the dissociated ions that replaces the stabilization that used to be provided by solvent molecules, which is *nano-confinement* (Figure 17.2).^{52,63,64} Here, the Coulombic charge carried by the ions is partially or completely balanced out by the host framework, either *via* direct interaction with the skeletal structure of the host materials, or *via* interaction with the functionalities that are part of the framework.

Among all the requirements for nano-confinement to occur, the size of the pores, voids or channels of the framework is a critical one. The sizes of most solvated ions usually range from ångstroms to nearly 1 nm, depending on the solvent molecules, the valence of the ion and solvation numbers. The emergence of diverse nanomaterials has made it easy to find a series of such hosts with adjustable sizes. It can be imagined that, when solvated ions are forced into the nano-sized pores or voids of such hosts, the spatial environment faced by these solvated ions is comparable in size to the solvation sheaths, and some of these solvated ions would engage in interactions with the host,

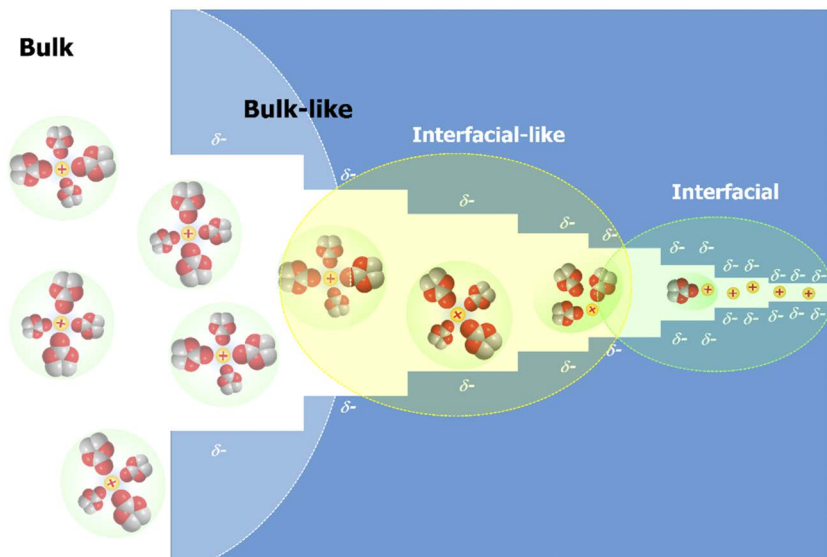


Figure 17.2 Forcing solvated ions into nano-confinement that is of similar size to the solvation sheath would induce partial or complete desolvation of the ions, whose formal charges would now be compensated by the space charges from the skeletal structure of the hosts. These desolvated ions and free solvent molecules, which actually represent new chemical states, are expected to generate bulk, transport and interfacial and interphasial properties.

resulting in partial or complete desolvation. As we have emphasized multiple times in earlier sections, *e.g.* Sections 16.6.1.1.1 and 16.7.2 (Figures 16.4 and 16.10), the location of the solvent molecules inside the primary solvation sheath dictates their reactivity, and hence their participation in interphasial chemistries. Therefore, upon removal of these solvent molecules from the solvation sheath, the solvent molecules would be in a new chemical state free from the influence of the Coulombic field from the working ions, and consequently exhibit unusual properties. Likewise, unusual properties would also be expected from the now “naked” working ions.

An interesting question then arises: what unusual properties can be expected? Or, on a more fundamental level, how would the solvated ions behave in these sub-nano structures?

The above nano-confinement concept has actually been sporadically reported for various electrolytes in various host frameworks, although in most cases the desolvation effect by the nano-confinement takes only a small portion of the bulk electrolyte, and the authors provided different explanations.

For example: (1) anomalous capacitance was generated when solvated tetraalkylammonium cations were forced into pores as small as 0.65 nm; (2) significantly different interphasial behaviors and morphologies of an Li⁺ anode emerged when infusing conventional lithium-ion electrolytes into nanopores of a ceramic–polymer composite host of mean diameter ~40 nm; (3) a significantly expanded electrochemical stability window arises when ether-based electrolytes are “frozen” into the sub-nano channels of 0.29 nm created by MOF structures; (4) extraordinarily fast ion transport far above that of the corresponding bulk polymer electrolyte occurs along the ceramic–polymer interfaces when the same polymer is embedded in the channels of a ceramic host as small as 40 nm in diameter; (5) in a more general context, the “soggy-sand” electrolyte⁵⁴ or the “ionic rectifier”⁶⁵ concept discussed in Section 17.3.2 should more or less involve the nano-confinement of electrolytes.

Although these scattered phenomena at first glance do not seem to be related, and the authors of each study offer widely different rationales, there is a common factor underneath it all: in the nano-structured environment the solvated ions are likely to interact with the surfaces of the host materials, during which partial or even complete desolvation of the ions occurs, producing electrolytes in new chemical states that have not been fully understood. A new avenue for electrolyte design could be opened up by leveraging these little-known chemical states.

17.5 Artificial Interphases

Since the indispensable role of interphases in lithium-ion batteries was first recognized, there has always been a motivation to artificially design and apply a protective layer on electrodes to replace the “naturally born”, *i.e. in situ*, interphases formed during the activation cycles of the batteries. Various materials, especially those already identified as effective interphasial ingredients such as LiF, Li₂O, Li₂CO₃, lithium oxalate, lithium alkoxide, *etc.*, have been coated on electrode surfaces using diverse techniques, including solution spraying, dip coating, dry application and radiofrequency sputtering, physical and chemical vacuum depositions and atomic layer deposition. However, although these artificial interphases did exhibit certain improvements, there were always irreversible capacities in the early cycles of the resultant batteries, which raises the question of whether the artificial coating is indeed effective or

necessary, because irreversible capacities indicate that *in-situ* interphase formation still occurs, while the coating procedures inevitably lead to higher costs and manufacturing uncertainties.

On a more fundamental level, there is also doubt about the scientific basis for artificial interphases, because such efforts aim at achieving an interphase of homogeneous morphology and singular chemical component, while the ion transport across the interphases, as we have discussed in Section 16.6.7, may very likely rely on the space-charge effect created by the interfacing between particles with different chemistries (Figure 16.7). On the other hand, an interphase of homogeneous morphology and singular chemical component may still be tantalizing, because one of the driving forces for the dendritic growth of Li^0 or other metal anode materials is the chemical and morphological inhomogeneity of the interphases, where the more conductive section would favor Li^0 deposition and growth than other more resistive regions (Section 10.2.2, Figures 10.2 and 10.3).

Hence the efforts to realize artificial interphases continue to receive intensive attention, especially for the development of lithium-metal batteries.

Although the presence of various fluorides, either organic or inorganic, has long been identified in both SEIs and CEIs, no simple linear relation between fluoride content and interphase performance could be extracted, and researchers have increasingly realized that how these fluorides are distributed in the interphase plays a much more important role than just their content. As indicated by the simulation studies of Qi and colleagues, when fluorides interface with other “impurities” such as oxides or carbonates at the nanometric scale, highly conductive pathways for Li^+ could be created along the grain boundaries.⁶⁶ This speculation has been partially confirmed by the results of experimental work, in which LiF and Li_2CO_3 were coated on a silicon anode surface *via* radiofrequency magnetron co-sputtering at various ratios, and the resultant artificial interphase with a 50:50 $\text{LiF}:\text{Li}_2\text{CO}_3$ ratio turned out to be the most conductive towards Li^+ , as indicated by the ${}^6\text{Li}-{}^7\text{Li}$ isotope exchange rate.

Nevertheless, a technique for precisely tailoring the nanometric morphology of these fluoride species is still lacking. A semiempirical approach widely adopted as the design philosophy is to pre-store fluorine in the structures of various solvents, additives or anions, which would become available only when electrochemically activated. This constitutes the fundamental reason why in recent years most of the newly developed electrolyte systems have been based on fluorinated solvent molecules. Fluorides formed in this manner would exist on a nanometric scale and be well interfaced with other interphasial

ingredients from the decomposition of other electrolyte components, including impurities such as oxygen or CO₂ dissolved in the electrolyte during preparation.

One particular approach recently adopted by Cui and colleagues is worth mentioning. When using cryogenic electron microscopy to analyze Li⁰ surfaces recovered from various electrolyte systems, they found that these highly fluorinated ether molecules actually do not contribute LiF to the interphases on Li⁰ as one would expect. Instead, the SEIs were found to consist mainly of Li₂O in high abundance. Under certain conditions, even a *monolithic* SEI based purely on Li₂O could be identified.^{18,67} On the other hand, these fluorinated solvent molecules did seem to have contributed LiF to the CEIs on the nickel-manganese-cobalt mixed oxides (NMC) cathode side. Based on this observation, they designed an artificial interphase strategy by suspending Li₂O nanoparticles in the electrolyte, in the hope that during the activation cycle of the battery these Li₂O nanoparticles would spontaneously deposit on the Li⁰ surface and form an Li₂O-rich SEI. This SEI with a singular chemical composition of Li₂O improved the Coulombic efficiency of a lithium-metal anode to 99.7%, one of the highest values ever reported in the literature thus far, and reduced the overpotential for Li⁰ nucleation, so that an even and reversible deposition and stripping of Li⁺ and Li⁰ ensued, leading to a significant prolonged cycle life of lithium-metal batteries.⁶⁸

It is anticipated that, with an increasing understanding of interphasial chemistry and morphology, we will witness further efforts in this direction with new chemical ingredients used. However, one should be cautious here about over-exercising this practice, because we actually understand very little about how LiF and Li₂O work in an interphase. The “correlation” that we think exists between their presence in the interphase and the improved interphase functions is still semiempirical. More fundamental understanding is critical for a truly rational design of interphases.

17.6 Dynamic Interphases

An interphase, no matter whether naturally born or artificially applied, is a permanent existence between the electrode and electrolyte, hence it inevitably brings undesirable aspects, such as the additional impedances at its own interfaces with the electrode and the bulk electrolyte, the irreversible capacities consumed in its formation, and the subsequent ever-growing process [eqn (16.73)] that keeps inducing

impedances and thickness of interphases and consuming the lithium source and electrolyte.

An ideal interphase should be free of all these shortcomings, while maintaining the protection and stabilization between the electrodes of extreme potentials and electrolytes of limited thermodynamic stability. Hence an unanswered question has been on researchers' minds: is it possible to design an interphase that only temporarily forms when the electrode/electrolyte interfaces require protection, and dissipates when the electrode potentials retreat from extreme values? Such an interphase would be non-permanent and transient, would not involve any reductive or oxidative decomposition of electrolyte components and would not induce excessive impedances for ion transport across the electrode/electrolyte interface.

One could immediately note the similarity of such a dynamic interphase to the classical 2D interface, where the electrified double layers instantaneously assemble or dissipate upon the application or removal of potential (Figure 16.1). In other words, the new concept of a dynamic interphase seeks to turn 3D interphases into traditional 2D interfaces. The only difference is that the dynamic interphases need to operate at much more extreme electrode potentials, hence placing stringent requirements on the electrolyte compositions.

According to a report by Xiao and colleagues, this new concept was partially enabled by the super-concentrated ethereal electrolyte, which proved to be an effective platform that can provide sufficient ions to enforce the formation of such a transient and dynamic interphase while remaining electrochemically stable at the potentials of the graphitic anodes.⁶⁹ They employed a super-concentrated ethereal electrolyte consisting of 5 M LiTFSI dissolved in DOL, which, upon negative polarization of the graphitic anode, formed a dense and temporary shielding consisting of layers of cations and anions, while the solvent molecules were excluded from the Helmholtz layers on the surface of the graphite (Figure 17.3).

This interphase does not invoke any electrochemical decomposition from the electrolyte components, as evidenced by the clean graphite surfaces revealed by various electron microscopic techniques, hence it relies only on the reversible reorientation, rearrangement and rapid assembly of these cations, anions and solvent molecules in the direction of the applied potential, and no permanent interphase has been formed. Most importantly, this interphase allows the cation (Li^+) to be intercalated into the graphitic structure, which occurs at a potential not far from that of lithium metal. Upon removal of the applied electric potential (*i.e.* discharge of the battery), such interphases are

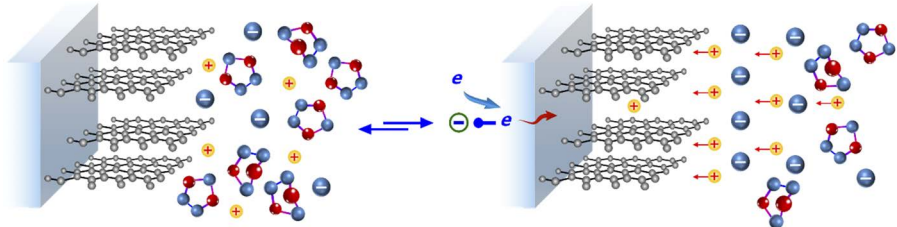


Figure 17.3 A dynamic interphase consisting of a layered arrangement of cations and anions in a super-concentrated ethereal electrolyte forms as the potential is applied on the electrode, and dissipates when the applied potential is removed. This interphase supports the reversible Li^+ intercalation chemistry in a graphite anode while consuming no Li^+ or solvent, and leaving behind no permanent chemical phases on the graphite surface.⁶⁹

disassembled accordingly as in electrochemical double layer capacitors, restoring the original electrolyte bulk and interfacial structures.

Although this concept of a dynamic interphase is still in its infancy and needs more verification and exploration, the potential behind this highly original concept is worth further exploration.⁷⁰

17.7 New Characterization Techniques

As Winter said in his now famous quotation, the interphases are “*the most important and the least understood*” component in advanced batteries.⁷¹ The accurate characterization of interphases, especially in their *in situ* and *operando* states, has always been, and still is, very difficult. For a very long time, most of the fundamental knowledge about interphases has been based on limited information gathered using traditional means of characterization. Thanks to the significant advances made during the past three decades in characterization and computer simulation techniques, we now can peer into the once elusive interphases at the atomic length scale and picosecond time scale.

Many of these “new” characterization techniques actually involve the innovative use of existing techniques assisted by equipment modifications and computation, such as the mapping of the ion solvation sheath structure by electrospray ionization mass spectrometry (ESI-MS) (Figure 12.3),⁷² quantification of the change in multinuclei chemical shifts in NMR spectroscopy to determine which solvent molecule and which site in that solvent molecule are preferentially interacting with working ions,⁷³ measurement of relative solvation power series for electrolyte solvents by NMR diffusion-ordered spectroscopy

(DOSY) (Table 12.1),⁷⁴ the weighing of mass changes during the interphase formation stage using the electrochemical quartz crystal microbalance (EQCM) technique,⁷⁵ the *in situ* mapping of ion solvation, interfacial and interphasial processes using liquid secondary ion mass spectrometry (LSIMS),⁷⁶ the various electron microscope techniques using either *in situ/operando* or cryogenic attachments,^{77,78} etc.

To shed further light on interphases, more novel characterization techniques, especially those operational under *in situ/operando* conditions and those with extremely high spatial and temporal resolution, are urgently needed. Although many advanced characterization tools have been introduced in other areas, such as chemistry, catalysis and biology, their application to electrolytes and interphases is still in the development stage. An example of such tools is cryogenic electron microscopy, the extra low dosage electron beam of which enables it to image and analyze extremely reactive species such as Li⁰.⁷⁹⁻⁸¹ On the other hand, the tools that directly probe and quantify the electrolytes and interphases are still insufficient. Given the non-crystalline and fast ion dynamics nature of typical electrolytes and interphases, spectroscopic methods with high chemical sensitivity and total scattering for local structure are especially desired, as they are tolerant towards long-range disordered arrangements and capture the complexities of the electrolytes and interphases at a statistical length scale. A comprehensive understanding of the solvation structure in electrolytes, the associated interphase chemistry and its distribution along 2D and 3D length scales, and also how the chemistry evolves during electrochemical processes, could be achieved based on large data sets collected using a combination of a variety of techniques, *e.g.* liquid and solid NMR spectroscopy, differential pair distribution function (d-PDF) analysis based on X-ray or neutron scattering using large-scale facilities such as a synchrotron, and cryogenic analytical electron microscopy equipped with tomography and electron energy-loss spectroscopy. Finally, the assistance of computational simulations, ML and AI will prove to be critical to interpret and rationalize the unprecedented data sets collected using these advanced characterization methods.

17.8 Computer Simulations

As highly powerful supercomputing facilities become more accessible than ever, and equally powerful algorithms are developed, complicated processes in the electrolyte bulk and interfaces can now be modeled with unprecedented accuracy. Computational methods no

longer just play the role of verifying or explaining experimental observations, but are now capable of predicting properties and designing new structures and materials.^{82–85}

First-principles quantum chemistry and density functional theory (DFT) calculations and molecular dynamics (MD) simulations using DFT or non-reactive force fields enable us to screen huge numbers of molecules with various structures and pre-select them according to their thermodynamic oxidative and reductive stabilities without carrying out laborious experiments. They also allow us to predict ion mobility, diffusivity and conductivity in highly intercorrelated electrolyte systems such as ionic liquids and super-concentrated and solid-state electrolytes. The molecular-scale insight into ion correlations and transport informs properties at the continuum scale in the Stefan–Maxwell formalism, providing a basis for developing electrolytes with enhanced ion and mass transport properties. Recently developed reactive and non-reactive force fields, together with advances in DFT and semiempirical methods, further make it possible to understand the elusive interfacial and interphasial processes, to predict chemical and electrochemical reactions and to identify the most favored materials and molecular structures with targeted properties, based on the huge databases constructed. These approaches have led to the development of infrastructures and associated databases that grant easy provision of electrolyte and interphase information to the wider community. With the increased interest in automated high-throughput experimentation, the so called “robotic laboratories”, these computational screening approaches are now aided by large volumes of experimental data, lending themselves to analysis using ML approaches. More and more calculation efforts have crossed the limits beyond thermodynamic calculations into predicting the kinetics of ion transport and charge transfer, or predicting the cascade of reactions that occur at interfaces leading to the formation of interphases. AI and ML methods thrive on the unprecedented scale of data now available for algorithm training, and forge tighter coupling between experimental methods and calculations. These computation tools are destined to grow into leading roles in all these endeavors. An imminent revolution in computational prediction and design of electrolyte materials is almost visible on the horizon.

17.8.1 Molecular Simulations

Computer simulations, no matter whether based on classical molecular dynamics (MD) or quantum mechanics (QM), seek to minimize the energy of the system. Each method looks at a system

consisting of a number of particles, and samples the phase space of their configurations distributed at an equilibrium state corresponding to a particular temperature. To attain such equilibrium, interaction energies are established among the particles, which can be obtained either from solution of the Schrödinger equation, density functional approximations or fits to quantum chemistry and/or experimental results. Phase-space sampling could be done *via* Monte Carlo (MC) or MD simulations. In the latter, a trajectory of molecular motion is created, which allows the extraction of linear transport coefficients *via* regression of equilibrium fluctuations. Alternatively, transport properties could also be extracted from non-equilibrium MD simulations by measuring the response to an externally applied field.

Energy minimization is the core principle of simulations. Consider a box containing a number (N) of particles, with each particle governed by certain laws of interactions, be they Coulomb, van der Waals, dipole–dipole, gravitational, *etc.* These N particles are then set off in any configuration and move in a random manner. For each move of each particle, an examination is conducted to see whether the move decreases the energy of the particle. If not, then the move is considered as not contributing to the final equilibrium of the system; if it does, then the move is accepted with a certain probability depending on the energy difference between the initial and final configurations and temperature, while a subsequent step is allowed. Repeating these steps a sufficiently large number of times, when the energy of the particles can no longer be reduced then the system is considered to have reached the final equilibrium state that represents accurate sampling of equilibrium configurations at this particular temperature. The collective behaviors of these particles at equilibrium, *i.e.* their velocity, location, distribution and energy, determine the properties of the system.

A few key factors dictate whether the properties thus predicted would be accurate: the number of particles, the time scale of the calculation and the laws that govern the interaction among particles. The first two require computing power and the last depends on the *force fields* established to govern the interactions among the particles or quality of the density functions.

In early classical MC and MD simulations, the well-known *Lennard-Jones 6–12 equation* was used to describe the interaction energies (U_{ij}) between two particles i and j in the electrolyte:

$$U_{ij} = -\frac{A}{r^6} + \frac{B}{r^{12}} \quad (17.1)$$

where r is the distance between the two particles and A and B are constants determined by the nature of the forces or energies that govern the interactions between the particles. These two terms represent attractive and repulsive forces between the particles as a function of their relative distance.

The basic assumption adopted in the classical MC and MD simulations is that the Coulombic interaction dominates the interparticle potential energies at distances comparable to and longer than the equilibrium distance (a_{ij}):

$$U_{ij} = -\frac{z_i z_j e_0^2}{\epsilon} \quad (17.2)$$

while at distances much shorter than a_{ij} , the strong repulsion between the two particles keeps them apart:

$$U_{ij} = \infty \quad (17.3)$$

At equilibrium, the attractive and repulsive forces balance each other out, and the system of the two particles realizes the minimum energy between them (Figure 17.4). Since the box contains N particles, interaction energies between all possible pairs should be considered, and the collective minimum energy should reflect the equilibrium state of the whole system:

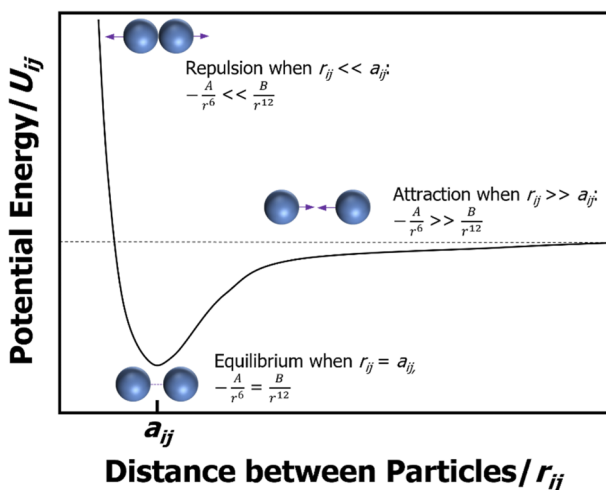


Figure 17.4 The Lennard-Jones potential relation between two particles as a function of the distances between them.

$$U_{\text{pair}} = \sum_i \sum_j \left[-\frac{A_{ij}}{r_{ij}^6} + \frac{B_{ij}}{r_{ij}^{12}} \right] \quad (17.4)$$

It is important to realize that this treatment of molecular interactions using Lennard-Jones and Coulombic terms is oversimplified for ionic systems. Additional terms such as polarization, improved electrostatics *via* inclusion of dipoles, quadrupoles, high-order dispersion terms and damping of interactions at short range are often added to improve further the description of intermolecular energies.

Of course, as mentioned in Section 4.1, the precise treatment of each particle pair in the box is in fact a multi-body problem, no matter whether the force is described by Coulombic or Lennard-Jones relations, which does not have an analytical solution unless approximations are made. The most popular approximation is the so-called “nearest neighbor only approximation”, which ignores the long-range Coulombic interactions between particles.

The more popular *molecular dynamics* (MD) simulations take more into account than just potential energies. In the box containing many particles, a force is applied on each particle, and the random movement of these particles is set off (Figure 17.5). Now all the quantities from classical Newtonian mechanics can be calculated, such as velocity, coordinates, momentum and energy exchange during each collision, at a time interval of every a few femtoseconds (10^{-15} s). Each individual particle is assumed to be an ideal mass point that obeys Newton’s second law:

$$\mathbf{F} = m\mathbf{a} \quad (17.5)$$

where \mathbf{a} is the acceleration, which can be related to the velocity by

$$\mathbf{a} = \frac{d\mathbf{v}}{dt} = \frac{d^2\mathbf{s}}{dt^2} \quad (17.6)$$

while the force \mathbf{F} is related to the interparticle potential energy by

$$\mathbf{F} = -\frac{d\psi}{dx} \quad (17.7)$$

These quantities of energy, force, coordinates and velocity can all be related to each other *via*

$$-\frac{d\psi}{dx} = m\frac{d\mathbf{v}}{dt} = m\frac{d^2\mathbf{s}}{dt^2} \quad (17.8)$$

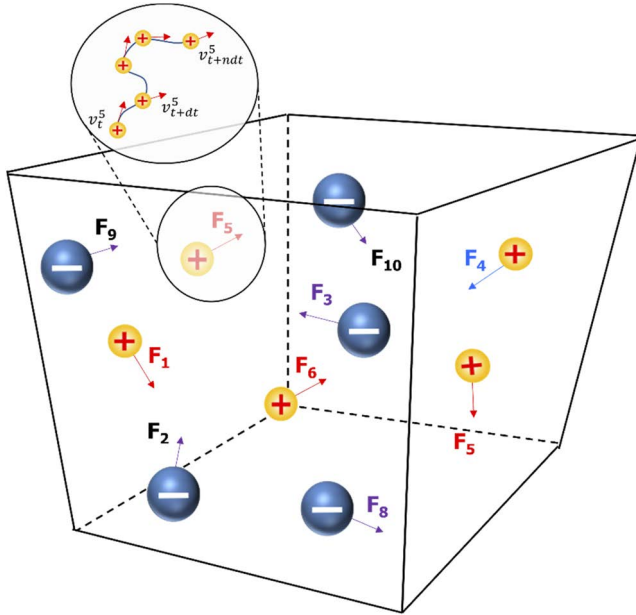


Figure 17.5 In MD simulations, each particle is considered an ideal mass point, and a set of force fields is established to govern the interaction between these particles. Their collective behavior at equilibrium reflects the properties of the system.

Unlike MC, classical MD simulations integrate the classical Newton equations of motion, producing a simulation trajectory, *i.e.* displacements of atoms *versus* time. In the box containing solvent, cations and anions, a force on each atom at time t is calculated from the negative gradient of intermolecular energy according to eqn (17.6) and (17.7), yielding acceleration, which is then used together with velocity to determine a new position of particles at a time $t + dt$. In order to yield stable integration of equations of motion, the simulation time step dt should be an order of the magnitude smaller than the period of the fastest motion, which is often the vibration of bonds, on the order of a fraction of a picosecond (10^{-12} s) or a few picoseconds if vibrations are restricted.

In theory, provided that the potential energy and the initial coordinates of the particles are known, the evolution of these quantities with time can be derived from the above equations. Of course, this is only the underlying principle, and the accuracy of actual predictions depends on both the accuracy of molecular interactions *via* the fitted molecular terms such as repulsion, dispersion, electrostatic (or DFT

functional for the DFT-based MD simulations) and ability to sample the phase space adequately so that equilibrium structural and transport properties from simulation trajectories can be extracted. While longer trajectories lead to improved sampling and smaller statistical uncertainty, as boundary conditions are applied in simulations, molecules inevitably interact with their images *via* a periodic boundary, leading to additional artifacts. The actual execution of the calculations is therefore very complicated, and depends on the force fields established to govern the forces and energies between the particles, while the box size and the time scale together determine how accurate the calculations could be.

Numerous force fields have been developed that are either commercially available or available in open sources, the most commonly used of which include *Optimized Potentials for Liquid Simulations* (OPLS), *Chemistry at Harvard Macromolecular Mechanics* (CHARMM), *Assisted Model Building with Energy Refinement* (AMBER), *All Atom* (AA), *Groningen Molecular Simulation* (GROMOS) and *Condensed Phase Optimized Molecular Potentials for Atomistic Simulation Studies* (COMPASS). The selection of the right force fields dictates whether the calculation results could be accurate enough to represent reality.

Differing from classical MD simulations, *ab initio* or DFT-based molecular dynamics is independent of force fields. Instead it relies on the solution of the Schrödinger equation and hence generates the interaction potential surfaces for particles at the basic quantum mechanics level. Based on QM calculations, often assisted by the Born–Oppenheimer approximation, Newtonian equations, eqn (17.5)–(17.8), are subsequently applied to calculate the trajectories of the particles. DFT-based Born–Oppenheimer MD is capable of predicting electrochemical reactions in addition to structural and transport properties, but the corresponding calculations are computationally much more expensive. Its extensive application to specific electrolyte and interphase problems relies on the advances in supercomputing infrastructure and capabilities. Meanwhile, the emerging ML methods have been more and more combined with classical and *ab initio* molecular dynamics, making these approaches more affordable and more accurate.

17.8.2 Prediction of Properties and Performances

Nowadays, the calculation *via* MD simulations of thermodynamic, structural and bulk properties such as density, viscosity, thermal capability, structure, *etc.*, has become fairly mature. For example, at equilibrium, when the particle distribution is accurately sampled at a

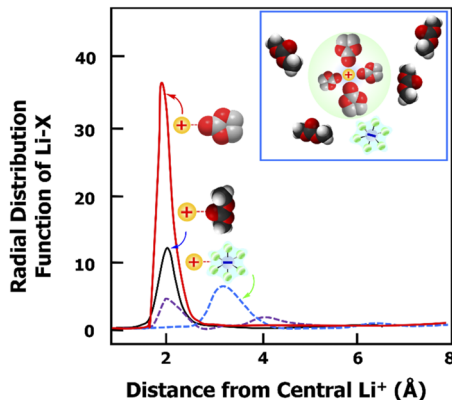


Figure 17.6 The radial distribution function of various oxygen atoms from EC and DMC and the fluorine atom from the anion PF_6^- around a central Li^+ . One can see that the solvation sheath is dominated by EC in its first layer, *i.e.* primary solvation sheath. The inset reflects this solvation sheath structure. Reconstructed based on data from ref. 87.

particular temperature, one could extract reliable information regarding the ion solvation sheath structure from the radial distribution function, as shown in Figure 17.6.⁸⁴

With correct force fields and models, MD simulations can also make fairly mature and reliable predictions about transport properties such as ion conductivity, diffusivity and mobility directly from the calculation of the mean square distance traveled by ions or solvent molecules during their random walk. Challenges remain with the simulation of the electrode/electrolyte interfacial structure, the prediction of interfacial charge transfer and the cascade of reactions that eventually lead to the formation of interphases. Studies by Borodin,⁹² Balbuena,⁹³ Persson⁹⁴ and their colleagues, respectively, addressed these challenges, and brought MD simulations into the new realms of predicting and designing new electrolytes and interphases. In particular, the emerging ML techniques have been trained and applied to predict comprehensive decomposition pathways, which allows one to bridge the atomic and microscopic states with macroscopic properties and their performances in devices.

17.8.3 Computational Design of Materials

With computational power undergoing rapid growth, the use of data mining coupled with neural network optimizations of ML has also been applied in the rational design of new materials, especially regarding

the structures of new electrode materials and solid electrolyte materials. Calculation-driven designs for the latter have been seen recently in the development of nudged elastic band (NEB) calculations,⁸⁶ which are especially effective in predicting Li⁺ conduction in newly proposed solid-state materials *via* the calculation of the activation barrier of ion transfer throughout the material's structure. This computational method led to the understanding of the anion arrangement/packing in the resulting Li⁺ transfer properties, a criterion now used to screen large numbers of compounds from a crystal structural database and narrowed down to a handful of materials that are predicted to exhibit the desired properties. This approach correctly identified Li₁₀GeP₂S₁₂, β-Li₃PS₄ and Li₇P₃S₁₁, among others, as Li⁺ superconductors, which was verified by experiments. Similarly, a data mining-driven ML process was adopted by Ceder and colleagues, who predicted and experimentally validated a series of Li⁺ and Na⁺ superconductors.⁹⁵

It is expected that more discoveries of new materials in the future will be guided by simulation-based material prediction studies.

References

1. The energy density numbers of lithium-ion batteries are so dynamic that almost any literature data are outdated. The most updated source is from the U. S. Department of Energy, Vehicle Technologies Annual Merit Review, 21–23 June 2022, <https://www.energy.gov/eere/vehicles/vehicle-technologies-annual-merit-review>.
2. T. Nagaura and K. Tozawa, Lithium Ion Rechargeable Battery, *Prog. Batteries Sol. Cells*, 1990, **9**, 209–217.
3. L. Trahey, F. R. Brushett, N. P. Balsara, G. Ceder, L. Cheng, Y. M. Chiang, N. T. Hahn, B. J. Ingram, S. D. Minteer, J. S. Moore, K. T. Mueller, L. F. Nazar, K. A. Persson, D. J. Siegel, K. Xu, K. R. Zavadil, V. Srinivasan and G. W. Crabtree, Energy storage emerging: A perspective from the Joint Center for Energy Storage Research, *Proc. Natl. Acad. Sci. U. S. A.*, 2020, **117**, 12550–12557.
4. K. Xu, Non-aqueous liquid electrolytes for lithium-based rechargeable batteries, *Chem. Rev.*, 2004, **104**, 4303–4417.
5. K. Xu, Electrolytes and interphases in Li-ion batteries and beyond, *Chem. Rev.*, 2014, **114**, 11503–11618.
6. M. Li, C. Wang, Z. Chen, K. Xu and J. Lu, New Concepts in Electrolytes, *Chem. Rev.*, 2020, **120**, 6783–6819.
7. K. Xu, Y. Lam, S. Zhang, T. R. Jow and T. Curtis, Solvation Sheath of Li⁺ in Non-aqueous Electrolytes and Its Implication of Graphite/Electrolyte Interface Chemistry, *J. Phys. Chem. C*, 2007, **111**, 7411–7421.
8. K. Xu, A. v. Cresce and U. Lee, Differentiating contributions to “ion transfer” barrier from interphasial resistance and Li⁺ desolvation at electrolyte/graphite interface, *Langmuir*, 2010, **26**, 11538–11543.
9. A. v. Cresce and K. Xu, Preferential solvation of Li⁺ directs formation of interphase on graphitic anode, *Electrochim. Solid-State Lett.*, 2011, **196**, 3906–3910.
10. O. Borodin, X. Ren, J. Vatamanu, A. v. W. Cresce, J. Knap and K. Xu, Modeling insight into battery electrolyte, electrochemical stability and interfacial structure, *Acc. Chem. Res.*, 2017, **50**, 2886–2894.

11. K. Leung and K. L. Jungjohann, Spatial Heterogeneities and Onset of Passivation Breakdown at Lithium Anode Interfaces, *J. Phys. Chem. C*, 2017, **121**, 20188–20196.
12. Y. Li, K. Leung and Y. Qi, Computational Exploration of the Li Electrode/Electrolyte Interface in the Presence of a Nanometer Thick Solid-Electrolyte-Interphase, *Acc. Chem. Res.*, 2016, **49**, 2363–2370.
13. W. R. McKinnon and J. R. Dahn, How to Reduce the Cointercalation of Propylene Carbonate in Li_xZrS_2 and Other Layered Compounds, *J. Electrochem. Soc.*, 1985, **132**, 364–366.
14. C. A. Angell, C. Liu and E. Sanchez, Rubbery solid electrolytes with dominant cationic transport and high ambient conductivity, *Nature*, 1993, **362**, 137–139.
15. K. Ueno, K. Yoshida, M. Tsuchiya, N. Tachikawa, K. Dokko and M. Watanabe, Glyme–Lithium Salt Equimolar Molten Mixtures: Concentrated Solutions or Solvate Ionic Liquids?, *J. Phys. Chem. B*, 2012, **116**, 11323–11331.
16. T. Tamura, T. Hachida, K. Yoshida, N. Tachikawa, K. Dokko and M. Watanabe, New glyme–cyclic imide lithium salt complexes as thermally stable electrolytes for lithium batteries, *J. Power Sources*, 2010, **195**, 6095–6100.
17. K. Yoshida, M. Tsuchiya, N. Tachikawa, K. Dokko and M. Watanabe, Change from Glyme Solutions to Quasi-ionic Liquids for Binary Mixtures Consisting of Lithium Bis(trifluoromethanesulfonyl)amide and Glymes, *J. Phys. Chem. C*, 2011, **115**, 18384–18394.
18. X. Cao, X. Ren, L. Zou, M. H. Engelhard, W. Huang, H. Wang, B. E. Matthews, H. Lee, C. Niu, B. W. Arey, Y. Cui, C. Wang, J. Xiao, J. Liu, W. Xu and J.-G. Zhang, Monolithic solid–electrolyte interphases formed in fluorinated orthoformate-based electrolytes minimize Li depletion and pulverization, *Nat. Energy*, 2019, **4**, 796–805.
19. O. Borodin, J. Self, K. Persson, C. Wang and K. Xu, Uncharted Waters: Superconcentrated Electrolytes, *Joule*, 2019, **4**, 69–100.
20. S. K. Jeong, M. Inaba, Y. Iriyama, T. Abe and Z. Ogumi, Electrochemical intercalation of lithium ion within graphite from propylene carbonate solutions, *Electrochim. Solid-State Lett.*, 2003, **6**, A13–A15.
21. M. Nie, D. P. Abraham, D. M. Seo, Y. Chen, A. Bose and B. L. Lucht, Role of Solution Structure in Solid Electrolyte Interphase Formation on Graphite with LiPF_6 in Propylene Carbonate, *J. Phys. Chem. C*, 2013, **117**, 25381–25389.
22. L. Ma, S. L. Glazier, R. Petibon, J. Xia, J. M. Peters, Q. Liu, J. Allen, R. N. C. Doig and J. R. Dahn, A guide to ethylene carbonate-free electrolyte making for Li-ion cells, *J. Electrochem. Soc.*, 2016, **164**, A5008–A5018.
23. K. Sodeyama, Y. Yamada, K. Aikawa, A. Yamada and Y. Tateyama, Sacrificial Anion Reduction Mechanism for Electrochemical Stability Improvement in Highly Concentrated Li-Salt Electrolyte, *J. Phys. Chem. C*, 2014, **118**, 14091–14097.
24. Y. Yamada, K. Furukawa, K. Sodeyama, K. Kikuchi, M. Yaegashi, Y. Tateyama and A. Yamada, Unusual Stability of Acetonitrile-Based Superconcentrated Electrolytes for Fast-Charging Lithium-Ion Batteries, *J. Am. Chem. Soc.*, 2014, **136**, 5039–5046.
25. K. Dokko, D. Watanabe, Y. Ugata, M. L. Thomas, S. Tsuzuki, W. Shinoda, K. Hashimoto, K. Ueno, Y. Umebayashi and M. Watanabe, Direct Evidence for Li Ion Hopping Conduction in Highly Concentrated Sulfolane-Based Liquid Electrolytes, *J. Phys. Chem. B*, 2018, **122**, 10736–10745.
26. J. Alvarado, M. A. Schroeder, T. P. Pollard, X. Wang, J. Z. Lee, M. Zhang, T. Wynn, M. Ding, O. Borodin, Y. S. Meng and K. Xu, Bisalt ether electrolytes: a pathway towards lithium metal batteries with Ni-rich cathodes, *Energy Environ. Sci.*, 2019, **12**, 780–794.
27. H. Kim, J. Hong, K.-Y. Park, H. Kim, S.-W. Kim and K. Kang, Aqueous Rechargeable Li and Na Ion Batteries, *Chem. Rev.*, 2014, **114**, 11788–11827.

28. L. Suo, O. Borodin, T. Gao, M. Olguin, J. Ho, X. Fan, C. Luo, C. Wang and K. Xu, "Water-in-salt" electrolyte enables high-voltage aqueous lithium-ion chemistries, *Science*, 2015, **350**, 938–943.
29. L. Suo, O. Borodin, W. Sun, X. Fan, C. Yang, F. Wang, T. Gao, Z. Ma, M. Schroeder, A. von Cresce, S. M. Russell, M. Armand, A. Angell, K. Xu and C. Wang, Advanced High-Voltage Aqueous Lithium-Ion Battery Enabled by "Water-in-Bisalt" Electrolyte, *Angew. Chem., Int. Ed.*, 2016, **55**, 7136–7141.
30. Y. Yamada, K. Usui, K. Sodeyama, S. Ko, Y. Tateyama and A. Yamada, Hydrate-melt electrolytes for high-energy-density aqueous batteries, *Nat. Energy*, 2016, **1**, 16129.
31. L. Suo, F. Han, X. Fan, H. Liu, K. Xu and C. Wang, "Water-in-Salt" electrolytes enable green and safe Li-ion batteries for large scale electric energy storage applications, *J. Mater. Chem. A.*, 2016, **4**, 6639–6644.
32. C. Yang, J. Chen, T. Qing, X. Fan, W. Sun, A. von Cresce, M. S. Ding, O. Borodin, J. Vatamanu, M. A. Schroeder, N. Eidson, C. Wang and K. Xu, 4.0 V aqueous Li-ion batteries, *Joule*, 2017, **1**, 122–132.
33. F. Wang, O. Borodin, T. Gao, X. Fan, W. Sun, F. Han, A. Faraone, J. A. Dura, K. Xu and C. Wang, Highly reversible zinc metal anode for aqueous batteries, *Nat. Mater.*, 2018, **17**, 543–549.
34. M. McEldrew, Z. A. H. Goodwin, A. A. Kornyshev and M. Z. Bazant, Theory of the Double Layer in Water-in-Salt Electrolytes, *J. Phys. Chem. Lett.*, 2018, **9**, 5840–5846.
35. O. Borodin, L. Suo, M. Gobet, X. Ren, F. Wang, A. Faraone, J. Peng, M. Olguin, M. Schroeder, M. S. Ding, E. Gobrogge, A. von W. Cresce, S. Munoz, J. A. Dura, S. Greenbaum, C. Wang and K. Xu, Liquid structure with nano-heterogeneity promotes cationic transport in concentrated electrolytes, *ACS Nano*, 2017, **11**, 10462–10471.
36. J. Lim, K. Park, H. Lee, J. Kim, K. Kwak and M. Cho, Nanometric Water Channels in Water-in-Salt Lithium Ion Battery Electrolyte, *J. Am. Chem. Soc.*, 2018, **140**, 15661–15667.
37. S. Chen, J. Zheng, D. Mei, K. S. Han, M. H. Engelhard, W. Zhao, W. Xu, J. Liu and J.-G. Zhang, High-Voltage Lithium-Metal Batteries Enabled by Localized High-Concentration Electrolytes, *Adv. Mater.*, 2018, **30**, 1706102.
38. L. Yu, S. Chen, H. Lee, L. Zhang, M. H. Engelhard, Q. Li, S. Jiao, J. Liu, W. Xu and J.-G. Zhang, A Localized High-Concentration Electrolyte with Optimized Solvents and Lithium Difluoro(oxalate)borate Additive for Stable Lithium Metal Batteries, *ACS Energy Lett.*, 2018, **3**, 2059–2067.
39. X. Ren, S. Chen, H. Lee, D. Mei, M. H. Engelhard, S. D. Burton, W. Zhao, J. Zheng, Q. Li, M. S. Ding, M. Schroeder, J. Alvarado, K. Xu, Y. S. Meng, J. Liu, J.-G. Zhang and W. Xu, Localized High-Concentration Sulfone Electrolytes for High-Efficiency Lithium-Metal Batteries, *Chem*, 2018, **4**, 1877–1892.
40. S. Chen, J. Zheng, L. Yu, X. Ren, M. H. Engelhard, C. Niu, H. Lee, W. Xu, J. Xiao and J. Liu, High-Efficiency Lithium Metal Batteries with Fire-Retardant Electrolytes, *Joule*, 2018, **2**, 1548–1558.
41. F. Wang, O. Borodin, M. S. Ding, M. Gobet, J. Vatamanu, X. Fan, T. Gao, N. Eidson, Y. Liang, W. Sun, S. Greenbaum, K. Xu and C. Wang, Hybrid aqueous/non-aqueous electrolyte for safe and high-energy Li-ion batteries, *Joule*, 2018, **2**, 927–937.
42. Z. Ma, J. Chen, J. Vatamanu, O. Borodin, D. Bedrov, X. Zhou, W. Zhang, W. Li, K. Xu and L. Xing, Expanding the low-temperature and high-voltage limits of aqueous lithium-ion battery, *Energy Storage Mater.*, 2022, **45**, 903–910.
43. C. S. Rustomji, Y. Yang, T. K. Kim, J. Mac, Y. J. Kim, E. Caldwell, H. Chung and Y. S. Meng, Liquefied gas electrolytes for electrochemical energy storage devices, *Science*, 2017, **356**, eaal4263.
44. Y. Yang, D. M. Davies, Y. Yin, O. Borodin, J. Z. Lee, C. Fang, M. Olguin, Y. Zhang, E. S. Sablina, X. Wang, C. S. Rustomji and Y. S. Meng, High-efficiency lithium-metal anode enabled by liquefied gas electrolytes, *Joule*, 2019, **3**, 1986–2000.

45. L. Ma, J. Z. Lee, T. P. Pollard, M. A. Schroeder, M. A. Limpert, B. Craven, S. Fess, C. S. Rustomji, C. Wang, O. Borodin and K. Xu, High-efficiency zinc-metal anode enabled by liquefied gas electrolytes, *ACS Energy Lett.*, 2021, **6**, 4426–4430.
46. T. Guo, T. Wang, H. Wei, Y. Long, C. Yang, D. Wang, J. Lang, K. Huang, N. Hussain, C. Song, B. Guan, B. Ge, Q. Zhang and H. Wu, Ice as Solid Electrolyte To Conduct Various Kinds of Ions, *Angew. Chem., Int. Ed.*, 2019, **58**, 12569–12573.
47. R. Chen, Q. Li, X. Yu, L. Chen and H. Li, Approaching Practically Accessible Solid-State Batteries: Stability Issues Related to Solid Electrolytes and Interfaces, *Chem. Rev.*, 2020, **120**, 6820–6877.
48. A. Banerjee, X. Wang, C. Fang, E. A. Wu and Y. S. Meng, Interfaces and Interphases in All-Solid-State Batteries with Inorganic Solid Electrolytes, *Chem. Rev.*, 2020, **120**, 6878–6933.
49. M. B. Armand, J. M. Chabagno and M. Duclot, Second International Meeting on Solid Electrolytes, St. Andrews, Scotland, 1978, 20–22.
50. *Sodium Sulphur Battery*, ed. J. Sudworth and A. R. Tiley, Chapman and Hall, New York, 1985.
51. N. B. Aetukuri, S. Kitajima, E. Jung, L. E. Thompson, K. Virwani, M.-L. Reich, M. Kunze, M. Schneider, W. Schmidbauer, W. W. Wilcke, D. S. Bethune, J. C. Scott, R. D. Miller and H.-C. Kim, Flexible Ion-Conducting Composite Membranes for Lithium Batteries, *Adv. Energy Mater.*, 2015, **5**, 1500265.
52. X. Zhang, J. Xie, F. Shi, D. Lin, Y. Liu, W. Liu, A. Pei, Y. Gong, H. Wang, K. Liu, Y. Xiang and Y. Cui, Vertically Aligned and Continuous Nanoscale Ceramic Polymer Interfaces in Composite Solid Polymer Electrolytes for Enhanced Ionic Conductivity, *Nano Lett.*, 2018, **18**, 3829–3838.
53. Y. Lu, Z. Tu and L. Archer, Stable lithium electrodeposition in liquid and nanoporous solid electrolytes, *Nat. Mater.*, 2014, **13**, 961–969.
54. C. Pfaffenhuber, M. Göbel, J. Popovic and J. Maier, Soggy-sand electrolytes: status and perspectives, *Phys. Chem. Chem. Phys.*, 2013, **15**, 18318–18335.
55. Z. Zou, Y. Li, Z. Lu, D. Wang, Y. Cui, B. Guo, Y. Li, X. Liang, J. Feng, H. Li, C.-W. Nan, M. Armand, L. Chen, K. Xu and S. Shi, Mobile ions in composite solids, *Chem. Rev.*, 2020, **120**, 4169–4221.
56. Z. Tu, P. Nath, Y. Lu, M. D. Tikekar and L. A. Archer, Nanostructured Electrolytes for Stable Lithium Electrodeposition in Secondary Batteries, *Acc. Chem. Res.*, 2015, **48**, 2947–2956.
57. Y. Lu, K. Korf, Y. Kambe, Z. Tu and L. A. Archer, Ionic-Liquid–Nanoparticle Hybrid Electrolytes: Applications in Lithium Metal Batteries, *Angew. Chem., Int. Ed.*, 2014, **53**, 488–492.
58. T. Hakari, M. Deguchi, K. Mitsuhashara, T. Ohta, K. Saito, Y. Orikasa, Y. Uchimoto, Y. Kowada, A. Hayashi and M. Tatsumisago, Structural and Electronic-State Changes of a Sulfide Solid Electrolyte During the Li Deinsertion–Insertion Processes, *Chem. Mater.*, 2017, **29**, 4768–4774.
59. D. Richards, L. J. Miara, Y. Wang, J. C. Kim and G. Ceder, Interface Stability in Solid-State Batteries, *Chem. Mater.*, 2016, **28**, 266–273.
60. E. J. Cheng, A. Sharafi and J. Sakamoto, Intergranular Li metal propagation through polycrystalline $\text{Li}_{6.25}\text{Al}_{10.25}\text{La}_3\text{Zr}_2\text{O}_{12}$ ceramic electrolyte, *Electrochim. Acta*, 2017, **223**, 85–91.
61. T. Swamy, R. Park, B. W. Sheldon, D. Rettenwander, L. Porz, S. Berendts, R. Uecker, W. C. Carter and Y.-M. Chiang, Lithium Metal Penetration Induced by Electrodeposition through Solid Electrolytes: Example in Single-Crystal $\text{Li}_6\text{La}_3\text{ZrTaO}_{12}$ Garnet, *J. Electrochem. Soc.*, 2018, **165**, A3648–A3655.
62. F. Han, A. S. Westover, J. Yue, X. Fan, F. Wang, M. Chi, D. N. Leonard, N. J. Dudney, H. Wang and C. Wang, High electronic conductivity as the origin of lithium dendrite formation within solid electrolytes, *Nat. Energy*, 2019, **4**, 187–196.
63. Z. Chang, Y. Qiao, H. Deng, H. Yang, P. He and H. Zhou, A liquid electrolyte with de-solvated lithium ions for lithium-metal battery, *Joule*, 2020, **4**, 1776–1789.

64. Z. Chang, Y. Qiao, H. Yang, H. Deng, X. Zhu, P. He and H. Zhou, Beyond the concentrated electrolyte: further depleting solvent molecules within a Li⁺ solvation sheath to stabilize high-energy-density lithium metal batteries, *Energy Environ. Sci.*, 2022, **13**, 4122–4131.
65. Z. Tu, M. J. Zachman, S. Choudhury, S. Wei, L. Ma, Y. Yang, L. F. Kourkoutis and L. A. Archer, Nanoporous Hybrid Electrolytes for High-Energy Batteries Based on Reactive Metal Anodes, *Adv. Energy Mater.*, 2017, **7**, 1602367.
66. Q. Zhang, J. Pan, P. Lu, Z. Liu, M. W. Verbrugge, B. W. Sheldon, Y. T. Cheng, Y. Qi and X. Xiao, Synergetic effects of inorganic components in solid electrolyte interphase on high cycle efficiency of lithium ion batteries, *Nano Lett.*, 2016, **16**, 2011–2016.
67. N. Kang, H.-W. Yang, W. S. Kang and S.-J. Kim, Improvement of Reversibility and Cyclic Stability: A Monolithic Solid Electrolyte Interphase in SiOx-Based Anode for Lithium-Ion Batteries, *J. Phys. Chem. C*, 2020, **124**, 2333–2339.
68. M. S. Kim, Z. Zhang, P. E. Rudnicki, Z. Yu, J. Wang, H. Wang, S. T. Oyakhire, Y. Chen, S. C. Kim, W. Zhang, D. T Boyle, X. Kong, R. Xu, Z. Huang, W. Huang, S. F. Bent, L.-W. Wang, J. Qin, Z. Bao and Y. Cui, Suspension electrolyte with modified Li⁺ solvation environment for lithium metal batteries, *Nat. Mater.*, 2022, **21**, 445–454.
69. D. Lu, J. Tao, P. Yan, W. A. Henderson, Q. Li, Y. Shao, M. L. Helm, O. Borodin, G. L. Graff, B. Polzin, C.-M. Wang, M. Engelhard, J.-G. Zhang, J. J. De Yoreo, J. Liu and J. Xiao, Formation of Reversible Solid Electrolyte Interface on Graphite Surface from Concentrated Electrolytes, *Nano Lett.*, 2017, **17**, 1602–1609.
70. W. Zhang, Q. Zhao, Y. Hou, Z. Shen, L. Fan, S. Zhou, Y. Lu and L. A. Archer, Dynamic interphase-mediated assembly for deep cycling metal batteries, *Sci. Adv.*, 2021, **7**, eabl3752.
71. M. Winter, The Solid Electrolyte Interphase – The Most Important and the Least Understood Solid Electrolyte in Rechargeable Li Batteries, *Z. Phys. Chem.*, 2009, **223**, 1395–1406.
72. A. v. Cresce and K. Xu, Preferential solvation of Li⁺ directs formation of interphase on graphitic anode, *Electrochim. Solid-State Lett.*, 2011, **196**, 3906–3910.
73. X. Bogle, R. Vazquez, S. Greenbaum, A. von W. Cresce and K. Xu, Understanding Li⁺-Solvent Interaction in Nonaqueous Carbonate Electrolytes with ¹⁷O NMR, *J. Phys. Chem. Lett.*, 2013, **4**, 1664–1668.
74. C. C. Su, M. He, R. Amine, T. Rojas, L. Cheng, A. T. Ngo and K. Amine, Solvating power series of electrolyte solvents for lithium batteries, *Energy Environ. Sci.*, 2019, **12**(4), 1249–1254.
75. T. Liu, L. Lin, X. Bi, L. Tian, K. Yang, J. Liu, M. Li, Z. Chen, J. Lu, K. Amine, K. Xu and F. Pan, In situ quantification of interphasial chemistry in Li-ion battery, *Nat. Nanotechnol.*, 2018, **14**, 50–56.
76. Y. Zhou, M. Su, X. Yu, Y. Zhang, J. G. Wang, X. Ren, R. Cao, W. Xu, D. R. Baer, Y. Du, O. Borodin, Y. Wang, X.-L. Wang, K. Xu, Z. Xu, C. Wang and Z. Zhu, Real-time mass spectrometric characterization of the solid-electrolyte interphase of a lithium-ion battery, *Nat. Nanotechnol.*, 2020, **15**, 224–230.
77. Z. Yu, N. P. Balsara, O. Borodin, A. A. Gewirth, N. T. Hahn, E. J. Maginn, K. A. Persson, V. Srinivasan, M. F. Toney, K. Xu, K. R Zavadil, L. A. Curtiss and L. Cheng, Beyond local solvation structure: nanometric aggregates in battery electrolytes and their effect on electrolyte properties, *ACS Energy Lett.*, 2021, **7**, 461–470.
78. L. C. Kao, X. Feng, Y. Ha, F. Yang, Y. S. Liu, N. T. Hahn, J. MacDougall, W. Chao, W. Yang, K. R. Zavadil and J. Guo, In-situ/operando X-ray absorption spectroscopic investigation of the electrode/electrolyte interface on the molecular scale, *Surf. Sci.*, 2020, **702**, 121720.
79. Y. Li, Y. Li, A. Pei, K. Yan, Y. Sun, C. L. Wu, L. M. Joubert, R. Chin, A. L. Koh, Y. Yu, J. Perrino, B. Butz, S. Chu and Y. Cui, Atomic structure of sensitive battery materials and interfaces revealed by cryo-electron microscopy, *Science*, 2017, **358**, 506–510.

80. X. Wang, M. Zhang, J. Alvarado, S. Wang, M. Sina, B. Lu, J. Bouwer, W. Xu, J. Xiao, J.-G. Zhang, J. Liu and Y. S. Meng, New insights on the structure of electrochemically deposited lithium metal and its solid electrolyte interphases *via* cryogenic TEM, *Nano Lett.*, 2017, **17**, 7606–7612.
81. J. Z. Lee, T. A. Wynn, M. A. Schroeder, J. Alvarado, X. Wang, K. Xu and Y. S. Meng, Cryogenic focused ion beam characterization of lithium metal anodes, *ACS Energy Lett.*, 2019, **4**, 489–493.
82. N. Yao, X. Chen, Z.-H. Fu and Q. Zhang, Applying classical, *Ab Initio*, and Machine-Learning Molecular Dynamics Simulations to the Liquid Electrolyte for Rechargeable Batteries, *Chem. Rev.*, 2022, **122**, 10971–11021.
83. O. Borodin, Polarizable force field development and molecular dynamics simulations of ionic liquids, *J. Phys. Chem. B*, 2009, **113**, 11463–11478.
84. A. Wang, S. Kadam, H. Li, S. Shi and Y. Qi, Review on modeling of the anode solid electrolyte interphase (SEI) for lithium-ion batteries, *Comput. Mater.*, 2018, **4**, 1–6.
85. M. W. Swift, H. Jagad, J. Park, Y. Qie, Y. Wu and Y. Qi, Predicting low-impedance interfaces for solid-state batteries, *Curr. Opin. Solid State Mater. Sci.*, 2022, **26**, 100990.
86. A. Van der Ven, Z. Deng, S. Banerjee and S. P. Ong, Rechargeable Alkali-Ion Battery Materials: Theory and Computation, *Chem. Rev.*, 2020, **120**, 6977–7019.
87. O. Borodin, *et al.*, *Phys. Chem. Chem. Phys.*, 2016, **18**, 164–175.
88. R. Yazami and Ph. Touzain, A reversible graphite-lithium negative electrode for electrochemical generations, *J. Power Sources*, 1983, **9**, 365–371.
89. M. S. Whittingham and F. R. Gamble, The Lithium Intercalates of the Transition Metal Dichalcogenides, *Mater. Res. Bull.*, 1975, **10**, 363–371.
90. Z. Tu, P. Nath, Y. Lu, M. D. Tikekar and L. A. Archer, Nanostructured Electrolytes for Stable Lithium Electrodeposition in Secondary Batteries, *Acc. Chem. Res.*, 2015, **48**, 2947–2956.
91. F. Han, A. S. Westover, J. Yue, X. Fan, F. Wang, M. Chi, D. N. Leonard, N. J. Duney, H. Wang and C. Wang, High electronic conductivity as the origin of lithium dendrite formation within solid electrolytes, *Nat. Energy*, 2019, **4**, 187–196.
92. O. Borodin, X. Ren, J. Vatamanu, A. von Wald Cresce, J. Knap and K. Xu, Modeling insight into battery electrolyte electrochemical stability and interfacial structure, *Acc. Chem. Res.*, 2017, **50**, 2886–2894.
93. Y. Wang, S. Nakamura, M. Ue and P. B. Balbuena, Theoretical studies to understand surface chemistry on carbon anodes for lithium-ion batteries: reduction mechanisms of ethylene carbonate, *J. Am. Chem. Soc.*, 2001, **123**, 11708–11718.
94. A. Jain, S. P. Ong, G. Hautier, W. Chen, W. D. Richards, S. Dacek, S. Cholia, D. Gunter, D. Skinner, G. Ceder and K. A. Persson, The Materials Project: A materials genome approach to accelerating materials innovation, *APL Mater.*, 2013, **1**, 011002.
95. G. Ceder, S. P. Ong and Y. Wang, Predictive modeling and design rules for solid electrolytes, *MRS Bull.*, 2018, **43**, 746–751.

18 Outlook

According to *Web of Science*™, in 2021 alone more than 35 000 papers were published on the topic of “battery”, which is equivalent to about 670 papers per week (Figure 18.1). Narrowing the topic down to “battery + electrolyte”, the numbers become 8260 per year and about 150 per week. Of course, while it reflects the global enthusiasm in seeking and discovering new battery chemistries and materials, it is essentially impossible for anyone to track such a publication trend thoroughly.

This accelerating trend seems to have started in the 2010s, when the governments around the world, led by the USA, China and the European Union, increased their investments in clean energy research as part of a stimulation plan to resuscitate the world economy from the subprime crisis in 2008. Fast forwarding to the 2020s, the post-Covid pandemic world now not only faces the challenges arising from natural causes such as climate change, crop shortages caused by disasters, and resource depletion of fossil energy, but also suffers more severely from human disasters: the war in Europe, trade conflicts, anxieties over supply chains, geopolitical mistrusts, surging nationalisms and the consequent hysteria and addictions to conspiracy theories.

All these unfortunate factors joined forces to make today's world much more dangerous and less habitable than just 5 years ago.

However, there is one thing that is invariable: the need for new chemistries and materials that enable more efficient energy storage.

The ultimate energy source for our planet is the Sun, which still has about 45 billion years of life left, but the process of energy transmission from the Sun to the Earth, and the time frame needed to naturally capture and store the transmitted energy, is terribly inefficient and sluggish.

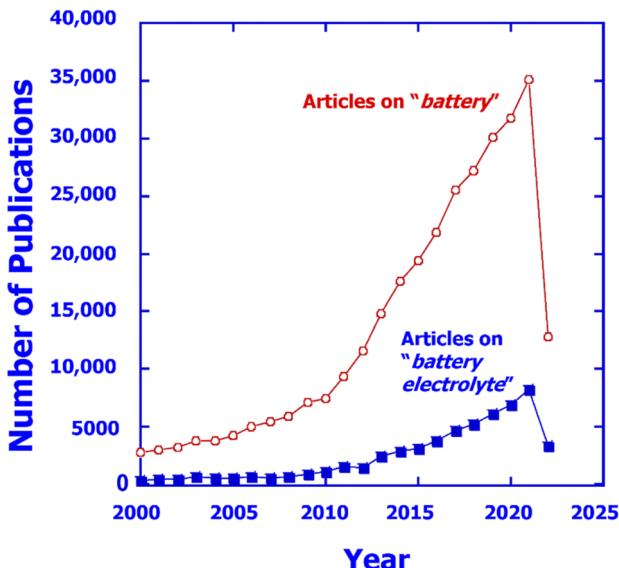


Figure 18.1 The number of research articles published each year since 2000 on the topic of “battery” or “battery + electrolyte”. Note that the data for 2022 reflect only the first half of the year (to mid-June). Source: Web of Science™.

The storage media involved in natural processes include rainwater that drives hydroelectric turbines, biomass used as direct fuels or as feedstock for chemical and biological processes to produce biofuels, and fossil fuels such as coal and petroleum. Rainwater and biomass either take years to realize or are restricted to geographic uniqueness, as exemplified by the limited location choices of water dams, or are characterized by low energy densities. Coal and petroleum are extremely energy dense, but take billions of years to realize, and therefore are essentially unsustainable in the lifespan of human civilization.

The process of capturing the energy from the Sun was significantly accelerated with the invention of solar energy technologies, either photovoltaic or photothermal, and other means of harvesting energy from the wind or ocean waves were added as part of the sustainable energy system. All these sustainable energy sources share one common and inconvenient nature, however: they convert solar, wind or wave energy to electricity in a rather intermittent manner, which is either periodic every day (depending on sunrise and sunset) or almost completely unpredictable (depending on local meteorological and hydrological conditions). Hence all of them require an energy storage system in order to work as a reliable grid. Further, the two major

means of energy consumption of modern society, namely transportation and mobile communication/computation, require the energy sources to be compact in volume and light in weight so that they are easy to carry.

In a broader context, there are other ways to generate, transmit and store energy, such as flywheels, heat, mechanical, gravitational, *etc.*, but electricity remains the most convenient, efficient and economical form of energy, with electrochemical devices being the most reliable way to store and transport electricity.

After all of the above constraints are applied, one finds that batteries remain the only viable and indispensable choice, and electrification of everything with batteries is the future of our civilization.

The last three decades, especially the 2010s, have witnessed an explosive growth of research activity on battery chemistry and materials, and astronomical amounts of investment have poured in from governmental and industry resources, driven by a curiosity for new discoveries, anticipation of the next lithium-ion battery technologies and overwhelming interest in, as well as anxieties about, both geopolitical and supply chain risks. This rapid growth of the battery and materials community has attracted an unprecedented number of scientists and engineers into the fervent frontier area.

It was also during the last three decades that the importance of electrolytes and interphases as key components in future batteries was increasingly recognized.

We have learned that any battery is a multicomponent system consisting of at least a positive electrode (cathode), a negative electrode (anode) and an electrolyte. In order for a designed battery chemistry to work, all these components must synchronize with each other, because the failure of a battery often occurs not as the result of a single malfunctioning component, but rather because of the interactions among the components.

Of all these components, the electrolyte is perhaps the most unique, as it must be simultaneously in physical contact with every other component in the battery, no matter whether they are active components such as the cathode and anode, or inactive components such as separators, current collectors and cell packaging. Simultaneously satisfying the diverse constraints is statistically difficult. Interphases are the natural consequences of electrolytes trying to work with electrode materials with extreme electrochemical potentials.

The development of electrolytes always evolves around the emergence of new battery chemistries, hence any discovery of new electrode materials must induce new demands for electrolytes and

interphases. The insatiable needs of humankind for higher energy and power densities, in addition to better safety, lower costs, sustainability and a wider service temperature range, keep pushing the boundaries of electrode materials to more challenging territories, and these challenges will eventually be passed on to electrolytes, partially or entirely. In this context, the quest for new electrolyte materials and developments in interface/interphase science, especially the fundamental understanding of interfacial/interphasial processes, chemistries and mechanisms, constitute the key frontiers for future energy storage science.

It is the sincere hope of the author that the knowledge summarized in this humble book will help the new generation of scientists in their quest for answers to the global energy demand. They should be more capable than our generation of making our planet a better place to inhabit for humankind.

Further Reading

1 The Classical Literature

- C. J. T. de Grotthuss, Sur la décomposition de l'eau et des corps qu'elle tient en dissolution à l'aide de l'électricité galvanique, *Ann. Chim.*, 1806, **58**, 54–73
- M. Faraday, *On Electrochemical Decomposition*, 1834, pp. 11–44
- W. Hittorf, Über die Wanderung der Ionen während der Elektrolyse, *Annu. Rev. Phys. Chem.*, 1853, **89**, 177
- S. Arrhenius, Development of the theory of electrolytic dissociation, Nobel Lecture, 11 December 1903, <https://www.nobelprize.org/uploads/2018/06/arrhenius-lecture.pdf>
- F. Kohlrausch, *Leitvermögen der Elektrolyte*, Benedictus Gotthelf Teubner, Leipzig, 1898
- F. G. Cottrell, Der Reststrom bei galvanischer Polarisation, betrachtet als ein Diffusionsproblem, *Zeitschrift für Physikalische Chemie*, Walter de Gruyter GmbH, 1903, vol. 42U (1), p. 385
- W. Ostwald, *On Catalysis*, Nobel Lecture, 12 December 1909, <https://www.nobelprize.org/prizes/chemistry/1909/ostwald/lecture/>
- G. N. Lewis and M. Randall, *Thermodynamics and the Free Energy of Chemical Substances*, McGraw-Hill Book Co., New York, 1st edn, 1923

- P. Debye and E. Hückel, Zur Theorie der Elektrolyte. I. Gefrierpunktserniedrigung und verwandte Erscheinungen, *Phys. Z.*, 1923, **24**, 185–206
- L. Onsager, Reciprocal Relations in Irreversible Processes I, *Phys. Rev.*, 1931, **37**, 405–426
- L. Onsager, Reciprocal Relations in Irreversible Processes II, *Phys. Rev.*, 1931, **38**, 2265–2279
- J. D. Bernal and R. H. Fowler, A Theory of Water and Ionic Solution, with Particular Reference to Hydrogen and Hydroxyl Ions, *J. Chem. Phys.*, 1933, **1**, 515–548
- L. Onsager, Theories and problems of liquid diffusion, *Ann. N. Y. Acad. Sci.*, 1945, **46**, 241–265
- R. H. Stokes and R. A. Robinson, Ionic hydration and activity in electrolyte solutions, *J. Am. Chem. Soc.*, 1948, **70**, 1870
- J. B. Perrin, *Atoms*, Translated by D. L. Hammick, Constable & Co. Ltd, London, 1916
- J. B. Hasted, D. M. Ritson and C. H. Collie, Dielectric properties of aqueous ionic solutions, *J. Chem. Phys.*, 1948, **16**, 1–21

2 The Three Foundational Books

- J. O. M. Bockris and A. K. N. Reddy, *Modern Electrochemistry*, Plenum Press, New York, 2nd edn, 1998
- A. J. Bard, L. R. Faulkner, *Electrochemical Methods. Fundamentals and Applications*, Wiley, New York, 2nd edn, 2001
- J. Newman and N. P. Balsara, *Electrochemical Systems*, Wiley, 4th edn, 2021

3 Reviews and Monographs

- Y. Marcus, Ionic Radii in Aqueous Solutions, *Chem. Rev.*, 1988, **88**, 1475–1498
- W. S. Price, Gradient NMR, in *Annual Reports on NMR Spectroscopy*, ed. G. A. Webb, Academic Press, London, 1996, pp 51–142
- N. Saunders and A. P. Miodownik, CALPHAD, Calculation of Phase Diagrams: A Comprehensive Guide, Elsevier Science, Oxford, UK, 1998
- K. Xu, Non-aqueous liquid electrolytes for lithium-based rechargeable batteries, *Chem. Rev.*, 2004, **104**, 4303–4417
- M. Inaba and Z. Ogumi, in *Li Ion Batteries: Solid Electrolyte Interphase*, ed. P. B. Balbuena and Y. Wang, Imperial College Press, Singapore, 2004, ch. 4

- E. Barsoukov and J. R. Macdonald, *Impedance Spectroscopy: Theory, Experiment and Applications*, Wiley-Interscience, New Jersey, 2nd edn, 2005
- R. A. Huggins, *Energy Storage*, Springer US, 2010
- S. Zugmann, M. Fleischmann, M. Amereller, R. M. Gschwind, H. D. Wiemhofer and H. J. Gores, Measurement of transference numbers for lithium ion electrolytes *via* four different methods, a comparative study, *Electrochim. Acta*, 2011, **56**, 3926–3933
- K. Xu, Electrolytes and interphases in Li-ion batteries and beyond, *Chem. Rev.*, 2014, **114**, 11503–11618
- Y. Shao-Horn, *et al.*, Inorganic Solid-State Electrolytes for Lithium Batteries: Mechanisms and Properties Governing Ion Conduction, *Chem. Rev.*, 2016, **116**, 140–162
- E. Peled and S. Menkin, SEI: Past, Present and Future, *J. Electrochem. Soc.*, 2017, **164**, A1703–A1719
- M. Winter, B. Barnett and K. Xu, Before Li-ion Batteries, *Chem. Rev.*, 2018, **118**, 11433–11456
- O. Borodin, J. Self, K. Persson, C. Wang and K. Xu, Uncharted Waters: Super-concentrated Electrolytes, *Joule*, 2019, **4**, 69–100
- *Linden's Handbook of Batteries*, ed. K. W. Beard, McGraw-Hill, New York, 5th edn, 2019
- M. Li, C. Wang, Z. Chen, K. Xu and J. Lu, New Concepts in Electrolytes, *Chem. Rev.*, 2020, **120**, 6783–6819
- Z. Zou, Y. Li, Z. Lu, D. Wang, Y. Cui, B. Guo, Y. Li, X. Liang, J. Feng, H. Li, C.-W. Nan, M. Armand, L. Chen, K. Xu and S. Shi, Mobile Ions in Composite Solids, *Chem. Rev.*, 2020, **120**, 4169–4221

4 Seminal Works

4.1 On Ion Solvation and Desolvation

- K. Xu, A. v. Cresce and U. Lee, Differentiating contributions to “ion transfer” barrier from interphasial resistance and Li^+ desolvation at electrolyte/graphite interface, *Langmuir*, 2010, **26**, 11538–11543
- K. Xu and A. v. Cresce, Interfacing electrolytes with electrodes in Li ion batteries, *J. Mater. Chem.*, 2011, **21**, 9849–9864
- A. v. Cresce and K. Xu, Preferential solvation of Li^+ directs formation of interphase on graphitic anode, *Electrochim. Solid-state Lett.*, 2011, **196**, 3906–3910
- X. Bogle, R. Vazquez, S. Greenbaum, A. von W. Cresce and K. Xu, Understanding Li^+ –Solvent Interaction in Nonaqueous Carbonate Electrolytes with ^{17}O NMR, *J. Phys. Chem. Lett.*, 2013, **4**, 1664–1668

- C. C. Su, M. He, R. Amine, T. Rojas, L. Cheng, A. T. Ngo and K. Amine, Solvating power series of electrolyte solvents for lithium batteries, *Energy Environ. Sci.*, 2019, **12**, 1249–1254
- A. M. Smith, A. A. Lee and S. Perkin, The Electrostatic Screening Length in Concentrated Electrolytes Increases with Concentration, *J. Phys. Chem. Lett.*, 2016, **7**, 2157–2163

4.2 On Phase Diagrams

- M. Ding, K. Xu and T. R. Jow, Liquid–Solid Phase Diagrams of Binary Carbonates for Lithium Batteries, *J. Electrochem. Soc.*, 2000, **147**, 1688–1694
- M. Ding, K. Xu and T. R. Jow, Phase diagram of EC–DMC binary system and enthalpic determination of its eutectic composition, *J. Therm. Anal. Calorim.*, 2000, **62**, 177–186
- Z.-K. Liu, Thermodynamic modeling of organic carbonates for lithium batteries, *J. Electrochem. Soc.*, 2003, **150**, A359–A365
- M. Ding, Excess Gibbs Energy of Mixing for Organic Carbonates from Fitting of Their Binary Phase Diagrams with Nonideal Solution Models, *J. Solution Chem.*, 2005, **34**, 343–359

4.3 On AC Impedance

- J. R. MacDonald, Simplified impedance/frequency-response results for intrinsically conducting solids and liquids, *J. Chem. Phys.*, 1974, **61**, 3977–3996
- R. G. Linford, in *Electrochemical Science and Technology of Polymers 2*, ed. R. G. Linford, Elsevier Applied Science, London, 1990, p. 281
- J. R. Macdonald and D. R. Franceschetti, Theory of small-signal ac response of solids and liquids with recombining mobile charge, *J. Chem. Phys.*, 1978, **68**, 1614–1637
- J. R. Macdonald, Precision of impedance spectroscopy estimates of bulk, reaction rate, and diffusion parameters, *J. Electroanal. Chem.*, 1991, **307**, 1–11
- E. Barsoukov and J. R. Macdonald, *Impedance Spectroscopy Theory, Experiment, and Applications*, John Wiley & Sons, 2nd edn, 2005

4.4 On Ion Transport

- D. N. Bennion, Phenomena at a gas-electrode-electrolyte interface, PhD thesis, University of California Berkeley, California, 1964

- T. W. Chapman, Transport Properties of Concentrated Solutions, PhD thesis, University of California Berkeley, California, 1967
- J. Newman and T. W. Chapman, Restricted Diffusion in Binary Solutions, *AICheJ.*, 1973, **19**, 343–348
- L. O. Valøen and J. N. Reimers, Transport properties of LiPF₆-based Li-ion battery electrolytes, *J. Electrochem. Soc.*, 2005, **152**, A882–A891
- C. W. Monroe and J. Newman, Onsager Reciprocal Relations for Stefan–Maxwell Diffusion, *Ind. Eng. Chem. Res.*, 2006, **45**, 5361–5367
- H. Tokuda, S. Tsuzuki, Md. A. bin H. Susan, K. Hayamizu and M. Watanabe How Ionic Are Room-Temperature Ionic Liquids? An Indicator of the Physicochemical Properties, *J. Phys. Chem.*, 2006, **110**, 19593–19600
- D. R. MacFarlane, M. Forsyth, E. I. Izgorodina, A. P. Abbott, G. Annat and K. Fraser, On the concept of ionicity in ionic liquids, *Phys. Chem. Chem. Phys.*, 2009, **11**, 4962–4967
- M. Gouverneur, F. Schmidt and M. Schöhoff, Negative effective Li transference numbers in Li salt/ionic liquid mixtures: does Li drift in the ‘Wrong’ direction? *Phys. Chem. Chem. Phys.*, 2018, **20**, 7470–7478
- N. M. Vargas-Barbosa and B. Roling, Dynamic Ion Correlations in Solid and Liquid Electrolytes: How do They Affect Charge and Mass Transport, *ChemElectroChem*, 2020, **7**, 367–385
- K. D. Fong, J. Self, B. D. McCloskey and K. A. Kristin, Ion Correlations and Their Impact on Transport in Polymer-based Electrolytes, *Macromol.*, 2021, **54**, 2575–2591
- D. J. Siegel, L. Nazar, Y.-M. Chiang, C. Fang and N. Balsara, Establishing a unified framework for ion solvation and transport in liquid and solid electrolytes, *Trends Chem.*, 2021, **3**, 807–818
- K. D. Fong, H. K. Bergstrom, B. D. McCloskey and K. K. Mandadapu, Transport phenomena in Electrolyte solutions: Non-equilibrium thermodynamics and statistical mechanics, *AICheJ.*, 2021, DOI: 10.1002/aic.17091
- B. Roling, Classifying Electrolyte Solutions by Comparing Charge and Mass Transport, *Energy & Environ. Mater.*, 2021,

4.5 On Ion Transference Number

- C. Turbandt, in *Handbuch der Experimentalphysik*, ed. W. Wein and F. Harms, Akademie Verlag, Leipzig, 1932, vol. XII, Part I
- C. A. Vincent and P. G. Bruce, Steady state current flow in solid binary electrolyte cells, *J. Electroanal. Chem. Interfacial Electrochem.*, 1987, **225**, 1–17

- J. Evans, C. A. Vincent and P. G. Bruce, Electrochemical measurement of transference numbers in polymer electrolytes, *Polymer*, 1987, **28**, 2324–2328
- K. Hayamizu, Y. Aihara, S. Arai and C. G. Martinez, Pulse-Gradient Spin-Echo ^1H , ^7Li , and ^{19}F NMR Diffusion and Ionic Conductivity Measurements of 14 Organic Electrolytes Containing $\text{LiN}(\text{SO}_2\text{CF}_3)_2$, *J. Phys. Chem. B*, 1999, **103**, 519–524
- K. Hayamizu, Temperature Dependence of Self-Diffusion Coefficients of Ions and Solvents in Ethylene Carbonate, Propylene Carbonate, and Diethyl Carbonate Single Solutions and Ethylene Carbonate + Diethyl Carbonate Binary Solutions of LiPF_6 Studied by NMR, *J. Chem. Eng. Data*, 2012, **57**, 2012–2017
- N. P. Balsara and J. Newman, Relationship between Steady-State Current in Symmetric Cells and Transference Number of Electrolytes Comprising Univalent and Multivalent Ions, *J. Electrochem. Soc.*, 2015, **162**, A2720–A2722
- F. Wohde, M. Balabajew and B. Roling, Li^+ Transference Numbers in Liquid Electrolytes Obtained by Very-Low-Frequency Impedance Spectroscopy at Variable Electrode Distances, *J. Electrochem. Soc.*, 2016, **163**, A714–A721
- M. Schönhoff, C. Cramer and F. Schmidt, Reply to the ‘Comment on “Negative effective Li transference numbers in Li salt/ionic liquid mixtures: does Li drift in the “Wrong” direction?”’, *Phys. Chem. Chem. Phys.*, 2018, **20**, 30046–30052
- D. P. Shah, H. Q. Nguyen, L. S. Grundy, K. R. Olsen, S. J. Mecham, J. M. DeSimone and N. P. Balsara, Difference between approximate and rigorously measured transference numbers in fluorinated electrolytes, *Phys. Chem. Chem. Phys.*, 2019, **21**, 7857–7866
- S. Pfeifer, F. Ackermann, F. Salzer, M. Schönhoff and B. Roling, Quantification of cation-cation, anion-anion and cation-anion correlations in Li salt/glyme mixtures by combining very-low-frequency impedance spectroscopy with diffusion and electrokinetic NMR, *Phys. Chem. Chem. Phys.*, 2021, **23**, 628–640

4.6 On Interfaces and Interphases

- J. N. Chazalviel, Electrochemical aspects of the generation of ramified metalltrodeposits, *Phys. Rev. A*, 1990, **42**, 7355–7367
- R. Fong, U. von Sacken and J. Dahn, Studies of lithium intercalation into carbons using nonaqueous electrochemical cells, *J. Electrochem. Soc.*, 1990, **137**, 2009–2013
- K. Xu, Y. Lam, S. Zhang, T. R. Jow and T. Curtis, Solvation Sheath of Li^+ in Non-aqueous Electrolytes and Its Implication of Graphite/

- Electrolyte Interface Chemistry, *J. Phys. Chem. C.*, 2007, **111**, 7411–7421
- M. Winter, The Solid Electrolyte Interphase – The Most Important and the Least Understood Solid Electrolyte in Rechargeable Li Batteries, *Z. Phys. Chem.*, 2009, **223**, 1395–1406
 - K. Xu, A. v. Cresce and U. Lee, Differentiating contributions to “ion transfer” barrier from interphasial resistance and Li^+ desolvation at electrolyte/graphite interface, *Langmuir*, 2010, **26**, 11538–11543
 - S. Shi, P. Lu, Z. Liu, Y. Qi, L. G. Hector Jr, H. Li and S. J. Harris, Direct Calculation of Li-ion Transport in the Solid Electrolyte Interphase, *J. Am. Chem. Soc.*, 2012, **134**, 15476–15487
 - Y. Li, K. Leung and Y. Qi, Computational Exploration of the Li Electrode/Electrolyte Interface in the Presence of a Nanometer Thick Solid-Electrolyte-Interphase, *Acc. Chem. Res.*, 2016, **49**, 2363–2370
 - O. Borodin, X. Ren, J. Vatamanu, A. v. W. Cresce, J. Knap and K. Xu, Modeling insight into battery electrolyte, electrochemical stability and interfacial structure, *Acc. Chem. Res.*, 2017, **50**, 2886–2894
 - L. Benitez and J. M. Seminario, Ion Diffusivity through the Solid Electrolyte Interphase in Lithium-Ion Batteries, *J. Electrochem. Soc.*, 2017, **164**, E3159–E3170
 - D. Lu, J. Tao, P. Yan, W. A. Henderson, Q. Li, Y. Shao, M. L. Helm, O. Borodin, G. O. Graff, B. Polzin, C.-M. Wang, M. Engelhard, J.-G. Zhang, J. J. De Yoreo, J. Liu and J. Xiao, Formation of Reversible Solid Electrolyte Interface on Graphite, *Nano Lett.*, 2017, **17**, 1602–1609
 - Y. Zhou, M. Su, X. Yu, Y. Zhang, J.-G. Wang, X. Ren, R. Cao, W. Xu, D. R. Baer, Y. Du, O. Borodin, Y. Wang, X.-L. Wang, K. Xu, Z. Xu, C. Wang and Z. Zhu, Real-time mass spectrometric characterization of the solid–electrolyte interphase of a lithium-ion battery, *Nat. Nanotechnol.*, 2020, **15**, 224–230
 - M. He, R. Guo, G. M. Hobold, H. Gao and B. M. Gallant, The intrinsic behavior of lithium fluoride in solid electrolyte interphases on lithium, *Proc. Natl. Acad. Sci. U. S. A.*, 2020, **117**, 73–79

4.7 On Concentrated Electrolytes

- J. R. Dahn and J. A. Seel, Energy and Capacity Projections for Practical Dual-Graphite Cells, *J. Electrochem. Soc.*, 2000, **147**, 899–901
- L. Suo, O. Borodin, T. Gao, M. Olguin, J. Ho, X. Fan, C. Luo, C. Wang and K. Xu, Water-in-Salt’ Electrolyte Enables High Voltage Aqueous Li-ion Battery Chemistries, *Science*, 2015, **350**, 938–943

- J. A. Read, *In Situ* Studies on the Electrochemical Intercalation of Hexafluorophosphate Anion in Graphite with Selective Cointercalation of Solvent, *J. Phys. Chem. C.*, 2015, **119**, 8438–8446
- O. Borodin, L. Suo, M. Gobet, X. Ren, F. Wang, A. Faraone, J. Peng, M. Olguin, M. Schroeder, M. S. Ding, E. Gobrogge, A. von W. Cresce, S. Munoz, J. A. Dura, S. Greenbaum, C. Wang and K. Xu, Liquid structure with nano-heterogeneity promotes cationic transport in concentrated electrolytes, *ACS Nano*, 2017, **11**, 10462–10471
- C. Yang, J. Chen, X. Ji, T. P. Pollard, X. Lü, C.-J. Sun, S. Hou, Q. Liu, C. Liu, T. Qing, Y. Wang, O. Borodin, Y. Ren, K. Xu and C. Wang, Aqueous Li-ion battery enabled by halogen conversion–intercalation chemistry in graphite, *Nature*, 2019, **569**, 245–250

4.8 On Simulations of Interfaces and Interphases

- M. M. Islam and T. Bredow, Density Functional Theory Study for the Stability and Ionic Conductivity of Li_2O Surfaces, *J. Phys. Chem. C.*, 2009, **113**, 672–676
- K. C. Lau, L. A. Curtiss and J. Greeley, Density Functional Investigation of the Thermodynamic Stability of Lithium Oxide Bulk Crystalline Structures as a Function of Oxygen Pressure, *J. Phys. Chem. C.*, 2011, **115**, 23625–23633
- S. Shi, P. Lu, Z. Liu, Y. Qi, L. G. Hector Jr, H. Li and S. J. Harris, Direct Calculation of Li-Ion Transport in the Solid Electrolyte Interphase, *J. Am. Chem. Soc.*, 2012, **134**, 15476–15487
- J. Pan, Y.-T. Cheng and Y. Qi, General method to predict voltage-dependent ionic conduction in a solid electrolyte coating on electrodes, *Phys. Rev. B.*, 2015, **91**, 134116
- H. Yildirim, A. Kinaci, M. K. Y. Chan and J. P. Greeley, First-Principles Analysis of Defect Thermodynamics and Ion Transport in Inorganic SEI Compounds: LiF and NaF, *ACS Appl. Mater. Interfaces*, 2015, **7**, 18985–18996
- Y. Li, K. Leung and Y. Qi, Computational Exploration of the Li-Electrode|Electrolyte Interface in the Presence of a Nanometer Thick Solid-Electrolyte Interphase Layer, *Acc. Chem. Res.*, 2016, **49**, 2363–2370
- Q. Zhang, J. Pan, P. Lu, Z. Liu, M. W. Berbrugge, B. W. Sheldon, Y.-T. Cheng, Y. Qi and Z. Xiao, Synergetic Effects of Inorganic Components in Solid Electrolyte Interphase on High Cycle Efficiency of Lithium Ion Batteries, *Nano Lett.*, 2016, **16**, 2011–2016

- K. Leung and K. L. Jungjohann, Spatial Heterogeneities and Onset of Passivation Breakdown at Lithium Anode Interfaces, *J. Phys. Chem. C.*, 2017, **121**, 20188–20196
- O. Borodin, X. Ren, J. Watamanu, A. von Wald Cresce, J. Knap and K. Xu, Modeling Insight into Battery Electrolyte Electrochemical Stability and Interfacial Structure, *Acc. Chem. Res.*, 2017, **50**, 2886–2894
- A. Wang, S. Kadam, H. Li, S. Shi and Y. Qi, Review on modeling of the anode solid electrolyte interphase (SEI) for lithium-ion batteries, *Comp. Mater.*, 2018, **4**, 15
- N. Yao, X. Chen, Z.-H. Fu and Q. Zhang, Applying Classical, *Ab Initio*, and Machine-Learning Molecular Dynamics Simulations to the Liquid Electrolyte for Rechargeable Batteries, *Chem. Rev.*, 2022,

4.9 On Diagnostics of Electrolytes in Practical Devices

- A. J. Smith, J. C. Burns, D. Xiong and J. R. Dahn, A High Precision Coulometry Study of the SEI Growth in Li/Graphite Cells, *J. Electrochem. Soc.*, 2011, **158**, A447–A452
- A. J. Smith, J. C. Burns, D. Xiong and J. R. Dahn, Interpreting High Precison Coulometry Results on Li-Ion Cells, *J. Electrochem. Soc.*, 2011, **158**, A1136–A1142
- C. P. Aiken, E. R. Logan, A. Eldesoky, H. Hebecker, J. M. Oxner, J. E. Harlow, M. Metzger and J. R. Dahn, Li[Ni_{0.5}Mn_{0.3}Co_{0.2}]O₂ as a Superior Alternative to LiFePO₄ for Long-Lived Low Voltage Li-Ion Cells, *J. Electrochem. Soc.*, 2022, **169**, 050512

Subject Index

References to figures are given in *italic* type. References to tables are given in **bold** type.

- 6 V super-battery, 353
- ab initio* molecular dynamic (AIMD) simulations, 162–163
- absolute mobility, 89, 94
- AC *see* alternating current
- accelerating rate calorimetry (ARC), 348
- acetic acid (HOAc), 7
- acetonitrile, 406
- acetonitrile-based electrolytes, 431
- acidic aqueous electrolytes, 214–215
- acids, 4, 5, 672
- AC impedance
 - elements, 449–454
 - connecting into circuits, 454–466
 - spectra, 458, 459, 467, 478
 - Sørensen-Jacobsen approach, 520, 520–522
 - spectroscopy, 444
 - technique, 535
- activation energy, 129
 - barrier, 170–172
- activity
 - coefficients, 23–25
 - gradient, 554
- additive(s)
 - electrolyte, 357, 618–619, 651–657, **653–654**
 - properties, 24
- Ag *see* silver
- aggregates (AGGs), 418
- AGGs *see* aggregates
- AI *see* artificial intelligence
- AIMD simulations *see ab initio* molecular dynamic simulations
- air
 - Greek element of universe, 6
- Al *see* aluminum
- Al₂O₃ *see* alumina
- alkaline aqueous electrolytes, 214–215
- alkoxides, 473, 629, 667
- alkylamides, 357
- alkyl carbonate esters, 124
- alkyl carbonates, 622
- alkyl esters, 376
- alternating current (AC), 16
 - techniques, 444–466, **445**
 - circuits with blocking electrodes, 457–459
 - circuits with non-blocking electrodes, 461–466
 - connecting AC impedance elements into circuits, 454
 - correcting with constant-phase element, 459–461
 - elements in AC impedance spectra, 449–454
 - equivalent circuits, 447–449, 454
 - R–C in parallel, 448, 455, 455–457
 - R–C in series, 448–449, 454–455, 455, 459
- alternative battery chemistry, 705
- alumina (Al₂O₃), 733, 741
- aluminum (Al), 305–306, 333–340, 740
- ambipolar diffusion, 563–565
 - coefficient (D_{ambp}), 114, 205, 521, 582

- ambipolar ionic movement, 112–116
transport, 112, 203–206
- ammonium salts, 729
- ammonium–superoxide complex, 357–358
- amorphous ceramics, 129
- amorphous solids, 129
- amperometry, 298
- Ancient Greeks, 3, 6
- Angell–Walden plot, 477–478, 479, 482–483
- ångstroms, 400
- anion, 3, 374
- anionic flux at steady state, 527–529
 - blocking condition, 443
 - concentration profile, 525
 - intercalation chemistries, 367–370
 - salt, 322, 323, 328
 - solvation, 429–432
- anisotropic properties, 309
- anisotropy, 129, 135–136, 141, 163, 694
- anode, 3, 212, 226, 333, 767
- copper, 246–247
 - cross-talk with cathode, 639–641
 - free lithium–metal cell, 617–618
 - graphitic, 369
 - graphitic carbon, 264
 - lithium, 257, 261
 - materials, 725
 - salts, 322, 323
- anode/electrolyte interface, 78, 253
- anodic current, 175
- anodic limit, 212
- antimony (Sb), 333
- antimony pentachloride ($SbCl_5$), 414
- antiperovskites, 128
- antiperovskite-type SSEs, 741–742
- aprotic, 119
- ARC *see* accelerating rate calorimetry
- Argentina, 292, 293
- argyrodite, 128
- Armand approach, 510–518, 546
- Arrhenius, Svante, 4–5, 24, 400, 439
- Arrhenius relation, 471
- Arrhenius's theory, 25–26
- artificial intelligence (AI), 715, 752
- artificial interphases, 746–748
- Asahi Kasei, 277, 306–307, 320
- Atacama salt flat in Peru, 292
- Au *see* gold
- Australia
- lithium reserves, 292
- Avogadro's number (N_A), 101, 390
- background current, 286
- BaCl₂ *see* barium chloride
- barium chloride (BaCl₂), 508
- barium sulfate (BaSO₄), 508
- bases, 4, 5
- BaSO₄ *see* barium sulfate
- batteries, 245–277
- battery chemistries: conversion reaction vs. intercalation, 273–277
 - capacity and energy, 257–266
 - charge separation, 255–257
 - comparison and transition with capacitors, 279–282
 - electrolyte engineering for battery applications, 472–477
 - energy quality, 271–273
 - how they work, 247–249, 767
 - invention of first, 3, 266
 - lessons learned from Nernst equation, 254–255
 - metal-air, 226
 - mistake often made, 268–271
 - primary, 226
 - rechargeable batteries:
 - Coulombic and energy efficiencies, 266–268
 - thermodynamics behind batteries: Nernst equation, 249–254
- BDM Model *see* Bockris–Devanathan–Müllen Model
- Be *see* beryllium
- benzene, 341
- Bernal–Fowler solvation sheaths, 420–421, 426, 716
- Bernal–Fowler Three-Layer Model, 400–401
- beryllium (Be), 349
- Berzelius, Jöns Jacob, 3
- beyond lithium-ion chemistries, 657–665
- CEIs in Li/O₂ and Li/Air chemistry, 658–660
 - CEIs on Conversion Reaction Chemistry, 664–665
 - SEIs on metals with multivalent chemistries, 662–664
 - SEIs on Na⁰/K⁰ electrodes and intercalation hosts for Na⁺/K⁺, 660–662

- BF₃, 671
 Bi *see* bismuth
 Big Bang, 292
 biofuels, 766
 bipolar, 328
 bipolarity, 12
 bis(fluorosulfonyl)imide (FSI), 323, 420
 bismuth (Bi), 333
 bis(oxalato)borate (BOB), 322
 bis(trifluoromethanesulfonyl)imide (TFSI), 215, 420–421
 Bjerrum length, 53–56, 126
 comparison with Debye–Hückel thickness, 56–57
 BOB *see* bis(oxalato)borate
 Bockris–Devanathan–Müllen (BDM) Model, 156–162, 236
 boiling point, 24, 377
 Bolivia, 292, 293
 Boltzmann distribution law, 34–35, 93
 Boltzmann equation, 33–35
 combining with Poisson equation, 36–40
 linearisation of, 35–36
 Boltzmann’s constant, 34
 Boltzmann’s entropy relation, 389
 borates, 322
 borohydrides, 662
 boundary conditions, 79
 brine water, 379
 bromide, 368
 Brownian motion, 101, 427
 Bruce–Vincent approach, 523–536, 546, 554, 556–557, 573
 cationic and anionic fluxes at steady state, 527–529, 594–595, 599
 cationic transference number in absence of interphases, 532–533
 cationic transference number in presence of interphases, 533–536
 potential profile across cell and electrolyte, 529–532
 revisiting in Newman’s formalism, 584–588
 salt (and ion) concentration profiles at the steady state, 524–527
 bubble point line, 377, 381, 381–382
 bulk region, 596–599, 597
 Butler–Volmer equation, 173–176, 174, 212, 613
 charge transfer coefficient (β), 182–186
 dependence on interface structure, 181–182
 electrochemical devices, in, 186–190
 quantifying polarisable and non-polarisable interfaces, 180–181
 three scenarios predicted by, 177–179
 equilibrium, at: Nernst equation, 177–178, 249, 252
 high overpotential, at a: Tafel behaviour, 178–179, 220–221
 small overpotential, at a: Ohmic behaviour, 178
 C *see* capacitor
 Ca *see* calcium
 Ca²⁺, 350, 350–351
 calcium (Ca), 662–663
 calorimetric technique, 385
 CALPHAD, 389, 396, 399
 capacitance, 258, 282–290, 450
 capacitor (C), 150–153, 151, 226, 449–453
 comparison and transition with batteries, 279–282
 leaky, 452, 460
 pure, 447, 451, 459
 simple, 155–156
 capacity
 energy, and, 257–266, 259, 293
 lithium metal, of, 294, 349
 carbonate-based electrolytes, 363, 374
 carbonate esters, 340, 624–625
 carbonates, 119, 375, 402, 659
 carbon dioxide (CO₂), 339, 353
 carbonic acid, 376
 carboxylate esters, 340
 carboxylates, 329, 473, 629
 carboxylic acids, 320
 CaSO₄, 26
 cathode, 3, 212, 226, 352–353, 767
 cross-talk with anode, 639–641
 graphitic, 369
 materials, 725
 oxygen, 359
 salts, 323, 324
 zinc, 246–247, 257
 cathode/electrolyte interface, 79, 253

- cathode/electrolyte interphase (CEI), 219, 608, 621, 632–639, 718
CEIs in Li/O₂ and Li/Air chemistry, 658–660
comparison between SEIs and CEIs, 641–644
electron energy levels, 606, 606
- cathodic challenge, 725, 726
- cathodic current, 175
- cathodic limit, 212
- cation, 3, 323, 324, 328
cationic conductivity, 534
cationic flux at steady state, 527–529
cationic transference number, 537, 541
absence of interphases, in, 532–533
presence of interphases, in, 533–536
concentration profile, 525
multivalent chemistries, 349–352
onium, 124
- CEI *see* cathode/electrolyte interphase
- center-of-mass frame (CoM frame), 546–547
- CH₂F₂ *see* difluoromethane
- chalcogenides (TiS₂), 740
- charge carrier number (n_i), 474
- charge density, 148
- charge quantity (Q), 279–280
- charge separation, 255–257, 400
- charge transfer
defined, 164–168
kinetics of across interfaces, 168–171, 169, 687, 690
presence of 2D interfaces and 3D interphases, in, 612–613
scenarios, 164–166
- charge transfer coefficient (β), 182–186, 183
- charge-transfer kinetics, 176
- charge-transfer limit, 74
- chelation, 415
- chemical potentials, 394, 396
- chemical stability, 375–376
- Chile, 292, 293
- China
lithium reserves, 292
- chloride, 368
- chlorine gas, 117
- CIPs *see* close ion pairs; contact ion pairs
- circuits
- blocking electrodes, with, 457–459, 458
- non-blocking electrodes, with, 461–466, 462
- circumventing irreversibility and safety hazards
birth of lithium-ion chemistries, 306–307
bypass *via* dual intercalation, 305–306
- clean energy research, 765
- cleavage, 629, 649
- close ion pairs (CIPs), 418
- Co *see* cobalt
- CO₂ *see* carbon dioxide
- coal, 766
- cobalt (Co), 365
- co-intercalation, 693–698, 695, 717
- Cole–Cole plot, 446
- colligative
law, 24
properties, 23–24, 26
- CoM frame *see* center-of-mass frame
- composition, 383, 394
- computer simulations, 751–759
computational design of materials, 758–759
molecular simulations, 752–757
prediction of properties and performances, 757–758
- Concentrated Solution Theory, 575–588
- Bruce–Vincent approach in Newmann's formalism, 584–588
limitations of, 588–589
self, ambipolar, salt and electrolyte diffusion coefficients, 582–584
- concentration cell, 510–518, 511
ion transference, with, 515
perturbed, 518–520
without ion transference, 515
- concentration gradient, 554
- concentration profiles
bulk region, in, 594, 596–599
interfacial region, in, 599–601
- condition of necessity, 220
- condition of sufficiency, 220
- conduction *see* migration (conduction)
- conductivity (σ), 5, 24, 83–87, 90–92, 94
cationic, 534
equivalence, 490
high to Li⁺, 611
maximum, 120, 121
molar (*see* molar conductivity)

- constant charge, 283
 constant-phase element (cpe), 449, 452–454
 correcting with, 459–461, 460
 constitutional properties, 24
 contact ion pairs (CIPs), 418
 convective diffusion coefficient, 115
 conventional mobility, 89
 conversion reaction, 361
 chemistry, 332, 664–665
 vs. intercalation, 273–277, 274
 copper (Cu), 246, 256, 365, 664
 copper sulfate (CuSO_4), 132–133, 133, 204, 509
 correlations, 560–562
 Cottrell equation, 200
 Coulombic efficiency, 266–268, 298, 345, 655, 700, 700
 Coulombic field, 17, 45, 105, 242
 Coulombic force (F_c), 18, 30, 35, 102, 275, 324
 Coulombic inefficiency, 303
 Coulombic repulsion, 149, 242, 322–323, 562
 Coulomb's law, 30, 46
 coulometry, 200, 212, 298
 Covid pandemic, 223
 post-Covid pandemic, 765
 cpe *see* constant-phase element
 Cu *see* copper
 cupric (Cu^{2+}) salt, 132
 Current Statement, 569
 CuSO_4 *see* copper sulfate
 CV *see* cyclic voltammetry
 cyclic voltammetry (CV), 212, 284–285, 285
 Daniell, John Frederic, 134
 Daniell cell, 134, 204, 246–248
 dative bond, 431
 DC *see* direct current
 DC potentiostatic polarisation technique, 535
 dead Li⁺, 302–304, 303, 336–337, 341–342, 345, 657–658, 661
 Debye–Hückel limiting law, 44
 Debye–Hückel–Onsager equation, 109–111
 Debye–Hückel Theory, 11, 29–64, 67
 combining the Poisson and Boltzmann equations, 36–40
 comparison between Debye–Hückel thickness and Bjerrum length, 56–57
 Constant K : Debye–Hückel thickness, 46–50, 48, 49
 ionic cloud, 29–31, 582
 linearisation of Boltzmann equation, 35–36
 liquid structures, 62–64
 refinement of model: finite-sized central ion, 50–52
 refinement of model: ion-pair formation and Bjerrum length, 53–56, 55
 refinement of model: ion-solvent interaction, 57–61, 58
 spatial distribution of ionic cloud Boltzmann equation, 33–35
 Poisson equation, 31–33
 successes and limitations of Debye–Hückel Model, 61–62
 verifications of the Debye–Hückel Model, 40–46
 Debye–Hückel thickness (constant K), 46–50, 48, 49, 110, 119, 593, 594
 comparison with Bjerrum length, 56–57
 DEC *see* diethylene carbonate
 decomposition, 212
 DEDOHC *see* diethyl-2,5-dioxahexane carboxylate
 de-electronation, 164, 225
 de-lithiation, 337
 dendrite formation, 300–302, 302, 341–342, 344, 741
 dendritic Li⁰, 302, 302, 336, 341–342, 364, 658, 739
 density, 91
 density functional theory (DFT), 752, 757
 denticity, 415, 427
 depositions, 299–302, 342, 644
 metal, 300
 deterministic approach, 69
 DFT *see* density functional theory
 1,2-dichloroethane, 414
 dielectrically saturated, 21, 22
 dielectric capacitors, 279
 dielectric constant, 13–17, 15, 23, 119, 414, 474
 effect of ions and unexpected application, 20–23
 water, of, 16, 16
 diethyl-2,5-dioxahexane carboxylate (DEDOHC), 436
 diethylene carbonate (DEC), 319, 321, 348, 623

- differential pair distribution function (d-PDF), 751
differential scanning calorimetry (DSC), 385
diffuse charge, 155–156
diffusion, 65–82, 100, 374, 499
ambipolar, 563–565
Einstein–Smoluchowski equation, 70–72
Fick's First Law: steady-state diffusion, 66–69
Fick's Second Law: non-steady state diffusion, 72–78, 73
solving for a few practical scenarios, 78–82
salt, 563–565
diffusional potential, 512
diffusion coefficient (D), 66, 80, 90, 90–92, 94, 101
diffusion control, 80
diffusion ordered spectroscopy (DOSY), 415, 750–751
diffusion thickness, 80
diffusivity (D), 66, 66, 71
difluoromethane (CH_2F_2), 730
dimethoxyethane, 730
dimethoxyethane (DME), 340, 347, 364, 413, 427, 647
dimethyl-2,5-dioxahexane (DMDOHC), 436, 437
dimethyl carbonate (DMC), 319, 321, 347–348, 436, 623
dimethyl methylphosphonate (DMMP), 339
1,3-dioxolane (DOL), 364, 415, 647
direct current (DC), 16, 440–441, 444
polarisation, 440–441, 442, 443, 494, 555
directional movement of ions, 87–88
disasters, 765
discharge current, 283
disproportionation, 421, 431
dissolution, 17, 18, 24
distortion parameter, 106
DMC *see* dimethyl carbonate
DMDOHC *see* dimethyl-2,5-dioxahexane
DME *see* dimethoxyethane
DMMP *see* dimethyl methylphosphonate
DN *see* donor number
DOL *see* 1,3-dioxolane
donicity, high, 427
donor number (DN), 414
DOSY *see* diffusion ordered spectroscopy
double-layer capacitance, 447, 462
double-layer capacitor, 457
downfield, 403
d-PDF *see* differential pair distribution function
drift velocity (v_d), 87, 88–89, 90–92, 100, 109, 547
driving force, 577
drunken sailor's random walk problem, 67–69
DSC *see* differential scanning calorimetry
dual intercalation, 305–306
battery, 276
chemistry, 276, 330, 331
dual-ion intercalation
cell, 369–370
chemistry, 369
dynamic equilibrium at an interface, 171–172
- earth
Greek element of universe, 6
EC *see* ethylene carbonate
EC–DEC solvent mixture, 436
EC–DMC solvent mixture, 385–387, 436, 498
phase diagram of, 384, 384
EC–EMC binary system, 476
ecm *see* electrocapillary maximum
EC–PC solvent mixture, 476, 701, 701
eigenpotentials, 229, 256, 333, 340, 607
Einstein equations, 490–492
Einstein relation, 92–94, 491, 574
Einstein–Smoluchowski equation, 70–72, 491, 582
EIS *see* electrochemical impedance spectroscopy
electric double layer, 135–141, 150, 169
classical understanding of, 141–150
electrocapillarity, 143–144
Gibbs Surface Excess, 141–142, 142
immeasurable potential, 137–139
polarisable and non-polarisable interfaces, 139–141
electric energy, 225–227
electricity, 3, 24, 766
electric vehicles, 223, 293
electric work (W_e), 42, 229
electrocapillarity, 141, 143–144, 150
electrocapillary maximum (ecm), 144, 148
electrocardiography, 224

- electrochemical concentration cell
see concentration cell
- electrochemical devices, 223–291
 batteries, 245–277
 Butler–Volmer equation, in, 186–190
 comparison and transition between capacitors and batteries, 279–290
 cyclic and linear voltammetry, 282–290
 electrochemical double-layer capacitors, 235–245
 four types of, 226–227
 fuel cells, 230–235
 how electrochemical energy device works, 228–290
 overview, 223–227
 pseudo-capacitors, 277–279
- electrochemical double-layer capacitors, 223, 226–227, 235–245
 electrolytes, 244–245
 how they work, 237, 237–241
 limiting factors, 241–244, 243
- electrochemical impedance spectroscopy (EIS), 444
- electrochemically dead, 303, 342
- electrochemical potential, 103
- electrochemical quartz crystal microbalance (EQCM), 674, 697, 699, 751
- electrochemical redox potential, 352
- electrochemical sensors, 224, 227
- electrochemical stability, 375–376, 476, 673–675
 exotic solvents, 721–722
- electrochemical stability window, 117, 212–219, 213
 aqueous and non-aqueous electrolytes, of, 214–216
 correlation with interphases, 220–221
 expanded by an interphase, 216–218
 water, 722–727
- electrode/electrolyte interface, 253, 404, 573
- electrode potential
 lithium metal, of, 293–294
- electrodes, 3–4, 135–136, 136
 blocking, 440, 447, 447, 457–459, 458
 ideally non-polarisable, 143
 ideally polarisable, 143
- negative, 227
- non-blocking, 443, 448, 448, 461–466, 462
- positive, 227
- reference/counter, 137, 143, 147
- SEIs on Na^0/K^0 electrodes, 660–662
- working, 137
- electrodics, 10, 116, 163–190, 373–374
 Butler–Volmer equation, 173–176
 charge transfer defined, 164–168
 dynamic equilibrium at an interface, 171–172
 kinetics of charge transfer across interfaces, 168–171
- electroencephalography, 224
- electrolysis, 224, 226
- electrolyte average diffusivity, 115
- electrolyte diffusion coefficients, 115, 580, 582–584
- electrolytes
 aqueous, 12, 244
 aqueous-nonaqueous hybrid, 727–729
 barrier, 134
 black box, as, 440, 466
 bulk, 11–28, 554, 569–570, 594–596
 classification of: ionic, super-ionic and sub-ionic, 480–482
 concentrated, 63, 418, 419
 defined, 3–5, 6
 dilute, 62–63
 electron insulator, as, 134
 engineering for battery applications, 472–477
 functional, 652
 function of, 377–378, 767
 ideal, 98, 492, 498
 ideality of, 490–492
 ionic conductor, as, 132, 134
 liquid, 376
 locally concentrated, 727–729
 locally high-concentration, 416, 728
 moderately concentrated, 63
 modern, 6–10
 multicomponent, 565–567
 multivalent ion, 705–708
 nano-confining, 744–746
 non-aqueous (*see* non-aqueous electrolytes)

- non-ideal, ionics for, 548–567
polymer-in-salt, 717
practical, 492, 501–504
requirements of, 375–377
salt solvate, 719
semi-solid, 735–736
soggy-sand, 735–736
solution, 10
strong or weak, 25–26
super-concentrated (*see* super-concentrated electrolytes)
term created by Faraday, 3
true solid, 737–744
types of, 6–10
water-in-salt (*see* water-in-salt electrolytes)
what qualifies as, 375–377
what they do, 377–378
- electrolytes, interfaces and interphases
in bulk electrolytes: ionics, 11–28
electrochemical devices, 223–291
interfaces, 592–601
interphases, 602–713
ion solvation, 400–434
ion transport in electrolytes, 65–130
ion transport: properties, 439–591
linking ionics with electrodics, 192–208
lithium-metal, lithium-ion and other batteries, 292–372
modern electrolytes, 6–10
new concepts and tools, 714–764
outlook, 765–768
phase diagrams of liquid electrolytes, 379–399
properties of electrolytes, interfaces and interphases, 373–378
quantification of ion–ion interaction: Debye–Hückel Theory, 29–64
static stability of electrolytes, 435–438
what is an electrolyte?, 3–5
when an electrode operates beyond electrode stability limits: interphase, 209–222
when electrolyte meets electrodes: interface, 131–191
electromotive force (emf), 134
electronation, 164, 225, 693
- electron energy levels, 605–609, 606
Electroneutrality Statement, 569–571, 573, 582, 592, 595
electron paramagnetic resonance spectroscopy, 626
electrophoresis effect, 46
electrophoresis force, 108–109
electrophoretic NMR (eNMR) spectroscopy, 537, 540, 540–543
electroplating, 224, 226
electropolishing, 224
electropositivity, 294
electro-spray ionisation mass spectrometry (ESI-MS), 347, 407, 411, 413, 430, 701, 750
electrostatic capacitors, 279
electrostatic field (ψ_r), 32, 35, 42, 45, 46, 235
electrostatic shield, 344
elements of universe, 6
EMC *see* ethylmethyl carbonate
emf *see* electromotive force
EMIM⁺ *see* 1-ethyl-3-methylimidazolium
endothermic, 385
energy
capacity, and, 257–266, 259, 293
efficiency, 266–268
quality, 271–273, 272
storage devices, 227
energy density, 332
eNMR spectroscopy *see* electrophoretic NMR (eNMR) spectroscopy
enthalpy, 17, 384
solvation, 400
entropy, 17, 35, 384, 390, 400
EP *see* ethyl propionate
EQCM *see* electrochemical quartz crystal microbalance
equilibrium, 254
equivalent conductivity (Λ), 86, 101
erf *see* error function
erfc *see* error complement function
error complement function (erfc), 80, 81
error function (erf), 80, 81
ESI-MS *see* electro-spray ionisation mass spectrometry
esters, 12, 646–647, 648
cathodically stable, 720–721
ethers, 12, 16, 340, 647–651, 648, 659, 720
anodically stable, 717–720
fluorinated, 650
polyfluorinated, 650–651

- ethylene carbonate (EC), 12, 13, 311, 348
 high melting point, 386
 “magic” EC-graphite chemistry, 311–313, 313, 330, 622
 vs. propylene carbonate (PC), 317–319, 318
- ethylene oxide, 731
- ethylmethyl carbonate (EMC), 319, 321, 347, 436, 623
- 1-ethyl-3-methylimidazolium (EMIM^+), 546
- ethyl propionate (EP), 436
- Euler’s formula, 452
- exchange current density (i_0), 172
- exfoliation, 309, 695–696, 697, 700
- exothermic, 385
- exotic solvents, 721–722
- extensive quantity, 257
- external electronic field
 absence of, 65, 105
 ion transport driven by, 82, 82–83
- extrinsic pseudo-capacitance, 279
- Exxon Corporate Research, 305, 334
- F *see* fluorine
- Faradaic process, 167, 288–290
- Faradaic reactions, 692
 capacitance, and, 282–290
- Faraday, Michael, 3–4, 24, 131, 223
- Faraday constant (F), 30, 91, 259
- Fe *see* iron
- FEC *see* fluoroethylene carbonate; monofluoroethylene carbonate
- feedstock, 766
- ferrocene, 690
- Fick’s first law, 66–69, 71–72, 114, 195, 200, 564–565, 572
- Fick’s second law, 67, 72–78, 97, 196–197, 199, 206, 572–573
 solving for a few practical scenarios, 78–82
- field strength X , 83
- fire
 Greek element of universe, 6
- fluorides, 638, 660, 676–677, 747
- fluorinated compounds, 357
- fluorinated ethers, 650
- fluorinated phosphates, 357
- fluorinated phosphites, 357
- fluorine (F), 352, 366, 676, 723
- fluorocarbons, 345
- fluoroethylene carbonate (FEC), 338
- fluoromethane, 730
- flux, 66, 77, 91, 499, 500, 577
 anionic, 527–529, 563
 cationic, 527–529, 563, 598
 conduction, 93
 constant, 75, 81, 196, 199
 diffusional, 93, 503, 526, 528, 563
 migrational, 528
- Flux Statement, 568–569, 572, 581, 583–584, 595
- formal charge, 164
- fossil
 energy, 765
 fuels, 766
- Fourier transform infrared (FTIR) spectroscopy, 20, 404, 430, 630, 679, 699
- frozen ice, 729–731
- FSI *see* bis(fluorosulfonyl)imide
- FTIR spectroscopy *see* Fourier transform infrared spectroscopy
- fuel cells, 223, 226, 230–235
 power conversion device, 230
- Fuji Photo Film Co., 334
- galvanodynamic conditions, 283
- galvanometry, 298
- galvanostatic conditions, 196–200, 197, 206, 283, 290, 519
- Gamow probability, 123–124
- Garnet-type SSEs, 739–741
- gas phase, 4
- Gauss error function complement, 79
- Gauss’s law, 31, 154, 595
- Geim, Andre, 309
- gel permeation chromatography, 437
- gel polymer electrolytes (GPEs), 124–125, 733
- geometric capacitance, 448, 462–464
- Gibbs–Duhem equation, 576, 589
- Gibbs–Duhem relation, 147
- Gibbs energy of the system, 391–392
- Gibbs free energy, 17, 133, 229, 389–396
 formation, of, 254–255, 266
- Gibbs mixing energy, 391–393
 excess, 391
- Gibbs Surface Excess, 141–142, 142
- gold (Au), 278, 333
- Goodenough, John B., 277, 305–307, 320, 331
- Gouy–Chapman Model, 151, 153–156, 161, 181
- GPEs *see* gel polymer electrolytes
- Grahame Model, 156–162, 157

- graphenes, 308–309
 hospitable host, 309, 311
 sheets, 308, 632
- graphite
 anode material, 269, 330, 336, 632, 692–694, 694, 749
 exfoliation, 695–696, 697
 hospitable host, 311
 intercalation host, 188, 189, 207
 interphases formed in electro-chemical process, 341
 Li⁺ host, as, 190, 307–311, 308
 “magic” EC-graphite chemistry, 311–313, 313, 622
 three electrochemical scenarios of, 314–317, 315, 316
- graphitic carbon, 264, 375, 606, 613, 692
- Grignard reagents, 662
- Grotthuss mechanism, 121–124, 122, 488, 681
- H *see* hydrogen
- H₃O⁺ *see* hydronium ion
- half-intercalation batteries, 304–305
- halides, 365–366, 473
- hard–soft acid–base (HSAB) model, 357
- Haven Ratio (H_R), 477, 480
- heat capacity, 384
- Helmholtz layers, 322–324, 749
- Helmholtz–Perrin Model, 150–153, 151, 155–156
- Henry’s law, 383
- HER *see* hydrogen evolution reactions
- n-hexane, 295, 341
- Hg *see* mercury
- highest occupied molecular orbital (HOMO), 607, 608, 612, 615–619, 632, 651–654
 energy levels, 690
- Hittorf approach
 disadvantages of, 507
 modified, 518–520
- Hittorf–Tubandt approach, 504–508, 505, 518, 543–544, 546
- HOAc *see* acetic acid
- HOMO *see* highest occupied molecular orbital
- host–guest chemistry, 275
- HSAB model *see* hard–soft acid–base model
- hydration, 18, 23
- hydrodynamics, 99
- hydroelectric turbines, 766
- hydrofluorocarbons, 729
- hydrogen (H), 118
 atom, 122
 bonding, 123, 275
 fuel cell, 231–232, 232, 444
 gas, 231, 678
- hydrogen evolution reactions (HER), 118, 118, 214
- hydronium ion (H₃O⁺), 123
- hydrophobic layer, 724
- ideal
 mixing, 389, 392, 392–393
 state, 443–444
- IHP *see* inner-Helmholtz plane
- imidazolium ionic liquid, 541–542
- impedance, 446, 446, 450, 452–453, 456–463
- In *see* indium
- in bulk electrolytes: ionics, 11–28
 activity coefficients, 23–25
 dielectric constant, 13–17
 effect of ions and
 unexpected application, 20–23
 ionic strength, 26–28
 Kohlrausch’s Law on Non-linear-ity, 25–26
 Lewis–Randall Empirical Law, 26–28
 solvation sheath, 17–20
 solvent molecules: dipole and
 dielectric medium, 12–13
- indium (In), 333
- inductance, 452
- inductor, 449
- inequilibria-equilibria process, 66
- initial
 condition, 78
 current, 523
 instant, at the, 554–555
- inner-Helmholtz plane (IHP), 157–160, 162, 165, 168
- inorganic
 salts, 418
 solid electrolytes, 9–10, 127–129, 128
- in situ/operando* characterisation techniques, 620
- instantaneous plane source, 74, 75, 76, 81
- insulation, electronic, 375
- intensive quantity, 257

- intercalation
chemistry, 332
vs. conversion reaction, 273–277, 274
hosts for Na^+/K^+ , 660–662
 Li^+ , 188–190, 189, 694
- interfaces, 4, 131–191
contemporary illustrations of
interfacial structure, 162–163
electric double layer, 135–141
free of any charge, 148
interface *vs.* interphase, 210–212
polarisable and non-polarisable,
139–141, 167
quantifying, 180–181
structure of an electrified
interface, 150–163
when charge transfers across
an interface: electrodics,
163–190
why interface matters, 131–134
- interfaces: properties, 592–601
charge transfer for 2D interfaces,
612–613
concentration profiles in the bulk
region, 596–599
concentration profiles in the
interfacial region, 599–601
interface defined, 592–595
ionic fluxes in bulk and across an
interface, 595–596
- interfacial
charge-transfer processes, 212,
707
region, 596, 599–601
resistance, 167
structure, 687–690, 688
contemporary illustrations
of, 162–163
tension, 146, 148–150, 152
- internal short-circuit, 362
- interphase formation, 160, 613–619
electrolyte additives, 618–619
instantaneous and indiscriminating, 614, 614–616
mechanism of: solvation–
interphase correlation,
686–708
preferential solvation leads to
preferential reduction,
698–702
- proto-interphase and interphase
in “anode-free” lithium-metal
cell, 617–618
- stepwise and discriminating,
616–617
- transient state before: co-intercalation, 693–698, 695
- interphase-free, 350–352, 608–609, 611
- interphases, 4, 209–222
artificial, 746–748
correlation between electrochemical
stability window and interphases,
220–221
destruction–reformation cycle of,
337
dynamic, 748–750
electrochemical stability window,
212–219
forming protective, 376
function of, 218–219
interface *vs.* interphase, 210–212,
211
- interphases, chemistry of, 620–686, 768
beyond lithium-ion chemistries,
in, 657–665
how interphases evolve, 685–686
how working ions travel across
interphases, 680–685
interphasial chemistries brought
by additives, 651–657
interphasial components under
debate, 675–679
lithium-ion batteries, in, 621–644
lithium–metal batteries, in,
644–651
stability of interphasial
ingredients, 665–675
chemical stability of
interphases, 671–673
electrochemical stability of
interphases, 673–675
solubility of interphasial
components, 666–667
thermal stability of interphases, 667–671
- interphases: properties, 602–713
charge transfer in presence of 2D
interfaces and 3D interphases,
612–613
chemistry of interphases,
620–686
good interphase, 609–612
interphase created by electrode–electrolyte mismatch in
electron energy levels,
605–609
interphase defined, 603–605, 604

- two distinct manners of forming interphases, 613–619
- interphasial chemistry, 690–708
altering the ion solvation sheath structure, 702–705
co-intercalation, 693–698
interphase formation in a lithium-ion battery: a special case, 692–698
preferential solvation leads to preferential reduction, 698–702
tailoring in multivalent ion electrolytes, 705–708
- interphasial components under debate, 675–679
over fluorides, 676–677
over Li_2CO_3 , 675–676
over LiH, 677–679
- intrinsic pseudo-capacitance, 279
- intrinsic resistance, 447
- ion conductivity, 439–489
AC (alternating current) techniques, 444–466
electrolyte engineering for battery applications, 472–477
- interphasial ingredients, of, 680, 680
- ionicity, 477
- parameters, 469–472
- practical battery electrolytes, for, 466–472
- ion diffusion coefficient (D_i), 439
- ion hopping, 129
- ionic cloud, 29–31, 582
spatial distribution of, 31–35
Boltzmann equation, 33–35
Poisson equation, 31–33
- total excess charge in, 40–41
- ionic density
limiting factors, 241–244, 243
- ionic electrolytes, 480–481
- ionicity, 102, 477
classification of electrolytes, 480–482
modifications to Walden analysis, 482–489
Walden Analysis and Haven Ratio, 477–480
- ionic liquids, 8–9, 25, 124–129, 357
inorganic solid electrolytes, 127–129
molten salts, 125–127, 480
- ionic radii
correction of, 482–484
 Li^+ , 350, 350
- ionics, 10–28, 373–374
activity coefficients, ionic strength and few empirical laws, 23–28
dielectric constant, 13–17
effect of ions and unexpected application, 20–23
- non-aqueous electrolytes, in, 116–121
- non-ideal electrolytes, for, 548–567
ambipolar diffusion: salt diffusion, 563–565
initial instant, at the, 554–555
multicomponent electrolytes, 565–567
Onsager transport coefficients, 559–563
steady state, at the, 555–559
- solvation sheath, 17–20
- solvent molecules: dipole and dielectric medium, 12–13
- ionic strength, 26–28
- ionic transference
reference frame for, 543–547, 545
- ion mobility (μ_i), 474
- ionogens, 7–8, 400
- ionophores, 7, 17, 400
- ion(s), 3–4
hydrated, 19
- pair formation, 53–56, 55
size parameter, 52, 52
solvated, 19
- ion solvation, 400–434
anion solvation, 429–432
Bernal–Fowler Three-Layer Model, 400–401
four basic questions, 401–402
- ion solvation in the concentrated regime, 418–420
- nano-heterogeneity in extended liquid structures, 422–424, 424
- preferential solvation, 408–414
quantifying solvation power, 414–418
- salt solvate electrolytes, 424–425
- solvating site, 402–405
- solvation disproportionation, 420–422
- solvation number, 405–408
- solvation sheaths, solvation cages and solvation sites, 426–429

- ion–solvent interactions, 11, 57–61, 58
 ion transference number *see*
 transference number
 ion transport in electrolytes, 65–130
 diffusion, 65–82
 migration (conduction), 89–129
 mobility (μ), 87–90
 relationships among D , σ , v_d and
 μ , 90–92
 requirements, 375
 ion transport number *see* transport
 number
 ion transport: properties, 439–591
 ion conductivity, 440–489
 ionics for non-ideal electrolytes,
 548–567
 mechanism of interphase
 formation: solvation–inter-
 phase correlation, 686–708
 Newman's Ion Transport Theory,
 568–589
 speciation, 489–547
 iron (Fe), 365, 664
 irreversibility, 298–299, 685
 circumventing and safety hazards,
 304–331
 irreversible reactions, 219, 221
 junctional potential, 512, 514, 517
- K *see* potassium
 K_2CrO_4 , 509
 KCl *see* potassium chloride
 kinetically reversible
 electrochemical reactions, 218
 kinetics, 599
 charge transfer across interface,
 of, 168–171, 169
 kinetic stability, 218, 295
 non-aqueous and aprotic
 solvents with lithium metal,
 295, 296–297
 Kirchhoff's law, 137
 Kohlrausch, Friedrich, 439
 Kohlrausch constant, 25
 Kohlrausch empirical law, 45–46,
 105, 110
 Kohlrausch independent ion migration
 law, 26, 86, 509
 Kohlrausch's law on non-linearity, 11,
 25–26, 28, 86
- laboratory reference frame, 546
 lactams, 357
- Laplace transformation, 77–78
 LEC *see* lithium ethyl carbonate
 $LEDC$ *see* lithium ethylene dicarbonate
 $LEMC$ *see* lithium ethylene
 monocarbonate
 Lennard–Jones potential, 754, 755
 Lewis acid, 414, 415, 435, 671
 Lewis basicity, 329
 Lewis empirical law, 27
 Lewis–Randall empirical law, 11, 26–28,
 41–45
 $LGPS$ *see* $Li_{10}GeP_2S_{12}$
 Li *see* lithium
 Li^+
 conduction across interphases,
 681–685, 682
 four basic questions, 401–402
 high conductivity, 611
 intercalation, 188–190, 189,
 309–312, 314–315, 367, 694
 ionic radii, 350, 350
 transference number, 538
- Li^0
 dead (*see* dead Li^0)
 dendritic (*see* dendritic Li^0)
 Li_2CO_3 *see* lithium carbonate
 Li_2O *see* lithium oxide
 Li_2O_2 *see* lithium peroxide
 Li_2OHX *see* lithium halide hydroxide
 Li_2S *see* lithium sulfide
 $Li_2S_2O_4$, 645
 Li_2SO_4 *see* lithium sulfate
 Li_3N *see* lithium nitride
 $Li_4Ti_5O_{12}$ *see* lithium titanate
 $Li_7La_3Zr_2O_{12}$ (LLZO), 739–741
 $Li_7P_3S_{11}$ (LPS), 742–743
 $Li_{10}GeP_2S_{12}$ (LGPS), 742–743
 Li/Air chemistry
 CEIs in, 658–660
 $LiAlCl_4$, 620
 $Li(AN)_6$, 406
 $LiAsF_6$, 716
 $LiBF_4$, 481, 671
 $LiBOB$ *see* lithium bis(oxalato)borate
 LiC_6 , 306–307, 309–310, 313, 616, 703
 $LiCF_3SO_3$ *see* lithium triflate
 Li/CF_x , 602
 $LiCl$ *see* lithium chloride
 $LiClO_4$ *see* lithium perchlorate
 $LiCoO_2$ *see* lithium cobalt oxide
 $LiCoPO_4$ *see* lithium cobalt phosphate
 $LiDFOB$ *see* lithium difluoro(oxalato)
 borate
 $Li(EC)_4$, 406
 LiF *see* lithium fluoride

- LiFePO₄** *see* lithium iron phosphate
LiFSI, 339, 364, 481
LiH *see* lithium hydride
LiHCO₃, 646–647, 672–673, 675
LiI *see* lithium iodide
limiting current, 202–203
LiMn₂O₄, 359, 636, 639
LiMnO₂, 602
LiN₃ *See* lithium azide
LiNbO₃ (LNO), 743
linear sweep voltammetry (LSV), 283
linking ionics with electrodeics,
192–208
 ambipolar ionic transport at an
 interface, 203–206
 further caution when applying
 diffusion-originated equations,
 206–208
 galvanostatic and potentiostatic,
 196–200
 limiting current, 202–203
 Nernst diffusion layer, 200–202
 steady state, 194–196
LiNO₃ *see* lithium nitrate
LiO₂ *see* lithium superoxide
Li/O₂ chemistry
 CEIs in, 658–660
LiOH *see* lithium hydroxide
LiPF₆ *see* lithium hexafluorophosphate
LiPO₂F₂ *see* lithium difluorophosphate
LiPON *see* lithium phosphorus
 oxynitride
Lippmann electrometer, 143
Lippmann equation, 148, 151
liquefied gas, 729–731
liquid chromatography, 437
liquid-inorganic interfacing, 735–736
liquid range, 377, 379
liquid secondary ion mass spectrometry
 (LSIMS), 410, 430, 751
liquid structures, 62–64
 nano-heterogeneity in extended,
 422–424, 424, 431
liquidus line, 377, 381, 381–383
LISICON *see* lithium superionic
 conductor
Li/SOCl₂, 602
LiTFSI *see* lithium bis(trifluoromethane-
 sulfonyl)imide
lithiation, 314, 315, 337
lithiophobicity, 740
lithium (Li)
 anode, 257, 261, 361, 363–364
 renaissance, 341
 reserves, 292
lithium/air batteries, 353, 355, 359
lithium alkylcarbonate, 339
lithium azide (LiN₃), 345
lithium bis(oxalato)borate (LiBOB), 339,
 481
lithium bis(trifluoromethanesulfonyl)
 imide (LiTFSI), 27, 64, 213, 215, 339,
 364, 420
 after 2010, modified version
 emerged as replacement for
 LiPF₆, 329–330
 dissolved in water, 566
 ionicity, 481
lithium carbonate (Li₂CO₃), 340, 356,
 615, 628, 634, 637, 646–647
 interphases, 672–673, 675–676,
 683–684
lithium chloride (LiCl), 418, 510, 620,
 645
lithium cobalt oxide (LiCoO₂), 306, 320,
 359, 621, 632, 635–637, 655
lithium cobalt phosphate (LiCoPO₄),
 607, 638
lithium difluoro(oxalato)borate
 (LiDFOB), 339
lithium difluorophosphate (LiPO₂F₂),
 438
lithium ethyl carbonate (LEC), 626
lithium ethylene dicarbonate (LEDC),
 410, 625, 666–667, 674
lithium ethylene monocarbonate
 (LEMC), 628, 667, 673
lithium fluoride (LiF), 340, 631, 646,
 656, 676–677, 683–684, 703
lithium halide hydroxide (Li₂OHX),
 742
lithium hexafluorophosphate (LiPF₆),
 124, 319, 329–330, 665, 671
 after 1990s adopted by lithium-ion
 battery industry, 329
 ionicity, 481
lithium hydride (LiH), 677–679
lithium hydroxide (LiOH), 340, 615
lithium iodide (LiI), 515, 743
lithium-ion batteries
 capacity, 269
 chemistry of interphases in,
 621–644
 on the anode: SEI, 621–622
 bias in studies towards SEIs,
 632–633
 on the cathode: CEI,
 632–639
 comparison of SEIs and
 CEIs, 641–644

- lithium-ion batteries (*continued*)
 cross-talk between anode and cathode, 639–641
 electrochemical rearrangement into permanent CEI, 636–639
 native passivation, spontaneous reaction and preferred adsorption, 633–636
 other SEI ingredients, 628–632
 semicarbonates, 622–628
 electrochemical stability limits of electrolytes, 206–207
 ethylene carbonate solvent used in, 12
 fire and explosion caused by, 302–303
 first-generation, 714
 interphase formation in: a special case, 692–698
 interphase-free, 608–609
 invention of, 223, 276–277
 Li⁺ intercalation, 188–190, 189
 most popular electrochemical device, 331, 374
 transport number, in, 95
- lithium-ion chemistries, 306–331
 birth of, 306–307
 EC *versus* PC, 317–319
 evolution of non-aqueous electrolytes, 319–330
 graphite as Li⁺ host, 307–311
 “magic” EC-graphite chemistry, 311–313
 modern lithium-ion battery, 330–331
 three electrochemical scenarios of graphite, 314–317
- lithium iron phosphate (LiFePO₄), 266, 367, 608, 621, 632, 732
- lithium metal, 340–346, 511
 capacity, of, 294, 349
 electrode potential, 293–294
 interphases formed in chemical process, 341
 kinetically stable non-aqueous and aprotic solvents with, 295, 296–297
 passivation layer, 602
- lithium-metal, lithium-ion and other batteries, 292–372
 circumventing irreversibility and safety hazards, 304–331
- emerging chemistries and electrolytes, 331–370
 anion intercalation chemistries, 367–370
 multivalent cation chemistries, 349–352
- lithium-ion chemistries, 306–331
- lithium-metal batteries, 294–304
 anode-free, 617–618
 chemistry of interphases, in, 644–651
 esters, 646–647
 ethers, 647–651
- dangerous morphology, 299–304, 341
 fire and explosion caused by, 302–304
- electrochemical stability limits of electrolytes, 206–207
 irreversibility, 298–299
 primary batteries, 602
- lithium methyl carbonate (LMC), 410, 626
- lithium nickel manganese cobalt oxide, 266
- lithium nitrate (LiNO₃), 345, 363–364, 418
- lithium nitride (Li₃N), 345–346, 615, 741
- lithium oxide (Li₂O), 340, 615, 646, 672
- lithium/oxygen batteries, 261–262, 353, 355–356, 358–359
 rechargeable, 356–357
- lithium perchlorate (LiClO₄), 124, 517
- lithium peroxide (Li₂O₂), 658–659
- lithium phosphorus oxynitride (LiPON), 129
- lithium propylene dicarbonate (LPDC), 625–626
- lithium salts, 322–324, 325–326, 328, 729
- lithium sulfate (Li₂SO₄), 645
- lithium sulfide (Li₂S), 361–362
- lithium/sulfur chemistry, 365
- lithium superionic conductor (LISICON), 128, 742
- lithium superoxide (LiO₂), 658–659
- lithium/thionyl chloride battery, 380
- lithium titanate (Li₄Ti₅O₁₂), 608, 621, 743
- Lithium Triangle, 292, 293
- lithium triflate (LiCF₃SO₃), 517

- LiTiS₂, 305
living fossil, 694
LLZO *see* Li₂La₃Zr₂O₁₂
LMC *see* lithium methyl carbonate
LNO *see* LiNbO₃
Lodge–Mason approaches, 508,
508–510, 544, 546
lowest unoccupied molecular orbital
(LUMO), 607, 608, 612, 615–619,
632, 651–654
 energy levels, 690
LPDC *see* lithium propylene dicarbonate
LPS *see* Li₇P₃S₁₁
LSIMS *see* liquid secondary ion mass
spectrometry
LSV *see* linear sweep voltammetry
LUMO *see* lowest unoccupied molecular
orbital
- machine learning (ML), 715, 752
macroscopically, 732
magnesium (Mg), 662–663
MALDI-MS *see* matrix-assisted laser
desorption/ionisation mass
spectrometry
manganese (Mn), 278
mass transfer, 193, 194
mass-transfer flux, 195
mass-transport limit, 74
Materials Balance Statement, 569–570,
572
matrix-assisted laser desorption/ionisa-
tion mass spectrometry (MALDI-MS),
630
maximum theoretical specific energy
(MTSE), 265–266
MC simulations *see* Monte Carlo
simulations
MD *see* molecular dynamics
mean square distance, 68, 71
melting point, 24, 124
mercury (Hg), 143
mercury electrode
 surface tension on, 143–145, 144
mercury/electrolyte
 interfacial tension, 146
mercury/electrolyte interface
 thermodynamics of, 145–150
metal halides, 480
metal–organic frameworks (MOFs), 733
metal oxides, 365–366
Mg *see* magnesium
Mg²⁺, 350, 350–351
MgCl₂, 26
MgSO₄, 95
microscopically, 732
migration (conduction), 89–129, 374,
499, 526–527
 conductivities, 83–87
 Einstein relation, 92–94
 Grotthuss Mechanism, 121–124,
 122
 ionic liquids, 124–129
 ionics in non-aqueous electrolytes,
 116–121
 Nernst–Einstein relation, 98–99
 Nernst–Planck Flux equation,
 102–105
 Onsager’s Laws, 105–116
 Stokes–Einstein relation, 99–100
 unexpected use of, 100–101
 transport number (t_+ and t_-),
 95–98
 Walden’s Rule, 101–102
 without any, 97
migration flux, 195
ML *see* machine learning
Mn *see* manganese
MnO₂, 278
mobility (μ), 87–92, 90, 547
MOFs *see* metal–organic frameworks
molar conductivity (A_m), 86, 126,
487–488, 490, 524
 limiting, 509
molecular dynamics (MD), 752
 DFT-based simulations, 756–757
 simulations, 242, 403, 422, 561,
 567, 715, 752–757
 prediction of properties and
 performances, 757–758
Moli Energy, 304–305, 321
molten salts, 8, 9, 25, 124–127, 400, 480
molybdenum sulfide (MoS₂), 321
monofluoroethylene carbonate (FEC),
654, 656, 660
monopolar, 324, 401
monopole, 12, 13
Monte Carlo (MC) simulations, 753, 754,
756
morphology, 611, 685
MoS₂ *see* molybdenum sulfide
MTSE *see* maximum theoretical specific
energy
multi-body problem, 30, 30
multinuclear NMR spectroscopy, 430
multivalent cation chemistries,
349–352
- Na *see* sodium
Na₂SO₄, 508

- NaBr, 156
 NaCl *see* sodium chloride
 NaF, 156
 Nafion, 231–234, 232
 NaI, 156
 nano-confinement, 744–745, 745
 nano-confining electrolytes, 744–746
 nano-heterogeneity, 727
 extended liquid structures, in,
 422–424, 431
 nanometers, 400
 nanoparticles, 735
 nanostructures, 338, 733
 NaOAc *see* sodium acetate
 NASICON *see* sodium superionic
 conductor
 native passivation, 633–634
 Nb *see* niobium
 NEB calculations *see* nudged elastic
 band calculations
 negative termini, 324
 Nernst diffusion layer, 200–202
 Nernst–Einstein equation, 473, 477,
 488, 492, 524, 549, 719
 Nernst–Einstein molar conductivity,
 479, 483
 Nernst–Einstein relation, 98–99,
 125–126, 490
 Nernst equation, 177–178, 514, 556
 lessons learned from, 254–255
 thermodynamics behind
 batteries, 249–254, 343
 Nernst–Planck Flux equation, 102–105
 new concepts and tools, 714–764
 artificial interphases, 746–748
 computer simulations, 751–759
 dynamic interphases, 748–750
 liquefied gas and frozen ice,
 729–731
 nano-confining electrolytes,
 744–746
 new characterisation techniques,
 750–751
 solidifying electrolytes, 731–744
 super-concentrating: unusual
 properties, 715–729
 Newman number, 586–587
 Newman's formalism, 584–588
 Newman's Ion Transport Theory,
 568–589
 Concentrated Solution Theory,
 575–588
 limitations of, 588–589
 Current Statement, 569
 Electroneutrality Statement,
 569–571, 573, 582, 592, 595
 Flux Statement, 568–569, 572,
 583–584, 595
 Materials Balance Statement,
 569–570, 572
 Newman theory, 373
 Newton's cradle, 122
 Newton's second law, 88, 755–756
 Newton's third law, 549
 Nextlion, 336
 Ni *see* nickel
 nickel (Ni), 664
 nickel-manganese-cobalt mixed oxides
 (NMC), 748
 niobium (Nb), 740
 nitriles, 12, 357
 NMC *see* nickel-manganese-cobalt
 mixed oxides
 NMR spectroscopy *see* nuclear
 magnetic resonance (NMR)
 spectroscopy
 non-aqueous electrolytes
 evolution of, 244, 319–330
 lower ion conductivity, 328
 salts, 322–330
 solvents, 320–322, 401–402
 non-Faradaic process, 240, 290
 non-ideal mixing, 391–392, 392
 non-polarisable interfaces, 139–141,
 180–181
 non-solvent, 728
 Novoselov, Konstantin, 309
 nuclear magnetic resonance (NMR)
 spectroscopy, 20, 403, 415–416, 439,
 484–489, 699
 correction *via*, 484–489
 liquid and solid, 750–751
 nudged elastic band (NEB) calculations,
 759
 Nyquist plot, 446

 O₂ *see* oxygen
 OER *see* oxygen evolution reactions
 Ohmic behaviour, 178
 Ohm's law, 85, 180, 440, 570
 OHP *see* outer-Helmholtz plane
 oil-drilling platforms, 224
 Onsager conductivity coefficients, 560,
 561, 563
 Onsager formalism, 548–549, 561, 577
 Onsager's Laws, 105–116
 ambipolar ionic movement,
 112–116

- Debye–Hückel–Onsager equation, 109–111
electrophoresis force, 108–109
relaxation force, 106–108
Onsager transport coefficients, 548–549, 558–563, 565–566, 575
order parameter, 429
osmotic pressure, 4–5
Ostwald, Wilhelm, 4–5, 24, 439
outer-Helmholtz plane (OHP), 157–162, 168, 181–182, 192, 194, 196–200
outlook, 765–768
overpotential (η), 175–176, 188, 212–214, 220
oxalates, 322, 629
oxidation, 117, 164, 171, 212, 225, 643, 676
oxidative decomposition, 607
oxidative pathway, 641
oxides, 128, 473, 669
oxygen (O_2), 353–360
atom, 122
oxygen evolution reactions (OER), 118, 118
- parasitic reactions, 686
passivation, 380
native, 633–634
PC *see* propylene carbonate
PC-DME solvent mixture, 474–475
pentafluorophosphorus (PF_5), 322, 671
PEO *see* poly(ethylene oxide)
Periodic Table, 294, 346, 353, 360
permittivity, 14
perovskites, 128, 741
Perrin, Jean Baptiste, 101
petroleum, 766
petroleum coke, 347
 PF_5 *see* pentafluorophosphorus
Pfeffer, Wilhelm, 4–5
pfg-NMR *see* pulsed field gradient NMR spectroscopy
PGSE-NMR *see* pulsed field gradient spin-echo
phase diagrams of liquid electrolytes, 379–399
experimental mapping of pseudo-binary phase diagrams, 384–388
phase diagram of pseudo-binary non-aqueous electrolyte, 382–384
thermodynamic calculation of higher order phase diagrams, 388–399
phase stability, 376
phosphates, 128
phosphoryl fluoride (POF_3), 664
phosphoryl trifluoride (POF_3), 322
physical properties, 379
plating, 299
platinum (Pt), 278
 POF_3 *see* phosphoryl fluoride; phosphoryl trifluoride
point charges, 30, 46, 47, 50, 324, 418
point of zero charge, 137, 158, 162
Poisson–Boltzmann equation, 36–40, 77
Poisson equation, 31–33, 595, 599
polarisable interfaces, 139–141, 180–181
polarisation, 248, 519, 687, 690
concentration, 496
DC polarisation, 440–441, 442, 443, 494
voltage, 241
polarographic analysis, 143
polar solvents, 400–402
polyelectrolyte, 232
poly(ethylene oxide), 124
poly(ethylene oxide) (PEO), 427
polyfluorinated ethers, 650–651
polyglymes, 427
polymer binders, 338
polymer electrolytes, 124, 429, 732–735
polymeric, 428
polymeric/oligomeric species, 667
polymer-in-salt concept, 425
polymerisation, 631
polysulfides, 361, 361–364
positron, 165
potassium (K)
- based batteries, 346
intercalation hosts for Na^+/K^+ , 660–662
metals, 346–349
SEIs on Na^0/K^0 electrodes, 660–662
potassium chloride (KCl), 478, 489, 509, 514
potential distribution, 529–532, 530
potential drop, 529–531, 530, 556
potentiodynamic conditions, 283, 287, 290
potentiometry, 200
potentiostatic conditions, 199–200, 283

- Pourbaix diagram, 118, 118
 power (*P*), 272–273
 power generation devices, 226
 preferred adsorption, 633, 635, 635–636, 636
 pressure, 394, 583, 588
 properties of electrolytes, interfaces and interphases, 373–378
 propylene carbonate (PC), 716
 vs. ethylene carbonate (EC), 317–319, 318
 proto-interphase, 617–618
 proton
 abnormal transport, 121–124
 protrusions, 300, 300, 302
 pseudo-binary electrolyte system, 383
 pseudo-binary system, 383
 pseudo-capacitance, 277
 pseudo-capacitors, 277–279
 pseudo-concentrated electrolytes, 416
 Pt *see* platinum
 pulsed field gradient NMR spectroscopy (pfg-NMR), 536–537, 727
 pulsed field gradient spin-echo (PGSE-NMR), 484–487
 pulse of instantaneous flux (J_{pulse}), 81
 pulverisation, 338
 pyrrolidinium (Py^+), 566
- QM *see* quantum mechanics
 quantum mechanics (QM), 123, 715, 752, 757
 quasi-equilibrium, 112
 quasi-ionic liquid systems, 424
 quasi-neutrality, 596
 quasi-two-dimensional reactions, 278
- R *see* resistor
 Raman spectroscopy, 20, 404, 430
 Randles–Sevcik equation, 288
 random ionic movement, 87, 87
 random walk of ions, 66–69, 71, 87, 100
 Raoult's law, 383
 rate-determining step (rds), 192–194
 RC networks, 449
 rds *see* rate-determining step
 reaction quotient, 254
 rechargeability, 295, 298–299
 rechargeable batteries, 212, 226–227, 245, 375, 602
 Coulombic and energy efficiencies, 266–268
 lithium-metal *vs.* lithium-ion batteries, 299
- reciprocity, 549
 redox flow batteries, 134
 redox reaction, 225, 254
 reduction, 117, 164, 212, 225, 367, 624–625, 659
 preferences for esters and ethers, 648, 648–649
 preferential, 698–702
 reduction potentials, 343–344, 344, 350, 350, 354
 reductive decomposition, 607
 reductive pathway, 641
 reference frame, 578
 external, 546
 internal, 544, 546
 ionic transference, for, 543–547, 545
- regular solution model, 391
 relaxation
 field, 46
 force, 106–108
 resistance, 138, 465, 535
 resistor (R), 449–453
 pure, 447, 450
 reversibility, 298, 332, 685
 reversible cell reactions, 375, 377
 reversible hydrogen electrode (RHE), 139, 143
 reversible intercalation chemistry, 316–317
 Reynolds number (Re), 99
 RHE *see* reversible hydrogen electrode
 robotic laboratories, 752
 room-temperature ionic liquids, 8, 124, 400
 round trip energy efficiency, 267
 RuO₂, 278
 Russia
 lithium reserves, 292
 ruthenium, 278
 Rutherford, Ernest, 3
- Salar de Uyuni (salt lake of Uyuni), 292, 293
 salt(s), 4, 5, 7, 322–330
 bridge, 514–515
 concentration, 469–471
 profile at steady state, 524–527
 diffusion, 563–565
 coefficients, 115, 582–584
 solubility, 328
 solvate electrolytes, 424–425
- Sand equation, 198

- Sand's time (τ_{Sand}), 198–199, 301
Sb *see* antimony
 SbCl_5 *see* antimony pentachloride
scalar quantities, 92
secondary ion mass spectrometry (SIMS), 689
SEI *see* solid/electrolyte interphase
self-diffusion coefficients, 115, 439, 487, 567, 582, 680
self-discharge, 362
semi-blocking condition, 443, 497–498
semicarbonates, 339, 622–629, 637, 646, 667, 670–672
semiconductors, 224
semi-solids, 428, 732
SEs *see* solid electrolytes
SFG vibrational spectroscopy *see* sum frequency generation vibrational spectroscopy
SHE *see* standard hydrogen electrode
silicates (SiO_4), 480, 733
silicon (Si), 188, 190, 207
 anode, as, 336–338
 capacity, 270
 interphases formed in electrochemical process, 341
 lithium-ion batteries, 333–340
silver (Ag), 333
SIMS *see* secondary ion mass spectrometry
single-electron pathway, 623
single-ion electrolyte, 232
 SiO_2 *see* silicates
smartphones, 223
 SOCl_2 *see* thionyl chloride
sodium (Na)
 -based batteries, 346
 intercalation hosts for Na^+/K^+ , 660–662
 metals, 346–349
 SEIs on Na^0/K^0 electrodes, 660–662
sodium acetate (NaOAc), 510
sodium chloride (NaCl), 4, 7–8, 17, 95, 418
 aqueous solution of, 379, 381, 381
 dissolution, 17, 18, 24
 Lodge–Mason approach, 510
 solutions, 26, 30, 124, 156
 static stability, 435
sodium/sulfur battery, 380
sodium superionic conductor (NASICON), 128
soft–soft interaction, 358
solar energy, 765, 766
solid/electrolyte interphase (SEI), 219, 321, 603, 608, 667
 anode, on the, 621–622, 702
 comparison between SEIs and CEIs, 641–644
 electron energy levels, 606, 606
 Li^+ -conducting and electron-insulating, 603
 SEIs on metals with multivalent chemistries, 662–664
 SEIs on Na^0/K^0 electrodes, 660–662
 thickness of, 610, 611
solid electrolytes (SEs), 737
solidifying electrolytes, 731–744
 liquid-inorganic interfacing, 735–736
polymer electrolytes, 732–735
true solid electrolytes and their interfaces/interphases, 737–744
solid polymer electrolytes (SPEs), 8, 9, 124–125, 733–734
solid-state electrolytes (SSEs), 737–744
 antiperovskite-type SSEs, 741–742
 Garnet-type SSEs, 739–741
 sulfide-type SSEs, 742–744
solidus line, 377, 382
solubility, 611
 interphasial components, of, 666–667
 salt, 328
 zero, 393, 395
solutes, 10
solutions, 10
solvating sites, 127, 402–405, 403
solvation, 18, 648, 648–649
 cages, 404, 426, 426–429
 disproportionation, 420–422
 number, 19, 405–408
 preferential, 408–414, 412, 416, 476, 698–702
 sites, 426, 426–429
solvation–interphase correlation, 686–708
 interfacial structure, 687–690, 688
 interphasial chemistry, 690–708
solvation power
 quantifying, 414–418
 relative, 415, 417

- solvation sheath, 17–20, 416, 426, 426–429
 Li^+ , of, 312, 624–625
 stability, 19–20
 structure, 702–705
 three-layer model, 18–19, 19
- solvent composition, 470
- solvent-free electrolytes, 124–125
- solvent-in-salt electrolytes, 425, 717
- solvent molecules: dipole and dielectric medium, 12–13
- solvents, 320–322
 constraints of formulation, 320–321
- solvent-separated ion pairs (SSIPs), 418, 420
- solvus line, 377
- Sony, 307, 334, 336
- Sørensen–Jacobsen approach, 520–522, 546
- speciation, 489–547
 ideality of electrolytes: Einstein equations, 490–492
 ionic transference, 543–547
 ion transport number, 493–500
 in practical electrolytes: transport number vs. transference number, 501–504
- specific adsorption, 156
- SPEs *see* solid polymer electrolytes
- spontaneous reaction, 633–635
- SSEs *see* solid-state electrolytes
- SSIPs *see* solvent-separated ion pairs
- stability of interphasial ingredients, 665–675
 chemical stability of interphases, 671–673
 electrochemical stability of interphases, 673–675
 solubility of interphasial components, 666–667
 thermal stability of interphases, 667–671
- standard hydrogen electrode (SHE), 139, 147, 247
- standard potentials, 343
 electrochemical series, 335, 335
- static stability of electrolytes, 435–438
- steady state, 100, 194–196, 442
 cationic and anionic fluxes at, 527–529
 ionics for non-ideal electrolytes, at the, 555–559
 ionics for non-ideal electrolytes at, 555–559
- salt (and ion) concentration profiles at, 524–527
- steady-state current, 523
- Stefan–Maxwell equation, 550, 575
- Stefan–Maxwell formalism, 373, 548, 577
- Stefan–Maxwell transport coefficient, 550, 575, 580
- Stern model, 155–156, 181
- Stern thickness, 161
- stochastic approach, 69
- Stokes–Einstein equation, 491
- Stokes–Einstein relation, 99–100, 125, 473, 477
 unexpected use of, 100–101
- Stokes law, 484
- Stokes radii, 483, 484
- stripping, 299, 303, 303
- structures and shapes of common ions, 484, 485
- sub-ionic electrolytes, 480
- sucrose, 24
- sulfides, 128, 365–366, 473
- sulfide-type SSEs, 742–744
- sulfoxides, 357
- sulfur (S), 353, 360–365
 chemistry, 362
- sum frequency generation (SFG)
 vibrational spectroscopy, 635
- supercapacitor, 279
- super-concentrated electrolytes, 8, 22, 61, 63, 158, 418, 419
 advantages of, 728
 disadvantages of, 728
 properties, 728–729
 solution, 492
- super-concentrating: unusual properties, 690, 715–729
 esters could be cathodically stable, 720–721
 ethers could be anodically stable, 717–720
 exotic solvents could be electrochemically stable, 721–722
 locally concentrated electrolytes, aqueous-nonaqueous hybrid electrolytes, 727–729
 water could have a wide electrochemical stability window, 722–727
- super-concentration, 716
- super-ionic electrolytes, 480–481
- surface excess, 141–142
 quantification of, 143

- surface tension
low, 376–377
mercury electrode, on, 143–145,
144
- sustainability, 377
- symmetric parameter (β), 182–186, 185
- Ta *see* tantalum
- Tafel behaviour, 178–179, 220–221
- Tafel empirical law, 179, 184
- tantalum (Ta), 740
- TCO *See* tin-based composite oxide
- teleporting, 123
- teleports, 122
- temperature (T), 101, 383, 394, 395
constant, 583, 588
ion conductivity parameter,
470–471
- ternary phase diagram, 397, 398, 398
- tetraalkylammonium, 746
- tetraethylammonium bis(trifluoromethanesulfonyl)imide, 27
- tetrahydrofuran (THF), 647, 730
- TFSI *see* bis(trifluoromethanesulfonyl)
imide
- thermal
decomposition, 668–670
energy, 35
motion, 35
runaway, 670
stability of interphases, 667–671
- thermodynamic factor (ϕ), 553–554
- thermodynamic properties, 254, 514
- thermodynamics, 23, 24, 35
batteries, behind, 249–254
- thermodynamic stability, 602,
686–687
- THF *see* tetrahydrofuran
- thiocarbonates, 363
- thioethers, 363
- thionyl chloride (SOCl_2), 602, 620
- Thomson, Joseph John “J.J.”, 3
- three-dimensional Faradaic behaviour,
277
- threshold current density level, 212
- Ti *see* titanium
- tin, 333–340
- tin-based composite oxide (TCO),
334, 336
- tin oxide, 336
- TiO_2 *see* titanate
- TiS_2 *see* chalcogenides; titanium
disulfide
- titanate (TiO_2), 278
- titanium (Ti), 278
- titanium disulfide (TiS_2), 320, 321
- titration, 212
- toluene, 341
- topotactic, 275
- toxicity, 349
- TPP *see* triphenyl phosphate
- transesterification reactions, 435,
437–438
- transference number (T_+ or T)
cationic, 532–537, 541
few classical approaches to, 504
Armand approach: electrochemical concentration cell, 510–518
- Bruce–Vincent approach:
combining AC and DC techniques, 523–536
- electrophoretic NMR spectroscopy, 537,
540–543
- Hittorf–Tubandt approach,
504–508
- Lodge–Mason approaches,
508–510
- modified Hittorf approach:
perturbed electrochemical concentration cell,
518–520
- pulsed field gradient NMR spectroscopy, 536–537
- Sørensen–Jacobsen approach: AC impedance spectra, 520–522
- Li^+ , 538
- transference number *vs.* transport number, 501–504
- transition metal oxides, 320, 375, 633
- transport number (t_+ or t), 95–98, 96,
97, 439, 489
real meaning of, 493–500
transport number vs. transference number, 501–504
- triphenyl phosphate (TPP), 339
- tris(pentafluorophenyl)borane, 358
- tris(perfluorobutyl)amine, 357
- two-dimensional non-Faradaic capacitance behaviour, 277
- ultracapacitor, 279
- unit field, 89
- upfield, 403
- USA
lithium reserves, 292

- van der Waals force, 275, 324
 van't Hoff, Jacobus Henricus, 4
 van't Hoff's law, 383
 vapor pressure, 4, 24
 VC *see* vinyl carbonate; vinylene carbonate
 vector, 92
 velocity, 504, 547
 vinyl carbonate (VC), 654–656
 vinylene carbonate (VC), 339, 438
 virtual chemical reaction, 257
 viscosity, 99, 101, 474
 Vogel–Tamman–Fulcher equation, 472
 Volta, Alessandro, 3, 223, 266, 273, 379
 voltage, 137, 138, 241, 248, 527
 battery, 212
 cell, 279–280, 293
 hysteresis, 267
 range, 212, 216
 upper limits for battery, 254–255
 window, 117
 voltaic pile, 3
 voltammetry, 200, 298
- Walden analysis
 modifications to, 482–489
 correction of ionic radii, 482–484
 correction *via* NMR spectroscopy, 484–489
- Walden Analysis, 477–480
 Walden plot, 478
 Walden's Rule, 101–102, 475, 477, 490
 Warburg element, 449, 454
 Warburg short element, 520
 water
 bulk, 21–23
 dielectric constant of, 16, 16
 electrochemical stability window, 722–727
 Greek element of universe, 6
 most universal solvent on Earth, 12, 13
 phase diagram of, 380, 380
 polar solvent molecule, 20, 20
 solvation sheath, 21–23
 water-in-bisalt electrolytes, 717
 water-in-salt electrolytes (WiSE), 27, 63, 421, 421–422, 425, 717, 726
 wave energy, 766
 *Web of Science*TM
 research articles on “battery” or “battery + electrolyte,” 765, 766
 wettability, 376
 Whittingham, Michael Stanley, 277, 305, 307, 320, 331
 wind energy, 766
 WiSE *see* water-in-salt electrolytes
 working ions, 493, 497, 574, 611, 680–685
- XANES spectra *see* X-ray absorption near-edge structure spectra
 XPS *see* X-ray photoelectron spectroscopy
 X-ray absorption near-edge structure (XANES) spectra, 639
 X-ray diffraction (XRD), 7, 321, 348, 679, 696–697
 X-ray photoelectron spectroscopy (XPS), 630
 X-ray scattering techniques, 20
 XRD *see* X-ray diffraction
- Yoshino, Akira, 277, 307, 331
- zinc (Zn), 246, 256, 257
 zinc batteries, 705–708, 706
 zinc-metal anode (Zn^0), 706–708
 zinc metal powder (Zn^0), 132
 Zn *see* zinc
 Zn^{2+} , 350, 351
 $ZnCl_2$, 480
 ZnF_2 , 480, 663
 $Zn(TFSI)_2$, 468, 472